Vol. 47 Nos. 1–4
December 1999

ISSN: 0263–8223

COMPOSITE STRUCTURES

EDITOR: I.H. MARSHALL

Special Issue

Tenth International Conference on Composite Structures

Guest Editors

I. H. Marshall & R. Jones

ELSEVIER

http://www.elsevier.com/locate/compstruct

COMPOSITE STRUCTURES

The past few decades have seen outstanding advances in the use of composite materials in structural applications. There can be little doubt that, within engineering circles, composites have revolutionised traditional design concepts and made possible an unparalleled range of new exciting possibilities as viable materials of construction. *Composite Structures*, an International Journal, disseminates knowledge between users, manufacturers, designers and researchers involved in structures or structural components manufactured using composite materials.

The journal publishes papers which contribute to knowledge in the use of composite materials in engineering structures. Papers may be on design, research and development studies, experimental investigations, theoretical analyses and fabrication techniques relevant to the application of composites in load-bearing components for assemblies. These could range from individual components such as plates and shells to complete composite structures.

Editor

PROFESSOR I. H. MARSHALL

Monash University, Department of Mechanical Engineering, Clayton Campus, Clayton 3168, Australia,
Fax: +61 (0) 3 9905 1825,
E-mail: ian.marshall@eng.monash.edu.au

Administrative Address

For submission of papers: Professor I. H. Marshall, 36 Gogoside Road, Largs,
Ayrshire KA30 9LX, UK, Tel./Fax: +44 (0) 1475 687444
E-mail: ian_marshall@talk21.com

Editorial Board

S. Adali
University of Natal, Republic of South Africa

W. M. Banks
University of Strathclyde, Glasgow, UK

P. Beardmore
Ford Motor Co., Dearborn, Michigan, USA

W. Becker
University of Siegen, Siegen, Germany

C. W. Bert
University of Oklahoma, Norman, USA

H. F. Brinson
University of Houston, Texas, USA

A. R. Bunsell
Ecole Nationale Superieure des Mines de Paris, France

R. Byron Pipes
Rensselaer Polytechnic Institute, Troy, USA

Lien-Wen Chen
National Cheng Kung University, Tainan, Taiwan

A. H. Cardon
Free University of Brussels, Pleinlann, Belgium

P. Gaudenzi
Università di Roma La Sapienza, Rome, Italy

R. Jones
Monash University, Clayton, Victoria, Australia

D. G. Lee
KAIST, Taejon-shi, Korea

A. W. Leissa
The Ohio State University, Columbus, USA

F. L. Matthews
Imperial College, London, UK

A. Miravete
University of Zaragoza, Spain

K. Moser
Universität Innsbruck, Austria

Y. Narita
Hokkaido Institute of Technology,
Sapporo, Japan

A. N. Palazotto
Air Force Institute of Technology,
Dayton, Ohio, USA

G. J. Turvey
University of Lancaster, Bailrigg, UK

J. F. M. Wiggenraad
National Aerospace Laboratory, Emmeloord,
The Netherlands

Publishing Office

Elsevier Science Ltd, The Boulevard, Langford Lane, Kidlington, Oxford OX5 1GB, UK
[*Tel*: (+44) (01865) 843730; *Fax*: (+44) (01865) 843969)]

Advertising information

Advertising orders and enquiries can be sent to: **Europe and ROW**: Rachel Leveson-Gower, Elsevier Science Ltd., Advertising Department, The Boulevard, Langford Lane, Kidlington, Oxford OX5 1GB, UK; phone: (+44) (1865) 843565; fax: (+44) (1865) 843976; e-mail: r.leveson-gower@elsevier.co.uk. **USA and Canada**: Elsevier Science Inc., Mr Tino DeCarlo, 655 Avenue of the Americas, New York, NY 10010-5107, USA; phone: (+1) (212) 633 3815; fax (+1) (212) 633 3820; e-mail: t.decarlo@elsevier.com. **Japan**. Elsevier Science K.K., Advertising Department, 9–15 Higashi-Azabu 1-chome, Minato-ku, Tokyo 106, Japan; phone (+81) (3) 5561-5033; fax: (+81) (3) 5561 5047.

Subscriptions

Publication information: *Composite Structures* (ISSN 0263-8223). For 2000, volumes 48–50 are scheduled for publication. Subscription prices are available upon request from the Publisher or from the Regional Sales Office nearest you or from this journal's website (http://www.elsevier.com/locate/compstruct). Further information is available on this journal and other Elsevier Science products through Elsevier's website: (http://www.elsevier.com). Subscriptions are accepted on a prepaid basis only and are entered on a calendar year basis. Issues are sent by standard mail (surface within Europe, air delivery outside Europe). Priority rates are available upon request. Claims for missing issues should be made within six months of the date of dispatch.

Orders, claims, and product enquiries: please contact the Customer Support Department at the Regional Sales Office nearest you:
New York: Elsevier Science, PO Box 945, New York, NY 10159-0945, USA; phone (+1) (212) 633 3730 [toll free number for North American customers: 1-888-4ES-INFO (437-4636)]; fax: (+1) (212) 633 3680; e-mail: usinfo-f@elsevier.com
Amsterdam: Elsevier Science, PO Box 211, 1000 AE Amsterdam, The Netherlands; phone: (+31) 20 4853757; fax: (+31) 20 4853432; e-mail: nlinfo-f@elsevier.nl
Tokyo: Elsevier Science K.K., 9–15 Higashi-Azabu 1-chome, Minato-ku, Tokyo 106, Japan; phone: (+81) (3) 5561 5033; fax: (+81) (3) 5561 5047; e-mail: info@elsevier.co.jp
Singapore: Elsevier Science, No. 1 Temasek Avenue, #17-01 Millenia Tower, Singapore 039192; phone: (+65) 434 3727; fax: (+65) 337 2230; e-mail: asiainfo@elsevier.com.sg
Rio de Janeiro: Elsevier Science: Rua Sete de Setembro 111/16 Andar, 20050-002 Centro, Rio de Janeiro - RJ, Brazil; phone: (+55) (21) 509 5340; fax: (+55) (21) 507 1991; e-mail: elsevier@campus.com.br [Note (Latin America): for orders, claims and help desk information, please contact the Regional Sales Office in New York as listed above]

Back Issues

Back issues of all previously published volumes are available direct from Elsevier Science Offices (Oxford and New York). Complete volumes and single issues can be purchased for 1995–1999. Earlier issues are available in high quality photo-duplicated copies as complete volumes only.

Periodicals postage paid at Rahway, New Jersey. *Composite Structures* (ISSN 0263–8223) is published (Monthly in January to December as three volumes per year, four issues per volume) by Elsevier Science Ltd., The Boulevard, Langford Lane, Kidlington, Oxford OX5 1GB, UK. The annual subscription in the USA is $2534.
Composite Structures is circulated by Mercury International Limited, 365 Blair Road, Avenel, NJ 07001, USA.
POSTMASTER: Please send address corrections to: *Composite Structures*, c/o Customer Services, Elsevier Science Inc., 655 Avenue of the Americas, New York, NY 10010, USA.

© 2000 Elsevier Science Ltd. All rights reserved

COMPOSITE STRUCTURES

VOL. 47 1999

Special Issue

Tenth International Conference on
Composite Structures

Guest Editors

I. H. Marshall & R. Jones

EDITOR
I. H. MARSHALL

Journal homepage: http://www.elsevier.com/locate/compstruct

ELSEVIER

20011130 018

AQ F02-02-0288

© 2000 Elsevier Science Ltd. All rights reserved.

This journal and the individual contributions contained in it are protected under copyright by Elsevier Science Ltd, and the following terms and conditions apply to their use:

Photocopying
Single photocopies of single articles may be made for personal use as allowed by national copyright laws. Permission of the publisher and payment of a fee is required for all other photocopying, including multiple or systematic copying, copying for advertising or promotional purposes, resale, and all forms of document delivery. Special rates are available for educational institutions that wish to make photocopies for non-profit educational classroom use.

Permissions may be sought directly from Elsevier Science Global Rights Department, PO Box 800, Oxford OX5 1DX, UK; phone (+44) 1865 843830, fax: (+44) 1865 853333, e-mail: permissions@elsevier.co.uk. You may also contact Global Rights directly through Elsevier's home page (http://www.elsevier.nl), by selecting 'Obtaining Permissions'.

In the USA, users may clear permissions and make payments through the Copyright Clearance Center, Inc., 222 Rosewood Drive, Danvers, MA 01923, USA; phone: (978) 7508400, fax: (978) 7504744, and in the UK through the Copyright Licensing Agency Rapid Clearance Service (CLARCS), 90 Tottenham Court Road, London W1P 0LP, UK; phone: (+44) 20 7631 5555; fax: (+44) 20 7631 5500. Other countries may have a local reprographic rights agency for payments.

Derivative Works
Subscribers may reproduce tables of contents or prepare lists of articles including abstracts for internal circulation within their institutions. Permission of the publisher is required for resale or distribution outside the institution.

Permission of the publisher is required for all other derivative works, including compilations and translations.

Electronic Storage
Permission of the publisher is required to store electronically any material contained in this journal, including any article or part of an article.

Except as outlined above, no part of this publication may be reproduced, stored in a retrieval system or transmitted in any form or by any means, electronic, mechanical, photocopying, recording or otherwise, without prior written permission of the publisher.

Address permissions requests to: Elsevier Science Global Rights Department, as the mail, fax and e-mail addresses noted above.

Notice
No responsibility is assumed by the Publisher for any injury and/or damage to persons or property as a matter of products liability, negligence or otherwise, or from any use or operation of any methods, products, instruction or ideas contained in the material herein. Because of rapid advances in the medical sciences, in particular, independent verification of diagnoses and drug dosages should be made.

Although all advertising material is expected to conform to ethical (medical) standards, inclusion in this publication does not constitute a guarantee or endorsement of the quality or value of such product or of the claims made of it by its manufacturer.

⊗ The paper used in this publication meets the requirements of ANSI/NISO Z39.48-1992 (Permanence of Paper).

Typeset in India by Scientific Publishing Services Ltd, Chennai
Printed by Nuffield Press, Abingdon, Oxon.

REPORT DOCUMENTATION PAGE

Form Approved OMB No. 0704-0188

Public reporting burden for this collection of information is estimated to average 1 hour per response, including the time for reviewing instructions, searching existing data sources, gathering and maintaining the data needed, and completing and reviewing the collection of information. Send comments regarding this burden estimate or any other aspect of this collection of information, including suggestions for reducing this burden to Washington Headquarters Services, Directorate for Information Operations and Reports, 1215 Jefferson Davis Highway, Suite 1204, Arlington, VA 22202-4302, and to the Office of Management and Budget, Paperwork Reduction Project (0704-0188), Washington, DC 20503.

1. AGENCY USE ONLY (Leave blank)	2. REPORT DATE	3. REPORT TYPE AND DATES COVERED
	December 1999	15-17 November 1999 Conference Proceedings - Final Report

4. TITLE AND SUBTITLE
International Conference on Composite Structures (10th) (ICCS/10) Held in Melbourne, Australia, 15-17 November 1999

5. FUNDING NUMBERS
F6256299M9104

6. AUTHOR(S)
I.H. Marshall and R. Jones, Editors

7. PERFORMING ORGANIZATION NAME(S) AND ADDRESS(ES)
Monash University
Department of Mechanical Engineering
Clayton 3168, VIC
Australia

8. PERFORMING ORGANIZATION REPORT NUMBER
ISSN: 0263-8223

9. SPONSORING/MONITORING AGENCY NAME(S) AND ADDRESS(ES)
US Department of the Air Force
Asian Office of Aerospace Research and Development (AOARD)
Unite 45002
APO AP 96337-5002

10. SPONSORING/MONITORING AGENCY REPORT NUMBER
CSP 98-20

11. SUPPLEMENTARY NOTES
Published in Composite Structures, Vol. 47 Nos. 1-4, December 1999. Published by Elsevier Science Ltd., The Boulevard, Langford Lane, Kidlington, Oxford OX5 1GB, UK. This work relates to a Department of Air Force contract/grant issued by the European Aerospace Office of Research and Development. The United States has a royalty free license throughout the world in all copyrightable material contained herein.

12a. DISTRIBUTION/AVAILABILITY STATEMENT
Approved for Public Release. U.S. Government Rights License. All other rights reserved by the copyright holder. (Code 1, 20)

12b. DISTRIBUTION CODE
A

13. ABSTRACT (Maximum 200 words)
See http://www.eng.monash.edu.au/iccs11/
This conference forms a natural extension from the previous ten International Conferences on Composite Structures (ICCS/1-10) held biennially since 1981. It is one of the longest running conferences on composites worldwide and continues to be the prime focus for structural aspects of composites. A wide spectrum of aspects of composite structures are addressed, ranging from precision fabrication techniques used in the space shuttle program to natural fiber composites used as building materials in developing countries, from automotive applications to prosthetic uses of composites, and so on. The common theme being the use of composites as structural materials. With this in mind the present series of international conferences was initiated to bring together Users, Manufacturers, Designers and Researchers in the field of composite structures, thereby promoting dissemination of knowledge between all sectors of this ever expanding technology. These proceedings include 49 articles.

14. SUBJECT TERMS	15. NUMBER OF PAGES
AOARD, Foreign reports, Conference proceedings, Composites, Structural materials..	16. PRICE CODE

17. SECURITY CLASSIFICATION OF REPORT	18. SECURITY CLASSIFICATION OF THIS PAGE	19. SECURITY CLASSIFICATION OF ABSTRACT	20. LIMITATION OF ABSTRACT
UNCLASSIFIED	UNCLASSIFIED	UNCLASSIFIED	UL

ELSEVIER

Composite Structures 47 (1999) iii–v

COMPOSITE STRUCTURES

www.elsevier.com/locate/compstruct

Contents

Special Issue: Tenth International Conference on Composite Structures
Guest Editors: I. H. Marshall & R. Jones

425 Editorial
I. H. MARSHALL (UK)

427 Foreword

429 Australian Composite Structures Society Composite Structures Award

431 Bonded composite repair of fatigue-cracked primary aircraft structure
A. BAKER (Australia)

445 Matrix dominated time dependent failure predictions in polymer matrix composites
H. F. BRINSON (USA)

457 Analysis and development of the angular twist type torque-meter
Y. D. CHEONG, J. W. KIM, S. H. OH & C. W. LEE (South Korea)

463 A simulation study on the thermal buckling behavior of laminated composite shells with embedded shape memory alloy (SMA) wires
H. J. LEE, J. J. LEE & J. S. HUH (South Korea)

471 A resin film infusion process for manufacture of advanced composite structures
B. QI, J. RAJU, T. KRUCKENBERG & R. STANNING (Australia)

477 Evaluation of elastic properties of 3-D (4-step) regular braided composites by a homogenisation method
C. ZUORONG, Z. DECHAO (People's Republic of China), M. LU (People's Republic of China, Australia) & L. YE (Australia)

483 An engineering approach for predicting residual strength of carbon/epoxy laminates after impact and hygrothermal cycling
B. QI & I. HERSZBERG (Australia)

491 Numerical investigation on thermal response of oil-heated tool for manufacture of composite products
Y. DING, W. K. CHIU & X. L. LIU (Australia)

497 Composite robot end effector for manipulating large LCD glass panels
J. H. OH, D. G. LEE & H. S. KIM (South Korea)

507 Composite heddle frame for high-speed looms
D. G. LEE, C. S. LEE, J. H. OH & H. S. JEON (South Korea)

519 Crack path selection in piezoelectric bimaterials
Q.-H. QIN & Y.-W. MAI (Australia)

525 Damage detection of CFRP laminates using electrical resistance measurement and neural network
D.-C. SEO & J.-J. LEE (South Korea)

531 Development of semianalytical axisymmetric shell models with embedded sensors and actuators
I. F. PINTO CORREIA, C. M. MOTA SOARES, C. A. MOTA SOARES (Portugal) & J. HERSKOVITS (Brazil)

543 Evaluation of durability and strength of stitched foam-cored sandwich structures
J. H. KIM, Y. S. LEE, B. J. PARK & D. H. KIM (South Korea)

551 Experimental and numerical study of the impact behavior of SMC plates
S.-M. LEE, J.-S. CHEON & Y.-T. IM (South Korea)

563 External failure pressure of a frangible laminated composite canister cover
T. Y. KAM, J. H. WU & W. T. WANG (Taiwan)

571 Flexure of pultruded GRP beams with semi-rigid end connections
G. J. TURVEY (UK)

581 Heat transfer and cure analysis for the pultrusion of a fiberglass-vinyl ester I beam
X. L. LIU & W. HILLIER (Australia)

589 Synthesis of in situ Al–TiB_2 composites using stir cast route
K. L. TEE, L. LU & M. O. LAI (Singapore)

595 Influence of SiC particles on mechanical properties of Mg based composite
B. W. CHUA, L. LU & M. O. LAI (Singapore)

603 Mesh design in finite element analysis of post-buckled delamination in composite laminates
T. E. TAY, F. SHEN, K. H. LEE (Singapore), A. SCAGLIONE & M. DI SCIUVA (Italy)

613 In situ synthesis of TiC composite for structural application
L. LÜ, M. O. LAI & J. L. YEO (Singapore)

619 On the dynamic response of metal matrix composite panels to uniform temperature loading
E. FELDMAN & R. GILAT (Israel)

625 Optimal design of piezolaminated structures
C. M. MOTA SOARES, C. A. MOTA SOARES & V. M. FRANCO CORREIA (Portugal)

635 Optimum in situ strength design of laminates under combined mechanical and thermal loads
J. WANG (People's Republic of China) & B. L. KARIHALOO (UK)

643 Post-fire mechanical properties of marine polymer composites
A. P. MOURITZ & Z. MATHYS (Australia)

655 Prediction of shrinkage and warpage in consideration of residual stress in integrated simulation of injection molding
D.-S. CHOI & Y.-T. IM (South Korea)

667 Resistance welding of carbon fibre reinforced thermoplastic composite using alternative heating element
M. HOU, M. YANG, A. BEEHAG, Y.-W. MAI & L. YE (Australia)

673 Stress analysis of adhesively-bonded lap joints
S.-C. HER (ROC)

679 The active buckling control of laminated composite beams with embedded shape memory alloy wires
S. CHOI, J. J. LEE, D. C. SEO & S. W. CHOI (South Korea)

687 The mechanical performance of 3D woven sandwich composites
M. K. BANNISTER, R. BRAEMAR & P. J. CROTHERS (Australia)

691 Application of thermodynamic calculation in the in-situ process of Al/TiB_2
N. L. YUE, L. LU & M. O. LAI (Singapore)

695 Thermal buckling and postbuckling analysis of a laminated composite beam with embedded SMA actuators
J. J. LEE & S. CHOI (South Korea)

705 Thermo-mechanical behaviour of shape memory alloy reinforced composite laminate (Ni–Ti/glass-fibre/epoxy)
Z. SU, H. MAI (People's Republic of China), M. LU (People's Republic of China, Australia) & L. YE (Australia)

711 Residual compressive strength of laminated plates with delamination
H. CHEN & X. SUN (People's Republic of China)

719 Design and evaluation of various section profiles for pultruded deck panels
L. H. GAN, L. YE & Y.-W. MAI (Australia)

727 On the mechanical behaviour of aging and recycled paper structures under cyclic humidity
S. DILLON, R. JONES & V. BUZZI (Australia)

737 Composite repairs to rib stiffened panels
T. TING, R. JONES, W. K. CHIU, I. H. MARSHALL (Australia) & J. M. GREER (USA)

745 Smart structure for composite repair
Y. L. KOH, N. RAJIC, W. K. CHIU & S. GALEA (Australia)

753 Impact resistance and tolerance of interleaved tape laminates
A. DUARTE, I. HERSZBERG & R. PATON (Australia)

759 Structural integrity analysis of embedded optical fibres in composite structures
R. HADZIC, S. JOHN & I. HERSZBERG (Australia)

767 The shear properties of woven carbon fabric
M. NGUYEN, I. HERSZBERG & R. PATON (Australia)

781 The bending properties of integrally woven and unidirectional prepreg T-sections
R. S. THOMSON, P. J. FALZON, A. NICOLAIDIS, K. H. LEONG (Australia) & T. ISHIKAWA (Japan)

789 Computer modelling of impact on curved fibre composite panels
Z. LEYLEK, M. L. SCOTT, S. GEORGIADIS & R. S. THOMSON (Australia)

797 Micromechanics models for the elastic constants and failure strengths of plain weave composites
P. TAN, L. TONG & G. P. STEVEN (Australia)

805 Reinforcement of concrete beam–column connections with hybrid FRP sheet
J. LI, S. L. BAKOSS, B. SAMALI & L. YE (Australia)

813 Development of a composite cargo door for an aircraft
H. G. S. J. THUIS (Netherlands)

821 An evaluation of higher-order effects on the eigenfrequencies of composite structures
P. GAUDENZI & R. CARBONARO (Italy)

827 A study on stress and vibration analysis of a steel and hybrid flexspline for harmonic drive
H. S. JEON & S. H. OH (South Korea)

ELSEVIER

Composite Structures 47 (1999) 425

COMPOSITE STRUCTURES

www.elsevier.com/locate/compstruct

Editorial

As we approach the new millenium it is fitting to reflect on the advances in composite structures which have been reported in ICCS and the Journal of Composite Structures, which started in 1983, over almost 20 years. Perhaps it is an auspicious coincidence that in that period almost exactly 2000 papers have been cumulatively published in these two forums! Unblessed with the requisite psychic ability to speculate on this coincidence the Writer can only peruse the scientific results which have been published to give some perspective of the journey traveled by our technology in that time.

It has been said by many that to know your past is to recognize your future. The last 20 years have witnessed unprecedented increases in the mechanical properties of composite materials along with the ability to withstand the severest of environmental conditions. The range and diversity of forms of reinforcement and matrix materials presently available is staggering by yesterday's standards. A much greater understanding of the interface region is also apparent. Process technology has fought to keep pace with both the challenges and the market opportunities offered by these new composites.

In parallel with the aforesaid developments have come substantial advances in the tools and methodology used to assess and design composite structures. This was an essential component to the catalyst of successful implementation of new concepts and innovative ideas. Today's finite element codes are distant relatives of their forefathers. Similarly our ability to analytically model structural response has increased by leaps and bounds as has an understanding of the damage mechanisms which can arise in service.

To all who have contributed to the advance of knowledge in either this Journal or ICCS go our thanks for a brighter future. In particular personal thanks is due to the Editorial Board who over the years have added immensely to the status of the Journal.

I.H. Marshall
36, Gogoside Road
Largs, Ayrshire
Scotland KA30 9LA
UK

0263-8223/99/$ - see front matter © 2000 Elsevier Science Ltd. All rights reserved.
PII: S0263-8223(00)00008-8

ELSEVIER

Composite Structures 47 (1999) 427

COMPOSITE STRUCTURES

www.elsevier.com/locate/compstruct

Foreword

This collection of papers form the Proceedings Volume of the Tenth International Conference on Composite Structures (ICCS/10) held in Monash University, Melbourne, Australia from 15 to 17 November 1999. As the name implies this was the tenth in a series of highly successful biennial international conferences which commenced in Scotland in 1981. They continue to be the only international forum which focuses on the structural aspects of composite materials and are one of the longest running international composites conferences. This was the first occasion ICCS was held in Australasia.

The success of ICCS/10 was due in no small way to a number of extremely hard working individuals.

Grateful thanks is due to:

The International Advisory Committee: A.M. Brandt (Poland), W.M. Banks (Scotland), A.R. Bunsell (France), P. Gaudenzi (Italy), J. Rhodes (Scotland).

The Local Organising Committee: W.K. Chiu, S. Dillon, Y. Ding, G.V. Ingram, J.P.G. Sawyer, T. Ting, P. Chaperon, M.L. Scott.

The Conference Secretary: Merrilyn Sorensen.

The Sponsor: Department of Mechanical Engineering, Monash University.

The Co-Sponsors: US Army Research Office – Far East, US Air Force Office of Scientific Research/Asian Office of Aerospace Research and Development (AFOSR/AOARD), Australian Composite Structures Society, CRC Advanced Composite Structures.

ICCS/10 was jointly Chaired by I.H. Marshall and R. Jones of Monash University.

0263-8223/99/$ - see front matter © 2000 Published by Elsevier Science Ltd.
PII: S0263-8223(00)00009-X

ELSEVIER

Composite Structures 47 (1999) 429

COMPOSITE STRUCTURES

www.elsevier.com/locate/compstruct

Tenth International Conference on Composite Structures (ICCS/10), Monash University, Melbourne, Australia, November 1999

Australian Composite Structures Society Composite Structures Award

The Australian Composite Structures Society (ACCS)–ICCS/10 Prize was bestowed on the paper *Damage Detection of CFRP Laminates using Electrical Resistance Measurement and Neural Network* by Dae-Cheol Seo and Jung-Ju Lee (Department of Mechanical Engineering, Korea Advanced Institute of Science and Technology).

The photograph shows from left to right, Murray L. Scott, President ACCS, Dae-Cheol Seo and Ian H. Marshall.

0263-8223/99/$ - see front matter © 2000 Published by Elsevier Science Ltd. All rights reserved.
PII: S0263-8223(00)00084-2

ELSEVIER

Composite Structures 47 (1999) 431–443

COMPOSITE STRUCTURES

www.elsevier.com/locate/compstruct

Bonded composite repair of fatigue-cracked primary aircraft structure

Alan Baker

Airframes and Engines Division, Defence Science and Technology Organisation, Fishermen's Bend, Aeronautical and Maritime Research Laboratory, Melbourne, Australia

Abstract

Repairs based on adhesively bonded fibre-composite patches or reinforcements are more structurally efficient and much less damaging to the parent structure than standard repairs based on mechanically fastened metallic patches. As a result of the high reinforcing efficiency of bonded patches "live" fatigue cracks can be successfully repaired. However, when such repairs are applied to primary structure a conservative certification approach is often taken in which *no credit* is given to the patch system for slowing crack growth or restoring residual strength. Thus, cracks approaching critical size cannot be repaired and inspection intervals must be based on the predicted growth behaviour of the unpatched crack. To allow credit to be given to the patch the need is to demonstrate either (a) that the likelihood of patch loss is acceptably low *or* (b) that its loss can be immediately detected. Two approaches are discussed: the first approach which addresses (a) is based on a demonstrated ability to predict the patch system's fatigue behaviour and to assure its environmental durability. The second approach that addresses (b) is based on the "smart patch" concept in which the patch system monitors its own health. Crown Copyright © 2000 Published by Elsevier Science Ltd. All rights reserved.

Keywords: Aircraft structure; Repair technology; Composites; Adhesive bonding; Fatigue cracking; Smart structures

1. Introduction

As a result of their excellent load transfer characteristics [1] bonded reinforcements or patches provide a stiff alternative load path so they can be used very effectively to repair "live" cracks. In contrast, standard (Structural Repair Handbook-SRM) repairs, based on mechanically fastened metallic patches provide a relatively compliant alternative load path so they cannot effectively repair cracks and require prior removal (or some other terminating treatment) of the cracked region.

Mechanical repairs also have several other disadvantages, compared to bonded repairs as highlighted in Fig. 1.

1.1. Background on patching technology

The high-performance fibre-composites boron/epoxy (b/ep) and graphite/epoxy (gr/ep) are highly suited for use as a patching or reinforcing material for defective or degraded metallic structure [2].

Briefly the attributes of these composites include:

- High Young's modulus and strength, which minimises the required patch thickness (b/ep is around 3× as stiff as aluminium).
- Highly resistant to damage by cyclic loads.
- Immunity to corrosion, forms excellent protective layer.
- High formability, which allows easy formation of complex shapes.
- Low electrical conductivity (b/ep only), which facilitates use of eddy current NDI for monitoring the patched cracks and eliminates concerns with galvanic corrosion.

The main disadvantage of composites as patching materials results from their relatively low coefficient of thermal expansion compared to the parent material which results in residual tensile mean stresses in the repaired component [2].

Although relatively costly, b/ep is chosen as the patch or reinforcement for most Australian bonded composite repair applications, mainly because of its excellent mechanical properties, low conductivity and relatively high coefficient of thermal expansion. However, gr/ep because of its better formability is chosen for regions with small radii of curvature and sometimes because of its low cost and much higher availability. Patches are generally bonded with an aerospace-grade structural epoxy-nitrile film adhesives, curing from 80°C to 120°C to provide a maximum temperature capability of around 100°C.

0263-8223/99/$ - see front matter Crown Copyright © 2000 Published by Elsevier Science Ltd. All rights reserved.
PII: S0263-8223(00)00011-8

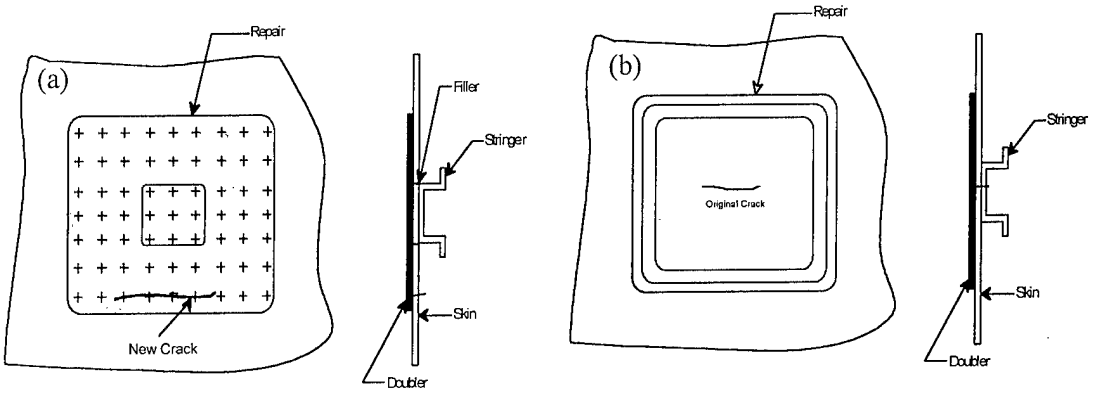

Fig. 1. (a) Some disadvantages of standard mechanically fastened repairs and (b) advantages of bonded composite repairs.

Composite reinforcement [3,4] can be used for a wide range of repairs/reinforcements to metallic aircraft components, many of which have been successfully exploited in Australia, these are categorised as follows:

Reduce stress intensity (crack patching)
- in regions with fatigue cracks,
- in regions with stress-corrosion cracks,
- increase damage tolerance in safe-life components.

Stiffen under-designed regions
- increase static strength,
- reduce fatigue strain at stress concentrators,
- reduce flutter,
- reduce deflection.

Restore residual strength or stiffness
- after corrosion removal,
- after flaw/crack removal,
- after reshaping to reduce stress concentration,
- in regions with widespread cracking.

1.2. Current limitations of crack patching

The economic benefits of patching live cracks are fully realised only when full credit can be given to the patch for the restoration of residual strength and reduction in fatigue crack growth rate. However, while application to non-flight critical structure is becoming widely accepted, application of bonded composite repairs to cracked primary structure is acceptable in most countries only on the basis that a margin on design limit load (DLL) capability is retained in the loss (total absence) of the patch [5,6]. This is the Fail-Safe approach, which can be applied:

- When a cracked single load path component maintains sufficient residual strength to withstand DLL times a safety factor (often 1.2). In this case inspection is required to ensure that the critical crack length for failure at this stress is not exceeded, based on the predicted growth rate for the *unpatched crack*.
- When a redundant (multiple) load path component can withstand DLL times the safety factor if the cracked path has failed. This is a standard procedure now for such structures so should not pose any particular problems. In this case inspection is required to ensure that the alternate load paths are not cracked to the extent that they could not withstand the elevated stress caused by the failure.

The single load path and redundant load path structural designs are, respectively, typical of fighter and large transport aircraft.

The inspection requirement based on growth of the unpatched crack in the single load path case may be acceptable (for example, if it coincides with the current inspection interval) where the initial crack size is small (or non-existent, for example, in the case of a preventative doubler rather than a patch). However, whilst the Fail-Safe approach is highly desirable, there will be some repairs, for example, those with crack approaching critical size or with small cracks having a high predicted growth rate, where this inspection requirement will not be cost-effective. The repair can then be certified only by giving full credit to the reinforcement in restoring residual strength and reducing the rate of crack growth.

The need to certify such a repair arose a few years ago in Australia, where a bonded composite repair [7] was developed for a fatigue crack in the lower wing skin of an F111 aircraft. This crack was very near to the critical size at DLL. Fig. 2 provides details on the repair, which has prevented crack growth in three years of further service.

Recently this cracking problem has become a fleet-wide issue with F111 since several similar cracks have

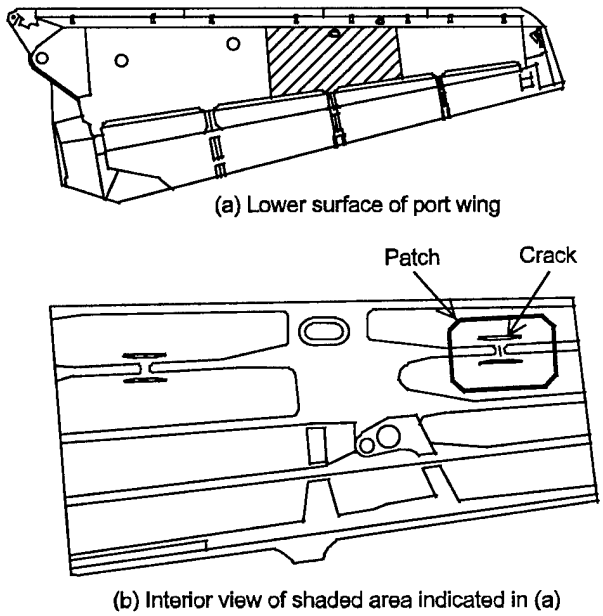

Fig. 2. Details of the location of a 45-mm fatigue crack in the F 111 lower wing-skin, at FASS 281 with an outline of the repair patch, which is made of 14 ply b/ep $(0_2, \pm 45, 0_3)_S$ bonded with adhesive. Patch dimensions are approximately 500 mm spanwise × 350 mm chordwise.

been detected. The aim is to patch these or, in the absence of cracking, to apply preventative reinforcements on all Australian F111 aircraft. The Fail-Safe approach can be adopted *initially* since the new cracks are below the critical size.There are essentially two ways of obtaining this justification. These are by showing:

(a) that the risk of significant loss in patching efficiency (defined later) is acceptably low, *or*

(b) that significant loss can be detected before it becomes a safety issue.

Fatigue strength of the patch system is considered not to be a concern where the static strength of the repair joint (crack spanned by the patch) is designed to exceed greatly the ultimate strength of the parent material [8,9]. However, fatigue is a concern with highly loaded primary structure where this margin cannot be achieved. In all repairs, thin or thick skin, environmental durability of the patch system is a concern.

Thus two approaches are discussed here: the first which addresses (a) is based on a demonstrated ability to predict the patch system's fatigue behaviour and to assure its environmental durability. The second, which addresses (b), is based on the "smart patch" concept in which the patch system monitors its own health.

2. Justifying credit for patching efficiency – fatigue concerns

This section addresses the situation where reduction in patching efficiency due to fatigue damage is the main concern. This includes consideration of degradation in fatigue properties of the patch system due to environmental agents such as temperature, moisture, fuel, hydraulic oil, etc.

Essentially the requirement is to prove by test or analysis that the patch can restore the residual strength of cracked structure to the required level (>1.2 × DLL) for the remaining service life. Thus, it is important to show that unacceptable loss in patch efficiency cannot result from the service cyclic loading (or from mechanical damage) and that the fatigue crack in the parent structure will grow at an acceptable rate which can be predicted for the purpose of setting inspection intervals.

Patching efficiency is defined here as (a) the recovery in residual strength following patching and (b) the reduction in crack growth rate of the fatigue crack provided by the patch. The patching efficiency depends largely on the reduction of stress intensity following patching and possibly on the level of mean stress [10] resulting from thermal mismatch between the patch and parent structure.

2.1. Influence of fatigue on patching efficiency

To satisfy these requirements there is a need to provide assurance that service loads cannot cause the patching efficiency to fall below an acceptable level due to fatigue damage in the patch system.

The patch efficiency could fall due to transverse fatigue failure (an unlikely event because of the relative fatigue immunity of these composites when loaded in the fibre direction, fibre-dominated mode) or to disbonding caused by fatigue crack growth through one or more of the following matrix/interface dominated modes:

- The adhesive.
- The adhesive (or primer) to metal interface.
- The adhesive composite interface.
- The surface matrix resin of the composite.
- The near-surface plies of the composite.

Fig. 3 illustrates some of these failure modes [2] in patched test specimen subjected to constant amplitude fatigue, $R = -1$. In each case the fatigue crack initiates in the high shear and peel region at the ends of the patch (strip).

In (a) the disbond propagates firstly through the adhesive very close to the metal interface and then into the middle of the adhesive layer; in (b) it propagates mainly through the adhesive, at approximately ±45° as a Mode 1 crack (normal to the nominal principal stresses); in (c) in which the b/ep patch is bonded with a epoxy-film adhesive (similar to that used in most Australian repairs) the crack has a preferred propagation path through the Dacron carrier fibres (presumably due to the weak fibre/resin interface) and through the surface matrix layer of the b/ep – above the glass fibre mat layer.

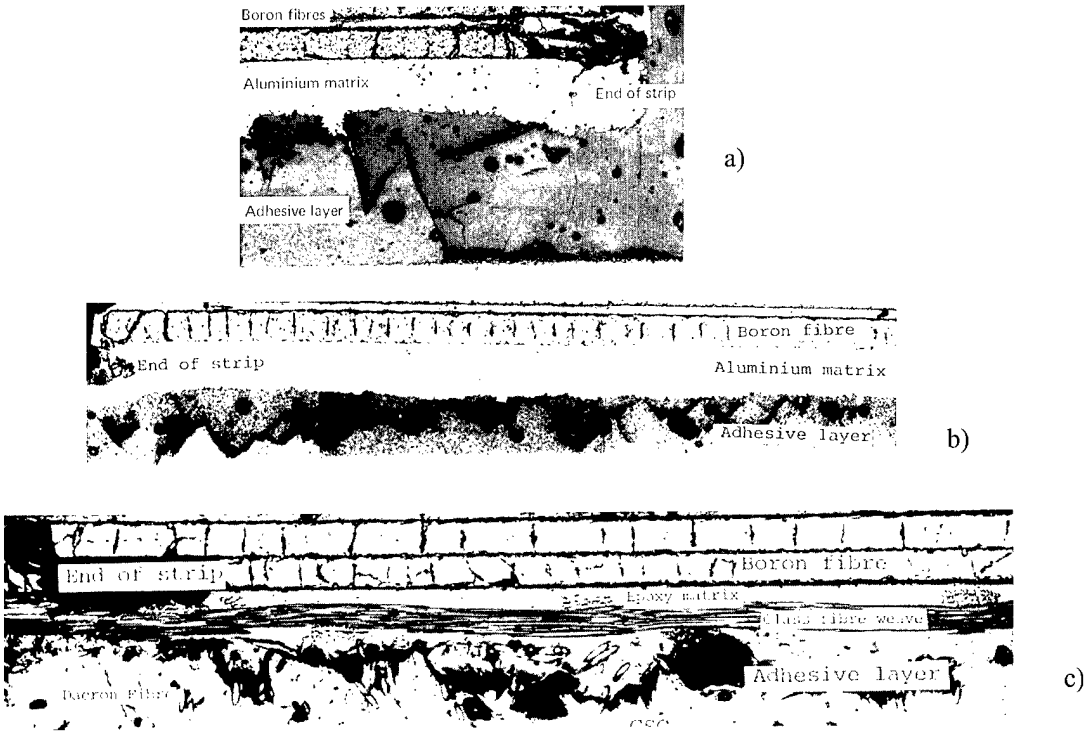

Fig. 3. Micrographs of taper sections through specimen with bonded b/ep or boron/aluminium (b/al) strips (patches) with the following patch-adhesive combinations (a) b/al-epoxy amine paste, (b) b/al-epoxy polyamide paste and (c) b/ep-epoxy nitrile film. The thickness of the adhesive is around 0.1 mm. Taken from Ref. [2].

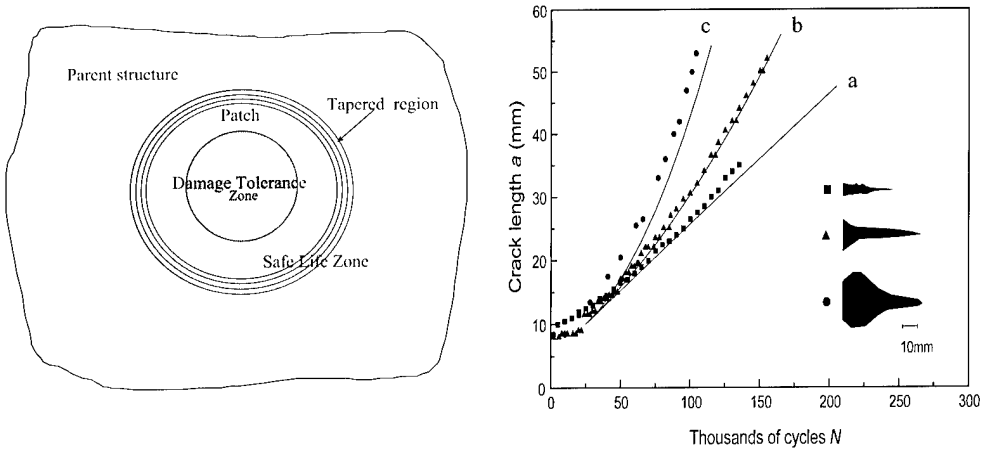

Fig. 4. (a) Schematic of an external bonded patch showing safe-life zone (no cracking allowed in patch system) and damage-tolerance zone (slow crack growth allowed in patch system). (b) Plot of crack growth versus cycles for three panels tested at 138 MPa, showing inset disbond size over crack. Taken from Ref. [4].

The predominantly matrix path for disbonding is often favoured for b/ep or gr/ep composites.

To discuss the influence of fatigue disbonding of the patch system the patch can be considered as two zones, Fig. 4(a):

- *Safe-life zone* at the tapered ends of the patch where damaging strains in the adhesive system are shear and peel.
- *Damage-tolerant zone* in the middle where damaging strains are mainly shear.

To prevent rapid loss of the patch due to fatigue disbonding, strains in the safe-life zone at the patch ends must not exceed the fatigue damage initiation threshold for a significant number of cycles. Even slow initial disbond growth in this region is unacceptable since once the disbond reaches the inner end of the taper region,

strains dramatically increase and growth will become rapid. Thus the patch system in this region must be designed on a safe-life basis. This is achieved [11] by limiting strains in the critical regions by design (e.g., appropriate end tapering, increased adhesive thickness, etc.) and use of appropriate strain allowables. With optimum patch design the strain levels in the tapered region can be designed to be quite low [12] so they should not be a concern in most repairs.

The forgoing considerations apply mainly to thick highly loaded structure. In thin-skin structure disbonding in the tapered region can be tolerated [13] as the load transfer stresses are acceptably low, even in the absence of the taper.

In the damage tolerance region, Fig. 4(a), limited disbond growth in the patch system is quite acceptable. Damage growth in this region is generally stable, and, if not large, has only a fairly small effect on reinforcing efficiency, Fig. 4(b) [4]. Since the patch/metal bond line is highly stressed in this region significant damage growth can be expected, particularly in demanding repairs involving thick skins and high loads.

Thus, assuming that the initial residual strength requirements are satisfied, full credit for the patch in slowing crack growth could be justified as follows:

- *Test/design certification approach*: Demonstration that: (a) strains are below threshold for fatigue damage initiation in the *safe-life zone*; (b) disbond growth is slow and predictable in the *damage-tolerant zone*, as described in the next section.
- *Continuous safety by inspection approach*: Based on self-assessment of the patch system integrity using the smart patch approach, described later.

2.2. Obtaining patch system fatigue allowables

To minimise certification costs suitably designed bonded joints [6] can be tested to provide a generic data base on patch system fatigue allowables. The proposed tests are outlined in Table 1. The joints, shown as inset in Table 1, have been used as the generic joints [2,14] to assess disbond initiation and growth rate in b/ep patch repairs to aluminium alloy specimen.

Table 1
Generic joint test program to obtain repair system allowables

Requirement	Approach
To find joint static and fatigue strain allowables and confirm validity of failure criteria based on coupon test data. *The failure criteria must hold for similar geometrical configurations, eg adherend thickness and stiffness and adhesive thickness.* 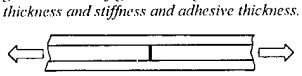 Generic Double Overlap Joint (Represents Cracked Region) 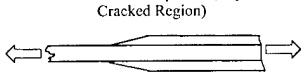 Generic Reinforcement Termination Joint	• Undertake static strength tests to: – check strength against predictions based on coupon data • Undertake fatigue tests to: – obtain **B**-basis threshold for fatigue disbond growth – rate of disbond growth at constant amplitude and spectrum loading • Find knockdown factors for: – hot/wet conditions – non-optimum manufacture – typical damage – more representative loading conditions

To characterise the allowable strains in the double-overlap joint the approach evaluated is to use the theoretical or the measured strain range in the adhesive $\Delta\gamma$ as the damage severity criteria. This is plotted against disbond growth rate db/dN, as shown in Fig. 5, where b is the disbond width and N is the number of cycles. The dotted line is arbitrarily defined as the initiation threshold in this case.

The patch-termination specimen shown in Table 1 is the more applicable generic joint specimen for characterising the threshold for damage growth in the safe-life zone, since this is representative of the geometry of this region and also represents the combination of peel and shear stresses that develops in this region. The total energy release rate G_T appears to be a suitable parameter to use as a damage severity criterion.

Since the patch system is expected to be insensitive to low loads and load sequences the allowables can probably be based directly on elevated stress constant-amplitude loading rather than using the constant-amplitude data to predict life under spectrum loading. A conservative approach could be to eliminate cycles at low loads from the spectrum (shown in prior testing) not to be damaging, then elevated all other loads to DLL and base allowable life on the number of cycles to damage initiation or acceptable damage growth.

A major issue is the relation of the generic joint to the actual loading situation in a particular repair. Providing the generic test is similar to the practical situation, limited testing using representative joints could be undertaken to find the knockdown factor for the difference. For example, the F111 repair was subjected to significant peel stresses [7] which could be simulated with an appropriate structural detail.

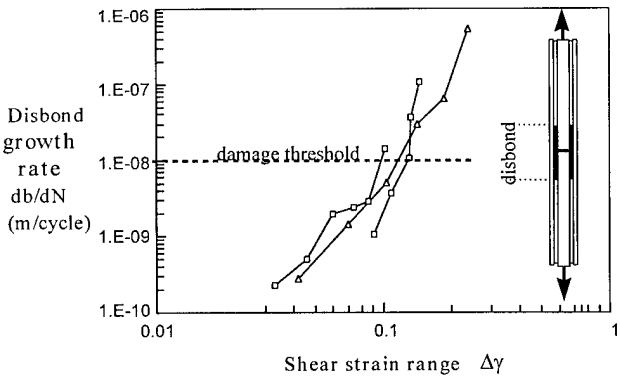

Fig. 5. Plot of disbond growth rate in the adhesive versus shear strain range obtained from tests on a double overlap joint, shown inset. The adhesive is FM73, around 0.3-mm thick, the inner adherend is 2024 T6 aluminium, around 3-mm thick, and the outer adherends are b/ep, around 1-mm thick.

2.3. Validation of patching analysis

The aim is to validate patch design approaches based on generic repair configurations. The approach is based on tests on a range of generic structural detail specimens, as indicated in Table 2. Again limited testing may be required on representative structural detail specimen to validate actual repair design, if this differs significantly from the generic structural detail [6].

Fig. 6(a) depicts a structural detail specimen tested under constant amplitude loading and Fig. 6(b) plots log da/dN versus log ΔK predicted using Rose's patching model [15]; where a is the crack length and K the stress intensity. These and other results [10] help to validate use of this model as a practical approach for predicting K in simple cracking geometries. The growth of disbonds in the damage-tolerant zone can be incorporated in the model [10] based on data from the generic joint tests [14].

Table 2
Validation of design approaches based on generic structural detail program

Requirement	Approach
Validate (F-E/analytical) design procedures and assess repair damage tolerance **Generic External Patch** 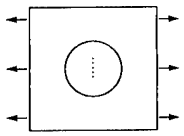	Undertake tests to assess: • Static strength under various environments • Fatigue strength, threshold for damage initiation in patch system • Threshold for growth and rate of growth of residual damage, eg cracks in metals • Influence of spectrum loading and environment Assess damage tolerance: • Residual strength before and after fatigue damage to patch system and residual damage • Influence of impact damage to patch and deliberate disbonds in patch system

Some success has been achieved in using the crack growth parameters obtained in the constant amplitude studies to predict growth of patched cracks under FALSTAF and F111 spectrum loading [16] using a modified crack closure model based on that developed by Newman [17]. The results for FALSTAF loading are shown in Fig. 7 using results taken from Ref. [18]. It can be seen that the predictions based on the equivalent crack method are in good agreement with the experimental results, noting that the effect of the thermal residual stress has been included. It is also interesting to note that, due to the increased mean stress resulting from the thermal residual stress, simple predictions based on simply integrating the crack growth equation on a cycle-by-cycle basis, using the steady-state crack-closure stress, are slightly conservative.

In addition to the fatigue studies, for direct comparison with model predictions [19] the stress intensity K was measured using K gauges bonded as the tip of a patched crack. The specimen used in this study was similar to that used in the fatigue experiments. As shown in Fig. 8 agreement between measured and predicted K is quite good up to a temperature of around 70°C.

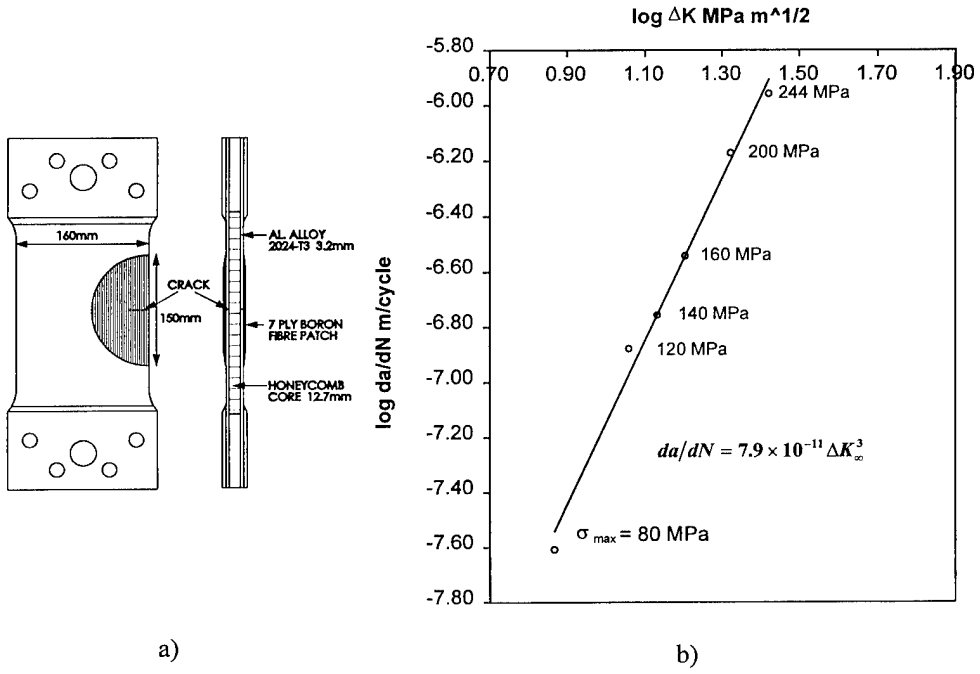

Fig. 6. (a) Generic structural detail test specimen for patched cracks in metallic structures used to validate the patching model and obtain crack growth parameters. (b) Plot of experimental log da/dN versus log ΔK, predicted from Rose's [15] analytical patching model.

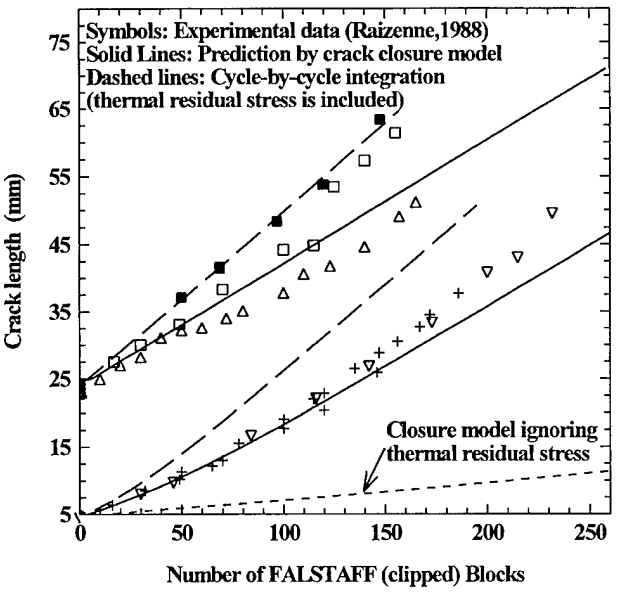

Fig. 7. Comparison between experimental and predicted growth behaviour of patched cracks under FALSTAFF spectrum.

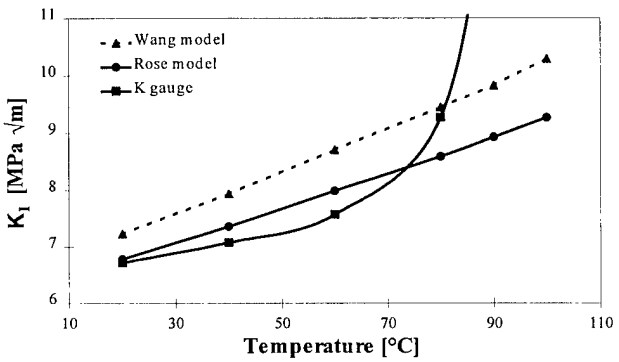

Fig. 8. Comparison of experimental and theoretical results for K_1 for $a = 30$ mm, patched specimen. The models used for the theoretical predictions are Rose's model and a related model developed more recently by Rose and Wang. Taken from Ref. [19]

3. Justifying credit for patching efficiency – environmental durability concerns

A key issue with the use of adhesive bonded repairs (as with structural adhesive bonding generally) is the need to assure environmental durability of the adhesive bond.

Environmental durability in bonded repairs impacts directly on structural integrity of the repair. Unlike fatigue it is not feasible to define either a strain threshold for environmental disbonding or a disbond growth rate. With inadequate environmental durability the threshold for disbonding can fall to zero so the disbond growth rate can be catastrophic. Thus it is not possible to set a safe inspection interval for this type of degradation.

It is important to note that environmental durability is generally a significant problem only with metals not with polymer–matrix composites such as b/ep or gr/ep. This is because of the moisture sensitivity of the metal interface if pre-bonding surface preparation is inadequate. Hydration of an unstable surface metal oxide results in a weak, easily disrupted interface.

The key point is that NDI techniques can detect only obvious disbonds, voids, etc. Bonds with *potentially* poor environmental durability cannot be detected as long as intimate contact at the bond interface is maintained. Developing an NDI capability to detect weak bonds is a very long-term prospect and may well prove infeasible. However, pre-bond NDI, that is, the development of techniques to check that the surfaces are correctly treated prior to bonding is feasible, as discussed later.

3.1. Assurance of patch system environmental durability

The requirement is to provide assurance at an acceptable level of probability that patch bond failure will not occur in the service environment during the required lifetime of the repaired component – or alternatively that the risk of bond failure is acceptable for the required service life.

This assurance revolves about quality control of the pre-bonding process because:

- This is the most critical process in the repair and is often applied under difficult conditions.
- The danger of incorrect application or surface contamination, for example, by organic species from fuel, etc, in the repair environment is significant.

Thus a simple-to-apply (non-hazardous) surface treatment, such as the silane process [2,20], increases application reliability, even though other more complex repair surface treatments, for example, those based on phosphoric acid anodising, may provide bonds with marginally superior environmental durability.

To provide the required assurance a suitable test is required to: (a) assess the process evaluation, (b) assess that it has been correctly applied, (c) qualify technicians. It is proposed that the Boeing wedge test (BWT), depicted in Fig. 9, fulfils this requirement for the following reasons:

- The BWT has been a US industry standard for adhesively bonded airframe components for many years and is an ASTM test.
- The BWT is a simple low-cost test which requires a minimum of equipment.
- Australian experience based on assurance of bond durability through BWT testing has been very positive, as described in the next section. Assurance is now based on RAAF Engineering Standard C5033 Composite Materials and Adhesive Bonded Repairs [9].

However, there are questions concerning whether the severity of the BWT is appropriate and how to quantify

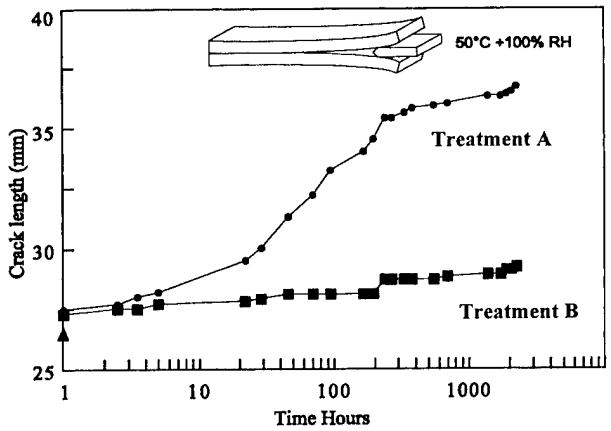

Fig. 9. The BWT to assess bond durability. The metallic adherends are made the aluminium alloy under investigation, generally about 3-mm thick bonded with the appropriate adhesive. The wedge is driven in under standard conditions.

it in terms of a failure probability. Neither of these questions can satisfactorily be answered at present.

Efforts are being made in Australia to establish if the required statistical data are available in the literature. There should also be a suitable statistical database held by the major aircraft manufacturers, but this is likely to be of a proprietary nature. At present the only information on which a decision can be based is on our extensive service experience discussed in Section 3.2.

Australia uses a severe version of the standard BWT. For example, an acceptable test result is generally less than 19 mm growth of the disbond in 1 h; whilst the Australian requirement is less than 5 mm growth in 24 h or 7 mm in 48 h.

More severe tests can be performed. These include the double-cantilever beam test, the constant-compliance cantilever-beam test [21] and the slow strain-rate test [22]. The advantage of these is that they are quantitative in that a Mode 1 fracture energy can be measured and correlated with exposure conditions and time. This is generally not possible with the BWT as with tougher adhesives some plastic bending of the metal adherend arms occurs when the wedge is driven in.

The disadvantages of the alternative tests are that they are much more costly to make and test compared with the BWT and they (probably) cannot be correlated with service behaviour, since a suitable database for these tests is unavailable. The ability to quantify a durability parameter, e.g., Mode 1 strain energy release rate G_1, is of limited use since it is not a useable design parameter. Thus these tests are more suitable for research purposes, for example, in the evaluation of new surface treatments.

Another issue is the value of a BWT made during the repair process, rather than simply to qualify technicians and processes. Separate test specimens made up in parallel and, as far as possible, under the conditions of the repair cannot capture all the variables associated with the repair process; for example, in the exact parent material, in the type and degree of contamination and in the cure cycle. Nevertheless, it is reasonable to assume that a good BWT result from the parallel specimen will provide considerable extra confidence in the repair procedure.

Other than the BWT for quality control of surface treatment there is also the possibility of pre-bond NDI, including simple wetting measurements. However, more sophisticated measurements for assessing, for example, contamination, degree of surface blasting [23], and production of the correct surface condition are also feasible and can be adapted for field use. These include surface potential measurement and infrared (IR) surface analysis.

3.2. Australian experience on service durability

Table 3 provides details on Australian bonded composite repair applications. Many repairs have survived over 20 years of service, without evidence of environmental or fatigue durability problems.

However, a few environmental durability failures were found in the Mirage III wing repairs. In these repairs the surface treatment was based on the phosphoric acid gel-anodising process (PAA). The failures were attributed to (a) the extreme porosity, which developed in the bond line of some of these repairs caused by moisture absorption under the tropical conditions in which these repairs were applied and (b) the absence of corrosion inhibiting primer. Use of staged adhesive and more careful drying of the surfaces prior to bonding would have reduced the moisture problems.

Fatigue durability of the patch system has been a problem in only one case: the F111 wing-pivot-fitting b/ep doublers which were primarily designed to reduce strains in the fitting during a cold (−40°C) proof load test – this they did successfully. A secondary aim for the doublers was to reduce fatigue strains in the fitting in service to increase the inspection interval (by a factor of around 3); however, fatigue failures are being experienced. Failure occurs mainly in the surface resin of the b/ep, as seen in part of Fig. 3(c). Whilst analysis of the cause of failure is not complete, the failures are thought to result from use of an excessive taper angle at the ends of the doubler resulting in adhesive strains above the fatigue threshold.

4. Justifying credit for patching efficiency – the smart patch approach

An alternative to certification procedures based on testing is the smart patch approach [6,24] illustrated in Fig. 10. The aim here is to develop a capability for

Table 3
Australian bonded patch repairs to military aircraft, experience on environmental durability[a]

Aircraft	Problem	Surface treatment (patch system)	Remarks on bond durability
C130	Stress corrosion cracked stiffeners in wing, aluminium alloy 7075	GB initially GB + S later (b/ep + FM73)	Over 20 years of service. No bond durability problems where bonding carried out as specified
Mirage III	Fatigue cracking in lower wing skin, aluminium alloy AU4SG	PANTA (b/ep + FM73)	180 wings repaired or reinforced. Eight bond durability problems over around eight years. Failures were associated with adhesive voiding caused by extreme humidity in the tropical repair station
F111-C	Secondary bending in wing pivot fittings leading to a fatigue problem. Steel D6ac fastened to aluminium alloy wing skin	GB + S (b/ep + FM73)	No bond durability failures to steel or aluminium surface over 10 years
F111-C	Stress corrosion cracking in weapon bay longeron flange, aluminium alloy 7075T6	GB + S (gr/ep cloth + ep)	Over 10 aircraft repaired. No bond durability problems over around eight years
F-111-C	Stress corrosion cracking in longeron adjacent to refuel receptacle, 7049-T6	GB + S (b/ep + EA 9321)	Over 10 aircraft repaired. No bond durability problems in eight years
F-111-C	Metal-to-metal and sandwich structure repairs. RAAF adopted GB + S and changed to FM 300 adhesive in 1992	GB + S FM300 FM 73, EA 9321	No bond durability failures in over seven years
F-111-C	Pork-chop panel (lower fuselage). Panels rebuilt after repeated in-service failures	GB + S FM 300	Repeat rebuild rate reduced from 95% to 0. No bond durability failures in seven years
C-141 (USAF)	Fatigue cracking in wing riser weep holes, 7075T6	GB + S + P (b/ep + FM73)	No bond durability problems around five years
P-3C	Full depth corrosion damage in horizontal tail, aluminium alloy 7075 T6	GB + S (al alloy + FM73)	No bond durability problems over around 10 years
Boeing 747	Simulated repairs to several regions including fuselage lap-joint, wing leading edge, trailing edge flap and engine thrust reverser cowl	GB + S + P (b/ep + FM73 or acrylic)	Demonstrator repairs; 37 000 flying hours, 7020 landings over a nine-year period with no significant bond durability problems
Sea King helicopter	Fatigue crack in frame	GB + S + P (b/ep + FM73)	Operated in am offshore ship-borne environment for four years with no problems
F-111-C	Fatigue cracking in lower wing skin at fuel flow hole under forward auxiliary spar	GB + SB/ep	No bond durability problems in over 2.5 years of service

[a] GB = alumina grit blasting; S = Silane; P = Primer; PANTA = Phosphoric Acid Non-Tank Anodising; b/ep = boron/epoxy; gr/ep = graphite/epoxy; AF 126, FM73, FM300 epoxy-nitrile film adhesives; ep = epoxy-paste adhesive; acrylic = toughened acrylic adhesive Flexon 241 EA 9321 epoxy paste adhesive.

continuous autonomous (self) monitoring of patch performance to ensure that the patch is performing in service as required. Although the need to follow the correct patch design and process procedures is unchanged, the "smart" approach should allow considerable relaxation in the certification requirements. However, failure of the patch system will still be a costly and therefore a highly undesirable event.

The most direct approach to assess the "health" of the patch system is to measure the level of load transfer in the safe-life zone, Fig. 4. This approach was successfully demonstrated on test specimen during the development of the b/ep doubler for the F111 wing-pivot fitting [25], using resistance strain gauges bonded at the ends of the tapered region, but was premature for in-flight application. The monitoring could also include automatic assessment of cracking in the parent structure and disbond growth in the patch system in the damage tolerance zone.

The demonstrator smart approach being developed for flight trials [24] is also based on strain gauges, bonded to the ends of the taper region, Fig. 11, and on the surface of the component away from the patch and monitoring the ratio (patch strains)/(strain in the component) during service life. Any decrease in the "patch health" ratio is an indication of disbonding of the patch

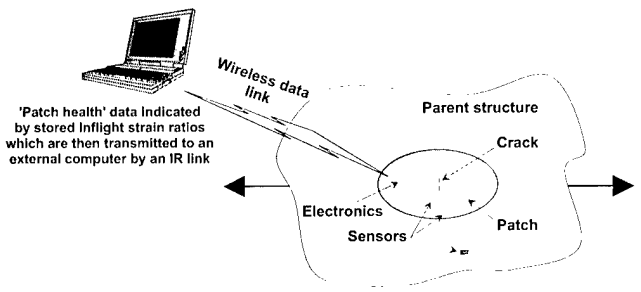

Fig. 10. Schematic diagram of the smart patch concept.

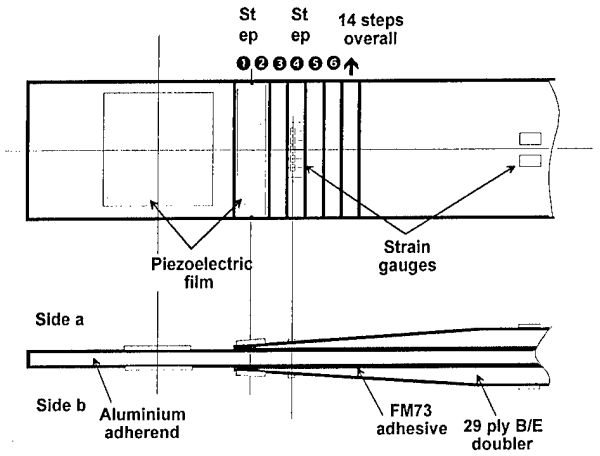

Fig. 11. Schematic of specimen showing strain gauge and piezoelectric film sensor locations on the steps at the ends of the doubler.

in this critical end region. In this approach there is no requirement for measurement of the actual loading, disbonding is indicated by the reduction in relative strain. The gauges are automatically monitored by an "on-board" miniaturised system that provides processed information. Data are transmitted to an external computer by an IR link.

The prototype device, shown in Fig. 12, was not optimised for size and weight; however, it easily fits in the palm of an average hand and has a mass of about 25 g and is powered by a single 3-V battery. Future approaches will be based on micro electro mechanical system (MEMS) [26] and will be very much smaller and more robust with much lower power requirements. The long-term aim is for a fully embedded system. However, in the near future the system (still fully self-contained) would have to be located in a nearby small cavity.

Experiments were undertaken to demonstrate this concept on the skin-doubler specimen depicted in Fig. 11. Resistance-foil strain gauges are located on the far field and the fourth step of the boron doubler on each side of this specimen. Two 28-μm thick piezoelectric film (PVDF) sensors, one located in the far-field on the aluminium adherend (parent structure) and the other located on the first two steps of the doubler. Fig. 13 shows the patch health ratio as a function of loading cycles. It is seen that the device satisfactorily monitors the damage growth at the end of the doubler.

IR (rather than radio waves) is being used for the data transmission. IR has the significant advantage of not interfering with (or being interfered by) any of the aircraft electrical functions, but may be difficult to use where the repair is deep in the airframe structure. However, it may prove viable to "pipe" the IR to an accessible region using optical fibres.

The viability of this smart approach revolves largely on how to prove its reliability under the aircraft temperature and environmental operating conditions. This is the reason why flight trials will be so important. These trials are planned within the next year to monitor the

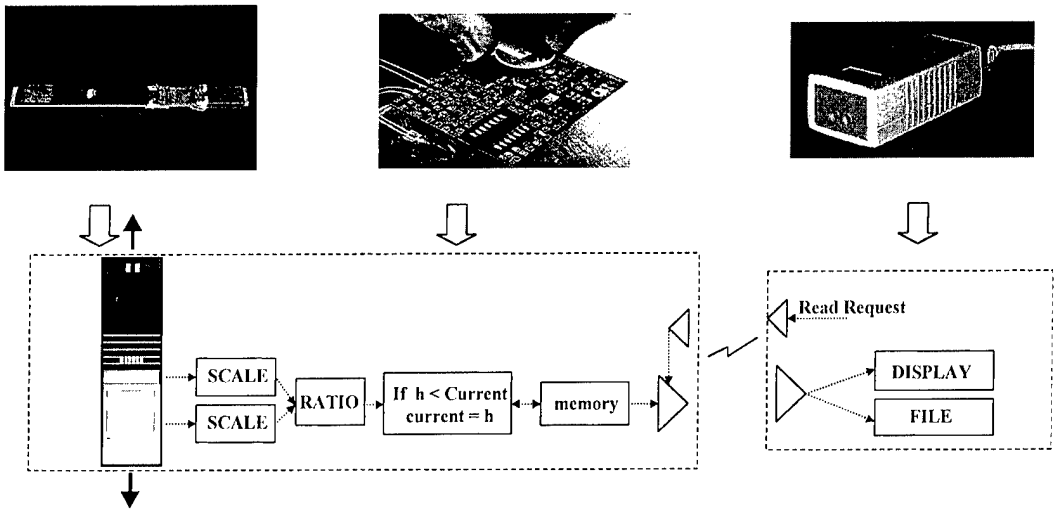

Fig. 12. Photographs and flow chart of the demonstrator experimental set-up.

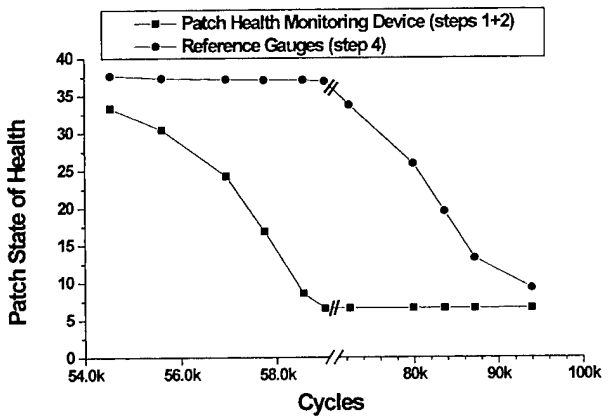

Fig. 13. Plot of variation of patch state of health (ratio of critical region strain/far-field strain) with increasing number of applied loading cycles.

performance of a b/ep doubler system recently developed [27] to extend the life of F/A-18 aileron hinges.

An alternative smart approach, being developed by Wilson [28], is based on the use of special chemical sensors embedded in the adhesive layer. These sensors detect chemical species produced at the metal surface during the process of bond degradation. This approach, complementary to the strain approach previously discussed, should provide warning of impending bond deterioration.

5. Discussion

A decision chart for management by slow-crack growth is provided in Fig. 14, based on the previous

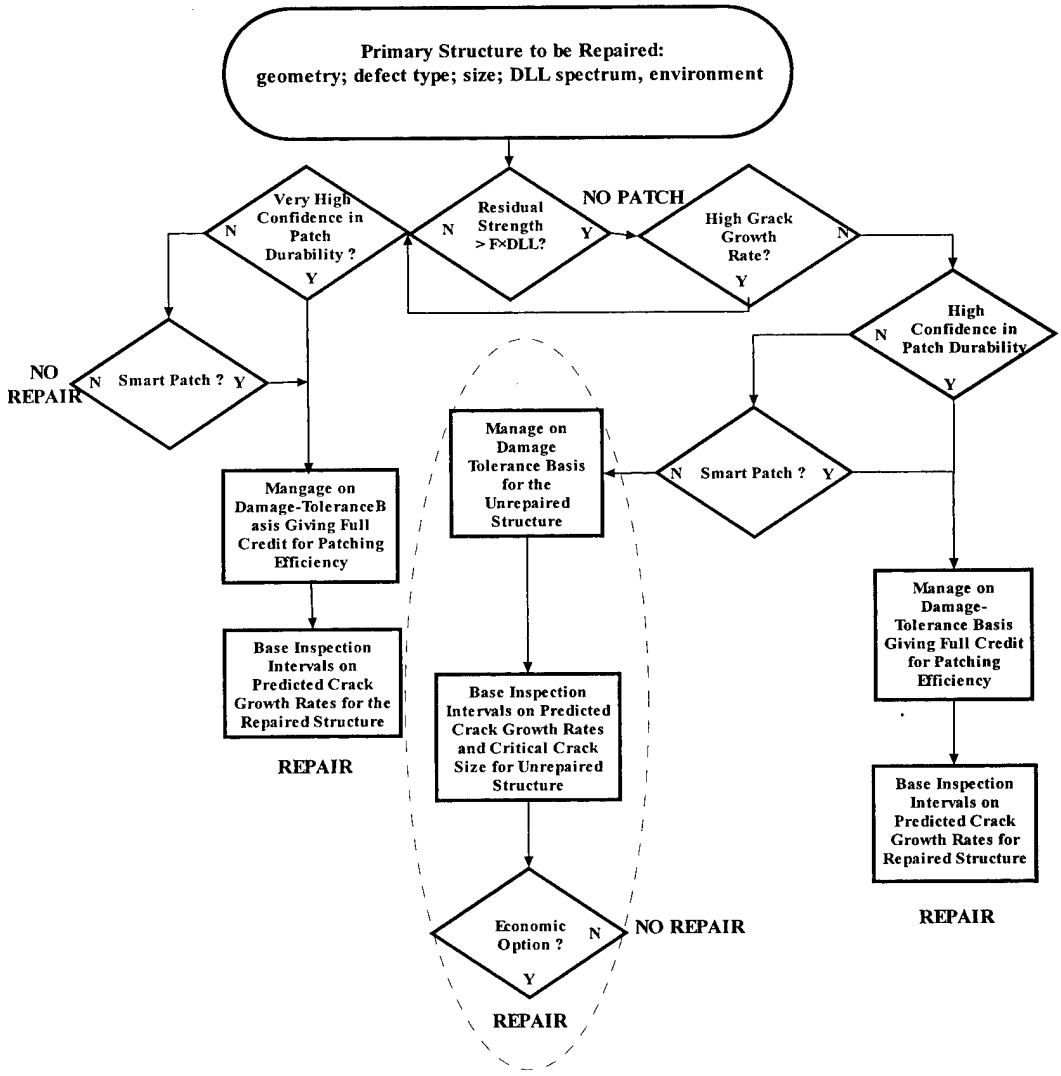

Fig. 14. Decision chart for certification of bonded patch repairs to cracked structure. The actions inside the dotted ellipse represent the conservative Fail-Safe approach.

discussion. This shows that certification requirements can be made much less stringent by the smart patch approach, as immanent loss or degradation of patch reinforcing ability will be immediately detected. However, where certification is based on this approach the key requirement becomes proving the smart system reliability in the aircraft operating environment. Generally, the smart patch approach appears technically feasible but will be economically viable mainly for repairs to costly primary structure

Where the smart patch approach is not used the key issue is how to provide assurance that the probability of unacceptable loss in patching efficiency is acceptably low. If bond environmental durability is shown not to be a concern then management can be based on patch system fatigue allowables, giving full credit for the patch in slowing crack growth and recovering residual strength. However, bond degradation is generally the major concern so the main issue here is of providing confidence that environmental degradation of the patch system will not occur. If this is not possible in the absence of the smart patch approach the repair must be based on the Fail-Safe approach, giving no credit to the patch.

To provide assurance of bond durability a validated accelerated test of bond quality is required. It is proposed that the BWT or some derivative of it is a suitable test. The BWT can be used to qualify surface treatment processes and technicians, as in the C141 repair program [29] and can be used for in-line quality control purposes. The question of what BWT result is and what is not acceptable is the current challenge. Sufficient information on service experience may exist in the literature on bonded aircraft components and in the Australian experience on bonded repairs to help provide the answer.

6. Conclusions

The certification requirements to permit management of bonded composite repairs by allowing full credit for the presence of the patch in slowing crack growth and recovering residual strength have been addressed.

The major structural integrity issue is to assure that disbonding of the patch due to environmental degradation will not occur during the required service life.

Methods based on a combined safe-life/damage tolerance approach can be applied to the patch system where bond environment durability is not a concern, based on patch system fatigue allowable and knock-down factors.

It is proposed that the BWT should be adopted as the principal accelerated test for quality control for bonding surface treatment. The main challenge is to correlate the BWT with a probability of failure, possibly based on service experience.

Use of the smart patch approach, based on self-monitoring would considerably alleviate the certification requirements, since loss of patching efficiency would be detected automatically. However, this approach brings its own problem of reliability assurance.

Acknowledgements

The author would like to acknowledge many stimulating discussions with his colleagues on this topic including: Max Davis, Loris Molent, Kevin Walker and Drs. Richard Chester, Steve Galea, Chun Wang, Francis Rose and David Bond.

References

[1] Baker AA. Joining and repair of aircraft composite structures. In: Mallick PK, editor. Part 14 Composite engineering handbook. New York: Marcel Dekker, 1997.

[2] Baker AA. Crack patching. In: Baker AA, Jones R, editors. Bonded repair of aircraft structures. Dordrecht: Martinus Nijhoff, 1988: pp. 107–73 [chapter 6: Experimental studies, practical applications].

[3] Baker AA. Repair of cracked or defective metallic aircraft components with advanced fibre composites – an overview of Australian work. Compos Struct 1984;2:153–81.

[4] Baker AA. Bonded composite repair of metallic aircraft components. AGARD-CP-550 Composite Repair of Military Aircraft Structures, Paper 1, 1994.

[5] Kerr A. Certification of bonded repairs. In: Proceedings of the USAF Aircraft Structural Integrity Program (ASIP), San Antonio, 1998.

[6] Baker AA. On the certification of bonded composite repairs to primary aircraft structures. In: Proceedings of the Eleventh International Conference on Composite Materials (ICCM-11), Gold Coast, Australia, 1997.

[7] Baker AA, Rose LRF, Walker KF, Wilson ES. Repair substantiation for a bonded composite repair to an F-111 lower wing skin. Appl Compos 1999;6:251–67.

[8] Davis M. The development of an engineering standard for composite repairs, AGARD-CP-550 Composite Repair of Military Aircraft Structures, Paper 24, 1994.

[9] Royal Australian Air Force Engineering Standard for Composite Materials and Adhesive Bonded Repairs, No. C5033 Issue 1. Department of Defence, Australia.

[10] Baker AA. Fatigue studies related to certification of composite crack patching for primary metallic structure. In: Proceedings of the FAA/NASA Symposium on Continued Airworthiness of Aircraft Structures, Atlanta USA, pp. 313–30.

[11] Hart-Smith LJ. An engineer's viewpoint on design and analysis of aircraft structural joints, Douglas Paper MDC 91K0067. In: Proceedings of the International Conference on Aircraft Damage Assessment and Repair, Australian Institute of Engineers, Melbourne, Australia, August 1991.

[12] Tran-Cong T, Heller M. Reduction in adhesive shear strains at the ends of bonded reinforcements, DSTO, AMRL Research Report, DSTO-RR-0115, 1997.

[13] Naboulsi S, Mall S, Denny JJ. Analysis of fatigue crack growth in imperfectly bonded composite patch repair of cracked aluminium panels. In: Proceedings of the International Conference on Aeronautical Fatigue 1997 (ICAF97).

[14] Chalkly P, Baker AA. Development of a generic repair joint for certification of bonded composite repairs. Int J Adhesion 1999;19:121 32.
[15] Rose LRF. In: Baker AA, Jones R, editors. Bonded repair of aircraft structures. Dordrecht: Martinus Nijhoff, 1988: pp. 107–73 [chapter 6: Theoretical analysis of crack patching].
[16] Wang CH, Rose LR, Baker AA. Modelling fatigue crack growth of patched cracks. Int J Frac 1998;88:L65–L170.
[17] Newman JC, FASTRANII – A fatigue crack growth structural analysis program. NASA Technical Memorandum 104195, NASA Langley Research Centre, 1992.
[18] Raizenne MD, Heath JBR, Benak T. TTCP PTP-4 Collaborative test program - variable amplitude loading of thin metallic materials repaired with composite patches, Laboratory Technical Report, LTR-ST-1662, National Aeronautical Establishment, Ottawa, Canada, 1988.
[19] Baker AA, Aktepe B. Sensor techniques to validate stress intensity models in cracked metallic panels repaired with bonded composite patches. In: Proceedings of the International Conference on Composite Materials (ICCM 12) Paris, 1999.
[20] Baker AA, Chester RJ. Minimum surface treatments for adhesively bonded repairs. Int J Adhesives Adhesion 1992;12:73–8.
[21] Kinloch AJ. Adhesion and adhesives: science and technology. London: Chapman & Hall, 1987 [chapter 7 – Fracture mechanics of adhesive joints].
[22] Kindermann MR, Wilson AR, Arnott DR. A multiple constant displacement-rate tensile testing machine. Measurement Sci Technol 1997;8:390–97.
[23] Olsson-Jacques CL, Arnott DR, Lambrianidis LT, Wilson AR, Kindermann MR, Theodossiou G. Toward quality monitoring of adherend surfaces prior to adhesive bonding in aircraft repairs. In: Proceedings of the International Aerospace Congress 1997 Seventh Australian Aeronautical Conference, Institution of Engineers Australia, 24–27 February, 1997, Sydney, Australia, pp. 511–20.
[24] Baker AA, Galea SC, Powlesland IG. A smart patch approach for bonded composite repairs to primary airframe structures. In: Proceedings of the Second Joint FAA/DOD/NASA Conference on Aging Aircraft, Williamsberg VA, 1998.
[25] Baker AA, Chester RJ, Davis MJ, Retchford JA, Roberts JD. The development of a boron/epoxy doubler system for the f111 wing pivot fitting – materials engineering aspects. Composites 1993;24:511–21.
[26] Web site: http://www.acq.osd.mil/es/dut/, Micromechanical Systems Opportunities.
[27] Chester R. Life extension of F/A-18 inboard aileron hinges by shape optimisation and composite reinforcement, DSTO – TR-0699, January 1999.
[28] Baker A, Meadows L. Air force research area critical issues paper: smart materials and structures for military airframes. Defence Science and Technology Report DSTO-GD-0176, May 1998.
[29] Schweinberg W, Jenson R, Fiebeg J. Advanced composite repairs of the C141 wing structure, International Conference of Composite Materials ICCM 10, 1995.

ELSEVIER

Composite Structures 47 (1999) 445–456

COMPOSITE STRUCTURES

www.elsevier.com/locate/compstruct

Matrix dominated time dependent failure predictions in polymer matrix composites

Hal F. Brinson *

Department of Mechanical Engineering, University of Houston, 4800 Calhoun, Houston, TX 78015, USA

Abstract

Various types of matrix dominated failures in polymer matrix composites (PMC) are reviewed. Current methods to evaluate the modulus degradation of PMC materials are discussed including viscoelastic/plastic and continuum damage models. It is pointed out that in each case the approach is based upon developing an analytical constitutive relation for the material in order to represent a measured stress–strain response. The suggestion is made that care must be used in the measurement of stress–strain behavior such that the modeling represents the true material behavior. New digital imaging methods are suggested as a means to determine in situ properties at a local scale commensurate with the continuum modeling procedure. A little used method to model viscoelastic/plastic (linear and non-linear) effects is discussed and modified to obtain a simple and easy to use time dependent failure law. Also, a little used energy based time dependent failure criterion is presented which can be combined with a non-linear viscoelastic integral approach to provide a prediction method for the time for creep rupture under simple stress states. Each is validated with experimental data for simple stress states but their generality is such that they could be used for complex (3-D) stress states. Advantages and limitations of both are addressed. Finally, a discussion of possible fruitful research areas are presented with the view of providing engineers in industry with an easy to use accelerated life prediction procedure. © 2000 Elsevier Science Ltd. All rights reserved.

1. Introduction

Engineering structures are most often designed to last for many years. It is usual for buildings, bridges, water systems, etc. to be designed for as long as 50 years. When materials such as steel or concrete are used, the principle concern relative to lifetime is associated with fatigue and corrosion. On the other hand, when polymers are used either alone or as the matrix component of polymer reinforced composites (PMC), another concern arises due to the viscoelastic or the inherent time dependent nature of the mechanical properties of the material. That is, strength as well as moduli or stiffness changes as a function of time due to the intrinsic or memory character of the molecular structure of the particular polymer being used.

Other applications where PMC materials are useful is in the automotive and aerospace industry. Again, a design lifetime of years is desired. A new and emerging application is in the offshore exploration and production of oil. Some reserves in the Gulf of Mexico have been discovered at a water depth of 6000 feet or more. Because of the large depth, structures (risers) made of metal to bring the oil to surface platforms may simply fail under their own weight. For this reason, PMC structures are being considered for use where the design lifetime is on the order of 40 yr. In addition, PMC materials are increasingly being considered for use in infra-structure applications either for repair or for complete new systems. Some specific applications include bridge structures, water and waste systems, etc. Again, a design life of 20–50 yr is required.

In all cases, it is not possible to perform tests on either materials or structures for periods long enough to guarantee structural integrity for periods over the design lifetime. As a result, there is a necessity for accelerated lifetime prediction procedures that can accurately predict the degradation of modulus and strength of PMC materials such that structural integrity and safety can be assured.

In the early stages of the development of polymeric composites, the need to address viscoelastic behavior was recognized [1]. Brinson et al. (1978) [2] proposed an accelerated characterization procedure for composites that would allow the prediction of long term properties from short term experiments using the well known time–temperature-superposition-principle (TTSP). Both,

* Tel.: +1-713-743-4509; fax: +1-713-743-4503.

0263-8223/99/$ - see front matter © 2000 Elsevier Science Ltd. All rights reserved.
PII: S0263-8223(00)00075-1

degradation of moduli and strength as a function of time were considered. The approach was modified several times to include time–stress-superposition-procedures (TSSP) and/or non-linear viscoelastic behavior as well as models to predict delayed failures such as creep ruptures [3–14].

In recent years, others have advanced approaches to model the time dependent degradation of the moduli and strength of PMC materials. The purpose of the present effort is to review our previous approaches as well as more recent theories of viscoplasticity, non-linear viscoelasticity and damage mechanics. While the latter are no doubt the preferred method to model degradation of properties, there is a question as to whether they will be widely used by design engineers. The difficulty is that many design engineers, for a variety of reasons, are reluctant to utilize the more advanced techniques in the intended manner. As an example, in the recent technology program for the high speed civil transport (HSCT) it was found that the use of techniques more advanced than linear viscoelasticity would not be easily accepted by those that design aircraft. As a result, development of data in the HSCT program was limited to a linear viscoelastic framework. For this reason, the principle thrust of the current effort is to review two relatively little known theories for predicting time dependent failures and assess their use for PMC materials. One is a viscoelastic/plastic failure theory due to Nagdi and Murch [15] and to Crochet [16]. The other is an approach utilizing deviatoric free energy as a basis for predicting failure due to Reiner and Weissenberg [17] which has been extensively investigated by Bruller [18,19]. The fundamental idea is to demonstrate that relatively simple TTSP and/or TSSP procedures can be used together with either failure law to accurately predict delayed failures in structural polymers or composites.

Before examining the various approaches to life prediction, it is appropriate to discuss briefly various matrix dominated failure modes and why they are important in the design of engineering structures made from PMC materials.

2. Matrix dominated failure modes

The usual failure modes attributed to the matrix are: matrix cracking, fiber matrix debonding and ply delaminations. These types of damage may initiate due to high stresses in regions of flaws arising during processing, at fiber breaks or other factors. Delaminations, are especially likely to occur in regions of high out-of-plane tensile stresses such as those found at a free edge or compressive stresses due to bending, thermal, or other effects. In fact, some might argue that fiber matrix debonding and ply delaminations are not matrix failures but are due to interface or interphase properties. That fiber breaks can lead to fiber matrix debonding was demonstrated by Gamstedt, Berlund and Peijjs [20] for a glass polypropylene laminate tested in fatigue as shown schematically in Fig. 1. In Fig. 1(a), fiber matrix debonding was observed at fiber breaks using a replication technique in a glass polypropylene laminate with a weak interface layer while little fiber matrix debonding was found in a similar polypropylene laminate with an additive to create better adhesion as shown in Fig. 1(b). It was also shown in the latter, that debonding was cohesive whereas in the former, debonding appeared to be adhesive.

Matrix failures can be seen in Fig. 2 for $[0°]_{8s}$, $[0°/90°]_{4s}$ and $[\pm 45]_{4s}$ graphite/epoxy laminates with a central crack or hole tested in tension using a photoelastic coating. In each case, the high stress field indicated by the photoelastic fringes suggests high deformations or damage in the matrix which can lead to splitting or fiber matrix debonding between the fibers.

Fig. 3 shows the results obtained in a separate test of a $\pm 45°$ specimen containing a central hole loaded in tension. The test was performed under stroke control (constant deformation rate) such that at any time during the test the distance between grips could be held fixed. In this manner, the test could be interrupted at selected intervals with the overall strain held constant such that the perimeter of the hole could be examined with a microscope to observe any damage that had developed. As seen in Fig. 3, the load dramatically decreased during the pause, even though the distance between grips was fixed. Apparently, a global stress relaxation process was taking place and in two cases, the specimen separated. The fact that the specimen failed while the load was decreasing significantly can be attributed to the viscoelastic behavior of the matrix which led to time delayed failure. Examination of the perimeter of the hole revealed small growing cracks in the outer plies in the $+45°$ direction while other cracks on the interior plies in

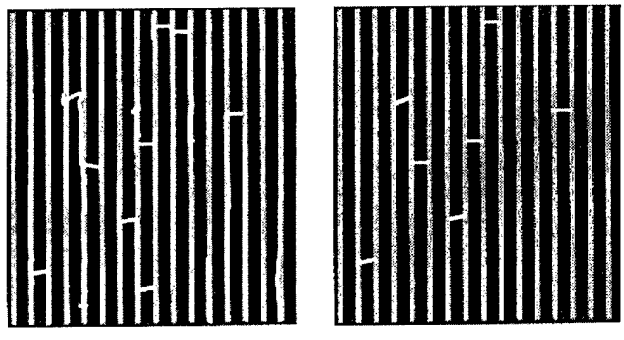

(a) (b)

Fig. 1. Schematic of failures in glass/polypropylene laminates tested infatigue: (a) fiber debonding at fiber breaks for a weak interface, (b) little debonding at fiber breaks for a strong interface [20].

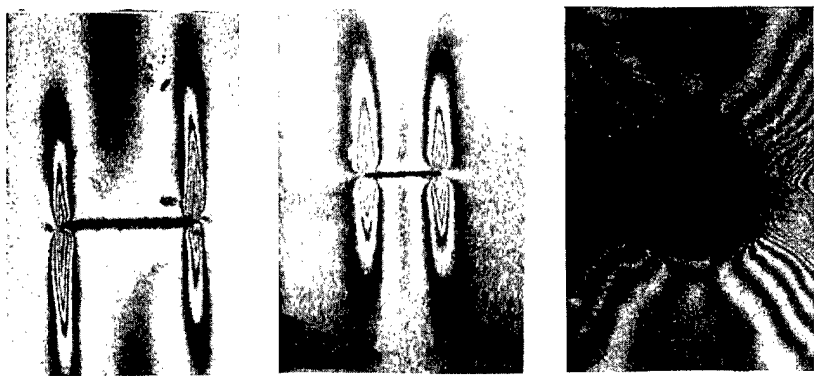

Fig. 2. Graphite/epoxy laminates with a photoelastic coating containing a central crack or hole tested in tension [21]. The isochromatic patterns indicate high deformations or damage in the matrix between fibers.

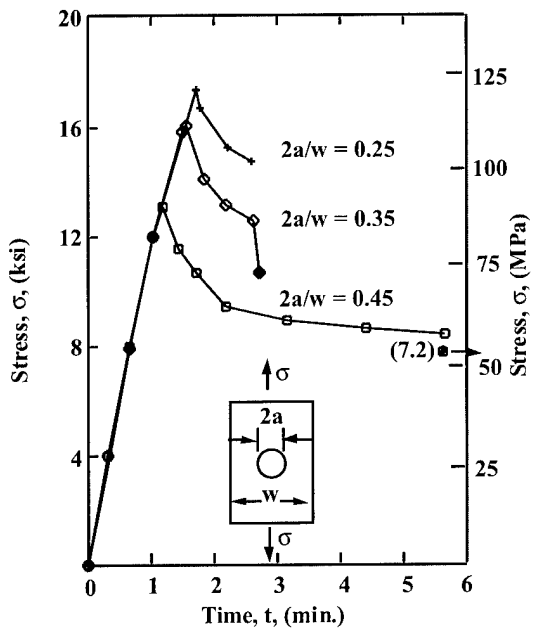

Fig. 3. Deformation control tensile test of a $[\pm 45°]_{4s}$ with ramp-relaxation response [21,22].

the −45° were growing in the opposite direction. For this reason, far field strains (and hence loads) were decreasing to compensate for the increased local strains in the cracked region in such a way that the overall (global) deformation could remain constant.

Fig. 4 shows examples of matrix dominated failures for three multi-directional glass/epoxy laminates tested in uniaxial tension from the work of Hahn [23]. Utilizing the measured stress–strain responses of 0°, 90°, ±45° laminates an excellent explanation is presented and an approximate analysis of the reduction of load in the $[0°/90°]_s$ when the first cracks appeared in the 90° plies and the further reduction in load for additional cracks. At a certain point, the matrix cracks turn and begin to grow along the interface and fiber/matrix debonding (or delamination) occurs. A similar circumstance occurs in the $[0°/\pm 45°]_s$ and $[0°/\pm 45°/90°]_s$ laminates. He further notes that similar cracking patterns occur for fatigue even in the first cycle. While not discussed in his work, undoubtedly a similar response will occur in creep (or static fatigue) but such failures depend upon the load and time. The possibility of such time dependent failures and their prediction is the principle subject of the current effort.

3. Approaches to model time dependent failures

Various approaches are used to mathematically model failure processes in engineering materials. Most frequently encountered are the traditional failure theories such as the maximum normal stress or strain, maximum shear stress and the maximum distortion (deviatoric) energy theories. Many variations of these have been used in an attempt to explain the progression of failure in a laminated composite. As an example, the Tsai–Hill criterion, which is a modification of the von Mises (distortion energy) approach has been frequently used to predict the failure of orthotropic laminates.

A recent effort by Christensen [24] briefly reviews the current status of yield/failure theories for composites and has concluded that stress based criteria are better suited for polymer composites rather than strain based criteria. Micro-mechanics is then used to guide the development of macroscopic stress based quadratic failure theories for both matrix and fiber dominated failure modes.

The elementary theories mentioned above do not account for strain hardening effects or take into account load carrying capability beyond a defined failure point. Nor do they include time or rate dependent effects. On the other hand, a more recent theories of linear and

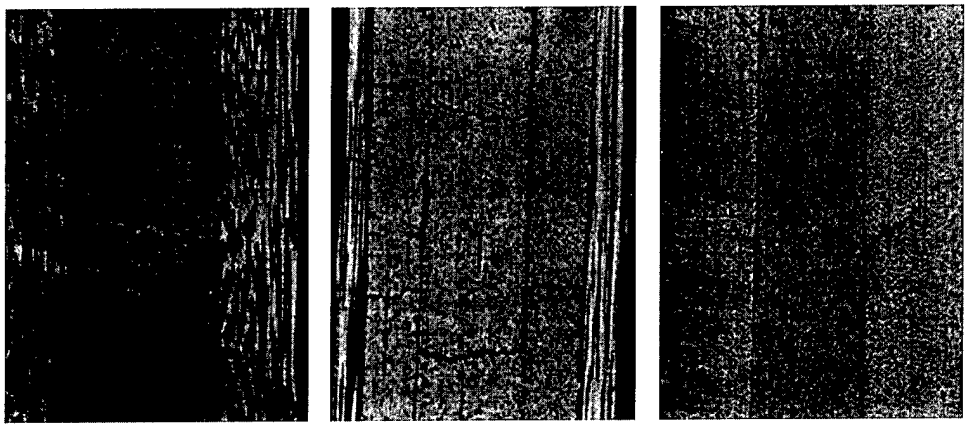

(a) $[0°/90°]_s$ (b) $[0°/\pm 45°]_s$ (c) $[0°/\pm 45°/90°]_s$

Fig. 4. The progression of failures in multi-axial laminate as demonstrated by Hahn [23].

non-linear viscoelasticity [1,25] and viscoplasticity [26] do account for time and rate effects and allow the calculation of stress or strain states in structural polymers and PMC materials when stressed beyond the linear range or when significant permanent deformations would be encountered upon unloading. Damage mechanics has been used to account for non-linear behavior in metals and polymer based materials [27,28] but has only recently been extended to included viscoelastic response [29–34]. A comprehensive survey of the viscoelastic nature of polymers and methods to evaluate aging, damage evolution and other issues can be found in Brinson and Gates [35].

One cautionary note is appropriate to the utilization of damage theories. Typically, evidence of modulus degradation in measured stress–strain behavior together with permanent deformation is used as a basis of the extent of damage in a PMC material. This assumption may be valid as long as the measurement technique to obtain strain is commensurate with the size of the inferred damage region or the "representative volume element". That is, a homogeneous state of strain is necessary at the location in which strain is measured and/or damage is inferred. This is especially true when a material exhibits crazing, necking or Luder's band development as occur in both thermoplastic and thermoset polymers. An example of crazing is shown in Fig. 5 for a modified epoxy tested to failure in uniaxial tension [36]. Crazes can be seen in Fig. 5(a) and (b) as small regions with a lighter color than the original material (sometimes referred to as "stress whitening") at various inclinations to the load axis. (An electrical strain gage is seen in the in the middle of the specimen.)

Apparently, even at failure, the crazing in the middle measurement region is not completely homogeneous and one might question if the strains measured by an electrical strain gage, clip gage or other macroscopic

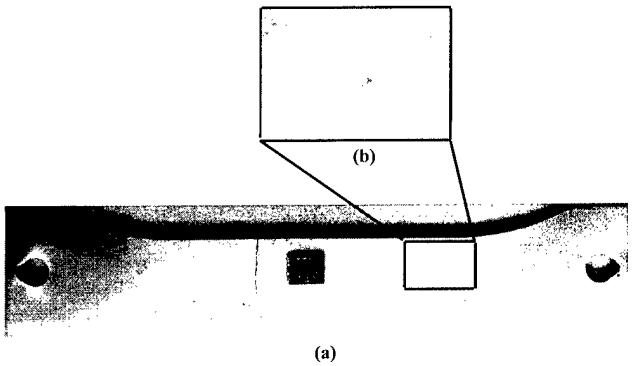

Fig. 5. Crazes (whitened regionsl in a modified epoxy [36]. (a) Failed tensile specimen, (b) enlargement of a central crazed area.

procedure is truly representative of the strains within crazes or damaged regions such as those shown in Fig. 5. Thus, moduli determined by global measurements may not be representative of local constitutive behavior and analytical models based upon gross observations may lead to non-conservative estimates of failure life. New non-contacting methods of strain measurement are under development, which will allow the accurate determination of strains within sub-micron regions such as crazes. One such approach utilizes high-resolution digital cameras to create a digital map from which deformations and strains can be obtained. An example is given in Fig. 6, which is a digital image micrograph of a [90°] graphite/epoxy specimen in three point bending [37]. The pixel map of individual fibers shown in the enlarged regions was used to measure the bending strain and obtain the transverse modulus therefrom. While the measurement was somewhat crude, the modulus found was within 15% of that determined with a tensile coupon and electrical strain gage measurements. Schapery [38] and Knauss [39] have successfully used this technique to

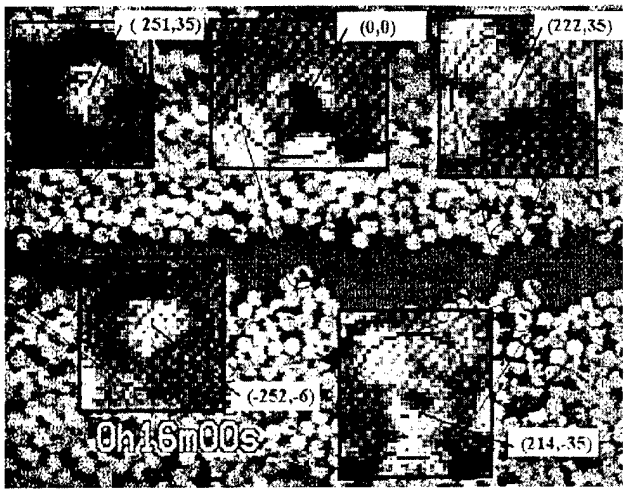

Fig. 6. Photomicrograph of a [90°] graphite/epoxy composite beam in three point bending. (Fiber diameters are about 5 μm. Resin rich layer is between outer two plies.) [37].

obtain accurate properties for polymers and composites with a digital image correlation procedure developed by Ransom and Sutton [40].

4. A model for viscoelastic–plasticity

A multi-axial yield/failure model for viscoelastic/plastic materials was developed by Nagdi and Murch [15] and later extended and refined by Crochet [16]. In this theory, the total strain is assumed to be the sum of the viscoelastic and plastic strains

$$\varepsilon_{ij} = \varepsilon_{ij}^{\mathrm{v}} + \varepsilon_{ij}^{\mathrm{p}}. \tag{1}$$

Stresses and strains are separated into elastic and viscoelastic deviatoric and dilatational components with the constitutive relations

$$e_{ij}^{\mathrm{E}} = \frac{1}{2G} s_{ij}^{\mathrm{E}} \quad \text{and} \quad \varepsilon^{\mathrm{E}} = \frac{1}{3K}\sigma^{\mathrm{E}}, \tag{2}$$

and

$$e_{ij}^{\mathrm{V}} = \int_{-\infty}^{t} J_1(t-\tau)\frac{\partial s_{ij}^{\mathrm{V}}}{\partial \tau}\,\mathrm{d}\tau \quad \text{and} \quad \varepsilon^{\mathrm{V}} = \int_{-\infty}^{t} J_2(t-\tau)\frac{\partial \sigma^{\mathrm{V}}}{\partial \tau}\,\mathrm{d}\tau, \tag{3}$$

where G and K are the elastic shear and bulk moduli, respectively and $J_1(t)$ and $J_2(t)$ are the viscoelastic shear and bulk compliances, respectively. The yield function is given as

$$f(\sigma_{ij}, \varepsilon_{ij}^{\mathrm{P}}, \chi_{ij}, \kappa_{ij}) = 0 \quad \text{and} \quad \chi_{ij} = \chi_{ij}(\varepsilon_{ij}^{\mathrm{V}} - \varepsilon_{ij}^{\mathrm{E}}), \tag{4}$$

where χ_{ij} is a time dependent function and κ_{ij} is a strain hardening function. Crochet gave specific form to the function χ_{ij} such that

$$\chi = [(\varepsilon_{ij}^{\mathrm{V}} - \varepsilon_{ij}^{\mathrm{E}})(\varepsilon_{ij}^{\mathrm{V}} - \varepsilon_{ij}^{\mathrm{E}})]^{1/2}, \tag{5}$$

and defined a time dependent uniaxial yield function as

$$Y(t) = \sigma_{yp}(t) = A + B\exp(-C\chi), \tag{6}$$

where A, B and C are material constants. In order to utilize the theory a viscoelastic stress analysis must be performed for the appropriate boundary value problem and the stresses and strains must satisfy Eq. (4). Crochet used the approach to perform a stress analysis of a viscoelastic/plastic hollow cylinder under internal pressure in a state of plane strain with a von Mises type yield criterion as well as the tensile yield equation given by (6).

The important feature of this viscoelastic/plastic theory is that a time dependent failure law contains the viscoelastic constitutive equation for the material. In order to predict yielding or failures over many years, the modulus or compliance would need to be known over the same period. One way to obtain long term modulus (compliance) properties from short term test data is through the use of a master curve produced with the TTSP. To obtain a master curve in this manner requires that short-term creep or relaxation tests be performed and the modulus (compliance) obtained therefrom be shifted horizontally (and sometimes vertically) to obtain the modulus (compliance) over a longer time scale. As given by Cartner [5,6], a relaxation modulus master curve produced in the described manner for the previously discussed modified epoxy is shown in Fig. 7. It is

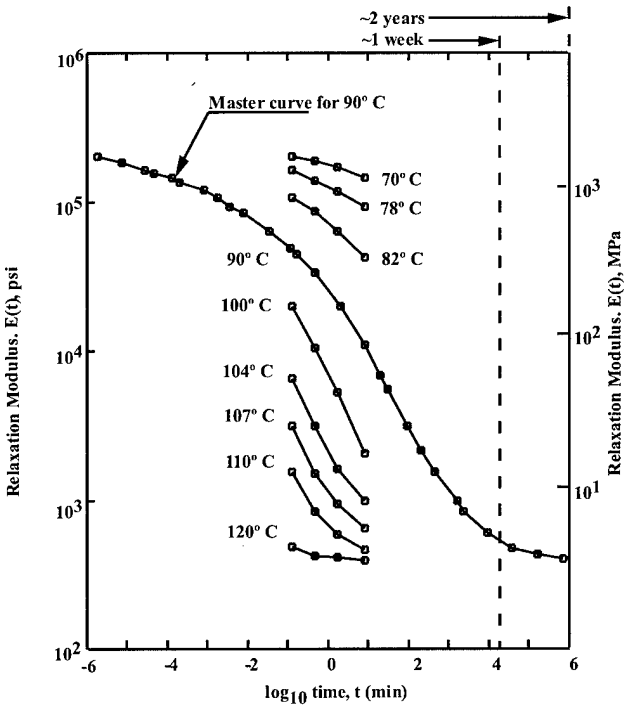

Fig. 7. Master curve for a modified epoxy.

to be noted that this master curve extends from 10^{-6} to 10^{16} or from a fraction of a second to about two years. This was accomplished using measured data from relaxation tests over a time interval of about 10 min. The resulting curve, if TTSP is valid, can be shifted to the right by one decade to become the master curve for 82° and the resulting master curve would provide data over 20 years. Obviously, an additional decade of shifting to be roughly equivalent to a master curve for 78° would provide data over approximately 200 yr. Clearly with this method predictions of behavior over a design lifetime of 40 or 50 yr is possible providing the approach is proven valid.

Another manner of producing a master curve is through the use of the TSSP. Here, creep or relaxation tests are performed at various stress levels over a short time and shifted to produce a master curve (see, Griffith [7,8] for a comprehensive review of shifting procedures). A non-linear viscoelastic procedure proposed by Schapery [25] is a formal mathematical statement of the TSSP method. His method, based upon irreversible thermodynamics, gives rise to the constitutive equation

$$\varepsilon(t,\sigma) = g_0 D_0 \sigma(t) H(t) + g_1 \int_0^t \tilde{D}(\psi - \psi') \left\{ \frac{\mathrm{d}[g_2 \cdot \sigma(\tau) H(\tau)]}{\mathrm{d}\tau} \right\} \mathrm{d}\tau, \quad (7)$$

where $\tilde{D}(\psi - \psi')$ is the transient linear viscoelastic compliance and g_0, g_1, g_2, a_σ are material parameters which are dependent on stress. The parameter a_σ is a shift factor which modulates the time scales given by ψ and ψ' through the equations

$$\psi(t,\sigma) = \int_{-\infty}^{t} \frac{\mathrm{d}t}{a_\sigma(t)} \quad \text{and} \quad \psi'(\tau,\sigma) = \int_{-\infty}^{\tau} \frac{\mathrm{d}\tau}{a_\sigma(\tau)}. \quad (8)$$

Schapery suggested a power law be used to represent the linear compliance as

$$D(t) = D_0 + \tilde{D} = D_0 + D_1 t^n, \quad (9)$$

and with this form Eq. (7) for a creep test becomes

$$\varepsilon(t) = \left[g_0 D_0 + g_1 g_2 D_1 \left(\frac{t}{a_\sigma} \right)^n \right] \sigma_0. \quad (10)$$

Using Eqs. (5), (6) and (10) an equation for the time-to-creep-to-yield for a non-linear viscoelastic material can be found and is given by [5,6],

$$t_f = \left[\frac{1}{C\beta\sigma_f} \ln \left(\frac{\sigma_f - A}{B} \right) \right]^{1/n}, \quad (11)$$

where n is the power law creep exponent and β is given by

$$\beta = D_1 \frac{g_1 g_2}{a_\sigma^n} \left(1 + 2\nu^2\right)^{1/2} \quad (12)$$

and ν is Poisson's ratio (which has been assumed to be constant).

Cartner used Eq. (10) to represent creep data with the result shown in Fig. 8. Notice the agreement is quite good for lower stress levels but not so good for high stress levels. The modified epoxy is quasi-brittle due to the inclusion of a rubber-toughening agent to create ductility. Where the original epoxy is quite brittle, the modified epoxy will have a strain at rupture of about 5% but crazing initially begins at about 2–3%. The crazing is a form of damage and likely one of the newer damage theories would be a better representation of behavior at higher stress levels.

Cartner also used Eq. (11) to represent the time-to-creep-to-failure (rupture) for the same material as shown in Fig. 8. Examination of the creep to rupture times in Fig. 9 indicate an excellent fit between theory and experiment. However, it is likely that the viscoelastic damage model developed by Weitzman [32] would also fit the data and would be a more rigorous approach. It is appropriate to note that Weitzman's method includes permanent deformation due to damage (i.e. such as microcracking or the crazes shown in Fig. 5) but does not include permanent deformation due to viscous effects which can be construed as a form of damage. On the other hand, the recent thermodynamic approach of Schapery [33] does include both types of permanent deformation and could also likely be used to represent the data of Fig. 9. The advantage of the Weitzman

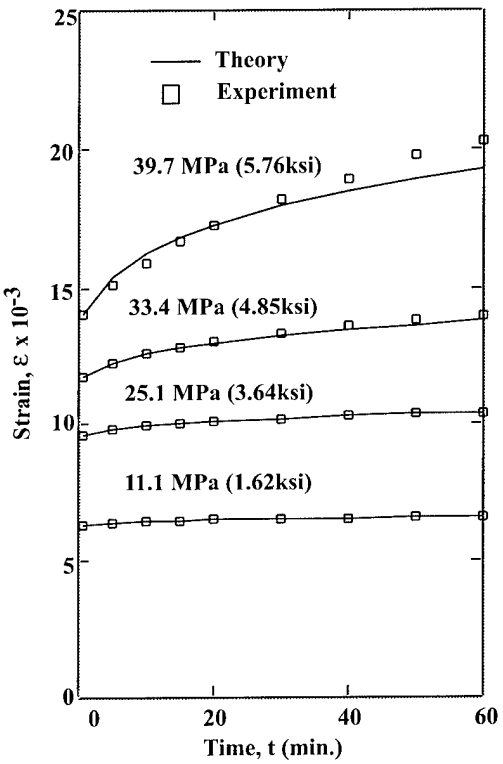

Fig. 8. Comparison between nonlinear theory and experiment for a modified epoxy in creep [5,6].

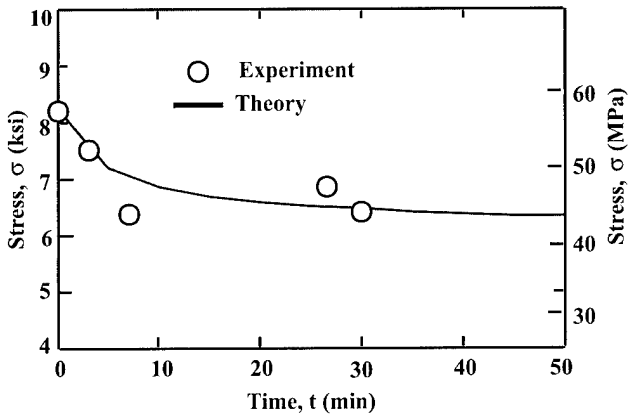

Fig. 9. Comparison between theory and experiment for creep to rupture failures in a modified epoxy.

model is that it does have a "built in" time dependent failure law.

The forgoing Schapery single integral non-linear viscoelastic method was used by Cartner et al. [5,6] to represent the creep behavior of a sheet molding compound (SMC-25) and the above modified viscoelastic/plasticity approach of Nagdi–Murch–Crochet was used to represent creep to rupture failures in the same material [5,6].

Before closing, it is to be noted that for laminated PMC materials the Tsai–Hill or one of the other failure theories for orthotropic materials may be modified to determine time dependent failures for individual plies under multi-axial stress states. In the case of the Tsai–Hill criterion, the law may be written as

$$\frac{\sigma_1^2}{X(t_r)^2} - \frac{\sigma_1\sigma_2}{X(t_r)^2} + \frac{\sigma_2^2}{Y(t_r)^2} + \frac{\tau_{12}^2}{S(t_r)^2} = 1, \tag{13}$$

where the denominators in (13) are the time dependent tensile strength in the fiber direction, transverse to the fiber direction and in-plane shear. Eq. (13) was first suggested and used by Dillard [9,10] with the exception that the well known Zhurkov equation was used instead of the failure law of Crochet.

Finally, it is clear the procedure to predict time dependent failure using Eq. (11) is only proven valid for a limited time frame. To predict failures over many years, a master curve in creep formed in a manner similar to the relaxation master curve given in Fig. 7 but for a time period equal to the design life must fitted with either the power law or a Prony series. As will be seen in the next section, the prony series approach is likely the better option. Further, this method, at present, does not allow the calculation of deformations beyond the yield point as do other models of viscoplasticity [26].

5. An energy based time dependent failure method

As reported by Hiel [11,12], Bruller [18,19] has made extensive studies of a time dependent failure theory originally proposed by Reiner and Weissenberg [17]. Their approach recognizes that a viscoelastic material when loaded (e.g. creep) both stores and dissipates energy. The total strain energy varies with time and is the sum of stored or free energy (recoverable portion) and dissipated energy (non-recoverable portion). The total energy as well as its components can be separated into a deviatoric part (shape change) and a part due to dilatation (volume change). The Reiner–Weissenberg (R–W) theory suggests the deviatoric free (stored) energy is responsible for failure. They also note that if energy is dissipated faster than energy is stored, failure will never occur. On the other hand, if the material stores energy faster than is dissipated, the stored energy will eventually reach a critical state and the material will fail. Hence a delayed yield/failure condition may occur for a viscoelastic material under arbitrary loading conditions in general and under uniaxial creep loading (constant stress) in particular. The theory assumes no permanent deformation due either to viscous effects or microcracking such as crazes. That is, the viscoelasticity is similar to that of a three-parameter solid. In order to predict long term behavior, it is necessary to represent stress–strain response over a long time which can best be accomplished with a master curve similar to the one given in Fig. 6 using either TTSP, TSSP or both. One method to mathematically model a master curve is to use a Prony series and this method is reported here.

Hiel [11,12], following Bruller's work, has shown that for a viscoelastic material under a creep load, the stored free energy in the springs, the dissipated energy in the dampers and the total energy of the system is given by

$$W_{\text{springs}} = \sigma_0^2\left[\frac{D_0}{2} + \sum_{i=1}^{n}\frac{D_i}{2}(1 - \exp(-t/\tau_i))^2\right], \tag{14}$$

$$W_{\text{dampers}} = \sigma_0^2\left[\sum_{i=1}^{n}\frac{D_i}{2}(1 - \exp(-2t/\tau_i))\right], \tag{15}$$

$$W_{\text{total}} = \sigma_0^2\left[\frac{D_0}{2} + \sum_{i=1}^{n}D_i(1 - \exp(-t/\tau_i))\right], \tag{16}$$

where D_0, D_i and τ_i are the necessary coefficients and relaxation times of the Prony series used to represent the compliance master curve of the material. Eqs. (14)–(16) are for total (shear and bulk) strain energy for a material in uniaxial tension and not just deviatoric (shear) free energy. However, Bruller [41] has shown, assuming Poisson's ratio to be a constant, that the deviatoric stored energy comprises 93% of the total energy in a uniaxial tension test. The stored energy due to volume

change is relatively small and for purposes, herein it is assumed that the deviatoric and total free energy is the same.

The master curve for a $[90°]_{8s}$ graphite/epoxy composite as determined by Hiel [9,10] using TTSP is shown in Fig. 10. A six-term Prony series representation of the data is also shown and as may be observed the agreement between the two is excellent.

Using the Prony series fit of the master curve in Fig. 10, it is now possible to compute the total energy, the stored free energy and the dissipated free energy from Eqs. (14)–(16). The results are shown in Fig. 11 normalized with respect to the initial total energy. (Because the calculation is made at $t = 0$ min. using the Prony series and not $t = 0.1$ min, the normalized total energy is slightly larger than one.) The total energy and the stored

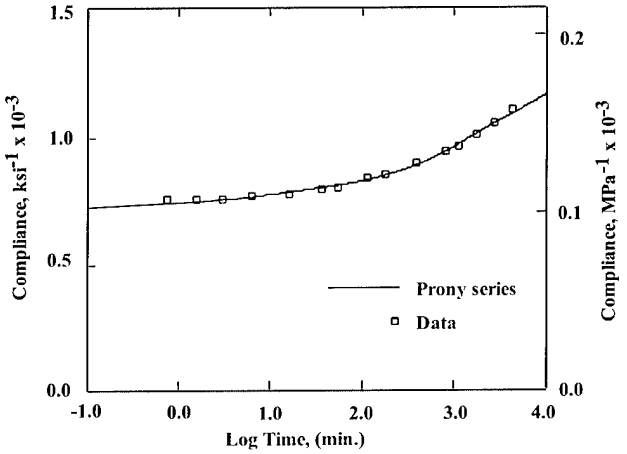

Fig. 10. Comparison between a TTSP master curve and a six term prony series for a [90°] graphite/epoxy composite at 160°C (320°F) and a stress of 35.7 MPa (5.18 ksi).

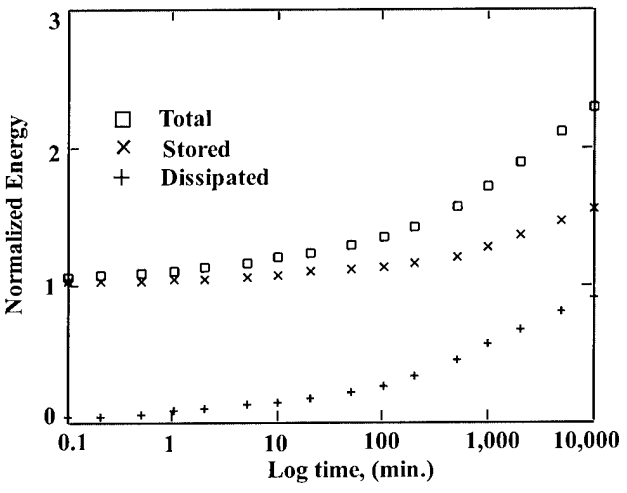

Fig. 11. Total stored and dissipated energy as calculated from Eqs. (14) (16) normalized with respect to the initial total energy ($t = 0$ min) using the prony series representation of the master curve in Fig. 10.

energy are the same initially and therefore, if sufficient creep stress is imposed, failure will occur upon loading. If a lower creep stress is imposed, dissipation will prevent failure until a critical stored energy is reached. The R–W theory suggests that the critical value of stored energy for failure at different creep stresses is a constant. In order to verify the theory, creep to rupture tests were performed by Hiel [11,12] on the same graphite/epoxy material. The results are shown in Fig. 12 along with the predictions using the R–W theory. The theory curve was obtained by finding a constant stored energy that would best fit the data. It should be recalled that in Fig. 11 the stored energy is the sum of the stored deviatoric and stored dilatational free energy. To use only the deviatoric free energy would require a small correction of about 7% and would only mean a small change in the precise value to the constant energy necessary to fit the data. Three-dimensional problems, on the other hand, may have much more energy associated with bulk behavior and the separation of stress states may be essential for accurate predictions. This point will be discussed further in the conclusions.

Instead of a Prony series, the power law given by Eq. (9) is sometimes used to represent the master curve given in Fig. 10. In fact, Hiel suggested this approach and developed the following simple equation for predicting the time-to-failure

$$t_f = \left[\frac{1}{\beta\sigma_f^2}\left(w - \frac{1}{2}g_0 D_0 \sigma_f^2\right)\right]^{1/n}, \tag{17}$$

where

$$\beta = D_1 \frac{g_1 g_2}{a_\sigma^n}\left(1 - 2^{n-1}\right). \tag{18}$$

In (17) and (18), it is assumed that material is non-linear and the constants D_0, D_1, and n as well as the parameters g_0, g_1, g_2 and a_σ are as previously defined. The quantity w is the dissipated deviatoric energy and is a

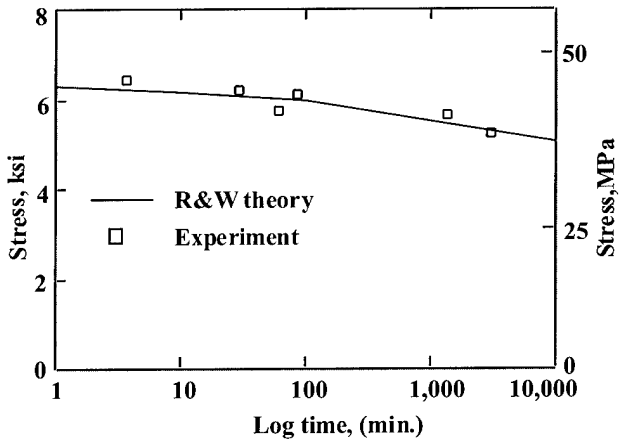

Fig. 12. Comparison between R–W theory and experiment [11,12].

material constant. This approach requires less parameters than that of Nagdi–Murch–Crochet method providing the power law is a good representation of the master curve. It would also require many less parameters than the Prony series method just discussed. Hiel concluded that the $[90°]_{8s}$ graphite/epoxy composite tested was linearly viscoelastic over the time frame of his measurements. For this reason the quantities g_0, g_1, g_2 and a_σ could be assumed to be equal to unity and Eq. (17) further simplified.

In the present investigation an attempt was made to use the power law defined by Eq. (9) with coefficients appropriate for the master curve of Fig. 10. However, with this approach it was not possible to find a constant stored energy that would represent the creep rupture data of Fig. 11. A likely reason can be visualized by examination of Fig. 13. In Fig. 13, the six term Prony series given previously in Fig. 10 is extended an additional two decades. It is to be noted that the series representation of the master curve reaches a plateau, which is typical of all polymers. The power law can be made to fit a portion of the master curve but will not reach a plateau and as is shown schematically will continue to rise without bound. As a result, it would be surprising if the time-to-failure given by Eq. (17) using the power law representation could adequately represent creep to rupture data over the glassy, transition and rubbery regions of a polymer. On the other hand, obviously from Fig. 13, the Prony series can adequately represent all the regions of behavior of a polymer.

Shown in Fig. 14 are the R–W predictions of creep rupture given in Fig. 12 extended an additional two decades together with Hiel's creep rupture data. Here it is seen that the failure stress prediction will also reach a plateau for a given constant stored energy at failure.

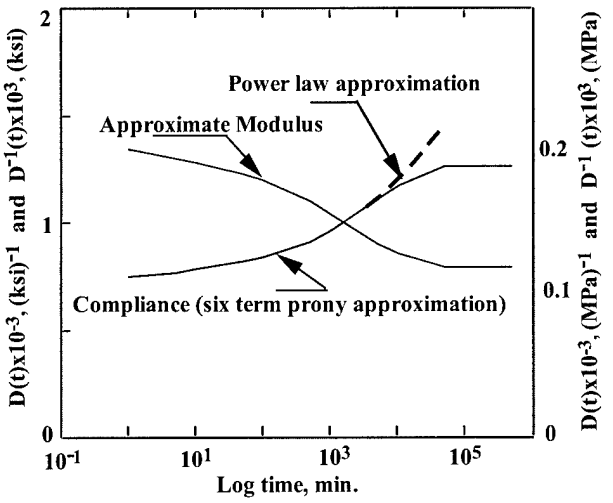

Fig. 13. Six term prony series representation of the compliance master curve of Fig. 8 extended to 10^6 min.

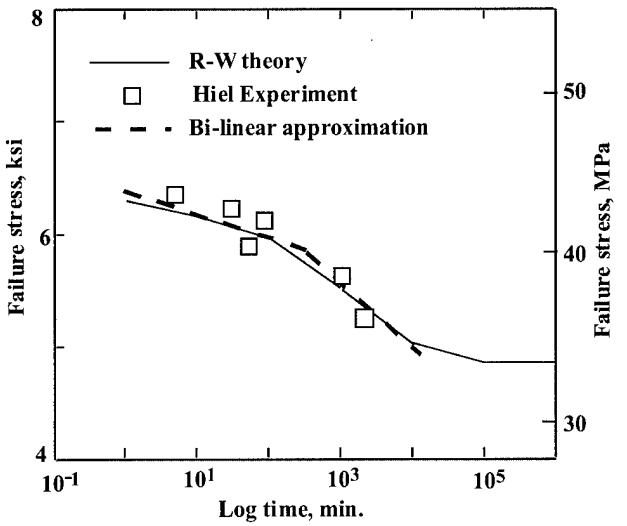

Fig. 14. R–W predictions of Fig. 12 extended to 10^6 min. Hiel's creep rupture data is also shown with an empirical bi-linear approximation.

Again, it is quite reasonable for the failure stress to become a constant in the rubbery plateau region of a polymer. The inverse of the Prony series representation of the compliance is given in Fig. 13 to approximate schematically the change in relaxation modulus with time. It is interesting to note that that variation in the measured and predicted failure stress with time have essentially the same shape as the variation of relaxation modulus with time. In other words, this seems to verify that a change in modulus does indeed represent a change in strength as is suggested by recent viscoplasticity or damage evolution theories.

Included in Fig. 14 is an empirical bi-linear approximation to the creep rupture data of Hiel. An examination of the R–W theory gives credence to the notion of "knee" in the creep to rupture life of a polymer as has been reported by others (see Kinloch [42], p. 213). It is reasonable to assume that the so-called knee is just a manifestation of the change of material properties when moving from the glassy region to the transition region of the polymer. In fact, it is likely that another "knee" would be found at longer times for a lower creep stress at the change of properties taking place in going from the transition to rubbery plateau region of a polymer.

Assuming a creep test was conducted at room temperature on the graphite/epoxy discussed here, the time-to-failure would be exceedingly long. The only reason that creep ruptures could be found within four decades of time was because, the tests were conducted at 160°C (380°F) and a high level of stress. In this instance, caution is suggested for the preceding interpretations as no data for the master curves shown in Fig. 13 or the strength curve shown in Fig. 14 was obtained for times longer than 4 decades and, therefore, the existence of a rubbery plateau was not verified for this composite.

6. Summary and conclusions

Various matrix dominated failure modes together with experimental verification have been reviewed for polymer based composites. In addition, evidence of a relaxation to failure phenomenon was demonstrated and it was suggested that all matrix-dominated failures are a function of time and may occur under constant load. Several new viscoplasticity and/or damage theories developed for the purpose of modeling degradation of the matrix dominated time dependent moduli of PMC materials were reviewed. It was noted that for models that consider changes in moduli as evidence of damage on the basis of measured stress–strain response, care must be taken to insure that homogeneous stress and strain states exist. Evidence of damage (craze) development in a modified epoxy was presented and a new digital imaging method to quantify stress–strain response in micro-domains was described. The digital imaging approach offers the possibility not only of measuring response within damage regions but also offers the opportunity to observe damage as it develops. In the near future, it will likely be possible to measure deformations within a similar sized region as the mesh used in finite element analyses creating the exciting prospects of interactive analysis and experiment within a region smaller than a micron.

While the rigor of viscoplastic or viscoelastic approaches to damage is not in doubt, it was suggested that they are not necessarily at a stage to be used by design engineers, especially those with insufficient training. As a possible means of placing rational methods to predict time dependent failure in the hands of design engineers, two much older approaches due to Nagdi et al. and Reiner et al. have been discussed. It has been shown that each is capable of predicting time dependent failures in both polymers and polymer composites where TTSP procedures are used to develop moduli over many decades of time. It has also been suggested that the degradation of the moduli of structural polymers and PMC materials over long periods of time can be obtained using a combination TTSP and TSSP testing procedures. While not yet proven, it is possible that the development of master curves in this manner can lead to accurate knowledge of PMC moduli for periods perhaps as long as the 20–50 year life of many engineering structures. A Prony series can be used to represent the master curves and either of the time dependent failure prediction methods discussed herein can be used to predict delayed failures. The master curves together with the time dependent failure laws can be incorporated into either lamination theory or finite element methods to predict the failure of complex structures. However, each approach needs more development. The Nagdi et al. method as used herein only predicts delayed failures in one dimension. In order to use the technique for multi-axial stress states, the theory needs to be extended for use beyond the yield/failure limit in a manner similar to the viscoplasticity theories that have been developed primarily for metals. Also, the χ_{ij} of Eqs. (4) and (5) needs to be further investigated to validate it's use for 3-D problems.

It is to be noted that the R–W criterion, as presented, is only valid for a viscoelastic solid which is suitable for a thermoset polymer or PMC materials where a thermosetting polymer is used as a matrix material. It is not likely to be valid for a thermoplastic polymer, which is best represented as a viscoelastic fluid. Neither does the approach include the possibility of damage such as craze development. However, the procedure is easily modified to include viscous permanent deformation and, because it is an energy technique, can be modified to include deformation due to damage. Arenz [43] used the theory in it's present form and found that it does not seem to work well in predicting the demarcation between linear and non-linear viscoelastic behavior for PVAc, a thermoplastic polymer. It would be interesting to see if a modified version would correlated theory and experiment for his material. Also it would be interesting to modify the theory to include the evolution of damage and to determine if the creep data of the modified epoxy in Fig. 8 could be better represented at higher stress levels.

The R–W energy approach is appealing as it is analogous to well known energy approaches for elastic materials and because only one additional parameter is needed beyond those normally found to represent moduli or compliances. The required parameter is a critical value of the stored deviatoric strain energy. Here, as previously explained, the total strain energy was used because for the case of uniaxial tension with a constant Poisson's ratio, the bulk behavior only contributes 7% to the total energy and therefore the difference between total stored energy and stored deviatoric strain energy was neglected. In some three-dimensional cases, the bulk behavior may be much more important. In fact, many polymers are more sensitive to bulk properties than is the case for structural metals. For example, in the case of a tubular riser being used to bring oil from a depth of 6000 feet of water or more, the stress state due to internal and external pressure would surely shorten the time-to-failure for a high axial tensile stress. As a result, it is felt that a critical value of total stored energy may be a better predictor of failure than only the stored deviatoric energy. Thus, it is suggested that to best predict failure, TTSP and/or TSSP master curves should be found using shear and bulk testing procedures such as those developed by Ravi-Chandar [44], Emri [45] or Wang [46].

Several issues exist to the rapid development of the procedures suggested above. First and foremost, TTSP and TSSP methods individually and in combination are

only known to be valid near or above the glass-transition temperature of a polymer. As polymers and composites are most often used as structural components in their glassy region, much better understanding of shifting procedures at lower temperatures need to be addressed. In addition, very little test information is available especially for the long times needed to gain confidence for engineering design. Unfortunately, industry users and government agencies are not willing to provide funds needed to sustain long term research programs that could develop model materials, short and long term data bases and the comparison of theory and experiment. The current efforts of Wang [46] to develop analytical and experimental lifetime design procedures (with industry support) for the use of PMC materials in offshore applications is a step in the right direction but progress will be slow until more *long term* dedicated fundamental research programs are initiated and funded by government agencies.

Only uniaxial tests data have been discussed here. There is a great need for multi-axial test data and for better procedures to measure strain distributions from initial load to failure. It is suggested that together with the acquisition of 3-D time dependent moduli and strength data for both shear and bulk behavior, the R–W criterion needs to be verified. Should the total stored strain energy in shear an bulk be found to be a constant at failure for different stress states, it would tend to verify that a the theory could be used much in the same manner that current failure theories are used for elastic materials.

There is little doubt to the author that all the procedures discussed herein could be developed in a user friendly manner for design engineers provided that resources are made available. Not only is it possible but such action is a necessity to insure the reliability and safety of the use of new and evolving light weight and high performance polymer matrix composites and to protect the public from unnecessary risks.

Acknowledgements

The author wishes to acknowledge to significant contributions of many former students and colleagues in producing the data and the development of the theories herein discussed.

References

[1] Schapery RA. Stress analysis of viscoelastic composite materials. J Compos Mater 1967;1:153–92.
[2] Brinson HF, Morris DH, Yeow YT. A new experimental method for the accelerated characterization and prediction of the failure of polymer-based composite laminates. In: Proceedings of the Sixth International Conference for Experimental Stress Analysis, Munich, West Germany. September 1978;395–400.
[3] Yeow YT. The time–temperature behavior of graphite/epoxy laminates. Ph.D. Thesis, Va. Tech. 1978.
[4] Yeow YT, Morris DH, Brinson HF. The time–temperature behavior of a unidirectional graphite/epoxy laminate. Composite Materials: Testing and Design, (5th Conference), STP 674, Philadelphia, PA: ASTM, 1979:263–81.
[5] Cartner JS. The non-linear viscoelastic behavior of adhesives and chopped fiber composites. M.S. Thesis, Va. Tech. 1978.
[6] Cartner JS, Griffith WI, Brinson HF. The viscoelastic behavior of composite materials for automotive applications. Compos Mater Automotive Industry, ASME 1978;159–69.
[7] Griffith WI. The accelerated characterization of viscoelastic composite materials. Ph.D. Thesis, Va. Tech. 1980.
[8] Brinson HF, Griffith WI, Morris DH. Creep rupture of polymer–matrix composites. In: Proceedings of the Fourth International Congress on Experimental Stress Analysis, and Experimental Mechanics, September 1981;329–35.
[9] Dillard DA. Creep and creep rupture of laminated graphite/epoxy composites. Ph.D. Thesis, Va. Tech. 1980.
[10] Dillard DA, Brinson HF. A numerical procedure for predicting creep and delayed failures in laminated composites. Long Term Behavior of Composites, ASTM-STP 31, Phil. PA 1983;23–37.
[11] Hiel C. The non-linear viscoelastic response of resin matrix composites. Ph. D. Thesis, U. of Brussels (VUB), 1983.
[12] Hiel C, Cardon AH, Brinson HF. The non-linear viscoelastic response of resin matrix composites. In: Marshall IH, editor. Compos Struct, vol. 2. Applied Science 1983;271–81.
[13] Tuttle M. Accelerated viscoelastic characterization of T300/5208 graphite/epoxy laminates. Ph.D. Thesis, Va. Tech. 1980.
[14] Tuttle ME, Brinson HF. Prediction of the long-term creep compliance of general composite laminates. Exp Mech 1986;26(1):89–102.
[15] Nagdi PM, Murch SA. On the mechanical behavior of viscoelastic/plastic solids. J Appl Mech September 1963;321–28.
[16] Crochet MJ. Symmetric deformations of viscoelastic–plastic cylinders. J Appl Mech June 1966;327–34.
[17] Reiner M, Weissenberg K. A thermodynamic theory of the strength of materials. Rheological Leaflet 12939;1:12–20.
[18] Bruller OS. The energy balance of a viscoelastic material. Int J Polym Mater 1973;2:137–48.
[19] Bruller OS. Energy-related failure of thermoplastics. Polym Eng Sci 1981;21(3):145–50.
[20] Gamstedt EK, Berglund LA, Peijs T. Influence of interfacial strength on micro- and macroscopic fatigue behavior of longitudinal glass fiber reinforced polypropylene. In: Reifsnider KL, Dillard DA, Cardon AH. editors. Progress in durability analysis of composite systems. Rotterdam: Balkema, 1998;137–42.
[21] Yeow YT, Morris DH, Brinson HF. The fracture behavior of graphite/epoxy laminates. Exp Mech 1979;19(1):1–8.
[22] Brinson HF, Griffith WI, Morris DH. Creep rupture of polymer matrix composites. Exp Mech 1981;21(9):329–36.
[23] Hahn HT. Fatigue behavior and life predictions of composite laminates. In: Tsai, editor. Composite materials: testing and design. STP 674. Philadelphia: ASTM, 1979;383–417.
[24] Christensen RM. Stress based yield/failure criteria for fiber composites. Int J Solids Structures 1997;34(5):529–43.
[25] Schapery RA. On the characterization of non-linear viscoelastic materials. Polym Eng Sci 1969;9(4):295–310.
[26] Gates TS. Experimental Characterization of non-linear, rate dependent behavior in advanced polymer matrix composites. Exp Mech 1992;32(1):68–73.
[27] Kachanov LM. An introduction to continuum damage mechanics. Boston: Martinu Nijhoff; 1986.
[28] Vujosevic M, Krajcinovic D. Creep Rupture of polymers – a statistical model. Int J Solids Structures 1997;34(9):1105–22.
[29] Weitsman YJ. A continuum damage model for viscoelastic materials. J Appl Mech 1988;55:773–80.

[30] Zocher MA, Allen DH, Groves SE. Stress analysis of a matrix-cracked viscoelastic laminate. Int J Solids Structures 1997;34(25):3235–57.
[31] Smith LV, Weitsman YJ. Inelastic behavior of randomly reinforced polymeric composites under cyclic loading. Mechanics of time dependent materials 1998;1:293–305.
[32] Abdel-Twab, Weitsman YJ, A coupled viscoelastic/damage model with applications to swirl-mat composites. Int J Damage Mechanics October 1998;7:351–80.
[33] Schapery RA. Non-linear viscoelastic and viscoplastic constitutive equations based on thermodynamics. Mechanics of time dependent materials 1997;1:209–40.
[34] Akshantala NV, Brinson LC. A damage evolution model for aging viscoelastic composite laminates. J Comp Tech Res (In review).
[35] Brinson LC, Gates TS. Viscoelasticity and aging of polymer matrix composites. In: Talreja R, editor. Comprehensive Composite Materials, vol. 2. New York: Elsevier (to appear in 2000).
[36] Renieri MP, Herakovich, CT, Brinson, HF. Rate and time dependent behavior of structural adhesives. Virginia Tech Report, VPI-E-76-7, April 1976.
[37] Brinson HF. Micro-measurement of mechanical properties of adhesives and composites based on a digital imaging technique. In: Proceedings of the 1995 Spring SEM Meeting, p. 484–90.
[38] Ha K, Schapery RA. A three-dimensional viscoelastic constitutive model for particulate composites with growing damage and its experimental verification. Int J Solids Structures 1998;35(26–27):3479–517.
[39] Lu HB, Vendroux G, Knauss WG. Surface deformation measurements via digital image correlation. GALCIT SM Report 96-1, California Institute of Technology, 1996.
[40] Chu TC, Ranson WF, Sutton MA, Peters WH. Application of digital-image-correlation techniques to experimental mechanics. Experimental mechanics, 25 September 1985;232.
[41] Bruller OS. Phenomenological characterization of the non-linear viscoelastic behavior of plastics. Private communication. 1989, Technical University of Munich.
[42] Kinloch AJ, Young RJ. Fracture Behavior of Polymers. London: Chapman and Hall; 1995.
[43] Arenz RJ. Non-linear shear behavior of poly(vinyl acetate) material. Mechanics of time dependent materials 1998–1999;2(4):287–305.
[44] Ravi-Chandar K. Pressure relaxation experiments in polycarbonate. In: Proceedings of the International Conference on Materials and Mechanics, Tokyo, July 20–22, 1997;497–90.
[45] Prodan T, Emri I. Pressure influence on mechanical properties of viscoelastic materials. International Conference on Advance Technology in Experimental Mechanics 1999, JSME-MMD, pp. 23–31.
[46] Karayaka M, Srinivasan S, Miyase A, Wang SS. Leakage damage and failure of glass-fiber reinforced composite tubular vessels under combined internal pressure and axial loading. In: Poursartip A, Street K. editors. Proceedings of the International Conference on Composite Materials (ICCM-10), vol. 1. August 14–18, Whistler, 1996;747–54.

ELSEVIER

Composite Structures 47 (1999) 457–462

COMPOSITE STRUCTURES

www.elsevier.com/locate/compstruct

Analysis and development of the angular twist type torque-meter

Yeon Doo Cheong [a], Ji Woong Kim [b,*], Se Hoon Oh [b], Chong Won Lee [b]

[a] *Department of Precision Mechanical Engineering, Samchok National University, Samchok-shi 245-711, South Korea*
[b] *Department of Mechanical Engineering, Chungang University, Dongjak-gu, Seoul 156-756, South Korea*

Abstract

The measurement of torque is essentially required for the precise machinery assembly, the improvement of machine performance and the control of power transmission system. The torque sensing part has a qualification such that the torsional stiffness is larger than the bending stiffness for high accuracy extent. Also the deflection of rotational part should be linearly proportional to the input torque and the power loss of coupling should be minimized. Now, the encoder technology is well developed enough to measure even a small twist angle. The type of rotating torque transducer discussed in this paper is the angular twist-type, which utilizes the principle of measuring the angular twist in a gage length proportional to the torque transmitted. This kind of shaft phase of torque-meter should have low stiffness in order to give a high resolution, but the low stiffness can cause a low resonant frequency, which will deteriorate the measuring system. In this paper, the torque-meter using two encoders are designed and manufactured with the rotating stainless steel bar. It is found that the values of axial strain calculated by the equation are in good agreement with the measuring values. Experiments also have been carried out to obtain strain distribution on the sensing plate surface and to investigate the effect of the surrounding conditions. The torque-meter using STS304 bar is designed and manufactured by the proposed equations. © 2000 Published by Elsevier Science Ltd.

Keywords: Torque-Meter; Glass fiber epoxy composite; Carbon fiber epoxy composite; Co-cured; Adhesively bonded

1. Introduction

The need of torque measurement is increased as the mechanical product capacity is developed. The measurement of torque is essentially required for the precise machinery assembly, the improvement of machine performance and the control part about power transmission system. A non-metal material is widely used in aircraft and electronic industries. For example, each of machinery part has to be solidly fastened in a tolerance limit when a machine is assembled.

The torque sensing part has a qualification to provide the greater torsional stiffness than the bending stiffness for high accuracy extent. The deflection of rotational part should be linearly proportional to input torque and the effect of coupling should be minimized as well. The torque range is limited by yield stress, and torsion angle of sensing part is restricted such as 0.25° per 1 m of shaft length. Due to this reason, the strain-gage type torque-meter is commonly used. The form of strain-gage type torque-meter is shown in Fig. 1.

The fourth strain-gages are bonded on the shaft surface in the direction of ±45° and are connected by the bridge type. The output signal goes to the amplifier by a slip ring. Strain-gages A, C are deformed by tension forces, and strain-gages B, D by shear forces. Therefore, bending and tension stresses are set-off so that the output signal from strain-gage would indicate the torque element. When DC voltage V is charged between A and C, the Eq. (1) shows the voltage between B and D.

$$E = \left[\frac{R_1R_3 - R_2R_4}{(R_1 + R_2)(R_3 + R_4)}\right]V. \tag{1}$$

Abrasion of the slip rings causes inferiority of the accuracy. This is the problem of strain-gage type torque-meter.

There have been many researches to develop an improved model. Buchele [1] proposed the brushless type torque-meter, which had the characteristics such that a slip ring and brush reading signal were replaced from the rotating shaft. Lapeyre [2] and Buchele [3] introduced that a refracted ray of light could check the twist angle. Eichenlaub [4] suggested the system to read the absolute position by inserting the reference tooth, intending to overcome a handicap of not reading the value when the torque-meter did not work. However the

* Corresponding author.
E-mail address: jiwoongl@nanmail.net (J. Woong Kim).

0263-8223/99/$ - see front matter © 2000 Published by Elsevier Science Ltd.
PII: S0263-8223(00)00010-6

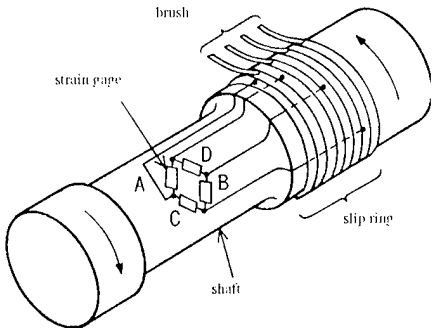

Fig. 1. Strain-gage type torque-meter.

functions brought about rotating motion, such as natural frequency, etc., prevented the torque-meter from being used for general industrial machines that was rotating about 5000 rpm.

Now the encoder technology is well developed enough to measure a small twist angle [5,6]. As shown in Fig. 2, the type of rotating torque transducer discussed in this paper is the angular twist-type. It employs the principle to measure the angular twist in a gage length, which is proportional to the transmitted torque. This kind of torque-meter should have low stiffness to give a high resolution, but the low stiffness can cause low resonance frequency, which will deteriorate the measuring system [7].

Here, the STS304 bar, a rotating shaft, is designed and manufactured by certain proposed conditions. It is found that the values of axial strain calculated by the equation are in good agreement with the measuring values. Experiments have been performed to obtain strain distribution on the surface of the sensing plate and to investigate the effect of surrounding conditions.

It is important for torque-meter to analyze the stiffness and linearity of rotating bar and to decide dimension for torque range. In this paper, the inside of the rotating bar was reinforced with glass and carbon fiber–epoxy composite co-cured and adhesively bonded, in order to enhance the damping capacity of the manufacturing productivity of the rotating bar that was manufactured using both composites and STS304. The composite part, as well known, increases the natural frequency and damping capacity of the torque-meter.

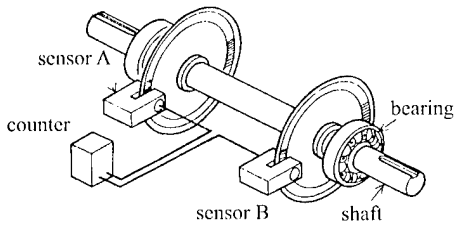

Fig. 2. The angle twist type torque-meter.

Here stress analysis and vibration characteristics were calculated using NASTRAN, a commercial finite element analysis software for the various types of conditions. Two kinds of model: a STS304 rotating bar and a STS304-composite bar bonded both sides are analyzed.

2. Manufacture of the rotating shaft

The properties of the STS304, composite materials and epoxy resin that were used for the rotating shaft are shown in Table 1, Table 2, Table 3, respectively [8,9].

The co-cured rotating bar was manufactured by laying-up composite prepreg on each side of the STS304 and curing in an autoclave with a cure cycle as shown in Fig. 3.

The surface of the STS304 was abraded by using #80 mesh sandpaper giving a better adhesion of the composite to the STS304.

The stacking sequences of the composites for the manufacture of the rotating shaft were $[\pm 30°/STS304]_{2s}$, $[\pm 45°/STS304]_{2s}$ and $[\pm 60°/STS304]_{2s}$. The shapes of the torque-meter discussed here are shown in Fig. 4.

3. Mechanical properties of torque-meter

The bar is twisted so that each section rotates about its torsion center. The torsional stiffness (k_t) of the bar can be expressed by the general Eq. (2).

Table 1
Properities of STS304

Tensile modulus (GPa)	193
Shear modulus (GPa)	76.8
Possion's ratio	0.25
Tensile strength (MPa)	640
Density (kg/m^3)	7700

Table 2
Properties of the composite materials

	Glass-fiber	Carbon-fiber
E_L (GPa)	43.5	130
E_T (GPa)	5	8
G_{TL} (GPa)	5	6
ν_{TL} (GPa)	0.25	0.28
ρ (kg/m^3)	1997	1661

Table 3
Properties of the epoxy resin (IPCO 9923)

Tensile modulus (GPa)	1.3
Shear modulus (GPa)	0.46
Possion's ratio	0.41
Tensile strength (MPa)	45
Shear strength (MPa)	29.5
Lap shear strength (MPa)	13.7
Density (kg/m^3)	1200

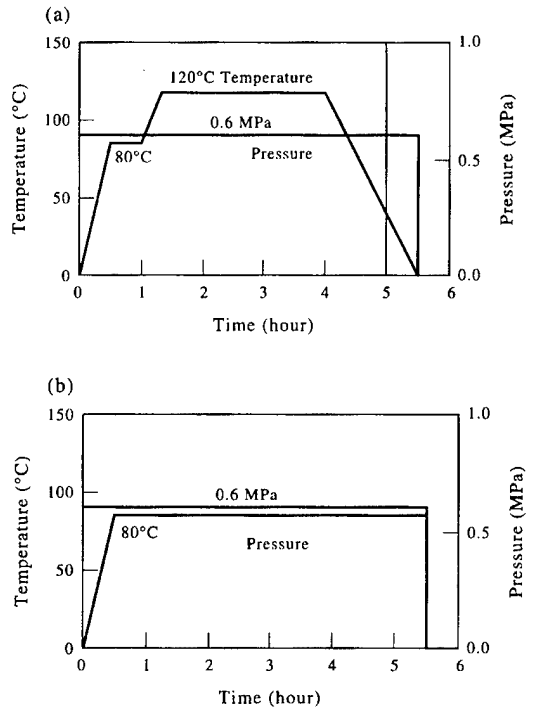

Fig. 3. Cure cycle for the composite materials and the epoxy resin.

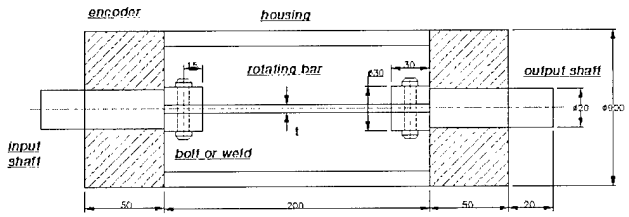

Fig. 4. The schematic diagram of torque-meter rotating shaft.

$$k_t = \frac{T}{\phi} = \frac{GJ}{L}. \tag{2}$$

J is a torsional constant dependent on the form and dimensions of the cross-section, and is defined in Table 4. Photographs of the torque-meter rotating shaft and manufactured torque-meter are shown in Fig. 5 and Fig. 6, respectively.

By using the properties of material, the torque range was determined. As STS304 is the ductile structure, a boundary between elasticity and plasticity is the yield stress. So the maximum stress was found by the yield stress $T_{max} = 23.675$ Nm. Therefore T_{max} was the basis of durability test and torque test.

4. Measurement of the spring constant of the torque-meter

The stiffness of the torque-meter in the radial direction must be high for the capacity of power transmission. It might be increased too much due to the reinforcement of the composite. The spring constant of the torque-meter was measured by extending the rotating shaft with tensile

Table 4
Properties of the torsional constant and maximum shear stress of STS304 shaft

Form and dimensions of cross-section	Solid rectangular section a a>b b a : the major axis b : the minor axis
Formula for J in $k_t = (GJ)/L$	J (torsional constant) $= ab^3(1 - 0.63(b/a) - 0.052(b^5/a^5))$
Formula for shear stress	τ_{max} (maximum shear stress) $= 3T/(ab^2(1 - 0.63(b/a) - 0.052(b^5/a^5))$ at midpoint of each longer side

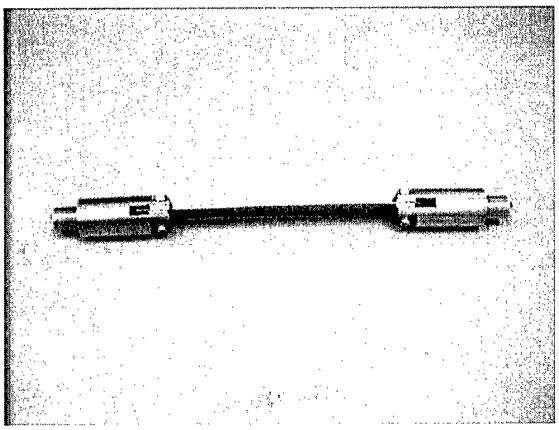

Fig. 5. The photograph of torque-meter rotating shaft.

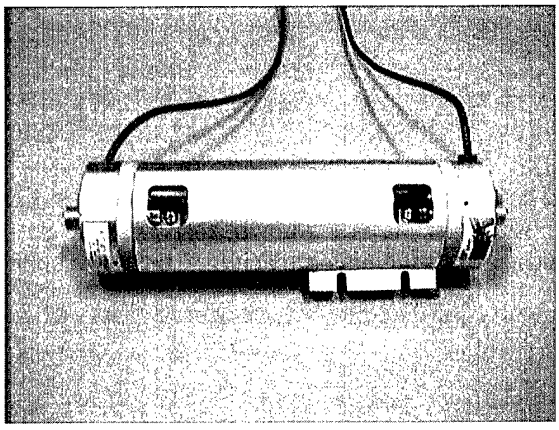

Fig. 6. The photograph of torque-meter.

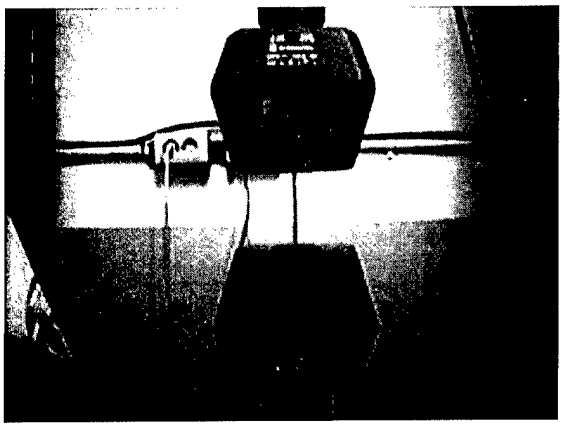

Fig. 7. The tensile tester of the rotating shaft.

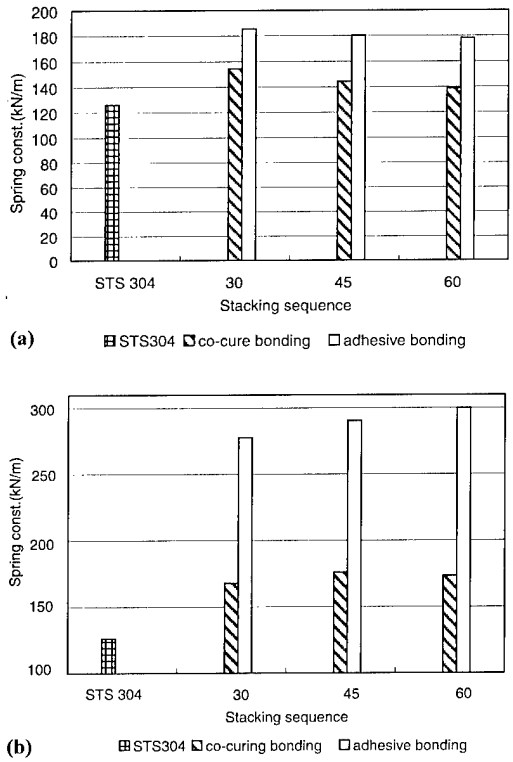

Fig. 8. Spring constants of the torque-meter with respect to the stacking sequence and bonding type: (a) reinforced with the glass fiber-epoxy composites; (b) reinforced with the carbon fiber-epoxy composites.

tester, as shown in Fig. 7. After tensile test, stiffness was determined by a grade of graph.

Fig. 8 shows the measured stiffness of the torque-meter in the radial direction with respect to stacking sequence and bonding type such as co-cure bonding and adhesive bonding. As shown in Fig. 8(a), in case of glass fiber–epoxy composite, the stiffness of the torque-meter in the radial direction was slightly decreased as the stacking angle was increased.

From the test results, it was found that the stiffness of the torque-meter was strongly dependent on the type of composite and the stacking sequence. When a 3-mm thick STS304 was reinforced by co-cure bonding with the carbon fiber–epoxy composite and with the glass fiber–epoxy composite, with a $[\pm 30°/\mathrm{STS304}]_{2s}$ stacking sequence, the radial stiffness was increased by about 35% and 23% compared with that of the unreinforced STS304 torque-meter.

When the STS304 rotating shaft was reinforced by adhesive bonding with the glass fiber–epoxy composite and with the carbon fiber–epoxy composite, with a $[\pm 30°/\mathrm{STS304}]_{2s}$ stacking sequence, the stiffness was increased about 50% and 137%. Therefore, it was concluded that the carbon fiber–epoxy composite material and the high stacking angle from the axis of the torque-meter were beneficial because the capacity of power transmission is high.

5. Vibration characteristics of the torque-meter

The vibration characteristics of the torque-meter were measured using the impulse-frequency response test. The test apparatus consists of an impulse hammer (B&K 8202), a dual-channel fast Fourier transform analyzer (B&K 3550), an amplifier (NTS 1250), an accelerometer (B&K 4383), and PC with an HCTL-1100 board for data acquisition and A/D card. The fundamental natural frequency and damping ratio were measured by giving radial impulses on the rotating shaft suspended with jig, as shown in Fig. 9.

Fig. 10 shows the fundamental natural frequency of the co-cured and adhesively bonded rotating shaft reinforced with the glass fiber–epoxy composite and carbon fiber–epoxy composite with respect to stacking sequence of the rotating shaft. Fig. 11 shows the damping ratio of the co-cured and adhesively bonded rotating shaft reinforced with the glass

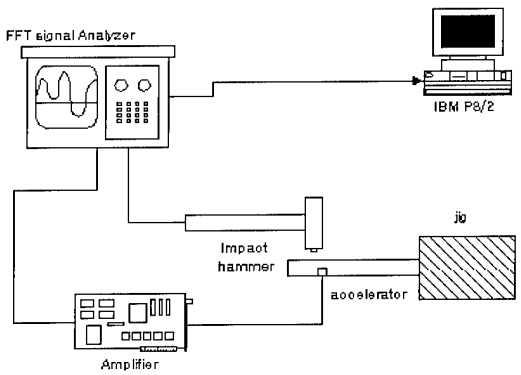

Fig. 9. Impulse-frequency response test of the rotating shaft.

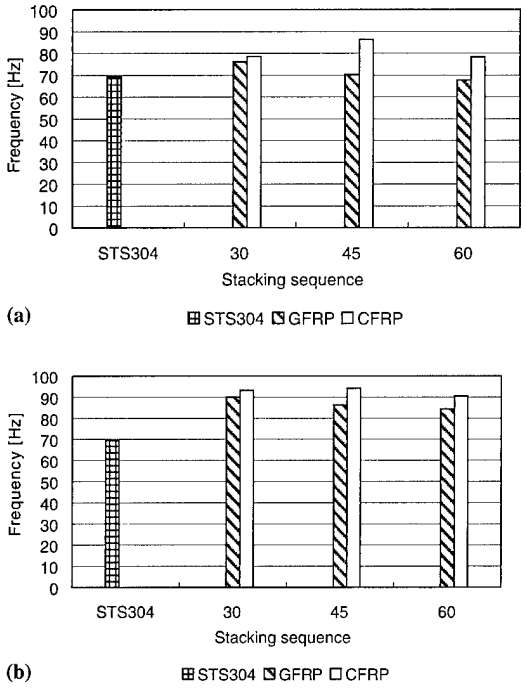

Fig. 10. Natural frequency of the torque-meter rotating shaft with respect to the stacking sequence and bonding type: (a) co-cured torque-meter rotating shaft; (b) adhesively bonded torque-meter rotating shaft.

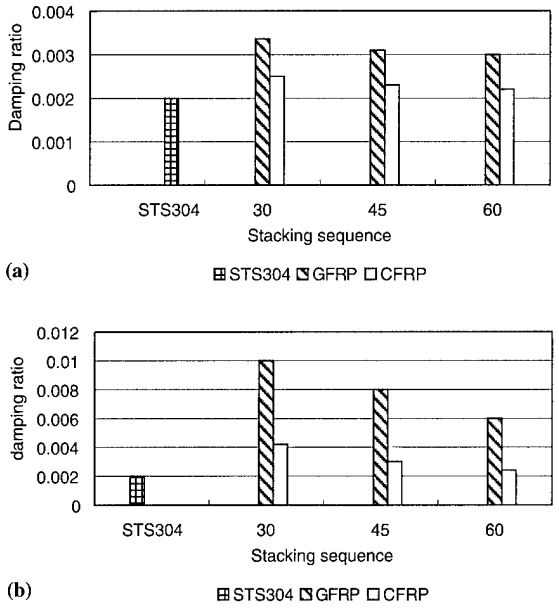

Fig. 11. Damping ratio of the torque-meter rotating shaft with respect to the stacking sequence and bonding type: (a) co-cured torque-meter rotating shaft; (b) adhesively bonded torque-meter rotating shaft.

fiber–epoxy composite and carbon fiber–epoxy composite with respect to stacking sequence of the rotating shaft.

As shown in Fig. 10(a), in case of glass fiber–epoxy composite, the fundamental natural frequency of the co-cured rotating shaft was decreased as the stacking angle was increased and in case of carbon fiber–epoxy composite in Fig.10(b), the fundamental natural frequency of the co-cured rotating shaft was symmetric.

The vibration characteristics of the rotating shaft were greatly dependent on the properties of the composite materials as stacking angle was increased. When the stacking angle was 45° of the rotating shaft reinforced with the carbon fiber–epoxy composite, the fundamental natural frequency was increased by 38% compared with that of the unreinforced rotating shaft of 3-mm thickness.

As shown in Fig. 11, the damping ratio of the rotating shaft was decreased as the stacking angle was increased. When the stacking angle was 30° of the rotating shaft reinforced with the carbon fiber–epoxy composite, the damping ratio was increased by about 500% compared with that of the unreinforced rotating shaft of 3-mm thickness.

From the test results, it is found that the adhesively bonded rotating shaft reinforced with the glass fiber–epoxy composite was more beneficial.

6. Torque test

The torque transmission capabilities of the torque-meter, manufactured either by co-curing or by adhesive bonding were tested. The test was on the rotating shaft which consisted of the glass fiber–epoxy composite with a stacking sequence of $[\pm 30°/STS304]_{2s}$, $[\pm 45°/STS304]_{2s}$, $[\pm 60°/STS304]_{2s}$ and a STS304 bar of thickness 3 mm.

Fig. 12 shows the apparatus for the torque test of the torque-meter. During the torque test, the welding-joint section of the torque-meter failed at the applied torque of 110 Nm. As the rated torque transmission capability of the torque-meter was 23.675 Nm, further tests were not performed. Therefore it was concluded that the torque-meter had a sufficient torque transmission capability.

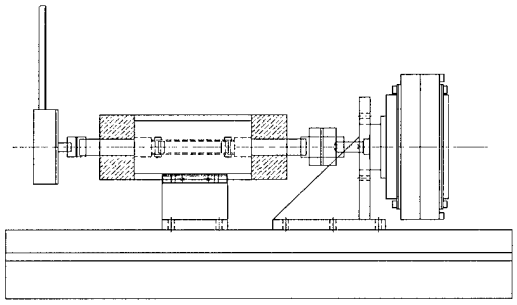

Fig. 12. The torque tester of torque-meter rotating shaft.

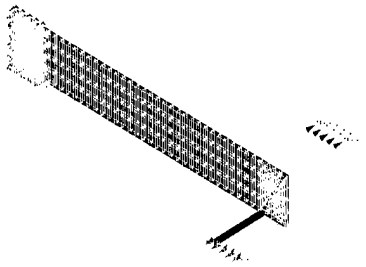

Fig. 13. Finite element model for the torque-meter rotating shaft applied by a couple of forces.

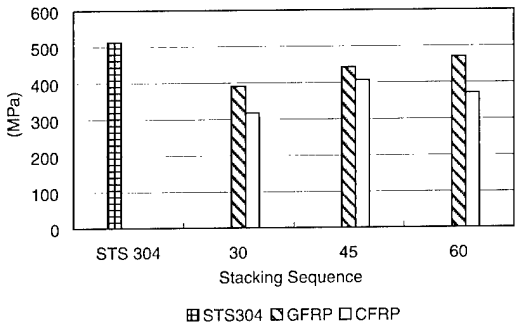

Fig. 14. Maximum Von-mises stresses with respect to the stacking sequence.

7. Finite element analysis of the torque-meter

The maximum Von-mises stresses with respect to the stacking sequence was calculated by finite-element method using NASTRAN, commercial software compared to the experimental results when it was subjected to the maximum rated torque of the torque-meter.

Polar coordinates are used for finding the twist-angle about torque.

For the torque analysis, the one end side element nodes were fixed in the radial and axial directions to prevent out-of-plane deformation. As shown in Fig. 13, the 23.675 Nm torque was applied to the another end nodes in the y-direction by means of couple of forces.

As shown in Fig. 14, when the rotating shaft was composed of 0.3 mm STS304 bar and the glass fiber–epoxy composite, with a stacking sequence of $[\pm 30°/\mathrm{STS304}]_{2s}$, the maximum stresses were 390.27 MPa. When the rotating shaft was composed of 0.3 mm STS304 bar and the carbon fiber–epoxy composite, with a stacking sequence of $[\pm 30°/\mathrm{STS304}]_{2s}$, the maximum stresses were 317.64 MPa. Therefore, it was concluded that the rotating shaft reinforced with the carbon fiber–epoxy composite had good torque transmissibility.

8. Conclusions

In this paper, the angular twist type torque-meter was designed and manufactured with STS304 and fiber-reinforced composite materials to improve the dynamic properties of the existing torque-meter. The carbon fiber–epoxy composite and glass fiber–epoxy composite were either co-cure bonded or adhesively bonded to the surface of STS304 to produce the rotating shaft of torque-meter.

Analysis has been applied on each kinds of model. Stress, stiffness, natural frequency and damping ratio were investigated as vibration characteristics.

From the experimental and numerical results, it was found that the adhesively bonded torque-meter rotating shaft had better dynamic characteristics than those of the co-cured and unreinforced torque-meter rotating shaft. For the torque-meter rotating shaft adhesively bonded and reinforced with the glass fiber–epoxy composite, with a stacking sequence of $[\pm 30°/\mathrm{STS304}]_{2s}$, the damping ratio and the radial stiffness was increased by 500% and 137% compared to those of the unreinforced torque-meter rotating shaft.

Finally, the conclusion is that the most appropriate shaft is the adhesively bonded torque-meter rotating shaft reinforced with the glass fiber–epoxy composite, with a stacking sequence of $[\pm 30°/\mathrm{STS304}]_{2s}$.

Acknowledgements

This research was supported by Chung-Ang University research grants in 1998.

References

[1] Buchele WF. Strain-gauge brushless torque-meter. United States patent, 3881347, 1975.
[2] Lapeyre JM. Optical shaft torque-meter. United states patent, 4188883, 1979.
[3] Buchele WF. Laser optical torque-meter. United states patent, 5705810, 1998.
[4] Eichenlaub IL. Torque measurement apparatus containing embedded data structure and related method. United states patent 4602515, 1986.
[5] Lee Dai-Gil. The manufacture of one-piece automotive drive shafts with aluminum and composite materials. Comp Struct 1997;38(1–4):309–19.
[6] Oh Se-Hoon. The properties of a steel-composite hybrid flexspline. Comp Struct 1997;38(1–4):251–60.
[7] Himmelsten S, et al. Manual of the choice of the right torque sensor. Bulletin 1995;705A.
[8] Roark JR. Formulas for stress and strain. New York: McGraw-Hill, 1975. p. 286–323.
[9] Pilkey DW. Formulas for stress, strain, and structural matrices. 1994:141–209.

ELSEVIER

Composite Structures 47 (1999) 463–469

COMPOSITE STRUCTURES

www.elsevier.com/locate/compstruct

A simulation study on the thermal buckling behavior of laminated composite shells with embedded shape memory alloy (SMA) wires

Hyo Jik Lee [a], Jung Ju Lee [a,*], Jeung Soo Huh [b]

[a] *Department of Mechanical Engineering, Korea Advanced Institute of Science and Technology, 373-1 Kusong-dong, Yusong-gu, Taejon 305-701, South Korea*

[b] *Department of Metallurgical Engineering, Kyung Pook National University, Sankyuk-dong, Taegu 702-702, South Korea*

Abstract

In this paper, numerical simulation analyses of the thermal buckling behavior of laminated composite shells with embedded shape memory alloy (SMA) wires were performed to investigate the effect of embedded SMA wires on the characteristics of thermal buckling. In order to simulate the thermomechanical behavior of SMA wires, the constitutive equation of the SMA wires was formulated in the form of an ABAQUS user subroutine. The computational program was verified by showing the response of the pseudoelasticity and shape memory effect (SME) at various temperatures and stress levels. Modeling of the laminated composite shells with embedded SMA wires and thermal buckling analyses were performed with the use of the ABAQUS code linked with the subroutine of the formulated SMA constitutive equations. The thermal buckling analyses of the composite shells with embedded SMA wires show that the critical buckling temperature can be increased and the thermal buckling deformation can be decreased by using the activation force of embedded SMA wire actuators. © 2000 Published by Elsevier Science Ltd.

Keywords: Thermal buckling; Critical buckling temperature; Shape memory effect; Constitutive equation; Smart structures

1. Introduction

Fiber-reinforced composite laminates show promise for increasing applications in engineering structures because of their high stiffness and strength-to-weight ratio. However, their resistance to buckling has been the major concern of research for a long time because their critical buckling load is lower than their compressive strength. Buckling can occur by the compressive forces caused by either external loads or thermal loads. Thermal loads are important factors in composite structures with large fluctuations in temperature. Fiber-reinforced composite laminates exhibit a passive response to the critical buckling temperature, which is dependent on the geometry and material properties of the structures. Recently, in order to increase thermal buckling resistance, research has focussed increasing attention on applications of the smart structure concept for composite structures, because smart structures display sensing and actuating capability. Shape memory alloy (SMA) actuators have advantages over other actuators in terms of a high power to volume ratio; they are suitable for problems of large deformation. SMA actuators also have the unique capability of changing their physical properties, such as stiffness, damping ratio and viscosity, in response to external stimuli and thus can be considered smart materials. Hence, SMA actuators have high control authority and are suitable for buckling problems that accompany large deformations. SMAs have two inherent characteristics: One is the shape memory effect (SME) and the other is superelasticity or pseudoelasticity.

Recently, Ro and Baz [1,2] showed that the static and buckling characteristics of flexible fiberglass SMA-reinforced composite plates were controlled by activating optimal sets of SMA wires embedded along the midplane of these plates. The SMA wires were pre-tensioned and activated to generate significant phase recovery forces in order to increase the membrane strain energy, which in turn increased the critical buckling load of the SMA-reinforced plates. Thompson and Loughlan [3] showed that restoration forces, associated with embedded activated pre-strained SMA wires, have been successfully employed to enhance the postbuckling behavior of laminated plate structures while under the influence of a uniaxial load. Also, Choi and Lee [4]

* Corresponding author. Tel.: +82-42-869-3033; fax: +82-42-869-3210 or 5210.

E-mail address: jjlee@sorak.kaist.ac.kr (J.J. Lee).

0263-8223/99/$ - see front matter © 2000 Published by Elsevier Science Ltd.
PII: S0263-8223(00)00020-9

studied the shape control of a composite beam with embedded SMA wire actuators, and the effects of the reactive moment of the SMA wire actuators on the shape control test were observed in detail.

The response of a cantilevered beam to an internal actuator force exerted by SMA wire was examined by Chaudhry and Rogers [5]. Contrary to normal expectations, such an internal force, although compressive, did not produce any buckling tendencies or any other instabilities in the beam.

Zhong et al. [6] investigated the thermal buckling and postbuckling behavior of composite plates with embedded SMA fibers. Their results showed that SMA fibers could greatly reduce or completely eliminate the postbuckling deflection at certain elevated temperatures.

In the present study, the thermal buckling behavior of composite laminated shells with embedded SMA wires under thermal loadings was investigated for the cases of two boundary conditions, clamped–clamped (CC) and simply supported–simply supported (SS), of composite laminated cylindrical shells and plates. Modeling and nonlinear thermal buckling analyses were performed through the ABAQUS [7] code linked with SMA's constitutive relation that was formulated in the form of an ABAQUS user subroutine.

2. Constitutive equation of SMA

Generally two phases, martensite (M) and austenite (A), exist in shape memory alloys and their fractions vary with temperature and stress conditions. Tanaka [8], Liang and Rogers [9], and Brinson and Lammering [10] have developed one-dimensional constitutive equations based on phenomenological thermo-mechanics. The constitutive equation by Tanaka relates the stress (σ) to the strain (ε), temperature (T) and martensite fraction (ξ) in the following form:

$$\dot{\sigma} = \frac{\partial \sigma}{\partial \varepsilon}\dot{\varepsilon} + \frac{\partial \sigma}{\partial T}\dot{T} + \frac{\partial \sigma}{\partial \xi}\dot{\xi} = D(\xi)\dot{\varepsilon} + \Theta\dot{T} + \Omega(\xi)\dot{\xi}. \tag{1}$$

Here, $D(\xi)$ is Young's modulus, Θ the thermoelastic tensor, and $\Omega(\xi)$ the transformation tensor, and the coefficients can be expressed as follows:

$$D(\xi) = D_a + \xi(D_m - D_a), \quad \Omega(\xi) = -\varepsilon_L D(\xi), \tag{2}$$

where D_m is the modulus value for the SMA of 100% martensite, D_a the modulus value for the SMA of 100% austenite, and ε_L the maximum recoverable strain or the recovery strain limit. Because the martensite fraction depends on the stress and temperature, transformation kinetics must be coupled with Eq. (1) to formulate a complete governing equation for SMA. Liang and Logers [9] developed a constitutive equation based on a cosine model to represent the martensite fraction as follows:

(i) Phase transformation from A to M:
For $C_M(T - M_s) < \sigma < C_M(T - M_f)$

$$d\xi = \frac{1-\xi_0}{2}(-)\sin[a_M(T - M_f) + b_M\sigma]\cdot a_M\, dT + \frac{1-\xi_0}{2}(-)\sin[a_M(T - M_f) + b_M\sigma]\cdot b_M\, d\sigma. \tag{3}$$

(ii) Phase transformation from M to A:
For $C_A(T - A_f) < \sigma < C_A(T - A_s)$

$$d\xi = \frac{\xi_0}{2}(-)\sin[a_A(T - A_s) + b_A\sigma]\cdot a_A\, dT + \frac{\xi_0}{2}(-)\sin[a_A(T - A_s) + b_A\sigma]\cdot b_A\, d\sigma. \tag{4}$$

The material constant ξ_0 is the martensite fraction before phase transformation begins and a_M, a_A, b_M and b_A are material constants in terms of the transition temperatures, A_s, A_f, M_s and M_f as follows:

$$a_M = \pi/(M_s - M_f),$$
$$a_A = \pi/(A_f - A_s),$$
$$b_M = -a_M/C_M,$$
$$b_A = -a_A/C_A,$$

where C_M, C_A are material constants related to the influence of stress on the phase transformation. In order to solve the stress–strain relations, Eqs. (3) and (4) must be substituted for Eq. (1); then the results are written in the incremental form as

(i) Phase transformation from A to M:

$$d\sigma = \frac{D}{1 + b_M\Omega((1-\xi_0)/2)\sin[a_M(T - M_f) + b_M\sigma]}\, d\varepsilon + \frac{\Theta - a_M\Omega((1-\xi_0)/2)\sin[a_M(T - M_f) + b_M\sigma]}{1 + b_M\Omega((1-\xi_0)/2)\sin[a_M(T - M_f) + b_M\sigma]}\, dT. \tag{5}$$

(ii) Phase transformation from M to A:

$$d\sigma = \frac{D}{1 + b_A\Omega(\xi_0/2)\sin[a_A(T - A_s) + b_A\sigma]}\, d\varepsilon + \frac{\Theta - a_A\Omega(\xi_0/2)\sin[a_A(T - A_s) + b_A\sigma]}{1 + b_A\Omega(\xi_0/2)\sin[a_A(T - A_s) + b_A\sigma]}\, dT. \tag{6}$$

Stress from these Eqs. (5) and (6) and martensite fraction from Eqs. (3) and (4) can be solved iteratively. The above process was programmed and processed in an ABAQUS user subroutine which is used in defining the mechanical constitutive equations of the material. In the user subroutine, it is important to define the tangent modulus ($\partial\sigma/\partial\varepsilon$) and the updated stress at every increment when the strain and temperature increments are passed information as shown in the flow chart of Fig. 1. To verify this program, we simulated the pseudoelastic behavior and the constrained recovery force by the SME as shown in Figs. 2 and 3 with the SMAs properties as shown in Table 1.

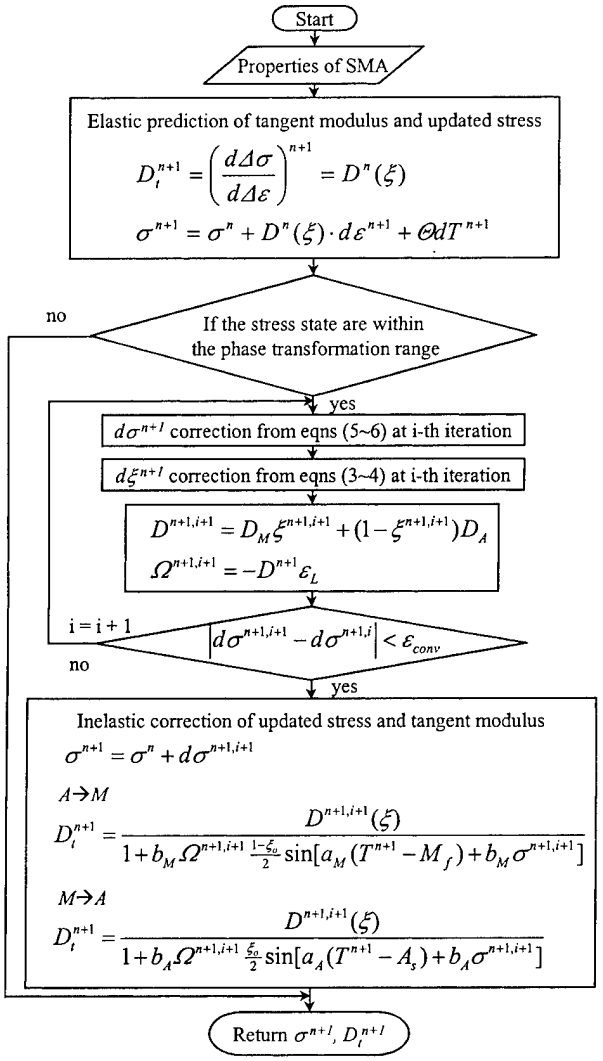

Fig. 1. Algorithm of SMA constitutive equation for ABAQUS user subroutine.

3. Modeling of laminated composite shells with embedded SMA wires

The incremental form of the SMA constitutive equation was formulated in the form of an ABAQUS user subroutine in which specific material behavior can be specified. Then, this subroutine was linked with an ABAQUS input file. Modeling of laminated composite shells and thermal buckling analysis were also performed through ABAQUS.

Two-node quadratic beam element B33 for the SMA wire and 4-node doubly curved general-purpose shell element S4R for the laminated composite shell were selected. B33 and S4R are ABAQUS element names. This shell element is appropriate for large-strain analysis. The multi point constraints (MPC) option was used for constraint conditions between the wires and shell.

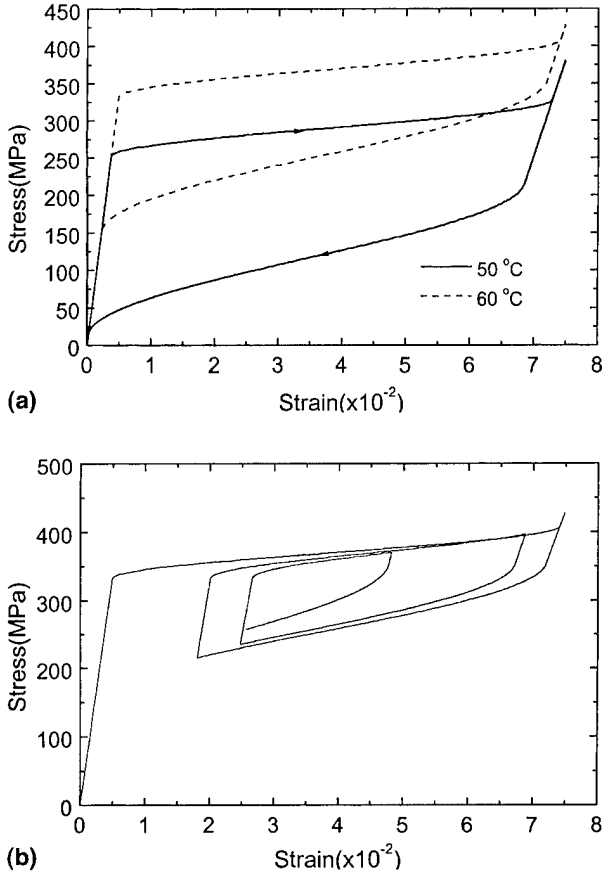

Fig. 2. (a) Pseudoelasticity with complete transformation; (b) pseudoelasticity with incomplete transformation.

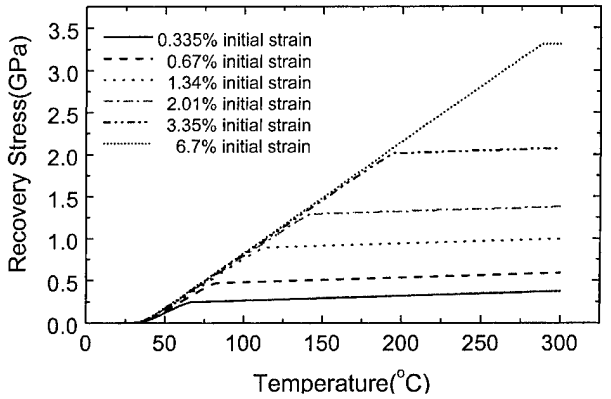

Fig. 3. Recovery stresses by shape memory effect with constraint initial strains.

The selected laminate composites were Carbon/Epoxy and the properties are listed in Table 2. In Table 2, subscript 1 denotes the direction parallel to the fiber orientation, subscript 2 denotes the direction transverse to the fiber orientation in plane, and subscript 3 denotes the direction perpendicular to the plane.

Table 1
Material properties of SMA

Coefficients of constitutive equation	$D_A = 67.0$ GPa
	$D_M = 26.3$ GPa
	$\Theta = 0.55$ MPa
Recovery strain limit	$\varepsilon_L = 0.067$
Four phase transformation temperatures	$M_f = 9°C$
	$M_s = 18.4°C$
	$A_s = 34.5°C$
	$A_f = 49°C$
Transition stiffness (stress/temperature)	$C_M = 8$ MPa/°C
	$C_A = 13.8$ MPa/°C
Diameter of wire	0.38 mm

Table 2
Properties of Carbon/Epoxy composite

$E_{11} = 135$ GPa
$E_{11} = 13$ GPa
$G_{12} = 6.4$ GPa
$G_{12} = 6.4$ GPa
$G_{12} = 4.3$ GPa
$\nu_{12} = 0.3$
$\alpha_{11} = -0.9°C^{-1}$
$\alpha_{22} = 27.0°C^{-1}$
$\alpha_{33} = 27.0°C^{-1}$

4. Thermal buckling analysis

The relationships between the temperature and normalized lateral displacement were obtained from the thermal buckling analysis. Thermal loads due to the change of temperature induced the thermal buckling because of the thermal expansion of the constrained composite structures. Geometric imperfections were required for the nonlinear thermal buckling analysis that was based on the mode shapes from a previous linear buckling analysis. The scaling factor of geometric imperfections controls the postbuckling behavior. Thus, nonlinear thermal buckling behavior is different if the scaling factor is different.

4.1. Laminated composite cylindrical panels

Thermal buckling occurs when structures are constrained and temperatures are increased. Fig. 4 shows the geometry, boundary conditions and position of the embedded SMA wires within the cylindrical shell. Through thermal buckling analyses, we investigated the effect of the number of embedded SMA wires and the effect of imperfections on the thermal buckling behavior. The size of the composite cylindrical shell was 200 mm × 100 mm × 45° ($L \times r \times \theta$) or 800 mm × 100 mm × 45° ($L \times r \times \theta$), and the thickness 0.5 mm. The stacking sequence was [90°/0°/SMA/0°/90°]. In the finite element modeling, the symmetric condition about mid line required only a half cylindrical shell modeling, and the numbers of meshes were 1200 shell elements for

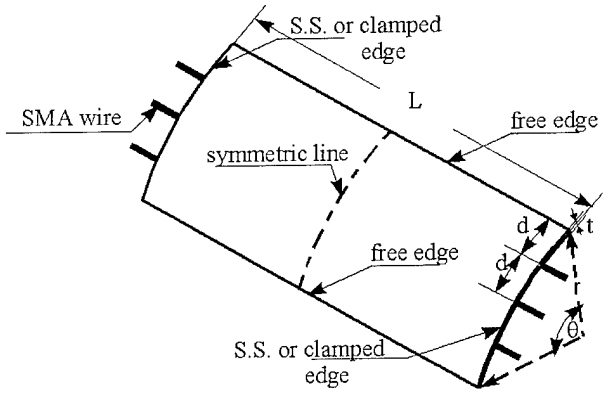

Fig. 4. Composite cylindrical panel with embedded SMA wires.

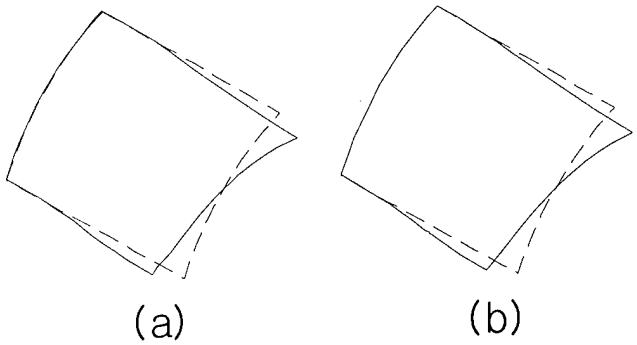

Fig. 5. First buckling mode of 1/2 composite cylindrical shells ($L/r = 2.0$) with (a) simply supported–simply supported boundary condition; (b) clamped–clamped boundary condition.

the cylindrical panel and 50 beam elements for one SMA wire.

Fig. 5 shows the results, obtained from the linear buckling analysis, of the thermal buckling modes. In Fig. 5, the first buckling mode with the CC boundary condition is similar to that with the SS boundary condition. Fig. 6 represents normalized lateral displacement of the center point at the free edge of Fig. 4 according to the temperature change without embedded SMA wires. In Fig. 7, three SMA wires are embedded. The results of Figs. 6 and 7 were obtained from nonlinear thermal buckling analyses. A comparison of Fig. 6 with Fig. 7 indicates that the critical buckling temperature increased by about 10°C. Here, the geometric imperfection determined the critical buckling temperature. The smaller the scaling factor of geometric imperfections, the higher the critical buckling temperature.

In Figs. 8 and 9, the normalized lateral displacement curves show the effect of the number of embedded SMA wires with the CC boundary condition and the SS boundary condition. The larger the number of embedded SMA wires, the higher the critical buckling temperature. Also, the larger the number of embedded SMA wires, the smaller the postbuckling deformations. In Figs. 8 and 9, a phase transformation does not occur in

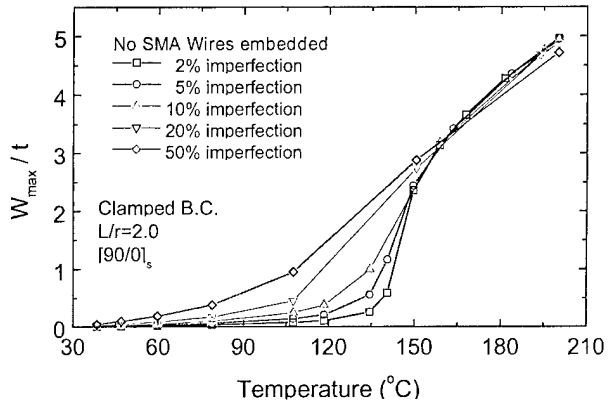

Fig. 6. Thermal buckling behavior of composite cylindrical panels without SMA wires.

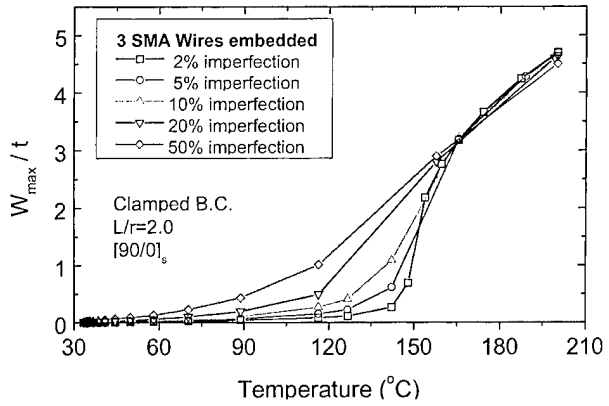

Fig. 7. Thermal buckling behavior of composite cylindrical panels with embedded SMA wires.

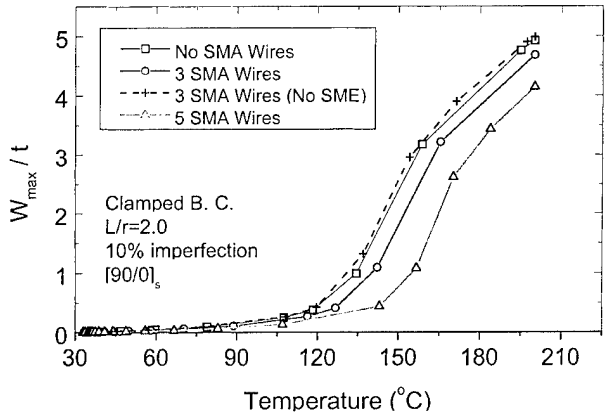

Fig. 8. Effects of embedded SMA wires on the thermal buckling behavior of composite cylindrical panels ($L/r = 2.0$) with clamped b.c.

the SMA wires without the SME in which case the phase is fixed to the martensite although the temperature changes. Thus, stiffeners without the SME never enhance the thermal buckling resistance.

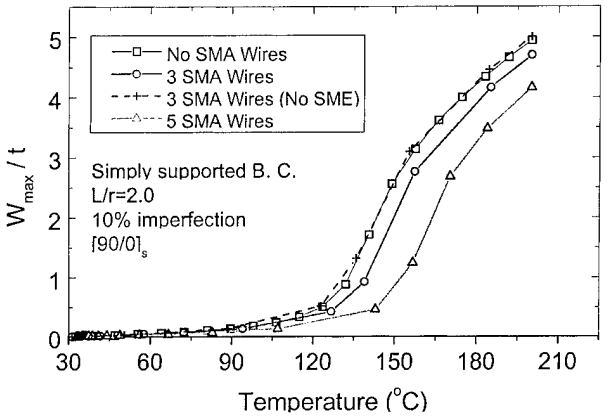

Fig. 9. Effects of embedded SMA wires on the thermal buckling behavior of composite cylindrical panels ($L/r = 2.0$) with simply surpported b.c.

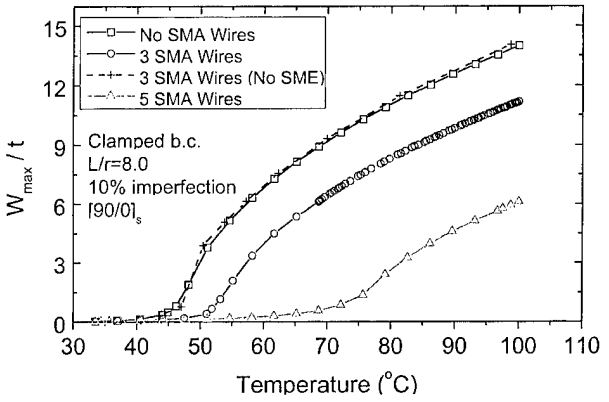

Fig. 10. Effects of embedded SMA wires on the thermal buckling behavior of composite cylindrical panels ($L/r = 8.0$) with clamped b.c.

Fig. 10 represents the thermal buckling behavior of longer cylindrical panels. In longer cylindrical panels, the critical buckling temperature is lower because they are susceptible to deformations. Here, SMA wires influence the thermal buckling behavior much more because the structure is much more flexible than short cylindrical panels.

4.2. Laminated composite plates

The schematic diagram of the composite plate is presented in Fig. 11. Since the plate is a symmetric cross-ply laminate, only a quarter of the plate was analyzed. The geometrical dimension is 300×200 ($L \times W$) mm, and in the finite element modeling of a quarter of the composite plate, the number of meshes are 720 shell elements for the composite plate and 24 beam elements for one SMA wire.

The nonlinear thermal buckling behavior of composite plates is represented in Figs. 12–14. The stacking sequences of laminated composite plates are [90°/0°$_2$/

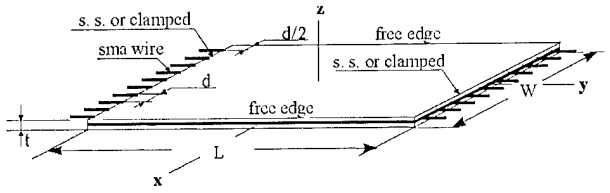

Fig. 11. Composite plate with embedded SMA wires.

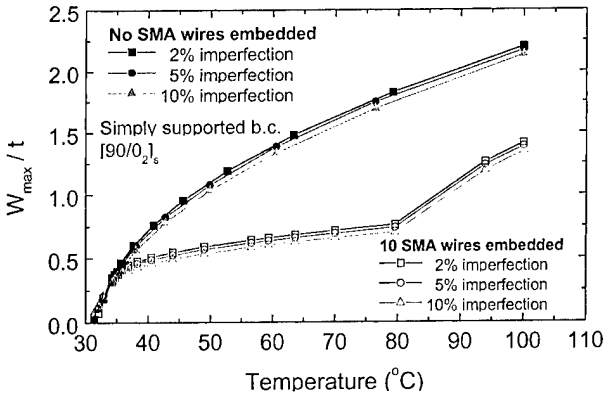

Fig. 12. Thermal buckling behavior of $[90/0_2]_s$ composite plates with embedded SMA wires and simply supported boundary condition.

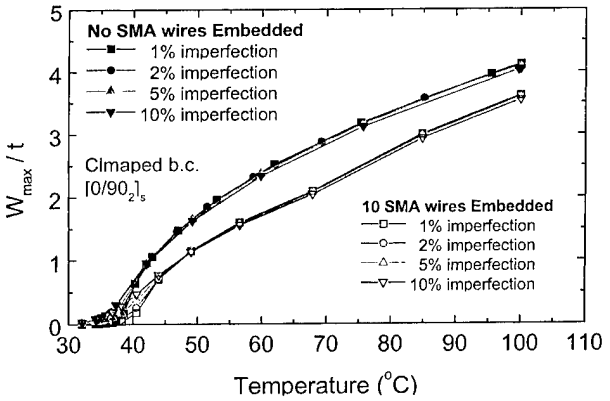

Fig. 13. Thermal buckling behavior of $[0/90_2]_s$ composite plates with embedded SMA wires and clamped boundary condition.

SMA/0°$_2$/90°] and [0°/90°$_2$/SMA/90°$_2$/0°], and effective coefficients of thermal expansion about the y-axis are 0.23×10^{-6} m/m per °C and 2.30×10^{-6} m/m per °C, respectively. In Figs. 13 and 14, the deformations are larger than those shown in Fig. 12. SMA wires are effective materials for decreasing postbuckling deformations in plates as well as in cylindrical panels but not effective materials for increasing critical buckling temperatures. In composite plates, geometric imperfections

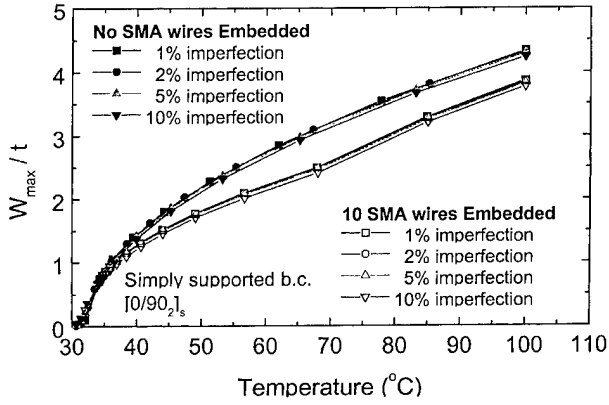

Fig. 14. Thermal buckling behavior of $[0/90_2]_s$ composite plates with embedded SMA wires and simply supported boundary condition.

do not influence thermal buckling behavior as much as in cylindrical shells.

5. Conclusion

We performed nonlinear thermal buckling analyses of laminated cylindrical composite panels and plates with embedded SMA wires using the ABAQUS code. The behavior of the SMA material was programmed in the form of an ABAQUS user subroutine and linked with an ABAQUS input file. This programmed constitutive equation of the SMA material was verified by showing the pseudoelasticity and SME.

The thermal buckling analysis revealed that embedded SMA wires can enhance the thermal buckling characteristics, which are critical buckling temperature and postbuckling deformations. In cylindrical panels, embedded SMA wires increased the critical buckling temperatures because of the contraction by the SME that takes place near A_s (34.5°C). But in plates, there was little increase of the critical buckling temperature because thermal buckling had already occurred below A_s (34.5°C). In plates, SMA wires only reduce postbuckling deformations. Thus, the austenite start temperature is significant in determining the critical buckling temperature. Thus, selection of the proper austenite start temperature in the SMA manufacturing process by considering the thermal buckling behavior of composite structures is important.

Acknowledgements

This study was supported by the HWRS–ERC project of KOSEF (Korea Science and Engineering Foundation). The authors wish to express their thanks for this support.

References

[1] Ro J, Baz A. Nitinol-reinforced plates: Part I. Thermal characteristics. Compos Eng 1995;5(1):65–75.

[2] Ro J, Baz A. Nitinol-reinforced plates: Part II. Static and buckling charateristics. Compos Eng 1995;5(1):77–90.

[3] Thompson SP, Loughlan J. Adaptive post-buckling response of carbon fibre composite plates employing SMA actuators. Compos Struct 1997;38:667–78.

[4] Choi S, Lee JJ. The shape control of a composite beam with embedded shape memory alloy wire actuators. Smart Mater Struct 1998;7(6):759–70.

[5] Chaudhry Z, Rogers CA. Response of composite beams to an internal actuator force. J Mech Design Trans ASME 1992;114:343–8.

[6] Zhong ZW, Chen RR, Mei C. Buckling and postbuckling of shape memory alloy fiber-reinforced composite plates. ASME 1994;AD-41/PDP-293:115–132.

[7] ABAQUS/Standard user's manual version 5.6, vol. I–III. Hibbitt, Karlsson & Sorensen, 1996.

[8] Tanaka K. A thermomechanical sketch of shape memory effect: One-dimensional tensile behaviour. Res Mech 1986;18:251–63.

[9] Liang C, Logers CA. One-dimensional thermomechanical constitutive relations for shape memory materials. J Intel Mat Syst Str 1990;1:207–34.

[10] Brinson LC, Lammering R. Finite element analysis of the behaviour of shape memory alloys and their applications. Int J Solids Struct 1993;30(23):3261–80.

ELSEVIER

Composite Structures 47 (1999) 471–476

COMPOSITE STRUCTURES

www.elsevier.com/locate/compstruct

A resin film infusion process for manufacture of advanced composite structures

B. Qi [a,*], J. Raju [b], T. Kruckenberg [a], R. Stanning [a]

[a] *The Cooperative Research Centre for Advanced Composite Structure Ltd., 361 Milperra Road, Bankstown, NSW 2200, Australia*
[b] *Hawker de Havilland, 361 Milperra Road, Bankstown, NSW 2200, Australia*

Abstract

This paper reports work conducted at the CRC-ACS for the manufacture of advanced composite structural demonstrators using a resin film infusion (RFI) process. The influences of a number of processing parameters on the quality of cured parts are discussed. A number of demonstrators are presented including an aileron skin panel, swaged wing rib and 3-bay aft-box structure. These demonstrators indicate the cost-effectiveness of the RFI process for manufacture of advanced composite structures. © 2000 Elsevier Science Ltd. All rights reserved.

Keywords: Resin film infusion; Autoclave; Composites; Lay-up

1. Introduction

Reduction of manufacturing cost and meeting quality requirements are critical for the application of composite materials in the aerospace industry. A variety of manufacturing methods have been researched and developed in the industry. Liquid moulding is an important method that could meet the above criteria.

Resin film infusion (RFI) is one of the liquid moulding techniques that has become attractive to composite manufacturers. It has been realised that the method has the potential to reduce tooling costs, as only a single sided tool is needed, and it compares favourably to the resin transfer moulding (RTM) process when the major technological and physical limitations are often the cost and weight of matched moulds. The process avoids pre-consolidation steps, utilised in prepreg process technology.

This paper reports the work conducted at the CRC-ACS on the development of a RFI process that was employed to manufacture a number of composite structural demonstrators.

2. RFI process

2.1. Materials

A commercially available resin film, Hexcel Composites M18 resin was used for the process development at the CRC-ACS [1]. M18 resin film is a high performance epoxy. Its dynamic viscosity is around 1000–10 000 cps at the temperature range of 100–175°C, depending on the temperature. This is shown in Fig. 1.

Different forms of textile preform reinforcements were used for the demonstrators. The fabric selection is mainly based on fabric cost and design criteria. The fabrics included non-tackified twill E3777 (12k tow) carbon fabric for the aileron skin panel, tackified 5HS G926 EPF (6k tow) for the swaged rib, and non-crimp carbon fabric for the 3-bay aft-box structure.

2.2. Lay-up and curing

A conventional RFI process (see Fig. 2) has been modified and developed at the CRC-ACS. The modification includes simplification of the lay-up and cure cycle based on the existing cure program for carbon fibre prepreg (180°C for 2 h at 650 kPa of autoclave pressure). The present demonstrators were cured based on the modified cure cycle using a production autoclave at Hawker de Havilland.

* Corresponding author. Fax: +61-2-9772-8432.
E-mail address: bqi@ozemail.com.au (B. Qi).

0263-8223/99/$ - see front matter © 2000 Elsevier Science Ltd. All rights reserved.
PII: S0263-8223(00)00025-8

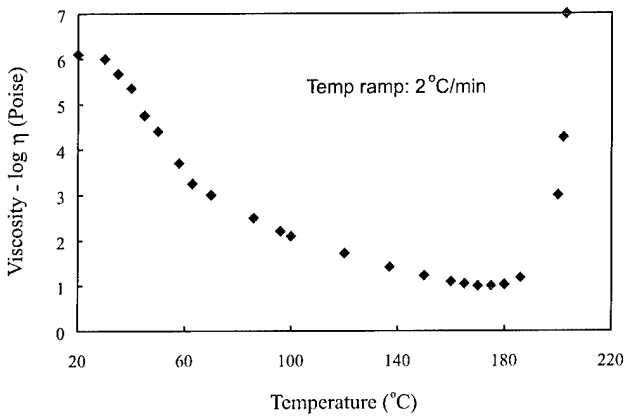

Fig. 1. Dynamic viscosity of M18 resin film.

In the process, a one-sided metal tool was used. On the other side of the part a caul plate, either rubber or aluminium, was used. This caul plate can consolidate the preform, provide strategically placed bleed-out holes (for excess resin removal and to guide resin flow), and improve surface finish of the cured parts.

The resin film (lightly cross-linked, or staged) is heated until it flows easily and penetrates into the dry preform before the final cure cycle commences [2,3]. The lay-up of solid resin film is easy and it is staged to prevent early resin bleed-out and excessive leakage.

In the modified cure cycle shown in Fig. 3, positive pressure (autoclave pressure) is applied at the start of the cure cycle before heat is applied. This allows the preform to be compacted prior to resin infusion and also helps extract volatiles or air bubbles from the lay-up. When the temperature increases, the resin melts and flows through the preform. Fig. 3 also shows the consolidation process for the M18 resin film.

2.3. Resin infiltration and bleed-out

The process is complex as a number of factors are not constant during the cure cycle. The degree of the compaction of the fibre preform changes during the cycle. As a result, the permeability is not constant as it is with RTM.

In order to fully impregnate the fibre reinforcement, achieve a required fibre volume fraction and to minimise porosity within a laminate, excess resin is generally required for bleed-out based on this resin system. Theoretically, the resin bleed-out behaviour can be used to estimate the resin content in the lay-up. For a given amount of resin used, the amount of resin bleed-out will affect the cured panel quality as follows.

1. Too many bleed-out holes may result in too much resin bleed-out. Consequently, resin starvation could occur. This also leaves several mark-off points on the surface, created by resin flash through the hole, which requires extra work to remove. A large bleed hole diameter can cause fibre distortion in the hole area and contribute to excessive bleed-out.
2. If there are insufficient numbers of holes, or too small a hole diameter is used, a high resin content will result. Volatiles and air bubbles may also be easily trapped in the reinforcement leaving porosity in the cured part.

The bleed-out holes allow access for vacuum to remove residual moisture and gas trapped inside the lay-up, assist in the driving force of resin flow, and assist in full impregnation of the fibres. The bleed-out, W_b, could be estimated by the following expression, which is schematically shown in Fig. 4(a):

$$W_b = \int_{t_1}^{t_2} Q_H \, dt, \tag{1}$$

where Q_H is the resin flow rate through the bleed-out holes, t_1 the time for resin to reach bleed-out holes and t_2 is the time when resin starts to gel or stop flowing.

In Fig. 4(a) Q_1 represents a bleed-out level above which resin starvation in the cured laminate could happen due to too much resin bleed-out, for a given amount of resin used. The amount of resin to be used

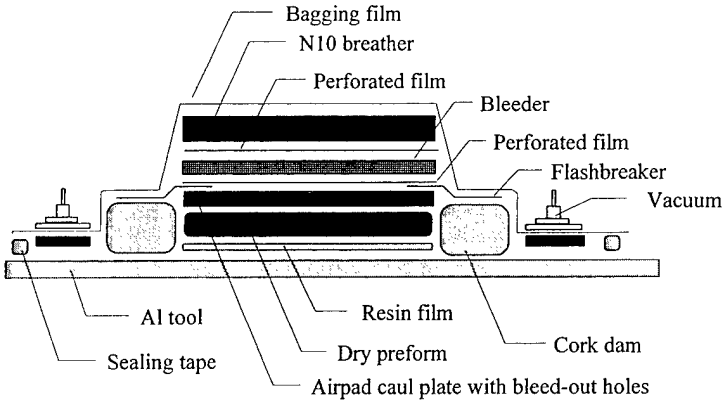

Fig. 2. A basic lay-up for the current RFI process (before modification).

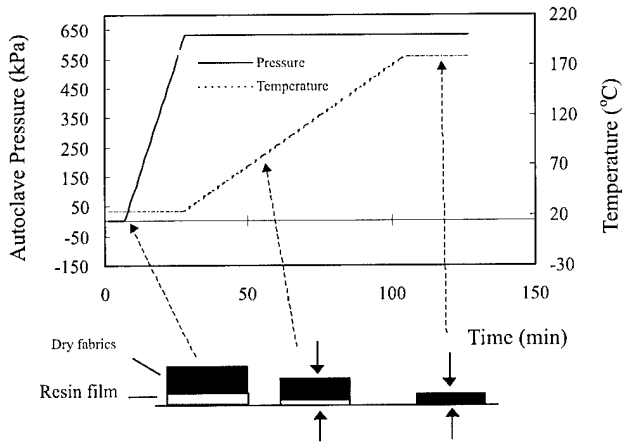

Fig. 3. A schematic of the initial cure profile and consolidation process.

can be calculated based on fibre volume fraction, V_f, required and excess resin for bleeding. A number of factors affecting the resin bleed-out will be discussed in the following section. A non-bleed-out system is also indicated in the figure if the resin starts to gel just after completing the wet-out. In this case a viscosity–temperature–time relationship needs to be well characterised.

According to Darcy's law, one-dimensional flow of Newtonian fluids through porous media can be described as

$$Q = \frac{KA}{\eta}\frac{\Delta P}{\Delta L}, \tag{2}$$

where K is the permeability of the porous medium, η the resin viscosity at time t, Q the flow rate, $\Delta P/\Delta L$ the pressure drop per unit length, and A is the cross-sectional area of the medium.

This can be extended to describe the resin flow behaviour in the porous breather materials

$$Q_H = \frac{K_H \times \Delta P \times A \times R_b}{\bar{L} \times \eta}, \tag{3}$$

where K_H is a constant that represents the permeability of breather material in the case, ΔP the pressure differential between autoclave pressure and the vacuum applied, A the panel area (normal to resin flow), $\bar{L}$ the effective distance resin travels after impregnation of dry preform, which is basically the breather thickness, and R_b is the bleed-out hole ratio (represented by the number holes per square meter, holes/m^2, for a constant hole diameter). This ratio can be determined experimentally. Fig. 4(b) is a sketch showing the resin flow through the thickness of the preform in the process.

All of the parameters except viscosity, η, can be treated as a constant after resin reaches the bleed-out holes, thus a relationship between resin bleed-out and processing parameters can be proposed as follows:

$$W_b = \left(\frac{A \times K_H \times \Delta P \times R_b}{\bar{L}}\right) \int_{t_1}^{t_2} \frac{1}{\eta}\, dt. \tag{4}$$

The complete filling in the lay-up occurs in the duration between t_0 and t_1, shown in Fig. 4(a). Thus, it is required that the time for resin to reach gel point must be longer than the duration to completely fill the part.

It can be seen in Eq. (4) that apart from the resin viscosity, there are a number of parameters that affect the bleed-out, including R_b. Experiments were conducted to investigate the influence of different bleed-out hole ratios on the general quality of cured panels such as fibre volume fraction, V_f, and porosity level. These were carried out using E3777/M18 materials. Eight panels (around 50×50 cm^2) were manufactured. The results are summarised in Figs. 5 and 6.

Areas between the two lines (V_f in 55% and 62%, respectively) in both figures represent an acceptable V_f range (based on a tolerance of ±5% in thickness). In Fig. 5, panels were made using a constant volume of resin, but with different bleed-out hole ratios. A panel made with one of the highest R_b and under standard vacuum level (before modification) gave the highest V_f. However, significant resin starvation and porosity were

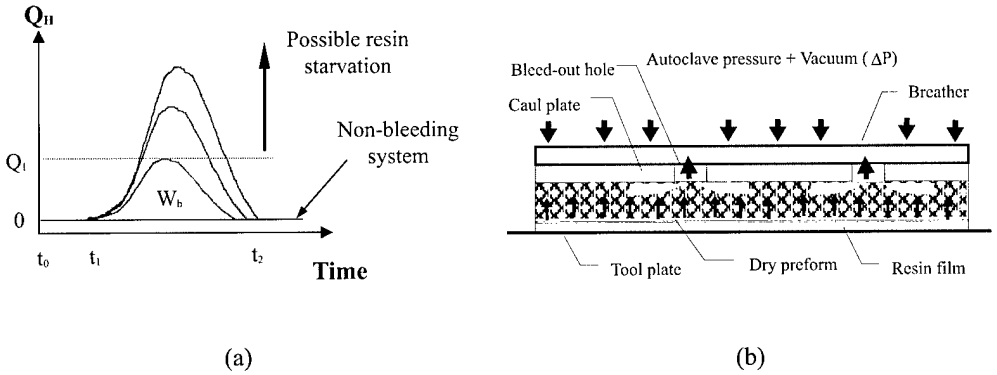

Fig. 4. (a) A sketch of resin bleed-out behaviour and (b) resin flow during curing.

observed in the cured panel. High resin bleed-out due to the large ratio used had caused resin starvation. To eliminate resin starvation, the bleed-out hole ratio was progressively reduced (this also reduced the mark-off on the panel surface).

Subsequently, in order to reduce the porosity, vacuum was applied for a longer period during the cure (until the estimated gel point is approached). This produced panels with a good surface quality, although the V_f was a little lower, it still meet the design criteria (see Fig. 5). Fig. 6 shows the influence of resin quantity on the V_f, where R_b is kept constant. It can be seen that when too much resin was used, for the given cure condition and bleed-out hole ratio, a lower V_f resulted. Thus, by employing an optimum bleed-out hole ratio, the modified cure program provided a good cure quality for the RFI lay-up.

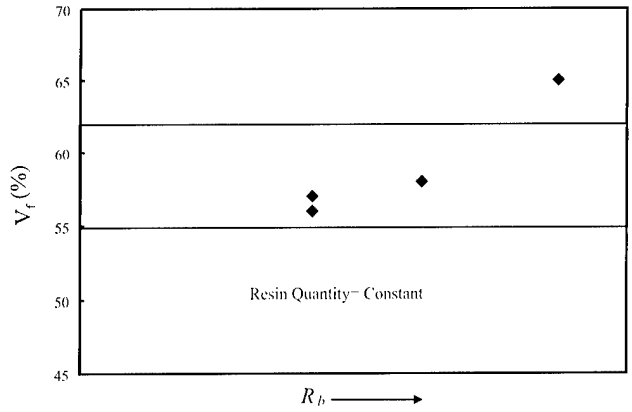

Fig. 5. Influence of bleed-out hole ratio on V_f of cured parts.

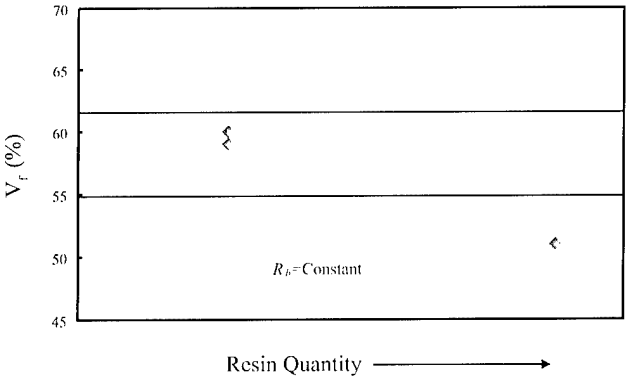

Fig. 6. Influence of resin quantity used on V_f of cured parts.

3. Manufacture of composite demonstrators

A number of composite structural demonstrators were manufactured using the RFI process. These included:

3.1. Aileron skin panel

These panels have a length of 3 m and width of 0.6 m (1.4-mm thick) and have a pad-up section in the middle for rib bonding. To achieve a good surface, a flexible caul plate bonded with FEP film was used. The caul plate was made of non-silicone tooling rubber, Airpad (supplied by Airtech), and reinforced with plain-woven carbon fabric/epoxy composites.

A total of four panels were made. Fig. 7(a) shows the outer surface (caul plate surface) of the cured panel after trimming. Fig. 7(b) shows two skins, one with internal structure, ready for assembly (mechanical fastening and secondary adhesive bonding).

Through transmission ultrasonic (TTU) inspection at 5 MHz was used to examine the quality of cured panels. No significant defects were detected in any of the four panels. Variation in thickness profile of about 5.5% was observed. Void rate is around 1%. Cross-sectional inspection of a cured panel under microscopy further verified the TTU inspection (Fig. 8 is an example).

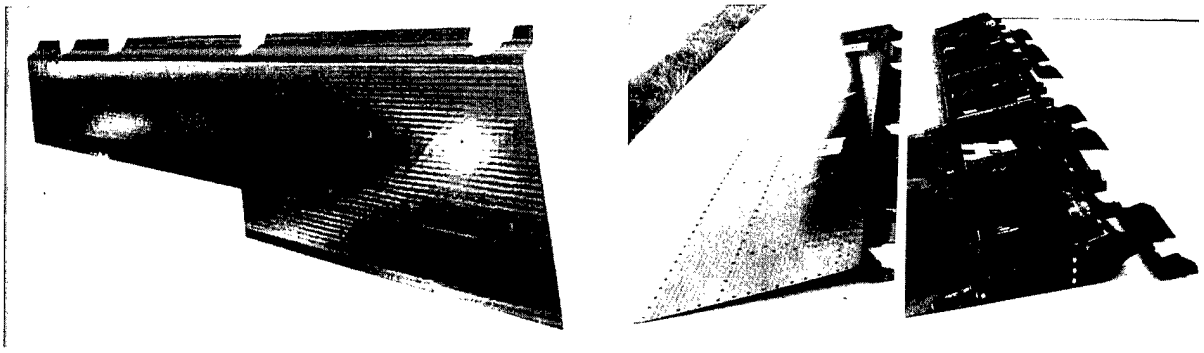

Fig. 7. (a) A contour of a upper RFI skin panel and (b) skin panels ready for assembly.

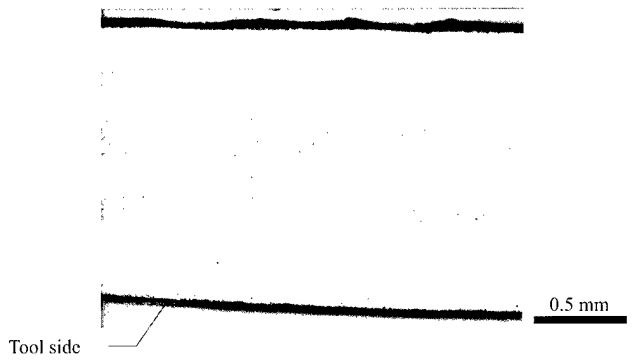

Fig. 8. A cross-section view of a cured RFI skin panel.

Fig. 9. An RFI G626/M18 composite swaged rib.

3.2. Swaged wing rib

Fig. 9 shows a RFI swaged rib. The rib has three washed swages, and the lay-up has 6 plies in the window area and 10 plies in the edges.

A steel tool containing a base plate with three female swages, was employed. A caul plate with protruding features was used to consolidate the preform and to form the swages. The part was manufactured near net shape. The final part perimeter, including mouseholes, was trimmed with the aid of a template. The ribs have been tested in a structural test wing box.

3.3. Three-bay aft-box structure

The co-moulded aft-box structure, which consisted of a 3-bay box and a hollow trailing edge section, has dimensions of $430 \times 405 \times 100$ mm^3, tapering to an apex, as shown in Fig. 10(a).

In the lay-up, M18 resin film was placed between the preformed fabrics rather than placed on the bottom of the stack. The tooling is shown schematically in Fig. 10(b). This tooling was originally used for co-cure of a prepreg aft-box. The preforms were made of CQX820B fabrics (non-crimp quadraxial).

Generally good quality was achieved. However, it was found that the degree of compaction in the middle ribs is difficult to control due to a number of factors including tool dimensional tolerance and materials in the conjunction areas that may cause mechanical locking of tooling. The current thick lay-up method could also significantly affect the rib compaction because it requires large tool movement. An existing prepreg tool was used for these trials and only a 93% compaction of the middle ribs was achieved with a corresponding lower desired V_f.

4. Cost estimation

Based on these experimental trials, manufacturing costs are estimated based on 100 parts production volume with an assumed learning curve reduction. This is summarised in Table 1. Compared to a prepreg hand lay-up method, these show a saving of nearly 18% for the swaged rib, up to 14% for the aileron skin and about 10% for a full size spoiler of similar construction (scaling up from the current study of the RFI 3-bay aft-box). The proposed RFI process represents a cost-effective method of manufacturing composite components with relatively complicated shapes.

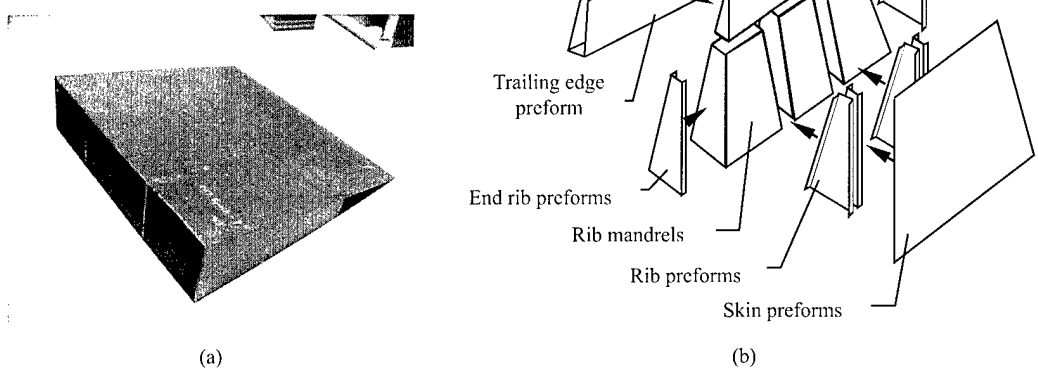

Fig. 10. (a) A co-moulded bond 3-bay aft-box and (b) tool for lay-up.

Table 1
Estimated recurring cost (labour hours and material cost) for the RFI composite demonstrators

Parts	Manufacture method	Comparison to prepreg hand lay-up
Aileron skin panel	RFI	86%
Swaged rib	RFI	82%
Spoiler[a]	RFI	90–95%

[a] It is estimated from scaling of the current study on a RFI 3-bay aft-box.

5. Conclusions

The trade-off studies showed that the RFI process is a cost-effective technique for these composite parts. The process is relatively robust and simple.

Research is continuing to optimise the process for thicker laminates and complex structures in terms of resin systems and their flow characteristics. Once the proposed relationship for bleed-out is experimentally verified, it can be used to improve the process design.

Acknowledgements

The authors wish to thank the director of the CRC-ACS, Dr. Ian Mair, for permission to present this paper. The assistance from Mark Croucher, Michael Baker, James Dunlop and Sam Dobson of HDH, and from HDH for use of its autoclave are gratefully acknowledged.

References

[1] Kruckenberg T, Allata P, Baker M, Blamires M, Croucher M, Szeyka S, Qi B, Raju J, Stanning R, Varbola M, Wells T. Innovation Network Program Manufacturing Report, CRC-ACS TM 97007, Australia, 1997.

[2] Gause LW, Apler JM. Braided to net section graphite/epoxy composite shapes. J Comp Technol Res 1988;10(2):3–36.

[3] Krusche T, Michaeli W. Resin infusion technology for the autoclave process. In: 41st International SAMPE Symposium. March 24–28, 1996:1542–50.

ELSEVIER

Composite Structures 47 (1999) 477–482

COMPOSITE STRUCTURES

www.elsevier.com/locate/compstruct

Evaluation of elastic properties of 3-D (4-step) regular braided composites by a homogenisation method

Chen Zuorong [a], Zhu Dechao [a], Meng Lu [a,b,*], Lin Ye [b]

[a] *Institute of Solid Mechanics, Beijing University of Aeronautics and Astronautics, Beijing 100083, People's Republic of China*

[b] *Department of Mechanical and Mechatronic Engineering, Centre for Advanced Material Technology, The University of Sydney, Sydney, NSW 2006, Australia*

Abstract

In this article a homogenisation method that considers the internal interface condition of a heterogeneous medium is established. The relevant formulae are developed based on a specific stratified medium with plane interfaces, but they can be obtained for more general cases in which curved interfaces are considered. A 3-D 4-step regular braid is studied, and its elastic properties are evaluated in terms of the homogenisation scheme. The present theoretical prediction shows a good agreement with experimental data. © 2000 Elsevier Science Ltd. All rights reserved.

Keywords: Braided fabrics; Homogenisation; Meso-mechanics; Fibre architecture

1. Introduction

The majority of analytical models for textile fabrics were primarily based on the concepts and methodologies developed previously for other types of composites, such as the composite cylinder assemblage method (CCAM) [1], the variation method [2], the generalised effective stiffness method [3], the self-consistent method [4], and the laminate plate theory [5], etc. A typical example was the Mosaic Model proposed by Ishikawa and Chow to study the elastic behaviour of woven hybrid composites. Later, the Bridge model [6], the 1-D fibre undulation model [7], and 2-D fibre crimp model [8], etc, were proposed to improve the Mosaic model in the cases where the Mosaic model does not apply. These models are successful in prediction of mechanical behaviour of 2-D woven fabrics, however, they are generally not applicable to 3-D braided composites. Therefore, other models were established for 3-D braided fabrics. Ko and Pastore [9] used four sets of idealised straight yarn segments to characterise a unit cell of a 3-D braid, and the stiffness tensor for each set of yarn segments was locally calculated and then rotated to a 3-D braided composite frame. In this way, the overall effective stiffness of the 3-D braided composite can be determined through summation of the stiffness of each yarn segment multiplied by its volume fraction. Yang et al. [10] established a fibre inclination model, which treats the unit cell of a 3-D braided composite as an assemblage of inclined unidirectional laminates.

These models have been extensively used to predict the elastic properties of 3-D braids. Although they are relatively simple, they were successful applied to the evaluation of the mechanical properties of 3-D textile fabrics. However, the fibre architectures in these models have to be significantly simplified. The interaction between yarn and matrix was also not taken into consideration, meanwhile some essential mechanical requirements, such as yarn–matrix interface conditions, have to be ignored.

The present study attempts to evaluate the effective elastic properties of 3-D braided fabrics using a homogenisation scheme which permits more meso-structural details to be included. With this scheme, the requirements of continuity at interfaces can be identified. That is, unlike a conventional homogenisation technique, the scheme is formulated by considering the continuity condition at interfaces inside a unit cell. Due to the limitation of space, the relevant formulae are presented only for a stratified medium with a plane interface, however, they can also be obtained for more general cases in which curved interfaces are considered.

* Corresponding author. Fax: +61-2-9351-3760.
E-mail address: menglu@mech.eng.usyd.edu.au (M. Lu).

0263-8223/99/$ - see front matter © 2000 Elsevier Science Ltd. All rights reserved.
PII: S0263-8223(00)00026-X

2. Formulation of the homogenisation scheme

Consider a stratified medium with n-layer laminates stacking together (see, Fig. 1), and the material of each layer is assumed to be linearly orthotropic elasticity, and all layers are perfectly bonded to each other at interfaces. The thickness of the kth layer is $h^{(k)}$. A representative volume element (RVE) of the medium is shown in Fig. 1.

The linearly elastic stress–strain relations for the kth layer can be written as

$$\sigma_{ij}^{(k)} = C_{ijpq}^{(k)}\varepsilon_{pq}^{(k)} \quad (i,j,p,q = 1,2,3;\ k = 1,2,\ldots,n), \tag{1}$$

where, $\sigma_{ij}^{(k)}$ is the stress tensor, $\varepsilon_{pq}^{(k)}$ the strain tensor, and $C_{ijpq}^{(k)}$ the elastic stiffness tensor.

The stress and strain tensors can be decomposed into two orthogonally complementary parts; one is normal to the interface and the other is tangential to the interface. Then Eq. (1) can be expressed in the in-plane and the out-of-plane components

$$\begin{bmatrix} \sigma_t^{(k)} \\ \sigma_n^{(k)} \end{bmatrix} = \begin{bmatrix} C_{tt}^{(k)} & C_{tn}^{(k)} \\ C_{nt}^{(k)} & C_{nn}^{(k)} \end{bmatrix} \begin{bmatrix} \varepsilon_t^{(k)} \\ \varepsilon_n^{(k)} \end{bmatrix} \quad (k = 1,2,\ldots,n), \tag{2a}$$

where

$$\left[\sigma_t^{(k)}\right] = \left[\sigma_{11}^{(k)} \quad \sigma_{22}^{(k)} \quad \tau_{12}^{(k)}\right]^{\mathrm{T}}, \tag{2b}$$

$$\left[\sigma_n^{(k)}\right] = \left[\sigma_{33}^{(k)} \quad \tau_{23}^{(k)} \quad \tau_{31}^{(k)}\right]^{\mathrm{T}}, \tag{2c}$$

$$\left[C_{tt}^{(k)}\right] = \begin{bmatrix} C_{11}^{(k)} & C_{12}^{(k)} & 0 \\ C_{12}^{(k)} & C_{22}^{(k)} & 0 \\ 0 & 0 & C_{66} \end{bmatrix}, \tag{2d}$$

$$\left[C_{tn}^{(k)}\right] = \begin{bmatrix} C_{33}^{(k)} & 0 & 0 \\ 0 & C_{44}^{(k)} & 0 \\ 0 & 0 & C_{55}^{(k)} \end{bmatrix}, \tag{2e}$$

and

$$\left[C_{tn}^{(k)}\right] = \left[C_{nt}^{(k)}\right]^{\mathrm{T}} = \begin{bmatrix} C_{13}^{(k)} & 0 & 0 \\ C_{23}^{(k)} & 0 & 0 \\ 0 & 0 & 0 \end{bmatrix}. \tag{2f}$$

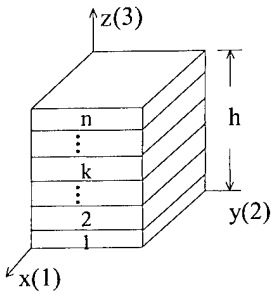

Fig. 1. RVE of a stratified medium with n layers.

Here, the subscripts t and n indicate the in-plane and out-of-plane components, respectively. The superscript T denotes transposition of matrix.

It follows from Eqs. (2a)–(2f) that

$$\begin{bmatrix} \varepsilon_t^{(k)} \\ \varepsilon_n^{(k)} \end{bmatrix} = \begin{bmatrix} D_{tt}^{(k)} & D_{tn}^{(k)} \\ D_{nt}^{(k)} & D_{nn}^{(k)} \end{bmatrix} \begin{bmatrix} \sigma_n^{(k)} \\ \sigma_t^{(k)} \end{bmatrix} \quad (k = 1,2,\ldots,n), \tag{3a}$$

where

$$D_{tt}^{(k)} = C_{tt}^{(k)} - C_{tn}^{(k)}C_{nn}^{(k)-}C_{nt}^{(k)}, \tag{3b}$$

$$D_{tn}^{(k)} = -D_{nt}^{(k)T} = C_{tn}^{(k)}C_{nn}^{(k)-}, \tag{3c}$$

$$D_{nn}^{(k)} = C_{nn}^{(k)-}. \tag{3d}$$

According to the continuity condition at a perfect interface, the in-plane components of strain tensor and the out-of-plane components of stress tensor must be continuous across the interface.

Assume

$$\begin{bmatrix} \varepsilon_t^{(k)} \\ \sigma_n^{(k)} \end{bmatrix} = [\xi(z)] \begin{bmatrix} \bar{\varepsilon}_t \\ \bar{\sigma}_n \end{bmatrix} \quad (k = 1,2,\ldots,n),$$

where $\bar{\varepsilon}_t$ and $\bar{\sigma}_n$ denote the averaged values of ε_t and σ_n over the entire unit cell, respectively. $[\xi(z)]$ is a diagonal matrix and its average over the unit cell is a unit matrix.

Jumps in σ_t and ε_n across the interface can be written in the form

$$\begin{bmatrix} \sigma_t^{(k+1)} \\ \varepsilon_n^{(k+1)} \end{bmatrix} - \begin{bmatrix} \sigma_t^{(k)} \\ \varepsilon_n^{(k)} \end{bmatrix} = \left\{ \begin{bmatrix} D_{tt}^{(k+1)} & D_{tn}^{(k+1)} \\ D_{nt}^{(k+1)} & D_{nn}^{(k+1)} \end{bmatrix} - \begin{bmatrix} D_{tt}^{(k)} & D_{tn}^{(k)} \\ D_{nt}^{(k)} & D_{nn}^{(k)} \end{bmatrix} \right\} [\xi_i(z)] \begin{bmatrix} \bar{\varepsilon}_t \\ \bar{\sigma}_n \end{bmatrix} \quad (k = 1,2,\ldots,n-1). \tag{4}$$

By expanding $\xi_i(z)$ in a series with respect to z, the first-order approximation gives

$$\begin{bmatrix} \bar{\sigma}_t \\ \bar{\varepsilon}_n \end{bmatrix} = \frac{1}{h}\int_0^h \begin{bmatrix} \sigma_t \\ \varepsilon_n \end{bmatrix}^k \mathrm{d}z = \left[\bar{D}_{nt}\right] \begin{bmatrix} \bar{\varepsilon}_t \\ \bar{\sigma}_n \end{bmatrix}, \tag{5}$$

where

$$\left[\bar{D}_{nt}\right] = \sum_{k=1}^{n} \alpha^{(k)} \left[D_{nt}^{(k)}\right], \quad \alpha^{(k)} = h^{(k)}/h, \quad \sum_{k=1}^{n} \alpha^{(k)} = 1. \tag{6}$$

Eqs. (5) and (6) are valid in the first-order approximation, and higher-order spatial fluctuations of stress and strain fields have been ignored.

Rearrange Eq. (6) in this form

$$\begin{bmatrix} \bar{\sigma}_t \\ \bar{\sigma}_n \end{bmatrix} = \begin{bmatrix} \bar{C}_{tt} & \bar{C}_{tn} \\ \bar{C}_{nt} & \bar{C}_{nn} \end{bmatrix} \begin{bmatrix} \bar{\varepsilon}_t \\ \bar{\varepsilon}_n \end{bmatrix}, \tag{7a}$$

where

$$\bar{C}_{tt} = \bar{D}_{tt} - \bar{D}_{tn}\bar{D}_{nn}^{-1}\bar{D}_{nt}, \tag{7b}$$

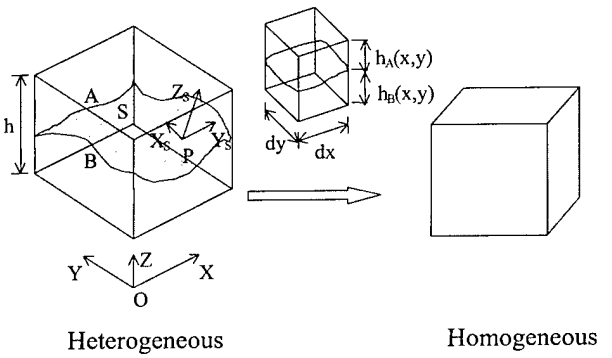

Fig. 2. RVE of a stratified medium with curved interface.

$$\bar{C}_{tn} = \bar{C}_{nt}^{\mathrm{T}} = \bar{D}_{tn}\bar{D}_{nn}^{-1}, \tag{7c}$$

$$\bar{C}_{nn} = \bar{D}_{nn}^{-1}. \tag{7d}$$

Thus, with some mathematical derivation, the effective elastic stress-strain relations for the stratified medium can be written as

$$\bar{\sigma}_{ij} = \bar{C}_{ijpq}\bar{\varepsilon}_{qp}, \tag{8}$$

where $\bar{C}_{ijpq}$ is the effective elastic tensor. The non-zero elements of $\bar{C}_{ijpq}$ can be , in the notation of engineering index, reduced as

$$\bar{C}_{ij} = \sum_{k=1}^{n}\alpha^{(k)}\left[C_{ij}^{(k)} - \frac{C_{i3}^{(k)}C_{3j}^{(k)}}{C_{33}^{(k)}}\right] + \sum_{k=1}^{n}\alpha^{(k)}\frac{C_{i3}^{(k)}}{C_{33}^{(k)}}\sum_{l=1}^{n}\alpha^{(l)} \times \frac{C_{3j}^{l}}{C_{33}^{l}}\left(\sum_{k=1}^{n}\frac{\alpha^{(k)}}{C_{33}^{k}}\right)^{-1} \quad (i,j=1,2,3), \tag{9a}$$

$$\bar{C}_{ij} = \left(\sum_{k=1}^{n}\frac{\alpha^{(k)}}{C_{ij}^{(k)}}\right)^{-1} \quad (i=j=4,5), \tag{9b}$$

$$\bar{C}_{66} = \sum_{k=1}^{n}\alpha^{(k)}C_{66}^{(k)}. \tag{9c}$$

Eqs. (9a)–(9c) are general and can be used for 3-D cases. For the cases in which interfaces are of any curvatures, the perfect interface-based homogenisation formulae can also be obtained, provided curvilinear orthogonal coordinate systems at interfaces are established and the corresponding transformation equations are introduced (Fig. 2).

3. Meso-structure of 4-step 3-D regular braided composites

Comprehensive descriptions of fibre architectures are essential in the prediction of the mechanical behaviours of textile composites. For braided fabrics, these parameters include braid configurations, fibre orientations, and fibre volume fraction, etc. To better characterise meso-structures and yarn interlacing patterns of braids, considerable insights into the microstructures of braided fabrics have been made in terms of analysis of braiding carrier motion, computer graphics simulation, computer solid modelling, and experimental observations [11–13], etc.

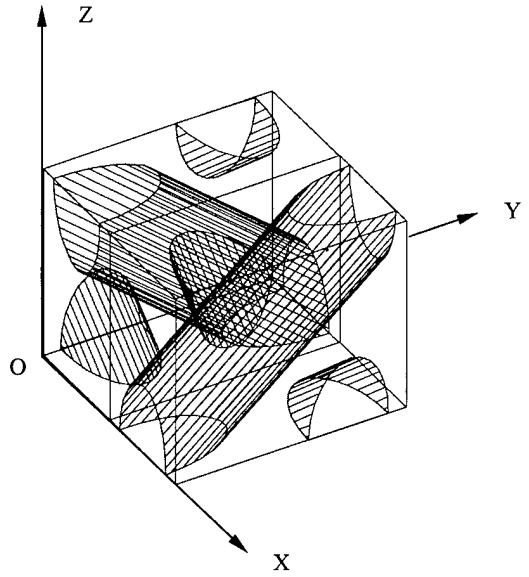

Fig. 3. Unit cell model.

Based on these studies [11–13], a solid unit cell model for the 3-D 4-step (1 × 1) rectangular braided fabric can be established in the following. The basic hypotheses about the geometrical unit cell model of the 3-D 4-step 1 × 1 braided fabric include

1. The cross-sections of yarns are elliptic and remain unchanged along their length;
2. All yarns in the unit cell have the same cross-section;
3. All yarns in the interior unit cell have no crimp owing to sufficiently high tension during braiding process.

A unit cell of the model is illustrated in Fig. 3, where a coordinate system is attached with the Z-axis (braiding direction) in the vertical direction. It is noted that the geometric parameters of the 3-D braided composites are constrained by some spatial relations [11–14]. In practical braiding processes, once the braiding angle is increased to a certain critical value, the stacking yarns in interlacing region will contact each other, and braiding movements can no longer proceed in this case. This is the so-called jamming condition.

4. Effective elastic properties of the 4-step 3-D braided composites

With Eqs. (9a) and (9b), and the meso-structural details of the composite, the effective elastic properties of the 4-step 3-D (1 × 1) rectangular braided can be evaluated.

Clearly, for a 3-D braided fabric, Eqs. (9a)–(9c) are no longer valid for the whole unit cell, i.e., the fibre volume-fraction, $\alpha^{(k)}$ $(k = 1, 2, 3, \ldots)$, is a function of coordinates and Eqs. (9a)–(9c) should be employed within sub-cells. Thus, it is essential to establish the relationship between volume-fractions of all the constituent materials and the configurations of (sub-cell of) the unit cell. Since it is difficult to obtain a global explicit expression of this relation, an analysis from local regions can be conducted. The procedure is first started with a 1/32 sub-cell, then a 1/8 sub-cell, then a 1/4 sub-cell, and so forth, till the entire unit cell is completed. This treatment is somewhat similar to that of the fibre undulation model [7], but the laminate theory used there does not apply to the present case. Instead, the local forms of Eqs. (9a)–(9c) [15,16] were used to evaluate the effective elastic properties of the 4-step 3-D textile composite.

A 1/32 sub-cell of RVE is shown in Fig. 4. A local coordinate system o_1–$x_1y_1z_1$ is located at a point (x', y', z') of the interface with the x_1-axis in the direction of yarn F1. The effective elastic properties of the 1/32 sub-cell can be obtained by considering the continuity conditions at interface S2 between yarn F2 and the effective medium consisting of (F1) and the matrix (M).

The effective elastic properties of a 1/16 sub-cell can be determined by considering the continuity condition between two 1/32 sub-cells. Using symmetry, the effective elastic properties of another 1/16 sub-cell can be easily obtained. Further, the effective elastic properties of a 1/8 sub-cell can be determined by considering the continuity condition between two 1/16 sub-cells. Following the same procedure, the effective elastic properties of the 1/8, 1/4, and 1/2 sub-cells can be successively determined, and finally the effective elastic tensor of the entire unit cell can be obtained. Through rotating the tensor $\pi/4$ with respect to the z'-axis, the effective elastic tensor of 3-D braided composites in the coordinate system o–xyz can be obtained.

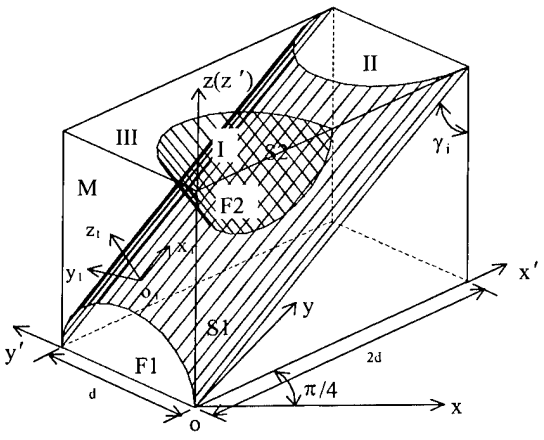

Fig. 4. A 1/32 sub-cell.

Figs. 5–10 illustrate the dependence of elastic properties on the braiding angle, with different fibre volume fractions. From these figures it can be seen that the effect of braiding angle and fibre volume fraction on the elastic modulus, E_Z, is as follows. E_Z decreases with the increasing of the braiding angle and it increases as the fibre volume fraction does. For the case of lower braiding angles, the effect of braiding angle on E_Z is dominant. As the braiding angle increases, the fibre volume fraction increases and the effect of fibre volume fraction on E_Z becomes stronger. As the braiding angle approaches the jamming braiding angle, in contrast, the effect of fibre volume fraction on E_Z is dominant, which makes E_Z increase. A similar situation can be seen for the effect of

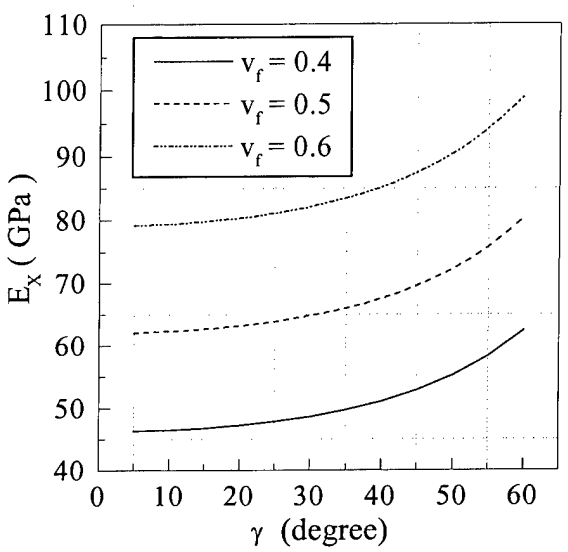

Fig. 5. Dependence of transverse modulus E_X on the braiding angle γ.

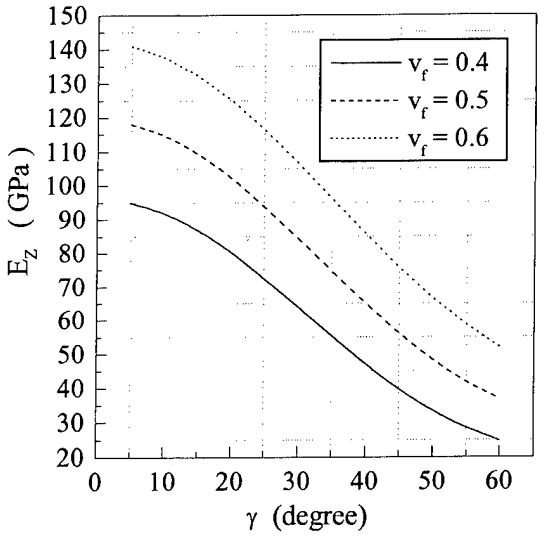

Fig. 6. Dependence of longitudinal modulus E_Z on the braiding angle γ.

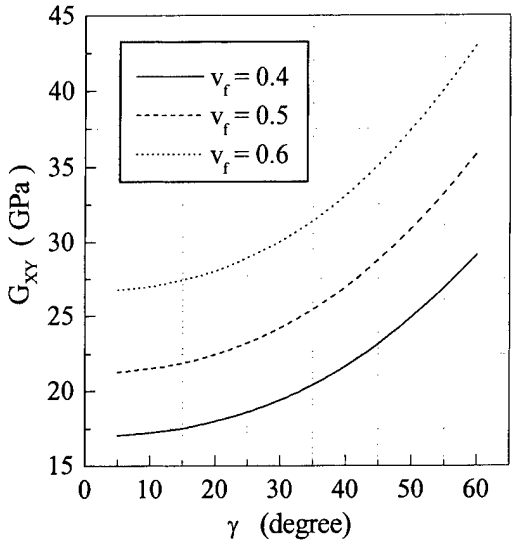

Fig. 7. Dependence of transverse shear modulus G_{XY} on the braiding angle γ.

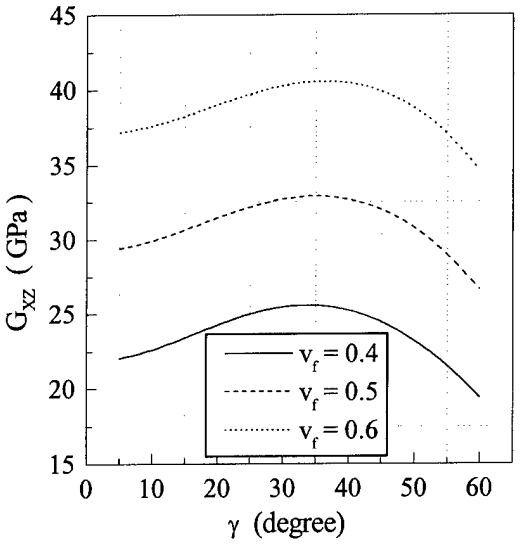

Fig. 8. Dependence of longitudinal shear modulus G_{XZ} on the braiding angle γ.

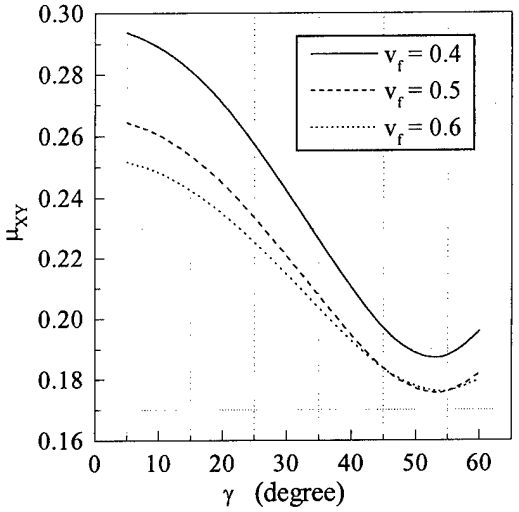

Fig. 9. Dependence of Poisson's ratio ratio μ_{XY} on the braiding angle γ.

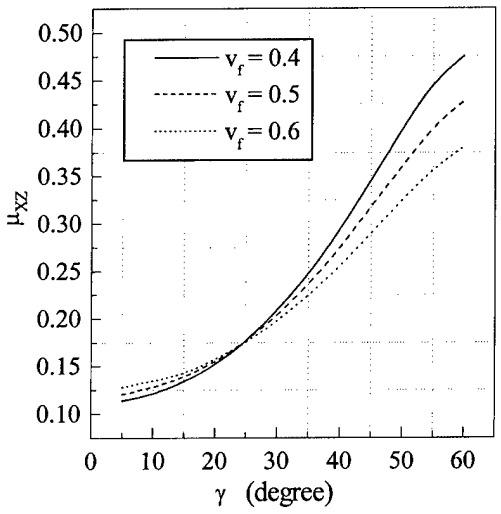

Fig. 10. Dependence of Poisson's ratio μ_{XZ} on the braiding angle γ.

the braiding angle and fibre volume fraction on the elastic modulus E_X which behaves in a similar way. That is, the increase of the braiding angle and fibre volume fraction makes E_X increase. It can be seen from Fig. 9 that the variation of E_X versus the braiding angle is higher than that of E_Z.

It can be noted that for the 4-step 3-D braided composite, the mechanical behaviours in the Z-direction (braiding direction) and in the X-direction are comparable due to their geometric comparability. The mechanical properties in the Z-direction at lower braiding angles are comparable with those in the X-direction at higher braiding angles. This feature allows a 3-D braided composite to achieve the well-balanced overall mechanical properties. The predicted results, as can be

Table 1
Comparison of the prediction and experimental results [17]

Surface braid angle (°)	Fiber volume fraction	Experimental results [17]		Present results	
		E_Z (GPa)	E_X (GPa)	E_Z (GPa)	E_X (GPa)
17	0.38	43.6 ± 1.9	6.21 ± 0.41	48.0	6.08
22	0.44	38.5 ± 2.4	6.02 ± 0.30	42.7	6.97

Table 2
Elastic properties of epoxy and yarn [17]

Epoxy resin		AS-4 Fibers				
E (GPa)	G (GPa)	E_1 (GPa)	E_2 (GPa)	G_{12} (GPa)	G_{23} (GPa)	μ_{12}
2.97	1.11	234.6	13.8	13.8	5.47	0.22

seen, also reflect this fact. With regard to G_{XY}, G_{XZ}, μ_{XY}, and μ_{XZ}, discussions can be made in a similar way.

Table 1 illustrates a comparison between the experimental data measured by Kalidindni [17] and the present predictions. The yarn and matrix properties [17] used are listed in Table 2. It is seen from Table 1 that a good agreement between the prediction and the experimental results is obtained.

5. Summary

In this article, we introduce a homogenisation method and establish a unit cell model to predict the elastic properties of a 3-D (4-step) braid. In comparison to the models based on the variation method, the CCAM, the generalised effective stiffness method and the self-consistent method, this method is easier to be carried out and can be applied to cases where complex geometry is involved. In comparison to models based on the laminate theory, this method can be used to predict not only in-plane properties but also the out-of-plane properties, of which the latter is very essential for 3-D braids.

Clearly, what we are here concerned with is a specific braid, yet the treatment can be extended to other textile forms of composites provided the microstructures of the fabrics can be adequately demonstrated. Also, although the assumptions used to define the unit cell are adequate for characterising the fibre architectures and yarn interlacing patterns, the geometrical model can be further improved and can be changed according to different fabrics under concern. For example, yarns in the unit cell do not necessarily have the same geometry, neither have they the same material properties. Studies on those fabrics are now under consideration.

Acknowledgements

The authors are grateful to the financial support from China General Corporation of Aerospace Industry.

References

[1] Hashin Z, Rosen RW. The elastic moduli of fibre-reinforced materials. J Appl Mech 1964;31(1):223–32.
[2] Hill R. Theory of mechanical properties of fibre-reinforced materials: I. Elastic behaviour. J Mech Phys Solids 1964;12:199–212.
[3] Aboudi J. Micromechanical analysis of composites by the method of cells. Appl Mech Rev 1989;42(7):103–28.
[4] Pastore CM, Gowayed YA. A self-consistent fabric geometry model: modification and application of a fabric geometry model to predict elastic properties of textile composites. J Composites Technol Res 1994;16(1):32–6.
[5] Ishikawa T, Chou TW. Stiffness and strength behaviour of woven fabric composites. J Mater Sci 1982;17:3211–20.
[6] Ishikawa T, Chou TW. In-plane thermal expansion and thermal bending coefficients of fabric composites. J Composite Mater 1983;17(2):92–104.
[7] Ishikawa T, Chou TW. One-dimensional micromechanical analysis of woven fabric composites. AIAA J 1983;21(12):1714–21.
[8] Naik NK, Shembekar PS. Elastic behaviour of woven fabric composite: I – Lamina analysis. J Composite Mater 1992;26(15):2197–225.
[9] Ko FK, Pastore CM. Structure and properties of an integrated 3-D fabric for structural composites. In: Vinson JR, Taya M, editors. Recent advances in Composites. The United States and Japan. ASTM STP 864. Philadelphia: American Society for Testing and Materials, 1985. p. 428–39.
[10] Yang JM, Ma CL, Chou TW. Fibre inclination model of three-dimensional textile structural composites. J Composite Mater 1986;20:472–84.
[11] Chou TW. Microstructural design of fibre composites. Cambridge: Cambridge University Press; 1992.
[12] Du GW, Ko FK. Unit cell geometry of 3-D braided structures. J Reinforced Plastics and Composites 1993;12(7):752–68.
[13] Pandey R, Hahn HT. Visualisation of representative volume elements for 3-dimensional 4-step braided composites. Composite Sci Technol 1996;51:161–71.
[14] Mohajerjasbi S. Fibre architecture of three-dimensional braided composites. AIAA J 1998;36(4):613–7.
[15] Chen ZR, Zhu DC, Lu M, Ye L. Evaluation of mechanical properties of 3-dimensional braids – Part 1 A homogenisation method. Composite B, submitted.
[16] Chen ZR, Zhu DC, Lu M, Ye L. Evaluation of mechanical properties of 3-dimensional braids – Part 2 Geometrical model and mechanical properties. Composite B, submitted.
[17] Kalidindi SR, Abusafieh A. Longitudinal and transverse moduli and strengths of low angle 3-D braided composites. J Composite Mater 1996;30(8):885–905.

ELSEVIER

Composite Structures 47 (1999) 483–490

COMPOSITE STRUCTURES

www.elsevier.com/locate/compstruct

An engineering approach for predicting residual strength of carbon/epoxy laminates after impact and hygrothermal cycling

B. Qi [a,*], I. Herszberg [b]

[a] *The Cooperative Research Centre for Advanced Composite Structure Ltd. 361 Milperra Road, Bankstown, NSW, 2200, Australia*
[b] *Department of Aerospace Engineering, Royal Melbourne Institute of Technology, P.O. Box 476V, Melbourne, Vic., 3001, Australia*

Abstract

A semi-empirical analysis on residual compressive strength (RCS) of carbon/epoxy woven composite laminate was developed which included the damage effects caused by impact and hygrothermal cycling. Impact damage is modelled as a soft inclusion with an exponentially reduced stiffness and the stiffness is further reduced due to hygrothermal cycling. A complex variable method was used to determine the in-plane stress distribution near the impact-induced damage and point stress failure criterion is then used to predict the failure load. Based on the semi-empirical model, the RCS can be related to damage width, damage intensity, undamaged strength and a degradation factor due to hygrothermal cycling. The results from the analysis coincide reasonably well with the experimental data for the plain-woven fabric laminates. © 2000 Elsevier Science Ltd. All rights reserved.

Keywords: Carbon/epoxy composites; Residual compressive strength; Hygrothermal; Compression after impact

1. Introduction

Residual compression strength of composite laminates after impact has been widely researched experimentally and theoretically [1–9]. Impact damage was either treated as a single delamination plane with an elliptical boundary [6], or was treated as an inclusion with reduced stiffness [7–9]. Prediction of residual strength has been mainly based on tape laminates [6–9], in which instability-related delamination growth is the dominant strength degradation phenomenon. The modulus in damage area was estimated based on relationship between compression after impact (CAI) and damage width.

Very little work has been done to incorporate the hygrothermal influence on the residual strength into the prediction, especially for textile composites. Under hygrothermal cycling, interlaminar and intralaminar cracking may occur within composite laminates. In particular, an initial impact damage may spread as a result of hygrothermal cycling due to the freeze-thaw or boiling cycle of any moisture absorbed in the damaged region [2,3].

This paper presents experimental results of the combined effects of hygrothermal cycling and low velocity impact (up to 6 J) on damage resistance and residual compressive strength (RCS) of thin carbon/epoxy laminates. These laminates were made from plain-weave fabrics that impregnated with epoxy resin by the resin transfer moulding (RTM) process. Based on the experimental results, a semi-empirical model is developed to predict the RCS of the composites.

2. Materials and experiments

The test specimens, produced from Ciba Composites G 1051 plain-weave (PW) fabric, comprising 3 K T300 tows, had a lay-up sequence of $[0/90, 0/90, \pm 45]_s$, impregnated with Ciba Composites GY260 epoxy resin HY917/DY070 by the RTM. The cured thickness is about 1.1 mm. The test specimens, of dimension 91×117 mm^2, were cut from the panel so that their length was in the 0° direction. The impact and CAI tests have been detailed in Ref [10] in which anti-buckling plates with a window were employed. The hygrothermal cycling exposure is described in the following paragraphs.

Four groups of specimens were tested. Each group comprised specimens that were damaged by impacting at energy levels ranging from 0 to 6 J and subjected to different hygrothermal conditioning. This included water immersion and standard hygrothermal cycling

* Corresponding author. Fax: +61-2 9772 8432.
E-mail address: bqi@ozemail.com.au (B. Qi).

0263-8223/99/$ - see front matter © 2000 Elsevier Science Ltd. All rights reserved.
PII: S0263-8223(00)00027-1

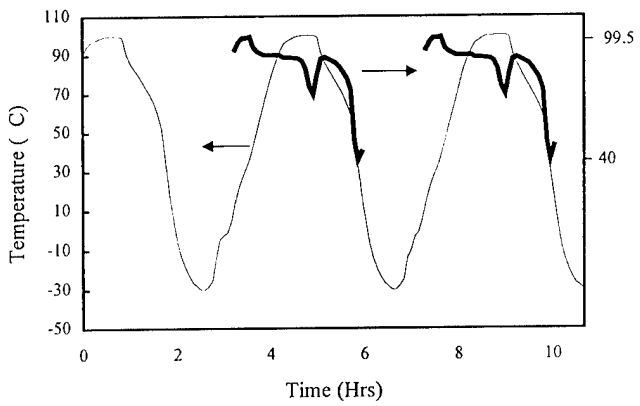

Fig. 1. SHC profile.

Table 1
Test matrix of PW laminates

Group	Test sequence	Number of specimens
A	Dry → Imp → CAI	PW:13
B	Wet → Imp → CAI	PW:4
C	Wet → Imp → SHC → CAI	PW:6
D	Wet → SHC → Imp → CAI	PW:4

(SHC). During SHC, the temperature ranges were −30°C to +100°C (measured at the specimen surface, and with average heating rate of 1.1°C/min). Relative humidity ranged from low to 99% (see Fig. 1). A total of 810 cycles was performed. All specimens were dried in an oven at 70°C until constant weight was reached, before testing. The edges of the test specimens were not sealed during conditioning. The testing sequence for each group before compression testing is shown in Table 1. Group A specimens were tested by impacting at different energy levels. Group B specimens were immersed in water at 70°C until their weight reached an equilibrium level. Then impact tests were conducted at different energy levels. Similar to Group B, Group C specimens were subjected to water immersion conditioning first. Impact tests were performed before SHC. Group D specimens were subjected to SHC after water immersion, then tested by impact.

3. Experimental results and discussion

3.1. Damage modes and growth caused by hygrothermal cycling

Three major damage modes were observed by visual inspection, optical microscopy and dye-enhanced X-ray radiography, respectively, during and after cycling. These included short transverse matrix cracks and surface debonding between resin and tow fibres, and delamination. The microcracks grew along fibres in the tows and they were arrested in the interlacing zone of warp and weft tows, while some delamination was found in the interlacing tows in the surface plies. Fig. 2 is an X-ray radiograph for an impacted PW specimen after SHC, showing these damage modes. The delamination was further investigated through cross-sectional inspection and shown in Fig. 3. The extent of damage apparently depends on resin type, hygrothermal cycling conditions.

3.2. Impact damage

Fig. 4 summaries the impact test results, in which damage area was plotted against impact energy. It seems that constant water exposure has improved damage resistance by improving the matrix toughness of the PW laminates (Group B and C). This result is quite similar to that obtained from tape laminates [10–12]. However, only slight improvement in impact resistance was

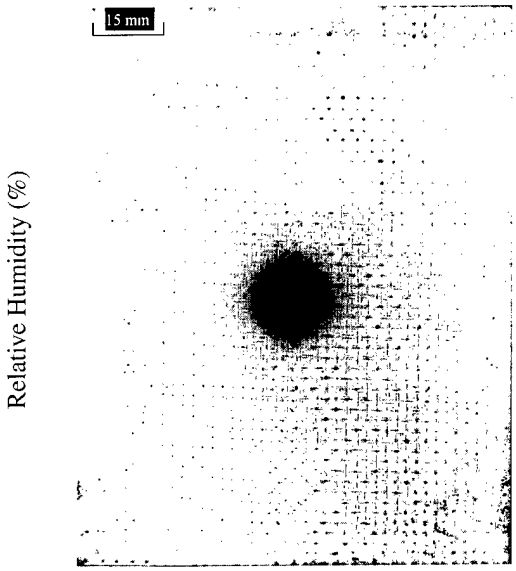

Fig. 2. Matrix cracking of an impacted PW specimen after cycling, shown by short and dark lines, and delamination in the interlacing area (X-ray radiography).

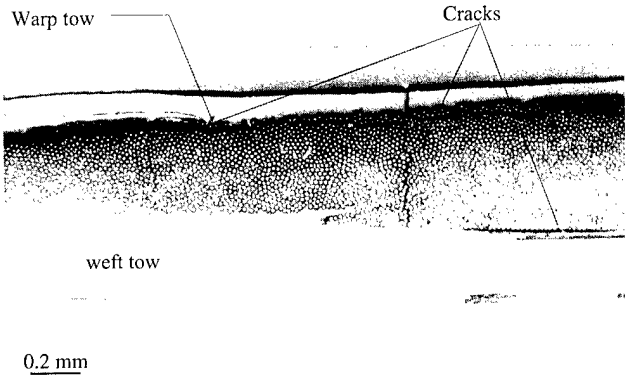

Fig. 3. Matrix cracking in a cycled PW specimen after 810 cycles.

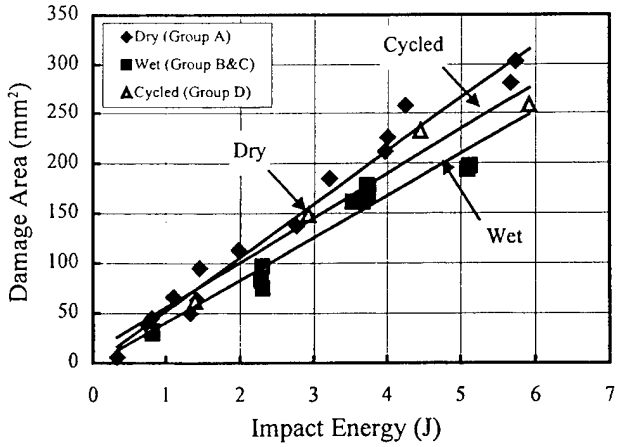

Fig. 4. Impact performance of PW laminates after different conditioning.

observed if damage width was used (comparison between dry and wet specimens).

Low velocity impact on PW laminates caused fibre breakage and tow separation. When impact energy increased, so did the extent of tow fibre breakage. The wavy tow structure provides great resistance for crack propagation and results in more localised damage and high impact resistance, compared to conventional tape laminates which suffers great delamination due to impact. It can be seen in Fig. 5 that when impact energy is further increased, the damage width is increased slowly. It is expected that when impact energy increased further, perforation will occur. Once perforation occurs, the damage area or damage width does not significantly increase with impact energy. The estimated perforation energy is indicated in Fig. 5, which is associated with a damage width of 21 mm. It is noted that the actual damage area will be bigger than the perforation area. The damage region was circular (based on C-scan inspection and X-radiography) and it can be modeled as a circular soft inclusion.

No significant damage growth was found in the impacted specimens after hygrothermal cycling (Group C), however, exposure to temperature and moisture during hygrothermal cycling could degrade interfacial properties at the crack tips of impact damage area. This could produce twofold effects: increases damage intensity; another reduces notch sensitivity.

3.3. Residual compression strength

An important observation was made, during compression after impact test, that no delamination growth occurred from the impact-induced damage up to final failure, in other words, sublaminate buckling did not happen as in the case of a tape laminate. Fig. 6 shows a comparison in damage propagation during compression loading between the impacted PW and tape laminates, in which they have been impacted at the similar energy level.

All failure started at the impact-induced damage edges and propagated in the width direction (normal to the loading direction), during compression loading. Significantly high local strains at the damage edge were recorded, and this indicated the stress concentration at the regions and thus is assumed to be the cause for onset of failure.

No significant difference in RCS, within data scatter, was found between Group A and Group B. This indicated that plasticisation in PW laminates did not affect RCS. It has been reported by a few workers [7,8] that resin toughness has little effect on the CAI strength when damage diameter is used. It mainly depends on undamaged strength, lay-up and failure mechanism.

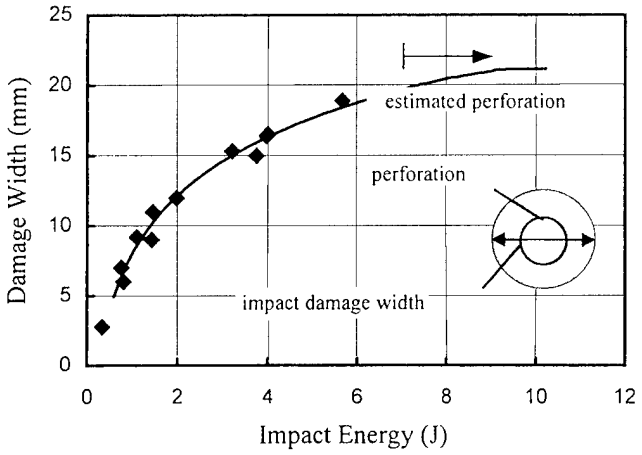

Fig. 5. Impact damage width and a proposed perforation diameter of dry PW laminate.

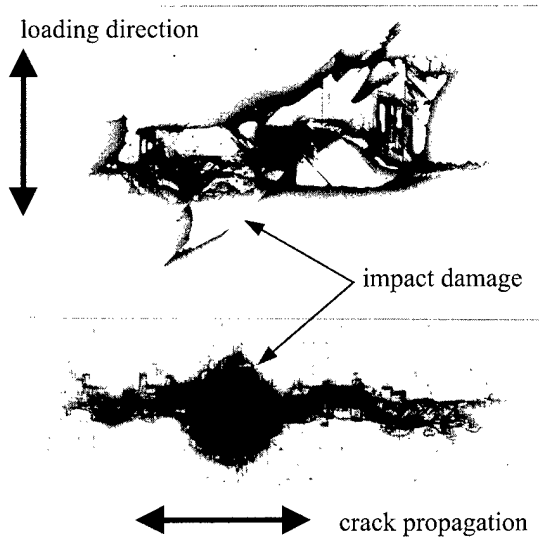

Fig. 6. Compression failure mode between impacted tape (upper) and (low) laminates during stepped loading (X-radiography, not scale).

This result will be shown in Fig. 11 together with the prediction developed in the present study.

Damage caused by cycling has a measurable influence on RCS. Both Group C and D specimens showed a lower residual strength than that of Group A and B, while Group C showed a slight higher residual strength compared to that of Group D in the range of bigger damage width. The placement of load-bearing plies (warp tows) on the surface makes their residual strength sensitive to damage caused by hygrothermal cycling. The degradation of matrix reduces its support to warp tow fibres, resulting in lower compression strength of non-impacted specimens.

4. Development of an analytical model

4.1. Estimation of reduced stiffness

In the present study, two mechanisms for stiffness reduction were considered: impact damage that reduces stiffness locally in the damage area, and damage due to hygrothermal cycling which is distributed over the whole surfaces of specimens.

4.1.1. Stiffness reduction due to impact damage

In principle, the extent of stiffness reduction due to impact or hygrothermal cycling could be measured directly. However, no significant difference in the measured modulus along the loading direction, at different hygrothermal conditions, was observed in which strain gauges were attached in a "far field" region. The average of these measured values was found to be in reasonable agreement with the calculated value based on a PW unit cell model [13].

Alternatively, an indirect method to estimate the stiffness of a soft inclusion such as impact damage, was used in the present study. The modulus retention ratio, M_r, is defined as

$$M_r = \frac{E^*}{E_0}, \tag{1}$$

where E^* is the reduced modulus of the damage area and E_0 is the elastic compressive modulus of an undamaged laminate in the loading direction (57.9 GPa, see Table 2). When the damage area is a hole, $M_r = 0$; when no damage exists, $M_r = 1$. However, for impact damage with perforation, $M_r > 0$, since the actual damage area is bigger than the perforation area. Based on Fig. 5, the damage width at perforation is estimated to be 21 mm. Consequently, at this point, M_r decreases to a minimum value. M_r may be written in the form

$$M_r = \exp(-ka), \tag{2}$$

where a is a damage width in mm, k represents a damage intensity in terms of failure mode, which is expected to be related to reinforcement form. The parameter is to be determined by the following iterative procedure, based on the point stress failure criterion [14]. It is assumed that all the elastic constants (except for Poisson's ratio) are reduced by the same factor.

For a selected value, k, M_r was calculated and used to determine the elastic constants in the damage area for a set of CAI data points corresponding to a particular group of specimens. Based on the stress distribution and measured undamaged strength, a characteristic length, d_0, was determined for each specimen and an average value of d_0 was determined for the group. The point failure stress criteria was then used to predict the failure stress as a function of a. This was then compared to the experimental values. The process was repeated for different values of k until a value of k was found which produced the best fit. For the present range of damage widths from 2 to 18 mm, the modulus retain ratio ranges from 0.28 to 0.87 for Group A and 0.11 to 0.78 for Group D specimens. Fig. 7 shows the implied results. The modulus retention ratio for group D or C will be discussed in the following section. Fig. 8 is an example of the application of this procedure, in which influence of k values on the prediction is shown.

It is found that using $M_r = 1 - ka$ to correlate the reduced stiffness and damage width will result in higher failure load in prediction in this case. This suggests that the actual stiffness reduction could be less than the predicted values.

4.1.2. Stiffness reduction due to hygrothermal cycling

Generally, damage is revealed by a variation of elastic modulus [15,16]. Similar approach was used in the present study to quantify the influence of damage caused by hygrothermal cycling on mechanical properties. This is represented by

$$E_H = (1 - D_H)E_0, \tag{3}$$

where E_H is the reduced stiffness of the cycled specimen and E_0 modulus of an undamaged specimen, in the

Table 2
Elastic constants of a PW laminate based on calculation and testing

Resource	E_1(GPa)	E_2(GPa)	G_{12}(GPa)	υ_{12}	Lay-up	v_f
CAI[a]	54.73	–	–	–	[0/90, 0/90, ±45]$_s$	0.59
PW unit cell model[b]	57.89	57.89	14	0.203		0.58

[a] Average result.
[b] Based on tensile loading [13].

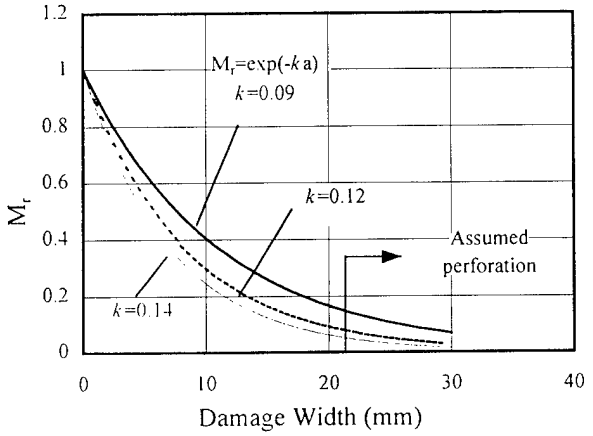

Fig. 7. Estimated stiffness reduction in the impact damage zone.

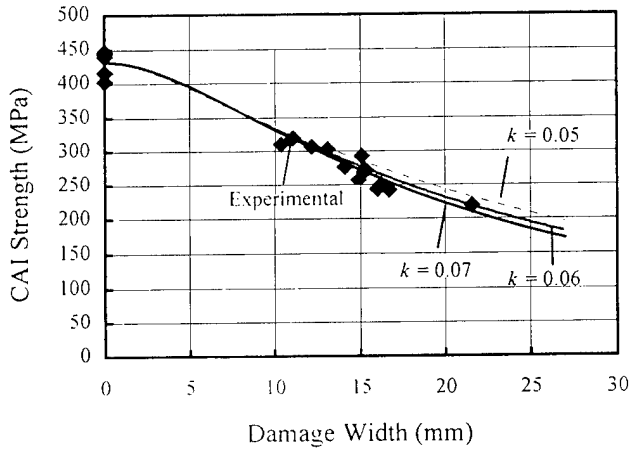

Fig. 8. Influence of damage intensity on prediction of RCS compared to experimental results for a 3 mm thick dry PW laminate.

loading direction, and D_H is the damage factor that defines the current level of damage caused by hygrothermal cycling. D_H is experimentally determined based on the percentage reduction in compression strength, using small non-impacted specimens (no buckling influence involved)

$$D_H = 1 - \frac{\sigma_{H,S}}{\sigma_{0,S}}, \tag{4}$$

where $\sigma_{H,S}$ and $\sigma_{0,S}$ are the strengths of cycled specimens and non-cycled specimens under compression loading, respectively. Thus, when $D_H = 0$, no damage occurs, while $D_H = 1$ is an extreme situation in which a complete failure is assumed to occur due to hygrothermal cycling. Therefore, the value of D_H is between 0 and 1, which apparently depends on loading type, cycling condition and resin matrix.

After cycling (up 810 cycles), the compressive strength of the cycled specimens is decreased by nearly 23% compared to non-cycled specimens based on Eq. (4).

4.1.3. Damage intensity and test sequence

Group C specimens (impacted first and then cycled) might be degraded in two ways, compared to Group D specimens (cycled first and then impacted): degradation in the global properties due to surface damage, and degradation in the properties of the impact-induced damage area. However, the difference in CAI strength was smaller between Group C and Group D (see Fig. 11).

Therefore, only one value of k for both Group D and Group C is used to take into account the hygrothermal cycling effect to predict failure strength. The variation of the implied modulus ratio in different conditions is shown in Table 3 and is summarised as follows:

$$M_{r,D} = M_{r,C} < M_{r,A}. \tag{5}$$

4.2. Analytical model

4.2.1. Basic assumptions

A point to be noted is that the ultimate failure stress of the thin laminates is above their local buckling stress. Since no sublaminate buckling occurs, it is assumed that the in-plane stress concentration causes failure starting at the edges of the damage (the stress gradients in the plane of the laminate and through the thickness are ignored because of the thin plate used).

The following assumptions are used in the present analysis:

1. The laminate is assumed to be quasi-isotropic.
2. Poisson's ratios are not changed due to damage.
3. After local buckling, stiffness in the damage area is assumed not to be changed. The buckled section (within the window area) will still be able to carry loads in the local postbuckling conditions. Since only ultimate failure load is to be predicted, the buckling history is ignored.
4. The damage causes stress redistribution during loading around the damage area. The discontinuous stiffness distribution induces stress concentration at the edge of the damage zone.

Table 3
The implied values used in the present model

Specimen type	Damage intensity, k	Characteristic length, d_0 (mm)	D_H	σ_0 (MPa)
Group A	0.09	1.21	0	340
Group C	0.14	1.38	0.23	270

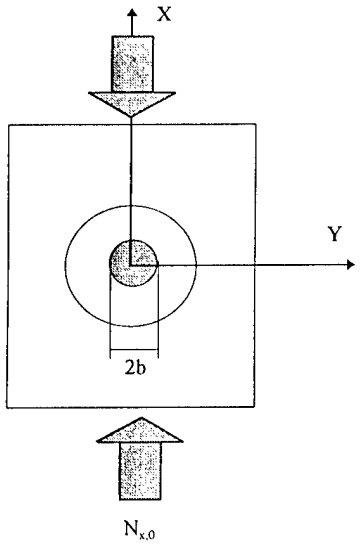

Fig. 9. A coordinate system for an impactded plate under compression.

4.2.2. Stress distribution

In-plane stress distribution around the damage area is determined based on Lekhiniskii's [17] theory. The impact damage is treated as a circular soft inclusion in a thin orthotropic plate and in-plane stress distribution can be calculated using the complex variable method. The inclusion is assumed to be small so that the laminate may be treated as on infinite quasi-isotropic plate. Then the residual strength of infinite width can be corrected using a finite-width correction (FWC) factor.

Fig. 9 shows a coordinate system in an orthotropic plate that contains circular damage with a diameter of $2b$. Under uniaxial compression loading, $N_{x,0}$, the stress in the damaged specimen can be described based on the superposition of stress in the inclusions and non-damaged part:

$$N_x = N_{x,0} + 2Re[\mu_1^2\varphi_1'(z_1) + \mu_2^2\varphi_2'(z_2)]. \tag{6}$$

The resultant normal force is N_x (N_Y is ignored) in the non-damaged area. The two resultant normal stresses in the inclusion are A and B, respectively (the shear stress in the inclusion is ignored). *Re* is the designation for the real part of the complex expression. The φ_1 and φ_2 are functions for an infinite plate with an opening, while μ_1 and μ_2 are the complex parameters of the plate, which are the roots of the following characteristic equation:

$$a_{11}\mu^4 + (2a_{12} + a_{66})\mu^2 + a_{22} = 0. \tag{7}$$

The compliance of the PW laminate, a_{ij}, that is calculated based on results obtained from a PW unit cell model shown in Table 2, are expressed as (note that Eq. (7) is applied):

$$\begin{aligned} \varepsilon_x &= a_{11}\sigma_x + a_{12}\sigma_y, \\ \varepsilon_y &= a_{12}\sigma_x + a_{22}\sigma_y, \\ \gamma_{xy} &= a_{66}\tau_{xy}. \end{aligned} \tag{8}$$

It is assumed that the laminate is in a state of plane stress when it is loaded in compression. Elastic constants, a_{ij}, in damage area, are discounted by

$$a_{ij}' = \frac{a_{ij}}{M_{r,A}}. \tag{9}$$

For cycled specimens, its elastic constants are presented by Eq. (4). The ratio, D_H, is also applied to the compliance of the laminate

$$a_{ij,H} = \frac{a_{ij}}{1 - D_H} \tag{10}$$

and its elastic constants in damage area, for Group C, similar to Eq. (9),

$$a_{ij,H}' = \frac{a_{ij}}{(1 - D_H)M_{r,C}}. \tag{11}$$

The complex potentials defined in Eqs. (8) and (9) satisfy the force boundary conditions between the laminate and inclusion (at contact surface). The stress components, A and B, in the inclusion are determined by a set of complex algebraic equations resulting from the displacement boundary conditions, given by Lekhiniskii [17]. The results in:

$$\begin{aligned} A = \frac{N_{X,0}}{\Delta}[&a_{11}a_{22}(k+n) + a_{11}a_{22}'k(1+n) \\ &+ a_{22}(a_{12} + a_{66} + a_{12}')], \end{aligned} \tag{12}$$

$$B = \frac{N_{X,0}}{\Delta}[a_{22}(a_{11} - a_{11}') + a_{11}(a_{12} - a_{12}')k(1+n)], \tag{13}$$

$$\begin{aligned} \Delta = &(a_{11}a_{22} + a_{11}'a_{22}')k + a_{22}(a_{66} + 2a_{12}') \\ &+ (a_{11}a_{22}'k + a_{22}a_{11}')n - (a_{12} - a_{12}')^2k, \end{aligned} \tag{14}$$

where $k = 1$ since the plate is treated as quasi-isotropic, while $n = -i(\mu_1 + \mu_2)$. Thus, the stress in the damaged specimen is

$$\sigma_x(y) = \frac{1}{h}N_X. \tag{15}$$

4.2.3. Failure criteria

For this work, the point stress failure criterion proposed by Whitney and Nuismer [14] is used to predict the residual strength of PW fabric laminates. For non-cycled specimens, ultimate failure occurs in the laminate when

$$\sigma_x(0, b + d_0) = \sigma_0. \tag{16}$$

For cycled specimens, ultimate failure occurs when

$$\sigma_x(0, b + d_0') = \sigma_{0,H}, \tag{17}$$

where d_0, and d_0' are the characteristic lengths of non-cycled and cycled laminates, respectively.

To account for the actual strength of a damaged laminate with a finite width, a finite-width correction

factor (FWC) for a quasi-isotropic plate containing impact damage, derived by Dost [6], is employed here. This result corrects the influence of specimen width on the residual strength for impacted laminates

$$Y = \left\{ \frac{2 + (1 - 2R/W)^3}{3(1 - 2R/W)} \right\}^{(1-M_r^N)^M}, \quad (18)$$

where N and M are constants, and they are 0.722 and 2.56, respectively [7]. Then the residual strength of a plate with finite width then is defined as

$$\sigma_r = \frac{\sigma_r^\infty}{Y}, \quad (19)$$

where it is assumed that stress concentration is the primary cause for strength reduction. It was found that the influence of FWC is only significant at larger damage width on the RCS.

Since Poisson's ratio is very small, it is assumed that damage caused by hygrothermal cycling did not influence the ratio. It was found that the result was insensitive to Poisson's ratio. A tenfold increase on Poisson's ratio led to an increase of less than 3% in stress concentration.

4.2.4. Characteristic length and stress concentration

Since pre-cracks exist in the impact-induced damage area, the characteristic length deduced is expected to be smaller than that in a case where a holed specimen is used. Groups C or D had a slight bigger d_0 value compared to Group A (1.38 mm versus 1.21 mm, average results). The reduction in RCS of these two group specimens is bigger than that of Group A specimens partly because the former had a much lower undamaged strength ($\sigma_H < \sigma_0$). The bigger d_0 value could also represent poor quality of the materials [14], which was due to damage caused by hygrothermal cycling in this case. Group C has a higher stress concentration factor than Group A, due to its lower modulus retention ratio. Table 3 summarises these values for the two groups.

It was found that the k value could significantly change d_0. Generally, within each group, d_0 and stress concentration increase with increasing k values. Consequently, σ_r/σ_0 decreases. Figs. 8 and 11 show the influence of d_0 and k on the prediction. However, the most important factors affecting the prediction are those undamaged strengths, σ_0 and σ_H, as well as the damage factor, D_H.

The ratio of elastic properties between the damaged area and the undamaged area affects both the stress concentration factor and the in-plane stress distribution. The relatively high stress concentration could occur when the retained modulus is significantly reduced. This could be related to the impact damage mode occurred in the PW laminate. When the laminates are subjected to cycling, damage intensity is further increased although the damage area is not significantly increased. Fig. 10 shows a comparison in stress concentration factors between Group A and Group C.

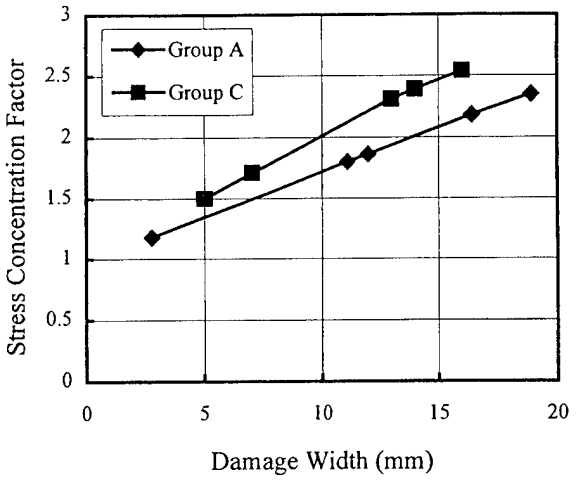

Fig. 10. Stress concentration factors calculated for Group A and C specimens.

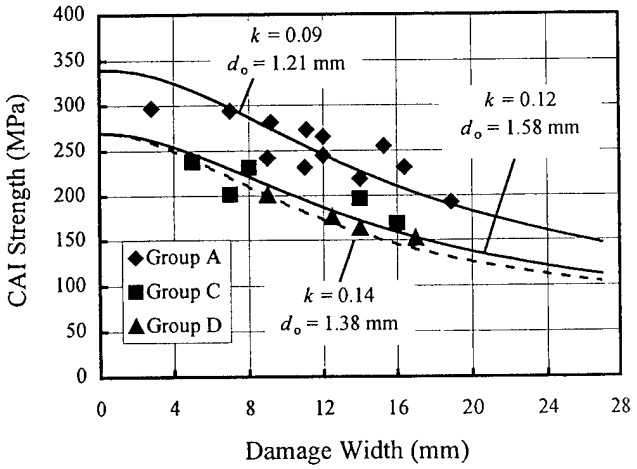

Fig. 11. Comparison of experimental results and the semi-empirical prediction for cycled and non-cycled PW laminates.

4.3. Comparison of experimental and analytical results

The analysis is verified through correlating the calculated results with measured experimental data. The comparisons are shown in Fig. 8 [18] and Fig. 11, respectively. It can be seen that in the range of impact energy used, a prediction is in good agreement. The experimental results shown in Fig. 8 was based on a PW laminate [18] with a thickness of 3 mm, with a stacking sequence of $[0, 0, \pm 45]_{3S}$ (elastic constants, E_1, G_{12} and υ_{12}, were assumed to be the same as the current PW laminates).

The semi-empirical analysis is reasonably simple and provides an engineering approach to predict the failure

strength of woven composite materials. It is noted that there are some limitations in the semi-empirical model. The model did not consider the progressive failure process although the actual failure starts at about 80% of the ultimate failure load. Subsequently, the fibre microbuckling and barrelling of warp tows were ignored. The form of reinforcement has an important effect on the notched strength, in which the formation of a damage zone can be largely suppressed, which was not included in the analysis. Also, to determine value of D_H, a hygrothermal cycling test is required for different laminates. In other words, a database of materials to hygrothermal response needs to be established.

5. Conclusions

From the present study, it can be concluded that the residual compression strength of composite laminate is further decreased due to the degraded matrix properties in the form of matrix cracking caused by hygrothermal cycling.

A semi-empirical model was developed which included the damage effects caused by impact and hygrothermal cycling. This model provides an engineering approach to predict RCS. Based on the semi-empirical model, the RCS can be related to damage width, damage intensity, undamaged strength and a degradation factor due to hygrothermal cycling. The results from the analysis coincide reasonably well with the experimental data for the PW laminates.

Acknowledgements

The first author would like to thank The Sir Lawrence Wackett Centre for Aerospace Design Technology, RMIT, and The CRC-ACS, for the financially support in the research program. Grateful acknowledgement is also given to AMRL, ASTA for access to the testing facilities employed in the program.

References

[1] Dow MB, Smith DL. Damage-tolerant composite materials produced by stitching carbon fabrics. In: 21st International SAMPE Technical Conference, 25–28 September, 1980.

[2] Lauraitis KN, Sandorff PE. Experimental investigation of the interaction of moisture, low temperature, and low level impact on graphite/epoxy composites. Lockheed-California company, NADC 79102–60, 1980.

[3] Stansfield KE, Pritchard G. Damage generation and healing during composite thermal spikes. In: 21st International SAMPE Conference, September 1989, p. 120–9.

[4] Mitrovic M, Carman GP. The influence of tensile fatigue damage on residual compressive strength of woven composites. In: Proceedings of the American Society for Composites, 10th Technical Conference, 18–20 October, 1995.

[5] Nejhad MNG. Effect of open holes and low velocity impact damage on the compressive strength of woven carbon fibre reinforced polymer composites, CCM Report 88–27. University of Delaware, 1987.

[6] Flanagan G. Two-dimensional delamination in composite laminates under compression loading. Composite Materials: Testing & Design, ASTM STP 972, 1988:180–190.

[7] Dost EF, Ilcewicz LB, Gosse JH. Sublaminate stability based modelling of impact-damaged composite laminates. In: Proceedings of the Third Technical Conference on American Society of Composites, Seattle, September 1988, p. 354–63.

[8] Guild FJ, Hogg PJ, Prichard JC. A model for the reduction in compression strength of continuous fibre composites after impact damage. Composites 1993;24(4):333–9.

[9] Xiong Y, Poon C. Failure prediction of composite laminates containing impact damage. LTR-ST-1898, NRC-CNRC, September 1992.

[10] Qi B, Herszberg I, Baker AA, Bannister M. The residual compression strength of stitched and unstitched plain-weave carbon/epoxy laminates after impact and hygrothermal cycling. ICCM-11, Gold Coast, July, 1997.

[11] Qi B, Herszberg I, Baker AA, Bannister M, Impact performance of carbon/epoxy laminates after environmental conditioning. In: International Aerospace Conference, Sydney, 25–27 February, 1997.

[12] Qi B, Herszberg I, Bannister MK. Moisture effect on interlaminar fracture toughness of unidirectional T300/914C composites. In: Karihaloo BL, Mai YW, Ripley MI, Ritchie RO. editors. Proceedings of the Ninth International Conference on Fracture: Advances in Fracture Research, vol. 2. Sydney: Pergamon Press, 1997, p. 875–84.

[13] Tan P, Tong L, Steven GP. A 3D modelling technique for predicting the linear elastic properties of opened-packing woven fabric unit cell. In: Presented at the Ninth International Conference on Composite Structure. UK: Paisley, 1–3 September 1997.

[14] Whitney JM, Nuismer RJ. Stress fracture criteria for laminated composites containing stress concentrations. Compos Mater 1974;8:253–65.

[15] Ladeveze P, Proslier PL. Damage and fracture of tri-directional composites. In: Progress in Science and Engineering of Composites. ICCM-IV, Tokyo, 1982:649–658.

[16] Beaumont PWR. Damage accumulation. In: Talreja R. editor. Composite Materials Series Vol. 9: Damage Mechanics of Composite Materials. Amsterdam: Elsevier, 1994:168.

[17] Lekhnitskii SG. Anisotropic Plate (Translated by Tsai, SW, Cheron). London: Gordon and Breach, 1986.

[18] Herszberg I, Leong KH, Bannister MK. The effect of stitching on the impact damage resistance and tolerance of uniweave carbon/epoxy laminates. In: Fourth International Conference on Automated Composites 1995;1:53–60.

ELSEVIER

Composite Structures 47 (1999) 491–495

COMPOSITE STRUCTURES

www.elsevier.com/locate/compstruct

Numerical investigation on thermal response of oil-heated tool for manufacture of composite products

Y. Ding [a,*], W.K. Chiu [a], X.L. Liu [b]

[a] *Department of Mechanical Engineering, Monash University, Clayton, Vic. 3168, Australia*

[b] *Cooperative Research Centre for Advanced Composite Structures, 506 Lorimer St., Fishermans Bend, Vic. 3207, Australia*

Abstract

In this paper, the thermal response of an oil-heated tool is studied using a commercial FEM package ABAQUS and the numerical results for laminar flows and fully turbulent flows in the oil are presented. The study is focused on the influence of the oil flow rates on the oil temperature distributions along the oil flow path and the thermal responses of the tool surface. It was determined that the higher a flow rate was, the shorter a transient heat transfer process took. Consequently, it is concluded that the heating process of an oil-heated tool can be controlled by the control of the thermal oil flow rates. Furthermore, since the oil-heated tool can also be used to cool the composite products by circulating cold oil through the tool, instead of hot oil, the cooling processes were also simulated. The results confirm that cooling can be similarly controlled by flow rates. © 2000 Elsevier Science Ltd. All rights reserved.

Keywords: Composite manufacturing; Oil-heated tool; Integral heating method; Transient heat transfer; Laminar flow; Turbulent flow; Finite element method; Forced convection/diffusion heat transfer

1. Introduction

Fiber-reinforced polymer composite materials are composed of high-strength fibers dispersed in a polymer matrix. The advantages of such advanced composite structures include weight reduction, design flexibility, corrosion resistance, and reduced noise transmission compared to those made from conventional materials. Particularly, the resin transfer molding (RTM) technique has been proven by composite manufacturers and material industries as possessing the most potential for overcoming the manufacturing difficulties involved in processing advanced composite components for medium to high volumes [2]. Due to the potential benefits of RTM in manufacturing, much research effort has been devoted in developing the technique during the last decade [1,3,5,7].

The RTM process is virtually a closed operation of a tool assembly or a mould whereby a dry fiber preform is placed between matched tools and impregnated with a liquid thermosetting resin. When the tool/mould is heated up according to a heating cycle, the resin is cured and the component is produced after opening up the tool assembly. Research involved in the past has been heavily focused on the curing process of the resin, assuming the tool/mould is heated up using the conventional heating method – heating the tool/mould in an autoclave or an oven. As the conventional heating method is time consuming and inefficient, some recent research effort has been focused on developing integrally heated tools, to which the heating elements are directly attached and no autoclave or oven is required. Liu and Lam [4] investigated the heating processes of a wing stringer RTM tool assembly using both the autoclave-heating method and the electric-strip-heaters-attached heating method. Their results showed that the electrical heating using strip heaters provided a much faster heating process for the tool compared to oven/autoclave heating. However, the temperature distribution on a cross-section of the tool during the electrical heating process was not as uniform as that during the oven heating process. To ensure a high quality of composite structure, one of the most important aspects to be considered in the tooling design is the temperature distribution in the tool during the heating up process. The temperature distribution not only has a direct impact on the curing cycle of the composite products, but also further influences the state of residual stress in the

* Corresponding author. Tel.: +010-61-3-565-4000; fax: +010-61-3-565-3409.

0263-8223/99/$ - see front matter © 2000 Elsevier Science Ltd. All rights reserved.
PII: S0263-8223(00)00028-3

structure. Thus, an alternative integral heating method, oil heating, for the manufacture of composite structures was investigated as a research program of the CRC-ACS, Australia. The method employs thermal oil as the heat transfer medium. The findings of the numerical simulation, using a commercial FEM package ABAQUS, on the heating process of an oil-heated tool, as a part of this program, are presented in this paper.

2. The oil-heated tool

Fig. 1 shows the oil-heated tool used in this investigation. The tool was made by embedding a copper tube into two aluminum plates to formulate 12 oil flow channels. The geometry parameters of the oil-heated tool are listed in Table 1. During the heating process, thermal oil, heated up in an oil heater, is forced to circulate through the tube, and heat is then transferred from the oil to the tool body by the forced convection.

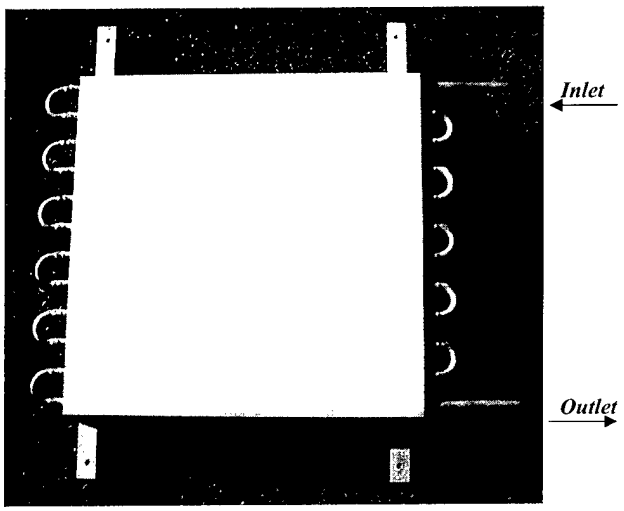

Fig. 1. The oil-heated tool for composite structures.

Table 1
Geometry parameters of the oil-heated tool (dimension of the oil-heated tool (mm))

Copper tube		Aluminum plate		
Inner diameter	Outer diameter	Length	Width	Thickness
10.5	12.5	450	450	22.5

The thermal oil used in this study was Shell Thermia Oil B. The properties of the oil and the tooling materials are given in Table 2.

3. Finite element modeling of heat transfer in the oil-heated tool

During a composite manufacturing process, the composite part is cured by the heat transferred from the tool surface. The heat transfer process in the composite is complex, involving heat conduction, heat convection caused by resin flow, and the exothermic heat of cure reaction. In the present study, only the heating up and cooling of the tool was considered. Focus was given to the investigation of the temperature distributions of the oil along its flow path at different times and the thermal responses of the tool at different points on the tool surface.

According to the principle of energy conservation and in the absence of heat generation within the tool, the governing equations for heat conduction over the tool and convection/diffusion via the thermal oil are described as

$$\frac{\rho_{\text{tool}} c_{\text{tool}}}{k_{\text{tool}}} \frac{\partial T}{\partial t} = \frac{\partial^2 T}{\partial x_1^2} + \frac{\partial^2 T}{\partial x_2^2} + \frac{\partial^2 T}{\partial x_3^2}, \tag{1}$$

$$\frac{\rho_{\text{oil}} c_{\text{oil}}}{k_{\text{oil}}} \left(\frac{\partial T}{\partial t} + u_1 \frac{\partial T}{\partial x_1} + u_2 \frac{\partial T}{\partial x_2} + u_3 \frac{\partial T}{\partial x_3} \right) = \frac{\partial^2 T}{\partial x_1^2} + \frac{\partial^2 T}{\partial x_2^2} + \frac{\partial^2 T}{\partial x_3^2}, \tag{2}$$

where ρ, c and k are density, specific heat and thermal conductivity of the tool and oil, as indicated. u_1, u_2 and u_3 are the velocity components of the oil flow, respectively.

Due to symmetry of the tool shown in Fig. 1, only half of the tool was modeled. Fig. 2 shows the FEM mesh of the model. The part of the oil channel outside of the tool (i.e., the 180° tube-bends) was not included in the model. It was assumed that there was no heat exchange at these tube-bends and consequently temperatures of oil at the two ends of a bend were the same. It was also assumed that the tool was well insulated and hence no surface convection and radiation were considered in the study. The temperature of the oil at the inlet was taken as constant at 180°C. The initial temperature of the tool used was 20°C.

Table 2
Properties of oil and the tool

Properties	Thermia Oil B	Aluminum	Copper
Density (ρ)	873 (kg/m^3)	2702 (kg/m^3)	8933 (kg/m^3)
Thermal conductivity (k)	0.121 (W/m K)	237 (W/m K)	401 (W/m K)
Specific heat (c_p)	2474.2 (J/kg K)	903 (J/kg K)	385 (J/kg K)
Viscosity (v)	4.3 (mm^2/s)	–	–

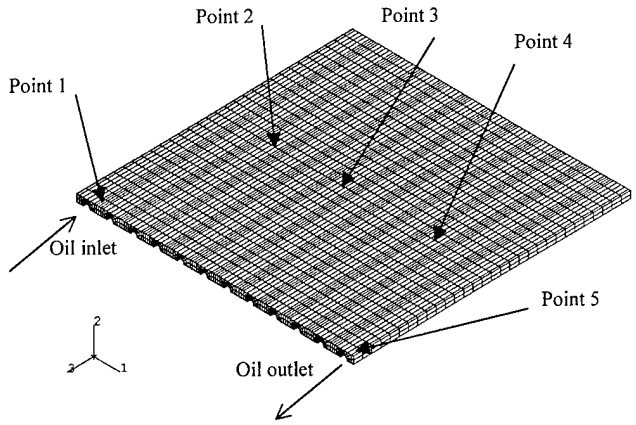

Fig. 2. The FEM model of the oil-heated tool.

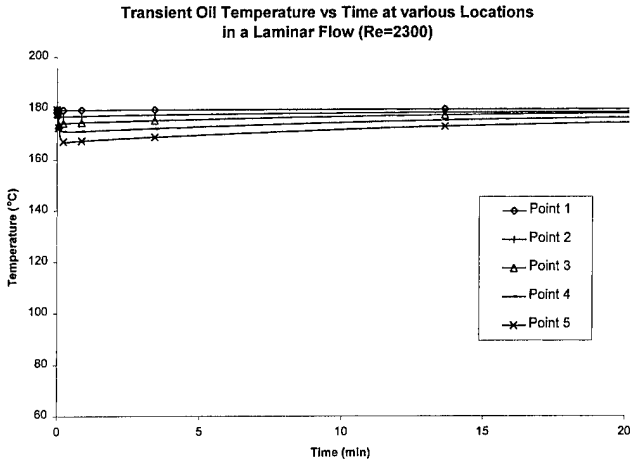

Fig. 3. Oil temperature change with time when $Re = 2300$.

Heat was transferred from the oil to the tool body by forced convection. A convective boundary was specified at the interface between the oil and the tube. The convective heat transfer coefficients, h_c, were calculated by the following equations [6]:

$$h_c = 3.66\frac{k_{oil}}{d} \quad (Re \leqslant 2300), \tag{3}$$

$$h_c = \frac{0.023k_{oil}^{0.6}\left(\rho_{oil}\ c_{oil}\right)^{0.4}}{d^{0.2}\ v_{oil}^{0.4}}u^{0.8} \quad (Re \geqslant 10,000), \tag{4}$$

where k_{oil}, ρ_{oil}, c_{oil} are defined in Eq. (2), v_{oil} the viscosity of the heat-transfer oil, d the diameter of the copper tube and u is the flow velocity of the oil along the tube. Re is the Reynolds number, which is defined as [6]:

$$Re = \frac{u \cdot d}{v_{oil}}. \tag{5}$$

A commercial FEM package, ABAQUS, was chosen for the numerical investigation, due to its ability to model forced convection and diffusion heat transfer. 3-D diffusive heat transfer elements were used for copper pipes and aluminum plate and 3-D forced convection/diffusion elements for the thermal oil. The results of the FEM model are presented and discussed in the following section.

4. Results and discussion

4.1. Transient oil temperature profiles during heating

Fig. 3 shows the oil temperature change with time. Points 1–5 in the figure are the surface nodes of the oil elements at the locations indicated in Fig. 2. Fig. 4 plots the oil temperature distributions along the oil flow channel at different times for a laminar flow of $Re = 2300$. The maximum oil temperature drop between the inlet and outlet was 13°C, and it occurred 6 s after heating began. As time increased, the oil temperature

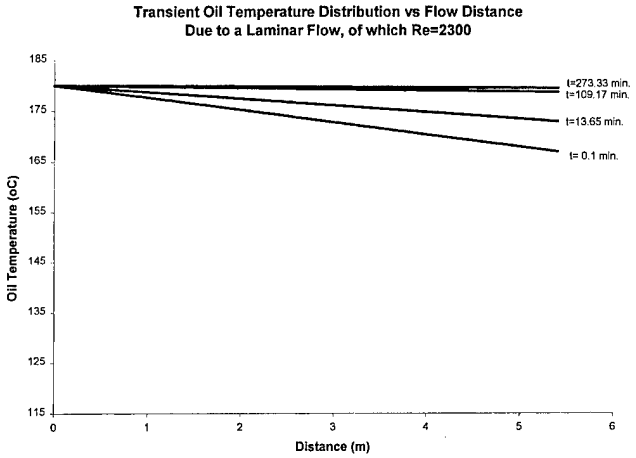

Fig. 4. Oil temperature distribution along the flow channel when $Re = 2300$.

distribution along the flow channel appeared to approach uniformity at an exponential rate.

The corresponding results for a fully developed turbulent flow of $Re = 10,000$ are given in Figs. 5 and 6, respectively. In this case, the maximum oil temperature drop between the inlet and outlet increased to approximately 106°C, and occurred 1.3 s after heating began. Compared to the laminar flow, the oil temperature profile approached uniformity at a much faster exponential rate.

4.2. Temperature distribution on the tool surface during heating

The thermal response of the tool during transient heat-transfer was analyzed and the results for the laminar flow and the turbulent flow are shown in Figs. 7 and 8, respectively. As shown in Fig. 6, the thermal responses at different points on the tool surface are almost

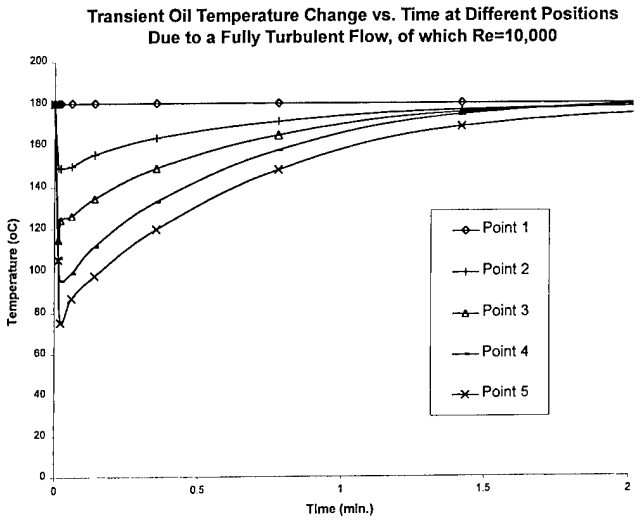

Fig. 5. Oil temperature change with time when $Re = 10,000$.

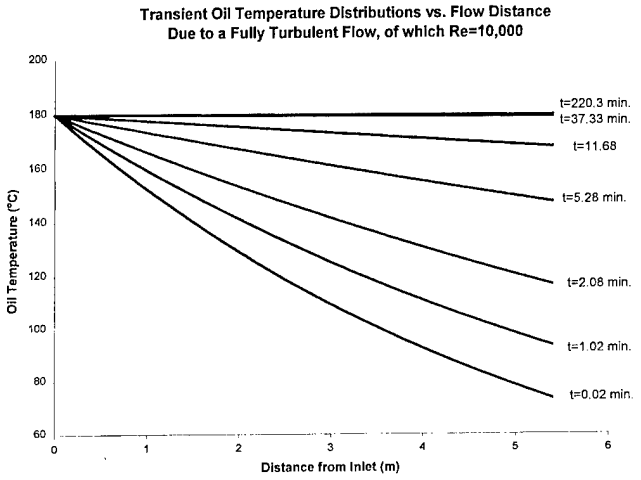

Fig. 6. Oil temperature distribution along the flow channel path when $Re = 10,000$.

identical, indicating that the transient temperature distribution over the tool surface was very uniform in laminar flows. For the turbulent flow, the temperature distribution on the tool surface was not uniform at the first few minutes of heating. The maximum temperature difference in the tool was approximately 33°C for the case of $Re = 10,000$. After a few minutes, the distribution became uniform.

The thermal responses at the center of the tool surface (point 3) are plotted in Fig. 9 for different flow rates. In the laminar flow region ($Re \leqslant 2300$), increasing the flow rate appeared to have little effect on the heating up rate of the tool. It took more than two hours for the point to reach the heating temperature. When the flow rate was increased to reach the turbulent flow region ($Re \geqslant 10,000$), the heating up rate increased with the Reynolds number. The temperature at point 3 reached the heating temperature in a few minutes.

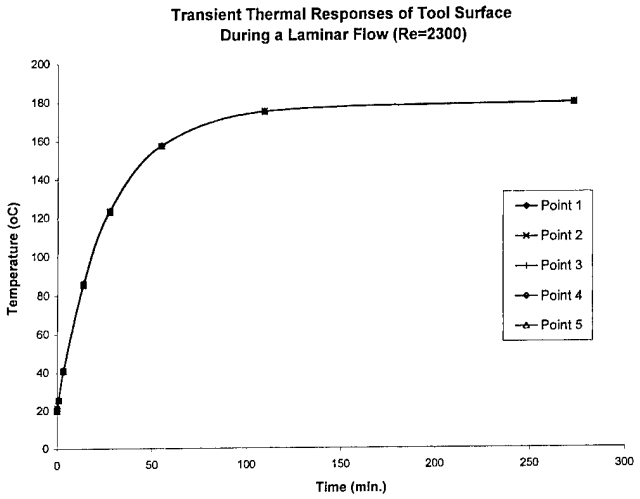

Fig. 7. Thermal responses of the tool surface at various locations when $Re = 2300$.

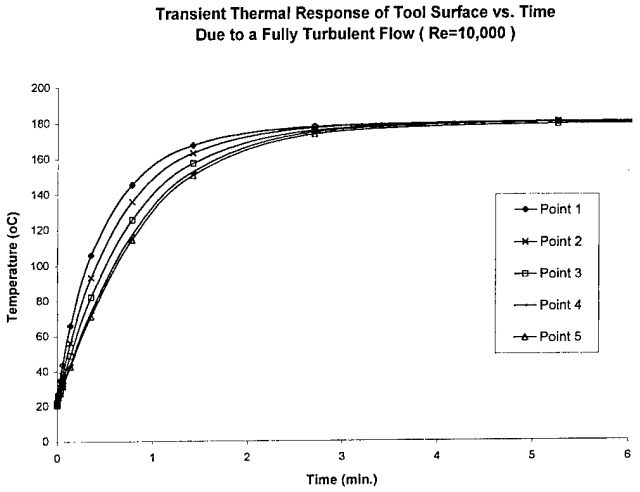

Fig. 8. Thermal responses of the tool surface at various locations when $Re = 10,000$.

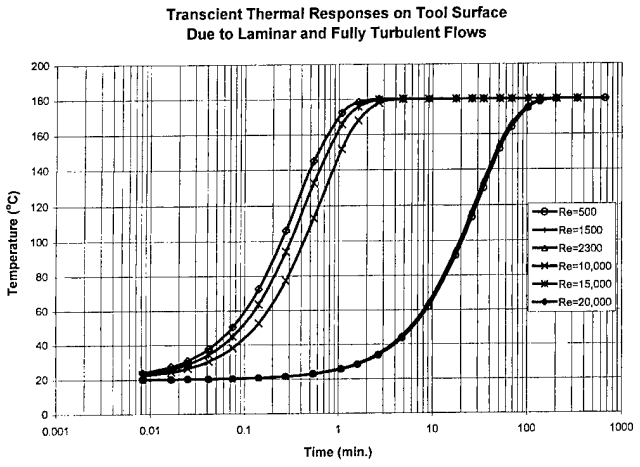

Fig. 9. Thermal responses at the center of the tool surface.

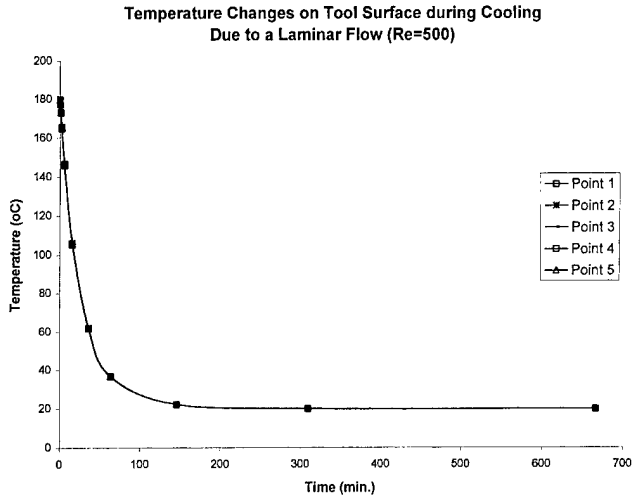

Fig. 10. Temperature changes of the tool surface during cooling when $Re = 500$.

4.3. Transient thermal responses of the tool surface during cooling

An advantage of an oil-heated tool is that it can also be used for cooling of the composite products. In the present study, temperature changes of the tool during the cooling process were also investigated. The cooling process was simulated for different flow rates, by taking the initial temperature of the tool body as 180°C and the temperature of the oil at the inlet as 20°C. The results indicated that the temperature responses of the oil and the tool changed in a similar fashion as those during heating up. Fig. 10 shows the temperature change versus time for a laminar flow of $Re = 500$.

5. Conclusions

According to the FEM simulations presented in this paper, the following conclusions are made:

(1) The heating and/or cooling process for the oil-heated tool can be controlled by the control of the oil flow rates.

(2) A laminar flow ($Re \leqslant 2300$) results in very uniform temperature distribution throughout the heating process. However, it is a relatively slow process, taking at least two hours for the tool to reach the heating temperature.

(3) A fully turbulent flow ($Re \geqslant 10,000$) generates a non-uniform temperature profile during the initial transient period of a few minutes. However, the tool can be heated up much faster as compared to the laminar flow.

(4) The optimal flow rate appears to be in the lower range of the fully turbulent flow region. This provides a high efficiency for the tool heating up and minimizes energy input.

References

[1] Gelin JG, Cherouat A, Boisse P, Sabhi H. Manufacture of the composite structures by the RTM process: numerical simulation of the shaping operation. Compos Sci Technol 1996;56:711–8.

[2] Johnson CF, Chavka NG, Jeryan RA. Resin transfer moulding of complex automotive structures. In: Proceedings of 41st Annual Conference of the Reinforced Plastics Composites Institute. The Society of the Plastics Industry, 1986 (Session 12-A).

[3] Johnson CF. Resin transfer moulding, In: Mallick PK, Newman S, editor. Composite materials technology – process and properties. Munich: Carl Hanser, 1990. p. 150–78.

[4] Liu XL, Lam YC. CRC-ACS report. Cooperative Research Centre for Advanced Composite Structures Ltd., Australia, 1997 (Confidential).

[5] Loos AC, MacRae JD. A process simulation model for the manufacture of a Blade-Stiffened panel by the resin film infusion process. Compos Sci Technol 1996;56:273–89.

[6] Mills AF. Heat transfer, Homewood, IL: Richard D. Irwin, 1992 (ISBN 0-256-12817-0).

[7] Molnar JA, Trevino L, Lee LJ. Mould filling in structural RIM and resin transfer moulding. In: Proceedings of 44th Annual Conference of the Composites Institutes. The Society of the Plastics Industry, 6–9 February, 1989. p. 1–10 (Session 20-A).

ELSEVIER

Composite Structures 47 (1999) 497–506

COMPOSITE STRUCTURES

www.elsevier.com/locate/compstruct

Composite robot end effector for manipulating large LCD glass panels

Je Hoon Oh [a], Dai Gil Lee [a,*], Hyun Surk Kim [b]

[a] *Department of Mechanical Engineering, Korea Advanced Institute of Science and Technology, ME 3221, Gusong-dong, Yusong-gu, Taejon-shi 305-701, South Korea*

[b] *Meerae Engineering Corporation, 54-2 Mok-ri, Dongtan-myon, Hwaseong-gun, Kyoungki-do 445-810, South Korea*

Abstract

Recently, the design and the manufacture of light robot end effectors with high stiffness have become important in order to reduce the deflection due to the self-weight and weight of glass panel, a part of LCD, as the size of glass panels as well as robot end effectors increases. The best way to reduce the deflection and vibration of end effectors without sacrificing the stiffness of end effectors is to employ fiber reinforced composite materials for main structural materials because composite materials have high specific stiffness and high damping. In this work, the end effector for loading and unloading large glass panels were designed and manufactured using carbon fiber epoxy composite honeycomb sandwich structures. Finite element analysis was used along with an optimization routine to design the composite end effector. A box type sandwich structure was employed to reduce the shear effect arising from the low modulus of honeycomb structure. The carbon fiber epoxy prepreg was hand-laid up on the honeycomb structure and cured in an autoclave. A special process was used to reinforce the two sidewalls of the box type sandwich structure. The weight reduction of the composite end effector was more than 50% compared to the weight of a comparable aluminum end effector. From the experiments, it was also found that the static and dynamic characteristics of the composite end effector were much improved compared to those of the aluminum end effector. © 2000 Published by Elsevier Science Ltd.

Keywords: LCD glass panel; End effector; Carbon/epoxy composite material; High specific stiffness; Damping; Optimum design; Sandwich structure

1. Introduction

Industrial robots are increasingly employed in clean room environment semiconductor industries to eliminate contamination from human workers. As the size of glass panel, a part of LCD, increases, the payload and stiffness of robots are required to increase accordingly. Recently, the thickness of aluminum robot end effector for loading and unloading of large glass panels has been increased much to reduce the deflection caused by the weight of large glass panels. However, the thickness increase of the aluminum end effector requires large working space of glass panel storage cassettes, which reduces the number of panels loaded in one cassette and therefore, reduces the productivity. When the height of storage cassettes is increased so as to increase the number of glass panels to be loaded, the size of the robot should be also increased, which requires larger motors to give the same acceleration. Therefore, the design and manufacture of slim but stiff end effectors have become important as the size of glass panels increases.

Since composite materials have high specific stiffness, high specific strength, high damping and low coefficient of thermal expansion, they have been widely used in aircraft and spacecraft structures as well as in sports and leisure goods. These properties cannot be obtained from conventional metals such as steel and aluminum [1]. In addition, the structures made up of composites have high natural frequencies as well as light weight, therefore, they are increasingly employed in rotating structures such as drive shafts, machine tool spindles and guide rollers [2–4], the nozzle dam for a steam generator [5] and hood for an automobile [6].

The structure of a robot should have both high specific stiffness and high damping in order to increase positional accuracy and dynamic performance. The specific modulus of the high modulus carbon/epoxy composite material can be increased more than five times that of steel or aluminum when the stacking angle of fibers from the axis is less than 15°. Also the damping

* Corresponding author. Tel.: +82-42-869-3221; fax: +82-42-869-3210.

E-mail address: dglee@kaist.ac.kr (D.G. Lee).

0263-8223/99/$ - see front matter © 2000 Published by Elsevier Science Ltd.
PII: S0263-8223(00)00013-1

capacity of the carbon/epoxy composite material is more than ten times larger than that of conventional metals [7,8]. Therefore, the carbon/epoxy composite material is a promising material for the end effector that requires lightweight and high stiffness to minimize the deflection due to the self-weight and the weight of glass panels.

Since composite materials have superior material properties and become cheaper, several researchers have attempted to employ composite materials as main structural materials in robot structures. Asada et al., [9] developed a direct-drive robot arm structure with carbon/epoxy composite material. The robot arm had hollow cylindrical shape and was used for an anthropomorphic type direct-drive robot. Lee et al. [10] designed and manufactured a SCARA type direct-drive robot for assembly operation with carbon/epoxy composite material. They also manufactured an aluminum robot arm with the same dimensions of the composite robot arm and showed that the static and dynamic characteristics of the composite robot arm as well as weight saving were considerably improved compared to those of the aluminum robot arm. A six degrees of freedom anthropomorphic robot arm with 70 N payload was designed and manufactured with high modulus carbon fiber epoxy composite by Lee et al. [11]. The static and dynamic performance of the composite arm were tested and compared to those of the steel arm with the same size. Kim et al. [12] developed the composite third robot arm of the six-axis articulated robot manipulator that has six degrees of freedom, 60 N payload and 0.1 mm positional accuracy of end effector.

In this work, a light end effector that can be used for loading and unloading large glass panels, parts of LCD, was designed and manufactured using carbon/epoxy composite material and honeycomb in order to reduce the deflection due to the self-weight of the end effector and weight of the glass panel without sacrificing the stiffness of the end effector. The box type sandwich structure whose two side walls and top and bottom faces were reinforced, was employed to reduce the shear effect arising from the low modulus of honeycomb structure. The carbon/epoxy prepreg was hand-laid up and cured using the autoclave vacuum bag degassing process. A special process was also used to reinforce the two sidewalls as well as the top and bottom faces.

In order to determine the optimum shape of the composite end effector, the finite element analysis in combination with an optimization routine was performed using ANSYS, a commercial finite element software, when the end effector was subjected to both the self-weight and the weight of the glass panel. Also, the static and dynamic characteristics of the composite robot end effector such as the static deflection, natural frequency and damping were measured and compared with those of a comparable aluminum robot end effector.

2. Characteristics of the end effector

Fig. 1 shows the typical robot system used for loading and unloading glass panels into a cassette. The robot that has three degrees of freedom (r, θ, and z), is composed of a base, arm, wrist block and end effector, respectively. In order to prevent particles from flowing

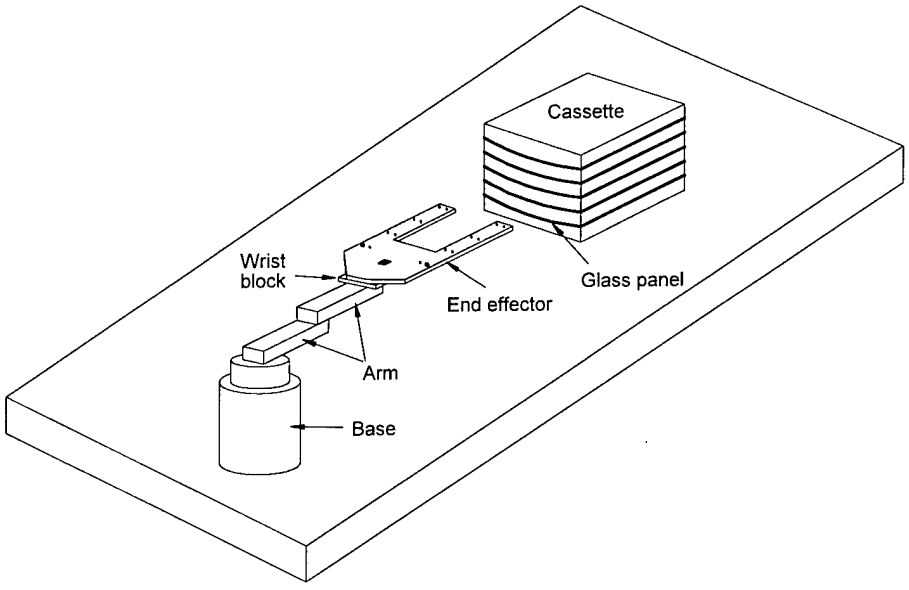

Fig. 1. Typical robot system for loading and unloading glass panels.

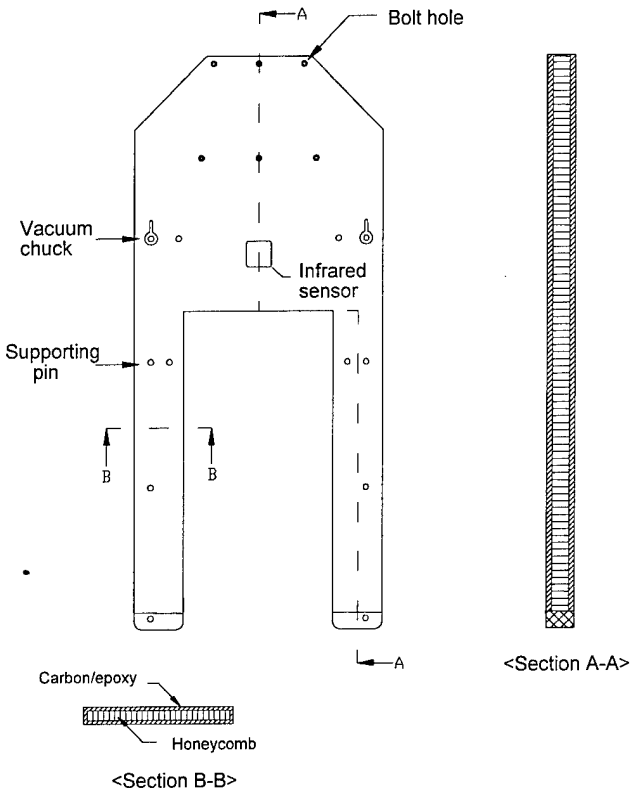

Fig. 2. Configuration of the composite end effector (sectional views are exaggerated for clarity).

into the clean environment, the arm joint sections are sealed with ferrofluidic materials. The robot with dual arm configuration has also been developed to reduce handling time of glass panels. The end effector for the single arm can be used directly for the dual arm because the configuration of end effector for the dual arm is the same as that of the end effector for the single arm as shown in Fig. 1.

The size of the end effector is dependent on the size of glass panel, which is a part of LCD. The current largest size of raw glass panel is 670 mm × 830 mm × 0.7 mm before machined to the required size of products. Thus, the aim of this work is to develop a composite end effector for manipulating the glass panels of 670 mm× 830 mm × 0.7 mm size. As shown in Fig. 1, the end effector is mounted on the wrist block located at the end of the second arm using six bolts. Fig. 2 shows the configuration of the composite end effector. Two vacuum chucks were located on the end effector to secure the glass panel on the end effector. The glass panel is loaded on the 10 cone-shaped pins mounted on the end effector, to prevent the glass panel from being scratched by the surface of end effector. An infrared sensor is used to detect the existence of the glass panel on the end effector. The central part of the end effector opposite to the wrist block is eliminated to reduce weight and interference with other equipments as shown in Fig. 2.

3. Design of the composite end effector

The total deflection δ_{total} of the end effector due to the weight of glass panel and the self-weight of the end effector is expressed as follows:

$$\delta_{\text{total}} = \delta_{\text{panel}} + \delta_{\text{self-weight}}, \tag{1}$$

where δ_{panel} and $\delta_{\text{self-weight}}$ are deflections due to the weight of glass panel and self-weight, respectively. The total thickness Δ required by the end effector when the glass panel is loaded, is given by

$$\Delta = \delta_{\text{total}} + t_{\text{endeffector}}, \tag{2}$$

where $t_{\text{endeffector}}$ is the thickness of the end effector.

Fig. 3 shows the schematic diagram of deformed shape of the end effector. As the total thickness required by the end effector increases, the pitch between the stacked panels increases, which reduces the number of glass panels loaded in one cassette. Thus, the total thickness Δ required by the end effector must be minimized to improve productivity.

In order to reduce the total thickness Δ required by the end effector, not only the end effector must be slim but also have high bending stiffness with low weight. The sandwich structure composed of carbon/epoxy face material and Nomex honeycomb was employed for the end effector to increase bending stiffness and decrease self-weight. The sidewalls were reinforced to reduce the shear deformations arising from the low rigidity of honeycomb structure. The unidirectional carbon/epoxy prepreg and Nomex honeycomb used in this work were USN 125 and HRH-10-1/8-4.0 manufactured by Sunkyung Chemicals (Suwon, Korea) and Hexcel Composites (USA), respectively. The material properties used in this work are listed in Table 1.

The stacking angle, thickness of the face and core, and dimensions of the end effector were determined through finite element analyses along with optimization routine. Before analyzing the characteristics of the end effector, a simply supported sandwich beam subjected to a uniform pressure on its top face was analyzed using ANSYS 5.3, a commercial finite element software, to verify the validity of the model for the end effector. The sandwich beam used in the verification was composed of the two aluminum skins and a foam core, whose material properties are shown in Table 2. Fig. 4 shows the sandwich beam used for the verification, which was subjected to a uniform distributed load of 1000 N/m. The mechanical characteristics of the point A at the interface between the top face and the core at coordinate $x = L/4$ as shown in Fig. 4 were calculated. The maximum displacement of the structure in the z-direction (U_z), σ_{xx} in the face and in the core, and σ_{xz} at point A were calculated using various elements such as solid, shell and plane element. The calculated results were also compared with those of Manet [13].

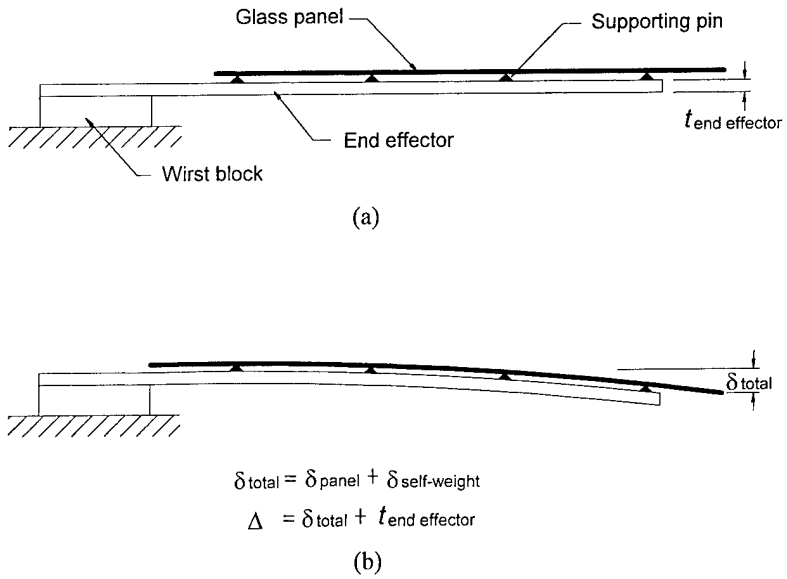

Fig. 3. Schematic diagram of the end effector with a glass panel: (a) before deformation; (b) after deformation (not to scale).

Table 1
Mechanical properties of carbon/epoxy, honeycomb and glass panel

	Carbon/epoxy (USN125)	Honeycomb (HRH-10-1/8-4.0)	Glass panel
E_1 (GPa)	128.0	-	57.5[a]
E_2 (GPa)	8.0	-	57.5[a]
G_{12} (GPa)	4.5	-	-
G_{23} (MPa)	-	32.4	-
G_{13} (MPa)	-	59.3	-
ν_{12}	0.30	-	0.2
X_T (MPa)	1900	-	-
Y_T (MPa)	60	-	-
S (MPa)	75	-	-
Density (kg/m^3)	1550	64	2440

[a] Property measured by vibration test.

Table 2
Material properties of the sandwich beam used in the verification

	E (GPa)	ν
Face	70	0.34
Core	0.34	0.4

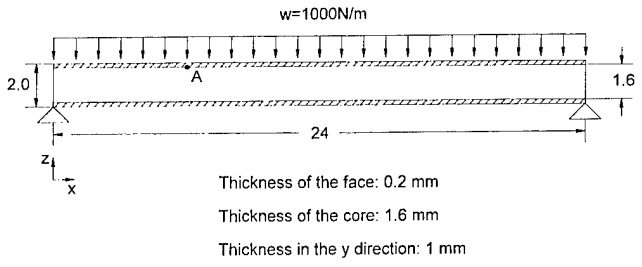

Fig. 4. Sandwich structure used in the verification of the model.

Table 3 shows the calculated results obtained from FEM analysis with respect to the element types as well as the result given by Manet. From results of the FEM analysis, it was found that all of three methods used for modeling the sandwich beam gave good approximation, from which the plane element gave the best result. However, the plane element was unstable for very coarse meshes, which required fine meshes for better approximation. Therefore, it was not suitable for three-dimensional problems such as the end effector. A good result was obtained when the solid elements were used for both the face and the core, however, the solid elements required fine meshes for good approximation, which resulted in long computation time. When the shell element and the solid element were used for the face and the core, respectively, a good approximation was obtained in short computation time inspite of relatively smaller number of elements. Therefore, considering the computation time and accuracy, the shell element and the solid element were used for the face and the core, respectively.

During analyses of the end effector, only half of the end effector was modeled due to its symmetry. The holes for bolts and supporting pins were not modeled in detail to keep the finite element model simple. The face, the core and the loaded glass panel were modeled using multi-layered 8-node shell elements, 20-node quadrilateral solid elements and 8-node structural shell elements, respectively. Since the stacking angle and ply thickness can be assigned in the multi-layered shell element of ANSYS 5.3, it is suitable for modeling of composite material. Fig. 5 shows the finite element model used for the analysis. As shown in Fig. 5, the nodes on the end effector located at the supporting pin positions were

Table 3
Calculated results for the sandwich beam in the verification

Face	Core	U_z	Face σ_{xx}	Core σ_{xx}	σ_{xz}	No. of elements
Plane[a]	Plane[a]	0.524	−102.3	−0.878	−3.295	16000
Solid[b]	Solid[b]	0.523	−101.3	−1.150	−3.296	8400
Shell[c]	Solid[b]	0.523	−101.8	−1.157	−3.297	1728
Ref. [13]		0.514	−103.7	−0.826	−3.296	–

[a] 8-node quadrilateral plane element.
[b] 20-node quadrilateral cubic element.
[c] Multi-layered 8-node quadrilateral shell element.

coupled in the z-direction with the corresponding nodes on the glass panel. For the boundary condition, all the displacements of nodes corresponding to the location of bolts were fixed and the gravitational acceleration was applied to both the end effector and the loaded glass panel.

The design optimization module within ANSYS 5.3 was used to optimize the end effector. The optimization module minimized the total thickness Δ required by the end effector with glass panel when the design was subjected to constraints imposed on the design variables.

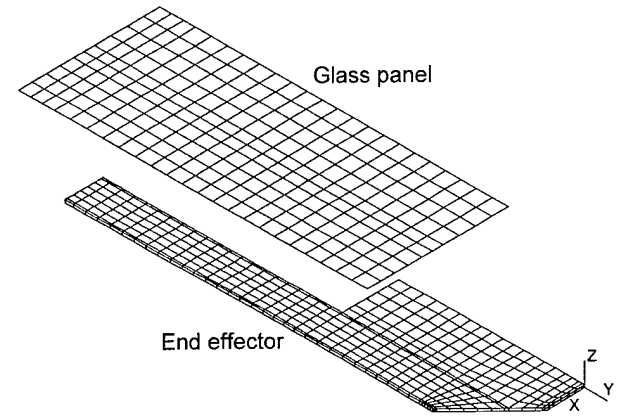

(a)

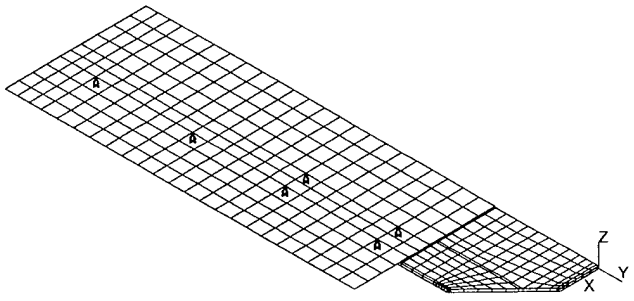

The symbol ▲ represents node coupling positions

(b)

Fig. 5. Finite element model used for the analysis: (a) before node coupling; (b) after node coupling.

The selected design variables for the optimization were the thickness of the honeycomb for the core (t_h), thickness of the carbon/epoxy for the faces (t_c), stacking angle of the carbon/epoxy ($\pm\theta$), lengths l_1 and l_2, and widths w_1, w_2, and w_3. Fig. 6 shows the geometric design variables used in the analysis.

The optimization technique used in the analysis was the sub-problem approximation method and the first order method offered by the optimization module of ANSYS [14]. The sub-problem approximation method uses approximation for the objective function and state variables, and converts the constrained optimization problem to an unconstrained problem. The search for a minimum of the approximated unconstrained objective function is carried out by applying a Sequential Unconstrained Minimization Technique (SUMT) at each iteration. Like the sub-problem approximation method, the first order method converts the problem to an unconstrained one by adding penalty functions to the objective function. The first order method uses gradient of the dependent variable with respect to the design variable. For each iteration, gradient calculations by a conjugate gradient method are performed in order to determine a search direction, and a line search strategy is adopted to minimize the unconstrained problem. Compared to the sub-problem approximation technique, the first order method requires more computation time

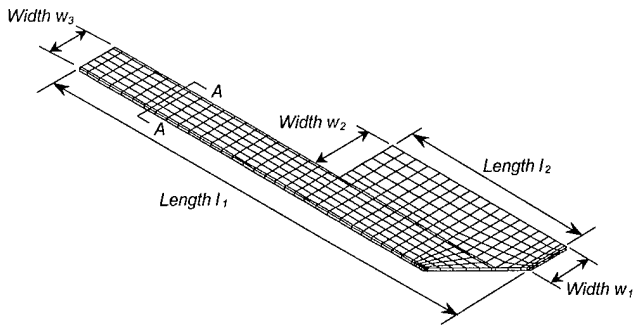

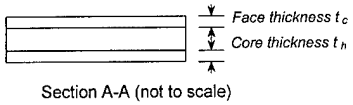

Section A-A (not to scale)

Fig. 6. Geometric design variables.

though it yields more accurate solution. Therefore, the sub-problem technique was used first and then with the result of the sub-problem technique, the objective function was minimized using the first order method.

Table 4
Determined optimum design variables

Design variables	Values
Core thickness t_h (mm)	6.0
Face thickness t_c (mm)	2.0
Stacking angle ($\pm\theta$)	14.5
Length l_1 (mm)	1010.0
Length l_2 (mm)	440.5
Width w_1 (mm)	90.0
Width w_2 (mm)	135.0
Width w_3 (mm)	90.0

From the results of the optimization, the optimum design variables were determined as shown in Table 4.

Although the structural failure by the applied loads seldom occurs in the stiffness-designed structure including the end effector, the failure index was also calculated using Tsai–Wu failure criterion to investigate the possibility of failure. The Tasi–Wu failure criterion is described by the tensor polynomial

$$F_i\sigma_i + F_{ij}\sigma_i\sigma_j = 1, \tag{3}$$

where the contracted notation $i,j = 1,2,\ldots,6$ is used and F_i and F_{ij} are experimentally determined strength tensor of the second and fourth rank with $F_{12} = 0.5$, respectively. The calculated maximum failure index was 0.02, which occurred near the bolted region.

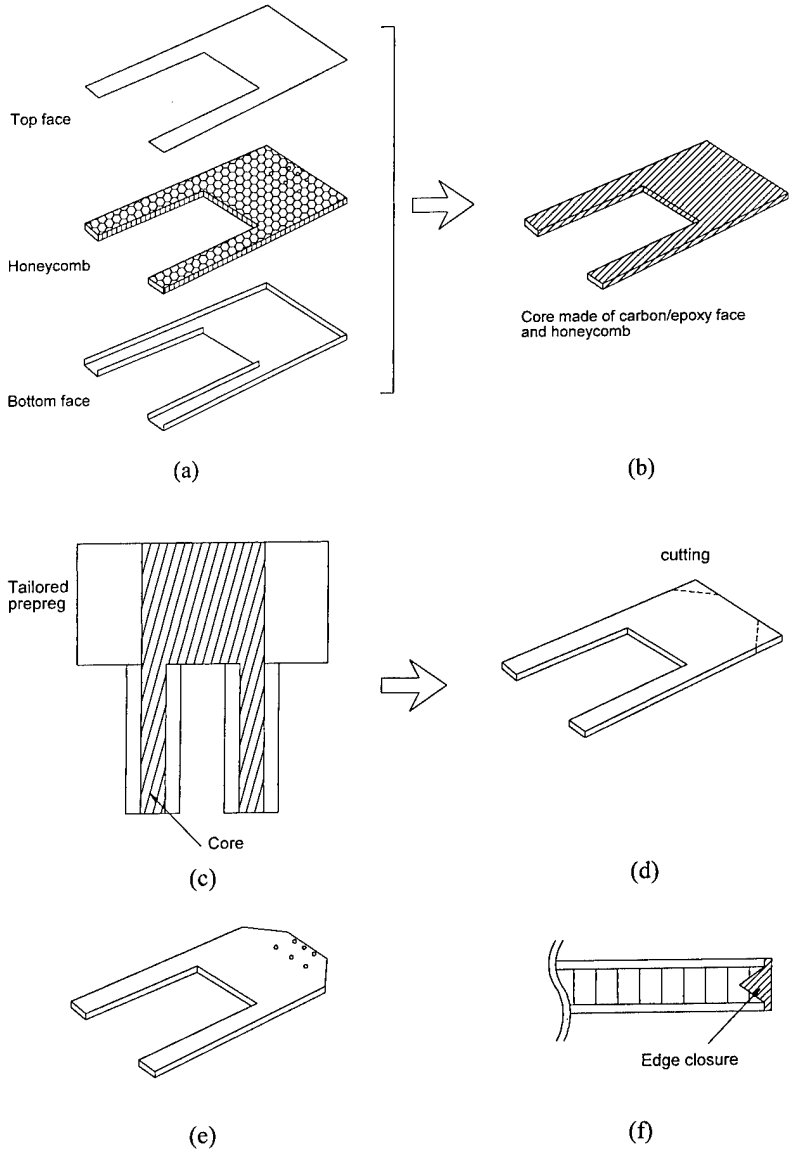

Fig. 7. Schematic diagram of the manufacturing sequence for the composite end effector.

4. Manufacture of the composite end effector

The composite end effector was manufactured using the prepreg lay-up method and autoclave vacuum bag degassing process. Since the ply thickness of USN 125 carbon/epoxy prepreg was 0.125 mm, total 16-ply carbon/epoxy prepreg was laid up to fabricate 2-mm thickness laminate. In order to prevent the thermal deformation due to temperature difference, the symmetric stacking sequence was employed in the manufacturing process.

Fig. 7 shows the manufacturing sequence for the end effector. First, the top and bottom faces were manufactured with stacking sequence of $[\pm\theta]_S$. As shown in Fig. 7(a), the two sidewalls of the bottom face were also reinforced to reduce shear effects arising from the low modulus of honeycomb. The core was fabricated by bonding the carbon/epoxy face to the 6 mm Nomex honeycomb using film adhesive as shown in Fig. 7(b). Then the prepreg tailored to the appropriate size was wrapped on the core as shown in Fig. 7(c). In order to spread the seam line through the surface, the core was turned upside down in every step of stacking. After stacking the tailored prepreg on the core, the end effector was placed in the mould and appropriate dams were put on the sides of the end effector. The end effector was cured under the recommended cure cycle in an autoclave after bagging the whole assembly with a vacuum bag. The cure cycle for the carbon/epoxy composite material is shown in Fig. 8.

After curing the end effector, two edges and six holes for bolts were machined using a diamond-cutting wheel and a tungsten carbide drill, respectively, as shown in Fig. 7(d) and (e). The machined areas were filled with nylon edge closures as shown in Fig. 7(f). The total stacking sequence of the composite end effector was

$$\left[\{(\theta/-\theta/-\theta/\theta)_{2T}\}_S/C_{48}/\{(-\theta/\theta/\theta/-\theta)_{2T}\}_S\right]_T.$$

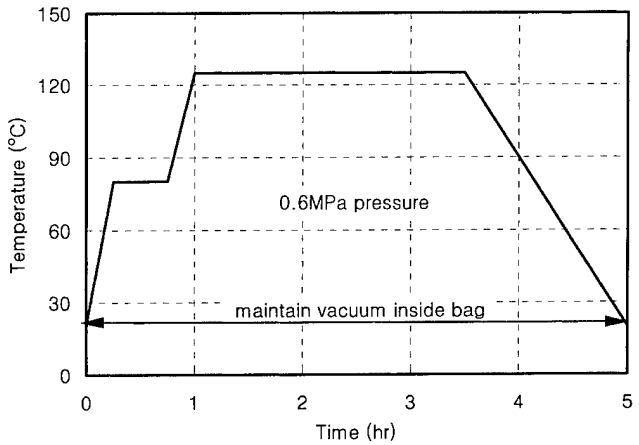

Fig. 8. Cure cycle for the carbon/epoxy composite material.

Fig. 9 shows the manufactured composite end effector before machining. The aluminum end effector that had the same dimensions as the composite end effector was also manufactured to compare the static and dynamic characteristics with those of the composite end effector.

The weight of the composite end effector was 21.5 N, while the aluminum end effector weighed 43.6 N. Therefore, the composite end effector had only 49% weight of the aluminum end effector.

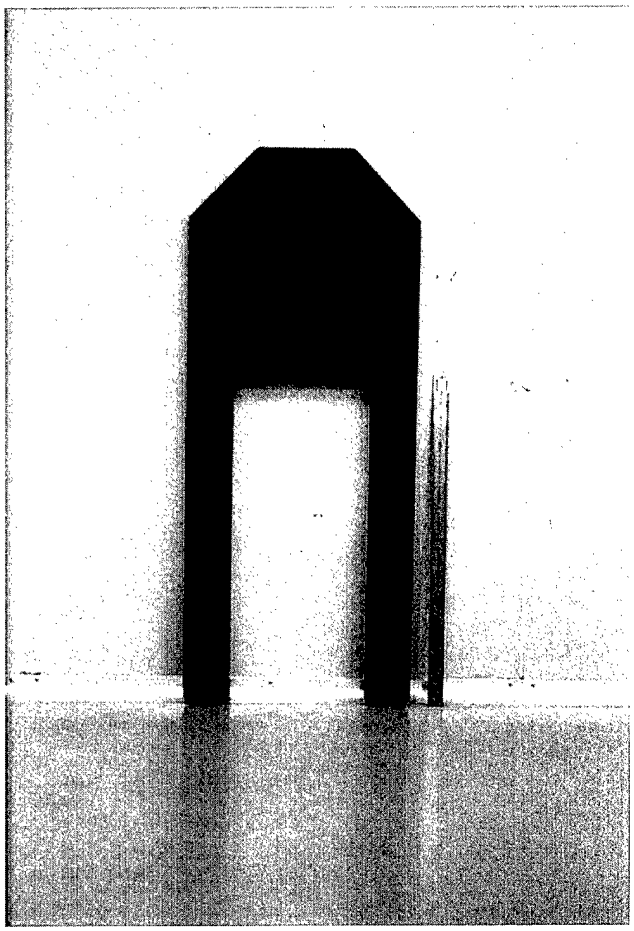

Fig. 9. Photograph of the composite end effector (right bar is a 600 mm long scale).

Table 5
Static deflection of the composite and the aluminum end effectors (mm)

Type	Deflection due to self-weight ($\delta_{\text{self-weight}}$)	Total deflection (δ_{total})
Composite end effector	1.55	2.52
Aluminum end effector	3.06	4.87

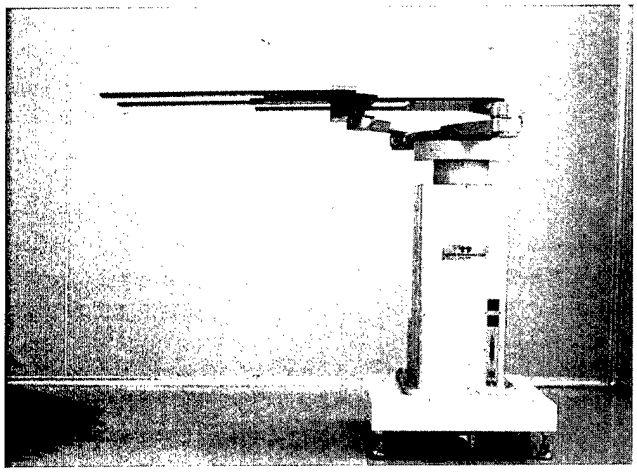

(a)

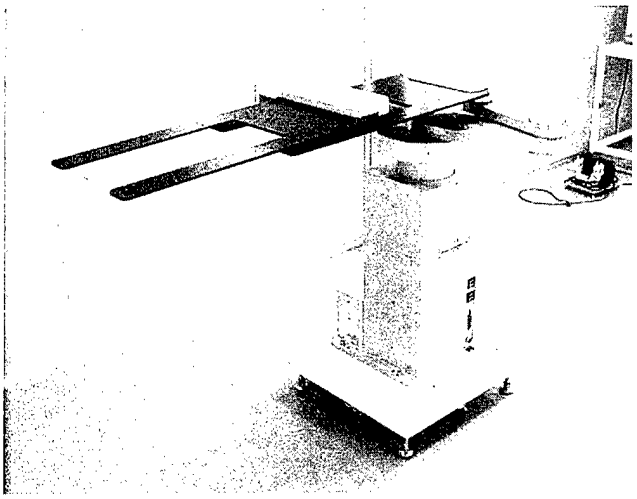

(b)

Fig. 10. Photograph of the robot with the two composite end effectors installed: (a) front view; (b) oblique view.

5. Static and dynamic characteristics of the composite end effector

The static and dynamic tests of the end effectors were performed to compare the characteristics of the composite end effector with those of the aluminum end effector. In order to measure the static deflection due to both the self-weight and the weight of glass panel, the composite and aluminum end effector were placed on the precision surface plate and the deflection was measured by a dial gauge.

The static deflection due to both the self-weight and the weight of glass panel was measured at the end of end effector. The static test results are shown in Table 5. The static stiffness of the composite end effector was 95% higher than that of the aluminum end effector.

The dynamic characteristics of the composite and the aluminum end effectors were measured by giving an impulse at the top surface of the end effector after assembling the end effector into the robot. Fig. 10 shows the photograph of the robot with the two composite end effectors. The vibration signal measured by an accelerometer (B&K 4374) at the end of the end effector was processed by an FFT signal analyzer (B&K 2032) to get frequency response. Fig. 11 shows the schematic diagram of vibration test and Fig. 12 shows the frequency response of the composite and the aluminum end effectors. The natural frequencies and damping ratios of the composite end effector at the first and second modes were 14.9, 20.0 Hz and 0.032, 0.031, respectively, whereas those of the aluminum end effector were 10.2, 16.8 Hz and 0.0088, 0.0060, respectively. From the experimental results, it was found that the fundamental natural frequency and damping ratio of the composite end effector were 1.5 and 3.6 times, respectively, compared with those of the aluminum end effector.

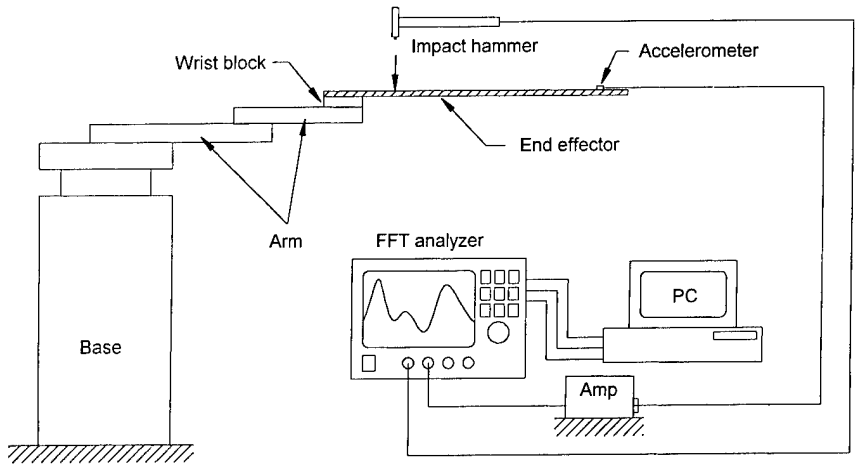

Fig. 11. Schematic diagram of the experimental set-up for vibration test.

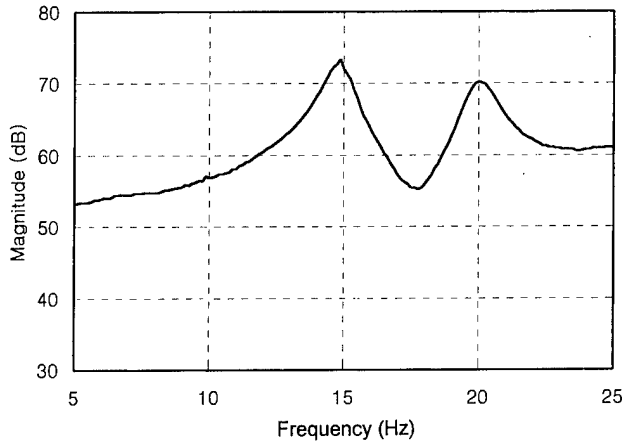

Mode	Frequency (Hz)	Damping ratio
1st	14.9	0.032
2nd	20.0	0.031

(a)

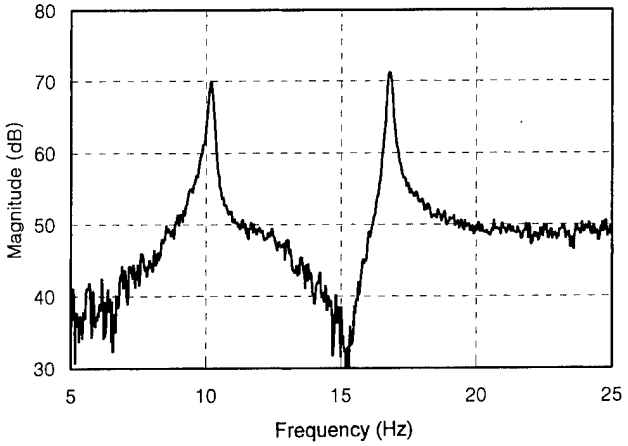

Mode	Frequency (Hz)	Damping ratio
1st	10.2	0.0088
2nd	16.8	0.0060

(b)

Fig. 12. Impulse frequency responses of: (a) the composite end effector; (b) the aluminum end effector.

6. Conclusions

In this work, a composite end effector for manipulation of large LCD glass panels was developed using carbon/epoxy composite material and honeycomb in order to reduce the deflection due to the self-weight of end effector and the weight of glass panel without sacrificing the stiffness. Finite element analysis was used along with the optimization routine to design the composite end effector. Through the finite element analysis, the optimum design variables were obtained and the Tsai–Wu failure index was also calculated.

The composite end effector was manufactured using the autoclave vacuum bag degassing process and another aluminum end effector that has the same dimensions of the composite end effector was also manufactured to compare the static and dynamic performances of the two end effectors. The box type sandwich structure whose two sidewalls as well as the top and bottom faces were reinforced, was employed to reduce the shear deformation arising from the low modulus of honeycomb structure. The weight of the composite end effector was 21.5 N whereas the aluminum end effector weighed 43.6 N. The composite end effector had only 49% weight of the aluminum end effector.

The static and dynamic characteristics of the composite and aluminum end effector were tested and compared. From the experiments, it was found that the static stiffness of the composite end effector was 95% higher than that of the aluminum end effector, and the fundamental natural frequency and damping ratio of the composite end effector were 1.5 and 3.6 times higher, respectively, compared with those of the aluminum end effector.

Acknowledgements

This work was financially supported by Meerae Engineering Corporation of Korea. Its support is gratefully acknowledged.

References

[1] Oh JH, Kim YG, Lee DG. Optimum bolted joints for hybrid composite materials. Compos Struct 1997;38:329–41.
[2] Cho DH, Lee DG, Choi JH. Manufacture of one-piece automotive drive shafts with aluminum and composite materials. Compos Struct 1997;38:309–19.
[3] Lee DG, Sin HC, Suh NP. Manufacturing of a graphite epoxy composite spindle for a machine tool. Ann CIRP 1985;27(1):365–9.
[4] Bang KG, Choi JK, Kim HS, Lee DG. Development of guide rollers using electroplated carbon fiber-epoxy composite for thin polymer film processing. Compos Struct 1997;38:321–8.
[5] Oh JH, Lee DG, Kim TR. Composite nozzle dam in the steam generator of a nuclear reactor. Compos Struct 1997;38:203–13.
[6] Kwak DY, Jeong JH, Cheon JS, Im YT. Optimal design of composite hood with reinforcing ribs through stiffness analysis. Compos Struct 1997;38:351–9.
[7] Reugg C, Habermeir J. Composite propeller shafts design and optimization. In: Advanced Composite Materials, Third International Conference on Composite Materials, vol. 2. Oxford: Pergamon Press, 1980:1740–55.
[8] Vorlicek PL, Material damping of aluminum and graphite/epoxy in a simulated zero-gravity environment. MS thesis. Boston, MA, Department of Aeronautics and Astronautics, Massachusetts Institute of Technology, 1981.
[9] Asada H, Youcef-Tourni K. Direct-drive robots. Boston, MA: MIT Press; 1987.
[10] Lee DG, Kim KS, Kwak YK. Manufacturing of a SCARA type direct-drive robot with graphite fiber epoxy composite material. Robotica 1991;9:219–29.

[11] Lee DG, Jeong KS, Kim KS, Kwak YK. Development of the anthropomorphic robot with carbon fiber epoxy composite materials. Compos Struct 1993;25:313–24.
[12] Kim YG, Jeong KS, Lee DG, Lee JW. Development of the composite third robot arm of the six-axis articulated robot manipulator. Compos Struct 1996;35:331–42.
[13] Manet V. The use of ANSYS to calculate the behaviour of sandwich structures. Compos Sci Technol 1998;58:1899–905.
[14] ANSYS Inc., ANSYS User's Manual vol. IV Theory. ANSYS. Inc., 1995.

ELSEVIER

Composite Structures 47 (1999) 507–517

COMPOSITE STRUCTURES

www.elsevier.com/locate/compstruct

Composite heddle frame for high-speed looms

Dai Gil Lee [a,*], Chang Sup Lee [a], Je Hoon Oh [a], Han Su Jeon [b]

[a] *Department of Mechanical Engineering, Korea Advanced Institute of Science and Technology, ME3221, Gusong-dong, Yusong-gu, Taejon-shi 305-701, South Korea*

[b] *Korea Institute of Industrial Technology Evaluation and Planning, 395-67 Shindaebang-dong, Dongjack-gu, Seoul 156-010, South Korea*

Abstract

A heddle (or heald) frame is the major part of a loom that produces woven cloth by insertion of weft yarns between warp yarns. Warp yarns are manipulated by many heddles fixed in a heddle frame. Recently, the up and down speed of heddle frames has been increased much for the increase of productivity, which induces higher inertial stresses and vibrations in the heddle frame. Conventional aluminum heddle frames have limits for the speed increase due to their low fatigue flexural strength as well as low bending stiffness. The estimated fatigue life of the aluminum heddle frame was 6 months at 600 rpm and infinite at 400 rpm, which was the same results reported by textile industries. Since carbon fiber epoxy composite materials have high specific fatigue strength (S/ρ), high specific modulus (E/ρ) and high damping capacity, in this paper a composite heddle frame was designed and manufactured. The optimum box type cross-sectional shape of the heddle frame and stacking sequence were determined by finite element analysis. The box type composite structure with several ribs was manufactured with prepregs by the autoclave vacuum bag process. Then the static and dynamic characteristics of the composite heddle frame and the aluminum heddle frame were measured and compared. © 2000 Published by Elsevier Science Ltd.

Keywords: Heddle frame; Loom; Composite materials; High specific strength; Stiffness; Fatigue; Buckling; Box beam; Honeycomb

1. Introduction

All woven fabrics are made of two sets of yarns: warp and weft. The warp yarns extend throughout the length of the fabric, whereas weft yarns go across the warp yarns. The weft yarns have to be moved between the warp yarns in weaving. A warp is inserted in the eye of a heddle (or heald) and many heddles are supported by the heddle frame. Consequently the heddle frame makes the warps move vertically up and down [1]. The structure of a commercial heddle frame is composed of two beams, stays, and joints as shown in Fig. 1. The stays and the joints fix the two beams. Generally aluminum heddle frames have the typical dimensions of 9 mm × 100 mm × 2000 mm and have about 2 kg mass.

There are three major types of shuttleless looms: rapier, gripper-shuttle and jet looms. Among them, the rapier looms in which the weft yarn is propelled by two rigid or flexible rapiers at each side of the loom are most widely used. Recently the rapier loom operated by high-speed positive cam systems has been developed. In the past, the loom with 4 heddle frames was operated by tappet cam systems at 200 rpm, but nowadays the loom with 12 heddle frames is operated at 600 rpm by positive cam systems. Accordingly the high-speed, variable, and high-dense weavings are today's trend of looms. Since the acceleration of the heddle frame becomes very severe as the cam rotation speed becomes faster, the heddle frame should be designed considering its specific flexural strength and the specific fatigue strength.

Carbon fiber epoxy composite materials have excellent properties for structures due to their high specific modulus (E/ρ), and high specific strength (S/ρ). They have high damping capacity because the composite materials have viscoelastic and interfacial characteristics, which reduces the noise and vibration of structures and decrease the resonance phenomena and settling time [2].

Therefore, carbon fiber epoxy composite materials have been employed in many lightweight structures such as aircraft wing structures, automobiles, and robot arms [3–6]. Also, carbon fiber epoxy composite materials have good fatigue characteristics; the fatigue strength of carbon fiber in the fiber direction remains almost 90% of the static strength after 10 million cycles [7]. Moreover, continuous fiber reinforced composite materials can be

* Corresponding author. Tel.: +82-42-869-3221; fax: +82-42-869-3210.

E-mail address: dglee@kaist.ac.kr (D. Gil Lee).

0263-8223/99/$ - see front matter © 2000 Published by Elsevier Science Ltd.
PII: S0263-8223(00)00012-X

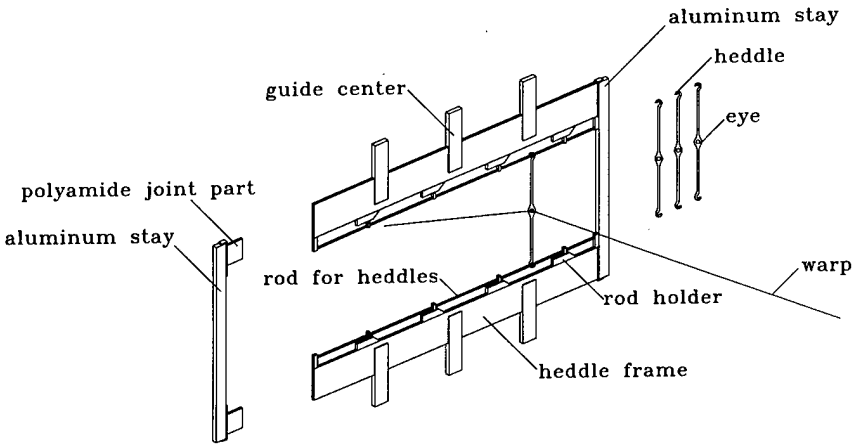

Fig. 1. Configuration of a heddle frame.

tailored to have desired mechanical properties by varying stacking angles and sequences [8]. Due to these beneficial effects, structures made of carbon fiber epoxy composite materials have been widely used in industry [9–11].

As already described, the heddle frame is required to have smaller mass and high fatigue endurance because the accelerating mass of the heddle frame contributes the major portion of the stresses.

Therefore, in this work, the carbon fiber epoxy composite materials were employed for manufacturing of the heddle frame for high-speed looms. First, in order to estimate the life of heddle frame the service load histories of the aluminum heddle frame were measured by using accelerometers. After the acceleration data were transformed into stresses, the fatigue life of the heddle frame was estimated by the rainflow counting method and the Palmgren–Miner rule. After the dimensions and stacking sequences of the composite heddle frame were calculated by finite element method, the composite heddle frames were manufactured with high strength carbon fiber epoxy composite materials. Finally, the static and dynamic properties of the aluminum and the composite heddle frames were tested and compared with each other.

2. Service load history of the heddle frame

The heddle frame is driven by a shedding cam system which is composed of two positive cams and a four bar linkage. Each cam mounted on each spindle makes the four bar linkage system move. Fig. 2 shows the schematic diagram of the cam and link system, in which the point E indicates the position of the heddle frame.

The stresses of the heddle frame come from the weight of heddle frame itself, the weight of heddles and warps, and the inertial forces induced by high acceleration. Since the heddle frame moves up and down repeatedly with high acceleration, the service load history was measured using accelerometers to estimate the fatigue life of the heddle frame at the cam rotation speeds

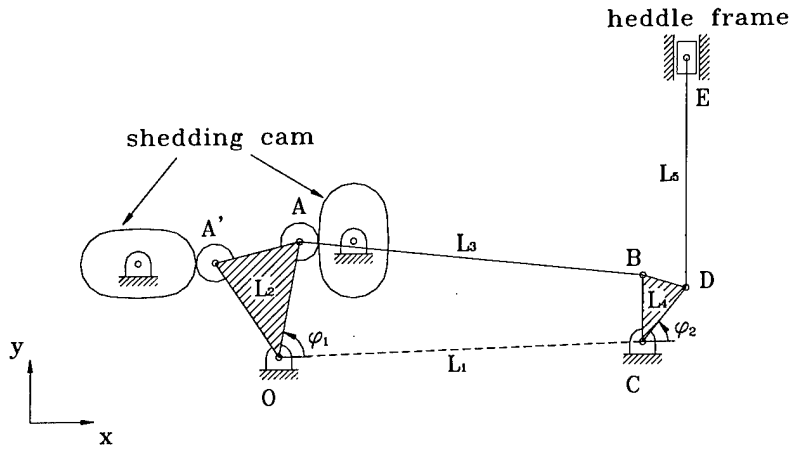

Fig. 2. Schematic diagram of the cam and link system.

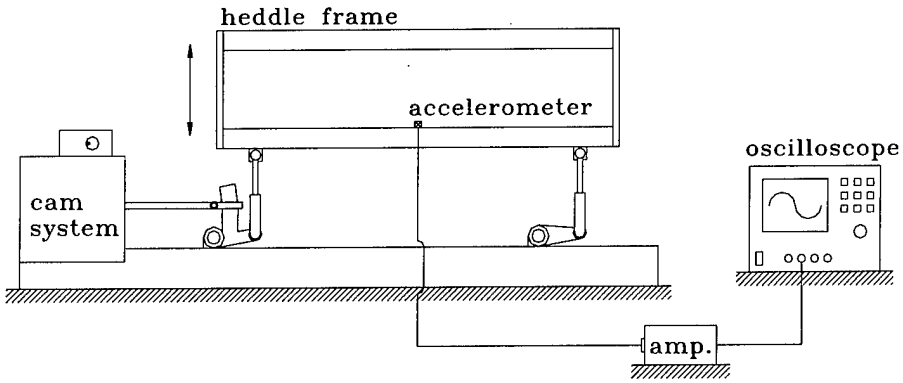

Fig. 3. Acceleration measurement set-up with respect to the cam angular speed.

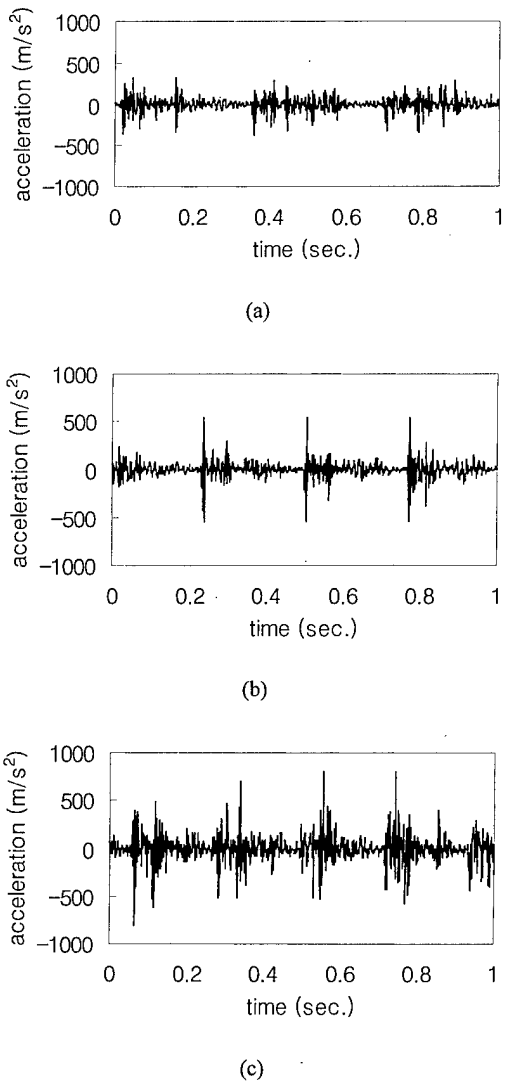

Fig. 4. Acceleration measurement signals of the heddle frame with respect to the cam rotation speed: (a) 350 rpm; (b) 450 rpm; (c) 550 rpm.

of 350, 450, and 550 rpm. Fig. 3 shows the acceleration measurement set-up and Fig. 4 shows the measured acceleration signals of the heddle frame.

At each cam rotation speed of 350, 450, and 550 rpm, the repetition appears in every 0.341, 0.267, and 0.218 s. The acceleration signals contain random vibration characteristics because they were caused by inertial forces, impact from the gap between the parts, and vibrations transferred from other looms. The relationship between the accelerations and the stresses of the heald frame was obtained by the finite element stress analysis, from which the life estimation of the heddle frame was made using the rainflow counting method and the Palmgren–Miner rule.

3. Finite element modeling

In order to find the relationship between the accelerations and the stresses of the heddle frame, the finite element stress analyses were performed using a commercial software ANSYS 5.3. Fig. 5 shows the cross-sectional shape of the aluminum heddle frame.

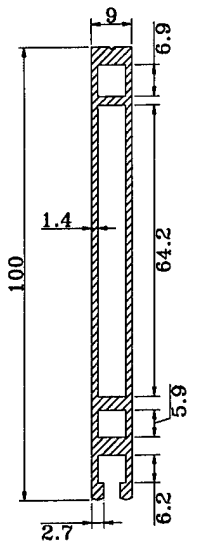

Fig. 5. Cross-sectional shape of the heddle frame.

The heddle frame structure is composed of two main plates with four ribs as shown in Fig. 5. The aluminum stays are joined by the polyamide joints as shown in Fig. 1. Since, it is difficult to determine the boundary conditions at both ends of the heddle frame with polyamide stays, the plates and the stays as well as the joints were included in the finite element model. The properties of aluminum and polyamide, which are used in the finite element model, are shown in Table 1.

Since the structure of the heddle frame is symmetrical, only 1/4 part of the heddle frame was analyzed in the finite element model. The solid 45 element of ANSYS 5.3 was used. Fig. 6 shows the finite element model of the heddle frame.

The total node number of finite element was 10 764 and the total element number of finite element was 19 133. The numbers of nodes and elements of the finite element model are shown in Table 2.

In the analysis, the nodes between the heddle frame and the joint were coupled to have the same displacements. However, the nodes whose nodal forces were tensile were excluded from the displacement coupling because some nodes might not contact with each other during bending. While, the nodes whose nodal forces were compressive were coupled to have the same displacements during several iterations [12]. Since the faces of the stay and the joint were in contact with each other during deformation, they were coupled to have the same displacements.

Table 1
Properties of aluminum and polyamide

Properties	Aluminum (Al 6061)	Polyamide
Tensile modulus (GPa)	68.9	1.6
Poisson's ratio	0.33	0.34
Density (kg/m^3)	2700	1130

Table 2
Number of nodes and elements of the finite element model

Part	Element	Node	Element
Heddle frame	Solid 45	16 160	8800
Joint	Solid 45	915	524
Stay	Solid 45	2058	1440
Total	–	19 133	10 764

To test the validity of the finite element analyses, the strain measurements of the heddle frame under vertical loads were performed. After mounting the stays on the 380 mm length heddle frame using the polyamide joints, the stays were inserted in the holes of a rigid steel metal block as shown in Fig. 7. Then the heddle frame specimen was loaded using a loading jig mounted on an Instron machine within elastic range. The loading jig had the diameter of 25.4 mm and the crosshead down speed was 1 mm/min.

As shown in Fig. 7, three strain gauges were bonded on the heddle frame. The strain gauge 1 measured ε_{1y} and ε_{1z} and the strain gauges 2 and 3 measured ε_{2z}, and ε_{3z}, respectively. Then the measured strains were compared to those obtained by analyses. Table 3 shows the strain comparison data.

The calculated stresses agreed well with the experimentally measured, from which it was concluded that

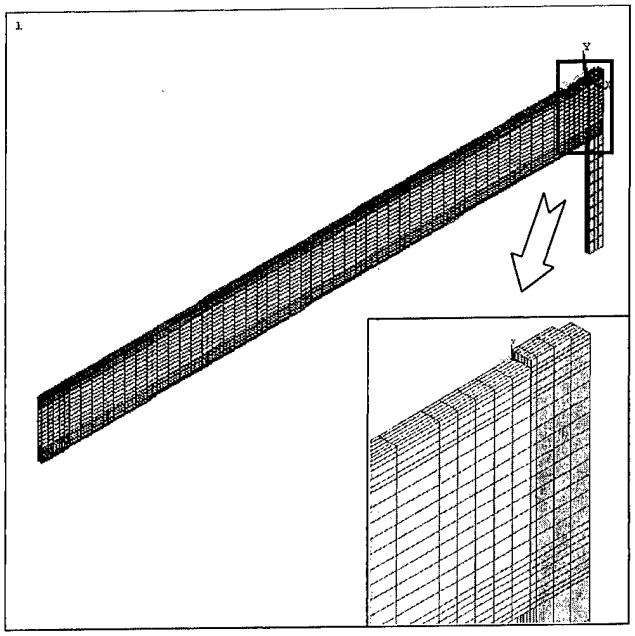

Fig. 6. Finite element model of the aluminum heddle frame.

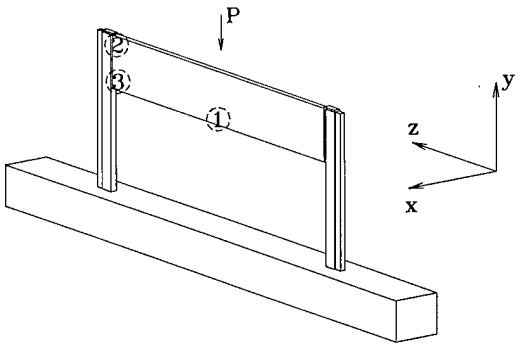

Fig. 7. Strain measurement position for the test.

Table 3
Strain comparison data between the calculated and the measured

Position	Calculated	Measured
Center (ε_{1y}, μS)	79	76
Center (ε_{1z}, μS)	236	227
Upper end part (ε_{2z}, μS)	2	5
Lower end part (ε_{3z}, μS)	31	38

the finite element model and the boundary condition were proper to predict the actual state.

4. Stress analysis of the aluminum heddle frame

The equivalent forces due to the weight of the heddle frame and the weight of the heddles and the warps were 10, 50 N/m, respectively. The force due to the heddle frame acceleration was 817 N/m because the acceleration of the heddle frame was 817 m/s^2 at the cam rotation speed of 550 rpm and the mass of the heddle frame was about 1 kg/m. The maximum stresses of the heddle frame are shown in Table 4.

Since the stresses due to the weights of the heddle frame and heddles were very small compared to that due to the inertial force, the weights of the heddle frame and heddles were neglected in further calculation.

Fig. 8 shows the stress contours of each component of the heddle frame at the acceleration of 817 m/s^2. The maximum stress occurred at the center of the heddle frame rather than at the end of the heddle frame and the stress concentrations occurred at the top and the bottom of the heddle frame. From these observations it was found that the beam boundary condition was similar to the simply supported condition at the end of the heddle frame under bending load. Also it was found that the stress levels of the joint and the stay were very low. As the relationship between the accelerations and the stresses were obtained, the life estimations of the aluminum heddle frame were performed.

5. Life estimation of the aluminum heddle frame

Since random stresses act on the heddle frame during operation, the fatigue life of the heddle frame was estimated using the Palmgren–Miner rule and the rainflow counting method. The rainflow counting method is one of the popular cycle counting methods from ASTM E1049-85 [13] and the Palmgren–Miner rule simply states that fatigue failure is expected when life fractions at different stress states sum to unity, that is, when 100% of the life is exhausted [14].

$$\frac{N_1}{N_{f1}}+\frac{N_2}{N_{f2}}+\frac{N_3}{N_{f3}}+\cdots=\sum\frac{N_j}{N_{fj}}=1, \tag{5.1}$$

where N_j is the number of cycles for σ_{aj}, N_{fj} the number of cycles to failure for σ_{aj} and σ_{aj} is the stress amplitude.

Fig. 9 shows the S–N curve of Al6061-T6. Table 5 shows the life estimations of the heddle frames calculated by Palmgren–Miner rule with S–N curve of the Al6061 at the cam rotation speeds of 350, 450, and 550 rpm.

The fatigue life estimations predicted that the failure of the aluminum heddle frame would occur after 5 months at the cam rotation speed of 550 rpm, which was close to the actual aluminum heddle frame failure. (The heddle frame life was reported to be 6–12 months by textile industries.) Since currently the speed of rapier looms is increasing for productivity, the aluminum heddle frame higher than 550 rpm may fail in much shorter time. Since carbon epoxy composite materials have higher specific strength and modulus and better fatigue properties than aluminum, the heddle frame made of carbon epoxy composite materials may outperform the aluminum heddle frame.

Table 4
Maximum stresses of the component of the heddle frame

	Heddle frame (MPa)	Joint (MPa)	Stay (MPa)
Due to the weight of the heddle frame	0.6	0.05	0.16
Due to the weight of the heddles and warps	2.8	0.2	0.7
Due to the inertial force	51.4	4.5	13.6

6. Design and manufacturing of the composite heddle frame

The heddle frame was designed and manufactured with high strength carbon fiber epoxy composite material whose properties are shown in Table 6.

Since the heddle frame is composed of two thin plates with some ribs, not only fracture but also buckling is important. Therefore, several factors such as bending strength, stiffness, buckling strength, and natural frequency were considered in the design of the composite heddle frame. The cross-section of the heddle frame was determined to be 9×100, which was the comparable size of conventional aluminum heddle frame to be installed on a normal rapier loom.

The heddle frame is composed of two thin plates and several ribs and has open section in the bottom because the heddles should be installed. Fig. 10 shows two cross-sectional shapes of the composite heddle frame with different rib shape in which one has two-rib section and the other has three-rib section. To determine the number of ribs, the Tsai–Wu failure indices (FI) of the heddle frames expressed in Eq. (6.1) were calculated with respect to thickness and stacking angle when the plate and the rib had the same thickness. Tsai and Wu assumed that the failure would occur when FI = 1.0 [15]:

$$\mathrm{FI}=F_1\sigma_1+F_2\sigma_2+F_6\sigma_6+F_{11}\sigma_{11}^2+F_{22}\sigma_{22}^2+F_{66}\sigma_{66}^2+2F_{12}\sigma_{12}, \tag{6.1}$$

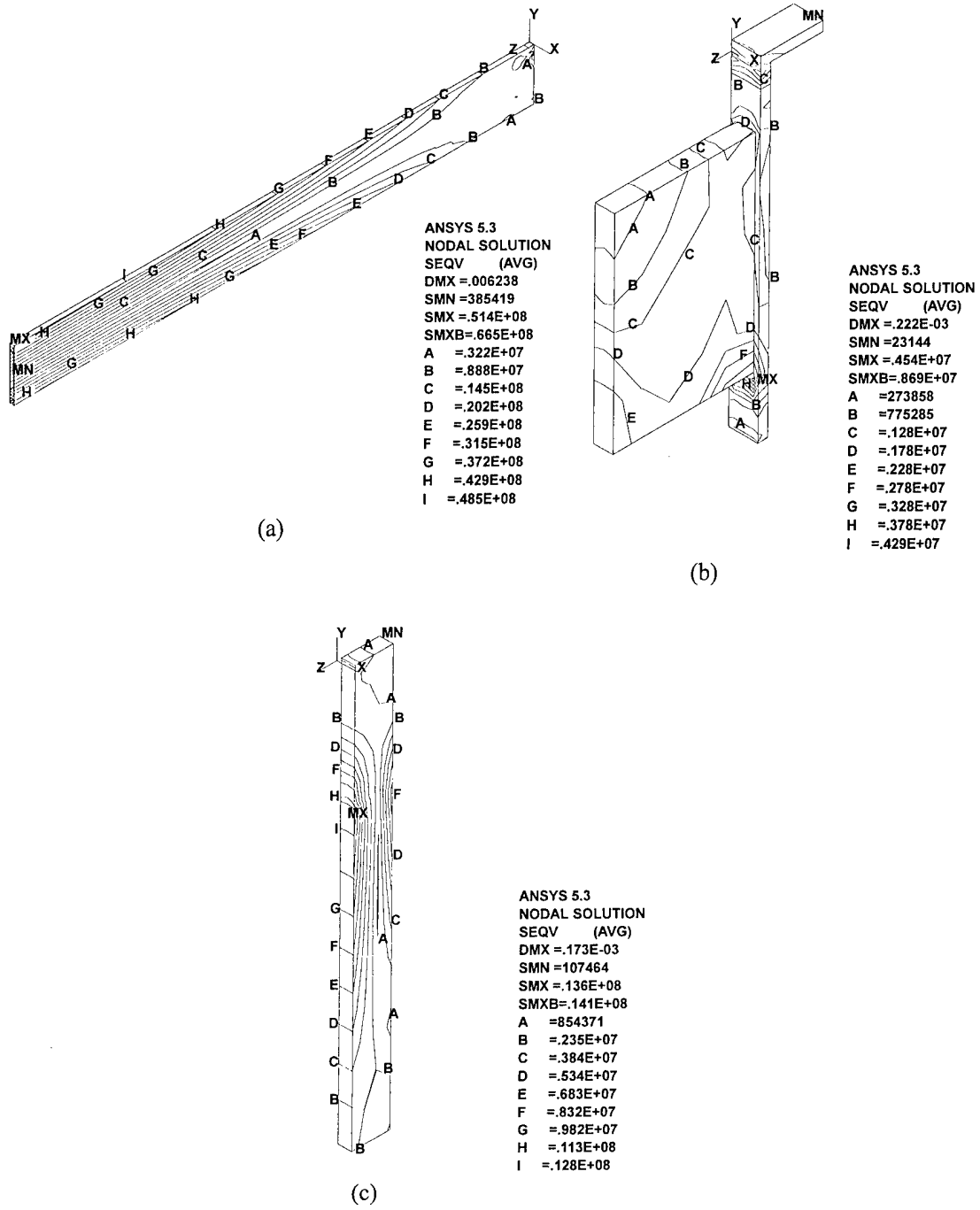

Fig. 8. Stress contours of each component: (a) heddle frame; (b) joint; (c) stay.

$$F_1 = \frac{1}{X_T} + \frac{1}{X_C}, \quad F_2 = \frac{1}{Y_T} + \frac{1}{Y_C}, \quad F_6 = 0,$$

$$F_{11} = -\frac{1}{X_T X_C}, \quad F_{22} = -\frac{1}{Y_T Y_C}, \quad F_{66} = -\frac{1}{S^2},$$

$$F_{12} = -\frac{1}{2}(F_{11}F_{22})^{1/2},$$

where X_T, X_C, Y_T, Y_C, and S represent the strength of the carbon fiber epoxy composite materials. Table 6 shows the mechanical properties of the carbon fiber epoxy composite materials.

As shown in Fig. 11, the failure indices of the heddle frame with three-rib section had smaller values with less variation with respect to thickness compared to the heddle frame with the two-rib section. Therefore, the heddle frame with three ribs was selected in this work. Although the fatigue characteristics and the strength of composite materials are best in the fiber direction, the

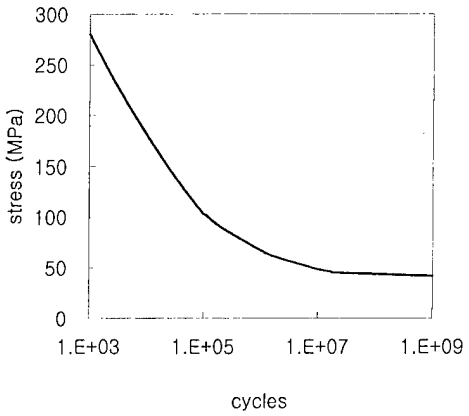

Fig. 9. S–N curve of Al6061-T6 at room temperature.

Table 5
Life estimations of the aluminum heddle frame with respect to the cam rotation speed

Cam rotation speed	Cycles	Years
350 rpm	1.0×10^{29}	2.8×10^{20}
450 rpm	6.5×10^{19}	1.4×10^{11}
550 rpm	2.5×10^{8}	4.3×10^{-1}

Table 6
Mechanical properties of the carbon fiber epoxy composite materials

Properties	Value
Longitudinal tensile strength (X_T, MPa)	1800
Longitudinal compressive strength (X_C, MPa)	1100
Transverse tensile strength (Y_T, MPa)	60
Transverse compressive strength (Y_C, MPa)	200
Shear strength (S, MPa)	75
Longitudinal tensile modulus (E_1, GPa)	130
Transverse tensile modulus (E_2, GPa)	8
Shear modulus (G_{12}, GPa)	4.5
Shear modulus (G_{23}, GPa)	3.5
Poisson's ratio (v_{12})	0.28
Poisson's ratio (v_{23})	0.40
Fiber volume fraction (v_f, %)	60
Density (ρ, kg/m^3)	1550

stacking angle of 10° was selected because some transverse load might be applied during operation.

The critical buckling load of the heddle frame was estimated by using the critical buckling load of plates, which is expressed as follows [16]:

$$P = \pi^2 h^2 L\left(k_1 \frac{D_1}{h^4} + k_2 \frac{D_2}{L^4} + k_3 \frac{D_3}{h^4 L^2}\right) \tag{6.2}$$

$$D_1 = \frac{E_z t^3}{12(1 - v_{yz}v_{zy})}, \quad D_2 = \frac{E_y t^3}{12(1 - v_{yz}v_{zy})},$$

$$D_3 = \frac{v_{yz}E_z t^3}{12(1 - v_{yz}v_{zy})} + G_{yz}t^3,$$

where h, L, and t represent the height, length, and thickness of the heddle frame and k_i are constants

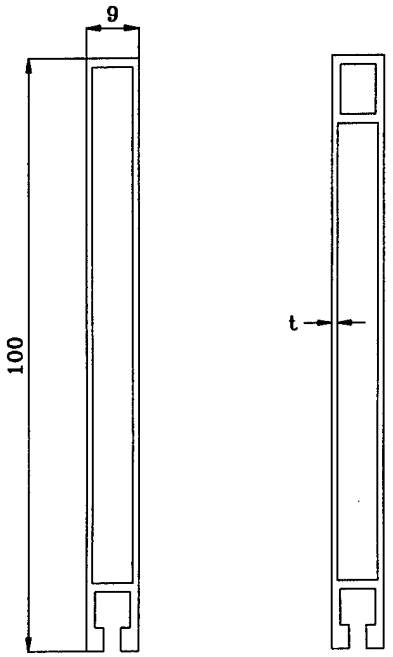

Fig. 10. Cross-sectional shapes of the composite heddle frames with different rib shape.

varying with respect to the boundary condition of the plate. D_1 and D_2 are the flexural stiffness in the longitudinal and transverse direction of the heddle frame, and D_3 is the flexural stiffness which is affected by Poisson's ratio and shear stiffness.

Fig. 12 shows the fracture and the buckling loads with respect to thickness in which the buckling and fracture loads had the same value when the thickness was 1.7 mm. However, the thickness of 1.5 mm was selected to make the number of stacked prepreg even because the thickness of the prepreg was 0.125 mm and 12 plies were stacked. Since the stiffness of the composite heddle frame was low in the transverse direction, the heddle frame was manufactured as a sandwich structure. Fig. 13 shows the manufacturing procedure of the composite heddle frame.

The manufacturing procedure is composed of two steps, fabricating inner beams and outer plate because there are some ribs in the section of the heddle frame. Composite prepregs were stacked with stacking sequence of $[\pm 10]_{2s}$ on the Nomex honeycomb core. Mechanical properties of Nomex honeycomb core are shown in Table 7.

Then the members were cured by the autoclave vacuum bag degassing molding method with the recommended cure cycle as shown in Fig. 14. After the three members were bonded with epoxy film adhesive, the prepregs were stacked on them with the stacking sequence of $[\pm 10]_s$ and cured again. Finally the bottom part was cut to make open section by a cut-off grinder. The mass of the composite heddle frame of 0.5 m length

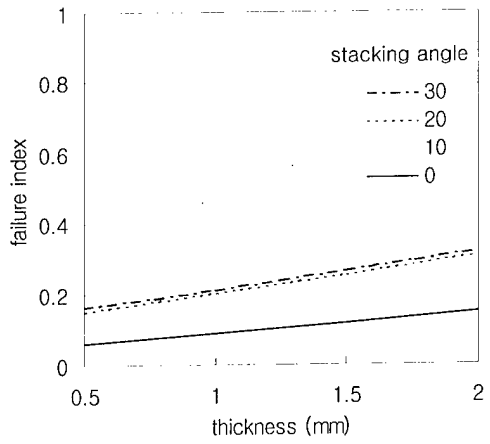

(a)

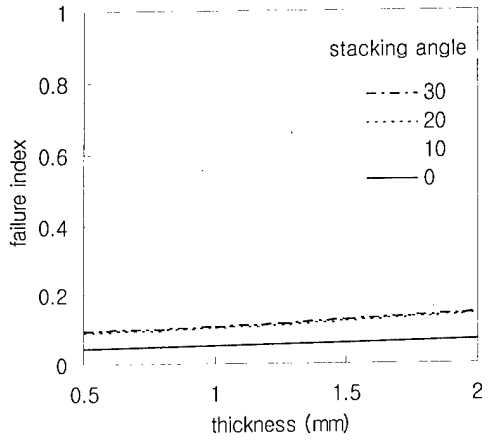

(b)

Fig. 11. Failure indices with respect to thickness and stacking angle: (a) two-rib section; (b) three-rib section.

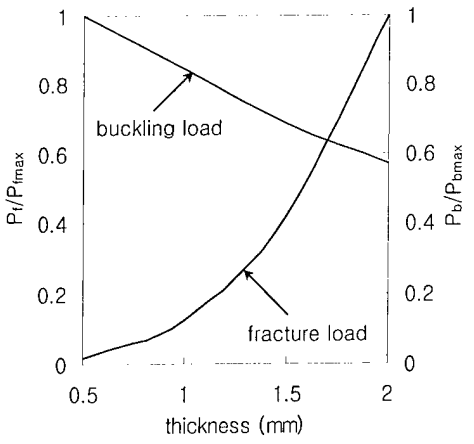

Fig. 12. Failure loads and buckling loads with respect to the thickness.

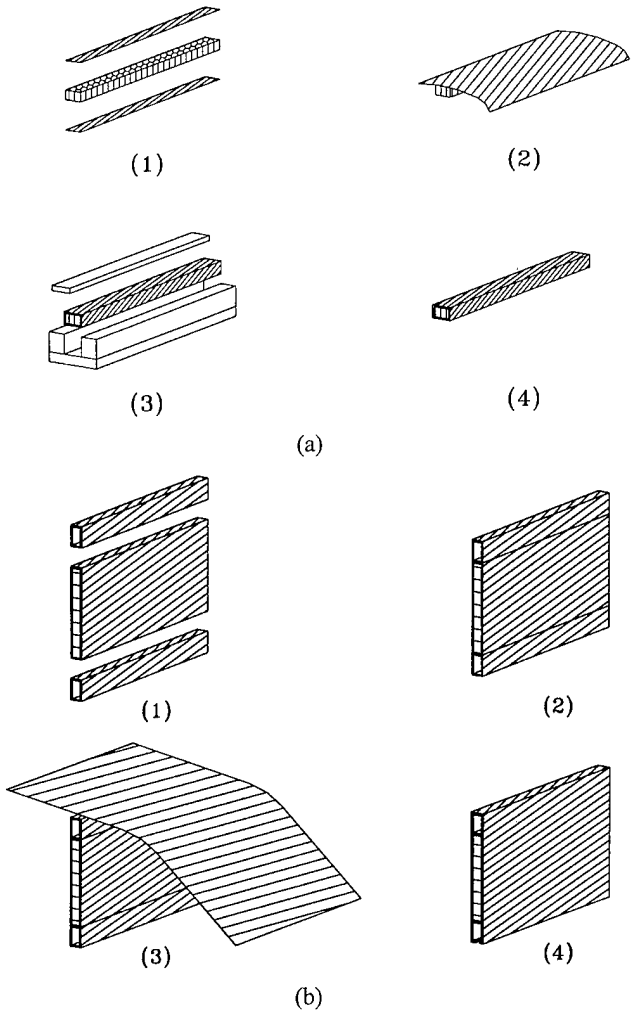

Fig. 13. Manufacturing procedure of the composite heddle frame: (a) inner beams; (b) outer plate.

Table 7
Mechanical properties of Nomex honeycomb core

	Nomex honeycomb core (HRH-10-1/8-4.0)
Shear modulus (G_{13}, MPa)	59.3
Shear modulus (G_{23}, MPa)	32.4
Density (kg/m^3)	64

was 0.315 kg, which was 36% less than that of aluminum heddle frame.

7. Test

The dynamic characteristics of the composite heddle frame were measured by the impulse frequency response method in the vertical and lateral directions. Fig. 15

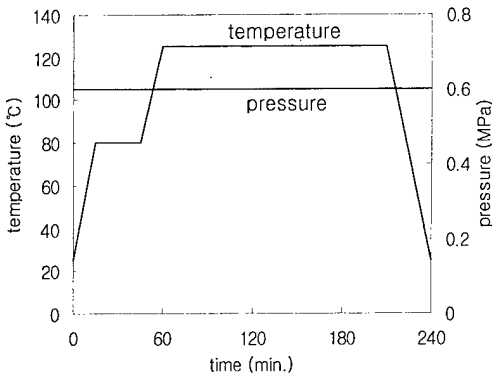

Fig. 14. Cure cycle of carbon fiber epoxy composite materials.

shows the vibration test set-up by the impulse frequency responses and Fig. 16 shows the test results.

Table 8 shows the natural frequencies and damping factors of the aluminum and composite heddle frames. The natural frequencies of the composite heddle frame in the vertical and lateral directions were improved 27% and 43%, respectively and the damping factors in the vertical and lateral directions were improved 4.4 and 1.3 times, respectively.

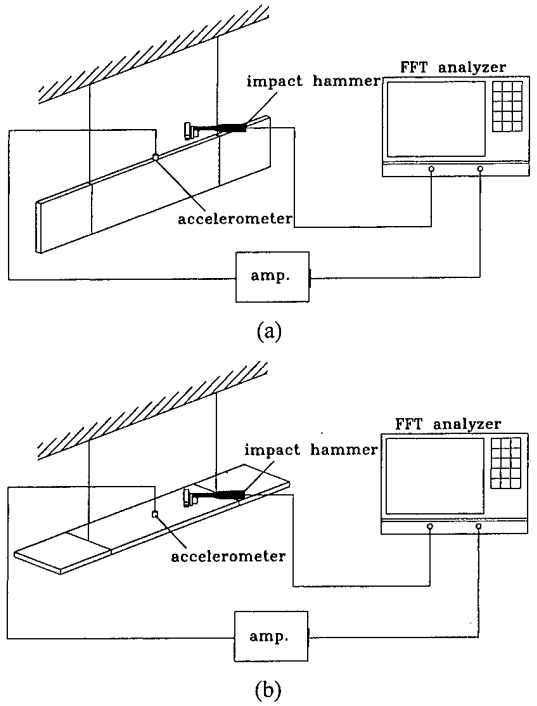

Fig. 15. Vibration test set-up: (a) vertical direction; (b) lateral direction.

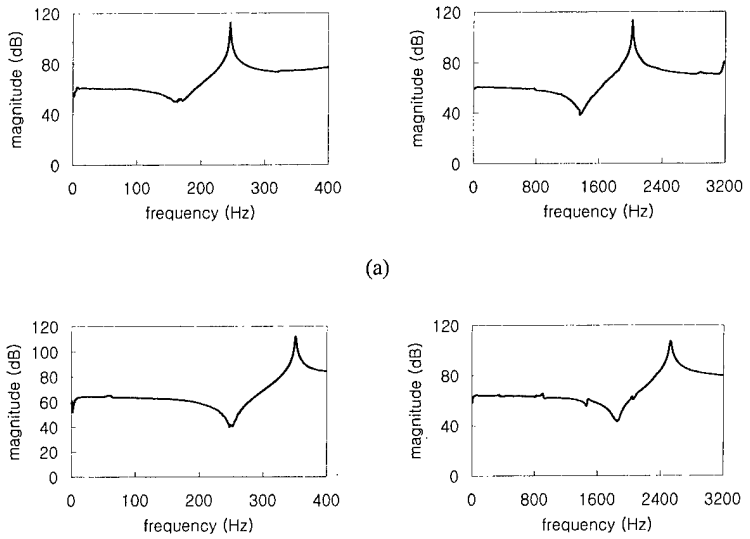

Fig. 16. Impulse frequency responses: (a) aluminum; (b) composite heddle frame.

Table 8
Natural frequencies and damping factors of the heddle frames

	Vertical direction		Lateral direction	
	Aluminum	Composite	Aluminum	Composite
Natural frequency (Hz)	1988	2528	246	414
Damping factor	0.0010	0.0044	0.0019	0.0024

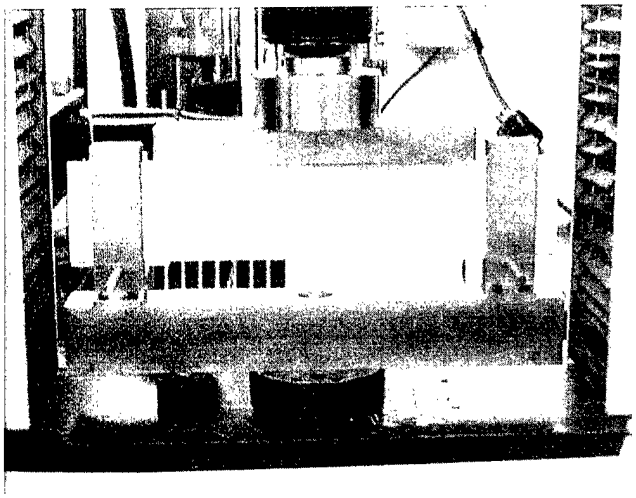

(a)

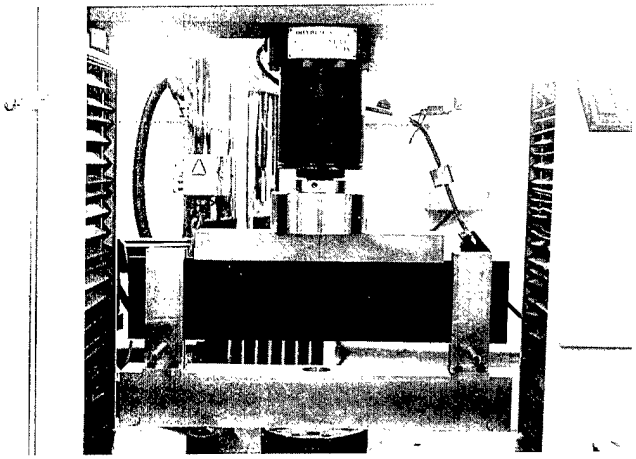

(b)

Fig. 17. Photographs of static bending test: (a) aluminum; (b) composite heddle frame.

The static bending strengths of the aluminum and composite heddle frames were tested using Instron machine using a loading bar composed of a steel bar and silicon rubber to distribute load on the heddle frames evenly. Fig. 17 shows the photograph of test.

During static test, the crosshead down speed of 1 mm/min was used. From the analysis, the buckling load and the fracture load of the aluminum heddle frame was 46.4 and 48.8 kN while the buckling load and the fracture load of the composite heddle frame was 123.8 and 50.4 kN. Accordingly the buckling of aluminum heddle frame was expected rather than fracture, on the other hand the fracture of composite heddle frame was expected rather than buckling.

Fig. 18 shows the load-displacement curves and the photographs of failure. As expected, the buckling of

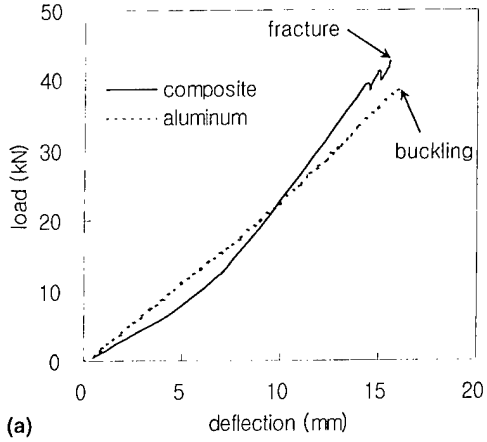

(a)

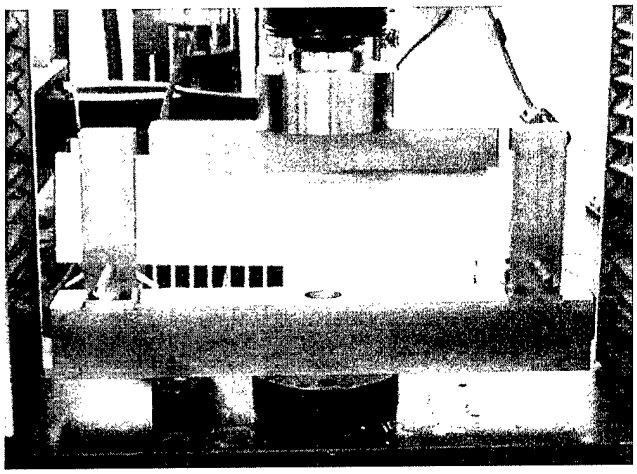

(b)

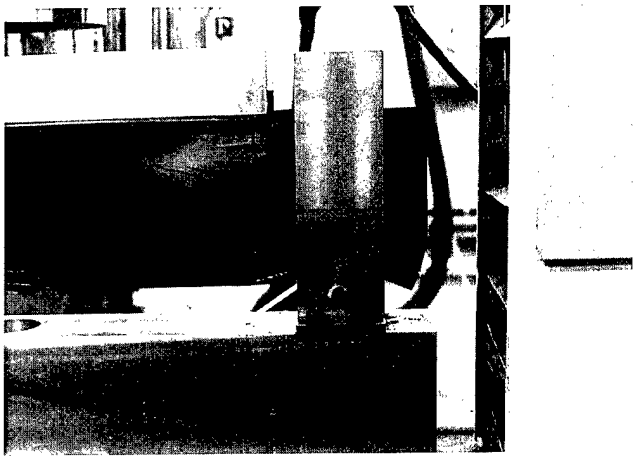

(c)

Fig. 18. Load–displacement curves and photographs of failure: (a) load–displacement curves; (b) buckling of aluminum heddle frame; (c) fracture of composite heddle frame.

aluminum heddle frame and the fracture of composite heddle frame occurred. The aluminum heddle frame buckled at 40.8 kN below the expected load because

some ribs affected the boundary conditions of the plates of aluminum heddle frame. The fracture of the composite heddle frame occurred at 42.7 kN also below the expected load near support pins due to the stress concentration before reaching the failure moment. Therefore it was expected that in real states the composite heddle frame might endure the load larger than 42.7 kN.

8. Conclusions

In this work, the life of aluminum heddle frame was estimated based on the service load history and was found that the life of aluminum heddle frames was too short to be used for high-speed looms operating over 500 rpm.

Since carbon fiber epoxy composite materials have high fatigue strength and low weight with high damping, they were employed for manufacturing of the heddle (or heald) frame for high-speed looms. From the analyses, the optimal number of ribs, stacking angle and thickness for the sandwich structural shape composite heddle frame were determined to be 4, 10°, and 1.5 mm, respectively. Then the composite heddle frames were manufactured by autoclave vacuum bag degassing molding and their static strength and vibrational characteristics were tested. From the tests, it was found that the natural frequencies of the carbon fiber epoxy composite materials were improved by 27% and 43% compared to those of the aluminum heddle frame in the vertical and lateral directions, respectively and the damping factor was increased 4.4 and 1.3 times higher in the vertical and lateral direction, respectively. Moreover, it was found that the calculated maximum stress of the composite heddle frame was only 66% of the aluminum heald frame at the cam rotation speed of 550 rpm because the weight of the composite heddle frame was 64% compared to that of the aluminum heddle frame.

Acknowledgements

This work was supported in part by the Bk21 project.

References

[1] Hall AJ. The standard handbook of textiles. 8th ed. London: Newnes, 1975.
[2] Lee DG. Manufacturing and testing of composite machine tool structures, Ph.D. Thesis. Cambridge, MA: MIT, 1985.
[3] Gibson RF. Principles of composite material mechanics. New York: McGraw-Hill; 1994.
[4] Cheon SS, Choi JH, Lee DG. Development of the composite bumper beam for passenger cars. Comp Struct 1995;32:491–9.
[5] Cho DH, Lee DG, Choi JH. Manufacturing of one-piece automotive driveshafts with aluminum and composite materials. Comp Struct 1997;38:309–19.
[6] Lee DG, Kim KS, Kwak YK. Manufacturing of a scara type direct-drive robot with graphite fiber epoxy composite materials. Robotica 1991;9:219–29.
[7] Mallick PK. Fiber-reinforced composites materials, manufacturing, and design. New York: Marcel dekker, 1988.
[8] Jones RM. Mechanics of composite materials. Scripta Book, 1975.
[9] Bang KK, Choi JK, Kim HS, Lee DG, Jeon HS. Development of the guide rollers using electroplated carbon fiber-epoxy composite for thin polymer film processing. Comp Struct 1997;38:321–8.
[10] Choi JK, Lee DG. Manufacture of a carbon fiber-epoxy composite spindle-bearing system for a machine tool. Comp Struct 1997;37:241–51.
[11] Jeong KS, Lee DG, Oh SH. Development of the composite flexspline for a cycloid harmonic drive by net shape manufacturing method. Comp Struct 1995;32:557–65.
[12] Ho H, Tsai MY, Morton J, Farley GL. Numerical analysis of the iosipescu specimen for composite materials. Comp Sci Tech 1993;46:115–28.
[13] Standard practices for cycle counting in fatigue analysis. American Society for Testing and Materials E 1049-85, 1996.
[14] Dowling NE. Mechanical behavior of materials. Englewood Cliffs: Prentice-Hall; 1993.
[15] Tsai SW, Hahn HT. Introduction to composite materials. Technomic Publishing, 1980.
[16] Vinson JR, Sierakowski RL. The behavior of structures composed of composite materials. Dordrecht: Martinus Nijhoff, 1987.

ELSEVIER

Composite Structures 47 (1999) 519–524

COMPOSITE STRUCTURES

www.elsevier.com/locate/compstruct

Crack path selection in piezoelectric bimaterials

Qing-Hua Qin *, Yiu-Wing Mai

Department of Mechanical Engineering, University of Sydney, Sydney NSW 2006, Australia

Abstract

The problem of crack path selection in piezoelectric bimaterials is considered in this paper. Based on the Stroh formulation for anisotropic material and Green's functions for piezoelectric bimaterials, the crack problem is expressed in terms of coupled singular integral equations at first, and then the equations are used to solve for stress and electric displacement fields numerically. A crack impinging an interface joining two dissimilar materials may arrest or may advance by either penetrating the interface or deflecting into it. The competition between deflection and penetration is investigated using the maximum energy release rate criterion. Numerical results are presented to study the role of remote electroelastic loads on the path selection of crack extension. © 2000 Elsevier Science Ltd. All rights reserved.

Keywords: Crack; Piezoelectric; Interface; Integral equation

1. Introduction

The crack problems with interfaces in dissimilar materials are of paramount importance for many micromechanics and numerical fracture mechanics. As such the interfacial failure mechanism has caused researchers to devote a great deal of attention to study the selection of crack growth path. Generally, fracture along and adjacent to bimaterial interfaces has several morphological manifestations. In some cases the fracture deflect into the interface, while in others fracture penetrate the interface into another material [1]. A number of studies dealing with crack kinking problem has been conducted for isotropic materials [2–4]. As to anisotropic materials, the problem of branched interface cracks between dissimilar anisotropic materials has been considered by Miller and Stock [5] in which the stress intensity factors are computed numerically for mismatch materials. The problem of two aligned orthotropic materials with a semi-infinite crack perpendicular to the interface was studied by Gupta et al. [6]. Wnag et al. [7] investigated the crack extension and singular fields at the tip of an interface crack in anisotropic solids, in which the emphasis was placed on establishing a framework to quantify fracture resistance under mixed mode conditions. Sung et al. [8] revealed some interesting phenomena for dependence of the stress intensity factor on elastic constants in their study on cracks perpendicular to an interface between dissimilar orthotropic materials. Recently, Chen [9] gave a further address on cracks normal to an interface between two orthotropic materials. In his study he showed that all elastic constants involved could be expressed by three independent parameters.

The present paper deals with the problem of crack path selection in two-dimentional piezoelectric bimaterials. The geometrical configuration analysed is depicted in Fig. 1. An inclined finite crack of length $2c$ in material 2 is shown impinging an interface between two dissimilar piezoelectric materials, with a branch of length a and angle θ_1 between the branch and the interface. The length a is assumed to be small compared to the length $2c$ of the inclined finite crack. Based on the Green's functions presented in [10], the branch crack problem is modeled by applying distributed dislocation along the cracks and placing a concentrated dislocation at the joint of the finite crack and the branch. Then, a set of singular integral equations is developed and solved numerically. Competition between deflection and penetration is investigated using the integral equations developed and the maximum energy release rate criterion. Numerical results are presented to study the role of remote electroelastic loads on the path of crack extension.

2. Problem formulations

2.1. Stroh's formalism

Based upon Stroh's formalism [11] in anisotropic elasticity, the general solutions for steady-state

* Corresponding author.

0263-8223/99/$ - see front matter © 2000 Elsevier Science Ltd. All rights reserved.
PII: S0263-8223(00)00014-3

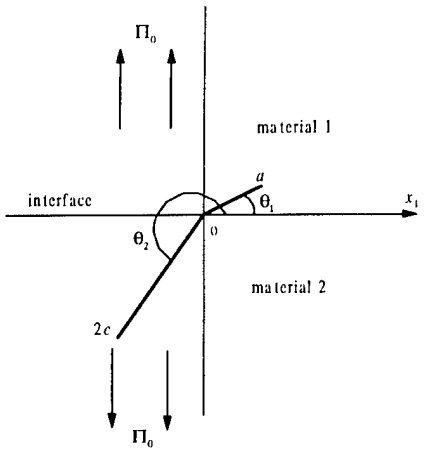

Fig. 1. Geometry of the branch crack.

piezoelectricity have been presented by Barnett and Lothe [12] as

$$\mathbf{u} = 2\mathrm{Re}[\mathbf{A}\mathbf{f}(\mathbf{z})], \quad \boldsymbol{\phi} = 2\mathrm{Re}[\mathbf{B}\mathbf{f}(\mathbf{z})],$$
$$\boldsymbol{\Pi}_1 = -\boldsymbol{\phi}_{,2}, \quad \boldsymbol{\Pi}_2 = \boldsymbol{\phi}_{,1}, \tag{1}$$

where

$$\mathbf{f}(\mathbf{z}) = \{f_1(z_1)\ f_2(z_2)\ f_3(z_3)\ f_4(z_4)\}^{\mathrm{T}}$$
$$z_i = x_1 + p_i x_2. \tag{2}$$

(x_1, x_2) is a fixed rectangular coordinate system, a comma (or a prime later) followed by an argument represents the differentiation with respect the argument, 'Re' stands for the real part of a complex number, $\mathbf{u} = \{u_1 u_2 u_3 \phi\}^{\mathrm{T}}$, $\boldsymbol{\Pi}_j = \{\sigma_{1j}\sigma_{2j}\sigma_{3j}D_j\}^{\mathrm{T}}$, $j = 1,2$; $i = \sqrt{-1}$, u_i and φ are the elastic displacement and electric potential (EDEP), σ_{ij} and D_i are stress and electric displacement (SED), p_i the electroelastic eigenvalues of the material whose imaginary parts are positive, **A** and **B** are well-defined in the literature (see [10,13], for example) and $f_i(z_i)$ are arbitrary functions with complex arguments z_i.

2.2. Green's function for an edge dislocation in a piezoelectric bimaterial

Consider a piezoelectric bimaterial subjected to a line dislocation at $z_0(x_{10}, x_{20})$. For convenience, we assume that z_0 be in material 1. The treatment for z_0 located in material 2 requires only a slight modification. The electroelastic Green's function due to the dislocation, say **b**, can be assumed in the form [14]

$$\mathbf{u}_1 = \frac{1}{\pi}\mathrm{Im}\left[\mathbf{A}_1\left\langle \ln(z_\alpha^{(1)} - z_{0\alpha}^{(1)})\right\rangle \mathbf{B}_1^{\mathrm{T}}\mathbf{b}\right] + \frac{1}{\pi}\mathrm{Im}\left[\sum_{\beta=1}^{4}\mathbf{A}_1\left\langle \ln(z_\alpha^{(1)} - \bar{z}_{0\beta}^{(1)})\right\rangle \mathbf{q}_\beta^{(1)}\right], \tag{3}$$

$$\boldsymbol{\phi}_1 = \frac{1}{\pi}\mathrm{Im}\left[\mathbf{B}_1\left\langle \ln(z_\alpha^{(1)} - z_{0\alpha}^{(1)})\right\rangle \mathbf{B}_1^{\mathrm{T}}\mathbf{b}\right] + \frac{1}{\pi}\mathrm{Im}\left[\sum_{\beta=1}^{4}\mathbf{B}_1\left\langle \ln(z_\alpha^{(1)} - \bar{z}_{0\beta}^{(1)})\right\rangle \mathbf{q}_\beta^{(1)}\right] \tag{4}$$

for material 1 in $x_2 > 0$ and

$$\mathbf{u}_2 = \frac{1}{\pi}\mathrm{Im}\left[\sum_{\beta=1}^{4}\mathbf{A}_2\left\langle \ln(z_\alpha^{(2)} - z_{0\beta}^{(1)})\right\rangle \mathbf{q}_\beta^{(2)}\right], \tag{5}$$

$$\boldsymbol{\phi}_2 = \frac{1}{\pi}\mathrm{Im}\left[\sum_{\beta=1}^{4}\mathbf{B}_2\left\langle \ln(z_\alpha^{(2)} - z_{0\beta}^{(1)})\right\rangle \mathbf{q}_\beta^{(2)}\right] \tag{6}$$

for material 2 in $x_2 < 0$, where the symbol $\langle(\ )_\alpha\rangle = \mathrm{diag}[(\ )_1\ (\ )_2\ (\ )_3\ (\ )_4]$ represents a diagonal matrix, overhead bar denotes the complex conjugate, $\mathbf{q}_\beta^{(i)}$ are unknown vectors to be determined, the superscripts (1) and (2) [or subscripts 1 and 2] label the quantities relating to the material 1 and 2, respectively. If the two materials are rigidly bonded we have

$$\mathbf{u}_1 = \mathbf{u}_2, \quad \boldsymbol{\phi}_1 = \boldsymbol{\phi}_2 \quad \text{at } x_2 = 0. \tag{7}$$

The substitution of Eqs. (3)–(6) into Eq. (7), leads to

$$\mathbf{q}_\beta^{(1)} = \mathbf{B}_\beta^{*}\mathbf{b}, \quad \mathbf{q}_\beta^{(2)} = \mathbf{B}_\beta^{**}\mathbf{b}, \tag{8}$$

where $\mathbf{I}_\beta = \mathrm{diag}[\delta_{1\beta}\ \delta_{2\beta}\ \delta_{3\beta}\ \delta_{4\beta}]$, $\delta_{ij} = 1$ for $i = j$; $\delta_{ij} = 0$ for $i \neq j$, and

$$\mathbf{B}_\beta^{*} = \mathbf{B}_1^{-1}\left[\mathbf{I} - 2(\mathbf{M}_1^{-1} + \bar{\mathbf{M}}_2^{-1})^{-1}\mathbf{L}_1^{-1}\right]\bar{\mathbf{B}}_1\mathbf{I}_\beta\bar{\mathbf{B}}_1^{\mathrm{T}},$$
$$\mathbf{B}_\beta^{**} = \mathbf{B}_2^{-1}(\bar{\mathbf{M}}_1^{-1} + \mathbf{M}_2^{-1})^{-1}\mathbf{L}_1^{-1}\mathbf{B}_1\mathbf{I}_\beta\mathbf{B}_1^{\mathrm{T}},$$
$$\mathbf{M}_j = -i\mathbf{B}_j\mathbf{A}_j^{-1} \quad (j = 1,2). \tag{9}$$

3. Singular integral equations

3.1. Boundary conditions

Consider a finite crack with length $2c$ and a branch with length $a(a \ll c)$ embedded in a bimaterial plane subjected to the remote load $\boldsymbol{\Pi}_0$ (see Fig. 1). The cracks are initially assumed to remain open and hence be free of tractions and charges. The corresponding boundaries are, then, as follows.

On the faces of each crack i:

$$\mathbf{t}_n^{(i)} = -\boldsymbol{\Pi}_1^{(i)}\sin\theta_i + \boldsymbol{\Pi}_2^{(i)}\cos\theta_i = 0 \quad (i = 1,2). \tag{10}$$

At infinity

$$\boldsymbol{\Pi}_2^{\infty} = \boldsymbol{\Pi}_0, \quad \boldsymbol{\Pi}_1^{\infty} = 0, \tag{11}$$

where n stands for the normal direction to the lower face of a crack and $\mathbf{t}_n^{(i)}$ the surface traction and charge vector acting on the faces of the ith crack.

To study the effect of cracks on the fracture behaviour, it is convenient to represent the solution as the sum

of a uniform SED in an unflawed solid and a corrective solution in which the boundary conditions are:

On the faces of each crack i:

$$\mathbf{t}_n^{(i)} = -\boldsymbol{\Pi}_1^{(i)} \sin\theta_i + \boldsymbol{\Pi}_2^{(i)} \cos\theta_i = -\boldsymbol{\Pi}_0 \cos\theta_i \quad (i = 1,2). \tag{12}$$

At infinity

$$\boldsymbol{\Pi}_2^{\infty} = \boldsymbol{\Pi}_1^{\infty} = 0. \tag{13}$$

3.2. Singular integral equations

The singular integral equations for the problem described above can be formulated by considering the stress and electric displacement fields on the prospective site of the branch crack configuration due to the distributed dislocation caused by all cracks. The assumed distribution of dislocation consists of two parts: (i) a concentrated dislocation with the intensity, $\hat{\mathbf{B}}$, applied at the joint of the finite crack and the branch (the origin in Fig. 1); (ii) distributed dislocation densities $\mathbf{b}_i(= b_{xi}, b_{yi}, b_{zi}, b_{Di};\ i = 1,2)$ applied along the ith crack.

Using the principle of superposition [15], the problem shown in Fig. 1 is decomposed into two sub-problems, each of which contains only one single crack. The boundary conditions in Eq. (12) can be satisfied by redefining the discrete Green's function $\mathbf{b}_i$ given in Section 2 in terms of distributing Green's function $\mathbf{b}_i(\xi)$ defined along each crack line, $z_k^{(i)} = \eta z_k^{*(i)}$, $z_{0k}^{(i)} = \xi z_k^{*(i)}$, $z_k^{*(i)} = \cos\theta_i + p_k^{(i)} \sin\theta_i$ $(i = 1, 2)$. Enforcing the satisfaction of the applied stress conditions on each crack face, a system of singular integral equations for Green's function is obtained as

$$\int_0^a \left(\frac{\mathbf{L}_1}{2(\eta-\xi)} + \mathbf{K}_{11}(\eta,\xi)\right) \mathbf{b}_1(\xi)\,\mathrm{d}\xi + \int_0^{2c} \mathbf{K}_{12}(\eta,\xi)\mathbf{b}_2(\xi)\,\mathrm{d}\xi + \frac{\boldsymbol{V}}{\eta}\hat{\mathbf{B}} = -\pi\boldsymbol{\Pi}_0 \cos\theta_1, \tag{14}$$

$$\int_0^{2c} \left(\frac{\mathbf{L}_2}{2(\eta-\xi)} + \mathbf{K}_{22}(\eta,\xi)\right) \mathbf{b}_2(\xi)\,\mathrm{d}\xi + \int_0^{a} \mathbf{K}_{21}(\eta,\xi)\mathbf{b}_1(\xi)\,\mathrm{d}\xi - \frac{\boldsymbol{V}}{\eta}\hat{\mathbf{B}} = -\pi\boldsymbol{\Pi}_0 \cos\theta_2, \tag{15}$$

where $\mathbf{K}_{ij}$ are 4×4 known kernel matrices and are regular within the related interval, which can be derived from Eqs. (1), (3)–(6). They are

$$\mathbf{K}_{11} = \mathrm{Im}\left[\sum_{\beta=1}^{4}\mathbf{B}_1\left\langle \frac{z_\alpha^{*(1)}}{\eta z_\alpha^{*(1)} - \xi \bar{z}_\beta^{*(1)}}\right\rangle \mathbf{B}_\beta^{*}\right], \tag{16}$$

$$\mathbf{K}_{12} = \mathrm{Im}\left[\sum_{\beta=1}^{4}\mathbf{B}_1\left\langle \frac{z_\alpha^{*(1)}}{\eta z_\alpha^{*(1)} - \xi \bar{z}_\beta^{*(2)}}\right\rangle \mathbf{B}_\beta^{**a}\right], \tag{17}$$

$$\mathbf{K}_{21} = \mathrm{Im}\left[\sum_{\beta=1}^{4}\mathbf{B}_2\left\langle \frac{z_\alpha^{*(2)}}{\eta z_\alpha^{*(2)} - \xi \bar{z}_\beta^{*(1)}}\right\rangle \mathbf{B}_\beta^{**}\right], \tag{18}$$

$$\mathbf{K}_{22} = \mathrm{Im}\left[\sum_{\beta=1}^{4}\mathbf{B}_2\left\langle \frac{z_\alpha^{*(2)}}{\eta z_\alpha^{*(2)} - \xi \bar{z}_\beta^{*(2)}}\right\rangle \mathbf{B}_\beta^{*a}\right], \tag{19}$$

$$\mathbf{V} = \frac{1}{2}\mathrm{Im}[\mathbf{B}_1(\mathbf{A}_1 - \bar{\mathbf{A}}_2\bar{\mathbf{B}}_2^{-1}\mathbf{B}_1)], \tag{20}$$

$$\mathbf{B}_\beta^{*a} = \mathbf{B}_2^{-1}[\boldsymbol{I} - 2(\mathbf{M}_2^{-1} + \bar{\mathbf{M}}_1^{-1})^{-1}\mathbf{L}_2^{-1}]\bar{\mathbf{B}}_1\mathbf{I}_\beta\bar{\mathbf{B}}_1^{T},$$
$$\mathbf{B}_\beta^{**a} = \mathbf{B}_1^{-1}(\bar{\mathbf{M}}_2^{-1} + \mathbf{M}_1^{-1})^{-1}\mathbf{L}_2^{-1}\mathbf{B}_2\mathbf{I}_\beta\mathbf{B}_2^{\mathrm{T}}. \tag{21}$$

The single-valued displacements around the closed contour surrounding the branch crack configuration requires that

$$\int_0^a \mathbf{b}_1(\xi)\,\mathrm{d}\xi + \int_0^{2c} \mathbf{b}_2(\xi)\,\mathrm{d}\xi = \hat{\mathbf{B}}. \tag{22}$$

The singular integral equations (14), (15) and (22) are too complicated to be evaluated exactly and consequently a numerical evaluation is necessary. To this end, let

$$\mathbf{b}_i(\xi_i) = \left(\frac{\xi_i}{d_i - \xi_i}\right)^{1/2} \mathbf{b}_i^{*}(\xi_i), \tag{23}$$

where $\mathbf{b}_i^{*}(\xi_i)$ are regular functions defined on the related interval $0 \leqslant \xi_i \leqslant d_i$, and $d_1 = a$, $d_2 = 2c$.

Employing the semi-open quadrature rule [16], Eqs. (14), (15) and (22) can be rewritten as

$$\sum_{m=1}^{M}\left[\left\{\frac{\mathbf{L}_1}{\eta_{1k} - \xi_{1m}} + \mathbf{K}_{11}(\eta_{1k},\xi_{1m})\right\}\mathbf{A}_{1m}\mathbf{b}_1^{*}(\xi_{1m}) + \mathbf{K}_{12}(\eta_{1k},\xi_{2m})\mathbf{A}_{2m}\mathbf{b}_2^{*}(\xi_{2m})\right] + \frac{V}{\eta_{1k}}\hat{\mathbf{B}} = \mathbf{t}_{n1}(\eta_{1k}), \tag{24}$$

$$\sum_{m=1}^{M}\left[\left\{\frac{\mathbf{L}_2}{\eta_{2k} - \xi_{2m}} + \mathbf{K}_{22}(\eta_{2k},\xi_{2m})\right\}\mathbf{A}_{2m}\mathbf{b}_2^{*}(\xi_{2m}) + \mathbf{K}_{21}(\eta_{2k},\xi_{1m})\mathbf{A}_{1m}\mathbf{b}_1^{*}(\xi_{1m})\right] - \frac{V}{\eta_{2k}}\hat{\mathbf{B}} = \mathbf{t}_{n2}(\eta_{2k}), \tag{25}$$

$$\sum_{m=1}^{M}[\mathbf{A}_{1m}\mathbf{b}_1^{*}(\xi_{1m}) + \mathbf{A}_{2m}\mathbf{b}_2^{*}(\xi_{2m})] = \hat{\mathbf{B}}, \tag{26}$$

where

$$\mathbf{A}_{im} = \frac{\pi d_i}{M}\sin^2\frac{m\pi}{2M} \quad (i = 1,2;\ m = 1,2,\ldots,M-1),$$

$$\mathbf{A}_{1M} = \frac{\pi d_1}{2M}, \quad \mathbf{A}_{2M} = \frac{\pi d_2}{2M},$$

$$\xi_{im} = d_i \sin^2 \frac{m\pi}{2M}, \quad \eta_{ik} = d_i \sin^2 \frac{(k-0.5)\pi}{2M}$$

$$(i = 1,2;\ m,\ k = 1,2,\ldots,M).$$

Eqs. (24) and (26) provide a system of $4(2M+1)$ algebraic equations to determine $\hat{\mathbf{B}}$, $\mathbf{b}_1^*(\xi_{1m})$ and $\mathbf{b}_2^*(\xi_{2m})$. Once these unknowns have been found from Eqs. (24)–(26), the SED, $\boldsymbol{\Pi}_n^{(1)}(\eta)$, in a coordinate local to the crack branch line can be expressed in the form

$$\boldsymbol{\Pi}_n^{(1)}(\eta) = \frac{1}{\pi}\boldsymbol{\Omega}(\theta_1)\left[\int_0^a \left(\frac{\mathbf{L}_1}{2(\eta-\xi)} + \mathbf{K}_{11}(\eta,\xi)\right)\mathbf{b}_1(\xi)\,\mathrm{d}\xi + \int_0^{2c} \mathbf{K}_{12}(\eta,\xi)\mathbf{b}_2(\xi)\,\mathrm{d}\xi + \frac{\boldsymbol{V}}{\eta}\hat{\mathbf{B}} + \pi\boldsymbol{\Pi}_0\cos\theta_1\right], \tag{27}$$

where the 4×4 matrix $\boldsymbol{\Omega}(\theta_1)$ whose components are the cosine of the angle between the local coordinates and the global coordinates is in the form

$$\boldsymbol{\Omega}(\theta) = \begin{bmatrix} \cos\theta_1 & \sin\theta_1 & 0 & 0 \\ -\sin\theta_1 & \cos\theta_1 & 0 & 0 \\ 0 & 0 & 1 & 0 \\ 0 & 0 & 0 & 1 \end{bmatrix}. \tag{28}$$

4. SED intensity factors and energy release rate

The SED intensity factors at the right tip of the branch crack are of interest and can be derived by first considering the traction and surface charge (TSC) on the direction of the branch line and considering the TSC very near the tip($\eta \to a$) which is given, from Eq. (27), as

$$\boldsymbol{\Pi}_n^{(1)}(r) \approx \boldsymbol{\Omega}(\theta_1)\frac{\sqrt{a}\mathbf{L}_1\mathbf{b}_1^*(a)}{2\sqrt{(\eta-a)}} = \frac{1}{2}\sqrt{\frac{a}{r}}\boldsymbol{\Omega}(\theta_1)\mathbf{L}_1\mathbf{b}_1^*(a), \tag{29}$$

where r is a distance ahead of the branch tip.

Using Eq. (29) we can calculate the SED intensity factors at the right tip of the branch by the following usual definition

$$\mathbf{K} = \{K_{II}K_I K_{III}K_D\}^{\mathrm{T}} = \lim_{r\to 0}\sqrt{2\pi r}\boldsymbol{\Pi}_n^{(1)}(r). \tag{30}$$

Combining with the results of Eq. (29), leads to

$$\mathbf{K} \approx \sqrt{\frac{a\pi}{2}}\boldsymbol{\Omega}(\theta_1)\mathbf{L}_1\mathbf{b}_1^*(a). \tag{31}$$

Thus the solution of the singular integral equation enables the direct determination of the stress intensity factors.

The energy release rate G can be computed by the closure integral [17]

$$G = \lim_{x\to 0}\frac{1}{2x}\int_0^x \boldsymbol{\Pi}_n^{(1)\mathrm{T}}(r)\Delta\mathbf{u}_n(x-r)\,\mathrm{d}r, \tag{32}$$

where x is the assumed crack extension and $\Delta\mathbf{u}$ is a vector of elastic displacement and electric potential jump across the branch crack. Noting that

$$\Delta\mathbf{u}(r) = \int_0^r \mathbf{b}_1(a-\xi)\,\mathrm{d}\xi, \tag{33}$$

we have

$$G = \lim_{x\to 0}\frac{1}{2x}\int_0^x \boldsymbol{\Phi}_n^{(1)\mathrm{T}}(r)\frac{\partial\Delta\mathbf{u}_n(x-r)}{\partial x}\,\mathrm{d}r, \tag{34}$$

where

$$\boldsymbol{\Phi}_n^{(1)}(r) = \int_0^r \boldsymbol{\Pi}_n^{(1)}(x)\,\mathrm{d}x. \tag{35}$$

During the derivation of Eq. (34), the following conditions have been employed

$$\Phi_n^{(1)}(0) = 0, \quad \Delta\mathbf{u}(x-r)|_{r=x} = 0. \tag{36}$$

Substituting Eqs. (23) and (33), and Eqs. (29) and (35), later into Eq. (34), one obtains

$$G = \frac{a\pi}{4}\mathbf{b}_1^{*\mathrm{T}}(a)\mathbf{L}_1[\boldsymbol{\Omega}^{\mathrm{T}}(\theta_1)]^2\mathbf{b}_1^*(a). \tag{37}$$

5. Criterion for crack propagation

A crack impinging an interface joining two dissimilar materials may advance by either penetrating the interface or deflecting into the interface. This competition can be assessed by comparing the ratio of the energy release rate for penetrating the interface and for deflecting into the interface, G_p/G_d, to the ratio of the mode I toughness of material 1 to the interface toughness, Γ_c/Γ_{ic}. Concretely, if

$$\frac{G_p}{G_d} > \frac{\Gamma_c}{\Gamma_{ic}}, \tag{38}$$

the impinging crack is likely to penetrate the interface, since the condition for penetrating across the interface will be met at a lower load than that for propagation in the interface. Conversely, if the inequality in Eq. (38) is reversed, the crack will tend to be deflected into the interface, where Γ_{ic} and Γ_c are the interface toughness and mode I toughness of material 1, respectively. For a given load condition, say $\boldsymbol{\Pi}_2^{\infty}$, the fracture toughness, Γ, is defined as the energy release rate G at the onset of the crack growth and has discussed in detail elsewhere [18]. G_d and G_p are the energy release rates for deflecting into the interface and for penetrating the interface, respectively.

6. Numerical results

Since the main purpose of this paper is to outline the basic principles of the proposed method, the assessment has been limited to a piezoelectric bimaterial plate with an inclined crack of length $2c$, a branch crack of length a and its interface coincided with x_1-axis shown in Fig. 1. In all calculations, the ratio of a/c is taken to be 0.1. The upper and lower materials are assumed to be PZT-5H and PZT-5 [19], respectively. The material constants for the two materials are as follows:

1. material properties for PZT-5H:

$$c_{11} = 117 \text{ GPa}, \quad c_{12} = c_{13} = 53 \text{ GPa},$$
$$c_{22} = c_{33} = 126 \text{ GPa}, \quad c_{44} = 35.5 \text{ GPa},$$
$$c_{23} = 55 \text{ GPa}, \quad c_{55} = c_{66} = 35.3 \text{ GPa},$$
$$e_{12} = e_{13} = -6.5 \text{ C/m}^2, \quad e_{11} = 23.3 \text{ C/m}^2,$$
$$e_{35} = e_{26} = 17 \text{ C/m}^2, \quad \kappa_{11} = 130 \times 10^{-10} \text{ C/Vm},$$
$$\kappa_{22} = \kappa_{33} = 151 \times 10^{-10} \text{ C/Vm},$$

2. material properties for PZT-5:

$$c_{11} = 111 \text{ GPa}, \quad c_{12} = c_{13} = 75.2 \text{ GPa},$$
$$c_{22} = c_{33} = 121 \text{ GPa}, \quad c_{44} = 22.8 \text{ GPa},$$
$$c_{23} = 75.4 \text{ GPa}, \quad c_{55} = c_{66} = 21.1 \text{ GPa},$$
$$e_{12} = e_{13} = -5.4 \text{ C/m}^2, \quad e_{11} = 15.8 \text{ C/m}^2,$$
$$e_{35} = e_{26} = 12.3 \text{ C/m}^2, \quad \kappa_{11} = 73.46 \times 10^{-10} \text{ C/Vm},$$
$$\kappa_{22} = \kappa_{33} = 81.7 \times 10^{-10} \text{ C/Vm}.$$

The ratio G_p/G_d vs. kink angle θ_1, with $\theta_2 = -90°$ and $\sigma_{23}^{\infty} = D_2^{\infty} = 0$, are shown in Fig. 2 for a number of loading combinations measured by $\psi = \tan^{-1}(K_{II}/K_I)$, where K_I and K_{II} are the conventional mode I and mode II stress intensity factors. The curve clearly shows that the maximum energy release rate occurs at different kink angle $\hat{\theta}$ for different loading phase ψ, where $\hat{\theta}$ is the critical knik angle for which the maximum energy release rate will occur under a given loading condition. For example, $\hat{\theta} = 43°$ for curves 1; $\hat{\theta} = 34°$ for curve 2; $\hat{\theta} = 28°$ for curve 3; $\hat{\theta} = 25°$ for curve 4 and $\hat{\theta} = 22°$ for curve 5. It is also found from Fig. 2 that the ratio G_p/G_d will increase along with the increase of phase angle ψ, which means that the possibility of the crack penetrating the interface will increase.

To study the effect of remote loading D_2^{∞} on the path selection of crack propagation, the numerical results of the ratio of G_p/G_d have been obtained and is plotted in Fig. 3 as a function of kink angle θ_1 for several values of remote loading D_2^{∞} with $\theta_2 = 180°$, $\sigma_{22}^{\infty} = 4 \times 10^6$ N/m^2 and $\sigma_{12}^{\infty} = \sigma_{23}^{\infty} = 0$.

In the calculation we found that the energy release rate may have negative value depending on the direction and magnitude of the remote loading D_2^{∞}. For this particular problem, the energy release rate G_i will be positive when $-1.8\times10^{-3}\text{C/m}^2 < D_2^{\infty} < 1.8\times10^{-3}\text{C/m}^2$ and be negative for other values of D_2^{∞}.

Fig. 4 shows the variation of G_p/G_d as a function of of kink angle θ_1 for several values of angle θ_2 with $D_2^{\infty} = 10^{-3}$ C/m^2, $\sigma_{22}^{\infty} = 4\times10^6$ N/m^2 and $\sigma_{12}^{\infty} = \sigma_{23}^{\infty} = 0$. It can be seen from the figure that the ratio of G_p/G_d will decrease along with the increase of angle θ_2. It is also found from Fig. 4 that the crack is likely to deflect into the interface under this particular loading condition.

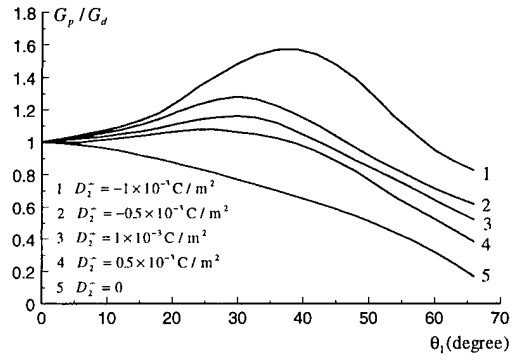

Fig. 3. Variation of G_p/G_d with kink angle θ_1 for several loadings $D_2^{\infty}(\theta_2 = 180°, \sigma_{22}^{\infty} = 4\times10^6$ N/m^2).

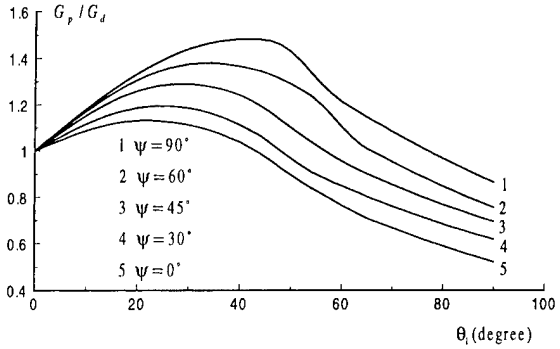

Fig. 2. Variation of G_p/G_d with knik angle θ_1 for several loading combinations specified by $\psi = \tan^{-1}(K_{II}/K_I)$.

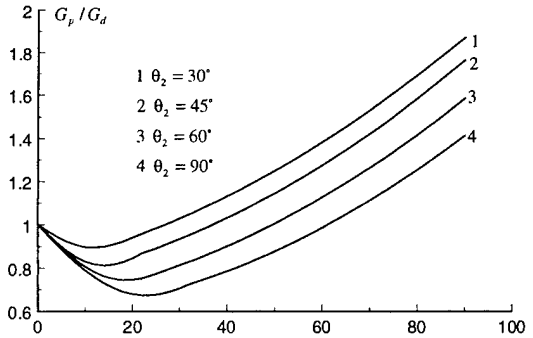

Fig. 4. Variation of G_p/G_d with kink angle θ_1 for several loadings $\theta_2(D_2^{\infty} = 10^{-3}$ C/m^2, $\sigma_{22}^{\infty} = 4\times10^6$ N/m^2).

7. Conclusions

The problem of crack path selection has been studied for piezoelectric bimaterial systems. In this investigation, the branched cracks are expressed in terms of coupled singular integral equations by way of Green's function approach. The unknowns for the resulting integral equations include the dislocation density function defined on each crack and a concentrated dislocation, $\hat{\mathbf{B}}$, applied at the joint of the main crack and the branch (the origin in Fig. 1). The energy release rate and SED intensity factors can be calculated from the solutions of the dislocation density functions. A particular example of a piezoelectric bimaterial containing an inclined crack and a branch was examined to see the application of the proposed formulation. By way of the criterion of maximum energy release rate, the numerical solution obtained can be used to assess whether an impinging crack will deflect into the interface or whether it will penetrate the interface. The analysis also shows that the energy release rate can have either positive or negative values in the presence of electric load, depending on the direction and the magnitude of the applied electric displacement. In other words, for a given mechanical load, presence of the applied electric displacement can either promote or retard crack extension. This conclusion may be useful in designing piezoelectric components with interface.

Acknowledgements

The authors wish to thank the Australian Research Council (ARC) for the continuing support of this work. Q.-H. Qin is supported by a Queen Elizabeth II fellowship from the ARC and the J.G. Russell Award from the Australian Academy of Science.

References

[1] He MY, Hutchinson JW. Crack deflection at an interface between dissimilar elastic materials. Int J Solids Struc 1989;25:1053–67.
[2] Erdogan F, Biricikoglu V. Two bonded half-planes with a crack going through the interface. Int J Engrg Sci 1973;11:745–66.
[3] Evans AG, Dalgleish BJ, He MY, Hutchinson JW. On crack path selection and the interface fracture energy in bimaterial systems. Acta Metall 1989;37:3249–54.
[4] He MY, Hutchinson JW. Kinking of a crack out of an interface. J Appl Mech 1989;56:270–8.
[5] Miller GR, Stock WL. Analysis of branched interface cracks between dissimilar anisotropic media. J Appl Mech 1989;56:844–9.
[6] Gupta V, Argon AS, Suo Z. Crack deflection at an interface between two orthotropic materials. J Appl Mech 1992;59:s79–87.
[7] Wang TC, Shih CF, Suo Z. Crack extension and kinking in laminates and bicrystals. Int J Solids Struc 1992;29:327–44.
[8] Sung JC, Liou JY, Lin YY. Some phenomena of cracks perpendicular to an interface between dissimilar orthotropic materials. J Appl Mech 1996;63:190–203.
[9] Chen DH. Stress intensity factor for a crack normal to an interface between two orthotropic materials. Int J Fracture 1997;88:19–39.
[10] Qin QH, Mai YW. Thermoelectroelastic Green's function and its application for bimaterial of piezoelectric materials. Arch Appl Mech 1998;68:433–44.
[11] Stroh AN. Dislocations and cracks in anisotropic elasticity. Philos Mag 1958;7:625–46.
[12] Barnett DM, Lothe J. Dislocations and line charges in anisotropic piezoelectric insulators. Phys Stat Sol (b) 1975;67:105–11.
[13] Chung MY, Ting TCT. Piezoelectric solid with an elliptic inclusion or hole. Int J Solids Struc 1996;33:3343–61.
[14] Ting TCT. Image singularities of Green's functions for anisotropic elastic half-space and bimaterials. Q J Mech Appl Math 1992;45:119–39.
[15] Horri H, Nemat-Nasser S. Elastic fields of interacting in homogeneities. Int J Solids Struc 1985;21:731–45.
[16] Boiko AV, Karpenko LN. On some numerical methods for the solution of the plane elasticity problem for bodies with cracks by means of singular integral equations. Int J Frac 1981;17:381–8.
[17] Park SB, Sun CT. Effect of electric field on fracture of piezoelectric ceramics. Int J Frac 1995;70:203–16.
[18] Hutchinson JW, Suo Z. Mixed mode cracking in layered materials, In: Hutchinson JW, Wu TY, editors, Advances in applied mechanics, 1992;29:63–191.
[19] Qin QH, Yu SW. An arbitrarily-oriented plane crack terminating at interface between dissimilar piezoelectric materials. Int J Solids Struc 1997;34:581–90.

ELSEVIER

Composite Structures 47 (1999) 525–530

COMPOSITE STRUCTURES

www.elsevier.com/locate/compstruct

Damage detection of CFRP laminates using electrical resistance measurement and neural network

Dae-Cheol Seo, Jung-Ju Lee *

Department of Mechanical Engineering, Korea Advanced Institute of Science and Technology, 373-1 Kusong-dong, Yusung-gu, Taejon 305-701, South Korea

Abstract

As carbon fibers are electrical conductors, the measurement of the electrical resistance appears to be a valuable technique for the in situ detection of various types of damage in carbon fiber reinforced polymers (CFRP) laminates. In such cases, carbon fibers are both the reinforcement and the sensor to detect damage in CFRP laminates. The damage-detecting method of CFRP laminates by electrical resistance measurement that are investigated in this study is made possible by attaching electrodes on the surface of the CFRP structures without special manufacturing.

In this paper, we investigate the electrical resistance change as a damage parameter of fatigue damage such as the degradation of residual strength and stiffness. The measured stiffness and electrical resistance change during fatigue tests showed a very similar trend of change. This is because cumulative fatigue damage is represented by the degradation of residual stiffness; these damages also cause change in electrical resistance. Thus, we can use this change in electrical resistance as a damage parameter. We also predict the future damage of composite laminates in fatigue loading from electrical resistance damage model by following a stiffness degradation model. Electrical resistance gradually increased as the stiffness reduced, and showed a very abrupt change when final fatigue failure was imminent. The predicted value showed good agreement with the experimental data except in the final stage, where stiffness and electrical resistance changed abruptly. © 2000 Published by Elsevier Science Ltd.

Keywords: Damage detection; Electrical resistance measurement; Fatigue; Carbon fiber sensor; Smart structures

1. Introduction

Owing to their superior mechanical properties such as high specific stiffness, high specific strength, corrosion resistance and fatigue resistance, advanced composite materials have been increasingly applied in aircraft and space structures which require light-weight design. Therefore, to ensure the safety of composite structures during their lifetime it is imperative to detect, analyze and evaluate the various types of damage caused by both static and dynamic loads and by environmental effects. To this end, researches on the integration of functional elements in composite laminates that allow in situ damage detection and in-service health monitoring have been widely pursued.

Since carbon fibers are electrical conductors, the measurement of variations in electrical resistance appears to be a valuable technique for the in situ detection of various types of damage in carbon fiber reinforced polymers (CFRP) laminates [1–6]. In such cases, carbon fibers are not only the reinforcement but also the sensor for damage detection in CFRP laminates. The method itself is similar to the potential drop technique used in metal specimen to detect crack propagation. However, in the case of metal, high input current (about several A) and high-resolution (about 0.1 μV) voltage meter are necessary. In the case of CFRP, only low input current (about mA) and low-resolution (about mV) voltage meter are required. The damage detection method of CFRP laminates by electrical resistance measurement that was investigated in this study is available by attaching electrodes on the surface of the CFRP structures without special manufacturing. This electric potential system can also be applied to structures in service without strength decrease.

Fatigue damage in composite laminates is a complicated phenomenon involving different mechanisms; these various damage mechanisms, in effect, take place simultaneously. Total cumulative fatigue damage can

* Corresponding author. Tel.: +82-42-869-3073; fax: +82-42-869-3210 or 5210.

E-mail address: jjlec@sorak.kaist.ac.kr (J.-J. Lee).

0263-8223/99/$ - see front matter © 2000 Published by Elsevier Science Ltd.
PII: S0263-8223(00)00016-7

be represented by changes in the strength, stiffness and other material properties. From a phenomenological standpoint fatigue damage can be evaluated in a global sense by the degradation of residual strength and stiffness [7]. Electrical resistance change in composite laminates is also a cumulative effect of damage caused by various damage mechanisms. Therefore, we investigated electrical resistance change as a damage parameter of fatigue damage such as the degradation of residual stiffness. The measured stiffness and electrical resistance change during fatigue tests showed a similar trend of change. The future damage of composite laminates in tensile fatigue loading from electrical resistance change could be predicted by following the stiffness degradation model proposed by Yang et al. [7–9]. The relationship between the electrical resistance damage parameter and fatigue life and stiffness reduction was also investigated using a neural network.

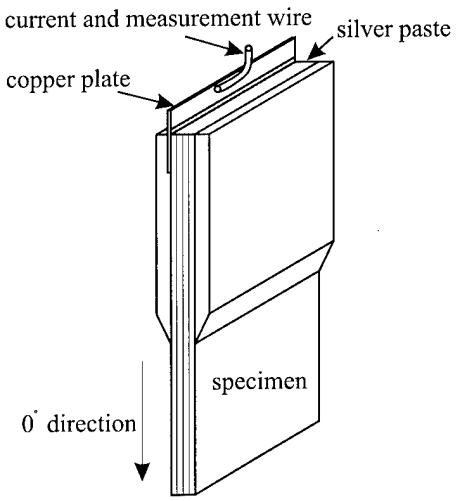

Fig. 1. Schematic diagram of specimen.

2. Specimens and test method

All specimens were fabricated from unidirectional carbon fiber/epoxy prepreg (UGN125 by SK Chemicals). CFRP laminates were cured using an autoclave, following the manufacturers recommended cure cycle; specimens were cut from the laminates using a water-cooled, diamond-coated saw machine. Specimen dimensions were 160 mm long, 24 mm wide and 1 mm thick. Two types of stacking sequences for composite laminates ($[0]_8$ and $[0_2/90_2]_s$) were used to investigate the difference in electrical resistance change due to different damage mechanisms such as reinforcement fiber breakage and matrix cracking. E-glass loading tabs were bonded with film adhesive at each end of the specimens to insulate them from grips and for load transfer. Next a 150 μm thick copper plate was inserted between each loading tab and specimen (Fig. 1). The copper plate was inserted to introduce input current and to measure resistance. Electrical contact between the carbon fibers and the copper plate was made with silver paste; measurement and current input wires were then soldered to the copper plate.

Fatigue tests were performed using a servo-hydraulic testing system. A constant current of 50 mA was introduced into the end faces of CFRP specimen with the aid of a copper plate that extended beyond the end of specimen. Electrical resistance was acquired by measuring voltages using a signal conditioning voltage amplifier and a personal computer with a data acquisition system. The tests were performed in tension–tension loading at a loading frequency of 4 Hz and stress ratio of $R = S_{min}/S_{max} = 0.1$. Five stress levels, 75%, 70%, 65%, 60% and 55% of the average static ultimate strength, were selected. For each of the selected stress levels six specimens were tested.

3. Results and discussion

3.1. Experimental results

The change in strain and electrical resistance of cross-ply and unidirectional CFRP specimens during constant amplitude fatigue test is shown in Fig. 2 and Fig. 3, respectively. They showed similar trend of change between strain and electrical resistance change as the number of cycles increased. This is because the cumulative fatigue damage was represented by the degradation of residual stiffness; this damage also causes the change in electrical resistance. Thus, we can use the change of electrical resistance as a damage parameter. Unlike the specimens, it is difficult to measure stiffness in real composite structure because both loading stress and strain are required; however, electrical resistance can be

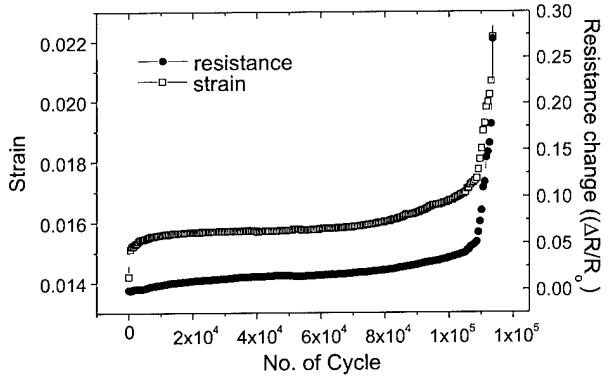

Fig. 2. Strain and electrical resistance change of cross-ply specimen during fatigue loading.

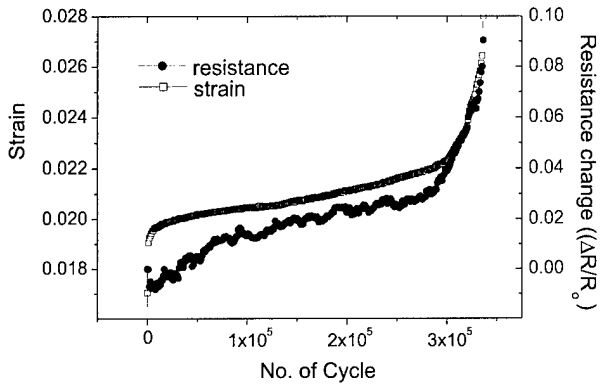

Fig. 3. Strain and electrical resistance change of unidirectional specimen during fatigue loading.

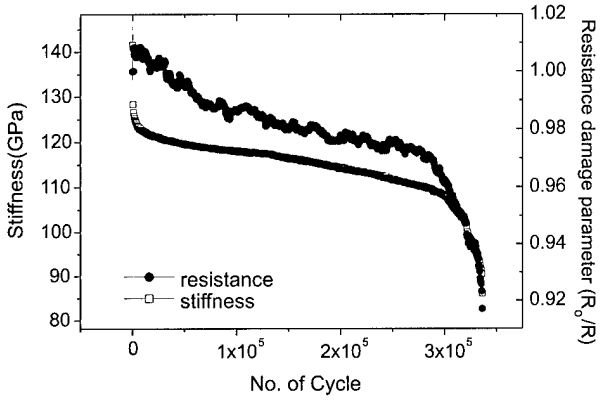

Fig. 5. Stiffness and electrical resistance damage parameter of unidirectional specimen during fatigue loading.

measured using simple devices if electrodes are provided. Thus, the electrical resistance measurement technique is easy to apply to structures in service.

Since the fatigue test is a force control test, only the strain changes in stiffness relation, $E = \sigma/\varepsilon$. Therefore, if we define a damage parameter, $D_r = R_0/R$, which is inversely dependent on resistance as stiffness is inversely dependent on strain, we can use this damage parameter, D_r, as a new parameter in predicting fatigue damage such as stiffness degradation. Electrical resistance gradually increased as the stiffness decreased and showed a very abrupt change when final fatigue failure was imminent, showing that specimen failure could be detected by monitoring electrical resistance change.

The change in the stiffness and electrical resistance damage parameter, D_r, of the cross-ply and unidirectional specimen is shown in Fig. 4 and Fig. 5, respectively. Both show acceptable agreement between stiffness reduction and change in the damage parameter. The cross-ply specimen, however, shows better agreement than does the unidirectional specimen. This is due to the difference in the damage mechanism. The matrix cracking of the cross-ply specimen occurs before the fiber breakage of the unidirectional specimen. The electrical resistance change in the CFRP laminate can be caused by the breakage of carbon fibers and by the damage in the perpendicular direction of reinforcement, because electric contact is possible between neighboring carbon fibers [1,5]. Thus, the damage mechanism, which alters the electrical contact of neighboring carbon fibers, i.e., matrix cracking and delaminating, also causes the electrical resistance change. In the cross-ply specimen, matrix cracking occurs before reinforcement fiber breakage and causes a uniform effect on fatigue damage. Thus, the stiffness reduction and the change in electrical resistance damage parameter of the cross-ply specimen showed better agreement than the unidirectional specimen.

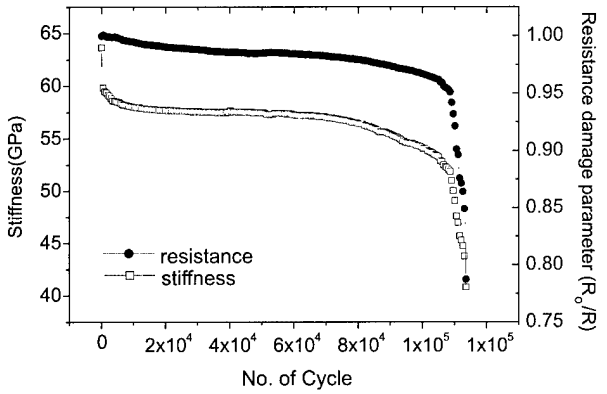

Fig. 4. Stiffness and electrical resistance damage parameter of cross-ply specimen during fatigue loading.

3.2. Electrical resistance damage parameter model

The stiffness degradation model proposed by Yang et al. [7–9] showed good agreement between predicted values and experimental results in predicting fatigue damage in carbon fiber reinforced epoxy composite laminates. This stiffness degradation model was based on the assumption that the residual stiffness degradation rate is a power function of the number of load cycles.

As mentioned in the previous section, the stiffness and electrical damage parameter D_r showed a very similar trend. We can therefore make a new model which predicts fatigue damage from the electrical resistance change by following the stiffness degradation model proposed by Yang et al. The change rate in the electrical resistance damage parameter D_r was assumed to be a power function of the number of load cycles, as in the following equation:

$$\frac{dD_r(n)}{dn} = -D_r(0)\,Qvn^{v-1}, \tag{1}$$

where n is the loading cycle, $D_r(0)$ the initial damage parameter, $D_r(n)$ the damage parameter at the nth

loading cycle, and Q and v are the material constants. Integrating the above equation from n_1 to n_2, one obtains

$$D_r(n_2) = D_r(n_1) - D_r(0)\,Q[n_2^v - n_1^v]. \quad (2)$$

For simplicity, let $n_1 = 0$ and $n_2 = n$ and from the definition of the electrical resistance damage parameter, $D_r = R_0/R$, $D_r(0)$ become unity. So the Eq. (2) becomes

$$D_r(n) = [1 - Qn^v]. \quad (3)$$

When base-line data are not available, there is no prior knowledge of the random variables Q and v appearing in the residual stiffness degradation model. Hence, the future stiffness degradation of a particular specimen will be predicted using only the initial measurement data [7]. This is the same in the electrical resistance damage parameter model. Let $D_r(n_1), D_r(n_2), \ldots, D_r(n_k)$ is the electrical resistance damage parameter of a particular specimen measured at $n_1, n_2, \ldots, n_k$ load cycle. We can then predict the future electrical resistance damage parameter $D_r(n_{k+1}), D_r(n_{k+2}), \ldots, D_r(n_{k+m})$ at $n_{k+1}, n_{k+2}, \ldots, n_{k+m}$ load cycles, based on the measured information, $D_r(n_1), D_r(n_2), \ldots, D_r(n_k)$. Let $Q(k)$ and $v(k)$ be the best estimates of the sample values of Q and v for a particular specimen at the current time n_k, and apply the boundary condition at the current time, i.e., $D_r(n) = D_r(n_k)$ for $n = n_k$. Eq. (3) leads to a relation between $Q(k)$ and $v(k)$ as follows:

$$Q(k) = [1 - D_r(n_k)]/(n_k)^{v(k)}. \quad (4)$$

Substitution of Eq. (4) into Eq. (3) yields

$$D_r(n) = D_r(n_k)(n/n_k)^{v(k)}. \quad (5)$$

Eq. (5) can be transformed into a linear regression form for $v(k)$

$$\ln[D_r(n)/D_r(n_k)] = v(k)\ln[n/n_k]. \quad (6)$$

Thus, $v(k)$ can be estimated from available measured data using the method of linear regression. Once $v(k)$ is obtained, the future damage parameter can be predicted using Eq. (5).

3.3. Comparison between predicted values and experimental results

Fig. 6 shows the predicted stiffness reduction and electrical resistance damage parameter and experimental results. The predicted values and experimental results show good agreement except in the final fracture region, where stiffness changes very abruptly. The final fracture region does not follow the assumption that the stiffness and electrical resistance damage parameter is a power function of the number of load cycles. It is therefore possible to predict future damage from the initially measured data in the region where the damage grew gradually. The effects of changing stress level, stiffness

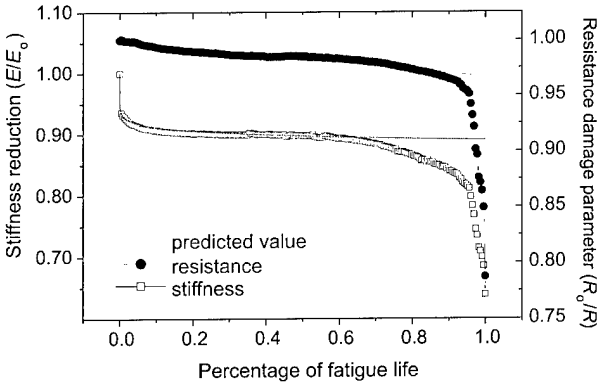

Fig. 6. Comparison of predicted stiffness reduction and electrical damage parameter with experimental value.

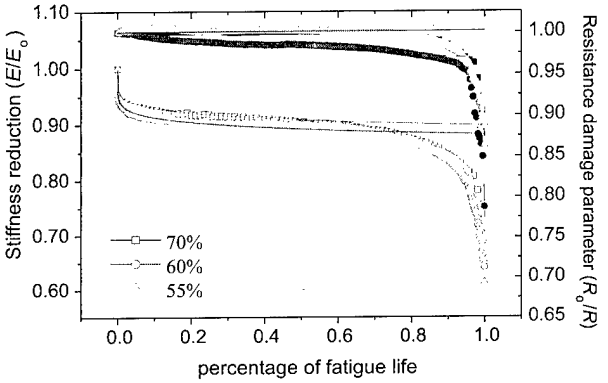

Fig. 7. Comparison of predicted stiffness reduction and electrical damage parameter with experimental value at different stress levels.

reduction and electrical resistance damage parameter of the specimen tested at 70%, 60% and 55% of static strength load level are shown in Fig. 7; the change in stress level resulted in no significant difference. Each specimen showed a slight difference, but the overall trends were the same. In the case of stiffness reduction, the difference from changing stress level was very small, but in the case of electrical resistance damage parameter, there was a small difference. However, this was due to the scatter of electrical resistance change rather than the effect of stress level change.

3.4. Neural network results

An artificial neural network provides a unique computing architecture that is used to address problems that are intractable or cumbersome with traditional methods. In this study, we analyzed the relationship between electrical resistance change and fatigue damage with such a neural network. As mentioned in the previous section, electrical resistance change can be used as a damage parameter representing fatigue damage such as the degradation of stiffness. However, the stiffness

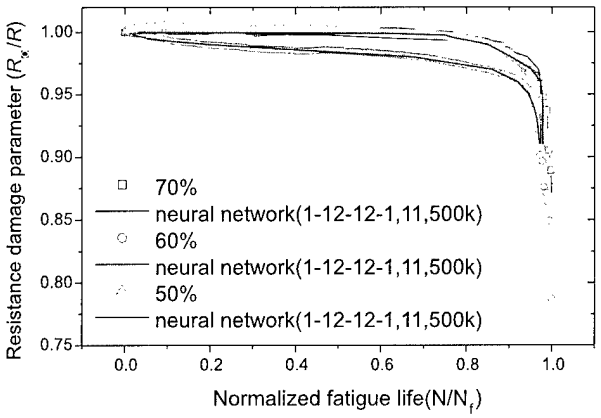

Fig. 8. Comparison of fatigue life and resistance damage parameter predicted by neural network and experimental results.

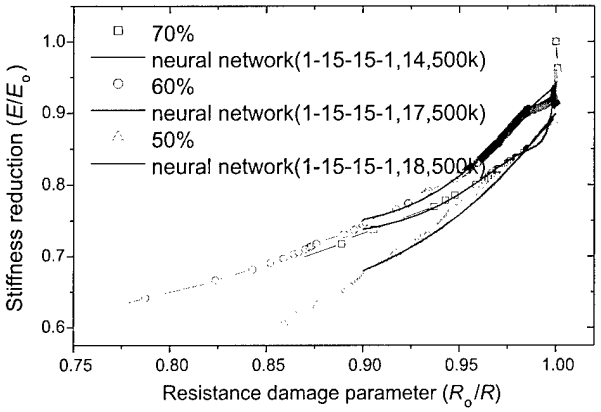

Fig. 9. Comparison of stiffness reduction and resistance damage parameter predicted by neural network and experimental results.

degradation and electrical resistance damage models rely on the assumption that damage is a power function of the number of load cycles, so this model cannot be used during the initial and final region of the fatigue test, where this assumption is not suitable. Hence, to apply the electrical resistance change as a damage parameter over the whole fatigue life, we investigated the relationship between electrical resistance change and fatigue life with a neural network by learning the electrical resistance, stiffness and fatigue cycle data.

Fig. 8 shows the results by learning the relationship between electrical resistance and fatigue life using a neural network; Fig. 9 shows the results by learning the relationship between electrical resistance and stiffness reduction using the neural network. The input node of the neural network is the electrical resistance damage parameter and the output node is fatigue life or stiffness reduction. The error convergence of the neural network relies on the structure of the hidden layer. In this case, it shows better results with two hidden layers than with one hidden layer. About 11–18 number of experimental data were used as learning input data. After the learning step, we acquired a graph very similar to the experimental results. Thus, it is possible to predict specimen damage by monitoring electrical resistance using a neural network.

4. Conclusion

From this study on fatigue damage detection of CFRP laminates by electrical resistance measurement, the following conclusions were obtained:

1. Electrical resistance change, which is easy to obtain through simple devices, can be a damage parameter representing the fatigue damage like the degradation of stiffness. The electrical resistance gradually increased as the stiffness reduced and showed very abrupt change when the final fatigue failure is imminent.
2. The measured stiffness and electrical resistance change during fatigue test showed very similar trends of change. We therefore defined a damage parameter, $D_r = R_0/R$, which is inversely dependent on resistance, as stiffness is inversely dependent on strain.
3. Fatigue damage was predicted using the electrical resistance damage parameter model formulated by following the stiffness degradation model. The predicted data showed good agreement with the experimental data, except in the final stage where stiffness and electrical resistance changed very abruptly.
4. The relationship between the electrical resistance damage parameter and fatigue life and stiffness reduction was investigated using a neural network. The predicted values using the neural network showed good agreement with the experimental results.

Acknowledgements

This study was supported by grant No. 971-1003-016-2 from the basic research program of the KOSEF.

References

[1] Schulte K, Baron Ch. Load and failure analyses of CFRP laminates by means of electrical resistivity measurements. Comp Sci Tech 1989;36:63–76.
[2] Prabhakaran R. Damage assessment through electrical resistance measurements in graphite fiber-reinforced composites. Exp Tech 1990;14:16–20.
[3] Fischer C, Arendts FJ. Electrical crack length measurement and the temperature dependence of the mode I fracture toughness of carbon fiber reinforced plastics. Comp Sci Tech 1993;46:319–23.
[4] Todoroki A, Kobayashi H. Application of electric potential method to smart composite structures for detection delamination. JSME Int A 1995;38(4):524–30.

[5] Sugita M, Yanagida H, Muto N. Materials design for self-diagnosis of fracture in CFGFRP composite reinforcement. Smart Mater Struct 1995;4:A52–7.
[6] Wang X, Chung DDL. Continuous carbon fiber epoxy-matrix composite as a sensor of its own strain. Smart Mater Struct 1996;5:796–800.
[7] Yang JN, Jones DL, Yang SH, Meskini A. A stiffness degradation model for graphite/epoxy laminates. J Comp Mater 1990;24:753–9.
[8] Yang JN, Yang SH, Jones DL. A stiffness-based statistical model for predicting the fatigue life of graphite/epoxy laminates. J Comp Tech Res 1989;11(4):129–34.
[9] Yang JN, Lee LJ, Sheu DY. Modulus reduction and fatigue damage of matrix dominated composite laminates. Comp Struct 1992;21:92–100.

ELSEVIER

Composite Structures 47 (1999) 531–541

COMPOSITE STRUCTURES

www.elsevier.com/locate/compstruct

Development of semianalytical axisymmetric shell models with embedded sensors and actuators

I.F. Pinto Correia [a], C.M. Mota Soares [b,*], C.A. Mota Soares [b], J. Herskovits [c]

[a] *ENIDH – Departamento de Máquinas Marítimas, Paco de Arcos, 2780 Oeiras, Portugal*
[b] *IDMEC – Instituto de Engenharia Mecânica, IST, Av. Rovisco Pais, 1049-001 Lisboa, Portugal*
[c] *COPPE – Universidade Federal do Rio de Janeiro, CP 68501, Rio de Janeiro, 21945-970 RJ, Brazil*

Abstract

This paper presents the development of two semianalytical axisymmetric shell finite element models, which have the possibility of having embedded and/or surface-bonded piezoelectric ring actuators and/or sensors. A mixed finite element approach is used, which combines the equivalent single-layer higher-order shear deformation theory, to represent the mechanical behavior with a layerwise discretization in the thickness direction to represent the distribution of the electrical potential of each piezoelectric layer of the frusta conical finite element. The electrical potential function is represented through a layerwise discretization in the thickness direction and can be assumed linear or quadratic with two or six electrical potential ring nodes per piezoelectric layer. The displacement field and the electrical potential are expanded by Fourier series in the circumferential direction, considering symmetric and anti-symmetric terms. Several examples are presented and discussed to illustrate the accuracy and capabilities of both models. © 2000 Elsevier Science Ltd. All rights reserved.

Keywords: Actuators; Axisymmetric shells; Electrical potential distribution; Finite element models; High-order theory; Piezoelectric layers; Sensors

1. Introduction

Laminated composite shells of revolution subjected to arbitrary loading have found extensive application in the pressure vessel, aircraft and spacecraft industries. The development of smart (adaptive) structures is currently receiving wide attention owing to potential applications in several branches of engineering. The concept of an intelligent structure involves an integrated control architecture with distributed sensors and actuators. Piezoelelectic materials have the advantage that they can be used for both sensing and actuation. This is particularly advantageous since closed loop control methods can be used. The combined effects of passive and active control on the static and vibration control of laminated plates and shells with embedded piezoelectric sensors and actuators has been studied by several authors [1–13]. It is expected that in the near future, more and more shells made of laminated materials with layers of piezoelectric materials will be used in order to achieve the growing mechanical demands of complex structures. Such applications increase the demand for numerical tools for the analyses of these structures with high accuracy and to use these tools to achieve efficient optimized designs. Related solutions for axisymmetric cylindrical shells have been proposed by Kapuria et al. [14] using three-dimensional elasticity solution and by Faria et al. [15] with a finite element cylinder model based on the Love–Kirchhoff formulation.

This paper presents two axisymmetric semianalytical finite element models, which are developed and applied on the static analysis of cylindrical/conical laminated thin and thick shells, with piezoelectric layers, using a higher order displacement field. The shell is modeled by cylindrical/conical finite elements and joined at their nodal circles, whose generalized displacements, electric potential and forces are expanded in the circumferential direction by Fourier series. These models take into consideration the coupling effect between the symmetric and anti-symmetric generalized displacement amplitudes, electrical potentials and applied loads. Related to this approach but for laminated axisymmetric structures, Sheinman and Weissman [16] and Mota Soares et al. [17] with Love–Kirchhoff models and more recently Pinto Correia et al. [18] using a higher order shear

* Corresponding author. Fax: +351-21-841-7915.
E-mail address: cmmsoares@alfa.ist.utl.pt (C.M. Mota Soares).

0263-8223/99/$ - see front matter © 2000 Elsevier Science Ltd. All rights reserved.
PII: S0263-8223(00)00017-9

deformable theory model, have discussed the importance of this coupling effect, which has been commonly disregarded until recently.

A mixed laminated theory for the analysis of piezoelectric composite axisymmetric shells is used, which combines an equivalent single-layer assumption for the displacements field and a layerwise representation for the electrical potential. This type of formulation has been used by Heyliger et al. [5], Saravanos [6] and Saravanos et al. [7] in numerical shell applications for the solution of static and dynamic problems.

In the conical shell models developed in this work, the distribution of the electrical potential is continuous in the longitudinal direction (along the elements) of the structure and the variation of the electrical potential across the thickness is either assumed linear or quadratic.

Three illustrative examples of axisymmetric laminated structures with sensors or actuators, under static loads are presented to show the response of the integrated structure and the capabilities of the proposed models.

2. Displacement and strain fields

The model is based on generic displacement field given by Palazotto [19] and Pinto Correia [20]:

$$\begin{aligned} u(s,\theta,z,t) &= \left(1+\frac{z}{R_s}\right)u_0 + z\beta_s + z^2u^* + z^3\beta_s^*,\\ v(s,\theta,z,t) &= \left(1+\frac{z}{R_\theta}\right)v_0 + z\beta_\theta + z^2v^* + z^3\beta_\theta^*,\\ w(s,\theta,t) &= w_0, \end{aligned} \tag{1}$$

where u_0, v_0, w_0 are displacements in the middle plane of the laminate referred to the local axes, β_s, β_θ are the rotations of the normal to the middle plane, about the s and θ axes and t is the time variable. The functions $u^*, v^*, \beta_s^*, \beta_\theta^*$ are high-order terms in the Taylor series expansion, also defined in the middle plane. All these functions depend only on s, θ and t. The principal radius of curvature of the surface in the θ and s directions are R_θ and R_s (Fig. 1). From the condition that the transverse shear stresses vanish on the shell top and bottom surfaces,

$$\gamma_{\theta z}\left(s,\theta,z=\pm\frac{h}{2},t\right) = \gamma_{sz}\left(s,\theta,z=\pm\frac{h}{2},t\right) = 0. \tag{2}$$

It is possible to express functions $u^*, v^*, \beta_s^*, \beta_\theta^*$ in terms of the generalized displacement field, u_0, v_0, w_0, β_s and β_θ. Due to the complexity of the shell strain displacement relations with a high-order displacement field it was necessary to use a symbolic manipulator [20,21]. After some cumbersome mathematical manipulations the displacement field takes the following form:

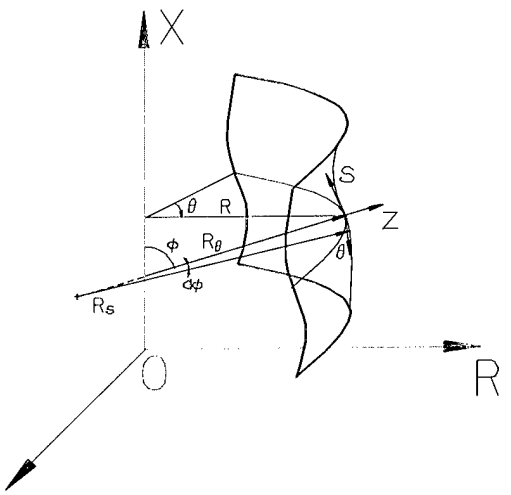

Fig. 1. Orthogonal curvilinear coordinate system (s, θ, z) of the shell with indication of the principal radius of curvature R_s and R_θ.

$$\begin{aligned} u(s,\theta,z,t) &= u_0 + \left(z-\frac{4}{3}\frac{z^3}{h^2}\right)\beta_s - z^3\frac{4}{3h^2}\frac{\partial w_0}{\partial s},\\ v(s,\theta,z,t) &= \left(1+\frac{z}{R_\theta}\right)v_0 + \left(z-\frac{4}{3}\frac{z^3}{h^2}\right)\beta_\theta - z^3\frac{4}{3R_\theta h^2}\frac{\partial w_0}{\partial \theta},\\ w(s,\theta,t) &= w_0. \end{aligned} \tag{3}$$

The linear strain–displacement relations for a generic conical geometry are represented, as deduced in [19,20], as a power series of the transversal coordinate z:

$$\begin{aligned} \varepsilon = \begin{Bmatrix} \varepsilon_s \\ \varepsilon_\theta \\ \gamma_{s\theta} \\ \gamma_{\theta z} \\ \gamma_{sz} \end{Bmatrix} &= \begin{Bmatrix} \varepsilon_s^0 \\ \varepsilon_\theta^0 \\ \gamma_{s\theta}^0 \\ \gamma_{\theta z}^0 \\ \gamma_{sz}^0 \end{Bmatrix} + z\begin{Bmatrix} \kappa_s^0 \\ \kappa_\theta^0 \\ \kappa_{s\theta}^0 \\ \kappa_{\theta z}^0 \\ 0 \end{Bmatrix} + z^2\begin{Bmatrix} 0 \\ \kappa_\theta^1 \\ \kappa_{s\theta}^1 \\ \kappa_{\theta z}^1 \\ \kappa_{sz}^1 \end{Bmatrix}\\ &\quad + z^3\begin{Bmatrix} \kappa_s^2 \\ \kappa_\theta^2 \\ \kappa_{s\theta}^2 \\ \kappa_{\theta z}^2 \\ 0 \end{Bmatrix} + z^4\begin{Bmatrix} 0 \\ \kappa_\theta^3 \\ \kappa_{s\theta}^3 \\ 0 \\ 0 \end{Bmatrix}. \end{aligned} \tag{4}$$

The explicit expressions of the strain and curvature terms at middle surface are detailed in Appendix A.

3. Constitutive equations

The constitutive relations for a thin ply k of both orthotropic and piezoelectric material in the shell referential axes, are defined as:

$$\begin{aligned} \boldsymbol{\sigma}^k &= \overline{Q}^k\boldsymbol{\varepsilon} - \overline{e}^kE^k,\\ D^k &= \overline{e}^k\boldsymbol{\varepsilon} + \overline{\xi}^kE^k, \end{aligned} \tag{5}$$

where $\boldsymbol{\sigma}^k = \{\sigma_{ss}\,\sigma_{\theta\theta}\,\sigma_{s\theta}\,\sigma_{\theta z}\,\sigma_{sz}\}^t$, $\boldsymbol{\varepsilon} = \{\varepsilon_{ss}\,\varepsilon_{\theta\theta}\,\varepsilon_{s\theta}\,\varepsilon_{\theta z}\,\varepsilon_{sz}\}^t$, $D^k = \{D_s D_\theta D_z\}^t$ and $E^k = \{E_s E_\theta E_z\}^t$ are the stress, strain, electric displacement and electric field vectors, respectively. $\bar{Q}^k$, $\bar{e}^k$ and $\bar{\xi}^k$ are the elastic stiffness matrix, the piezoelectric stiffness matrix and the dielectric permittivity matrix. The angle between the principal axis of the kth layer and the s axis of the shell referential is α_k. The reduced transformed stiffness matrix coefficients $\bar{Q}_{ij}^k$ in the shell coordinate system are obtained from the material stiffness matrix in lamina coordinate through a fourth-order tensor transformation and are given explicitly in [22]. Eq. (5) can also be presented in a single explicit form, for a generic kth layer, in the shell coordinate system:

$$\begin{Bmatrix} \sigma_{ss} \\ \sigma_{\theta\theta} \\ \tau_{s\theta} \\ \tau_{\theta z} \\ \tau_{sz} \\ \hline D_s \\ D_\theta \\ D_z \end{Bmatrix}^k = \left[\begin{array}{ccccc:ccc} \bar{Q}_{11} & \bar{Q}_{12} & \bar{Q}_{16} & 0 & 0 & 0 & 0 & \bar{e}_{31} \\ \bar{Q}_{12} & \bar{Q}_{22} & \bar{Q}_{26} & 0 & 0 & 0 & 0 & \bar{e}_{32} \\ \bar{Q}_{16} & \bar{Q}_{26} & \bar{Q}_{66} & 0 & 0 & 0 & 0 & \bar{e}_{36} \\ 0 & 0 & 0 & \bar{Q}_{44} & \bar{Q}_{45} & \bar{e}_{14} & \bar{e}_{24} & 0 \\ 0 & 0 & 0 & \bar{Q}_{45} & \bar{Q}_{55} & \bar{e}_{15} & \bar{e}_{25} & 0 \\ \hdashline 0 & 0 & 0 & \bar{e}_{14} & \bar{e}_{15} & \bar{\xi}_{11} & \bar{\xi}_{12} & 0 \\ 0 & 0 & 0 & \bar{e}_{24} & \bar{e}_{25} & \bar{\xi}_{12} & \bar{\xi}_{22} & 0 \\ \bar{e}_{31} & \bar{e}_{32} & \bar{e}_{36} & 0 & 0 & 0 & 0 & \bar{\xi}_{33} \end{array}\right]^k \begin{Bmatrix} \varepsilon_{ss} \\ \varepsilon_{\theta\theta} \\ \gamma_{s\theta} \\ \gamma_{\theta z} \\ \gamma_{sz} \\ \hline E_s^k \\ E_\theta^k \\ E_z^k \end{Bmatrix}. \tag{6}$$

The transformed piezoelectric stiffness and permittivity matrix coefficients are [10]:

$$\begin{aligned}
\bar{e}_{31}^k &= e_{31}^k \cos^2\alpha_k + e_{32}^k \sin^2\alpha_k, \\
\bar{e}_{32}^k &= e_{31}^k \sin^2\alpha_k + e_{32}^k \cos^2\alpha_k, \\
\bar{e}_{36}^k &= \left(e_{31}^k - e_{32}^k\right)\cos\alpha_k \sin\alpha_k, \\
\bar{e}_{14}^k &= \left(e_{15}^k - e_{24}^k\right)\cos\alpha_k \sin\alpha_k, \\
\bar{e}_{24}^k &= e_{24}^k \cos^2\alpha_k + e_{15}^k \sin^2\alpha_k, \\
\bar{e}_{15}^k &= e_{15}^k \cos^2\alpha_k + e_{24}^k \sin^2\alpha_k, \\
\bar{e}_{25}^k &= \left(e_{15}^k - e_{24}^k\right)\cos\alpha_k \sin\alpha_k, \\
\bar{\xi}_{11}^k &= \xi_{11}^k \cos^2\alpha_k + \xi_{22}^k \sin^2\alpha_k, \\
\bar{\xi}_{22}^k &= \xi_{11}^k \sin^2\alpha_k + \xi_{22}^k \cos^2\alpha_k, \\
\bar{\xi}_{12}^k &= \left(\xi_{11}^k - \xi_{22}^k\right)\cos\alpha_k \sin\alpha_k, \\
\bar{\xi}_{33}^k &= \xi_{33}^k.
\end{aligned} \tag{7}$$

The poling direction of the piezoelectric layer is always coincident with the z axis. It is also assumed linear piezoelectricity and the applied and resultant electrical potential are always within the admissible values so that the resultant electrical field does not cause any damage by depoling of the piezoelectric material.

4. Finite element formulation

The structural analysis is carried out using a frustra conical finite element, Fig. 2, with two nodal circles and 24 displacement degrees of freedom. To account for the circumferential dependency, the generalized displacement field is expanded by a Fourier series, in the variable θ, which in a matricial form is expressed as

$$q = \begin{Bmatrix} u_0 \\ v_0 \\ w_0 \\ \beta_s \\ \beta_\theta \end{Bmatrix} = \sum_{n=0}^{NF} \left[\begin{array}{ccccc:ccccc} \cos n\theta & 0 & 0 & 0 & 0 & \sin n\theta & 0 & 0 & 0 & 0 \\ 0 & \sin n\theta & 0 & 0 & 0 & 0 & \cos n\theta & 0 & 0 & 0 \\ 0 & 0 & \cos n\theta & 0 & 0 & 0 & 0 & \sin n\theta & 0 & 0 \\ 0 & 0 & 0 & \cos n\theta & 0 & 0 & 0 & 0 & \sin n\theta & 0 \\ 0 & 0 & 0 & 0 & \sin n\theta & 0 & 0 & 0 & 0 & \cos n\theta \end{array}\right] \begin{Bmatrix} q_n^1 \\ q_n^2 \end{Bmatrix} = \sum_{n=0}^{NF} C_n q_n, \tag{8}$$

where $q_n = \{q_n^1 q_n^2\}^t$ are the symmetric and anti-symmetric terms of Fourier expansion of the generalized displacement field and NF is the number of terms in the truncated series.

The components of the nth term of the Fourier series of the generalized displacement field are related to the nodal degrees of freedom through

$$q_n = \begin{Bmatrix} q_n^1 \\ q_n^2 \end{Bmatrix} = \begin{bmatrix} N & 0 \\ 0 & N \end{bmatrix} \begin{Bmatrix} q_{no_n}^1 \\ q_{no_n}^2 \end{Bmatrix} = N q_{no_n}, \tag{9}$$

where N is the shape function matrix. For the present models, C^1 continuity shape functions of Hermite polynomials [23] and linear Lagrangian shape functions [24], are used for the transversal amplitudes, w_0, and u_0, v_0, β_s, β_θ, respectively. The vector q_{no_n} is the nth term of

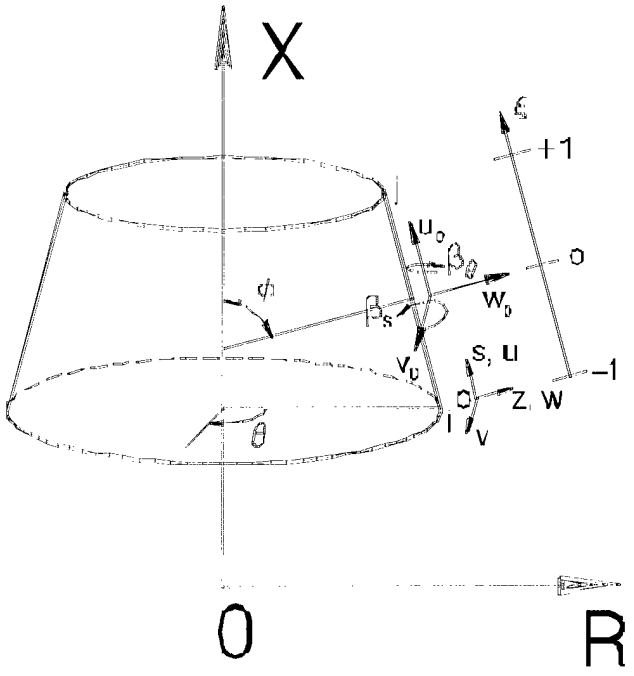

Fig. 2. Conical element and displacement field components.

the Fourier series of the vector of degrees of freedom of the generalized displacements,

$$q_{no_n} = \left\{ \left(u_0^1 v_0^1 w_0^1 \ \frac{\partial w_0^1}{\partial s} \ \beta_s^1 \ \beta_\theta^1 \ u_0^2 \ v_0^2 \ w_0^2 \ \frac{\partial w_0^2}{\partial s} \ \beta_s^2 \ \beta_\theta^2 \right)^i \left(u_0^1 v_0^1 w_0^1 \ \frac{\partial w_0^1}{\partial s} \beta_s^1 \ \beta_\theta^1 \ u_0^2 \ v_0^2 \ w_0^2 \ \frac{\partial w_0^2}{\partial s} \ \beta_s^2 \ \beta_\theta^2 \right)^j \right\}_n^t, \tag{10}$$

where superscripts i, j indicate the element node, and 1,2 are the symmetric and anti-symmetric terms. The electrical potential layerwise assumption implies that in each of the total number of layers NL, the electric potential scalar field is represented by an independent function ϕ_i. Thus the electrical potential vector whose components are the NL functions, can be expressed similarly as

$$\phi = \begin{Bmatrix} \phi_1 \\ \vdots \\ \phi_{NL} \end{Bmatrix} = \sum_{n=0}^{NF} \left[\begin{array}{ccc|ccc} \cos n\theta & \cdots & 0 & \sin n\theta & \cdots & 0 \\ \vdots & \ddots & \vdots & \vdots & \ddots & \vdots \\ 0 & \cdots & \cos n\theta & 0 & \cdots & \sin n\theta \end{array} \right] \begin{Bmatrix} \phi_1^1 \\ \vdots \\ \phi_{NL}^1 \\ \phi_1^2 \\ \vdots \\ \phi_{NL}^2 \end{Bmatrix} = \sum_{n=0}^{NF} C_n^{\phi} \phi_n, \tag{11}$$

where $\phi_n = \{\phi_n^1 \phi_n^2\}^t$ are the symmetric and anti-symmetric terms of Fourier expansion of the electrical potential. In the case of non-piezoelectric layers it is considered that there does not exist a electrical potential function for that layer.

The electric field components are related to the electrostatic potential ϕ through the relation:

$$E = \{E_r \quad E_\theta \quad E_z\}^t = -\nabla\phi \tag{12}$$

taking into account that the poling direction is always along the z axis,

$$E = \{0 \quad 0 \quad E_z\}^t = -\left\{0 \quad 0 \quad \frac{\partial\phi}{\partial z}\right\}^t. \tag{13}$$

In the present work, layerwise laminate theories [5–7] are employed to model the electric potential variation through the thickness of the piezoelectric layers.

This work considers the possibility of modeling linearly or parabolically the electrical potential distribution through the ply thickness.

4.1. Linear variation of potential

For each of the piezoelectric layers the potential is assumed to vary linearly, and the potential value represents the potential differential variation through the layer thickness. Thus the derivative term of expression (13) is replaced by the ratio $\partial\phi/\partial z \approx \Delta\phi/h_k$.

The electrical field in the kth piezo layer is then given by

$$E_z^k = -\frac{1}{h_k}\phi_k. \tag{14}$$

To allow the distribution of the electrical potentials along the longitudinal axis of the element, pseudo nodes located at the edges of each kth layer are considered, Fig. 3.

The Fourier series expansion of the electrical potential is now given by

$$\phi^k = \sum_{n=0}^{NF} \theta_n^{\phi} N_s \phi_n^k \tag{15}$$

with:

$$\theta_n^{\phi} = [\cos n\theta \quad \sin n\theta], \qquad N_s = \begin{bmatrix} L_1 & 0 & L_2 & 0 \\ 0 & L_1 & 0 & L_2 \end{bmatrix}, \tag{16}$$

where L_1 and L_2 are linear Lagrangian shape functions [24] and the electrical potential nodal values (symmetric and anti-symmetric terms) are:

$$\phi_n^k = \left\{ \left(\phi_1^k \quad \phi_2^k\right)^i \quad \left(\phi_1^k \quad \phi_2^k\right)^j \right\}_n^t, \tag{17}$$

where the superscripts k, i, j indicate the kth layer and the pseudo nodes respectively and the subscript the nth harmonic.

The electrical field obtained from Eq. (15), for a generic kth piezo layer is

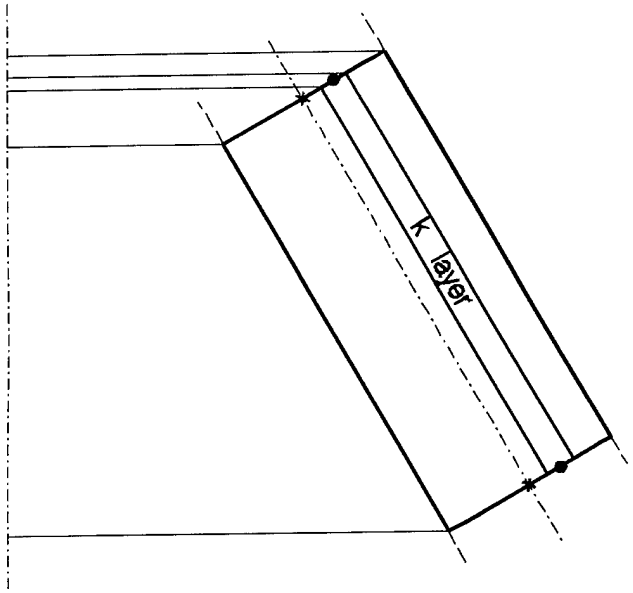

Fig. 3. S2P2 element with indication of the two displacement nodes (×) and of the two pseudo nodes (•) for lamina k .

$$E_z^k = -\frac{1}{h_k}\sum_{n=0}^{\mathrm{NH}} \boldsymbol{\theta}_n^{\phi} N_s \boldsymbol{\phi}_n^k = \sum_{n=0}^{\mathrm{NH}} \boldsymbol{\theta}_n^{\phi} B_k^{\phi} \boldsymbol{\phi}_n^k. \tag{18}$$

The number of electrical potential degrees of freedom, for this element is $4\times\mathrm{NL}$, and the total number of degrees of freedom is $24+4\times\mathrm{NL}$ (element S2P2).

4.2. Quadratic variation of potential

In order to model a quadratic variation of potential through the layer thickness three electrical potential values are needed for each piezoelectric layer, $\boldsymbol{\phi}_z^k = \left\{\phi_b^k \quad \phi_m^k \quad \phi_u^k\right\}^{\mathrm{t}}$ corresponding to the bottom, middle and upper face of the layer, Fig. 4.

Hence the electrical potential within a piezoelectric layer is

$$\boldsymbol{\phi}^k = H_{\phi}^k \boldsymbol{\phi}_z^k, \qquad H_{\phi}^k = \left[H_1^k \quad H_2^k \quad H_3^k\right], \tag{19}$$

where H_i^k are the quadratic interpolation functions

$$H_1^k = \frac{2}{h_k^2}z^2 - \frac{z_k^i + 3z_k^s}{h_k^2}z + \frac{z_k^s\left(z_k^i + z_k^s\right)}{h_k^2},$$
$$H_2^k = -\frac{4}{h_k^2}z^2 + \frac{4\left(z_k^i + z_k^s\right)}{h_k^2}z - \frac{4z_k^i z_k^s}{h_k^2}, \tag{20}$$
$$H_3^k = \frac{2}{h_k^2}z^2 - \frac{3z_k^i + z_k^s}{h_k^2}z + \frac{z_k^i\left(z_k^i + z_k^s\right)}{h_k^2}$$

and z^i and z^s are the z coordinate of the bottom and upper face and h_k is the layer thickness.

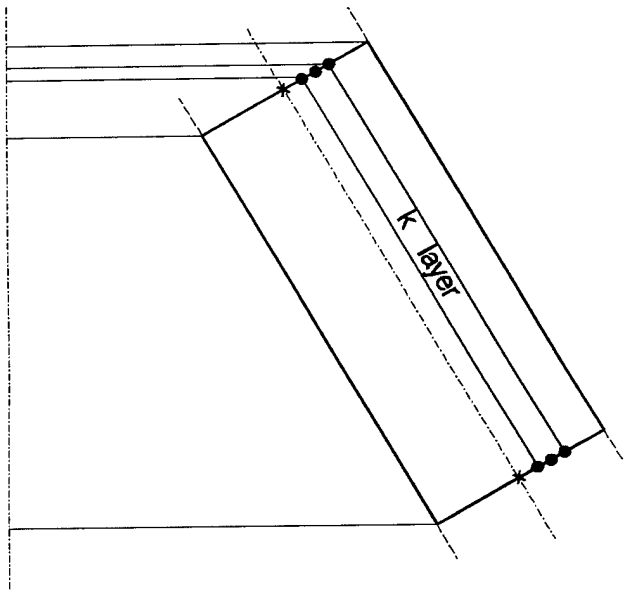

Fig. 4. S2P6 element with with indication of the two displacement nodes (×) and of the six pseudo nodes (•) for lamina k.

From Eq. (13), the electrical field is

$$E_z^k = -\frac{\partial}{\partial z}H_{\phi}^k \boldsymbol{\phi}_z^k = \left(L_k^{e\phi} + zL_k^{0\phi}\right)\phi_z^k, \tag{21}$$

where

$$L_k^{0\phi} = \frac{1}{h_k^2}\left[4 \quad -8 \quad 4\right],$$
$$L_k^{e\phi} = \frac{1}{h_k^2}\left[-z_k^i - 3z_k^s \quad 4z_k^i + 4z_k^s \quad -3z_k^i - z_k^s\right]. \tag{22}$$

Considering that the electrical potential can vary linearly along the element and quadratically across the thickness, the electrical potential in a generic kth piezo layer is given by

$$\boldsymbol{\phi}^k = \sum_{n=0}^{NF} \boldsymbol{\theta}_n^{\phi} N_s N_{\phi}^k \boldsymbol{\phi}_n^k, \tag{23}$$

where N_s is the shape function matrix defined in (16),

$$\mathrm{N}_{\phi}^k = \left[\begin{array}{cccccc|cccccc} \mathrm{H}_1^k & 0 & \mathrm{H}_2^k & 0 & \mathrm{H}_3^k & 0 & 0 & 0 & 0 & 0 & 0 & 0 \\ 0 & \mathrm{H}_1^k & 0 & \mathrm{H}_2^k & 0 & \mathrm{H}_3^k & 0 & 0 & 0 & 0 & 0 & 0 \\ \hline 0 & 0 & 0 & 0 & 0 & 0 & \mathrm{H}_1^k & 0 & \mathrm{H}_2^k & 0 & \mathrm{H}_3^k & 0 \\ 0 & 0 & 0 & 0 & 0 & 0 & 0 & \mathrm{H}_1^k & 0 & \mathrm{H}_2^k & 0 & \mathrm{H}_3^k \end{array}\right] \tag{24}$$

$$\boldsymbol{\phi}_n^k = \left\{\left(\phi_1^b \quad \phi_2^b \quad \phi_1^m \quad \phi_2^m \quad \phi_1^u \quad \phi_2^u\right)^i \left(\phi_1^b \quad \phi_2^b \quad \phi_1^m \quad \phi_2^m \quad \phi_1^u \quad \phi_2^u\right)^j\right\}_n^{\mathrm{t}} \tag{25}$$

and $\boldsymbol{\phi}_n^k$ is the vector for the nth term of the Fourier series of the electrical potential degrees of freedom at locations in the bottom, middle and upper surfaces at both edges of a generic kth piezo layer for an element.

The number of electrical potential degrees of freedom, for this element is therefore $2\times(2+4\times\mathrm{NL})$, and the total number of degrees of freedom is $24+2\times(2+4\times\mathrm{NL})$, (element S2P6).

The electrical field for a generic kth piezo layer is obtained from Eqs. (21), (23) and (24), yielding:

$$E_z^k = \sum_{n=0}^{NH} \boldsymbol{\theta}_n^{\phi} N_s \left(B_k^{e\phi} + zB_k^{0\phi}\right)\boldsymbol{\phi}_n^k, \tag{26}$$

where

$$\mathrm{B}_k^{\phi} = \frac{1}{\mathrm{h}_k^2}\left[\begin{array}{cccccc|cccccc} \mathrm{B}_1^{\phi k} & 0 & \mathrm{B}_2^{\phi k} & 0 & \mathrm{B}_3^{\phi k} & 0 & 0 & 0 & 0 & 0 & 0 & 0 \\ 0 & \mathrm{B}_1^{\phi k} & 0 & \mathrm{B}_2^{\phi k} & 0 & \mathrm{B}_3^{\phi k} & 0 & 0 & 0 & 0 & 0 & 0 \\ \hline 0 & 0 & 0 & 0 & 0 & 0 & \mathrm{B}_1^{\phi k} & 0 & \mathrm{B}_2^{\phi k} & 0 & \mathrm{B}_3^{\phi k} & 0 \\ 0 & 0 & 0 & 0 & 0 & 0 & 0 & \mathrm{B}_1^{\phi k} & 0 & \mathrm{B}_2^{\phi k} & 0 & \mathrm{B}_3^{\phi k} \end{array}\right] \tag{27}$$

with

$$B_1^{\phi k} = z_i + 3z_s,$$
$$B_2^{\phi k} = -4z_i + 4z_s, \tag{28}$$
$$B_3^{\phi k} = 3z_i + z_s$$

and

$$\mathbf{B}_k^{0\phi} = \frac{1}{h_k^2}\left[\begin{array}{cccccc|cccccc} 4 & 0 & -8 & 0 & 4 & 0 & 0 & 0 & 0 & 0 & 0 & 0 \\ 0 & 4 & 0 & -8 & 0 & 4 & 0 & 0 & 0 & 0 & 0 & 0 \\ \hline 0 & 0 & 0 & 0 & 0 & 0 & 4 & 0 & -8 & 0 & 4 & 0 \\ 0 & 0 & 0 & 0 & 0 & 0 & 0 & 4 & 0 & -8 & 0 & 4 \end{array}\right]. \tag{29}$$

From the expressions of the generalized displacement field and of the strain–displacement relations, one obtains the expressions of the strains and the associated curvatures at the middle surface, given by

$$\left\{\begin{array}{c} \varepsilon_s^0 \\ \varepsilon_\theta^0 \\ \gamma_{s\theta}^0 \end{array}\right\} = \varepsilon^0 = 0_n B_e^* q_{no_n}$$

$$\left\{\begin{array}{c} \kappa_s^p \\ \kappa_\theta^p \\ \kappa_{s\theta}^p \end{array}\right\} = \kappa^p = 0_n B_B^{p^*} q_{no_n} \qquad \text{with } p = 0, \ldots, 3. \tag{30}$$

and also for the shear transverse strains:

$$\left\{\begin{array}{c} \gamma_{\theta z}^0 \\ \gamma_{sz}^0 \end{array}\right\} = \gamma^0 = 0_n^s B_{cS}^* q_{no_n}$$

$$\left\{\begin{array}{c} \kappa_{\theta z}^q \\ \kappa_{sz}^q \end{array}\right\} = \kappa_S^q = \boldsymbol{\theta}_n^S B_S^{q^*} q_{no_n} \qquad \text{with } q = 0, \ldots, 2. \tag{31}$$

Matrices $\boldsymbol{\theta}_n, \boldsymbol{\theta}_n^S, B_e^*, B_B^{p^*}, B_{cS}^*$ and $B_S^{q^*}$ are described in [20,18].

In order to obtain the governing equations for the element Hamilton's variational principle is used. The Lagragian function is

$$L = T - H + W, \tag{32}$$

where T, H and W are the kinetic energy, the electric enthalpy and the work of external applied force, given for a generic element e as

$$T(\dot{u}) = \frac{1}{2}\sum_{k=1}^{NL}\int_{V_k} \rho_k \dot{u}\dot{u}\, \mathrm{d}V, \tag{33}$$

$$H(\varepsilon, E) = \sum_{k=1}^{NL}\int_{V_k}\left(\frac{1}{2}\boldsymbol{\varepsilon}^t \overline{Q}_k \boldsymbol{\varepsilon} - \boldsymbol{\varepsilon}^t \overline{e}_k E_k - \frac{1}{2}E_k^t \overline{\xi}_k E_k\right)\mathrm{d}V, \tag{34}$$

$$W(u,p) = \int_S u^t p\, \mathrm{d}S, \tag{35}$$

where u and p are, respectively, the element displacement field and the surface-forces vectors, V is the volume of the element and S is the surface under applied loads.

The coupling effect between the electrical potential and the mechanical deformation fields in a piezoelectric laminated shell with the poling direction aligned with the z axis is only due to the in-plane shear action. This is due to the fact that the only non-zero component of the electrical field is along the z axis, and because of the sparse nature of the piezoelectric stiffness matrix, the product $\boldsymbol{\varepsilon}^t \overline{e}_k E_k$, from Eq. (34), is simplified to

$$\boldsymbol{\varepsilon}^t \overline{e}_k E_k = \varepsilon_{ss}\overline{e}_{13}^k E_z^k + \varepsilon_{00}\overline{e}_{23}^k E_z^k + \gamma_{s\theta}\overline{e}_{63}^k E_z^k. \tag{36}$$

From Eq. (36) it is noticeable that only the in-plane components of the strain field contribute to the electrical mechanical coupling.

In a similar way, the product $E_k^t \overline{\xi}_k E_k$, from Eq. (34), is

$$E_k^t \overline{\xi}_k E_k = E_z^{k^t}\overline{\xi}_{33}^k E_z^k. \tag{37}$$

The equations of motion are deduced by carrying out the variational process

$$\delta\int_{t_1}^{t_2} L\, \mathrm{d}t = \delta\int_{t_1}^{t_2}(T - H + W)\, \mathrm{d}t = 0. \tag{38}$$

Substituting in Eq. (32), the expressions (33)–(35) and considering that the displacement, strain and electrical fields are expanded in Fourier series of the n terms nodal values and bearing in mind the orthogonal condition of the trigonometric functions in the interval $[0,2\pi]$, the finite element equations get uncoupled in harmonics, and one obtains, from Eq. (38), a set of NF independent equations, which written in a compact form are

$$\left[\begin{array}{cc} M_{uu}^e & 0 \\ 0 & 0 \end{array}\right]_n \left\{\begin{array}{c} \ddot{q} \\ \ddot{\phi} \end{array}\right\}_n + \left[\begin{array}{cc} K_{uu}^e & K_{u\phi}^e \\ K_{\phi u}^e & K_{\phi\phi}^e \end{array}\right]_n \left\{\begin{array}{c} q \\ \phi \end{array}\right\}_n = \left\{\begin{array}{c} F^e \\ 0 \end{array}\right\}_n. \tag{39}$$

The quantities M_{uu}^e and K_{uu}^e are the mass and stiffness matrices commonly used in structural analysis, which have been deduced in [18,20], $K_{\phi u}^{e^t} = K_{u\phi}^e$ is the electrical mechanical coupled stiffness matrix, $K_{\phi\phi}^e$ is the electrical stiffness matrix and F^e is the force vector for element e.

The electrical coupled stiffness matrix and the electrical stiffness matrix for the nth term of the Fourier series, are for both models, given by the following.

4.3. Electrical mechanical coupled and electrical stiffness matrices—Linear variation of potential

$$\begin{aligned} K_{u\phi}^e &= K_{\phi u}^{e^t} \\ &= \sum_{k=1}^{NL}\int_0^{2\pi}\int_{-1}^{1}\int_{z_i}^{z_s} T_c^t\Big[B_e^{*t}\boldsymbol{\theta}_n^{Bt}\overline{e}_k\boldsymbol{\theta}_n^{B\phi}B_k^\phi \\ &\quad + zB_B^{0*t}\boldsymbol{\theta}_n^{Bt}\overline{e}_k\boldsymbol{\theta}_n^{B\phi}B_k^\phi + z^2 B_B^{1*t}\boldsymbol{\theta}_n^{Bt}\overline{e}_k\boldsymbol{\theta}_n^{B\phi}B_k^\phi \\ &\quad + z^3 B_B^{2*t}\boldsymbol{\theta}_n^{Bt}\overline{e}_k\boldsymbol{\theta}_n^{B\phi}B_k^\phi \\ &\quad + z^4 B_B^{3*t}\boldsymbol{\theta}_n^{Bt}\overline{e}_k\boldsymbol{\theta}_n^{B\phi}B_k^\phi\Big]\, \det J\, \mathrm{d}z\, \mathrm{d}\zeta\, \mathrm{d}\theta, \end{aligned} \tag{40}$$

$$K^e_{\phi\phi} = \sum_k^{NL} \int_0^{2\pi} \int_{-1}^{1} \int_{z_i}^{z_s} \left[B_k^{\phi^t} \theta_n^{B\phi^t} \bar{\xi}_k \theta_n^{B\phi} B_k^{\phi} \right] \det J \, dz \, d\zeta \, d\theta. \tag{41}$$

4.4. Electrical mechanical coupled and electrical stiffness matrices—Quadratic variation of potential

$$\begin{aligned} K_{u\phi} &= K^t_{\phi u} \\ &= \sum_{k=1}^{NL} \int_0^{2\pi} \int_{-1}^{1} \int_{z_i}^{z_s} T_c^t \Big[B_e^{*t} \theta_n^{Bt} \bar{e}_k \theta_n^{B\phi} N_s B_k^{e\phi} \\ &\quad + z B_B^{0*t} \theta_n^{Bt} \bar{e}_k \theta_n^{B\phi} N_s B_k^{e\phi} + z^2 B_B^{1*t} \theta_n^{Bt} \bar{e}_k \theta_n^{B\phi} N_s B_k^{e\phi} \\ &\quad + z^3 B_B^{2*t} \theta_n^{Bt} \bar{e}_k \theta_n^{B\phi} N_s B_k^{e\phi} + z^4 B_B^{3*t} \theta_n^{Bt} \bar{e}_k \theta_n^{B\phi} N_s B_k^{e\phi} \\ &\quad + z B_e^{*t} \theta_n^{Bt} \bar{e}_k \theta_n^{B\phi} N_s B_k^{0\phi} + z^2 B_B^{0*t} \theta_n^{Bt} \bar{e}_k \theta_n^{B\phi} N_s B_k^{0\phi} \\ &\quad + z^3 B_B^{1*t} \theta_n^{Bt} \bar{e}_k \theta_n^{B\phi} N_s B_k^{0\phi} + z^4 B_B^{2*t} \theta_n^{Bt} \bar{e}_k \theta_n^{B\phi} N_s B_k^{0\phi} \\ &\quad + z^5 B_B^{3*t} \theta_n^{Bt} \bar{e}_k \theta_n^{B\phi} N_s B_k^{0\phi} \Big] \det J \, dz \, d\zeta \, d\theta, \end{aligned} \tag{42}$$

$$\begin{aligned} K^e_{\phi\phi} = \sum_{k=1}^{NL} \int_0^{2\pi} \int_{-1}^{1} \int_{z_i}^{z_s} & \Big[B_k^{e\phi^t} N_s^t \theta_n^{B\phi^t} \bar{\xi}_k \theta_n^{B\phi} N_s B_k^{e\phi} \\ & + z B_k^{e\phi^t} N_s^t \theta_n^{B\phi^t} \bar{\xi}_k \theta_n^{B\phi} N_s B_k^{0\phi} \\ & + z B_k^{0\phi^t} N_s^t \theta_n^{B\phi^t} \bar{\xi}_k \theta_n^{B\phi} N_s B_k^{e\phi} \\ & + z^2 B_k^{0\phi^t} N_s^t \theta_n^{B\phi^t} \bar{\xi}_k \theta_n^{B\phi} N_s B_k^{0\phi} \Big] \det J \, dz \, d\zeta \, d\theta, \end{aligned} \tag{43}$$

where T_c is the coordinate transformation matrix, which relates the nodal displacements of the element expressed in the local coordinate system (element) to the shell coordinate system (global), ζ is the longitudinal normalized integration variable and the Jacobian is:

$$J = R_{lam} \left(1 + \frac{z}{R_{lam}} \right) \frac{l_e}{2}. \tag{44}$$

The element length and the mean radius of each layer are l_e and R_{lam}, respectively. The integration is carried out analytically in the circumferential coordinate taking into account the orthogonality properties of the trigonometric functions and also along the z coordinate and for the longitudinal direction, numerical integration with two Gauss points is used. When integrating through the thickness of the shell, any layer that is not a piezoelectric material does not contribute to the coupling nor to the electrical stiffness matrices, and the corresponding electrical potential values are not considered.

The equations of motion for the nth term of the Fourier series expansion of the discretized structure are obtained from the element equation (39) using the standard assembly techniques, yielding

$$\begin{aligned} &\begin{bmatrix} M^{\Omega}_{uu} & 0 \\ 0 & 0 \end{bmatrix} \begin{Bmatrix} \ddot{d} \\ \ddot{V}^S \end{Bmatrix} + \begin{bmatrix} K^{\Omega}_{uu} & K^{\Omega}_{u\phi} \\ K^{\Omega}_{u\phi} & K^{\Omega}_{\phi\phi} \end{bmatrix} \begin{Bmatrix} d \\ V^S \end{Bmatrix} \\ &= \begin{Bmatrix} F^{\Omega} - K^{\Omega}_{u\phi} V^A \\ -K^{\Omega}_{\phi\phi} V^A \end{Bmatrix}, \end{aligned} \tag{45}$$

where d are the system displacement degrees of freedom and V^A, V^S are the values of the applied and sensory electrical potential.

Uncoupling Eq. (45), a new set of independent equations is obtained

$$\begin{aligned} &M^{\Omega}_{uu} \ddot{d} + \left(K^{\Omega}_{uu} - K^{\Omega}_{u\phi} K^{\Omega^{-1}}_{\phi\phi} K^{\Omega}_{\phi u} \right) d \\ &\quad = F^{\Omega} + \left(K^{\Omega}_{u\phi} K^{\Omega^{-1}}_{\phi\phi} K^{\Omega}_{\phi\phi} - K^{\Omega}_{u\phi} \right) V^A, \\ &V^S = -K^{\Omega^{-1}}_{\phi\phi} \left(K^{\Omega}_{u\phi} d + K^{\Omega}_{\phi\phi} V^A \right). \end{aligned} \tag{46}$$

From these equations, it is possible to obtain the sensory electrical potential values of either the modal characteristics (free vibration) or the forced vibration response of the structure for the nth harmonic, once the boundary conditions are introduced.

5. Numerical applications

5.1. Cylindrical shell with outside surface-bonded ring piezoactuators

In this example, the static response of a composite cylindrical thin shell with piezoelectric rings perfectly bounded to the outside surface, all around the shell, Fig. 5, is studied. The cylinder is a simply supported laminated shell, with ply orientation $[0°/\pm 45°]_s$ and the following geometric data: length $L = 2.2$ m, radius $R_0 = 65$ mm, total thickness $h_s = 2.0$ mm. The actuator rings have a thickness $h_p = 0.2$ mm and a length of 2×50.0 mm for the symmetric case and 2×100.0 mm for the anti-symmetric case. The material properties are: for the composite layers (T300/976): $E_1 = 65.0$ GPa, $E_2 = 9.0$ GPa, $\nu_{12} = 0.3, G_{12} = G_{23} = G_{23} = 7.1$ GPa and for the piezoceramic (G1195N): $E_1 = E_2 = 63.0$ GPa, $\nu_{12} = 0.3, G_{12} = G_{23} = G_{23} = 24.2$ GPa, piezoelectric coefficients $e_{31} = 22.86$ C m^{-2}, $e_{32} = 17.58$ C m^{-2} (obtained by the relation $e^k = Q^k d^k$ using the piezoelectric strain coefficients $d_{31} = d_{32} = 254$ pm V^{-1}) and the electrical permittivity $\xi_{33} = 15.0$ nF m^{-1}. A discretization with 30 elements is used. Two different cases are analysed:

(a) symmetric actuation, where both actuator rings are subject to an applied electrical potential differential $\Delta V = 100$ V,

(b) anti-symmetric actuation in which the electrical potential differential applied to the actuators has opposite signs, $\Delta V = \pm 100$ V.

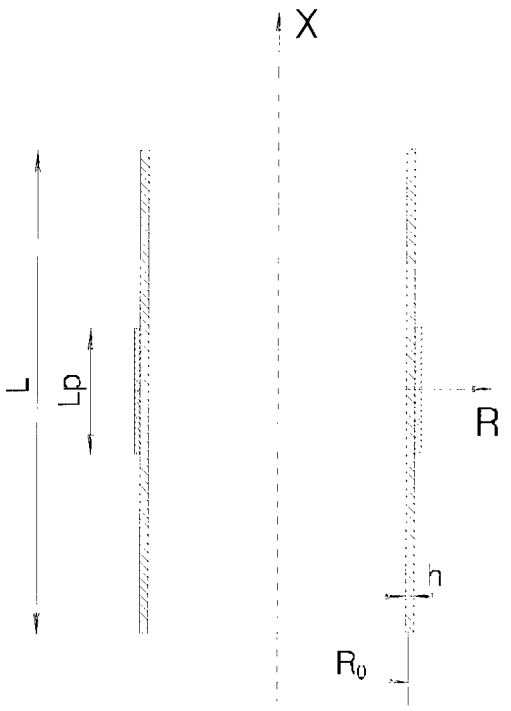

Fig. 5. Laminated cylinder with two equal size outside surface-bonded ring piezoactuators.

The value of the radial displacement for the case of an infinitely long cylinder with an actuator also infinitely long spanning over all the length of the shell and subject to an applied electrical potential differential of $\Delta V = 100$ V is used as a reference value to normalize the radial displacement. Figs. 6 and 7 show the normalized radial displacement distribution and since the curves are symmetric and anti-symmetric with respect to the middle of the cylinder, only one half is represented. The radial displacement distributions versus the axial coordinate are compared with Faria et al. [15], using a finite element model and a close form

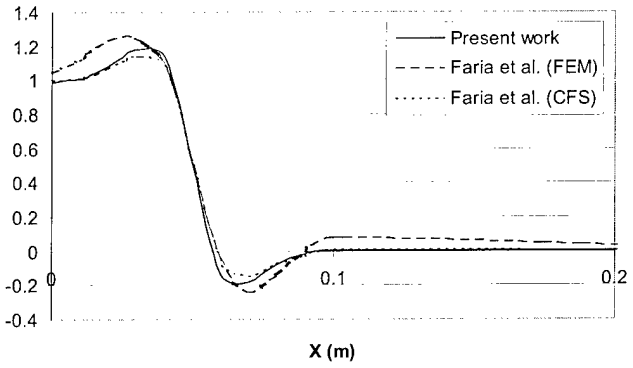

Fig. 6. Normalized radial displacement versus axial coordinate, for symmetric actuation with two 50 mm long actuators ($Lp = 2 \times 50$ mm).

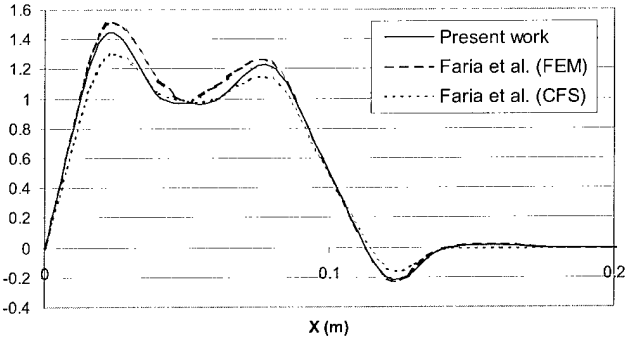

Fig. 7. Normalized radial displacement versus axial coordinate, for anti-symmetric actuation with two 100 mm long actuators ($Lp = 2 \times 100$ mm).

solution based on Love–Kirchhoff theory. The values obtained with the present model are in good agreement with the two alternative solutions [15]. Concerning the type of electrical potential distribution employed (linear or quadratic), both models were used without any difference being noticed, due to the fact that the electrical potential in this example is a constant imposed value.

5.2. Cylinder of PVDF subject to uniform pressure on its outer surface

The cylinder has a length to radius ratio $L/R = 4$ and a radius-to-thickness ratios, $S = R/h$ of 6, 10 and 100. Material properties for the polyvinyledene fluoride (PVDF) are: $E_1 = E_2 = E_3 = 2.0$ GPa, $\nu_{12} = \nu 12 = \nu_{12} = 1/3$, $e_{31} = 2.25 \times 10^{-3}$ C m^{-2}, $e_{32} = 1.725 \times 10^{-3}$ C m^{-2}, $e_{63} = -2.25 \times 10^{-2}$ C m^{-2} ($d_1 = -30 \times 10^{-12}$ C N^{-1}, $d_2 = 23 \times 10^{-12}$ C N^{-1}, $d_3 = 3 \times 10^{-12}$ C N^{-1}), $\varepsilon_1 = \varepsilon_2 = 0.3141 \times 10^{-10}$ F m^{-1} and $\varepsilon_3 = 0.3078 \times 10^{-10}$ F m^{-1}. The boundary displacement conditions are $w(x = 0, L) = 0$ and $u(x = L/2) = 0$. At the edges of the cylindrical shell, as well, on its inner and outer surface the electrical potential is held at 0 value. The load is a uniform unitary radial pressure p_0 applied on the outer surface. A discretization with forty elements is used. The axial and radial displacements are calculated at one edge of the cylinder $u(x = 0)$ and at half length $w(x = L/2)$. The electrical potential is calculated at a distance $0.025 \times L$ from the edge, $\phi(x = 0.025L)$. Table 1 shows the normalized results of the present model which are compared with a three-dimensional elasticity solution obtained by Kapuria et al. [14]. In this example, the model S2P6, is able to satisfy the electrical potential boundary conditions of zero potential at the inner and outer surfaces simultaneously. A maximum discrepancy of 5% and 1.7% for the axial and radial displacement and 1.6% for the electrical potential was found for the $S = 10$ radius-to-thickness ratio cylinder.

Table 1
Effect of radius-to-thickness ratio on the normalized values of the radial and axial displacements and electrical potential $\left(\overline{u}=\frac{uE_T}{S^2hp_0}, \overline{w}=\frac{wE_T}{S^2hp_0}, \overline{\phi}=1000\frac{\phi d_I E_T}{Rp_0}\right)$

	Present work (S2P6)	Kapuria et al. [14]	Present work (S2P6)	Kapuria et al. [14]	Present work (S2P6)	Kapuria et al. [14]
$S=R/h$	6	6	10	10	100	100
$\overline{u}(x=0)$	0.6755	0.7336	0.6615	0.6962	0.6563	0.6604
$\overline{w}(x=L/2)$	1.08213	1.04985	1.0508	1.0326	1.005	1.0034
$\phi(x=0.025L)$	−0.41887	−0.2437	−0.4806	−0.4733	−0.01011	−0.01184

5.3. *Laminated cylindrical shell subjected to hydrostatic pressure*

A typical illustrative case of a four-layer cylindrical shell with both edges clamped, Fig. 8, has the following geometric properties: $D=0.1905$ m (diameter), $L=0.381$ m (length) and $h_T=0.00051$ m (overall thickness). The shell is made of a core-resistant three layer composite, $h=3\times0.0001667$ m and of an outer piezoelectric layer, $h=0.00001$ m, used as an integrated sensor. The material properties for the composite passive layers are: $E_1=206.9$ GPa, $E_2=E_3=18.62$ GPa, $G_{12}=G_{13}=G_{23}=4.48$ GPa and $\nu_{12}=\nu_{13}=\nu_{23}=0.28$ with ply orientation: [60°/0°/60°] and for the piezoelectric layer: $E_1=E_2=E_3=63.0$ GPa, $\nu_{12}=\nu_{13}=\nu_{23}=0.3$, piezoelectric coefficients $e_{31}=22.86$ C m^{-2}, $e_{32}=17.56$ C m^2 and the electrical permittivity $\xi_{33}=15.0$ nF m^{-1}. The cylindrical shell is under the action of an internal surface load: $p(\theta)=p_0(1+\cos\theta)$, with: $p_0=1000$ N m^{-2}. A finite element model with 25 ring elements of equal length is used.

Both models (S2P2 and S2P6) are used to study the sensory behavior. Table 2 shows electrical potential differentials registered between the outer and the inner faces of the piezoelectric layer for both models. The effect of coupling between the symmetric and anti-symmetric terms of the electrical potential is shown in Table 3. The maximum deviation is only 0.9%, due to the small magnitude of the piezoelectric contribution to the displacements field. This deviation is a much smaller value when compared with the radial displacement deviation that was recorded by Pinto Correia et al. [18] for the same core resistant laminated, where a maximum deviation of about 45% was found.

Table 2
Electrical potential differential distribution for a laminated cylinder subjected to hydrostatic pressure

X (m)	$\Delta\phi$ (V) (linear distribution element S2P2)	$\Delta\phi$ (V) (quadratic distribution element S2P6)
0	0.10838	0.10840
0.01524	−0.05054	−0.05054
0.03048	−0.12797	−0.12797
0.04572	−0.09256	−0.09260
0.06096	−0.11794	−0.11790
0.0762	−0.11321	−0.11321
0.09144	−0.12006	−0.12007
0.10668	−0.12164	−0.12160
0.12192	−0.12455	−0.12456
0.13716	−0.12630	−0.12630
0.1524	−0.12782	−0.12780
0.16764	−0.12876	−0.12880
0.18288	−0.12926	−0.12926
0.19812	−0.12926	−0.12926
0.21336	−0.12877	−0.12882
0.2286	−0.12783	−0.12783
0.24384	−0.12632	−0.12632
0.25908	−0.12457	−0.12459
0.27432	−0.12167	−0.12170
0.28956	−0.12008	−0.12008
0.3048	−0.11327	−0.11327
0.32004	−0.11795	−0.11791
0.33528	−0.09263	−0.09259
0.35052	−0.12848	−0.12848
0.36576	−0.05078	−0.05077
0.381	0.10863	0.10870

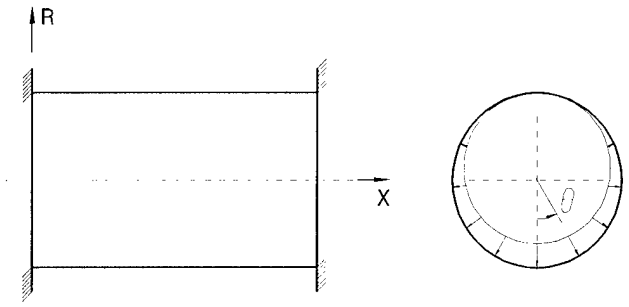

Fig. 8. Clamped laminated cylindrical shell subjected to an internal hydrostatic pressure.

6. Conclusions

Two axisymmetric finite element models based on a mixed laminated theory for the analysis of laminated shell with embedded and/or surface-bonded piezoelectric layer actuators and/or sensors have been developed. A high-order shear deformation model has been used in the displacement field with the condition of zero transverse shear stresses at the bottom and top surfaces of the

Table 3
Electrical potential differential distribution for a laminated cylinder subjected to hydrostatic pressure (quadratic distribution – element S2P6)

x (m)	$\Delta\phi^{*}$ (V)	$\Delta\phi^{**}$ (V)	Relative deviation (%)
0	0.10830	0.10840	0.1
0.01524	−0.05010	−0.05054	0.9
0.03048	−0.12725	−0.12797	0.6
0.04572	−0.09230	−0.09260	0.3
0.06096	−0.11750	−0.11790	0.3
0.0762	−0.11280	−0.11321	0.4
0.09144	−0.11970	−0.12007	0.3
0.10668	−0.12120	−0.12160	0.3
0.12192	−0.12410	−0.12456	0.4
0.13716	−0.12592	−0.12630	0.3
0.1524	−0.12740	−0.12780	0.3
0.16764	−0.12830	−0.12880	0.4
0.18288	−0.12880	−0.12926	0.4
0.19812	−0.12887	−0.12926	0.3
0.21336	−0.12840	−0.12882	0.3
0.2286	−0.12740	−0.12783	0.3
0.24384	−0.12594	−0.12632	0.3
0.25908	−0.12420	−0.12459	0.3
0.27432	−0.12130	−0.12170	0.3
0.28956	−0.11970	−0.12008	0.3
0.3048	−0.11287	−0.11327	0.4
0.32004	−0.11750	−0.11791	0.3
0.33528	−0.09230	−0.09259	0.3
0.35052	−0.12776	−0.12848	0.6
0.36576	−0.05030	−0.05077	0.9
0.381	0.10850	0.10870	0.2

* Coupling disregarded.
** Coupling allowed for:

$$\text{Relative deviation} = \frac{\Delta\phi^{*} - \Delta\phi^{**}}{\Delta\phi^{**}} \times 100.$$

shell, which avoids the need of shear correction factors. To account for the dependence in the circumferencial coordinate the generalized displacement field components and electrical potential are expanded in Fourier series considering both the symmetric and anti-symmetric terms. The coupling effect between the symmetric and anti-symmetric terms of the Fourier expansion of the electrical potential is analyzed in this work. The importance of this effect has already been shown [16–18] for the displacements field in laminated axisymmetric anisotropic shells. In the present work it is shown that this effect also exist in the case of the electrical potential field, although with a much reduced magnitude when compared to the displacement coupling effect, which for the illustrative example of a laminated cylindrical shell subjected to hydrostatic pressure is about 45%. Two different models, concerning the type of electrical distribution across the thickness, are presented: one linear (S2P2) and the other quadratic (S2P6). The main advantage of the S2P2 model is its finite element formulation simplicity when compared to S2P6 model, the number of pseudo nodes (related to the electrical potential) of the first model is less than half the number of pseudo nodes of S2P6. One of the advantages of the more refined quadratic distribution is the its wider possibility to satisfy boundary conditions, such as zero electrical potential at the bottom and upper face of a piezoelectric layer.

Acknowledgements

The authors wish to thank FCT, Fundacão para a Ciência e Tecnologia, Project PRAXIS/P/EME/12028/1998 and FCT/ICTI(Portugal)/CNPQ(Brazil) for the financial support.

Appendix A

The strain and curvature terms at the middle surface are as follow:

$$\begin{Bmatrix} \varepsilon_s^0 \\ \varepsilon_\theta^0 \\ \gamma_{s\theta}^0 \\ \gamma_{\theta z}^0 \\ \gamma_{sz}^0 \end{Bmatrix} = \begin{Bmatrix} \frac{\partial u_0}{\partial s} \\ \frac{\cos\phi}{R} u_0 + \frac{1}{R}\frac{\partial v_0}{\partial \theta} + \frac{\sin\phi}{R} w_0 \\ \frac{1}{R}\frac{\partial u_0}{\partial \theta} - \frac{\cos\phi}{R} v_0 + \frac{\partial v_0}{\partial s} \\ \frac{1}{R}\frac{\partial w_0}{\partial \theta} + \beta_\theta \\ \frac{\partial w_0}{\partial s} + \beta_s \end{Bmatrix},$$

$$\begin{Bmatrix} \kappa_s^0 \\ \kappa_\theta^0 \\ \kappa_{s\theta}^0 \\ \kappa_{\theta z}^0 \\ \kappa_{sz}^0 \end{Bmatrix} = \begin{Bmatrix} \frac{\partial \beta_s}{\partial s} \\ -\frac{\cos\phi\sin\phi}{R^2} u_0 - \frac{\sin^2\phi}{R^2} w_0 + \frac{\cos\phi}{R}\beta_s + \frac{1}{R}\frac{\partial \beta_\theta}{\partial \theta} \\ -\frac{\sin\phi}{R^2}\frac{\partial u_0}{\partial \theta} - \frac{\cos\phi\sin\phi}{R^2} v_0 + \frac{\sin\phi}{R}\frac{\partial v_0}{\partial s} + \frac{1}{R}\frac{\partial \beta_s}{\partial \theta} - \frac{\cos\phi}{R}\beta_\theta + \frac{\partial \beta_\theta}{\partial s} \\ -\frac{\sin\phi}{3R}\left(\frac{1}{R}\frac{\partial w_0}{\partial \theta} + \beta_\theta\right) \\ 0 \end{Bmatrix},$$

$$\begin{Bmatrix} \kappa_s^1 \\ \kappa_\theta^1 \\ \kappa_{s\theta}^1 \\ \kappa_{\theta z}^1 \\ \kappa_{sz}^1 \end{Bmatrix} = \begin{Bmatrix} 0 \\ -\frac{3\sin^2\phi}{R^3}\frac{\partial v_0}{\partial \theta} + \frac{\sin\phi}{3R^2}\left(\frac{1}{R}\frac{\partial^2 w_0}{\partial \theta^2} + \frac{\partial \beta_\theta}{\partial \theta}\right) - \frac{\cos\phi\sin\phi}{R^2}\beta s - \frac{\sin\phi}{R^2}\frac{\partial \beta_\theta}{\partial \theta} \\ -\frac{\sin\phi}{R^2}\frac{\partial \beta_s}{\partial \theta} + \frac{\cos\phi\sin\phi}{3R^2}\beta_\theta + \frac{\sin\phi}{3R}\left(\frac{1}{R}\frac{\partial^2 w_0}{\partial s \partial \theta} + \frac{\partial \beta_\theta}{\partial s}\right) - \frac{2\cos\phi\sin\phi}{3R^2}\frac{1}{R}\frac{\partial w_0}{\partial \theta} \\ -\frac{4}{h^2}\left(\frac{1}{R}\frac{\partial w_0}{\partial \theta} + \beta_\theta\right) \\ -\frac{4}{h^2}\left(\frac{\partial w_0}{\partial s} + \beta_s\right) \end{Bmatrix},$$

$$\begin{Bmatrix} \kappa_s^2 \\ \kappa_\theta^2 \\ \kappa_{s\theta}^2 \\ \kappa_{\theta z}^2 \\ \kappa_{sz}^2 \end{Bmatrix} = \begin{Bmatrix} -\frac{4}{3h^2}\left(\frac{\partial^2 w_0}{\partial s^2} + \frac{\partial \beta_s}{\partial s}\right) \\ -\frac{4\cos\phi}{3h^2 R}\left(\frac{\partial w_0}{\partial s} + \beta_s\right) - \frac{4}{3h^2 R}\left(\frac{1}{R}\frac{\partial^2 w_0}{\partial \theta^2} + \frac{\partial \beta_\theta}{\partial \theta}\right) \\ -\frac{4}{3h^2}\left(\frac{1}{R}\frac{\partial \beta_s}{\partial \theta} + \frac{\partial \beta_\theta}{\partial s}\right) + \frac{4\cos\phi}{3h^2 R}\left(\frac{1}{R}\frac{\partial w_0}{\partial \theta} + \beta_\theta\right) - \frac{8}{3h^2 R}\frac{\partial^2 w_0}{\partial s \partial \theta} \\ \frac{4\sin\phi}{3h^2 R}\left(\frac{1}{R}\frac{\partial w_0}{\partial \theta} + \beta_\theta\right) \\ 0 \end{Bmatrix}$$

and

$$\begin{Bmatrix} \kappa_s^3 \\ \kappa_\theta^3 \\ \kappa_{s\theta}^3 \\ \kappa_{\theta z}^3 \\ \kappa_{sz}^3 \end{Bmatrix} = \begin{Bmatrix} 0 \\ \frac{4\sin\phi\cos\phi}{3h^2 R^2}\left(\frac{\partial w_0}{\partial s} + \beta_s\right) + \frac{4\sin\phi}{3h^2 R}\left(\frac{1}{R}\frac{\partial^2 w_0}{\partial \theta^2} + \frac{\partial \beta_\theta}{\partial \theta}\right) \\ \frac{4\sin\phi}{3h^2 R^2}\left(\frac{1}{R}\frac{\partial \beta_s}{\partial \theta} + \frac{\partial^2 w_0}{\partial s \partial \theta}\right) - \frac{4\cos\phi\sin\phi}{3h^2 R^2}\left(\frac{1}{R}\frac{\partial w_0}{\partial \theta} + \beta_\theta\right) \\ 0 \\ 0 \end{Bmatrix}.$$

References

[1] Allik H, Hughes TJR. Finite element method for piezoelectric vibration. Int J Numer Meth Eng 1970;2:151–7.

[2] Hwang WS, Park HC, Hwang W. Vibration control of a laminated plate with piezoelectric sensor/actuator: finite element formulation and modal analysis. J Intell Mater Syst Struct 1993;4:317–29.

[3] Tzou HS, Gadre M. Theoretical analysis of a multi-layered thin shell coupled with Piezoelectric shell actuators for distributed vibration controls. J Sound Vibration 1989;132(3):433–50.

[4] Pletner B, Abramovich H. Consistent methodology for the modeling of piezolaminated shells. AIAA J 1997;35(8):1316–26.

[5] Heyliger P, Pei KC, Saravanos D. Layerwise mechanics and finite element model for laminated piezoelectric shells. AIAA J 1996;34(11):2353–60.

[6] Saravanos DA. Mixed laminate theory and finite element for smart Piezoelectric composite shell structures. AIAA J 1997;35(8):1327–33.

[7] Saravanos DA, Heyliger PR, Hopkins DA. Layerwise mechanics and finite element for the dynamics analysis of Piezoelectric composite plates. Int J Solids Struct 1997;34(3):359–78.

[8] Mitchell JA, Reddy JN. A refined hybrid plate theory for composite laminates with piezoelectric laminae. Int J Solids Struct 1995;32(16):2345–67.

[9] Reddy JN. Theory and analysis of laminated composite plates. In: Mota Soares CA, Mota Soares CM, Freitas MJM, editors. Mechanics of composite materials and structures. Netherlands: Kluwer Academic Publishers, 1999: 1–79.

[10] Reddy JN. On laminated composite plates with integrated sensors and actuators. Eng Struct 1999;21:568–93.

[11] Correia VMF, Mota Soares CM, Mota Soares CA. Optimal Design of composite structures with integrated piezoelectric laminae. In: Mota Soares CA, Mota Soares CM, Freitas MJM, editors. Mechanics of composite materials and structures. Netherlands: Kluwer Academic Publishers, 1999: 389–408.

[12] Tzou HS, Ye R. Analysis of piezoelastic structures with laminated piezoelectric triangle shell elements. AIAA J 1996;34(1):110–5.

[13] Suleman A, Venkayya VB. A simple finite element formulation for a laminated composite plate with piezoelectric layers. J Intell Mater Syst Struct 1995;6:776–82.

[14] Kapuria S, Sengupta S, Dumir PC. Three-dimensional solution for simply-supported piezoelectric cylindrical shell for axisymmetric load. Comput Meth Appl Mech and Eng 1997;140:139–55.

[15] Faria AR, Almeida SFM. Axisymmetric actuation of composite cylindrical thin shells with piezoelectric rings. Smart Mater Struct 1998;7:845–50.

[16] Sheinman I, Weissnam S. Coupling between symmetric and antisymmetric modes in shells of revolution. J Comp Mat 1978;21:988–1007.

[17] Mota Soares CM, Cordeiro NM, Barbosa JI. A discrete model for the design sensitivity analysis of multilayered composite shells of revolution. Comp Eng 1995;5(5):533–50.

[18] Pinto Correia IF, Barbosa JI, Mota Soares CM, Mota Soares CA. A finite element semi-analytical model for laminated axisymmetric shells: statics, dynamics and buckling. Comput and Struct 2000;76(1–3):299–317.

[19] Palazotto AN, Dennis ST. Nonlinear analysis of shell structures. Washington, DC: AIAA Education Series; 1992.

[20] Pinto Correia IF. Análise estrutural de cascas axissimétricas laminadas pelo método dos elementos finitos com campo de deslocamento de alta ordem. M.Sc. thesis (in portuguese). Lisboa: Instituto Superior Técnico, Universidade Técnica de Lisboa, 1997.

[21] Char BW, Geddes KO, Gonnet GH, Leony BL, Monagan MB, Watt SM. First leaves: a tutorial introduction to MAPLE V. New York: Springer; 1996.

[22] Reddy JN. Mechanics of laminated composite plates – theory and analysis. Boca Raton, USA: CRC Press; 1997.

[23] Crisfield MA. Non-Linear finite element analysis of solids and structures. Volume 1: Essentials. Chichester: Wiley, 1994.

[24] Zienkiewicz OC. The finite element method in engineering science. 3rd ed. London: McGraw-Hill, 1982.

ELSEVIER

Composite Structures 47 (1999) 543–550

COMPOSITE STRUCTURES

www.elsevier.com/locate/compstruct

Evaluation of durability and strength of stitched foam-cored sandwich structures

Jae Hoon Kim *, Young Shin Lee, Byoung Jun Park, Duck Hoi Kim

Department of Mechanical Design Engineering, Chungnam National University, Taejon, 305-764, South Korea

Abstract

The static and fatigue characteristics of polyurethane foam-cored sandwich structures are investigated. Three types of specimens with glass fabric faces and polyurethane foam core are used; non-stitched, stitched and stiffened sandwich specimens. The bending strength of the stitched specimen is improved by 50% compared with the non-stitched specimen, and the stiffened specimen is over 10 times stronger than the non-stitched specimen. After fatigue loading of 10^6 cycles, the static bending strengths of all specimens decrease compared with those of the static test. To verify the aging effect of polyurethane foam, ultrasonic C-scanning equipment is used to detect damage of the skin laminate alone after the fatigue test for non-stitched specimens. From the results of UT C-scanning images, no damage is found to have occurred during the fatigue test. Results indicate that the decrease in bending strength of foam-cored sandwich structures is caused by the degradation of stiffness due to the aging of the polyurethane foam core during fatigue cycles. To investigate the effect of distance and diameter of stitching thread, four types of stitched specimens are used. The strength of stitched specimen is improved by increasing the stitching thread diameter and decreasing the stitching thread distance. But fatigue characteristics are not predominantly affected by the variation of stitching thread diameter and distance. © 2000 Published by Elsevier Science Ltd.

Keywords: Sandwich structures; Durability; Strength

1. Introduction

The main benefits of using the sandwich concept in structural components are the high stiffness and strength-to-weight ratios. Sandwich structures may successfully be used in a variety of areas of vehicle applications, including components in spacecrafts, aircraft structures, marine vessels, transportation structures, tanks, refrigerator containers and car body shells [1–6].

Conventional sandwich structures consist of a metallic skin and polyurethane foam core material as an insulating layer. These conventional structures have been used very widely for structural components. However, the durability of those panels becomes degraded due to delamination at the bonding interfaces and stiffness degradation through aging of the foam core over the period of service life. Improvements in durability of panels along with weight reduction have been strongly proposed. In order to overcome the shortcomings of conventional sandwich structures, the reinforcement to thickness of sandwich structures through the stitching process is one of the solutions to the problem of averting delamination and minimizing the degradation of stiffness.

In a recent paper, Shenoi et al. [7] investigated the static and flexural fatigue characteristics of foam core polymer composite sandwich beams. The applied load in a 10-point configuration approximates a uniformly distributed load throughout the span of the beam that is simply supported at the ends. Failure modes relate to both core shear and skin failure. Burmen et al. [8] also tested the fatigue characteristics of two cellular foam core materials as used in load carrying sandwich structures. Judawisastra et al. [9] reported on the bending fatigue behavior of pure-epoxy and 3D woven sandwich composites. Panels with different core properties were selected. During the fatigue test, the displacement was monitored with a constant load applied to obtain the stiffness degradation. The results of the property degradation correlated with the mechanical properties of the different sandwich panels. Thomsen [10] verified that the local bending effects are strongly influenced by the modular ratio (E_f/E_C) and the thickness of the loaded face through analysis. Theulen et al. [11] verified the minimum weight criterion of a sandwich panel with

* Corresponding author.
E-mail address: kimjhoon@hanbat.chungnam.ac.kr (J.H. Kim).

0263-8223/99/$ - see front matter © 2000 Published by Elsevier Science Ltd.
PII: S0263-8223(00)00019-2

respect to a given bending stiffness and strength. From this study, sandwich constructions consisting of a PVC core and glass fiber-reinforced epoxy faces are tested in a four-point bending test. A composite sandwich panel can be optimized with regard to some specific characteristics. The optimum core-to-face weight ratio for bending stiffness is about two and for bending strength it is about one. The increase in panel weight for panels with a core to face weight ratio near the optimum is relatively low. Yoon et al. [12] demonstrated that a stitched sandwich specimen reveals higher impact force than a non-stitched sandwich specimen. Therefore, research on stitched sandwich structures is demanded.

In this study, the bending strength and bending fatigue strength are evaluated on a foam-cored sandwich structure which is manufactured and installed in refrigerator containers by Hankuk Fiber Glass Co., Ltd. Three types of specimens with glass fabric faces and polyurethane foam core are used. To evaluate the advantage of reinforcement stitching, it is necessary to understand the fatigue behavior of foam-cored sandwich structures. The purpose of this reinforcement is to characterize the mechanical behavior caused by fatigue loading.

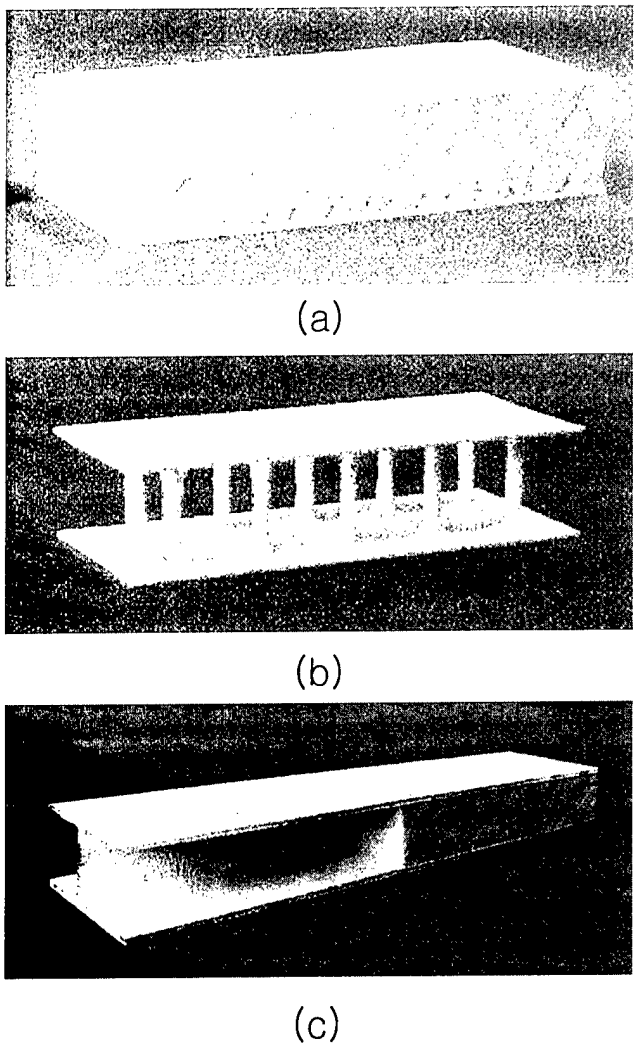

Fig. 1. Configurations for three types of specimens: (a) non-stitched sandwich specimen, (b) stitched sandwich specimen, and (c) stiffened sandwich specimen.

2. Materials and specimens

Fig. 1 shows the configurations of non-stitched, stitched and stiffened sandwich specimens used in this study. All sandwich specimens were made by Hankuk Fiber Glass Co., Ltd., according to the manufacturer's specifications. These sandwich specimens consist of a glass fabric and polyurethane foam core. Table 1 shows the materials of the specimen.

The manufacturing process of a non-stitched sandwich specimen is

- Lay-up a woven glass fabric on a polyurethane foam core.
- Lay-up a resin sheets on each face of the materials.
- Lay-up reinforcement fibers on each side again.
- Cure by hot-press (pressure: 1.5 ± 0.1 kg/cm^2).

Fig. 2 shows the curing cycle of specimens.

A stitched sandwich specimen is prepared by stitching the glass fabric and foam core material together with stitching thread. Especially as reinforcing to thickness direction, twisted glass and polyester thread is stitched together to combine the upper and lower faces through the core of the stitched specimen. Then, epoxy resin is impregnated into the stitching thread during the curing process. To investigate the effect of distance and diameter of the stitching thread, four types of the stitched

Table 1
Materials of specimen

Construction	Material	Remark
Skin	Glass fabric	G.R.C Glass Roving cloth 3D fabric
Resin	Epoxy	R340S/R340G/ R680G
Foam	P.U. foam	Density 40–60 kgf/m^3
Stitched fiber	Nylon + Glass yarn	Diameter, distance

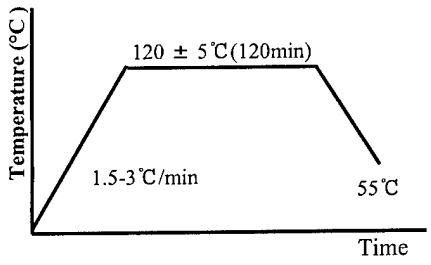

Fig. 2. Curing cycle of specimen.

specimens are used; 50×50 (ϕ3), 50×50 (ϕ5), 50×75 (ϕ5) and 50×100 (ϕ5).

The stiffened sandwich specimen is continuously stiffened by woven glass/epoxy prepreg which has the same curing characteristics as resin sheet.

3. Test setup and procedures

The static bending test is conducted according to ASTM Standard C-393 [13]. The experimental setup used in the static and fatigue test is presented in Fig. 3. The test is performed with a fatigue test machine (Shimadzu, Model EHF-ED10) at a constant crosshead speed of 0.5 mm/min.

The span length is chosen as $L = 457.2$ mm. Strain gages are attached to the outer skin in order to measure the strain caused by the bending load. Fig. 4 shows the gage position on the specimens. The strain value is obtained using a strain indicator (Micro-measurement, Model P3500) and a switch and balance unit (Micro-measurement, Model SB 100).

The bending fatigue test is performed under load control with stress ratio $R = 0.1$. A frequency of 3 Hz is chosen. The maximum value of fatigue load that is 20% of maximum load under static bending test, is applied to the range of 10^5–10^6 cycles. After the fatigue test, bending strength degradation and fatigue characteristics due to cyclic loads are evaluated by static test.

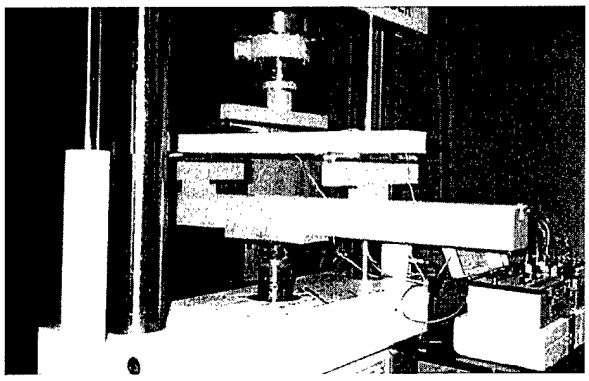

Fig. 3. Configuration of experimental setup.

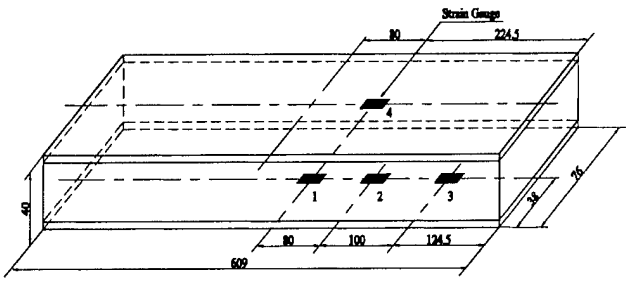

Fig. 4. Dimension and strain measurement sites of specimen used in static and fatigue test.

4. Static bend test result

Fig. 5 shows the load–displacement curves of the static bending test for the three types of specimens. The bending strength of the stitched specimen was found to be 50% greater than the non-stitched specimen, and the stiffened specimen was 10 times greater than the non-stitched specimen. In the case of the non-stitched and stitched specimens, as the displacement increases, the load–displacement curves form a parabola shape. Therefore, maximum load is defined by the maximum value of the load–displacement curves. The maximum load of the specimens for the static bend test is summarized in Table 2.

Fig. 6 shows the load–strain curves of the static bending test for the three types of specimens. The strain values of the stitched and non-stitched specimens have similar values. However, the strain value of the stiffened specimen is 69% lower at gage 1, and 53% lower at gage 2 compared with the non-stitched specimen. Comparing gage positions 2 and 4, strain values on the stitched and the stiffened specimens are similar but the strain value on the non-stitched specimen is about twice as large-gage 2 of the upper skin. Table 3 gives the maximum strain values at each gage position for the three types of specimens.

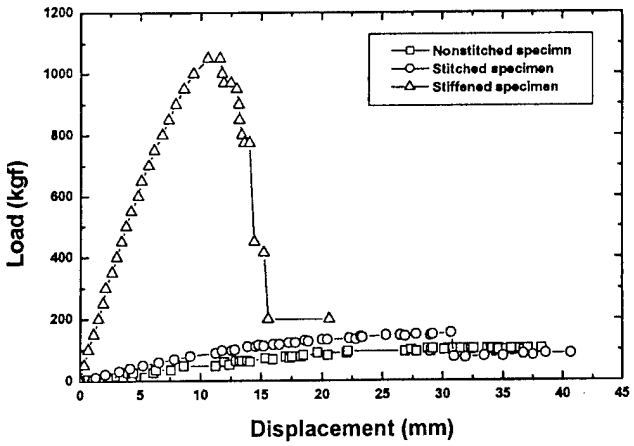

Fig. 5. Load–displacement curves of static test.

Table 2
Maximum loads of static test

Type of specimen	Maximum load (kgf)
Non-stitched specimen	100
Stitched specimen	150
Stiffened specimen	1050

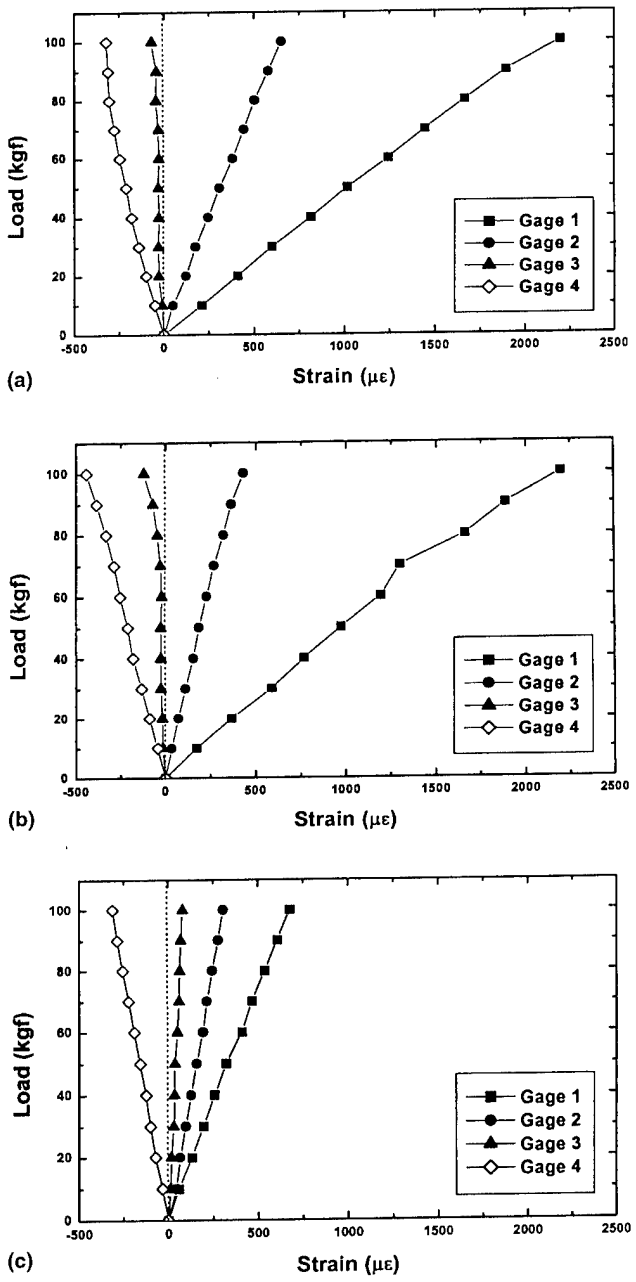

Fig. 6. Load–strain curves of static test: (a) non-stitched sandwich specimen, (b) stitched sandwich specimen, and (c) stiffened sandwich specimen.

Table 3
Maximum strains at gage positions for three types of specimens

Gage position	Strain of non-stitched (με)	Strain of stitched (με)	Strain of stiffened (με)
Gage 1	2167	2199	679
Gage 2	652	413	306
Gage 3	−61	−121	80
Gage 4	−311	−422	−311

The results show that bending strength of foam-cored sandwich specimens can be improved with a stiffener. Reinforcement by stitching increases static bending strength.

5. Bending fatigue test result

Fig. 7 shows the load–displacement curves of the non-stitched specimen for the static bending test and the specimens subjected to fatigue loading.

Results of the fatigue bending test are obtained from the static bending test after fatigue loading of 10^5, 3×10^5, 5×10^5 and 10^6 cycles. The bending strength of the non-stitched specimen is 10% lower compared with that of the static test for 10^5 fatigue cycles, 15% for 5×10^5 fatigue cycles and 27% for 10^6 fatigue cycles. From the load–strain curves of the non-stitched specimen at gage 2 shown in Fig. 8, it can be seen that the strain of the non-stitched specimen which is applied a fatigue loading of 10^6 cycles increases largely compared with those of other specimens, and as fatigue cycles increase, the nonlinear position of the load–strain curves appears ahead.

To verify the aging effect of polyurethane foam, ultrasonic C-scanning equipment is used to detect the damage to the laminated skin alone and degradation of

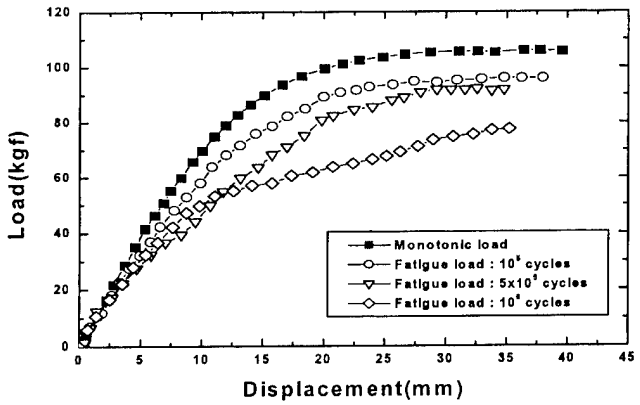

Fig. 7. Load–displacement curves of non-stitched sandwich specimen.

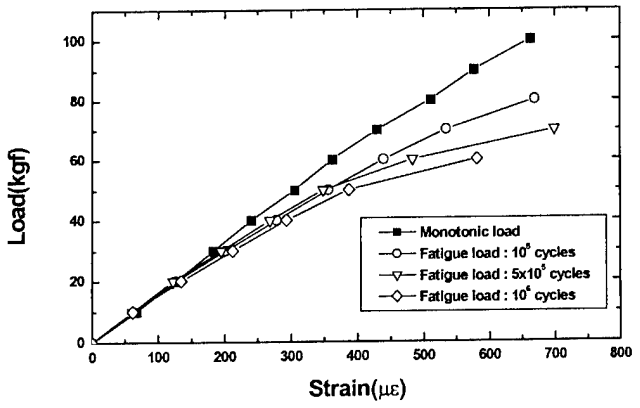

Fig. 8. Load–strain curves of non-stitched sandwich specimen at gage 2.

stiffness after the fatigue test. Fig. 9 shows the images generated with ultrasonic C-scanning on the skin of the non-stitched specimen after the fatigue loading. There are no defects that can be considered to be damaged resulting from the fatigue test even though there is a slight difference of dB value due to the foam remnant attached locally to the skin after the foam materials have been removed thoroughly from the sandwich panel, however, this can also be considered as deviation which can occur during the manufacturing process. From the results of the ultrasonic C-scanning, it is conclusive evidence to show that the decrease in bending strength of foam-cored sandwich structures is caused by stiffness degradation due to the aging of polyurethane foam during the bending fatigue test.

Fig. 10 shows the load–displacement curves of the static test for the stitched specimen and the specimens subjected to fatigue loading. Compared with the monotonic bending strength, the bending strength of the stitched specimen decreases by 29% for 10^5 fatigue cycles, 38% for 5×10^5 fatigue cycles and 39% for 10^6 fatigue cycles. The strain values of the stitched specimen at gage 2 are shown in Fig. 11. With an increase in fatigue cycles, the strain value also increases. To verify the degradation of the bending strength due to fatigue loading, foam materials were removed from the specimen.

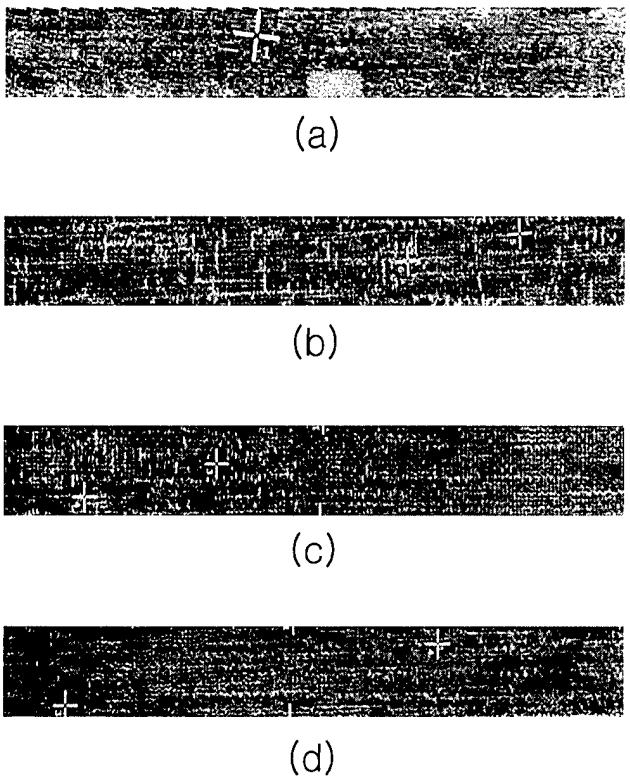

Fig. 9. Ultrasonic C-scan images for skins of non-stitched sandwich specimen after fatigue loading: (a) specimen without fatigue loading, (b) 10^5 fatigue loading, (c) 5×10^5 fatigue loading, and (d) 10^6 fatigue loading.

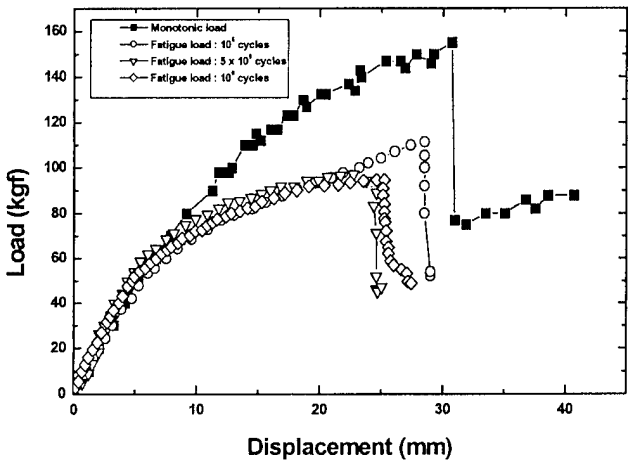

Fig. 10. Load–displacement curves of stitched sandwich specimen.

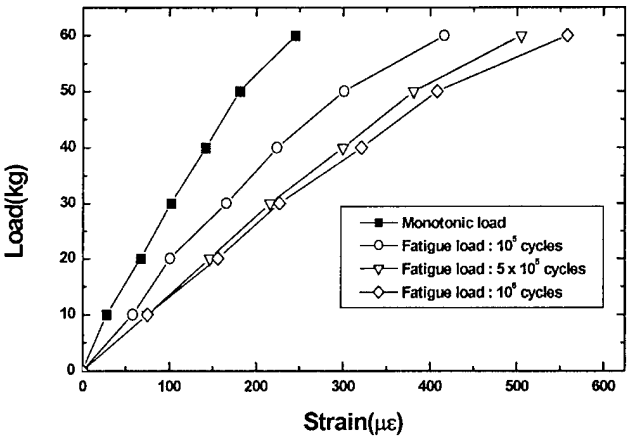

Fig. 11. Load–strain curves of stitched sandwich specimen at gage 2.

Fig. 12 presents the photographs of stitched specimens after fatigue loading. As fatigue cycles increase, the damage to resin around the stitching thread increases very rapidly and is the main cause of stiffness degradation. It is understood that the stitched specimen can increase the static bending strength considerably but cannot increase the bending fatigue strength, because the characteristics of the resin built-up around the stitching thread are generally very brittle and easily broken under fatigue loading condition.

Fig. 13 shows the load–displacement curves of the static test for the stiffened specimen and the specimens subjected to fatigue loading. Compared with the monotonic bending strength, the bending strength of the stitched specimen decreases by 7% for 5×10^5 fatigue cycles, and 20% for 10^6 fatigue cycles. The strain value versus the load curve of the stiffened specimen at gage 2 is shown in Fig. 14. With increases in fatigue cycles, the strain levels show little linear difference.

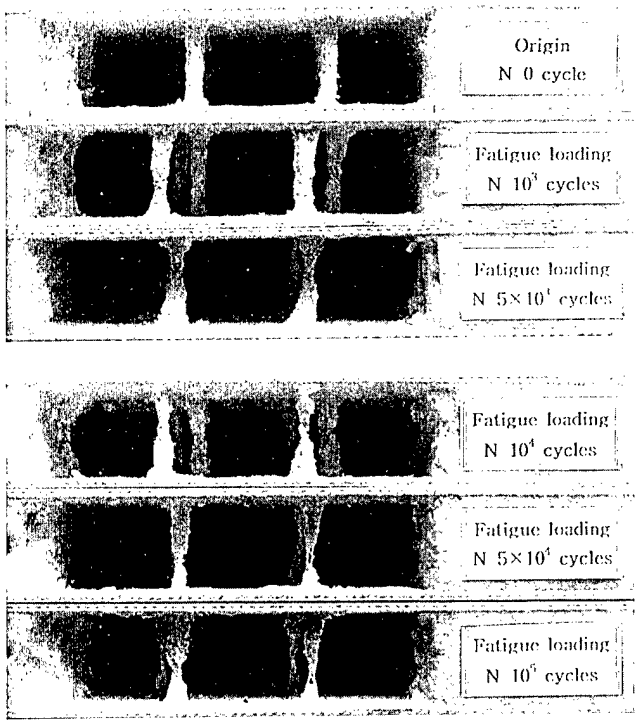

Fig. 12. Photos of stitched reinforced thread after fatigue loading.

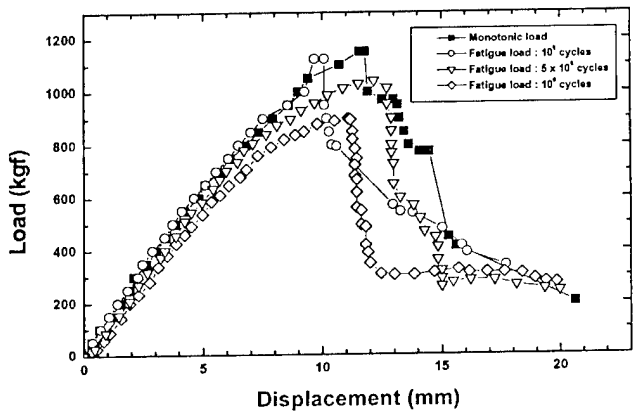

Fig. 13. Load–displacement curves of stiffened sandwich specimen.

It is concluded that the degradation of static bending strength for the non-stitched specimen after fatigue loading is caused by aging of foam materials. In the case of stitched polyurethane foam-cored structures, static bending strength improves. However, the stitched specimen is weak for fatigue loads because epoxy resin itself is brittle. The static bending strengths of stiffened polyurethane foam-cored structures are greater than the other specimens and they have predominant fatigue characteristics.

The deflection versus number of cycle curves for the three types of specimens after fatigue loading of $N = 5\times10^5$ cycles are shown in Fig. 15. With an increase in fatigue cycles, the deflection in the stiffened specimen reveals a little increase at both maximum and minimum loading, but those of the other specimens increase gradually with a similar trend.

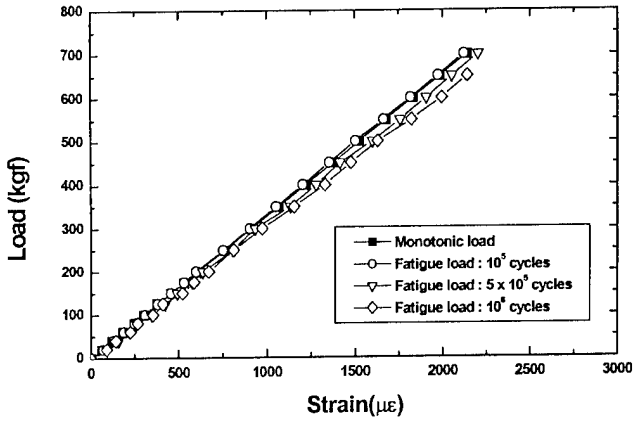

Fig. 14. Load–strain curves of stiffened sandwich specimen at gage 2.

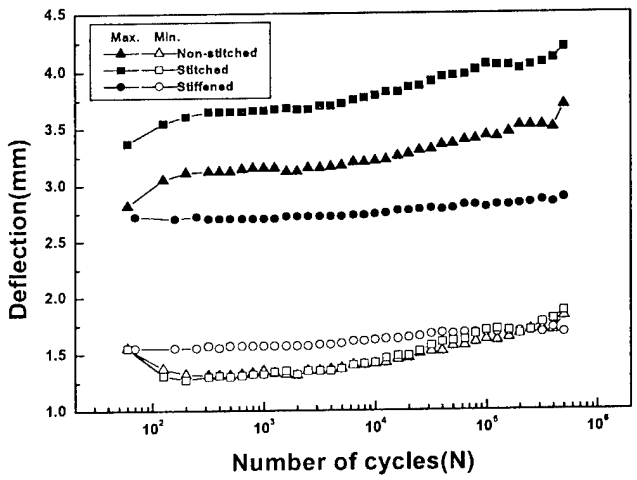

Fig. 15. Deflections as a function of cycles under during fatigue loading of $N = 5\times10^5$ cycles.

6. Effect of stitching thread diameter and distance

To investigate the effects of stitching thread diameter and distance, four types of stitched specimens are used; 50×50 mm^2 ($\phi3$ mm), 50×50 mm^2 ($\phi5$ mm), 50×75 mm^2 ($\phi5$ mm) and 50×100 mm^2 ($\phi5$ mm).

Fig. 16 is the load–displacement curves of the four types of stitched specimens. In the case of the stitched specimens which were described in the previous sections, the skins of the stitched specimen were three ply. However, the stitched specimens which are described in the present section, are two-ply skins. Therefore, the maximum load of the stitched specimens decreases by 30 kgf compared with that of Section 5.

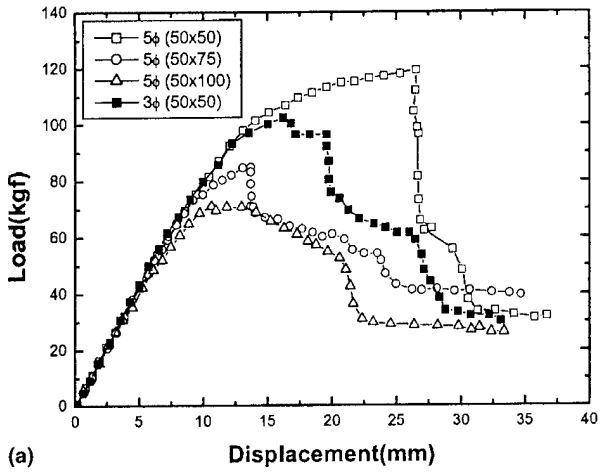

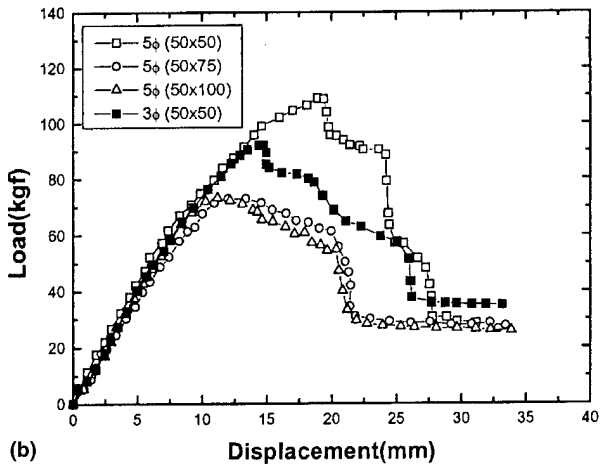

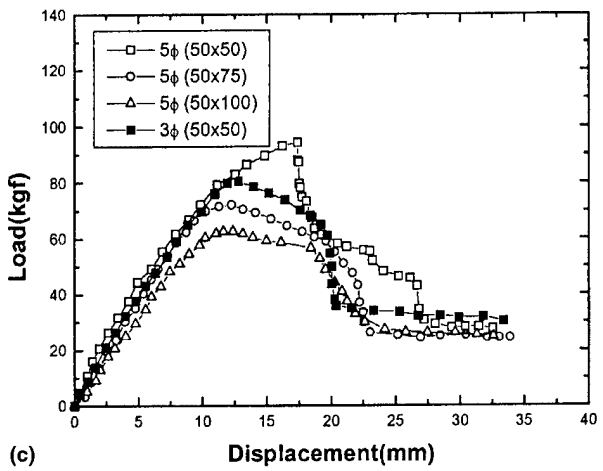

Fig. 16. Load–displacement curves of stitched specimen for variation of stitching thread diameter and distance: (a) monotonic load, (b) after $N = 10^5$ fatigue cycles, and (c) after $N = 5\times10^5$ fatigue cycles.

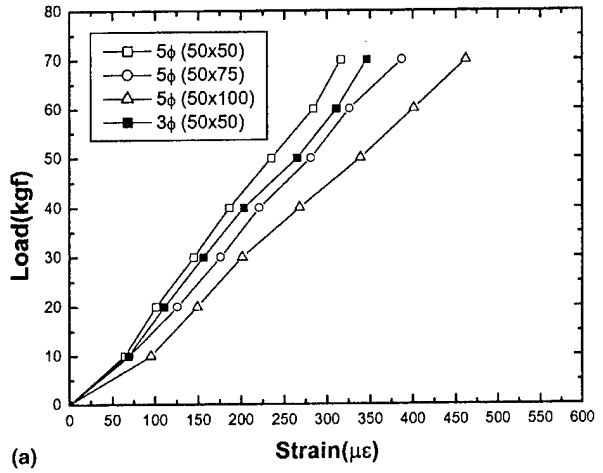

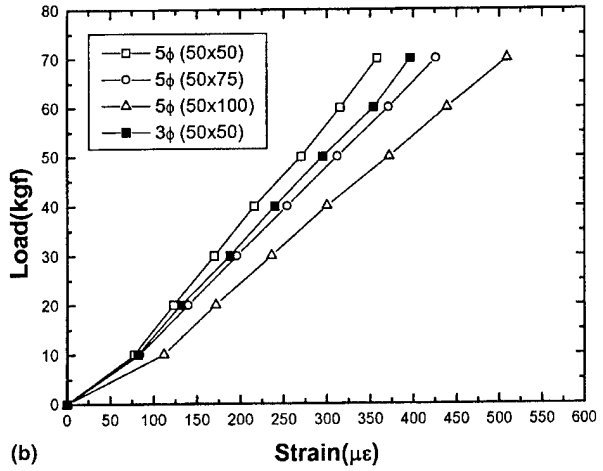

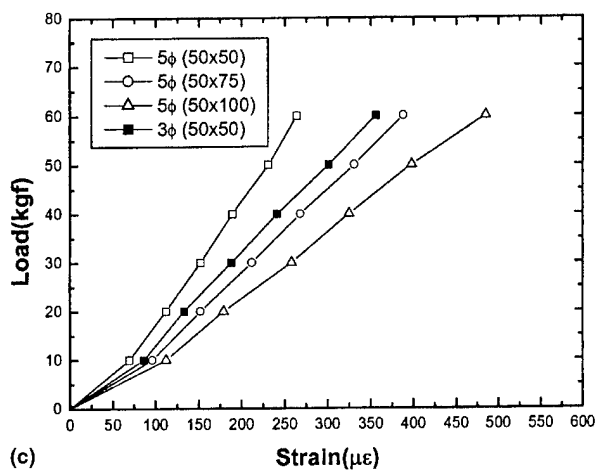

Fig. 17. Load–strain curves of stitched specimen for variation of stitching thread diameter and distance: (a) monotonic load, (b) after $N = 10^5$ fatigue cycles, and (c) after $N = 5\times10^5$ fatigue cycles.

As the stitching thread diameter varies from $\phi3$ to $\phi5$ mm, the bending strength of the stitched specimen increases by 17% for the monotonic load, 17% for 10^5 fatigue cycles and 12% for 5×10^5 fatigue cycles.

Also, when the stitching thread distance varies from 50×50 mm^2, 50×75 mm^2 and 50×100 mm^2, the bending strength of the stitched specimens ($\phi5$ mm) decreases by 28% and 48% for the monotonic load compared with

50×50 mm^2, respectively. In the case of 10^5 fatigue cycles, the bending strength of the stitched specimens decreases by 33% and 34%, and, the bending strength of the stitched specimens decreases by 25% and 35% for 5×10^5 fatigue cycles, respectively.

Fig. 17 shows the load–strain curves for the four types of stitched specimens. The strain level of the stitched specimen with 50×50 mm^2 ($\phi3$ mm) increases largely compared with that of the specimen with 50×50 mm^2 ($\phi5$ mm). As the stitching thread distance increases, the strain of the stitched specimen increases.

The experimental results indicate that the strength of the stitched specimen is improved by increasing the stitching thread diameter and decreasing the stitching thread distance, but the fatigue characteristics of the stitched form core structures are not predominantly affected by the variation of stitching thread diameter and distance.

The present study is a preliminary research which is to be applied to foam-cored sandwich structures used in engineering components such as railway vehicles, etc. At the present time, the effects of stitching thread diameter, stitching distance in foam-cored sandwich structures and control methods for stitching thread resin content have been investigated. The detailed effects will be established later.

7. Conclusions

The static bending and fatigue characteristics for polyurethane foam-cored sandwich specimens are investigated. The conclusions obtained from the present results are as follows:

1. The bending strength of the stitched specimen is improved by 50% compared with the non-stitched specimen, and the stiffened specimen is over 10 times stronger than the non-stitched.
2. After fatigue loading of 10^6 cycles, the bending strengths of all specimens decrease compared with those in the static test. The reduction of bending strength of foam-cored sandwich specimens is caused by the stiffness degradation of foam due to the aging of polyurethane foam during fatigue cycles.
3. The stitched specimen can increase the static bending strength considerably but cannot increase the bending fatigue strength, because the characteristics of the resin built-up around the stitching thread are generally very brittle and easily broken under fatigue loading condition.
4. The static bending strengths of stiffened polyurethane foam-cored structures are greater than the other specimens and they have predominant fatigue characteristics.
5. The strength of the stitched specimen is improved by increasing the stitching thread diameter and decreasing the stitching thread distance. However, fatigue characteristics are not predominantly affected by the variation of stitching thread diameter and distance.

Acknowledgements

We wish to thank the Korea Research Foundation for the financial support. The authors wish to thank Hankuk Fiber Glass Co., Ltd. for supplying polyurethane foam-cored sandwich specimens.

References

[1] Gibbson RF. Principles of Composite Material Mechanics. New York: McGraw-Hill; 1994.
[2] Burchanrdt C. Fatigue of sandwich structures with inserts. Comp Struct 1998;40:201–11.
[3] Shenoi RA, Aksu A, Allen HG. Flexural fatigue characteristics of FRP sandwich beams. Fatigue Fracture Eng Mater Struct 1993;6:649–62.
[4] Grenestedt JL, Hallstrom S, Kuttenkeuler J. Cracks emanating from wedges in expanded PVC foam. Eng Fracture Mech 1996;54:445–56.
[5] Bergan PG, Buene L, Echtermeyer AT, Hayman B. Assessment of FRP sandwich structures for marine applications. Mar Struct 1994;7:457–73.
[6] Papanicolaou GC, Bakos B. Interlaminar fracture behavior of sandwich structures. Composites 1996;27A:165–73.
[7] Shenoi RA, Clark SD, Allen HG. Fatigue behavior of polymer composite sandwich beams. J Comp Mater 1995;29:2423–45.
[8] Burmen M, Zenkert D. Fatigue of foam core sandwich beams-1: Undamaged specimens. Int J Fatigue 1997;19:551–61.
[9] Judawisastra H, Ivens J, Verpoest I. Bending fatigue behavior of pure-epoxy and phenolic 3D woven sandwich composites. Mech Sandwich Struct 1998:297–294.
[10] Thomsen OT. Analysis of local bending effects in sandwich plates with orthotropic face layers subject to localized loads. Comp Struct 1993;25:511–20.
[11] Theulen JCM, Peijs AAJM. Optimization of the bending stiffness and strength of composite sandwich panels. Comp Struct 1991;17:87–92.
[12] Yoon SH, Lee SC, Cho SH, Park BJ, Cho JM. Low energy impact behaviors of non stitched and stitched foam cored sandwich structures. In: Proceedings of the Twelfth International Conference on Composite Materials. CD edition. Paris, France, Extended Abstracts, 1999. p. 373.
[13] ASTM, C393–94, Standard Test Method for Flexural Properties of Sandwich Constructions 1996:21–24.

ELSEVIER

Composite Structures 47 (1999) 551–561

COMPOSITE STRUCTURES

www.elsevier.com/locate/compstruct

Experimental and numerical study of the impact behavior of SMC plates

Sang-Min Lee [a], Jae-Seung Cheon [b], Yong-Taek Im [b,*]

[a] *R&D Department, Kimhae Plant, Korea Airlines Co., Pusan 618-242, South Korea*

[b] *Computer Aided Materials Processing Laboratory, ME3227, Department of Mechanical Engineering, Korea Advanced Institute of Science and Technology, 373-1 Gusongdong, Yusonggu, Taejon 305-701, South Korea*

Abstract

Steel components absorb impact energy by plastic deformation whilst composite materials absorbing it by damage mechanisms such as fiber debonding, fiber fracture, and matrix cracking. Therefore, in order to properly substitute metal components with composite ones in industrial applications, the impact property of composite materials must be well known. In this study, the impact behavior of sheet molding compounds (SMC), which is widely used in automobile industry due to its relatively low cost and high productivity, was examined both experimentally and numerically. In order to investigate the impact behavior of SMC, an experimental study was carried out by setting up a drop weight impact test system. Using this system, the dissipated impact energies of SMC flat plates were measured to investigate the influence of the mass and shape of impactor, initial velocity, and specimen thickness on the impact behavior.

For numerical predictions, a modified damage model for SMC was developed and adopted in the user defined material subroutine of the commercial simulation program LS-DYNA3D. For the sake of improving efficiency of impact simulations, the SMC material property was determined in consideration of the local differences of the fiber volume fractions. The dissipated impact energies under various conditions and the reliability of the developed impact simulation process were examined through comparisons of the predicted data with the experimental results.

From this comparison, it was found that, in the scope of current study, the specimen thickness is the most important parameter that should be considered in the design of SMC components for the aspect of impact behavior. © 2000 Published by Elsevier Science Ltd.

Keywords: Impact energy; Impact behavior; Sheet molding compounds (SMC)

1. Introduction

The effective use of materials to absorb impact energy in automotive applications has received increased attention because material and structural based energy absorbing devices can be fabricated using simpler designs compared to devices based on pneumatic or hydraulic principles. Also, the need for more light-weight and fuel efficient vehicles has made composite materials suitable substitutes for conventional metal parts. Among composite materials, sheet molding compounds (SMC) is widely used because of its high stiffness-to-weight ratio, high strength-to-weight ratio, and high volume-to-low cost production. As the use of SMC in automotive applications increases, the need to determine the impact property of these materials becomes very important to ensure the stability and safety of the designed structures. For this purpose, the impact behavior of SMC flat plates was examined experimentally and numerically in this study.

The experimental studies on the impact behavior of composite materials can be largely categorized into either high velocity or low velocity impact tests [1]. In high velocity impact tests, the entire structure does not have time to respond, leading to very localized damage. On the other hand, in low velocity impact tests, the contact duration is long enough for the entire structure to respond to the impact. The low velocity impact testing devices can be divided into pendulum type (Izod, Charpy) and the drop weight type [2]. The pendulum type is usually used to measure the in-plane impact resistance, but it has limitations in terms of the size of

* Corresponding author. Tel.: +82-42-869-3227; fax: +82-42-869-3210.

E-mail address: ytim@convex.kaist.ac.kr (Y.-T. Im).

0263-8223/99/$ - see front matter © 2000 Published by Elsevier Science Ltd.
PII: S0263-8223(00)00021-0

specimen, impact direction, and boundary conditions. On the other hand, the drop weight type impact tester, which better represents situations of bumper collisions or falling debris, enables to measure the impact behavior of an entire structure for the out-of-plane impact loads. Also, the drop weight type can be easily adapted to various situations by changing the boundary conditions, impactor shapes, and impact directions. Considering these benefits, a drop weight impact tester was designed and constructed to examine the impact behavior of SMC plates in the current study.

In previous studies of the low velocity impact, Siow et al. [3] carried out an experimental and numerical study on the residual strength and stiffness after impact. Zhou [4] and Lagace [5] studied the correlation between the damaged area and absorbed impact energy, while the effect of geometry on the dissipated impact energy rate was investigated by Cantwell et al. [6] and Kumar et al. [7]. These previous studies have dealt with laminated composites reinforced with continuous fibers. In comparison, the impact behavior of SMC plates, which are reinforced with chopped fibers and manufactured by compression molding, was examined in the present study. For this, numerous drop weight impact tests were carried out for SMC flat plates under varying conditions of impactor mass, initial impact velocity, impactor shape, and specimen thickness.

Although experimental studies are invaluable in that they provide actual raw data, they require much time and cost. In this sense, numerical simulations have an advantage in decreasing the lead time for the designing process. In order to simulate the impact behavior of SMC plates, the characteristics of SMC must be well known. Compared to metals, which absorb impact energy by plastic deformation, brittle SMC absorbs energy by damage mechanisms such as fiber debonding, fiber breakage, and matrix cracking. In order to represent such damage characteristics, Kachanov [8] suggested damage mechanics for a continuum. Based on this theory, numerous studies have been carried out to determine the damage behavior of composite materials. Murakami [9] recognized the non-linearity in stress–strain relations, and in order to represent this non-linearity induced by the stiffness reduction, Pickette et al. [10] introduced the damage function.

However, in these previous damage models, the absorbed impact energy was over predicted because of the limit of the failure mode considered. Thus, a revised damage model with an elimination routine to consider failure elements was developed and coded into the user defined material subroutine of LS-DYNA3D [11]. This damage model is depending on the elastic material property of the material to be tested. In order to increase the efficiency of numerical simulations, it is practical to be able to predict the material property rather than making experimental tests to determine it. Hill [12] and Hashin [13] carried out the prediction of material property in uniformly distributed short fiber reinforced composites, and based on these studies the material property of randomly distributed fiber reinforced composites was predicted by Christensen et al. [14]. However, since this work did not consider the contribution of the filler, which is a major component in SMC, Chang et al. [15] improved the theory to include the effect of filler. Also, the distribution of fibers plays an important role in determining the material property of SMC and the non-uniformity of the distribution of fibers induces variation in local stiffness which influences the impact behavior. Thus, the fiber volume fraction distribution of compression molded SMC plates was made by the approach suggested by Cheon et al. [16].

In the present study, the material property of SMC was estimated with knowledge of the distribution of fibers and SMC constituents' material properties. This material property was used in the aforementioned revised damage model to conduct numerical simulations of the impact of SMC flat plates under various conditions. The numerical results were compared to the experimental data to examine the reliability of the impact simulation process. In the scope of the current study, the experimental and numerical results showed that the specimen thickness is the most important parameter that should be considered in the design of impact structures made of SMC.

2. Experimental study on the impact behavior of SMC

An experimental study to examine the impact behavior of SMC was carried out by measuring the dissipated energy of the impactor under various conditions. For this, a drop weight impact tester, which is a type of low velocity impact tester, was set up as follows.

2.1. Drop weight impact tester

A drop weight impact test system was constructed to measure the dissipated impact energies for complete failure of SMC flat plates as shown in Fig. 1. The drop height of the impactor, which was attached to guiding rods, ranged from 100 to 1100 mm for an impact velocity range from 1.40 to 4.75 m/s. The impactor was composed of three parts, namely, the body, contacting tup, and added mass samples, as shown in Fig. 2. Four impacting tup types, cone, flat, hemi-sphere, and semi-cylinder, as shown in Fig. 3, were designed to be easily assembled and disassembled. The added masses ranged 100, 200, 500, and 1000 g to give an impactor mass range of 1.0–4.5 kg.

Two ends of the specimen were simply supported using the jig as shown in Fig. 2. In order to measure the velocity of the impactor, a micro-photosensor, which

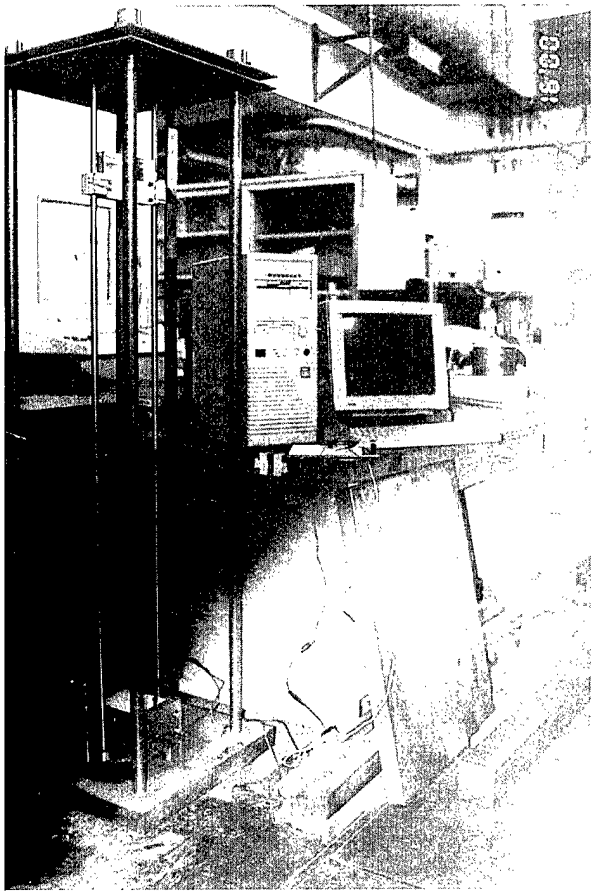

Fig. 1. The constructed experimental setup for drop weight impact test.

generates 5 V of voltage when an object passes, was used. The analog signal from the sensor was transformed into a digital signal for the purpose of calculating the velocity. A U-shaped bracket was attached to the impactor as shown in Fig. 2. The velocity of the impactor was measured three times as the U-shaped bracket passed the sensor and the velocity of the impactor was calculated by averaging the three measurements as follows:

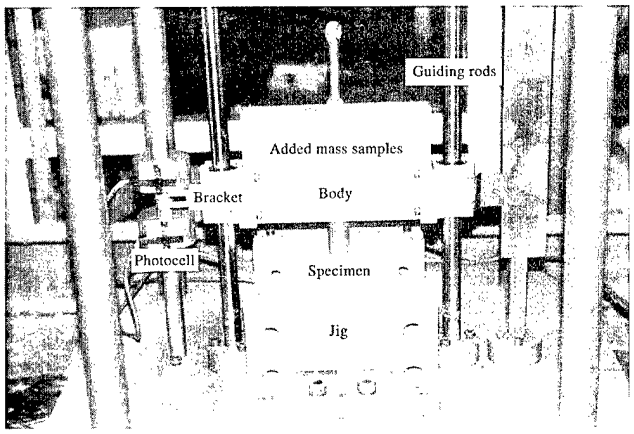

Fig. 2. Photograph showing the impactor with added mass samples, U-shaped bracket, guiding rods, scale to measure the drop height, and the photocells to measure the velocity.

$$l_j = 0.5\ \text{mm}, \quad t_j = N \times \Delta t_s, \quad V_j = l_j/t_j,$$
$$V = (V_1 + V_2 + V_3)/3.0, \qquad j = 1, 2, 3. \tag{1}$$

Here, l_j is the length of a flanged part and hole in the U-shaped bracket, t_j the required time to travel the distance l_j, N the number of measured sampling times, $\Delta t_s = 0.2$ ms the sampling time, and V is the impacting velocity. Then, the dissipated impact energy can be calculated from the measured initial and residual impact velocities as follows:

$$E_d = E_i - E_r = \frac{1}{2}M((V_i)^2 - (V_r)^2). \tag{2}$$

Here, the subscripts d, i, and r indicate dissipated, initial, and residual, respectively, and M is the mass of the impactor.

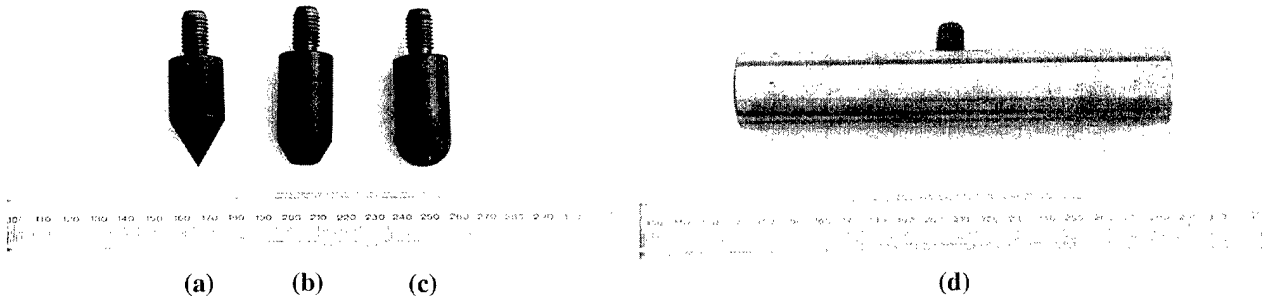

(a) (b) (c) (d)

Fig. 3. Photographs of the (a) conical, (b) flat, (c) hemi-spherical, and (d) semi-cylindrical shape penetration impactors.

2.2. Compression molding of SMC flat plate specimen

An hydraulic 150 ton press was used to fabricate the specimen to be used for the impact tests. The heating rods inserted in the lower and upper molds were controlled by a temperature controller to maintain the molds at 120°C. The dimensions of the initial charge were 101.0 mm × 76.7 mm × thickness to cover 60% of the lower mold area as shown in Fig. 4. The fiber weight fraction of SMC used in the current study was 30%. The percentage of constituents and their properties are given in Tables 1 and 2, respectively. The compression molding required forming loads of 10–20 tons and the fabricated SMC plate had dimensions of 101.0 mm × 127 mm × thickness. At least five specimens were compression molded for each of the impact test conditions to be described in the following section.

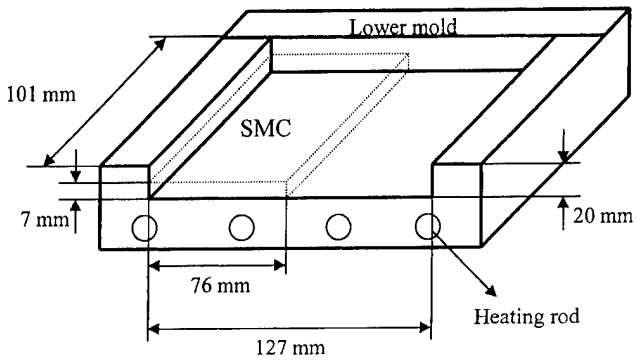

Fig. 4. Dimension and location of the initial SMC charge on the lower mold.

Table 1
Constituents of SMC

Material	Ingredient	Weight percent (%)
SMC-R24	Resin (polyester, styrene monomer, low profile additive)	27.35
	Filler	40.70
	Catalyst	0.25
	Thickener	0.70
	Internal release	1.00
	25.4 mm chopped E-glass	30.00

2.3. The impact test of SMC flat plates

Drop weight impact tests were carried out on compression molded SMC flat plates with simply supported boundary conditions. The tests were carried out for four different cases to investigate the major influencing factors on impact behavior as follows.

(1) *Thickness variation of the specimen*: The thicknesses of the rectangular specimen were varied for five cases of 2.4, 3.2, 3.6, 4.3, and 4.9 mm. The semi-cylindrical shaped impactor with the radius of 10 mm was used for the experiments. The initial impacting velocity was 4.75 m/s and the impactor mass was 4.5 kg to give an initial impact energy of 102 J.

(2) *Initial velocity variation of impactor*: The initial velocity of the impactor was varied for five cases of 3.4, 3.6, 3.9, 4.1, and 4.4 m/s by controlling the height of the impactor. The specimen thickness was 2.4 mm and the semi-cylindrical shaped impactor was used with an impactor mass of 3.5 kg for the experiments. This varied the initial impact energy as 21–34 J.

(3) *Mass variation of impactor*: Five impact masses of 2.7, 3.1, 3.5, 3.9, and 4.3 kg were used. The specimen thickness used for the experiments was 2.4 mm and the initial velocity of the impactor in the shape of semi-cylindrical head was 3.9 m/s. This made the varying initial impacting energy to be coincident with the previous impact test case of velocity variation.

(4) *Shape variation of impactor*: The impactor shapes were varied as cone, flat, hemi-sphere, and semi-cylinder. The specimen thickness was 2.4 mm and the initial velocity and impactor mass were 3.94 m/s and 3.5 kg, respectively, to give an initial impact energy of 54.5 J.

3. Numerical study on the impact behavior of SMC

Experimental studies such as mentioned in the previous section are very useful in determining the impact behavior of materials. However, such methods are too time-consuming and expensive. Thus, in the present study, a numerical process to simulate impact reactions of materials was developed in an effort to increase the efficiency of the design of impact resisting structures. A damage model of SMC in consideration of failed

Table 2
Constituent properties of SMC

Composite constituents	Young's modulus (E) (GPa)	Poisson's ratio (ν)	Density (ρ) (g/cm^3)
Polyester (resin)	3.5	0.45	1.12
Calcium carbonate (filler)	41.4	0.21	2.77
Glass fiber	72.4	0.22	2.54
Kevlar fiber	131.0	0.25	1.44
Carbon fiber	227.0	0.25	1.72
High-modulus carbon fiber	482.0	0.25	1.90

elements was programmed into the user defined material subroutine of LS-DYNA3D to conduct simulations of the impact of SMC plates. Also, the material property of SMC was numerically predicted with knowledge of the fiber volume fraction distribution and constituents' material properties in an effort to increase the efficiency of simulations.

3.1. Damage model of SMC

Most composites are so brittle that they absorb energy mainly by elastic deformation and damage mechanisms. Damage mechanics must be well modeled to predict the energy dissipation rate accurately as it is the dominant energy absorbing mechanism. Generally, the material deterioration of SMC is initiated by internal defects such as cracks. Thus, continuum damage mechanics suggested by Kachanov [8] was applied to construct a damage model for SMC. The fundamental notion of this theory is to represent the damaged state of materials by cavities in terms of appropriate mechanical variables, and then to establish mechanical equations to describe the mechanical behavior of damaged materials.

For example, consider the tensile bar of Fig. 5 in which the cross-sectional area in the undamaged initial state and that in the current damaged state under stress σ are represented by A_0 and A, respectively. The damaged state of Fig. 5(b) can be represented by the damage variable d ($0 \leqslant d \leqslant 1$) where 0 and 1 indicate the initial undamaged state and the final fracture state, respectively. This variable is often interpreted as the effective area reduction caused by the internal cracks due to material damage. In other words, it is assumed that the load-carrying effective area of the bar is decreased from A to a certain smaller value A^* due to the generation of distributed cavities, and the damage variable d can be related to A^* as follows:

$$1 - d = A^*/A. \tag{3}$$

Reduction of the load-carrying effective area increases the stress induced by the external load T. The increased stress σ^* is usually called the effective stress and is given as follows:

$$\sigma^* = T/A^* = \sigma/(1-d). \tag{4}$$

Based on the above theory, a damage model for SMC was constructed using the linear damage function suggested by Pickett et al. [10]. A characteristic tensile stress–strain curve of SMC is shown in Fig. 6. It can be seen that SMC acts as an elastic material until the applied stress exceeds a certain limit, whereafter the stiffness of the material drastically decreases. The curve exhibits four distinct phases as follows:

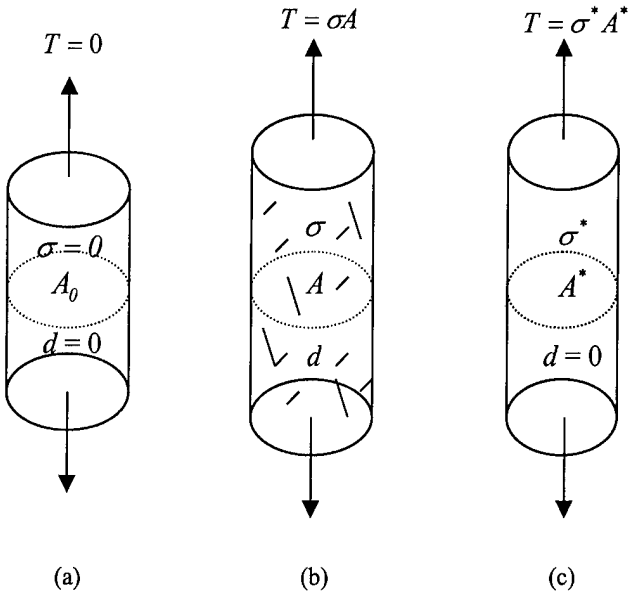

Fig. 5. Damage of a bar under uniaxial tension: (a) initial undamaged state, (b) current damaged state, and (c) fictitious undamaged state.

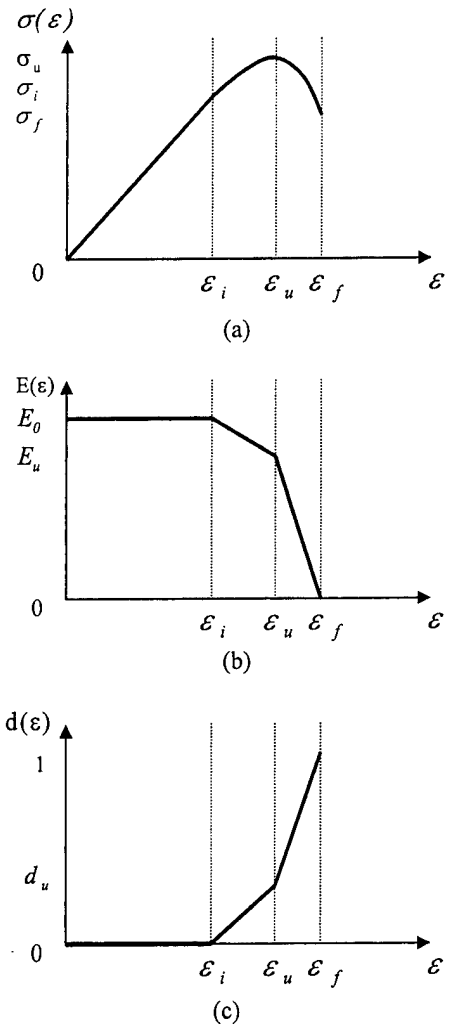

Fig. 6. Curves of (a) stress, (b) Young's modulus, and (c) damage versus strain.

1. In the initial linear state ($\varepsilon < \varepsilon_i$), there is no permanent deformation or damage.
2. In the first damaged state ($\varepsilon_i \leqslant \varepsilon < \varepsilon_u$), the stiffness decreases gradually.
3. In the second damaged state ($\varepsilon_u \leqslant \varepsilon < \varepsilon_f$), the load-carrying ability drastically decreases.
4. In the final failure state ($\varepsilon_f \leqslant \varepsilon$), complete failure occurs.

At each state, the damage function $D(\varepsilon)$ can be given as follows:

$$D(\varepsilon) = \begin{cases} 0, \varepsilon < \varepsilon_i, \\ \dfrac{\varepsilon - \varepsilon_i}{\varepsilon_u - \varepsilon_i} d_u, \quad \varepsilon_i \leqslant \varepsilon < \varepsilon_u, \\ \dfrac{\varepsilon - \varepsilon_u}{\varepsilon_f - \varepsilon_u}(d_f - d_u) + d_u, \quad \varepsilon_u \leqslant \varepsilon < \varepsilon_f, \\ 1, \varepsilon_f \leqslant \varepsilon. \end{cases} \tag{5}$$

Here, d is the damage variable and subscripts i, u, and f represent the initial damage occurring point, the ultimate stress point, and the final failure point, respectively. From this, the elastic modulus in relation to the damage function can be represented as follows:

$$E(\varepsilon) = (1 - D(\varepsilon))E_0. \tag{6}$$

Here, E_0 is the initial elastic modulus. And the stress–strain relationship in consideration of the damage effect can be given as follows:

$$\sigma(\varepsilon) = \begin{cases} E_0\varepsilon, \varepsilon < \varepsilon_i, \\ E_0\varepsilon\left(1 - \dfrac{d_u}{\varepsilon_u - \varepsilon}(\varepsilon - \varepsilon_i)\right), \quad \varepsilon_i \leqslant \varepsilon < \varepsilon_u, \\ E_0\varepsilon\left(1 - d_u - \dfrac{d_f - d_u}{\varepsilon_f - \varepsilon_u}(\varepsilon - \varepsilon_u)\right), \quad \varepsilon_u \leqslant \varepsilon < \varepsilon_f, \\ 0, \varepsilon_f \leqslant \varepsilon. \end{cases} \tag{7}$$

3.2. Prediction of SMC material property

The basic approach for predicting the material property suggested by Chang et al. [15] is shown in Fig. 7. First, the resin and filler are combined to form an effective matrix, which is then combined with the chopped fibers to form the final composites. Then, the effective bulk modulus and shear modulus of the matrix can be obtained from Hashin's expressions [13] as follows:

$$K_m = K_r + (K_p - K_r)\frac{(4G_r + 3K_r)v_p^*}{4G_r + 3K_p + 3(K_r - K_p)v_p^*}, \tag{8}$$

$$G_m = G_r\left(1 + \frac{15(1 - v_r)(G_p - G_r)v_p^*}{(7 - 5v_r)G_r + 2(4 - 5v_r)[G_p - (G_p - G_r)v_p^*]}\right). \tag{9}$$

$$v_p^* = \frac{v_p}{v_p + v_r}. \tag{10}$$

Here, the subscripts m, r, and p refer to the matrix, resin, and filler, respectively, v is the Poisson's ratio, G the shear modulus, K the bulk modulus, and v_p^* the effective filler volume fraction of the matrix component. Under the assumptions of the filled matrix being quasi-homogeneous and quasi-isotropic, the elastic modulus and Poisson's ratio, which are effective stiffness properties of the filled matrix, can be derived as follows:

$$E_m = \frac{9K_mG_m}{3K_m + G_m}, \tag{11}$$

$$v_m = \frac{3K_m - 2G_m}{2(3K_m + G_m)}. \tag{12}$$

Once the effective stiffness properties of the filled matrix component are known, the three-component composites can be represented as a fiber/matrix mixture. Then the stiffness properties of a two-dimensional, randomly

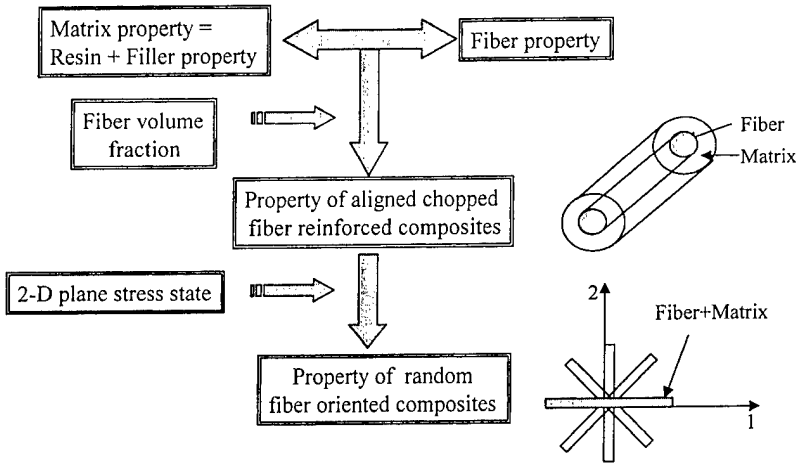

Fig. 7. Schematic diagram of the material property prediction process.

oriented fiber composites can be generated from that of a transversely isotropic, uni-directionally aligned fiber composites by assuming the fibers to be evenly oriented from 0 to π as follows:

$$E_c = \frac{1}{\pi}\int_0^{\pi} E(\theta)\,d\theta, \tag{13}$$

where E_c represents a stiffness property of the composites and $E(\theta)$ represents the stiffness property of an uni-directional composite oriented at an angle θ with respect to the material axis.

A transversely isotropic material has five independent elastic constants that are designated as E_{11}, v_{12}, G_{23}, G_{12}, and K_{23}. Here, the 2–3 plane represents the isotropic plane while the 1-direction is the fiber direction. As derived by Hill [12], the modulus and contraction ratio for the uni-axial condition are given as follows:

$$E_{11} = v_f E_f + v_m E_m + \left[4 v_f v_m (v_f - v_m)^2 \Big/ \left(\frac{v_m}{K_f + G_f/3} + \frac{v_f}{K_m + G_m/3} + \frac{1}{G_m}\right)\right], \tag{14}$$

$$v_{12} = v_f v_f + v_m v_m + \left[v_f v_m (v_f - v_m) \times \left(\frac{1}{K_m + G_m/3} - \frac{1}{K_f + G_f/3}\right) \Big/ \left(\frac{v_m}{K_f + G_f/3} + \frac{v_f}{K_m + G_m/3} + \frac{1}{G_m}\right)\right], \tag{15}$$

v_m and v_f refer to the volume fractions of the matrix and fibers, respectively. Based on the variational principle developed by Hashin [13], G_{23}, G_{12}, and K_{23} are obtained as follows:

$$G_{23} = G_m\left[1 + \left\{v_f \Big/ \left[\frac{G_m}{G_f - G_m} + \frac{(K_m + \frac{7}{3}G_m)v_m}{2(K_m + \frac{4}{3}G_m)}\right]\right\}\right], \tag{16}$$

$$G_{12} = G_m \frac{G_f(1 + v_f) + G_m v_m}{G_f v_m + G_m(1 + v_f)}, \tag{17}$$

$$K_{23} = K_m + \frac{G_m}{3} + \left(v_f \Big/ \left[\frac{1}{K_f - K_m + \frac{1}{3}(G_f - G_m)} + \frac{v_m}{(K_m + \frac{4}{3}G_m)}\right]\right). \tag{18}$$

Using the concept of Eq. (13) and Hill and Hashin's results given by Eqs. (14)–(18), Christensen et al. [14] obtained the effective stiffness properties of a two-dimensional randomly oriented fiber reinforced composites as follows:

$$E_c = \frac{1}{u_1}(u_1^2 - u_2^2), \tag{19}$$

$$v_c = \frac{u_2}{u_1}. \tag{20}$$

Here, the subscript c represents the final composite and u_1 and u_2 are given as follows:

$$u_1 = \frac{3}{8}E_{11} + \frac{G_{12}}{2} + \frac{(3 + 2v_{12} + 3v_{12}^2)G_{23}K_{23}}{2(G_{23} + K_{23})}, \tag{21}$$

$$u_2 = \frac{1}{8}E_{11} - \frac{G_{12}}{2} + \frac{(1 + 6v_{12} + 3v_{12}^2)G_{23}K_{23}}{2(G_{23} + K_{23})}. \tag{22}$$

Also, as the distribution of fibers is an important aspect influencing the mechanical properties of the final compression molded SMC product, the distribution of fiber volume fractions was considered in predicting the material property of SMC. The fiber volume fraction distribution was predicted in the manner proposed by Cheon et al. [16] in which the charge flow, heat transfer from molds, and curing reaction during compression molding were considered.

3.3. Impact simulation process and conditions

Impact simulations were carried out by using the commercial program LS-DYNA3D. The damage model of SMC was coded into the user defined material subroutine of LS-DYNA3D. In order to carry out more accurate simulations, an elimination routine of failed elements was added to represent cracks in the damaged specimen. If such an elimination routine is not considered, cracks in the specimen are not well taken into consideration such that the calculated dissipated impact energies will be overestimated since the failed elements will continue to absorb energy beyond its failure point. Also, the material property of SMC was predicted to be used in the impact simulations. The entire simulation process can be summarized as follows:

1. The fiber volume fraction distribution in the SMC flat plate is calculated by the finite element method as suggested by Cheon et al. [16].
2. Based on the fiber volume fraction distribution and constituents' material property, the material property of SMC is predicted by Eqs. (19) and (20) as given in Table 3.
3. The predicted material property is used in the damage model of SMC, represented in Eq. (7), which is coded into LS-DYNA3D.
4. Impact simulation is carried out and when an element is determined to be failed from damage model that element is eliminated from the current mesh system.
5. The dissipated impact energy is calculated from the difference between the initial and residual velocities of the impactor.

The simulation conditions were made to be consistent with the experimental tests and the simulations were carried out until complete failure was reached. The flat

Table 3
Predicted material properties of SMC used in simulations

Specimen	Material No.	Volume fraction	Young's modulus (E), GPa	Shear modulus (G), GPa	Poisson's ratio (ν)	Density (ρ) 10^3 (kg/m^3)
SMC-R30	1	0.2181	13.59	4.935	0.377	1.882
	2	0.2175	13.60	4.936	0.377	1.882
	3	0.2162	13.60	4.937	0.377	1.882
	4	0.2161	13.64	4.953	0.377	1.882
	5	0.2160	13.66	4.961	0.377	1.883

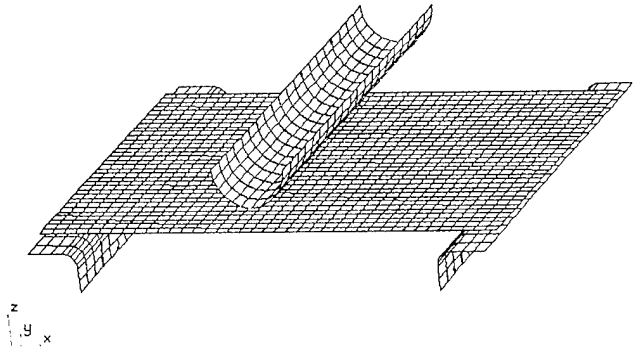

Fig. 8. Initial shape of the impactor, jig, and specimen for an impact analysis.

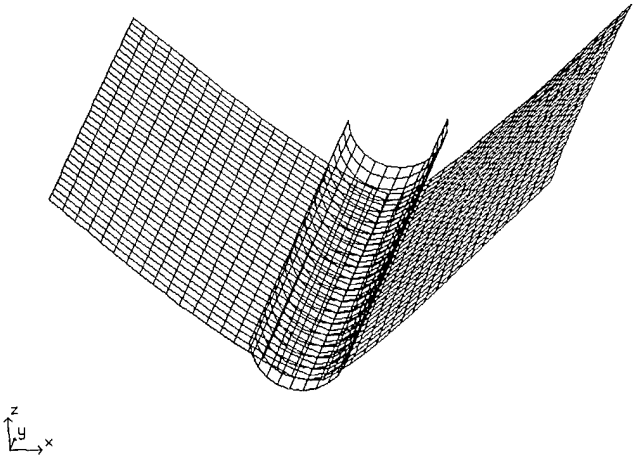

Fig. 9. Final deflection state of the specimen for an impact analysis.

plate specimen was modeled by 1300 shell elements and the jig and impactor were represented as rigid bodies. The friction coefficient between the specimen and both the jig and impactor was assumed to be 0.3. The specimen was assumed to be simply supported at two ends. The initial and final shapes of the specimen, jig, and impactor are shown in Figs. 8 and 9, respectively.

4. Results and discussion

In order to examine the factors which influence the dissipated impact energies of SMC plates, drop weight impact tests and numerical analyses were carried out for the following cases of thickness variation of SMC specimen and initial velocity and mass variation of the impactor. And the results of experiments and numerical simulations were compared to investigate the reliability of the developed simulation process. Also, impact tests were conducted with variation in impactor shapes to experimentally examine the effect of failure mechanisms on the level of dissipated impact energy.

4.1. Thickness variation of SMC specimen

The experimental and simulation data of dissipated impact energies calculated from the difference between the initial and residual velocities of the impactor are given in Fig. 10. It was found that the experimental data showed deviation of about 15%. This is due to inconsistent factors such as the vibrations of the specimen and jig, friction between the specimen and impactor, and energy dissipated into noise. Both the experimental and numerical results show that as the specimen thickness increases, the amount of dissipated impact energy increases. This is the reason why the ability of elastic absorption of impact energy is enhanced with increasing specimen thickness and more energy is required to cause damage for the thicker specimen. It can be seen that the trend of simulation

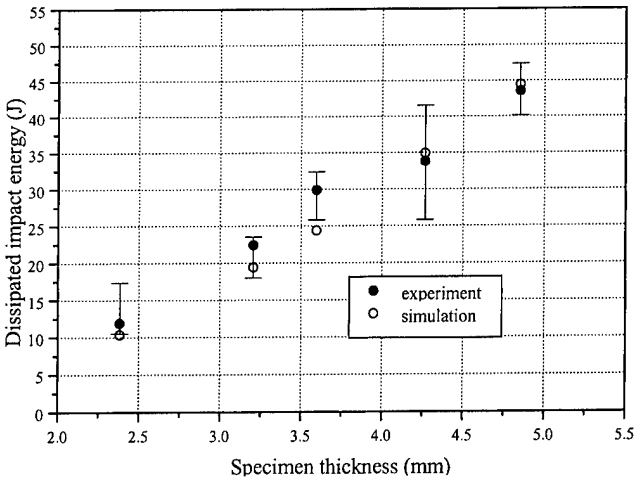

Fig. 10. Comparison of dissipated impact energy between simulation and experimental results for varying specimen thicknesses.

results coincides with experimental findings but the predicted numerical values are about 10–20% lower than the experimental values. Such discrepancy is invoked from the fact that energy dissipation mechanisms such as jig vibration, energy dissipated into noise, and force transfer to the jig were neglected in the simulation process. Although, such errors exist in the simulation process, the results can be considered satisfactory in the design perspectives since the predicted amount of dissipated energy is lower than the actual values. This means that the designed structure will have a certain amount of safety factor included.

A damaged specimen sample from the impact tests is shown in Fig. 11. Cracks propagated vertically from the middle of the bottom side of the specimen and fiber pull-out occurred due to the tensile stress induced by bending. In contrast, cracks can not be examined on the top side, where compressive stress acted to close voids and the cracks. In simulations, after the specimen was damaged and bent to the extent that it lost contact, it fell through the jig setting with the impactor. Such simulation results resembled the experimental observations.

4.2. Initial velocity and mass variation of impactor

In the case of the initial velocity variation of impact tests, the dissipated impact energies from experiment and simulation results did not change significantly although the initial impacting velocity was increased from 3.4 to 4.4 m/s as shown in Fig. 12. Generally, in the case of high velocity impact (impact velocity exceeding 10 m/s), major energy dissipation occurs in the form of local deformation and failure as the contact duration time is too short for the entire structure to react. So, velocity variation will likely invoke different dissipation modes and influence impact resistance. In contrast, when the contact duration time is long enough for the entire structure to react as in low velocity impact (impact velocity below 10 m/s), the dissipated impact energies remain almost constant regardless of the local strength and impact velocity. That is, the geometric structure of the specimen plays a much more important role in determining the amount of energy dissipation compared to velocity change in low velocity impact. The experimental and numerical results of dissipated impact energy in the case of mass variation are compared in

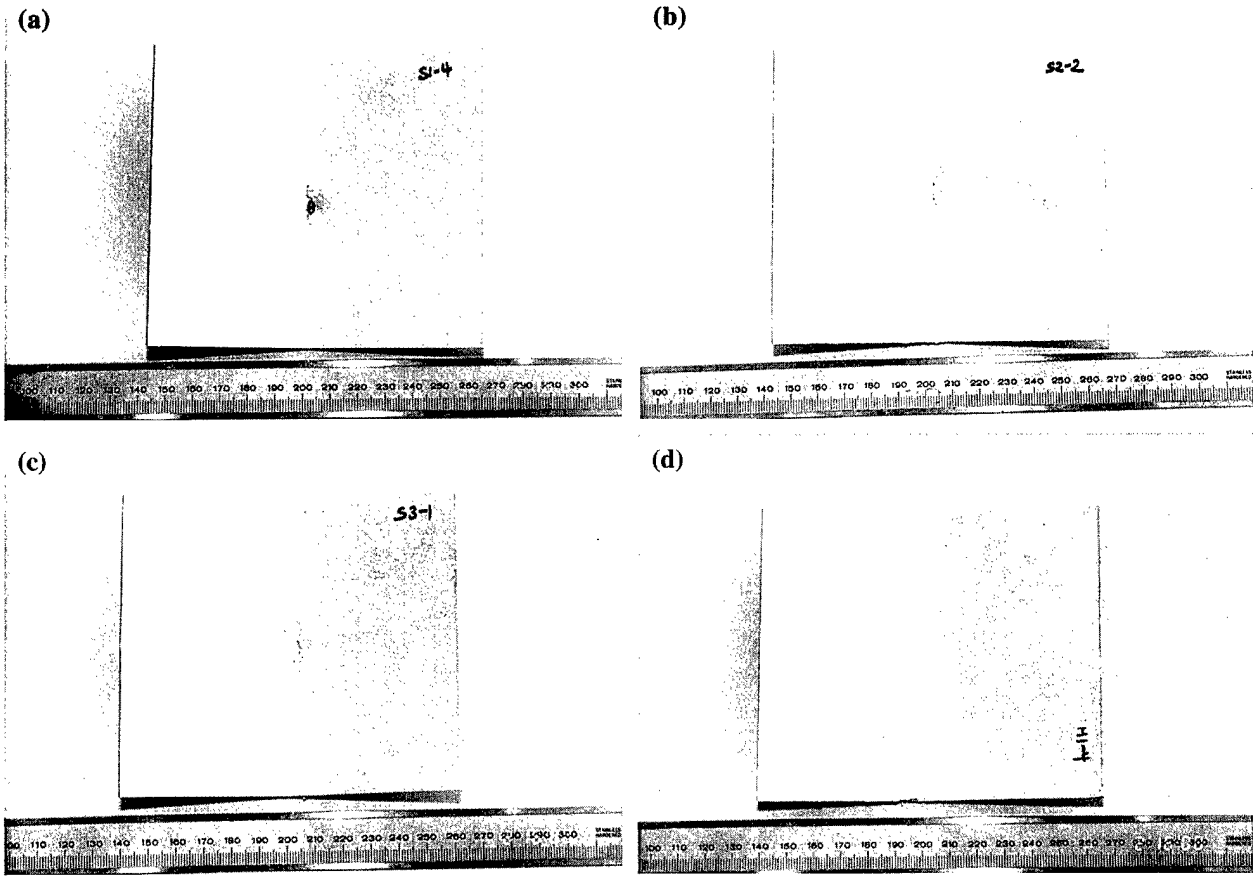

Fig. 11. Photographs of the resulting matrix cracking and indentation in specimens of the impact tests: the (a) conical, (b) flat, (c) hemi-spherical, and (d) semi-cylindrical shape impactors.

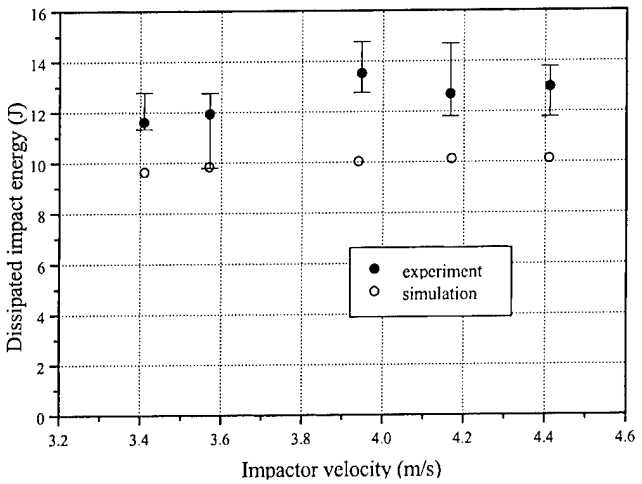

Fig. 12. Comparison of dissipated impact energy between simulation and experimental results for varying impacting velocities.

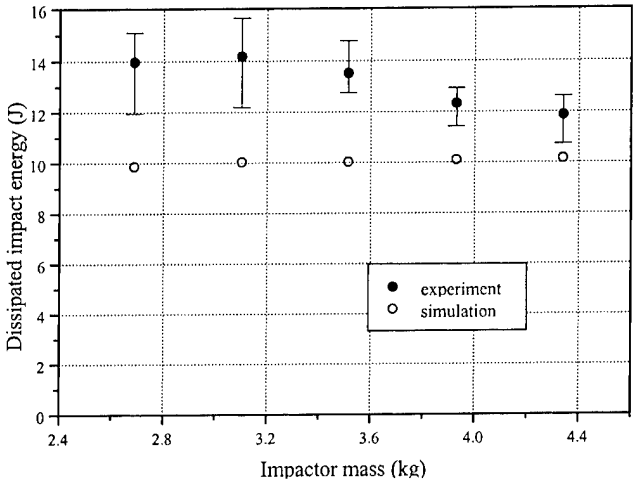

Fig. 13. Comparison of dissipated impact energy between simulation and experimental results for varying the masses of impactor.

Fig. 13. The initial impacting energies for this case were made to be consistent with these energies of the velocity variation tests. The results can be seen to be similar to the results of the velocity variation test results and comparison of simulation results with experiments follows the pattern discussed in the previous section.

Based on the above results, it was found that a specimen has a limited capacity to endure impact. Thus, impact behavior of SMC is mainly governed by the specimen geometry, however, the impactor mass and velocity do not significantly influence the amount of energy dissipation. It is likely that if experiments were conducted in a manner such that complete failure of the specimen did not occur then the variation of initial impact energy would have influenced the amount of dissipated impact energy due to impact. However, in the scope of the current study, in which complete failure of

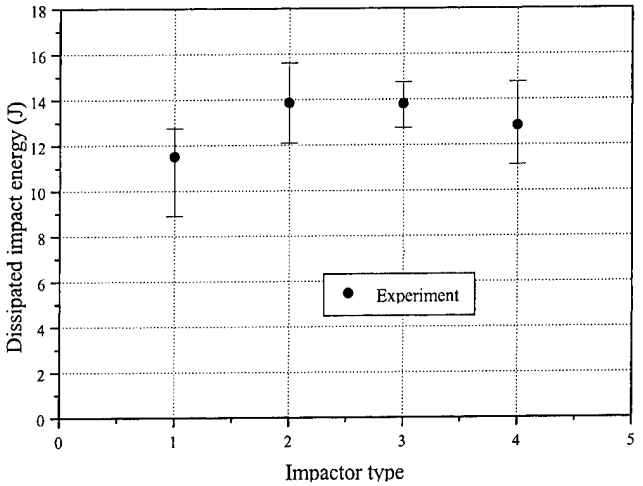

Fig. 14. Experimental graph of dissipated impact energy according to impactor types: (1) conical, (2) flat, (3) hemi-spherical, and (4) semi-cylindrical.

the specimen occurred, it was found that the specimen geometry determines the energy dissipation, and this is not influenced by variations in initial impact energy.

4.3. Shape variation of impactor

In order to examine the effect of failure mechanisms on the level of dissipated impact energies, experimental tests were conducted with different impactor types, namely, the cone, flat, hemi-sphere, and semi-cylinder types as shown in Fig. 3. The results are shown in Fig. 14, in which it can be seen that the different failure mechanisms induced by each impactor type affected the amount of dissipated impact energies. First, the flat and hemi-spherical types displayed similar energy dissipation levels and failure mechanisms. Compared to the semi-cylindrical type in which only a vertically propagating crack was observed, in the case of the flat and hemi-spherical types local indentation occurred and this extra failure mechanism acted to increase the energy dissipation capability of the specimen. In case of the conical type impactor, it was observed that local penetration occurred in the specimen. This penetration acted to drastically decrease the strength of the entire specimen such that the dissipated impact energy was the lowest among the tested impactor types. Thus, although the initial impact energy level had little influence, the type of failure mechanism induced by the impactor type affects the energy dissipation capacity of the specimen.

5. Conclusions

An experimental and numerical study was carried out to investigate the impact behavior of SMC plates. Drop

weight impact tests were carried out to examine the dissipated impact energies under different conditions of varying specimen thickness, initial impact velocity, and impactor mass. Also, in an effort to reduce the lead time of the design process, a numerical simulation process was developed. The results showed that geometry governed the impact energy dissipation capacity of the specimen and that this capacity was not significantly influenced by variations in initial impacting energies. However, it was found that different failure mechanisms induced by different impactor types affected this capacity. Also, comparison of experimental and numerical results showed that the numerical process provided results consistent with experimental observations. Although the predicted numerical values possessed errors, the results were such that the impact energy dissipation capacity of the specimen was underpredicted, which can lead to safer designs.

Acknowledgements

The authors wish to thank the Grant from the Ministry of Trade, Industry and Energy and the continuous financial support from Cheil Chemical Co. under which this work was possible. The support from Aekyung Chemical Co. for providing the material for this research is greatly appreciated also.

References

[1] Richardson MOW, Wisheart MJ. Review of low-velocity impact properties of composite materials. Composites A 1996;27:1123–31.
[2] Kakarala N, Roche JL. Experimental comparison of several impact test methods. Instrumented impact testing of plastics and composites materials. ASTM STP 1987;936:144–162.
[3] Siow YP, Shim VPW. An experimental study of low velocity impact damage in woven fiber composites. J Comp Mater 1998;32:1178–203.
[4] Zhou G. Damage mechanics in composite laminates impacted by a flat-ended impactor. Comp Sci Tech 1995;54:267–73.
[5] Lagace PA. Impact damage resistance of several laminated material systems. AIAA J 1995;33:1106–13.
[6] Cantwell WJ, Morton J. Geometrical effects in the low velocity impact response of CFRP. Comp Struct 1989;12:39–59.
[7] Kumar P, Rai B. Impact damage on single interface GFRP laminates- an experimental study. Comp Struct 1991;18:1–10.
[8] Kachanov LM. On rupture time under condition of creep. Izvestia Akademi Nauk SSSR, Otd Tekhn Nauk 1958;8:26–31.
[9] Murakami S. Mechanical modeling of material damage. J Appl Mech 1988;55:280–6.
[10] Pickett AK, Haug E, Rückert J. A fracture damaging law suitable for anisotropic short fibre/matrix materials in an explicit finite element code. Composites 1996;21(4):297–304.
[11] Hallquist JO. LS-DYNA3D USER'S MANUAL. Livermore Software Tech. Corporation, 1993.
[12] Hill R. Theory of mechanical properties of fiber-strengthened materials: I. Elastic behavior. J Mech Phys Solids 1964;12:199–212.
[13] Hashin Z. On elastic behavior of fiber reinforced materials of arbitrary transverse phase geometry. J Mech Phys Solids 1965;13:119–34.
[14] Christensen RM, Waals FM. Effective stiffness of randomly oriented fibre composites. J Comp Mater 1972;6:518–32.
[15] Chang DC, Weng GJ. Elastic moduli of randomly oriented, chopped-fibre composites with filled resin. J Mater Sci 1979;14:2183–90.
[16] Cheon JS, Im YT. Determination of short glass-fiber volume fractions in compression molded thermoset composites-numerical. J Comp Mater 1999;33(6):525–46.

ELSEVIER

Composite Structures 47 (1999) 563–569

COMPOSITE STRUCTURES

www.elsevier.com/locate/compstruct

External failure pressure of a frangible laminated composite canister cover

T.Y. Kam *, J.H. Wu, W.T. Wang

Department of Mechanical Engineering, National Chiao Tung University, Hsin-Chu 30050, Taiwan, ROC

Abstract

The static failure strength of a frangible laminated composite canister cover subjected to uniform external pressure is studied via both theoretical and experimental approaches. The frangible canister cover, which is fabricated with four plate-like laminated composite parts, which is designed in such a way that it will fail in a predetermined pattern when subjected to an impulsive internal pressure and its external failure pressure is much higher than its internal failure pressure. The stress distribution in the canister cover is determined using the finite element method and the failure of the cover identified on the basis of an appropriate failure criterion. A number of laminated composite canister covers were fabricated and subjected to static external pressure testing. The failure modes of the frangible covers are studied and the experimental results are used to verify the theoretical predictions. Close agreements between the experimental and theoretical results have been observed. The present study shows that the design of frangible covers with external failure pressure much higher than the internal failure pressure can be achieved. © 2000 Elsevier Science Ltd. All rights reserved.

Keywords: Laminated composite materials; Finite element method; Failure analysis; Frangible cover; Structure; Failure criterion

1. Introduction

The functions of a canister cover are to prevent the leaking out of the inert gas stored in a canister and protect the encanistered missile from attack by foreign objects. In the past, different types of canister covers have been designed and fabricated [1–6]. For instance, canister cover through which missiles exit from missile launchers have used rigid doors or covers that are ruptured by explosive means prior to missile launch. Recently, laminated composite materials have been used in the fabrication of canister covers. For instance, Doane [6] has designed a frangible fly through diaphragm for missile launch canisters using glass/epoxy laminae. The composite canister diaphragm was designed to fail in a predetermined pattern when impacted by the missile nose cone during launch. The disadvantage of this type cover is that it may damage the surface of the missile during the fly through process. Recently, Wu et al. [7] have developed a laminated composite frangible cover, which will not cause any damage on the missile during the fly through process. The special feature of the cover is that it will burst open in accordance with a predetermined pattern and let the encanistered missile fly out of the canister unharmedly when subjected to an internal impulsive pressure generated by the missile engine. Some preliminary results on the static internal failure pressure of the frangible cover have been reported in the literature [7]. In general, canister covers are used for a cluster of canisters. Therefore, the previously proposed frangible cover must also be able to sustain the thrust pressure induced by neighboring missiles during after launch. To ensure no failure occurs, the external failure pressure of the frangible cover must be properly determined.

In this paper, results on the external pressure resistance of the previously proposed frangible cover are presented. The static external failure pressure of the canister cover is studied via both theoretical and experimental approaches. A finite element model of the frangible cover is established and used for analyzing the stress distribution in the cover. The theoretical failure pressure of the canister cover is determined on the basis of the buckling or stress failure criteria. Static burst strength tests on a number of laminated composite canister covers were performed. Experimental results are used to validate the suitability of the design and verify the accuracy of the theoretical method for failure pressure prediction.

* Corresponding author. Tel.: +886-3-5725-634; fax: +886-3-5728-504.

E-mail address: tykam@cc.nctu.edu.tw (T.Y. Kam).

0263-8223/99/$ - see front matter © 2000 Elsevier Science Ltd. All rights reserved.
PII: S0263-8223(00)00022-2

2. Frangible laminated composite cover

The geometries of the previously proposed frangible laminated composite canister covers, namely, types CA and CB, are shown in Figs. 1 and 2, respectively. The covers (types CA and CB) are convex structures, which are fabricated with four plate-like laminated composite parts and a laminated composite frame. All the laminated composite components are adhesively bonded together along with their edges in forming the cover. The canister cover is designed in such a way that when subjected to an impulsive pressure, the adhesive bonds between the components will be broken and the severed plate-like laminated composite parts are blown away from the opening of the frame.

The laminated composite components of the canister cover are fabricated with two types of glass fabric/epoxy plies, namely, glass fabric A/epoxy and glass fabric B/epoxy. All the glass fabric/epoxy plies are balanced orthotropic materials for which the in-plane Young's moduli in material (fiber and matrix) directions, i.e., E_1 and E_2, are the same. The laminated composite components are fabricated in such a way that the stack of glass fabric B/epoxy plies is sandwiched in between those of glass fabric A/epoxy plies. The material properties of different cured glass fabric/epoxy plies are listed in Table 1. Referring to the lamina material directions, the stress–strain relations of a balanced orthotropic lamina can be expressed as

$$\begin{Bmatrix} \sigma_1 \\ \sigma_2 \\ \sigma_6 \end{Bmatrix} = \begin{bmatrix} Q_{11} & Q_{12} & 0 \\ Q_{12} & Q_{11} & 0 \\ 0 & 0 & Q_{66} \end{bmatrix} \begin{Bmatrix} \varepsilon_1 \\ \varepsilon_2 \\ \varepsilon_6 \end{Bmatrix}, \tag{1}$$

where σ_1, σ_2 are normal stresses, σ_6 is shear stress, $\varepsilon_1, \varepsilon_2$ normal strains, ε_6 is engineering shear strain. The components of the lamina stiffness matrix, Q_{ij}, are obtained as

$$Q_{11} = \frac{E_1}{1 - \nu_{12}^2}, \quad Q_{12} = \frac{\nu_{12} E_1}{1 - \nu_{12}^2}, \quad Q_{66} = G_{12}, \tag{2}$$

where ν_{12} is the Poisson's ratio, G_{12} is the in-plane shear modulus. The in-plane stress–strain relations of a balanced orthotropic laminate are expressed as

$$\begin{Bmatrix} \overline{\sigma}_1 \\ \overline{\sigma}_2 \\ \overline{\sigma}_6 \end{Bmatrix} = \frac{1}{h} \begin{bmatrix} A_{11} & A_{12} & 0 \\ A_{12} & A_{11} & 0 \\ 0 & 0 & A_{66} \end{bmatrix} \begin{Bmatrix} \varepsilon_1 \\ \varepsilon_2 \\ \varepsilon_6 \end{Bmatrix}, \tag{3}$$

where $\overline{\sigma}_i$ are average stresses, h is laminate thickness. The components of the laminate stiffness matrix, A_{ij} are obtained as

$$A_{ij} = \int_{-\frac{h}{2}}^{\frac{h}{2}} Q_{ij}\, \mathrm{d}z, \quad i,j = 1,2,6. \tag{4}$$

By inversion, Eq. (3) can be rewritten as

$$\begin{Bmatrix} \varepsilon_1 \\ \varepsilon_2 \\ \varepsilon_6 \end{Bmatrix} = h \begin{bmatrix} a_{11} & a_{12} & 0 \\ a_{12} & a_{11} & 0 \\ 0 & 0 & a_{66} \end{bmatrix} \begin{Bmatrix} \overline{\sigma}_1 \\ \overline{\sigma}_2 \\ \overline{\sigma}_6 \end{Bmatrix}, \tag{5}$$

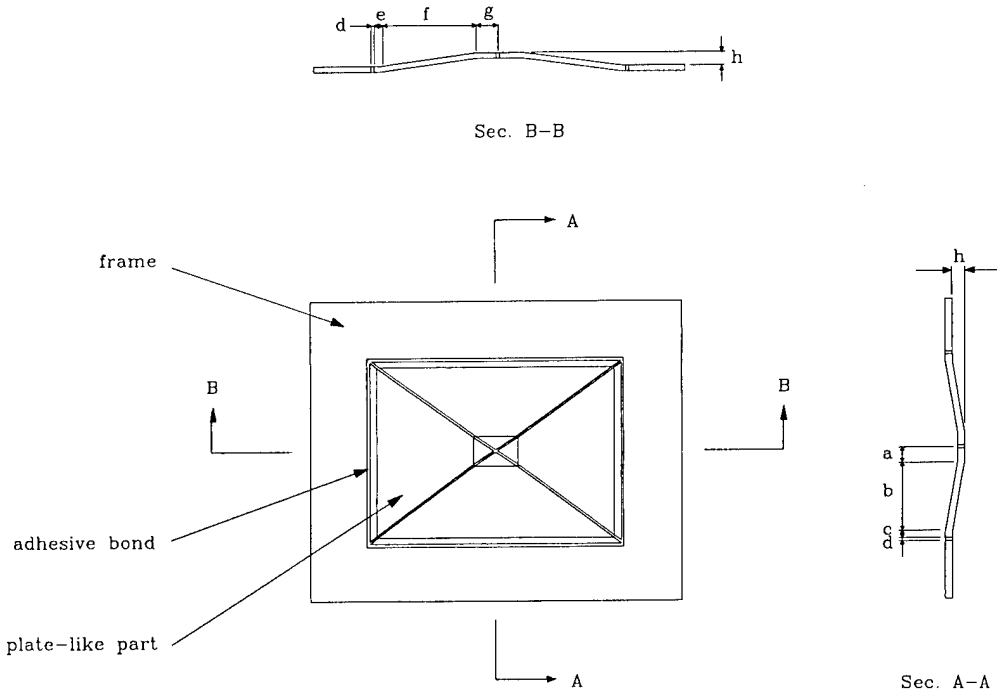

Fig. 1. Geometry of frangible canister cover CA.

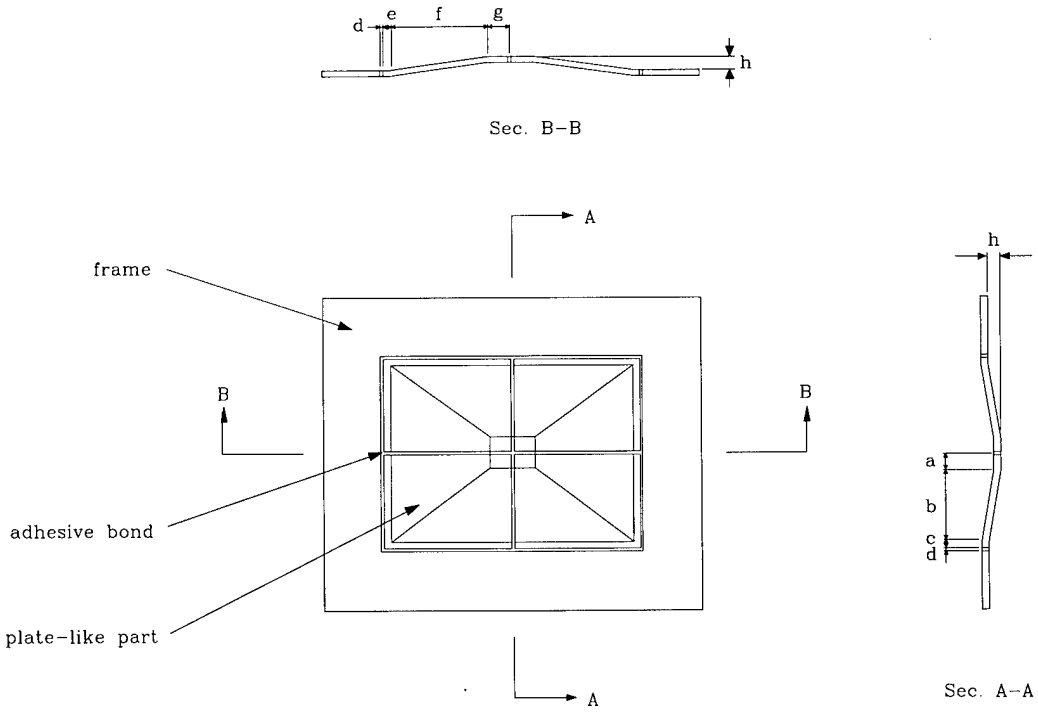

Fig. 2. Geometry of frangible canister cover CB.

Table 1
Properties of different composite laminae

Material type	Material constant[a]			Strength parameter[b]			Lamina thickness (mm)
	E_1 (GPa)	G_{12} (GPa)	ν_{12}	X_T (MPa)	X_C (MPa)	S (MPa)	
Glass fabric A/epoxy	19.70	1.03	0.106	184.33	251.56	57.48	0.22
Glass fabric B/epoxy	24.95	2.00	0.143	369.00	504.03	44.91	0.44

[a] Coefficients of variation are about 5%.
[b] Coefficients of variation are about 8%.

where a_{ij} are the components of the laminate compliance matrix. Once a_{ij} are known, the effective engineering constants of the balanced orthotropic laminate can be obtained as

$$\overline{E}_1 = \frac{1}{a_{11}h}, \quad \overline{\nu}_{12} = -\frac{a_{12}}{a_{11}}, \quad \overline{G}_{12} = \frac{1}{a_{66}h}, \tag{6}$$

where $\overline{E}_1, \overline{\nu}_{12}, \overline{G}_{12}$ are the effective in-plane longitudinal Young's modulus, Poisson's ratio, and shear modulus, respectively.

3. Failure analysis of frangible cover

The finite element method formulated on the basis of the theory of linear elasticity is used to evaluate the stress distribution in and buckling strength of the composite canister cover. In order to include all possible buckling mode shapes, the full cover is considered in the finite element analysis. Since the width, d, of the adhesive bond is much smaller than its depth. It will be more appropriate to model using the adhesive bond in three-dimensional (3D) brick elements than in two-dimensional (2D) plate elements. Therefore, all the components of cover CA are modeled by eight-node brick and six-node wedge elements while those of cover CB by eight-node brick elements. When constructing the finite element mesh, a number of layers of elements are considered in the thickness directions of the components and the aspect ratios of the elements are chosen in such a way that no numerical instability occurs. The material constants for the elements of the laminated composite components are determined on the basis of the concept of effective engineering constants as mentioned in the previous section. Furthermore, since the length-to-thickness ratios of the laminated components are large, it is reasonable to assume that the stress in the thickness direction is negligible. For simplicity, it is assumed that the material constants in the thickness direction have the following properties

$$\overline{E}_3 = \overline{E}_1, \quad \overline{\nu}_{13} = \overline{\nu}_{12}, \quad \overline{G}_{13} = \overline{G}_{12}, \tag{7}$$

Table 2
Properties of different types of adhesive

Adhesive type	Material constant[a]			Strength parameter[b]	
	E (GPa)	G (GPa)	v	X_T (MPa)	S (MPa)
I	1.264	0.498	0.269	31.57	6.837
II	1.251	0.496	0.261	21.5	4.125
III	1.231	0.491	0.253	18.3	4.524
IV	1.157	0.464	0.247	12.4	4.860
V	2.152	0.784	0.373	35.7	11.68

[a] Coefficients of variation are about 5%.
[b] Coefficients of variation are about 10%.

where $\overline{E}_3, \overline{\nu}_{13}, \overline{G}_{13}$ are effective Young's modulus, Poisson's ratio, and transverse shear modulus in the thickness direction, respectively. On the other hand, the adhesive is assumed to be isotropic. Different types of adhesive have been used in bonding the cover components and their material properties are listed in Table 2.

In the failure analysis of the canister cover, two types of failure modes, namely, material failure and structural instability are considered. For the case of material failure, two phenomenological failure criteria, namely, the Tsai–Wu and maximum stress criteria are used to study the incipient failures in the components. In particular, the incipient failure in the laminated composite components is identified using the Tsai–Wu criterion [8].

$$F_{11}\sigma_1^2 + 2F_{12}\sigma_1\sigma_2 + F_{22}\sigma_2^2 + F_{66}\sigma_6^2 + F_1\sigma_1 + F_2\sigma_2 = 1 \quad (8)$$

with

$$F_1 = \frac{1}{X_T} - \frac{1}{X_C}, \qquad F_{12} = -\frac{1}{2\sqrt{X_T^2 X_C^2}},$$

$$F_2 = F_1, \qquad F_{66} = \frac{1}{S^2}, \quad (9)$$

$$F_{11} = \frac{1}{X_T X_C}, \qquad F_{22} = F_{11},$$

where X_T, X_C are the in-plane lamina tensile and compressive strengths in the fiber direction, respectively, S is the in-plane shear strength. It is noted that the actual stresses rather than the average stresses in each lamina of the laminated composite components are used in the above failure criterion for failure prediction. On the other hand, the incipient failure in the adhesive bonds is identified using the maximum stress failure criterion, which states that failure of the material is assumed to occur if any of the following conditions is satisfied

$$\sigma_{max} \geqslant X_T' \quad \text{or} \quad \tau_{max} \geqslant S', \quad (10)$$

where σ_{max}, τ_{max} are the maximum principal and shear stresses, respectively, X_T', S' are adhesive tensile and shear strengths, respectively. It is noted that failure of an adhesive bond line is always induced by the maximum tensile stress developed in the adhesive. The value of the maximum shear stress is small and its effect on the failure of adhesive is minimal. Since the adhesive used in fabricating the frangible covers is brittle, it is thus appropriate to predict adhesive failure using the maximum stress criterion. For the case of structural instability, the buckling pressure is determined by solving the following eigenvalue problem.

$$KD = \lambda K_g D, \quad (11)$$

where K, K_g are structural stiffness and geometric stiffness matrices, D the vector of nodal displacements, λ is the buckling pressure.

4. Experimental investigation

A number of frangible laminated composite canister cover specimens were fabricated and subjected to external static pressure tests. The dimensions of the test specimens are listed in Table 3. The notation used for denoting the lay-up of a laminated composite component is $[A_n/B_m]_s$ where A and B denote the laminae of fabric A/epoxy and fabric B/epoxy, n and m numbers of plies, and s is symmetric lamination. A schematic description of the experimental setup for external static pressure test is shown in Fig. 3. The frame of the cover specimen under testing was properly clamped on the lug at one end of the cylindrical pressure tank while air was pumped into the tank from the other end. It is noted

Table 3
Dimensions of different cover specimens

Cover specimen	Dimensions (mm)							
	a	b	c	d	e	f	g	h
Small scale	10	50	5	1	5	65	15	8
Full scale	50	250	10	2	10	325	75	40

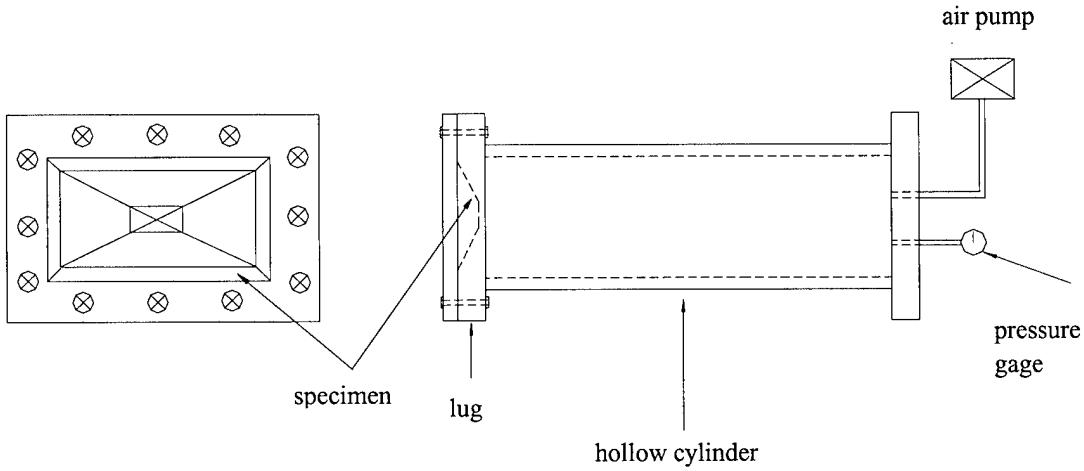

Fig. 3. Experimental setup for burst strength test.

that the convex side of the cover is facing toward the cylindrical pressure tank. The flow rate of the air pumped into the tank was slow enough that no excitation of the specimen was induced. The ultimate pressure that the specimen could sustain was measured via a pressure gauge attached to the tank. Visual inspection of the cover specimens, which had been tested and showed that failure always occurred at the adhesive bond lines between the plate-like parts and the rectangular frame. It is noted that since both buckling and material failure may lead to the same failure pattern of the frangible covers, the failure modes of the covers cannot be identified directly by pure visual inspection of the failed specimens.

Table 4
Convergence test of the finite element model for the full-scale $[A_2/B_5]_s$ cover CB

Mesh type	Number of nodes	Number of elements	Buckling pressure (kPa)
I	2489	2416	115.66
II	3217	3136	115.68
III	3952	4041	115.70

5. Results and discussion

The aforementioned methods for failure prediction are used to predict the external failure pressure of the frangible laminated composite canister covers that are to

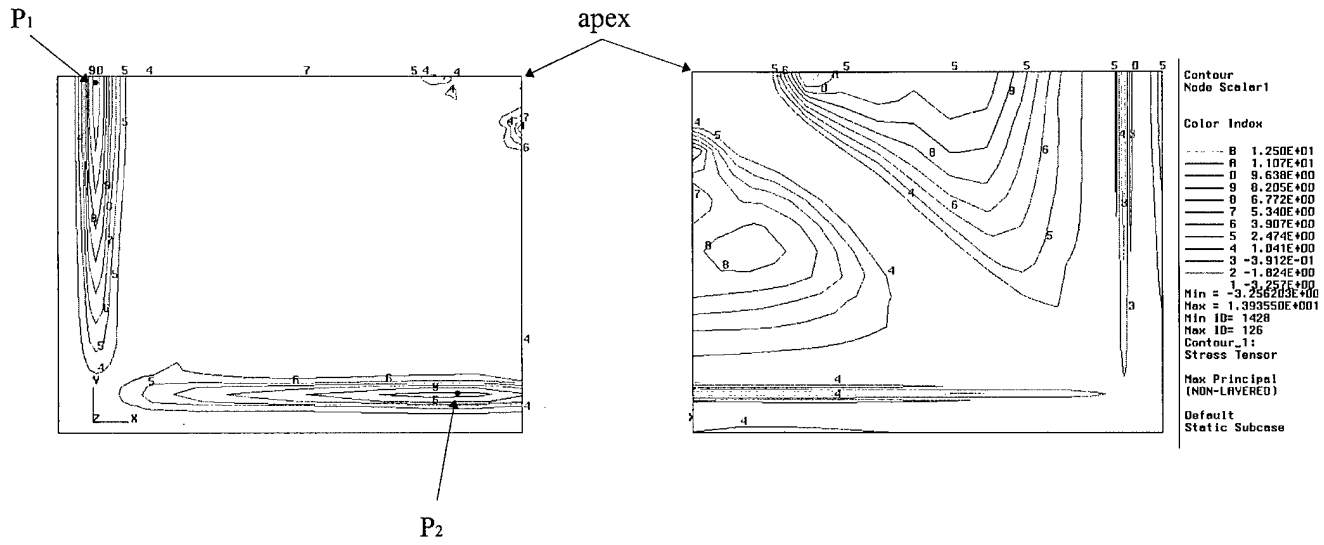

Fig. 4. Distribution of the maximum principal stress in $[A_2/B_2]_s$ quarter cover CA.

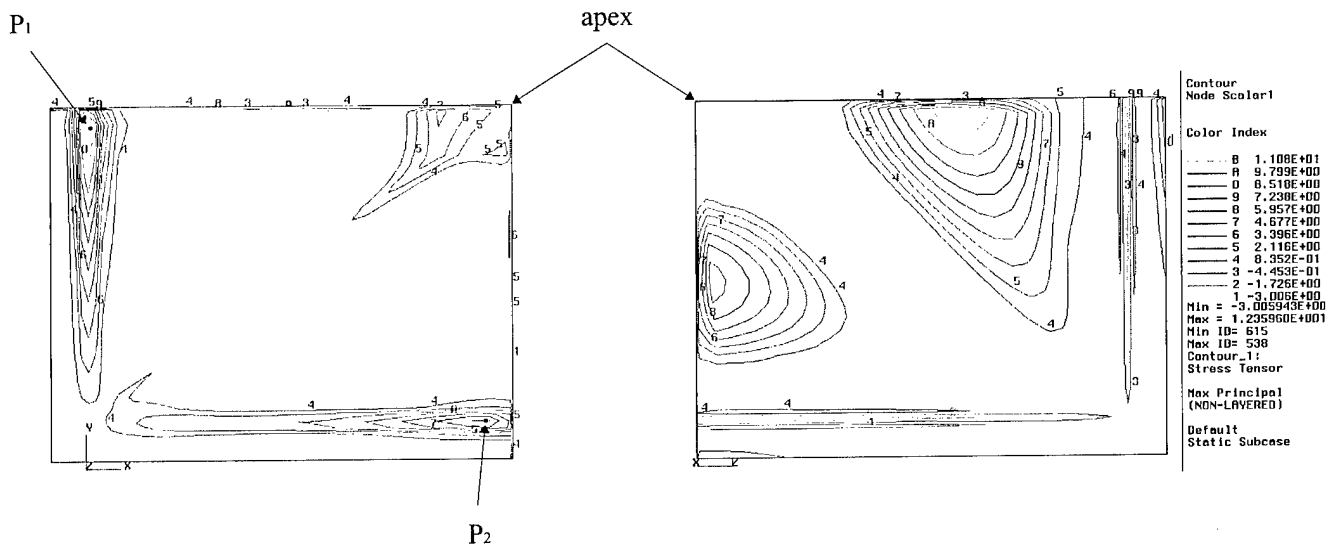

(a) Top view (b) Bottom view

Fig. 5. Distribution of the maximum principal stress in $[A_2/B_2]_s$ quarter cover CB.

Table 5
External failure pressure of small-scale frangible canister covers

Cover specimen			External failure pressure (kPa)					Internal failure pressure (kPa)
Lay-up	Adhesive type	Cover type	Experimental (I)	Theoretical		Percentage difference		
				Buckling (II)	Material failure (III)	$\left\|\frac{I-II}{I}\right\| \times 100$	$\left\|\frac{I-III}{I}\right\| \times 100$	
$[A_2/B_2]_s$	II	CA	172.4	617.8	153.1	258.4	11.2	86.19
		CB	165.5	582.6	148.9	252.0	10.3	96.53
$[A_2/B_3]_s$	II	CA	>206.9	933.6	256.5	–	–	103.43
		CB	>206.9	862.6	253.7	–	–	110.32
	III	CA	>206.9	924.6	217.9	–	–	93.08
		CB	>206.9	857.7	212.4	–	–	93.08

Table 6
External failure pressure of full-scale frangible canister covers

Cover specimen			External failure pressure (kPa)			Percentage difference	
Lay-up	Adhesive type	Cover type	Experimental (I)	Theoretical		$\left\|\frac{I-II}{I}\right\| \times 100$	$\left\|\frac{I-III}{I}\right\| \times 100$
				Buckling (II)	Material failure (III)		
$[A_2/B_2]_s$	IV	CB	72.4	273.0	79.3	277.1	9.5
$[A_2/B_3]_s$	IV	CB	103.4	390.3	99.3	277.5	4.0

be tested. Herein the commercial finite element code NASTRAN [9] is used to perform the finite element analysis of the covers. All the laminated composite components and adhesive bond lines of the frangible covers are modeled by the aforementioned 3D elements. A convergence test of the finite element model for buckling analysis is first performed to determine the suitable finite element mesh. For illustration, the buckling pressure of the $[A_2/B_{10}]_s$ cover CB has been determined using different types of finite element mesh and the results are listed in Table 4. It is noted that the differences among the buckling pressures predicted by the various types of finite element mesh are small. For the sake of saving computing time, mesh type I will be adopted in the failure analyses of the other frangible covers. It's worth noting that the buckling mode associated with the buckling pressure is symmetric with respect to the planes of symmetry of the covers. The

maximum principal stress distributions of the quarter $[A_2/B_2]_s$ covers CA and CB (full-scale) subjected to external pressure of magnitude 68.95 kPa are shown in Figs. 4 and 5. If failure of frangible covers is predicted on the basis of the maximum stress criterion then it is obvious that points P1 and P2 in the adhesive bond lines between the rectangular frame and the plate-like parts are likely to be the locations, where incipient failure will be incurred in the frangible cover. The theoretically predicted failure locations of the cover specimens seem to conform with those observed experimentally. Based on different failure criteria, the theoretical failure pressures of various frangible cover specimens are computed and the results listed in Tables 5 and 6 in comparisons with the experimental results. In Table 5, the experimental failure pressures of the $[A_2/B_3]_s$ covers CA and CB exceed 206.9 kPa at which the tests were terminated. In view of the results in Tables 5 and 6, it is obvious that the failure mode of the covers is material failure and the theoretical method can produce reasonable predictions of the failure pressure of the covers. The errors in the theoretical predictions of the failure pressure based on the material failure criterion can be attributed to the existence of uncertainty in the material properties. It is also noted that the covers with same size, cover CA is generally stronger than cover CB. The thickness of the bond lines, i.e., the thickness of the laminated components has important effects on the failure pressure of the covers. The increase in the thickness of the bond lines can raise the failure pressure of the covers. A comparison between the external and internal failure pressures of the small-scale covers is also performed. As indicated by the results listed in Table 5, it is obvious that the external failure pressure of the covers is much higher than their internal failure pressure.

6. Conclusions

The external failure pressures of two new frangible laminated composite canister covers were studied via both theoretical and experimental approaches. The failure mode of the frangible covers under external pressure was identified to be material failure. Good agreements between the theoretical and experimental results were observed. The thickness of the bond lines between the rectangular frame and the plate-like parts of the covers had important effects on the failure pressure of the covers. It was also shown that different types of cover designs (CA or CB) could have different external pressure resistance. It is recommended that both external and internal pressure resistance of a frangible cover be considered simultaneously if a proper design of the cover is to be pursued.

Acknowledgements

This research was supported by the National Science Council of the Republic of China under grant No. NSC 86-2623-D-009-008. Their support is gratefully acknowledged.

References

[1] Bell RE. Missile weapon system. US Patent No. 5239909, 1992.
[2] Boeglin PH. Plate-glass fitted with an explosion-cutting device. US Patent No. 4333381, 1982.
[3] Mussey RA. Launch tube closure. US Patent No. 4301708, 1981.
[4] Copeland RL, Greene RF. Protective cover for a missile nose cone. US Patent No. 3970006, 1976.
[5] Krol UB. Frangible cover assembly for missile launchers. US Patent No. 3742814, 1971.
[6] Doane WJ. Frangible fly through diaphragm for missile launch canister. US Patent No. 4498368, 1985.
[7] Wu JH, Wang WT, Kam TY. Failure analysis of a frangible laminated composite canister cover. In: Proc Inst Mech Eng, vol. 213, Part G, 1999, p. 187–95.
[8] Tsai SW, Hahn HT. Introduction to composite materials. Westport, Connecticut: Technomic Publishing Company, 1980.
[9] Caffrey JP, Lee JM. MSC/NASTRAN linear static analysis user's guide version 68. Los Angeles, USA: The Macneal-Schwendler Corporation, 1994.

ELSEVIER

Composite Structures 47 (1999) 571–580

COMPOSITE STRUCTURES

www.elsevier.com/locate/compstruct

Flexure of pultruded GRP beams with semi-rigid end connections

G.J. Turvey *

Engineering Department, Faculty of Applied Sciences, Lancaster University, Bailrigg, Lancaster LA1 4YR, UK

Abstract

Details of a series of three point flexure tests on 101.6×101.6×6.4 mm Wide Flange (WF)-section, pultruded Glass Reinforced Plastic (GRP) beams are presented. The beams were tested at four spans ($L/d = 21$–45) under four sets of end conditions: clamped, bolted web and flange cleats, bolted web cleats and simply supported. Mid-span deflections and beam end rotations were recorded in the tests. The observed deflections and end rotations are compared with semi-rigid shear deformable beam theory predictions. Reasons are given for the differences (not large in the majority of cases) between the observed deflections and end rotations and the theoretical predictions. It is shown that deflection reduction and load enhancement performance indices provide a better basis for comparison of the experimental results and the theoretical predictions. The comparisons demonstrate and quantify the improvements in structural performance, arising from the inherent rotational stiffness of practical end connections, which could be utilised at no extra cost by adopting a semi-rigid design philosophy. © 2000 Elsevier Science Ltd. All rights reserved.

Keywords: Beams; Connections; Flexure; GRP; Pultrusions; Semi-rigidity; Testing; Theory

Notation

A	gross area of beam cross-section
A_w	web area of beam cross-section
d	beam depth
E	longitudinal elastic modulus of beam
G	shear modulus of beam
I	second moment of area of beam cross-section
$k_i (i = 1$–$4)$	constants which depend on the load configuration
K	rotational stiffness of the end connection
Q	point load at the mid span of the beam
$\alpha (= EI/GAL^2, EI/GA_wL^2)$	dimensionless shear flexibility of the beam
$\beta (= EI/KL)$	dimensionless flexibility of the beam end connection
λ_δ	deflection reduction index
λ_Q	load enhancement index

1. Introduction

Pultruded Glass Reinforced Plastic (GRP) beams are used in both secondary and primary load bearing structures in those sectors of the engineering industry where their advantageous properties, e.g., low weight, high corrosion resistance etc, may be exploited to full advantage. Typically, they are used in frameworks supporting platforms, storage vessels, pipework etc. Such frames usually have bolted connections similar to those in steel construction. Presently, knowledge of the behaviour of bolted connections in pultruded GRP materials remains limited, even though research directed towards acquiring this knowledge has been in progress for almost a decade (see Refs. [1–6]). Procedures for the design of bolted, bonded or combined connections to transmit bending moments and shear forces between pultruded GRP structural profiles are not at all well developed. The guidance given in manufacturers' and other design manuals (see Refs. [7–10]) is mostly concerned with axial load transfer in plate to plate type joints. Limited knowledge of the behaviour of connections in which moment transfer across the connection arises and the absence of reliable procedures for their design has forced structural engineers to adopt a conservative approach to the design of joints in pultruded GRP frame structures. In consequence, joints are generally assumed to behave as if pinned and

* Tel.: +44-01524-593088; fax: +44-01524-381707.
E-mail address: engineering@uk.ac.lancs.comp (G.J. Turvey).

0263-8223/99/$ - see front matter © 2000 Elsevier Science Ltd. All rights reserved.
PII: S0263-8223(00)00024-6

bracing is used to resist any horizontal loading on the frame. Such conservatism reduces the competitiveness of pultruded GRP profiles relative to conventional structural materials such as aluminium and stainless steel.

One approach to improving the structural performance and, hence, the competitiveness of pultruded GRP profiles is to account for end connection stiffness (there is always some rotational stiffness present in practical connections) in design, i.e. to adopt a semi-rigid design philosophy. However, designers need to be persuaded of the benefits of adopting what, even for structural steelwork, is widely regarded as a radically new and less conservative approach to design. Some progress has been made towards *making the case* for moving to a semi-rigid design philosophy for pultruded GRP frame structures. Mottram and Zheng [11] and Turvey [12] have developed analyses for beams with semi-rigid end connections and, using rotational stiffnesses derived from connection tests, have shown that beam deflections may be reduced significantly (10–40%) compared to simply supported beams. Further theoretical research by Zheng and Mottram [13] and Mottram and Zheng [14] has shown similar benefits for plane frames with semi-rigid joints. However, if structural designers are to be convinced of the benefits of adopting a semi-rigid design philosophy, theoretical evidence is not enough-test data are also needed. Recognition of this need was the catalyst for undertaking the investigation reported herein. The aim was to demonstrate, using simple test procedures, that the benefits in structural performance predicted by analysis are indeed realisable in practice. It was, therefore, expected that load-deformation response data from tests on beams with practical end connections could provide the information needed to show the structural performance benefits achievable with semi-rigid design. A review of the literature on flexural testing of pultruded GRP profiles, especially profiles with a variety of end connections, revealed, rather to the author's surprise, that tests of this nature had not been undertaken. A number of short span, simply supported beam tests have been carried out to determine elastic moduli for different profiles (see Refs. [15–17]) and also to study buckling phenomena, especially local and lateral buckling (see Refs. [18–21]). Some of the latter test work has involved beams with practical end connections. However, it appears that no tests have been reported in the literature on serviceability testing (maximum deflections up to about $L/100$) of beams with various end connections. Thus, it was decided to undertake a series of small deformation flexure tests on pultruded GRP beams with idealised and practical (semi-rigid) end connections in order to generate the data needed to show that the performance benefits predicted by semi-rigid beam theory are indeed realisable in practice.

Three point flexure tests were carried out on a pultruded GRP Wide Flange (WF) section beam for a range of spans between 2 and 5 m. For each span the beam was tested under four sets of end conditions. Two were idealised, viz. rigidly clamped and simply supported, and two were bolted web and flange and web cleat connections. Details of the test setup, joint configurations and test procedure are described. Mid-span deflections and associated loads recorded in the tests are compared with theoretical predictions evaluated using the formulae given in [12] and good agreement between experiment and theory is demonstrated for three of the four end conditions. Moreover, for practical end connections, the test results quantify the reductions in mid-span deflection and the increases in load carrying capacity relative to simply supported beams and also provide quantitiative evidence that using a semi-rigid approach to design does indeed lead to structural performance and efficiency gains compared with the current conservative design approach.

2. Beam details

As no data on flexure testing of pultruded GRP beams with practical end connections was available for comparison with the semi-rigid beam analysis presented in Ref. [12], it was decided to undertake a series of three point flexure tests. A 101.6×101.6×6.4 mm EXTREN® 500 Series WF section was chosen for the beam. The constituents of this WF-section are: *E*-glass reinforcement (rovings and continuous filament mat), polyester resin and filler. Typically, their volume percentages are: 40% glass, 55% polyester resin and 5% filler. Fig. 1 shows the fibre architecture in a short length of this profile after burning off the resin matrix.

Minimum values of the elastic moduli of this WF-profile are given in Ref. [7] based on both coupon and beam flexure tests. In order to check the manufacturer's

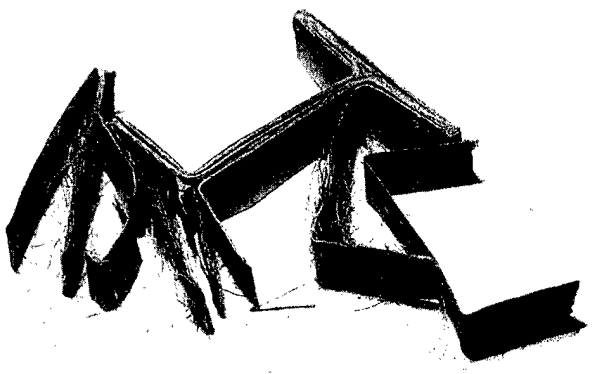

Fig. 1. Fibre architecture of a 101.6×101.6×6.4 mm^3 WF-section after resin burn-off test.

values three parallel-sided coupons, each nominally 25 mm wide, were cut (longitudinally) from the web and flanges of a length of the profile. They were tested in tension without end tabs up to a load of 15 kN (nearly one third of the failure load). The longitudinal extensions of each coupon were recorded using a pair of mechanical extensometers, each with a 50 mm gauge length, arranged back to back on the coupon. The average value of the longitudinal tension modulus was 19.4 kN/mm^2 which is about 8.4% higher than the minimum value of 17.9 kN/mm^2 given in [7].

The intention was to conduct three point flexure tests for a range of beam spans and generate load and deformation data in order to verify the theoretical structural performance benefits attributable to the end connection stiffnesses. As the WF-profiles are supplied in standard lengths of about 6 m, this determined the upper limit on the span for the beam tests. Two other factors, viz. the size and layout of the end connections and the grid spacing of the reaction points on the laboratory strong floor, also influenced the selection of the test spans. Taking account of these constraints, it would have been feasible to carry out three point flexure tests at six spans, ranging from 1.320 to 5.382 m, i.e., span to depth (L/d) ratios ranging from about 13 to 53. Because of time constraints, no tests were carried out at the shortest span. Moreover, only one test (under clamped end conditions) was carried out at the longest span, because lateral buckling tended to arise before the serviceability deflection limit (about $L/100$) was reached. Consequently, beam flexure tests were conducted for the following spans: 2.135 m ($L/d=21$), 2.950 m ($L/d=29$), 3.746 m ($L/d=36.9$) and 4.570 m ($L/d=45$).

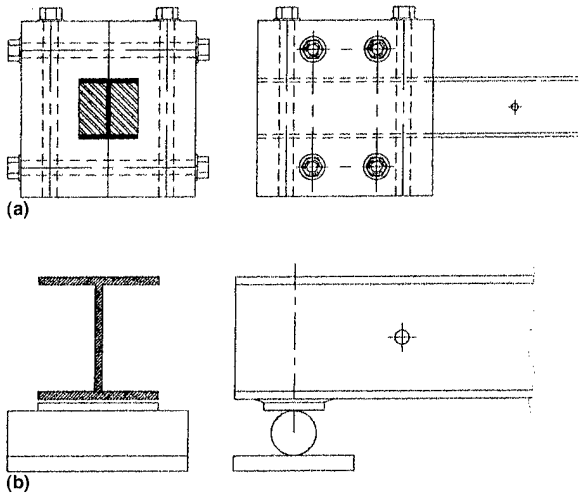

Fig. 2. Idealised end support conditions: (a) clamped and (b) simply supported.

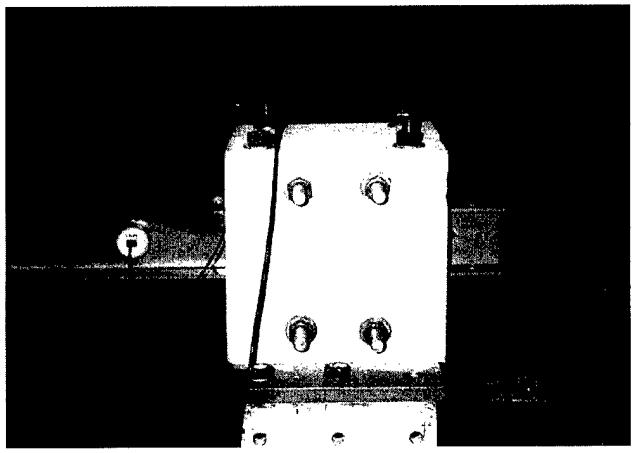

Fig. 3. Concrete blocks used to simulate clamped end support conditions.

3. End connection details

The beams were tested with nominally identical support conditions at each end. Four sets of support conditions were considered. Two of the conditions – rigidly clamped and simply supported – are idealised and constitute two extremes of the spectrum of practical end conditions. The clamped end condition was simulated with a pair of recessed concrete blocks (300×300×150 mm) and timber packing pieces, as shown in Fig. 2(a). Four bolts, which passed through horizontal holes in the concrete blocks, were used to clamp them firmly to the beam ends. A further four bolts, which passed through vertical holes, clamped the blocks to a horizontal, rigid steel base and prevented them from rotating in a vertical plane (see Fig. 3). The simply supported end condition was provided by a solid circular cross-section steel rod in contact with a flat aluminium plate bonded to the beam soffit, as shown in Fig. 2(b).

The two practical end connections were bolted web and flange and bolted web cleat arrangements. Details of the layout of the web and flange cleat connection are shown in Fig. 4. The layout details of the web cleat connection are as shown in Fig. 4 but with the flange cleats removed. The cleats were cut from 101.6×101.6×9.5 mm EXTREN® 500 Series pultruded GRP angle. 10 mm diameter mild steel bolts were used in close tolerance holes with the smooth parts of their shanks in contact with the cylindrical walls of the holes. The bolts were torqued to 20 Nm. The legs of the angles not connected to the flanges and web of the beam were bolted to the vertical leg of a 20 mm thick welded mild steel angle which was braced against rotation by means welded triangular side stiffeners (see Fig. 5). The horizontal leg of the mild steel angle was bolted to a horizontal, rigid steel base.

The layouts of the bolted cleat connections were similar to those described in Ref. [5] and their initial rotational stiffnesses are stated as 85 kNm/rad for the

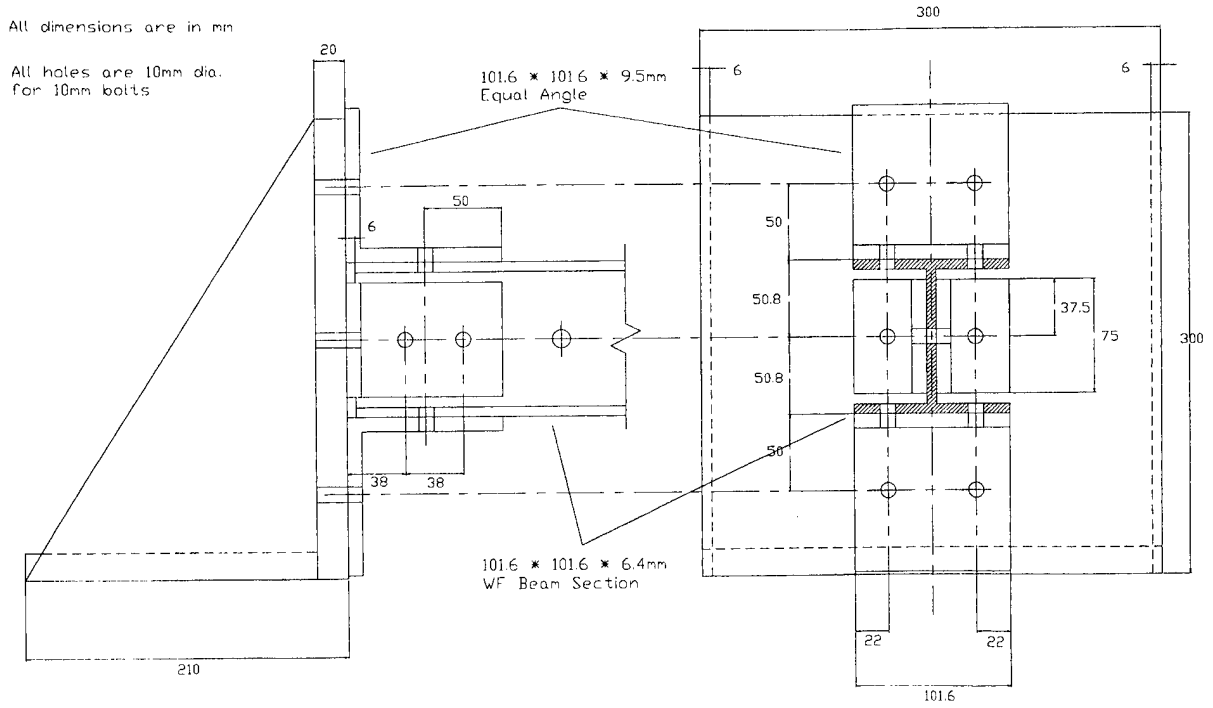

Fig. 4. Details of bolted web and flange cleat connection (*Note*: The bolted web cleat connection details are similar but with the flange cleats removed).

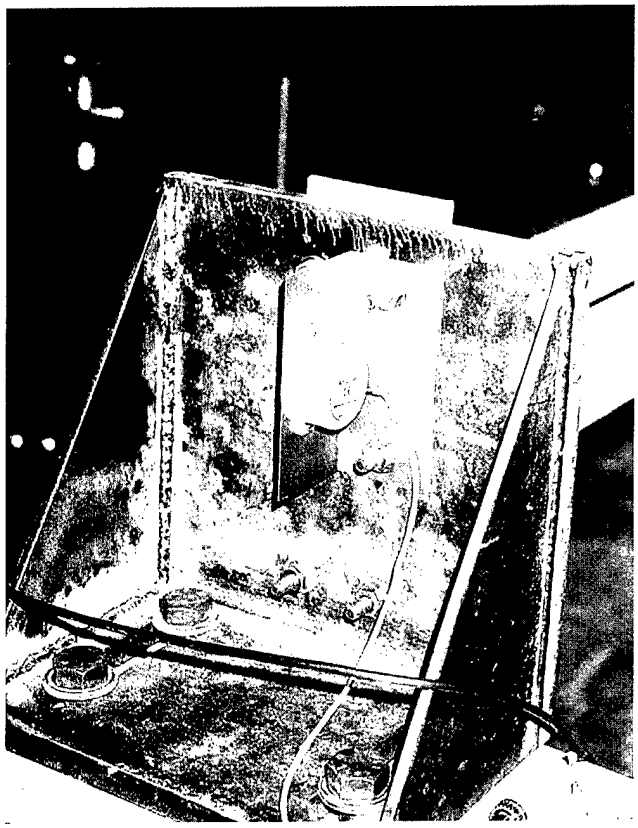

Fig. 5. Welded steel angle with triangular welded side plates.

web and flange cleat connection and 14 kNm/rad for the web cleat connection.

4. Test set up and test procedure

The beam flexure tests were carried out using a single 6 m length of 101.6×101.6×6.4 mm pultruded GRP WF-section in order to economise on the use of the material. Consequently, it was necessary to carry out the tests in a particular order. Testing started at the longest beam span and all flexure tests were completed at this span before the ends of the beam were removed for testing at the next shorter span. For each span the overall length of the beam varied slightly in order to satisfy the particular requirements of each type of end connection. For clamped ends, the beam needed to be 600 mm longer than the test span, so that the concrete blocks could be tightened against the beam section over their whole lengths. Likewise, for simply supported ends, the beam needed to be 100 mm longer than the test span. And, for the bolted cleat connections, the beam needed to be 12 mm shorter than the test span. Thus, for a particular test span the beam was tested first with clamped ends, followed by simply supported ends and finally with bolted cleat end connections. In the latter case, for practical reasons, the web and flange cleat

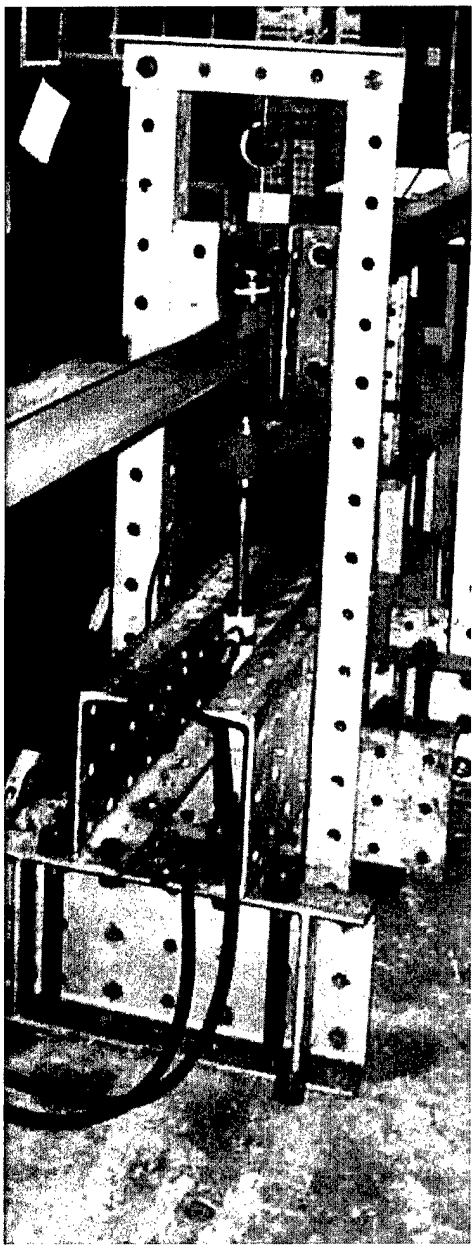

Fig. 6. Mid-span loading arrangement.

connection was tested before the web cleat connection (the presence of open holes in the beam flanges after the removal of the flange cleats was deemed not to affect the behaviour of the beam with web cleat end connections).

The beams were subjected to single point loading at mid-span. The load was applied by means of a tension jack pulling down on the lower part of a load hanger, the upper part of which was reacted against a ball joint bonded to the upper flange of the beam. The load was measured by a 10 kN capacity load cell (with a 10 N load resolution) connected to the ram of the jack and the lower part of the load hanger. This loading arrangement is shown in Fig. 6.

The mid-span deflection of the beam was recorded using a 100 mm travel dial gauge with an accuracy of 0.01 mm. Electronic clinometers were used to record the end rotations of the beam to the nearest 0.001°. For practical and consistency reasons, the clinometers were positioned on the centreline of the web 140 mm in from the ends of the span.

A number of preliminary load tests were carried out on the GRP beam in order to check that the instrumentation was functioning correctly and to ensure that the rotation of the concrete blocks and the vertical legs of 20 mm steel angles was negligible.

The procedure for the main series of tests was to increase the mid-span deflection in 1mm increments and to record the associated load and beam end rotations. After reaching the prescribed maximum deflection, generally not greater than $L/100$, the mid-span deflection was reduced to zero in 1mm decrements, again recording the associated loads and end rotations. This procedure was repeated three times for each span and each end connection arrangement. The measured loads and rotations recorded turned out to be highly consistent in all cases, though perfect symmetry of the end rotations was not achieved.

5. Analysis of beams with semi-rigid end connections

The analysis of pultruded GRP beams with semi-rigid end connections is dealt with at length in Ref. [12]. Here, for the sake of completeness, it is convenient to reiterate some of the formulae, as they have been used in the theoretical – experimental results correlations described in Section 6.

The relationships between deflection and load and end rotation and load, as given in Ref. [12], are

$$\delta = \frac{QL^3}{k_1 EI}\left(\frac{1 + 48\alpha + k_2\beta + 96\alpha\beta}{1 + 2\beta}\right), \tag{1}$$

and

$$\theta = \frac{QL^2}{k_3 EI}\left(\frac{\beta}{1 + 2\beta}\right). \tag{2}$$

In Eqs. (1) and (2) Q is the mid-span point load, E the longitudinal modulus of the beam material, I the second moment of area of the beam cross-section, $k_1(= 192)$, $k_2(= 8)$ and $k_3(= 8)$ are constants, L the beam span, δ the mid-span deflection, θ the end rotation, $\alpha(= EI/GAL^2$ or $EI/GA_wL^2)$ the dimensionless shear flexibility of the beam and $\beta(= EI/KL)$ is the dimensionless rotational flexibility of the end connection. Note that two forms of the shear flexibility parameter, α, are given in terms of the shear modulus, G, of the beam material and the gross and web cross-sectional areas, A and A_w, respectively of the beam.

Eqs. (1) and (2) have been derived on the assumption that the rotational stiffness, K, of the connection has a linear characteristic. The inverse forms of these equations have been used to predict the load – deflection and load – rotation responses for each of the spans and end connection layouts tested. In the theoretical calculations the nominal cross-section dimensions and shear modulus ($G = 2.93$ kN/mm^2), given in Ref. [7], were used in conjunction with the measured spans and the longitudinal modulus and connection rotational stiffness values determined by experiment.

The effect of the rotational stiffness of the end connections on the response of a beam under central point loading may be assessed in terms of three performance indices given in Ref. [12]. Two of these, viz. the deflection reduction index, λ_δ, and the load enhancement index, λ_Q, are used here to demonstrate that the test data do conform with the theoretical structural performance improvements. These indices may be expressed as

$$\lambda_\delta = \left(\frac{1 + 48\alpha + k_2\beta + 96\alpha\beta}{k_4 + 48\alpha + k_2\beta + 96\alpha\beta} \right) \tag{3}$$

and

$$\lambda_Q = \frac{1}{\lambda_\delta}. \tag{4}$$

In Eq. (3) k_4 ($=4$ for a point load at mid-span) is a constant which depends on the loading configuration.

For a beam under central point loading, λ_δ varies from 1 to 0.25, corresponding to simply supported and clamped end conditions respectively. Beams with semi-rigid end connections have λ_δ values which lie within this range. Thus, in physical terms, the λ_δ value is a measure of the reduction in the mid-span deflection of a beam with semi-rigid connections relative to a simply supported beam of the same span and subjected to the same loading.

6. Comparison of theoretical predictions with experimental results

The predicted load – deflection response, calculated from the inverse form of Eq. (1), is compared with the

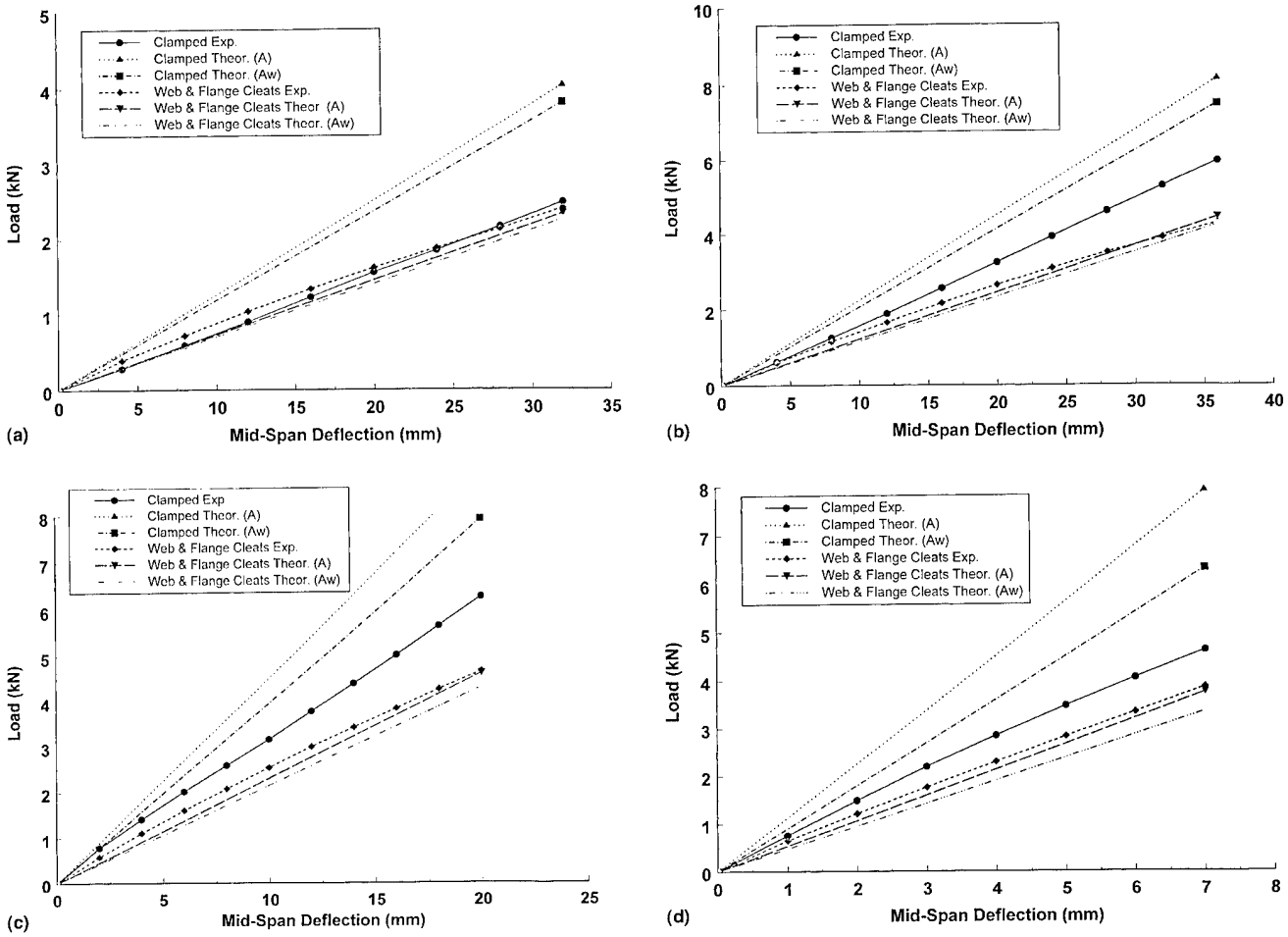

Fig. 7. Comparison of theoretical and experimental load – deflection responses for clamped and bolted web and flange cleat end conditions: (a) $L = 4.570$ m; (b) $L = 3.746$ m; (c) $L = 2.950$ m and (d) $L = 2.135$ m.

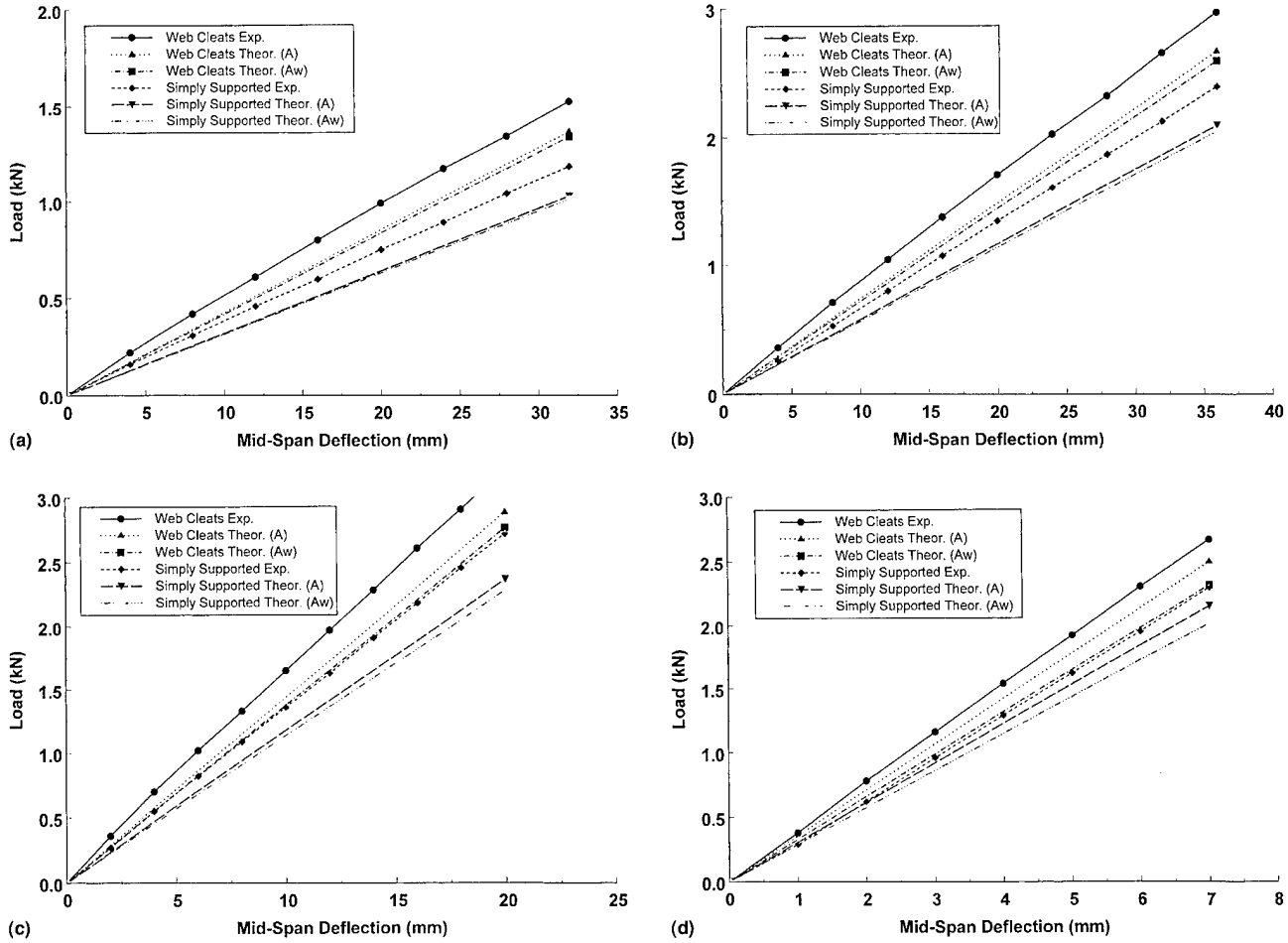

Fig. 8. Comparison of theoretical and experimental load – deflection responses for bolted web cleat and simply supported end conditions: (a) $L = 4.570$ m; (b) $L = 3.746$ m; (c) $L = 2.950$ m and (d) $L = 2.135$ m.

response measured in the tests in Figs. 7 and 8. Because of the large differences in flexural stiffness of the beams under the four sets of end conditions, it is convenient to compare clamped and web and flange cleat connections separately from simply supported and web cleat connections. Therefore, the former and latter comparisons are shown in Figs. 7 and 8, respectively. In these figures two theoretical predictions are shown for each end connection arrangement. One prediction uses the gross cross-sectional area, A, to evaluate the shear flexibility parameter, α, and the other uses the web cross-sectional area, A_w. Thus, these theoretical predictions provide upper and lower bounds on the influence of shear flexibility on the beam response.

The theoretical and experimental results comparisons for the beams with clamped and web and flange cleat connections, shown in Fig. 7, all show similar trends. It is obvious that there is poor agreement between the theoretical predictions and the experimental results for clamped ends. This is not altogether surprising, as it is generally recognised that it is impossible to simulate a rigid end connection accurately in an experiment. Clearly, the concrete blocks used in the beam tests do not achieve this. At the longest span (4.570 m) the concrete blocks, apparently, do not even provide as much rotational restraint as the web and flange cleat connections. However, for the other three, shorter spans they do provide significantly more rotational restraint. In these figures the comparison between the theoretical predictions and the experimental results for the web and flange cleat end connections is much better. It appears that, for this type of end connection, theory indicates that the beam has a slightly lower stiffness than was observed in the tests. This discrepancy between the theoretical and experimental results for the web and flange cleat end connections may be due, in part, to the longitudinal modulus, based on coupon test data, being somewhat low (other research on portal frames made from this WF-section appears to suggest that its modulus may be as high as 22 kN/mm^2). It may also be due to the fact that in the tests to determine the rotational stiffness of the web and flange cleat connection (see Ref. [5]) one leg of each cleat was bolted to the flange of a similar section column, whereas in the beam tests these

cleat legs were bolted to a 20 mm thick mild steel plate. Therefore, the rotational stiffnesses used in the theoretical predictions may be somewhat low.

The theoretical predictions and experimental results comparisons for web cleat connections and simply supported end conditions are shown in Fig. 8 for each of the four spans considered. It is obvious, in all cases, that web cleat end connections provide a worthwhile improvement in flexural stiffness for all spans. Here too, the theoretical predictions suggest that the beams are less stiff than was observed in the tests. The difference between theory and experiment appears to be of a similar order for both types of end support. This suggests that the rotational stiffness, taken from [12] and used in the calculations for the web cleat connections, was probably quite accurate. Indeed, for these connections the effect of bolting one leg of the angle cleats to a 20 mm thick steel plate rather than the flange of a similar GRP WF-section would be much less significant. Thus, it would appear that the low value of the longitudinal modulus, determined from the coupon tests, is the mostly likely reason for the theoretical predictions overestimating the experimental deflection values.

As stated earlier, the end rotations were recorded during the flexure tests and to demonstrate how well the predicted rotations compare with the experimental values Fig. 9 has been compiled for the 3.746 m span beam. The comparison for the clamped and web and flange cleat end conditions is presented in Fig. 9(a). The experimental results for the clamped beam should, of course, lie along the load axis, but do not do so, because the concrete block clamps did not fully restrain the ends of the beam against rotation. For the web and flange cleat end connections, the comparison is much better, especially at lower loads. At higher loads, however, the theoretical predictions under-estimate the observed end rotations. This is, most probably, due to the onset of nonlinearity in the moment – rotation response of the connections, which reduces their stiffness. The comparison of the predicted and observed load – rotation responses for web cleat and simply supported end conditions is shown in Fig. 9(b). Clearly, there is very good agreement between theory and experiment for both sets of end conditions.

An alternative means of comparing the theoretical predictions with the experimental results is in terms of the performance indices. This approach has the merit that it eliminates the effects of errors/difficulties in determining the material properties (longitudinal and shear moduli) from the comparison. The theoretical values for the deflection reduction index, λ_δ, and the load enhancement index, λ_Q, have been evaluated using Eqs. (3) and (4) with the same geometric and material properties as were used to calculate deflections and rotations from Eqs. (1) and (2). The same index values may also be calculated for the test data. The simplest

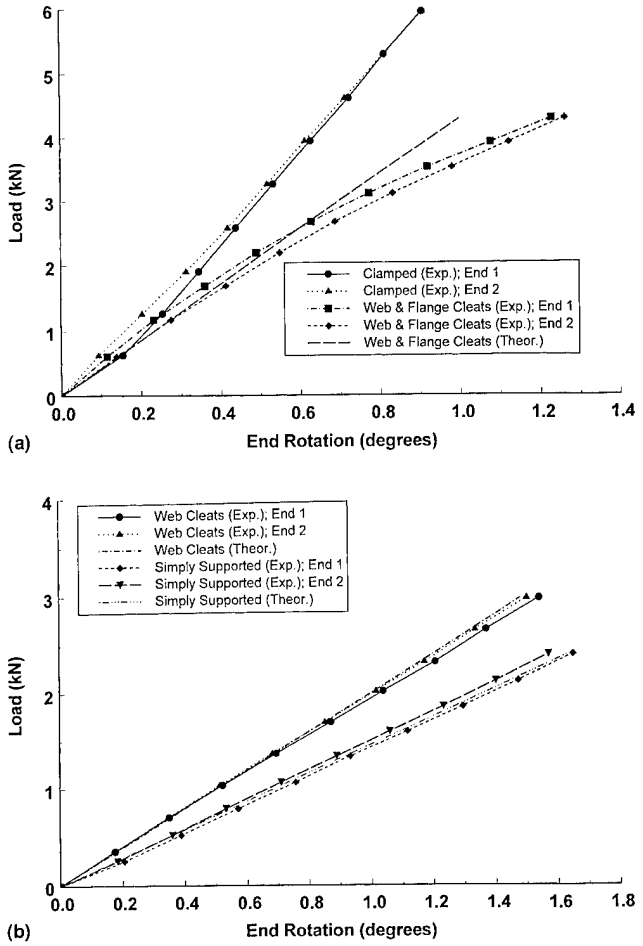

Fig. 9. Comparison of theoretical and experimental load – end rotation responses for a 3.746 m span beam: (a) clamped and bolted web and flange cleat end conditions and (b) bolted web cleat and simply supported end conditions.

approach is to establish the load to cause a prescribed deflection for a given span in, for example, a simply supported beam test and a beam test with web cleat connections. The value of the load enhancement index, λ_Q, is then obtained by dividing the load for the beam with web cleats by the load for the simply supported beam. The deflection reduction index, λ_δ, is simply the reciprocal of this value. These computations have been carried on the experimental results for the four main spans and the results are presented graphically in Fig. 10. Fig. 10(a) shows the deflection reduction index plotted as a function of the span-depth ratio. In this figure the continuous and broken line curves represent the theoretical results for the three end support conditions, clamped, web and flange cleats and web cleats, and for the upper and lower limits on the shear flexibility parameter. The experimental results are shown as points. Clearly, there is poor agreement between theory and experiment in the case of clamped end conditions. As explained above, this is because the concrete blocks did not provide rigid clamping conditions. However, the

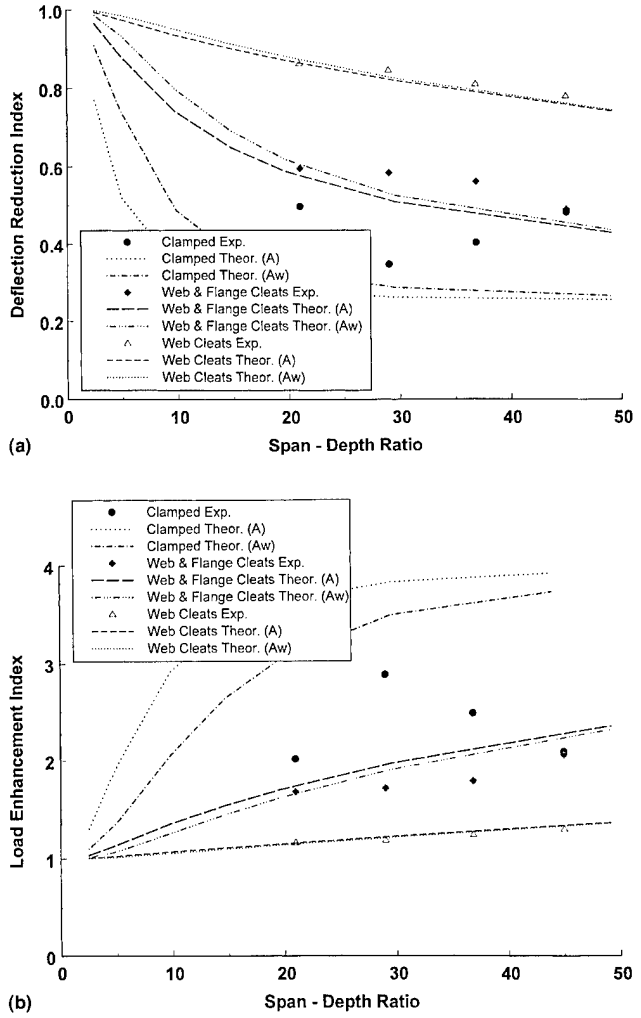

Fig. 10. Comparison of theoretical and experimental performance indices: (a) deflection reduction index, λ_δ, versus span–depth ratio and (b) load enhancement index, λ_Q, versus span–depth ratio.

agreement between the theoretical and experimental results is much better for the web and flange cleat end connections. Indeed, the agreement appears to be superior to that shown Fig. 7. Likewise, for the case of web cleat end connections, the agreement between theory and experiment is excellent and, moreover, is also superior to that shown in Fig. 8.

The comparison between the theoretical predictions and the experimental results for the load enhancement index, λ_Q, is shown in Fig. 10(b). Since these results are directly related to the those presented in Fig. 10(a), it is not surprising that they reflect the same level of agreement between the results sets for each of the three types of end support condition.

7. Concluding remarks

Three point flexure tests have been carried out on a pultruded GRP WF-section beam at four spans and under four sets of end conditions – two idealised and two practical. The test results show that within the serviceability range of mid-span deflections, i.e., up to a maximum of $L/100$, the beam response is linear. They also show that shear deformable beam analysis incorporating a linear rotational stiffness model of the semi-rigid end connections is capable of simulating the response of beams with bolted cleat end connections with good accuracy.

Moreover, the test results suggest that even the bolted web cleat connections provide a significant increase in the overall flexural stiffness of the beam, especially at the higher L/d ratios, compared to a simply supported beam. Currently, this stiffness is disregarded, as pultruded GRP beams are usually designed assuming their ends to be simply supported. Thus, the results presented herein demonstrate that semi-rigid design could lead to considerable improvements in the structural performance of pultruded GRP profiles at no extra cost, because the connection stiffness benefits are present, but not utilised.

Acknowledgements

The author wishes to record his appreciation to Mr. Andrew Foster who, under the author's direction, carried out the beam flexure tests as part of his final year undergraduate project. His comprehensive and meticulous records of load and deformation data and other test details greatly simplified the task of preparing this paper. The author is also grateful for continuing support from colleagues in the Engineering Department.

References

[1] Bank LC, Mosallam AS, Gonsior HE. Beam-to-column connections for pultruded FRP shapes. In: Proceedings of the ASCE First Materials Engineering Congress. Colorado: Denver, 1990. p. 804–13.

[2] Bank LC, Mosallam AS, McCoy GT. Design and performance of connections for pultruded frame structures. J. Reinforced Plastics and Composites 1994;13(4):199–212.

[3] Bass AJ, Mottram JT. Behaviour of connections in frames of fibre reinforced-polymer section. The Structural Engineer 1994; 72(17):280–5.

[4] Mottram JT. Tests on nominally pinned connections for pultruded frames. In: Clarke JL. editor. Structural design of polymer composites: EUROCOMP design code and handbook. London: E. & F.N. Spon, 1996. p. 705–18.

[5] Turvey GJ, Cooper C. Semi-rigid pultruded GRP frame connections: tests to determine static moment – rotation characteristics. In: ECCM-7 (Seventh European Conference on Composite Materials: Realising their Commercial Potential), Cambridge: Woodhead Publishing Limited, 1996. p. 295–300.

[6] Turvey GJ, Cooper C. Characterisation of the short term static moment – rotation response of bolted connections between pultruded GRP beam and column WF-sections. In: El-Badry M. editor. Advanced composite materials in bridges and structures.

Montreal: The Canadian Society for Civil Engineering, 1996. p. 927–34.
[7] Anon., EXTEN Fiberglass Structural Shapes Design Manual, Morrison Molded Fiberglass Company (now Strongwell), Bristol, Virginia, 1989.
[8] Anon., Creative Pultrusion Design Guide, Creative Pultrusions, Alum Bank, Pennsylvania, 1988.
[9] Anon., Fibreline Design Manual for Structural Profiles in Composite Materials, Fibreline Composites A/S, Kolding, Denmark, 1995.
[10] Clarke JL. editor. Structural design of polymer composites: EUROCOMP design code and handbook. London: E. & F.N. Spon, 1996.
[11] Mottram JT, Zheng Y. State-of-the-art review on the design of beam-column connections for pultruded frames. Composite Struct 1996;35(4):387–401.
[12] Turvey GJ. Analysis of pultruded GRP beams with semi-rigid end connections. Composite Struct 1997;38(1–4):3–16.
[13] Zheng Y, Mottram JT. Analysis of pultruded frames with semi-rigid connections. In: El-Badry, MM. editor, Advanced composite materials in bridges and structures. Montreal: Canadian Society for Civil Engineering, 1996. p. 919–27.
[14] Mottram JT, Zheng Y. Analysis of a pultruded frame with various connection properties. In: Saadatmanesh H, Ehsani MR. editors, Fiber composites in infrastructure, Tucson: University of Arizona, Vol. II, 1998. p. 261–74.
[15] Sims GD, Johnson AF, Hill RD. Mechanical and structural properties of a GRP pultruded section. Composite Struct 1987;8(3):173–87.
[16] Bank LC. Flexural and shear moduli of full-section fiber reinforced plastic (FRP) pultruded beams. ASTM J Testing and Evaluation 1989;17(1):40–5.
[17] Mottram JT. Structural properties of a pultruded *E*-glass fibre-reinforced polymeric I-beam. In: Marshall IH. editor. Composite Structures 6. Barking: Elsevier Applied Science, 1991. p. 1–28.
[18] Bank LC, Gentry TR, Nadipelli M. Local buckling and failure of pultruded fiber-reinforced plastic beams. ASME J Eng Mater Technol 1994;116(2):233–7.
[19] Mottram JT. Lateral-torsional buckling of a pultruded I-beam. Composites 1992;23(2):81–93.
[20] Turvey GJ. Lateral buckling tests on rectangular cross-section pultruded GRP cantilever beams. Composites Part B Eng 1996;27B(1):35–42.
[21] Turvey GJ, Brooks RJ. Lateral buckling tests on pultruded GRP I-Section beams with simply supported – simply supported and clamped – simply supported end conditions. In: Proceedings of the First International Conference on Composites in Infrastructure (ICCI'96). USA: University of Arizona, 15–17 January, 1996. p. 651–64.

ELSEVIER

Composite Structures 47 (1999) 581–588

COMPOSITE STRUCTURES

www.elsevier.com/locate/compstruct

Heat transfer and cure analysis for the pultrusion of a fiberglass-vinyl ester I beam

X.L. Liu [a,*], W. Hillier [b]

[a] *Cooperative Research Center for Advanced Composite Structures, 506 Lorimer Street, Fishermens Bend, Vic. 3207, Australia*
[b] *Cooperative Research Center for Advanced Composite Structures, 361 Milperra Road, Bankstown, NSW 2200, Australia*

Abstract

In the present paper, the heat transfer and curing process during the pultrusion of a fiberglass-vinyl ester I beam is simulated using a finite element/control volume procedure developed at the Cooperative Research Centre for Advanced Composite Structures (CRC-ACS). The governing equations for the pultrusion process are introduced. The numerical algorithm adapted to solve the equations is briefly described. Numerical simulations are conducted to obtain the temperature and curing profiles for different temperature settings and pull speeds. The predicted temperature profiles are compared with those obtained experimentally. Good agreement is observed. The result of the present work enhances our confidence in applying the numerical procedure as a routine design and analysis tool for the pultrusion tooling and process development. © 2000 Elsevier Science Ltd. All rights reserved.

Keywords: Heat transfer; Curing analysis; Pultrusion processes; Numerical modelling

1. Introduction

Pultrusion is a continuous process used to produce polymer composite materials of constant cross-sections. In pultrusion, fiber reinforcements are saturated in a resin tank with the thermoset resin and then continuously pulled through a heated die. Inside the die, the resin gradually cures and solidifies to form a composite part with the same cross-sectional profiles as the die. A puller continuously draws the part through the die, and a travelling cutoff saw cuts the part into desired lengths. This process is illustrated schematically in Fig. 1.

The curing of the thermoset resin is an exothermic reaction in which significant amount of heat may be produced. For a given resin, the reaction can only be vigorously activated when the temperature reaches a certain level and it takes a certain time to complete. In order to obtain parts of good quality by pultrusion, care must be taken, through proper tooling and process design, to ensure that a relatively uniform and sufficient degree of cure is achieved in the parts. For the same reason, it is also important to prevent the parts from overheating which may be happening due to the exothermic resin reaction and low conductivity of the composites. Therefore, it is very desirable to be able to predict the temperature and curing profiles under different tooling design and process conditions. Due to the complexity of the problem, this can only be achieved using a numerical method.

A number of numerical procedures have been developed for heat transfer and curing analysis of pultrusion processes [1–10]. However, with the exception of those reported by Roux and his co-workers [7–9], the majority of the procedures published were of two-dimensional nature. Consequently, the part geometries were generally limited to either circular rods or flat plates and the geometry of the die and the heating configuration could not be modeled with reasonable accuracy. It was also a general practice in the numerical works reported that pultrusion was assumed to be a steady process for which the temperature and the cure profiles would not change with time. While this assumption is valid when the steady state of pultrusion has been established, it requires that the die-wall temperature be specified as a known boundary condition. However, in practice the die-wall temperature is unknown and is one of the most important variables to be predicted by the modeling. It is also necessary, for a steady simulation, to provide the initial guesses for temperature and the degree of cure profiles on which iterations have to be performed to obtain the true temperature and the degree of cure profiles. Convergence may not be achieved if the initial

* Corresponding author. Tel.: +61-3-9646-6544; fax: 61-3-9646-8352.
E-mail address: liu@duigen.dsto.defence.gov.au (X.L. Liu).

0263-8223/99/$ - see front matter © 2000 Elsevier Science Ltd. All rights reserved.
PII: S0263-8223(00)00029-5

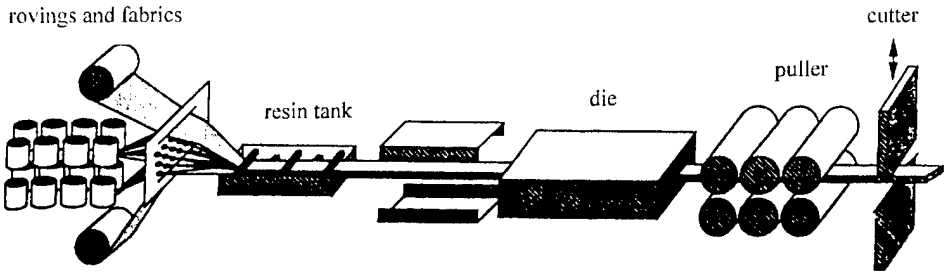

Fig. 1. Schematic illustration of pultrusion process.

guesses provided are poor. This was proved by some of the results reported in [10].

Recently, a finite element/control volume procedure was developed at the Cooperative Research Centre for Advanced Composite Structures (CRC-ACS) [11]. The procedure is of three dimensional and transient nature. A number of modeling options have been implemented to allow for the selection of, among others, resin cure kinetic models, fiber volume fraction distributions, pull speeds, initial temperature and degree of cure profiles, and different heating (and heating control) methods. These options should ensure that modeling requirements for different situations, or at least those most commonly encountered, are catered for. Another distinguishing feature of the procedure is that it is implemented on general-purpose finite element packages, currently on both LUSAS and MSC/NASTRAN. This approach results in not only considerable savings in development time and costs but also makes available to the users the modeling features provided by the FE packages, such as broad options on pre- and post-processing, element types and boundary conditions. Perhaps more importantly, the approach makes it more convenient if a structural analysis is to be conducted for the part by the same FE package or if the stress is to be coupled into the heat transfer and cure simulation.

In the present paper, the theoretical background of the procedure is first described. The procedure is then used to simulate the pultrusion of a fiberglass-vinyl ester I beam. The predicted temperature profiles in both the part and the die are compared with those measured experimentally. Temperature and cure profiles under various pull speeds and heater control temperatures are investigated to determine proper process conditions for the I beam.

2. Theory

2.1. Energy equation for the tool

The part of the pultrusion tool to be included in the thermal analysis usually consists of the heated die and a number of electrical heaters arranged in the pull direction and controlled at different temperatures. Heat transfer in the tool is governed by the following equation in the Cartesian coordinate system:

$$\rho c_p \frac{\partial T}{\partial t} = \frac{\partial}{\partial x}\left(\kappa_x \frac{\partial T}{\partial x}\right) + \frac{\partial}{\partial y}\left(\kappa_y \frac{\partial T}{\partial y}\right) + \frac{\partial}{\partial z}\left(\kappa_z \frac{\partial T}{\partial z}\right) + q, \tag{1}$$

where T is the temperature in Kelvin, ρ, c_p the density and specific heat of the tooling materials, respectively, $\kappa_x,\kappa_y,\kappa_z$ the thermal conductivities in x, y and z directions, respectively; q is the rate of energy exchange at the boundary.

2.2. Energy equation for the part

In pultrusion, the reinforcement is saturated with the resin before entering the heated die. Therefore, it is reasonable to assume that the resin does not flow. The pultruded part is moving in the pull direction at the pull speed. The energy equation for the part can be written as

$$\bar{\rho} c_p \left(\frac{\partial T}{\partial t} + u\frac{\partial T}{\partial x}\right) = \frac{\partial}{\partial x}\left(\bar{\kappa}_x \frac{\partial T}{\partial x}\right) + \frac{\partial}{\partial y}\left(\bar{\kappa}_y \frac{\partial T}{\partial y}\right) + \frac{\partial}{\partial z}\left(\bar{\kappa}_z \frac{\partial T}{\partial z}\right) + V_r Q, \tag{2}$$

where V_r is the resin volume fraction, u the pull speed, $\bar{\rho}, \bar{c}_p$ the lumped density and specific heat for the composite material, respectively, $\bar{\kappa}_x,\bar{\kappa}_y,\bar{\kappa}_z$ the lumped thermal conductivities in x, y and z directions, respectively, Q is the rate of internal heat generation caused by the resin reaction.

The lumped properties are evaluated by the following equations [7]:

$$\begin{aligned} \bar{\rho} &= (1 - V_r)\rho_f + V_r\rho_r, \\ \bar{c}_p &= \frac{(1 - V_r)\rho_f c_{pf} + \rho_r V_r c_{pr}}{\bar{\rho}}, \\ \bar{\kappa} &= \frac{\kappa_f \kappa_r \bar{\rho}}{(1 - V_r)\rho_f \kappa_r + V_r \rho_r \kappa_f}. \end{aligned} \tag{3}$$

2.3. Species equation for the resin

The internal heat generation Q is caused by the exothermic resin cure reaction. In pultrusion, governing the

rate of the reaction is the following chemical species equation

$$\frac{\partial \alpha}{\partial t} = R - u\frac{\partial \alpha}{\partial x}, \tag{4}$$

where α is the degree of cure which is defined as a ratio of the amount of heat evolved during the curing up to time t, $H(t)$, to the total heat of reaction H_{tr}:

$$\alpha = \frac{H(t)}{H_{tr}}. \tag{5}$$

R is the rate of resin reaction, i.e.

$$R = \frac{\mathrm{d}\alpha}{\mathrm{d}t} = \frac{\mathrm{d}H(t)}{H_{tr}\mathrm{d}t}. \tag{6}$$

From Eq. (6), the rate of internal heat generation per unit volume caused by the resin reaction is:

$$Q = \frac{\mathrm{d}H(t)}{\mathrm{d}t} = H_{tr}R. \tag{7}$$

For a given resin, H_{tr} and R can be determined using differential scanning calorimetry (DSC) measurements. The results are often fitted to an Arrhenius type equation to represent R as a function of temperature and the degree of cure.

Temperature distribution in the part and the tool, and the degree of cure profile in the part are obtained by solving the above governing equations.

2.4. Numerical procedure

The energy equations and the species equation are coupled in that the rate of the cure reaction is a function of temperature. Therefore they are non-linear even if the physical properties of the composites are assumed to be constant.

In the present numerical procedure, the governing equations are solved using the following mixed time integration

$$\begin{aligned}\bar{\rho}c_p\left(\left[\frac{\partial T}{\partial t}\right]^n + \left[u\frac{\partial T}{\partial x}\right]^{n-1}\right) &= \frac{\partial}{\partial x}\left(\bar{\kappa}_x\frac{\partial T}{\partial x}\right)^n + \frac{\partial}{\partial y}\left(\bar{\kappa}_y\frac{\partial T}{\partial y}\right)^n + \frac{\partial}{\partial z}\left(\bar{\kappa}_z\frac{\partial T}{\partial z}\right)^n \\ &\quad + [V_r Q]^{n-1}.\end{aligned} \tag{8}$$

And the species equation is integrated explicitly:

$$\left[\frac{\partial \alpha}{\partial t}\right]^n = \left[R - u\frac{\partial \alpha}{\partial x}\right]^{n-1}, \tag{9}$$

where n is the time step index.

Nodal control volumes are constructed based on the finite element mesh. The centers of the control volumes coincide with the nodal points of the finite elements.

The species equation is solved using the control volume method to obtain the degree of cure at each nodal point. The effect of the convection term and the exothermic term on temperature is computed from the known temperatures of the previous time step. A finite element package is then used for the solution of the remaining transient heat conduction problem to obtain the temperature for the current time step. If necessary, sub-stepping and/or iteration can be performed to improve the accuracy of the solution in a time step.

The previous numerical results have indicated that this procedure is able to produce stable solutions for both temperature and the degree of cure even when a relatively large discretization in the pull direction is used [11].

3. Process modeling for I beam

3.1. Fiberglass-vinyl ester I beam

The problem under consideration was the pultrusion of a fiberglass-vinyl ester I beam. The cross-sectional profile of the beam is shown in Fig. 2. The beam was made of fiberglass reinforcement and vinyl ester resin VE3 (a blend of DERAKANE 411-45).

The pultrusion was conducted using a pultrusion die of 1020 mm in length. Heating was provided by four electrical heat platens placed on the top and bottom surfaces of the die and two electrical strip heaters at the two sides, see Fig. 3. The die was cooled at the entrance by water to prevent excessive curing at the die entrance side.

3.2. Numerical model

Using symmetry, only a quarter of the pultrusion tool and the pultruded part was considered in the numerical model. The finite element/control volume mesh consisted of 1218 elements for the part, 4216 elements for the die and 1360 elements for the heat platens. The length of the part considered in the model was 1305 mm which was 28 5mm longer than that of the die. The additional

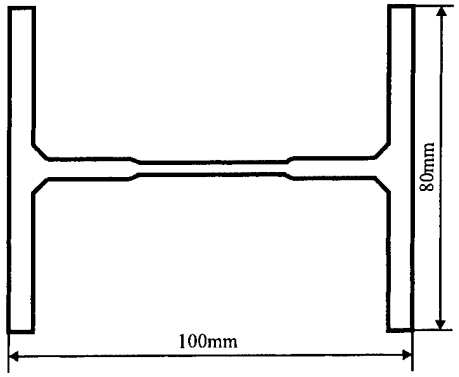

Fig. 2. Cross section of the I beam.

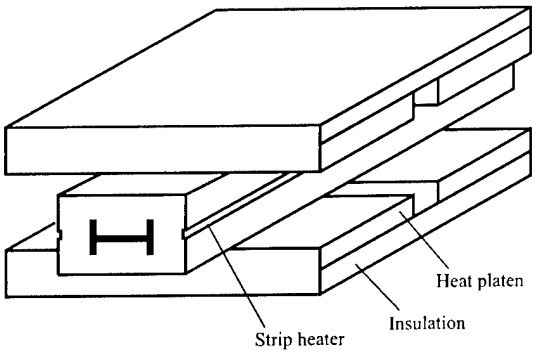

Fig. 3. Heating configuration.

length of the part was arranged at the exit side such that heat transfer and curing analysis of the part was extended to the post-die region. The 3D finite element/control volume model is illustrated in Fig. 4.

The temperature control process of the electrical heating was simulated by placing a control node at each of the locations where control thermocouples existed. For a time step, the applied heating powers were turned on or off automatically according to the temperatures at the control nodes. The control tolerance used was 0.5°C. Only free convection heat transfer was considered for the exposed surfaces. The convective heat transfer coefficient used was 10 W/m^2 K. Other material properties used in the simulation are given in Table 1.

3.3. Resin kinetic model

DSC tests were conducted to establish reaction kinetic model for the VE3 resin. These included dynamic DSCs at a scanning rate of 20°C/s and isothermal DSCs at 100°C, 120°C and 140°C, respectively. Using nonlinear regression, the results were fitted to the following Arrhenius equation by assuming a second-order reaction:

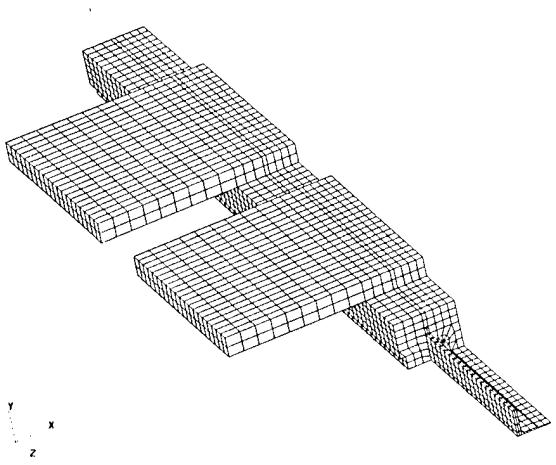

Fig. 4. 3D FE model.

Table 1
Material properties

Material	ρ (kg/m^3)	c_p (J/kg K)	κ (W/m K)
Die	7860	486	51.0
Heater	2700	896	180.0
Fiberglass	2560	670	1.04, 11.4
Resin	1100	1640	0.169

Table 2
Kinetic parameters for VE3

Parameters	Values
k_0 (1/s)	186958305
E (J/mol)	71688
m	0.7147
n	1.2853

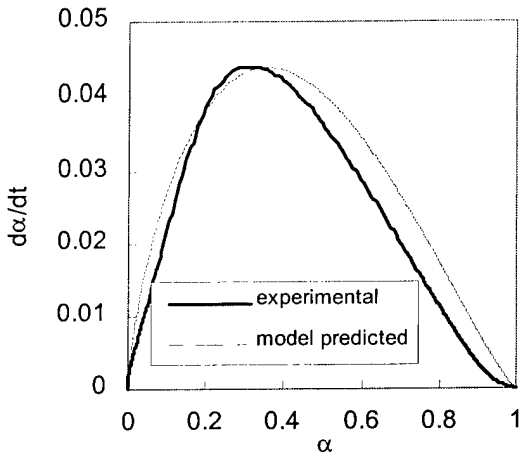

Fig. 5. Reaction rate at 140°C.

$$\frac{d\alpha}{dt} = \frac{k_0}{\alpha_{max}} \exp\left(\frac{-E}{RT}\right)\alpha^m(\alpha_{max} - \alpha)^n. \quad (10)$$

In the equation, α_{max} is the highest degree of cure achieved at a given temperature. In the present work, it was taken as an average value of 0.97 for the temperature range considered.

Parameters in the kinetic model are listed in Table 2. A comparison between the experimental and the predicted resin kinetics at 140°C is given in Fig. 5.

4. Results and discussion

4.1. Experimental verification

Pultrusion experiments were conducted to verify the numerical procedure. The experiment conditions were:

$u = 300$ mm/min, $T_c = 123$°C (process 1)

and

$u = 360$ mm/min, $T_c = 128$°C (process 2),

respectively, where T_c is the control temperature for the electrical heaters. The fiber volume fraction was maintained at 45%.

As shown in Fig. 6, temperature profiles in the pull direction at points A (both processes), B (process 1) and C (process 2) were investigated. To record the temperature profiles at points B and C of the moving part during pultrusion, thermocouples were placed there at the die entrance and pulled through together with the part. The temperature profiles at point A of the die were obtained using 10 thermocouples in the pull direction.

The numerical temperature profiles under the above two process conditions are compared with those experimentally obtained in Figs. 7 and 8, respectively. Very good agreement exists between the numerical and the experimental results, reconfirming that the numerical procedure can produce relatively accurate prediction on temperature distribution in both the part and the die.

4.2. Curing state at die exit

It can be observed from Fig. 7(a) and Fig. 8(a) that, under the two process conditions investigated, temperatures in the part continued to increase significantly after exiting the die. This was particularly true for process 2 in which temperature at point C increased by about 80°C in the post-die region. Such phenomenon implies that sufficient degree of cure was not reached by the part within the pultrusion die. Instead, a significant amount of cure reaction happened in the post-die region.

The predicted degree of cure profiles at the die exit is plotted in Fig. 9(a) and (b) for processes 1 and 2, respectively. It is interesting to note that, in both cases, point C was close to the place where the degree of cure reached was the lowest on the cross-section at the die exit. Therefore, this point can be used as a reference to determine if sufficient degrees of cure were reached in the part at the die exit. The degrees of cure at the die exit for both processes distributed non-uniformly, with the

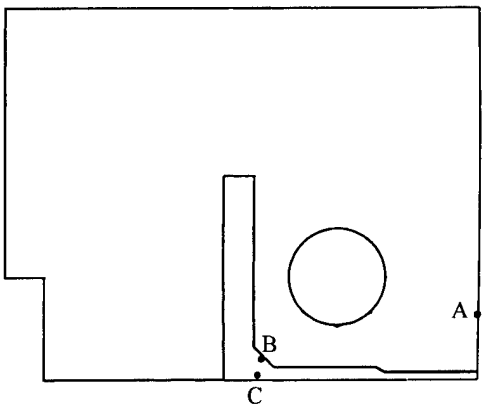

Fig. 6. Sampling positions on a section.

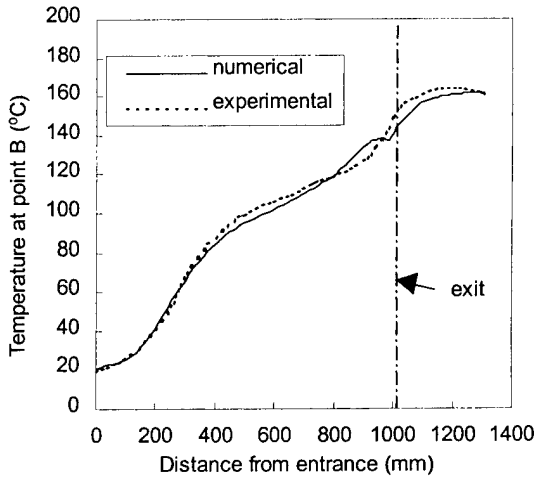

(a) part

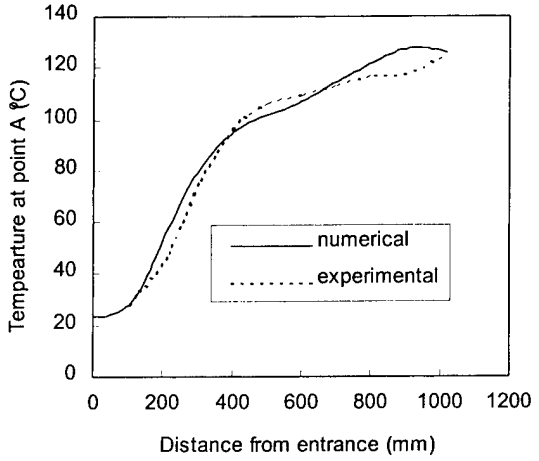

(b) die

Fig. 7. Temperature profiles for process 1.

difference between the maximum and the minimum degrees of cure being about 0.8. However, for process 1, the non-uniformity was located at the junction of the flange and the web. For process 2, very non-uniform distribution in the degree of cure was observed on the flange and part of the web. This is because less time is available for heat transfer and cure reaction before the part travels through the die at a relatively high pull speed such as that used in process 2.

4.3. Effect of pull speed

It is generally agreed that the pull speed has significant effect on the temperature distribution, and hence the degree of cure profile in the part. An important task in pultrusion process design is the selection of a proper pull speed, at a given heating configuration, to ensure that sufficient degrees of cure (>0.8) are reached before the part is pulled out of the die.

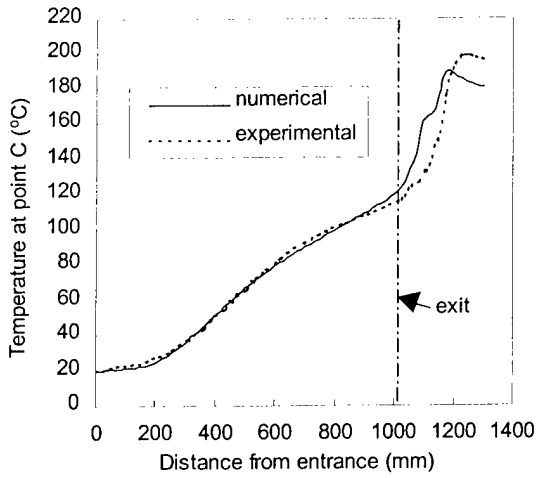

(a) part

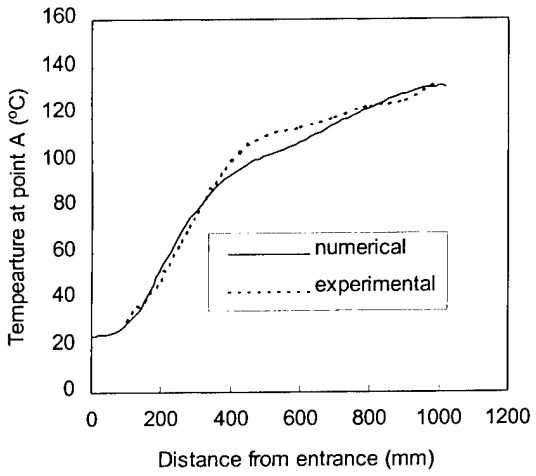

(b) die

Fig. 8. Temperature profiles for process 2.

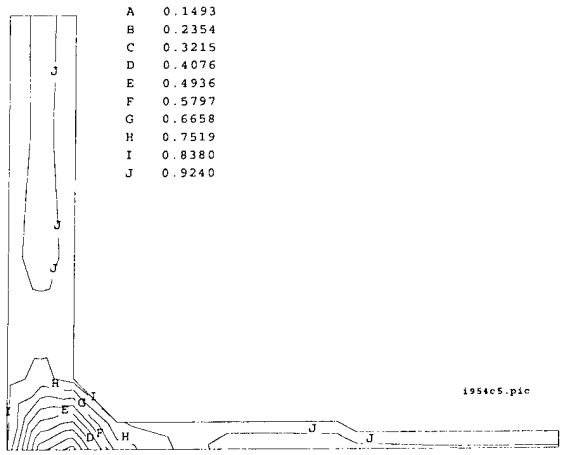

(a) process 1

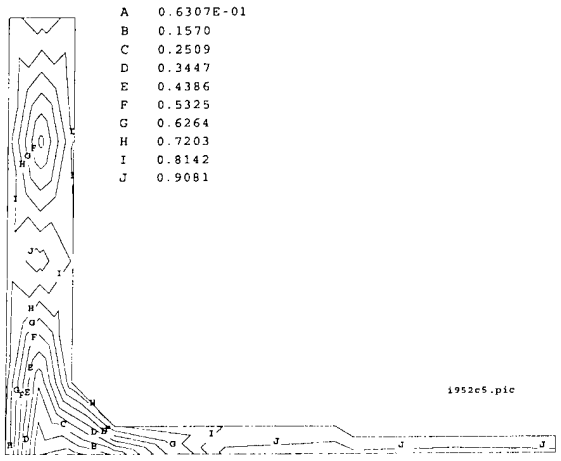

(b) process 2

Fig. 9. Degree of cure profile at exit.

Simulation was performed for pultrusions at the speeds of 240, 300 and 360 mm/min while the control temperature was maintained at 128°C. Temperature and the degree of cure profiles at point C are compared in Figs. 10 and 11, respectively.

Both temperature and the degree of cure at a lower pull speed lead those at higher speeds. Within a certain distance from the die entrance, temperature of the die was higher than that of the part and more heat could transfer from the die to the part at a lower pull speed. This resulted in higher temperature and the degree of cure as compared to those obtained at higher pull speeds.

When the pull speed approached and exceeded about 300 mm/min, sufficient degree of cure at point C could not be accomplished within the die and the peak exothermic temperature was reached in the post-die region. Therefore, if the heaters are controlled at 128°C, pull speeds should be kept lower than 300 mm/min to obtain

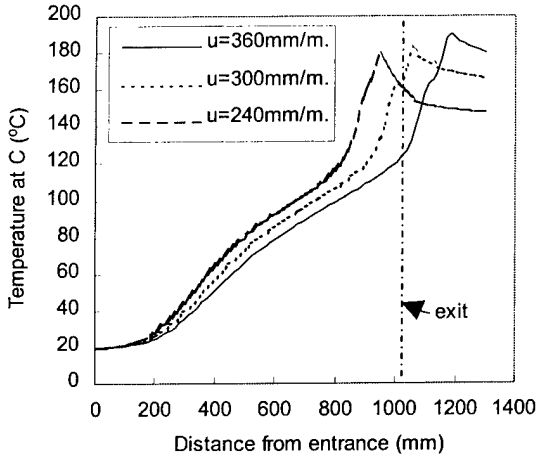

Fig. 10. Effect of pull speed on T.

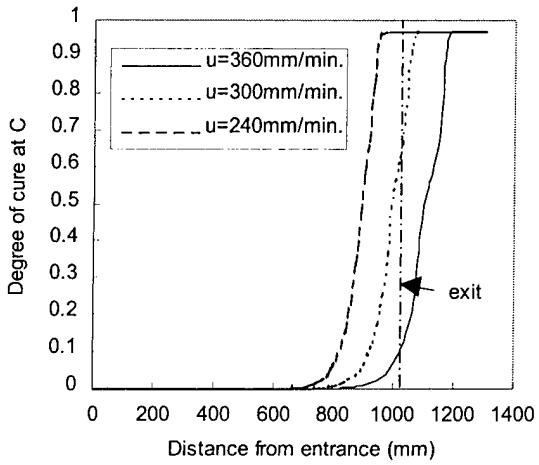

Fig. 11. Effect of pull speed on α.

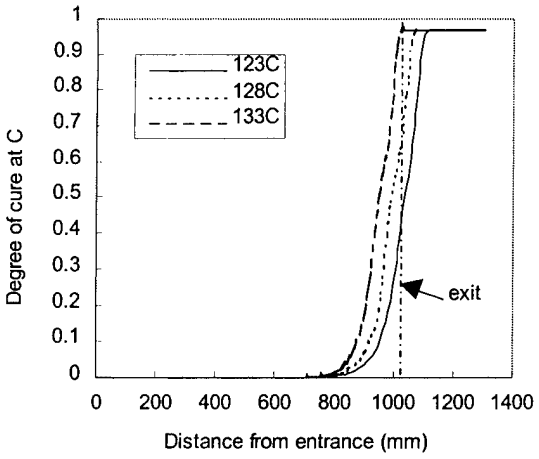

Fig. 13. Effect of control temperature on α.

good quality part. It is also observed from Fig. 10 that the peak temperature increased with the pull speed. This is because at a higher pull speed, more cure reaction was accomplished in the post-die region and less exothermic heat could transfer to the die.

4.4. Effect of control temperature

The effect of the control temperature for the electrical heaters was investigated by simulation at three different temperature settings of 123°C, 128°C and 133°C, using a constant pull speed of 300 mm/min. The predicted temperature and degree of cure profiles at C are compared in Figs. 12 and 13, respectively.

Increasing the control temperature had a similar effect on temperature and the degree of cure profiles as that of reducing pull speed. At a higher control temperature, more heat transferred from the die to the part, resulting in higher temperature and the degree of cure.

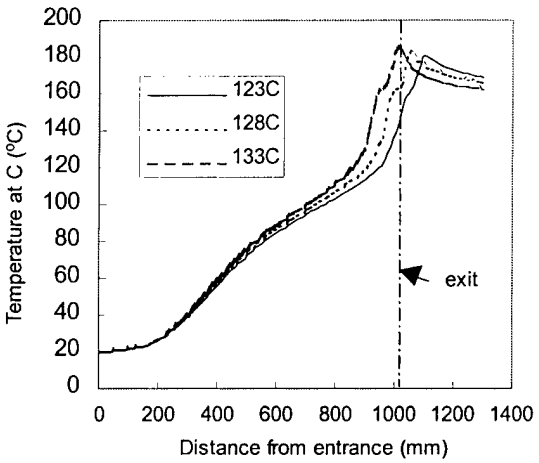

Fig. 12. Effect of control temperature on T.

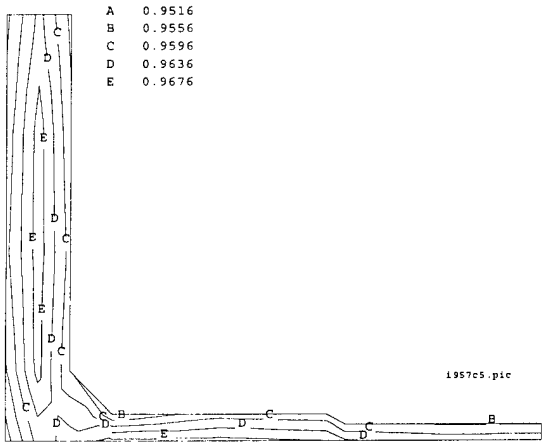

u=300mm/min., T_c=133°C

Fig. 14. Degree of cure profile at exit.

The degree of cure at point C reached 0.404, 0.657 and 0.967 for control temperature 123°C, 128°C and 133°C, respectively at the die exit. Combined with the results of the previous section, the proper process condition for the I beam pultrusion could be selected as: $u = 300$ mm/min and $T_c = 133$°C. Sufficient and relatively uniform degree of cure at the die exit was predicted under this process condition, see Fig. 14.

5. Conclusions

It can be concluded from the work reported in this paper that:

1. The numerical procedure, developed at the CRC-ACS, for three dimensional heat transfer and curing analysis of pultrusion processes can produce relatively

accurate prediction on temperature distribution in both the pultrusion die and the pultruded part.

2. Pull speed and the control temperature for the heaters have significant effect on both the temperature and the degree of cure profiles in the pultruded part. A proper combination of these two process parameters can be determined with the help of numerical simulation.

3. The fiber glass-vinyl ester I beam investigated in this paper should be pultruded at 300 mm/min while the control temperature is set to 133°C.

Acknowledgements

The DSC experiments for the vinyl ester resin were organized by Mr. P. Andrews of the CRC-ACS and conducted by Mr. G. Mathys of the Aeronautical and Maritime Research Laboratory, DSTO, Australia. Their assistance is gratefully acknowledged.

References

[1] Aylward L, Douglas C, Roylance D. A transient finite element model for pultrusion processing. Poly Proc Eng 1985;3:247.

[2] Han CD, Lee DS. Development of a mathematical model for the pultrusion process.. Polymer Eng Sci 1986;26:393–404.

[3] Wu HT, Joseph B. Model based and knowledge based control of pultrusion processes. SAMPE J 1990;26(6):59–70.

[4] Hackett RM, Zhu SZ. Two-dimensional finite element model of the pultrusion process. J Reinforced Plastics and Composites 1992;11:1322–51.

[5] Batch GL, Macosko CW. Heat transfer and cure in pultrusion: model and experimental verification. AIChE J 1993;39:1228–41.

[6] Ruan Y, Liu J. A steady state heat transfer model for fiber-reinforced-thermoplastic pultrusion processes using the finite element method. J Mater Process & Manufacturing Sci 1994; 3:91–113.

[7] Gorthala R, Roux JA, Vaughan JG, Donti RP. Comparison of processing parameters for pultruded graphite/epoxy and fiberglass/epoxy: a heat transfer and curing model. J Reinforced Plastics and Composites 1994;13:288–300.

[8] Chachad YR, Roux JA, Vaughan JG. Three-dimensional characterization of pultruded fiberglass-epoxy composite materials. J Reinforced Plastics and Composites 1995;14:495–512.

[9] Roux JA, Vaughan JG, Shanku R, et al. Comparison of measurements and modeling for pultrusion of a fiberglass/epoxy I-beam. J Reinforced Plastics and Composites 1998;17:1557–79.

[10] Suratno BR, Ye L, Mai YW. Simulation of temperature and curing profiles in pultruded composite rods. Composite Sci Technol 1998;58:191–7.

[11] Liu XL, Crouch IG, Lam YC. Simulation of heat transfer and cure in pultrusion using a general purpose FE package. Composites Sci Technol., accepted.

ELSEVIER

Composite Structures 47 (1999) 589–593

COMPOSITE STRUCTURES

www.elsevier.com/locate/compstruct

Synthesis of in situ Al–TiB_2 composites using stir cast route

K.L. Tee [a], L. Lu [b,*], M.O. Lai [b]

[a] *School of Engineering, Nanyang Polytechnic, 180, Ang Mo Kio Av.8, 569830 Singapore*

[b] *Department of Mechanical and Manufacturing Engineering, National University of Singapore, 10 Kent Ridge Crescent, 119260 Singapore*

Abstract

When elemental Ti and B powders were added to molten Al at above 1000°C, fine in situ TiB_2 particulates were formed through Al–Ti–B exothermic reaction. By optimising the nucleation of TiB_2, the tensile and yield strengths of a synthesised Al–$15V_f$%TiB_s composite were twice that of matrix material. Modification of Al-matrix with 4.5 wt%Cu tripled the tensile and yield strengths at peak-aged condition. Owing to the co-presence of brittle Al_3Ti flakes with TiB_2 particles in the composites synthesised by the Al–Ti–B system, ductility was reduced to 68% and 84% in composites with Al- and Al–Cu matrices, respectively. When the (Ti + B) mixture was incorporated with 3 wt%C, TiB_2 and TiC reinforcing phases were simultaneously produced in the composite with Al–Cu matrix. Such an approach reduced Al_3Ti compound in the composite considerably. Although the presence of Cu in the composite was found to promote the formation of Al_3Ti, its effect on the fluidity caused the melt recovery to increase from 33% to 52%. © 2000 Elsevier Science Ltd. All rights reserved.

Keywords: In-situ synthesising: Al–TiB_2 composite; Stir casting

1. Introduction

Al-base MMCs reinforced with ceramic particulates have been the subject of numerous research works. Owing to the low density, low melting point, high specific strength and thermal conductivity of aluminium, a wide variety of ceramic particulates such as SiC [1–6], B_4C [5]. Al_2O_3 [6], TiC [5,7] and graphite [8] have been reinforced into it. Among these particulates, TiB_2 has emerged as an outstanding reinforcement. This is due to the fact that TiB_2 is stiff, hard and more importantly, does not react with aluminium to form any reaction product at the interface between the reinforcement and matrix [9].

In situ synthesising of MMCs involves the production of reinforcement within the matrix during composite fabrication. This technique offers an attractive set of features: fine reinforcement, clean interface and process economy [10]. Al–TiB_2 composite is particularly adaptable to in situ synthesising. Reaction between Ti and B is highly exothermic in behaviour and the heat generated helps to accelerate the formation of TiB_2 readily [11]. In addition, TiB_2 is particularly suitable to serve as a reinforcing phase for Al-base composites because of its thermodynamic stability in aluminium [12]. Apart from using the salt route to synthesise the in situ Al–TiB_2 composite [13], no attempt has been made to stir cast the composite from the elemental metals.

This paper investigates the synthesising of Al–TiB_2 composite by the stir casting approach. The processing parameters which influence the formation of TiB_2 and mechanical properties of the composites are studied.

2. Experimental procedures

Ti powder (99.5% purity; average size 150 μm), amorphous B powder (96.1% purity; average size 1 μm) and commercial aluminium AA1100 were used as the starting materials. The (Ti + B) powders with stoichiometric composition corresponding to $15V_f$%TiB_2 were added into molten aluminium after 2 h of preheating at 200°C. Melting of the Al was carried out in a graphite crucible that had been repeatedly brush-coated with alcohol-based zirconium oxide. A vertical chamber furnace operating under normal atmospheric condition was used to do the heating. Argon gas, introduced through an alumina tube, was used to perform the stirring at intervals.

Three composite samples, one in Al-matrix (sample A), one in Al–4.5 wt%Cu matrix (sample B) and the

* Corresponding author. Tel.: +65 874 2236; fax: +65 779 1459.
E-mail address: mpeluli@nus.edu.sg (L. Lu).

0263-8223/99/$ - see front matter © 2000 Elsevier Science Ltd. All rights reserved.
PII: S0263-8223(00)00030-1

other also with Al–Cu but using (Ti + B) mixture incorporated with 3 wt%C (sample C) were synthesised. In all samples, the (Ti + B) mixture was introduced into molten Al at 1040°C, held for 12 min, raised to 1080°C and then held for another 18 min before they were cast into billets. The cast billets were extruded at 350°C at an extrusion ratio of 12:1 and at a rate of 2.85 mm/s. For each billet, three tensile specimens with 6 mm throat diameter were machined. Sample B was solutionised at 500°C for an hour and then aged at 160°C for 18 h so that the matrix was hardened to peak-aged condition. The samples were tested at a ramp rate of 0.005 mm/s. The elongation was measured by attaching a 25 mm extensometer to each tensile sample during testing. Tensile properties were obtained through averaging the results of the three tests carried out for each composite. The phases in the composites were measured by means of XRD and the microstructural features were examined under optical and scanning microscopes.

3. Results and discussion

3.1. XRD analysis

Several reactions had transpired between Al, Ti, B and C. Fig. 1 shows the XRD spectra of the composites synthesised after 30 min of reaction. Analysis shows that

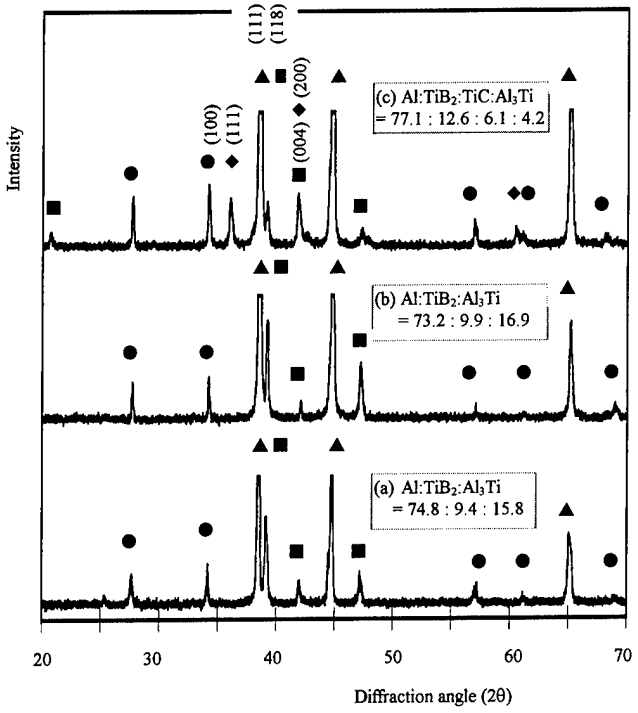

Fig. 1. XRD spectra of (a) Al–15V_f%TiB_2; (b) AlCu–15V_f%TiB_2 and (c) AlCu-15V_f%TiB_2 with 3 wt%C composites: ▲ Al; ● TiB_2; ◆ TiC; ■ Al_3Ti.

the composite samples A and B synthesised by Al–Ti–B system give rise mainly to Al, TiB_2 and Al_3Ti phases (Fig. 1(a) and (b)). This confirms that the addition of the (Ti + B) mixture simultaneously into molten aluminium leads to the reaction of

$$2Ti + 2B + 3Al \rightarrow TiB_2 + Al_3Ti \quad (1)$$

To reflect a clearer comparison, the relative fractions of these 3 phases are calculated based on the intensity of TiB_2 (1 0 0), Al_3Ti (1 1 8) and aluminium (1 1 1) diffraction peaks. The results are shown along with the diffractographs in Fig. 1.

From the figure, it is seen that the relative fractions of Al:TiB_2:Al_3Ti change from 74.8:9.4:15.8 to 73.2:9.9:16.9 as the matrix is changed from Al to Al–Cu. In particular, the relative proportion of TiB_2 increases from 9.4 to 9.9% with the modification of the matrix. This suggests that the presence of Cu promotes nucleation of TiB_2 in the composite. When the amount of TiB_2 increases, the relative proportion of Al_3Ti should reduce since more Ti is consumed to form the TiB_2 phase. However, this situation is seen in reverse in the present work. The relative proportion of Al_3Ti is found to increase from 15.8% to 16.9% after the modification. This phenomenon may probably be attributed to the presence of Cu in the matrix which, apart from increasing the reaction, promotes a more complete formation of Al_3Ti [14]. This occurrence is probably related to the increased reaction when Cu is incorporated into the matrix. The increase in the reaction is likely to be attributed to a more exothermic behaviour of Cu–Ti than Cu–B reaction [14].

For composite sample C, an additional TiC phase is formed as a result of incorporating C to the starting materials. This indicates that C reacts with Ti in accordance to the following reaction at the reaction temperature:

$$3Ti + 2B + C + 3Al \rightarrow TiB_2 + TiC + Al_3Ti \quad (2)$$

Prominent TiC peaks occur in (1 1 1) and (2 0 0) planes, with the latter being overlapped by Al_3Ti (0 0 4) from 41.7 to 42° diffraction angles. Using the peaks of Al, TiB_2 and Al_3Ti phases as described for composite samples A and B together with TiC (1 1 1), the relative fractions of Al:TiB_2:TiC:Al_3Ti are again calculated and presented in Fig. 1(c). The ratios indicate that the amount of TiB_2 is increased from 9.9 to 12.6% while the total (TiB_2 + TiC) reinforcement takes up to 18.7% of the composite. The amount of Al_3Ti is seen to reduce to 4.2%. This suggests that the incorporation of C in the composite suppresses the activity of Ti with Al to form Al_3Ti while inducing some of the Ti to react with C and B to form TiB_2 and Ti simultaneously in the composite. According to Gotman and Koczak [12], Al_3Ti is the first phase to form by a direct reaction between Ti and Al in the Al–Ti–C system. The Al_3Ti further reacts with C to form Ti_2AlC before it is decomposed into TiC particles.

This proposal can be extended to the Al–Ti–B–C system in the sense that TiC and TiB_2 form simultaneously when (Ti + B + C) mixture is added to the molten Al after the decomposition of Ti_2AlC.

3.2. Formation of TiB_2 and Al_3Ti

From Fig. 1, TiB_2 and Al_3Ti were observed to be the two predominant phases when the Al–Ti–B reaction took place at above the melting point of aluminium. The use of process schedule, viz. introducing the mixture at 1040°C and held, raised to 1080°C and held, was the result of a series of experimental melting and casting. It was found by XRD that both Al_3Ti and TiB_2 started to appear at about 800°C. Their formation intensified with the increase in the reaction temperature. The choice of introducing (Ti + B) mixture at 1040°C was made in order to minimise the growth sensitivity of Al_3Ti towards temperature. However, holding at this temperature for the reaction to take place gave rise to low intensity of TiB_2 while maintaining the melt composite at higher temperature caused the formation of a viscous melt. According to Kobashi et al. [15], there exists an incubation period for the wetting of the particles to take place in molten Al. By applying their finding to hold the melt composite at the temperature after the introduction of the mixture for a brief period led to an increase in the nucleation of TiB_2 reinforcement. This increase was also partly attributed to a fuller conversion of $(Al,Ti)B_2$ into TiB_2 [16] when the melt composite was later subject to a higher temperature to induce the reaction to take place.

3.3. Tensile properties

Table 1 compares the tensile properties of the composites with respect to the matrix material. The presence of TiB_2 in the composite (sample A) causes the tensile and yield strengths to increase to more than two orders while the modulus of composite at about 20%. However, when the matrix is modified with the addition of Cu, there is a dramatic improvement especially in tensile and yield strengths. Both of them are seen to increase to three orders. The increment is derived from two factors: an increase in the amount of TiB_2 as shown in Fig. 1(b) and the age hardening of the matrix. The modulus of the composite in this instance also increases correspondingly although the increment is quite small relative to tensile and yield strengths. This shows that the small increase in the modulus is derived from the enhancement of the nucleation of TiB_2 promoted by the Cu and not from the matrix ageing. However, the benefits of these increments are marred by a loss of ductility. The decrease in ductility amounts to as much as 84%. Such a low ductility is associated with the presence of large fraction of Al_3Ti compound. Its presence degrades the mechanical properties through crack propagation manifested from the microstructural analysis (see Fig. 5).

By introducing C to produce the Al–TiB_2–TiC composite (sample C), there is a prominent change in ductility. Table 1 shows that the loss of ductility in this composite is only 27% as compared to the matrix material. Comparing with the Al–TiB_2 composite (sample A), ductility of this composite is higher by two orders. This improvement is accredited to two factors: a reduction of brittle Al_3Ti compound (4.2% against 15.8%) and the improved fracture toughness probably provided by the TiC reinforcement. According to Zdaniewski [17]. TiC is an efficient toughening phase as compared to the TiB_2 of poor fracture toughness. The presence of a combined (TiB_2 + TiC) reinforcement that amounts to 18.7% (Fig. 1(c)) improves the tensile and yield strengths by 2.5 orders. This high amount of total reinforcement also contributes towards an improvement in the modulus of the composite in accordance with McDanels' modulus-reinforcement dependent relationship [18].

3.4. Microstructure

Optical microstructure of Al–TiB_2 composites with both Al- and Al–Cu matrices shows a dispersion of reinforcing particles and Al_3Ti that assumes a flaky form. Fig. 2 shows a typical microstructure. It is seen that the presence of Al_3Ti hinders the uniform distribution of the reinforcement. On the other hand, the Al–TiB_2–TiC

Table 1
Tensile parameters for matrix and reinforced composites. Data in [ ] and ( ) parentheses refer to order of increment and percentage change with respect to the aluminium matrix, respectively[a]

Sample	UTS (MPa) [% increment]	0.2% σ_y (MPa) [% increment]	Modulus (GPa) [% increment]	Elongation (%) [% reduction]
AA1100	102.4	82.1	74.4	14.2
(A) Al–15V_f%TiB_2	223.5	171.3	91.2	4.6
	z[2.2X]	[2.1X]	[1.2X]	(−68%)
*(B) AlCu–	333.0	248.1	93.1	2.3
15V_f%TiB_2	[3.3X]	[3X]	[1.3X]	(−84%)
**(C) AlCu–	257.6	202.8	96.7	10.3
15V_f%TiB_2	[2.5X]	[2.5X]	[1.3X]	(−27%)

[a] * Peak aged; ** With 3 wt%C.

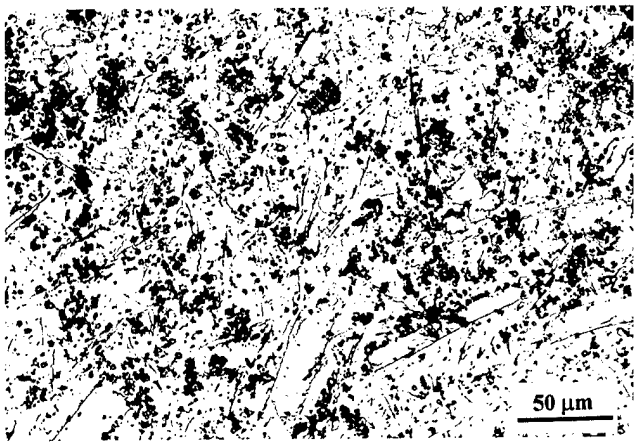

Fig. 2. Reinforcement co-exists with Al_3Ti in Al $15V_f\%TiB_2$ composite.

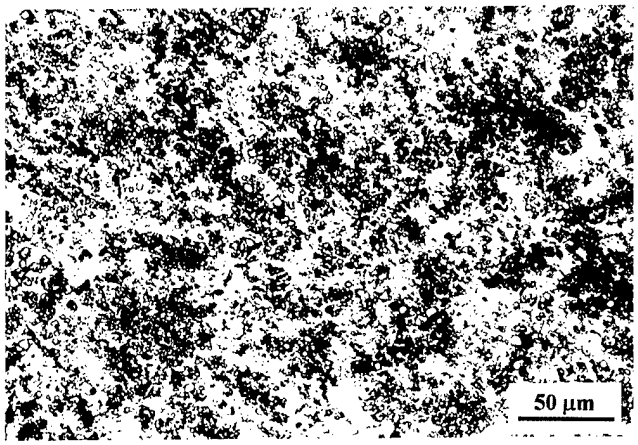

Fig. 3. Relatively uniform distribution of reinforcing particles in AlCu $15V_f\%TiB_2$ composite with 3 wt%C.

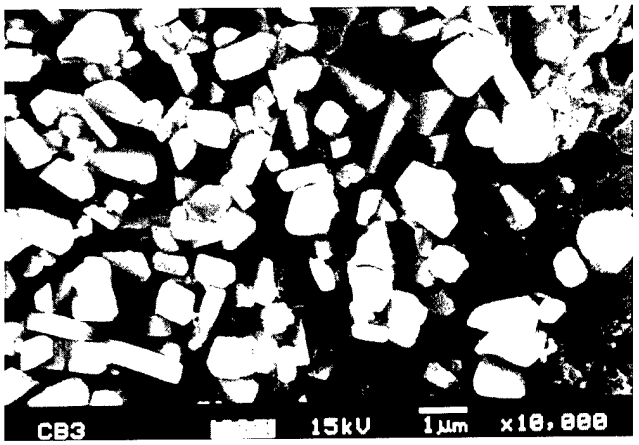

Fig. 4. Reinforcing particulates in AlCu–$15V_f\%TiB_2$ composite with 3 wt%C.

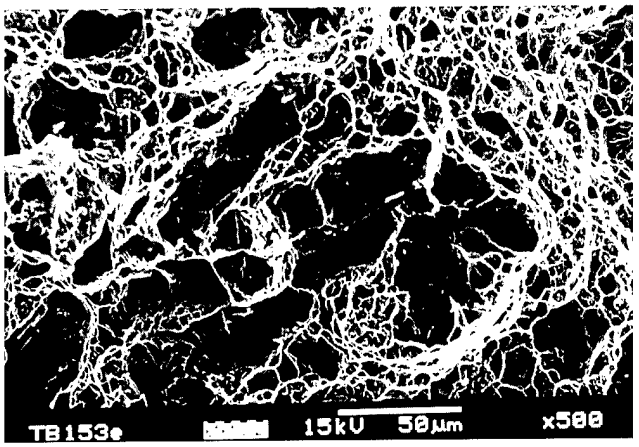

Fig. 5. Crack initiation evidently shown on Al_3Ti flakes.

composite shows scanty evidence of Al_3Ti. Thus, the reinforcement is seen to be uniformly distributed throughout the matrix. Fig. 3. shows a representative structure from such a composite. The apparent increased amount of reinforcement shown in Fig. 3 is attributed to the presence of both TiB_2 and TiC particles. SEM examination reveals the characterised morphology of TiB_2 particulates that assume a hexagonal structure. In Al–TiB_2–TiC composite, apart from the hexagonal TiB_2 particles, some of the reinforcing particulates tend to take a cubic form. Although it is difficult to distinguish between TiB_2 and TiC particulates microstructurally due to the crystallographic orientation of TiB_2, those ill-defined hexagonal structure shown in Fig. 4 are thought to be TiC reinforcement. Fractography reveals a widespreading of crystalline Al_3Ti flakes. The manifestation of cracks in the majority of the flakes, as shown in Fig. 5, explains the cause of low ductility in the composite synthesised from the Al–Ti–B system. This occurrence contrasts with the composite synthesised from the Al–Ti–B–C system where there is a limited amount of Al_3Ti to cause the premature failure.

3.5. Composite yield

Viscosity of a melt increases as a result of increased reinforcement in the composite [19]. In synthesising the in situ Al–TiB_2 composite by stir casting technique, great difficulty was encountered especially in the composite with $15V_f\%$. The composite yield was only 46% during the synthesising of composite sample A. When the same composite was incorporated with 3 wt%C to eliminate the Al_3Ti completely, the composite yield reduced to 21%. The poor recovery was due to the formation of powdery dross on the melt surface and had to be skimmed off before pouring. When Cu was added to the matrix (composite sample C), the composite yield increased to 52%. Cu appeared to provide fluidity to the composite melt. However, the presence of Cu in the composite also promoted the nucleation of Al_3Ti. In

the present work, this was found to be in the region of 4.2%, a level which would not hamper tensile properties appreciably. Thus, casting route is deemed a viable technique to synthesise Al–TiB_2 composite.

4. Conclusions

(a) In situ Al–TiB_2 composite has been successfully synthesised using the traditional casting technique.
(b) The Al–TiB_2 composite synthesised by Al–Ti–B system improved tensile and yield strengths by two orders. The presence of Al_3Ti caused a loss of 68% of ductility.
(c) Modification of the Al-matrix with 4.5 wt%Cu further increased to tensile and yield strengths to three orders.
(d) Alleviated the undesirable presence of Al_3Ti through the formation of additional TiC reinforcement. The composite showed an order of 2.5 improvement in tensile properties as compared to the matrix material. High ductility was maintained in the composite.

References

[1] Alpas AT, Zhang J. Wear 1992;155:83–104.
[2] Rana F, Stefanescu DM. Metall Trans A 1989;20:1564–6.
[3] Lee CS, Kim YH, Han KS. J Mater Sci 1992;27:793–800.
[4] Alpas AT, Embury JD. Scri Metall 1990;24:931–5.
[5] Roy M, Venkataraman B, Bhanuprasad VV, Mahajan YR, Sundararajan G. Metall Trans A 1992;23:2833–47.
[6] Zhang ZF, Zhang LC, Mai YW. J Mater Sci 1995;30:1961–6.
[7] Khatri S, Koczak M. Mater Sci Eng 1993;A162:153–62.
[8] Das S, Prasad SV. Wear 1989;133:137–87.
[9] Wang L, Arsenault RJ. Metall Trans A 1991;22:3013–8.
[10] Aikin RM. J Metals 1997;8:35–9.
[11] Taneoka Y, Odawara O. J Amer Cer Soc 1989;72(2):1047–9.
[12] Gotman I, Koczak MJ. Mater Sci Eng A 1994;189:189–99.
[13] Wood JV, Davies P, Kellie JLF. Mater Sci Techn 1993;9:833–40.
[14] Brinkman HJ, Duszczyk J, Katgerman L. Mater Sci Eng 1998;14:873–6.
[15] Kobashi M, Mohri T, Choh T. J Mater Sci 1993;28:5707–12.
[16] Marcantonio JA, Mondolfo LF. Metall Trans 1971;2:465–71.
[17] Zdaniewski WA. Amer Cer Bull Soc 1986;63:1408–14.
[18] McDanels DL. Metall Trans A 1985;16:1105–15.
[19] Thomas DG. J Colloid Sci 1965;20:267–77.

ELSEVIER

Composite Structures 47 (1999) 595–601

COMPOSITE STRUCTURES

www.elsevier.com/locate/compstruct

Influence of SiC particles on mechanical properties of Mg based composite

B.W. Chua, L. Lu *, M.O. Lai

Department of Mechanical and Production Engineering, The National University of Singapore, 10 Kent Ridge, Crescent 119260, Singapore

Abstract

AZ91 magnesium alloy reinforced with different sizes of SiC particulates has been fabricated using powder metallurgy route. Mechanical properties of the specimens have been studied. Yield and ultimate tensile stresses show a decrease with the increase in the size of SiC particulates. The influence of thermal shock between 400°C and 30°C on the mechanical properties was also investigated. The results show a decrease in yield stress and elongation to fracture with the number of thermal shock cycles. © 2000 Elsevier Science Ltd. All rights reserved.

Keywords: Powder metallurgy; Mg based composites; Thermal shock; Mechanical properties; Microstructure

1. Introduction

Magnesium alloys reinforced by particulates have proven to be advantageous. There are several methods to fabricate Mg metal matrix composites (MMCs) including solid process, infiltration and powder metallurgy (P/M). In P/M, the magnesium matrix composite is fabricated from powders without passing through a fully melting state. P/M technique can attain a more uniform distribution of particulates in the metal matrix without or with less excessive reactions between matrix and the reinforcement.

AZ91 Mg alloy as the matrix material has been investigated. Mg has a hexagonal lattice, lower cold workability and poor corrosion resistance [1]. To improve its mechanical properties and corrosion resistance, several additions have been introduced to Mg, such as Al, Zn and Mn forming AZ91 [2]. Most Mg–Al alloys contain 8–9% Al with small amount of Zn to give some increase in tensile properties. Mn about 0.1–0.3 wt% improves corrosion resistance. The maximum solubility of Al in Mg is 11.8 at.% at the eutectic temperature of 437°C. δ-phase, $Mg_{17}Al_{12}$, sometimes referred to as Mg_4Al_3, appears in alloys containing more than 2% Al. An incoherent, coarse precipitate of the equilibrium $Mg_{17}Al_{12}$ phase is produced without the formation of GP zone or an intermediate metastable precipitate. This precipitate is not fine and dense enough to produce a strong strengthening effect. A network of the δ-phase is formed around the grain boundaries as the Al content is increased and the ductility of the alloy decreases rapidly above 8% Al content [3]. Furthermore, Mg cannot be alloyed with more than about 10% of Al plus Zn or else the ductility of the alloy decreases drastically due to the formation of brittle intermediate compound [3].

The major difficulty in the synthesis of Mg MMCs is the high reactivity of Mg leading to significant problem in producing Mg-based MMCs. Improper fabrication process can cause degradation rather than improvement to the mechanical properties of the composite. Special attentions should be given to the reaction products at the interface between SiC particles and the Mg matrix [4]. Due to the high reactivity of Mg, SiC particles are frequently separated from the matrix by an interfacial film composed of nanocrystalline MgO particles (10–70 nm diameter) to a depth that depends upon the fabrication conditions. These films attain a thickness of up to 500 nm and can promote interparticle fracture. MgO may arise from oxide formation on the surface of the SiC as a result of heating during the fabrication process, as well as from the reduction of oxide such as Al_2O_3. In addition to the oxide films, secondary phase Mg_2Si and $Al_{12}Mg_{17}$ phase have been observed. Mg_2Si in the form of fine particles that are occasionally of 10–400 nm in size, appears to originate from the reaction between the

* Corresponding author. Tel.: +65-874-2236; fax: +65-779-1459.
E-mail address: mpeluli@nus.edu.sg (L. Lu).

0263-8223/99/$ - see front matter © 2000 Elsevier Science Ltd. All rights reserved.
PII: S0263-8223(00)00031-3

SiO_2 on the surface of SiC and the Mg matrix. Mg_2Si, formed by the following reactions, is expected to cause embrittlement [5,6]:

$$2Mg + Si \rightarrow Mg_2Si,$$
$$4Mg + SiO_2 \rightarrow Mg_2Si + 2MgO.$$

The purpose of this study is to investigate the influence of particulate size and thermal shock on the mechanical properties of AZ91-based MMCs arising from the effect of the reactions between the matrix and the reinforcement.

2. Experimental procedures

Mg9Al0.7Zn0.15Mn (wt%) reinforced with 10 vol%SiC particulates with sizes varying from 15 to 50 μm were prepared from elemental powders. The size of the Mg powder was about 60–300 μm. The Mg, Al, Zn, Mn powders and SiC particulates were mixed in a double cone blender at a rotation speed of 50 rpm for 1 h. After mixing, the powder mixture was cold compacted to a size of 40 mm height and 35 mm diameter. The green compact was heated at 400°C for 30 min followed by extrusion. Standard tensile specimens of 5 mm diameter and 25 mm gauge length were machined from the extruded sample according to ASTM E 8M

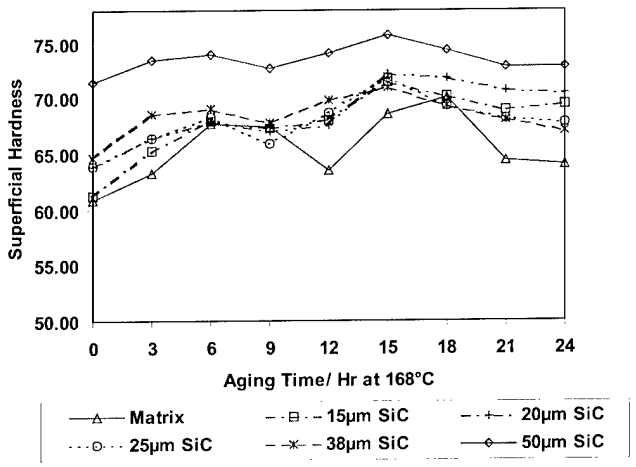

Fig. 1. Variation of hardness with aging time at 168°C.

Table 1
Results of aging studies

Size of SiC (μm)	Peak aging time (h)	Peak hardness (HR15T)
Matrix alloy	18	70.03
15	15	71.47
20	15	72.17
25	15	71.78
38	15	70.93
50	15	75.78

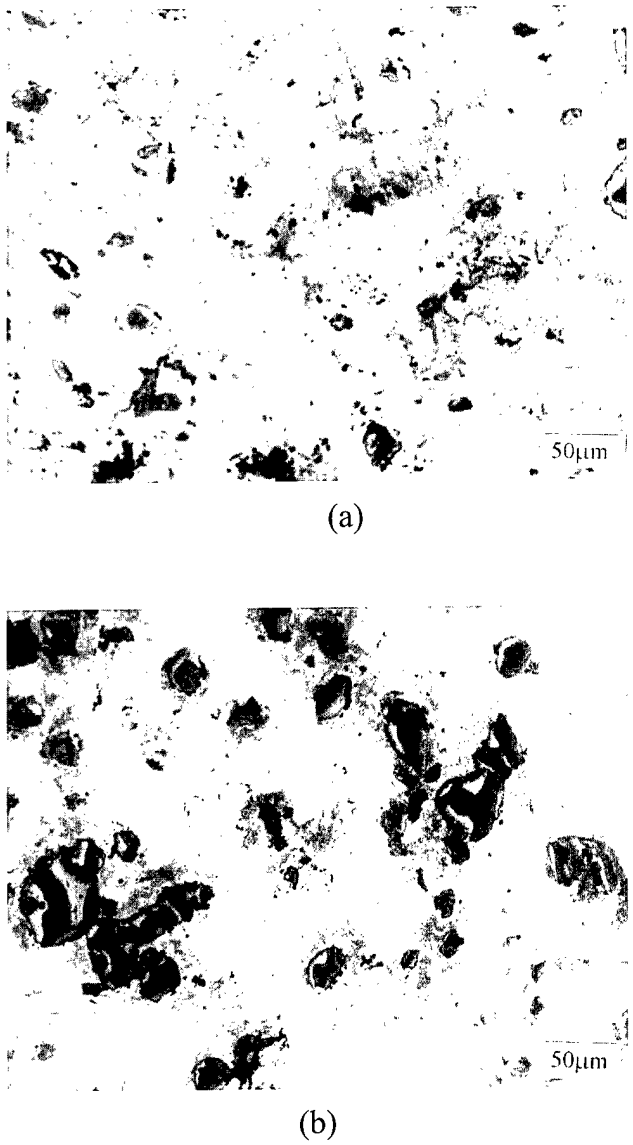

Fig. 2. Optical micrographs of: (a) etched solutionized Mg alloy and (b) etched aged alloy at 168°C for 18 h at 200×.

standard. The specimens were solution treated at 410°C for 2.5 h and quenched into water at room temperature and then artificially aged at 168°C for various durations.

Superficial hardness test in accordance with ASTM E18-94 was conducted on an HR15T-scale Rockwell digital hardness tester with a 1/16 in. steel ball indenter to determine the duration of peak aging. The specimens were artificially aged at 168°C at various time intervals. Hardness at each aging interval was taken. All specimens for tensile testing were solution treated and finally peak aged.

Specimens used for thermal shocking process were first solution treated at 410°C for 2.5 h followed by thermal shock. Thermal shock was performed by heating the specimens to 400°C for 30 min and quenched into water bath at room temperature. To minimise deformation

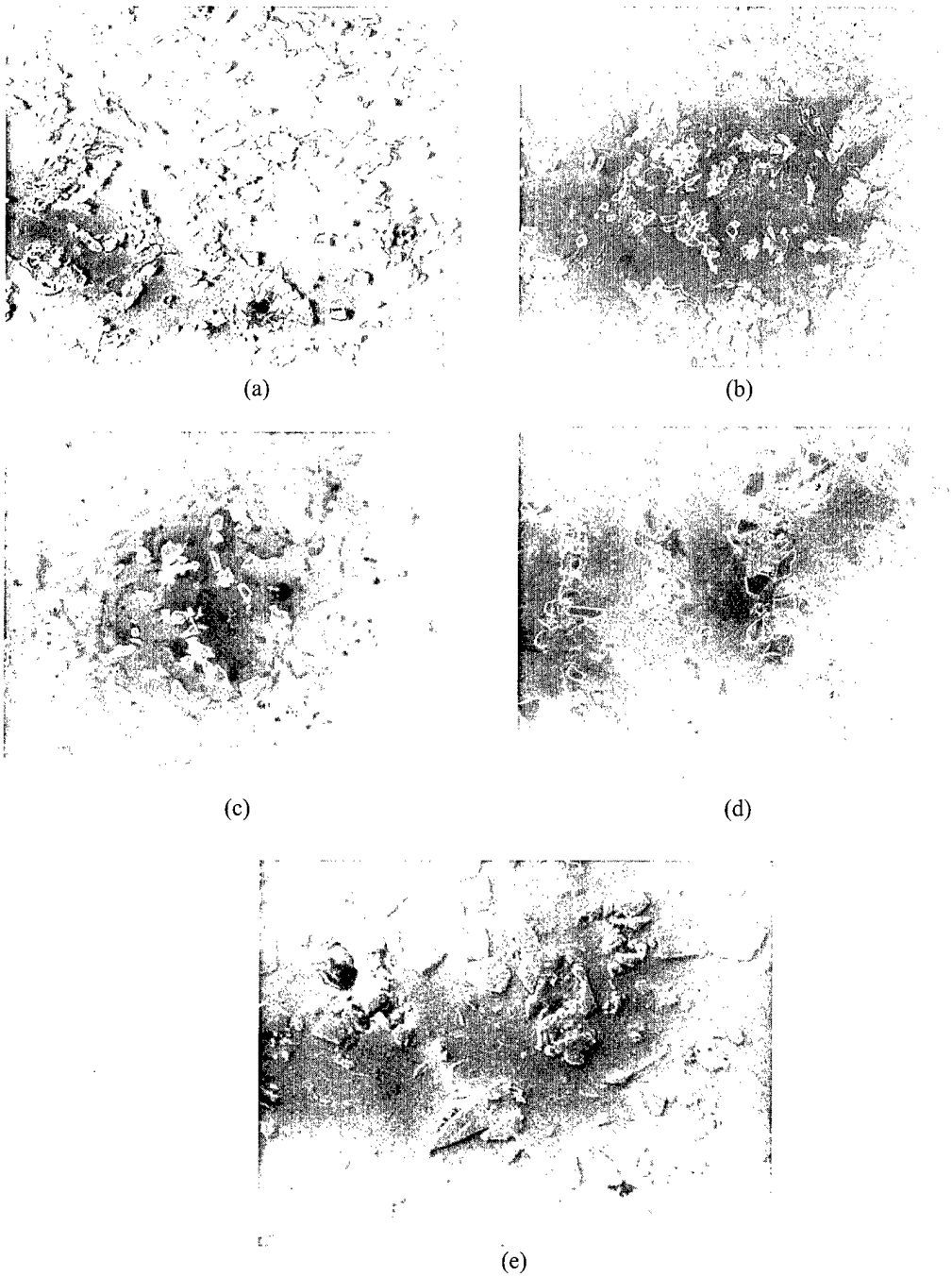

Fig. 3. SEM micrographs of Mg matrix composite (transverse direction) reinforced with SiC of sizes: (a) 15, (b) 20, (c) 25, (d) 38 and (e) 50 μm.

induced by the heating and cooling, the specimens were vertically placed on a ceramic board. A total of 5–20 thermal shocking cycles was conducted. After thermal shock, tensile test was carried out on these thermal shock specimens by using the same testing condition.

Fracture surfaces of specimens after tensile and thermal shock tests were examined under a JEOL JSM-T330A SEM at an accelerating voltage of 15 kV to study the morphologies and microstructure of the fracture surfaces. Crystallographic and phase analyses were performed on an X-ray diffractometer by using monochromatic CuKa radiation. The detection range was from 30° to 80° with a step size of 0.05° and a scanning speed of 2°/min. Identification of crystalline phases was carried out by comparison of XRD patterns with JCPDS database.

3. Results and discussion

Hardness measurement as a function of artificial aging duration at an aging temperature of 168°C is given

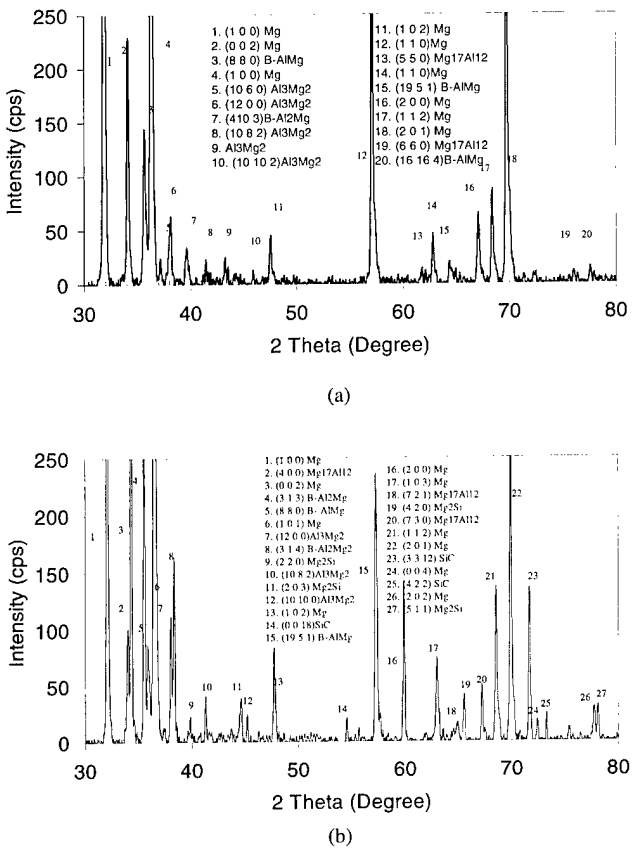

Fig. 4. XRD spectrum of: (a) matrix alloy and (b) reinforced with 50 μm SiC.

in Fig. 1. The peak hardness for the samples with reinforced SiC are summarized in Table 1. The mean hardness readings suggest that the matrix Mg alloy achieved peak age at 18 h while its composites peak aged at 15 h. However, the increase in hardness after aging for both the composites and the alloy is not significant. Hence, aging response of the composite was not very obvious and conclusive enough to justify for aging kinetics.

The optical micrographs in Fig. 2 show the microstructure of the matrix Mg alloy in the transverse direction. Fig. 2(a) shows the microstructure of the solutionised alloy. Precipitate is hardly observed indicating that the structure may be in supersaturated condition. Discontinuous precipitates appeared in the aged alloy from Fig. 2(b).

The SEM micrographs in Fig. 3 show the microstructure of the composites reinforced with the different sizes of SiC in the transverse direction. Although some agglomeration of SiC particles could be observed, the distribution generally appeared to be reasonably homogeneous.

From the results of XRD shown in Fig. 4, presence of $Mg_{17}Al_{12}$ phase was detected in both matrix and reinforced composites. In addition, secondary phase, mainly Mg_2Si was detected in the reinforced matrix composites. Mg_2Si phase appears to originate from the reaction between the SiO_2 on the surface of SiC and the Mg matrix. Based on [5,6], the phase will form from the reaction between SiO_2 on the surface of SiC and the Mg matrix. Mg_2Si is expected to cause embrittlement and could weaken the interfacial bonding and in turn affect the mechanical properties of the composites.

Results of tensile tests including 0.2% yield strength (YS), elastic modulus, ultimate tensile strength (UTS) and percentage of elongation with different particle sizes are shown in Table 2 and Fig. 5. There are only little differences in the 0.2% YS and tensile strength of the 15–25 μm SiC reinforced composites but that with 50 μm particulate possesses a much lower 0.2% YS and tensile strength. It could also be seen that an increase in particle size gave an increase in the Young's modulus as predicted according to the theory of the Tsai Halpin Model [7]. The ductility was however severely reduced. As compared to the matrix, the composites exhibit an overall lower 0.2% YS and tensile strength. There are several possible reasons for this observation. Firstly, the extrusion ratio may be too low for the extruded composites investigated. The low extrusion force created such defects as voids between the SiC and matrix interface as could be seen from the SEM micrographs in Fig. 3, thus resulted in poor bonding between SiC with the matrix interface. Secondly, the interfacial reactions between the reinforcement/matrix interface may have degraded the mechanical properties in that the reaction product such as Mg_2Si may have weakened the interfacial bonding between the SiC and the matrix.

Tensile strength was the lowest for the material with the biggest particle size. K_{IC} values of a particle-

Table 2
Mechanical properties of composites reinforced with SiC of different sizes

Size of SiC (μm)	0.2% YS (MPa)	Elastic Modulus (GPa)	UTS (MPa)	Elongation (%)	Predicted fracture toughness, K_{IC} (MPa $m^{1/2}$)
Matrix alloy	150.00	42.00	190.00	1.15	–
15	120.00	44.50	135.00	0.47	17.70
20	117.00	45.10	120.00	0.24	19.38
25	117.50	42.15	127.50	0.33	21.60
38	110.00	42.00	120.00	0.45	25.80
50	105.00	49.80	110.00	0.23	9.75

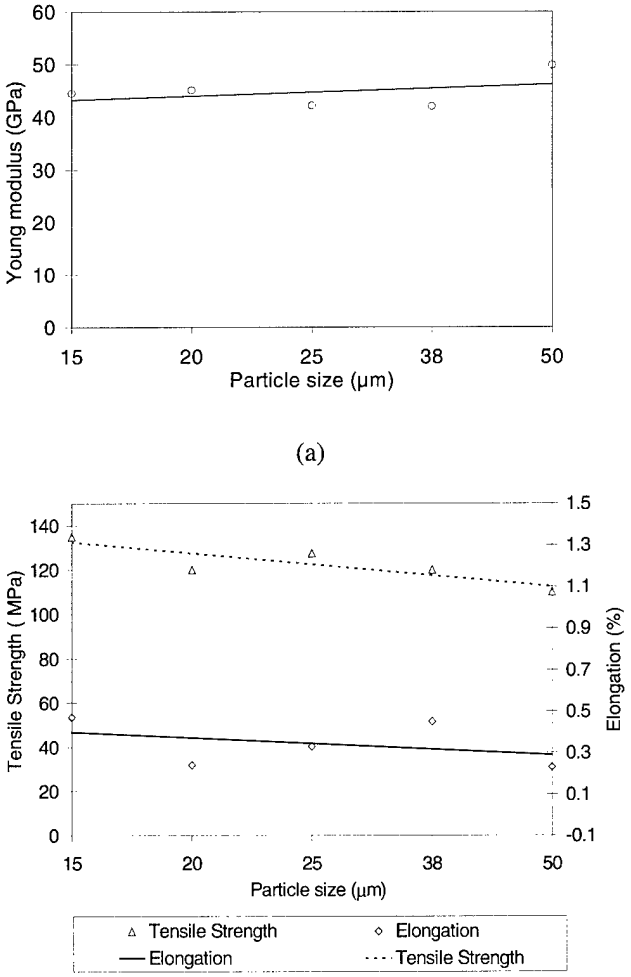

Fig. 5. Influence of SiC particulate reinforcement on: (a) Young modulus and (b) tensile strength and elongation.

reinforced composite may be related to the yield stress σ_y, elastic modulus E, particle diameter D and volume fraction of the particles V according to the relation [8]

$$K_{IC} = [2\sigma_y E(\pi/6)^{1/3} D]^{1/2} V^{-1/6}. \quad (1)$$

Eq. (1) considers that the particles are more resistant to cracking than the matrix. The fracture toughness of a Mg MMC therefore depends on the extent of the heavily strained region of the crack tip that is a function of the yield strength and modulus of elasticity. It is also dependent upon the size and the volume fraction of the particles. From Table 2, the theoretical fracture toughness of the different size of SiC is calculated. The largest particle size gives rise to the lowest fracture toughness value. Large ceramic particles are known to fracture at a given applied stress more likely than smaller particles since they are more likely to contain flaw of critical size.

The tensile strength was the highest for the smallest particle size even though the smaller size particles had a greater surface area that would lead to greater interfacial reaction between the SiC and the matrix and that degrades the mechanical properties. In this case, the more dominating effect on the mechanical properties is due to grain size (Hall–Petch relationship) and the spacing between SiC particulates (Orowan strengthening). The grain size for the different size of particles and yield strength are shown in Table 3 where the values of k and σ_0 for the Hall–Petch relationship can be evaluated to be 273.31 and 60.081 MPa, respectively. The tensile strength is the highest for the 15 μm SiC reinforced composite because of smaller grains.

The thermal shock cycling and tensile tests were carried out on the same specimens under the same testing conditions. The results of the two different sizes of SiC at various thermal shock times are summarised in

Table 3
Mean grain size of composites reinforced with SiC with different sizes

Size of particle	15 μm	20 μm	25 μm	38 μm	50 μm
Mean grain size (μm)	22.40	26.70	27.10	36.00	41.70
Tensile strength (MPa)	135.00	120.00	127.50	120.00	110.00
$D^{-1/2}$ ($\mu m^{-1/2}$)	0.21	0.19	0.19	0.16	0.15

Table 4
Effects of thermal shock cycles on mechanical properties of composites with 15 and 50 μm SiC particles

No of thermal shock cycles	0.2% YS (MPa)	Elastic Modulus (GPa)	UTS (MPa)	Elongation (%)
15 μm SiC				
5	117.50	41.70	125.00	0.46
10	120.00	41.10	125.00	0.38
15	117.50	43.60	135.00	0.48
20	100.40	42.60	101.50	0.23
50 μm SiC				
5	94.00	43.00	93.00	0.27
10	97.50	43.00	98.50	0.25
15	82.00	44.00	83.00	0.15
20	94.00	40.00	90.00	0.15

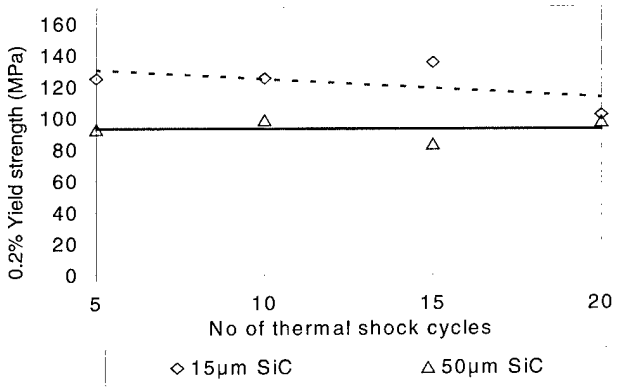

(a)

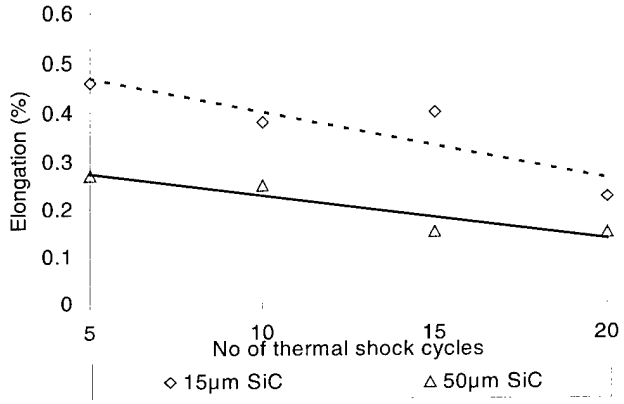

(b)

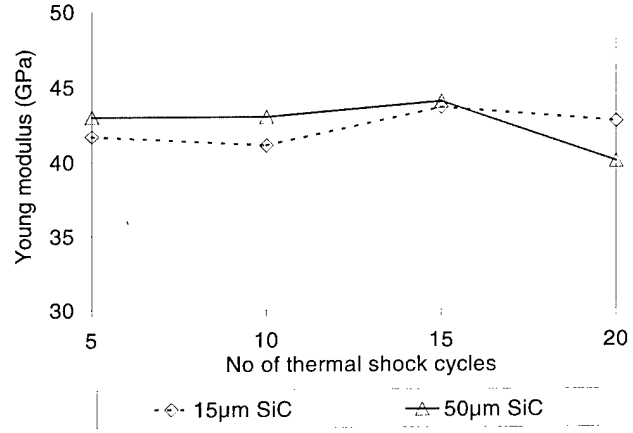

(c)

Fig. 6. Influence of thermal shock cycles on: (a) 0.2% yield strength, (b) elongation and (c) Young's modulus.

Table 4 and graphically shown in Fig. 6. Both the 15 and 50 μm SiC reinforced composites in general show almost no change in Young's modulus. Quenching generated large dislocation density owing to mismatch in the thermal expansion coefficients of the two phases. These dislocations are believed to increase the pile up stresses generated by the geometrically necessary dislocation during plastic flow and hence increasing the likelihood of particle fracture [9]. Elongation for both reinforced composites decreased as the thermal shock cycles increased. The difference in coefficient of thermal expansion (CTE) between the two phases had been related to a high dislocation density in the matrix. The CTE of Mg was six times larger than that of SiC (Mg CTE $\approx 24 \times 10^{-6}$/K, SiC CTE $\approx 4 \times 10^{-6}$/K). The thermal mismatch occurring at the interface had induced high density of dislocations causing debonding between the matrix and the SiC particulates, hence leading to decrease in both strength and elongation. By comparison, the 15 μm SiC reinforced Mg composites had higher tensile strength and percentage of elongation than the 50 μm SiC reinforced composites. This could be attributed to the effect of the Hall–Petch relationship was still dominant as the tensile strength, σ_y, is proportional to the grain size, $D^{-1/2}$. Consequently, the smaller SiC particles would cause grain refinement in the composites that resulted in higher tensile strength. Moreover, the additional SiC particles were carried out in the softer matrix and they hindered the motions of the dislocations and enhanced the strength of the composite.

4. Conclusions

The influence of SiC particle size on the microstructure, thermal shock behaviour and mechanical properties of Mg matrix composites with composition of Mg-9 Al-0.7 Zn-0.15 wt% Mn/10 vol% SiC particles has been studied. The increase in hardness after aging for both the matrix and composites was not significant. Major phase such as $Mg_{17}Al_{12}$ was detected. Secondary phase, namely Mg_2Si, had been detected in the reinforced matrix composites. Mg_2Si may have caused embrittlement that could weaken the interfacial bonding, and defects from low extrusion ratio (19:1) could have affected the mechanical properties of the composites.

The smaller particle size in the composite resulted in relatively higher elastic modulus and tensile strength with the number of thermal shock cycles. The difference in CTE between the matrix and SiC particulates led to a higher dislocation density and thermal residual stress, causing, cracking and debonding. The tensile strength and elongation decreased as the number of thermal shock cycles increased.

References

[1] Emley EF. Principles of magnesium technology, First ed.. Oxford, New York: Pergamon Press; 1966.

[2] Polmear IJ. Light alloys, Second ed.. London: Edward Arnold; 1989.
[3] Smith WF. Structure and properties of engineering alloys. New York: McGraw-Hill; 1981.
[4] Mordike BL, Kainer KU, Schroder J. Powder metallurgical preparation of composite materials. Trans Powder Metallurgy Assoc India 1990;17:7–17.
[5] Inem B, Pollard G. Interface structure and fractography of a magnesium-alloy, metal-matrix composite reinforced with SiC particles. J Mater Sci 1993;28(16):4427–34.
[6] Molins R, Bartout JD, Bienvenu Y. Microstructural and analytical characterization of Al_2O_3-(Al–Mg) composite interfaces. Mater Sci Engrg A 1991;135-137(1–2):111–7.
[7] Lloyd DJ. Particle reinforced aluminium and magnesium matrix composites. Int Mater Rev 1994;39(1):1-23.
[8] Lu L, Lai MO, Chen FL. Al-4 wt% Cu composite reinforced with in situ TiB2 particles. Acta Materialia 1997;45(10):4297–309.
[9] Dunand D, Mortensen A. Thermal mismatch dislocation produced by large particles in a strain-hardening matrix. Mater Sci Engrg 1991;135:179–84.

ELSEVIER

Composite Structures 47 (1999) 603–611

COMPOSITE STRUCTURES

www.elsevier.com/locate/compstruct

Mesh design in finite element analysis of post-buckled delamination in composite laminates

T.E. Tay [a,*], F. Shen [a], K.H. Lee [a], A. Scaglione [b], M. Di Sciuva [b]

[a] *Department of Mechanical and Production Engineering, National University of Singapore, 10 Kent Ridge Crescent, Singapore 119260, Singapore*
[b] *Departimento di Ingegneria Aeronautica e Spaziale, Politecnico di Torino, Corso Duca Degli Abruzzi, 24, 10129, Torino, Italy*

Abstract

The role of mesh design in the post-buckling analysis of delamination in composite laminates is addressed in this paper. The determination of the strain energy release rate (SERR) along the crack front is central to the analysis. Frequently, theoretical analysis is limited to treatment of the problem in two dimensions, since considerable complexity is encountered in extending the analysis to three dimensions. However, many practical problems of embedded delamination in composite laminates are inherently three-dimensional in nature. Although in such cases, the finite element (FE) method can be employed, there are some issues that must be examined more closely to ensure physically realistic models. One of these issues is the effect of mesh design on the determination of the local SERR along the delamination front. There are few studies that deal with this aspect systematically. In this paper, the effect of mesh design in the calculation of SERR in two-dimensional (2D) and three-dimensional (3D) FE analyses of the post-buckling behavior of embedded delaminations is studied and some guidelines on mesh design are suggested. Two methods of calculation of the SERR are considered: the virtual crack closure technique (VCCT) and crack closure technique (CCT). The 2D analyses confirm that if the near-tip mesh is symmetric and consists of square elements, then the evaluation of the SERR is not sensitive to mesh refinement, and a reasonably coarse mesh is adequate. Despite agreement in the global post-buckling response of the delaminated part, the SERR calculated using different unsymmetrical near-tip meshes could be different. Therefore, unsymmetrical near-tip meshes should be avoided, as convergence of the SERR with mesh refinement could not be assured. While the results using VCCT and CCT for 2D analyses agree well with each other, these techniques yield different quantitative results when applied to 3D analyses. The reason may be due to the way in which the delamination growth is modeled. The CCT allows simultaneous delamination advance over finite circumferential lengths, but it is very difficult to implement and the results exhibit mesh dependency. Qualitatively, however, the two sets of results show similar distributions of Mode I and Mode II components of the SERR. This is fortunate, since the VCCT is relatively easy to implement. © 2000 Elsevier Science Ltd. All rights reserved.

Keywords: Mesh design; Finite element analysis; Post-buckled delamination; Composite laminates

1. Introduction

Much research work has been carried out on the analysis of delamination growth in laminated composites. In most of the work, 2D plane strain conditions are assumed in order to simplify the analysis. The problem then corresponds to the post-buckling behavior of a through-width thin-film delamination of the test coupon [1,2]. The results obtained from such analyses are often used to infer the general behavior of delaminations in composite structures. However, delaminations in laminated structures are usually 3D in nature [3,4]. Typically, delaminations occur during low velocity impact, around fastener holes, or as manufacturing defects. Near surface multiple delaminations can result from impact damage. The post-buckling response of such delaminations under compressive loads can be complicated. It is unlikely that simplified 2D analyses will be adequate in describing all the characteristics of real structural delaminations. Therefore, in order to understand the mechanism of delamination growth more fully, it is hoped that more accurate and realistic models can be built and analyzed. Furthermore, these models must be validated, together with appropriately formulated growth and fracture criteria, by comparison with experimental results [5,6]. Towards this end, some finite element (FE) analyses of delaminations in composite laminates, with varying levels of complexities, have been performed. A number of them are 2D plane strain analyses [7,8]. However, the majority of investigations may

* Corresponding author.
E-mail address: mpetayte@nus.edu.sg (T.E. Tay).

0263-8223/99/$ - see front matter © 2000 Elsevier Science Ltd. All rights reserved.
PII: S0263-8223(00)00033-7

be classified as quasi-3D analyses, employing plate or shell elements in order to reduce computational effort [9–14]. In some cases, releasing selected node pairs advances the delamination crack front. The virtual crack closure technique (VCCT) [15–18] is commonly used to determine the strain energy release rates (SERRs) and the locations where the node pairs are to be released. However, while the use of plate or shell elements enables the determination of the total SERR along the delamination front, generally it does not permit the separation of the SERR into its three components (i.e., the opening and two shearing modes) [11]. For this reason, several researchers [19–25] have used fully 3D FE models, although the analyses are much more computationally intensive. It should also be noted that although the VCCT is commonly used because it requires only a single solution, it is an indirect method of computing the SERR based on linear elastic fracture mechanics. One of the objectives of this paper is to compare the use of the VCCT with a more direct (albeit more inefficient) crack closure method [26] of computing the SERR. Also implicit in the use of the VCCT is the assumption of self-similarity in crack growth. While this does not present a problem in 2D analyses, in 3D or quasi-3D cases the final and initial shapes of the delamination front are usually very different. The use of VCCT in the latter cases implies an incremental uniform crack growth along the entire crack front, which is not observed experimentally. Despite this, the VCCT is likely to remain popular due to its simplicity, ease of implementation and computational efficiency. A 3D analysis also introduces the possibility of modeling local crack closure along parts of the delamination front [22,24]. It has been shown in some studies that under high compressive loads, it is important to include contact surface definitions in FE models to prevent inter-penetration of crack surfaces. Local crack closure is likely to be influenced by the stacking sequence of the sub-laminate.

Although many studies have employed the FE method, relatively few have addressed the influence of mesh design or refinement on the computation of the SERR. Papers that deal with mesh refinement include references [19,24,26,27]. It will be shown in this paper that the VCCT produces values of SERR that are relatively insensitive to mesh refinement, compared to values produced by the direct crack closure technique (CCT). It will also be shown that 2D analysis produces results that are different from those using 3D analysis. In the following, the VCCT and its assumptions will be reviewed. Issues involved in the implementation of the VCCT and the calculation of SERR using CCT, especially in 3D analysis of delaminations, will be discussed. Several 2D FE models with different mesh designs and refinements for post-buckling analysis of delaminated plates under plane strain conditions will be described. The effect of varying the depth of the delamination is studied. It is found that the depth of the delamination has a significant effect on the relative magnitudes of the Mode I (opening) and Mode II (sliding) components of SERR. The observations gained from the 2D analysis are used to guide the construction of several 3D FE meshes of a compressively loaded rectangular composite plate containing a circular embedded delamination. Results of the SERRs along the delamination front, computed using VCCT and CCT are compared and discussed. The effect of mesh refinement along the circumferential direction of the delamination front is also considered. All analyses are conducted using an in-house finite element code for post-buckled delamination.

2. Virtual crack closure and direct crack closure techniques

At this point, it should be noted that since delamination in laminated composites usually propagates in between two plies of different fibre orientations, the problem can be considered as that of a crack embedded between two dissimilar orthotropic materials. In such interfacial crack problems, the near-tip stress singularity exhibit an oscillatory nature [28]. It can be shown that while the total SERR does not show oscillatory behavior, the Mode I and Mode II components of the SERR do [28,29]. However, it is generally recognized that the oscillatory stress and displacement solutions are non-physical. Some researchers have therefore proposed alternative measures of SERR components that do not exhibit this oscillatory behavior [29,30]. Fortunately, the dominance of this oscillatory behavior of the stresses and displacements is confined to a small region near the crack tip. Outside this region (estimated to be about 0.25 of the ply thickness [27]), the VCCT can be effectively applied to yield physically reasonable values of Mode I and Mode II components of the SERR [27,29]. We therefore exclude from our discussion here the determination of SERR within the zone of oscillating stress singularity. Another usual way of avoiding this issue of oscillating singularity is to assume that the crack tip is, in reality, embedded within a very thin isotropic matrix-rich layer between the plies. Within this even smaller length scale, the familiar non-oscillatory square root singularity prevails and the SERR components are well defined. However, it is impractical to generate a 3D model containing this interlaminar resin-rich layer, since an inordinately large number of elements and nodes would be required.

Suppose a crack extends by a small amount Δc; in the CCT, it is assumed that the strain energy released in the process is equal to the work required to close the crack to its original length. When applied in a numerical method, two analyses are needed to obtain the components of SERR. The first is performed for the case just prior to crack growth, which yields the nodal forces at

the crack tip. In the second analysis, the relevant crack tip nodes are released, providing the required corresponding nodal displacements. The nodal forces obtained in the first step are the forces required to close the crack. The work done during this process can then be obtained by multiplying one-half of the nodal forces with the corresponding displacements. The components of SERR can be obtained by separating the total work into its corresponding components.

The VCCT, however, is an approximate method that dispenses with the need for two analysis steps. The nodal forces at the crack front and the displacements behind the crack front are used to calculate the SERR. It should be noted that the VCCT implies self-similarity in crack growth, a fact generally not crucial for 2D delamination problems, but clearly not generally true for 3D delamination growth. Fig. 1 shows the near crack front region for 2D and 3D finite element problems.

In 2D cases, the SERR components G_{I} and G_{II} can be expressed as:

VCCT

$$\begin{aligned} G_{\mathrm{I}} &= \frac{1}{2\Delta c}[Y_5(v_1 - v_2) + Y_6(v_3 - v_4)] \\ G_{\mathrm{II}} &= \frac{1}{2\Delta c}[X_5(u_1 - u_2) + X_6(u_3 - u_4)], \end{aligned} \tag{1}$$

CCT

$$\begin{aligned} G_{\mathrm{I}} &= \frac{1}{2\Delta c}(Y_5\delta v_5 + Y_6\delta v_6) \\ G_{\mathrm{II}} &= \frac{1}{2\Delta c}(X_5\delta u_5 + X_6\delta u_6). \end{aligned} \tag{2}$$

In 3D cases, G_{I}, G_{II} and G_{III} are approximated by:

VCCT

$$\begin{aligned} G_{\mathrm{I}} &= \frac{1}{2\Delta A}\left\{Z_{c_3}(w_{a_3} - w_{A_3}) + Z_{d_2}(w_{b_2} - w_{B_2}) + \frac{1}{2}[Z_{c_2}(w_{a_2} - w_{A_2}) + Z_{c_4}(w_{a_4} - w_{A_4})]\right\} \\ G_{\mathrm{II}} &= \frac{1}{2\Delta A}\left\{X_{c_3}(u_{a_3} - u_{A_3}) + X_{d_2}(u_{b_2} - u_{B_2}) + \frac{1}{2}[X_{c_2}(u_{a_2} - u_{A_2}) + X_{c_4}(u_{a_4} - u_{A_4})]\right\} \\ G_{\mathrm{III}} &= \frac{1}{2\Delta A}\left\{Y_{c_3}(v_{a_3} - v_{A_3}) + Y_{d_2}(v_{b_2} - v_{B_2}) + \frac{1}{2}[Y_{c_2}(v_{a_2} - v_{A_2} + Y_{c_4}(v_{a_4} - vA_4)]\right\}, \end{aligned} \tag{3}$$

CCT

$$\begin{aligned} G_{\mathrm{I}} &= \frac{1}{2\Delta A}(Z_{c_3}\delta w_{c_3} + Z_{d_2}\delta w_{d_2} + Z_{c_2}\delta w_{c_2} + Z_{c_4}\delta w_{c_4}) \\ G_{\mathrm{II}} &= \frac{1}{2\Delta A}(X_{c_3}\delta u_{c_3} + X_{d_2}\delta u_{d_2} + X_{c_2}\delta u_{c_2} + X_{c_4}\delta u_{c_4}) \\ G_{\mathrm{III}} &= \frac{1}{2\Delta A}(Y_{c_3}\delta v_{c_3} + Y_{d_2}\delta v_{d_2} + Y_{c_2}\delta v_{c_2} + Y_{c_4}\delta v_{c_4}). \end{aligned} \tag{4}$$

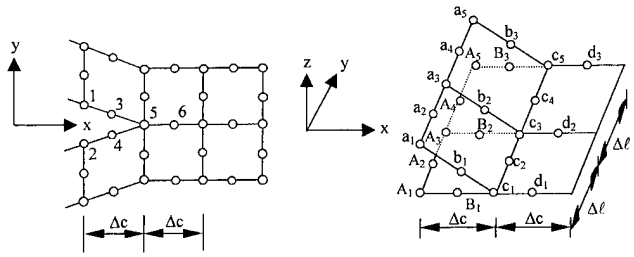

Fig. 1. Schematic of crack front region in 2D and 3D cases.

In the above equations, X, Y and Z are nodal force components, and u, v and w are nodal displacement components in the x, y and z directions, respectively. The subscripts denote the corresponding nodes in Fig. 1. For the CCT, δu, δv and δw are the differences in nodal displacement components before and after node release. The delaminated area is given by $\Delta A = \Delta c \cdot \Delta l$.

In the preceding equations, it is assumed that the element sizes ahead of and behind the crack tip are equal. If they are not equal, Rybicki and Kanninen [15] have shown that the nodal forces can be corrected by considering the fact that for isotropic materials, the stresses near the crack tip vary as $1/r^{1/2}$.

3. 2D analysis of post-buckled delamination

In this section, the effect of mesh design on 2D analysis of the post-buckling behavior of delamination is considered. The isotropic material properties chosen are given in Table 1. The problem is defined as the post-buckling of a through-width delamination of an isotropic plate, with the dimensions shown in Fig. 2. The plate is fully clamped at both ends, where in-plane compressive loads are applied. The length of the plate is $L = 120$ mm, the length of the delaminated part is $l = 40$ mm, the thickness of the plate is $T = 4$ mm, and the thickness

Table 1
Material properties

Isotropic	Composite (graphite/epoxy)
$E = 10$ GPa	$E_{11} = 145.6$ GPa
$\nu = 0.3$	$E_{22} = 10.5$ GPa
	$\nu_{12} = 0.3$
	$G_{12} = 5.25$ GPa

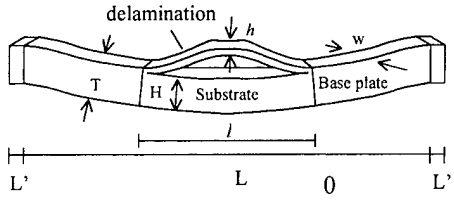

Fig. 2. Dimensions of a through-width delamination of plate.

of the delaminated part is $h = 0.4$ mm. Due to symmetry, only half of the plate needs to be meshed. Eight-node plane strain quadrilateral elements are used in an in-house code, which has been developed specifically for the finite element analysis of post-buckled delamination. The first and coarsest mesh used is shown in Fig. 3, where the amplified post-buckling shape is also shown. An eigenvalue analysis produced a critical buckling load of the delaminated part of 14.21 N. A separate analysis using the same mesh in the FE software ABAQUS showed a comparable value of 14.22 N.

In non-linear analysis of the post-buckling behavior of delaminations, it is usual to introduce a small transverse displacement to the delaminated part in order to initiate the buckling behavior. Here, three values of the initial transverse displacement d are chosen to determine its effect on the results ($d/h = 0.15\%$, 1.5% and 15%). Fig. 4 shows the applied load versus maximum transverse displacement of the delaminated part for the three cases, and Fig. 5 shows the crack tip nodal opening forces as a function of the applied load (normalized with respect to the critical buckling load). The effect is only significant very close to the critical buckling load. The behavior is not affected at all for values of d/h at or less than 1.5%. Hence, the value of 1.5% is selected for all subsequent analyses.

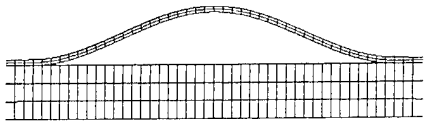

Fig. 3. Typical post-buckling shape with a coarse mesh.

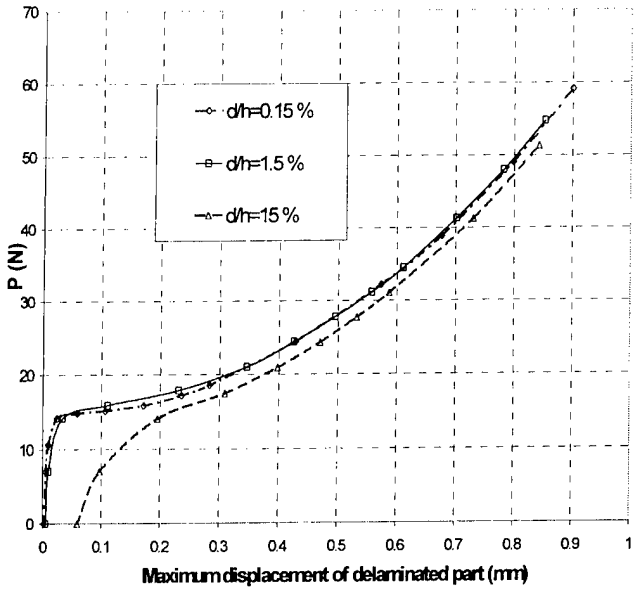

Fig. 4. Applied load vs maximum transverse displacement.

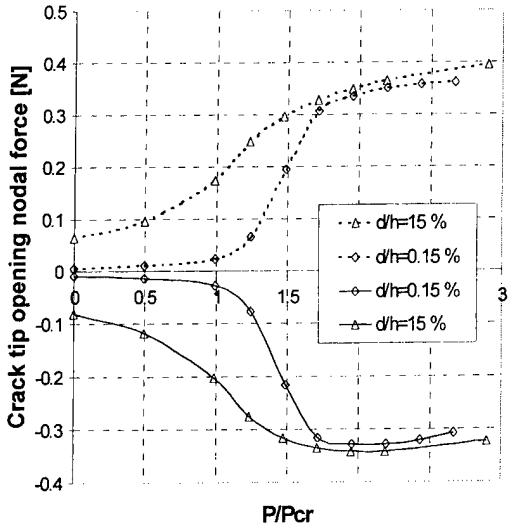

Fig. 5. Crack tip nodal opening forces.

Two sets of FE meshes are generated. The first five meshes (labeled $a1$–$a5$ in Table 2) contain rectangular elements. Elements ahead of the crack tip are not identical to those behind the crack tip. The former are smaller in size and aspect ratio than the latter. The mesh is progressively finer with consecutive numbering. The crack tip element size c refers to the length of the element directly ahead of the crack tip, in the x-direction. Examples of the meshes are shown in Fig. 6. The second set consists of four meshes (labeled $s1$–$s4$). These contain square elements, and the mesh behind the crack tip is a mirror image of the mesh ahead of the crack tip. In other words, the meshes are symmetrical. Some of these meshes are shown in Fig. 7. All nine meshes did not have a significant effect on the critical buckling load, which remains at about 14.2 N, and the subsequent applied load versus maximum transverse displacement curves are identical.

Although the global response of the delamination behavior is similar in every case, the SERR calculated using CCT differs considerably in cases where mesh symmetry is not present. Figs. 8 and 9 show the non-dimensionalized Mode I and Mode II SERR, for meshes $a1$–$a5$, respectively. ε_0 is the applied strain, ε_{cr} is the Euler critical strain for the delaminated part, and the normalized SERRs are defined as $G_i = (2G_i/Eh) \times 10^5$. Clearly, there is no convergence with mesh refinement.

Table 2
Meshes for 2D analysis

Mesh	c (mm)	c/l
$a1$, $s1$	1	0.025
$a2$, $s2$	0.5	0.0125
$a3$, $s3$	0.25	0.00625
$a4$, $s4$	0.125	0.003125
$a5$	0.0625	0.0015625

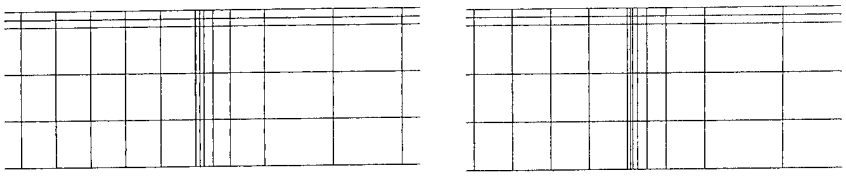

Mesh *a*4 Mesh *a*5

Fig. 6. 2D Unsymmetric near-tip meshes.

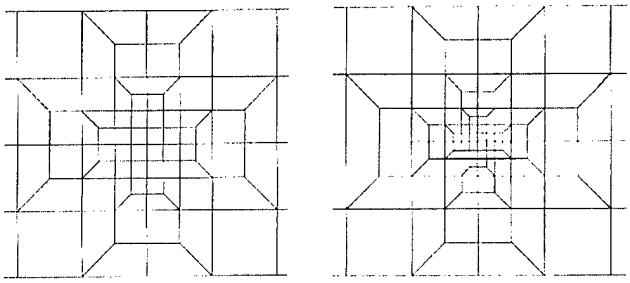

Fig. 7. 2D symmetric near-tip meshes.

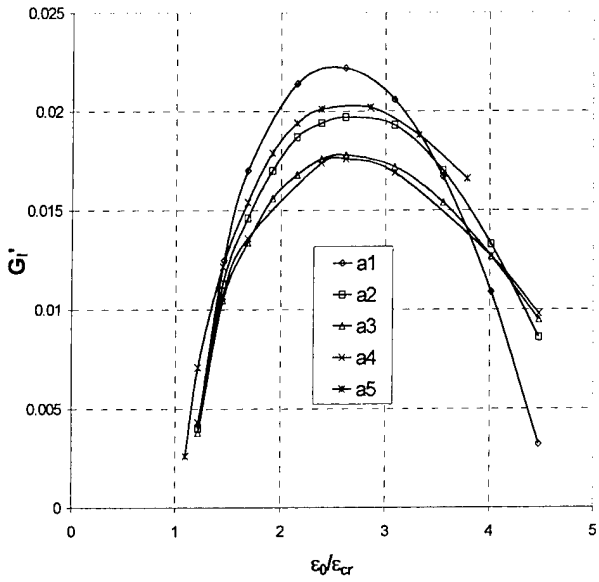

Fig. 8. Mode I SERR for unsymmetric near-tip meshes.

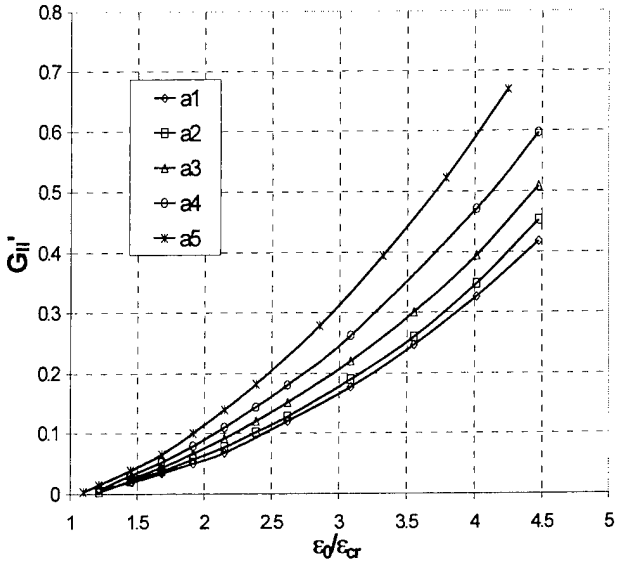

Fig. 9. Mode I SERR for unsymmetric near-tip meshes.

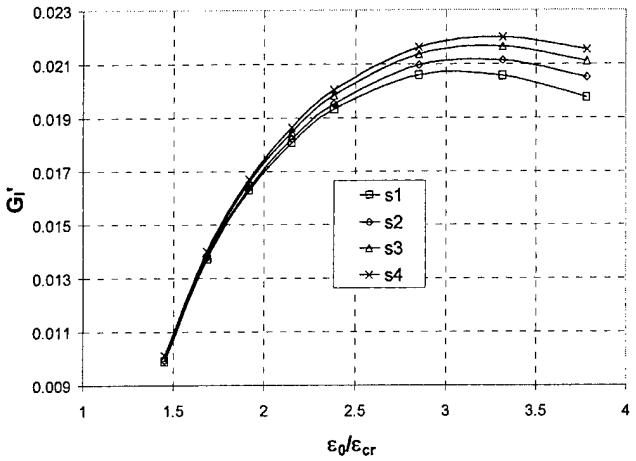

Fig. 10. Mode I SERR for symmetric near-tip meshes.

The value of G_{II} continues to rise with greater mesh refinement. However, in the case of symmetrical meshes, i.e. *s*1–*s*4, the results for both G_I and G_{II} are nearly independent of the mesh fineness (Figs. 10 and 11, respectively). Indeed, the coarsest mesh *s*1 appears to be sufficient for producing accurate results. When the SERR is calculated using the VCCT, the results are identical to those calculated using the CCT, confirming the expected conclusion that in 2D analysis, the use of CCT and VCCT yields equivalent results.

In the problem discussed above, the Mode II SERR appears to be the dominating component, compared to the Mode I SERR. This is due to the position of the delamination being close to the top surface of the plate. With increasing depth of the delamination, the magnitude of G_I relative to G_{II} will increase. If material properties are now changed to those of a unidirectional graphite-epoxy composite (Table 1), and the delamination depth is increased to $h/T = 0.2$, the relative magnitudes of G_I and G_{II} are shown in Fig. 12. Two different

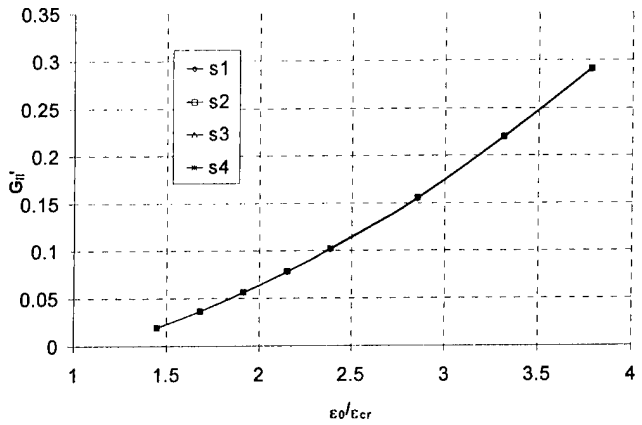

Fig. 11. Mode II SERR for symmetric near-tip meshes.

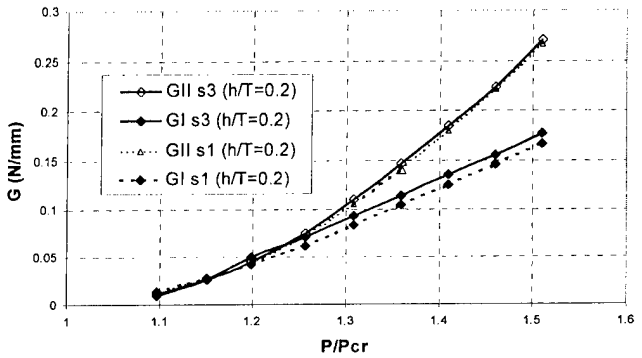

Fig. 12. Mode I and Mode II SERR calculations for graphite-epoxy composite plate.

symmetric meshes near the crack tip are used, *s*1 and *s*3. Again, the results show that mesh refinement has little effect on the SERRs.

The conclusion of the 2D analysis is that if the near-tip mesh is symmetric and consists of square elements, then the evaluation of G_I and G_{II} is not sensitive to mesh refinement, and a reasonably coarse mesh is adequate. Despite agreement in the global post-buckling response of the delaminated part, the SERR calculated using different unsymmetrical near-tip meshes could be different. Unsymmetrical near-tip meshes should be avoided, as convergence of the SERR with mesh refinement could not be assured.

4. 3D analysis of post-buckled circular delamination

The results of the 2D analysis in the preceding section are used as a guide for the construction of 3D FE meshes for the analysis of a circular delamination in a rectangular composite plate subjected to compressive loads. The problem considered is a 12-ply plain weave ECS0002 graphite fabric composite plate of length 250 mm and width 50 mm, with a centrally located hole of 5 mm diameter. The total thickness of the laminate is 3.6 mm. A circular delamination, in the form of a 20 mm diameter Teflon sheet and centred with the hole, was inserted between the first and second plies before fabrication by the autoclave method. Twelve specimens were mounted onto an anti-buckling device and tested under fatigue with fully reversed compression-tension loading ($R = -1$) and a peak load of 28 kN. This peak load corresponds to 65% of the ultimate compressive strength of the notched laminate. Details of the experiment and the results can be found in Ref. [31]. The delamination began to grow transverse to the loading direction across the width of the specimen at about 10,000 cycles. C-scan images showed that the delamination continued to grow in the same direction until final failure at between 300,000 and 380,000 cycles.

Three 3D FE meshes with local symmetry at the near-tip region, are constructed (Fig. 13). These are labeled *S*1–*S*3. Because of symmetry, only a quarter of the plate is modeled. Mesh *S*1 has the coarsest radial section mesh design. Mesh *S*2 is a slight improvement over *S*1, having more elements near the crack tip region. The third mesh *S*3 is considerably more refined than the previous two. The mesh design in the plane of the plate is also shown in Fig. 13. There is more refinement in the circumferential direction near the region of observed delamination growth. For computations using VCCT and CCT, coarser meshes in this region are also used to observe the effect of mesh design on the components of the SERR.

The CCT is applied to each mesh at the region of experimentally observed delamination growth. The delamination front is advanced incrementally by releasing appropriate node pairs. However, the decision has to be made a priori concerning the shape of the newly formed delamination front (and hence, the magnitude of the increment in crack area). This decision has to be considered during construction of the mesh, since for example, if a small increment in crack area is desired, then a very fine mesh will be necessary near the region where node release is to take place. In each case, geometrically non-linear analysis is carried out for the peak applied compressive load of 28 kN, distributed uniformly on the loading face. Appropriate constraints are applied to the other two faces, representing the two planes of symmetry. Eigenvalue analyses using the in-house code for each of the meshes yield an identical critical buckling load of the delaminated part of 13.50 kN. When analyzed using the commercial code ABAQUS, the model *S*1 yields a critical buckling load of 13.23 kN. After application of the compressive load of 28 kN, the relevant node pairs are released. The resulting displacements of the nodes on the newly formed crack surfaces and the nodal forces obtained just before node release are used to compute the components of the SERR. In each case, the delamination front is advanced only one element at a time along the initial front, thereby

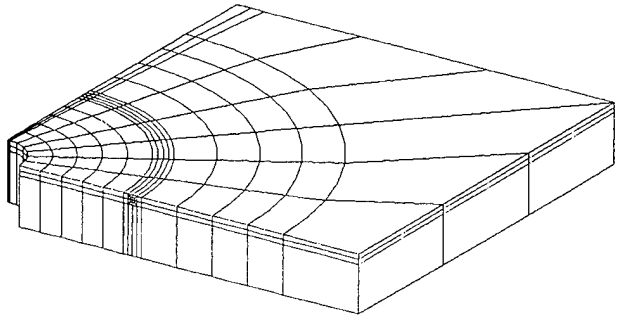

Typical model used in 3D mesh analysis

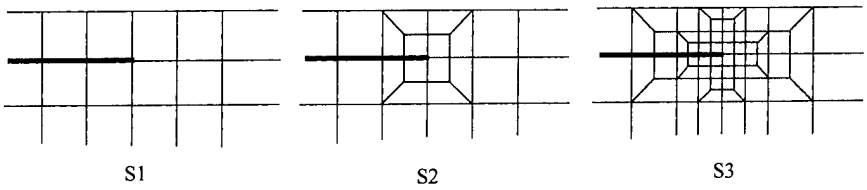

Fig. 13. 3D meshes with local symmetry at near-tip region.

providing the SERRs at discrete positions. In the case of the VCCT, there is no need for nodal release, and the components of SERR are computed at the end of the application of the maximum compressive load.

The results for Mode I and Mode II components of the SERR computed using VCCT are shown in Fig. 14 and those computed using CCT are shown in Fig. 15. The results are for the position on the delamination front at 90° to the loading direction. In the figures, the element aspect ratio is defined as the ratio of the length of the crack tip element (in the circumferential direction) to the height of the same element (in the plate thickness direction). The height of the element is maintained constant. In this problem, where the laminate is composed of woven fabric layers, the Mode III fracture component of the SERR is found to be negligible. The results using CCT (Fig. 15) show a surprising lack of convergence as the element aspect ratio is decreased, suggesting that mesh refinement in the circumferential direction does not lead to unique values of G_I and G_{II}. However, the values do approach constant values with increasing aspect ratio, with the exception of $S1$, which may be too coarse. G_I approaches a value of about 120 J/m^2 only after an aspect ratio of about 8, while G_{II} approaches a value of about 35 J/m^2 after an aspect ratio of about 4. The lack of convergence is more pronounced for G_I than G_{II}. It appears that the larger the aspect ratio, the closer the VCCT SERR is to the CCT SERR. The SERR obtained by CCT is not a pointwise value but an averaged value for the crack area released. There is perhaps greater justification for the use of pointwise SERR (as calculated using the VCCT) in regions of locally uniform crack growth. The result of a C-scan of the delaminated area is shown in Fig. 16. It

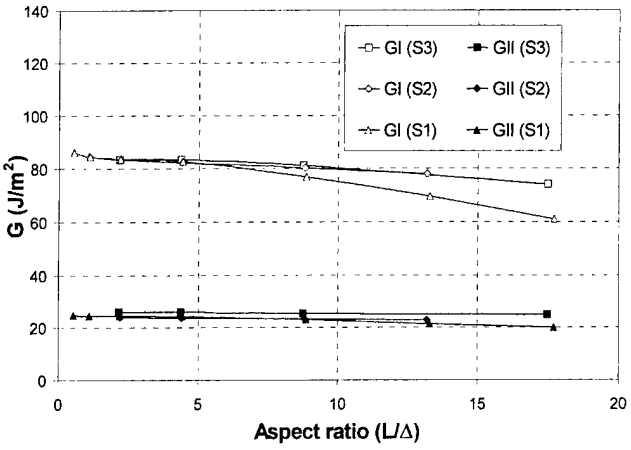

Fig. 14. Mode I and Mode II SERRs using VCCT.

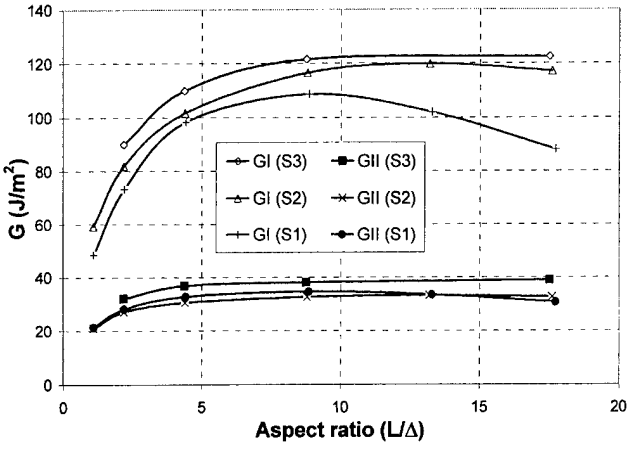

Fig. 15. Mode I and Mode II SERRs using CCT.

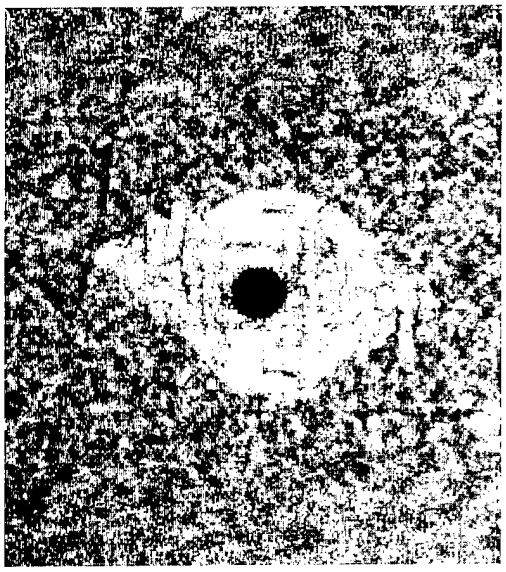

Fig. 16. Typical C-scan image of delamination Ref. [31] (load direction is vertical).

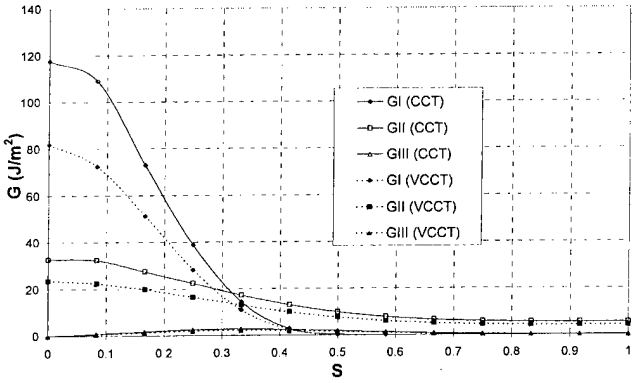

Fig. 17. Distribution of G_I, G_{II} and G_{III} using VCCT and CCT.

appears that in order to obtain meaningful values of the SERR the node release scheme employed must bear some resemblance to physical evidence of the shape and extent of delamination growth. The delamination front could have advanced in a finite circumferential length simultaneously, although this could not be determined experimentally, since the C-scans were obtained after the specimens were fatigue loaded under pre-specified load cycle intervals. The growth of the delamination front was therefore not observed in real time.

The values of G_I and G_{II} obtained using the VCCT (Fig. 14) show a lack of dependence on mesh refinement, with again the exception of mesh S1. For this mesh, G_I is significantly affected by increasing element aspect ratio, although G_{II} is not similarly affected. The value of G_I of about 80 J/m^2 and G_{II} of about 25 J/m^2 are significantly lower than the corresponding values obtained through CCT. However, the mode mixity ratios G_I/G_{II} for VCCT and CCT are very close, at 3.2 and 3.4, respectively. As mentioned previously, the VCCT is a convenient and efficient method of computing SERR, but lacks a sound theoretical basis for application to 3D delamination problems because of the assumption of uniform crack growth along the delamination front. In this case, it also underestimates the components of the SERR, by about 50% in the case of G_I, and 40% in the case of G_{II}. Finally, the distribution of Mode I, Mode II and Mode III components of the SERR along the entire delamination front is shown in Fig. 17. In the figure, S is the circumferential coordinate measured along the circular delamination front. $S = 0$ corresponds to the position on the delamination front at 90° to the loading direction, and $S = 1.0$ to the position 0° to the loading direction. In this problem, the Mode III component is negligible. The results show that although the values of the SERR components differ when calculated using CCT and VCCT, the distributions appear very similar. This implies that while VCCT may underestimate the values of G_I and G_{II}, it is still useful in predicting the direction of delamination growth.

5. Conclusion

The results of 2D analyses confirm that if the near-tip mesh is symmetric and consists of square elements, then the evaluation of G_I and G_{II} are not sensitive to mesh refinement, and a reasonably coarse mesh is adequate. Despite agreement in the global post-buckling response of the delaminated part, the SERR calculated using different unsymmetrical near-tip meshes could be different. Therefore, unsymmetrical near-tip meshes should be avoided, as convergence of the SERR with mesh refinement could not be assured. While the results using VCCT and CCT for 2D analyses agree well with each other, these techniques yield different quantitative results when applied to 3D analyses. The reason may be due to the way in which the delamination growth is modeled. The CCT is able to allow for simultaneous delamination advance over a finite circumferential length but is very difficult to implement. Qualitatively, however, the two sets of results show similar distribution of Mode I and Mode II components of the SERR. This is fortunate, since the VCCT is relatively easy to implement.

References

[1] Chai H, Babcock CD, Knauss WG. One-dimensional modelling of failure in laminated plates by delamination buckling. Int J Solids Struct 1981;17:1069–83.
[2] Chai H, Babcock CD. Two-dimensional modelling of compressive failure in delaminated laminates. J Comp Mater 1985;19:67–98.
[3] Chai H. Three-dimensional fracture analysis of thin-film debonding. Int J Fract 1990;46:237–56.
[4] Peck SO, Springer GS. The behavior of delaminations in composite plates-analytical and experimental results. J Comp Mater 1991;25:907–29.

[5] Davidson BD. Prediction of delamination growth in laminated structures. Failure mechanics in advanced polymeric composites, ASME 1994; AMD-196:43–65.
[6] Davidson BD. Delamination buckling: theory and experiment. J Comp Mater 1991;25:1351–78.
[7] Gaudenzi P, Perugini P, Spadaccia F. Post-buckling analysis of a delaminated composite plate under compression. Comp Struct 1998;40:231–8.
[8] Buchholz F-G, Rikards R, Wang H. Computational analysis of interlaminar fracture of laminated composites. Int J Fract 1997;86:37–57.
[9] Klug J, Wu XX, Sun CT. Efficient modeling of postbuckling delamination growth in composite laminates using plate elements. AIAA J 1996;1:178–84.
[10] Lachaud F, Lorrain B, Michel L, Barriol R. Experimental and numerical study of delamination caused by local buckling of thermoplastic and thermoset composites. Comp Sci Tech 1998;58:727–33.
[11] Nilsson K-F, Asp LE, Alpman JE. Delamination buckling and growth at global buckling. In: Rossmanith, editor. Damage and failure of interfaces. Rotterdam: Balkema, 1997. p. 193–202.
[12] Nilsson K-F, Giannakopoulos AE. A finite element analysis of configurational stability and finite growth of buckling driven delamination. J Mech Phys Solids 1995;43:1983–2021.
[13] Nilsson K-F, Thesken JC, Sindelar P, Giannakopoulos AE, Storakers B. A finite element analysis of configurational stability and finite growth of buckling driven delamination. Theoretical and experimental investigation of buckling induced delamination growth. . J Mech Phys Solids 1993;41:749–82.
[14] Naganarayana BP, Atluri SN. Strength reduction and delamination growth in thin and thick composite plates under compressive loading. Comput Mech 1995;16(3):170–89.
[15] Rybicki EF, Kanninen MF. A finite element calculation of stress intensity factors by a modified crack closure integral. Engrg Fract Mech 1977;9:931–8.
[16] Shivakumar KN, Tan PW, Newman jr JC. A virtual crack-closure technique for calculating stress intensity factors for cracked three dimensional bodies. Int J Fract 1988;36:R43–50.
[17] Raju IS. Calculation of strain-energy release rates with higher order and singular finite elements. Eng Fract Mech 1987;28(3): 251–74.
[18] Narayana KB, George S, Dattaguru B, Ramamurthy TS, Vijayakumar K. Modified crack closure integral (MCCI) for 3D problems using 20 noded brick elements. Fatigue Fract Eng Mater Struct 1994;17(2):145–57.
[19] Whitcomb JD. Three-dimensional analysis of a postbuckled embedded delamination. J Comp Mater 1989;23:862–89.
[20] Whitcomb JD. Delamination growth in a laminate with a postbuckled edge delamination. J Comp Tech Res 1991;13:175–8.
[21] Whitcomb JD. Analysis of delamination growth near intersecting ply cracks. J Comp Mater 1992;26:1844–58.
[22] Whitcomb JD. Analysis of a laminate with a postbuckled embedded delamination including contact effects. J Comp Mater 1992;26:1523–35.
[23] Whitcomb JD. Predicted and observed effects of stacking sequence and delamination size on instability related delamination growth. J Comp Tech Res 1989;11(3):94–8.
[24] Tian Z, Swanson SR. Effect of delamination face overlapping on strain energy release rate calculations. Comp Struct 1992;21:195–204.
[25] Suemasu H, Kumagai T, Gozu K. Compressive behavior of multiply delaminated composite laminates Part finite element analysis. AIAA J 1998;36(7):1286–90.
[26] Moorthy CMD, Reddy JN. Modelling of laminates using a layerwise element with enhanced strains. Int J Numer Meth Eng 1998;43:755–79.
[27] Raju IS, Crews Jr. JH, Aminpour MA. Convergence of strain energy release rate components for edge-delaminated composite laminates. Eng Fract Mech 1988;30(3):383–96.
[28] Hutchinson JW, Suo Z. Mixed mode cracking in layered materials. In: Hutchinson JW, Wu TY. editors. Advances in Applied Mechanics, vol. 29. New York: Academic Press, 1992.
[29] Beuth JL. Separation of crack extension modes in orthotropic delamination models. Int J Fract 1996;77:305–21.
[30] Qian W, Sun CT. Methods for calculating stress intensity factors for interfacial cracks between two orthotropic solids. Int J Solids Struct 1998;35(25):3317–30.
[31] Pradhan SC, Tay TE. Three-dimensional finite element modeling of delamination growth in notched composite laminates under compression loading. Eng Fract Mech 1998;60(2):157–72.

ELSEVIER

Composite Structures 47 (1999) 613–618

COMPOSITE STRUCTURES

www.elsevier.com/locate/compstruct

In situ synthesis of TiC composite for structural application

L. Lü *, M.O. Lai, J.L. Yeo

Department of Mechanical and Production Engineering, The National University of Singapore, 10 Kent Ridge Crescent, 119260 Singapore, Singapore

Abstract

In situ TiC reinforced Al composite has been synthesized from the reaction between Ti and activated carbon. The size of in situ TiC is in the range from sub-micron to a maximum of 1.7 μm. Degree of reaction between Ti and activated carbon increases with increasing reaction temperature and amount of carbon. At low reaction temperature, the tensile strength of the composite is low as a result of the presence of unreacted activated carbon retained in the material. The retained carbon can be reduced by increasing reaction temperature. It has been observed that at low reaction temperature formation of Al_3Ti is a dominant phenomenon while at high reaction temperature Al_3Ti is not stable. Along with its disappearance, formation of TiC becomes favorable. © 2000 Elsevier Science Ltd. All rights reserved.

Keywords: In situ reaction; Stir casting; X-ray diffraction; Al-based composite

1. Introduction

In situ processes represent a category of techniques used to synthesize metal matrix composites (MMCs) [1–3]. The processes involve the synthesis of composites such that the desirable reinforcement(s), matrices and interfaces are formed during processing [4–6]. The success of the process to obtain the desirable end product requires a good understanding of thermodynamics and reaction kinetics. The resultant composites generally exhibit the presence of uniform distribution of reinforcement that tends to be fine and associated with a clean interface with the metallic matrix. The latter also renders the formation of strong bonds between the reinforcement and the metallic matrix. Other advantages of in situ processing include cost-effectiveness, improved wettability between reinforcement and matrix, and the elimination of deleterious interface reaction [7–9].

In the in situ processing of TiC reinforced Al MMCs, Al_3Ti is the first phase that has been observed after the chemical reaction [10]. According to thermodynamic equilibrium, Al_3Ti will further react with carbon to form the more thermodynamically stable TiC as illustrated in the following equations [10]:

$$\text{Divergent reaction: } 2TiAl_3 + C \rightarrow Ti_2AlC + 5Al \quad (1)$$

$$\text{Convergent reaction: } Ti_2AlC + C \rightarrow 2TiC + Al \quad (2)$$

Besides the formation of Al_3Ti in such a multi-component system, it is also possible that Al_4C_3 is formed during the reaction. According to Colters et al. [11], the free energy change of formation based on the equation $Ti + C \rightarrow TiC$ is

$$\Delta G^\circ = -186606 + 13.22T \text{ J mol}^{-1}, \quad (3)$$

where T is the temperature.

On the other hand, the free energy of change of formation of Al_4C_3 is

$$\Delta G^\circ = -88840 + 32.1T \text{ J mol}^{-1}. \quad (4)$$

Comparing the two values of ΔG°, it can be seen that Ti is a much stronger carbide former than Al_4C_3. However, as Ti depletion occurs on the formation of TiC, the activity of Al relative to Ti increases and formation of Al_4C_3 takes place below a certain Ti concentration level. Knowledge of the composition is necessary to calculate the minimum Ti content required to prevent the following reaction [9]:

$$13Al(l) + 3TiC(s) \rightarrow Al_4C_3(s) + 3TiAl_3 \quad (5)$$

Svendsen et al. [12] reported that the four-phase reaction depicted in Eq. 5 occurs at 754°C. Thus if the time of cooling from the combustion temperature to the melting temperature T_m of Al is long, Al_4C_3 will form. Al_4C_3 was reported to be formed on TiC in Al–Ti liquids containing carbon at temperatures below 1000°C [10].

* Corresponding author. Tel.: +65-874-2236; fax: +65-779-1459.
E-mail address: mpeluli@nus.edu.sg (L. Lü).

0263-8223/99/$ - see front matter © 2000 Elsevier Science Ltd. All rights reserved.
PII: S0263-8223(00)00032-5

The objective of the present investigation is to study the formation of in situ TiC from the reaction between Ti and carbon, and between K_2TiF_6 salt and carbon in molten Al.

2. Experimental procedures

The nominal composition of the in situ MMC was Al4.5%Cu/10wt%TiC. Commercially pure AA1050 Al ingots (99.5% pure) and 50 μm Cu powder (99% pure) were used for the preparation of metal matrix. K_2TiF_6 salt and activated carbon granules were employed in the reaction synthesis. The amount of carbon used in the process was 200% of the stoichiometric amount. This is to promote the formation of TiC. Before in situ synthesis, the K_2TiF_6 and carbon granules were ball-milled for 10 min to mix the salt as well as crush the 2.5 mm carbon granules. The mixture was then preheated at 250°C for 60 min to remove any trace of moisture.

Reaction synthesis was initially carried out in two different powder mixtures, namely Al, Ti and activated carbon powder mixture, and Al, K_2TiF_6 salt and activated carbon powder mixture. The powder mixtures were first ball-milled and then compacted into small pellets. Reaction of the powder mixtures was determined by using Rheometric 1500 simultaneous thermal analyzer (STA) at a heating rate of 10°C/min.

Final synthesis was performed using stir casting method in which Al was first melted with Cu in a graphite crucible at 850°C under the protection of argon gas. The molten Al was stirred continuously using a graphite stirrer for 10 min to assist the dissolution of the Cu into the Al melt. The mixture of K_2TiF_6 and activated carbon was slowly added into the molten Al through a ceramic tube for a period of 20 min. At the same time, the graphite stirrer was held near the surface of the melt to ensure a good mix of the salts with the molten metal. After the addition of the K_2TiF_6 and carbon mixture, the melt was held for 30 min for further reaction. Three different reaction temperatures of 850°C, 1000°C and 1200°C were employed. Melts were cast into a ∅35 mm steel mold which was preheated at 400°C. The cast rods were later extruded at an extrusion ratio of 13:1. The specimens were solutionised at 540°C for 2 h and quenched into cold water. The solutionised specimens were finally artificially aged at 170°C to obtain peak ageing.

Structural examination of the in situ MMC was carried out using a Schimazu Lab-6000 X-ray diffractometer. To quantitatively evaluate the amount of TiC after the in situ reaction, four standard Al-4.5 wt%Cu specimens containing 5, 10, 15 and 20 wt% of TiC were likewise fabricated using Al, Cu and TiC powders. Tensile properties were determined using an Instron 8500 automatic servo-hydraulic test system at a loading speed of 0.5 mm/min.

3. Results and discussion

3.1. Structural evaluation

Fig. 1(a) shows the STA curve of Al–Ti–C mixture. A strong endothermic peak at about 660°C indicates the melting of Al. Following the endothermic peak, a big exothermic peak starting at about 760°C can be observed indicating reaction in powder mixture during heating. By heating the powder mixture to higher temperature, other two small endothermic peaks can be seen. To understand the reaction, the powder mixtures were heated to three different temperatures of 850°C, 1000°C and 1200°C. Fig. 2 shows the XRD diffraction peaks of Al–Ti–C after heat treatment at the three different temperatures. After heating at 850°C, the appearance of (1 1 2), (0 0 4), (2 0 0), (2 2 0) and (1 1 6) Al_3Ti diffraction peaks as shown in Fig. 2(a) indicates that the first compound formed is Al_3Ti [10]. A very

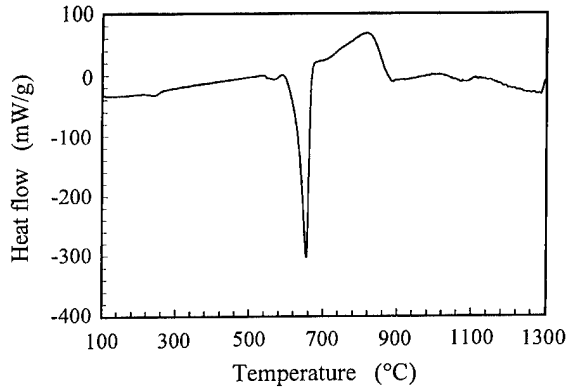

(a)

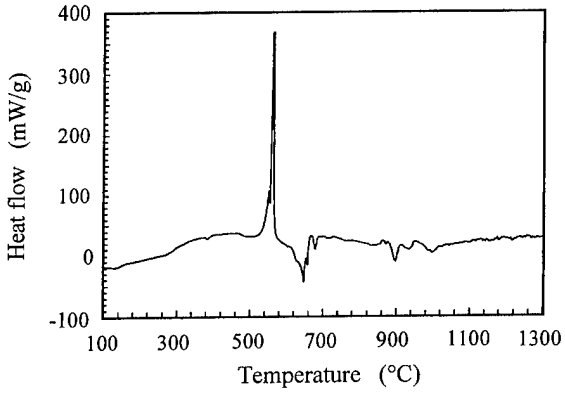

(b)

Fig. 1. DSC measurement of formation of in situ Al/TiC composites. (a) Reaction in Al–Ti–C mixture and (b) reaction in Al–K_2TiF_6–C mixture.

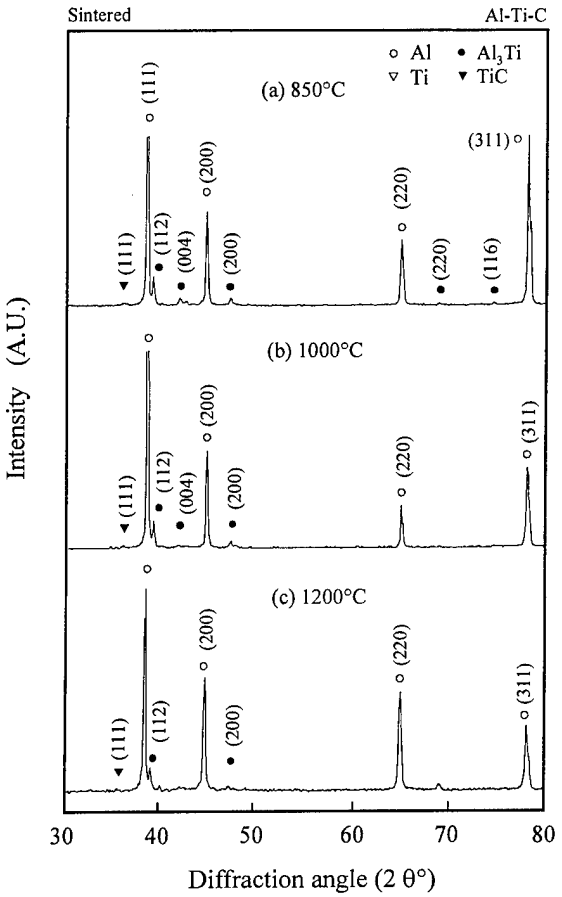

Fig. 2. XRD spectra of Al–Ti–C mixture after reaction at: (a) 850°C, (b) 1000°C and (c) 1200°C.

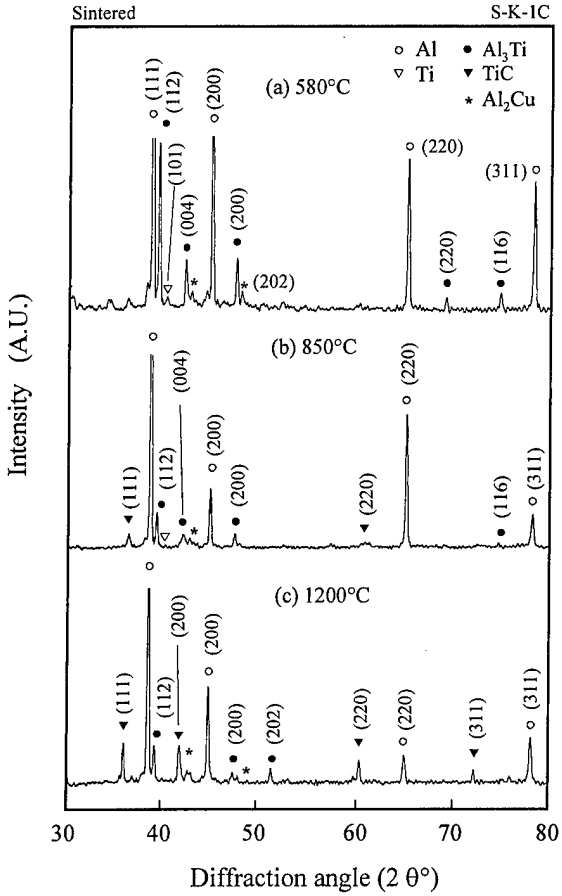

Fig. 3. XRD spectra of Al–K_2TiF_6–1C mixture after reaction at: (a) 580°C, (b) 850°C and (c) 1200°C.

weak peak at about 35.5° is probably an indication of the initial formation of TiC but the evidence is not conclusive. There is no significant difference in the diffraction spectra between the samples heat treated at 850°C and 1000°C. With an increase in reaction temperature to 1200°C, there is still no clear indication of the formation of TiC even though the intensity of Al_3Ti has decreased relative to Al diffraction one. This implies that the direct reaction between Ti and carbon in Al does not easily form in situ TiC.

Result of STA measurement on Al–K_2TiF_6–C in Fig. 1(b) shows totally different characteristics from those of Al–Ti–C reaction. An exothermic reaction at about 570°C was recorded, followed by an endothermic peak of melting of Al. Other endothermic peaks at about 890°C, 920°C and 990°C can be observed. From the STA result, three batches of Al–K_2TiF_6–C were respectively heat treated at 580°C, 850°C and 1200°C. Very different XRD spectra compared to those for Al–Ti–C system can be observed from Fig. 3. After heat treatment at 580°C, strong Al_3Ti diffraction spectrum can be seen although Ti still co-exists indicating that K_2TiF_6 salt has been dissociated at 570°C releasing Ti and part of it has reacted with Al to form Al_3Ti. Besides the formation of Al_3Ti, weak (1 1 1) TiC diffraction peak can also be observed. This implies that in the salt reaction, formation of TiC is easier than direct formation of TiC from the reaction between Ti and carbon. Formation of Al_3Ti and TiC at low temperature is probably the result of the heat released from the dissociation of K_2TiF_6 salt which raised the local temperature of the powder mixture. After reaction at 850°C, the intensity of Al_3Ti was dramatically reduced indicating the dissociation of the Al_3Ti phase at this temperature (Fig. 3(b)). After the reaction at 1200°C, strong TiC (1 1 1), (2 0 0), (2 2 0) and (3 1 1) diffraction peaks have been detected (Fig. 3(c)) but some trace of Al_3Ti phase could still be detected.

During heat treatment of Al–K_2TiF_6–C, some of activated carbon might be reacted with O_2 to form CO and CO_2 and released before reacting with Ti forming TiC. The stoichiometric composition of TiC might not be obtainable. Some excessive activated carbon is therefore needed. Fig. 4 shows the diffraction spectra of Al–K_2TiF_6–C system with 200% of original activated carbon (designated as Al–K_2TiF_6–2C). At the low reaction temperatures of 580°C and 850°C, although no significant difference could be observed between Figs. 3

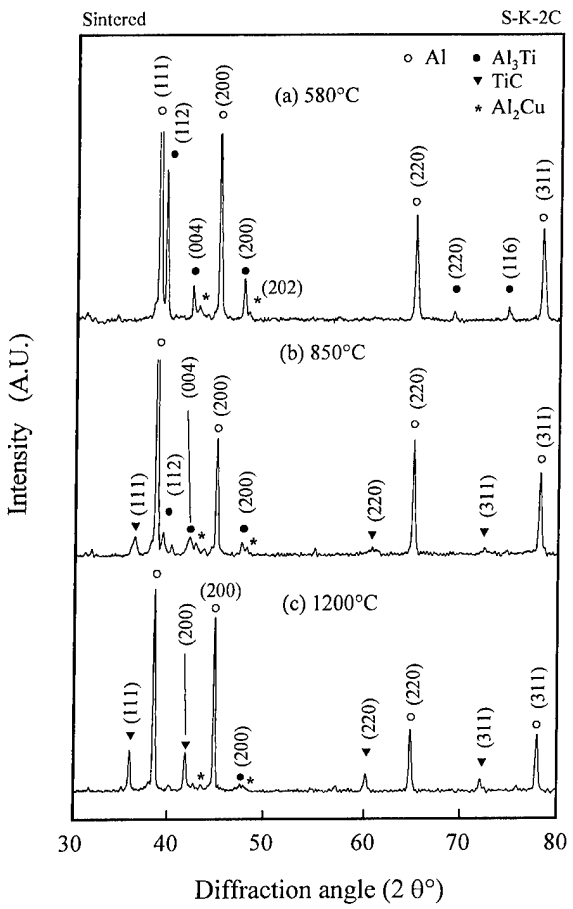

Fig. 4. XRD spectra of Al–K_2TiF_6–2C mixture after reaction at: (a) 580°C, (b) 850°C and (c) 1200°C.

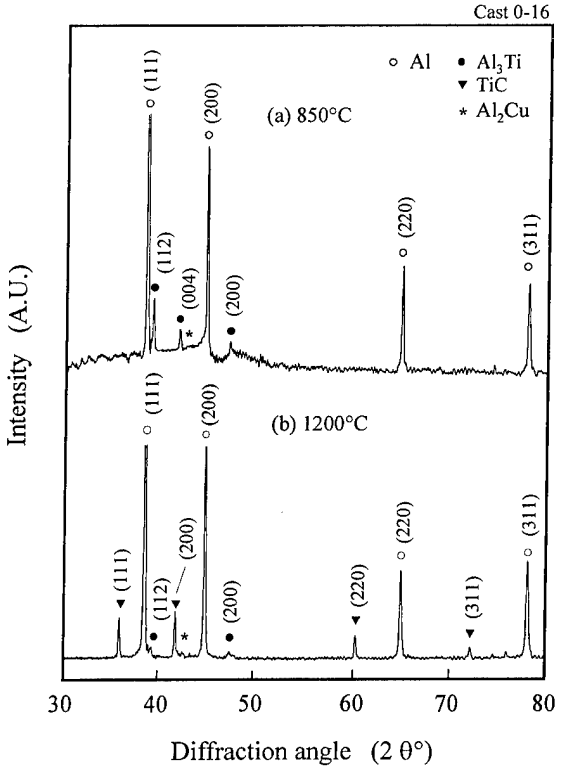

Fig. 5. XRD spectra of stir cast Al–K_2TiF_6–2C after reaction at: (a) 850°C and (b) 1200°C.

Table 1
Quantitative measurement of TiC at different casting temperature

Temperature	850°C	1000°C	1200°C
TiC (vol.%)	1.1	5.3	6.5

and 4, the relative intensity of Al_3Ti is obviously lower than those in Fig. 2. After the reaction at 1200°C, Al_3Ti phase in Fig. 4 almost completely disappears implying that a more completed reaction can be obtained by the addition of activated carbon. The diffraction of TiC is much stronger than those in Fig. 3.

The final stir castings based on composition of Al–K_2TiF_6–2C were carried out at 850°C, 1000°C and 1200°C. XRD spectrum shows that for the reaction carried out at 850°C, strong Al_3Ti phase can be detected (Fig. 5(a)) with almost no evidence of formation of in situ TiC. However, when the reaction is carried out at 1000°C and 1200°C, strong diffraction peaks of TiC phase could be found while only very weak Al_3Ti phase could be detected (Fig. 5(b)). This observation indicates that, the formation of Al_3Ti is favored at 850°C while at higher temperatures Al_3Ti becomes unstable. Table 1 gives the quantitative measurement of volume percentage of TiC measured by X-ray diffraction. It can be seen that higher temperature better assists the formation of TiC.

Fig. 6 reveals the microstructures of matrix and in situ MMC. In the microstructure of Al the matrix shows equiaxed grains with average grain size of about 80 μm. Some grains with large size can also be observed. After the in situ reaction, the grain size was reduced to about 21 μm. A closer view of the microstructure clearly shows TiC particulates of size ranging from sub-micron to 1.7 μm.

3.2. Mechanical properties

Mechanical properties of the composite obtained from tensile tests are given in Table 2. It is noted that strength of the in situ MMC cast at 850°C is lower than that of its matrix. Microstructure characterization shows that the MMC reacted at 850°C contains some retained activated carbon which is located along the grain boundaries. In Fig. 7, the black areas indicated by arrows show the presence of unreacted activated carbon. Some agglomerations of activated carbon are in the range of about a few microns in size. Besides the activated carbon, the Al_3Ti with gray needle like structure can also be observed. It is known that the bonding

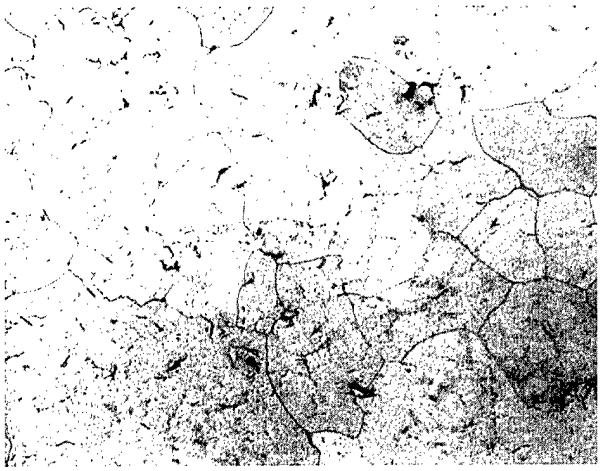

(a)

(b)

Fig. 6. Microstructure of: (a) Al matrix and (b) in situ of TiC composite.

Table 2
Summary of mechanical properties

Specimen	Matrix	850°C	1000°C	1200°C
0.2% YS (MPa)	133 ± 4	98 ± 3	126 ± 2	155 ± 10
UTS (MPa)	289 ± 2	222 ± 14	279 ± 9	320 ± 14
Elongation (%)	27 ± 0.4	6 ± 2	11 ± 4	13 ± 0.8

between carbon and Al is very week as strength of carbon is very low. During tension, high stress concentration around the retained carbon leads to early failure of the composite so that the elongation of the MMC cast at 850°C is much lower than its matrix. When the reaction temperature is increased, reaction rate between activated carbon and matrix increases and the degree of reaction becomes more complete resulting in less retained carbon after casting. Decrease in retained carbon leads to increase in the amount of TiC and reduction in the

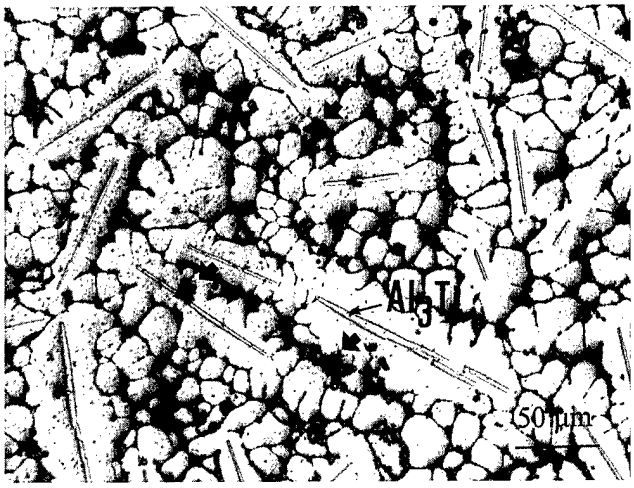

Fig. 7. Microstructure of MMC at 850°C.

amount of impurity along the grain boundaries. Consequently, both tensile strength and elongation are improved.

4. Conclusion

In situ TiC reinforced Al composite has been successfully synthesized from the reaction between Ti salt and activated carbon. Based on the present work, the following conclusions can be drawn:

1. In situ reaction of TiC must be carried out at a temperature above 1000°C. The first phase formed during the reaction is Al_3Ti the amount of which first increases with reaction temperature. Al_3Ti tends to decrease when the temperature is above 1000°C.
2. Excessive carbon may assist the reaction with Ti to form TiC since carbon is easy to be burnt away without reaction with Ti. The size of in situ TiC is in the range from sub-micron to a maximum of 1.7 μm.
3. At low reaction temperature, the tensile strength of the composites is low due mainly to the presence of unreacted carbon. The amount of retained carbon can be reduced by increasing the reaction temperature.

References

[1] Aghajanian MK, Rocazella MA, Burke JT, Keck SD. J Mater Sci 1991;26:447.
[2] Ward-close CM, Minor R, Doorbar PJ. Intermetallics 1996;4:217.
[3] Terry B, Jones G. Metal matrix composites: current developments and future trends in industrial research and applications. Amsterdam: Elsevier; 1990.
[4] Shtessel V, Sampath S, Koczak M. In: Singh M, Lewis D, editors. In situ composites: science and technology. The Minerals, Metals & Materials Society, 1994:37.
[5] Chen Y, Ohung DDL. J Mater Sci 1996;31:311.

[6] Fishman SG. In: Singhand M, Lewis D, editors. In situ composites: science and technology. The Minerals, Metals & Materials Society, 1994:1.
[7] Fan Z, Miodownik AP, Chandrasekaran L, Ward-close M. J Mat Sci 1994;29:1127.
[8] Koczak MJ, Premkumar MK. J Met 1993;1:44.
[9] Sahoo P, Koczak MJ. Mater Sci Eng A 1991;144:37.
[10] Gotman I, Koczak M, Shtessel E. Mater Sci Eng A 1994;187:189.
[11] Colters RG. Mater Sci Eng A 1985;70:1.
[12] Svendsen L, Jarfors A. Mater Sci Tech 1993;9:948.

ELSEVIER

Composite Structures 47 (1999) 619–624

COMPOSITE STRUCTURES

www.elsevier.com/locate/compstruct

On the dynamic response of metal matrix composite panels to uniform temperature loading

Esther Feldman [a], Rivka Gilat [b,*]

[a] *Department of Solid Mechanics, Materials and Structures, Faculty of Engineering, Tel Aviv University, Ramat Aviv 69978, Israel*
[b] *Faculty of Engineering, Academic College JAS, Ariel 44837, Israel*

Abstract

Thermal dynamic response of antisymmetrically laminated metal matrix composite flat and curved panels subjected to uniform time-dependent temperature field is studied. Temperature dependence of both elastic and viscoplastic properties of the metallic matrix is taken into account. The structural analysis is combined with a micromechanical approach which is employed to establish the instantaneous thermo-inelastic constitutive law of the composite at every point of the structure at each time increment. Results are presented for SiC/Al panels. The effects of boundary conditions, panel curvature and inelastic behavior of the metallic matrix on the thermally induced vibrations are illustrated. The thermal dynamic buckling behavior of flat and curved panels is studied.
© 2000 Elsevier Science Ltd. All rights reserved.

Keywords: Dynamic thermal loading; Dynamic stability; Inelastic behavior; Metal matrix composite

1. Introduction

Thin panels that are exposed to a rapid change in temperature respond by oscillating. This phenomenon is widely encountered in structural applications, consequently, the thermally induced vibrations of thin panels have gained a considerable attention as is described in the surveys by Tauchert [1] and Noor and Burton [2]. The possibility of dynamic buckling occurring due to thermal load was treated only in a few works including those of Ray [3] and Birman [4].

While most of the studies were devoted to the analysis of elastic structural elements, the inelastic material behavior was taken into account in a limited number of investigations. Thermally induced vibrations of viscoelastic homogeneous plates were studied by Mazumdar et al. [5]. Viscoplastic effects were considered by Takezono and Tao [6] and by Karagiozova and Manoach [7] for structures made of isotropic homogeneous materials. The effects of inelastic behavior of metal matrix composite (MMC) material on the structural response to thermal shock were addressed by Gilat and Aboudi [8] for infinitely wide laminated plates.

In the present work the dynamic response of metal matrix composite structural elements to thermal loading is studied. Both rectangular plates and shallow cylindrical panels are considered. The temperature field is assumed to be spatially uniform and time dependent. The effective thermo-inelastic behavior of the metal matrix composite material is established by the micromechanical method of cells of Aboudi [9].

The governing equations are formulated in the framework of the classical shell theory, in terms of the stress function and the transverse displacement. An approximate solution is obtained using spatial Galerkin procedure and the Runge–Kutta temporal integration. Due to the evolution of plasticity and the temperature dependence of the material properties, the analysis is carried out incrementally; at each time step and at every point of the structure, the micromechanical analysis is employed in order to establish the current thermo-inelastic constitutive law.

Numerical results are presented for SiC/Al antisymmetric laminated rectangular flat and cylindrical panels subjected to rapid heating. The inelastic effects of the metallic matrix on the thermally induced dynamic response are illustrated. Furthermore, the thermal dynamic buckling of the panels is studied by adopting the approach used by Gilat and Aboudi [8].

* Corresponding author. Tel.: +972-3-640-8158; fax: +972-3-640-7617.
E-mail address: gilat@eng.tau.ac.il (R. Gilat).

0263-8223/99/$ - see front matter © 2000 Elsevier Science Ltd. All rights reserved.
PII: S0263-8223(00)00034-9

2. Problem formulation

Consider an antisymmetric angle-ply shallow cylindrical panel of length a in the longitudinal direction x, width b in the circumferential direction y, thickness h in the normal direction z, and radius of curvature R (z axis is directed towards the center of curvature). The panel is subjected to a time-dependent uniform temperature field. In the framework of the classical shell theory, when neglecting the inplane inertia, the equations of motion can be expressed in terms of the stress function Φ and the transverse displacement w in the following non-dimensional form [10]

$$M_{\xi\xi,\xi\xi} + 2\lambda M_{\xi\eta,\xi\eta} + \lambda^2 M_{\eta\eta,\eta\eta} + \frac{1}{R}\Phi_{,\xi\xi} + \frac{\lambda^2}{a^2}\left(\Phi_{,\eta\eta}w_{,\xi\xi} - 2\Phi_{,\xi\eta}w_{,\xi\eta} + \Phi_{,\xi\xi}w_{,\eta\eta}\right) = I\ddot{w}, \tag{1}$$

$$\lambda^2\varepsilon^0_{\xi\xi,\eta\eta} + \varepsilon^0_{\eta\eta,\xi\xi} - \lambda\varepsilon^0_{\xi\eta,\xi\eta} = -\frac{1}{R}(w-w^0)_{,\xi\xi} + \frac{\lambda^2}{a^2}\left[-w_{,\xi\xi}w_{,\eta\eta} + (w_{,\xi\eta})^2 + w^0_{,\xi\xi}w^0_{,\eta\eta} - (w^0_{,\xi\eta})^2\right]. \tag{2}$$

Here w^0 is initial transverse displacement, $\xi = x/a$ and $\eta = y/b$ are the non-dimensional inplane coordinates, $\lambda = a/b$ stands for the panel aspect ratio, and dot denotes time derivative. $M_{\alpha\beta}$ are the moment resultants and $I = a^2\int_{-(h/2)}^{(h/2)}\rho\,\mathrm{d}z$, where $\rho(z)$ is the effective density of the material. The midplane strains which correspond to the von Karman kinematic relations are:

$$\begin{aligned}
\varepsilon^0_{\xi\xi} &= \frac{1}{a}u_{,\xi} + \frac{1}{2a^2}\left[(w_{,\xi})^2 - (w^0_{,\xi})^2\right],\\
\varepsilon^0_{\eta\eta} &= \frac{\lambda}{a}v_{,\eta} - \frac{w-w^0}{R} + \frac{\lambda^2}{2a^2}\left[(w_{,\eta})^2 - (w^0_{,\eta})^2\right],\\
\varepsilon^0_{\xi\eta} &= \frac{\lambda}{a}u_{,\eta} + \frac{1}{a}v_{,\xi} + \frac{\lambda}{a^2}\left[w_{,\xi}w_{,\eta} - w^0_{,\xi}w^0_{,\eta}\right],
\end{aligned} \tag{3}$$

where u and v are the in-plane displacements in the x and y directions, respectively.

The effective behavior of the thermo-viscoplastic MMC is obtained using the micromechanical method of cells [9]. Assuming a state of plane stress, the constitutive law for the composite can be written in the following form:

$$\boldsymbol{\sigma} = \mathbf{Q}(\boldsymbol{\varepsilon} - \boldsymbol{\varepsilon}^{\mathrm{P}} - \boldsymbol{\varepsilon}^{\mathrm{T}}), \tag{4}$$

where $\mathbf{Q}$ is effective reduced stiffness matrix, $\boldsymbol{\varepsilon}^{\mathrm{P}}$ is the plastic strain, and $\boldsymbol{\varepsilon}^{\mathrm{T}} = \boldsymbol{\alpha}\Delta T$ is the thermal component of the strain with $\boldsymbol{\alpha}$ being the effective thermal expansion and ΔT being the temperature change.

Substitution of Eq. (4) into the definitions of stress and moment resultants yields the corresponding constitutive relations of the panel (see [11]). These are then used to eliminate $\varepsilon^0_{\alpha\beta}$ and $M_{\alpha\beta}$ from Eqs. (1) and (2). Thus, the equations which govern the thermally induced motion of an antisymmetric angle-ply panel can be written in terms of Φ and w as follows:

$$\begin{aligned}
&D^*_{11}(w-w^0)_{,\xi\xi\xi\xi} + 2\lambda^2(D^*_{12} + 2D^*_{66})(w-w^0)_{,\xi\xi\eta\eta} + \lambda^4 D^*_{22}(w-w^0)_{,\eta\eta\eta\eta} - \frac{a^2}{R}\Phi_{,\xi\xi} + \lambda(2B^*_{26} - B^*_{61})\Phi_{,\xi\xi\xi\eta}\\
&+ \lambda^3(2B^*_{16} - B^*_{62})\Phi_{,\xi\eta\eta\eta} + a^2\left(G^P_{\xi\xi,\xi\xi} + 2\lambda G^P_{\xi\eta,\xi\eta} + \lambda^2 G^P_{\eta\eta,\eta\eta}\right)\\
&- \lambda^2\left(\Phi_{,\eta\eta}w_{,\xi\xi} - 2\Phi_{,\xi\eta}w_{,\xi\eta} + \Phi_{,\xi\xi}w_{,\eta\eta}\right) = -a^2 I\ddot{w},
\end{aligned} \tag{5}$$

$$\begin{aligned}
&A^*_{22}\Phi_{,\xi\xi\xi\xi} + \lambda^2(2A^*_{12} + A^*_{66})\Phi_{,\xi\xi\eta\eta} + \lambda^4 A^*_{11}\Phi_{,\eta\eta\eta\eta}\\
&= -\frac{a^2}{R}(w-w^0)_{,\xi\xi} + (2B^*_{16} - B^*_{62})(w-w^0)_{,\xi\eta\eta\eta} + \lambda(2B^*_{26} - B^*_{61})(w-w^0)_{,\xi\xi\xi\eta}\\
&+ \lambda^2\left[(w_{,\xi\eta})^2 - w_{,\xi\xi}w_{,\eta\eta} - (w^0_{,\xi\eta})^2 + w^0_{,\xi\xi}w^0_{,\eta\eta}\right]\\
&+ a^2\left(\lambda\gamma^P_{\xi\eta,\xi\eta} - \lambda^2\gamma^P_{\xi\xi,\eta\eta} - \gamma^P_{\eta\eta,\xi\xi}\right).
\end{aligned} \tag{6}$$

Here $\mathbf{A}^*, \mathbf{B}^*$ and $\mathbf{D}^*$ are stiffness matrices (see, for example, [12]). Due to the fact that the material properties of the metallic matrix are highly temperature dependent, these stiffnesses are function of the temperature, namely of time. The expressions for the plastic functions $G^{\mathrm{P}}_{\alpha\beta}$ and $\gamma^{\mathrm{P}}_{\alpha\beta}$, which depend on the spatial coordinates ξ, η and time t, may be found in [13].

The governing equations of motion (5) and (6) are accompanied by initial and boundary conditions. For a panel being at rest when loading commences, the initial conditions are

$$\text{at } t = 0: \quad w = w^0, \ \dot{w} = 0. \tag{7}$$

As to the boundary conditions, simply supported (S) and clamped (C) panels with two types of inplane conditions are considered. These have the following form:

$$\begin{array}{lll}
\text{S1} & \text{at } \xi = 0,1: & \Phi_{,\xi\eta} = w = M_{\xi\xi} = \bar{\Delta}_x = 0;\\
 & \text{at } \eta = 0,1: & \Phi_{,\xi\eta} = w = M_{\eta\eta} = \bar{\Delta}_y = 0;\\
\text{S2} & \text{at } \xi = 0,1: & \Phi_{,\xi\eta} = w = M_{\xi\xi} = \bar{\Delta}_x = 0;\\
 & \text{at } \eta = 0,1: & \Phi_{,\xi\xi} = \Phi_{,\xi\eta} = w = M_{\eta\eta} = 0;\\
\text{C1} & \text{at } \xi = 0,1: & \Phi_{,\xi\eta} = w = w_{,\xi} = \bar{\Delta}_x = 0;\\
 & \text{at } \eta = 0,1: & \Phi_{,\xi\eta} = w = w_{,\eta} = \bar{\Delta}_y = 0;\\
\text{C2} & \text{at } \xi = 0,1: & \Phi_{,\xi\eta} = w = w_{,\xi} = \bar{\Delta}_x = 0;\\
 & \text{at } \eta = 0,1: & \Phi_{,\xi\xi} = \Phi_{,\xi\eta} = w = w_{,\eta} = 0.
\end{array} \tag{8}$$

Here $\bar{\Delta}_x$ and $\bar{\Delta}_y$ are average edge shortening in both inplane directions

$$\begin{aligned}
\bar{\Delta}_x &= \int_0^1 [u(1,\eta) - u(0,\eta)]\,\mathrm{d}\eta,\\
\bar{\Delta}_y &= \int_0^1 [v(\xi,1) - v(\xi,0)]\,\mathrm{d}\xi,
\end{aligned} \tag{9}$$

which can be expressed in terms of Φ, w [11].

3. Solution procedure

In order to obtain an approximate solution of the initial-boundary value problem (5)–(8), the unknown

functions are assumed to have the following form which satisfies the boundary conditions:

$$\Phi(\xi,\eta,t) = -\frac{a^2}{\lambda^2}P_x(t)\frac{\eta^2}{2} - a^2P_y(t)\frac{\xi^2}{2} + \sum_{p=1}^{P}\sum_{q=1}^{Q}F_{pq}(t)X_p(\xi)X_q(\eta),$$

$$w(\xi,\eta,t) = \begin{cases} \sum_{m=1}^{M}\sum_{n=1}^{N} W_{mn}(t)\sin\pi m\xi\sin\pi n\eta \\ \quad \text{(for S-cases)}, \\ \sum_{m=1}^{M}\sum_{n=1}^{N} W_{mn}(t)X_m(\xi)X_n(\eta) \\ \quad \text{(for C-cases)}. \end{cases} \tag{10}$$

Here $X_i(\alpha)$, $i = 1,2,\ldots$, are beam eigenfunctions satisfying the kinematic boundary conditions $X_i = X_{i,\alpha} = 0$ at $\alpha = 0,1$. The functions $P_x(t)$, $P_y(t)$ are the normal in-plane stress resultants developing at the edges $x = 0, a$ and $y = 0, b$, respectively; they are determined in terms of the coefficients F_{ij}, W_{ij} by meeting the inplane boundary conditions.

The form of the initial imperfection w^0 is assumed to be in accordance with the form of the out-of-plane displacement w

$$w^0(\xi,\eta) = \begin{cases} \sum_{m=1}^{M}\sum_{n=1}^{N} W^0_{mn}\sin\pi m\xi\sin\pi n\eta \\ \quad \text{(for S-cases)}, \\ \sum_{m=1}^{M}\sum_{n=1}^{N} W^0_{mn}X_m(\xi)X_n(\eta) \\ \quad \text{(for C-cases)}. \end{cases} \tag{11}$$

By substituting expressions (10) and (11) into the compatibility equation (6) and employing the Galerkin procedure with $X_i(\xi)X_j(\eta)$ being the weighting functions, the latter is reduced to a set of algebraic equations. Thus, the coefficients F_{pq} can be expressed in terms of W_{mn}. A further substitution of the latter expression in conjunction with Eqs. (10) and (11) into Eq. (5), and application of the Galerkin procedure with either $\sin\pi i\xi\sin\pi j\eta$ or $X_i(\xi)X_j(\eta)$ being the weighting functions (for the S and C boundary conditions, respectively) yields the following set of ordinary differential equations:

$$Q^{(0)}_{pq} + \sum_m\sum_n Q^{(1)}_{pqmn}W_{mn} + \sum_m\sum_n\sum_i\sum_j Q^{(2)}_{pqmnij}W_{mn}W_{ij} + \sum_m\sum_n\sum_i\sum_j\sum_k\sum_l Q^{(3)}_{pqmnijkl}W_{mn}W_{ij}W_{kl} = Q^{(4)}\ddot{W}_{pq} \quad (p = 1,\ldots,M, \quad q = 1,\ldots,N). \tag{12}$$

Here $Q^{(0)}_{pq},\ldots,Q^{(3)}_{pqmnijkl}, Q^{(4)}$ are complicated expressions containing the geometrical parameters of the panel, the amplitudes of the initial imperfection $W^{(0)}_{mn}$, and various line and surface integrals involving the elements of the stiffness matrices, as well as different plastic and thermal functions. The Eq. (12) together with the initial conditions (7) govern the behavior of a geometrically nonlinear imperfect laminated panel, made of metal matrix composite material, and subjected to uniform time-dependent temperature loading.

This initial value problem with variable coefficients is solved by the Runge–Kutta method. This in done in conjunction with incrementally following both the development of plasticity and the change of the material properties due to the variation of the temperature field [8]. At the end of each time increment, $t = t^{(l)}$, at all points of the structure, the micromechanical analysis is employed to obtain the plastic strains, plastic strain rates and the local current stiffness matrix. Then the coefficients of the system (12) and their time derivatives are evaluated. Assuming that the derivatives remain constant within the following time increment, Eq. (12) is integrated over the time increment Δt to obtain the amplitudes of the transverse displacement W_{mn} at the end of the current time increment $t = t^{(l)} + \Delta t$.

4. Application

The thermally induced dynamic behavior of anti-symmetric angle-ply SiC/Al flat and curved panels is investigated. The SiC fibers are considered to be elastic isotropic with temperature independent properties: Young's modulus $E = 414$ GPa, Poisson's ratio $v = 0.3$, density $\rho = 3210$ Kg/m^3, and thermal expansion coefficient $\alpha = 4.8\,10^{-6}$ /°C. The density of the aluminum matrix is $\rho = 2700$ Kg/m^3; the fiber volume fraction is taken to be $v_f = 0.3$.

The aluminum matrix is assumed to be a thermo-viscoplastic isotropic work-hardening material, whose rate-dependent behavior is described by the unified theory of plasticity by Bodner and Partom [14]. The corresponding material properties of aluminum alloy 2024-T4 at various temperatures are given in Table 1; piecewise linear interpolation is used for determining properties at intermediate temperatures.

Let the panel, being initially at a temperature $T_{ref} = 21$°C, be subjected to a rapid uniform heating of its upper and lower surfaces. In general, the resulting temperature distribution is governed by the heat conduction equation. Addressing thin panels and neglecting the mechanical coupling in the heat conduction equation, it is assumed that the temperature distribution through the panel thickness is uniform.

Rectangular panels having thickness ratio $b/h = 100$ are considered, and the initial geometric imperfection is assumed to have a one-mode form given by Eq. (11) with $M = N = 1$. For all the cases considered below, the first term in the series (10) for w was found to be a predominant one.

Table 1
Material constants of the 2024-T4 aluminum alloy: isotropic material in the elastic region; isotropic work-hardening material in the plastic region[a]

T (°C)	E (GPa)	ν	α (1/°C)	D_0 (1/s)	Z_0 (MPa)	Z_1 (MPa)	$\bar{m}$	$\bar{n}$
21.0	72.4	0.33	22.5×10^{-6}	10 000	340	435	300	10.0
148.9	69.3	0.33	22.5×10^{-6}	10 000	340	435	300	7.0
204.4	65.7	0.33	22.5×10^{-6}	10 000	340	435	300	4.0
260.0	58.4	0.33	22.5×10^{-6}	10 000	340	435	300	1.6
371.0	41.5	0.33	22.5×10^{-6}	10 000	340	435	300	0.6

[a] Here E, ν, and α are Young's modulus, Poisson's ratio, and thermal expansion coefficient, respectively; D_0 is the limiting strain rate, Z_0 is related to the 'yield stress' of a uniaxial stress–strain curve, Z_1 is proportional to the ultimate stress, $\bar{m}$ determines the rate of work hardening, and the rate-sensitivity is controlled by the parameter $\bar{n}$.

4.1. Flat panels

Consider a flat unidirectional square panel with lamination angle $\theta = 0°$ and $b = 0.5$ m. Plate's temperature is assumed to be increased with constant rate $\dot{T} = 10^4$°C/s such that $T(t) = T_{\text{ref}} + \dot{T}t$. The behavior of the plate is obtained from the previously presented formulation by setting R to be infinitely large. The response of plates having two kinds of boundary conditions, S1 and C1, with initial imperfection amplitude $W_0/h = 10^{-5}$, are shown in Fig. 1. Dotted lines represent the elastic solutions obtained by neglecting all the inelastic effects. It is observed that the viscoplastic effects become more pronounced as time elapses and temperature increases. As expected, the vibrations of the simply supported plate are of larger amplitudes and smaller frequency then those of the stiffer clamped plate. For both plates, the evolution of plasticity gradually reduces the amplitude of the thermally induced vibrations.

A similar effect of the viscoplasticity is observed in Fig. 2. Fig. 2 shows the response of a unidirectional square clamped C1 plate , with $b = 0.2$ m, $\theta = 0°$, and $W_0/h = 0.01$, and subjected to a sudden rapid increase in temperature such that $T(t) = T_{\text{ref}} + T_{\max}(1 - e^{-500t})$. The graphs corresponds to $T_{\max} = 150$°C. While the elastic plate seems to reach a steady state, the visco-plastic vibrations are suppressed. Yet the value of the displacement around which the plate oscillates is the same for both elastic and inelastic cases.

Let the amplitude A of the thermally induced vibration at about $t = 0.01$ s be chosen to characterize the panel response to the thermal shock. Fig. 3 illustrates the influence of the thermal shock magnitude $T_{\max}$ on the response of the viscoplastic plate. The corresponding elastic results are included as well. The transition from elastic to viscoplastic behavior occurs at a temperature magnitude of about $T_{\max} = 50$°V. The effect of inelastic behavior of the metallic matrix is pronounced, yielding an increasing reduction of the vibrations amplitude with increase in temperature magnitude.

The curves presented in Fig. 3 exhibit an essential change in the response at about $T_{\max} = 25$°C. Under thermal loads of lower magnitude, the amplitude of the thermally induced vibrations is small, of about the same order as the initial imperfection. Thermal shocks of magnitude greater then $T_{\max} = 25$°C induce vibrations

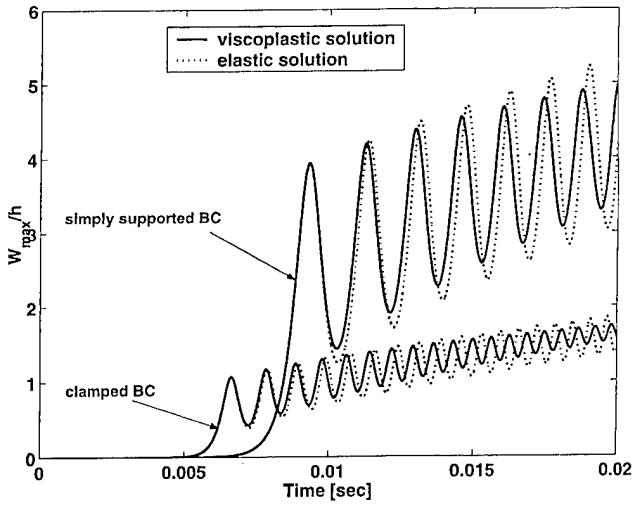

Fig. 1. Response of unidirectional [0°] simply supported (S1) and clamped (C1) plates to uniform temperature linearly increasing with time.

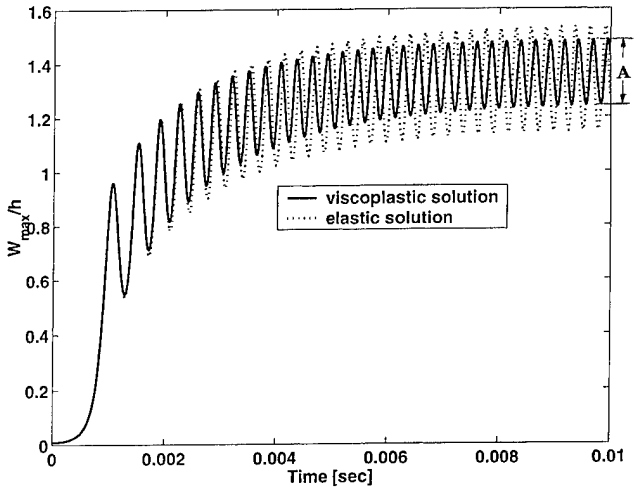

Fig. 2. Response of a unidirectional [0°] clamped (C1) plate to a step-like temperature change.

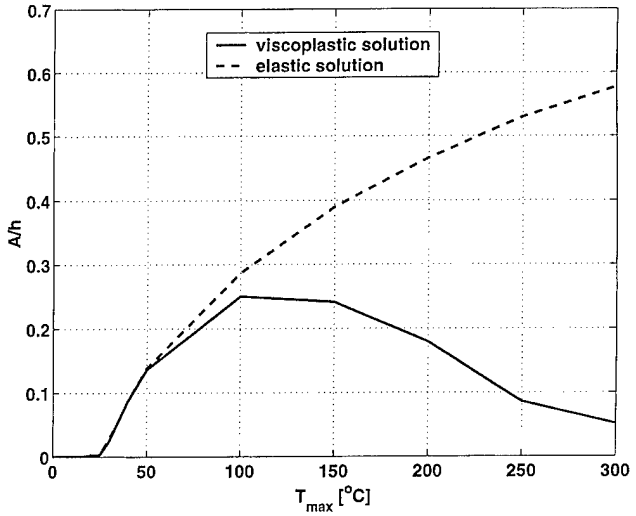

Fig. 3. Dynamic buckling behavior of a unidirectional [0°] clamped (C1) plate due to step-like thermal loading.

with increasing amplitudes. Consequently, according to the concept of Budiansky [15], $T_{max} = 25°C$ can be thought to be a critical value, the dynamic thermal buckling load.

Fig. 3 indicates that under the considered circumstances, the viscoplastic behavior of the metallic matrix does not effect the dynamic thermal buckling load.

4.2. Cylindrical panels

A typical response of a [±45°] clamped C2 square cylindrical panel to the previously described thermal shock of amplitude $T_{max} = 350°C$ is displayed in Fig. 4(a). The panel curvature is $b/R = 0.3$ with $b = 0.5$ m; the initial imperfection amplitude is $W_0/h = 0.001$. The effects of the viscoplasticity are similar to those found in the flat panel response, yet they are definitely less pronounced. It is worthwhile noting that for C2 boundary conditions the edges $y = 0, b$ are free to move in the normal direction; this leads to a bifurcational behavior of the panel. In the case of immovable edges (either S1 or C1 boundary conditions), for which transverse displacement develops simultaneously with the load application even for geometrically perfect panels, the inelastic effects were found to be almost negligible.

The panel response, as obtained while keeping the material properties constant (with values corresponding to the reference temperature) is presented in Fig. 4(b). From a comparison between Fig. 4(a) and (b) it may be concluded that the panel behavior is affected by the temperature dependence of the material properties and disregarding it yields an underestimation of the inelastic effects.

The dynamic buckling behavior of cylindrical panels having various curvatures is illustrated in Fig. 5. It can

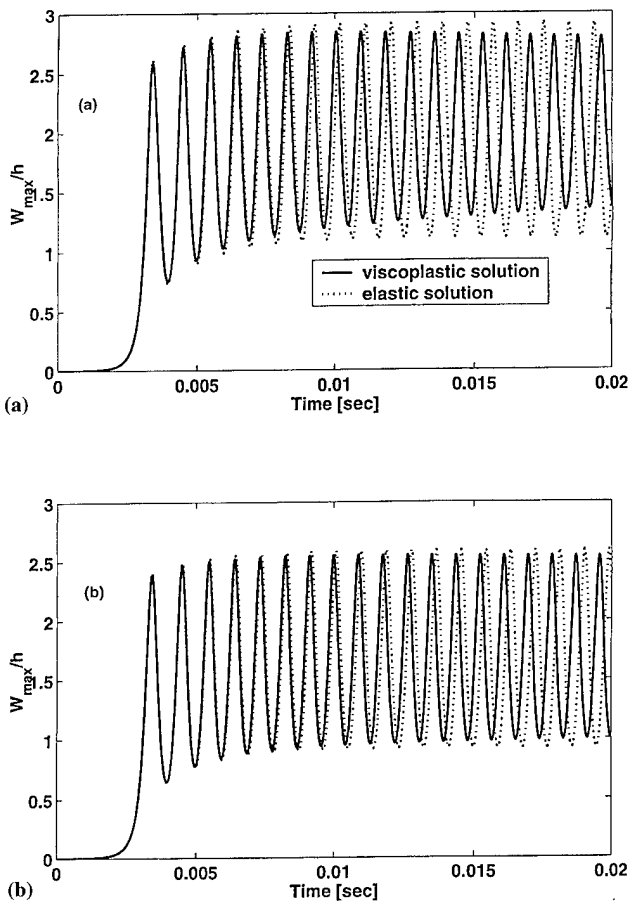

Fig. 4. Response of a [±45°] clamped (C2) cylindrical panel to a step-like thermal loading: (a) temperature dependence of the material properties is included; (b) temperature dependence of the material properties is disregarded.

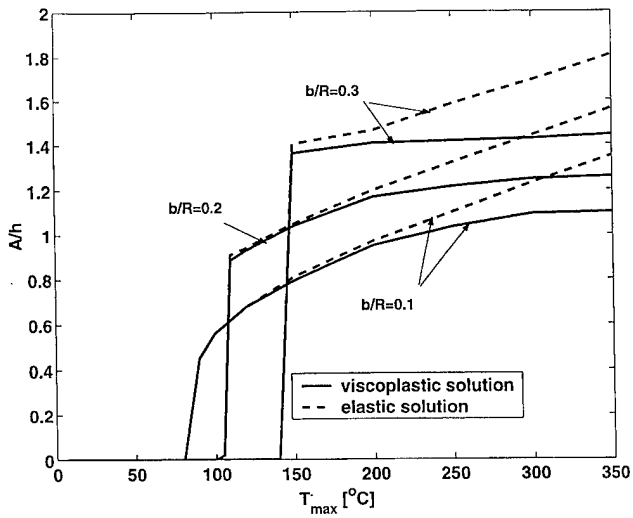

Fig. 5. Effect of curvature on the dynamic thermal buckling behavior of [±45°] clamped (C2) cylindrical panels.

be seen that as the curvature increases, inelastic effects become more pronounced. The dynamic thermal buckling load increases with the increase of the curvature, and is not effected by the inelastic behavior of the MMC.

5. Conclusions

Response of antisymmetrically laminated MMC plates and cylindrical panels to dynamic thermal loading is studied. Out-of-plane inertia effects are included. To treat the problem, a method based on a combination of micromechanical and structural analyses is used.

Results are presented for simply supported and clamped SiC/Al plates and curved panels exposed to a uniform temperature change $T(t)$. Two types of applied thermal loading are considered: (1) linear change of temperature with time ($\dot{T} = \text{const}$), and (2) a step-like temperature change.

Inelastic effects in the metallic matrix may influence significantly the thermally induced vibrations of MMC structures; both vibrations amplitude and their frequency are affected. The inelastic effects are found to be more pronounced for dynamically heated flat plates than for cylindrical panels.

The dynamic buckling due to a step-like temperature change is not affected by the inelastic behavior of the metallic matrix. Yet, the viscoplasticity does influence the postbuckling behavior of MMC panels.

Temperature dependence of material properties (both elastic and viscoplastic) affects the behavior of the structure and must be properly accounted for.

References

[1] Tauchert TR. Thermally induced flexure buckling and vibrations of plates. App Mech Rev 1991;44:347–60.
[2] Noor AK, Burton WS. Computational models for high-temperature multilayered composite plates and shells. App Mech Rev 1992;45:419–45.
[3] Ray H. Dynamic instability of suddenly heated angle-ply laminated composite cylindrical shells. Comp Struct 1993;16:119–24.
[4] Birman V. Thermal dynamic problems of reinforced composite cylinders. J Appl Mech 1990;57:941–7.
[5] Mazumdar J, Hill D, Clements DL. Thermally induced vibrations of a viscoelastic plate. J Sound Vibration 1980;73:31–9.
[6] Takezono S, Tao K. Elasto-visco-plastic dynamic response of thin shells of revolution subjected to mechanical or thermal loads or both. Int J Pres Vessels Piping 1990;44:309–27.
[7] Karagiozova D, Manoach E. Coupling effects in an elastic-plastic beam subjected to heat impact. Nucl Eng Des 1992;135:267–76.
[8] Gilat R, Aboudi J. Dynamic inelastic response and buckling of metal matrix composite infinitely wide plates due to thermal shock. Mech Comp Mat Struct 1995;2:257–71.
[9] Aboudi J. Mechanics of composite materials a unified micromechanical approach. Amsterdam: Elsevier, 1991.
[10] Simitses GJ. Dynamic stability of suddenly loaded structures. Berlin: Springer, 1990.
[11] Feldman E, Aboudi J. Thermal postbuckling of metal matrix laminated plates. J Thermal Stresses 1995;18:197–218.
[12] Whitney JM. Structural Analysis of Laminated Anisotropic Plates. Technomic, Lancaster, PA, 1987.
[13] Feldman E. The effect of temperature-dependent material properties on elasto-viscoplastic buckling behavior of non-uniformly heated MMC plates. Comp Struct 1995;35:65–74.
[14] Bodner SR, Partom Y. Constitutive equations for elastic-viscoplastic strain-hardening materials. J Appl Mech 1975;42:385–9.
[15] Budiansky B. Dynamic buckling of elastic structures: criteria and estimates. In: G. Hermann, editors. Dynamic stability of structures. Oxford: Pergamon, 1967.

ELSEVIER

Composite Structures 47 (1999) 625–634

COMPOSITE STRUCTURES

www.elsevier.com/locate/compstruct

Optimal design of piezolaminated structures

Cristóvão M. Mota Soares [a,*], Carlos A. Mota Soares [a], Victor M. Franco Correia [b]

[a] *IDMEC – Instituto de Engenharia Mecânica, Instituto Superior Técnico, Av. Rovisco Pais, 1049-001 Lisboa, Portugal*

[b] *ENIDH – Escola Náutica Infante D. Henrique, Av. Eng. Bonneville Franco, 2780-569 Paço de Arcos, Portugal*

Abstract

This paper presents refined finite element models based on higher-order displacement fields to study the mechanical and electrical behavior of laminated composite plate structures with embedded and/or surface bonded piezoelectric actuators and sensors. Sensitivity analysis and optimization techniques are also applied in order to maximize the piezoelectric actuator efficiency, improve the structural performance and/or minimize the weight of the structure. The application of structural optimization to the static shape control of adaptive structures is also addressed. To show the performance of the proposed models, several illustrative and simple examples are presented. © 2000 Elsevier Science Ltd. All rights reserved.

Keywords: Higher-order plate models; Piezoelectric actuators and sensors; Sensitivities; Structural optimization

1. Introduction

Piezoelectric materials are able to produce an electrical response when mechanically stressed (sensors) and inversely high precision motion can be obtained with the application of an electrical field (actuators). Developments in smart composite structures incorporating integrated piezoelectric sensors and actuators offer potential benefits in a wide range of engineering applications such as structural health monitoring, vibration and noise suppression, shape control and precision positioning. Accurate and reliable numerical tools able to model the structural behavior of these types of materials are very important. Crawley [1] presented an overview of the technology leading to the development of adaptive structures incorporating actuators and sensors.

Many of the developed models for laminated composite plates are based on classical laminate and first-order shear deformation plate theories [2]. It has been demonstrated that these theories can lead to substantial errors in the prediction of stresses of highly anisotropic and/or moderately thick composite plates [3–5]. The same behavior has been observed with embedded or surface bonded piezoelectric layers [6,7]. Accurate numerical models of laminated composite structures using three-dimensional finite elements can give accurate results by setting computationally expensive refined meshes with acceptable aspect ratios. A compromising less expensive situation can be achieved by using single layer models based on higher-order displacement fields [8,9] involving higher-order expansions of the displacement field in powers of the thickness coordinate. These models can accurately account for the effects of transverse shear deformation yielding quadratic variation of out-of-plane strains and therefore do not require the use of artificial shear correction factors and are suitable for the analysis of highly anisotropic plates ranging from high to low length-to-thickness ratios. Several researchers [4,5,10–12] have carried out critical reviews of higher-order models applied to the analysis of laminated composite structures. An extensive survey on the advances and trends on finite element formulations and applications to smart structural elements has been presented by Benjeddou [13]. Recently, Wang et al. [14] discussed a finite element formulation applied to the static shape control of plate structures containing distributed piezoelectric sensors and actuators.

Optimization and sensitivity analysis techniques have been applied to improve the efficiency of piezoelectric actuators and sensors to control the behavior of adaptive structures. Donthireddy and Chandrashekhara [15] studied the influence of boundary conditions, ply orientation and actuator voltage on changes in the shape of laminated beams with piezoelectric actuators, by using a

* Corresponding author. Tel.: +351-1-841-7455; fax: +351-1-841-7915.

E-mail address: cmmsoares@alfa.ist.utl.pt (C.M. Mota Soares).

0263-8223/99/$ - see front matter © 2000 Elsevier Science Ltd. All rights reserved.
PII: S0263-8223(00)00036-2

one-dimensional finite element beam formulation. Carman and Reifsnider [16] presented an elasticity solution for the problem of a continuous cylindrically shaped coated sensor/actuator embedded in a material system subjected to transverse strains. The optimum interface coating thickness and modulus that minimize the stress state are discussed. Kim and Jones [17], investigated the effect of piezo-actuator thickness on the vibration control of a cantilever beam using the Euler–Bernoulli beam theory. Also, the optimal thickness that maximizes the static beam deflection was analyzed. Meric and Saigal [18] derived shape sensitivity expressions for linear piezoelectric structures with coupled mechanical and elastic field. The adjoint variable method and the material derivative formulation of shape variation were used in a systematic procedure to evaluate the total variation of a general performance criterion with respect to shape variation. Silva et al. [19] proposed an optimal design method of piezoelectric composite microstructures using topology optimization techniques and homogenization theory to optimize the performance characteristics, subject to constraints such as property symmetry and stiffness. Batra and Liang [20] used a three-dimensional linear theory of elasticity to find the optimal location of an actuator on a simply supported rectangular laminated plate with embedded PZT layers that leads to the maximum out-of-plane displacement for a given distribution of the applied voltage. The optimal design is obtained by fixing the applied voltage and the size of the actuator and moving it around in order to find the maximum out-of-plane displacement. Liang et al. [21] proposed a model for the optimization of the induced-strain actuator location and configuration for active vibration control based on the actuator power factor that guarantees the highest energy efficiency for single-frequency and broad-band applications. Leeks and Weisshaar [22] studied a self-strained actuator mounted on one side of a panel to find the features of the actuator that produces the largest deflection of simply-supported rectangular panels using a Rayleigh–Ritz model associated to classical plate theory. Seeley and Chattopadhyay [23] presented a multiobjective optimization procedure to address the combined problems of structures/control synthesis and actuator locations for the design of intelligent structures where multiple design objectives such as vibration reduction, dissipated energy, power and a vibration performance index are combined in a multiobjective optimization formulation. Abdullah [24] presented a method for the optimal design of the placement and gains of actuators and sensors at discrete locations in output feedback control systems to reduce structural vibrations. Kang et al. [25] investigated the optimization of the sensor/actuator placement for structural vibration control of laminated composite plates for various fiber orientations in the plates, where damping and stiffness of the adhesive layer and the piezoceramics are taken into account in the finite element formulation. Varadarajan et al. [26] studied the shape control of laminated composite plates with integrated piezoelectric actuators using finite element models based in the first-order shear deformation theory, where the effectiveness of piezoelectric actuators and position sensors was investigated for shape control under the influence of quasistatically varying unknowns. Recently, Laxminarayana and Kota [27] introduced an approach to static shape control of smart structures using compliant mechanisms powered by a single input actuator and combining the first principles of mechanics and kinematics through a structural optimization scheme. Adali et al. [28] used piezoelectric actuators to minimize the deflection of antisymmetrically laminated thick rectangular plates, where the deformation generated by the piezoelectric effect counteracts the deflections induced by mechanical and/or thermal loads. Padula and Kincaid [29] presented a survey of optimization strategies for sensor and actuator placement in adaptive structures. Han and Lee [30] used genetic algorithms to find the efficient locations of piezoelectric sensors and actuators in composite plates.

In the present work, finite element models based on higher-order and first-order displacement fields have been extended to incorporate the piezoelectric effects and incorporated in an in-house computer package applied to the sensitivity analysis and optimal design of laminated composite plates with integrated piezoelectric layers working both as sensors or actuators. A gradient-based optimization procedure is used where the objective is to minimize the mass of the structure or maximize the structural and/or piezoelectric actuator performance subject to behavior constraints. The design variables are the fiber angles in orthotropic layers, thickness of the substrate composite and piezoelectric layers and the electric potentials applied to the actuators. For the static shape control the objective function is to minimize the mean-squared error between the desired and achieved shape and the design variables are the input voltages at the piezoelectric actuators. The gradients of the objective function and constraint equations with respect to the design variables are evaluated analytically or semi-analytically. Simple and illustrative examples are discussed.

2. Displacement field and constitutive equations

The displacement components u, v and w at any point in the laminate space in the x, y and z directions, respectively, are expanded in a Taylor's series powers of the thickness coordinate z. Each component is a function of x, y, z and t, where t is the time. The following higher-order displacement field can be written [8,9]:

$$u = u_0 + z\theta_x + z^2 u_0^* + z^3 \varphi_x^*,$$
$$v = v_0 + z\theta_y + z^2 v_0^* + z^3 \varphi_y^*, \quad (1)$$
$$w = w_0 + z\varphi_z + z^2 w_0^*,$$

where u_0, v_0, w_0 are the displacements of a generic point on the reference surface, θ_x, θ_y the rotations of normal to the reference surface about the y and x axes, respectively, and $\varphi_z, u_0^*, v_0^*, w_0^*, \varphi_x^*, \varphi_y^*$ are the higher-order terms in Taylor's series expansions, defined at the reference surface.

The linear piezoelectric constitutive equations coupling the elastic field and the electric field, can be written as [2,31]

$$\sigma = \bar{\mathbf{Q}}\varepsilon - \bar{\mathbf{e}}\mathbf{E}, \quad (2)$$

$$\mathbf{D} = \bar{\mathbf{e}}^{\mathrm{T}}\varepsilon + \mathbf{p}\mathbf{E}, \quad (3)$$

where $\sigma = \{\sigma_{xx}\sigma_{yy}\sigma_{zz}\sigma_{xy}\sigma_{yz}\sigma_{xz}\}^{\mathrm{T}}$ is the elastic stress vector and $\varepsilon = \{\varepsilon_{xx}\varepsilon_{yy}\varepsilon_{zz}\gamma_{xy}\gamma_{yz}\gamma_{xz}\}^{\mathrm{T}}$ the elastic strain vector. $\bar{\mathbf{Q}}$ the elastic constitutive matrix in the laminate (x, y, z) coordinate system, $\bar{\mathbf{e}}$ the piezoelectric stress coefficients matrix in the same coordinate system, $\mathbf{E}$ the electric field vector, $\mathbf{D}$ the electric displacement vector and $\mathbf{p}$ is the dielectric matrix. The electric field vector $\mathbf{E}$ is the negative gradient of the electric potential, i.e.

$$\mathbf{E} = -\nabla\phi. \quad (4)$$

In the present work, within the context of the plate theory, it is assumed that the electric field is applied through the thickness direction and thus

$$\mathbf{E} = \{0, 0, E^z\}^{\mathrm{T}}, \quad (5)$$

where E^z is the electrical field in the thickness direction.

The stresses for an arbitrary ply k, written in the laminate (x, y, z) coordinate system are evaluated by

$$\sigma_k = \bar{\mathbf{Q}}_k\varepsilon_k - \bar{\mathbf{e}}_k\mathbf{E}_k, \quad (6)$$

where the non-zero element of $\mathbf{E}_k$ vector for kth layer is given by

$$E_k^z = -\phi_k/t_k \quad (7)$$

and ϕ_k is the electric voltage applied across the kth layer and t_k is the thickness of the kth layer. Eq. (6) can also be written as

$$\sigma_k = \bar{\mathbf{Q}}_k(\varepsilon_k - \bar{\mathbf{d}}_k\mathbf{E}_k), \quad (8)$$

where $\bar{\mathbf{d}}_k$ is the piezoelectric strain coefficient matrix in the (x, y, z) coordinate system, for the kth layer, related with $\bar{\mathbf{e}}_k$ by

$$\bar{\mathbf{e}}_k = \bar{\mathbf{Q}}_k\bar{\mathbf{d}}_k. \quad (9)$$

The terms of constitutive matrix $\bar{\mathbf{Q}}_k$ of the kth layer referred to the laminate axes (x, y, z) are also obtained from the $\mathbf{Q}_k$ matrix referred to the material coordinate system $(1, 2, 3)$ with the usual coordinates transformation given explicitly in Reddy [2].

3. Finite element models

The finite element model based on the displacement field represented by Eq. (1) is referred to as Q9-HSDT 11P. This model has 11 degrees of freedom at each node for the elastic behavior and one additional electric potential degree of freedom for each piezoelectric layer for the piezoelectric behavior. By deleting the higher-order terms in the w component of the displacement field we can obtain the Q9-HSDT 9P higher-order model with 9 degrees of freedom per node plus the electric potential degrees of freedom. Also the first-order model Q9-FDSDT 5P with 5 degrees of freedom per node, plus the electric potential degrees of freedom, can be obtained by deleting all higher-order terms and introducing the shear correction factors on the transverse shear terms of constitutive matrix. Details regarding the development of the above finite numerical models for the mechanical behavior are fully described in Mota Soares et al. [5].

In the present models, there is one electric potential degree of freedom for each piezoelectric layer to represent the piezoelectric behavior [32,33] and the vector of electrical degrees of freedom is

$$\phi^e = \left\{ \dots \phi_j^e \dots \right\}^{\mathrm{T}}, \quad j = 1, \dots, \mathrm{NPL}, \quad (10)$$

where NPL is the number of piezoelectric layers in a given element. The vector of degrees of freedom for the element, $\mathbf{q}^e$ is

$$\mathbf{q}^e = \left\{\mathbf{u}_1^e \dots \mathbf{u}_9^e \phi^e\right\}^{\mathrm{T}}, \quad (11)$$

where $\mathbf{u}_i^e$ is the mechanical displacements vector for node i. Further details regarding the development of the finite element models for the electric behavior can be found in Franco et al. [32].

4. Equilibrium equations

The equilibrium equations of the laminate composite plate with embedded piezoelectric layers can be written as

$$\begin{bmatrix} \mathbf{M}_{uu} & 0 \\ 0 & 0 \end{bmatrix} \begin{Bmatrix} \ddot{\mathbf{u}} \\ \ddot{\phi} \end{Bmatrix} + \begin{bmatrix} \mathbf{K}_{uu} & \mathbf{K}_{u\phi} \\ \mathbf{K}_{\phi u} & \mathbf{K}_{\phi\phi} \end{bmatrix} \begin{Bmatrix} \mathbf{u} \\ \phi \end{Bmatrix} = \begin{Bmatrix} \mathbf{F}_u(t) \\ \mathbf{F}_\phi(t) \end{Bmatrix}, \quad (12)$$

where $\mathbf{M}_{uu}$ is the mass matrix $\mathbf{K}_{uu}$ the elastic stiffness matrix, $\mathbf{K}_{\phi\phi}$ the dielectric 'stiffness' matrix and $\mathbf{K}_{u\phi} = \mathbf{K}_{\phi u}^{\mathrm{T}}$ are the coupling matrices between elastic mechanical and electrical effects. $\{u, \phi\}^{\mathrm{T}}$ is the vector of the unknown electromechanical response of the structure, that is, the system generalized displacements and voltages at sensors. $\{\mathbf{F}_u(t), \mathbf{F}_\phi(t)\}^{\mathrm{T}}$ is the force vector of the structure including the mechanical loads and the applied electrical charges and t is the time. For static type situations, we have

$$\begin{bmatrix} \mathbf{K}_{uu} & \mathbf{K}_{u\phi} \\ \mathbf{K}_{\phi u} & \mathbf{K}_{\phi\phi} \end{bmatrix} \begin{Bmatrix} \mathbf{u} \\ \phi \end{Bmatrix} = \begin{Bmatrix} \mathbf{F}_u \\ \mathbf{F}_\phi \end{Bmatrix}. \tag{13}$$

In practice, voltage may also be specified as input to the actuators. In this case the following equilibrium equation, for static type situations, can be written as

$$\mathbf{K}_{uu}\mathbf{u} = \mathbf{F}_u - \mathbf{F}_{\text{act}}, \tag{14}$$

where $\mathbf{F}_{\text{act}} = K_{u\phi}\phi$ is an additional force vector due to the voltage ϕ applied to the actuators. The system matrices $\mathbf{K}_{uu}$, $\mathbf{K}_{u\phi}$, $\mathbf{K}_{\phi\phi}$ and $\mathbf{M}_{\phi\phi}$ are obtained by assembling the corresponding element matrices $\mathbf{K}^e_{uu}$, $\mathbf{K}^e_{u\phi}$, $\mathbf{K}^e_{\phi\phi}$ and $\mathbf{M}^e_{uu}$ of the finite elements in the domain.

For free harmonic vibrations and considering the nth mode, Eq. (12) can be written as

$$\begin{aligned} &\left(\mathbf{K}_{uu} - \omega_n^2\mathbf{M}_{uu}\right)\mathbf{u} + \mathbf{K}_{u\phi}\phi = 0, \\ &\mathbf{K}_{\phi u}\mathbf{u} + \mathbf{K}_{\phi\phi}\phi = 0, \end{aligned} \tag{15}$$

where ω_n is the natural frequency of mode n. By performing the condensation of the electrical potential degrees of freedom we can write

$$\left(\mathbf{K}^* - \omega_n^2\mathbf{M}_{uu}\right)\mathbf{u} = 0, \tag{16}$$

where

$$\mathbf{K}^* = \mathbf{K}_{uu} - \mathbf{K}_{u\phi}\mathbf{K}_{\phi\phi}^{-1}\mathbf{K}_{\phi u}. \tag{17}$$

5. Sensitivity analysis

For static type situations represented by the equilibrium Eqs. (13) or (14) the sensitivities with respect to changes in the design variables, $\mathbf{b}$, of a generic function $\varphi_j = \varphi_j(\mathbf{q}, \mathbf{b})$ are given by

$$\frac{\mathrm{d}\varphi_j}{\mathrm{d}b_i} = \frac{\partial\varphi_j}{\partial b_i} + \psi_j^{\mathrm{T}}\left(\frac{\partial\mathbf{F}}{\partial b_i} - \frac{\partial\mathbf{K}}{\partial b_i}\mathbf{q}\right), \tag{18}$$

where ψ_j is the adjoint displacements vector obtained from

$$\mathbf{K}\psi_j = \frac{\partial\varphi_j}{\partial\mathbf{q}} \tag{19}$$

and matrix $\mathbf{K}$ is the stiffness matrix containing the mechanical, electrical and coupling submatrices as in Eq. (12), $\mathbf{F}$ is the force vector including the mechanical and electrical components as well as the force vector due to the applied voltages at the actuators $\mathbf{F}_{\text{act}}$ and $\mathbf{q}$ is the displacement vector.

The sensitivities represented by Eq. (18) can be evaluated at the element level by

$$\frac{\mathrm{d}\varphi_j}{\mathrm{d}b_i} = \frac{\partial\varphi_j}{\partial b_i} + \sum_{\ell\in E}\psi_j^{e^\ell\mathrm{T}}\left(\frac{\partial\mathbf{F}^{e^\ell}}{\partial b_i} - \frac{\partial\mathbf{K}^{e^\ell}}{\partial b_i}\mathbf{q}^{e^\ell}\right), \tag{20}$$

where $\psi_j^{e^\ell}$ is the adjoint displacements vector for element ℓ, and E the set of elements for which the design variable b_i is defined. The function φ_j can represent either the objective function of the optimization problem or a constraint equation. The sensitivities $\partial\mathbf{K}^e/\partial b_i$ at the element level are evaluated analytically.

The derivatives of the load vector in order to the considered design variables are equal to 0 for the mechanical component, i.e.

$$\frac{\partial\mathbf{F}_u}{\partial b_i} = 0 \tag{21}$$

and for the actuators, Eq. (14), they are evaluated analytically by

$$\frac{\partial F_{\text{act}}}{\partial b_i} = \frac{\partial\mathbf{K}_{u\phi}}{\partial b_i}\phi + \mathbf{K}_{u\phi}\frac{\partial\phi}{\partial b_i}. \tag{22}$$

For the free vibration case, the solution of the eigenvalue problem represented by Eq. (16) consists of N eigenvalues ω_n^2 and corresponding eigenvectors $\mathbf{u}_n$. For single eigenvalues, if we consider a vibration mode $\mathbf{u}_p$ corresponding to the natural frequency ω_p normalized through the relation $\mathbf{u}_p^{\mathrm{T}}\mathbf{M}_{uu}\mathbf{u}_p = 1$, the sensitivity of natural frequency with respect to changes in the design variable b_i is given by

$$\frac{\mathrm{d}\omega_p}{\mathrm{d}b_i} = \frac{1}{2\omega_p}u_p^{\mathrm{T}}\left(\frac{\partial\mathbf{K}^*}{\partial b_i} - \omega_p^2\frac{\partial\mathbf{M}_{uu}}{\partial b_i}\right)\mathbf{u}_p \tag{23}$$

where $\mathbf{u}_p$ is the pth mode vector and the derivatives $\partial\mathbf{K}^*/\partial b_i$ given by

$$\frac{\partial\mathbf{K}^*}{\partial b_i} = \frac{\partial\mathbf{K}_{uu}}{\partial b_i} - 2\frac{\partial\mathbf{K}_{u\phi}}{\partial b_i}\mathbf{K}_{\phi\phi}^{-1}\mathbf{K}_{\phi u} + \mathbf{K}_{u\phi}\mathbf{K}_{\phi\phi}^{-1}\frac{\partial\mathbf{K}_{\phi\phi}}{\partial b_i}\mathbf{K}_{\phi\phi}^{-1}\mathbf{K}_{u\phi} \tag{24}$$

can be obtained by working directly with the global matrices. These derivatives $\partial K^*/\partial b_i$ are more efficiently obtained by forward finite difference at the structure level. The sensitivities $\partial\mathbf{M}_{uu}/\partial b_i$ are obtained by adding the contributions of the derivatives at the element level $\partial M^e_{uu}/\partial b_i$.

In the case of multiple eigenvalues they are not, in general, differentiable with respect to design variables and Eq. (23) becomes inapplicable. This is because the eigenvectors corresponding to the repeated eigenvalues are not unique and any linear combination of the eigenvectors will satisfy the eigenvalue problem represented by Eq. (16). In this case, the sensitivities can be obtained by calculating the directional derivatives [34–37] evaluated by considering a simultaneous change of all the design variables.

6. Optimal design

The structural optimization problem can be stated as

$$\begin{aligned} &\min\{\Omega(\mathbf{b})\} \\ &\text{subject to}: \quad b_i^l \leqslant b_i \leqslant b_i^u, \quad i = 1,\ldots,n\,\mathrm{d}v, \\ &\qquad\qquad \Psi_j(\mathbf{q},\mathbf{b}) \leqslant 0, \quad j = 1,\ldots,m, \end{aligned} \tag{25}$$

where $\Omega(\mathbf{b})$ is the objective function, $\Psi_j(\mathbf{q},\mathbf{b})$ are the m inequality constraint equations, b_i^l and b_i^u are respectively, the lower and upper limits of the design variables and $n\,dv$ is the total number of design variables.

In the developed optimization package the constrained optimization problems are solved by using the method of feasible directions [38] and the unconstrained problems are solved by using the BFGS (Broydon-Fletcher-Goldfarb-Shanno) method [38].

7. Static shape control

The present approach assumes that the shape of the plate structure is described by the transverse displacement w in any arbitrary location in the (x,y) plane. Let γ_i and w_i, respectively, represent the desired transverse displacement and the actual transverse displacement corresponding to node i. In order to control the shape of the plate structure in static type situations, by using piezoelectric actuators, we want to calculate the appropriate electrical voltages, to be applied to the actuators, such that the mean-squared error between the desired and the achieved shape is minimized [26]. Hence the following objective function can be written

$$\Omega_{sc} = \sum_{i=1}^{ns} [\gamma_i - w_i]^2, \tag{26}$$

where ns represents the number of discrete nodal points used to control the shape of the plate. The design variables in the optimization problem are the electrical voltages that should be applied to the piezoelectric actuators, ϕ_i, in order to minimize the above objective function. In this case the optimization problem can be written as

$$\begin{aligned} &\min\{\Omega_{sc}\} \\ &\text{subject to}: \quad \phi_i^{\min} \leqslant \phi_i \leqslant \phi_i^{\max} \quad i = 1,\ldots,n\,dv, \\ &\qquad\qquad \Psi_j(\mathbf{q},\mathbf{b}) \leqslant 0, \quad j = 1,\ldots,m, \end{aligned} \tag{27}$$

where $\phi_i^{\max}$ and $\phi_i^{\min}$ represent the upper and lower saturation voltages of the actuator and also inequality behavior constraints $\Psi_j(\mathbf{q},\mathbf{b})$ can be imposed.

8. Numerical applications

8.1. Cantilever piezoelectric actuator/substrate plate

The first numerical application is used to validate the developed finite element models and is based on the experiments conducted by Crawley and Lazarus [39]. The experiment specimen consists of a cantilevered laminate composite graphite/epoxy substrate plate with distributed G-1195 piezoelectric actuators bonded to the top and bottom surfaces as represented in Fig. 1. A constant voltage with an opposite sign is applied to the piezoceramic actuators on each side of the plate. The plate graphite/epoxy substrate has six layers of equal thickness with a lamination sequence of $[0°/+45°/-45°]$s and a total thickness of 0.83 mm. The following material properties are assumed: $E_1 = 150$ GPa, $E_2 =$

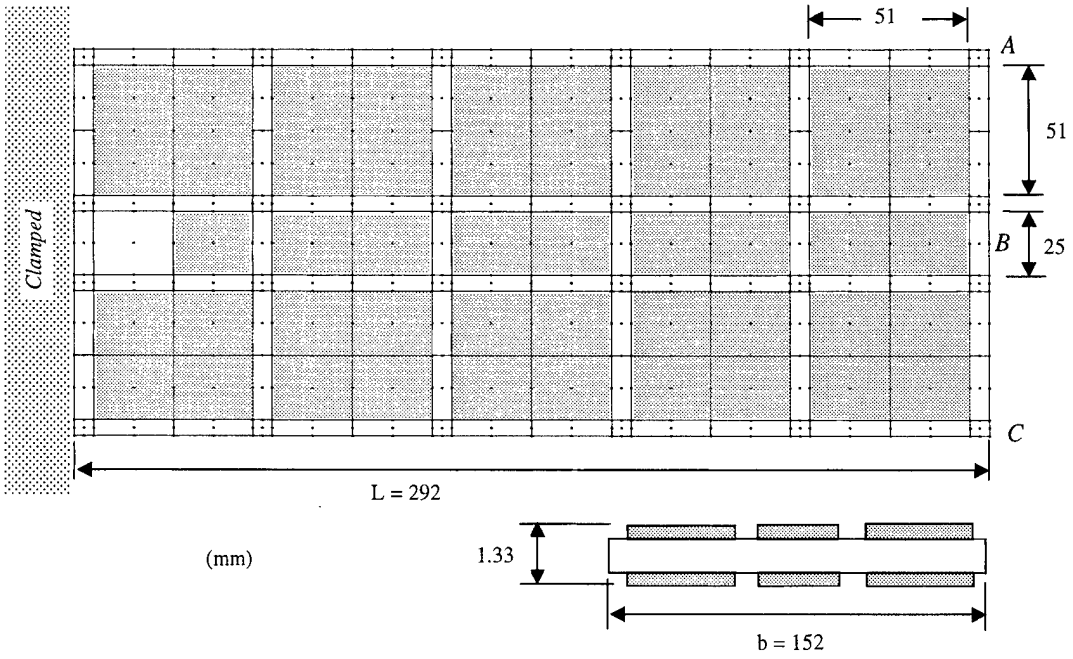

Fig. 1. Cantilever piezoelectric actuator/substrate plate.

Table 1
Non-dimensional longitudinal bending (w_1), twist deformation (w_2) and transverse bending (w_3)

	Experiment [39]	Ritz solution [39]	Q9-FSDT5P	Q9-HSDT9P	Q9-HSDT11P
w_1	0.034	0.028	0.03488	0.03474	0.03461
w_2	0.0038	0.0036	0.004065	0.004040	0.004051
w_3	0.0028	0.0032	0.003521	0.003494	0.003506

$E_3 = 9$ GPa, $G_{12} = G_{13} = 7.1$ GPa, $G_{23} = 2.5$ GPa, $\nu_{12} = \nu_{23} = \nu_{13} = 0.3$. The G-1195 piezoelectric actuators have 0.25 mm thickness each and the following material and piezoelectric properties are used: $E_1 = E_2 = E_3 = 63$ GPa, $G_{12} = G_{13} = G_{23} = 24.2$ GPa, $\nu_{12} = \nu_{23} = \nu_{13} = 0.3$, $d_{31} = d_{32} = -166 \times 10^{-12}$ m/V, $p_{33} = 15 \times 10^{-6}$ F/m. The d_{33} coefficient for the Q9-HSDT11P model is assumed to be $d_{33} = 360 \times 10^{-12}$ m/V, according to the product catalog of G-1195 piezoceramic material.

In the experiment, the deflection of the plate was measured in points A, B and C (Fig. 1). The following non-dimensional displacements are defined

$$w_1 = \frac{w_B}{b}, \quad w_2 = \frac{w_C - w_A}{b}, \quad w_3 = \frac{w_B - (w_C + w_A)/2}{b}, \tag{28}$$

where b is the width of the plate, w_B the tip deflection at the center of the plate, w_A and w_C are the tip deflections at the outer transverse edges of the plate. The non-dimensional displacement w_1 represents the longitudinal bending, w_2 the twist deformation and w_3 the transverse bending. The results obtained with the present models for an applied field of 315 V/mm are compared in Table 1 with Crawley and Lazarus [39] experimental results and also with a Ritz solution [39]. The agreement of the present models with the experimental results is reasonably good for the longitudinal bending w_1 and also for the twist w_2 and slight differences are obtained for the transversal bending w_3. In this last case, the agreement with the Ritz solution is better. Both first-order and higher-order models gave very similar results.

8.2. Optimal design of cantilever plate with surface bonded piezoelectric actuator patches

The illustrative example of a cantilever rectangular plate with two surface bonded piezoelectric actuator patches is now considered. The plate consists of a four-ply Aramid/Epoxy composite substrate and two surface bonded piezoceramic PXE-52 patches with 80 mm×40 mm on each side of the plate as represented in Fig. 2. A point load $P = 0.05$ N is applied at point A. Also, a constant electric voltage of +160 V is applied to the top piezoceramic layer and −160 V is applied to the bottom piezoceramic layer.

The assumed material properties of the Aramid/Epoxy layers are: $E_1 = 76$ GPa, $E_2 = E_3 = 5.5$ GPa, $G_{12} = G_{23} = G_{13} = 2.1$ GPa, $\nu_{12} = \nu_{23} = \nu_{13} = 0.34$, $\rho = 1380$ kg/m^3. The lamination sequence of the Aramid/Epoxy layers is $[+45°/-45°]$s. The material and electric properties for the piezoelectric PXE-52 are: $E_1 = E_2 = E_3 = 62.5$ GPa, $G_{12} = G_{13} = G_{23} = 24$ GPa, $\nu_{12} = \nu_{13} = \nu_{23} = 0.3$, $d_{31} = d_{32} = -280 \times 10^{-12}$, $d_{33} = 700 \times 10^{-12}$ m/V, $p_{33} = 3.45 \times 10^{-8}$ F/m.

The objective of the optimization problem is to minimize the overall mass of the plate and the design variables are the thicknesses of both substrate and piezoceramic layers, $t_1, \ldots, t_6$, as represented in Fig. 3. A constraint is imposed on the transversal displacement in point A, with a maximum allowable displacement of $w_{max} = 1.5$ mm. Also, lower and upper limits of 0.2 and 1.0 mm, respectively, are introduced to limit the possible variations of the layer thicknesses.

The results of the optimization problem are summarized in Table 2, showing the initial and optimal designs, obtained with the present numerical models. A reasonable mass reduction is achieved in the optimal design and slightly higher thicknesses are obtained by the first-order model.

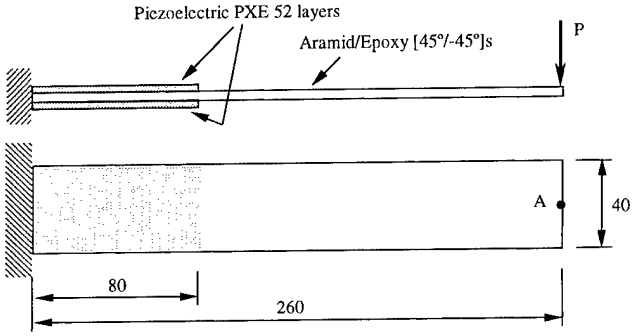

Fig. 2. Cantilever plate with surface bonded piezoelectric actuator patches.

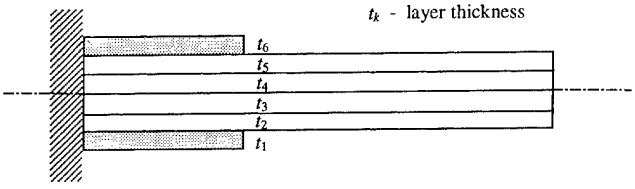

Fig. 3. Definition of design variables t_i.

Table 2
Optimal design of cantilever plate with piezoelectric actuator patches

	Initial design		Optimal design	
	Mass (kg)	Thickness distribution $(t_1,\ldots,t_3)$s (mm)	Mass (kg)	Thickness distribution $(t_1,\ldots,t_3)$s (mm)
Q9-HSDT 11P	0.048672	0.4; 0.5; 0.5	0.026125	0.2559; 0.2325; 0.2325
Q9-HSDT 9P	0.048672	0.4; 0.5; 0.5	0.027022	0.2699; 0.2360; 0.2360
Q9-FSDT 5P	0.048672	0.4; 0.5; 0.5	0.028420	0.2754; 0.2556; 0.2556

8.3. Static shape control of a rectangular panel

This example is used to illustrate the application of the static shape control optimization scheme. A rectangular plate made of 4-ply S-Glass/Epoxy with the lamination sequence of [0°/45°/−45°/0°] represented in Fig. 4, is considered. Three pairs of piezoceramic actuator patches PC5K (lead zirconate titanate) are bonded to each side of the plate as shown in Fig. 4. The plate is simply supported along the shorter edges and free at the longer edges. The plate is subjected to a uniformly distributed load of 1000 N/m^2.

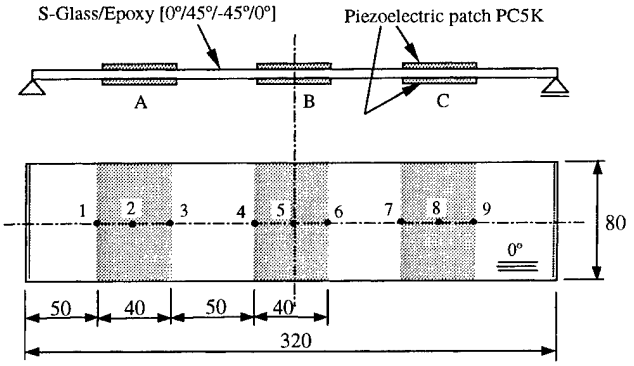

Fig. 4. Rectangular plate with three pairs of piezoelectric actuator patches.

Table 3
Transversal displacements in the shape control process

Control points (Fig. 4)	1 and 9	2 and 8	3 and 7	4 and 6	5
Desired shape: γ_i (mm)	0.400	0.580	0.730	0.900	0.920
	Actual shape in the initial design: w_i^{ini} (mm)				
Q9-HSDT 11P	0.338	0.482	0.612	0.758	0.770
Q9-HSDT 9P	0.338	0.483	0.613	0.759	0.770
Q9-FSDT 5P	0.337	0.481	0.611	0.756	0.767
	Achieved shape in the optimal design: w_i^{opt} (mm)				
Q9-HSDT 11P	0.405	0.578	0.725	0.902	0.920
Q9-HSDT 9P	0.406	0.578	0.727	0.903	0.922
Q9-FSDT 5P	0.405	0.578	0.725	0.901	0.921

The assumed material properties of the S-Glass/Epoxy substrate layers are: $E_1 = 55$ GPa, $E_2 = E_3 = 16$ GPa, $G_{12} = G_{23} = G_{13} = 7.6$ GPa, $\nu_{12} = \nu_{23} = \nu_{13} = 0.28$, $\rho = 2000$ kg/m^3. The thickness of the 0° outside layers is 1 mm each and the thickness of the inside 45° and −45° layers is 0.5 mm each.

The material and electric properties for the piezoelectric PC5K (lead zirconate titanate) are: $E_1 = E_2 = 60.24$ GPa, $E_3 = 49.02$ GPa, $G_{12} = G_{13} = G_{23} = 23.0$ GPa, $\nu_{12} = \nu_{13} = \nu_{23} = 0.31$, $d_{31} = d_{32} = -306 \times 10^{-12}$, $d_{33} = 800 \times 10^{-12}$ m/V, $p_{33} = 5.04 \times 10^{-8}$ F/m. The thickness of the piezoceramic patches is 0.5 mm.

The shape of the plate, i.e. the transversal displacements w_i will be controlled in the nine points $(i = 1,\ldots,9)$ shown in Fig. 4. The objective is to find the appropriate electric voltages that should be applied to the three pairs of piezoelectric actuator patches in order to minimize the mean-squared error between the actual shape of the plate and the desired shape. The lower and upper voltage limits are taken as −200 and 200 V, respectively. The transversal displacements corresponding to the desired shape γ_i, actual shape in the initial design, w_i^{ini}, and achieved shape in the optimal design, w_i^{opt}, are shown in Table 3. The electric voltages corresponding to the initial design and to the optimal design are presented in Table 4. A very good agreement between the higher-order and first-order models is obtained.

8.4. Maximum natural frequency design of a skewed plate with piezoelectric sensor strips

This last example consists of a 6-ply Graphite/Epoxy skewed plate with two surface bonded pairs of piezo-

Table 4
Static shape control of a rectangular plate with actuator patches

	Electric voltages applied to the actuator pairs (V)					
	Initial design			Final design		
	Pair A	Pair B	Pair C	Pair A	Pair B	Pair C
Q9-HSDT 11P	0/0	0/0	0/0	−81.7/81.6	−129.4/130.1	−81.1/81.6
Q9-HSDT 9P	0/0	0/0	0/0	−82.1/81.7	−130.5/130.5	−81.2/81.8
Q9-FSDT 5P	0/0	0/0	0/0	−82.6/82.4	−131.2/131.4	−82.6/83.0

electric sensor strips, as represented in Fig. 5. The skewed plate is simply supported along the sides marked with SS and free along the sides marked with F in Fig. 5. The electric boundary conditions are open circuit, which means that the electric voltages at the piezoelectric sensors remain free.

The assumed material properties of the Graphite/Epoxy substrate layers are: $E_1 = 220$ GPa, $E_2 = E_3 = 6.9$ GPa, $G_{12} = G_{23} = G_{13} = 4.8$ GPa, $\nu_{12} = \nu_{23} = \nu_{13} = 0.25$, $\rho = 1640$ kg/m^3. All layers are assumed to have equal thickness: 6×0.5 mm $= 3$ mm (total thickness).

The piezoelectric sensor strips (PZT 5A) are surface bonded to the top and bottom sides of the 6-ply composite plate and the following material and electric properties are considered: $E_1 = E_2 = 69.4$ GPa, $E_3 = 106.4$ GPa, $G_{12} = G_{13} = G_{23} = 26.5$ GPa, $\nu_{12} = \nu_{13} = \nu_{23} = 0.31$, $\rho = 7700$ kg/m^3, $d_{31} = d_{32} = -171 \times 10^{-12}$, $d_{33} = 374 \times 10^{-12}$ m/V, $p_{33} = 1.5 \times 10^{-8}$ F/m. The thickness of the piezoelectric strips is 0.15 mm.

The objective of the optimization problem is to maximize the fundamental natural frequency of the skewed plate. The design variables are the fiber angles in each one of the Graphite/Epoxy layers. Table 5 presents the natural frequencies corresponding to the first four vibration modes for the initial design and optimal design. The assumed initial design and optimal lamination sequence obtained with the higher-order models and first-order model are also presented in Table 5. As in previous examples, a very good agreement between the higher-order and first-order models is obtained.

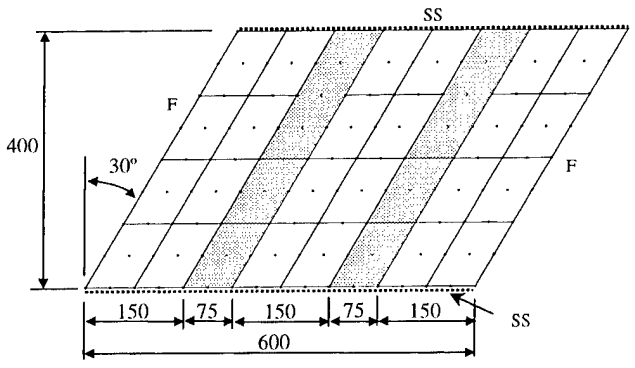

Fig. 5. Skewed plate with piezoelectric sensor strips.

9. Conclusions

In this work, finite element models based on high-order and first-order displacement fields, applied to the analysis of laminated plates with embedded and/or surface bonded piezoelectric laminae have been presented. It has been shown elsewhere [6,7,40] that the first-order models can lead to significant errors in the stress prediction of highly anisotropic and/or moderately thick composite laminated plates and also when piezoelectric laminae are involved.

The developed models have been applied to the design sensitivity analysis and optimal design of laminated plates with piezoelectric laminae. The design objectives are the minimization of weight/mass of the structure subject to behavior constraints, maximization of the piezoelectric actuator performance and/or the maximization of natural frequencies of specified vibration modes. The design variables are the fiber angles in the substrate orthotropic layers, the thicknesses of substrate and piezoelectric layers and also the electric potentials applied to the actuators. The sensitivities of constraint equations and objective functions with respect to the design variables are evaluated analytically.

As shown in the simple examples presented, important improvements in the structural performance and/or weight savings can be achieved with the developed optimization schemes. Only thin plate situations are involved in the presented illustrative applications and in

Table 5
Maximum frequency design of skewed plate with piezoelectric sensor strips

	Initial design		Optimal design	
	Natural frequencies (rad/s)	Lamination sequence	Natural frequencies (rad/s)	Lamination sequence
Q9-HSDT 11P	191.79	[30°/30°/30°]s	532.34	[74.1°/73.3°/70.6°]s
	334.84		540.64	
	659.76		612.25	
	786.33		776.09	
Q9-HSDT 9P	192.57	[30°/30°/30°]s	532.47	[73.8°/74.4°/70.8°]s
	335.52		540.51	
	662.16		612.60	
	788.52		778.07	
Q9-FSDT 5P	192.60	[30°/30°/30°]s	532.78	[75.9°/72.2°/70.3°]s
	336.07		539.20	
	662.59		613.93	
	789.02		779.89	

this case, as expected, the higher-order models and first-order model gave very similar results. The present finite element models have been implemented in an in-house software package for the structural optimization of laminated structures with piezoelectric actuator and sensors.

Acknowledgements

This work was supported by F.C.T. – Fundação para a Ciência e Tecnologia, Ministério da Ciência e Tecnologia – Project PRAXIS/P/EME/12028/1998. The authors also wish to thank Fundação Calouste Gulbenkian and FLAD – Fundação Luso Americana para o Desenvolvimento, for their financial support.

References

[1] Crawley EF. Intelligent structures for aerospace: a technology overview and assessment. AIAA J 1994;32(8):1689–99.
[2] Reddy JN. Mechanics of laminated composite plates: theory and applications. Boca Raton: CRC Press; 1997.
[3] Pagano NJ, Hatfield SJ. Elastic behavior of multilayered bidirectional composites. AIAA J 1972;10:931–3.
[4] Mallikarjuna, Kant T. A critical review and some results of recently developed refined theories of fiber-reinforced laminated composites and sandwiches. Comp Struct 1993;23:293–312.
[5] Mota Soares CM, Mota Soares CA, Franco Correia VM. Optimization of multilaminated structures using higher-order deformation models. Comput Meth Appl Mech Eng 1997;149:133–52.
[6] Chattopadhyay A, Seeley CE. A higher order theory for modeling composite laminates with induced strain actuators. Composites B 1997;28:243–52.
[7] Robbins DH, Reddy JN. Analysis of piezoelectrically actuated beams using a layer-wise displacement theory. Comput Struct 1991;41(2):265–79.
[8] Lo KH, Christensen RM, Wu EM. A high-order theory of plate deformation. Part 1: Homogeneous plates. J Appl Mech 1977;663–68.
[9] Lo KH, Christensen RM, Wu EM. A high-order theory of plate deformation. Part 2: Laminated plates. J Appl Mech 1977;669–76.
[10] Reddy JN. An evaluation of equivalent single-layer and layerwise theories of composite laminates. Comp Struct 1993;25:31–5.
[11] Noor AK, Burton WS. Assessment of computational models for multilayered anisotropic plates. Comp Struct 1990;14:233–65.
[12] Reddy JN, Robbins Jr DH. Theories and computational models for composite laminates. Appl Mech Rev 1994;47(6):147–69.
[13] Benjeddou A. Advances in finite element modeling of smart structural elements. In: Mota Soares CA, Mota Soares CM, Freitas MJM, editors. Proceedings of NATO Advanced Study Institute, Mechanics of Composite Materials and Structures, vol. IV, IDMEC/IST, Instituto Superior Técnico, Lisbon, Portugal, 1998. p. 171–92.
[14] Wang Z, Chen S, Han W. The static shape control for intelligent structures. Finite Elements Anal Design 1997;26:303–14.
[15] Donthireddy P, Chandrashekhara K. Modeling and shape control of composite beams with embedded piezoelectric actuators. Comp Struct 1996;35:237–44.
[16] Carman G, Reifsnider K. Analytical optimization of coating properties for actuators and sensors. J Intell Mater Syst Struct 1993;4:89–97.
[17] Kim SJ, Jones JD. Influence of piezo-actuator thickness on the active vibration control of a cantilever beam. J Intell Mater Syst Struct 1995;6:610–23.
[18] Meric RA, Saigal S. Shape sensitivity analysis of piezoelectric structures by the adjoint variable method. AIAA J 1991;29(8):1313–8.
[19] Silva ECN, Fonseca JSO, Kikuchi N. Optimal design of piezoelectric microstructures. Comput Mech 1997;19:397–410.
[20] Batra RC, Liang XQ. The vibration of a rectangular laminated elastic plate with embedded piezoelectric sensors and actuators. Comput Struct 1997;63(2):203–16.
[21] Liang C, Sun FP, Rogers CA. Determination of design of optimal actuator location and configuration based on actuator power factor. J Intell Mater Syst Struct 1995;6:456–64.
[22] Leeks TJ, Weisshaar TA. Optimizing induced strain actuators for maximum panel deflection. In: Proceedings of AIAA/ASME Adaptive Structures Forum, AIAA-94-1774-CP, 1994. p. 378–87.
[23] Seely CE, Chattopadhyay A. Development of intelligent structures using multiobjective optimization and simulated annealing. In: Proceedings of AIAA/ASME Adaptive Structures Forum, AIAA-94-1777-CP, 1994. p. 411–21.
[24] Abdullah MM. Optimal location and gains of feedback controllers at discrete locations. AIAA J 1998;36(11):2109–16.
[25 Kang YK, Park HC, Agrawal B. Optimization of piezoceramic sensor/actuator placement for vibration control of laminated plates. AIAA J 1998;36(9):1763–5.
[26] Varadarajan S, Chandrashekhara K, Agarwal S. Adaptive shape control of laminated composite plates using piezoelectric materials. AIAA J 1998;36(9):1694–8.
[27] Laxminarayana S, Kota S. Static shape control of smart structures using compliant mechanisms. AIAA J 1999;35(5):572–8.
[28] Adali S, Verijenko VE, Tauchert TR, Richter A. Minimization of deflection using piezo effect and ply angles for thick laminated plates. In: Adali A, Morozov EV, Verijenko VE, editors. Proceedings of the Second International Conference on Composite Science and Technology, Department of Mechanical Engineering, University of Natal, Durban, South Africa, 1998. p. 389–94.
[29] Padula SL, Kincaid RK. Optimization strategies for sensor and actuator placement, NASA/TM-1999-209126, NASA, Langley Research Center, 1999.
[30] Han J, Lee I. Optimal placement of piezoelectric sensors and actuators for vibration control of a composite plate using genetic algorithms. Smart Mater Struct 1999;8:257–67.
[31] Allik H, Hughes TJR. Finite element method for piezoelectric vibration. Int J Numer Meth Eng 1970;2:151–7.
[32] Franco Correia VM, Mota Soares CM, Mota Soares CA. Optimal design of composite structures with integrated piezoelectric laminae. In: Soares CAM, Soares CMM, Freitas MJ, editors. Mechanics of composite materials and structures. Nato Science series. Netherlands: Kluwer Academic Publishers, 1999. p. 389–408.
[33] Suleman A, Venkayya VB. A simple finite element formulation for a laminated composite plate with piezoelectric layers. J Intell Mater Syst Struct 1995;6:776–82.
[34] Seyranian AP, Lund E, Olhoff N. Multiple eigenvalues in structural problems. Struct Optim 1994;8:207–27.
[35] Rodrigues HC, Guedes JM, Bendsoe MP. Necessary conditions for optimal design of structures with a non-smooth based criterion. Struct Optim 1997;9:52–6.
[36] Mota Soares CM, Mota Soares CA, Franco Correia VM. Multiple eigenvalue optimization of composite structures using discrete third order displacement models. Comp Struct 1997;38:99–110.

[37] Mateus HC, Rodrigues HC, Mota Soares CM, Mota Soares CA. Sensitivity analysis and optimization of thin laminated structures with a nonsmooth eigenvalue based criterion. Struct Optim 1997;14(4):219 24.

[38] Vanderplaats GN. Numerical optimization techniques for engineering design: with applications. New York: McGraw-Hill; 1994.

[39] Crawley EF, Lazarus KB. Induced strain actuation of isotropic and anisotropic plates. AIAA J 1991;29(6):944–51.

[40] Franco Correia VM, Gomes MA, Suleman A, Mota Soares CM, Mota Soares CA. Modeling and design of adaptive composite structures. Comput Meth Appl Mech Eng 2000;185(2–4): 325–346.

ELSEVIER

Composite Structures 47 (1999) 635–641

COMPOSITE STRUCTURES

www.elsevier.com/locate/compstruct

Optimum in situ strength design of laminates under combined mechanical and thermal loads

J. Wang [a,*], B.L. Karihaloo [b]

[a] *Department of Mechanics and Engineering Science, Peking University, Beijing 100871, People's Republic of China*
[b] *Division of Civil Engineering, Cardiff School of Engineering, Cardiff University, Queen's Buildings, P.O. Box 686, Newport Road, Cardiff CF2 3TB, UK*

Abstract

In this paper, optimum laminate configurations are sought for multidirectional fibre-reinforced composite laminates under combined in-plane mechanical and thermal loads. The design objective is to enhance the value of the loads over and above the first-ply-failure loads which are judged by a transverse failure criterion and the Tsai-Hill criterion, respectively. The in situ strength parameters previously obtained are incorporated in these criteria. It is found that the optimum designs under combined mechanical and thermal loads are not the same as those under pure mechanical loads for three of the four loading cases studied. For all cases the optimum loads are significantly larger than those for a quasi-isotropic design. © 2000 Elsevier Science Ltd. All rights reserved.

Keywords: In situ strength; Optimum design; Thermal load; Failure criterion; First-ply-failure

1. Introduction

Optimum strength designs of continuous fibre-reinforced composite laminates have been pursued since the early days of these materials. For example, Sandhu [1] used a parametric study to investigate the fibre orientation of a unidirectional lamina yielding maximum strength under in-plane stress conditions. Brandmaier [2] found that the strength of a unidirectional lamina under in-plane stresses could be maximized analytically with respect to the fibre orientation. The results based upon Tsai-Hill failure criterion indicated that the optimum fibre orientation depended upon the stress state and the relative value of the transverse and in-plane shear strengths of the lamina. When the strength of a multidirectional composite laminate is to be maximized, more complicated and explicit optimization techniques are needed. The work by Chao et al. [3] was probably the earliest study that sought the optimum strength design of multidirectional laminates using a search technique. Many studies have been devoted to the optimum strength design of multidirectional laminates in the recent two decades. Among these are the works by Park [4], Fukunaga and Chou [5], Miravete [6], Fukunaga and Vanderplaats [7]. Considering that most of the advanced fibre-reinforced composite laminates are prone to cracking and delamination, and that the properties of laminates are tailorable, Wang and Karihaloo [8–10] posed optimum strength design problems of multidirectional laminates in a different way from the conventional ones. They applied fracture mechanics analyses in the optimum strength designs of multidirectional laminates against delamination and transverse cracking.

In measuring the in situ transverse strength of unidirectional laminae in laminates, it was found by Flaggs and Kural [11] that the thermal residual stress resulting from the manufacturing process might consist of a large portion of the in situ strength (more than half for $[0_2/90_n]_s$ and $[\pm 30/90_n]_s$ for $n = 1, 2, \ldots, 8$). A composite structure will also experience temperature variations in service. Because of the remarkable difference in the thermal expansion coefficients as well as the stiffnesses of a unidirectional lamina in its longitudinal and transverse directions, the stresses caused by temperature variations may be quite significant in practice. It is obvious that the thermal stresses in a multidirectional laminate are functions of the laminate configuration, that is, functions of the ply angles in the laminate. In the present paper, we shall pursue the optimum in situ strength design of multidirectional composite laminates subjected to combined mechanical and thermal loads. In the main part of this paper, we shall first introduce the in situ

* Corresponding author. Fax: +81-3-3920-3824.
E-mail address: jxwang@pku.edu.cn (J. Wang).

0263-8223/99/$ - see front matter © 2000 Elsevier Science Ltd. All rights reserved.
PII: S0263-8223(00)00040-4

strength parameters, and then incorporate them into the formalism of optimization problems. The optimization problems will be solved by a nonlinear mathematical programming technique.

2. In situ strength formulae

Chang and Lessard [12] fitted experimental data with two formulae to calculate the in situ transverse tensile and in-plane shear strengths of unidirectional laminae in general multidirectional laminates, namely,

$$\frac{Y_t}{Y_t^0} = 1 + \frac{A}{N^B}\sin(\Delta\theta), \tag{1}$$

$$\frac{S_c}{S_c^0} = 1 + \frac{C}{N^D}\sin(\Delta\theta), \tag{2}$$

where Y_t^0 and S_c^0 are the transverse tensile strength and in-plane shear strength measured with a thick unidirectional lamina. A, B, C and D are to be determined by experiments. N is the number of plies in a unidirectional lamina in a multidirectional laminate. $\Delta\theta$ represents the minimum difference between the ply angle of a lamina and those of its neighbouring plies.

In order to reveal the physics of the phenomenon of in situ strengths, Wang and Karihaloo studied the in situ strengths using fracture mechanics [9]. Based upon the fracture mechanics analyses, they proposed two formulae to calculate the in situ strengths [9]

$$\frac{Y_t}{Y_t^0} = 1 + \frac{A}{N^B} f_t(\Delta\theta), \tag{3}$$

$$\frac{S_c}{S_c^0} = 1 + \frac{C}{N^D} f_s(\Delta\theta). \tag{4}$$

Here, the two functions $f_t(\Delta\theta)$ and $f_s(\Delta\theta)$ represent the influence of the neighbouring laminae on the strengths of a lamina. They are given by

$$f_t(\Delta\theta) = \min\left[\frac{\sin^2(\Delta\theta_a)}{1+\sin^2(\Delta\theta_a)}, \frac{\sin^2(\Delta\theta_b)}{1+\sin^2(\Delta\theta_b)}\right], \tag{5}$$

$$f_s(\Delta\theta) = \min\left[\frac{\sin^2(2\Delta\theta_a)}{1+\sin^2(2\Delta\theta_a)}, \frac{\sin^2(2\Delta\theta_b)}{1+\sin^2(2\Delta\theta_b)}\right]. \tag{6}$$

The parameters A, B, C and D in formulae (1)–(4) are to be determined from experimental results. As these formulae also contain the ply-angle influence functions, i.e. $\sin(\Delta\theta)$, $f_t(\Delta\theta)$ and $f_s(\Delta\theta)$, the investigation of the dependence of A, B, C and D on the laminate configuration is very important. They must be independent of the laminate configuration, if they are to be regarded as material constants. Otherwise the above in situ strength formulae cannot be applied to a general multidirectional laminate. Therefore, in order to determine the values of these constants for a particular composite material, extensive experiments are needed. Currently, there are very few experimental results available, of which the results of the in situ transverse tensile strength obtained by Flaggs and Kural [11] are widely cited in the literature. Regarding the in-plane shear strength, Chang and Chen [13] studied its dependence on the ply thickness in unidirectional and cross-ply laminates. There is a dearth of experimental data to determine the dependence of the in situ shear strength on the laminate configuration.

In Fig. 1, the in situ transverse strength predicted by Eqs. (1) and (3) are compared with the experimental results of Flaggs and Kural [11] for the material T300/934. In fitting the experimental data, different values of A are used in Eqs. (1) and (3) (1.7 and 3.4, respectively). Chang and Lessard [12] used $A = 1.3$ and $B = 0.8$ previously to fit the experimental data. It is seen that both the theoretical formulae fit the experimental data reasonably well. The most important conclusion drawn from Fig. 1 is that for the material and laminate configurations studied by Flaggs and Kural [11], the parameters A and B appear to be independent of the laminate configuration. It appears that they can indeed be treated as material constants. On the other hand, due to lack of experimental data, the dependence of the parameters C and D on the laminate configuration cannot be judged. Chang and Lessard [12] found that formula (2) fits the experimental data well for T300/976 cross-ply laminates with $D = 2.0$ and $C = 1.0$ In the sequel, we shall use formula (3), which has a fracture mechanics basis, to calculate the in situ shear strength of laminae in multidirectional laminates with $C = 4.0$ and $D = 1.0$.

In most cases, transverse cracking is the first noticeable damage in a laminate. Although the transverse cracks generally do not result in the immediate failure of the whole laminate, they have the potential to induce failure by stress concentration and delamination. For instance, the experimental results of Herakovich [14]

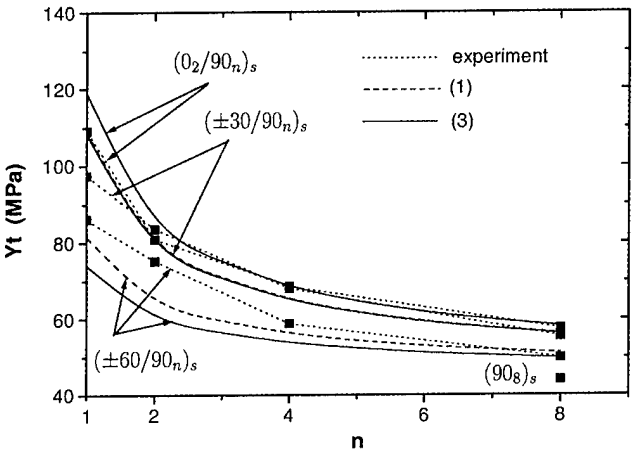

Fig. 1. Comparison of theoretical and experimental results of the in situ transverse tensile strength. $A = 1.7$ and $B = 0.8$ are used in formula (1), and $A = 3.4$ and $B = 0.8$ are used in formula (3).

indicate that the failure of angle-ply laminates with thick laminae under in-plane unidirectional tension is entirely due to transverse cracking. In the optimum strength design to follow, we shall use a transverse tensile failure criterion [12] to judge the transverse failure of a unidirectional lamina in a multidirectional laminate. This criterion, into which the in situ strengths are incorporated, is written as

$$\left(\frac{Y}{Y_t}\right)_i^2 + \left(\frac{S}{S_c}\right)_i^2 \leqslant 1 \quad (i = 1, 2, \ldots, L), \tag{7}$$

where Y and S are the in-plane transverse and shear stresses in the lamina. L is the total number of unidirectional laminae in the laminate. In the previous optimum strength design of laminates by Wang and Karihaloo [10], it was found that the optimizer aims at distributing the stresses according to the strengths of an anisotropic material in different directions. In the failure criterion (7), the strength and stress in the fibre direction are not taken into account. Therefore, the optimizer always gives optimum designs of laminates in which the stresses in the fibre directions of the laminae are very large. This may increase the risk of failure in the fibre direction. Thus, in the present paper, we also use the following simplified Tsai-Hill criterion to consider the effect of the stress in the fibre direction in the optimum design

$$\left(\frac{\sigma_L}{F_L}\right)_i^2 + \left(\frac{Y}{Y_t}\right)_i^2 + \left(\frac{S}{S_c}\right)_i^2 \leqslant 1 \quad (i = 1, 2, \ldots, L), \tag{8}$$

where σ_L and F_L are the stress and strength of a unidirectional lamina in the fibre direction.

3. Formulation of optimization problem

For a multidirectional laminate subjected to in-plane loads, let us denote the left-hand terms of Eqs. (7) and (8) by q_i^2. For a composite laminate under given in-plane loads, if the ply angles and thicknesses of the constituent laminae are so chosen that the values of q_i^2 for all laminae are reduced, then the loads corresponding to the transverse cracking or failure will be enhanced. This objective is achieved by minimizing the maximum value of q_i^2. Following the procedure in the work by Wang and Karihaloo [10], the optimization problem is formulated as

$$\min_{\theta_i, t_i, \gamma} \quad \gamma \tag{9}$$

subject to

$$q_i - \gamma \leqslant 0, \tag{10}$$

$$-\frac{\pi}{2} \leqslant \theta_i \leqslant \frac{\pi}{2}, \tag{11}$$

$$\sum_i t_i = h \quad (i = 1, \ldots, L), \tag{12}$$

$$\underline{t} \leqslant t_i \leqslant \bar{t}. \tag{13}$$

The above optimization problem is solved by a constrained variable metric method. The non-differentiability of $f_t(\Delta\theta)$ and $f_s(\Delta\theta)$ with respect to the design variables θ_i is treated using the procedure in the work by Wang and Karihaloo [10].

As mentioned in Section 1, the thermal residual stresses resulting from the manufacturing process may constitute a large portion of the in situ strength (more than half for $[0_2/90_n]_s$ and $[\pm 30/90_n]_s$ for $n = 1, 2, \ldots, 8$ [11]). It is obvious that the thermal residual stresses in a multidirectional laminate are also functions of the laminate configuration, that is, functions of the ply angles in the laminate. Therefore, in the optimum strength design of laminates, the laminates are assumed to be under combined thermal and mechanical loads. Thus, following the classical lamination theory, the total stresses in a generic lamina in a multidirectional laminate are calculated from

$$\sigma_i = \bar{Q}_{ij}\left[A_{jk}^{-1}(N_k + N_k^t) - \varepsilon_j^t\right] \quad (i, j, k = 1, 2, 6), \tag{14}$$

where σ_i the stress components in the reference coordinate system for the laminate, $\bar{Q}_{ij}$ the off-axis stiffnesses of the lamina, and A_{ij} the in-plane stiffnesses of the laminate, N_k^t the equivalent thermal loads, and ε_j^t the thermal strains.

4. Design examples

The above optimization procedure was applied to the optimum design of a multidirectional laminate shown in Fig. 2. Fig. 2(a) shows the in-plane loads, and Fig. 2(b) shows the detailed configuration of one half of the laminate. This laminate is composed of L laminae of different ply angles and thicknesses. It is physically symmetric with respect to its geometric middle plane, i.e. the laminae are stacked in the order $(\theta_{L/2}/\ldots/\theta_1)_s$. The stiffness and strength constants used in the calculation of the in situ strengths are adapted from the work by Chang and Lessard [12] on T300/976. The thermal expansion coefficients are taken as those of T300/934 [11], i.e. $\alpha_L = 0.09\,\mu\text{strain}/^\circ\text{C}$, $\alpha_T = 28.8\,\mu\text{strain}/^\circ\text{C}$. The thickness of a single ply is assumed to be 0.14 mm. The temperature variation is taken as $\Delta T = -147^\circ\text{C}$, i.e. the temperature drop in the manufacturing process [11]. It can be arbitrary otherwise.

Because of the highly nonlinear nature of the functions q_i and of the fact that they can attain their minima at different combinations of design variables, the above optimization problem can have many local minima. In the computational scheme, the global minimum is sought by a random search technique. The optimization process is begun from different initial design points $(x_j^0)_m^T$ $(j = 1, \ldots, L; m = 1, \ldots, M)$ (m denotes the mth initial design point) in the space of design variables

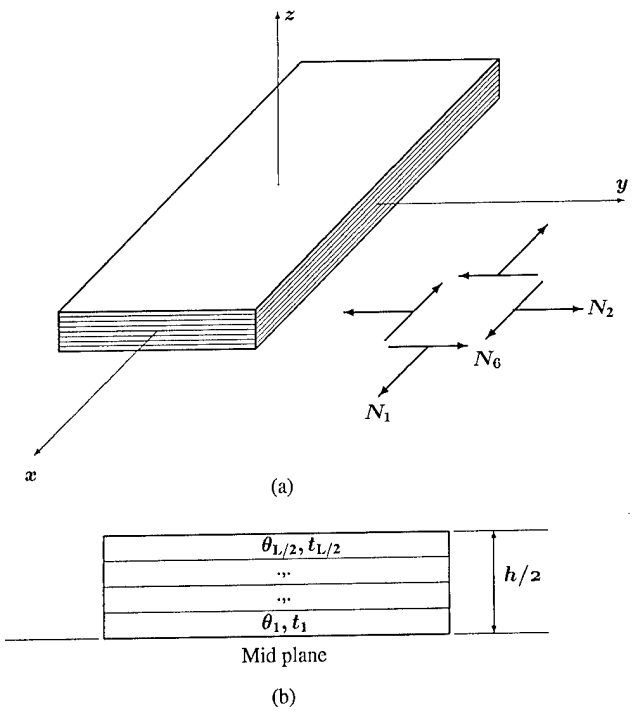

Fig. 2. The laminate configuration. The in-plane loads shown represent the resultant mechanical forces over the thickness.

$\{x_j\}^T$ $(j = 1, \ldots, L)$. These random initial design points are chosen so that they are uniformly distributed in the design space, and the global minimum is sought from among the local minima corresponding to these randomly chosen initial designs. In all cases, M was chosen to be equal to 400.

The above optimum design is demonstrated on an eight-ply symmetric laminate with the four ply angles being the design variables. Given a mechanical load $[N_1^0, N_2^0, N_6^0]$, the improvement in the design is represented by

$$k = \frac{1}{\max q_i} \quad (i = 1, 2, \ldots, 4). \tag{15}$$

We first seek the optimum designs without the thermal effect, that is, the laminate is only subjected to mechanical loads. The change of the load factor k during the optimization process for four in-plane loading combinations is shown in Figs. 3 and 4 for the failure criteria (7) and (8), respectively. The initial guesses to ply angles (chosen pseudo-randomly) and their final optimum values, the optimum load factor k_{max} and the ratio of k_{max} to the initial load factor k_{in}, are given in Table 1, where the load factor k_{iso} is for a quasi-isotropic laminate design $[45/90/-45/0]_s$.

The results shown in Table 1 and in Figs. 3 and 4 exhibit several features. First, for each of the loading cases (a)–(c), the mechanical load corresponding to the first-ply-failure in the optimally designed laminate is increased several fold compared with that of a randomly

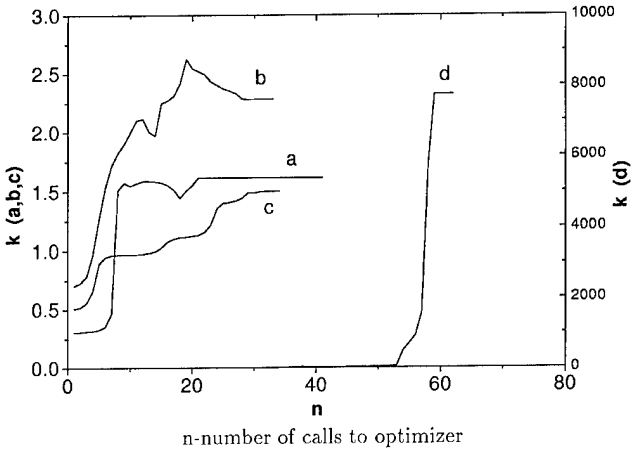

Fig. 3. Evolution of load factor k for a symmetric laminate of four ply angles for four mechanical loading cases without thermal effect: (a) $[N_1^0, N_2^0, N_6^0]^T = [200, 200, 0]^T$ kN/m; (b) $[N_1^0, N_2^0, N_6^0]^T = [200, 0, 200]^T$ kN/m; (c) $[N_1^0, N_2^0, N_6^0]^T = [400, 200, 0]^T$ kN/m; (d) $[N_1^0, N_2^0, N_6^0]^T = [200, 200, 200]^T$ kN/m. The transverse cracking criterion (7) is used.

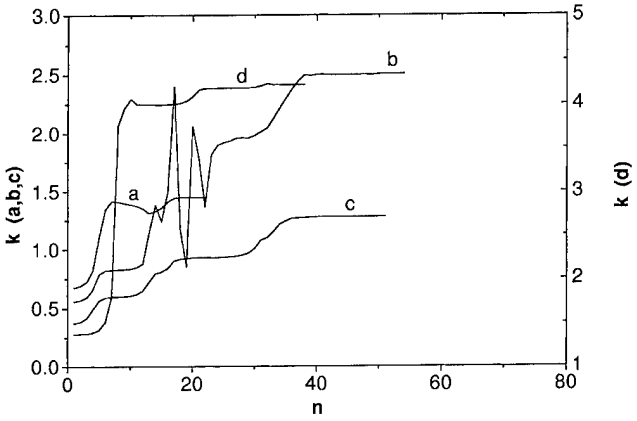

Fig. 4. Evolution of load factor k for a symmetric laminate of four ply angles without thermal effect. The mechanical loading cases are the same as those in Fig. 3. The Tsai-Hill failure criterion (8) is used.

chosen design. Secondly, when the transverse cracking criterion (7) is used in the optimization, the optimizer aims at reducing the transverse and in-plane shear stresses and distributing the stress in the fibre direction of a lamina in a laminate. For example, for loading case (b) in Fig. 3, the final stresses in the four laminae in the optimized laminate are $\{\sigma_1, \sigma_2, \sigma_6\} = [\{-349, 39, 0.5\}, \{541, -19, 0.3\}, \{-36, 18, -38\}, \{540, -19, 3\}]$ MPa. For loading case (c), these values are $\{\sigma_1, \sigma_2, \sigma_6\} = [\{439, 48, 24\}, \{364, 53, -23\}, \{436, 28, 24\}, \{726, 29, -5\}]$ MPa. In terms of the optimum design under loading case (b), the failure load corresponding to the first transverse cracking will be $k_{max} \times [N_1^0, N_2^0, N_6^0]$, in which case the maximum tensile stress in the fibre direction of the second ply (lamina) will be 2.28×541 MPa $= 1233$ MPa. This value is close to

Table 1
Summary of optimized ply angles in a symmetric laminate of four ply angles without thermal effect

In-plane loading	Initial design $\theta_1, \theta_2, \theta_3, \theta_4$	Final design $\theta_1, \theta_2, \theta_3, \theta_4$	k_{max}	k_{max}/k_{in}	k_{iso}
	Transverse cracking criterion				
a	82.4, 88.5, 75.3, 46.6	46.8, 89.6, 44.0, −30.4	1.62	5.34	1.37
b	−78.1, 72.5, 82.5, 18.2	−56.6, 32.7, 86.6, 30.5	2.28	3.27	0.93
c	−0.9, 76.1, −2.2, 48.3	−33.5, 70.0, −33.8, 20.4	1.5	3.0	1.40
d	33.9, 27.3, 35.2, 38.9	45.0, 45.0, 45.0, 45.0	∞	∞	0.77
	Tsai-Hill failure criterion				
a	27.1, 7.2, 38.6, −40.9	40.6, −4.4, 54.7, −58.5	1.45	2.13	1.32
b	−61.5, 10.6, −59.7, 86.1	−58.4, 32.0, −57.6, 31.3	2.50	4.5	0.90
c	13.6, 54.2, −74.0, 61.7	−48.9, 52.3, −44.7, 10.6	1.28	3.46	1.18
d	23.0, 55.2, 52.5, 21.4	45.5, 43.6, 47.0, 43.7	4.22	3.08	0.76

the longitudinal tensile strength 1515 MPa of the material T300/976. For this reason, optimum strength designs are pursued using the Tsai-Hill failure criterion (8) in which the contribution of the stress component in the fibre direction is also taken into account.

The results obtained using the Tsai-Hill failure criterion are also shown in Table 1. However, it is found that the use of the Tsai-Hill criterion does not result in a significant change in the stress distribution in the laminae in the optimally designed laminate. For instance, for loading case (b) in Fig. 4, the final stresses in the four laminae in the optimized laminate are $\{\sigma_1, \sigma_2, \sigma_6\} = [\{-213, 41, 2\}, \{537, -8, -5\}, \{-213, 41, 10\}, \{537, -8, 3\}]$ MPa. The reason for this may be due to the large strength of the unidirectional lamina in the fibre direction. The optimizer always distributes the stresses according the strengths in different directions of the anisotropic material.

Loading case (d) is simply to check the "smartness" of the optimizer. As this loading case is simply a unidirectional tension along 45° with respect to the 1-axis of the reference coordinate system for the laminate, the theoretical optimum design should be a unidirectional laminate in which all the fibres are along 45°. In this case, all q_i are 0, which is obviously the absolute minimum of the optimization problem. This theoretical optimum design is captured by the optimizer for both failure criteria, as shown in Table 1. This theoretical optimum design was not obtained in the previous work by Wang and Karihaloo [15].

The results of the optimum designs when the thermal effect is included are shown in Table 2 again for the two failure criteria. The evolutions of the load factor k are shown in Figs. 5 and 6 for the two failure criteria, respectively. Due to the thermal stresses, the absolute enhancement of the load factor is not as large as those in Table 1. However, the values of the ratio k_{max}/k_{in} are of the same level as those in Table 1. Because all the optimum designs are sought starting from multiple random initial designs, the initial designs in Table 2 are not necessarily the same as those in Table 1. Although the optimum values of k_{max} in Tables 1 and 2 are likely to be the global maxima in the design domain, the optimum ply angles as well as the initial ply angles leading to the same optimum angles are not unique because of the high nonlinearity and the inherent symmetry of the problem. To get a better insight into the influence of the thermal effect on the optimum strength design, we use the initial ply angles in Table 1 to seek the optimum designs of the laminate when subjected to the combined mechanical and thermal loads. The results are shown in Table 3.

Table 2
Summary of optimized ply angles in a symmetric laminate of four ply angles with thermal effect

In-plane loading	Initial design $\theta_1, \theta_2, \theta_3, \theta_4$	Final design $\theta_1, \theta_2, \theta_3, \theta_4$	k_{max}	k_{max}/k_{in}	k_{iso}
	Transverse cracking criterion				
a	−29.9, −13.6, −75.6, 13.6	−56.3, −30.5, −49.2, 44.4	0.81	1.66	0.60
b	−7.1, −35, −19.2, 16.4	23.7, −36.5, 23.7, 27.0	2.24	8.75	0.72
c	−27.37, −63.1, 69.8, −63.4	43.7, −51.1, 43.7, −18.6	0.82	3.31	0.62
d	57.3, 41.3, 45.8, 35.6	45.0, 45.0, 45.0, 45.0	∞	∞	0.50
	Tsai-Hill failure criterion				
a	−32.6, −27.7, −77.8, 14.9	−53.0, −29.2, −47.2, 45.8	0.79	1.56	0.60
b	86.6, 73.4, −36.0, 61.2	27.4, 24.3, −36.6, 24.3	1.91	5.66	0.71
c	−64.8, 11.1, −88.6, −44.0	−42.8, 49.1, −42.8, 19.4	0.77	1.95	0.60
d	86.7, 61.6, 22.8, 22.6	45.0, 45.0, 45.0, 45.0	4.24	5.75	0.50

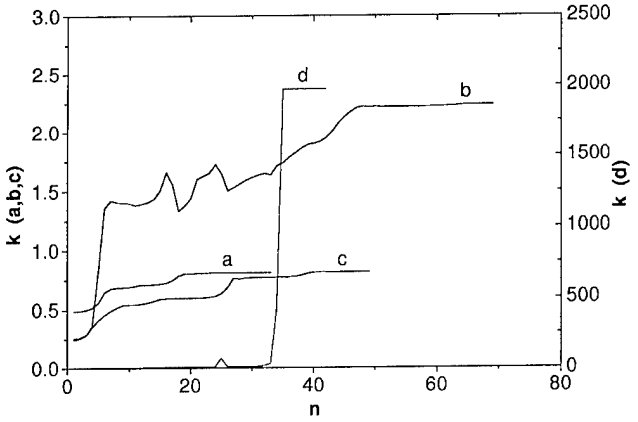

n-number of calls to optimizer

Fig. 5. Evolution of load factor k for a symmetric laminate of four ply angles subjected to mixed thermal and mechanical loads. The mechanical loading cases are the same as those in Fig. 3. The transverse cracking criterion (7) is used.

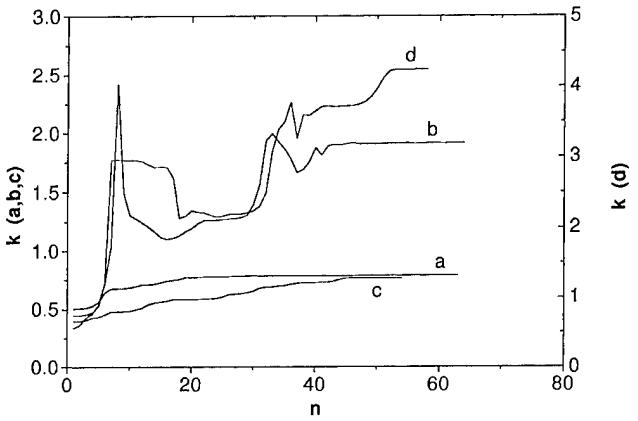

n-number of calls to optimizer

Fig. 6. Evolution of load factor k for a symmetric laminate of four ply angles subjected to mixed thermal and mechanical loads. The mechanical loading cases are the same as those in Fig. 3. The Tsai-Hill failure criterion (8) is used.

A comparison of the results in Tables 1 and 3 shows that for loading cases (a), (b), and (c), the optimum designs without the thermal effect are not the optimum designs under mixed mechanical and thermal loads. On the other hand, for loading case (d), the optimum design under pure mechanical loads is the optimum design under mixed mechanical and thermal loads, for both the failure criteria.

5. Conclusions

In this paper, using a transverse cracking criterion and the Tsai-Hill failure criterion, the optimum strength designs are sought for a symmetric laminate under in-plane mixed mechanical and thermal loads. For all loading cases, the optimizer aims at distributing the stresses in the laminate according to the strengths in different directions of the orthotropic laminae. This creates a "smart" structure which fully takes advantage of the anisotropic properties of the composite material. It is found that the optimum designs under mixed mechanical and thermal loads are not the same as those under pure mechanical loads for three of the four loading cases studied. For all loading cases the optimum loads are significantly larger than those for a quasi-isotropic design, especially for loading case (b).

Acknowledgements

The support of the State Education Ministry of the People's Republic of China to J. Wang through the Excellent Young Teacher Foundation and the SRF is gratefully acknowledged. Thanks are also due to Professor G. Cheng of Dalian University of Science and Technology for helpful discussions.

Table 3
Summary of optimized ply angles in a symmetric laminate of four ply angles with thermal effect using the initial designs in Table 1

In-plane loading	Initial design $\theta_1, \theta_2, \theta_3, \theta_4$	Final design $\theta_1, \theta_2, \theta_3, \theta_4$	k_{max}	k_{max}/k_{in}
	Transverse cracking criterion			
a	82.4, 88.5, 75.3, 46.6	35.2, 60.7, 41.8, −44.9	0.81	2.7
b	−78.1, 72.5, 82.5, 18.2	−84.7, 39.6, 37.0, 37.0	1.78	2.59
c	−0.9, 76.1, −2.2, 48.3	−43.9, 50.9, −43.9, 18.4	0.82	2.16
d	33.9, 27.3, 35.2, 38.9	45.0, 45.0, 45.0, 45.0	∞	∞
	Tsai-Hill failure criterion			
a	27.1, 7.2, 38.6, −40.9	54.2, 30.3, 48.1, −45.1	0.79	1.37
b	−61.5, 10.6, −59.7, 86.1	−55.9, 33.2, −69.0, 32.9	1.66	4.05
c	13.6, 54.2, −74.0, 61.7	−42.9, 49.2, −42.9, 19.3	0.77	2.64
d	23.0, 55.2, 52.5, 21.4	45.5, 45.0, 45.0, 45.0	4.24	4.08

References

[1] Sandhu RS. Parametric study of Tsai's strength criterion for filamentary composites. TR-68-168, Air Force Flight Dynamic Laboratory, Wright-Patterson AFB, 1969.

[2] Brandmaier HE. Optimum filament orientation criteria. J Comp Mater 1970;4:422–5.

[3] Chao CC, Sun CT, Koh SL. Strength optimization for cylindrical shells of laminated composites. J Comp Mater 1975;9:53–66.

[4] Park WJ. An optimal design of simple symmetric laminates under the first ply failure criterion. J Comp Mater 1982;16:341–55.

[5] Fukunaga H, Chou T-W. On laminate configurations for simultaneous failure. J Comp Mater 1988;22:271–86.

[6] Miravete A. Optimization of symmetrically laminated composites rectangular plates. In: Wu Y, Gu Z, Wu R, editors. Proceedings of the Seventh International Conference on Composite Materials, vol. 3. Beijing: International Academic Publishers, 1989: 289–94.

[7] Fukunaga H. Vanderplaats GN. Strength optimization of laminated composites with respect to layer thickness and/or layer orientation angle. Comput and Struct 1991;40:1429–39.

[8] Wang J, Karihaloo BL. Cracked composite laminates least prone to delamination. Proc. Roy. Soc. London A 1994;44:17–35.

[9] Wang J, Karihaloo BL. Optimum in situ strength design of composite laminates Part I: in situ strength parameters. J Comp Mater 1996;30:1314–37.

[10] Wang J, Karihaloo BL. Optimum in situ strength design of composite laminates Part II: optimum design. J Comp Mater 1996;30:1338–58.

[11] Flaggs DL, Kural MH. Experimental determination of in situ transverse lamina strength in graphite/epoxy laminates. J Comp Mater 1982;16:103–16.

[12] Chang F-K, Lessard LB. Damage tolerance of laminated composites containing an open hole and subjected to compressive loadings Part I: analysis. J Comp Mater 1991;25:2–43.

[13] Chang F-K, Chen MH. The in situ ply shear strength distributions in graphite/epoxy laminated composite. J Comp Mater 1987;21:708–33.

[14] Herakovich CT. Influence of layer thickness on the strength of angle-ply laminates. J Comp Mater 1982;16:216–27.

[15] Wang J, Karihaloo BL. Fracture mechanics and optimization – a useful tool for fibre-reinforced composite design. Comp Struct 1995;31:151–62.

ELSEVIER

Composite Structures 47 (1999) 643–653

COMPOSITE STRUCTURES

www.elsevier.com/locate/compstruct

Post-fire mechanical properties of marine polymer composites

A.P. Mouritz *, Z. Mathys

DSTO, Aeronautical and Maritime Research Laboratory, P.O. Box 4331, Melbourne, Vic. 3001, Australia

Abstract

Changes to the tensile and flexure properties of marine-grade glass-reinforced polyester, vinyl ester and resole phenolic composites after exposure to radiant heat are investigated. The properties were determined at room temperature after the composites had been exposed to heat fluxes of 25–100 kW/m^2 for 325 s or to a heat flux of 50 kW/m^2 for increasing times up to 1800 s. The stiffness and failure load of all three composites decreased rapidly with increasing heat flux or time due mainly to the thermal degradation of the resin matrix. The post-fire tension and flexure properties of the resole phenolic composite were similar to the properties of the other composites, despite its superior fire resistance. Models are presented for determining the post-fire mechanical properties of fire-damaged composites, and are used to estimate the reductions in failure load of composite ship materials caused by fire. © 2000 Elsevier Science Ltd. All rights reserved.

Keywords: Post-fire mechanical properties; Glass-reinforced polymer composites; Polyester matrix; Vinylester matrix; Phenolic matrix

1. Introduction

Glass-reinforced polymer (GRP) composites are used increasingly in the construction of marine craft such as life-boats, racing yachts, coastal patrol boats and naval mine-hunting ships. GRP composites are also used in marine structures such as radomes, sonar domes and submarine casings and are candidate materials for propellers, propeller shafts and masts. The most common polymer used in marine composites is polyester resin because of its low cost and good durability in the marine environment. Vinyl ester resin is used occasionally instead of polyester in marine composites because of its higher heat-distortion temperature, better water resistance and slightly higher mechanical properties. However, vinyl ester resins are 1.5–2 times more expensive then polyester, and therefore are used only in small, high-performance craft such as racing canoes and speedboats. Phenolic resins are used in marine composites requiring excellent fire resistance, however their mechanical properties are lower and absorb more seawater than polyester or vinyl ester composites. Other types of resins, such as epoxies and thermoplastics (such as polyethersulphone and polyetherimide), are seldom used in marine composites because of their high cost [1].

A major problem with using composites in marine craft is that the polymer matrix can ignite within a short time when exposed to a fire. Fires on ships can be caused by electrical faults, ignition of spilt hydraulic oil or petroleum, and in warships by strikes from missiles and bombs. As the composite burns, large amounts of heat, smoke and toxic fumes are released that poses a risk to passengers and crew and makes it difficult for fire fighters to extinguish the fire [2–6]. The poor fire resistance of composites has been a contributing factor to the limited use of GRP in some marine craft such as large passenger ships and naval submarines. Another limitation is that when composites are damaged by fire their mechanical properties are degraded [7–14]. For example, Sorathia et al. [10] showed that thin composites usually suffer reductions of more than 80% in flexural strength after exposure to a relatively low-intensity fire (radiating an incident heat flux of 25 kW/m^2) for 20 min. While the effect of fire on the mechanical properties of aircraft composites, such as carbon-reinforced epoxy laminates, fire has been investigated in detail [7–13], the degradation of the properties of marine composites has not been extensively studied.

The purpose of this paper is to compare the post-fire mechanical properties of GRP composites with a polyester, vinyl ester or phenolic matrix. These are the only three types of composites used in any significant amount in marine craft. The composites were exposed for 325 s to heat fluxes of 25, 50, 75 and 100 kW/m^2, which

* Corresponding author. Tel.: +61396268276; fax: +61396268999.
E-mail address: adrian.mouritz@dsto.defence.gov.au (A.P. Mouritz).

0263-8223/99/$ - see front matter © 2000 Elsevier Science Ltd. All rights reserved.
PII: S0263-8223(00)00043-X

Sorathia et al. [12] suggest are approximately the fluxes radiated by a small fire, a large trash can fire, a significant room fire and an oil fire, respectively. The composites were also exposed to a constant heat flux of 50 kW/m^2 for increasing times up to 1800 s. This is the minimum time that composite materials used on US Naval ships are expected to retain their mechanical properties in a fire [5]. After fire testing, the tensile and flexural properties were determined at room temperature. These data are then used to validate models for estimating the post-fire mechanical properties of composites.

2. Materials and experimental techniques

2.1. Composites

The composites were reinforced with a woven E-glass fabric (DF1400 made by Colan Industries) containing 2400 tex plain roving tows in the warp direction and 5600 tex spun roving tows in the weft direction. The weight fraction of glass fibre in the warp and weft directions was 0.36 and 0.64, respectively, and the areal weight of the dry fabric was 1.35 kg/m^2. The polymers used were an isophthalic polyester resin (Synolite 0288-T-1 made by Dulux Australia), vinyl ester resin (Derakane® 411 C-350 made by Dow Chemical) and a low-temperature acid–cure resole phenolic resin (Resinox® 1916 made by Huntsman Chemical Australia). The composites were laminated using the wet lay-up process, which is used in the fabrication of most marine structures, into panels that were 240 mm long in the warp fibre direction, 160 mm wide in the weft direction, and 11.5–12.0 mm thick. These panels were used in the determination of the post-fire mechanical properties of the composites. Additional panels were laminated up to 30 mm thick for measurements of the char thickness in the composites, but the post-fire mechanical properties of these thicker specimens were not determined.

The polyester and vinyl ester composites were cold-cured under ambient conditions for several weeks, and had polymer contents of 43 and 47 wt%, respectively. The phenolic composite was cured at room temperature for 24 h and then post-cured at 60°C for 1 h and 80°C for 2 h. The polymer content of the phenolic composite was 41 wt%.

2.2. Fire testing

Composite panels were fire-tested in a Stanton Redcroft cone calorimeter. The panels were placed horizontal to an electric radiant heat source and exposed to incident heat fluxes of 25, 50, 75 or 100 kW/m^2 for 325 s or to a heat flux of 50 kW/m^2 for different heat-exposure times up to 1800 s. A spark igniter located between the heat source and panel was used to ignite combustible gases released from the composite. The time-to-charring was also measured for composites exposed to heat fluxes ranging from 15 to 100 kW/m^2. After testing, the flames were extinguished and the composite was cooled slowly to room temperature before the tensile and flexural properties were determined.

2.3. Tensile and flexural testing

After fire testing, the composite panels were cut into five specimens measuring 240 mm long (in the warp direction) and 25 mm wide for tensile and flexural testing. The tensile tests were performed at room temperature in close accordance with ASTM D3039 to determine the stiffness and failure load. The specimens had a gauge length of 105 mm, and were loaded at a cross-head speed of 1 mm/min to failure. Five specimens were tested in tension for each heat flux and heat-exposure time.

The flexural modulus and failure load were determined at room temperature using the four-point bend method in ASTM D790M. The specimens were loaded at a cross-head speed of 5 mm/min in 1/4-point loading with load and support spans of 92 and 184 mm, respectively. The surface of the specimen exposed to the heat source was placed against the two load points of the four-point bend fixture, so it experienced bending-induced compression. Five specimens were tested for each heat flux and heat-exposure time.

3. Results and discussion

3.1. Fire damage to composites

Log–log plots of ignition time against incident heat flux for the polyester, vinyl ester and phenolic composites are shown in Fig. 1. The ignition time is the time required for the composite to sustain flaming when exposed to a heat flux. The ignition times for the composites decreased exponentially with increasing heat flux above 15–25 kW/m^2. Similar ignition times to these have been determined for other types of polyester, vinyl ester and phenolic composites [3,6]. The polyester composite had the shortest ignition times, although the times for the vinyl ester composite were only slightly longer. Both composites ignited in less than 60 s when irradiated with a heat flux above 35–45 kW/m^2, and the ignition times dropped to less than 10 s when the heat flux rose towards 100 kW/m^2. The low-ignition times of polyester and vinyl ester composites is a reason for the restricted use of these materials in some types of marine craft, such as large passenger ferries and naval submarines. Fig. 1 shows that the ignition times for the phenolic composite were much longer than the times for the polyester and

vinyl ester composites. The long ignition times are one reason for the increasing use of phenolic composites on ships where fire is a potential hazard.

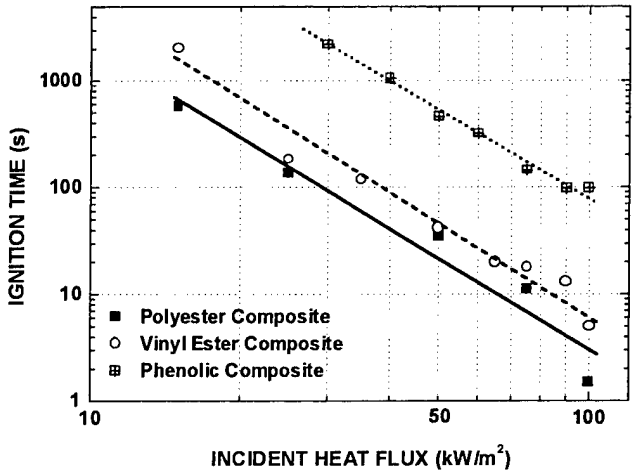

Fig. 1. Log–log plots of incident heat flux against time-to-ignition.

During the fire tests performed in the cone calorimeter, it was observed that when the polyester and vinyl ester composites ignited they immediately started to char. However, charring of the phenolic composite occurred prior to ignition. Charring is observed as a blackened layer, as shown in Fig. 2, that developed at the surface exposed to the heat source and then spread into the composite. Examination of the materials after fire testing using scanning electron microscopy (SEM) revealed that the structure of the char was similar in the polyester and vinyl ester composites but different to the char formed in the phenolic composite. The resin matrix within the charred region of the polyester and vinyl ester composites was consumed, leaving only the glass fibres as shown in Fig. 3. During fire testing within the cone calorimeter, the temperature of composite surface exposed to the heat source ranges from 500°C to 550°C when tested at a heat flux of 25 kW/m^2 up to 850–900°C at a heat flux of 100 kW/m^2 [15,16]. Isophthalic polyester and vinyl ester resins begin to thermally decompose at 350–400°C and are completely and rapidly consumed

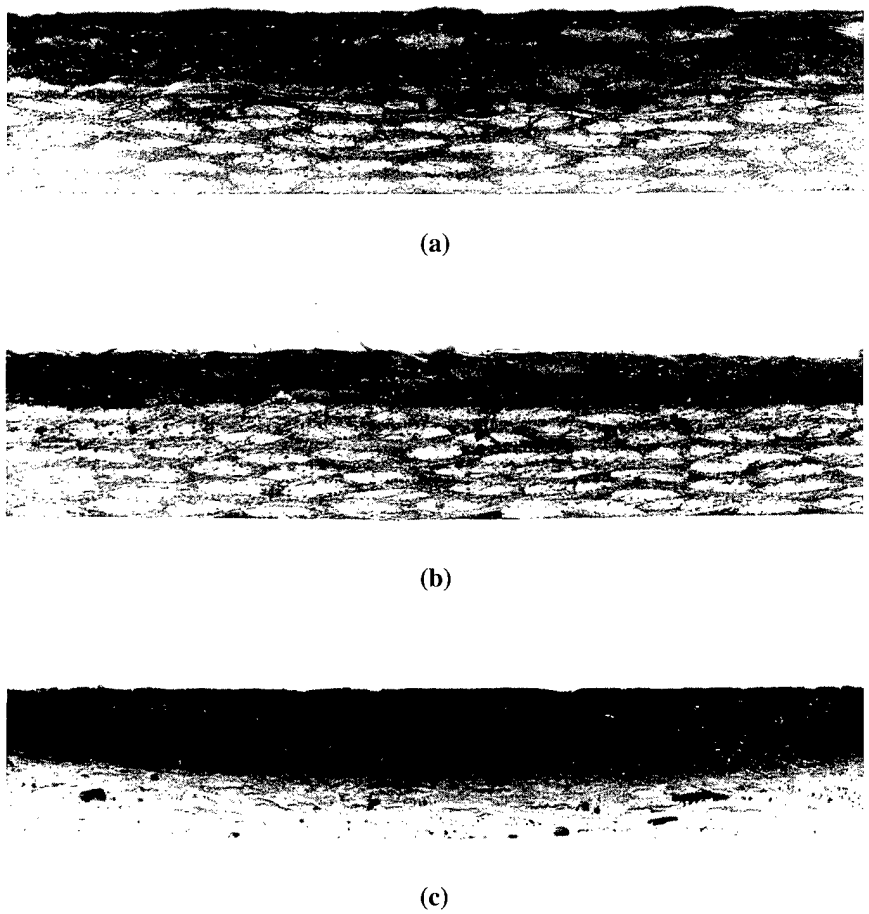

Fig. 2. Side-views of the (a) polyester, (b) vinyl ester and (c) phenolic composites showing the char layer. The heat-exposed surface is at the top and was irradiated with 50 kW/m^2 for 325 s. The char is the dark layer.

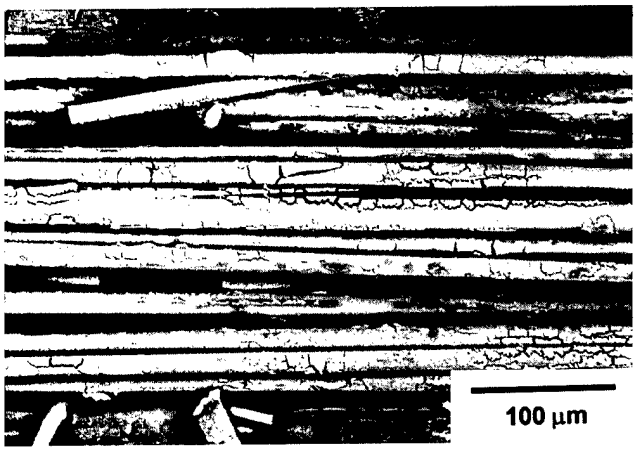

Fig. 3. Scanning electron micrograph of the char in the polyester composite. The exposed fibres are coated with a heavily cracked layer of thermally degraded resin. Char in the vinyl ester composite had the same appearance.

at 500–550°C [17,18]. Therefore, the heat fluxes used in the fire tests generate high enough surface temperatures to completely consume the matrix of the polyester and vinyl ester composites. However, the temperatures are not hot enough to cause melting of the glass fibres that occurs at 1065–1120°C [19]. In addition to char formation, the radiant heating also caused delamination cracking within the polyester and vinyl ester composites. The delaminations occurred immediately beneath the char layer, as shown in Fig. 4. Some delaminations almost caused complete separation of the char from the unburnt portion of the composite. Charring and delamination cracking were the only types of fire damages observed in the polyester and vinyl ester composites.

Fire damage to the phenolic composite appeared less severe than that observed for the polyester and vinyl ester composites when examined using SEM. While the phenolic composite was visibly blackened due to charring (Fig. 2(c)), the microstructure of the char had the same appearance as the composite before fire testing, as shown in Fig. 5. St John et al. [20] examined the thermal decomposition processes of glass-reinforced resole phenolic composites. St John [21] suggests that the mechanical properties of resole phenolic composites begin to degrade when heated to 200–400°C due mainly to the conversion of ether cross-linkages to form methylene cross-links in the polymer network structure. This temperature range 200–400°C was exceeded in the fire tests because the heat fluxes of 25–100 kW/m^2 are expected to generate much higher surface temperatures of ~500–900°C. St John et al. [20] found, however, that the main chemical network structure of a resole phenolic resin remains reasonably stable until the temperature rises above ~550°C, when the phenol rings and methylene cross-links in the network break-down. At this stage in the decomposition process a stable char forms that degrades slowly with increasing temperature or heating time. In comparison, polyesters and vinyl esters degrade rapidly above 350–400°C. As a result, the charred

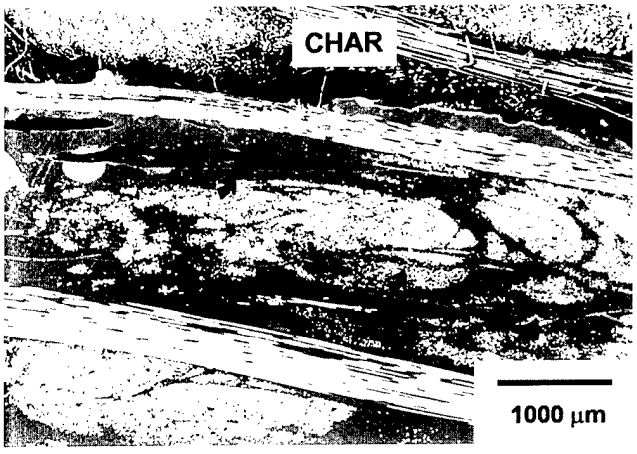

Fig. 4. Delaminations (indicated with arrows) beneath the char in the polyester composite.

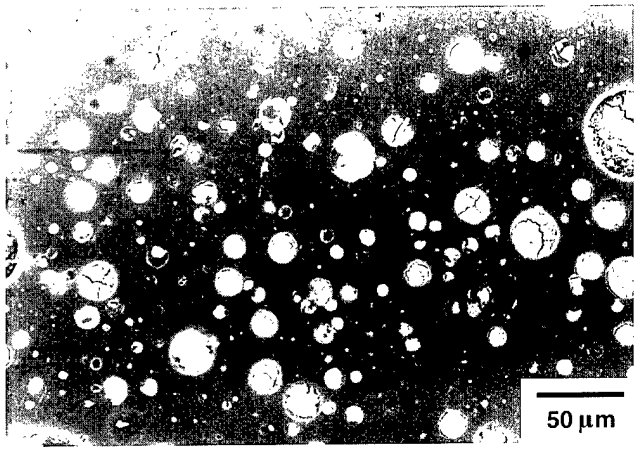

(a)

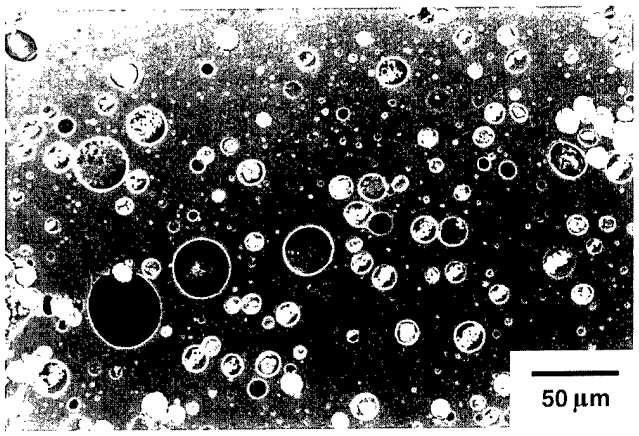

(b)

Fig. 5. Microstructure of the matrix to the phenolic composite (a) before fire testing and (b) within the char region. The voids are present before fire-testing, and are formed during curing of the resin.

phenolic composite showed much less thermal damage after the fire tests, although the phenolic resin matrix is expected to be brittle [21]. Physical damage to the phenolic composite as a result of heating in the cone calorimeter only occurred after exposure to a high heat flux ($\geqslant$ 50 kW/m^2) for a considerable time (longer than 1500 s). Damage then occurred close to the heat-exposed surface, and consisted of fine-scale cracking of the phenolic matrix due to the brittleness of the thermally degraded resin as well as some combustion of the resin matrix leaving partially exposed glass fibres (Fig. 6).

The heat-exposure time needed to induce the first visible appearance of char, known as the time-to-char, t_c, decreased exponentially with increasing heat flux as shown by log–log plots in Fig. 7. The char times for the polyester and vinyl ester composites are the same values as the ignition times given in Fig. 1 because char formation and ignition occurred at the same time. The phenolic composite had the longest char times. Presumably, this is because the decomposition temperature

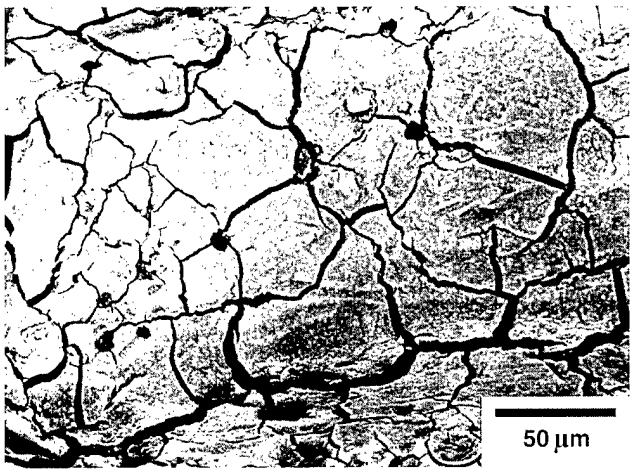

(a)

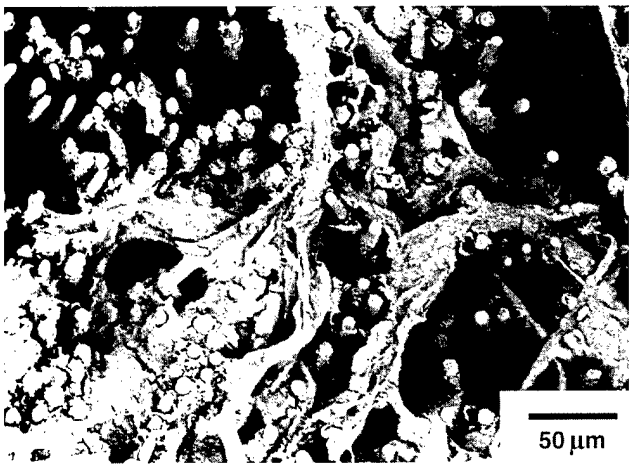

(b)

Fig. 6. (a) Cracking of the matrix and (b) exposure of fibres in the phenolic composite caused by intense and prolonged radiant heating.

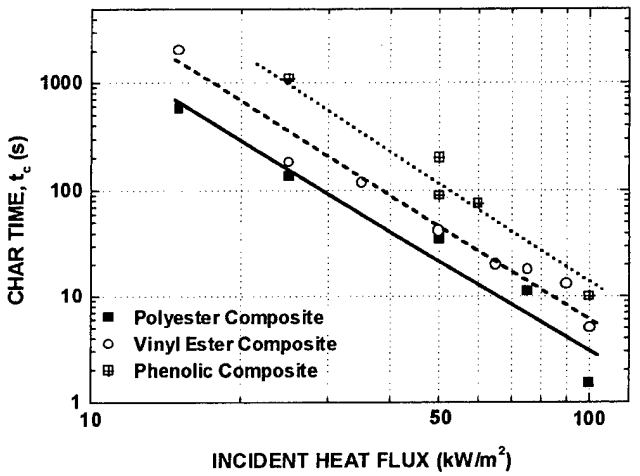

Fig. 7. Log–log plots of incident heat flux against time-to-charring.

of the phenolic resin (~550°C) was higher than for the polyester and vinyl ester resins (350–400°C). All three composites experienced a reduction in char time (t_c) with increasing incident heat flux (q) that can be expressed by

$$t_c \approx \beta_1 e^{-(q-q_0)/\lambda_1} + \beta_2 e^{-(q-q_0)/\lambda_2}, \quad (1)$$

where q_0 is the minimum heat flux used in the fire test, and β_1, β_1, λ_1 and λ_2 are empirical constants determined from time-to-char tests. Values for these constants together with q_0 values for the composites are given in Table 1.

As mentioned earlier, charring of the three composites occurred as a well-defined layer that can be clearly distinguished from the underlying (uncharred) material because of its dark appearance. Therefore it was possible to measure the char thickness after the composites had been tested in the cone calorimeter. When the char was less than 10 mm thick the layer thickness was measured from the standard sized composite test panels (that were 11.5–12.0 mm thick). After testing at high heat fluxes or long heat-exposure times the char was much thicker than 10 mm, and therefore it was necessary to use composite test panels up to 30 mm thick. It is important to note, however, that using composite panels with different thicknesses did not affect the thickness of the char layer. The char thickness values are plotted in Fig. 8 against the char heat-exposure time, which is the total heat-exposure time (t) less the time-to-charring (t_c). The char thickness values were measured after the composites were tested at 25, 50, 75 or 100 kW/m^2. The char thickness initially increased rapidly with the post-char heat-exposure time up to ~500 s. Within this time the char thickness values for the three composites were similar. With longer heat-exposure times the char layers continue to thicken, although at steadily decreasing rates. This trend indicates that as the char grows in thickness this slows the rate of the thermal degradation processes at the char/composite interface that leads to

Table 1
Thermal and mechanical property constants

Property	Polyester composite	Vinyl ester composite	Phenolic composite
q_0 (W/m^2)	15000	15000	25000
β_1 (s)	189	698	649
β_2 (s)	383	1340	420
λ_1 (W/m^2)	18621	13119	15164
λ_2 (W/m^2)	3709	2314	1699
$S_{T(0)}$	1	1	1
$S_{T(c)}$	0.08	0.08	0.21
$P_{T(0)}$ (kN)	58.6	54.6	51.5
$P_{T(c)}$ (kN)	10.0	10.0	5.3
$(EI)_{F(0)}$ (N m^2)	66.5	65.8	53.2
$(EI)_{F(c)}$ (N m^2)	0	0	14.6
$P_{F(0)}$ (kN)	6.4	5.8	3.1
$P_{F(c)}$ (kN)	0	0	0.26

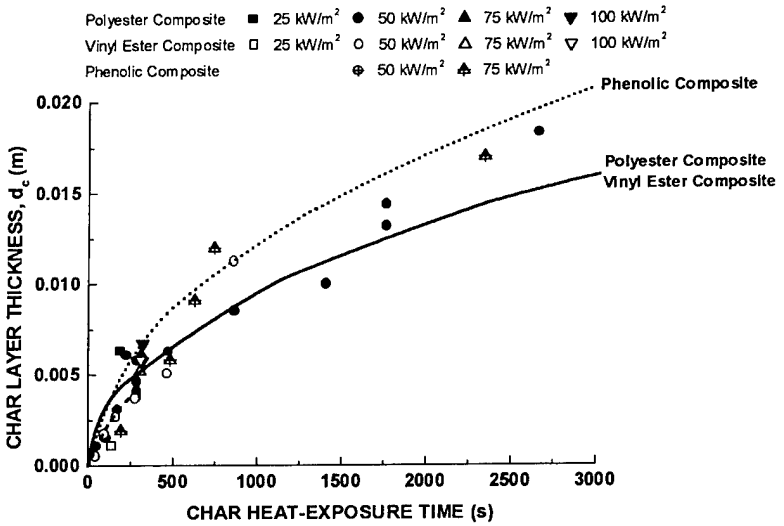

Fig. 8. Effect of char heat-exposure time on the thickness of the char in the composites.

the formation of more char. The char thickness values for the polyester and vinyl ester are similar. In comparison, above ~500 s the char thickness values for the phenolic composite become slightly higher than for the other two composites.

The relationship shown in Fig. 8 between the char thickness (d_c) and char heat-exposure time ($t - t_c$) can be approximately expressed as

$$d_c \approx [a(t - t_c)]^{1/2}, \quad (2)$$

where t is the total heat-exposure time, t_c the charring time (which is determined using Eq. (1)), and a is a empirical constant that for the polyester and vinyl ester equals 8.7×10^{-8} m^2/s and for the phenolic composites equals 14.6×10^{-8} m^2/s. The curves in Fig. 8 were determined using Eq. (2). The difference between the calculated and measured char thickness values is usually less than 2 mm, showing that Eq. (2) can be used to accurately determine the char thickness in the three composites for any heat flux between 25 and 100 kW/m^2.

3.2. Post-fire mechanical properties

The effect of heat-exposure time on the post-fire tensile and flexural properties is shown in Fig. 9. The properties were determined at room temperature after the composites had been exposed to a heat flux of 50 kW/m^2 for times up to 1800 s. In this figure, the data points are the experimental post-fire properties, with each point being the average value determined from five tensile or flexural tests. The curves, on the other hand, show the calculated reductions in the post-fire properties with increasing heat-exposure time determined from a theoretical model that is described below. Therefore, the curves do not represent lines-of-best fit through the data points.

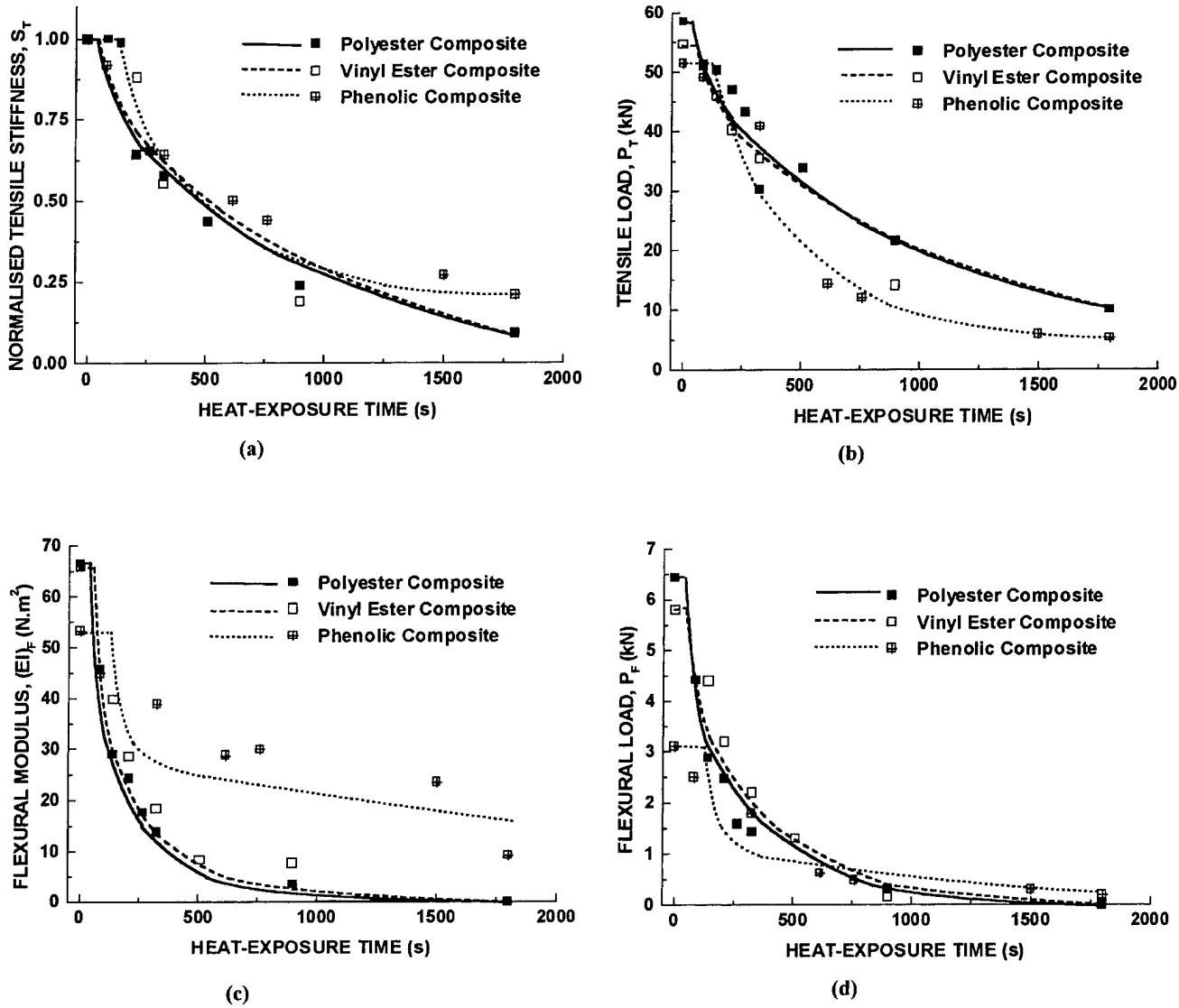

Fig. 9. Effect of heat-exposure time on the post-fire mechanical properties.

In Fig. 9(a) the normalised tensile stiffness values were determined by dividing the gradient of the linear region of the tensile load–displacement curve for a fire-tested composite with the gradient of the curve for the same composite measured before fire-testing. The tensile failure loads of the three composites were similar before fire testing, as shown in Fig. 9(b). The tensile failure load of the vinyl ester composite is slightly lower than for the polyester composite, even though the tensile strength of the vinyl ester matrix is expected to be higher than for the polyester resin (see resin strength data in Smith [1]). The vinyl ester composite has a lower failure load because its glass fibre reinforcement content (of 53 wt%) was lower than for the polyester composite (57 wt%). Figs. 9(c) and (d) show that the flexural modulus and flexural failure load of the phenolic composite were much lower than the flexural properties of the polyester and vinyl ester composites. This occurs despite the phenolic composite having the highest glass fibre content (of 59 wt%) of the three materials. St John and Brown [22] have compared the flexural properties of glass-reinforced resole phenolic composites with glass-reinforced isophthalic polyester composites. They found phenolic composites had slightly lower flexural moduli and substantially lower flexural strengths than polyester composites. The lower flexural properties of phenolic composites were attributed to three factors:

1. poor compatibility between the reinforcing fibres and phenolic matrix, resulting in low fibre/resin interfacial bond strength,
2. low strength of the phenolic resin, and
3. voids in the polymer matrix that form during the acid–cure reaction of the phenolic resin (such as those shown in Fig. 5).

Fig. 9 shows the post-fire mechanical properties of all three composites dropped rapidly with increasing heat-exposure time up to 750–1000 s, particularly the flexural properties. For longer times, the properties declined more slowly and after 1800 s most properties were less than 10–20% of their original value. The rapid reductions to the properties with increasing time up to 750–1000 s were due mainly to the rapid charring of the composites within this time. The delaminations beneath the char in the polyester and vinyl ester composites are also expected to contribute to the fall in properties, particularly under flexural loading. After ~1000 s the composites were nearly or were completely charred, and therefore longer heat-exposure times did not cause any further charring. As a result, the post-fire properties dropped more gradually with increasing heat-exposure time from 1000 to 1800 s. It is interesting to find that most post-fire properties of the phenolic composite were similar to the properties of the polyester and vinyl ester composites. The only post-fire property of the phenolic composite that was significantly higher was flexural modulus. The results therefore indicate that the tensile and flexural properties of fire-damaged ship structures made with glass-reinforced resole phenolic composite will usually be degraded by about the same amount as the properties of glass-reinforced polyester and vinyl ester composite structures. This is expected to occur despite the superior fire resistant properties (e.g. longer ignition and char times) of phenolic composites.

As reported earlier, the char formed within the three composites is a well-defined layer that can be clearly distinguished from the underlying (uncharred) material (Fig. 2). The charred composites can therefore be considered as bi-layer materials with one layer being the char and the other layer the uncharred composite, as shown in Fig. 10. When the mechanical properties of the two layers are different, the normalised tensile stiffness (S_T) and tensile failure load (P_T) of a bi-layer material such as the fire-damaged composites can be determined using

$$S_T = \frac{(d - d_c)}{d} S_{T(0)} + \frac{d_c}{d} S_{T(c)} \tag{3}$$

and

$$P_T = \frac{(d - d_c)}{d} P_{T(0)} + \frac{d_c}{d} P_{T(c)}, \tag{4}$$

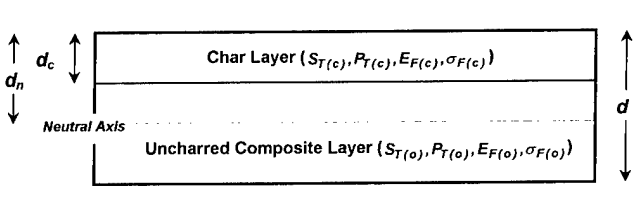

Fig. 10. Cross-sectional drawing of the fire-damaged composite treated as a bi-layer.

where d is the composite thickness and d_c is the char layer thickness that is calculated using Eq. (2). $S_{T(0)}$ and $S_{T(c)}$ are the normalised tensile stiffness values for the uncharred composite and char, respectively, and $P_{T(0)}$ and $P_{T(c)}$ are the tensile failure loads for the uncharred composite and char, respectively. Tensile tests were performed on the composites before fire-testing to measure $S_{T(0)}$ and $P_{T(0)}$ and on the fully charred composites to determine $S_{T(c)}$ and $P_{T(c)}$. Measured values for these properties are given in Table 1.

When fire-damaged composites are treated as a bi-layer beam loaded in 1/4-point bending, it can be shown that their flexural modulus $(EI)_F$ is determined by

$$(EI)_F = \left\{ \frac{4(d - d_n)^3 + 4(d_n - d_c)^3}{d^3} + 4\frac{E_{F(c)}}{E_{F(0)}} \frac{\left[d_n^3 - (d_n - d_c)^3\right]}{d^3} \right\} (EI)_{F(0)}, \tag{5}$$

where $(EI)_{F(0)}$ is the flexural modulus of the uncharred composite. d_n is the distance from the outer surface of the char layer to the neutral stress axis of the beam, which is calculated using

$$d_n = \frac{(E_{F(0)} d^2) - d_c^2 (E_{F(0)} - E_{F(c)})}{(2E_{F(0)} d + 2E_{F(c)} d_c - 2E_{F(0)} d_c)}. \tag{6}$$

The flexural failure load (P_F) for fire-damaged composites can be calculated using

$$P_F = \frac{8}{L} \left\{ \frac{\sigma_{F(0)} b}{3} \frac{(d - d_n)^3 + (d_n - d_c)^3}{(d - d_n)} + \frac{\sigma_{F(c)} E_{F(c)} b}{3E_{F(0)}} \frac{\left[d_n^3 - (d_n - d_c)^3\right]}{(d - d_n)} \right\}, \tag{7}$$

where L is the load span and b is the beam width. $\sigma_{F(0)}$ and $\sigma_{F(c)}$ are the flexural strengths of the composite without fire-induced damage and the char, respectively. Values for $(EI)_{F(0)}$, $E_{F(0)}$ and $\sigma_{F(0)}$ were determined from flexural tests on the composites before fire-testing while values for $E_{F(c)}$ and $\sigma_{F(c)}$ were determined from flexural tests on the fully charred composites. The values are given in Table 1.

Reductions to the post-fire properties of the composites with increasing heat-exposure time determined using Eqs. (3)–(7) are shown by the curves in Fig. 9. No change in the post-fire tensile and flexural properties is predicted using the model until the composites begin to char. For this reason the curves show no reduction in the post-fire properties until the heat-exposure time reaches 35, 48 and 125 s for the polyester, vinyl ester and phenolic composites, respectively, at which times charring of the heat-exposed surface occurs. The curves then show a rapid reduction in the post-fire mechanical

properties with increasing heat-exposure time. The agreement between the measured and calculated post-fire mechanical properties is excellent.

Fig. 11 shows the influence of heat flux on the post-fire tensile and flexural properties. The composites were exposed to heat fluxes of 25, 50, 75 or 100 kW/m^2 for 325 s before the properties were measured at room temperature. As with Fig. 9, the data points are the measured post-fire properties and the curves are determined from the model. The post-fire properties of the three composites dropped rapidly with increasing heat flux, particularly to 50 kW/m^2. Again it is found that the post-fire mechanical properties of the phenolic composite are in most cases similar to the properties of the polyester and vinyl ester composites, the only difference being that the flexural modulus is higher for the phenolic composite.

The curves in Fig. 11 show the theoretical reductions in properties with increasing heat flux calculated using the model. It is predicted (using Eq. (2)) that no charring occurs within 325 s until the polyester, vinyl ester and phenolic composites are irradiated with heat fluxes above 15, 26 and 36 kW/m^2, respectively. Consequently, the curves show no change in the post-fire properties until these heat fluxes are exceeded, and then large reduction occurs with increasing heat flux. In most cases the agreement between the measured and calculated post-fire properties is good, particularly for the polyester and vinyl ester composites. However, the model over-predicts significantly the post-fire properties of the phenolic composite after exposure to 25 kW/m^2. The experimental results show large reductions in the properties of the phenolic composite after testing at 25 kW/m^2 for 325 s, with the flexural and tensile failure loads

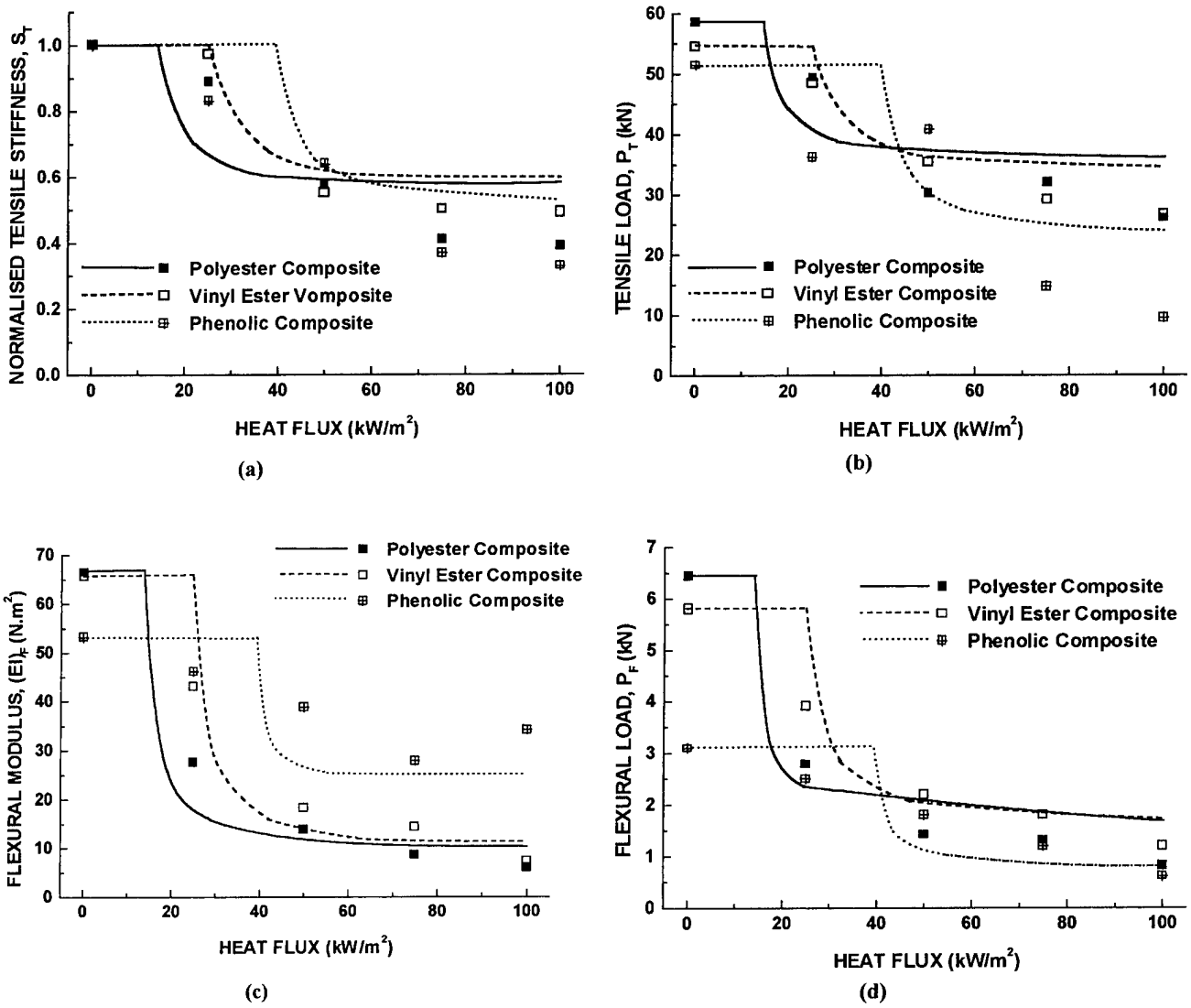

Fig. 11. Effect of heat flux on the post-fire mechanical properties.

falling by 20% and 30%, respectively. It was concluded by Mouritz and Mathys [13] that these reductions in the post-fire properties were probably due to partial thermal degradation of the phenolic resin, which caused the matrix to become brittle without charring being experienced. It is predicted using the model, however, that the properties of the phenolic composite are not affected by exposure to a heat flux of 25 kW/m^2 for 325 s because charring has not occurred. The model also fails to accurately predict the post-fire tensile failure load and flexural modulus of the phenolic composite when exposed to heat fluxes above 50 kW/m^2.

3.3. Predictions of the post-fire properties of marine composite structures

The effect of radiant heat from a fire on the mechanical properties of composite ship structures (e.g. decks, bulkheads and superstructures) has not been studied in detail. It is generally recognised that large fires can degrade the structural properties of composite marine craft [2,4,5], however engineering design rules for estimating reductions in stiffness and failure load are not available. For this reason, most composite ship structures are designed without consideration being given to the reduction in properties that may be experienced from a fire. In addition, the maximum allowable reduction in properties due to fire is usually not specified. The only requirement is that the US Navy recommends that composites used on their ships must retain adequate stiffness and strength when exposed to fire for at least 30 min.

It was shown earlier that the post-fire tensile and flexural properties of the composites are accurately predicted with the models for most heat fluxes and heat-exposure times. It is proposed that the models can be used to perform a preliminary assessment of the load-bearing capacity of composite ship structures damaged by fire. The use of the models for estimating the post-fire load-bearing capacity of composite ship structures with different thicknesses up to 50 mm is demonstrated in Fig. 12. In this analysis the post-fire properties were determined after the glass-reinforced polyester, vinyl ester and phenolic composites had been exposed for 30 min to 50 kW/m^2, which is about the heat flux of a medium intensity shipboard fire. The parameters $P_T/P_{T(0)}$ and $P_F/P_{F(0)}$ are the failure loads of the fire-damaged ship structure loaded in tension and flexural, respectively, normalised against the failure load of the undamaged composite of the same thickness. Also shown in Fig. 12 are typical thickness values for the decks (5–8 mm), superstructure (10–15 mm) and hull (greater than 20 mm) of a large composite ship such as a navy minesweeping vessel.

When exposed to the heat flux for 30 min it is calculated using Eq. (2) that the polyester and vinyl ester

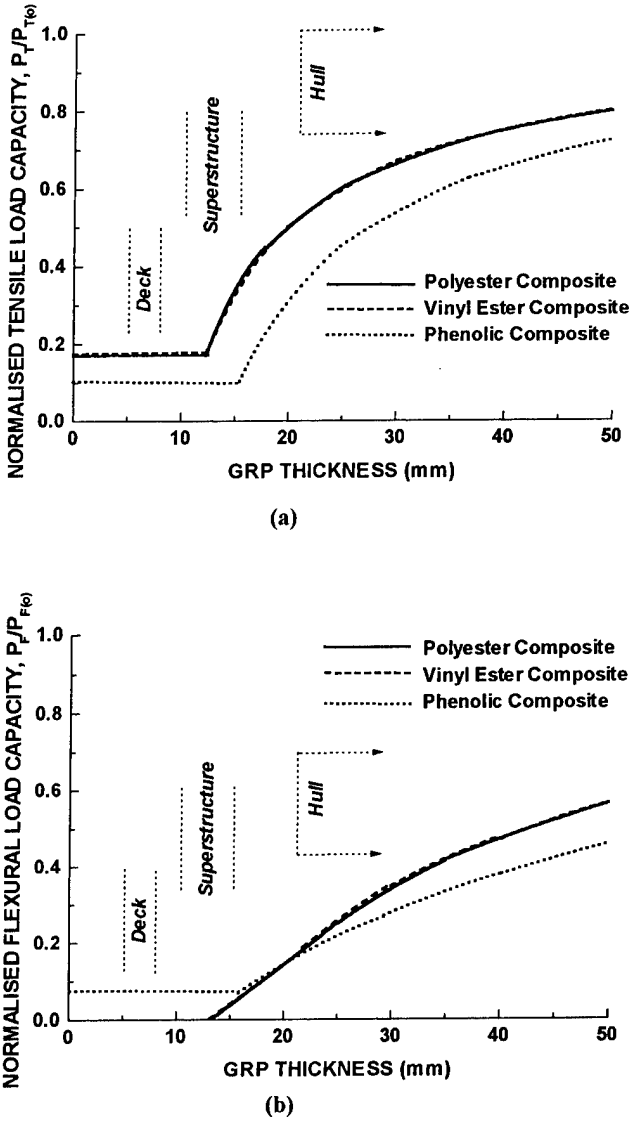

Fig. 12. Effect of GRP thickness on the (a) normalised tensile failure load, $P_T/P_{T(0)}$ and (b) normalised flexural failure load, $P_F/P_{F(0)}$, of composites after exposure to a heat flux of 50 kW/m^2 for 30 min.

composites are charred to a depth of 12.5 mm. Under the same fire conditions the phenolic composite is charred to a depth of 15.6 mm. As a consequence, $P_T/P_{T(0)}$ and $P_F/P_{F(0)}$ are low and constant up to these thickness values because the composites are completely charred. In Fig. 12 it is seen that the load parameters for relatively thin structures (e.g. decks, superstructure) are very low, indicating that they have little or no load-bearing capacity. The load parameters increase steadily with GRP thickness above 12.5–15.6 mm, although even relatively thick structures (e.g. hull) are severely weakened. Other information that can be provided from the curves are, firstly, that the load-bearing capacity is reduced more for bending than tension and, secondly, the load-bearing capacity of the phenolic composite is reduced more than for polyester and vinyl ester

composites. The curves are therefore useful for providing general information on the effect of fire on the load-bearing capacity of composite ship structures. However, it should be clearly understood that the curves are at this stage speculative and must be validated with large-scale failure tests on fire-damaged ship structures.

4. Conclusions

The mechanical properties of GRP composites used in marine craft can be severely degraded when exposed to intense radiant heat from a fire. This study has shown for the first time that the tensile and flexural properties of marine-grade glass-reinforced polyester, vinyl ester and phenolic composites are rapidly reduced with increasing heat flux or heat-exposure time. All three composites had similar post-fire mechanical properties. This is despite the phenolic composite having fire-resistant properties (e.g. longer ignition times) that are superior to those of the polyester and vinyl ester composites. Phenolic composites are being used increasing in marine craft because of their excellent fire resistance, but it is revealed in this study that this does not result in post-fire mechanical properties that are superior to conventional marine composites such as glass-reinforced polyester and vinyl ester composites. The properties are degraded mainly by thermal decomposition of the resin matrix that forms a char. The char in the polyester and vinyl ester composite consists of exposed glass fibres coated with a thin layer of heavily decomposed resin. The char in the phenolic composite, on the other hand, was more thermally stable and hence pyrolysis of the resin and char did not occur until after exposure to a high heat flux for a long time ($\sim$1800 s). Fire-induced delamination cracks beneath the char also contributed to the reduction in properties of the polyester and vinyl ester composites. Models have been proposed that allow the post-fire properties of polymer composites to be accurately determined for most heat-fluxes and heat-exposure times. It is suggested that the models could be used to make preliminary estimations of the reductions in the mechanical properties of composites used in ship structures after exposure to fire.

Acknowledgements

The authors thank Dr. C. Flockhart and Dr. P.J. Burchill for their helpful comments about the models, Dr. N. St John for his discussions about the thermal degradation of phenolic composites, and Mr. J. Triantofillou and Mr. C. Townsend for performing some of the experimental work.

References

[1] Smith CS. Design of marine structures in composite materials. London: Elsevier; 1990.
[2] Rollhauser CM. Solving the fire, smoke and toxicity problem for US Navy surface ships. In: Proceedings of the Use of Composite Materials in Load-Bearing Structures, vol II. 1990. p. 85–90.
[3] Egglestone GT, Turley DM. Flammability of GRP for use in ship superstructures. Fire Mats 1994;18:255–60.
[4] Caplan IL. Marine composites – The US Navy experience. In: Proceedings of the First International Workshop on Composite Materials for Offshore Operations, 26–28 October 1993. p. 91–114.
[5] Fisher KJ. Is fire a barrier to shipboard composites? Adv Comp 1993;20:20–26.
[6] Scudamore MJ. Fire performance studies on glass-reinforced plastic laminates. Fire Mats 1994;18:313–25.
[7] Gibson AG, Hume J. Fire performance of composite panels for large marine structures. Plast Rubb Comp Process Appl 1995;23:175–83.
[8] Pering GA, Farrell PV, Springer GS. Degradation of tensile and shear properties of composites exposed to fire or high temperature. In: Springer GS, editor. Environmental effects on composite materials. CT: Technomic Publishing, 1981. p. 145–59.
[9] Chang GI. Thermal effects on polymer composite structures. Theoret Appl Frac Mech 1986;6:113–20.
[10] Sorathia U, Lyon R, Gann R, Gritzo L. Materials and fire threat. SAMPE J 1996;32:8–15.
[11] Dao M, Asaro RJ. A study on failure prediction and design criteria for fiber composites under fire degradation. Comp A 1999;30:123–31.
[12] Griffis CA, Nemes JA, Stonesifer FR, Chang CI. Degradation in strength of laminated composites subjected to intense heating and mechanical loading. J Comput Math 1986;20:216–35.
[13] Mouritz AP, Mathys Z. Mechanical properties of fire-damaged glass-reinforced phenolic composites. Fire Mat, in press.
[14] Mouritz AP, Mathys Z. Post-fire mechanical properties of glass-reinforced polyester composites. Comput Sci Tech, submitted.
[15] Sorathia U, Beck C, Dapp T. Residual strength of composites during and after fire exposure. J Fire Sci 1993;11:255–70.
[16] Grabovac I, Mathys Z. Unpublished data.
[17] Bansal RJ, Mittal J, Singh P. Stability and degradation studies of polyester resins. J Appl Poly Sci 1989;37:1901–8.
[18] Regnier N, Mortaigne B. Analysis by pyrolysis/glass chromatography/mass spectrometry of glass fibre/vinyl ester thermal degradation products. Poly Degrad Stab 1995;49:419–28.
[19] Gupta PK. Glass fibers for composite materials. In: Bunsell AR, editor. Fibre reinforcements for composite materials. Amsterdam: Elsevier, 1988. p. 19–71.
[20] St John NA, Fawell PD, Brown JR. Improved fire-retardant fibre-reinforced phenolic composites. GIRD Project 15048 Technical Report, Defence Science and Technology Organisation Report DSTO-1P1C-0012, 1995.
[21] St John N. Private communication.
[22] St John NA, Brown JR. Flexural and interlaminar shear properties of glass-reinforced phenolic composites. Comp A 1998;29:939–46.

ELSEVIER

Composite Structures 47 (1999) 655–665

COMPOSITE STRUCTURES

www.elsevier.com/locate/compstruct

Prediction of shrinkage and warpage in consideration of residual stress in integrated simulation of injection molding

Du-Soon Choi, Yong-Taek Im *

Computer Aided Materials Processing Laboratory ME3227, Department of Mechanical Engineering, Korea Advanced Institute of Science and Technology, 373-1 Gusongdong, Yusonggu, Taejon 305-701, South Korea

Abstract

The accurate prediction of shrinkage and warpage of injection molded parts is important to achieve successful mold design with high precision. In this study, the numerical analysis of shrinkage and warpage of injection molded parts made of amorphous polymers was carried out in consideration of the residual stresses produced during the packing and cooling stages of injection molding. The temperature and pressure fields were obtained from the coupled analysis of the filling and post-filling stages. For residual stress analysis, a thermo-rheologically simple viscoelastic material model was introduced to consider the stress relaxation effect and to describe the mechanical behavior according to the temperature change. The effect of the additional material supply during the packing stage was modeled by assigning the reference strain. The deformation of injection molded parts after ejection induced by the residual stress and temperature change was analyzed using a linear elastic three-dimensional finite element approach. In order to verify the numerical predictions obtained from the developed program, the simulation results were compared with the available experimental data in the literature. In the case of residual stress, it was found that the present simulation results over-predicted the tensile residual stresses at the surface of injection molded parts. However, the predicted shrinkage was found to be reasonable to describe the effects of processing conditions well. Finally, an analysis of the shrinkage and warpage was successfully extended for a part with a more complex curved shape. © 2000 Published by Elsevier Science Ltd.

Keywords: Shrinkage; Warpage; Residual stress; Injection molding

1. Introduction

Injection molding is one of the manufacturing processes in which a pressurized polymer melt is injected into the cavity and solidified. In the filling stage, the polymer melt is injected into the cavity through the sprue, runner and gate. In packing stage, additional polymer melt is pushed into the cavity in order to compensate for the shrinkage caused by cooling of the material. During these processes, the residual stress is produced due to high pressure, temperature change, and relaxation of polymer chains, resulting in shrinkage and warpage of the part. In order to yield a product with high precision, optimum mold geometry and processing parameters must be found. To reduce the cost and time at the design stage, it is important to simulate shrinkage and warpage of the injection molded part considering residual stress. In this study, an integrated simulation program for the calculation of the shrinkage and warpage considering residual stress was developed as a part of computer-aided engineering of injection molding.

In the past, Jacques [1] analyzed thermal warpage in injection molded flat parts due to unbalanced cooling. Tompson and White [2] and Akay and Ozden [3] measured thermal residual stresses and distortions of injection molded parts and analyzed the effects of temperature gradients. Boitout et al. [4] calculated residual stresses in injection molding considering thermal shrinkage and the frozen-in pressure, assuming the polymer to be an elastic material. Jansen and Titomanlio [5–7] calculated residual stresses and shrinkage of thin products using an elastic model to study the effect of in-mold shrinkage on the final product dimensions and measured the shrinkage under various molding conditions. Zoetelief et al. [8] investigated the influence of the holding stage on the thermal residual stress using a linear viscoelastic constitutive law and compared this with experimental results. Liu [9] simulated and predicted the residual stress and warpage using a viscoelastic phase transformation model, which assumed the solidified polymer to be a

* Corresponding author. Tel.: +82-42-869-3227; fax: +82-42-869-3210.

E-mail address: ytim@mail.kaist.ac.kr (Y.-T. Im).

0263-8223/99/$ - see front matter © 2000 Published by Elsevier Science Ltd.
PII: S0263-8223(00)00045-3

linear solid and the polymer melt to be a viscous fluid. Bushko and Stokes [10,11] used the solidification of a molten layer of amorphous thermoplastic between cooled parallel plates to model the mechanics of part shrinkage, warpage and the build-up of residual stresses during the injection molding process, assuming thermo-viscoelastic behavior of the material. Kabanemi et al. [12,13] simulated residual stresses and residual deformations using three-dimensional finite element method for a thermo-viscoelastic model and applied it to a complex shape. Matsuoka et al. [14] developed an injection molding analysis program considering mold cooling and polymer filling-packing-cooling to predict warpage. Hastenberg et al. [15] measured the residual stress distributions in injection molded flat plates using a modified layer-removal method. Jansen et al. [16] systematically studied the effect of processing conditions such as holding pressure, injection velocity, and mold and melt temperatures on shrinkage.

A viscoelastic model for polymers gives more accurate results than an elastic model. Present investigation showed that the frozen-in stress caused by packing pressure is very important. Therefore, in this study, the model proposed by Bushko and Stokes [10] was used for analyzing residual stresses during the packing and cooling stages. This model considers additional material to be added by high pressure during packing stage. A general constitutive model for thermo-rheologically simple materials was implemented also. For the analysis of shrinkage and warpage, a linear elastic three-dimensional finite element method was used for an efficient numerical integration. This approach enables the analysis for thin complex injection molded geometries. Finally, the numerical results of residual stress and shrinkage was verified by comparing them with the available experimental data in the literature.

2. Residual stress analysis

During the filling stage of injection molding, high pressure is applied to force polymer melt into the mold. In this process, a thin layer solidifies at the contact with the mold surface. However, this thin layer has little effects on the shrinkage and warpage of the parts, because the pressure of the filling stage is much lower than that of the packing stage. Therefore, in this study, only the packing and cooling stages of injection molding were considered for the analysis of residual stresses.

Amorphous polymers behave as a viscoelastic liquid above the glass transition temperature T_g and as rubbery or glassy solid below T_g. The model of Bushko and Stokes [10] well represents these viscoelastic properties of amorphous polymers and the mechanics in the cavity during the packing stage. This model is available in the case of amorphous polymer between cooled parallel plates where the temperature field is independent of the in-plane x and y coordinates. However, in order to adopt this model to a general thin geometry, the following assumptions were needed:

(a) there is no bending of parts in the mold;
(b) there is no in-plane deformation of the solid polymer in the mold;
(c) there is no deformation of the mold.

During the packing stage, the polymer is fixed to the mold strongly by high pressure, and so the assumptions (a) and (b) are reasonable. Assumption (c) means that the mold is assumed to be rigid. By (a)–(c), the shear stress components become much smaller than tensile or compressive stress components and can be neglected. For a thin geometry, the temperature gradient of the in-plane direction is much smaller than that of the thickness direction and it can be assumed that the temperature field is independent of the in-plane x and y coordinates at a local area. Therefore, it is thought that there is no problem in adopting this model to a general thin geometry.

The following is a brief explanation about this model. By the symmetry, the temperature field is independent of the in-plane coordinates of x and y. Therefore, the equilibrium equation is simplified as follows:

$$\frac{\partial \tau_{xz}(z,t)}{\partial z} = 0, \quad \frac{\partial \tau_{yz}(z,t)}{\partial z} = 0, \quad \frac{\partial \sigma_z(z,t)}{\partial z} = 0. \tag{1}$$

Due to boundary conditions and symmetry condition, all shear stress components become zero and the remaining stress components are $\sigma_x(z,t)$, $\sigma_y(z,t)$, and $\sigma_z(t)$.

2.1. Constitutive equations

During the packing and cooling stages, the polymer is assumed to be an isotropic thermo-rheologically simple viscoelastic material. By using time–temperature equivalence to consider mechanical properties of the polymer over a wide range of temperature, the constitutive equation becomes

$$\sigma(t) = \int_0^t L(\xi(t) - \xi(t'))\,\mathrm{d}\{\varepsilon(t') - \theta(t')\}, \tag{2}$$

where $L(t)$ is the relaxation modulus of the material. The material time ξ and the thermal strain θ are, respectively, defined by

$$\xi(t) = \int_0^t \Phi\{T(t')\}\,\mathrm{d}t', \tag{3}$$

$$\theta(t) = \int_{T_0}^{T(t)} \alpha\{p(T'), T'\}\,\mathrm{d}T', \tag{4}$$

where α is the thermal expansion coefficient.

The shift function Φ is defined by time–temperature equivalence on the basis of the Williams, Landell and Ferry (WLF) equation as

$$\log \Phi = \frac{c_1(T - T_g)}{c_2 + (T - T_g)}, \tag{5}$$

where c_1 and c_2 are constants, and T_g is the glass transition temperature of the material.

In case of the isotropic elastic material, the relation between stress and strain can be represented by Hooke's law and from this, the relaxation modulus $L(t)$ can be represented as follows:

$$\begin{bmatrix} \sigma_x \\ \sigma_y \\ \sigma_z \end{bmatrix} = [L] \begin{bmatrix} \varepsilon_x \\ \varepsilon_y \\ \varepsilon_z \end{bmatrix},$$
$$[L] = \frac{2}{3} \begin{bmatrix} 2 & -1 & -1 \\ -1 & 2 & -1 \\ -1 & -1 & 2 \end{bmatrix} G(t) + \begin{bmatrix} 1 & 1 & 1 \\ 1 & 1 & 1 \\ 1 & 1 & 1 \end{bmatrix} K(t). \tag{6}$$

The shear relaxation modulus $G(t)$ and the bulk relaxation modulus $K(t)$ were described by the following models:

$$G(t) = \sum_{\beta=1}^{m} G^{(\beta)} e^{-t/\tau^{\beta}}, \tag{7}$$

$$K(t) = K_0. \tag{8}$$

In Eq. (7), $G(t)$ was assumed to have the form of generalized Maxwell model where $G^{(\beta)}$ are constants and τ^{β} are relaxation times. In Eq. (8), the bulk modulus is assumed to be constant.

2.2. Packing pressure effects

The effect of the added material during the packing stage was taken into account by introducing the concept of reference strain ε_r. The reference strain is determined as the strain state when the material turns into a rubbery solid possibly under pressure. The strain in the constitutive equation must be defined based on the stress-free state. Therefore, this reference strain affects constitutive equation.

First, consider the strain state in a pressurized melt. The strain of a melt, which is initially in stress-free state and is pressurized by the hydrostatic stress $\boldsymbol{\sigma} = -p\mathbf{I}$ at time t, is

$$\boldsymbol{\varepsilon}_{melt} = \frac{1}{3} \ln\{v(t)/v(0)\}\mathbf{I}, \quad \mathbf{I} = [1 \quad 1 \quad 1]^T. \tag{9}$$

Here, v is the specific volume of the material.

Eq. (9) can be used to calculate the reference strain $\boldsymbol{\varepsilon}_r$ of the melt having pressure p_s and temperature T_s when solidification occurs as follows:

$$\boldsymbol{\varepsilon}_r(z) = -\boldsymbol{\varepsilon}_{melt}\{p_s(z), T_s(z)\} = -\frac{1}{3} \ln \frac{v\{p_s(z), T_s(z)\}}{v\{0, T_s(z)\}} \mathbf{I}, \tag{10}$$

where $p_s(z)$ and $T_s(z)$ are position-dependent because each material point solidifies at a different thermodynamic condition.

The constitutive equation can be re-written considering the reference strain as,

$$\boldsymbol{\sigma}(z,t) = \int_0^t \mathbf{L}\{\xi(z,t) - \xi(z,t')\}\, \mathrm{d}[\varepsilon(z,t') - \{\boldsymbol{\varepsilon}_r(z,t') + \boldsymbol{\theta}(z,t')\}]. \tag{11}$$

As the boundary conditions, following assumptions were used:

- the material is constrained in the in-plane directions: $\varepsilon_x = \varepsilon_y = 0$;
- a packing pressure is applied: $\boldsymbol{\sigma}_z(t) = -p(t)$;
- when the polymer is confined between mold walls during solidification, the change in the plaque thickness must be zero as long as $\boldsymbol{\sigma}_z < 0$:

$$\Delta l_0(t) = \int_{-l_0/2}^{l_0/2} \varepsilon_z(z,t)\, \mathrm{d}z = 0;$$

- the reference strain can only be increased in the liquid region:

$$\Delta\boldsymbol{\varepsilon}_r(z,t) = \begin{cases} \Delta\boldsymbol{\varepsilon}_r\mathbf{I}, & \text{liquid state,} \\ 0, & \text{solid state.} \end{cases}$$

In order to determine whether the material is in a liquid or solid state, the no-flow temperature is used.

2.3. Temperature and pressure fields

For the analysis of residual stress, only the packing and cooling stages of injection molding were considered. However, analysis of the temperature and pressure fields in the filling stage is also required to obtain initial fields for the packing stage. Temperature and pressure fields were obtained from the results of a coupled analysis of the filling and post-filling stages following the approach suggested by Han and Im [17].

Because most injection molded parts are thin plate geometries, thermal energy is transferred mostly in the in-plane direction. Neglecting thermal diffusion along the plane direction, the energy equation can be expressed by,

$$\rho C_{pl}\left(\frac{\partial T}{\partial t} + U_x\frac{\partial T}{\partial x} + U_y\frac{\partial T}{\partial y}\right) = k_l\frac{\partial^2 T}{\partial z^2} + \eta\dot{\gamma}^2, \tag{12}$$

$$\rho C_{ps}\frac{\partial T}{\partial t} = k_s\frac{\partial^2 T}{\partial z^2}, \tag{13}$$

where (U_x, U_y) are the velocity components in the (x, y) directions, T the temperature, t the time, C_p the specific heat, ρ the density, η the shear viscosity, $\dot{\gamma}$ the shear rate, and k the thermal conductivity of the material with subscripts l and s denoting the liquid and solid phases, respectively.

In addition, the following boundary conditions should be applied:

$$U_x = U_y = 0,\ T = T_w \quad \text{at } z = \pm h,$$
$$\frac{\partial U_x}{\partial z} = \frac{\partial U_y}{\partial z} = 0 \quad \text{at } z = 0, \tag{14}$$
$$k_s \frac{\partial T_s}{\partial z} = k_l \frac{\partial T_l}{\partial z} \quad \text{at } z = \delta,$$

where δ is the half thickness of liquid zone.

After filling stage, flow in the cavity can be neglected and so only Eq. (13) becomes important.

For the pressure field in the plane direction, following equations were used:

$$\frac{\partial \rho}{\partial t} + \frac{\partial}{\partial x}(\rho U_x) + \frac{\partial}{\partial y}(\rho U_y) = 0, \tag{15}$$

$$\frac{\partial}{\partial z}\left(\eta \frac{\partial U_x}{\partial z}\right) - \frac{\partial p}{\partial x} = 0, \tag{16}$$

$$\frac{\partial}{\partial z}\left(\eta \frac{\partial U_y}{\partial z}\right) - \frac{\partial p}{\partial y} = 0, \tag{17}$$

where p is the pressure.

During the packing and cooling stages, the pressure over most regions in the cavity becomes equal to the packing pressure p_{pack}.

To describe the shear thinning effect, a Cross-type model was employed as follows:

$$\eta(\dot\gamma, T, p) = \frac{\eta_0(T,p)}{1 + \left\{(\eta_0(T,p)\dot\gamma)/(\tau^*)\right\}^{1-n}}. \tag{18}$$

Here, n is the power-law index, τ^* the stress level of the asymptotic transition region between the power-law and Newtonian fluids, and $\eta_0(T, p)$ the zero shear rate viscosity represented by the WLF functional form as follows:

$$\eta_0(T,p) = D_1 \exp\left\{ -\frac{A_1[T - T^*(p)]}{A_2 + D_3 p + [T - T^*(p)]} \right\}, \tag{19}$$

$$T^*(p) = D_2 + D_3 p. \tag{20}$$

For accurate modeling of density, the Tait state equation was used as follows:

$$v(T,p) \equiv \frac{1}{\rho} = v_0(T)\left[1 - 0.0894 \ln\left(1 + \frac{p}{B(T)}\right)\right]. \tag{21}$$

To accurately model density in both the liquid and the solid regions, $v_0(T)$ and $B(T)$ were represented by:

$$v_0(T) = \begin{cases} b_{1,l} + b_{2,l}(T - b_5) & \text{for } T > T_g, \\ b_{1,s} + b_{2,s}(T - b_5) & \text{for } T \leqslant T_g, \end{cases} \tag{22}$$

$$B(T) = \begin{cases} b_{3,l} \exp\{-b_{4,l}(T - b_5)\} & \text{for } T > T_g, \\ b_{3,s} \exp\{-b_{4,s}(T - b_5)\} & \text{for } T \leqslant T_g, \end{cases} \tag{23}$$

$$T_g(p) = b_5 + b_6 p, \tag{24}$$

where T_g is the glass transition temperature for an amorphous polymer.

3. Shrinkage and warpage analysis

When the polymer melt in the cavity is cooled and solidified until it has enough strength, it is demolded. After demolding, the injection molded parts undergo shrinkage and warpage caused by residual stresses and temperature change. At ejection, the temperature profiles along thickness direction have wall temperature at the surface and some higher temperature in the core. In this high temperature region, the relaxation time of polymer becomes very long and can take several days. Thus, in this study, the polymer after demolding was assumed to behave as a linear elastic material.

The parts with a general curved shape have shrinkage in plane direction and warpage in thickness direction. Thus, the analysis of deformation is carried out with a three-dimensional finite-element method.

The constitutive equation of a linear elastic body of which body forces are neglected is represented by

$$\sigma_{ij} = E_{ijkl}\varepsilon_{kl} - \beta_{ij}(T - T_0) + (\sigma_r)_{ij}, \tag{25}$$

where σ_r is the residual stress calculated in parts and β_{ij} is the material tensor related to thermal expansion coefficient and bulk modulus which is represented by

$$\beta_{ij} = K\alpha\delta_{ij}. \tag{26}$$

The tensor E of isotropic materials can be represented by

$$E_{ijkl} = \frac{2\upsilon}{(1 - 2\upsilon)} G\delta_{ij}\delta_{kl} + G(\delta_{ik}\delta_{jl} + \delta_{il}\delta_{jk}), \tag{27}$$

where υ is Poisson's ratio and G is shear modulus of the material. G can be obtained from Eq. (7) when the relaxation time τ approaches infinity such as

$$G = \sum_{\beta=1}^{m} G^{(\beta)}. \tag{28}$$

The weak form of Eq. (25) is

$$\int_\Omega E_{ijkl} u_{k,l} \bar u_{i,j}\, d\Omega - \int_\Omega \beta_{ij}(T - T_0)\bar u_{i,j}\, d\Omega + \int_\Omega (\sigma_r)_{ij}\bar u_{i,j}\, d\Omega = 0, \tag{29}$$

where u_k are displacements and $\bar u_k$ are virtual displacements.

4. Verification of residual stress profiles

In order to verify the numerical results obtained from the developed program, the simulation results were compared with the available experimental data

measured by Zoetelief et al. [8]. Specimen A shown in Fig. 1 molded of polystyrene (PS) was used for comparison. The material data for PS are listed in Tables 1–4 supplied by Zoetelief et al. [8]. The melt temperature was 200°C, the mold temperature 55°C, the injection rate 7.6×10^{-6} m^3/s, and the packing pressure 50 MPa.

Fig. 2 shows the evolution of the in-plane residual stress distribution while in the mold. It shows tensile stresses at the surface, followed by a region with compressive stresses more inward, and lower compressive stresses in the core. At the surface where the polymer melt solidified during the filling stage, high tensile stresses were generated as the material cooled. At more inward region, compressive stresses were generated due to frozen-in stresses caused by high pressure during the packing stage, but in the core, the compressive stresses became lower because of cooling after gate freezing time.

Fig. 3 shows the experimental and calculated in-plane residual stress distribution of parts cooled to 20°C after ejection. In Fig. 3, the predicted residual stress profile is in qualitative agreement with experimental results, but

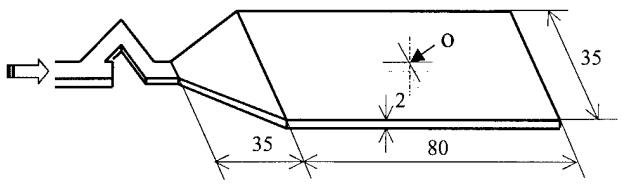

(a)

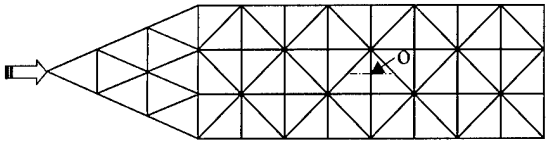

(b)

Fig. 1. (a) Geometry of specimen A; (b) its mesh layout.

Table 1
Material data for the PS used in numerical calculations [8]

Material Data	Symbol	Value
Young's modulus	E	2.446 GPa
Poisson's ratio	ν	0.35
Specific heat (liquid state)	C_l	2289 J/kg K
Specific heat (glassy state)	C_g	1785 J/kg K
Glass transition temperature	T_g	100°C
Thermal expansion coefficient (liquid state)	α_l	0.1966×10^{-3}°C^{-1}
Thermal expansion coefficient (glassy state)	α_g	0.0770×10^{-3}°C^{-1}
Thermal conductivity (average value)	K	0.16 W/m K

Table 2
7-Constant model constants for the PS used in numerical calculations [8]

Symbol	Value
N	0.2520
τ^*	3.080×10^4 Pa
D_1	4.76×10^{10} Pa s
D_2	100°C
D_3	5.1×10^{-7}°C/Pa
A_1	25.74
A_2	61.06°C

Table 3
Specific-volume model constants for the PS used in numerical calculations [8]

Symbol	Value
$b_{1,l}$	9.72×10^{-4} m^3/kg
$b_{2,l}$	5.44×10^{-7} m^3/kg°C
$b_{3,l}$	1.68×10^8 Pa
$b_{4,l}$	4.08×10^{-3}°C^{-1}
$b_{1,s}$	9.72×10^{-4} m^3/kg
$b_{2,s}$	2.24×10^{-7} m^3/kg°C
$b_{3,s}$	2.62×10^8 Pa
$b_{4,s}$	3.00×10^{-3}°C^{-1}
b_5	100°C
b_6	5.1×10^{-7}°C/Pa

Table 4
Shear relaxation data for the PS used in numerical calculations [8]

i	G_i (Pa)	τ_i (s)
1	6.919×10^7	4.769×10^{-8}
2	5.958×10^7	2.498×10^{-6}
3	1.203×10^8	1.178×10^{-4}
4	2.220×10^8	6.660×10^{-3}
5	3.433×10^8	3.000×10^{-1}
6	9.136×10^7	4.496×10^0

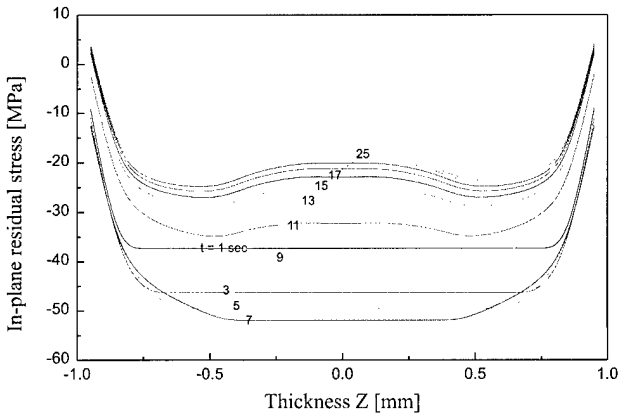

Fig. 2. In-plane residual stress distribution according to time variation in the thickness direction at point O of specimen A.

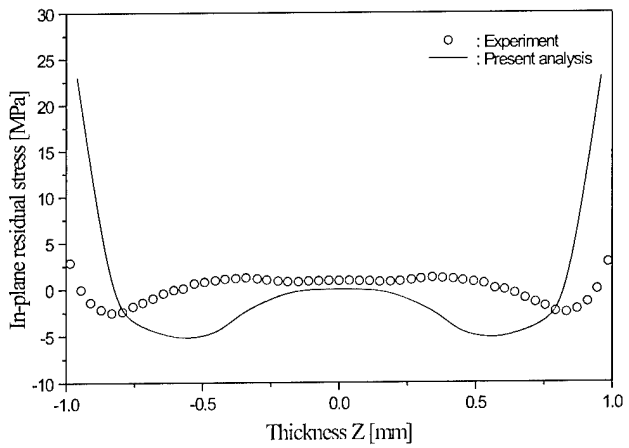

Fig. 3. Comparison of in-plane residual stress distribution between the predicted and measured values [7].

magnitudes of tensile stresses at the surface do not agree with each other. Also, in the core the calculated stresses are not tensile but nearly zero. Such disagreement can be explained as follows.

First, in the present analysis, the boundary conditions for the energy equation were imposed as a fixed temperature on the mold wall for the sake of simplicity. Thus, high temperature gradients were formulated near the wall. But, in real injection molding, the wall temperature can be changed as the polymer melt fills the cavity. Therefore, at the surface, the mold temperature is actually higher than the prescribed wall temperature and the calculated tensile residual stress overpredicts the experiment. For better prediction, heat transfer in the mold must be considered.

Second, the specimen used in the experiment had been stored for about one week at room temperature. Though the polymer has a very long relaxation time at room temperature, some relaxation may occur in polymer chains after one week. Therefore, the tensile stresses in the surface after ejection will decrease actually.

Third, the boundary condition of constraining the material in the in-plane direction was used in residual stress analysis. Fig. 2 shows that at the end of filling a relatively high tensile stress is generated at surfaces. But in real process, the polymer can shrink at surface in the in-plane direction during filling stage, and so the magnitude of the tensile stress at surfaces will not be too high.

5. Verification of shrinkage

The verification of the numerical results of shrinkage was carried out by comparing it to the experimental data measured by Jansen et al. [16]. PS and acrylonitrile-butadiene-styrene (ABS) was used and the material data of ABS is listed in Tables 5–8 as supplied by Zoetelief et al. [8]. Specimen B, shown in Fig. 4, was also used for verification. The standard molding conditions of two materials are listed in Tables 9 and 10. Varying the processing conditions such as packing pressure, injection velocity, mold temperature, and melt temperature,

Table 5
Material data for the ABS used in numerical calculations [8]

Material Data	Symbol	Value
Young's modulus	E	2.732 GPa
Poisson's ratio	ν	0.35
Specific heat (liquid state)	C_l	2289 J/kg K
Specific heat (glassy state)	C_g	1785 J/kg K
Glass transition temperature	T_g	90°C
Thermal expansion coefficient (liquid state)	α_l	$0.2 \times 10^{-3}\,°C^{-1}$
Thermal expansion coefficient (glassy state)	α_g	$0.0840 \times 10^{-3}\,°C^{-1}$
Thermal conductivity (average value)	k	0.16 W/m K

Table 6
7-Constant model constants for the ABS used in numerical calculations [8]

Symbol	Value
n	0.2030
τ^*	1.175×10^5 Pa
D_1	1.669×10^5 Pa s
D_2	170°C
D_3	0°C/Pa
A_1	13.15
A_2	117.0°C

Table 7
Specific-volume model constants for the ABS used in numerical calculations [8]

Symbol	Value
$b_{1,l}$	9.73×10^{-4} m^3/kg
$b_{2,l}$	5.60×10^{-7} m^3/kg°C
$b_{3,l}$	1.84×10^8 Pa
$b_{4,l}$	$3.90 \times 10^{-3}\,°C^{-1}$
$b_{1,s}$	9.73×10^{-4} m^3/kg
$b_{2,s}$	2.27×10^{-7} m^3/kg°C
$b_{3,s}$	2.11×10^8 Pa
$b_{4,s}$	$4.10 \times 10^{-3}\,°C^{-1}$
b_5	90°C
b_6	1.47×10^{-7} °C/Pa

Table 8
Shear relaxation data for the ABS used in numerical calculations [8]

i	G_i (Pa)	τ_i (s)
1	5.074×10^7	4.706×10^{-9}
2	8.688×10^7	4.410×10^{-6}
3	2.904×10^8	2.082×10^{-3}
4	4.091×10^8	6.198×10^{-1}
5	3.573×10^5	3.035×10^6
6	1.185×10^5	2.749×10^8

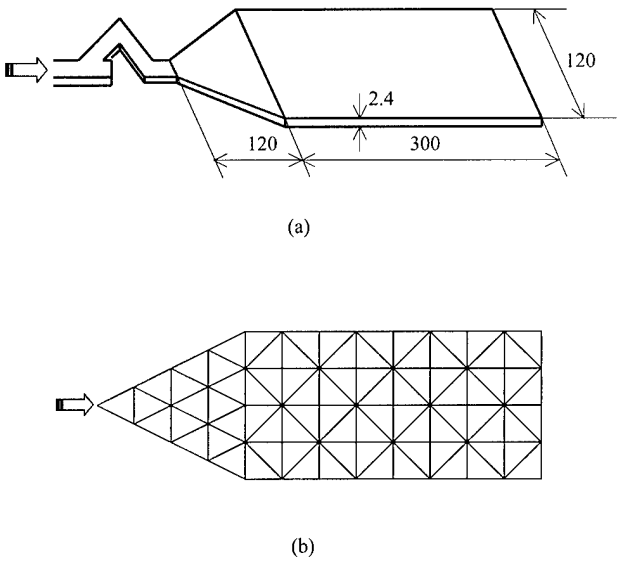

Fig. 4. (a) Geometry of specimen B; (b) its mesh layout.

Table 9
Standard processing parameters for the PS

Processing parameter	Value
Melt temperature	503 K
Mold temperature	323 K
Packing pressure	35 MPa
Injection rate	9.818×10^{-5} m^3/s
Holding time	15 s

Table 10
Standard processing parameters for the ABS

Processing parameter	Value
Melt temperature	503 K
Mold temperature	323 K
Packing pressure	58.35 MPa
Injection rate	1.964×10^{-4} m^3/s
Holding time	15 s

the effects of processing conditions on shrinkage and the accuracy of the developed program were checked.

For comparisons of the magnitude of shrinkage, the following measure was used in the present investigation:

$$S = \frac{d_{\text{mold}} - d_{\text{product}}}{d_{\text{mold}}} \times 100[\%]. \tag{30}$$

5.1. Effect of flow path

Length and width shrinkage along the flow path were calculated and compared to the experimental data. As can be seen in Fig. 5, the shrinkage for PS and ABS is constant along the flow path. It is known that for amorphous polymers, length and width shrinkage along the flow path are constant because of good pressure

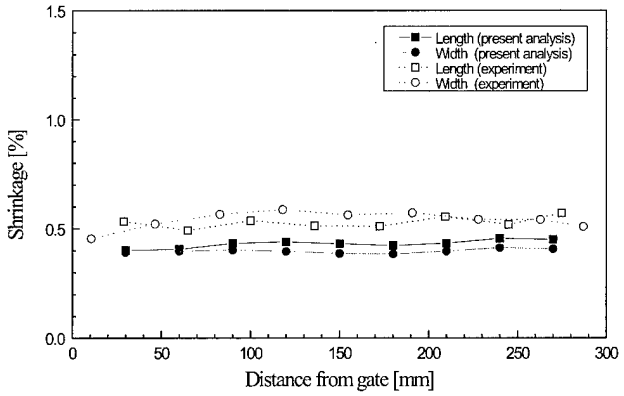

Fig. 5. Comparison of in-plane shrinkage variation along the flow path for the PS between the predicted and measured values [16].

transfer at liquid state. Thus, it is concluded that the numerical results are found to be accurate. The in-plane residual stresses along the flow path are shown in Fig. 6. It shows that the in-plane residual stress along the flow path is also similar. However, tensile stress at surfaces becomes smaller as it is far from the gate which causes the shrinkage of the polymer at surfaces during the filling stage to decrease.

5.2. Effect of packing pressure

Shrinkage as a function of packing pressure was calculated and compared to the experimental data [16]. The result in Fig. 7 shows that the shrinkage decreases as the packing pressure increases for both PS and ABS. It is because much material is added during the packing stage as the packing pressure increases.

Fig. 8 shows in-plane residual stresses for different packing pressure levels. It shows that as the packing pressure increases, the difference between tensile and compressive stresses becomes large. It is because high packing pressure induces high compressive frozen-in stress.

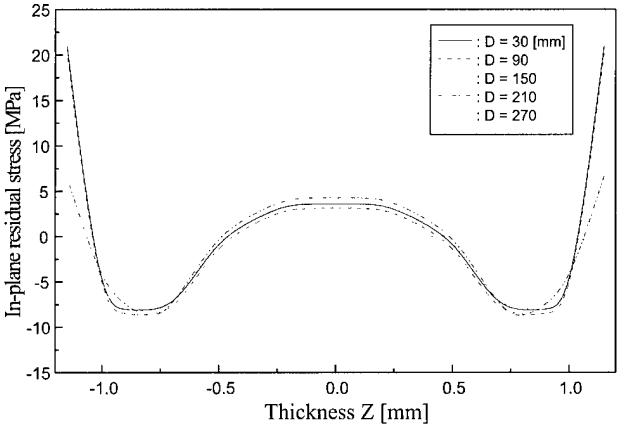

Fig. 6. Calculated in-plane residual stress distribution for different distances from the gate for the PS.

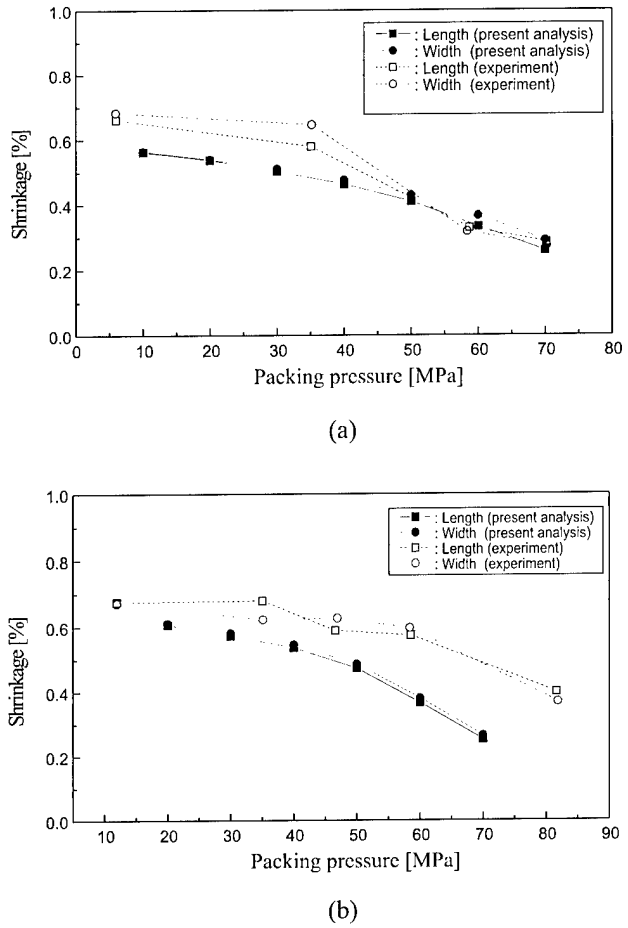

Fig. 7. Comparison of in-plane shrinkage variation for different packing pressures between the predicted and measured values [16] (a) for the PS, and (b) for the ABS.

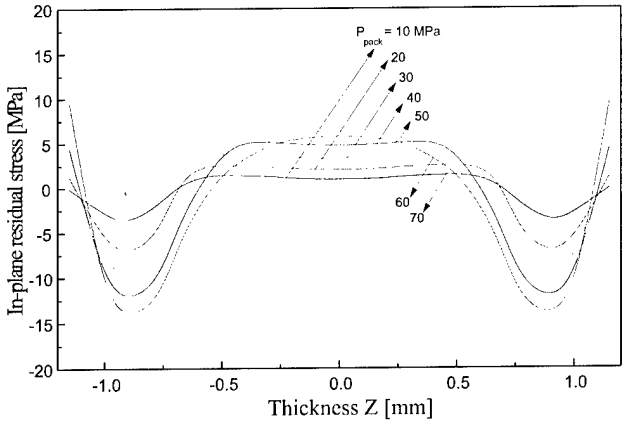

Fig. 8. Calculated in-plane residual stress distribution for different packing pressures for the PS.

5.3. Effect of melt temperature

Shrinkage as a function of melt temperature was calculated and compared to the experimental data [16] for PS and ABS as shown in Fig. 9. The shrinkage of both materials decreases with increasing melt temperature. The calculated results show this tendency well. As melt temperature increases, the gate freezing is delayed such that more materials can be added to decrease the amount of shrinkage. Fig. 10 shows in-plane residual

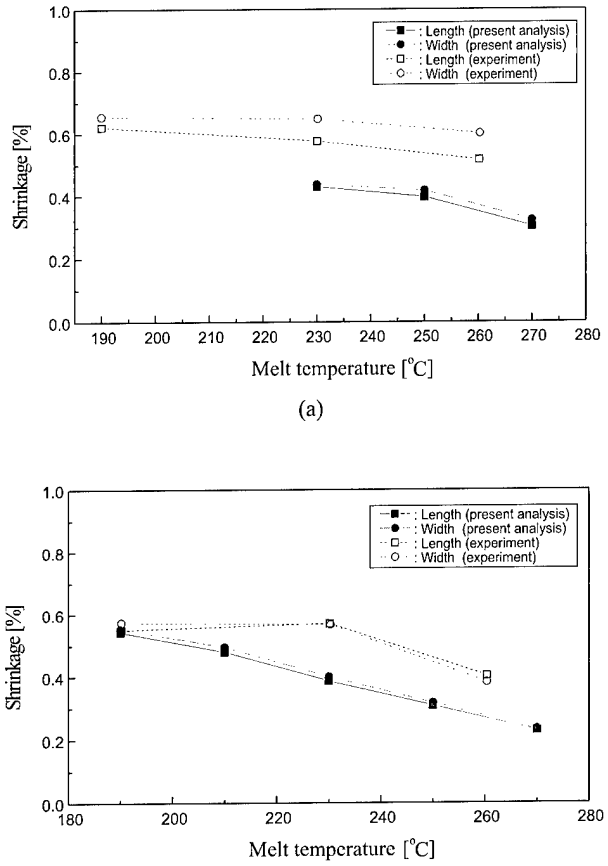

Fig. 9. Comparison of in-plane shrinkage variation for different melt temperatures between the predicted and measured values [16] (a) for the PS, and (b) for the ABS.

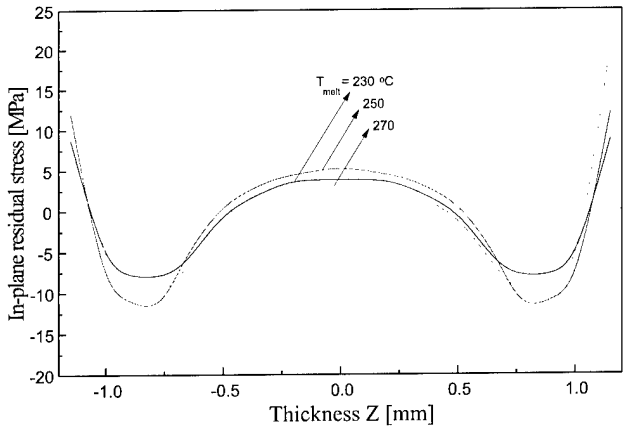

Fig. 10. Calculated in-plane residual stress distribution for different melt temperatures for the PS.

stresses for different melt temperatures, and in this case, all profiles have a very similar shape.

5.4. Effect of mold temperature

Shrinkage as a function of mold temperature was calculated and compared to the experimental data [16] for PS and ABS. Fig. 11 shows that the trend of shrinkage in terms of mold temperature is different for each material. In general, increase of mold temperature delays the gate freezing time which decreases shrinkage while increasing thermal shrinkage after ejection. The results in Fig. 11 are due to these two effects whose extents of influence are different according to the material. Fig. 12 shows in-plane residual stresses for different mold temperatures. The width of the central parabolic portions in the residual stress profile increases with the mold temperature. This increase is caused by the slower rate of propagation of the solid-liquid boundary at higher mold temperatures.

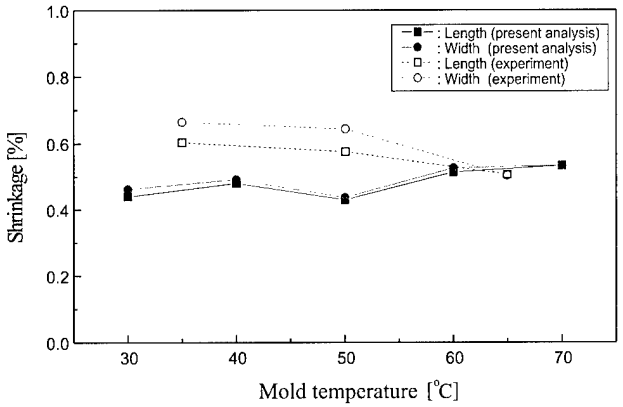

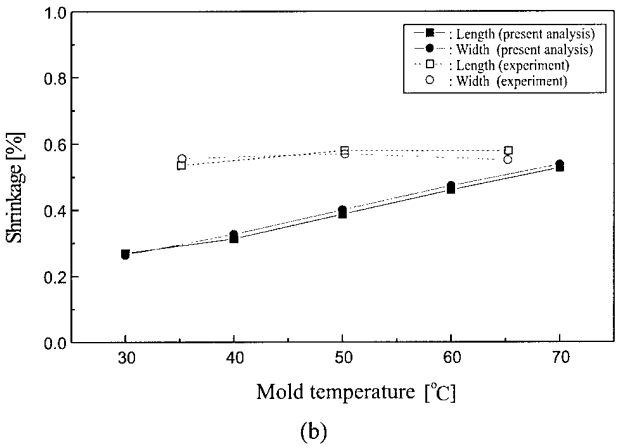

Fig. 11. Comparison of in-plane shrinkage variation for different mold temperatures between the predicted and measured values [16] (a) for the PS, and (b) for the ABS.

5.5. Effect of injection velocity

Shrinkage for different injection velocities was represented in Fig. 13 for both the calculated and measured

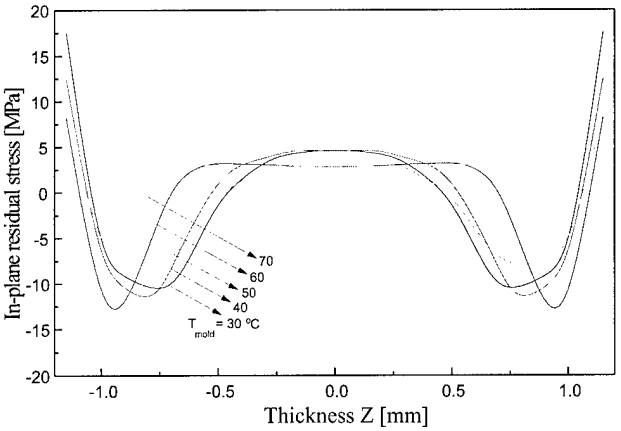

Fig. 12. Calculated in-plane residual stress distribution for different mold temperatures for the PS.

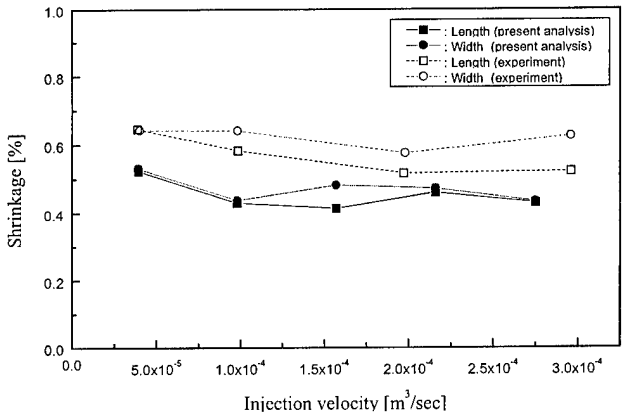

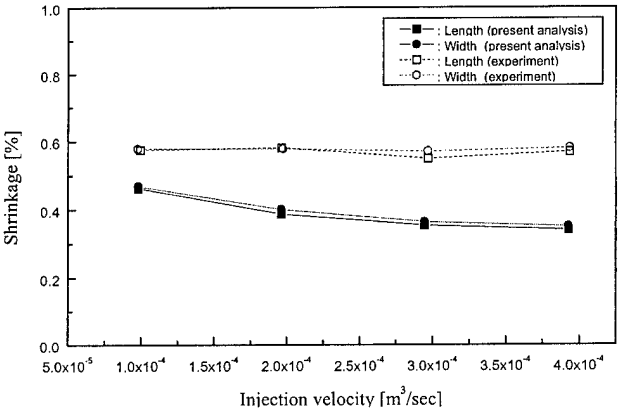

Fig. 13. Comparison of in-plane shrinkage variation for different injection velocities between the predicted and measured values [16] (a) for the PS, and (b) for the ABS.

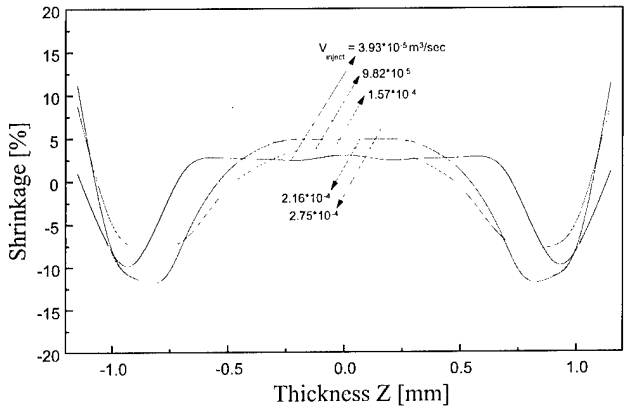

Fig. 14. Calculated in-plane residual stress distribution for different injection velocities for the PS.

cases. It was found that injection velocity has no effect on shrinkage in this case.

Fig. 14 shows in-plane residual stress for different injection velocities. The injection velocity also has no effect on residual stresses. Thus, it is construed that the injection velocity has no effect on the parts quality. But it can affect the processing time.

As can be known from the above results, all calculated shrinkages are in agreement with experimental results except they are slightly smaller.

6. The analysis for thin curved shape

Analysis of shrinkage and warpage was carried out for a part with a curved shape. The position of the gate and the shape of the part are shown in Fig. 15. It is a sector of a spherical shell with a radius of 50 mm and thickness of 2 mm. The material was PS and the processing parameters were listed in Table 9.

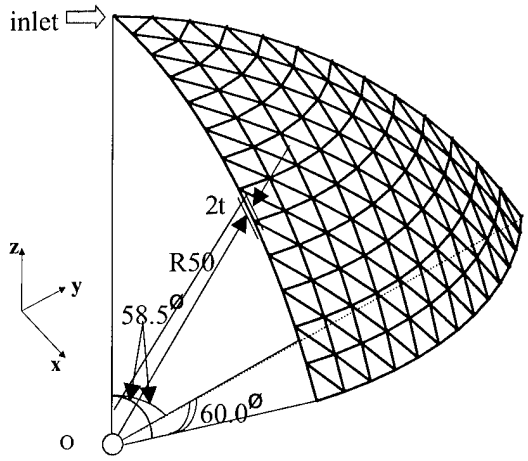

Fig. 15. Mesh layout for the thin curved shell.

Fig. 16 shows the final deformation of the part. Three corner points A, B, and C were constrained to move only in x, y, and z directions, respectively. Width shrinkage along the flow path (curve CD) was calculated and is shown in Fig. 17. The shrinkage along the flow path was nearly constant. However, slightly larger shrinkage occurred in the central region of the curved shell. This was because the curved shell was deformed to a flatter shape. The distances between two points CA and CB were reduced by 0.9% whereas AB was reduced by 0.7%. This indicates that the displacement of point C was larger than those of points A or B, because the gate is located at point C and the shrinkage along the flow path is larger than those in the other directions.

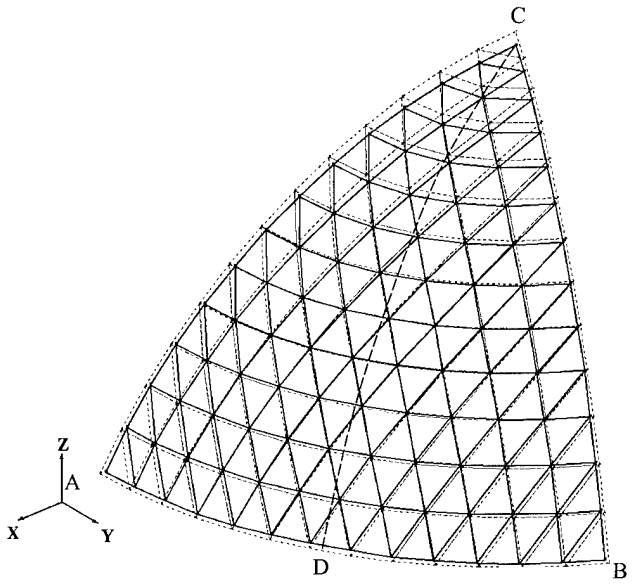

Fig. 16. Shrinkage and warpage of the thin curved shell. Displacements were amplified by a factor of 10. Three points of A, B, and C were constrained to move only in the x, y, and z directions, respectively.

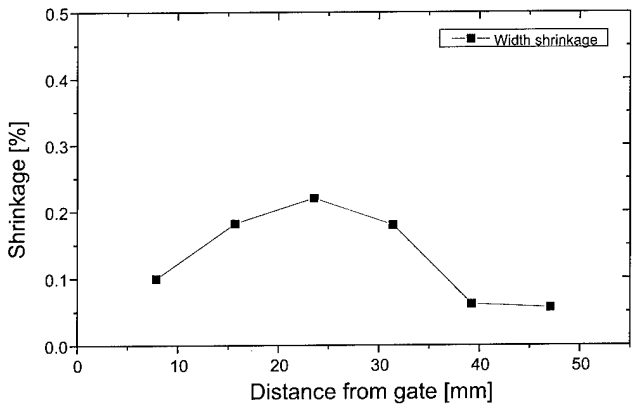

Fig. 17. Shrinkage variation along the flow path for the thin curved shell.

It is construed that the currently developed program can adequately analyze the shrinkage and warpage of a thin curved geometries in three-dimensions.

7. Conclusion

An integrated injection molding analysis program for the calculation of residual stress, shrinkage, and warpage coupled with filling and post-filling stages was developed. To calculate residual stress in the mold, the polymer was assumed to be thermo-viscoelastic. A model which can consider the effect of the additional material during the packing stage was implemented. With residual stress and temperature profiles obtained from this calculation, shrinkage and warpage of the final product was calculated by the linear elastic three-dimensional finite element method. The accuracy of the developed program was verified by comparing the results to the experimental data in the literature under various molding conditions of packing pressure, mold temperature, melt temperature, and injection velocity. Also, analysis was carried out for a curved geometry. Although the residual stress profiles were not completely accurate quantitatively, it was found that the currently developed program was useful in the analysis of shrinkage and warpage under various molding conditions.

Acknowledgements

The authors are grateful for the grant from Korea Science and Engineering Foundation (KOSEF) through the Engineering Research Center for Net Shape and Die Manufacturing at Pusan National University under which this work was possible.

References

[1] Jacques M. An analysis of warpage in injection molded flat parts due to unbalanced cooling. Polym Eng Sci 1982;22(4):241–7.
[2] Thompson M, White JR. The effect of a temperature gradient on residual stresses and distortion in injection molding. Polym Eng Sci 1984;24(4):227–41.
[3] Akay M, Ozden S, Tansey T. Prediction of process-induced warpage in injection molded thermoplastics. Polym Eng Sci 1996;36(13):1839–46.
[4] Boitout F, Agassant JF, Vincent M. Elastic calculation of residual stresses in injection molding. Int Polym Process 1995;10:237–42.
[5] Jansen KMB, Titomanlio G. Effect of pressure history on shrinkage and residual stresses-injection molding with constrained shrinkage. Polym Eng Sci 1996;36(15):2029–40.
[6] Titomanlio G, Jansen KMB. In-mold shrinkage and stress prediction in injection molding. Polym Eng Sci 1996;36(5):2041–9.
[7] Jansen KMB, Pantani R, Titomanlio G. As-molded shrinkage measurements on polystyrene injection molded products. Polym Eng Sci 1998;38(2):254–64.
[8] Zoetelief WF, Douven LFA, Ingen AJ. Residual thermal stresses in injection molded products. Polym Eng Sci 1996;36(14):1886–96.
[9] Liu SJ. Modeling and simulation of thermally induced stress and warpage in injection molded thermoplastics. Polym Eng Sci 1996;36(6):807–18.
[10] Bushko WC, Stokes VK. Solidification of thermoviscoelastic melts. Part I: Formulation of model problem. Polym Eng Sci 1995;35(4):351–64.
[11] Bushko WC, Stokes VK. Solidification of thermoviscoelastic melts. Part II: Effects of processing conditions on shrinkage and residual stresses. Polym Eng Sci 1995;35(4):365–83.
[12] Kabanemi KK, Crochet MJ. Thermoviscoelastic calculation of residual stresses and residual shape of injection molded parts. Int Polym Process 1992;7:60–70.
[13] Kabanemi KK, Vallancourt H, Wang H, Salloum G. Residual stresses, shrinkage, and warpage of complex injection molded products: numerical simulation and experimental validation. Polym Eng Sci 1998;38(1):21–37.
[14] Matsuoka T, Takabatake J, Koiwai A, Inoue Y, Yamamoto S, Takahashi H. Integrated simulation to predict warpage of injection molded parts. Polym Eng Sci 1991;31(14):1043–50.
[15] Hastenberg CHV, Wildervanck PC, Leanen AJH. The measurement of thermal stress distribution along the flow path in injection-molded flat plates. Polym Eng Sci 1992;32(7):506–15.
[16] Jansen KMB, Dijk DJV, Husselman MH. Effect of processing conditions on shrinkage in injection molding. Polym Eng Sci 1998;38(5):838–46.
[17] Han KH, Im YT. Compressible flow analysis of filling and post-filling in injection molding with phase-change effect. Comp Struct 1997;38(1–4):179–90.

ELSEVIER

Composite Structures 47 (1999) 667–672

COMPOSITE STRUCTURES

www.elsevier.com/locate/compstruct

Resistance welding of carbon fibre reinforced thermoplastic composite using alternative heating element

Meng Hou [a,*], Mingbo Yang [b], Andrew Beehag [a], Yiu-Wing Mai [b], Lin Ye [b]

[a] *Cooperative Research Centre for Advanced Composite Structures Ltd., 361 Milperra Road, Bankstown, NSW 2200, Australia*

[b] *Department of Mechanical and Mechatronic Engineering, Centre for Advanced Materials Technology (CAMT), The University of Sydney, Sydney, NSW 2006, Australia*

Abstract

The focus of this work is the use of a metal mesh as an alternative heating element for the joining of carbon fibre fabric reinforced polyetherimide composite laminate. A more homogeneous temperature distribution was generated by the metal mesh at the bonding surface. Glass fibre fabric reinforced PEI (GF/PEI) was used as an electrical insulator between the heating element and adherend laminates. Experimental results show that the GF/PEI prepreg could effectively prevent current leakage and enlarge the welding area. Welding parameters, such as input power level, welding time and pressure, were optimized according to the results of mechanical and microstructure characterization. Mechanical performance of composite specimens joined using metal mesh, in terms of lap shear strength and Mode I interlaminar fracture toughness, was equivalent to that of compression moulded benchmarks. Fracture surfaces of welded specimens showed mostly cohesive failure or intralaminar failure, indicating that good bonding between the PEI matrix and metal mesh was achieved. © 2000 Elsevier Science Ltd. All rights reserved.

Keywords: Thermoplastic composite; Resistance welding; Heating element

1. Introduction

Thermoplastic matrix composites offer the possibility of fusion-bonding as a joining method [1]. Fusion bonding of thermoplastic composites is accomplished by raising the temperature of the bond area above the melting/softening temperature of the polymer matrix, then allowing the joint to cool while intimate contact is maintained. Heating of the thermoplastic matrix can be done in several ways and a number of techniques exist for developing the heat needed to melt the polymer matrix [2–8]. It seems that the most attractive heating techniques would be those that heat only a thin layer of the composite in the vicinity of the bond surface. Resistance welding has been identified as one of the most promising fusion bonding methods and offers a number of advantages [4–6].

Resistance welding with carbon fibre reinforced thermoplastics has been investigated experimentally in several papers [4–6,9] and the most commonly used heating element is made out of either UD CF prepreg or CF fabric prepreg, in order to maintain integrity between the heating element and the composite substrate. Reasonable bond strengths can be obtained using a carbon fibre heating element, although not without large amounts of scatter in the results. The reason is believed to be due to the large degree of scatter in the resistivity of CF prepreg, which may result in uneven heating of the joint area. Other defects of CF-prepreg heating elements, which could be introduced through the preparation procedure, including fibre breakage and incomplete removal of matrix from the fibre surface at the electrical contact, can also cause uneven current distribution across the width of the heating element and result in a partially or incompletely bonding surface. Therefore, consistent quality of the heating element is essential to achieving reproducible, reliable performance and quality of welded joints. The results of our previous study [6] show that overheating of the part edges may induce localized melting and undesirable fibre motion. This squeeze flow may eventually cause the fibre bundles of the heating element to come into contact with those of the adherend laminate and create new current paths within the adherend laminate. This phenomenon is referred as "current leakage" in the literature [4,9] and can dramatically reduce the heating efficiency and intensify temperature non-uniformity of the heating element.

* Corresponding author.

0263-8223/99/$ - see front matter © 2000 Elsevier Science Ltd. All rights reserved.
PII: S0263-8223(00)00047-7

The aims of the present work are to explore the feasibility of using: (a) alternative electric conductive materials as heating elements and (b) an electric isolation layer between the heating element and adherend in resistance welding of thermoplastic composites. The relationship between welding conditions and mechanical performance, in terms of lap shear strength and Mode I interlaminar fracture toughness, was studied. The efficiency of the welded joints is quantified by comparing test results with compression moulded benchmarks. Fracture surfaces of welded specimens were examined by both optical microscopy and SEM techniques.

2. Experimental

2.1. Laminates

Carbon fabric and glass fabric reinforced polyetherimide (Ultem 1000) prepregs supplied by Ten Cate Advanced Composites, The Netherlands, were used in this study. The CF-PEI prepreg has a 5H satin woven construction with a resin content of 44 wt%, while the GF-PEI prepreg has an 8H satin fabric with a resin content of 36 wt%. Two different laminates were manufactured and used as the adherend laminates. One laminate consisted of 10-ply CF-PEI and the other was a 12-ply hybrid laminate (referred to as GF/CF-PEI) made of 10-ply CF-PEI sandwiched between two GF-PEI prepregs. Consolidation of these laminates was performed using compression moulding. The prepregs were placed between two aluminium platens and UPILEX films introduced between the composites and aluminium platens for easy de-moulding. The stack was then consolidated in a hot press. Moulding conditions were adopted from Ref. [10] and the void content of the consolidated laminates was less than 0.2%. The thicknesses of fully consolidated laminates are about 3.0 mm for CF-PEI and 3.6 mm for GF/CF-PEI panel, respectively. Adherend specimens, with dimensions of 100 mm in length and 25 mm in width for lap shear samples, and 170 mm in length and 20 mm in width for Mode I samples, were cut from the consolidated laminates with a water cooled diamond saw. In addition, compression moulded lap shear and Mode I specimens ($[CF/PEI]_{20}$ and $[GF/PEI, CF/PEI_{10}, GF/PEI]_s$) were also prepared using a special mould to provide a benchmark for comparison.

2.2. Heating element

Stainless steel mesh was used as the conductive material in the heating element to generate Joule heat. The metal mesh made of steel wires with a diameter of 25 μm has an aperture of about 30 μm and a thickness of about 50 μm. To obtain compatibility between metal mesh and composite adherends, the metal mesh was impregnated with PEI polymer. This was achieved by co-moulding a single metal mesh between either two pure PEI films with a thickness of 0.076 mm (Type I heating element) or between two GF/PEI prepregs (Type II heating element). Before co-moulding the metal mesh was cleaned with acetone. Compression moulding was used to manufacture these two types of heating elements. The moulding conditions were the same as for the moulding of laminate except that a much lower moulding pressure was used in order to prevent excessive flow of PEI resin. The final thickness of Type I heating element and Type II heating element were 0.10 and 0.46 mm, respectively. The polished cross-sections of these two heating elements (Fig. 1) show that a full impregnation/consolidated state was achieved. In the preparation of the heating element only the "would-be-bonded" area was impregnated with PEI, while the remaining section of the metal mesh was kept from any contamination, which gave good electrical conductivity between the heating element and the connector of the electric power supply. More importantly, the ductility of metal wire can effectively prevent any damage of the heating element, such as breakage of the wires.

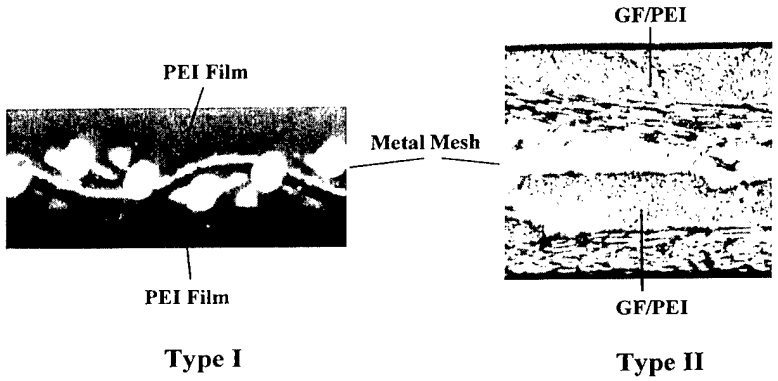

Fig. 1. Heating elements.

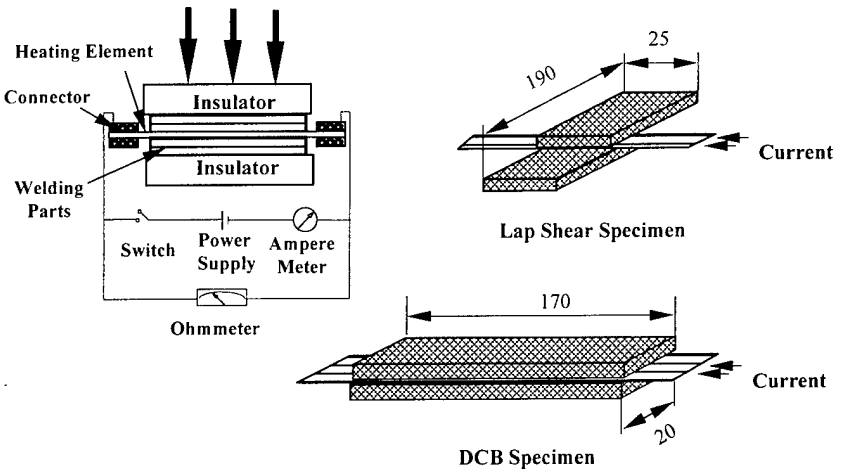

Fig. 2. Schematic illustration of resistance welding set-up.

2.3. Resistance welding

The experimental set-up for resistance welding is shown in Fig. 2. An Instron 5567 testing machine was used to provide a constant compressive load on the specimen to be welded. The loading shaft between the cross-head and welding stack was composed of a ball and socket coupling, which guaranteed a homogenous pressure distribution throughout the whole welding surface. A power supply, which can supply up to 32 A current and 30 V voltage, was used to provide electrical current for welding. Voltage was automatically regulated by the power supply to maintain a constant current output. Two pairs of brass blocks serving as connectors were bolted together to provide a contact pressure to the heating element.

Lap shear and Mode I (DCB) specimens were prepared by resistance welding. The overlap length of the lap shear specimen was approximately 12 mm. The surfaces to be bonded were sanded and cleaned with acetone before welding. Welding was conducted under constant load control and the motion of the cross-head was recorded. Fig. 3 shows a typical displacement–welding time curve, which can be divided into six regions, namely: (1) initial compaction, (2) thermal expansion and compaction, (3) thermal expansion, (4) melt flow, (5) solidification and (6) contraction. It is found that a reduction of bonding thickness, ΔE, which is defined as the distance between the first plateau that occurs before the volume expansion and the last plateau that takes place after the consolidation, could be used as an indicator of the extent of bonding of the joints. For the particular sample geometry of the present study, ΔE was found to be in the range from -0.15 to -0.3 mm for good bonding quality. If ΔE is less than this range it is believed that the specimen has not been fully heated. With larger ΔE values, on the other hand, the specimen has suffered prolonged heating and excessive micro-flow has occurred during welding.

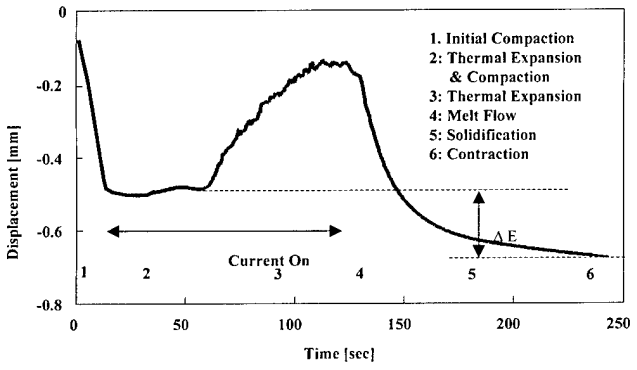

Fig. 3. Typical displacement–welding time curve of resistance welding.

2.4. Characterization

Lap shear testing (ASTM D1002) was used to evaluate the welding quality of all joint specimens. The specimen was 190 mm long and 25 mm wide with an overlap length of 12 mm. The free length between the grips was 140 mm. At least three replicates were tested for each set of processing parameters, at 25°C and 50% RH. The cross-head speed was 1 mm/min. DCB testing (ASTM D 5528) was performed on specimens welded with representative welding conditions. The cross-head speed was 1 mm/min. Three specimens were tested for each benchmark laminate and two specimens were tested for each set of processing parameters. The initiation value ($G_{IC,ini}$) and crack propagation value ($G_{IC,prop}$) were determined by visual observation using a microscope and the modified compliance calibration method, respectively. Before testing all welded specimens were polished by about 0.1 mm on each side so that the edge irregularities obtained during the welding process due to transverse matrix flow could be removed.

Fracture surfaces of welded specimens were examined by both optical microscopy and SEM techniques.

3. Results and discussion

3.1. Lap shear strength

It is well known that the welding quality is influenced by many processing factors, such as power level (current density), welding time and holding pressure. It is, therefore, important to explore the best combination of these factors to obtain the best welding result. Hou et al. [6] have investigated the effect of the power level, welding pressure and welding time on lap shear strength in the resistance welding of CF/PEI composites using carbon fibre as the heating element and a processing window has been optimized. His processing window [6] was used as a guideline in determining processing parameters for the current study. Type I heating element and CF-PEI laminate were used in the preparation of lap shear specimens. The welding parameters used in the present study are indicated by open and closed circles in Fig. 4. These combinations of welding parameters were selected in such a way that they were either near or inside the processing window generated in Ref. [6]. The influence of welding conditions on lap shear strength can be more clearly seen in Table 1. It can be seen that the lap shear strength of several specimens reach that of the benchmark material made by compression moulding (i.e., ~31 MPa). When the lap shear values are compared with that given in Ref. [6], it is clear that the mean strength values do not significantly vary from process to process. However, the metal mesh heating element does produce more consistent joint strengths than the CF heating element. Data points with lap shear strengths higher than 27 MPa, which is equivalent to 87% of the compression moulded benchmark, are assumed as the baseline of satisfactory strength and are indicated using open circles, while lower strength values are shown with closed circles in Fig. 4. The processing window, bounded by the open circles and indicated by the broken lines, is wider than the old processing window from Ref. [6]. This clearly demonstrates that CF/PEI laminates can be satisfactorily bonded by resistance welding using metal mesh as the heating element under broader processing conditions.

Table 1
Processing conditions and resultant lap shear strength

Power level (kW/m^2)	Welding energy (kJ/m^2)	Holding pressure (MPa)	Mean lap shear strength (MPa)
150	2700	0.3	30.31
	3267	0.2	30.50
125	2717	0.3	28.90
	4450	0.2	31.73
120	3913	0.4	30.00
	5217	0.2	27.50
	5987	0.3	19.47
105	4300	0.4	29.30
	5150	0.2	31.48
	5700	0.3	27.26
100	3260	0.4	31.47
	4076	0.2	34.46
	4347	0.4	27.78
	5434	0.4	33.19
80	2609	0.2	15.00
	3478	0.3	23.00
	4347	0.4	29.30

The failure mode of the welded part was found to be cohesive or intralaminar, i.e., fracture occurred either within the bulk of the composites or occurred from one laminate through the heating element and then into another laminate, as shown in Fig. 5. Furthermore, there is evidence of metal mesh being torn off leaving depressions on the fracture surface and the elongated wires of the heating element could also be clearly seen in Fig. 5. Further understanding of the adhesion behaviour

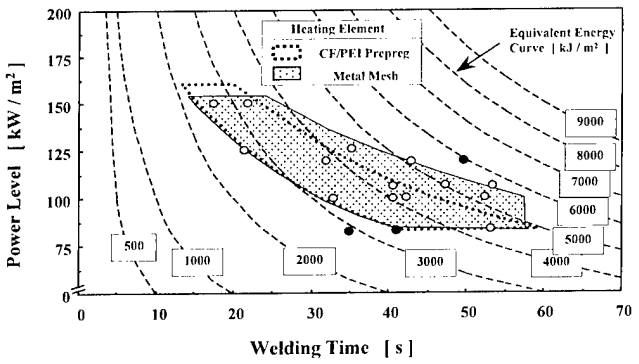

Fig. 4. Processing window for resistance welding of CF/PEI composites.

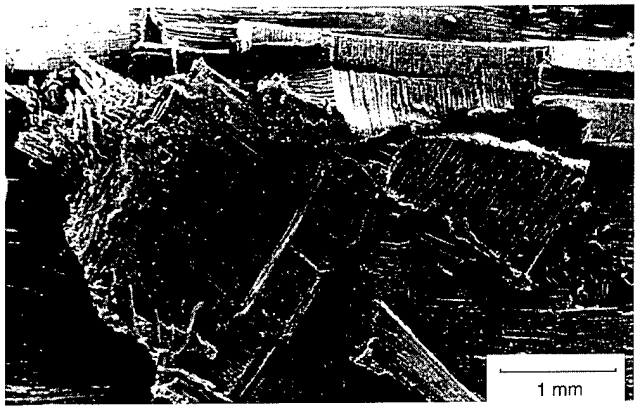

Fig. 5. SEM photograph showing fracture across layers in the lap shear test.

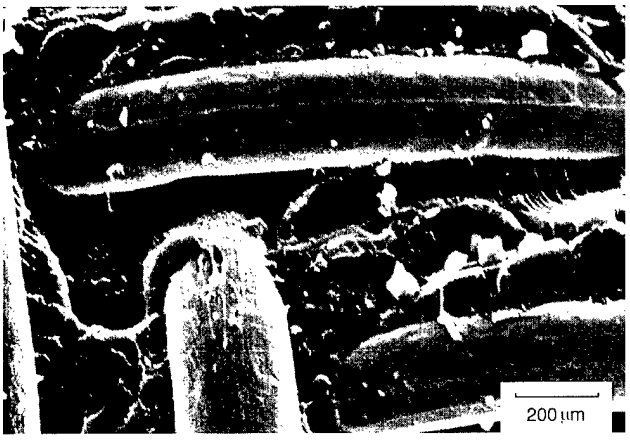

Fig. 6. Enlarge SEM photography of fracture surface from lap shear test.

between the metal mesh and the matrix resin can be obtained from Fig. 6. Clearly, there is a lot of matrix material attached to the surface of the metal wire indicating good adhesion strength between metal wire and matrix. It is noted that the metal mesh element was pretreated by PEI film and therefore compatible with the PEI resin resulting in a strong bond. Alternatively, it might be assumed that the metal ions, generated by electric current passing through the mesh, could diffuse into and react with the polymer domain either physically or chemically. In this way, the bonding between metal mesh and matrix resin could be further strengthened.

3.2. Welding of large area

3.2.1. Electrical current leakage

An unusual phenomenon found in welding a Mode I specimen using a Type I heating element and CF-PEI laminate was that joining could not be completed irrespective of welding time. When the electric current was switched on the matrix material was rapidly melted at the two ends of the specimen and the resin was subsequently squeezed out. After the specimen was split open at the interface, localized melting at the end of specimen was clearly seen, while the middle of the specimen was not bonded at all, even after long welding times. Through an on-line monitoring system it was found that the resistance of the heating element decreased drastically during the welding process. Since more thermal energy was generated at both ends of the specimen [6], the matrix at the sample end would be melted long before the whole specimen surface was uniformly heated to the flow temperature. As soon as the resin was melted and squeezed out, the heating element would be in contact with the carbon fibre of the adherend laminate, thereby creating new current paths inside the adherend laminate. This effect led to an increase in the conductive cross-sectional area and the whole laminate would eventually act as a heating element. Consequently, it must produce a decrease in the global resistance and a loss in heat energy generation at the surface. Because of the high temperature at both ends, matrix flow, polymer thermal degradation and fibre motion occur in these regions, while the middle part of the specimen remains completely un-welded. This phenomenon did not occur in the lap shear specimen because the welding area was too small, but would be greatly amplified with the increase of welding length.

To prevent current leakage, GF-PEI was used as an electric isolation layer between heating element and adherend laminate. This was achieved for joining: (1) CF-PEI laminate with Type II heating element and (2) hybrid laminate [GF-CF-PEI] with Type I heating element. The results of on-line monitoring revealed that no current leakage has occurred. Small amounts of matrix resin were squeezed out of the bonding line, suggesting that the laminates have been well bonded. Thus, the heating elements, Type I and Type II, can be used for resistance welding of large GF/CF-PEI and CF-PEI laminates, respectively. Both of them give good welding results; however, Type II is more convenient to apply since laminates to be welded are rarely pre-laminated with GF/PEI prepregs in advance. The welded area reached 3400 mm^2 (width mm $\times$ length 170 mm) for the Mode I specimen. This was almost nine times larger than the welded area of the lap shear specimen (300 mm^2). Indeed, parts as large as 7200 mm^2 (45 mm in width and 160 mm in length) have been welded using both types of heating element without any current leakage.

3.2.2. Mode I interlaminar fracture toughness

To simplify the experimental work, the welding parameters of Mode I specimens were selected from the established processing window (Fig. 4). Two power levels of 100 and 125 kW/m^2, welding energies ranging from 3000 to 5000 kJ/m^2 and a welding pressure of 0.2 MPa were used in the demonstration. The Mode I interlaminar fracture toughnesses of welded specimens are summarized in Fig. 7. To explore the behaviour of crack propagation of the composite, Madhukar and Drzal [11] suggest that the average value for stable crack growth should be used. Therefore, the plateau value of the R-curve was used to calculate the average value of $G_{IC,Prep}$. It is clear that the fracture toughnesses of welded specimens are at least as good and sometimes are even better than that of the benchmark materials. Relatively speaking, given the same welding process parameters, the Type II heating element is not as effective as Type I for toughness enhancement. This difference in toughness behaviour could be caused by the location of the starter crack being different in these two specimens, as schematically illustrated in Fig. 8. For Type I heating elements, the starter crack is located between the GF/PEI

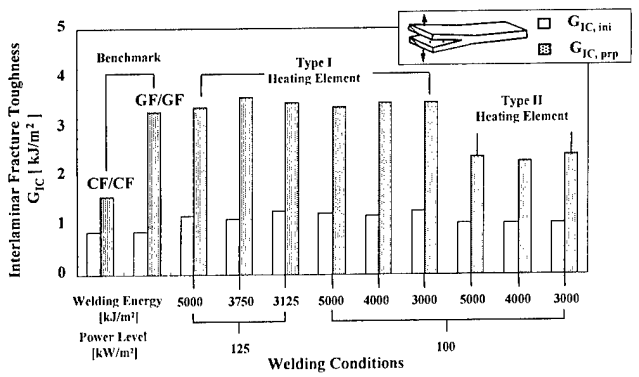

Fig. 7. Mode I interlaminar fracture toughness of welded CF/PEI composites.

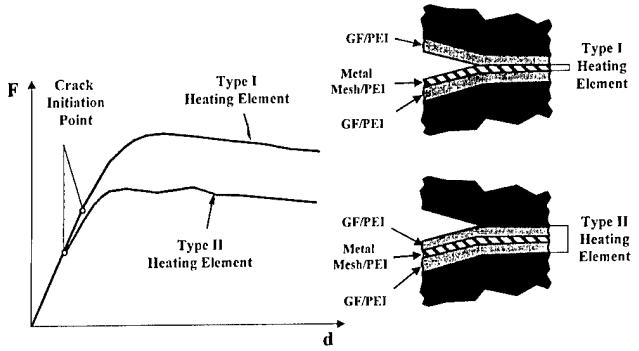

Fig. 8. Schematics of load–displacement diagrams.

laminate and PEI/metal mesh so that the crack propagates through the interface consisting of GF/PEI, metal mesh and GF/PEI. For Type II heating elements, the starter crack is placed between the GF/PEI layer and CF/PEI laminate. Crack growth between these two layers requires less fracture energy. From that, the thickness of resin is greater adjacent to the metal mesh in Type I, due to the use of PEI film. Therefore, we would expect the deformation zone ahead of the crack tip to be larger in the Type I element than the Type II, leading to higher fracture energy.

4. Conclusions

An experimental investigation of resistance welding of carbon fibre reinforced polyetherimide laminates was conducted, in which stainless steel mesh was used as the conductive material in the heating element. Experimental results indicate that CF/PEI laminates can be satisfactorily bonded using metal mesh heating elements and the maximum lap shear strength achieved is equivalent to that of compression moulded specimens. Fracture surface analysis shows that a very good bond existed between the metal mesh and polymer matrix, and the main failure mode of the welded part was cohesive or intralaminar failure due to tearing of the metal mesh and the elongation of the metal wire. Compared with CF/PEI heating elements, metal mesh heating elements gave a bigger processing window. Current leakage was identified as a main reason for incomplete bonding of large areas. The use of an insulation layer on the surface of the heating element or laminate has proved to be an effective method to prevent current leakage and can be used to join large welding area specimens. The Mode I interlaminar fracture toughnesses of welded specimens were equivalent to that of the co-moulded benchmark (GF-PEI), and were considerably tougher than the benchmark (CF-PEI).

Acknowledgements

This work was carried out as a part of the Cooperative Research Centre for Advanced Composite Structures (CRC-ACS) Research Program (Task 2.1.3 Alternative Prepreg). Thanks are due to the technicians in the Materials Laboratories of the CAMT at the University of Sydney for their assistance in the experiments.

References

[1] Lambing CLT, Don RC, Andersen SM, Holmes ST, Leach BS, Gillespie JW. Design and manufacture of an automated resistance welder for thermoplastic composites. ANTEC '91, p. 2527–31.
[2] Strong AB, Johnson DP, Johnson BA. Variables interactions in ultrasonic welding of thermoplastic composites. SAMPE Quart, January 1990;36–41.
[3] Harras B, Cole KC, Vu-Khanh T. Optimization of the ultrasonic welding of PEEK-carbon composites. J Reinforced Plastics Compos 1996;15:174–82.
[4] Eveno EC, Gillespie Jr. JW. An experimental investigation: resistance welding of graphite polyetheretherketone composites. J Thermoplastic Compos 1988;1:322–37.
[5] Hou M, Friedrich K. Resistance welding of continuous carbon fibre polypropylene composites. Plastics Rubber Compos 1992;18:205–13.
[6] Hou M, Ye Y, Mai Y-W. An experimental study of resistance welding of carbon fibre reinforced polyetherimide composite material. Appl Compos Mater 1999;6:35–49.
[7] Maguire DM. Joining thermoplastic composites. SAMPE J 1989;25(1):11–4.
[8] Fink B, Gillespie Jr. JW, McCullough RL. A local theory of heating in cross-ply carbon fibre thermoplastic composites by magnetic induction. Polym Eng Sci 1992;32(5):357–69.
[9] Ageorges C, Ye L, Hou M. Experimental investigation of the resistance welding for thermoplastic matrix composites. Part I: heating element and heat transfer. Compos Sci Technol, 2000, to appear.
[10] Hou M, Ye L, Lee HJ, Mai YW. Manufacture of carbon fibre fabric reinforced polyetherimde (CF/PEI) composite material. Compos Sci Technol 1998;58:181–90.
[11] Madhukar M, Drzal LT. Fibre-matrix and its effect on composite mechanical properties: IV. Mode I and Mode II fracture toughness of graphite/epoxy composite. J Compos Mater 1992;26:936–45.

ELSEVIER

Composite Structures 47 (1999) 673–678

COMPOSITE STRUCTURES

www.elsevier.com/locate/compstruct

Stress analysis of adhesively-bonded lap joints

Shiuh-Chuan Her *

Department of Mechanical Engineering, Yuan-Ze University, 135 Yuan-Tung Road, Chung-Li, Tao-Shian 320, Taiwan, ROC

Abstract

The adhesively-bonded joints considered in this investigation include single-lap joint and double-lap joint. A simplified one-dimensional model based on the classical elasticity theory is presented. The shear deformation in the adhesive is assumed constant across the adhesive thickness. The analytical solutions of shear stress in the adhesive and longitudinal stress in the adherend are obtained and compared with the numerical solutions determined by the two-dimensional finite element method. © 2000 Elsevier Science Ltd. All rights reserved.

Keywords: Adhesively-bonded; Single-lap joint; Double-lap joint; Finite element method

1. Introduction

Joint which connects two components together is a common technology for assembling structures, and is increasingly being used in aerospace and automotive industries. Statistics shows that approximately 70% of the failure of structures is initiated from joints. Thus, to ensure the safety of joints in structures, it is necessary to analyse the stress distribution on the joint. The single-lap joint with the characteristics of simplicity and efficiency has been used widely in many applications and becomes a standard test specimen for determining the mechanical properties of adhesives. Although the stress analysis of the single-lap joint has been investigated by many researchers for a long period of time, some controvertible issues still remain [1–6], e.g. the maximum shear stresses, some results show it occurs at the free end of adhesive layer [3], however, others show that it occurs at a short distance from the free ends [6].

Kinloch [7] proposed a simple shear lag model which considered the shear deformation in the adhesive layer. Goland and Reissner [8] performed the analysis of a cylindrically bent plate that include the effects of the joint edge moment due to the eccentricity of the loading path. Hart–Smith [9] modeling the adherends as an elastic foundation obtained the stress solutions for a linear elastic and elastic–plastic adhesive. Du Chen et al. [10] presented an analytical solution based on two-dimensional elasticity theory in conjunction with variational principal of complementary energy. The analysis of joints which connects two orthotropic materials can be found in Refs. [11–16]. In this investigation a simplified model is presented for both single-lap joint and double-lap joint. Analytical solutions based on the classical elasticity are obtained and compared with the numerical results computed by two-dimensional finite element method.

2. Problem statement and basic assumption

Most of structures are formed by connecting different components through the joints. In adhesive bonding, the load is transmitted from one adherend to another adherend smoothly through the adhesive layer in the overlap region, i.e. the adhesive serves as a medium for load transmission. The objective of this investigation is to provide a simple but accurate solution to calculate the shear stress in the adhesive. The major difference between adhesive bonding and mechanical fastener is the bonded area. The area of adhesive bonding is larger than that of mechanical fastener. The stress concentration is minimized due to the larger bonded area, and the stress distributions become more uniformly in the overlap region. Fig. 1 shows the geometric model for a single-lap joint. The models presented here are one-dimensional, i.e. all stress components vary with the x-axis only. For a joint connecting two composite materials, the material constants are transformed to effective engineering constants.

* Fax: +3-4558013.
E-mail address: mesch@saturn.yzu.tw (S.-C. Her).

0263-8223/99/$ - see front matter © 2000 Elsevier Science Ltd. All rights reserved.
PII: S0263-8223(00)00052-0

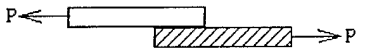

Fig. 1. Single-lap joint.

The eccentric loading path may result in bending deflections and joint edge moment at the free ends of the overlap region for a single-lap joint. To simplify the model, the thickness is assumed to be small enough so that the bending effect can be neglected. The basic assumptions are as follows:

1. The shear stress in the adhesive layer do not vary through the thickness.
2. The longitudinal stresses in the adherends do not vary through the thickness.
3. The adherends and adhesive layer are linear elastic, and joint edge moment is neglected.

3. Single-lap joint

The geometric profile of a single-lap joint is shown in Fig. 2. The free-body-diagram of an infinitesimal element in the overlap region is shown in Fig. 3. The force equilibrium of upper and lower adherend in Fig. 3 yields to the following differential [17]:

$$\frac{dT_o}{dx} + \tau = 0, \tag{1a}$$

$$\frac{dT_i}{dx} - \tau = 0, \tag{1b}$$

where T_o, T_i in Eqs. (1a) and (1b) represents longitudinal tension per unit width in the upper and lower adherend, respectively, τ is the shear stress in the adhesive layer.

The longitudinal displacement-strain relations of adherends are:

$$\frac{du_o}{dx} = \varepsilon_o = \frac{T_o}{E_o t_o}, \tag{2a}$$

$$\frac{du_i}{dx} = \varepsilon_i = \frac{T_i}{E_i t_i}, \tag{2b}$$

where u_o, ε_o, E_o and t_o are the longitudinal displacement, strain, Young's modulus, and thickness of the upper adherend, respectively. u_i, ε_i, E_i and t_i are the respective components relative to the lower adherend.

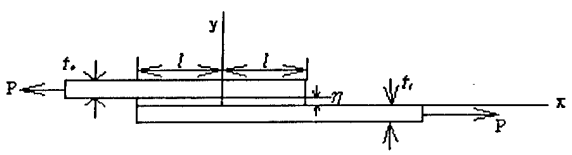

Fig. 2. Geometric profile of a single-lap joint.

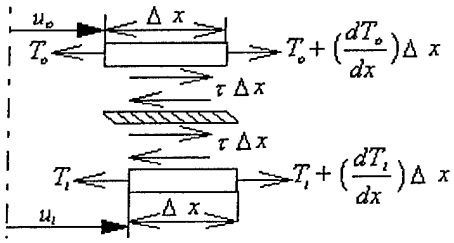

Fig. 3. The free-body diagram of a single-lap joint.

The differential equations (1a) and (1b) can be combined together through the shear deformation in the adhesive layer as follows:

$$\tau = G_a \gamma = \frac{G_a}{\eta}(u_i - u_o), \tag{3}$$

where G_a is the shear modulus of adhesive, γ and η are the shear strain and thickness of the adhesive layer, respectively.

Taking the derivative with respect to x of Eqs. (3) and (1a), yields

$$\frac{d\tau}{dx} = \frac{G_a}{\eta}\left(\frac{du_i}{dx} - \frac{du_o}{dx}\right), \tag{4}$$

$$\frac{d^2 T_o}{dx^2} = -\frac{d\tau}{dx}. \tag{5}$$

Substituting Eqs. (4) and (2a), (2b) into Eq. (5) yields

$$\frac{d^2 T_o}{dx^2} = -\frac{G_a}{\eta}\left(\frac{du_i}{dx} - \frac{du_o}{dx}\right) = -\frac{G_a}{\eta}\left(\frac{T_i}{E_i t_i} - \frac{T_o}{E_o t_o}\right). \tag{6}$$

The force balance in Fig. 3 requires that the sum of the longitudinal forces in upper and lower adherend equals to the applied force P, i.e.

$$P = T_i + T_o \quad \text{or} \quad T_i = P - T_o. \tag{7}$$

Substituting Eq. (7) into Eq. (6), one can obtain a second-order differential equation of T_o with respect to x as follows:

$$\frac{d^2 T_o}{dx^2} - \lambda^2 T_o = -\frac{G_a P}{E_i t_i \eta}, \tag{8}$$

where

$$\lambda^2 = \frac{G_a}{\eta}\left(\frac{1}{E_i t_i} + \frac{1}{E_o t_o}\right).$$

The associated boundary conditions are

$$\begin{aligned} T_o &= 0, \quad x = l, \\ T_o &= P, \quad x = -l, \end{aligned} \tag{9}$$

where l is the half length of the bonded region.

The solution of differential Eq. (8) can be written as

$$T_o = A\sinh(\lambda x) + B\cosh(\lambda x) + \frac{PE_o t_o}{(E_o t_o + E_i t_i)}. \tag{10}$$

The integration constants A and B can be solved by applying the boundary conditions in Eq. (9). As a result, the longitudinal tensions, T_o and T_i, in upper and lower adherend and the shear stress τ in the adhesive layer can be expressed as the following forms:

$$T_o = P\left[-\frac{1}{2}\frac{\sinh(\lambda x)}{\sinh(\lambda l)} + \frac{E_i t_i - E_o t_o}{2(E_i t_i + E_o t_o)}\frac{\cosh(\lambda x)}{\cosh(\lambda l)} + \frac{E_o t_o}{(E_i t_i + E_o t_o)}\right], \tag{11a}$$

$$T_i = P\left[1 + \frac{1}{2}\frac{\sinh(\lambda x)}{\sinh(\lambda l)} - \frac{E_i t_i - E_o t_o}{2(E_i t_i + E_o t_o)}\frac{\cosh(\lambda x)}{\cosh(\lambda l)} - \frac{E_o t_o}{(E_i t_i + E_o t_o)}\right], \tag{11b}$$

$$\tau = \frac{P\lambda}{2}\left[\frac{\cosh(\lambda x)}{\sinh(\lambda l)} - \frac{E_i t_i - E_o t_o}{(E_i t_i + E_o t_o)}\frac{\sinh(\lambda x)}{\cosh(\lambda l)}\right]. \tag{11c}$$

The constants E_i and E_o are the equivalent longitudinal moduli in upper and lower adherends, respectively.

4. Double-lap joint

The geometric profile of a double-lap joint is shown in Fig. 4. The free-body-diagram of an infinitesimal element in the overlap region is shown in Fig. 5. The force equilibrium of outer and inner adherend in Fig. 5 yields to the following differential equations:

$$\frac{dT_o}{dx} + \tau = 0, \tag{12a}$$

$$\frac{dT_i}{dx} - 2\tau = 0, \tag{12b}$$

where T_o, T_i in Eqs. (12a) and (12b) represents longitudinal tension per unit width in the outer and inner adherend, respectively, τ is the shear stress in the adhesive layer.

The longitudinal displacement-strain relations of adherends are:

$$\frac{du_o}{dx} = \varepsilon_o = \frac{T_o}{E_o t_o}, \tag{13a}$$

$$\frac{du_i}{dx} = \varepsilon_i = \frac{T_i}{E_i t_i}, \tag{13b}$$

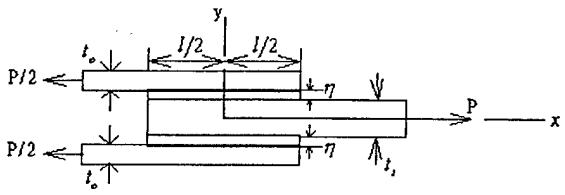

Fig. 4. Geometric profile of a double-lap joint.

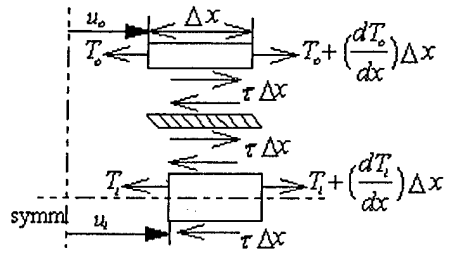

Fig. 5. The free-body diagram of a double-lap joint.

where u_o, ε_o, E_o and t_o are the longitudinal displacement, strain, Young's modulus, and thickness of the outer adherend, respectively. u_i, ε_i, E_i and t_i are the respective components relative to the inner adherend.

The differential equations (12a) and (12b) can be combined together through the shear deformation in the adhesive layer as follows:

$$\tau = G_a\gamma = \frac{G_a}{\eta}(u_i - u_o), \tag{14}$$

where G_a is the shear modulus of adhesive, γ and η are the shear strain and thickness of the adhesive layer, respectively.

Taking the derivative with respect to x of Eq. (14) and Eq. (12a), yields

$$\frac{d\tau}{dx} = \frac{G_a}{\eta}\left(\frac{du_i}{dx} - \frac{du_o}{dx}\right), \tag{15}$$

$$\frac{d^2T_o}{dx^2} = -\frac{d\tau}{dx}. \tag{16}$$

Substituting Eqs. (15) and Eqs. (13a) and (13b) into Eq. (16) yields

$$\frac{d^2T_o}{dx^2} = -\frac{G_a}{\eta}\left(\frac{du_i}{dx} - \frac{du_o}{dx}\right) = -\frac{G_a}{\eta}\left(\frac{T_i}{E_i t_i} - \frac{T_0}{E_o t_o}\right). \tag{17}$$

The force balance in Fig. 7 requires that the sum of longitudinal forces in outer and inner adherend equals to the applied force P, i.e.

$$P = T_i + 2T_o \text{ or } T_i = P - 2T_o. \tag{18}$$

Substituting Eqs. (18) into (17), one can obtain a second-order differential equation of T_o with respect to x as follows:

$$\frac{d^2T_o}{dx^2} - \lambda^2 T_o = -\frac{G_a P}{E_i t_i \eta}, \tag{19}$$

where

$$\lambda^2 = \frac{G_a}{\eta}\left(\frac{2}{E_i t_i} + \frac{1}{E_o t_o}\right).$$

The associated boundary conditions are

$$T_o = 0; \quad x = \frac{l}{2},$$

$$T_o = \frac{P}{2}; \quad x = -\frac{l}{2}, \tag{20}$$

where l is the length of the bonded region.

The solution of differential Eq. (19) can be written as

$$T_o = A\sinh(\lambda x) + B\cos(\lambda x) + \frac{PE_o t_o}{(2E_o t_o + E_i t_i)}. \tag{21}$$

The integration constants A and B can be solved by applying the boundary conditions in Eq. (20). As a result, the longitudinal tensions, T_o and T_i, in outer and inner adherend and the shear stress τ in the adhesive layer can be expressed as the following forms:

$$T_o = \frac{P}{2}\left[-\frac{1}{2}\frac{\sinh(\lambda x)}{2\sinh(\frac{\lambda l}{2})} + \frac{E_i t_i - 2E_o t_o}{2(E_i t_i + 2E_o t_o)}\frac{\cosh(\lambda x)}{\cosh(\frac{\lambda l}{2})} + \frac{2E_o t_o}{(E_i t_i + 2E_o t_o)}\right], \tag{22a}$$

$$T_i = P\left[1 + \frac{1}{2}\frac{\sinh(\lambda x)}{\sinh(\frac{\lambda l}{2})} - \frac{E_i t_i - 2E_o t_o}{2(E_i t_i + 2E_o t_o)}\frac{\cosh(\lambda x)}{\cosh(\frac{\lambda l}{2})} - \frac{2E_o t_o}{(E_i t_i + 2E_o t_o)}\right], \tag{22b}$$

$$\tau = \frac{P\lambda}{4}\left[\frac{\cosh(\lambda x)}{\sinh(\frac{\lambda l}{2})} - \frac{E_i t_i - 2E_o t_o}{(E_i t_i + 2E_o t_o)}\frac{\sinh(\lambda x)}{\cosh(\frac{\lambda l}{2})}\right]. \tag{22c}$$

The constants E_i and E_o are the equivalent longitudinal moduli in inner and outer adherends, respectively.

5. The finite element analysis

The high stress concentrations on the free ends of overlap region have been proven to be responsible for the failure of the adhesively bonding joint. The stresses that cause the failure of joints include the shear stress and transverse normal (peeling) stress in the adhesive layer. Previously one-dimensional model provides simple solution for the shear stress. However, it is unable to determine the transverse normal stress. In the section, a two-dimensional finite element method is employed to determine the transverse normal stress in the adhesive layer.

Reddy [2] analyzing the single-lap joint by finite element method concluded that mesh size and boundary conditions could affect the stress distribution. The results indicated that the finer mesh should be imposed on the high stress gradient area.

The geometric model for the single-lap joint used in the finite element analysis is shown in Fig. 6, and the associated dimensions are as follows:

- $a = 32$ mm;
- overlap length $2l = 16$ mm;

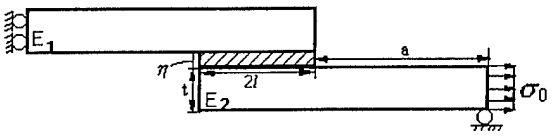

Fig. 6. Boundary conditions and geometric model for the single-lap joint.

- adhesive thickness $\eta = 0.32$ mm;
- adherend thickness $t = 1.6$ mm.

The upper and lower adherends are the same material with the Young's modulus $E_1 = E_2 = 71$ GPa and Poisson's ratio $v = 0.3$. The Young's modulus and Poisson's ratio of adhesive layer are $E_a = 56.5$ GPa and $v_a = 0.33$, respectively. An uniformly distributed stress, $\sigma_0 = 9.81$ MPa, is applied to the right side of the joint, and a roller is deployed to the left side as shown in Fig. 6.

The finite element mesh in the overlap region is shown in Fig. 7, where the four-node isoparametric element is employed. There are six elements and two element through the thickness of adherends and adhesive, respectively. In order to obtain the high stress concentration on the both ends of overlap region, a finer mesh is deployed to these areas as shown in Fig. 7. In the following results, the stresses of adhesive layer are represented by the stresses at the middle nodes in the adhesive layer. To examine the accuracy of the finite element method, the transverse normal stress obtained by present method is compared with the numerical results from Ref. [2] . Both of the results agree very well as shown in Fig. 8.

The numerical results of shear stress in the adhesive layer obtained by the finite element method, are compared with the analytical solution, Eq. (11c), derived in Section 4. The comparison presented in Fig. 9, shows

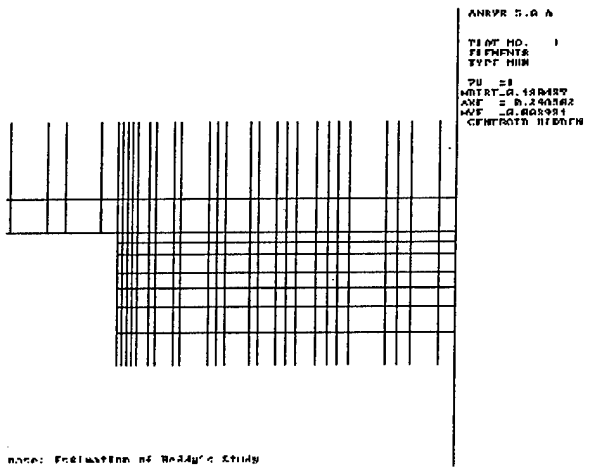

Fig. 7. The finite element mesh in the adhesive region.

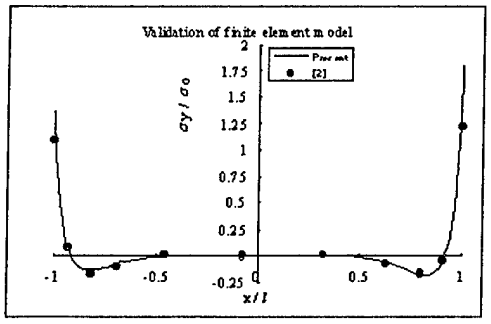

Fig. 8. The validation of finite element model.

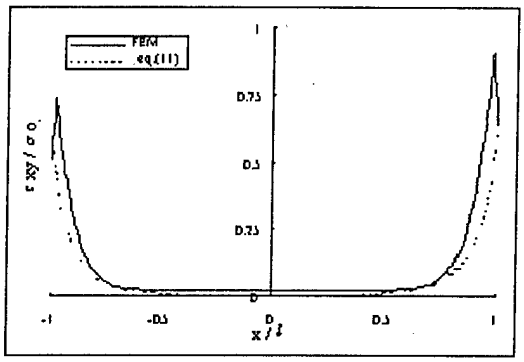

Fig. 9. The shear stress obtained by Eqs. (11a)-(11c) and FEM along the adhesive region for a single-lap joint.

that both results agree well in overall. From these results one can observe:

1. The stress obtained by finite element method is higher than the analytical solution. It may be due to the bending effect caused by the eccentric load which has been ignored in the analytical solution.
2. The result of maximum shear stress in the analytical solution is occurred on both the ends of overlap region. However, the maximum shear stress occurs at a short distance away from the ends in the finite element result.

6. Parametric study

By examining the failure of adhesively bonding joints, the shear stress (τ_{xy}) and normal stress (σ_y) are the most responsible for the failure. In the following parametric study, we focus on the single-lap joints which are utilized mostly.

The parameters that influence the stress distributions in the adhesively bonding region can be classified into two categories. One is called material parameters which includes the adherend material and the shear modulus of the adhesive. The other is called geometric parameters which includes the thickness of the adhesive layer, the thickness of the adherend and the length of overlap.

A single-lap joint with simplified one-dimensional model as shown in Fig. 6 is investigated with respect to the following geometric and material parameters:

1. the adhesive thickness η;
2. the ratio of the thickness between the upper and lower adherend t_o/t_i;
3. adhesive shear modulus: G_a/E (shear modulus of adhesive/Young's modulus of adherend);
4. stiffness ratio: E_1/E_2 (ratio of Young's modulus between upper and lower adherends).

Fig. 10 shows the result of shear stress (τ_{xy}) versus adhesive thickness (η). It indicates that the thinner of the adhesive thickness the higher of the shear stress. Thus, high stress concentration on the free ends of adhesive layer can be reduced by increase of the adhesive thickness.

Fig. 11 depicts the variation of shear stress at the two free ends of adhesive layer versus the ratio of the thickness between upper and lower adherends. The maximum shear stress occurs at the free end of adhesive layer which is near to the side of thinner adherend.

Fig. 12 depicts the results of shear stress varied with the shear modulus of adhesive. It shows that as the shear modulus increases the shear stress increase.

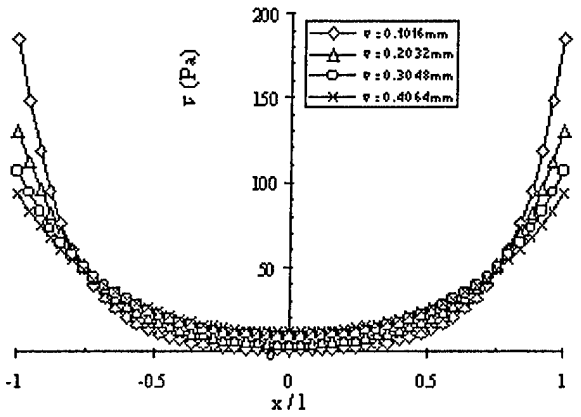

Fig. 10. Shear stress vs adhesive thickness.

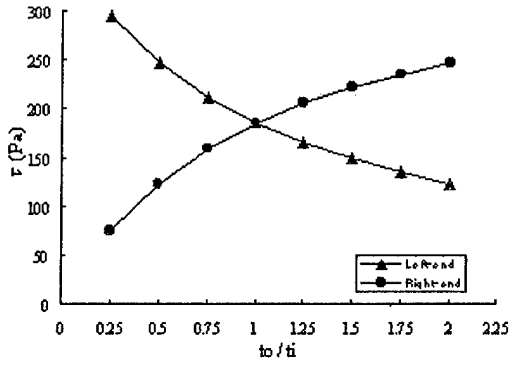

Fig. 11. The thickness at the two free ends vs the ratio of thickness between upper and lower adherends.

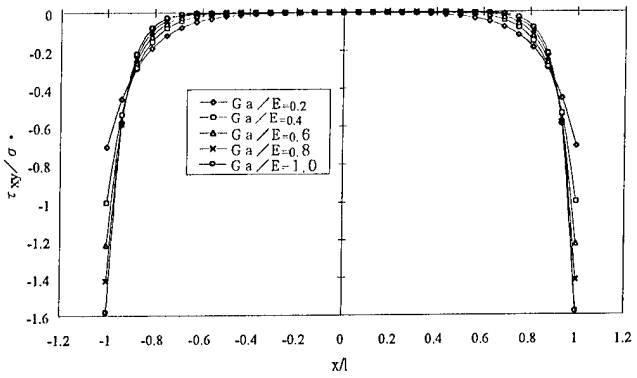

Fig. 12. Shear stress vs adhesive shear modulus.

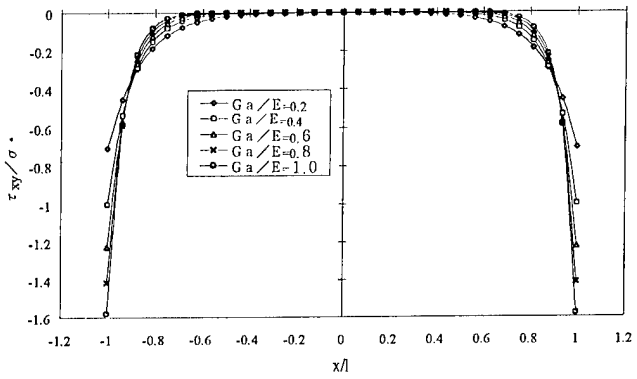

Fig. 13. Shear stress vs ratio of Young's modulus between upper and lower adherend.

When the adhesively bonding joint is used to connect two different adherends, the shear stresses are varied with the ratios of the Young's modulus between these two adherends as shown in Fig. 13. The maximum shear stress occurs at the free end of adhesive region near to the adherend with higher modulus.

7. Conclusions

A simplified one-dimensional approach has been developed to model the adhesive bonding for single-lap joint and double-lap joint. A simply analytical solution is obtained, and compared with the two-dimensional finite element results. Good agreement between these two results demonstrate that present approach can provide a simple but accurate solution which is very useful in joint design.

The effects of varying parameters such as thickness of adhesive and adherend, modulus of adhesive and adherend can be concluded as follows:

1. High stress concentration occurs on the free ends of adhesively bonding region. The shear stress and transverse normal stress in the adhesive layer are responsible for the initiation of the failure of the adhesively bonding joints.
2. Increase of the thickness of the adhesive layer, leads to the lower shear stress in the adhesively bonding region. Thus, thicker adhesive layer is able to improve the strength of the adhesively bonding joint.
3. In the case of two different adherends connected by the adhesive joint, the maximum shear stress occurs at the free end of adhesive region near to the adherend with higher stiffness.
4. As the thickness of adherents is different, the maximum shear stress occurs at the free end of adhesive region near to the thinner adherend.

References

[1] Delate F, Erdogan F. Viscoelastic analysis of adhesively bonded joints. J Appl Mech 1981;48:331–8.
[2] Reddy JN, Roy S. Non-linear analysis of adhesively bonded joints. Int J Non-Linear Mech 1988;23(2):97–112.
[3] William CC. A comparison of numerous lap joint theories bonded joints. J Adhesion 1991;35:55–73.
[4] Richardson G, Crocombe AD, Smith PA. A comparison of two- and three-dimensional finite element analyses of adhesive joints. Int J Adhesion and Adhesives 1993;13(3):193–200.
[5] Chien-Chang L, Yee-Shown L. A finite element model of single-lap adhesive joints. Int J Solids Struct 1993;30(12):1679–92.
[6] Tsai MY, Morton J. An evaluation of analytical and numerical solutions to the single-lap joint. Int J Solids Struct 1994;31(18):2537–63.
[7] Kinloch AJ. Adhesion and adhesives. London: Chapman & Hall, 1987.
[8] Goland M, Reissner E. The stresses in cemented joints. ASME J Appl Mech 1994;11:A17–22.
[9] Hart-Smith LJ. Adhesive-bonded single-lap joints. NASA CR-112236 1973.
[10] Du C, Shun C. An analysis of adhesive-bonded single-lap joints. J Appl Mech 1983;50:109–15.
[11] Yadagiri S, Papi C, Reddy T. Viscoelastic analysis of adhesively bonded joints. Comput Struct 1987;27(4):445–54.
[12] William CC. Two finite elements for modeling the adhesive in bonded configurations. J Adhesion 1989;30:25–46.
[13] Umur Y, Dean PU. Stress analysis of bonded plates and joints. J Engrg Mech Division:1980;37–56.
[14] Umur Y, Dean PU. Bending and Shear Deformation Effects in Lap Joints. J Engrg Mech Division:1981;55–76.
[15] Delale F, Erdogan F, Aydinoglu MN. Stresses in adhesively bonded joints: a closed-form solution. J Comp Mater 1981;15: 249–71.
[16] Chamis CC, Murphy PLN. Simplified procedures for designing adhesively bonded composite joints. J Reinforced Plastics and Composites 1991;10:29–41.
[17] Liyong T. Bond shear strength for adhesive bonded double-lap joints. Int J Solids Struct 1994;31(21):2919–31.

ELSEVIER

Composite Structures 47 (1999) 679–686

COMPOSITE STRUCTURES

www.elsevier.com/locate/compstruct

The active buckling control of laminated composite beams with embedded shape memory alloy wires

Sup Choi [a], Jung Ju Lee [b,*], Dae Cheol Seo [b], Sun Woo Choi [c]

[a] *Agency for Defense Development, P.O. Box 35, Yusung-gu, Taejon 305-600, South Korea*

[b] *Department of Mechanical Engineering, ME3033, Korea Advanced Institute of Science and Technology, 373-1 Kusong-dong, Yusung-gu, Taejon 305-701, South Korea*

[c] *Korea Aerospace Research Institute, P.O. Box 113, Yusung-gu, Taejon 305-333, South Korea*

Abstract

In this paper, the results of an experimental analysis on the active buckling control behaviour of a laminated composite beam with embedded shape memory alloy (SMA) wires are presented. For the purpose of enhancing the critical buckling load, active buckling control was investigated through the use of the reaction time associated with the shape recovery force of SMA wires. An increased critical buckling load and altered deflection shape due to the effects of activation of embedded SMA wires are represented qualitatively and quantitatively on the load–deflection behaviour records. The results obtained from this active buckling control test confirm that the buckling resistance in a composite beam with embedded SMA wires can be increased by the use of an activation force of the embedded SMA wires. Based on our experimental analysis, a new formula for the behaviour control of active buckling in a laminated composite beam with embedded SMA wires is also suggested. © 2000 Published by Elsevier Science Ltd.

Keywords: Shape memory alloy wires; Recovery force; Reactive moment; Cut and paste; Active buckling control; Snapthrough

1. Introduction

The application of laminated composite materials to various engineering structures, such as aircraft, marine and space structures, has increased significantly in recent years because of their inherent highly specific stiffness and strength. Most composite shell structures are thin, and hence their buckling behaviour is a major design consideration for the integrity of thin composite structures. In order to enhance the buckling resistance of these flexible composite structures which are sensitive to buckling, due to initial geometric imperfections caused by variable environments and loading conditions, the use of smart materials such as shape memory alloy (SMA) wires which have high forces over a large strain can be useful. Recently, smart composite structure concepts are receiving a lot of attention for improving the stability of laminated composite structures which are susceptible to buckling [1,2].

In buckling control of a flexible composite structure, the main principle is to maintain the original structural shape in order to avoid buckling. Two types of smart materials are employed for this purpose: piezoelectric materials and SMAs. Firstly, the use of piezoelectric actuators for controlling the buckling behaviour of the composite structures has a limitation because of its inherent characteristics, such as small available strain and force [3]. Secondly, SMAs which are embedded in a composite beam can generate the shape memory effect (SME) which has significant forces [4]. SMAs have good characteristics as actuators, converting thermal energy into mechanical energy as they undergoes their unique phase transformation by temperature change [5,6]. Although there has been considerable research on buckling control using piezoelectric materials, few studies on the buckling control of composite structures with embedded SMA wires have yet been reported. The application of SMA wires to the composite laminated structures started in 1990 [7–9]. Typical research examples are as follows:

Rogers et al. [7] reported that the embedded SMA wires essentially superimpose an additional external compressive load on the composite plate, and his numerical analytical results have shown that the activation of SMA wires embedded in a laminated composite plate alone can cause a buckling of that plate. Therefore, they

* Corresponding author. Tel.: +82-42-869-3033; fax: +82-42-869-3210/5210.

E-mail address: jjlee@sorak.kaist.ac.kr (J.J. Lee).

0263-8223/99/$ - see front matter © 2000 Published by Elsevier Science Ltd.
PII: S0263-8223(00)00053-2

proposed that the adverse buckling effect of SMA should be considered for the safe design of composite structures, when the shape recovery force of SMA is intended for use. Baz et al. [8] performed experiments on active buckling control using a composite beam with embedded SMA wires, which is covered by a sleeve, within the neutral plane of the composite beam. His experimental results showed that the critical buckling load could be increased three times compared to that of a composite beam without SMA wires. However, one noticeable point from his results is the boundary conditions of the specimens in which the embedded SMA wires were fixed to the external supports. It seems that, in his experiments, the effect of embedded SMA wires on the critical buckling load was caused by tension between the SMA strings fixed to the external support, rather than the activation force of the SMA wires itself. Thompson and Loughlan [9] performed an experimental study of the post-buckling behaviour of laminated SMA-composite plates which were fabricated by the insertion of SMA wires through sleeves located within the neutral plain of composite plates. They reported that the buckling behaviour was dependent upon the laminate stacking sequence, because of the influence of thermal effects. Therefore, the foregoing studies mentioned above [8,9] have been restricted to fixing the SMA actuators to external supports and then inserting them in sleeves which are embedded in the composite.

Based on the literature survey, the unique feature and main purpose of this study can be explained as follows: Firstly, the embedded SMA wires used in this study, unlike that of previous studies, is neither fixed to the external support nor inserted into the sleeve in order to confirm the effects of the activation force of SMA wires on the buckling characteristics, as shown in Fig. 1. Secondly, through these experiments and analyses, the pure effect of embedded SMA wires on the buckling behaviour of a composite beam is confirmed and explained qualitatively and quantitatively. Finally, based on the basic analysis of the experimental results, the theoretical formula to account for the effect of SMA wires on the active buckling control behaviour, which is confined to a small deflection prior to the postbuckling of a composite beam, is suggested in this paper.

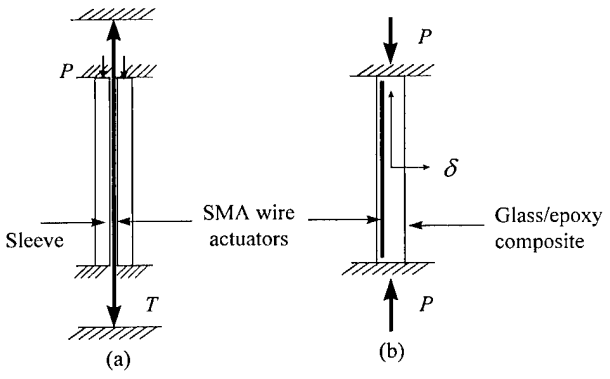

Fig. 1. Models for active buckling control of a composite beam with embedded SMA wires. (a) Model of previous studies [8], (b) model of this study.

2. An analysis of active buckling control behaviour

Although nonlinear analysis is required to strictly investigate the buckling behaviour of the beam for simplicity, we suggest a theoretical formula to show the effect of the SMA wires on the control of active buckling. In order to investigate the effects of the shape recovery force on buckling behaviour in the composite beam with embedded SMA wires (SMA-composite beam), two methods are used: one is the Euler method, which evaluates the buckling response within a small deflection, and the other is the cut and paste method [10] which evaluates the internal stress and displacement field of the SMA-composite beam.

At the model having a length $2l$ and fixed-ends condition, assuming an initial curvature of the beam as shown in Fig. 2, an initial curvature is given by

$$y_0 = \frac{a}{2}\left(1 - \cos\frac{\pi x}{l}\right). \tag{1}$$

When the ends of the beams are not free to rotate during compression, any eccentricities in the application of the compressive forces do not result in the bending of the beam, and a straight beam will undergo only a uniform compression. Hence in the discussion of geometric initial imperfection of beams with fixed-ends, only the initial curvature needs to be considered. The bending moments

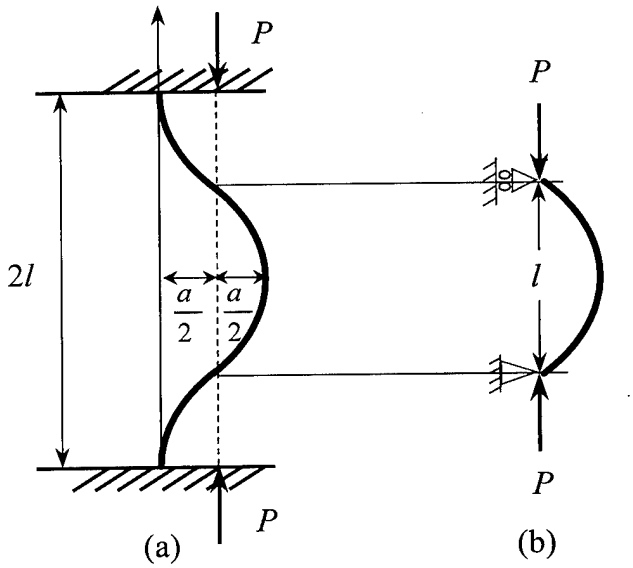

Fig. 2. Analytical model for the active buckling control behaviour with initial geometric imperfections under fixed-ends condition.

under a fixed-ends boundary condition naturally will depend on the shape of the initial curvature of the beam. Therefore, to analyze the slender beam which has fixed-ends, it has been recommended to take the effective length of the beam, which is proposed by Timosenko [11]. By the applied axial compression load, the lateral deflection with the initial imperfection of $a/2$ at the middle of the beam is given by

$$y = \frac{1}{1-\alpha}\frac{a}{2}\left(\sin\frac{\pi x}{l}\right), \tag{2}$$

where α is the ratio of the axial compression load to its critical value.

To understand the cut and paste method, consider the equilibrium state of the SMA-composite beam which is being activated by a flow of current. The idea is to cut the SMA wires separately and then paste the SMA wires into the composite beam. The stress distribution of the SMA wires and the composite beam, into which the SMA wires are pasted, are presented in Fig. 3(b) and (c), respectively. In Fig. 3(b) the SMA wires are contracted by SME. In order to meet the geometric boundary condition, the SMA wires are subjected to tension, P_{SMA}, which does not contribute to the lateral deflection of the composite beam. After pasting the wires into the composite, the composite beam is subjected to an eccentric compressive load to meet the traction free condition for the initial state in Fig. 3(a). In Fig. 3 both the end effect of Saint-Venant's principle and the local nonuniform stress due to the embedded SMA wires having a small volume fraction are neglected, and thus the bending stress is uniformly distributed along the embedding axis. The uniform compressive load P_{SMA} in the composite beam does not have an effect on the buckling behaviour. The resulting shape recovery force of SMA times the distance to the neutral axis of the beam, generates a uniform moment distribution along the embedding axis as shown in Fig. 3(c) and can be expressed simply

$$M_{SMA} = P_{SMA} \times e, \tag{3}$$

where P_{SMA} is the shape recovery force of the SMA wires and e is the offset distance of the embedding wires from the neutral axis. The M_{SMA} is the reactive moments by SMA wires, and the moment distribution along the axial direction of the beam is expressed as a pure bending state. The direction of the M_{SMA} must be carefully considered when analyzing the buckling behaviour of the SMA-composite beam under a fixed-ends condition. Assuming the beam has an initial imperfection as shown in Fig. 2, the moments at the ends and at the middle are always numerically equal and have opposite signs under the fixed-ends boundary condition of the beam. Therefore, the moment by SME for the simply-supported condition is in the opposite direction from that of the fixed-ends condition at the middle.

Consider the model for the SMA-composite beam, as shown in Fig. 4. This beam has a positive lateral deflection at the middle point of the beam. In this, we can equilibrate the fixed-ends beam with length $2l$ with a simply-supported beam with length l, and then obtain the resultant deflection of the beam by superimposition of the reactive moment M_{SMA} upon the deflection due to an axial loading. The lateral deflections, δ_P and $\delta_{M_{SMA}}$, are expressed as Eqs. (4) and (5), respectively.

$$\delta_P = \left(\frac{a}{2(1-\alpha)} - \frac{a}{2}\right), \tag{4}$$

$$\delta_{M_{SMA}} = \frac{M_{SMA}\, l^2}{8EI}. \tag{5}$$

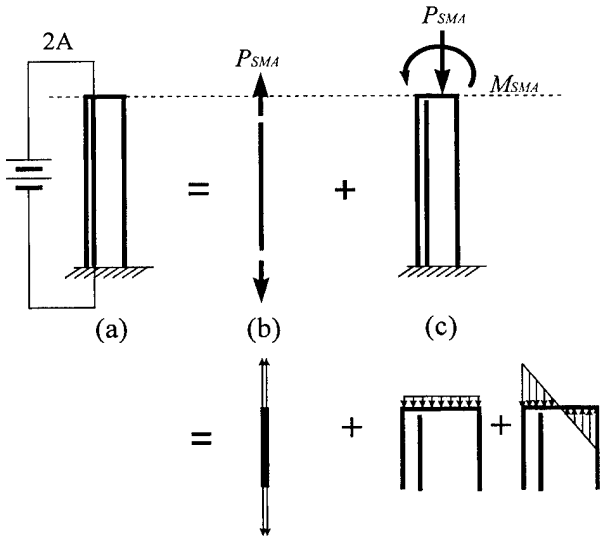

Fig. 3. Analytical model for stress analysis using the cut and paste method.

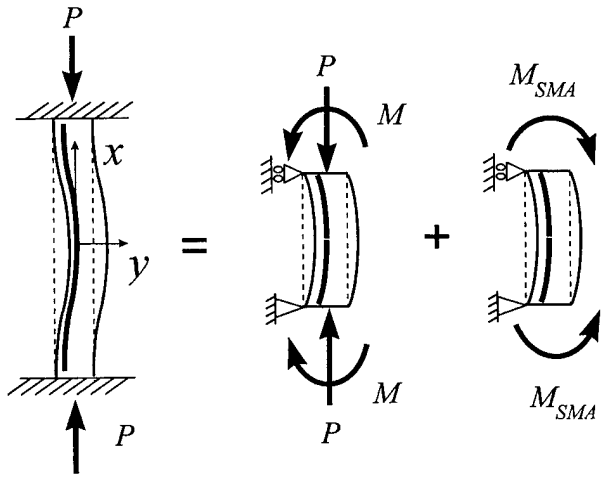

Fig. 4. Effects of the reactive moment, M_{SMA}, on the buckling behaviour with equivalence between fixed-ends conditions of length $2l$, and simply-supported conditions of length l.

The resultant lateral deflection of a composite beam with embedded SMA wires can be expressed simply as Eq. (6), which is confined to a small deflection prior to the postbuckling.

$$\delta = \delta_P - \delta_{M_{SMA}}. \tag{6}$$

In this analysis, the flexural stiffness EI and initial geometric imperfection, a, in Eq. (4) are obtained from the test results. On analyzing the buckling behaviour, the magnitude of the initial curvature is chosen based on the test results so as to compensate not only for the crookedness of the beam but also for eccentricity in application of the load. In order to investigate the reactive moment, M_{SMA}, the initial lateral deflections are adjusted to 0 in comparing the test results which measure the relative deflection from the initial imperfections position. The activation of the SMA wires by the flow of electrical current influences the temperature of the composite beam resulting in a thermal compression load under a fixed-ends condition. It is assumed that the recovery force of the SMA wires varies linearly with the thermal load up to the buckling loads. The shape recovery force, P_{SMA}, is taken as 36 N based on the experimental results.

3. Experimental

3.1. Test specimens

The test specimens were cut from a laminated composite panel fabricated with glass fibre/epoxy matrix prepregs with unidirectional rovings supplied by Sunkyung Industry. The dimensions of the specimens, with embedded SMA wires of 0.38 mm diameter, were 170 mm in length, 23 mm in width and 1.0 mm in thickness. Either the SMA wires or NiCr wires are eccentrically embedded within the middle of a 0° layer of specimens, with the stacking sequence of specimen (A); $[0_4/90]_s$ and specimen (B); $[90/0_4]_s$. The interval between the embedded SMA wires are 4 mm resulting in a volume fraction of 2.78% for the wires, and the offset distance of embedded wires from the neutral axis of specimen (A) and (B) is 0.3 and 0.2 mm, respectively, as shown in Fig. 5(a). The test specimens were designed to have the beneficial effects of a reactive moment by SMA wires, M_{SMA}, for the buckling behaviour. As shown in Fig. 5(b), the optical micrography of test specimen (A) shows that placing SMA wires parallel to the longitudinal axis of the composite laminate is clearly an advantageous position to minimize the problem in the fabrication of test specimens. Table 1 shows the material properties of composite laminates, SMA and NiCr wires, used in these experiments.

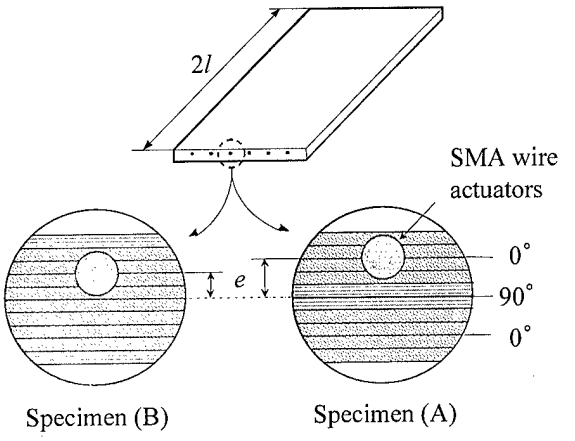

(a)

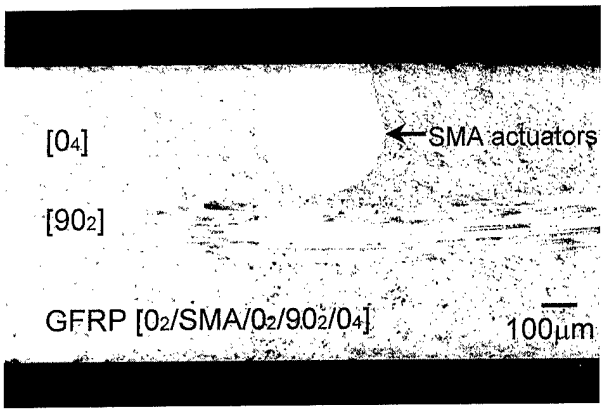

(b)

Fig. 5. Cross-sections of the SMA-composite beam of: (a) the schematic diagram, (b) the optical micrography.

3.2. Active buckling control test

The active buckling control test was performed using the INSTRON tester at a constant loading rate of 0.01 mm/min, and non-contact gap sensors for measuring the lateral deflection under the fixed-ends boundary condition using a specially fabricated jig. The signals from the sensors were first transmitted to a controller on real time to compare with a pre-set lateral deflection, and then the start of activation of the SMA wires was determined. Once the lateral deflection reached pre-set values, δ_{act}, the controller was then linked to a power supplier to provide the flow of current required to drive the SMA wires. From this testing system, the activation force of SMA wires which produced the reactive moment, M_{SMA}, can be generated. Fig. 6 shows an experimental setup for the buckling test used in these experiments. Thermal activation of SMA wires was achieved by applying the flow of electrical current leading to the electrical resistance heating. In order to minimize the thermal effects of SMA wires heated by the flow of current on the

Table 1
Material properties of glass/epoxy composites and wires

	Glass/epoxy		Wires	
			SMA	NiCr
E_1 (GPa)	40.77	Resistance (Ω/m)	10.0	9.8
E_2 (GPa)	11.70			
ν_{12}	0.31	Diameter (mm)	0.38	0.4
G_{12} (GPa)	4.89			

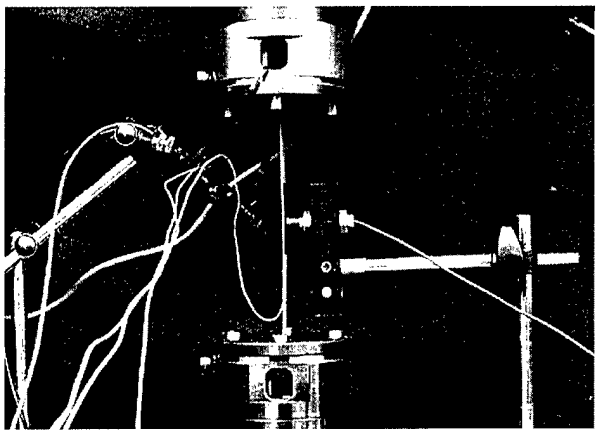

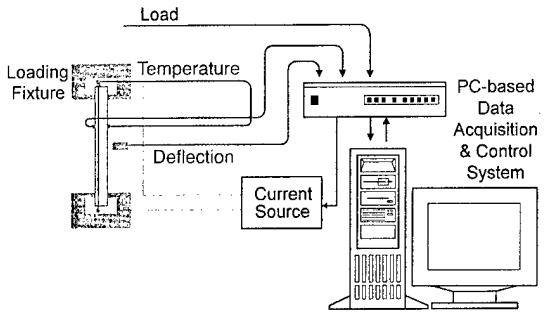

Fig. 6. Experimental setup for the active buckling control tests.

composite beam, it was adopted to employ an impulse current activation within 1–2 s.

4. Results and discussion

Due to the effects of the reaction of SMA embedded M_{SMA}, either the deflection of the beam is considerably reduced, or snapped. This indicates sudden changes in deflection to the opposite direction of the deformed composite beam occurring under the same compression load. These effects are described quantitatively on the load–deflection plots, which show the increment of the critical buckling load and snapthrough in comparison with the buckling behaviour. This is denoted by no activation, as shown in the Figures, since it was subjected to only an external load. The lateral deflection as denoted by δ_{cr} is confined to 1/10 of the thickness of the beam, which is assumed to be a small deflection of the SMA-composite beam, in comparison with the critical buckling loads. The purpose of introducing a composite beam with embedded NiCr wires (a NiCr-composite beam), is to calculate its recovery force by comparing with the SMA-composite beam and to prove whether or not the thermal moment affects buckling behaviour. The dimensions and electrical resistance of NiCr wires are chosen to be almost the same as those of the SMA wires, but the NiCr wires do not have the capability for shape recovery force. While the activation of the SMA wires exert both a thermal force and a shape recovery force on the SMA-composite beam, the activation of NiCr wires exerts only a thermal force on the NiCr-composite beam. The quantity of thermal forces between SMA-composite and NiCr-composite beams can be regarded as an identical value under the same conditions of thermal activation.

4.1. Mechanical characteristics

Prior to the active buckling control test, buckling tests were performed to characterize how the eccentrically embedded wires affect the buckling behaviour. An effort was made to account for the differences in the critical buckling loads between the beams which are reinforced by either SMA or NiCr wires and having different Young's modulus. The critical buckling load depends on the flexural stiffness, EI, which is proportional to the critical buckling loads, P_{cr}. The flexural stiffness of the SMA-composite and NiCr-composite beams increases approximately 8% and 12%, respectively, compared to that of a composite beam without any embedded wires. In this study, we neglect the 4% difference in flexural stiffness between the SMA-composite and NiCr-composite beams because of the negligible effects on the buckling behaviour.

4.2. The characterization of the shape recovery force, P_{SMA}

The shape recovery force depends on many variables, such as pre-strain, volume fraction, temperature, stress, and cycling effects of SMA wires [12–15]. Therefore, an

indirect method is employed to calculate the recovery force, by comparing characteristics of the applied force induced by the flow of current between the SMA-composite and NiCr-composite beams. In order to calculate the recovery force of SMA wires, buckling tests were performed with a fixed-ends condition without an external compressive load, and these results are shown in Fig. 7(a). All compressive stresses are induced by the thermal expansion accompanied by the flow of current through the wires, and these stresses induced by the flow of current caused abrupt buckling of the composite beams. The recovery force of SMA wires, P_{SMA}, can be confirmed from the load–deflection behaviour of two differently fabricated SMA-composite and NiCr-composite beams. This behaviour can be seen in Fig. 7(a), where the load difference between points A and C indicates the reality of the activation force of SMA wires embedded in a composite beam. The quantity of load differences are 32–36 N. The points A and C indicate the states when stopping the activation by the flow of electrical current in SMA and NiCr wires. After stopping activation of the SMA wires the compression load increased, by the gradual decrement of activation force, up to point B which is the cool down state of the SMA wires by natural convection. Path A–B shown in Fig. 7(a) means physically that the activation force of SMA by the flow of current is decaying, because of stoppage of the flow of current from A. There are two opposite forces: the one is a compressive force by thermal heating from SMA wires, and the other is a contraction force in the SMA wires to B, where the thermal expansion force is dominant due to the decaying of the activation force in the SMA wires. Thus, the suppressed deflection of point A by the activation force of SMA returns to point B, where the deflection increases.

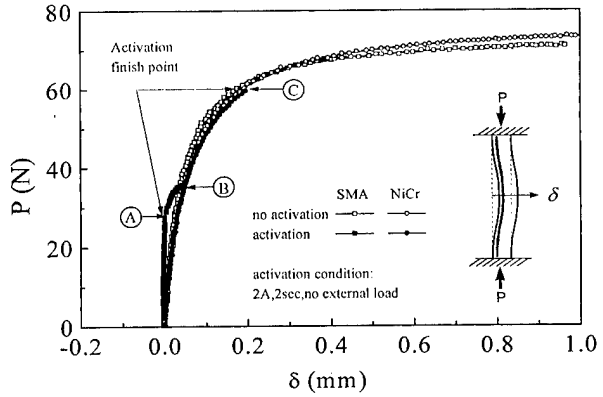

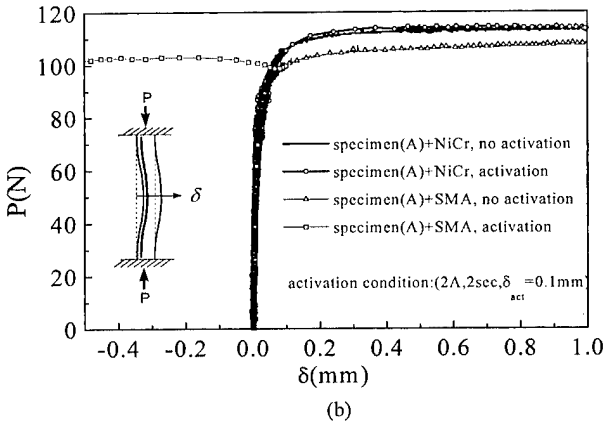

Fig. 7. Buckling behaviours of: (a) the specimen (B) without an external compression load, (b) the specimen (A) after lateral deflection, δ_{act}, when the external compression load has occurred, under activation from both the SMA-composite and the NiCr-composite beams.

4.3. The effects of the reactive moment, M_{SMA}

To check whether there are any other factors, apart from the activation force of embedded SMA wires, which can affect the buckling behaviour, the effects of the moment induced by thermal expansion due to heating of the SMA wires eccentrically embedded were investigated. Therefore, an indirect method is employed to investigate the effects of the reactive moment, M_{SMA}, by comparing characteristics of the buckling behaviours between the SMA-composite and NiCr-composite beams as shown in Fig. 7(b). When we initiate activation at $\delta_{act} = 0.1$ mm of lateral deflection of beams subjected to external compression load, the behaviour of the NiCr-composite beam under activation is the same as load–deflection caused by only the external load. That means the effects of the thermal moment does not contribute to the buckling behaviour of the composite beams. On the other hand, the alteration of the deflection shape of SMA-composite beams occurs, as shown in Fig. 7(b). Therefore, it can be said that the dominant and decisive factor which can influence the buckling behaviour of the SMA-composite beam, is the reactive moment, M_{SMA}, induced by the shape recovery force.

4.4. The effects of the embedding position of SMA wires

In Fig. 8, the results of the buckling test for two different types of specimens are presented to observe how the embedding position of SMA wires affects the active buckling control behaviour. Two types of specimens indicate that the one, case (A), contains SMA wires on the left-hand side of thickness (negative position from the centre), and the other, case (B), at the opposite side, that is, the right-hand side of thickness. Hereafter, the left and right directions indicate the negative and positive sides, respectively. In this test, the activation of SMA wires takes place when the deflection by the external load becomes 0.05 mm ($\delta_{act} = 0.05$ mm). For the case (A), the activation of the embedded SMA wires by the flow of current is beneficial for buckling

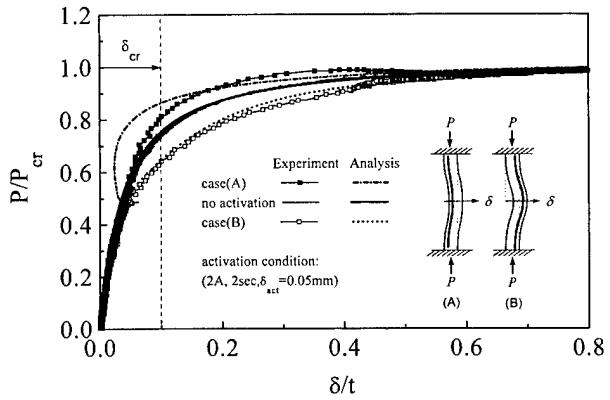

Fig. 8. Comparison of normalized load–deflection curves (specimen (B)) between experimental and analytical results.

resistance resulting in an increased critical buckling load. The embedded SMA wires help the deformed shape of the composite specimen to recover its original position, which results in a 10.8% increment of the critical buckling load around δ_{cr}, as shown in Fig. 8. On the other hand, for the case (B), the activation of the SMA wires embedded is detrimental to buckling resistance. These effects from SMA wires are presented quantitatively in Fig. 8 as load–deflection curve. The increased and decreased buckling loads of cases (A) and (B), respectively, at the deflection, δ_{cr}, are compared in Fig. 8. Based on the above results, it can be said that our analytical result by using Eq. (6) shows a good correlation with the experimental result within small deflection prior to the postbuckling of the SMA-composite beam.

4.5. The effects of an initial imperfection on the buckling behaviour

Fig. 9 shows the effects of the activation force of SMA wires embedded within composite beams, which have different initial imperfections. The initial imperfections, a, are calculated from Eq. 4(a) and these imperfections, a, are then shifted to the original point of Fig. 9 for comparisons with each other. In the cases of the specimens having a large initial imperfection ($a = 0.075$ mm), the activation force of embedded SMA wires increased the buckling load. The increased buckling load in this case can be explained from Eq. (6), where δ_P, having a large initial imperfection, a, is larger than $\delta_{M_{SMA}}$. However, in the case of a small initial imperfection, $\delta_{M_{SMA}}$ is larger than δ_P, which results in negative deflection showing a snapthrough.

4.6. The effects of activation time from SMA wires

Fig. 10 shows the effects of activation time from SMA wires on the active buckling control behaviour of the SMA-composite beams. In the case of a 1 s activation time, about a 20% increment of the buckling load at δ_{cr} was obtained. On the other hand, in the case of a 2 s activation time, a snapthrough from shape deflection occurred because of highly increased M_{SMA} values, as shown in Fig. 10. These results indicate that we can implement active buckling control in composite beams by using the activation force from SMA wires.

4.7. The effects of the activation starting position of deflection

Fig. 11 shows how the starting point in the activation of SMA wires affects the active buckling control behaviour. It also shows the conclusions in comparing experimental results to analytical results, calculated from Eq. (6) for the load–deflection curves. If the initiation deflection points of activation are relatively small, $\delta_{act} = 0.025$ mm, the activation of SMA wires result in a snapthrough. Both the analytical and experimental results show snapthrough of the SMA-composite beams due to M_{SMA} when the SMA wires are activated.

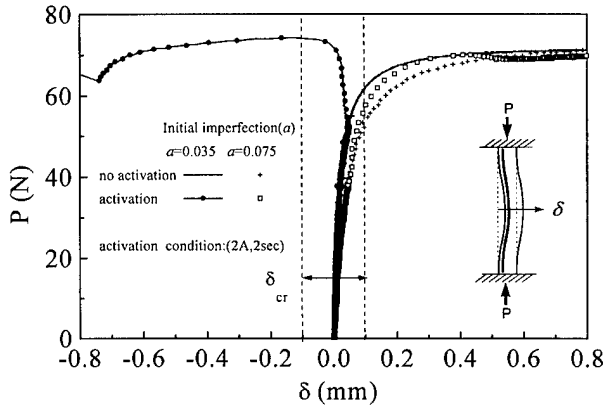

Fig. 9. Load–deflection curves for the SMA-composite beam (specimen (B)) with different initial imperfections.

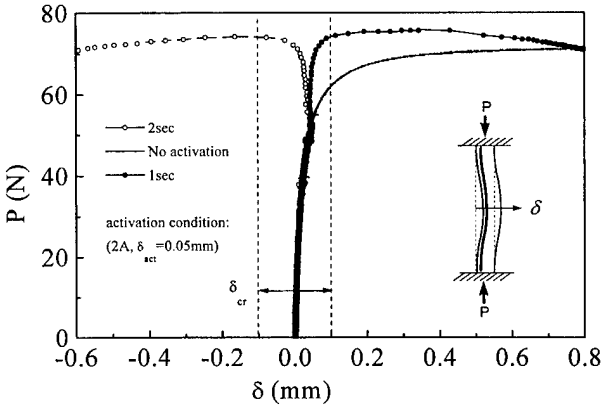

Fig. 10. Load–deflection curves for the SMA-composite beam (specimen (B)) with different activation times for the SMA wires.

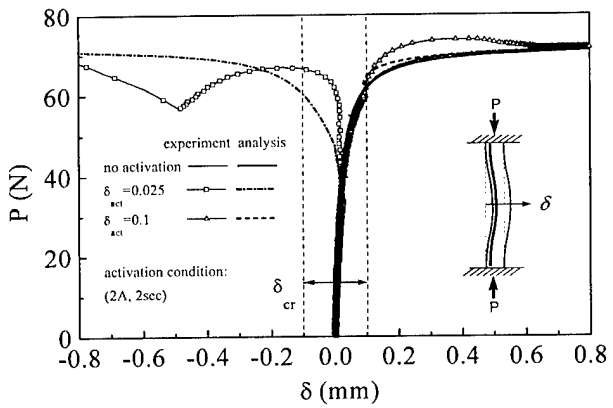

Fig. 11. Comparison between experimental and analytical results for the load–deflection curves of the SMA-composite beam (specimen (B)) with different activation starting positions before deflection.

However, in the case of a relatively large deflection, $\delta_{act} = 0.1$ mm, an increased buckling load is observed without snapthrough. From these results, it can be said that the analytical results by using Eq. (6) show a good correlation with the experimental results. Furthermore, the analytical formula can positively describe the active buckling control behaviour of the SMA-composite beams within a small deflection, which is either incremental of the buckling load or a snapthrough.

5. Conclusions

In this paper, an experimental study on the active buckling control of a laminated composite beam was performed with test specimens with eccentrically embedded SMA wires along the axial direction. From these results, the following conclusions were obtained:

1. An increment of buckling load or snapthrough observed in the active buckling control behaviour of the SMA-composite beams using a reactive moment induced by an activation force of SMA wires. These results confirm that SMA wires can be used for the buckling control of laminated composite beams which were subjected to mechanical loading and then exposed to an elevated temperature which influences phase transformation of SMA wires.
2. The new formula, which can describe the active buckling control behaviour of laminated composite beams with embedded SMA wires, is suggested based on both the Euler equation and cut and paste methods. This model, which is confined to a small deflection prior to the postbuckling, shows good agreement with the experimental results.

References

[1] Thompson SP, Loughlan J. The active buckling control of some composite column strips using piezoceramic actuators. Comp Struct 1995;32:59–67.
[2] Loughlan J. The buckling of composite stiffened box sections subjected to compression and bending. Comp Struct 1996;35:101–16.
[3] Meressi T, Paden B. Buckling control of a flexible beam using piezoelectric actuators. ASME J Guidance, Control Dynam 1993;16:977–80.
[4] Sun G, Sun CT. Bending of shape-memory alloy-reinforced composite beam. J Mater Sci 1995;30:5750–4.
[5] Gandhi MV, Thompson BS. Smart material and structures. London: Chapman and Hall; 1992.
[6] Perkins J. Shape memory effects in alloys. New York: Plenum Press; 1975.
[7] Rogers CA, Liang C, Jia J. Structural modification of simply-supported laminated plates using embedded shape memory alloy fibers. Comput Struct 1991;38:569–80.
[8] Baz A, Ro J, Mutua M, Gilheany J. Active buckling control of reinforced composite beams. In: Proceedings of the ADPA/AIAA/ASME/SPIE Conference on Active Materials and Adaptive Structures, 1992:167–175.
[9] Thompson SP, Loughlan J. Adaptive post-buckling response of carbon fiber composite plates employing SMA actuators. Comp Struct 1997;38:667–78.
[10] Suo Z, Hutchison JH. Interface crack between two elastic layers. Int J Fracture 1990;43:1–18.
[11] Timoshenko S, Gere J. Theory of elastic stability. Englewood Cliffs, NJ: McGraw-Hill; 1963.
[12] Shaw JH, Kyriakides S. Thermomechanical aspects of NiTi. J Mech Phys Solids 1995;43:1243–81.
[13] Brison LC, Huang MS. Simplifications and comparisons of shape memory alloy constitutive models. J Intell Mater Syst Struct 1996;7:108–14.
[14] Friend CM, Morgan N. The actuation response of model SMA hybrid laminates. J Phys IV 1995;5:415–20.
[15] Liang C, Rogers CA. One-dimensional thermomechanical constitutive relations for shape memory materials. J Intell Mater Syst Struct 1990;1:207–34.

ELSEVIER

Composite Structures 47 (1999) 687–690

COMPOSITE STRUCTURES

www.elsevier.com/locate/compstruct

The mechanical performance of 3D woven sandwich composites

M.K. Bannister [a,*], R. Braemar [b], P.J. Crothers [c]

[a] *Cooperative Research Centre for Advanced Composite Structures Ltd. (CRC-ACS), 506 Lorimer Street, Fishermens Bend, Vic. 3207, Australia*
[b] *Department of Aerospace Engineering, RMIT University, 226 Lorimer Street, Fishermens Bend, Vic. 3207, Australia*
[c] *ASTA Components, 226 Lorimer Street, Fishermens Bend, Vic. 3207, Australia*

Abstract

Composite sandwich structures were manufactured from a 3D woven fabric consisting of two face fabrics interconnected by pile yarns (Distance Fabric). Specimens were produced from Distance Fabric (DF) consolidated with vinyl ester resin with and without a polyurethane foam core and compared to specimens produced from a precast polyurethane foam core with composite skins added separately. Flatwise compression, edgewise compression, climbing drum peel and flexure tests were conducted and all demonstrated a dramatic improvement in properties from the combination of DF and foam core. These improvements are postulated to arise from the mutual reinforcement of the pile yarns and foam core. © 2000 Elsevier Science Ltd. All rights reserved.

Keywords: Sandwich structure; Distance Fabric; Textiles; Flexure; Compression; Foam core

1. Introduction

Sandwich construction, producing two structural composite faces separated by a light-weight honeycomb or foam core, has been one of the most traditional and successful structural designs using composite materials due to the advantage of a dramatically increased stiffness to weight ratio when compared to other materials. However, the manufacture of conventional sandwich structures usually consists of the strengthening skins being adhesively bonded to the foam or honeycomb core. This can be a costly process due to the requirement for the manufacture to take place in several stages; machining of the core followed by the lay-up and bonding of the skins. There also is the difficulty of obtaining a strong bond line between the skin and the core, which can often lead to reductions in performance or failure of the component when subjected to impact conditions.

The development of advanced textile technology has made it possible to manufacture 3D woven structures which can be used to reinforce polymer matrices [1]. Integrally woven sandwich structures, or Distance Fabrics (DF), in which the core is directly interwoven with the skins through vertical pile yarns (Fig. 1), has been produced commercially for a number of years and has been shown to give improved mechanical performance [2–7]. However, the commercial use of these materials has been limited due to difficulties in developing a cost-effective, automated, manufacturing process utilising these fabrics. Recent work at the Cooperative Research Centre for Advanced Composite Structures (CRC-ACS) has lead to a significant breakthrough in the development of a manufacturing technique that can produce good quality sandwich structures from DF in a highly automated process (Fig. 2). This technique also allows the incorporation of extra structural skins as well as a foam core in a one-step consolidation process that could lead to significant cost benefits.

This paper presents the results of a number of mechanical tests that were performed on composite sandwich structures manufactured using this technique. The specimens were manufactured from E-glass DF with and without a polyurethane foam core and compared to sandwich specimens made from precast polyurethane cores and E-glass fabric skins.

2. Materials and experiments

The test specimens were manufactured from DF obtained from Vorwerk GmbH and was designated TechnoTex 13822. This was an E-glass DF and had a fabric weight of 1400 g/m^2 and a fully extended

* Corresponding author. Fax: +61-3-9646-0583.
E-mail address: mbcrcas@ozemail.com.au (M.K. Bannister).

0263-8223/99/$ - see front matter © 2000 Elsevier Science Ltd. All rights reserved.
PII: S0263-8223(00)00035-0

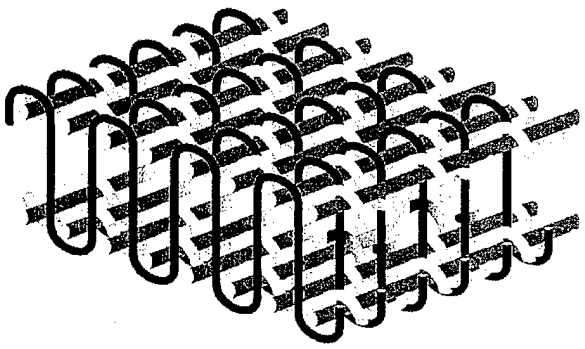

Fig. 1. Illustration of DF showing fabric skins connected by vertical yarns.

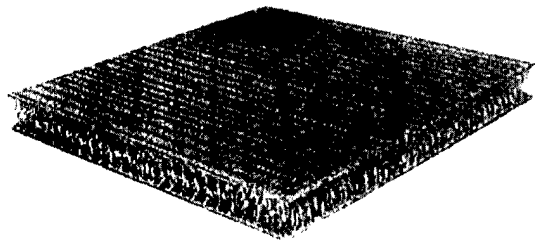

Fig. 2. Sandwich structure manufactured with DF and noncrimp skins.

sandwich height of approximately 25 mm. The fabric was consolidated in a liquid moulding process with Derakane 411-350 vinyl ester resin, with Andonox catalyst, using the proprietary CRC-ACS technique. The samples were postcured for 4 h at 40°C to fully cure the vinyl ester.

Specimens consisting only of the consolidated DF were manufactured in this way to examine the performance of the DF alone (specimens referred to as DF). To investigate the performance of the DF material with a foam core some of the cured specimens were filled with a Type G rigid polyurethane foam (specimens referred to as DF + PU). Foam densities obtained were on an average 100 kg/m^3. Specimens were also manufactured from precast blocks of polyurethane foam of similar density to which was added E-glass fabric skins comparable to the areal weight and weave architecture of the DF skins (specimens referred to as SW). The skins of the specimens were consolidated directly onto the core through a resin infusion process with the Derakane 411-350 vinyl ester resin. These specimens were produced to compare the performance of the two types of DF specimens against a similar, traditional sandwich structure.

A number of tests relevant to sandwich structures were performed in order to characterise the mechanical performance of the DF sandwich specimens (all samples were, on an average, 25 mm high). These tests were Flatwise Compression (ASTM C 365-94), Flexure (3-point bend) (ASTM 393-62), Climbing Drum Skin Peel (ASTM D 1781-93) and Edgewise Compression (ASTM C 643-94).

3. Experimental results and discussion

3.1. Flatwise compression

The test samples for flatwise compression were 100 mm × 100 mm and the results of the tests are shown in Fig. 3. The DF and SW samples were found to have comparable compression strengths, however, the combination of the DF and the polyurethane core produced strengths almost 4.5 times higher. This result was much greater than the simple addition of the two separate strengths and showed that there is a synergistic effect of the material combination.

The DF samples failed through buckling of the pile yarns. These yarns flexed significantly before matrix cracking was heard, following which the yarns began to fail catastrophically leading to complete sample failure. The foam samples failed through a crushing of the foam cells with flecks of foam falling from the specimen. Failure of the DF + PU samples was first observed in the foam with small cracks forming and flecks of foam falling from the specimen. Buckling of the pile yarns was observed but at a much higher load than the DF samples, leading to the conclusion that the presence of the foam was supporting the pile yarns against buckling. Following buckling, matrix cracking occurred in the pile yarns, followed by yarn failure and final specimen failure.

3.2. Flexure

The 3-point bend tests were conducted to determine the shear characteristics of the various samples and the results are presented in Fig. 4. The specimen dimensions (180 mm long × 50 mm wide × 25 mm high) were chosen to try and ensure that the specimens failed by shear failure of the core. This type of failure occurred in

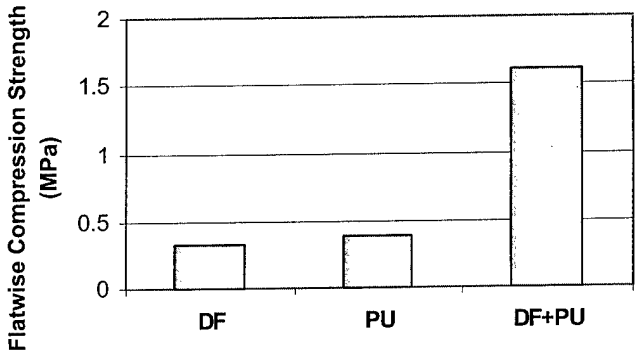

Fig. 3. Flatwise compressive strength.

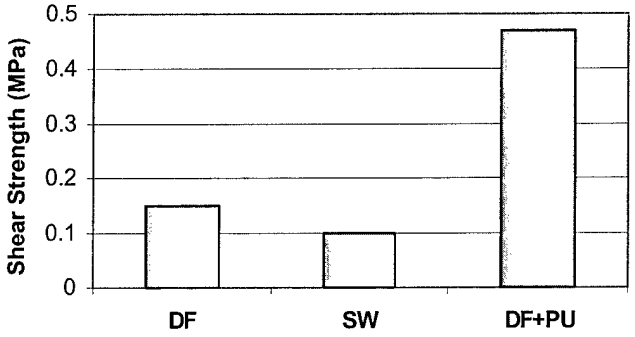

Fig. 4. Shear strength measured in 3-point bend.

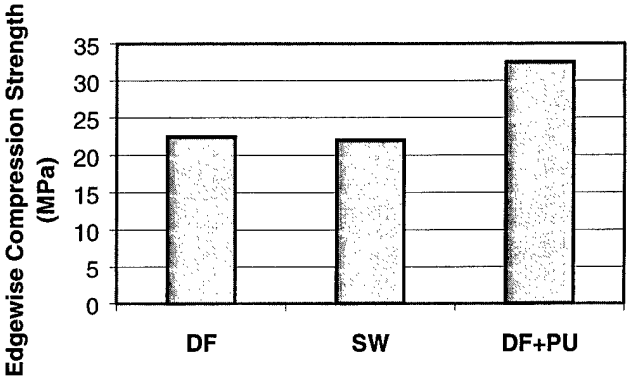

Fig. 5. Edgewise compressive strength.

the DF and SW specimens but the DF + PU specimens were observed to fail in the compressive surface skin, therefore, the true core shear failure strength for this specimen would be higher than the measurement given here.

It is clear from the data in Fig. 4 that the combination of the DF and the polyurethane core again leads to a dramatic improvement in the flexural properties of the sandwich specimens, far greater than the performance of the individual components. Again it is thought that the presence of the foam supports the pile yarns and prevents them from collapsing under the action of a shear force. Similarly, the presence of the pile yarns stiffens and strengthens the foam, preventing failure from occurring at low shear loads. The shear performance due to the DF component of the specimens is also thought to be helped by the fact that the pile yarns are not completely vertical. These yarns tend to have an equal distribution of "S" & "Z" shapes oriented in the length direction of the test specimens which is a result of the weaving technique used to manufacture the raw DF itself. These curvatures in the pile yarns would tend to prevent shear failure to a larger degree than specimens with completely vertical pile yarns.

3.3. Climbing drum peel

The climbing drum peel test specimens had overall dimensions of 76 mm width and 300 mm length with 25 mm long grip areas machined into the specimens (as per ASTM specifications). The results of these tests were mixed. The SW specimens all failed in the appropriate manner with the skin being cleanly peeled off the polyurethane core at an average peel load of 21 kg. The DF specimens resisted any attempts to peel the skin away, instead of peeling the samples bent and folded around the test drum. In order to obtain relevant results it would be necessary to stiffen the back face in order to resist the specimen bending. The DF + PU specimens produced varied results. Of the four specimens tested, two resisted peeling and failed in a similar manner to the DF samples. The remaining two specimens peeled over a small length (approximately 10 mm) at average loads of 250 and 175 kg, respectively, but this load increased as the peel continued until the specimen was eventually pulled out of the rig.

Although it is not possible to make absolute comparisons between the different types of specimens based upon these results, it is obvious that the presence of the pile yarns in the DF and DF + PU samples has dramatically increased the peel resistance of the sandwich structures compared to a conventional structure. Further testing with improved specimens are needed before strict comparisons can be made.

3.4. Edgewise compression

The specimens for edgewise compression were identical to those used for flatwise compression and the results are shown in Fig. 5. Both the DF and SW samples failed at similar stresses and both failed by cracking of the faces in the centre of the gauge section with the faces of the SW specimen also delaminating slightly from the core. These data suggest that the presence of the pile yarns in the DF specimens provides a similar level of support against buckling of the faces as the foam core in the SW specimens. The DF + PU samples failed at stresses 40% greater than that carried by the DF samples, again with the faces cracking in the centre of the gauge section. It is not clear why this increase in failure stress was observed but the results again demonstrate the benefits of combining a foam core with DF to achieve a sandwich structure with improved mechanical performance.

4. Conclusions

A proprietary manufacturing process has been developed at the CRC-ACS that allows high quality composite sandwich structures to be produced using DF materials. This manufacturing technique also allows the incorporation of extra structural skins as well as a foam core in a one-step consolidation process that could lead

to significant cost benefits when compared to traditional methods of forming sandwich structures.

Specimens of 25 mm high DF were consolidated with vinyl ester resin using this process, following which, half of the specimens were filled with a polyurethane foam core. Specimens were also manufactured from precast polyurethane cores that had composite skins added to the face through a liquid moulding process. These skins had comparable properties to the DF skins.

Flatwise compression, edgewise compression, climbing drum peel and flexure tests were carried out on all three specimen types and the results clearly showed significant improvements in performance through the combination of the DF and the foam core. This improvement is thought to be due to the mutual reinforcement of the core and pile yarns, where the core is supporting the pile yarns from buckling or shearing and the pile yarns generally stiffen and strengthen the foam core.

Further work is needed to evaluate the mechanical performance of these materials, in particular, the impact performance and peel resistance, but these initial results clearly demonstrate the potential of these materials to produce composite sandwich structures with dramatically improved performance.

References

[1] Arendts FJ, Drechsler K, Brandt J. Manufacturing and mechanical performance of composites with 3D woven fiber reinforcement. In: Proceedings of the 38th International SAMPE Symposium, 1989. p. 2118.

[2] Verpoest I, Ivens J, Willem van Vuure A, Efstratiou V. Research in textile composites at K.U. Leuven. Fiber-Tex 1992 – NASA Conference Publication 3211, 1993. p. 49–68.

[3] Verpoest I, Ivens J, van Vuure AW, Meerding K. Survey of intermediate pile length 3D sandwich fabric composites. In: Proceedings of the 38th International SAMPE Symposium, 1993. p. 1710 19.

[4] Verpoest I, Wevers M, Ivens J, De Meester P. 3D fabrics for compression and impact resistant composite sandwich structures. In: Proceedings of the 35th International SAMPE Symposium, 1990. p. 296–305.

[5] Zic I, Ansell MP, Newton A, Price RW. Mechanical properties of composite panels reinforced with integrally woven 3D fabrics. J Text Inst 1990;81(4):461–79.

[6] Preller T, Brandt J, Drechsler K. Manufacturing and mechanical properties of new textile fibre preforms for structural sandwich applications. In: Textiles in composite building construction, Part 3, 1990. p. 307–17.

[7] Nakatani T, Nakai A, Fujita A, Egami M, Hamada H. Mechanical behaviour in glass 3D woven fabric composites. In: Proceedings of the Fourth Japan International SAMPE Symposium, 1995. p. 1473–78.

ELSEVIER

Composite Structures 47 (1999) 691–694

COMPOSITE STRUCTURES

www.elsevier.com/locate/compstruct

Application of thermodynamic calculation in the in-situ process of Al/TiB_2

N.L. Yue, L. Lu *, M.O. Lai

Department of Mechanical and Production Engineering, National University of Singapore, 10 Kent Ridge Crescent, 119260 Singapore, Singapore

Abstract

A thermodynamic model describing the formation of in-situ TiB_2 reinforced Al metal matrix composite (MMC) has been established. Based on thermodynamic principles, the Gibbs free energies of formation of TiB_2, AlB_2, and Al_3Ti were evaluated. Experimental investigation was carried out to verify the validity of the thermodynamic model. KBF_4 and K_2TiF_6 were used to synthesize in-situ particulates in molten Al at different temperatures. X-ray diffraction was employed to characterize the formation of different phases in the composite. © 2000 Elsevier Science Ltd. All rights reserved.

Keywords: Thermodynamic calculations; In-situ TiB_2; Al based composites; Gibbs free energy

1. Introduction

Al based composites reinforced by hard ceramic particles have become more and more attractive in the research of structural composites. The addition of ceramic particles such as TiB_2, SiC or Al_2O_3 to an Al based matrix does not considerably change the density of the material but instead it usually leads to a significant rise in specific strength and modulus of the composite. This improvement in strength-to-weight ratio of the composite plays a key role optimizing as weight-saving material for use in structural applications. Several fabricating techniques for such materials have been introduced and developed in the past. The feasible techniques include reactive gas injection (RGI), salt–metal reactions, XD process, reactive sintering, powder metallurgy (P/M) and mechanical alloying (MA).

In spite of many processing techniques developed, mechanisms of the reactions that occur in the process are not well understood. For example, in Al–Ti–B system, several different reactions have been proposed between Al, Ti and B. Maxwell and Hellawell [1] suggested a ternary peritectic reaction of L (liquid) + Al_3Ti + TiB_2 → (Al) above 665°C and a ternary eutectic reaction of L (liquid) → (Al) + Al_3Ti + TiB_2 below 659°C.

Abdel Hamid and Durand [2] proposed two transition reactions of $L + Al_3Ti \rightarrow (Al) + TiB_2$ and $L + TiB_2 \rightarrow (Al) + AlB_2$ to occur within the temperature range of 659–665°C. Thermodynamic calculation [3] has consistently shown the presence of compound phases of AlB_2, TiB_2, Al_3Ti and mixed boride phase of $(Al, Ti)B_2$. Most of the studies on Al based metal matix composites (MMCs) reinforced by TiB_2 were limited to experimental investigations. There is a long traditional debate [4–16] on whether AlB_2 and TiB_2 exist as two separate phases or as a continuous series of solid solution of the form $(Al,Ti)B_2$. Although several investigators [9–16] have reported that AlB_2 and TiB_2 can coexist together. Both AlB_2 and TiB_2 exhibit the same crystal structures and have lattice parameters that are very similar. Al_3Ti was also discovered among component phases when the mixture of salts and Al were heated up to 850°C and held for 35 min. As the reaction duration increased, the amount of Al_3Ti decreased [17]. In the present study, an alternative theoretical method is formulated to evaluate the change in Gibbs free energy. The calculated results have been successfully verified by the experimental investigation.

2. Theoretical formulation

In general, excess free energy, ΔG has been used to determine the possibility of a reaction. The free energy of a system at a temperature, T, can be written as

* Correspondent author. Tel.: +65-874-2236; fax: +65-779-1459.
E-mail address: mpeluli@nus.edu.sg (L. Lu).

0263-8223/99/$ - see front matter © 2000 Elsevier Science Ltd. All rights reserved.
PII: S0263-8223(00)00037-4

$$\Delta G = \Delta H - T\Delta S, \tag{1}$$

where ΔH and ΔS are respectively the changes in enthalpy and entropy of two states.It can be seen from Eq. (1) that ΔG is only a function of temperature. However, as ΔG is also dependent on the concentration of the reactants, the influence of composition on the reaction must be taken into consideration. Consider the following reaction:

$$n_1A_1 + n_2A_2 \rightarrow n_3A_3 + n_4A_4, \tag{2}$$

where n_i is the weight of composition A_i. For the reactant, n_i is negative; while for the product, positive.

In the reaction, ΔG in a reaction may be expressed as

$$\begin{aligned}\Delta G_{T,P} &= \Delta G^{\circ}_{T,P} + \sum_i n_i RT \ln \alpha_i \\ &= \Delta G^{\circ}_{T,P} + \sum_i n_i RT \ln \chi_i + \sum_i n_i RT \ln \gamma_i,\end{aligned} \tag{3}$$

where $\Delta G^{\circ}_{T,P}$ is the standard free energy, χ_i, the molar concentration of the component i in the solution, and γ_i is the activity coefficient of component i. From Eq. (3), it can be seen that if γ_i is known, the free energy $\Delta G_{T,P}$ of the reaction in Eq. (2) can be calculated. Lupis [18] has presented a feasible method to estimate the activity coefficient γ_i. In this study, this method has been applied to the reaction of salts KBF_4 and K_2TiF_6 in the molten aluminum. While Eq. (1) is only limited to cases in which reactants are stoichiometrically mixed together, Eq. (3) can widely be used in every case. The reason is that ΔG is not only dependent on temperature, but also on the concentration of the component, especially for liquid solution. Based on Lupis method [18], the concepts of first order interaction coefficient ε and second order interaction coefficient ρ were introduced to interpret how concentration affects the excess free energy as well as activity by using the central atom model [19] of a metallic solution which is limited to qualitative interpretation of the results. The central atom model assumes that forces between atoms are short range, and neglects the effect of non-nearest neighbors. This assumption of short range forces appears realistic for metallic solutions whether or not one or more neighboring atom shells are being considered. The activity of the solution can be obtained by summation of the contributions of each atom in the solution. Assume Z to be the coordination number, namely, the number of atoms in the nearest-neighboring shell. $\ln \gamma_B^{\infty}$ represents essentially the contribution to the activity of a B atom surrounded by Z atoms of A. Choosing a reference energy state for any central atom to correspond to a nearest-neighbor shell, ε_B^B represents the contribution of a configuration which has a central atom B surrounded by a B atom and $(Z-1)$ A atoms. If B is surrounded by a C atom and $(Z-1)$ A atoms or if C is surrounded by a B atom and $(Z-1)$ A atoms (Fig. 1), ε_B^C should be identical to ε_C^B, namely

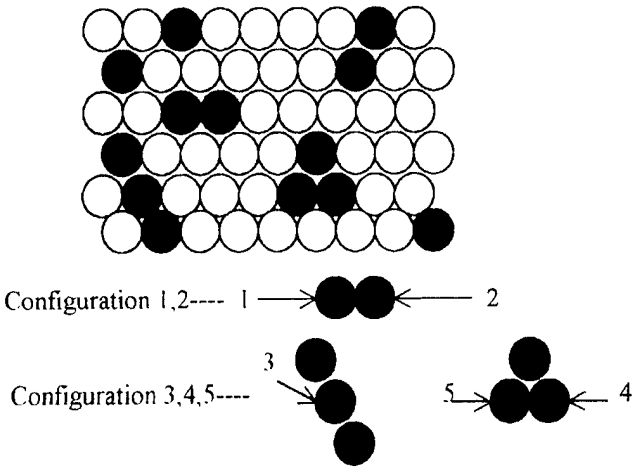

Fig. 1. Illustration of central atom model. Configuration 1 corresponds to ε_B^C , 2 to ε_C^B, 3 and 4 to $\rho_B^{B,C}$, and 5 to ρ_C^B.

$$\varepsilon_C^B = \varepsilon_B^C. \tag{4}$$

ρ is used to describe the second order activity coefficient when one solute atom interacts with two other solute atoms. For example, $\rho_B^{(B,C)}$ is used to describe the contribution of a B atom surrounded by a B atom, a C atom, and $(Z-2)$ A atoms. Some of these configurations entail the presence of a C atom surrounded by two B atoms and $(Z-2)$ A atoms. Based on Gibbs–Duhem equation, the relationship between $\rho_B^{(B,C)}$ and $\rho_C^{(B)}$ can be formulated as follows:

$$\rho_B^{(B,C)} + \varepsilon_C^B = 2\rho_C^{(B)} + \varepsilon_B^B. \tag{5}$$

The key to solve Eq. (3) is to calculate the activity coefficient γ_i. Lupis and Elliot [20] introduced a creative approach to calculate γ_i according to Taylor Series equation

$$\begin{aligned}\ln \gamma_i = \ln \gamma_i^{\circ} &+ \sum_{j=2}^{N} \varepsilon_i^j \chi_j + \sum_{j=2}^{N} \rho_i^j \chi_j^2 + \sum_{j=2}^{N}\sum_{k=j}^{N} \rho_i^{j,k} \chi_j \chi_k \\ &+ O(\chi^3),\end{aligned} \tag{6}$$

where ε_i^j is the first order interaction coefficient among the components, and ρ_i^j, $\rho_i^{j,k}$ are the second order interaction coefficients among component units and can be expressed as follows:

$$\varepsilon_i^j = \left(\frac{\partial \ln \gamma_i}{\partial \chi_i}\right)_{X\text{solvent}\rightarrow 1}, \tag{7}$$

$$\rho_i^j = \frac{1}{2}\left(\frac{\partial^2 \ln \gamma_i}{\partial^2 \chi_j}\right)_{X\text{solvent}\rightarrow 1}, \tag{8}$$

$$\rho_i^{j,k} = \frac{1}{2}\left(\frac{\partial^2 \ln \gamma_i}{\partial \chi_j \partial \chi_k}\right)_{X\text{solvent}\rightarrow 1}. \tag{9}$$

In addition, γ_i° is the activity coefficient of component i under standard state.

3. Experimental procedures

A mixture of potassium hexafluorotitanate (K_2TiF_6) and potassium tetrafluoroborate (KBF_4) salts was heated to 250°C for 1 h before being added to molten Al. Two batches of Al were melted at 1023 and 1123 K. In the molten state, the salt mixture was slowly added, and stirred for 10 min followed by holding for another 25 min. During the synthesizing process, protective argon gas was constantly introduced into crucible. The cast samples were cut for X-Ray diffraction analysis.

4. Results and discussion

Figs. 2 and 3 show the XRD diffraction spectra of the two batches of in-situ MMCs reacted at 1023 and 1123 K, respectively. It can be seen that TiB_2 and Al_3Ti have been formed after the reaction. Since diffraction peaks for Al_2B fully overlap with those of TiB_2, it is not possible to differentiate them. Besides the formation of TiB_2 and Al_3Ti, some traces of TiB can also be observed. To evaluate relative amounts of compound formed during the reactions, relative intensity of XRD spectra, D, is evaluated

$$D_i(\%) = \frac{I_i}{I_i + I_j + I_k}(\%), \tag{10}$$

where I_i is the intensity of compound i. Three typical peaks from Al (1 1 1), TiB_2 (1 0 0) and Al_3Ti (1 1 2) are used for the evaluation.

At the high temperature, both K_2BF_6 and KBF_4 would decompose. The elements K and F decomposed from the two salts would form slag floating on top of the Al melt. While the metallic melt is supposed to be Al–Ti–B ternary system. Since the designed fraction of TiB_2 is very low, the system can be approximated to be a dilute solution consisting of Al as the solvent, and Ti

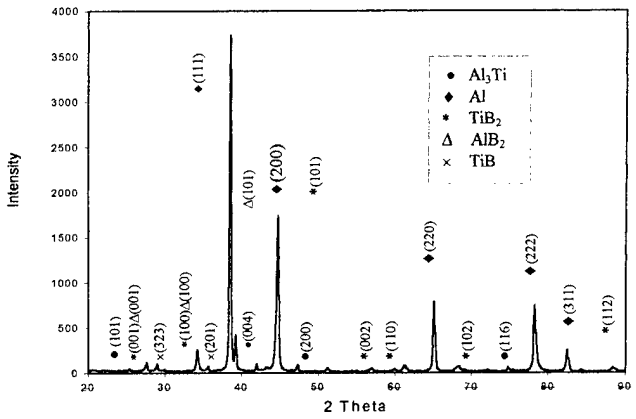

Fig. 2. Results of the XRD of Al/TiB_2 composite prepared by in-situ process at 750°C.

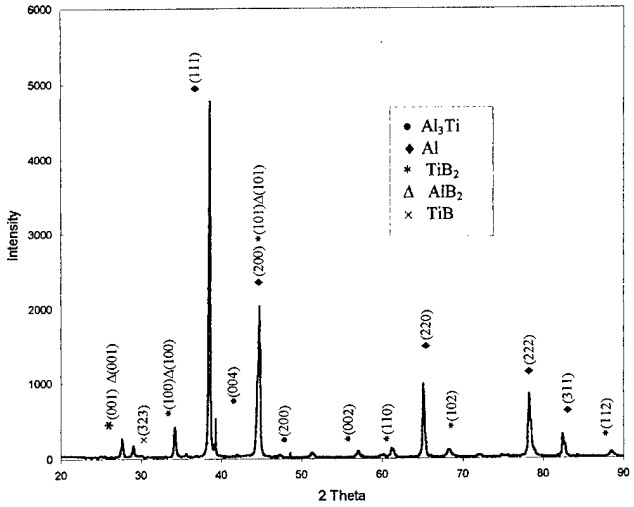

Fig. 3. XRD of Al/TiB_2 composite prepared by in-situ process at 850°C.

and B as the solutes. According to Eq. (6), the contributions of Ti and B can be expressed as follows:

$$\ln \gamma_{Ti} = \ln \gamma^{\circ}_{Ti} + \varepsilon^{Ti}_{Ti}\chi_{Ti} + \varepsilon^{B}_{Ti}\chi_{B}, \tag{11}$$

$$\ln \gamma_{B} = \ln \gamma^{\circ}_{B} + \varepsilon^{Ti}_{B}\chi_{Ti} + \varepsilon^{B}_{B}\chi_{B}. \tag{12}$$

In Eqs. (11) and (12), the second interaction coefficient ρ is neglected because χ_i^2 is close to zero. During the in-situ reaction, the following three reactions are possible to occur:

$$Ti + 3Al \rightarrow TiAl_3, \tag{13}$$

$$Ti + 2B \rightarrow TiB_2, \tag{14}$$

$$Al + 2B \rightarrow AlB_2. \tag{15}$$

The presence of possible phases at different temperature in the Al melt can be evaluated by comparing the ΔG of the three reactions. Based on available thermodynamic data, the calculated results are illustrated in Fig. 4. It can be observed that ΔG_{TiB_2} is far more negative than ΔG_{Al_3Ti}

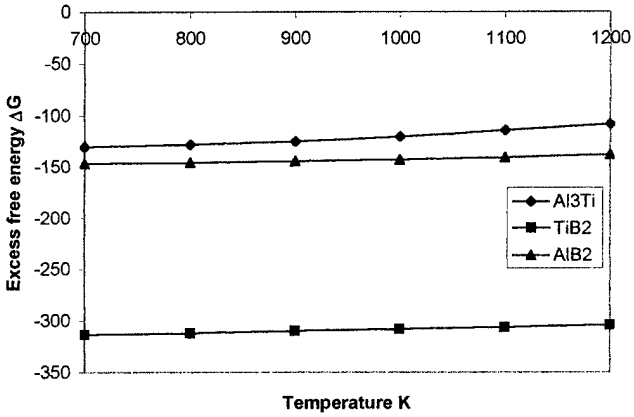

Fig. 4. Relation between excess free energy and temperature.

and ΔG_{AlB_2} at the temperature range from 700 to 1200 K while ΔG_{Al_3Ti} is less negative than ΔG_{AlB_2}. In other words, TiB_2 phase is easier to form than Al_3Ti and AlB_2 phases. With increase in temperature, the changes in Gibbs free energies of TiB_2 and AlB_2 are almost constant while that of Al_3Ti has become small. However, if the second order activity coefficient had been taken into account when $\ln \gamma$ was calculated, the change in Gibbs free energy of Al_3Ti would have been larger. This implies that Al_3Ti becomes unstable in comparison with TiB_2 and AlB_2. Based on Eq. (10), $D_{(TiB_2)}$ and $D_{(Al_3Ti)}$ at 1023 K have been calculated to be 3.55% and 9.15%, respectively. When the temperature is raised to 1123 K, D_{TiB_2} increases to 6.8% while $D_{(Al_3Ti)}$ decreases to 3.0%. The results agree well with the theoretical prediction that Al_3Ti become unstable when reaction temperature is increased. Besides thermodynamic considerations, kinetics of the reaction should also be considered since the rate and degree of the reaction and the growth of TiB_2 particulates are kinetically dependent. This consideration is however beyond the scope of the present paper.

5. Conclusion

1. Al/TiB_2 composite synthesized by reaction between K_2TiF_6 and KBF_4 in molten Al has successfully been carried out. It was found that the formation of TiB_2 occurred at as low as 1023 K but the amount increased with increase in reaction temperature.
2. Theoretical analysis showed that the decrease in the change in Gibbs free energy of Al_3Ti decreased with increase in reaction temperature, implying that Al_3Ti is unstable at high temperature.
3. By comparing the theoretical prediction with experimental results, it can be concluded that the present model is suitable for the analysis of in-situ reaction of TiB_2/Al composites.

References

[1] Maxwell I, Hellawell A. Metall Trans 1972;3:1487.
[2] Abdel-Hamid A, Durand F. Z Metallkd 1985;76:744.
[3] Murray JL, Liao PK, Spear KE. Bull Alloy Phase Diagrams 1986;7:550.
[4] Marcantonio JA, Mondolfo LF. Metall Trans 1971;2:465.
[5] Cornish AJ. Metal Sci 1975;9:477.
[6] Kiusaalas R. Relation between phases present in master alloys of Al–Ti–B type. Chemical Communications. Stockholm University, 1986;(1).
[7] Backerud L. Jernkont Ann 1971;155:422.
[8] Johnsson M, Jansson K. Z Metallkd 1998;89:394.
[9] Moriceau J. Revue De L'Aluminium 1972;(December):977.
[10] Maxwell I, Hellawell A. Metall Trans 1972;3:1487.
[11] Maxwell I, Hellawell A. Acta Metall 1975;23:895.
[12] Morimunc F, Shingu H, Kobayashi K, Ozaki R. J Jpn Inst Met 1977;41:444 (In Japanese).
[13] Collons DLW. Metall Trans 1972;3:2290.
[14] Abdel-Hamid A, Hamar-Thibaul S, Durand F. J Crystal Growth 1984;66:195.
[15] Abdel-Hamid A, Curand F. Metall Trans 1986;17A:349.
[16] Zupanic F, Spaic S, Krizman A. Mater Sci Technol 1998;14:601.
[17] Lu L, Lai MO, Chen FL. Acta Mater 1997;45(10):429.
[18] Lupis CHP. Chemical Thermodynamics of Materials, PTR Prentice Hall, 1983:235.
[19] Lupis CHP, Elliott JF. Acta Metall 1967;15:265.
[20] Lupis CHP, Elliott JF. Acta Metall 1966;14:529.

ELSEVIER

Composite Structures 47 (1999) 695–703

COMPOSITE STRUCTURES

www.elsevier.com/locate/compstruct

Thermal buckling and postbuckling analysis of a laminated composite beam with embedded SMA actuators

Jung Ju Lee [a,*], Sup Choi [b]

[a] *Department of Mechanical Engineering, Korea Advanced Institute of Science and Technology, 373-1 Kusong-dong, Yusung-gu, Taejon 305-701, South Korea*

[b] *Agency for Defense Development, P.O. Box 35, Yusung-gu, Taejon 305-600, South Korea*

Abstract

In this paper, the thermal buckling and postbuckling behaviours of a composite beam with embedded shape memory alloy (SMA) wires are investigated analytically. For the purpose of enhancing the critical buckling temperature and reducing the lateral deflection for the thermal buckling, the characteristics of thermal buckling are investigated through the use of the shape recovery force associated with SMA wire actuators. The results of both thermal buckling and postbuckling behaviours present quantitatively how the shape recovery force affects the thermal buckling behaviour. The analytical results show that the shape recovery force reduces the thermal expansion of the composite laminated beam, which results in both an increment of the critical buckling temperature and also a reduction of the lateral deflection of postbuckling behaviours. A new formula is also proposed to describe the critical buckling temperature of the laminated composite beam with embedded SMA wire actuators. © 2000 Published by Elsevier Science Ltd.

Keywords: Thermal buckling and postbuckling; Shape recovery force; Cut and paste method; Critical buckling temperature

List of symbols

CC	clamped–clamped boundary condition
CS	clamped–simply supported boundary condition
D	Young's modulus of the SMA wire actuators
E	Young's modulus
E_{eff}	engineering constants of the composite laminated beam
EI	flexural rigidity
P_{SMA}	shape recovery force
S	slenderness ratio
SMA	shape memory alloys
SS	simply supported–simply supported boundary condition
ΔT	temperature change ($= T - T_0$)
ΔT_{cr}	critical buckling temperature change ($= \Delta T_{\text{crl}} + \Delta T_{\text{SMA}}$)
ΔT_{crl}	critical buckling temperature change caused by thermal strains
ΔT_{SMA}	buckling temperature change caused by the shape recovery force
T	operating temperature
T_0	room temperature
α_{com}	effective thermal expansion coefficient
ε_{o}	initial strain of the SMA wire actuators
ε_{SMA}	compressive strain caused by the shape recovery force
ε_{t}	total strain of the SMA-composite beam ($= \varepsilon_{\text{th}} - \varepsilon_{\text{SMA}}$)
ε_{th}	thermal strain of the SMA-composite beam
v_{SMA}	volume fraction of SMA wire actuators
σ_{SMA}	stress induced by the shape recovery force
ξ_{M}	initial martensite fractions of the SMA wire actuators
ξ	martensite fractions of the SMA wire actuators

1. Introduction

Because of their inherent high specific stiffness and strength, use of laminated composite materials has increased in the design of thin-walled structural

* Corresponding author. Tel.: +82-42-869-3033; fax: +82-42-869-3210 or 5210.

E-mail address: jjlee@sorak.kaist.ac.kr (J.J. Lee).

0263-8223/99/$ - see front matter © 2000 Published by Elsevier Science Ltd.
PII: S0263-8223(00)00038-6

components for aerospace vehicles, such as high-speed aircraft, rockets and spacecraft, all of which are subjected to thermal loads due to aerodynamic and/or radiation heating. Such thin-walled laminated composite structures may become unstable at a relatively low temperature difference, and thus cause buckling in the elastic region. Therefore, thermal buckling is a significant failure mode governing the design of thin-walled structural components under severe thermal environments [1,2]. Recently, smart structure concepts have received a lot of attention for their capability in improving the stability of laminated composite structures subjected to severe thermal environments. Considerable attention has been given to shape memory alloys (referred to as SMA hereafter) for developing smart structures that are capable of adapting their reaction to the given environment [3]. Shape memory alloys (SMA) have good characteristics as actuators, converting thermal energy into mechanical energy as it undergoes its unique phase transformation during a temperature change. The use of SMA as actuators is motivated by their ability, that is, a shape memory effect, which can generate a significant shape recovery force with phase transformation during shrinkage from the martensitic phase of a low temperature to the austenitic phase of a high temperature [4,5].

Research efforts have been made to apply the shape recovery force by SMA wire actuators to the buckling control [6] and the shape control [7] of flexible structures. However, few studies on the thermal buckling and postbuckling of a composite laminated structure with embedded SMA wire actuators exist currently in the literature. Thompson and Griffin [8] investigated the effects of the shape recovery force on the buckling behaviours of structures with embedded SMA wire actuators using *ABAQUS*. In their study, the quantity of the shape recovery force is used by manipulating the thermal expansion coefficient of the SMA wire actuators which then results in inaccurate behaviour of composite structures. Zhong et al. [9] investigated the thermal buckling and postbuckling behaviour of composite plates with embedded SMA wire actuators using a finite element analysis. They reported that embedded SMA wire actuators could both increase the critical buckling temperature as well as reduce the postbuckling deflection at certain elevated temperatures. However, in their study, the characteristics of the shape recovery force employed not the constitutive equation, but excerpted the quantity of the shape recovery force from other experimental results [10].

A lot of research effort has been performed in order to quantify the effect of the shape recovery force on the composite structures with embedded SMA wire actuators. In order to characterize the interaction between directly embedded SMA wire actuators and composite laminates, the classical lamination theory and a shear-lag model to express resultant forces and moments were introduced [11,12]. Up to now, many previous workers evaluated the distributed axial compressive force, bending moment due to a phase transformation in the SMA wire actuators, and mechanical behaviours of the composite structures by using a shear-lag model. However, this method can lead to some errors at the ends of structures, because it has two limitations: the one is that the shear interaction parameters should be determined and the other is that an inadmissible stress state at the ends of structure has taken place [13]. Because of such limitations in shear-lag analysis, in this study, we introduced the cut and paste method to evaluate the stress and displacement fields due to the shape recovery forces.

The main purpose of this study is to investigate the capability of the shape recovery force on the thermal buckling and postbuckling behaviours of a composite beam with embedded SMA wire actuators (referred to as a SMA-composite beam hereafter), by evaluating the critical buckling temperature, using the constitutive relation of SMA wire actuators and the cut and paste method. A theoretical formula to account for the effect of the shape recovery force on the critical buckling temperature of thermal buckling of the SMA-composite beam is also suggested.

2. Analysis of critical buckling temperature

Consider the model of a composite beam with embedded SMA wire actuators within the midplane of beam thickness (SMA-composite beam) at a fixed-ends boundary condition, as shown in Fig. 1. Let T be the operational temperature and T_0 be an ambient temperature, so that $\Delta T = T - T_0$ is the temperature change which causes the thermal strains of the composite beam. When T is increased by ΔT, the beam tends to expand axially. However, the resistance to the thermal expansion is caused by the fixed-ends of the composite beam so that an axial compressive load is induced within the composite beam [14]. For simplicity of the analysis, the following three assumptions are made: (1) perfect

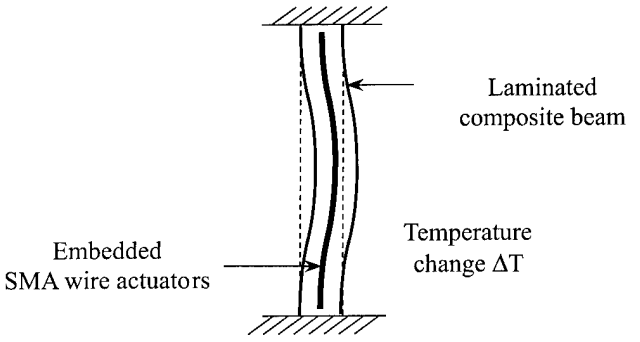

Fig. 1. Model of the SMA-composite beam for thermal buckling in this study.

bonding between the composite laminate and SMA wire actuators, (2) a uniform temperature distribution throughout the beam's thickness and length directions, and (3) independence of the material properties from the temperature.

Although nonlinear analysis is required to investigate the thermal buckling behaviour of the beam, linear analysis is employed for simplicity to show the effect of the shape recovery force from the analysis. Assuming that the critical buckling load, at which the thermal buckling of the beam occurs, is equal to the Euler load of a composite beam without any embedded wires, the critical buckling load, P_{cr}, can be expressed as [15]:

$$P_{cr} = \alpha_{com}\Delta T_{cr} EA = \frac{\pi^2 EI}{l_e^2}, \tag{1}$$

where ΔT_{cr} is the changed quantity of the critical buckling temperature, A, EI, α_{com} and l_e are the cross-sectional area, the flexural rigidity,the effective thermal expansion coefficient and the effective length of the composite beam, respectively. The critical buckling temperature change, ΔT_{cr}, is given by

$$\Delta T_{cr} = \frac{\pi^2}{\alpha_{com} S^2}, \tag{2}$$

where $S = l_e/r$ is the slenderness ratio and r is the radius of gyration. The effective thermal expansion, α_{com}, is calculated based on the classical lamination theory. The critical buckling temperature of the beam is independent of Young's modulus and inversely proportional to α_{com}, as shown in Eq. (2) [14,15]. For this analysis, the following three boundary conditions are considered [16]: (1) simply supported–simply supported (SS), (2) clamped–clamped (CC), and (3) clamped–simply supported (CS). The effective lengths with these end conditions are determined by noting the length of a composite beam corresponding to a pin-ended beam.

In order to investigate the effect of the shape memory force by SMA wire actuators on the thermal buckling of the SMA-composite beam, two methods are applied: one is the *Euler* method [17], which evaluates the buckling load within a small deflection, and the other is a *cut and paste* method, which evaluates the internal stress and displacement field of the SMA-composite beam [18]. To understand the cut and paste method, consider the equilibrium state of a composite beam with embedded SMA wire actuators, which is activated by electrical resistance heating, as shown in Fig. 2(a). The theory of the cut and paste method is to cut the SMA wire actuators separately as shown in Fig. 2(b) and to paste the SMA wire actuators into the composite beam. The SMA wire actuators are contracted by the shape recovery forces, according to temperature changes presented in Fig. 2(c). In order to meet the geometric boundary condition, the SMA wire actuators are subjected to tension, P_{SMA}. After pasting the SMA wire actuators into the composite as shown in Fig. 2(d), the SMA-composite beam is then subjected to the compressive load to meet the traction free condition of the initial state in Fig. 2(a). Both the end effect of Saint-venant's principle and the nonuniform local stress due to the embedded SMA wire actuators having a small-volume, fraction are not considered, and thus the compressive load P_{SMA} in the SMA-composite beam contributes to suppressing the thermal expansion of the composite. Since a state of self-equilibrium is involved as shown in Fig. 2(e), the stress distribution over a cross-section of the SMA-composite beam entails compressive as well as tensile stresses. If the temperature is increased uniformly to the amount of ΔT_{cr} throughout the beam's thickness and the beam is also not axially restrained, it would then expand freely. As shown in Fig. 2, the total axial strains of the composite beam with embedded SMA wire actuators, ε_t, consist of the thermal strain of

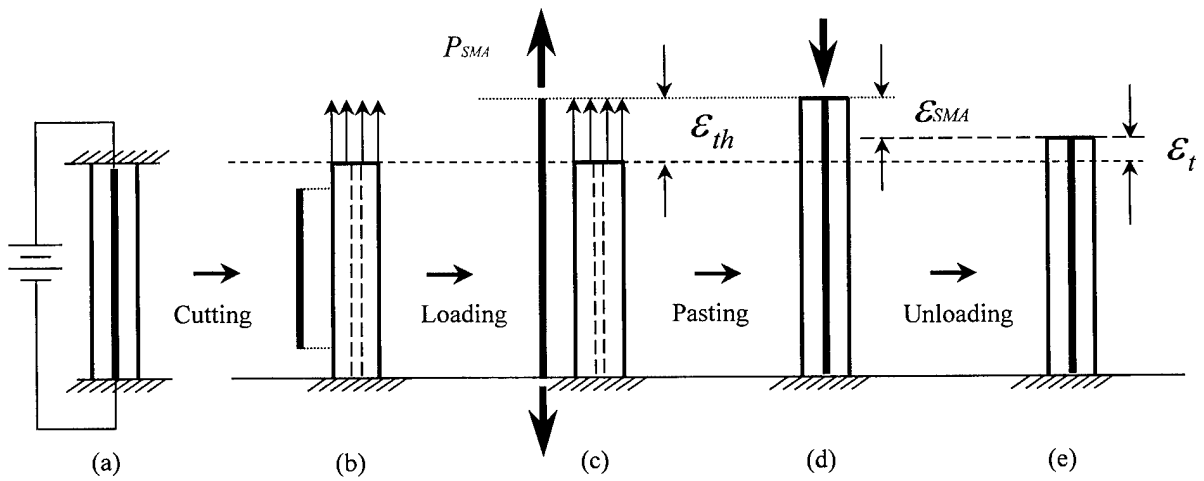

Fig. 2. Analytical model of the SMA-composite beam using the cut and paste method.

the composite laminate subjected to a uniform temperature rise, ε_{th}, and the compressive strain of the composite laminated beam, ε_{SMA}, caused by the shape recovery force, P_{SMA}. They can be expresses as follows:

$$\varepsilon_{th} = \alpha_{com}\Delta T, \tag{3}$$

$$\varepsilon_{SMA} = \frac{P_{SMA}}{E_{eff}A}, \tag{4}$$

$$\varepsilon_t = \alpha_{com}\Delta T - \varepsilon_{SMA}, \tag{5}$$

where E_{eff} is the engineering constant of the composite laminate beam. This concept is simple so that it is therefore convenient to apply it to more complex problems [6,7] when analysing the internal stress and displacement field of composite structures which consist of two or more constituent materials, having different mechanical and thermal properties when subjected to temperature changes in the elastic region. The shape recovery force, P_{SMA} can be expressed in Eq. (6) as a function of the number of embedding, n, the cross-section, A_{SMA}, and recovery stress, σ_{SMA}, of SMA wire actuators. At the SMA-composite beam, the effective thermal coefficient of expansion, α_{com}, can be related to the total axial strain, ε_t, by Eq. (7):

$$P_{SMA} = nA_{SMA}\sigma_{SMA}, \tag{6}$$

$$\alpha_{com} = \frac{\varepsilon_t}{\Delta T}, \tag{7}$$

$$v_{SMA} = \frac{nA_{SMA}}{A}. \tag{8}$$

Substituting (6)–(8) and (5) for (2), we obtain

$$\Delta T_{cr} = \left(\frac{\pi^2}{S^2} + \frac{v_{SMA}\sigma_{SMA}}{E_{eff}}\right) \Big/ \alpha_{com} = \Delta T_{crl} + \Delta T_{SMA}. \tag{9}$$

Eventually, the changed quantity of critical buckling temperature, ΔT_{cr}, when considering the effects of the shape recovery force, can be expressed as a function of S, σ_{SMA}, α_{com}, E_{eff} and v_{SMA}. For convenience, in Eq. (9), it is denoted by ΔT_{crl} for the first temperature change caused by thermal strains of the composite beam subjected to the uniform temperature change and ΔT_{SMA} for the second temperature change caused by the shape recovery force, P_{SMA}. For all these results, the thermal buckling temperature change is denoted by ΔT_{cr}, unless otherwise specified.

3. Constitutive equation of SMA wire actuators

The formulations of various constitutive models have been developed to describe the thermo-mechanical behaviours of SMA. Many researchers [19,20] reported that the constitutive models described in the following uniaxial form equation to characterize the thermo-mechanical behaviour of SMA wire actuators during the course of stress-induced martensite transformation:

$$\sigma - \sigma_0 = D(\varepsilon - \varepsilon_0) + \Theta(T - T_0) + \Omega(\xi - \xi_0), \tag{10}$$

where D, Θ, Ω, ξ represent the elastic modulus, thermoelastic tensor, transformation tensor and the martensite fraction of the SMA wire actuators, respectively. During the course of the phase transformation from martensite to austenite (M → A), it was assumed that D is a function of ξ and ξ is a function of T and σ as follows [20]:

$$D(\xi) = \frac{D_M - D_A}{2}(\cos\xi\pi + 1) + D_M, \tag{11}$$

$$\xi^{M\to A} = \frac{\xi_M}{2}\left\{\cos\left[a_A\left(T - A_s^\sigma\right)\right] + 1\right\}, \tag{12}$$

where

$$A_f^\sigma = A_f + \frac{\sigma}{C_A}, \quad a_A = \frac{\pi}{A_f - A_s}, \tag{13}$$

where the austenite start temperatures, A_s^σ, are linearly proportional to the stress [20], a_A is the material constant, and ξ_M is the initial martensite fraction of the SMA wire actuators.

The differential relation of σ, ε and T can be expressed as Eq. (14) [21]:

$$\begin{aligned} d\sigma &= D\,d\varepsilon + \Theta\,dT + \Omega\,d\xi, \\ &= D\,d\varepsilon + \left(\Theta + \Omega\frac{\partial\xi}{\partial T}\right)dT + \Omega\frac{\partial\xi}{\partial\sigma}d\sigma, \\ d\varepsilon &= \frac{1}{D}\left(1 - \Omega\frac{\partial\xi}{\partial\sigma}\right)d\sigma - \frac{1}{D}\left(\Theta + \Omega\frac{\partial\xi}{\partial T}\right)dT. \end{aligned} \tag{14}$$

The condition $d\varepsilon = 0$ means that two ends of the composite beam are restrained in the axial direction. The relation of σ and T can be obtained by numerical integration, such as the Runge–Kutta method.

Fig. 3 shows the analytical predictions of the restrained recovery stress, versus temperature for different

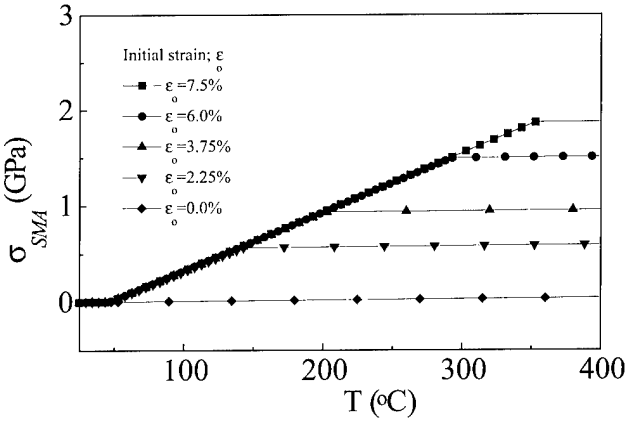

Fig. 3. Analytical results of the shape recovery force versus temperature for different initial strains of the SMA wire actuators.

initial strains. It can be seen that the recovery stress increases in sigmoidal fashion over the temperature. Note that the A_s–A_f range is generally broadened and displaced to higher temperatures by the stress induced transformation, as shown in Eq. (13). The maximum shape recovery stresses depend on the initial pre-strain which can be expressed by adjusting ξ_M which is inversely proportional to the recovery strain limit, ε_L [20]. Therefore, the quantity of the shape recovery force as shown in Fig. 3 is utilized along with Eq. (9) to compute critical buckling temperatures in the SMA-composite beam.

Fig. 4 shows the change of the martensite fraction, ξ and Young's modulus, D, in the course of M → A transformation, when heating under the stress-induced transformation. Once the temperature is reached A_s^{σ}, the SMA wire actuators will be completely in the austenite phase, and no phase transformation will be taking place, therefore the change in the total martensite volume fraction is 0. It is also shown that the Young's modulus of the SMA wire actuators changes when they undergo martensinic transformation, which is one of the important characteristics of the SMA wire actuators. However, in this study, because the volume fraction of SMA wire actuators is a small amount, the increment of Young's modulus on the SMA-composite beam can be assumed to be negligible. In the stress-free state, SMA wire actuators can be considered to have, martensite start (M_s), martensite finish (M_f), austenite start (A_s), and austenite finish (A_f) temperature. These temperatures are determined by a differential scanning calorimeter (DSC), and the results are presented in Table 1.

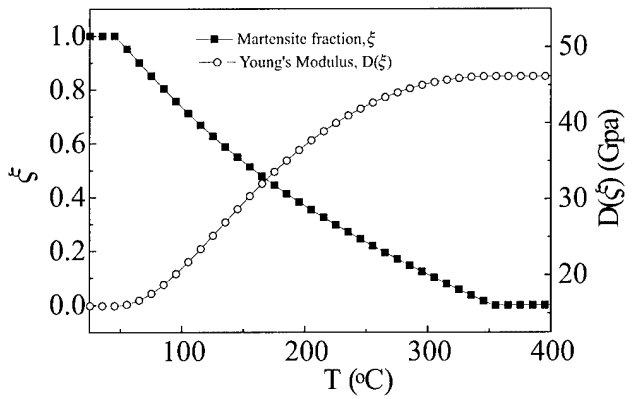

Fig. 4. Analytical results of Young's modulus and martensite volume fraction of SMA wire actuators versus temperature.

Table 1
Phase transition temperatures

Phase	Temperature (°C)
M_s	48.5
M_f	41.0
A_s	45.0
A_f	52.5

Table 2
Material constants of the SMA wire actuators for constitutive equation

Material constants	Experimental results
C_M	7.09 MPa
C_A	6.21 MPa
D_M	15.96 GPa
D_A	46.12 GPa
Θ_M	1.06 KPa/°C
Θ_A	1.06 KPa/°C
ε_L	0.075
Ω	$-D(\xi)^* \varepsilon_{trans}$

The coefficients used in the above constitutive relations are determined through the testing of the SMA wire actuators, and the results are presented in Table 2.

4. Results and discussion

Results are presented and discussed to investigate how the shape recovery force affects the thermal buckling and postbuckling behaviours of the SMA-composite beam. For this analysis, we considered the stacking sequence, the slenderness ratio, the laminated composite material, the boundary condition of the beam, and the volume fraction of the SMA wire actuators. Prior to the thermal buckling analysis, an effort was made to account for the mechanical characteristics of the composite beam reinforced by SMA wire actuators. On the results of the critical buckling loads of the SMA-composite subjected to only an external load, the flexural rigidity, EI, of the SMA-composite are the same values as compared to those of composite beams without embedded SMA wire actuators. Thus, in this study, we neglect this difference in the flexural rigidity, EI, between the SMA-composite and the composite beam, because of its negligible effect on the thermal buckling in composite beams. The material properties of three types of composite, graphite/epoxy, glass/epoxy, and boron/Al composite used in the present analysis are shown in Table 3 [22], and the room temperature, $T_0 = 25°C$, is assumed in this analysis. The dimensions of the model, with embedded SMA wire actuators with a 0.38 mm diameter, are 170 mm in length (l), 23 mm in width (b)

Table 3
Material properties used in this analysis

	Glass/ epoxy	Graphite/ epoxy	Boron/Al
E_1 (GPa)	38.61	181.00	220.00
E_2 (GPa)	9.65	10.30	95.00
ν_{12}	0.26	0.28	0.26
G_{12} (GPa)	6.21	7.17	48.00
α_{11} (m/m/°C) × 10^{-6}	4.0	0.02	3.74
α_{22} (m/m/°C) × 10^{-6}	16.0	22.5	14.74

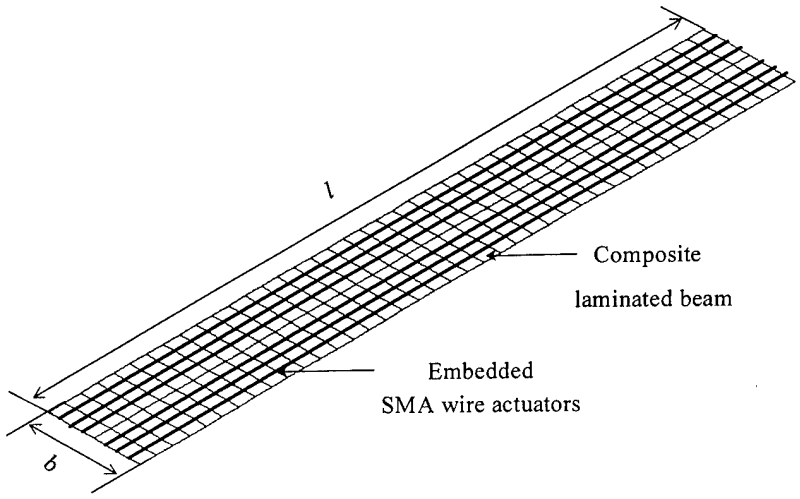

Fig. 5. A finite element model for the SMA-composite beam.

and 0.125 mm*ply number in thickness (t), unless otherwise specified. As shown in Fig. 5, the number of embedded SMA wire actuators is 6, resulting in the volume fraction of 1.97% of SMA wire actuators in the case of the stacking sequence $[0/\pm(\theta)_2/90]_s$.

4.1. Thermal buckling

Fig. 6 shows the effect of the shape recovery force on the critical buckling temperature change, ΔT_{cr}, with fibre orientations for different stacking sequences. The effective thermal coefficient for expansion in the axial direction, α_{com}, is changed by the fibre orientation, which is inversely proportional to the thermal critical buckling, as shown in Eq. (2). The quantity of the shape recovery force, P_{SMA}, corresponding to ΔT_{crI} enhances the critical buckling temperature, ΔT_{cr}, of the symmetric angle-ply laminates in the amount of ΔT_{SMA}. Therefore, the thermal critical buckling temperature, ΔT_{cr}, can be obtained by the superimposition ΔT_{crI} and ΔT_{SMA}, as shown in Eq. (9).

Fig. 7 shows the effect of the shape recovery force on the critical buckling temperature change, ΔT_{cr}, with the slenderness ratios for different stacking sequences. The critical buckling temperature change is proportional to the square of slenderness ratio, S, as shown in Eq. (9). The critical buckling temperature increases as the slenderness ratio decreases, which then results in a higher quantity in the shape recovery force. As shown in Fig. 7, the difference in temperature rate of increase with the different slenderness ratio, can be attributed to the quantity of the shape recovery force to temperature.

Fig. 8 shows the effects of the shape recovery force on the critical buckling temperature change, with slenderness ratios for a different volume fraction of SMA wire actuators, v_{SMA}. The critical buckling temperature change, ΔT_{cr}, increases when the volume fraction of the SMA wire actuators increases, as shown in Eq. (9). We

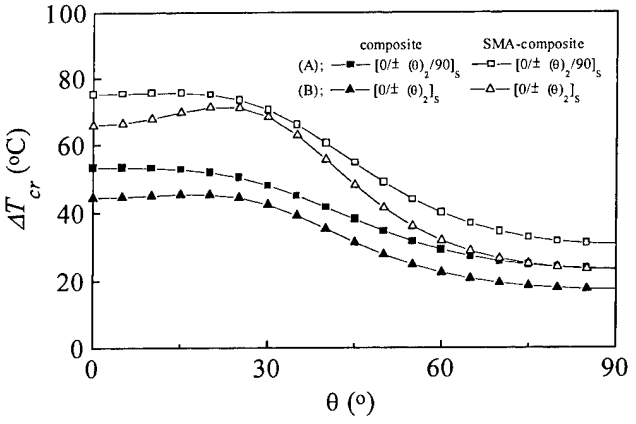

Fig. 6. Variation of the critical buckling temperature with fibre orientation for different stacking sequences (BC; CC, Gl/ep, (A); $v_{SMA} = 1.97\%$, $S = 196.3$, (B); $v_{SMA} = 2.36\%$, $S = 235.6$).

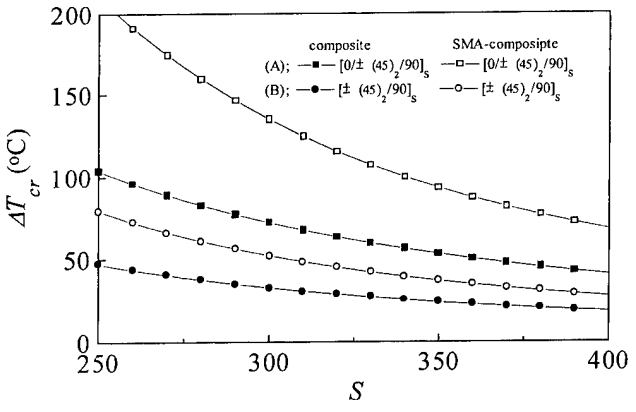

Fig. 7. Variation of the critical buckling temperature with slenderness ratio for different stacking sequences (BC; SS, Gr/ep, (A); $v_{SMA} = 1.97\%$, (B); $v_{SMA} = 2.36\%$).

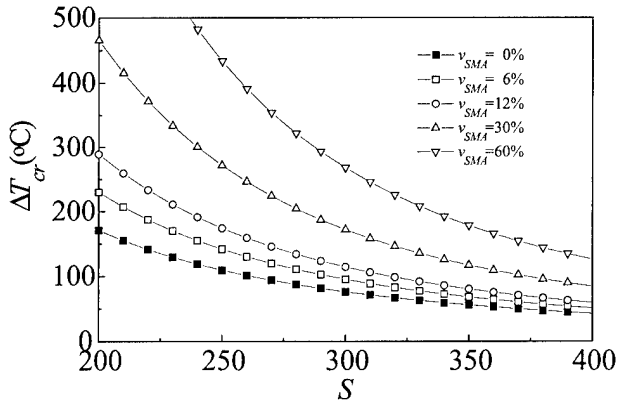

Fig. 8. Variation of the critical buckling temperature with slenderness ratio for different volume fractions of the SMA wire actuators ($[0/\pm(30)_2/90]_s$, BC; CC, boron/Al).

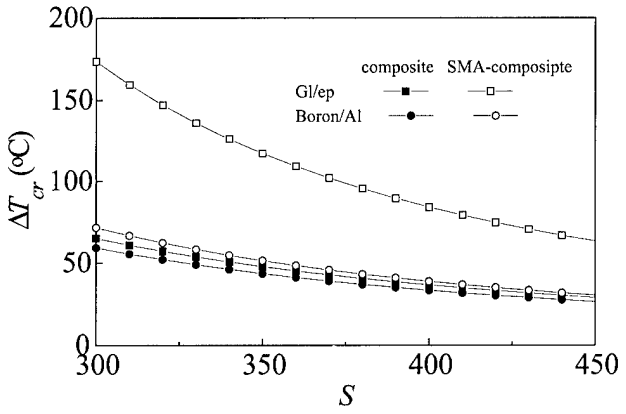

Fig. 10. Variation of the critical buckling temperature with slenderness ratio for different laminated composite materials ($[0/\pm(45)_2/90]_s$ BC; *CC*, $v_{SMA} = 6.0\%$).

can say that practical applications are possible by adjusting the volume fraction of the embedded SMA wire actuators.

Fig. 9 shows the effect of the shape recovery force on the critical buckling temperature change, with fibre orientations for different boundary conditions. The increasing rates of change in critical buckling temperatures, ΔT_{cr}, are different from each other at the condition of the CC, CS and SS boundary conditions. The critical buckling temperature, ΔT_{cr1}, under clamped boundary conditions, is higher than that under hinged–hinged boundary conditions. The shape recovery force, at the case of the fixed–fixed boundary condition, corresponding to the critical buckling temperature change, ΔT_{cr1}, is higher than those of the SS or CS boundary conditions. This difference of the shape recovery force causes a difference in the increasing rates of critical buckling temperature changes with respect to boundary conditions.

Fig. 10 shows the effect of the shape recovery force on the critical buckling temperature change with slenderness ratios, for different composite laminated materials. The increasing rate of critical buckling temperatures, ΔT_{cr}, are different between glass/epoxy and boron/Al composite. At the condition of almost the same shape recovery force corresponding to ΔT_{cr1}, the effect of the shape recovery force on the critical buckling temperature change for the glass/epoxy is much higher than that of the boron/Al composite. The difference in the increasing rate of temperature for the composite laminated material can be attributed to the engineering constants of the composite laminate beam, E_{eff}, as shown in Eq. (9).

From the results mentioned above, we can lead to the conclusion that the embedded SMA wire actuators can contribute to increasing the service temperature of the composite structures exposed to an elevated temperature, which can then cause phase transformation of SMA wire actuators. An analytical model to describe the critical buckling temperature of the SMA-composite, as shown in Eq. (9), can explain how the shape recovery force affects the critical buckling temperature.

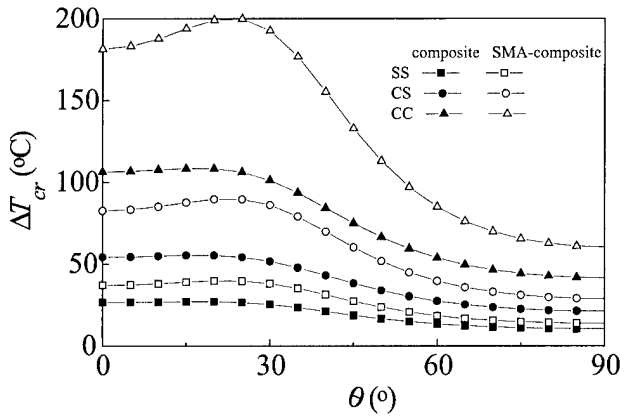

Fig. 9. Variation of the critical buckling temperature with fibre orientation for different boundary conditions ($[0/\pm(45)_2]_s$, $v_{SMA} = 2.36\%$, $l = 100$ mm, Gl/ep).

4.2. Postbuckling behaviours

As mentioned above, because the idea of cut and paste method is valid for the elastic region, it is also employed in the finite element analysis to describe the thermal postbuckling of the SMA-composite beam. The finite element model is constructed using *ABAQUS*, and the SMA wire actuators are modelled with beam elements, while the composite laminate are modelled with shell elements, as shown in Fig. 5. In order to describe the behaviour of embedded SMA wire actuators, constitutive equations based on Eqs. (10)–(13) are formulated in the form of *ABAQUS* user subroutine [23]. Modelling of laminated composite shells with embedded SMA wires and thermal buckling and postbuckling analysis, are performed by the use of a *ABAQUS* code

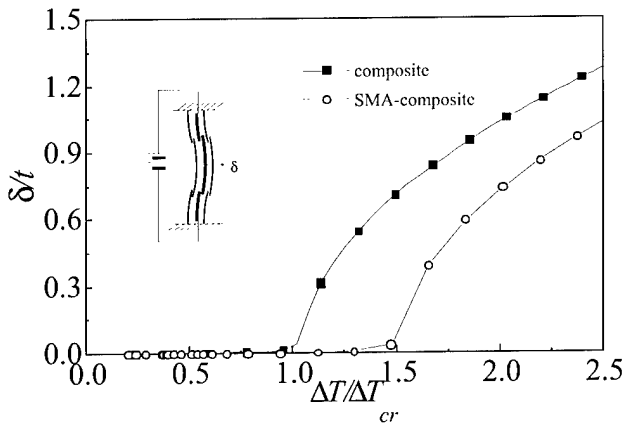

Fig. 11. Thermal buckling responses of the SMA-composite and the composite beam on the normalized deflection-temperature ($[0/\pm(45)_2/90]_s$, $S = 392.6$, $v_{SMA} = 1.97\%$, BC; SS, Gr/ep).

linked with the subroutine of the suggested the SMA constitutive relations. All the nodes of embedded SMA wire actuators are tied to that of the shell element, which allows constraints to be imposed between different degrees of freedom in the model.

A geometrical nonlinear temperature-deflection analysis is performed to predict thermal postbuckling behaviours. The postbuckling deflections at the centre of beam, normalized by the beam's thickness, as a function of $\Delta T/\Delta T_{cr}$ of the SMA-composite beam, are illustrated in Fig. 11. As might be expected, as the temperature ΔT is increased from 0, the lateral deflection of the composite beam remains around zero value, until the temperature reaches the critical buckling temperature, ΔT_{cr}. After ΔT_{cr}, the lateral deflection is suddenly increased with the temperature's rise. The critical buckling temperatures of the SMA-composite beam are increased by 50% compared with those of the composite beam. It is also shown in Fig. 11 that the lateral deflections are $0.7t$ and $0.03t$ (t = beam thickness) for the composite and the SMA-composite beam, respectively, at the temperature change $\Delta T/\Delta T_{cr} = 1.5$ which is the critical buckling temperature change of the SMA-composite beam. The shape recovery force, P_{SMA}, can reduce the thermal expansion strain of composite laminates in the amount of ε_{SMA}, as shown in Fig. 2 and Eq. (6), which results in a decrease in the thermal load acting on the SMA-composite beam. From these results, the lateral deflection of the composite structure can be significantly reduced at any temperature, and the critical buckling temperature can be increased by the shape recovery force.

5. Conclusions

In this paper, an analytical study on the thermal buckling and postbuckling of the composite beams with embedded SMA wire actuators subjected to a uniform temperature change are performed. The constitutive equations of the SMA wire actuators are formulated in the form of ABAQUS user subroutine, and the results are then applied to the thermal postbuckling behaviours. From this study, the following conclusions are obtained.

1. The critical buckling temperature can be increased and the lateral deflection of the laminated composite beam can be reduced at any temperature by the use of shape recovery force. These results indicate that the application of SMA wire actuators to the thermal buckling problem of real composite structures which work under a severe thermal environment can be implemented.
2. An analytical model is proposed to describe the thermal buckling of laminated composite beams with embedded SMA wire actuators based on *Euler* equation and *cut and paste* methods under a uniform temperature distribution of the beam. This theoretical formula positively shows how the shape recovery force affects the critical buckling temperatures.

References

[1] Liaw DG. Supersonic flutter of laminated thin plates with thermal effects. J Aircraft 1993;30(1):105–11.
[2] Chen LW, Liu WH. Thermal buckling of antisymmetric angle-ply laminated plates – an analytical levy-type solution. J Thermal Stress 1993;16:401–19.
[3] Thompson SP, Loughlan J. Adaptive post-buckling response of carbon fiber composite plates employing SMA actuators. Composite Struct 1997;38(1–4):667–78.
[4] Technical information of shape memory alloys, Inc. (http://www.sma-inc.com).
[5] Perkins J. Shape memory effects in alloys. New York: Plenum Press; 1975.
[6] Choi S, Lee JJ, Seo DC. A study on the buckling and postbuckling control of composite beam with embedded NiTi actuators. J Composite Mater 2000;34.
[7] Choi S, Lee JJ. The shape control of composite beam with embedded shape memory alloy wire actuators. Smart Mater Struct 1998;7(6):759–70.
[8] Thompson DM, Griffin OH. Finite element prediction of active buckling control of stiffened panels. J Intell Mater Sys Struct 1993;4:243–7.
[9] Zhong ZW, Roger RC, Chun M, Pates III CS. Proceedings of the ADPA/AIAA/ASME/SPIE Conference on Active Materials and Adaptive Structures, 1994. p. 115–32.
[10] Cross WB, Kariotis AH, Stimler FJ. Nitinol characterization study, NASA-CR-1433, 1970.
[11] Lagoudas DC, Tadjbakhsh IG. Active flexible rods with embedded SMA fibers. Smart Mater Struct 1992;1:162–7.
[12] Lin MW, Rogers CA. Analysis of stress distribution in a shape memory alloy composite beam. AIAA-91-1164-CP, 1991. p. 169–77.
[13] Nairn JA. A variatioal mechanics analysis of the stresses around breaks in embedded fibers. Mech Mater 1992;13:131–54.
[14] Hetnarski RB. Thermal stresses III. Amsterdam: North-Holland; 1989.
[15] Britvec SJ. Stability and optimization of flexible space structures. Basel: Birkhauser; 1995.

[16] Mathew TC, Singh G, Rao MD. Thermal buckling of cross-ply composite laminates. Comput Struct 1992;42(2):281–7.
[17] Timoshenko S, Gere J. Theory of elastic stability. New York: McGraw-Hill; 1963.
[18] Suo Z, Hutchison JH. Interface crack between two elastic layers. Int J Fracture 1990;43:1–18.
[19] Tanaka K. A thermomechanical sketch of shape memory effects: one-dimensional tensile behavior. Res Mechanica 1986;18:251–63.
[20] Liang C, Rogers CA. One-dimensional thermomechanical constitutive relations for shape memory materials. J Intell Mater Sys Struct 1990;1:207–34.
[21] Sun G, Sun CT. One-dimensional constitutive relation for shape-memory alloy-reinforced composite lamina. J Mater Sci 1993; 28:6323–8.
[22] Taya M, Arsenault RJ. Metal matrix composites. Oxford: Pergamon Press; 1989.
[23] ABAQUS/standard user's manual, Hibbitt, Karlsson & Sorensen, Inc., 1996.

ELSEVIER

Composite Structures 47 (1999) 705–710

COMPOSITE STRUCTURES

www.elsevier.com/locate/compstruct

Thermo-mechanical behaviour of shape memory alloy reinforced composite laminate (Ni–Ti/glass-fibre/epoxy)

Zhongqing Su [a], Hanchao Mai [a], Meng Lu [a,b,*], Lin Ye [b]

[a] *Institute of Solid Mechanics, Beijing University of Aeronautics and Astronautics, Beijing 100083, People's Republic of China*

[b] *Centre for Advanced Material Technology (CAMT), Department of Mechanical and Mechatronic Engineering, The University of Sydney, Sydney, NSW 2006, Australia*

Abstract

The thermo-mechanical behaviour of a shape memory alloy reinforced composite (SMARC) laminated plate (Ni–48.8Ti/Glass-fibre/Epoxy) was studied. A theoretical frame of the constitutive law was first proposed using irreversible thermodynamics. Expressions were derived in details in terms of some approximations based on meso-mechanics. Typical experiments, including uniaxial tension, restrained recovery, free recovery tests, etc., were carried out to determine the material coefficients. The results obtained include the constitutive relationship between stress and strain, the expression of entropy, and the dependence of the effective "elastic" coefficients on temperature. © 2000 Elsevier Science Ltd. All rights reserved.

Keywords: Shape memory alloy; Fibre reinforced composites; Thermodynamics; Constitutive relations

1. Introduction

Since the early 1980s, the concept of smart materials has increasingly attracted attentions in engineering communities, particularly in aviation and aerospace industry. In fact, technologies of smart materials have been successfully applied to such occasions as suppression of thermo-vibration of spaceship's antennas, control of configurations of large-size structures in the space, and monitoring of damage in aviation structures, etc.

Researchers have developed quite a few sorts of "smart" materials. Shape memory alloy reinforced composites (SMARC) are one of them. A SMARC is made of a conventional composite material (laminated or textile fabric) embedded with shape memory alloy filaments. SMA filaments are used as distributed actuators. When the driven actions (say, temperatures) are applied subject to a control procedure, especially to an adaptive control loop, therefore, a component of SMARC may behave like "intelligent" [1–3].

As is known, the thermo-mechanical properties of shape memory alloys themself have been extensively studied by many researchers [1,4–9]. For example, Lei and Wu [5] studied the thermo-mechanical behaviour of Ni–Ti-based shape memory alloys, including the theoretical background of SMA. Tang and Sandstrom [7] discussed some practical applications of SMA, and investigated limitations of constitutive models for Ni–Ti shape memory alloys, with improved methods.

However, shape memory alloys are scarcely used as structural elements in engineering applications to undertake primary loadings. Alternatively, they are normally embedded into other materials (say, composites) to form an SMA reinforced "composites". Therefore, it is important in the structural design to investigate the thermo-mechanical properties of SMARCs. That is, one needs to establish the average stress–strain–temperature relationship of SMARC. Recently, considerable insights have been made into the thermo-mechanical properties of various SMARCs. For example, Xiong and Tao [10] investigated the thermo-behaviour of a SMARC, and established a one-dimensional constitutive relationship on the basis of thermodynamics. Wang and Wu [11] studied the thermo-mechanical characteristics of a composite reinforced with shape memory alloy filaments, and discussed its potential application to intelligent structures.

The objective of the present study is to investigate the two-dimensional effective thermo-mechanical properties of a glass-fibre/epoxy laminated plate embedded with Ni–Ti shape memory alloy filaments. For this purpose,

* Corresponding author. Fax: +61-2-9351-3760.
E-mail address: menglu@mech.eng.usyd.edu.au (M. Lu).

0263-8223/99/$ - see front matter © 2000 Elsevier Science Ltd. All rights reserved.
PII: S0263-8223(00)00039-8

the required Helmholtz free energy was first established. With the expression of the free energy, the stress–strain relation and the entropy expression can be formally obtained in terms of the principle of thermodynamics. The material coefficients in the constitutive equations can be determined by some experiments that include uniaxial tensions, restrained recovery, and free recovery tests, etc.

2. Constitutive relations of the SMARC

The SMARC laminated plate is schematically shown in Fig. 1. Like treating conventional composite laminates, it is assumed as an orthotropic but a uniform medium.

Suppose that the concerned characteristic time scale is sufficiently slow so that the local temperature balance can be reached within this time scale. Meanwhile, it is assumed that the spatial fluctuations of the stress, the strain and the temperature in the plate can be neglected, compared with their average values. In this way, the SMARC laminated plate can be dealt with as an "effective" uniform medium in the sense of not only space but also time.

According to the thermodynamic theory [12,13], a general constitutive relation can be formally described by

$$\psi = \hat{\psi}(\varepsilon_{ij}, T, g_i, \{\xi\}), \tag{1}$$

$$\sigma_{ij} = \hat{\sigma}_{ij}(\varepsilon_{ij}, T, g_i, \{\xi\}), \tag{2}$$

$$s = \hat{s}(\varepsilon_{ij}, T, g_i, \{\xi\}), \tag{3}$$

$$\hat{q}_i = \hat{q}_i(\varepsilon_{ij}, T, g_i, \{\xi\}), \tag{4}$$

$$\dot{\xi} = \hat{\xi}(\varepsilon_{ij}, T, g_i, \{\xi\}), \tag{5a}$$

where ψ is the Helmholtz free energy, s the entropy, σ_{ij} the stress, ε_{ij} the strain, T the temperature, $g_i = T_{,i}$ the temperature gradient, q_i the heat flux, and ξ is an internal variable which can be taken as the volume fraction of the Martensite phase of SMA. Clearly, $1-\xi$ denotes the volume fraction of the Austenite phase.

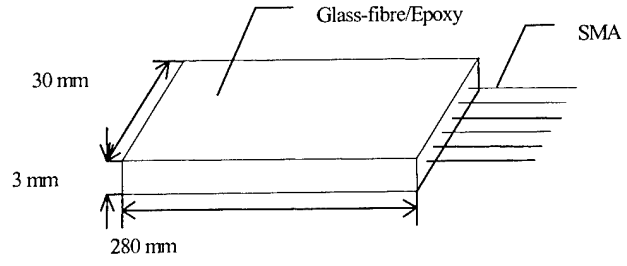

Fig. 1. Schematic of SMARC specimen.

Since ξ only relates the SMA, the evolution laws of ξ, previously developed by Liang and Roger [4], can be adopted.

1. *For the reverse transformation*:

$$\xi/\xi_M = 1 - (1/2)\exp[a_A(A-T)^n], \quad A \geqslant T \geqslant A_s,$$

$$\xi/\xi_M = (1/2)\exp[a_A(T-A)^n], \quad A_f \geqslant T \geqslant A,$$

or, equivalently,

$$\dot{\xi} = a_A \xi_A n(A-T)^{n-1}\left(\frac{\xi}{\xi_M} - 1\right), \ A \geqslant T \geqslant A_s, \tag{5b}$$

$$\dot{\xi} = a_A \xi_A n(A-T)^{n-1}\frac{\xi}{\xi_M}, \quad A_f \geqslant T \geqslant A, \tag{5c}$$

2. *For the Martensite transformation*:

$$\xi = 1 - (1/2)\xi_M \exp[a_M(M-T)^n], \quad M \geqslant T \geqslant M_f,$$

$$\xi = (1/2)\xi_M \exp[a_A(T-M)^n], \quad M_s \geqslant T \geqslant M,$$

or, equivalently,

$$\dot{\xi} = a_A \xi_A n(A-T)^{n-1}\left(\frac{\xi}{\xi_M} - 1\right), \quad M \geqslant T \geqslant M_f, \tag{5d}$$

$$\dot{\xi} = a_A \xi_A n(A-T)^{n-1}\frac{\xi}{\xi_M}, \quad M_s \geqslant T \geqslant M. \tag{5e}$$

Here

$$a_M = [2^n \ln(2 \times 0.01)]/(M_s - M_f)^n,$$

$$a_A = [2^n \ln(2 \times 0.01)]/(A_f - A_s)^n,$$

$$M = \frac{1}{2}(M_s + M_f),$$

$$A = \frac{1}{2}(A_s + A_f).$$

In the above equations, n is the transformation coefficient, and ξ_M is the percentage of Martensite at the beginning of transformation, which depends on properties of the SMA. A_s, A_f, M_s and M_f are the transformation temperatures determined by experiments.

The second law of thermodynamics, in the form of the entropy production in inequality, indicates

$$\rho\dot{s} - (\rho r/T) + (q_i/T)_{,i} \geqslant 0. \tag{6}$$

Introduction of the Helmholtz free energy per unit mass gives

$$\psi = e - Ts. \tag{7}$$

Then, substitution of Eq. (7) into Eq. (6) yields

$$-\rho(\dot{\psi} + s\dot{T}) + \sigma_{ij}\dot{\varepsilon}_{ij} - \left(\frac{1}{T}\right)q_i T_{,i} \geqslant 0. \tag{8}$$

Substituting Eq. (1) into Eq. (8) we have

$$\left(\sigma_{ij}-\rho\frac{\partial\psi}{\partial\varepsilon_{ij}}\right)\dot{\varepsilon}_{ij}+\rho\left(s+\frac{\partial\psi}{\partial T}\right)\dot{T}+\frac{\partial\psi}{\partial g_i}\dot{g}_i+\frac{\partial\psi}{\partial\xi}\dot{\xi}-\frac{q_i g_i}{T}\geqslant 0. \tag{9}$$

In light of the rational thermodynamics [12,13]

$$\sigma_{ij}=\rho\frac{\partial\psi}{\partial\varepsilon_{ij}}, \tag{10}$$

$$s=-\frac{\partial\psi}{\partial T}, \tag{11}$$

$$\frac{\partial\psi}{\partial g_i}=0. \tag{12}$$

Eqs. (10) and (11) indicate such a fact that if the expression of the Helmholtz free energy is available, the expressions for stress and entropy can be obtained by differentiating with respect to strain and temperature, respectively. Eq. (12) indicates that the free energy, as well as stress and entropy, is independent of the gradient of temperature.

For small deformation, the Helmholtz free energy can be expanded in a power series of the strain, namely,

$$\psi=\frac{1}{\rho}\left[\psi_0(T,\{\xi\})+\alpha_{ij}(T,\{\xi\})\varepsilon_{ij}+\frac{1}{2}C_{ijkl}(T,\{\xi\})\varepsilon_{ij}\varepsilon_{kl}\right]+o\left\{\|\varepsilon_{ij}\|^2\right\}, \tag{13}$$

in which the terms up to $\|\varepsilon_{ij}\|^2$ are retained and the higher order ones are neglected.

Substitution of Eq. (13) into Eqs. (10) and (11) leads to

$$\sigma_{ij}=C_{ijkl}(T,\{\xi\})\varepsilon_{kl}+\alpha_{ij}(T,\{\xi\}), \tag{14}$$

$$s=-\frac{1}{2\rho}C'_{ijkl}(T,\{\xi\})\varepsilon_{ij}\varepsilon_{ij}+\alpha'_{ij}(T,\{\xi\})\varepsilon_{ij}+\psi'_0(T,\{\xi\}), \tag{15}$$

where $(\cdot)'=\frac{\partial}{\partial T}(\cdot)$.

For a two-dimensional orthotropic laminated plate, in the material coordinate system, in terms of engineering index notations, Eq. (14) may be written as

$$\begin{bmatrix}\sigma_1\\ \sigma_2\\ \sigma_6\end{bmatrix}=\begin{bmatrix}Q_{11}(T,\{\xi\}) & Q_{12}(T,\{\xi\}) & 0\\ Q_{12}(T,\{\xi\}) & Q_{22}(T,\{\xi\}) & 0\\ 0 & 0 & Q_{66}(T,\{\xi\})\end{bmatrix}\begin{bmatrix}\varepsilon_1\\ \varepsilon_2\\ \varepsilon_6\end{bmatrix}+\begin{bmatrix}\alpha_1(T,\{\xi\})\\ \alpha_2(T,\{\xi\})\\ \alpha_6(T,\{\xi\})\end{bmatrix}, \tag{16}$$

where

$$Q_{11}=\frac{E_{11}(T,\{T\})}{1-\nu_{12}(T,\{\xi\})\nu_{21}(T,\{\xi\})}, \tag{17}$$

$$Q_{22}=\frac{E_{22}(T,\{T\})}{1-\nu_{12}(T,\{\xi\})\nu_{21}(T,\{\xi\})}, \tag{18}$$

$$Q_{12}=\frac{\nu_{21}(T,\{\xi\})E_{11}(T,\{T\})}{1-\nu_{12}(T,\{\xi\})\nu_{21}(T,\{\xi\})}=\frac{\nu_{12}(T,\{\xi\})E_{22}(T,\{T\})}{1-\nu_{12}(T,\{\xi\})\nu_{21}(T,\{\xi\})}, \tag{19}$$

$$Q_{16}=Q_{26}=0, \tag{20}$$

$$Q_{66}=G_{12}(T,\{\xi\}), \tag{21}$$

$$\nu_{12}(T,\{\xi\})E_{11}(T,\{\xi\})=\nu_{21}(T,\{\xi\})E_{22}(T,\{\xi\}). \tag{22}$$

Linear approximation for α_i leads to

$$\alpha_i=\alpha_j(\{\xi\})Q^0_{ij}(\{\xi\})(T-T_0), \tag{23}$$

where T_0 is the reference temperature, and Q^0_{ij} is the value of Q_{ij} at T_0.

For the entropy relation, a linear approximation is used

$$s=\frac{1}{\rho}\alpha_i(\{\xi\})Q^0_{ij}(\{\xi\})\varepsilon_j+C_e(\{\xi\})(T/T_0-1), \tag{24}$$

where the quantity C_e is the specific heat at constant strains, evaluated at $\varepsilon_{ij}=0$, $T=T_0$.

In the above equations, the dependence of the material coefficients, such as E_{11}, on the temperature T, can be determined by the experiments which will be discussed in the next section.

The constitutive relations, Eqs. (16) and (25), describe the thermo-mechanical behaviour of the SMARC in which both the fibre composite and SMA filaments play the role simultaneously.

However, it can be expected that the major influence of SMA filaments on the whole system is in the X_1-direction. Hence, as a first order approximation, the material constants in Eqs. (17)–(22), namely, E_{22}, ν_{12}, ν_{21}, α_2, and α_{12} except E_{11} and α_6, can be obtained by evaluating the corresponding composite laminates without SMA filaments. The longitudinal Young's modulus E_{11} is defined by both the reinforcing fibres and the SMA filaments, and it could be determined by experiments.

Regarding the thermal expansion coefficient α_1, it can be approximated using the glass-fibre/epoxy system without SMA, if the volume fraction of SMA in the SMARC system is rather low (less than 1% in the present case).

3. Experimental determination of thermo-mechanical properties

The specimen of the SMARC laminate used in experimental study (see Fig. 1) consists of ten layers of glass-fibre/epoxy laminae $(0°/90°)_{10}$. The glass-fibre

volume fraction is about 10%. The thermal expansion coefficient in X_1-direction of the glass-fibre/epoxy, α_M, is $6.6 \times 10^{-6}/°C$, at the ambient temperature.

The length of the specimen is 280 mm, the width is 30 mm, and the thickness is 3 mm. At the mid-plane of the plate, five Ni–50.8%Ti shape memory alloy filaments were uniformly distributed along the width of the specimen, with their length in the X_1-direction. The diameter of SMA filament is 0.5 mm, and each filament was pre-strained by 3%. The physical parameters for the SMA are listed in Table 1.

Determination of the relationship between E_{11} and T needs comprehensive experimental data. Experiments were carried out in three different ways, which include the uniaxial tension, restrained recovery, and free recovery tests.

Uniaxial tension tests were conducted at constant but different environmental temperatures, respectively. Fig. 2 shows the stress and strain curves at 30°C, 65°C and 80°C, respectively. From these curves, it can be seen that the relation of stress and strain is approximately linear at a certain temperature, which implies that the constitutive form described by Eq. (16) is a good approximation to the problem. In order to be compared with SMA, the corresponding relationships of SMA at 15°C, 58°C, 65°C are shown in Fig. 3.

Table 1
Properties of SMA

Density (g/cm^3)	6.25
Electrical resistivity (Ω m)	7×10^{-7}
Specific heat capacity (J/mol °C)	29.5
Conductivity (J/mol °C s)	0.21
General transformative temperature (°C)	
M_f	−3
M_s	2
A_f	45
A_f	60
Coefficient of change of phase	−489.8

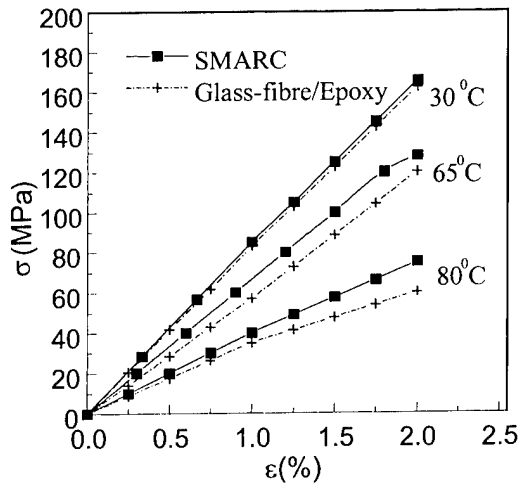

Fig. 2. Axial tension of SMARC under different temperatures.

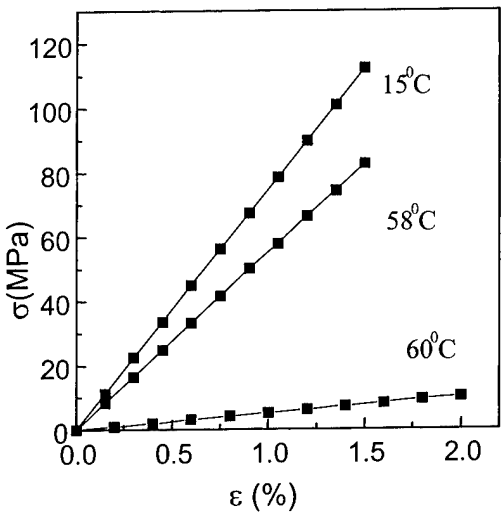

Fig. 3. Axial tension of SMA under different temperatures (after [10]).

To further determine the effective Young's modulus of the SMARC, the so-called "parallel model" is used to establish the relation of the Young's moduli of the glass-fibre/epoxy system and the SMA filaments. In this way, experimental data for the pure glass-fibre/epoxy and the SMA are needed to obtain E_{11} of the SMARC laminate (see Appendix A for details),

$$E_{11} = E(\xi) + \frac{V_m E_m}{V_a}\left(1 - \Omega \frac{\partial \xi}{\partial \sigma_a}\right) \tag{25}$$

and

$$\frac{\partial \xi}{\partial \sigma_a} = \begin{cases} \frac{\xi_m}{2}\frac{a_A}{C_A}\sin[a_A(T - A_s)] - \frac{a_A}{C_A}\sigma_a \\ \quad \text{for Austenite to Martensite,} \\ \frac{1-\xi_A}{2}\frac{a_M}{C_M}\sin[a_M(T - M_f)] - \frac{a_M}{C_M}\sigma_a \\ \quad \text{for Martensite to Austenite,} \end{cases} \tag{26}$$

where $E(\xi)$ and E_M are Young's moduli of the composite (without SMA) and SMA, respectively, and V_m and V_a the corresponding volume fractions. C_A and C_M are material constants. The expression of σ_a is given in Appendix A.

Determination of Young's modulus, $E(\xi)$, of SMA as a function of temperature can be fitted with the experimental data of the restrained recovery test and the free recovery test [10], which are illustrated in Figs. 4 and 5, respectively. Note that the dependence of E_m on T can be obtained in terms of the result shown in Fig. 2.

Hence, based on the parallel model and the experimental results shown in Figs. 2, 4 and 5, the relationship between E_{11} and T of SMARC can be obtained, which is illustrated in Fig. 6. For practical convenience, the curve of E_{11} versus T in Fig. 6 can be approximately fitted by a polynomial

$$E_{11} = a_0 + a_1 T + a_2 T^2 + a_3 T^3 + a_4 T^4 + a_5 T^5 + a_6 T^6, \tag{27}$$

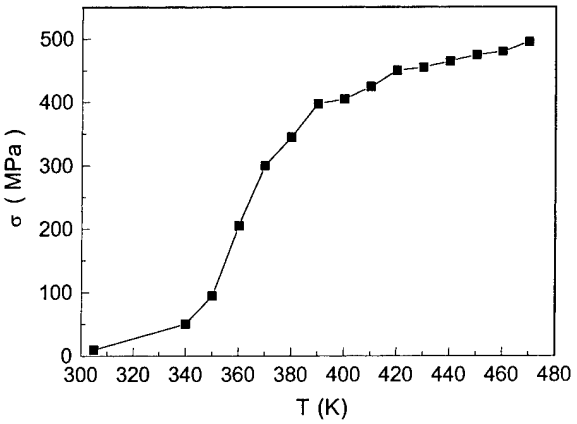

Fig. 4. σ–T curve of Ni–Tinol in restrained tension test (after [10]).

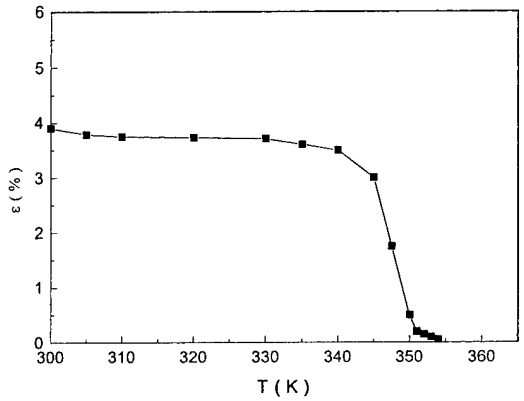

Fig. 5. ε–T curve of Ni–Tinol in free tension test (after [10]).

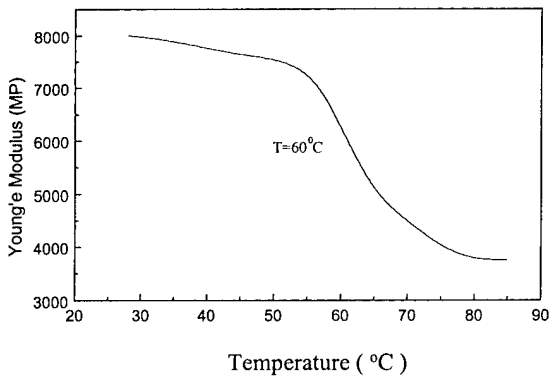

Fig. 6. Dependence of Young's modulus of SMARC on temperature T.

where

$a_0 = 9.50567$, $a_1 = -1.455 \times 10^{-2}$,

$a_2 = 1.76 \times 10^{-3}$, $a_3 = -5.83585 \times 10^{-5}$,

$a_4 = 6.81021 \times 10^{-7}$, $a_5 = -3.35067 \times 10^{-9}$,

$a_6 = 5.94068 \times 10^{-12}$.

4. Conclusion

Based on experimental data and thermodynamics theory a two-dimensional constitutive model for a SMARC laminate was established. Since the laminate is reinforced with the SMA filaments only in one direction, its properties in other directions can be approximately regarded as unchanged in comparison to those of the composite. This approximation allows us to use experimental data of unidirectional tests to fit the material coefficients in the filament direction. Theoretically, the method can be extend to the case where a SMA "net" rather than SMA filaments are used to reinforce the composite laminated plate. In that case bi-axial testing techniques must be used.

Acknowledgements

The authors are grateful to Institute of Smart Materials and Structures, Nangjing University of Aeronautics and Astronautics, for providing all the experimental data. Financial support from Xi'an Institute of Aircraft Design is gratefully acknowledged.

Appendix A

The parallel model is used to derive the effective Young's modulus, E_{11}, of the SMARC. According to the basic assumption of the parallel model, the SMARC laminated plate, the glass-fibre/epoxy laminate, and SMA filaments have the same strain in the X_1-direction when subjected to an external loading in the direction. That is

$$d\varepsilon_m = d\varepsilon_a = d\varepsilon, \tag{A.1}$$

where ε is the total strain of the specimen, ε_m the strain of the glass-fibre/epoxy plate, and ε_a is the strain of the SMA filaments. Note that for convenience the subscripts, such as "11" indicating directions, have been omitted, but all the derivation below is referred to in the X_1-direction.

Suppose that σ is the total stress on the SMARC, σ_a the stress on the SMA filaments, and σ_m the stress on the glass-fibre/epoxy laminate, then

$$d\sigma = V_a\, d\sigma_a + V_m\, d\sigma_m, \tag{A.2}$$

where V_a and V_m indicate the volume-fractions of SMA and glass-fibre/epoxy, respectively.

Let E_A be the elastic modulus of the SMA in the Austenitic phase, E_M the elastic modulus of the SMA in the Martensite phase, E_m the elastic modulus of glass-fibre/epoxy, α_m the corresponding thermal expansion coefficient. For glass-fibre/epoxy system, we have

$$d\varepsilon_m = (d\sigma_m/E_m + a_m\, dT). \tag{A.3}$$

Substitution of Eqs. (A.2) and (A.3) into Eq. (A.1) yields

$$d\varepsilon_m = (d\sigma - V_a\, d\sigma_a)/E_m V_m + a_m\, dT. \tag{A.4}$$

In a similar way, expression for $d\varepsilon_a$ can be obtained.

The constitutive equation of the SMA can be expressed as

$$\dot{\sigma}_a = E_a(\xi)\,\dot{\varepsilon}_a + \alpha_a \dot{T} + \Omega\,\dot{\xi}, \tag{A.5}$$

where E_a is the elastic modulus of the SMA, α_a the thermal elastic coefficient, and Ω denotes the phase transformation coefficient, which can be taken as a constant for the whole composite including glass-fibre/epoxy. Take

$$d\xi = \frac{\partial \xi}{\partial \sigma_a} d\sigma_a + \frac{\partial \xi}{\partial T} dT. \tag{A.6}$$

Substitution of Eq. (A.6) into Eq. (A.5) produces

$$d\varepsilon_a = \frac{1}{E(\xi)} \left\{ \left(1 - \Omega \frac{\partial \xi}{\partial \sigma_a}\right) d\sigma_a - \left(0 + \Omega \frac{\partial \xi}{\partial T}\right) dT \right\}. \tag{A.7}$$

Using Eqs. (A.1), (A.4) and (A.7), the effective Young's modulus E_{11} can be written as

$$E_{11} = E(\xi) + \frac{V_m E_m}{V_a} \left(1 - \Omega \frac{\partial \xi}{\partial \sigma_a}\right). \tag{A.8}$$

For the transform from the Austenite phase to Martensite phase

$$\frac{\partial \xi}{\partial \sigma_a} = \frac{\xi_M}{2} \frac{a_A}{C_A} \sin\left[a_A(T - A_s) - \frac{a_A}{C_A}\sigma_a\right]. \tag{A.9}$$

For the transform from the Martensite phase to Austenite phase

$$\frac{\partial \xi}{\partial \sigma_a} = \frac{1 - \xi_A}{2} \frac{a_M}{C_M} \sin\left[a_M(T - M_f) - \frac{a_M}{C_M}\sigma_a\right]. \tag{A.10}$$

σ_a in Eq. (A.8) can be expressed as

$$\sigma_a = \frac{1}{V_a}\{\sigma - V_m E_m[\varepsilon - \alpha_m(T - T_0)]\}, \tag{A.11}$$

where T_0 denotes the reference temperature.

References

[1] Schetky LM, Wu MH. The properties and processing of shape memory alloys for use as actuators in intelligent composite materials. Smart Struct Mater 1991;24:65–71.

[2] Liang C, Rogers CA, Malafeew E. Preliminary investigation of shape memory polymers and other hybrid composites. Smart Struct Mater 1991;24:97–105.

[3] Giurgiutiu V, Rogers CA, Craig A. Design and preliminary tests of an active composite. Smart Struct Mater 1997;30:206–16.

[4] Liang C, Rogers CA. Design of shape memory alloy springs with application invibration control. J Vibration Acoustics 1993;115:97–112.

[5] Lei CY, Wu MH. Thermo-mechanical properties of NiTi shape memory alloys. Smart Struct Mater 1991;24:73–7.

[6] Boyd JG, Lagoudas W. Thermomechanical response of shape memory alloys. J Intelligent Mater Syst Struct 1993;5:34–48.

[7] Tang WJ, Sandstrom R. On the material parameters in the constitutive relations for shape memory alloys. In: Proceedings of the International Symposium on Shape Memory Materials. China Academic Publishers, 1994:535–41.

[8] Tang WJ, Sandstrom R. Limitations of constitutive relations for NiTi shape memory alloys. J Phys 1995;11:185–90.

[9] Gao S, Shen YP. The mechanical analysis of shape memory alloys and its application in engineering. Adv Mech 1997;27:301–12.

[10] Xiong K, Wang Z, Tao BQ. One-dimension constitute relations for shape memory alloy reinforced composites. Trans NUAA 1996;28:551–5.

[11] Wang Z, Wu JS. Thermo-mechanical characteristics of composites reinforced with shape memory alloy wires – Research on smart composites. Acta Mater Compositae Sinica 1997;10:52–6.

[12] Coleman BD. Thermodynamics of materials with memory. Arch Rational Mech Anal 1964;17:1–46.

[13] Colemen BD, Gurtin ME. Thermodynamics with internal state variables. J Chem Phys Solids 1967;47:597–613.

ELSEVIER

Composite Structures 47 (1999) 711–717

COMPOSITE STRUCTURES

www.elsevier.com/locate/compstruct

Residual compressive strength of laminated plates with delamination

Haoran Chen *, Xiannian Sun

State Key Laboratory of Structural Analysis of Industrial Equipment, Department of Engineering Mechanics, Dalian University of Technology, Dalian 116024, People's Republic of China

Abstract

A study of residual compressive strength in delaminated laminates is presented. A methodology is proposed for simulating the whole compressive failure responses, such as initial buckling, postbuckling, contact of delamination front region, delamination propagation, fiber breakage, and matrix cracking etc. An finite element analysis (FEA) of the residual compressive strength is conducted on the basis of the Von Karman's nonlinearity assumption and the first-order shear deformation plate theory, combined with a stiffness degradation scheme. The numerical analysis models and methods are briefly introduced in this paper and some numerical examples are presented to illustrate it. From numerical results and discussion, it is clear that the compressive failure response involves complex multi-failure modes during compressive process. The method and numerical conclusions provide in this paper should of great value to engineers dealing with composite structures. © 2000 Elsevier Science Ltd. All rights reserved.

Keywords: Laminates; Delamination; Finite element analysis (FEA); Residual compressive strength; Failure prediction

1. Introduction

Compression behavior of the laminated plates containing delaminations has recently drawn considerable attention among researchers, because delaminated plates resulting from impact or manufacturing defects can cause significant reductions in stiffness and strength under compressive loads. Therefore, a clear understanding of the compressive failure behavior and residual load carrying capacity for the delaminated plates is of extremely importance in designing and maintaining laminated structures. Thus, investigation and analysis of the compressive failure behavior for the delaminated plates are of great interest to engineers and mechanics scientists, and many valuable papers have been published. Most of previous investigators only addressed to study on the failure behavior of delamination prebuckling, post-buckling and growth, because they believe that the failure of the laminated composites with delaminations would undergo delamination buckling and growth process [1–12]. However, according to observation experimental phenomena [1,4], the failure mode appears not only in delamination fracture, but also in other multiple failure modes, e.g., compressive failure caused by matrix cracking and fibrous breakage etc. Hence, those research works are not appropriate for simulating the complex multiple failure modes. Several researchers have developed some semi-experiential engineering approaches to analyze the residual strength of the damaged laminated composites, which are considered the delamination zone as an open hole or soft zone based on enormous experimental results [13,14]. It is obvious that those approaches are very simple, but the effects of delamination buckling and propagation on the residual strength are ignored. In fact, the progressive and ultimate failure configurations of the delaminated plates could appear in different modes, which are affected by the many factors, e.g., location, shape and size of the delamination, and ply orientation, stacking sequence and edge constrained condition, etc. of the plates. For examples, the progressive failure process of the laminated plates with shallow delamination is from initial buckling, delamination growth, postbuckling till final failure, while for the lamination length being shorter and deeper, the initial and final failures would be compressive failure without undergoing buckling process. Therefore, it is very important to identify different failure mechanisms for different delaminated laminates in advance.

The objective of this study is to establish the numerical analysis models and methods for predicting the residual compressive strength of the laminated plates

* Corresponding author. Tel.: +86-411-470-8393; fax: +86-411-470-8116.

E-mail address: chenhr@gingko.dlut.edu.cn (H. Chen).

0263-8223/99/$ - see front matter © 2000 Elsevier Science Ltd. All rights reserved.
PII: S0263-8223(00)00041-6

with a delamination and simulating the compressive responses such as initial buckling, postbuckling, contact of delamination front region, fiber and matrix failure. A virtual crack closure technique is adopted to calculate the value of the strain energy release rate (SERR) along the delamination front, and a virtual interface spring element approach is employed to avoid the overlap between upper and lower sublaminates of the delaminated region. Numerical results and conclusions for some typical examples show the effects of location, shape and size of the delamination upon the progressive and ultimate failure modes of the delaminated plates. Hence, the present paper is believed to form a significant contribution to the engineering understanding of the failure mechanism of the laminated plates.

2. Numerical analysis models

2.1. Delamination model

Fig. 1 shows a typical composite plate embedded a delamination under compressive loads, which consists of three parts forming an upper, lower and base sublaminate. The finite element nodes for each of the sublaminates are assumed to be located on their mid-planes.

According to the first-order shear deformation plate theory, the displacement fields for each sublaminates can be expressed as follows:

$$\begin{aligned} u &= u^0(x,y) + z\theta_y(x,y), \\ v &= v^0(x,y) - z\theta_x(x,y), \\ w &= w^0(x,y), \end{aligned} \tag{1}$$

where u, v, w and θ_x, θ_y denote translational displacement components in the x, y and z directions, and rotational components about the x-, y-axis's, respectively. The superscript "0" presents the mid-plane of the sublaminate. Using the von Kármán-strains nonlinearity assumption, the non-linear strain–displacement equations are formulated

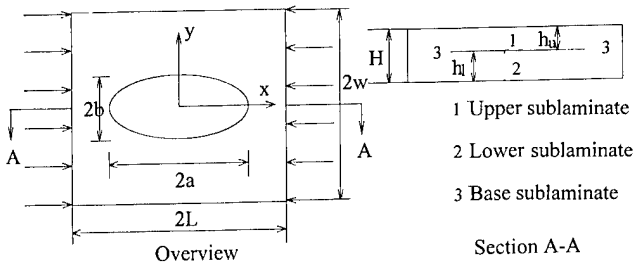

Fig. 1. Configuration of laminated plate with an elliptical delamination.

$$\begin{Bmatrix} \varepsilon_x \\ \varepsilon_y \\ \varepsilon_{xy} \\ \varepsilon_{yz} \\ \varepsilon_{zx} \end{Bmatrix} = \begin{Bmatrix} u_{,x} + z\theta_{y,x} + w_{,x}^2/2 \\ v_{,y} - z\theta_{x,y} + w_{,y}^2/2l \\ u_{,y} + v_{,x} - z\theta_{x,x} + z\theta_{y,y} + w_{,x}w_{,y} \\ w_{,y} - \theta_x \\ w_{,x} + \theta_y l \end{Bmatrix}. \tag{2}$$

The continuity of the displacements and rotations along the delamination front between the upper, lower and base sublaminates must be strictly satisfied, hence the constraint equations imposed can be written as:

$$\begin{aligned} &w = w_1 = w_2 = w_3, \\ &\theta_x = \theta_{x1} = \theta_{x2} = \theta_{x3}, \quad \theta_y = \theta_{y1} = \theta_{y2} = \theta_{y3}, \\ &u_1 = u_3 + \theta_{y3}(H - h_l)/2, \quad u_2 = u_3 - \theta_{y3}(H - h_u)/2, \\ &v_1 = v_3 - \theta_{x3}(H - h_l)/2, \quad v_2 = v_3 + \theta_{x3}(H - h_l)/2, \end{aligned} \tag{3}$$

where the subscripts 1, 2, 3 are the upper, lower and base sublaminates, h_u, h_l and H denote the thickness' of the upper, lower and base sublaminates, respectively, as shown in Fig. 1.

2.2. Contact analysis model

For certain combinations of delamination size, shape and strain level, the closure appearance would occur over parts of the delamination front. Unless constraints are imposed, the delamination faces will appear in overlap during the analysis process and then the numerical error will be introduced in the results. Assume that there is no friction in the contact area, a virtual truss element can be used to prevent penetration between the upper and lower sublaminates. Every two nodes with the same values of x and y coordinates located in the mid-planes of the upper and lower sublaminates form a node pair. The expressions of the contact condition for every node pair can be defined as:

$$\begin{aligned} &w_i^1 - w_i^2 > 0 \quad \text{not contacted,} \\ &w_i^1 - w_i^2 = 0 \quad \text{contacted, no pressure,} \\ &w_i^1 - w_i^2 < 0 \quad \text{contacted,} \end{aligned} \tag{4}$$

where the superscripts 1 and 2 are upper and lower sublaminates, as shown in Fig. 1.

When a node pair is contacted, a virtual truss element should be imposed between the two nodes of the node pair. The stiffness matrix of the truss element is

$$[K]^e = k\begin{bmatrix} 1 & -1 \\ -1 & 1 \end{bmatrix}, \tag{5}$$

where k is a specified stiffness for avoiding penetration between the upper and lower sublaminates of the delaminated region.

2.3. Failure model

The failure models of the delaminated composite plates consist of buckling, delamination initiation, postbuckling, delamination propagation and local compressive damage. The buckling and postbuckling models were introduced in Refs. [6–9], therefore omitted here.

(1) *Delamination initiation and propagation* [10,11]: Using linear elastic fracture mechanics theory to predict delamination initiation, a modified crack closure technique [15] is employed to calculate the value of the strain energy release for each delamination front. The strain energy released during crack extension process is assumed to be equal the work to close the opened crack surfaces.

Fig. 2 shows a typical model of a pair of four elements in the upper and lower sublaminates at the delamination front. Generally, the length of the virtual crack extension Δa taken is less than that of delamination to meet the need of calculating precision. As shown in Fig. 2, the value of the closure energy of the node i_1 can be written as

$$2U = N_x\Delta u + N_y\Delta v + N_z\Delta w + M_x\Delta\theta_x + M_y\Delta\theta_y, \tag{6}$$

where Δu, Δv, Δw and $\Delta\theta_x$, $\Delta\theta_y$ are the differences of the nodal displacements and rotations between the nodes i'_1 and i'_2; N_x, N_y, N_z, M_x, M_y denote the components of the internal forces and moments between nodes i_1 and i_2, respectively. The strain energy release rate can be expressed as

$$G = U/A, \tag{7}$$

where A is the crack closure area and

$$A = \frac{1}{2}\overline{j'_1k'_1} \times \overline{i'_1i_1}. \tag{8}$$

(2) *Local compressive damage*: The Tsai–Hill failure criteria combined with corresponding stiffness degradation rules is adopted for predicting the occurrence and modes of the local damage failure, and determining the reduced material properties after damage. The Tsai–Hill failure criteria for the plane stress state is as follows:

$$\left(\frac{\sigma_1}{X}\right)^2 + \left(\frac{\sigma_2}{Y}\right)^2 - \frac{\sigma_1\sigma_2}{X^2} + \left(\frac{\sigma_6}{S}\right)^2 = 1, \tag{9}$$

where σ_1, σ_2, σ_6 are the on-axis normal and shear stresses; and X, Y, S are the on-axis tension and shear strength, respectively. A lamina would be damage when the left value of Eq. (9) is greater than and/or equal 1. Accordingly, the reduced material properties can be obtained by the following degradation rules proposed by Tsai [16]:

$$\begin{aligned} &E_1^* = E_1, \quad E_2^* = 0.56E_2, \\ &\mu_{12}^* = \mu_{12}, \quad G_{12}^* = 0.44G_{12}, \end{aligned} \tag{10}$$

where the superscript "$*$" denotes the degraded material properties.

3. Methodology

A modified Newton–Raphson iteration scheme combined with the analysis models described in the preceding section is used for study of the failure process and residual compressive strength of the delaminated plates. The basic steps of the finite element iteration method are briefly summarized as following:

1. a virtual transverse load is applied at the center of the delaminated region to initiate transverse deflections of the delaminated plates;

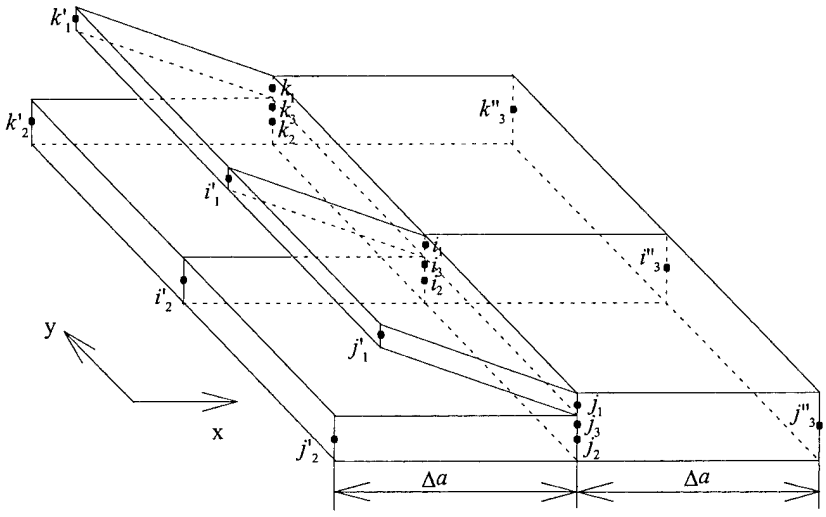

Fig. 2. Schematic of delamination front region.

2. an external incremental load ΔP defined and the ΔP is applied to the delaminated plates for forming an initial load state P;
3. the finite element analysis (FEA) based on the first-order shear deformation and Vor Karman nonlinear plate theory is used to calculate the stress field of the delaminated plates;
4. the contact condition is employed to check the front of the delaminated region. If any node pair appears in overlap, a virtual truss element is used to modify the contact state of the corresponding node pair and then the next return step 3;
5. the Tsai–Hill failure criteria is used to check the stress states for all the elements and if any element appears in failure, the stiffness matrix of the corresponding elements is modified according to the Tsai' stiffness degradation rule, and then the next step returns to step 3;
6. the values of energy release rate of the nodes in the front of the delaminated region are calculated;
7. if the current load P is not reached at a specified load, the current load P is added to the incremental load ΔP for forming a new load, and then the next step returns to step 3;
8. iteration stops.

A C computer program, called DAMAGE, has been developed by authors to utilize the above-mentioned procedure.

4. Results and discussion

Consider a T300/5208 laminated plate embedded a circular delamination under compression, as shown in Fig. 1. The dimensions for the plate are $2L = 2W = 100$ mm. For simplicity, let $\bar{a} = a/L = b/W$ and $\bar{h} = h_u/H$. The boundary conditions along the four edges are clamped. The stacking sequences of the laminated plates are $[0]_{32}$, $[0]_{64}$, $[0/90/90/0]_{4S}$ and $[0/90/90/0]_{8S}$, respectively. The thickness of a lamina $h = 0.127$ mm. The mechanical properties and strengths of the composite are:

$$E_1 = 181.0\ \text{GPa}, \quad E_2 = E_3 = 10.3\ \text{GPa},$$
$$G_{12} = G_{13} = 7.17\ \text{GPa}, \quad G_{23} = 4.02\ \text{GPa},$$
$$\mu_{12} = \mu_{13} = 0.28, \quad \mu_{23} = 0.28,$$

$$X_T = X_C = 1500\ \text{MPa}, \quad Y_T = 40\ \text{MPa},$$
$$Y_C = 246\ \text{MPa}, \quad S = 68\ \text{MPa},$$

where, the subscripts "T" and "C" denote the tension strength and compressive strength, respectively.

4.1. Buckling loads and compressive strength

Figs. 3 and 4, respectively illustrate the normalized buckling loads P_{cr}/P_S versus the delamination areas and depths for $[0]_{32}$ and $[0]_{64}$ plates, where P_S represents the values of compressive strength for the corresponding perfect plates. The ratios between the spans and thickness' for two kinds of plates are 24.6 and 12.3, respectively. Comparing Fig. 3 with 4, It can be found that, the values of the normalized buckling loads are less than one for all $[0]_{32}$ plates, i.e., the buckling is a control failure mode prior compressive strength failure for these laminated plates, while for $[0]_{64}$ plates with a large and shallow delamination, $P_{cr} < P_S$, i.e. the buckling is still a control failure mode, but for $[0]_{64}$ plates with a small and deep delamination, $P_{cr} > P_S$ i.e. the compressive strength failure is a control failure mode prior to buckling. Hence, it is necessary to identify their failure modes in advance of analyzing the compressive load capabilities of the delaminated plates.

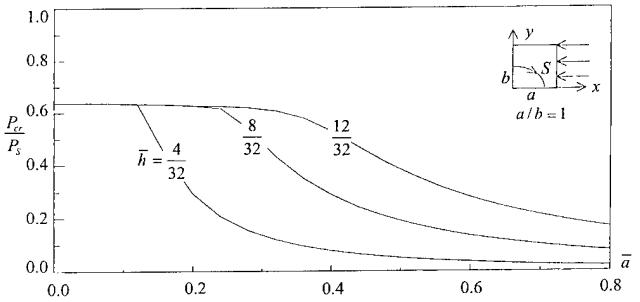

Fig. 3. Variations of buckling loads of $[0]_{32}$ with delamination areas and depths.

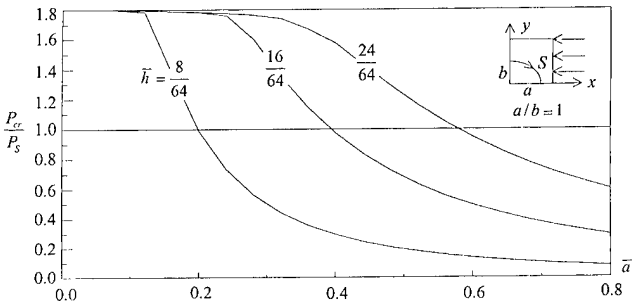

Fig. 4. Variations of buckling loads of $[0]_{64}$ laminated plate with delamination areas and depths.

4.2. Effect of stiffness degradation on buckling loads

The effect of stiffness degradation induced by progressive failure on the buckling loads of the delaminated plates should be considered, if the first ply failure (FPF) appears prior to initial buckling. Let σ_{cr} and σ_{cr}^{d} be the buckling stresses with and without considering the property degradation of the delaminated plate, respectively. The buckling stress is defined by the ratio between the buckling loads and transverse section area of the delaminated plate.

Calculating the stresses of buckling and compressive failure for $[0/90/90/0]_{4S}$, and $[0/90/90/0]_{8S}$ plates without delaminations, respectively. During the loading process of the laminated plates, the FPF arises in the 0° sublaminates prior to buckling, and the corresponding stress of the plates is 795.3 MPa. Therefore, according to the stiffness degradation rule defined in Eq. (10), the properties of the 0° sublaminates need to be reduced. Then with increasing load, the buckling failure arises prior to the compressive strength failure in the 90° sublaminates, the values of the ultimate stresses for the two kinds of laminated plates are 862.6 and 2099.7 MPa, respectively. However, the buckling stresses for the two kinds of laminated plates are 927.4 and 2566.9 MPa, respectively, without considering property degradation caused by FPF. Hence, it is very important to identify the changes of the failure modes during the loading process.

Tables 1 and 2 show the buckling stresses for $[0/90/90/0]_{4S}$, and $[0/90/90/0]_{8S}$ plates versus the delamination sizes and locations, respectively. From these tables, it can be seen that the buckling stresses increase with increasing the thicknesses of the delaminated plates, which results in the compressive strength failure prior to buckling for the 0° sublaminates. In contrast, the buckling stresses decrease with increasing the delamination radius, which results in the buckling prior to the compressive strength. Hence, it should be noted that, the effect of delamination sizes and depths on the failure modes of the laminated plates must be considered for analyzing the residual load capability of the delaminated plates.

4.3. Effect of stiffness degradation on postbuckling deflection

Consider two kinds of $[0/90/90/0]_{4S}$ laminated plates with a circular delamination, the depths of delaminations for both plates are the same and $\bar{h} = 4/32$, whereas the values of the delamination radius are 15 and 30 mm, respectively. The midpoint deflections curves of upper and lower sublaminates of the delaminated plates are shown in Figs. 5 and 6. The ordinate of the figures ε presents the external uniform compressive strains subjected to the edges $x = a$, $-a$. Comparing Fig. 5 with 6, it can be found that the values of midpoint deflections for the plates with considering the stiffness degradation are larger than that without considering the stiffness degradation, and the effect of stiffness degradation on the midpoint deflections for the plate with a smaller delamination is more severe than that with large delamination.

4.4. Effect of stiffness degradation on distribution of strain energy release rate at delamination front

Fig. 7 presents the values of the strain energy release rate on the delamination front for $[0/90/90/0]_{4S}$ laminated plate with a circular delamination, which dimensions are $a = b = 30$ mm and $\bar{h} = 4/32$. It can be seen that the peak values of strain energy release rate with considering the stiffness degradation are much higher than that without considering the stiffness degradation during the loading process. Hence, the stiffness degradation will accelerate delamination growth of the delaminated plate.

Table 1
Variations of buckling stresses of $[0/90/90/0]_{4S}$ plates versus delamination sizes and locations (in MPa)

	$\bar{h} = 4/32$			$\bar{h} = 8/32$			$\bar{h} = 12/32$		
$\bar{a}$	σ_{cr}	σ_{cr}^{d}	$(\sigma_{cr} - \sigma_{cr}^{d})/\sigma_{cr}$	σ_{cr}	σ_{cr}^{d}	$(\sigma_{cr} - \sigma_{cr}^{d})/\sigma_{cr}$	σ_{cr}	σ_{cr}^{d}	$(\sigma_{cr} - \sigma_{cr}^{d})/\sigma_{cr}$
0.2	432.2	432.2	0.000	907.8	844.5	0.070	909.9	846.2	0.070
0.3	200.9	200.9	0.000	686.8	686.8	0.000	859.8	818.3	0.048
0.4	114.9	114.9	0.000	413.3	413.3	0.000	724.9	724.9	0.000
0.5	74.1	74.1	0.000	272.9	272.9	0.000	524.4	524.4	0.000
0.6	51.7	51.7	0.000	193.1	193.1	0.000	388.4	388.4	0.000

Table 2
Variations of buckling stresses of $[0/90/90/0]_{8S}$ plates versus delamination sizes and locations (in MPa)

	$\bar{h} = 8/64$			$\bar{h} = 16/64$			$\bar{h} = 24/64$		
$\bar{a}$	σ_{cr}	σ_{cr}^{d}	$(\sigma_{cr} - \sigma_{cr}^{d})/\sigma_{cr}$	σ_{cr}	σ_{cr}^{d}	$(\sigma_{cr} - \sigma_{cr}^{d})/\sigma_{cr}$	σ_{cr}	σ_{cr}^{d}	$(\sigma_{cr} - \sigma_{cr}^{d})/\sigma_{cr}$
0.2	909.9	846.2	0.070	2519.2	2061.1	0.182	2525.9	2068.1	0.181
0.3	859.8	818.3	0.048	2033.6	1696.4	0.166	2437.1	1994.0	0.182
0.4	724.9	724.9	0.000	1345.2	1200.0	0.108	2067.3	1727.6	0.164
0.5	524.4	524.4	0.000	944.4	867.6	0.081	1621.4	1406.1	0.133
0.6	388.4	388.4	0.000	693.2	693.2	0.000	1277.0	1140.0	0.107

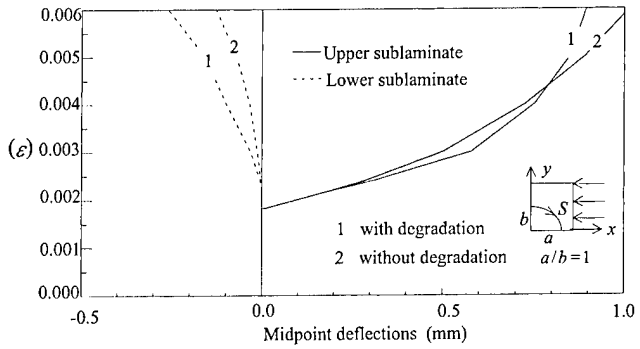

Fig. 5. Midpoint deflections of upper and lower sublaminates of $[0/90/90/0]_{4S}$ plate with a circular delamination ($a \times b = 15$ mm $\times$ 15 mm, $\bar{h} = 4/32$).

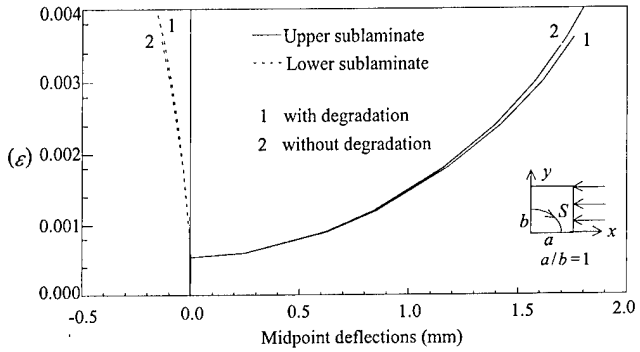

Fig. 6. Midpoint deflections of upper and lower sublaminates of $[0/90/90/0]_{4S}$ plate with a circular delamination ($a \times b = 30$ mm $\times$ 30 mm, $\bar{h} = 4/32$).

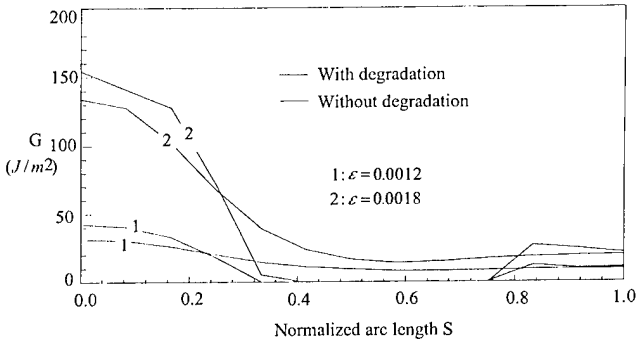

Fig. 7. Distributions of strain energy release rate for $[0/90/90/0]_{4S}$ plate with a circular delamination ($a \times b = 30$ mm $\times$ 30 mm, $\bar{h} = 4/32$).

5. Conclusions

1. The progressive and ultimate failure configuration of the delaminated plates under compressive loads could appears in different modes, thus, it is necessary to identify their failure modes in advance of analyzing the compressive load capabilities of the delaminated plates.
2. If the progressive strength failure modes appear prior to buckling, the effect of stiffness degradation induced by progressive failure on the buckling loads of the delaminated plate should be considered.
3. On the postbuckling path, the values of midpoint deflections for the plate with considering the stiffness degradation are larger than that without considering the stiffness degradation, and the effect of stiffness degradation on the midpoint deflection for the plate with a smaller delamination is more severe than that with a larger delamination.
4. The stiffness degradation caused by progressive strength failures will accelerate delamination growth of the delaminated plate.
5. The failure mechanisms for different delaminated laminates are affected by many factors, e.g., location, shape and size of the delamination, and ply orientation, stacking sequence and edge constrained condition, etc. of the plates.
6. The methodology, model and numerical analysis methods proposed in the paper can be used for simulating the whole compressive failure responses, such as initial buckling, postbuckling, contact of delamination front region, delamination propagation, fiber-breakage, and matrix cracking, etc.

Acknowledgements

This work has been supported by the National Natural Science Foundation of China, under the grant No. 19672014, and the Special Doctoral Science Foundation of Chinese Education Ministry under grant No. 96014111.

References

[1] Abrate S. Impact on laminated composites: recent advances. Appl Mech Rev 1994;47:517–44.
[2] Whitcomb JD. Finite element analysis of instability-related delamination growth. J Compos Mater 1981;15:403–26.
[3] Whitcomb JD. Three-dimensional analysis of a postbuckled embedded delamination. J Compos Mater 1989;23:862–89.
[4] Davidson BD. Delamination buckling: theory and experiment. J Compos Mater 1991;25:1351–78.
[5] Xiong Y, Poon C, Staznicky PV, Vietinghoff H. A prediction method for the compressive strength of impact damaged composite laminates. Compos Struct 1995;30:357–67.
[6] Klug J, Wu XX, Sun CT. Efficient modeling of postbuckling delamination growth in composite laminates using plate elements. AIAA J 1996;34:178–84.
[7] Kim HJ. Postbuckling analysis of composite laminates with a delamination. Comput & Struct 1997;52:975–83.
[8] Rinderknecht S, Kroplin B. A computational method for the analysis of delamination growth in composite plates. Comput & Struct 1997;64:359–74.
[9] Sun XN, Chen HR. Pre-post buckling analysis of composite laminates with delamiantion damage. Acta Aeronautica ET Astronautica SINICA 1988;20:224–9 in Chinese.

[10] Sun XN, Chen HR. Study of energy release rate of composite laminates with symmetric edge-delaminations considering geometric nonlinearity. J Dalian Univ Technol 1998;38:249–54 in Chinese.
[11] Sun XN, Chen HR. Quasi-three dimensional geometric nonlinear analysis of composite laminates containing symmetrical through-the width delaminations. J Dalian Univ Technol 1999;39:705–16 in Chinese.
[12] Kim H, Kedward KT. A method for modeling the local and global buckling of delaminated composite plates. Compos Struct 1999;44:45–53.
[13] Starnes JH Jr., Rhodes MD, Williams JG. The effect of impact damage and circular holes on the compressive strength of a graphite–epoxy laminate. NASA Technical Memorandum 1978;78796.
[14] Guild FJ, Hogg PJ, Prichard JC. A model for the reduction in compression strength of continuous fiber composites with impact damage. Composites 1993;24:333–9.
[15] Ribyki EF, Kannien MF. A finite element calculation of stress intensity factors by a modified crack closure integral. Eng Frac Mech 1977;19:931–8.
[16] Tsai SW. Composite design – 1986. United States Air Force Materials Laboratory Press, 1986.

ELSEVIER

Composite Structures 47 (1999) 719–725

COMPOSITE STRUCTURES

www.elsevier.com/locate/compstruct

Design and evaluation of various section profiles for pultruded deck panels

Lian Hong Gan, Lin Ye *, Yu-Wing Mai

Department of Mechanical and Mechatronic Engineering, Centre for Advanced Materials Technology, The University of Sydney, Sydney, NSW 2006, Australia

Abstract

Local high stresses and buckling may be critical to the composite deck panels with moderately thick walls. Design and evaluation of section profiles for pultruded deck panels with the reduced local stress and improved buckling strength are discussed. The deck panels with several different cross-sectional profiles are assessed based on finite element analysis. The assessment covers the global and local stiffness, the maximum stresses and buckling strength. Compared to the original design, one of the panels with the modified profiles possesses significant improvement in all aspects evaluated. Most profiles provide lower compressive stress and higher local stiffness and significantly higher buckling strength. © 2000 Elsevier Science Ltd. All rights reserved.

Keywords: Deck panel; Pultrusion; Section profile; Finite element analysis; Buckling

1. Introduction

Application of fibre reinforced composites to bridge structures has attracted great attention to the transportation industry. A number of fibre reinforced plastic (FRP) bridge decks have been manufactured and put into service in the world. The composite decks are not only for pedestrian bridges, but also for traffic bridges. Some of many important achievements on composite decks have been reported [1–7].

One of the main driving forces to use composites in bridge structure is to construct light and easy-to-erect deck systems. To achieve this, moderately thin walls and multi-cellular structure are usually employed in composite decks. They may, however, lead to high compressive stresses under wheel pressures, resulting in a large difference between the maximum compressive and tensile stresses in the decks. Considerable difference in the maximum stresses is detrimental to the strength of the structural components, as the flanges do not equally contribute to the global strength. Large compressive stresses can cause local buckling in the top flange of the deck. Breaks were found in the top surface of the composite deck in a bridge in Britain, which occurred within a small area, a certain period after it was put into service. The real reasons for this are not clear at the moment, but it is possible due to the high local stresses, which may be related to local buckling. Therefore, it is important to fully understand the local stress and buckling in FRP deck panels, which allows design of panels with the high buckling strength and improved properties for the top flange to increase their ultimate strength.

The main aims of this work are to design such panels through constructing suitable section profiles and assessing their performance using finite element analysis. The section profiles presented in this work were developed by modifying a typical panel used in applications. This paper presents a comparative study on the decks with some typical profiles and the proposed ones.

2. Design of section profiles

The sectional shapes assessed in this study are shown in Fig. 1, where the section (a) was taken from [1] and sections (b) and (c) were from [2]. The first three sections are named as hexagonal (H), triangle (T) and rectangular (R4), respectively, for simplicity. They can be considered as the representatives for those have been used in composite decks, as they are unique but typical in the way how the top and bottom flanges are

* Corresponding author. Tel.: +61-2-9351-4798; fax: +61-2-9351-7060.

E-mail address: ye@mech.eng.usyd.edu.au (L. Ye).

0263-8223/99/$ - see front matter © 2000 Elsevier Science Ltd. All rights reserved.
PII: S0263-8223(00)00042-8

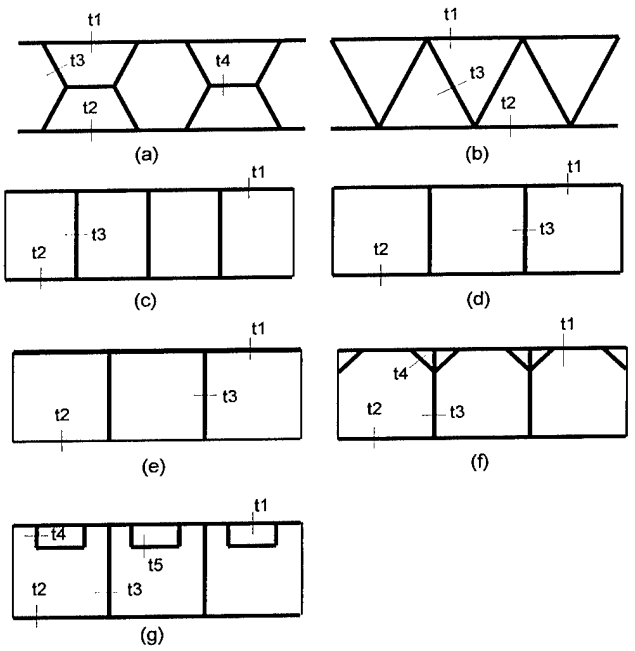

Fig. 1. Section profiles for pultruded deck modules, where t1 to t5 are the flange or web thickness.

connected. A 3-cell rectangular section (S3) is also considered, which is basically the same as R4, but composed of square cells which are different in the wall thickness. Decks with these sections all belong to multi-cellular structures, but are different in the cell shape, being hexagon, triangle and rectangle, respectively.

The deck panels with the first three profiles fabricated with the specific dimensions [1,2] have shown satisfactory mechanical performance. The dimensions of the profiles in this study are, however, chosen to be slightly different from those in literature to ensure the same cross-section area, which leads to the same volume of material for each panel for the purpose of comparison (Table 1). It is clear that for each section there are many combinations available for the thickness of the top flange, bottom flange and webs to comply with the requirement of the equal section area. However, a simple choice of using the same (approximately) thickness for each part was made for all the sections in the present study. The wall thickness for the 3-cell section was designed to be 12 mm, which is in between those used in literature [1–3,7]. The thicknesses for other profiles are adjusted by forming the same cross-section area to S3.

Table 1
Geometric dimensions of section profiles (mm)

	S3	H	T	R4	TT	TE	CE
T1	12	9	9	11	14	11	11
T2	12	9	9	11	10	9	9
t3	12	8	8.2	10.6	12	12	10
t4						5.7	5
t5							7

Our preliminary study reveals that overall the S3-section has better stiffness and strength than the others, and thus it is selected as the basis to develop new profiles. There are various ways to improve a profile to achieve higher buckling strength and enhanced compression strength for the top flange. The approach in this study stems from the understanding of the local buckling and deformation of the top flange, whose analysis can be simplified as a plate subject to elastic supports. According to structural buckling theories [8] the local buckling strength can be increased through the improvements in the constraints to the flange, its bending stiffness and the buckling wavelength. The modification on the selected section S3, to implement these improvements results in the new section profiles in Fig. 1(e)–(g).

A most straightforward method to increase the bending stiffness of the panel is to increase the thickness of the top flange, implemented in the section (e). This section, termed as thick top section (TT), involves no change in geometrical shape, except the thickness of the flanges. In sections (f) and (g), the thickness of the bottom flange is reduced by 17%, and that of the webs reduced by 8%, compared to R3-section. The cut material is used to build the stiffeners for the top flange. The section (f) is enhanced using extra stiffeners to join the top flange and webs, termed as triangle-enhanced (TE). This enhancement can effectively reduce the buckling wavelength when the top flange buckles into such a shape that a wave forms between two contiguous webs. This is usually the case in our preliminary study, and therefore this connection will effectively increase the anti-buckling capacity of the deck panels. The enhancement also increases the resistance to the local deformation of the top flange, which will bring about reduction in local stresses. The cut material in the section (g) is used to form a C-section channel fixed to the top flange. To get an enough volume of material for the C-channels with a reasonable wall thickness, the webs are also cut by 8%. This C-channel enhanced section, or CE for short, will improve the bending stiffness of the top flange primarily in the axial direction.

3. Finite element modelling

The panels with these profiles as cross-section are assumed to be supported by four solid beams uniformly placed in a span of 8/3 m (Fig. 2), which is typical in bridge structure. The maximum bending moment will be generated when the loads are applied at the middle span of the panel (Fig. 2). The loads are uniformly distributed on a small area to simulate the wheel pressures.

A deck panel in loading conditions will be subjected to the constraints from the adjacent panels. The

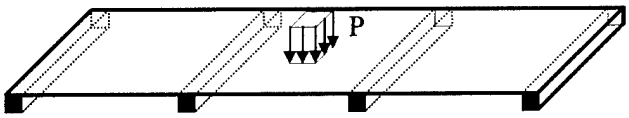

Fig. 2. Schematic expression of loading and boundary conditions for the deck panel.

Table 2
Material properties used in finite element analysis

	E_{11}[a] (GPa)	E_{22} (GPa)	G (GPa)	v
Flange	22	8	4	0.27
Web/ stiffener	14	14	4	0.27

[a] The subscript "11" refers to the axial direction and "22" to the lateral direction of the flanges, webs, or stiffeners.

constraints are difficult to be defined, but are simplified in this study as two basic cases. In the first case, no constraints from the adjacent panels are considered, which means that the panel is free to deform at its both sides. This case corresponds to the most common test conditions in a laboratory. The other case considers that both top and bottom flanges have no in-plane transverse movement at their side edges.

The panels are assumed to be produced with pultrusion. Strictly speaking, the micro-structure of the composite produced with this technology is normally different from the layered composite. However, it is justified to apply the laminate composite theory to the analysis of the pultruded composites, as exercised by a number of researchers [9]. For the present purpose, the material was assumed to be orthotropic, and the properties in Table 2, estimated using [10], were used in the computations.

To obtain accurate results for stress distributions, 3D elements with composite material properties were adopted for the static analysis [11]. For buckling analysis, shell elements were employed for the sake of computational efficiency. Fine mesh definitions with either 3D or shell elements were used for the computations to ensure accurate numerical results (Fig. 3). The computations were performed using ABAQUS, a finite element package for general purposes [11].

4. Assessment of the profiles based on numerical results

It was found that the numerical results for both simplified cases of constraints from the adjacent panels show no clear difference as to which section profile has better properties. Therefore, only the results for the free side edges assumption are presented.

4.1. Global stiffness

The deformations of the deck panels under the applied loads are shown in Figs. 4 and 5. The maximum deflections of the bottom flange, f_m, which occurs at the middle span of the deck panels, are given in Table 3. It can be seen that of four original sections, the S3 panel possesses the highest global stiffness (the lowest deflection), while R4 possesses the lowest. This is because S3 has more material distributed to the flanges to sustain

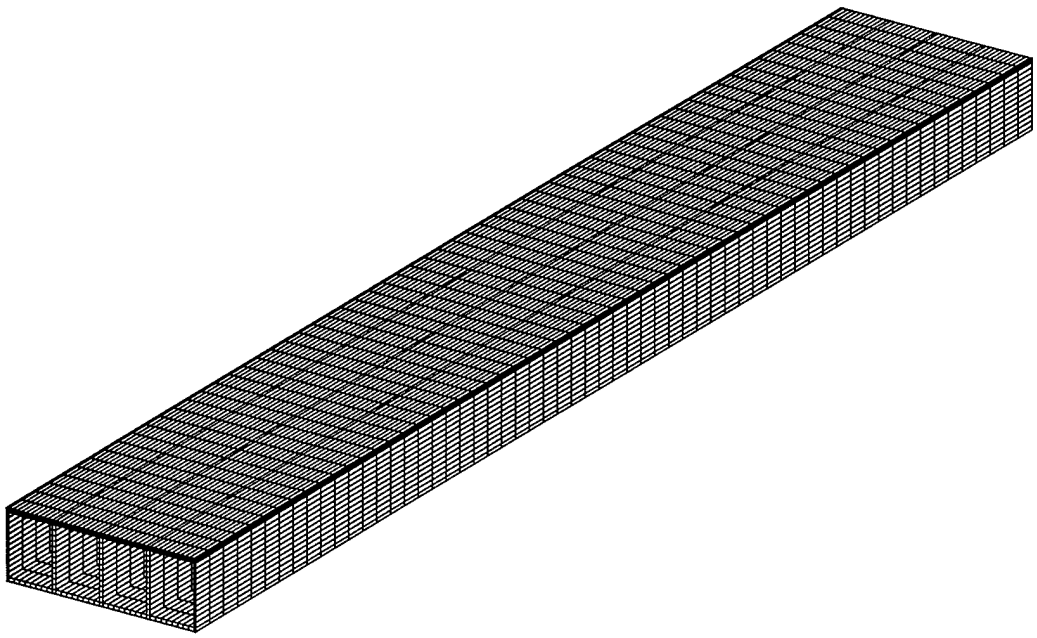

Fig. 3. Finite element mesh for a deck panel.

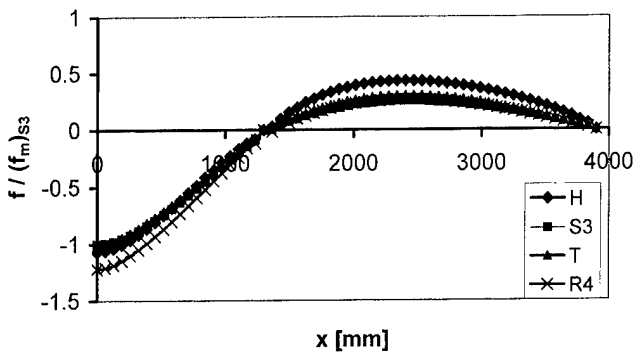

Fig. 4. Deflections of deck panels with original section profiles.

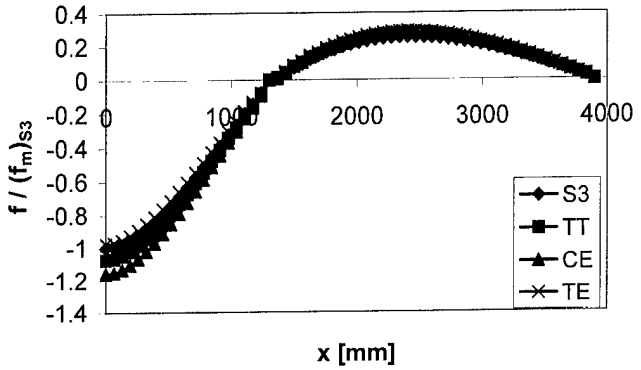

Fig. 5. Deflections of deck panels with modified section profiles.

bending deformation. A reverse situation exists in R4 and H, which results in a lower global stiffness. The differences in the global stiffness between H, T and S3 are minor, being within 7%. R4 produces a deflection 21% larger than that of S3. This shows the importance of using appropriate combination of the number of walls and the thickness for the webs in rectangular multi-cellular panel. Of the panels with the improved profiles, the TE panel provides the best global stiffness. Its stiffness is also slightly higher than that of S3, even with some material in the top and bottom flanges being cut. However, the CE panel appears to lose 16% global stiffness compared to S3.

The numerical results show that TE and its original, S3, are suitable for a panel to achieve the high global stiffness.

4.2. Local stiffness

It has been found that the out-of-plane displacement in the top flange is much larger than that in the bottom one. This deformation directly reflects the local stiffness and strength of the deck panel, which is important to the assessment of the deck properties. For the deck panels with various section profiles, the out-of-displacements across the width at the middle span are shown in Figs. 6 and 7. The maximum value of the displacement, D_m, is used to measure the local stiffness.

Of four panels with the original profiles, the difference in the local stiffness is significant (Table 3). In comparison, S3 gives a D_m twice larger than H, and 30% larger than T. However, even with a smaller global stiffness, R4 gives a D_m 48% smaller than S3. This is, in part, due to more webs being used in this section, which spreads the loads on the top flange over more than one cell. As the bending stiffnesses of the top flange are enhanced, TT and TE panels show far better properties in the local stiffness than S3 (Fig. 7). Their maximum out-of-plane displacements are 84% and 59% of the S3 panel, respectively. However, CE gives a slight improvement in local stiffness. The local stiffness of the top flange is mainly dependent on the supports from the webs. As such, the H panel with inclined plates to support the top flange generates a weaker constraint than the straight plates in the S3 panel, as in the former the supporters will be bent, while in the latter they are mainly compressed. In the TE panel, the supports to the top flange are further improved and it provides better local stiffness.

Table 3
Normalized maximum deflection, out-of-plane displacement, maximum tensile and compressive stress and critical loads for panels with various section profiles

	H	T	R4	S3	TT	CE	TE	
f_m[a]	1.07	1.01	1.22	1.00	1.07	1.16	0.97	Free
	1.11	1.01	1.21	1.00	0.99	1.13	0.96	x-Fixed
D_m	2.26	1.30	0.51	1.00	0.84	0.97	0.59	Free
	1.28	1.27	0.49	1.00	0.75	0.94	0.58	x-Fixed
σ_c	0.79	1.26	0.66	1.00	0.91	0.92	0.67	Free
	0.77	1.25	0.66	1.00	0.85	0.93	0.67	x-Fixed
σ_t	0.95	1.00	0.94	1.00	0.95	0.95	0.96	Free
	0.95	1.00	0.94	1.00	0.95	0.95	0.96	x-Fixed
σ_c/σ_t	1.62	2.47	1.37	1.97	1.88	1.91	1.36	Free
	1.59	2.44	1.36	2.50	1.86	1.91	1.36	x-Fixed
P_{cr}	0.52	0.45	0.76	1.00	1.38	1.11	1.26	Free

[a] f_m: maximum deflection; D_m: maximum out-of-plane displacement; σ_c: maximum compressive stress; σ_t: maximum tensile stress; p_{cr}: critical load factor. f_m, D_m, σ_c, σ_t, p_{cr} are normalized by those of S3.

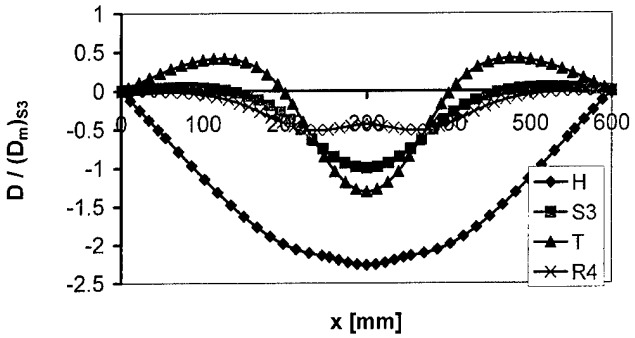

Fig. 6. Out-of-plane deflections of deck panels with original section profiles.

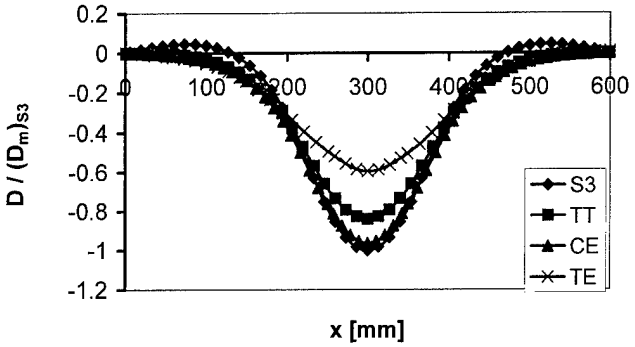

Fig. 7. Out-of-plane deflections of deck panels with modified section profiles.

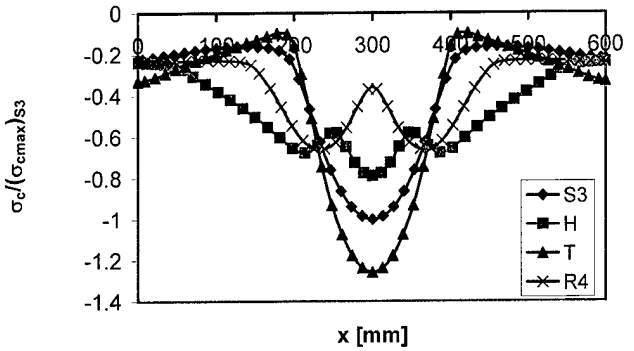

Fig. 8. Compressive stress in deck panels with original section profiles.

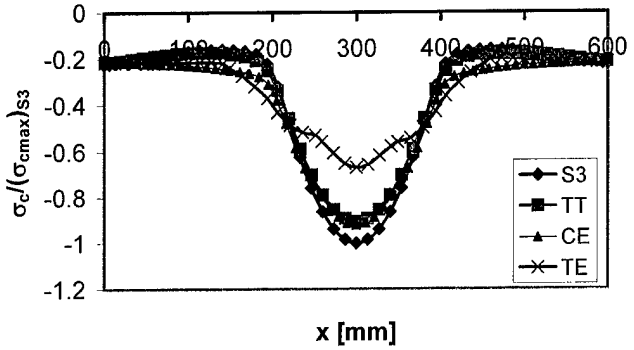

Fig. 9. Compressive stress in deck panels with modified section profiles.

4.3. Maximum stresses

With the present loading conditions, the axial stress is found to be the dominant stress component, and only this component is analysed. The maximum tensile stress, σ_t, occurring at the bottom flange, is listed in Table 3 for various deck panels. It can be seen that the difference in the maximum stresses for all panels except for R4 is only within 5%.

The compressive stress across the width of the top flanges varies significantly at the middle span. For the deck panels with the original profiles, the stress distributions across the panel width are shown in Fig. 8. It can be seen that among four panels with the original profiles, T shows the largest variation in the stress distribution with a ratio between the maximum and the minimum stress, $\sigma_{max}/\sigma_{min}$, being about 5.7, and R4 has the least variation with $\sigma_{max}/\sigma_{min} = 3$. The maximum compressive stress (σ_c) is higher than the maximum tensile stress (σ_t) in all panels. The ratio of σ_c/σ_t is approximately 2.5 for T, and 1.6 for H, 2.0 for S3 and 1.4 for R4, respectively (Table 3).

It is found that the compressive stress in the top flange is influenced by the web number and the distances between two contiguous webs. This explains why H and R4 have a lower compressive stress than the others.

The enhancement to the top flange in the modified panels improves the local stress distribution, shown in Fig. 9. Compared to S3, the maximum compressive stress is reduced by about 8%, 9% and 33% for CE, TT and TE, respectively. As a result of this, the variation in stress distribution across the width is correspondingly diminished. The enhancement also diminishes the difference between σ_c and σ_t. The ratio of σ_c/σ_t is 2.0 for S3, but reduced to 1.88 for TT, and 1.4 for TE. However, CE panel did not show significant reduction in the local compressive stress.

It is clear from the numerical results that the TE and R4 sections are effective for deck panel in reducing the local compressive stress.

4.4. Buckling properties

With a relatively thin thickness for the elements, the deck panels can be viewed as a plate structure and would buckle locally under wheel pressures. The buckling mode shapes under bending for these panels are shown in Fig. 10. It is clear from Fig. 10 that large local

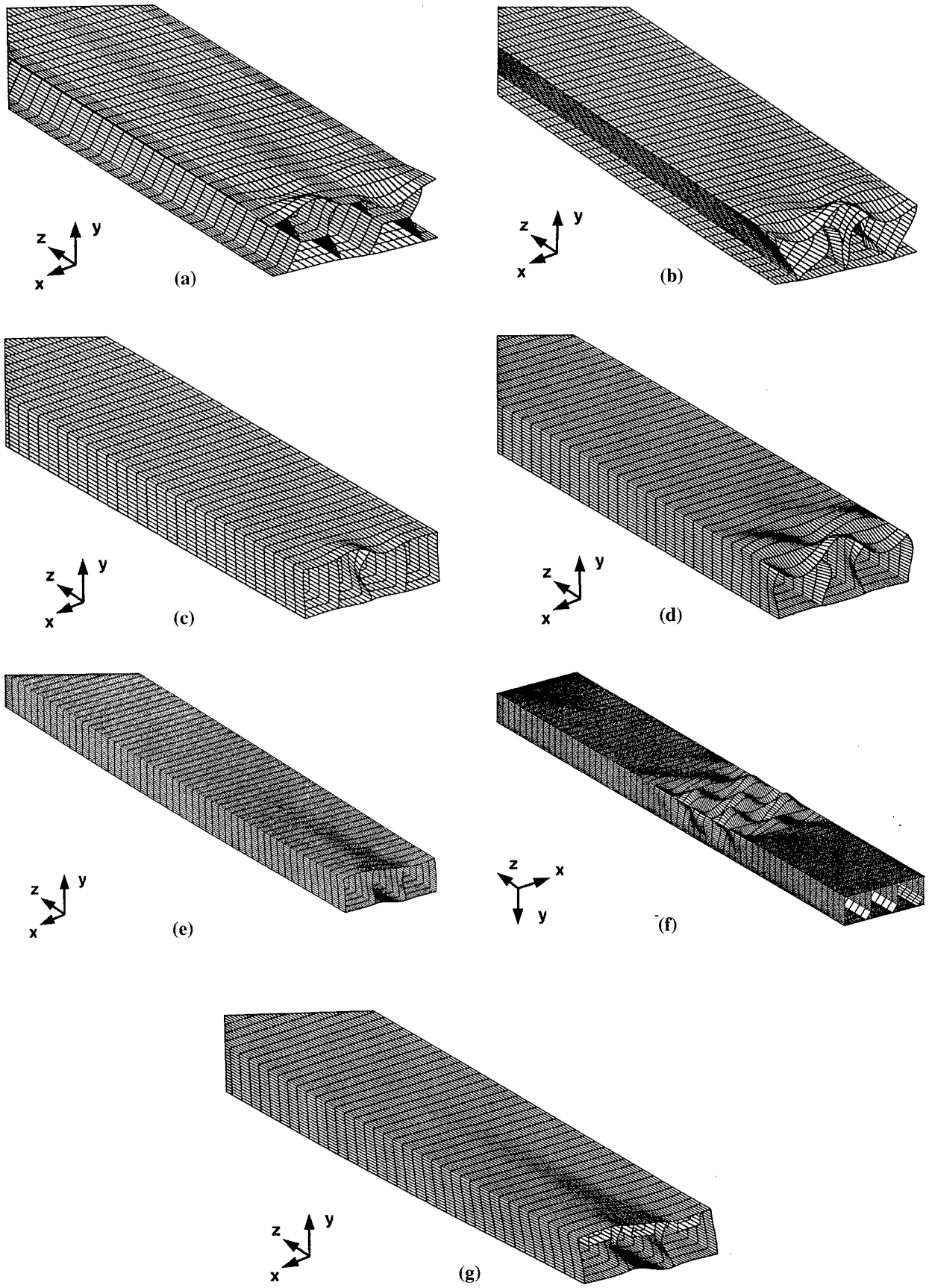

Fig. 10. Buckling mode shapes ford deck panels with various section profiles: (a) H, (b) T, (c) R4, (d) S3, (e) TT, (f) TE, (g) CE.

deformation will develop when the panel buckles. For these four panels with the original sections, buckling is clearly seen in the top flanges and webs (Fig. 10(a)–(d)). However, when the top flange is stiffened as in the improved sections, the top flange may not buckle before the webs, as the local deformation amplitudes in the webs are larger than that in the top flange. With the TE section panel, buckling does not occur at the top flange, but at the bottom flange at the location around the support beam (Fig. 10(f)).

The S3 panel has the highest buckling strength among panels with the original sections (Table 3). The critical load for S3 is about twice higher than those for H and T, and 24% higher than that of R4. The critical loads for buckling are significantly increased when the top flange is stiffened. Compared to the critical load of the R panel, it increases by 26% for the TE panel, and by 11% and 33% for the CE and TT panels, respectively. Although the T-enhanced panel does not have the highest critical load, the method to construct this section is rather effective in improving the buckling strength.

5. Summary and conclusions

Among four panels with the original profiles, the 4-cell panel has a significantly lower global stiffness than the others, whose global stiffness is almost the same. The maximum tensile stresses in all panels are almost the same and substantially lower than the maximum compressive stresses in value. The panels with 3-cell section can provide better properties in local stiffness and buckling strength than the T and H section panels. However, the maximum compressive stresses in the 4-cell section and H-section panels are significantly lower than those in the others.

Three modified section decks possess a substantially higher buckling strength than the original, with almost the same maximum tensile stress. They also provide significant improvement in local stiffness, resulting in considerable reduction in the maximum compressive stress and the difference between the maximum tensile and compressive stresses. Compared to the 3-cell panel, the T-enhanced panel has a slightly higher global stiffness, while the other two modified panels have some loss in the global stiffness. Overall, the T-enhanced section is an optimum design of all the sections evaluated, which provides the highest global stiffness and significant improvements in local stiffness and buckling strength.

Acknowledgements

This study was financially supported by ARC (Australia Research Council) SPIRT grant through the research project on pultruded composites between the University of Sydney and Australia Defence Industry (ADI).

References

[1] Sotiropoulos S, GangRao H, Barbero E. Static response of Bridge superstructures made of fibre reinforced plastic. In: AMD, Use of composite materials in transportation system, vol. 129. New York: ASME, 1991.
[2] Karbhari V, Seible F, Hegemier G, Zhao L. Fiber reinforced composite decks for infrastructure renewal – results and issues. In: Proceedings, International Composites Expo, 1997, Session 3-C. p. 1–6.
[3] Lopez-Anido R, Gangarao H, Vedam V, Overby N. Design and evaluation of a modular FRP bridge deck. In: Proceedings, International Composites Expo, 1997, Session 3-E. p. 1–6.
[4] Lopez-Anido R, Gangarao H, Trovillion J, Busel J. Development and demonstration of a modular FRP deck for bridge construction and replacement. In: Proceedings, International Composites Expo, 1997, Session 16-D. p. 1–6.
[5] Bodamer D. A composite sketch. Civil Eng, January 1998;57–9.
[6] Khalifa M, Tadros M. The world's longest cable-stayed footbridge using fiber reinforced plastics. In: ASCE, infrastructure: new materials & methods of repair, Proceedings of the Third Materials Engineering Conference, 1994. p. 207–13.
[7] Mcghee K, Furman W, Mckeel W. Optimum design of composite bridge deck panels. In: Advanced Composite Materials. p. 360–9.
[8] Bazant ZP, Cedolin L. Stability of structures. Oxford: Oxford University Press, 1991.
[9] Vakiener R, Zureick A, Will KM. Prediction of local flange buckling in pultruded shapes by finite element analysis. In: Srinivasa LI, Rajan S, editors. Advanced composites materials in civil engineering structures, Proceedings of the Specialty Conference. American Society of Civil Engineers, 1991. p. 302–12.
[10] Kelly A. Concise encyclopedia of composite materials. Oxford: Pergamon Press, 1989.
[11] Hibbitt, Karlsson & Sorensen, Inc. ABAQUS/standard user's mannual. Pawtucket: Hibbitt, Karlsson & Sorensen, Inc., 1994.

ELSEVIER

Composite Structures 47 (1999) 727–736

COMPOSITE STRUCTURES

www.elsevier.com/locate/compstruct

On the mechanical behaviour of aging and recycled paper structures under cyclic humidity

S. Dillon [a,*], R. Jones [a], V. Buzzi [b]

[a] *Centre of Expertise in Structural Mechanics, Department of Mechanical Engineering, Monash University, Clayton, Victoria 3168, Australia*
[b] *Amcor Research and Technology, 17 Rex Avenue, Alphington, Victoria 3078, Australia*

Abstract

This paper begins by briefly outlining the behaviour of paper structures under mechanical and hygrothermal loading. The results of an experimental test program are then presented and it is shown that the strain to failure is not a suitable parameter for adequately differentiating between the virgin and recycled paper structures. Indeed, the present paper postulates that the accumulated inelastic work may be a better tool for assessing the effect of furnish. The results of a creep test program are also presented and a possible extension of the master curve concept, which was developed for the visco-elastic response of amorphous polymers to the visco-plastic regime is discussed. © 2000 Elsevier Science Ltd. All rights reserved.

Keywords: Paper structures; Hygrothermal effects; Recycling; Creep response; Stress–strain response

1. Introduction

In today's global market, Australia is vitally dependent on its ability to export. Much of our primary produce and manufactured goods are shipped in paperboard structures. As a packaging material, it is extremely successful in terms of its effectiveness in protecting goods from damage using a relatively small amount of packaging mass. However, it is prone to behavioral changes as a result of changes in the relative humidity (RH) and temperature of its environment, i.e., it behaves in a hygrothermo elastic fashion. These behavioural changes can be deleterious, manifesting themselves generally as high rates of creep, and can lead to buckling in the case of rigid containers, or rupture in the case of paper sacking. This hygrothermal effect often results in manufacturers significantly over designing their containers, which results in a commensurate increase in costs, and is one of the driving forces behind industry research into paper structures. The problem manifests itself severely in particular with fibre board boxes, which are very commonly used in the Australian packaging industry. For example, in the transport of refrigerated foodstuffs by ship or truck it has long been noted that, with these containers, high rates of creep often occur, especially under the conditions of cyclic humidity in the container environment. This of course results in produce damage, particularly in boxes low in the stack, driving up costs both for the primary producer, and the packager.

Australia is presently attempting to increase the extent of its primary produce markets in the Pacific and in Southeast Asia, both areas prone to high and changeable humidity levels. This produce is commonly shipped in cardboard cartons that contain a mixture of virgin and recycled pulps. Indeed, there are increased environmental, economic and social pressures to use less virgin pulp and to increase the usage of recycled paper materials. To this end a means of assessing, and quantifying, the structural performance and the acceptability of recycled paper materials for use in the Pacific and ASEAN regions is highly desirable.

This paper begins by briefly summarising the current status in the analysis and testing of paper structures concentrating both on the topics outlined above as well as on techniques for assessing the acceptability of recycled paper. A series of experimental tests are then performed to evaluate the structural performance of the virgin and recycled paper. From this test program it was found that, at any given age, although the stress–strain response differs markedly the strain to failure does not appear to significantly vary between virgin and recycled material. Thus the strain to failure cannot be used to differentiate between virgin and recycled material.

* Corresponding author. Tel.: +61-03-9905-1417; fax: +61-03-9905-1825.
E-mail address: dillon@its-eng1.eng.monash.edu.au (S. Dillon).

0263-8223/99/$ - see front matter © 2000 Elsevier Science Ltd. All rights reserved.
PII: S0263-8223(00)00044-1

Indeed, the present paper postulates that the accumulated inelastic work may be a better tool for assessing the effect of furnish.

The present test program also reveals a possible extension of the master curve concept, which was developed for the visco-elastic response of amorphous polymers, to the visco-plastic regime.

2. Techniques for characterising the structural response

When designing paper structures a number of facets of its behaviour need to be considered, viz, creep response, stress–strain behaviour, hygrothermal effects (coupled moisture, temperature and load history), visco-plasticity, cyclic fatigue, static strength, and aging and deaging. The specific design objectives need to be identified and the ability of virgin, recycled or mixtures of virgin and recycled paper to meet these design objectives needs to be considered. In this design process, it must be noted that paper behaves in a visco-plastic fashion and can experience both aging and deaging effects, see [1–4,7–17] for more details. To this end a number of relatively simple visco-elastic models have been developed. Unfortunately, as can be seen from Fig. 1, prior to failure the inelastic response of paper dominates the elastic response, for more details see [3]. As such there is a need to extend current approaches into the inelastic regime.

Fig. 1 also shows that, very early in the unloading process, paper experiences a reverse yielding phenomenon which can result in large open hysteresis loops. This is clearly shown in Fig. 1 where the cyclic stress varied from ~18 to ~1 MPa. This phenomenon is particularly important since merely unloading, in this case to near zero load, produces open loops and therefore increases the damage done to the paper. Ref. [3] also found that when subjected to strain holds paper was found to exhibit quite large changes in stress. This behaviour is also seen in structural adhesives [6] and resulted in the

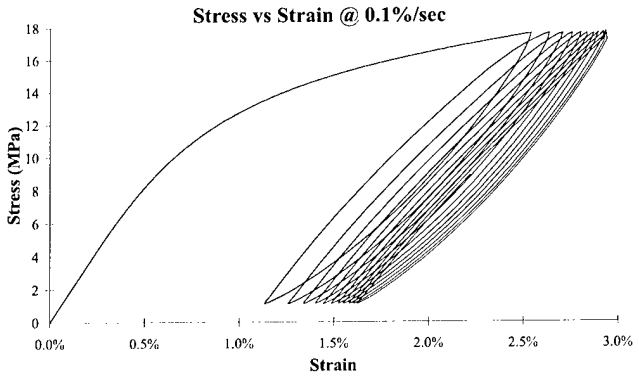

Fig. 1. Typical cyclic response of packaging materials, from [3].

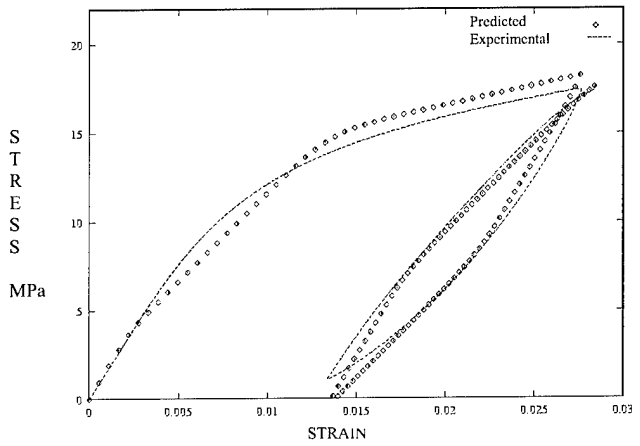

Fig. 2. Comparison of the predicted and experimental cyclic response of packaging materials.

development of an "overstress" concept which is now widely used to model the structural response of polymers, for more details see [6].

To account for these phenomena Sawyer et al. [4] have recently developed two quite distinct formulations for modeling the stress–strain response of paper. These approaches used a unified constitutive theory in which the strain tensor ε_{ij} was expressed as

$$\varepsilon_{ij} = \varepsilon_{ij}^{e} + \varepsilon_{ij}^{I} + \varepsilon_{ij}^{T} + \varepsilon_{ij}^{M}, \tag{1}$$

where ε_{ij} are the total strains, ε_{ij}^{e} the elastic components of the strain, ε_{ij}^{I} the inelastic components of the strain, ε_{ij}^{T} the components of the strain induced by thermal effects, and ε_{ij}^{M} are the components of the strain induced by changes in moisture content. In both the formulations the inelastic ε_{ij}^{I} was assumed to be a function of the overstress, see [4] for more details. This approach differs quite markedly from the conventional formulations where the strain tensor is expressed in the form

$$\varepsilon_{ij} = \varepsilon_{ij}^{e} + \varepsilon_{ij}^{ve} + \varepsilon_{ij}^{p} + \varepsilon_{ij}^{vp} + \varepsilon_{ij}^{c} + \varepsilon_{ij}^{T} + \varepsilon_{ij}^{M}. \tag{2}$$

Here the strain components have been divided into a visco-elastic component ε_{ij}^{ve}, a plastic component ε_{ij}^{p}, a visco-plastic component ε_{ij}^{vp} and a creep component ε_{ij}^{c}. In classical formulations each component is governed by a different mathematical law. In contrast, the unified constitutive theories have a single mathematical law relating the inelastic strain ε_{ij}^{I} to the applied stress, for more details see [4,5]. To date Sawyer's GUV model [1] has only been used for prediction of the behaviour of paper under iso-moisture and iso-temperature conditions, i.e., constant temperature and moisture. Whilst the predictions appear quite promising, see Fig. 2, the formulation has not yet been extended to allow for hygrothermal effects.

[1] In Ref. [4], the authors stated a preference for the so-called "General Unified Viscosity" (GUV) model as a means of predicting the behaviour of paper materials.

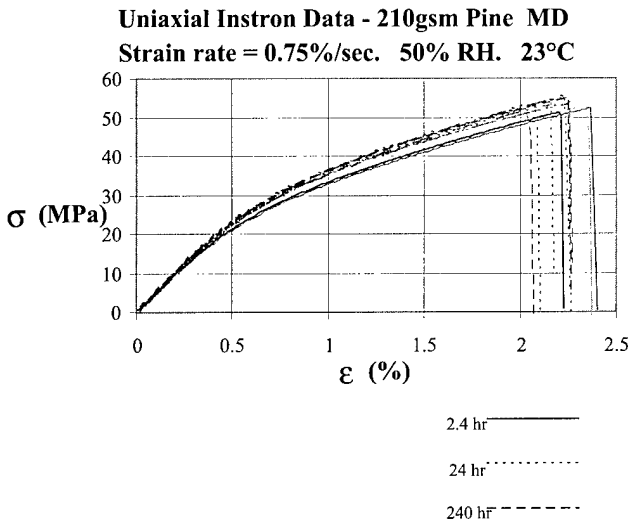

Fig. 3. Stress strain response: pine (MD) at various ages.

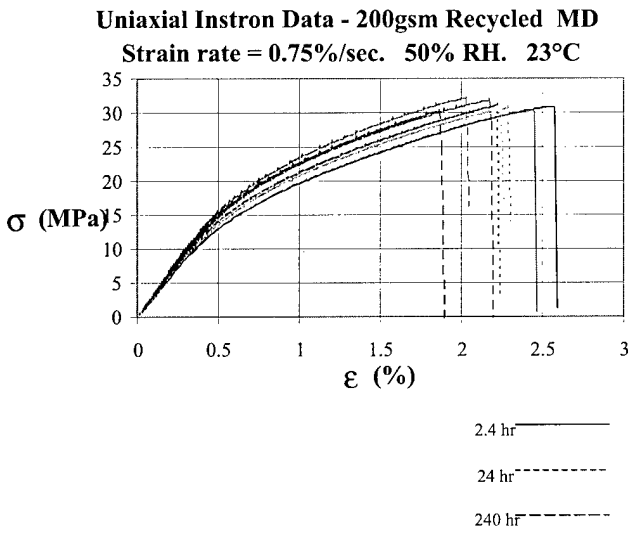

Fig. 4. Stress strain response: recycled (MD) at various ages.

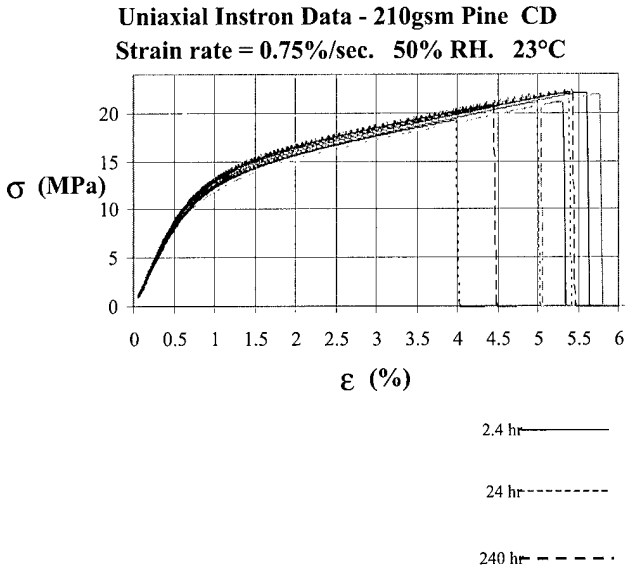

Fig. 5. Stress strain response: pine (CD) at various ages.

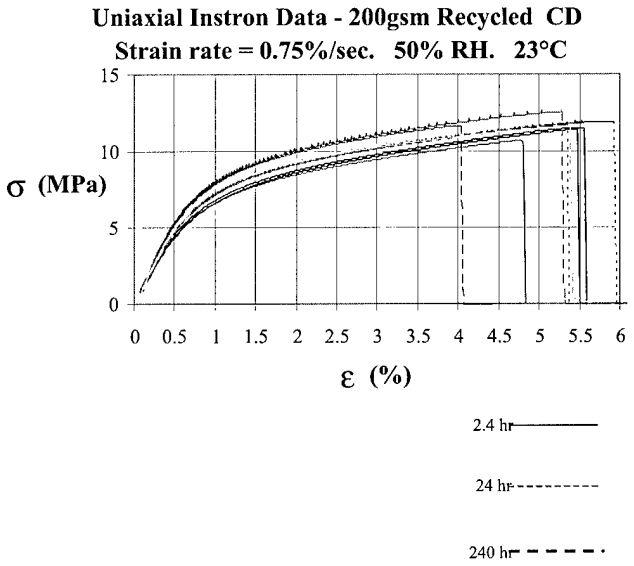

Fig. 6. Stress strain response: recycled (CD) at various ages.

2.1. Creep response

The creep response of paper has frequently been used as a tool to characterise the structural response of paper, and many researchers have investigated its creep response [7–11]. Creep is essentially an inelastic time dependant response to a constant load, and varies with the environmental conditions. Under high humidity, the creep rates of many hydrophilic materials are commonly noted to increase markedly. Creep due to hygrothermal effects is commonly termed mechano-sorptive creep, and is exhibited by some amorphous polymeric materials, which undergo significant deformations as a result of a change in the RH of their environment. Interestingly, this change in humidity levels can be either positive or negative and still produce increased rates of creep.

As we have previously remarked classical approaches to characterising the behaviour of paper implicitly assume that the strain can be split into its creep, viscoplastic and other components. This formulation requires special purpose creep tests to be performed before the creep response of the sample can be characterised, see [5]. This approach is not necessarily required when a unified constitutive formulation is used.

2.2. Hygrothermal effects

A number of investigations have been performed into the effect of temperature and moisture on paper structures [8,9,11]. There is strong evidence indicating that

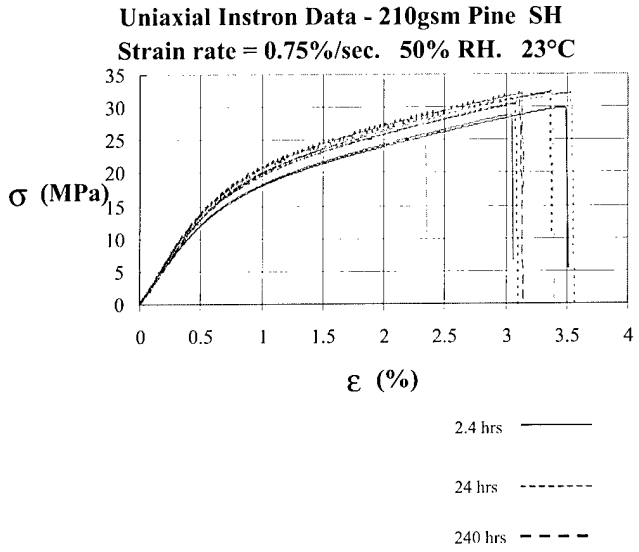

Fig. 7. Stress strain response: pine (SH) at various ages.

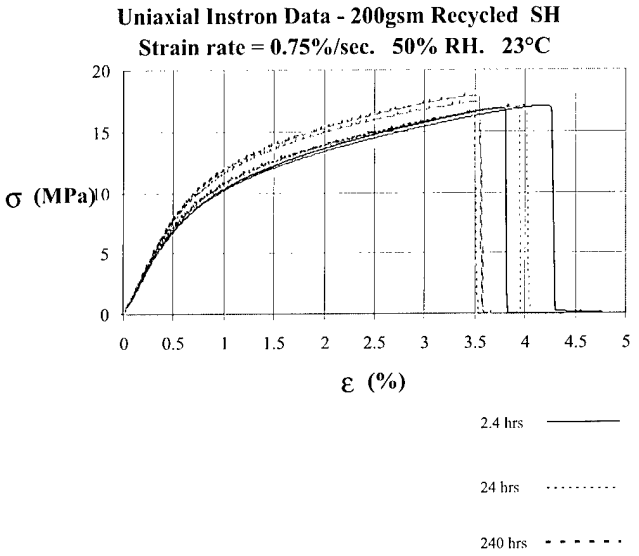

Fig. 8. Stress strain response: recycled (SH) at various ages.

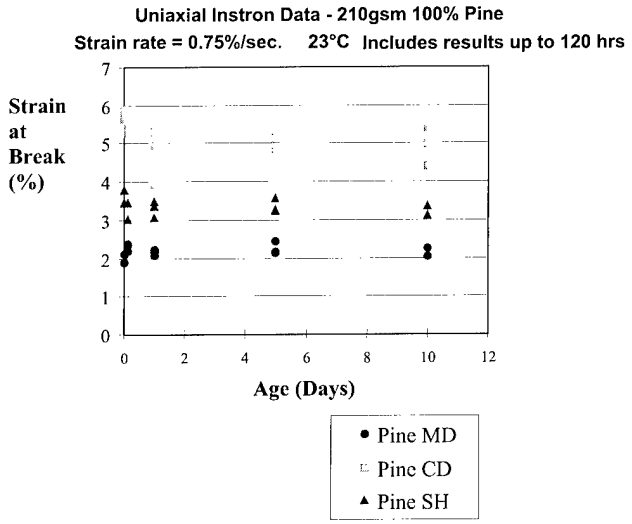

Fig. 9. Strain to failure vs age (pine).

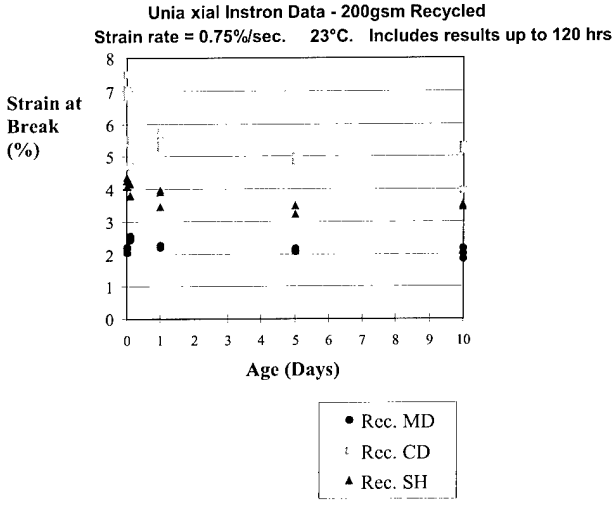

Fig. 10. Strain to failure vs age (recycled).

the volumetric recovery of a partly amorphous polymeric sample may be greatly influenced by small changes in the crystallinity during the physical aging [12,17]. The level of crystallinity in a sheet of paper is quite likely to be of the order of 70% [16]. Consequently the structural response of paper, unlike a purely amorphous polymer, will be dependent upon its crystallinity. This, in turn, depends upon the moisture content of the paper. Salmen [7] states that the glass transition temperature (T_g) depends significantly upon the level of plasticisers, such as water, within the material, i.e., the T_g is lowered by increasing the water content. The water content is related to the environment. Due to the time dependence of hygroscopic effects such as the percolation of moisture, there will inevitably be some time lag before moisture level equilibration.

Coffin and Boese [11] state that, for a paper sheet, this time lag is likely to be of the order of minutes. In contrast, Serra-Tosio and Chave [12] assert that the equilibration process for papers up to a weight of 100 gsm is likely to require ~1 h. Foss et al. [13] also present data that indicate that the moisture equilibration for certain types of paper sheets is essentially achieved after a period of about 1 h, assymptoting to equilibrium values after approximately 2 h.

In his examination of the behaviour of packaging papers, Chalmers [14] presented data that appeared to indicate that this material was particularly sensitive to the upper level of the humidity that the sample experienced in the course of the test. His data were expressed

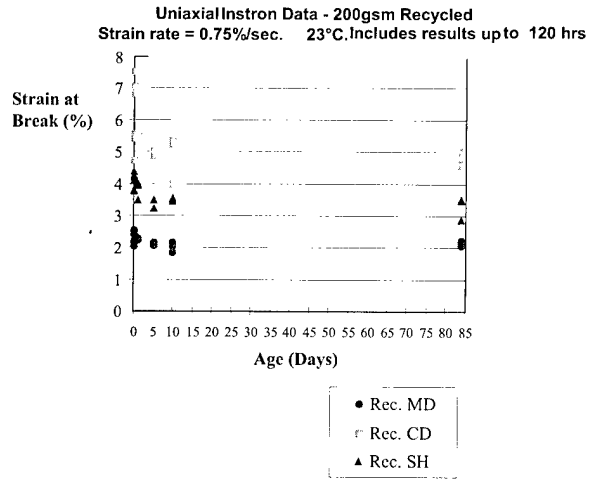

Fig. 11. Strain to failure vs age (recycled).

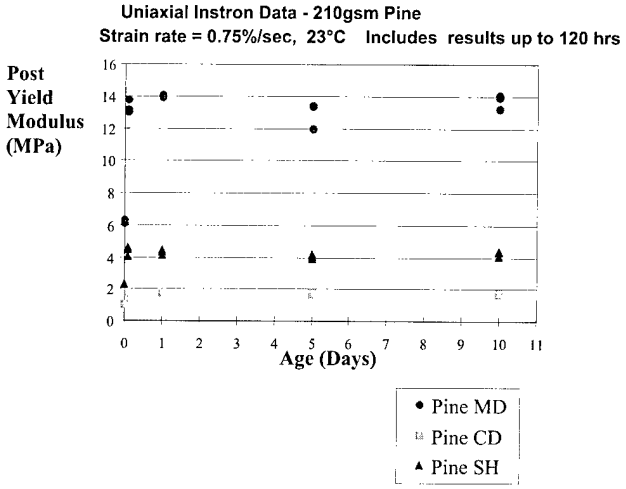

Fig. 12. Post yield modulus vs age (pine).

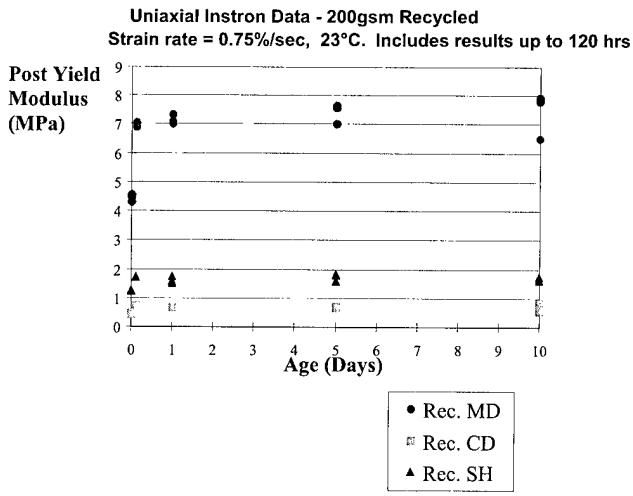

Fig. 13. Post yield modulus vs age (recycled).

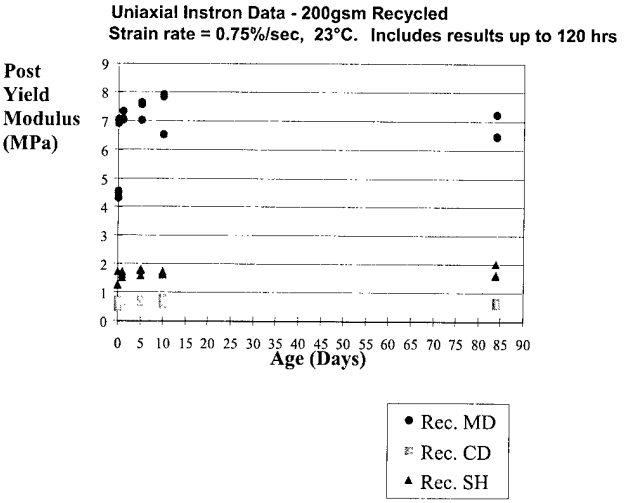

Fig. 14. Post yield modulus vs age (recycled).

as a series of curves for the compressive loading of paper samples under different loads, demonstrating a relationship between the life of the sample and the maximum RH it had experienced. It has been found to be inherently difficult to accurately maintain a deaging humidity of the order of 90%, and this RH level tends to vary slightly with machine temperature fluctuations over time. If Chalmer's results are accepted then, unless the researcher can establish that the RH level was extremely stable, many of the published results for high humidity testing must be considered to be questionable.

2.3. Mathematical models

A variety of mathematical models have been proposed for the structural response of paper. In the previous section we briefly discussed a particular unified constitutive formulation. In this section, we will briefly outline the so-called KWW approach. This approach models the distribution of relaxation times in an amorphous polymer, where the response is assumed to decay

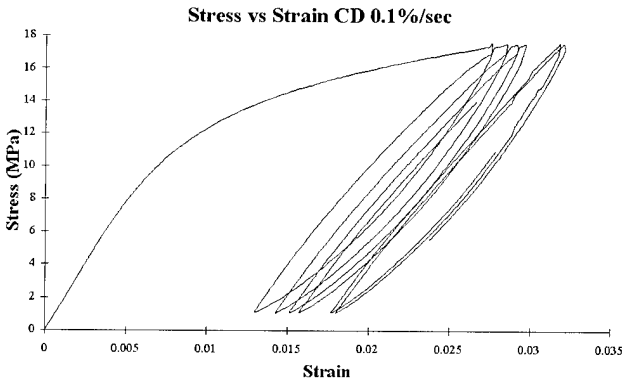

Fig. 15. Cyclic stress–strain response of paper, from [3].

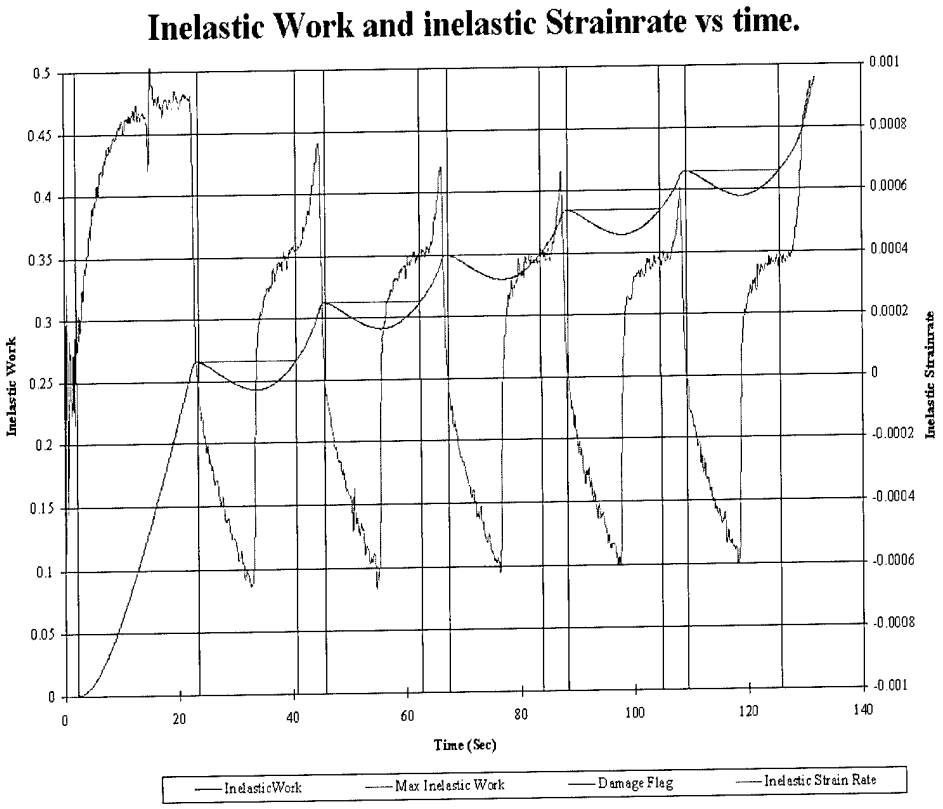

Fig. 16. Inelastic strain with respect to inelastic work, from [3].

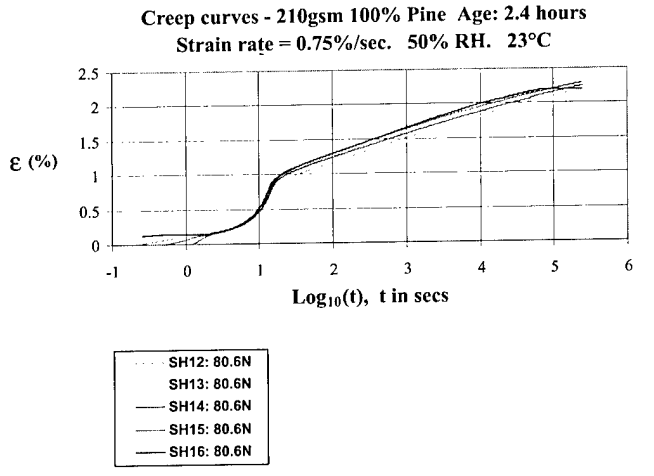

Fig. 17. Shear creep results, age 2.4 h.

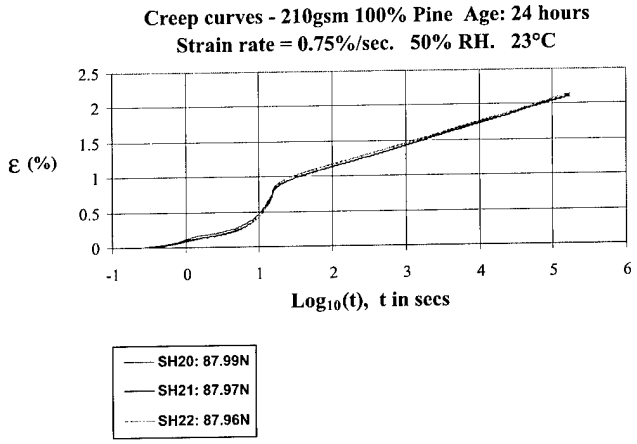

Fig. 18. Shear creep results, age 24 h.

exponentially with time. The term KWW is an acronym standing for Kohlrausch, Williams and Watts, who pioneered and developed this approach [1]. In this formulation, the response is assumed to be proportional to $\exp[-(t/\tau)^{\beta}]$, where τ and β are constants. The term β is termed the exponential stretching factor and must be $0 < \beta < 1$. Padanyi [10] found that using the values of β ranging from 0.09 to 0.27, with 0.142 being the most commonly occurring value, the KWW equation was useful in predicting the short-term creep.

Unfortunately, this relatively simple equation has difficulties in characterising the long-term creep, as this form of the equation predicts a value of zero for the relaxation modulus at equilibrium, and also no final value for the creep at equilibrium. Consequently, application of the KWW law to long-term creep is questionable. The KWW equation also uses a continuous distribution of relaxation times, which restricts its

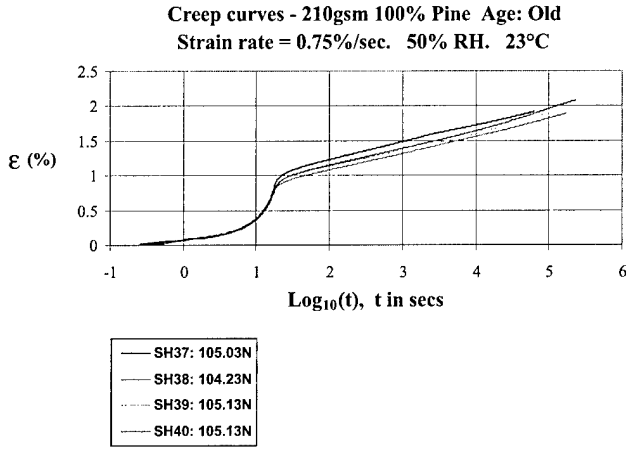

Fig. 19. Shear creep results, age 6 yr.

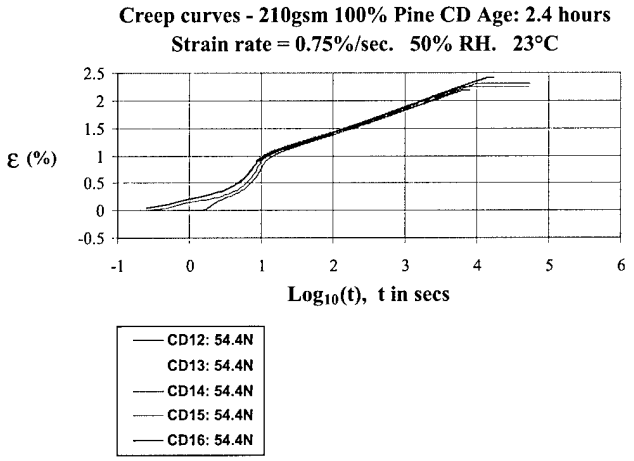

Fig. 20. CD creep results, age 2.4 h.

usefulness as regards its ability to examine the distribution of free volume during the relaxation process.

2.4. Load history effects

Loading history has a profound effect on the aging and deaging of an amorphous polymer. There is experimental evidence that at high stress levels, where the Boltzsman superposition principle no longer applies, the intermittent application of large stresses causes a higher rate of creep in polymers than when the stresses are applied continuously. Indeed, Struik [2] has produced graphs of data for rigid PVC showing the departure from the normal continuous stress position of creep curves where stresses were applied intermittently. This departure has been explained by Struik [2] as being due to the deaging effects which large stresses have upon a polymer sample. This is consistent with the experimental results shown in Fig. 1 which show that, at high stresses, the unloading process itself can produce additional damage in the structure.

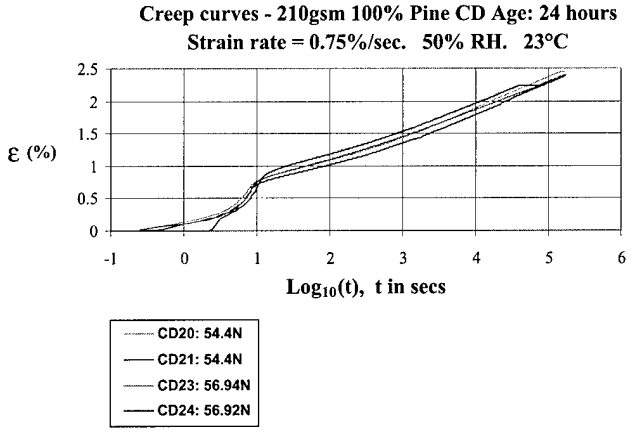

Fig. 21. CD creep results, age 24 h.

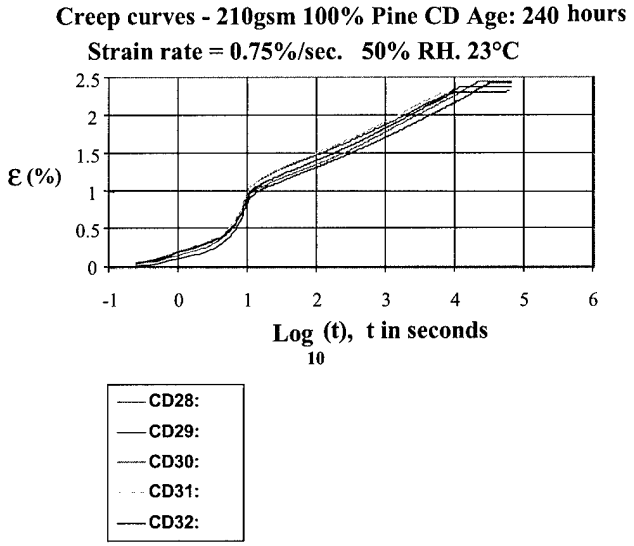

Fig. 22. CD creep results, age 240 h.

3. Structural response of recycled and virgin paper

Having briefly introduced the topic of the mechanical response of paper and the effect of temperature and moisture, let us now examine the structural response of both recycled and virgin paper. To this end, a series of (Instron) uniaxial tensile tests are presented to illustrate the differences in the structural performance of virgin pine liner (210 gsm) and recycled liner (200 gsm). The samples were at varying physical ages and were stressed to failure, under ISO conditions, viz, 23°C and 50% RH. Tests on the "near zero age" specimens were performed at 23°C and 90% RH. The test specimens were rectangular with a width of 15 mm, a length of 250 mm, and a gauge length of 200 mm. Three configurations were tested. These tests will be labeled as follows: CD (cross direction), where the major fibre direction was normal to the length of the specimen, MD (machine direction), where the major fibre direction was along the length of

the specimen, and SH (shear tests), where the load was applied 45° to the CD and MD directions. In each case a range of ages were tested, typically 2.4, 24 and 240 h. The results of this test program are shown graphically in Figs. 3–14.

Figs. 3–8 show that the structural response of virgin and recycled paper is quite different. However, from Figs. 9 and 10 it can be seen that, at any given age, the strain to failure does not appear to significantly vary between the virgin and recycled material. Furthermore, in contrast to the accumulated inelastic strain, the failure strains do not vary greatly with age. Thus, the strain to failure is not a criterion by which the quality of the finish of paper can be adequately judged, i.e., it cannot differentiate between the virgin and recycled material. This has potential implications for creep tests in which the stress is held constant and performance is supposedly judged by the strain time history.

Creep tests attempt to reveal an insight into the time dependent irreversible behaviour of the material. However, given that strain may not be the best way to differentiate between the furnish, alternative tests such as stress relaxation tests performed at a constant strain, or stress–strain tests performed over several decades of strain rate may be viable alternatives. Stress relaxation tests provide information on the relative peak stress (strength) that the sample can achieve, the asymptotic level to which the stress will decay and the time scale over which this will occur. During this decay process elastic strains are converted into inelastic strains. One advantage of stress relaxation tests, and stress–strain tests, is that differences in the furnish of the test samples produce significant differences in the load carrying capacity of the samples and the total inelastic work to failure (see Figs. 12 and 13).

In this context it should also be noted that in the cyclic fatigue tests described in [3], the accumulated inelastic work was found to be very useful in predicting the point, in the cyclic strain history, where significant inelastic effects would re-occur. In this case for the cyclic stress–strain response shown in Fig. 15, it was found that the inelastic strain rate began to increase rapidly at approximately the same time as the inelastic work surpassed its previous maximum value, see Fig. 16. As such the accumulated inelastic work may be a useful tool to assess furnish. This finding is consistent with the work of Mast et al. [18–20] who found inelastic work to be an excellent measure of the damage induced in composite specimens. They also found that failure could be correlated with the amount of inelastic work.

The present test program also found that above the apparent yield stress, (i.e. the stress at 0.2% inelastic strain,) the slope of the post yield curves for stress vs strain equilibrated very rapidly with age. As with the strains to failure, the final asymptotic values were achieved after approximately one day.

3.1. Creep tests

To further illustrate the inelastic response of paper and the effect of aging on its structural performance a series of CD and SH creep tests were also performed. In these tests, attention was confined to virgin material at various ages. In all creep tests, the stress level held was chosen to correspond to that at ~0.2% inelastic strain. This approach was adopted in an attempt to ensure that an identical amount of inelastic work (damage) had been experienced by each sample, regardless of age, orientation or furnish. The results of this test program can be seen in Figs. 17–22.

From these figures it is clear that as a first approximation the creep vs log time response was essentially linear and that the slope of the curve rapidly asymptotes to a constant value as the age of the sample increases. This asymptotic behaviour is similar to that discussed above. As a result of this behaviour it is possible to create a single master inelastic strain vs log time creep curve, for this stress level. As such this highlights the potential to extend the master curve concept as used by Struik [2], which was developed for the visco-elastic response of amorphous polymers, to the visco-plastic regime. However, this would involve both horizontal and vertical shifting of the creep log time curves.

4. Conclusions

This paper has briefly summarised the behaviour of paper structures under mechanical and hygrothermal loading. The experimental test program has shown that, at any given age, although the stress–strain response differs markedly the strain to failure does not appear to vary significantly between the virgin and recycled material. Thus the strain to failure does not adequately differentiate between the virgin and recycled material.

In the cyclic fatigue tests described in [3], the accumulated inelastic work was found to be very useful in predicting the point, in the cyclic strain history, where significant inelastic effects would re-occur. As such it is hypothesised that the accumulated inelastic work may be a better tool for assessing the effect of furnish. Indeed, this finding may be considered as an extension of the work of Mast et al. [18–20], who found the inelastic work to be an excellent measure of the damage induced in fibre composite specimens, to paper structures.

If this hypothesis is true, then the philosophy underlying creep tests can be re-visited. Creep tests are generally performed to establish the nature of the

strain–time response of the (paper) structure. However, since we have established that strain is a poor indicator of the quality of the furnish, it would be better to determine the inelastic work (dissipated energy) time history of the paper. This could be achieved via a traditional creep test. However, creep testing is relatively slow and other test procedures may be suitable.

Appendix A. The GUV Model

The formulation of the GUV Model arose from an investigation, into the structural response of paper [3 4], of a distributed viscosity model approach to representing the stress–strain response of paper structures. In its simplest form, this model can be expressed as

$$\varepsilon_{ij}^{\mathrm{I}} = D\exp\{eK_2\}\sinh\{eK_2\}\frac{(S_{ij}-\Omega_{ij})}{\sqrt{K_2}}, \tag{A.1}$$

$$\dot{\Omega}_{ij} = F_{ij} + g_{ij}\left(\bar{\varepsilon}^{\mathrm{I}}\right), \tag{A.2}$$

$$F_{ij} = k_{ijkl}(\varepsilon_{kl} - \chi_{kl}), \tag{A.3}$$

$$\dot{x}_{ij} = A_{ij}\exp\left\{b_{ijkl}F_{kl}\right\}\sinh\left\{c_{ijkl}F_{kl}\right\}, \tag{A.4}$$

$$K_2 = \sqrt{\frac{3}{2}(S_{ij}-\Omega_{ij})(S_{ij}-\Omega_{ij})}, \tag{A.5}$$

$$\bar{S} = \sqrt{\frac{3}{2}S_{ij}S_{ij}}, \tag{A6}$$

$$\varepsilon_{\mathrm{eff}} = \frac{\varepsilon_{ij}S_{ij}}{\bar{S}}, \tag{A.7}$$

where

$$\left[\exp(A_{ij}) = \begin{matrix} \exp(A_{11}) & \exp(A_{12}) & \dots \\ \exp(A_{21}) & \exp(A_{22}) & \dots \\ \vdots & \vdots & \ddots \end{matrix}\right]. \tag{A.8}$$

Here D, e, E, g_{ij}, k_{ijkl}, A_{ij}, b_{ijkl} and c_{ijkl} are material constants and Ω, S, $\bar{S}$, $\dot{\varepsilon}^{\mathrm{I}}$ and $\varepsilon_{\mathrm{eff}}^{\mathrm{I}}$ are the back stress, the deviatoric stress, the effective deviatoric stress, the inelastic strain rate and the effective inelastic strain, respectively. F and x are the additional state variables.

Ref. [4] revealed that this level of complexity was not required and that the equations could be simplified by reducing the tensor forms to equivalent vector terminology, viz:

$$\varepsilon_i^{\mathrm{I}} = D\exp\{eK_2\}\sinh\{eK_2\}\frac{(S_i-\Omega_i)}{\sqrt{K_2}}, \tag{A.9}$$

$$\dot{\Omega}_i = F_i + g_i(\bar{\varepsilon}^{\mathrm{I}}), \tag{A.10}$$

$$F_i = k_{ij}(\varepsilon_j - \chi_j), \tag{A.11}$$

$$\dot{\chi}_i = A_i\exp\left\{b_{ij}\,F_j\right\}\sinh\left\{c_{ij}F_j\right\}, \tag{A.12}$$

where we have defined

$$\exp(A_i) = [\exp(A_1), \exp(A_2), \dots]. \tag{A.13}$$

Here K_2, and $\bar{S}$ are calculated as in the tensor form of the model, see [4] for more details.

References

[1] Hutchinson JM. Physical aging of polymers. Progr Polym Sci 1995;20(4):703–60.

[2] Struik LCE. Physical aging in amorphous polymers and other materials. Amsterdam: Elsevier, 1978.

[3] Sawyer JPG, Jones R, Mckinlay P. An experimental description of paper. J Compos Struct 1996;38:101–111.

[4] Sawyer JPG, Jones R, McKinlay P. A unified constitutive theory for paper. J Compos Struct 1998;42(1):93–100.

[5] Dame LT, Stouffer DC. Inelastic deformations in metals. New York: Wiley, 1995.

[6] Chiu WK, Chalkley P, Jones R. Effects of temperature on the shear stress–strain behaviour of structural adhesives FM73. Comput Struct 1994;53(3):101–4.

[7] Salmen L. Responses of paper properties to changes in moisture content and temperature. Oxford Products of Paper Making Conference 1993;1:369–431.

[8] Salmen L, Fellers C. Moisture induced transients and creep of paper and Nylon 66: a comparison. Nordic Pulp and Paper Res J 1996;3.

[9] Soremark C, Fellers C. Mechano-sorptive creep and hyrdoexpansion of corrugated boards in bending. J Pulp and Paper Sci 1993;19(1):J19–26.

[10] Padanyi ZV. Reversible age dependence of creep and stress relaxation in paperboard. Proceedings Moisture Induced Creep Behaviour of Paper and Board, Stockholm, 5–7 December 1994, pp. 67–87.

[11] Coffin DW, Boese SB. Tensile creep behaviour of single fibres and paper in a cyclic humidity environment. In: Proceedings of the third International Symposium, Moisture and Creep Effects on Paper, Board and Containers. Rotorua, New Zealand. Feb. 1997, p. 39.

[12] Serra-Tosio JM, Chave Y. Internal stress in paper revealed by hygroexpansivity measurements and its influence upon creep behaviour. In: Proceedings of the third International Symposium, Moisture and Creep Effects on Paper, Board and Containers, Rotorua, New Zealand. Feb. 1997, p. 99.

[13] Foss WR, Bronkhorst CA, Bennett KA, Riedemann JR. Transient moisture transport in paper in the hygroscopic range and its role in the mechano-sorptive effect. In: Proceedings of the third International Symposium, Moisture and Creep Effects on Paper, Board and Containers, Rotorua, New Zealand. Feb. 1997, p. 221.

[14] Chalmers I. The effect of humidity of packaging grade paper elastic modulus. In: Proceedings of the third International Symposium, Moisture and Creep Effects on Paper, Board and Containers, Rotorua, New Zealand. Feb. 1997, p. 201.

[15] Chalmers I. The performance of packaging grade paper in high and cycling relative humidity. In: Proceedings Moisture-induced Creep Behaviour of Paper and Board, Stockholm, Sweden 5–7 December 1994, p. 233.

[16] Salmen NL, Back EL. Moisture dependent thermal softening of paper evaluated by its elastic modulus. Tappi J 1980;63(6):118.

[17] Spinu I, McKenna GB. Physical aging of NYLON 66. Polym Engrg Sci ISSN:0032-3888 1994;34:1808-1814.

[18] Mast PW, Nash GE, Michopoulos JG, Badaliance TR, Wolock I. Characterisation of strain induced damage in composites based on dissipated energy density Part I: Basic scheme and formulation. J Theoret Appl Fracture Mech 1997;22(3):71–96.
[19] Mast PW, Nash GE, Michopoulos JG, Badaliance TR, Wolock I. Characterisation of strain induced damage in composites based on dissipated energy density Part II: Composite specimens and naval structures. J Theoret Appl Fracture Mech 1997;22(3):71–96.
[20] Mast PW, Nash GE, Michopoulos JG, Badaliance TR, Wolock I. Characterisation of strain induced damage in composites based on dissipated energy density Part III: General material and constitutive relation. J Theoret Appl Fracture Mech 1997;22(3):71–96.

ELSEVIER

Composite Structures 47 (1999) 737–743

COMPOSITE STRUCTURES

www.elsevier.com/locate/compstruct

Composite repairs to rib stiffened panels

T. Ting [a,*], R. Jones [a], W.K. Chiu [a], I.H. Marshall [a], J.M. Greer [b]

[a] *Department of Mechanical Engineering, Monash University, Clayton, Vic. 3168, Australia*

[b] *Department of Engineering Mechanics, USAFA Center for Aircraft Structural Life Extension, HQ USAFA/DEFM, 2354 Fairchild Dr. Ste 6H2, US AirForce Academy, CO 80840-6240, USA*

Abstract

There are several methods available for obtaining a first estimate for the design of composite repairs to cracks in thin metallic skins. One approach uses analytical formulae, which build on an analogy with the problem of a bonded symmetric lap joint (Rose LRF. An application of the inclusion analogy for bonded reinforcements. Int J Solid Struct 1981;17:827–838; Fredell RS. Damage tolerant repair techniques for pressurized aircraft fuselages. PhD Thesis, Delft University of Technology, June 1994; Baker AA, Jones R. Bonded repair of aircraft structures. Dordrecht: Martinus Nijhoff, 1988). The present paper extends this methodology to include the bonded repair to rib stiffened wing skins. To this end the present paper presents the results of a series of 3-D finite element analysis of various composite repair configurations. This study reveals that, after repair, the stress intensity factors exhibits an asymptotic behaviour as the crack length increases and that this stress intensity factor is a weak function of the stiffener spacing. © 2000 Elsevier Science Ltd. All rights reserved.

Keywords: Bonded repair; Composites; Boron patches; Stiffened wing skins; Fracture

1. Introduction

Externally bonded composite patches have proved to be an effective method of repairing cracked, or damaged, structural components [1–9]. A variety of approaches are now available for the design of composite repairs to cracks in thin metallic skins, i.e., typical thickness less than ~3 mm. One such technique is based on the fact that the stress intensity factor for a patched crack approach a constant (limiting) value defined as K_∞, as the crack length increases. This approach was based on the premise that, for a sufficiently long crack in a structure which is subjected to a remote uniform stress field, the central region of the patch, over the crack, behaves like an overlap joint [1,2]. From this premise it follows that the stress distribution in this central region and the stress intensity factor should become independent of crack length.

As a result of this analogy it has been found that the problem of a bonded symmetric lap joint can be used in the initial design process. Indeed, the resultant analytical formulae are particularly easy to use and provide a first estimate for the patch design.

It is possible to increase the accuracy of the current approximate 2-D formulae, initially developed by Rose in [1], for the limiting stress intensity factor K_∞ for a crack repaired with an externally bonded composite repair, by (partially) accounting for through-the-thickness effects. To this end the value of K_∞ can be approximated by the formulae

$$K_\infty = Y\Omega_L\sigma_o\sqrt{\pi\lambda}, \tag{1}$$

where

$$\sigma_o = \sigma E_p t_p/(E_p t_p + E_r t_r). \tag{2}$$

Y is a geometry factor, which accounts for repairs to centre or edge cracks:

$$Y = \begin{cases} 1 & \text{for a repair to a centre crack,} \\ 0.9 & \text{for a repair to an edge crack,} \end{cases}$$

and Ω_L is the load attraction factor. For long uni-directional fibre patches it has been found that the term σ_L can be approximated as follows:

$$\Gamma = 3/8\ 1/(1 + XE_r t_r/(BE_p t_p)) - E_p t_p/(E_r t_r + E_p t_p), \tag{3}$$

$$\Omega_L = (E_p t_p/(E_r t_r + E_p t_p) + \Gamma)/\sigma_o, \tag{4}$$

$$\pi\lambda = \sqrt{E_p t_p/\beta(1 + t_p E_p/E_r t_r)} \tag{5}$$

* Corresponding author.

0263-8223/99/$ - see front matter © 2000 Elsevier Science Ltd. All rights reserved.
PII: S0263-8223(00)00046-5

and

$$\beta = (t_a/G_a + t_r/3G_r + t_p/3G_p) / (t_a/G_a + 3t_r/8G_r + 3t_p/8G_p)^2. \quad (6)$$

Here X is the width of the patch, B the width of the plate/skin, t_a, t_p and t_r are the thicknesses of the adhesive, plate, and patch, respectively, G and E denote the shear and Young's modulus and the subscripts a, p and r denote their values for the adhesive, plate, and patch, respectively.

These formulae ignore bending effects. However, even if the plate (wing skin) is in a state of plane stress, the location of the neutral axis of the patch-adhesive-skin section will differ from the neutral axis of the wing skin itself. Hence, forces applied to the skin will result in an out of plane bending, which will reduce the efficiency of the repair.

There are several methods that can be used to account for bending effects. One approach, developed at Northrop, is presented in [3]. In this method, the apparent stress intensity factor K_p^* at the mid surface of the sheet is given by

$$K_p^* = (1 + BC)K_p, \quad (7)$$

where BC is a bending correction factor. Here,

$$BC = a\, y_{max}(1 - K_p/K_s)(t_p + t_r)/I, \quad (8)$$

where K_s is the value of the stress intensity factor before patching, t_p and t_r the thicknesses of the sheet and patch, respectively, y_{max} the distance of the lower unpatched surface of the plate from the neutral axis of the section (i.e., sheet plus patch), I the moment of inertia of the section and a is the crack half length.

The value of K_p^* can be related to J, the energy release rate for self similar crack growth, in the usual way, viz

$$J = K_p^{*2}/E. \quad (9)$$

However, since the growth is not self-similar with the maximum growth occurring at the lower free surface, it may be best not to use K_p^* or J but to design on the basis of the maximum stress intensity factor K_p^{max} which is given by

$$K_p^{max} = (1 + 2BC)K_p. \quad (10)$$

To extend the technology base the present paper focuses on the bonded repair to (cracked) rib stiffened wing skins, a topic that has received little attention. This study reveals that, after repair, the stress intensity factors exhibits an asymptotic behaviour as the crack length increases and that this stress intensity factor is a weak function of the stiffener spacing.

2. Repair of thin skins

To illustrate the accuracy of these formulae let us first consider an externally bonded composite repair (patch) to a centre crack in a 3-mm thick aluminium panel with $E = 72,000$ MPa and $\nu = 0.33$. Two patch thicknesses were analysed, viz, 1.0 and 1.85 mm, and the patch was assumed to have the following mechanical properties: $E_{11} = 208,000$ MPa, $E_{22} = 25,432$ MPa, $\nu_{12} = 0.183$, and $G_{12} = G_{13} = G_{23} = 7241$ MPa. The plate was assumed to have dimension of 200 (length) × 290 (width) × 3 mm and the patch was assumed to have a platform of 100 (length) mm × 82 (width) mm. The adhesive was taken to be 0.25-mm thick with a shear modulus of 375 MPa and $\nu = 0.33$. The analysis used 20 noded isoparametric 3-D brick elements with 2 layers of elements through each of the plate, patch and adhesive. The plate was subjected to a remote uniform stress of 229.8 MPa and global bending, after patching, was prohibited.

In this analysis symmetry was used and only a quarter of the structure was modeled. The resultant mesh consisted of 4889 nodes and 1132 elements and, to simulate the crack tip singularity, the near tip elements had the mid side nodes moved to the 1/4 points. The resultant solution was well conditioned and the accuracy of the solution was evaluated by performing two separate analyses. The first used optimum integration, i.e. 2 × 2 × 2 Gaussian quadradture points, to form the stiffness matrices of the elements whilst the second used full integration, i.e. 3 × 3 × 3 Gaussian quadradture points, to form the stiffness matrix. Both analyses gave results, which agreed to within 1%. Following this analysis a range of other problems were then considered. The results for these repair configurations are presented in Tables 1–4.

From these tables we see that the simple closed form solutions are reasonably accurate. The analytical formulae are also quite accurate for the case when bending is allowed (Tables 5–7). However, in this case the accuracy of the simple analytical formulae decreases when

Table 1
K_∞ for a repaired edge notch panel, 1.85-mm thick patch

	Crack length				
	5 mm	6 mm	7 mm	10 mm	20 mm
Patched surface	10.6	10.8	10.9	10.9	10.4
Middle	11.6	11.7	11.9	12.1	12.9
Bottom	11.7	11.9	12.0	12.2	12.7

Table 2
K values for repaired centre notch panel, 1.85-mm thick patch

	Crack half length				
	5 mm	6 mm	7 mm	10 mm	20 mm
Patched surface	11.2	11.5	11.8	12.0	11.6
Middle	11.9	12.4	12.7	12.2	14.3
Bottom	12.0	13.16	12.9	13.4	14.1

Table 3
K for a repaired centre notch panel, 1-mm thick patch

	Crack half length				
	5 mm	6 mm	7 mm	10 mm	20 mm
Patched surface	14.6	15.2	15.6	16.1	15.7
Middle	15.5	16.3	16.8	17.8	19.4
Bottom	15.6	16.4	17.0	17.9	19.1

Table 4
Comparison of prediction for K_{∞} for various patch configurations

Crack configuration	Crack length (mm)	Configuration	Predicted	K finite element
Edge crack $\sigma = 344.8$ MPa	20	Skin[a] 2 mm, patch = 0.75 mm, $G_a = 375$ MPa, $t_a = 0.25$ mm	21.6	17.8–22.4
Centre crack $\sigma = 344.8$ MPa	20	Skin[a] 2 mm, patch = 0.75 mm, $G_a = 375$ MPa, $t_a = 0.25$ mm	23.6	19.8–24.0
Centre crack $\sigma = 229.8$ MPa	20	Skin[a] 3 mm, patch = 1.00 mm, $G_a = 375$ MPa, $t_a = 0.25$ mm	19.2	15.7–19.1
Centre crack $\sigma = 299.8$ MPa	20	Skin[b] 3 mm, patch = 0.889 mm, $G_a = 750$ MPa, $t_a = 0.165$ mm	16.2	15.7–15.8

[a] The platform of the skin and patch were as previously described.
[b] Plate was 320 mm × 150 mm (wide) with a semi-circular patch, 80 mm radius.

Table 5
Comparison of prediction for bending problems, case 1

K_{max} MPa $\sqrt{m}$	Edge centre	a (mm)	t_p (mm)	E_p (MPa)	t_r (mm)	G_r (MPa)	t_a (mm)	G_a (MPa)	σ (MPa)	X (mm)	B (mm)
	Centre	40	3.16	72,000	1	208,030	0.2	375	158	200	200
Predicted	48.3										
f.e.	47.4										

the crack length approaches a half of the patch width (X).

3. Analysis of repairs to rib stiffened panels

3.1. Finite element analysis

Let us now turn our attention to composite repairs to cracked repairs to (cracked) rib stiffened panels where the stiffeners are assumed to be riveted to the skin. Symmetry considerations enabled only a 1/4 of the structure to be model (Fig. 1). In this study the crack length, patch thickness, skin thickness, stiffener width, stiffener spacing and stiffener depth were varied to determine their effects on the stress intensity factors.

3.2. Results for stress-intensity calculations from the finite element analysis of a boron epoxy composite repair of a crack over a stiffening element

This study focused on composite repairs to centre cracks in a 2.5, 3.16 or 4-mm thick aluminium stiffened panel with $E = 72,000$ MPa, and $v = 0.33$. Three patch thickness were considered, i.e., 1, 1.4 and 1.85-mm thick and the modulii of the patch were taken to be $E_{11} = 208,000$ MPa, $E_{22} = 25,432$ MPa, $v_{12} = 0.183$, $G_{12} = G_{13} = G_{23} = 7241$ MPa.

Table 6
Comparison of prediction for bending problems, case 2

K_{max} MPa $\sqrt{m}$	Edge centre	a (mm)	t_p (mm)	E_p (MPa)	t_r (mm)	G_r (MPa)	t_a (mm)	G_a (MPa)	σ (MPa)	X (mm)	B (mm)
	Edge	20	2	72,000	0.75	208,030	0.25	375	345	200	200
Predicted	85.2										
f.e.	83.4										

Table 7
Comparison of prediction for bending problems, case 3

K_{max} MPa $\sqrt{m}$	Edge centre	a (mm)	t_p (mm)	E_p (MPa)	t_r (mm)	G_r (MPa)	t_a (mm)	G_a (MPa)	σ (MPa)	X (mm)	B (mm)
	Centre	20	3	71,000	0.89	208,000	0.17	750	230	41	145
Predicted	62.7										
f.e.	59.2										

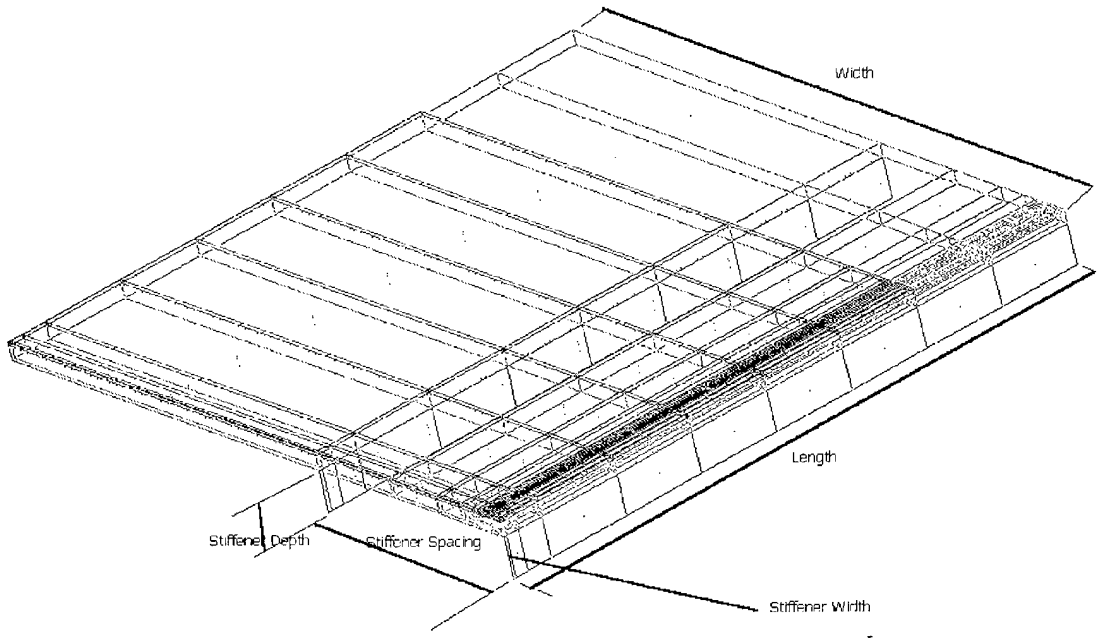

Fig. 1. Schematic of 3-D 1/4 finite element model of stiffened panel. Note the definitions with respect to stiffener dimensions.

The panel had dimension of 375 mm (length)× 400 mm (width) and the platform of the composite repair was 275 mm (length) × 400 mm (width). The adhesive was taken to be 0.20-mm thick with a shear modulus of 375 MPa and $\nu = 0.33$. The analysis used 20 noded isoparametric 3-D bricks with single layer of elements through the skin, adhesive and patch. 15 noded isoparametric 3-D wedge shaped bricks were used at the crack tip location through the entire thickness of the specimen. The skin in the panel was subjected to a remote uniform stress of 229.8 MPa.

To illustrate the asymptotic effects of the solution the results for repairs to centre notch cracks will now be presented. To this end various plots of stress intensity factors vs crack length are presented. They are used to illustrate the effects of varying the various individual geometrical parameters on K_1.

The values presented in these analyses are taken from the bottom surface of the skin (just above the stringer). As expected, these gave consistently higher values of K_1 when compared to the stress intensity values at the skin-adhesive interface.

3.2.1. Comparison of results for several different stiffener spacing and two different skin thicknesses

This study focused on determining the effect of stiffener spacing on the stress intensity factor. The geometrical parameters considered are shown in Table 8. The results are summarised in Figs. 2 and 3, where in each case the stiffener width and depth was 3.5 mm and 12 mm, respectively. From these figures we see that the stress intensity factor K_I is a weak function of the stiffener spacing.

3.2.2. Comparison of results for several stiffener spacings and stiffener depths and two different skin thicknesses

This study focused on confirming the effect of stiffener spacing on the stress intensity factor. In this study the stiffener depths were varied, (Table 9), and the results are summarised in Figs. 4 and 5 and we again see that the stress intensity factor K_I is a weak function of the stiffener spacing.

Table 8
Geometrical parameters considered

Skin thickness (mm)	Stiffener spacing (mm)	Patch thickness
2.5	75	1.0
3.6	127.5	1.8
	150	

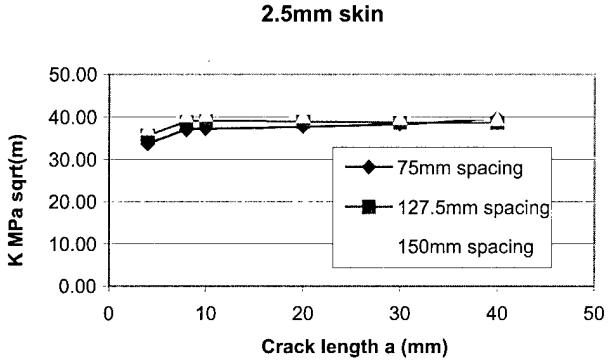

Fig. 2. Plot of K_I vs a for 2.5 mm stiffened skin with three different stiffener spacings.

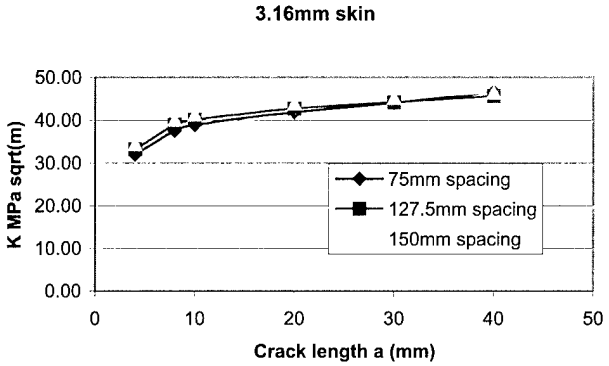

Fig. 3. Plot of K_I vs a for 3.16 mm stiffened skin with different stiffener spacings.

3.2.3. Comparison of results for various stiffener spacing and patch thickness for two different skin thicknesses

This study focused on confirming the effect of stiffener spacing on the stress intensity factor. In this study the patch thickness was varied (Table 10) and the results

Table 9
Geometrical parameters considered

Skin thickness (mm)	Stiffener spacing (mm)	Patch thickness	Stiffener depth (mm)
2.5	75	1.0	12
3.6	127.5		50
	150		

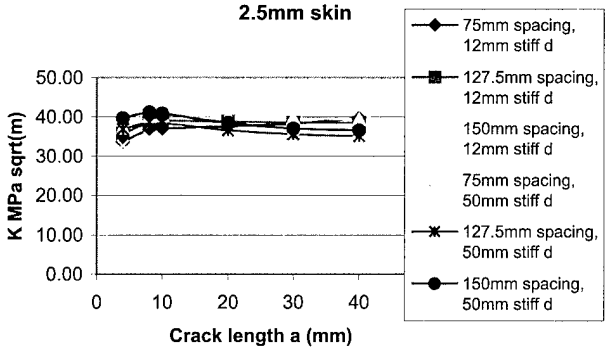

Fig. 4. Plot of K_I vs a for 2.5 mm stiffened skin with three different stiffener spacings and two different stiffener depths.

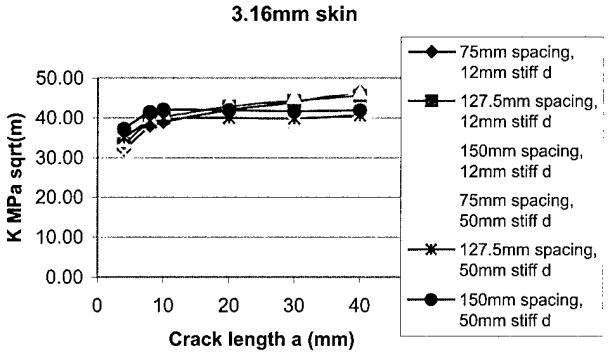

Fig. 5. Plot of K_I vs a for 3.16 mm stiffened skin with three different stiffener spacings and two different stiffener depths.

Table 10
Geometrical parameters considered

Skin thickness (mm)	Stiffener spacing (mm)	Patch thickness	Stiffener depth (mm)
2.5	75	1.0	12
3.6	127.5	1.8	
	150		

are summarised in Figs. 6 and 7. From this study we again see that the stress intensity factor K_I is a weak function of the stiffener spacing.

Figs. 2–7 also show that the stress intensity factors K_I exhibit an asymptotic behaviour as the crack length increases. However, as the skin thickness increases the crack length required to achieve this asymptote, K_∞ also increases. Indeed, for the 2.5-mm sheet thickness with a 1 mm patch the limiting value of K_∞ has essentially been reached at a crack length of between 20 and 30 mm (Fig. 6). In contrast for the 3.16-mm sheet thickness with a 1 mm patch the limiting value has not been reached by 40 mm (Fig. 7). Similarly the crack length required to reach K_∞ is also a function of the patch thickness. For example, in the case considered above when the 3.16-mm sheet thickness has a 1.8-mm thick patch this limiting value is essentially achieved with a crack length of (say) 20 mm (Fig. 7).

This asymptotic process is also a function of the depth of the stiffener. For example for a 2.5 mm skin by the time the crack length is 40 mm the limiting value of K_∞ has been reached for stiffener depths of both 12 and 50 mm (Fig. 4). In contrast for the 3.16 mm thick skin with a crack length of 40 mm the solution associated with a 50 mm deep stiffener has reached its asymptote whilst that for a 12 mm deep stiffener has not (Fig. 5).

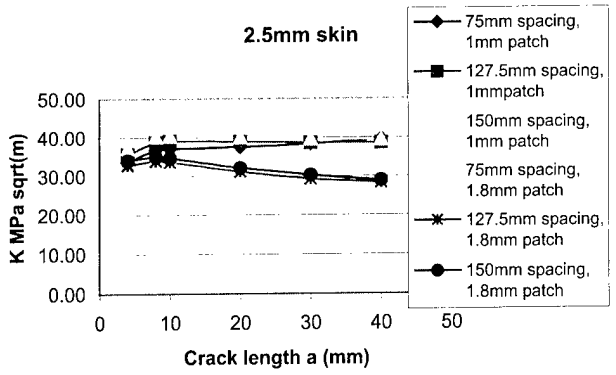

Fig. 6. Plot of K_I vs a for 2.5 mm stiffened skin with three different stiffener spacings and two different patch thicknesses.

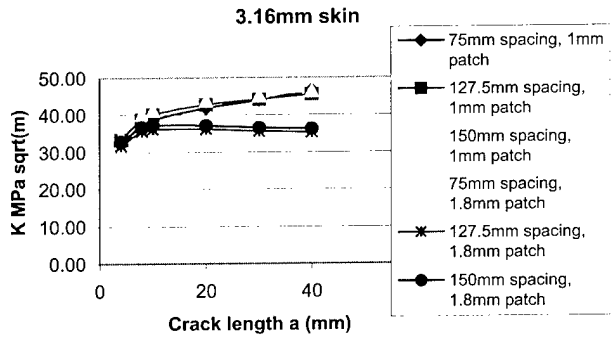

Fig. 7. Plot of K_I vs a for 3.16 mm stiffened skin with three different stiffener spacings and two different patch thicknesses.

3.3. Simple analytical formulae for predicting the limiting behaviour

The finite element result would indicate that as a first approximation the simple analytical formulae for the case when bending was allowed but the stiffeners were ignored can be used to obtain a first estimate of the limiting stress intensity factors (K_∞) for composite repairs to cracked rib stiffened panels. This dramatically simplifies the analysis and design methodologies. In general the maximum magnitude of the differences between this simple approach and the finite element results was approximately 10%. This can be seen from Tables 11 and 12.

Table 11
Comparison of prediction for bending problems, case 1

K_∞ MPa $\sqrt{m}$	Edge centre	A (mm)	t_p (mm)	E_p (MPa)	t_r (mm)	G_r (MPa)	t_a (mm)	G_a (MPa)	σ (MPa)	X (mm)	B (mm)
	Centre	80	2.5	71,000	1	208,000	0.25	375	158	200	200
Predicted f.e.	35.6 c.f. 33.9 for a 50 mm deep stiffener c.f. 38.3 for a 12 mm deep stiffener										

Table 12
Comparison of prediction for bending problems, case 2

K_∞ MPa $\sqrt{m}$	Edge centre	A (mm)	t_p (mm)	E_p (MPa)	t_r (mm)	G_r (MPa)	t_a (mm)	G_a (MPa)	σ (MPa)	X (mm)	B (mm)
	Centre	40	3.16	71,000	1	208,000	0.25	375	158	200	200
Predicted f.e.	48.3 c.f. 41.9 for a 50 mm deep stiffener c.f. 46.2 for a 12 mm deep stiffener A f.e. analysis found that this value asymptotes to 47.4 as the stiffener depth approached zero										

4. Conclusion

This paper has examined the problem of composite repairs to rib stiffened panels. As a result of this study it appears that:

a) The solution for the stress intensity factors K_1 exhibits an asymptotic behaviour as the crack length increases.

b) The stress intensity factor K_1 is a weak function of the stiffener spacing.

c) The stress intensity factor K_1 is more strongly effected by stiffener depth than stiffener width. Thus it is more dominantly a function of I for the stiffener than the area of the stiffener.

d) Simple closed form solutions can be used to obtain an accurate first approximation for the asymptotic value of the stress intensity factors K_∞.

References

[1] Rose LRF. An application of the inclusion analogy for bonded reinforcements. Int J Solid Struct 1981;17:827–38.

[2] Fredell RS. Damage tolerant repair techniques for pressurized aircraft fuselages. PhD Thesis, Delft University of Technology, June 1994.

[3] Baker AA, Jones R. Bonded repair of aircraft structures. Dordrecht: Martinus Nijhoff, 1988.

[4] Callinan RJ, Sanderson S, Keeley D. Finite element analysis of an F-111 lower wing skin fatigue crack repair, DSTO, Melbourne. DSTO-TN-0067, 1997.

[5] Roach D, Walkington P. Full scale structural and NDI validation tests of bonded composite doublers for aircraft applications, Sandia Report, SAND98-1015, February 1999.

[6] Roach D. Damage tolerance assessment of bonded composite doublers for commercial aircraft applications, Sandia National Laboratories/Department of Energy, Sandia Report, SAND98-1016, August 1998.

[7] Molent L, Callinan RJ, Jones R. Structural aspects of the design of an all boron/epoxy reinforcement for the F-111C wing pivot fitting. J Composite Struct 1989;11(1):57–83.

[8] Jones R, Chiu WK, Sawyer JPG. Composite repairs to cracks in thick metallic components. J Composite Struct 1999;44(1):17–29.

[9] Massar JJA. The fatigue characteristics of repaired and unrepaired C141 panels, Internal Report, HQ USAF Academy/ADFEM, February 1999.

ELSEVIER

Composite Structures 47 (1999) 745–752

COMPOSITE STRUCTURES

www.elsevier.com/locate/compstruct

Smart structure for composite repair

Y.L. Koh [a,*], N. Rajic [b], W.K. Chiu [a], S. Galea [b]

[a] *Department of Mechanical Engineering, Monash University, Wellington Road, Clayton, Vic. 3168, Australia*

[b] *Defence Science and Technology Organisation, Aeronautical and Maritime Research Laboratory, Airframes and Engines Division, 506, Lorimer Street, Fishermans Bend, Vic. 3207, Australia*

Abstract

This paper reports on an experimental study aimed at assessing the feasibility of detecting damage in a bonded composite structure by means of surface mounted PZT sensor/actuator elements. A boron/epoxy composite patch repair is artificially degraded through the introduction of teflon inserts at the bond line. PZT elements attached to the patch and host structure are then excited and sensed in both transfer function and self-impedance configurations and the measurements examined to assess whether bond degradation is detectable. These measurements indicate that both methods offer good prospect of detecting debonds however, some limitations have been identified. © 2000 Published by Elsevier Science Ltd. All rights reserved.

Keywords: PZT; PZT sensor/actuator; Damage detection; Impedance method; Transfer function method

1. Introduction

A smart structure can be defined as a structure that senses its internal state and external environment and based on the information-gained responds in a manner that fulfills its functional requirements. The primary advantage of moving towards smart structures technology is the potential cost benefit of condition-based maintenance strategies and the prospective life extension that may be achieved through in situ health monitoring. The monitoring of operational health and performance, and diagnosis of any faults as they occur, is a relatively new concept that is being developed to provide advantages of safer, and more reliable and affordable structures. Health monitoring can be achieved by positioning (embedded or surface mounted) sensor systems on a structure to measure those physical parameters that are informative with respect to the state of structural health. Specifically, information relating to the severity, significance and location of damage is required.

The condition monitoring of operational health and performance and the diagnosis of faults as they occur are relatively new approaches that are being developed in leading laboratories with the aim of improving the safety and reliability of structures. Monitoring can be achieved by placing a sensor system on a structure/machine to measure physical quantities such as vibration signature, power flow, strain, acoustic emission, to mention but a few. Schulz et al. [5] reported that measurements from sensor systems can be interpreted to provide four possible levels of diagnosis or action:

1. damage detection,
2. damage location,
3. damage force magnitude,
4. the remaining life of the structure.

By augmenting existing structural fabrication practices with smart materials technology, it is possible to develop structural components that contain networks of embedded sensors, microprocessors and dynamically tuneable actuator materials, that would all work in concert to affect an advanced smart structure. Such a structure would be able to diagnose, interpret and correct structural faults in situ as they occur. In this respect, one of the collaboration projects between the Australian Defence Science and Technology Organisation and Monash University involved the application of smart materials for the detection and monitoring of damage in a composite repair. This paper reports the experimental work performed to validate a series of numerical studies performed by Chiu et al. [1].

Chiu et al. [1] reported on the concept of a 'perceptive repair' or 'smart' system, which was proposed as a means to assess the in-service performance of a composite patch repair on a host structure. The concept is attractive in the composite repair context because of the stringent certification requirements demanded of such repairs when applied to aircraft. The vision is for a

* Corresponding author.

0263-8223/99/$ - see front matter © 2000 Published by Elsevier Science Ltd. All rights reserved.
PII: S0263-8223(00)00048-9

composite repair that would incorporate actuation and sensor elements and thereby offer the capacity to detect damage in the repair as well as monitor damage growth in the parent structure. Chiu et al. [1] reported on the possibilities of utilising a single sensor/actuator or multiple sensors/actuators approaches to monitor disbond in a composite repair patch. The study highlighted the efficacy of both electromechanical impedance and transfer function techniques in this role and made the following general observations:

- For the single sensor/actuator (i.e., electromechanical impedance approach) to be effective, the sensor/actuator has to be located very close to the damage area.
- The electromechanical impedance of the sensor/actuator was noted to decrease with increasing damage size.
- For the multiple sensors approach, it was found that the accumulated area under frequency response function between a pair of sensor/actuator decreases with increasing damage size.
- With the multiple sensors approach, the sensor or the actuator has to be located close to the damage. However, it appears that this technique is more sensitive to the presence of damage than the single sensor/actuator approach.

The present article will provide some experimental evidence to support the findings summarised above.

2. Statement of problem

Fig. 1 shows the schematic of the problem discussed in this paper. Here a 5-ply unidirectional boron/epoxy patch was bonded onto an aluminium plate to simulate a typical bonded repair arrangement. Five of these specimens were prepared. Four had single teflon strips inserted at the bondline marked 'A', each with a different strip size: 5×5, 10×10, 15×15 and 20×20 mm, whilst the fifth was left unmodified to serve as a reference. The incremental increase in teflon strip size was intended to reflect the progressive enlargement of a disbond during active service. Three PZT elements were bonded onto the specimen as shown in Fig. 1. Whilst PZT element 1 was bonded immediately over the disbond, PZT elements 2 and 3 were bonded on the aluminium substrate.

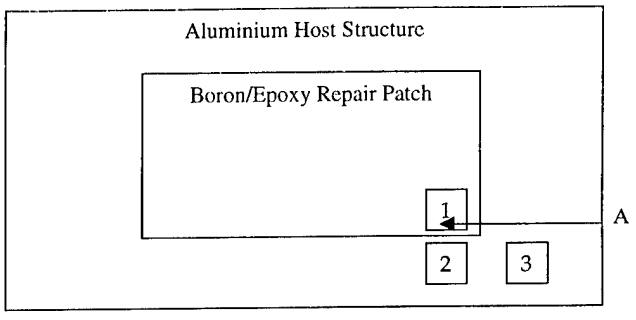

Fig. 1. Schematic of the test specimen and the locations of the PZT sensors/actuators.

One of the advantages of using PZT elements in a health monitoring role is their ability to act both as an actuator and as a sensor. When the single sensor approach is used (i.e., the electromechanical impedance technique), each PZT element is interrogated separately as a collocated sensor/actuator. In a transfer function arrangement, a pair of elements is involved, where one acts as an actuator and the other as a sensor.

3. Impedance method

Non-destructive evaluation techniques commonly utilise the characteristic of impedance to detect structural degradation. The method has been developed over several years with interest from the aeronautical industry growing as relevant technologies and techniques progressively advance. There are doubts however regarding the accuracy of predictions and conclusions made from tests conducted thus far. However, work is continuing because of the significant benefits that would be obtained if the impedance method could be made to work.

A typical application, where the impedance method is suitable can be described using a structure with the presence of a disbond reported by Summerscales [4]. Unlike other vibration techniques, a dry interface is used between the PZT and the structure under analysis. However, this introduces another stiffness to the problem. We therefore modelled stiffness of the disbond as well as the stiffness relating to the two surfaces in contact acting in series. In this respect, it is most desirable to achieve a high contact stiffness between the two surfaces, increasing the sensitivity of the method [2].

Another unique property of this vibration analysis technique is that it utilises simultaneous actuation and sensing of the structural response. This means that a single piezoelectric is used to fulfill the task of the direct as well as the converse effect, as mentioned previously.

In order to understand how piezoelectric materials can be used to obtain a vibrational structural response, it is necessary to have a clear understanding of how they interact with the structure. The PZTs are actuated using a fixed alternating electric field. The PZT provides the induced vibration, and, at the same time, serves as a sensor of the dynamic response. This response, which is largely characteristic of the host structure, modulates the current flowing through the PZT and thereby changes the measured impedance.

3.1. Results and discussion

This section will present experimental results to demonstrate how the impedance method can be used on critical sections of a composite boron/epoxy patch repair to an aluminium host structure. In this experiment, a disbond was created at the corner of the patch (see Fig. 1), since this was the most likely location for a disbond to initiate under actual service conditions.

An HP Impedance Analyser was used for this experiment. This analyser applies a 1 V (rms) single frequency signal to the PZT element and evaluates the impedance based on the response voltage. Since the voltage produced by the PZT is a function of the local stiffness, any decrease in the local stiffness will result in an increase in the PZT voltage output giving rise to a reduction in the measured impedance.

It is known that a flaw such as the kind described in Fig. 1 is likely to have minimal effect on the global dynamic properties of the structure [1]. However, it can compromise the local stiffness. In this paper, we seek to use this change in local stiffness to determine the severity of the disbond. When there is a change in local stiffness, it is envisaged that a given force over the damaged region will result in a change in the displacement or strain response. To this end, we are seeking to use PZT to enable us to relate this change to the size of the damaged region.

It is possible in most situations to model a disbond as a spring, with a stiffness of k. This is shown in relation to a model of PZT bonded to a host structure shown schematically in Fig. 2, as suggested by Chaudry [2]. Mechanical impedance, Z_m, is defined as the ratio of the force acting on the surface or system to the velocity of the system at the point of the application of the force.

A frequency-dependent electrical admittance equation has been developed from the solution to the wave equation for such a structure [2]

$$Y(\omega) = \mathrm{i}\omega a\left(\varepsilon_{33}^{\mathrm{T}}(1-\mathrm{i}\delta) - \frac{Z_{\mathrm{struc}}(\omega)}{Z_{\mathrm{PZT}}(\omega)+Z_{\mathrm{struc}}(\omega)} d_{3x}^2 Y_{xx}^E\right),$$

where Z_{struc} is the structures' mechanical impedance and Z_{PZT}, the PZTs mechanical impedance. All others are constants of the PZT.

As the size of disbonds increases, the stiffness of the spring in the model decreases. This leads to an increase in velocity which in turn leads to a decrease in impedance. As the impedance of the structure decreases, admittance will decrease proportionately.

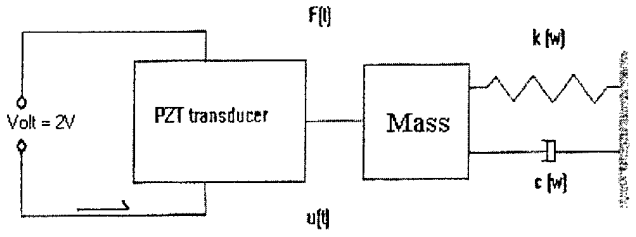

Fig. 2. Model to represent a PZT-driven dynamic structural system.

The size of disbond in the composite patch was successfully monitored with a microprocessor-based electrical impedance analyser connected to PZT elements mounted to the specimen (Fig. 1). High-resolution amplitude and phase measurements were made across two frequency bands: (i) 400 Hz–1 kHz and (ii) 1–25 kHz, at the frequency intervals given in Table 1. The experimental results for the repair patch are presented in Figs. 3 and 4 in relation to impedance measurements taken from sensor/actuator (1).

Fig. 3 shows a marked change in impedance. Notably, increasing disbond size is shown to produce a reduction in impedance across the frequency range considered (400 Hz to 1 kHz). When a higher frequency range was considered, the impedance curves tended to bunch closer together (see Fig. 4). This shows that the choice of frequency range is an important factor.

The results showed that placing a PZT element on the host structure yields a much smaller indication of the disbond. This is evident in the smaller separation between the curves in Figs. 5 and 6 as compared to those in Figs. 3 and 4. This finding is consistent with that of Chiu et al. [1], where a similar problem was investigated numerically. The main findings from these experiments can be summarised as follows:

- The PZT elements can be used to evaluate the electromechanical impedance of a bonded repair.
- The electromechanical impedance can be used to determine the size of the disbond under in the bonded repair.
- For this method to be effective, the PZT element has to be located over the disbond area.
- This method has shown to be less effective when the PZT element was located in the aluminium structure.

The impedance method has been shown to offer a useful means of detecting disbond growth in composite patch repairs. This technique has the following principal advantages:

- The method is not based on any model, and thus can be easily applied to complex structures.
- Given the typically small size of PZT elements, the method is largely unobtrusive.
- The method can be implemented for real-time health monitoring.
- The continuous monitoring provides a better assessment of the current status of the structure, which can eliminate the need for scheduled inspection.

Table 1
Frequency range and interval used for frequency response acquisition

	Range	Interval
Higher frequency	1–25 kHz	0.08 kHz
Lower frequency	0.4–1 kHz	0.002 kHz

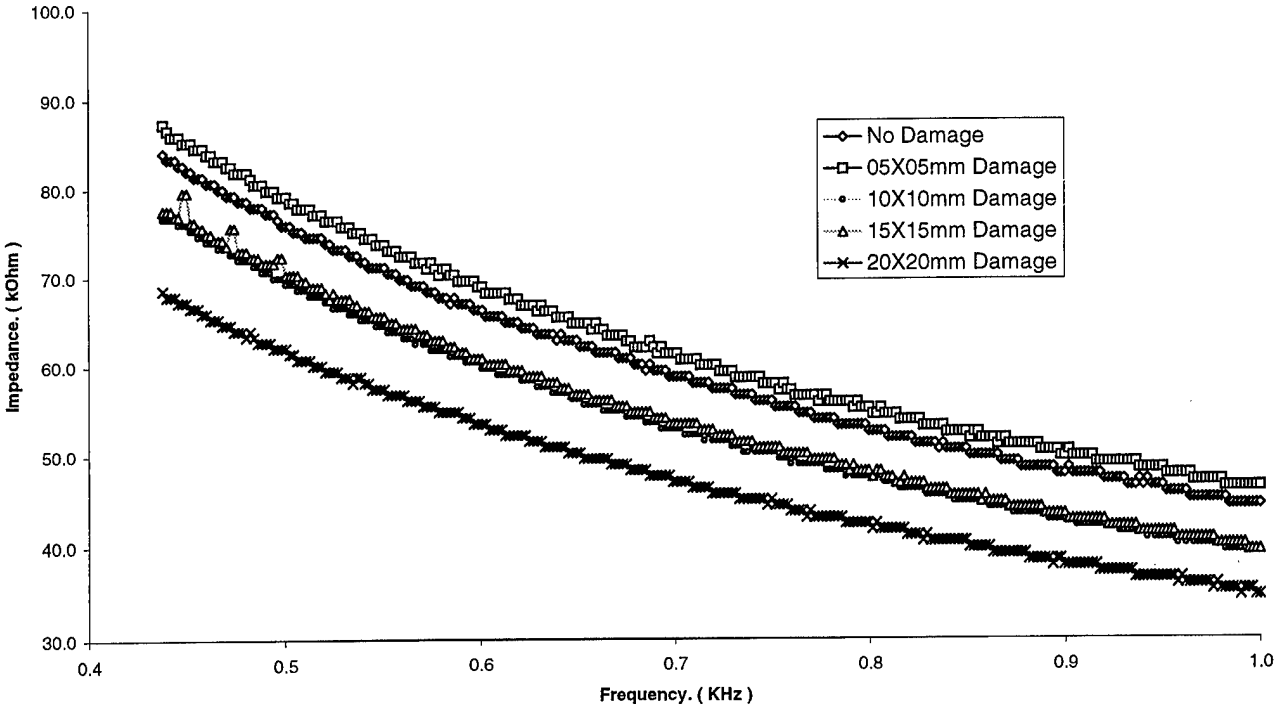

Fig. 3. Effect of disbonding on impedance magnitude (low frequency) (PZT element 1 was used as actuator/sensor).

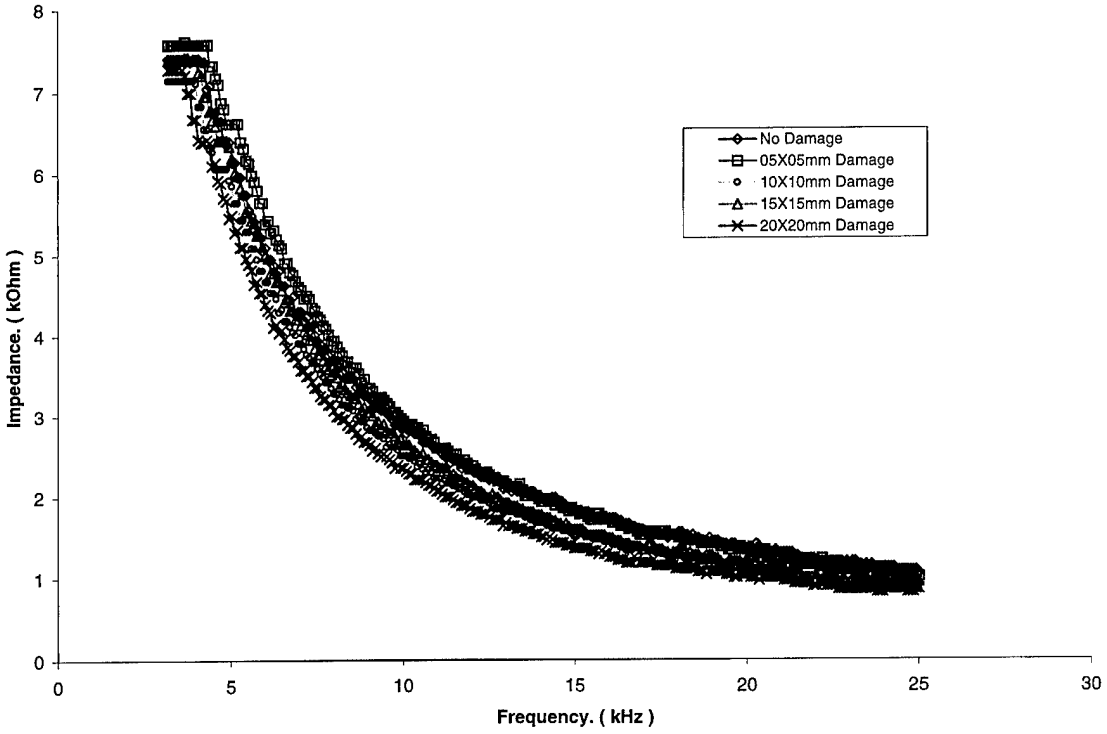

Fig. 4. Effect of disbonding of impedance magnitude (high frequency) (PZT element 1 was used as actuator/sensor).

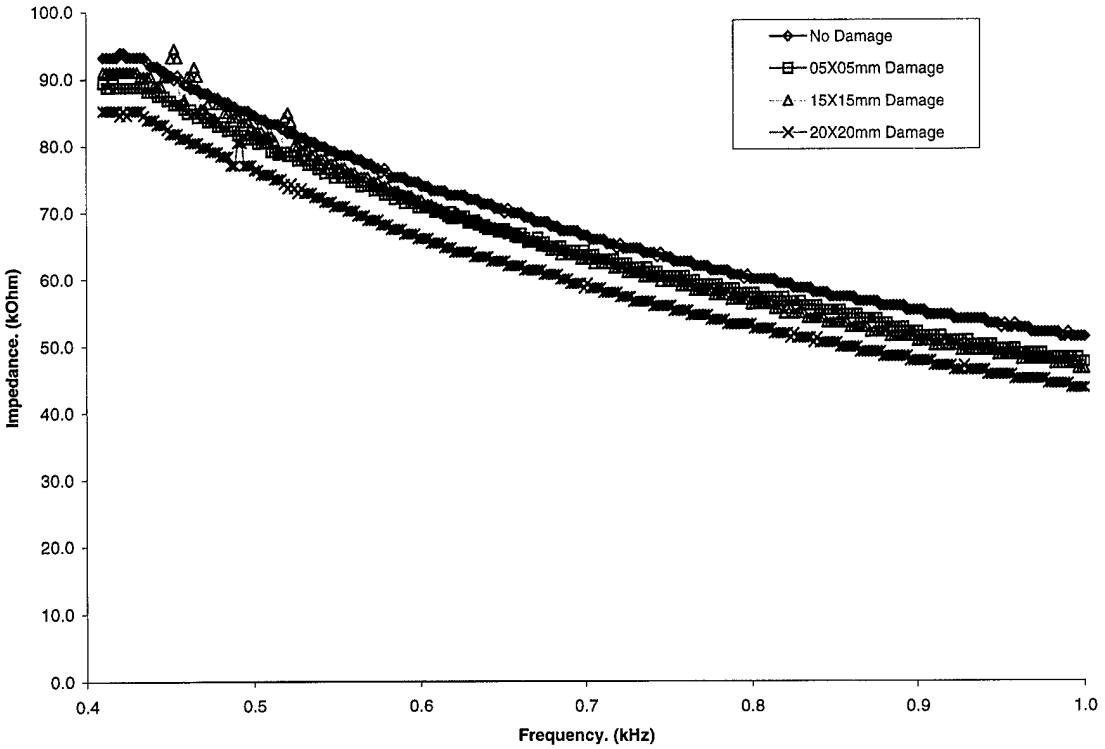

Fig. 5. Effect of distance on impendance magnitude (low frequency) (PZT element 2 was used as actuator/sensor).

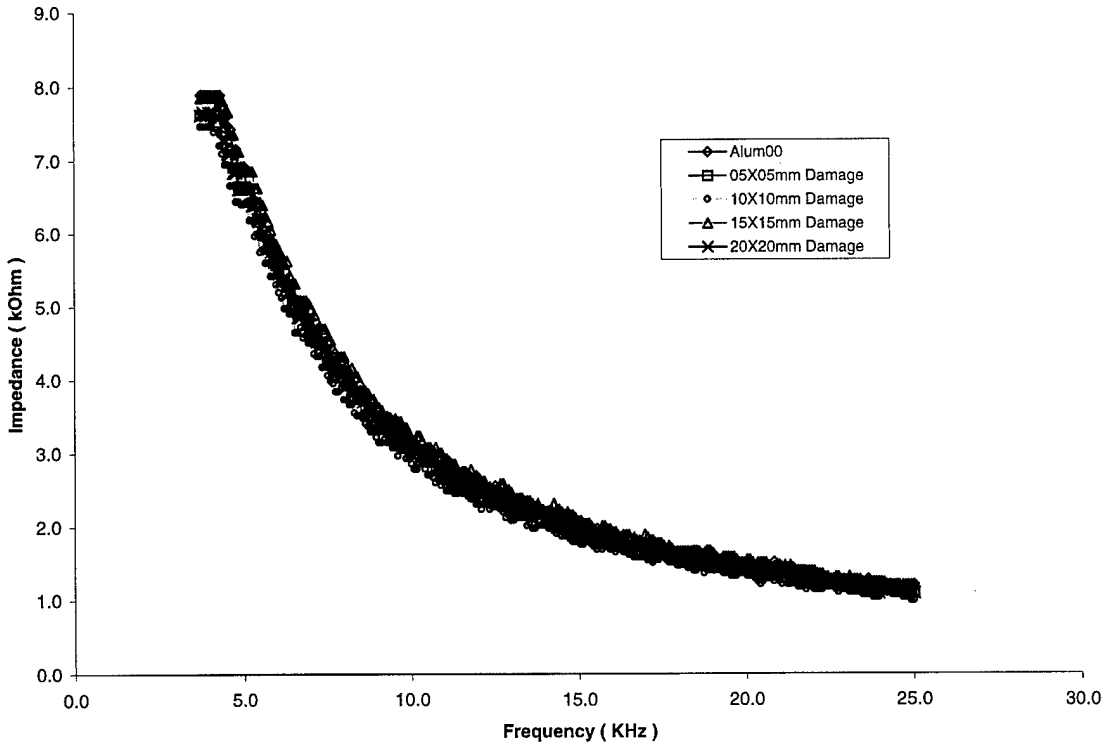

Fig. 6. Effect of distance on impendance magnitude (high frequency) (PZT element 2 used as actuator/sensor).

4. Transfer function method

The transfer function method presented in this investigation is based on the system transfer function between pairs of PZT transducers. This technique utilises both the converse and direct effect of the piezoelectric material for actuation and sensing, respectively.

To acquire the frequency response of the structure, the PZT actuator was excited with a broadband random vibration. The transfer function between this actuator and the sensor can be expressed as follows:

$$\mathrm{TF} = \frac{\text{Signal obtained from sensor}}{\text{Signal input to actuator}}.$$

4.1. Results and discussions

The specimens used for the Impedance Method experiments were also used to assess the effectiveness of the transfer function method. The following three different actuator/sensor configurations were tested (refer Fig. 1):

1. PZT (1) as the sensor and PZT (2) as the actuator.
2. PZT (2) as the sensor and PZT (1) as the actuator.
3. PZT (2) as the sensor and PZT (3) as the actuator.

A broadband signal was produced using an analogue and digital AD-3525 FFT analyser, with a frequency bandwidth of 250 Hz to 100 kHz and an RMS signal amplitude of 2 V. This broadband signal was supplied to the PZT serving as the actuator, whilst simultaneously acquiring the signal from the PZT sensor. In this manner, the transfer function of the various actuator/sensor combinations was obtained. When calculating the transfer function, a total of 30 spectral averages were taken (Table 2).

Fig. 7 shows the transfer function obtained for the case where PZT (1) was used as a sensor and PZT (2) was used as an actuator. For clarity, Fig. 7 only shows the results obtained from the no-damage case and with a 20 mm × 20 mm disbond. Given this configuration, Chiu et al. [1] predicted that the magnitude of the transfer function would decrease with an increase in the size of the disbond. As a means of reducing the effects of experimental noise and thus improving the clarity of genuine trends, an accumulative integral of measured transfer function was performed. This is similar to the technique reported by Lichtenwalner et al. [3]. Fig. 8 provides a plot of this integration. It is clear from this figure that the magnitude of the transfer function decreases with the size of disbond under the patch, which is consistent with the earlier predictions.

Fig. 9 shows the results obtained when PZT (2) was used as a sensor and PZT (3) was used as an actuator. This figure indicates that the sensor has to be located over the damage area if integrity assessment is to be successful. When PZT (2) (i.e., on aluminium structure)

Table 2
Frequency ranges used for transfer function acquisition

Frequency interval	Frequency range	Averages
0.25 kHz	0.25–100 kHz	30

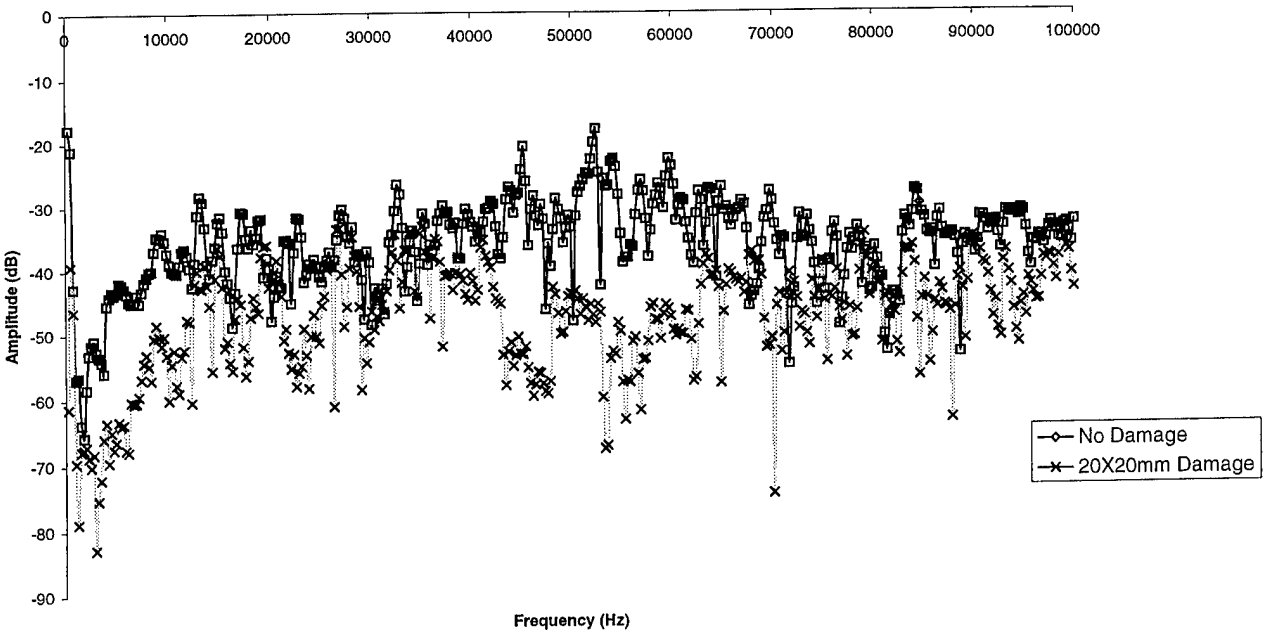

Fig. 7. Transfer function for no damage and 20 mm damage (PZT element 1 used as sensor; PZT element 2 used as actuator).

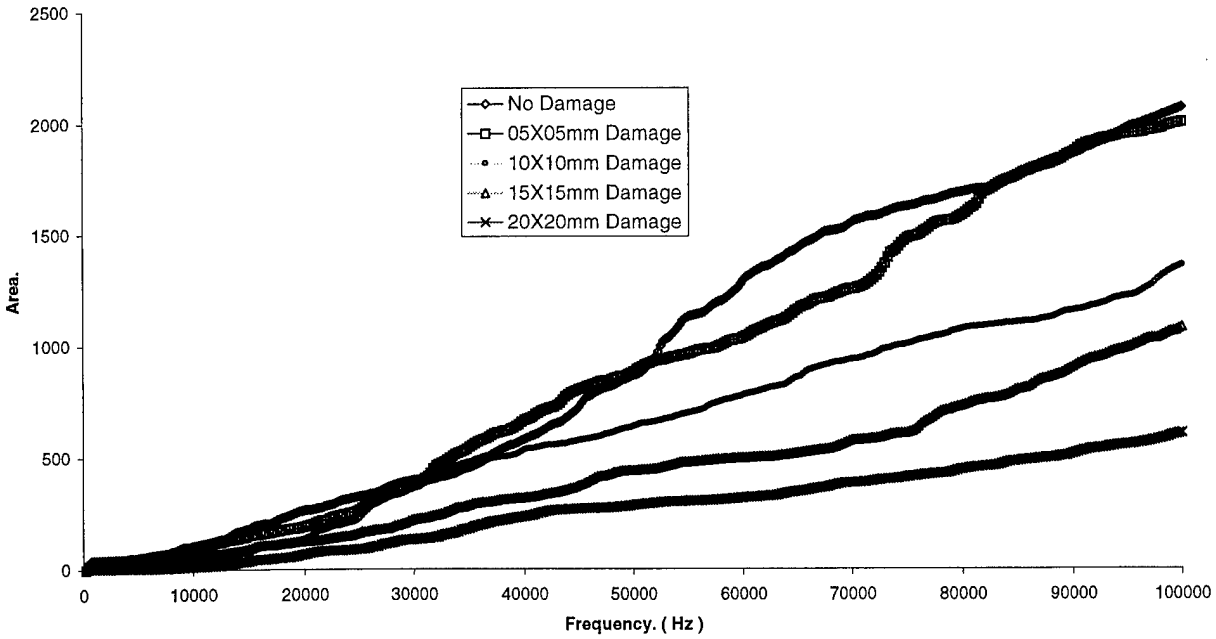

Fig. 8. Effect of debonding on transfer function magnitude area (PZT element 1 used as sensor; PZT element 2 used as actuator).

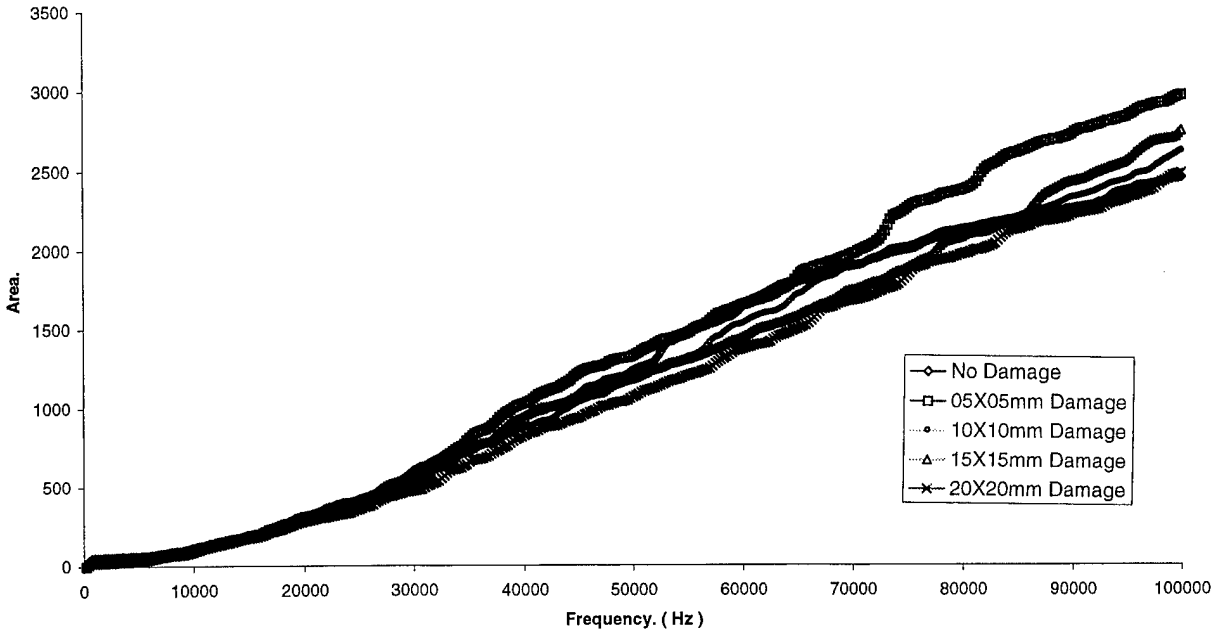

Fig. 9. Accumulative transfer function when PZT element 2 used as sensor; PZT element 3 used as actuator.

was used as sensor and PZT (1) (i.e., over damage) was used as an actuator, the results (Fig. 10) are similar to those for the converse configuration (Fig. 9). This shows that the method is capable of detecting the disbond as long as either a sensor or an actuator is located over the damage area.

We can summarise the experimental results for the transfer function approach as follows:

- The transfer function of a pair of sensor and actuator decreases with an increase in the disbond size in the composite repair.
- This decrease in the transfer function is obtained as long as a sensor or an actuator was located on the damage zone.
- The results described above revealed that locating both the sensor and actuator on the aluminium

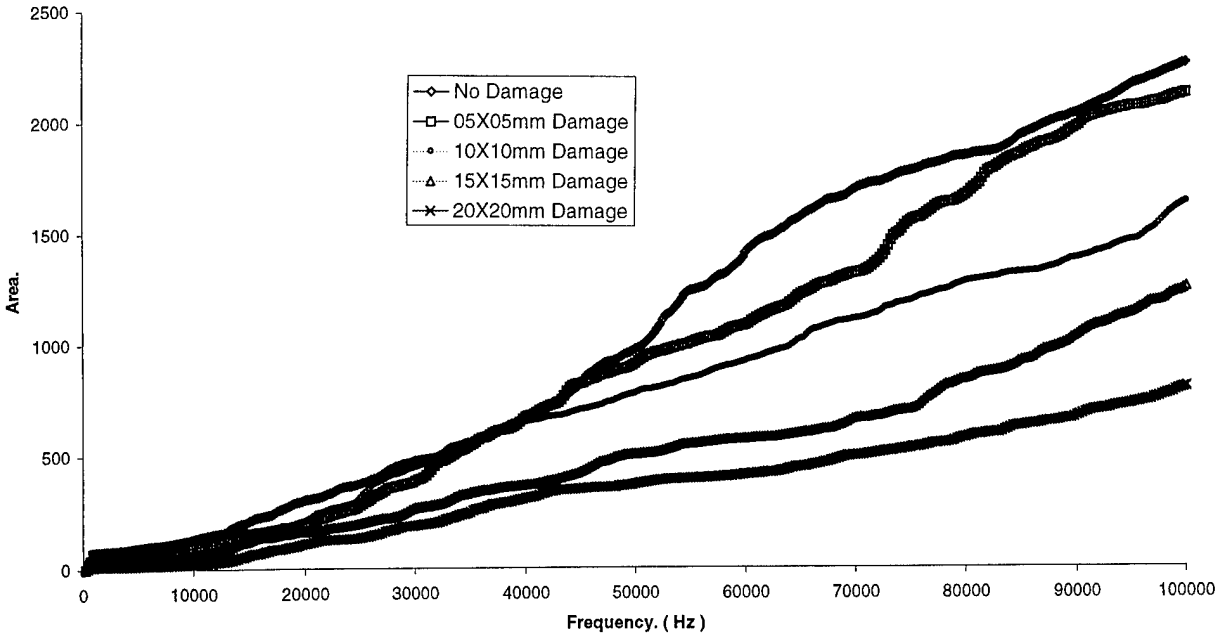

Fig. 10. Effect of debonding on transfer function magnitude area (PZT element 2 used as sensor; PZT element 1 used as actuator).

substrate is not likely to provide any information on the size of the disbond.

4.2. Advantages of the transfer function method

The transfer function approach appears to offer an effective non-destructive technique for locating disbonds in a layered structure. Some of the advantages of this technique are:

- It provides cost-effective distributed actuation/sensing technology towards the development of smart composites.
- Enhances the inspectability of composites and provides a new technology for improved material diagnostics.
- Can be implemented for real-time in situ health monitoring or for in-production quality control.

5. Conclusion

In this paper, a series of experimental results were presented to confirm some preliminary numerical findings obtained by Chiu et al. [1]. The two different methods offer different features that can be more easily matched with the needs of a particular application. The impedance-based method can offer real-time localised inspection of critical sections if bonded over the damaged region; while the transfer function method offers better alternative in cases where remote sensing is required. In most practical situations, it should be possible to incorporate both approaches in the same application. This should ensure that the maximum amount of information relating to a structural problem is obtained and provides some measure of redundancy should one of the techniques fail. An important practical advantage of the transfer function technique is that it need not involve mounting sensors in regions of high stress. Instead, the actuating PZT can be located in a low stress region, while the sensor placed in the high stress region can be made from PVDF, a material with better fatigue resistance properties.

References

[1] Chiu WK, Galea SC, Koss LL, Rajic N. Damage detection in bonded repairs using PZT material. Smart Mater Struct 1999 (submitted).
[2] Chaudry Z, et al. Monitoring the integrity of composite patch structural repair via piezoelectric actuators/sensors. Centre of Intelligent Material Systems and Structures 12212, 1995.
[3] Lichtenwalner PF, Dunne JP, Becker RS, Baumann EW. Active damage interrogation system for structural health monitoring. SPIE 1997;3044:186–94.
[4] Summerscales J. Non-destructive testing of fibre-reinforced plastics composites. London: Elsevier; 1987.
[5] Pierce SG, Staszewsik WJ, Gachagan A, James IR, Philip WR, Worden K, Schulz M, Pai PF, Smith EC, Tu PKC. Adaptive real-time structural health monitoring. AIAA J 1998.

ELSEVIER

Composite Structures 47 (1999) 753–758

COMPOSITE STRUCTURES

www.elsevier.com/locate/compstruct

Impact resistance and tolerance of interleaved tape laminates

Andre Duarte [a,*], Israel Herszberg [b], Rowan Paton [c]

[a] *Sir Lawrence Wackett Centre for Aerospace Design Technology, Royal Melbourne Institute of Technology, GPO Box 2476V, Melbourne, Vic. 3001, Australia*

[b] *Department of Aerospace Engineering, Royal Melbourne Institute of Technology, GPO Box 2476V, Melbourne, Vic. 3001, Australia*

[c] *Cooperative Research Centre for Advanced Composites Structures Limited, 506 Lorimer Street, Fishermen's Bend, Vic. 3207, Australia*

Abstract

This paper presents and discusses the results of low-velocity impact and compression-after-impact (CAI) tests conducted on interleaved and non-interleaved carbon/epoxy tape laminates. Olefin film interleaves provided a strong interface bond, resulting in a reduction in projected damage area. These interleaves changed the stress distribution under impact and restricted delamination formation at the ply interface. An investigation into the compression behaviour of these laminates revealed a reduction in undamaged strength using olefin interleaves. This was attributed to the lack of lateral support for fibres at the fibre/interleaf interface, allowing fibre microbuckling to occur at a low load. Low modulus copolyamide web interleaves resulted in an increase in damage area and minor changes to CAI strength. Examination of laminate cross-sections revealed that this was due to both the open structure of the interleaf and poor resin/interleaf adhesion. High shear modulus polyethylene interleaves resulted in a significant decrease in damage area at various impact energies, with CAI strength improved compared to the non-interleaved laminates. © 2000 Published by Elsevier Science Ltd. All rights reserved.

Keywords: Interleaving; Impact resistance; Damage tolerance; Compression after impact; Carbon/epoxy tape

1. Introduction

The use of structural composites has been limited by their low impact resistance and damage tolerance properties. Much work has been conducted to address this problem, with various techniques developed including resin modification and 3D reinforcements. However, many of these techniques involve costly manufacturing processes or result in degradation of the mechanical properties of the composite. One method used to improve impact properties in prepreg laminates is the technique of interleaving, which involves the insertion of thin, tough, polymer layers (interleaves) between selected plies of the composite laminate. Fig. 1(a) and (b) show cross-sections of a non-interleaved and interleaved laminate respectively, with the interleaf appearing as dark bands at the ply interfaces in Fig. 1(b). Various researchers have reported improvements in impact resistance and damage tolerance with interleaved carbon/epoxy tape laminates, including Masters [1], Evans et al. [2], Sun and Rechak [3] and Gandhe and Griffin [4]. In the current work, this technique has been applied to carbon/epoxy tape laminates incorporating various thermoplastic interleaf materials, and using relatively thin specimens (2 mm). This paper presents and discusses the results of low-velocity impact tests and compression-after-impact (CAI) tests conducted on interleaved and non-interleaved laminates.

2. Test apparatus and materials

2.1. Materials and specimen definition

The interleaved and non-interleaved carbon/epoxy prepreg specimens were produced using T300/914C tape manufactured by Ciba–Geigy. All laminates were cured in an autoclave at 177°C and 650 kPa. The non-interleaved specimens used a 16 ply quasi-isotropic lay-up $[+45,0,-45,90]_{2S}$ as recommended by the SACMA test specification [5], while the interleaved specimens had an interleaf (I) between dissimilar orientation tape plies such that the lay-up was $[+45,I,0,I,-45,I,90,I,+45,I,0,I,-45,I,90]_S$. The following interleaf materials were chosen for impact and CAI testing, each with different material properties. These are described in detail in Table 1, with three different interleaf types shown

* Corresponding author.

0263-8223/99/$ - see front matter © 2000 Elsevier Science Ltd. All rights reserved.
PII: S0263-8223(00)00049-0

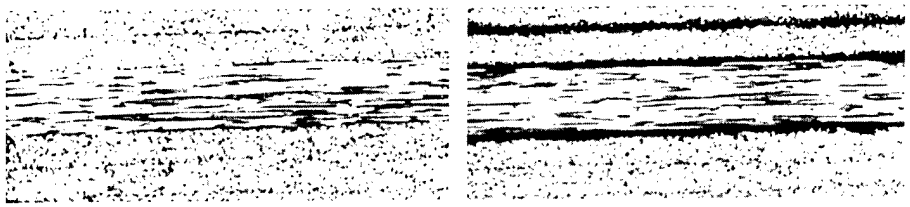

Fig. 1. Cross-sectional micrographs of non-interleaved and interleaved specimens: (a) non-interleaved; (b) 2210 interleaved.

Table 1
Interleaf details

Designation	Material	Manufacturer	Moulded thickness (mm)	Melting temperature (°C)
XAF2210	Polylefin	XIRO	0.030	145
XAF2210P	Polyolefin	XIRO	0.030	145
XAF2065	Polyolefin	XIRO	0.039	125
1a8s18	Copolyamide	Protechnic	0.018	145
Ultem 1000	Polyetherimide	General Electric	0.048	225

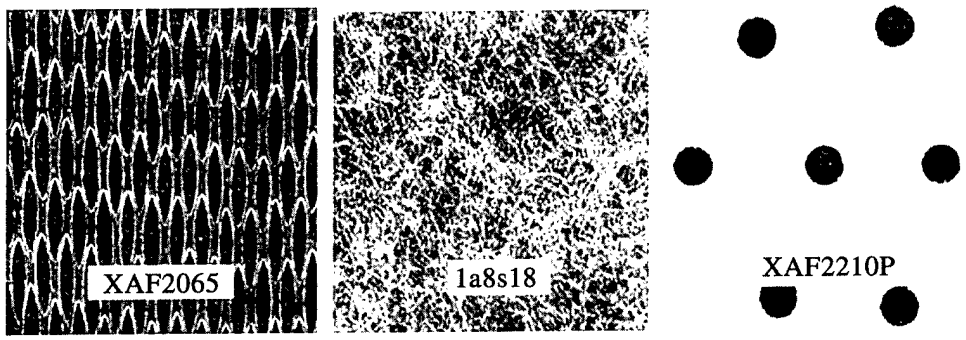

Fig. 2. Interleaf structure.

in Fig. 2. The last two listed interleaf materials were tested to investigate the influence of interleaf perforations on impact and CAIS.

- XAF2210 – thermofusible polyolefin film,
- 1a8s18 – thermofusible copolyamide web,
- Ultem 1000 – polyetherimide film,
- XAF2210P – perforated XAF2210, hole size $\frac{1}{4}$ in. at 20 mm staggered spacing,
- XAF2065 – open net form of XAF2210.

2.2. Drop weight impact test

Low velocity impact tests were conducted in accordance with the CRC-ACS impact test specification [6], using a drop weight test rig as shown in Fig. 3. The specimens measured 90×115 mm^2, and were machined with tolerances as designated by the specification. The specimens were clamped using an edge support frame with an impact window of 80×90 mm^2. The impactor used a hemispherical steel tup of diameter 12.5 mm, and used variable weights and heights to impact the specimen at incident energies up to 7 J/mm. Following impact, the specimens were c-scanned to determine the projected damage area, with selected specimens sectioned and viewed under a microscope to investigate failure paths and mechanisms.

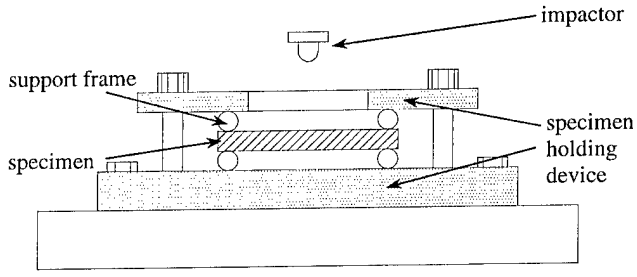

Fig. 3. Schematic of drop weight impact test rig.

2.3. Compression after impact test

Compression tests were conducted on impacted and non-impacted specimens using a modified rig developed

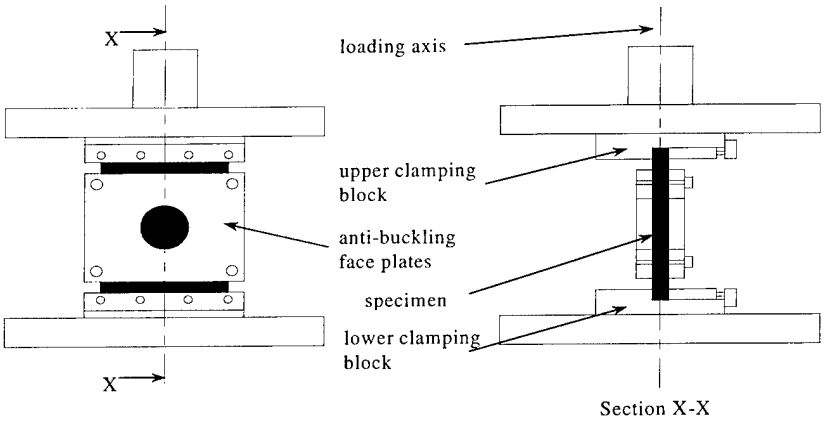

Fig. 4. Schematic of CAI test rig.

at the CRC-ACS, and following the CRC-ACS CAI test specification [7]. A schematic of the rig is shown in Fig. 4. The CAI tests were conducted at a displacement rate of 0.5 mm/min and were concluded at the first onset of failure.

3. Results

3.1. Low-velocity impact

The olefin film interleaves (XAF2210) provided a strong bond at the interleaf/epoxy interface. These interleaves restricted delamination propagation at the interface and changed the formation and distribution of interlaminar stresses under impact. As shown in Fig. 5, the XAF2210 interleaves produced a significant reduction in projected damage area at all impact energies (≈55% reduction at 6 J/mm), with the threshold energy for damage initiation increased to 2 J/mm. At this impact energy of 2 J/mm, the non-interleaved specimen resulted in an extrapolated damage area of around 200–250 mm^2. The perforated film (XAF2210P), produced similar results, with slightly higher damage areas compared to the non-perforated film.

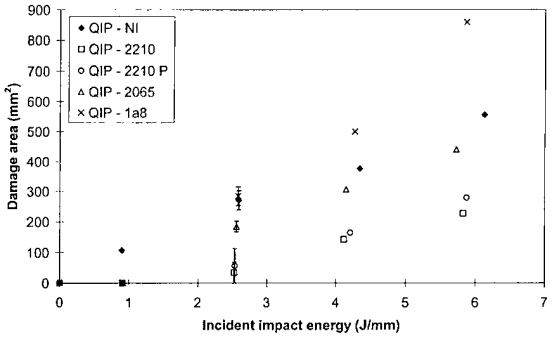

Fig. 5. Damage area (non-interleaved and various interleaved).

The XAF2065 interleaf produced only a slight improvement in damage resistance over the non-interleaved (≈15% at 6 J/mm), with the initiation energy increased to approximately 1 J/mm. At this impact energy level, 100 mm^2 damage area was produced in the non-interleaved specimen. The behaviour of the XAF2065 interleaved composite was very different to that using the XAF2210 film interleaves because of the large amount of matrix resin at the interface dominating the stress–strain behaviour of the specimen under impact.

The 1a8s18 interleaves resulted in an increase in damage area, particularly at higher impact energies. It was suggested that this was due to the interleaf having a very open web structure, allowing cracks to propagate easily between the gaps in the thermoplastic. Another reason for the lack of delamination suppression was the poor bond between the copolyamide interleaf and the epoxy resin, possibly providing weak points for the initiation of matrix cracks. A similar behaviour was shown using 1a8s18 interleaved RTM composites in a paper previously published by the authors [8].

The polyetherimide interleaf material was chosen for its high shear modulus, to overcome problems with lack of lateral support under compression loading associated with the low modulus olefin interleaves (see Section 3.2). The results presented in Fig. 6 show a substantial increase in impact resistance, with damage initiation energy increased to 2.7 J/mm. At this impact energy, the non-interleaved specimen had a projected damage area of approximately 250–300 mm^2. The improvement was not as significant at the higher impact energies, with 5 J/mm extrapolated as a damage energy at which no improvement was realised. The proposed reason for the reduced effect of interleaving at higher impact energies is the increased localised fibre breakage. The impactor began penetrating the impact surface of the non-interleaved specimen at around 3–4 J/mm. It will also be shown later that the reduction in CAIS of the

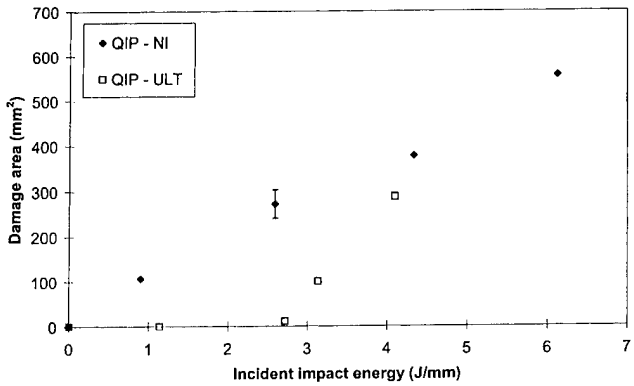

Fig. 6. Damage area (non-interleaved and ultem interleaved).

non-interleaved laminate was minimal after 3 J/mm (saturation energy). Hence, a large proportion of the impact energy was absorbed by breakage of fibres in and around the impacted site, reducing the effectiveness of the interleaf material.

The micrographs in Fig. 7 show cross-sections of an ultem-interleaved specimen impacted at 3 J/mm. It is seen that crack propagation occurred preferentially through the lamina, rather than at the fibre/matrix interface. This indicated a significant increase in the bond strength at the interface, and an increase in interlaminar fracture toughness of the interleaved composite. The second figure shows numerous transverse cracks through the lamina, inclined at 45° to the lamina. The noticeable phenomenon here is the suppression of delamination formation at the interfaces, with relatively few transverse cracks forming delaminations. With those that do form delaminations, the propagation distance is very small, indicating increased resistance to delamination at the interface.

3.2. Compression after impact

The different types of interleaf resulted in very different CAI strengths, as shown in Fig. 8. The reduction in undamaged compression strength was very severe with the XAF2210 olefin interleaves (almost 65% reduction), particularly due to the separation of the 0° plies. The low compression strength of these specimens was due to fibre microbuckling at the edge of the lamina. This was due to a lack of out-of-plane support for the fibres under compression loading, as the olefin interleaf had a very low shear modulus. The failure of these laminates is seen in the micrograph in Fig. 9. This was also described by Evans and Masters [9], indicating fibre microbuckling would occur as the shear modulus of the interleaf material decreased. Further reductions in CAIS were evident only at very high energy impacts. The discrete perforations in the XAF2210P specimens made

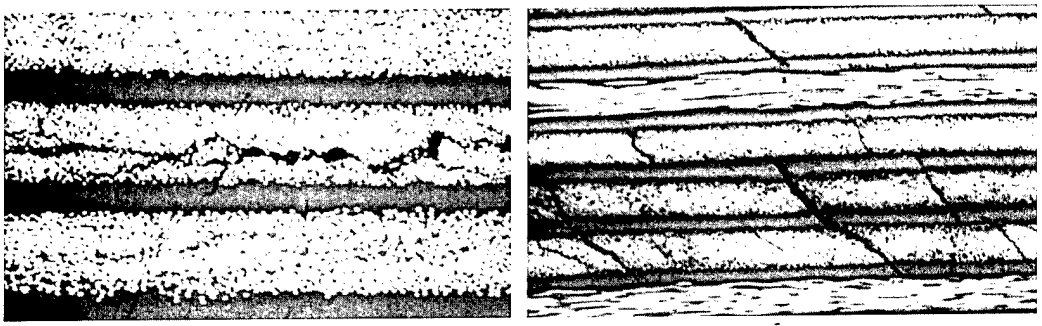

Fig. 7. Intra-tow cracks and transverse cracks (ultem interleaved – 3 J/mm).

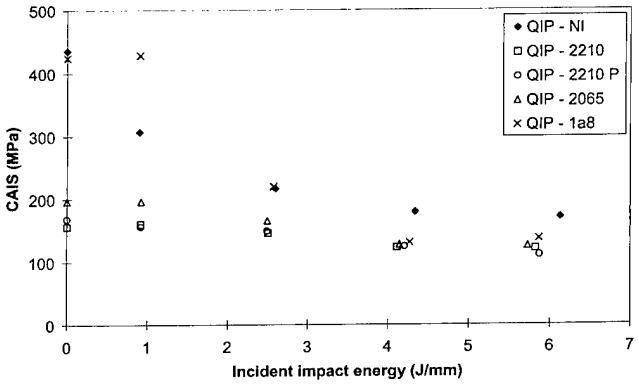

Fig. 8. CAIS (non-interleaved and various interleaved).

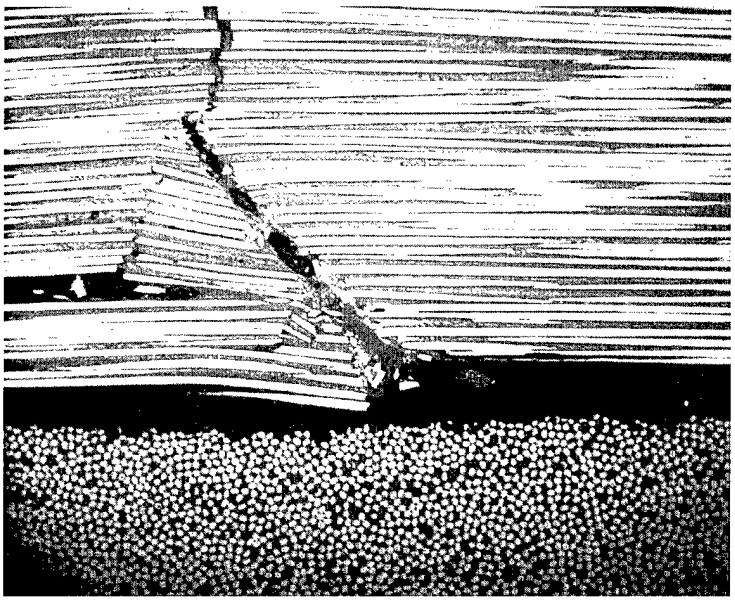

Fig. 9. Fibre microbuckling (2210 interleaved).

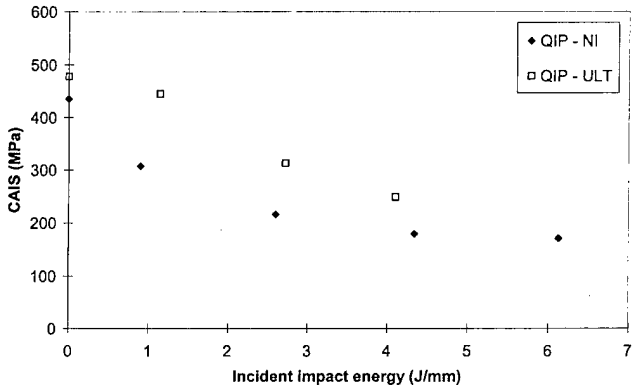

Fig. 10. CAIS (non-interleaved and ultem interleaved).

no difference to the CAIS results. The XAF2065 resulted in slightly higher undamaged and low-energy impact compression strength. This was due to the open net providing larger resin regions at the interface to support the fibres and a shorter buckling length. The 1a8s18 interleaves seemed to indicate a tolerance to very low-energy impacts, with no damage reduction seen at 1J/mm. However, the strength dropped suddenly at 2J/mm, to a level similar to the non-interleaved.

As seen in Fig. 10, the introduction of ultem interleaves produced a very small reduction in compression strength (7%) at 1 J/mm impact. In contrast, the non-interleaved laminate suffered a 30% reduction in compression strength for a similar impact. This was similar at higher impact energy, however the damage tolerance improvement reduced as the impact energy increased. The last result recorded was a compression strength reduction of 47% at 4.1 J/mm compared to a 60% reduction at 4.3 J/mm for the non-interleaved composite. This is a significant result, indicating the damage tolerance of quasi-isotropic tape laminates can be increased to a large degree with high shear modulus thermoplastic interleaving.

4. Conclusions

The different types of interleaf material investigated offer different property tailoring options for interleaved RTM composites. Low modulus olefin interleaves were successfully used to increase impact resistance, shown by a decrease in projected damage area. However, this was accompanied by a reduction in compression strength, due to a lack of lateral support for the fibres. Therefore, this reduction in visible damage area may be of use in lightly or non-loaded non-structural components only.

For structural components, the compression strength may be improved using a higher shear modulus interleaf material. This was shown using a polyetherimide film, which produced reductions in damage area, and significant improvements in compression after impact strength.

References

[1] Masters J. Improved impact and delamination resistance through interleafing. Key Eng Mater 1989;37:317–48.
[2] Evans R, Hirschbuehler K. (American Cyanamid Company). Thermoplastic interleafed resin matrix composites with improved impact strength and toughness. United States Patent No. 4,604,319, 1986.
[3] Sun C, Rechak S. Effect of adhesive layers on impact damage in composite laminates. In: Whitcomb JD, editor. Composite Materials: Testing and Design (Eighth Conference), ASTM STP 972.

Philadelphia: American Society for Testing and Materials, 1988. p. 97–123.

[4] Gandhe G, Griffin Jr. O. Post-impact characterization of interleaved composite materials. SAMPE Quarter 1989;20(4):55–8.

[5] Anon., SACMA recommended test method for compression after impact properties of oriented fibre resin composites. Suppliers of Advanced Composite Materials Association, SRM 2R-94, 1994.

[6] Callus P, Test method for the generation of impact damage in polymer matrix composite materials. Co-operative Research Centre for Advanced Composite Structures – Internal Publication, CRC-ACS-TS-131-002, 1997.

[7] Callus P, Test method for the compression-after-impact properties of impacted polymer matrix composite materials. Co-operative Research Centre for Advanced Composite Structures – Internal Publication, CRC-ACS-TS-131-003, 1997.

[8] Duarte AJ, Herszberg I, Paton R. Impact resistance and tolerance of interleaved RTM laminates. In: Proceedings of the International Conference on Composite Materials 12 (ICCM-12). France: Paris, July 1999.

[9] Evans R, Masters J. A new generation of epoxy composites for primary structural applications: materials and mechanics. In: Johnston N, editor. Toughened Composites, ASTM 937. Philadelphia: American Society for Testing and Materials, 1987. p. 413–36.

ELSEVIER

Composite Structures 47 (1999) 759–765

COMPOSITE STRUCTURES

www.elsevier.com/locate/compstruct

Structural integrity analysis of embedded optical fibres in composite structures

R. Hadzic [a,*], S. John [a], I. Herszberg [b]

[a] *Department of Mechanical and Manufacturing Engineering, RMIT, University, Bundoora East Campus, Vic. 3083, Australia*

[b] *Department of Aerospace Engineering, RMIT, University, The Sir Lawrence Wackett Centre for Aerospace Design Technology, G.P.O. Box 2476V, Melbourne, 3001, Australia*

Abstract

The virtues of having sensors in manufactured goods for increased functionality purposes have been well documented. Benefits include sophisticated structures requiring less maintenance and repair, increased safety and reliability, and avoidance of 'over design'. Though many schemes of sensing are available, these so-called 'smart' products in the near future, will increasingly rely on the optical fibres (OF) principles because of numerous inherent advantages. Optical fibres are small, lightweight, possess geometrical flexibility, Electromagnetic interference (EMI) immunity, operate over a wide range of environmental conditions, and can be configured to respond to many physical parameters.

This paper will report on the suitability of embedding OF in commonly used carbon-fibre composites. These panels will be designed, manufactured and tested for the effects of typical fibre-optic geometrical and physical parameters such as types of fibre coating polymers, fibre diameter and fibre distribution. Corroboration of these test results with finite element (FE) results will be shown. Based on tensile and compression tests on OF-embedded composites, it is shown that significant deterioration on strength is observed beyond a certain OF density level. This paper will focus on the macroscopic effect of having optical fibres in composites from a structural integrity point of view. To this end, an exposition on the theoretical considerations using continuum mechanics and energy principles is provided. © 2000 Elsevier Science Ltd. All rights reserved.

Keywords: Structural integrity; Embedded optical fibres; Composite structures

1. Introduction

As mentioned above, one of the key issues to be addressed in this paper is the embedding of optical fibre (OF) in composite structures and its effect on the material properties of the laminated composite. Future aerospace applications can be expected to require structures with ever lower weight and higher temperature and strength capability. Composite materials offer a potential means of enabling these structural properties, but manufacturing difficulties and adequate methods of verifying structural integrity have slowed their development.

Optical fibre sensors may be embedded directly into the material and used to monitor the manufacturing process. The same OF sensors may be used in conjunction with non-destructive evaluation methods to evaluate the integrity of parts, once they have been manufactured to check for flaws that may result from processing or handling. Once the parts have been installed into the structure, the sensors may be interconnected into a health monitoring network that could be used to determine maintenance requirements and operational readiness.

Benefits of using 'Smart' structure technology, include safe and reliable structures giving optimum performance under varying conditions with minimal human interference. Since the concept is in the embryonic stage, a number of technical issues need to be addressed before successful applications become a reality.

This research focuses on the effect of embedding OF sensors on the mechanical properties of carbon-epoxy composite materials. Using Finite Element Analysis (FEA) and experimental tensile test results, the interplay between the OF and mechanical property degradation is monitored and quantitatively modelled.

1.1. Experimental

Mechanical testing of composite panels with OF was undertaken to determine the tensile strength. Some of

* Corresponding author.

0263-8223/99/$ - see front matter © 2000 Elsevier Science Ltd. All rights reserved.
PII: S0263-8223(00)00050-7

the details are described below, but the comprehensive overview of this experimental program can be obtained from Hadzic [2].

1.2. Design and computational

To verify the reliability of the experimental results, FEA was performed using the COSMOS/M package.

Finite element analysis was performed to investigate the stress/strain distributions within the composite material and the embedded optical fibre. For example, how strain is transferred from the carbon-epoxy host to the core/cladding of the optical fibre through resin-rich region which acts as an interface.

1.3. Mathematical modelling

The verification of experimental and computational results was undertaken through the development of the theoretical models of optimum optical fibre embeddability and spatial distribution. Here, an exposition on the theoretical considerations using continuum mechanics and energy principles is provided.

2. Macromechanical experiments

The effects of embedded OF on the mechanical properties of carbon-epoxy composite as a host material were studied. Optical Fibres, 125/250 μm in diameter were embedded in AS4/3501-6 carbon/epoxy and Fibredux 914 unidirectional carbon pre-preg. The static performance of the material was evaluated. The OF were placed in the middle plane and near the surface of the specimens both parallel to the loading direction. The mechanical tests included 0° tensile, and compression with a first ply failure of specimens.

2.1. Introduction

The approach taken in this work, conducting static tests on laminates with embedded Optical Fibres, is not new. Various workers such as Culshaw and Gardiner [1] found it is possible to choose composite host systems with embedded OF sensors that do not have degraded static mechanical properties.

Transverse tensile (90°) testing on two different host materials produced different results in their study. One material produced failures at the OF inclusion, while the other did not. Longitudinal (0°) compression strengths were reduced when OF were embedded orthogonally.

The laminate approach differs from a micromechanical approach that concentrates on the region immediately surrounding the individual OF. The micromechanical approach has been used to look at the stress and strain in and around the OF, and the interface between the OF and host material.

2.2. Experimental procedure

In the first part of the experimental program, composite laminates were made from commercial AS4/3501-6 (carbon-epoxy) tape from Hercules Inc. The pre-preg stacks were laminated as eight ply ($90°_4$, $0_4°$)s and 16 ply ($90_8°$, $0_8°$)s panels. Each ply was 0.125 mm thick for the nominal fibre volume content 62%. Optical fibres were embedded in the middle plane or near the surface of the laminate.

In the second part of the experimental program, composite laminates were made from Fibredux 914 unidirectional carbon pre-preg with a fibre content of 59.45%. In this case, OF were embedded below the surface and near the bottom of the laminate. Laminates contained 0.24% fiber optics. Note that in all cases, the OF were aligned with the carbon reinforcing fibres and were placed between two plies of identical orientation.

Experimental and analytical studies have shown that this is an optimal orientation to minimize the effect that the embedded optical fiber has on the surrounding host material, see [1]. Optical Fibres were placed in the middle plane of the laminate, or below the surface ply and aligned with the fibre direction to the 0°-plies, by the following procedure: The two symmetrical halves of each lay-up were stacked up individually. One half was placed on the lay-up table. The OF were placed across the stack and temporarily taped to the table. The second half of laminate was then placed on top, sandwiching the OF between two halves, as shown in Fig. 1.

The laminate was then ready for curing in the autoclave. There were no special precautions taken in the cure and bagging to restrict the OF from shifting position. Curing followed the manufacturer's recommended cycle at a maximum temperature of 177°C and pressure of 5.5 MPa for 5 h.

Several assumptions were made in these experiments. First, it was assumed that the temperature is constant throughout the composite specimen and that all the OF experience the same temperature, regardless of location in the laminate.

It is believed that the specimen was thin enough (approximately 1 mm) so that the heat transfer was rapid and temperature gradients were minimised. After autoclaving, the plies were then peeled carefully from the panel, and mechanical test specimens were cut using a water-cooled diamond saw. The specimens had the dimensions of 150 by 30 mm for tensile testing and 60 by 25 for compression test. Specimen edges were inspected for cutting flaws, and specimens with visible edge defects were eliminated. The laminate configurations of tested (AS4/3501-6) and (Fibredux 914) are shown in Tables 1–4.

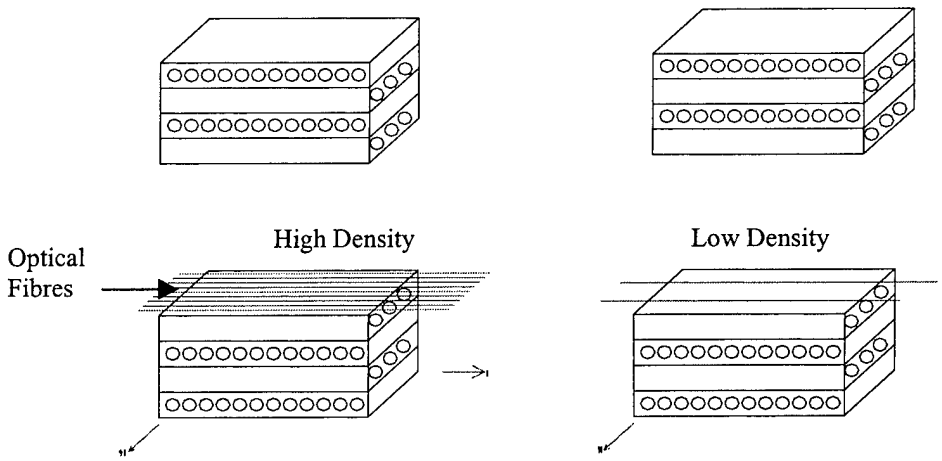

Fig. 1. Schematic of specimens with different densities of OF.

Table 1
Laminates (AS4/3501-6) tested-tensile test[a]

Laminate	Optical fibres		Specimens		
	Diameter (μm)	Number of OF	Width (mm)	Thickness (mm)	Gauge length (mm)
$[90_4, 0_4]_s$	250	N/A	30	1	80
$[90_4, 0_4, 0\,\mathbf{OF2}]_s$	250	2	30	1.35	80
$[90_4, 0_4, 0\,\mathbf{OF5}]_s$	250	5	30	1.35	80
$[90_4, 0_4, 0\,\mathbf{OF9}]_s$	250	9	30	1.35	80
$[90_8, 0_8]_s$	250	N/A	30	2.36	80
$[90_8, 0_8, 0\,\mathbf{OF2}]_s$	250	2	30	2.36	80
$[90_8, 0_8, 0\,\mathbf{OF5}]_s$	250	5	30	2.36	80
$[90_8, 0_8, 0\,\mathbf{OF9}]_s$	250	9	30	2.36	80

[a] *Explanation of the laminate ID coding*:
$[90_4, 0_4]_s$ – Specimen with 8-ply symmetrical orientation of 90° and 0°.
$[90_8, 0_8, 0\,\mathrm{OF2}]_s$ – Symmetric crossply laminate (16 layers) with two OF embedded in middle plane.
$[90_8, 0_8, 0\,\mathrm{OF9}]_s$ – Symmetric crossply laminate (16 layers) with nine OF embedded in middle plane.

Table 2
Laminates (AS4/3501-6) tested-compression test

Laminate	Optical fibre		Specimens		
	Diameter (μm)	Number of OF	Width (mm)	Thickness (mm)	Gauge length (mm)
$[90_4, 0_4]_s$	250	N/A	25	1	20
$[90_4, 0_4, 0\,\mathbf{OF2}]_s$	250	2	25	1.35	20
$[90_4, 0_4, 0\,\mathbf{OF5}]_s$	250	5	25	1.35	20
$[90_4, 0_4, 0\,\mathbf{OF9}]_s$	250	9	25	1.35	20
$[90_8, 0_8]_s$	250	N/A	25	2.36	20
$[90_8, 0_8, 0\,\mathbf{OF2}]_s$	250	2	25	2.36	20
$[90_8, 0_8, 0\,\mathbf{OF5}]_s$	250	5	25	2.36	20
$[90_8, 0_8, 0\,\mathbf{OF9}]_s$	250	9	25	2.36	20

Table 3
Laminates (Fibredux 914) tested-tensile test

Laminate	Optical fibre		Specimens		
	Diameter (μm)	Number of OF	Width (mm)	Thickness (mm)	Gauge length (mm)
$[0_4, 90_4]_s$	250	N/A	30	1	80
$[0, 0\,\mathbf{OF28}, 0, 90, 0, 0, 90, 0, 0\,\mathbf{OF28}, 0]$	250	56	30	1.70	80

Table 4
Laminates (Fibredux 914) tested-compression test

Laminate	Optical fibre		Specimens		
	Diameter (μm)	Number of OF	Width (mm)	Thickness (mm)	Gauge length (mm)
[0, 0, 90, 0, 0, 90, 0, 0]	250	N/A	30	1	20
[0, 0 **OF28**, 0, 90, 0, 0, 90 0 0 **OF28**, 0]	250	56	30	1.70	20

Table 5
Results of tensile test (AS4/3501-6)

Laminate	Specimens Tested	Maximum Load (kN)
$[90_4,0_4]_s$	5	21.30
$[90_4,0_4,0$ **OF2**$]_s$	5	20.36
$[90_4,0_4,0$ **OF5**$]_s$	5	19.17
$[90_4,0_4,0$ **OF9**$]_s$	5	20.01
$[90_8,0_8]_s$	5	34.66
$[90_8,0_8,0$ **OF2**$]_s$	5	34.46
$[90_8,0_8,0$ **OF5**$]_s$	5	35.41
$[90_8,0_8,0$ **OF9**$]_s$	5	35.71

3. Tension and compression testing

Tensile tests were conducted in accordance with ASTM-D3039M-93 and compression testing in accordance with ASTM-D3410-87, with strict compliance of specimen dimensions. A servo hydraulic load frame was used in all coupon tests and Test Star II data acquisition software for recording load and strain data.

3.1. Results and discussion

3.1.1. Tension test

Experiments were conducted on specimens with and without embedded OF. In the experiments, specimens were loaded in continuously increasing tensile load. A Physical Acoustics Local AT acoustic emission detector was used to monitor acoustic events, while each specimen was being loaded. When a significant acoustic event occurred, loading was stopped and the specimen removed from the load frame and inspected for cracks.

These results indicated that the presence of Optical Fibres (shaded rows in Table 5) did not seriously degrade the mechanical properties of the host material. This can be seen in Table 5, where the shaded rows (with OF) are compared with identical specimens without OF (unshaded rows in Table 5).

This, however, contrasts markedly with the findings in Table 6 on tests conducted on the Fibredux panels.

Here, it is seen that the failure load of composite laminates with comparatively more densely embedded OF (28 fibres near each surface) decreased by approximately 33%.

Table 6
Results of tensile test (Fibredux 914)

Laminate	Specimens tested	Maximum load (kN)
[0, 0, 90, 0, 0, 90, 0, 0]	3	14.20
[0, 0 **OF28**, 0, 90, 0, 0, 90, 0, 0 **OF28**, 0]	3	9.46

4. Computational analysis

The FE modelling was used to provide an insight into the behaviour of the fibre (core/cladding) inclusion and the carbon-epoxy host. The analysis provided an understanding of the local interaction mechanisms between the embedded fibre and the composite host. The Young's Moduli were experimentally determined as shown in Table 7.

Table 7
Experimentally determined Young's Modulus

	E_z (longitudinal axis) (GPa)
(AS4/3501-6)-$[90_4,0_4]_s$	104.5
(AS4/3501-6)-$[90_4,0_4,0$ **OF9**$]_s$	74.6
(Fibredux 914)-[0,0,90,0,0,90,0,0]	179.2
(Fibredux 914)-[0,0 **OF28**,0,90,0,0,90,0,0 **OF28**,0]	79.64

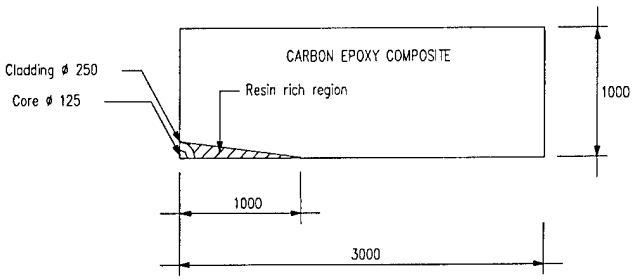

Fig. 2. A sketch of the FEA model.

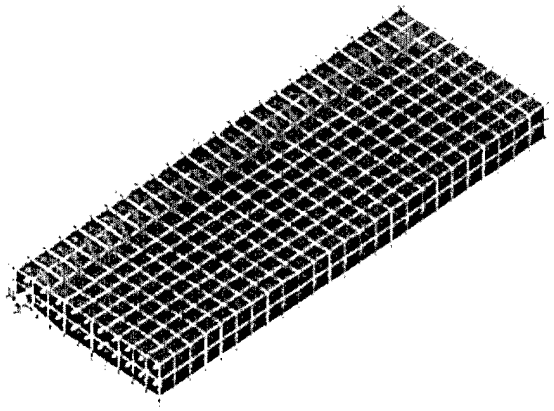

Fig. 3. Quarter of model with constrained conditions.

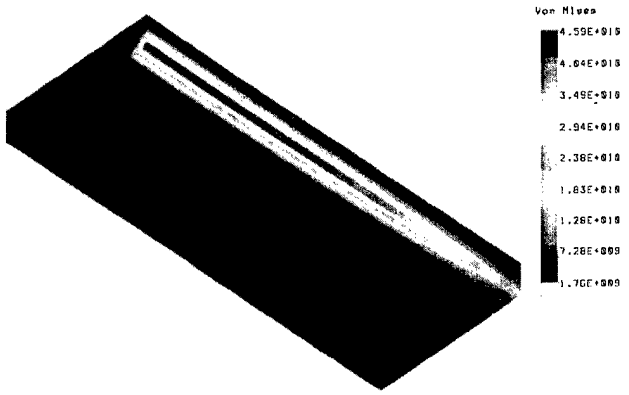

Fig. 4. Von-Mises stress distribution (GPa).

4.1. Finite element model

To study the behaviour of the stress–strain distributions of the system under consideration, a three-dimensional (3D) linear elastic finite element model was developed. A sketch of the model is shown in Fig. 2. Interfacial and non-linear behaviour of the resin-rich portion of the laminate was not modelled in this study.

The model was created using 3D solid elements under the plane stress assumptions. The boundary and loading conditions applied to the quarter of model are shown in Fig. 3. The boundary conditions used in the FE model were such that they closely represent the condition specimens in the 10 kN Instron tensile testing machine.

Material properties used in the model are given in Table 8, where E_x, E_y and E_z are the elastic moduli in directions X, Y and Z, respectively, and v_{xy}, v_{xz}, v_{yz} are Poisson's ratios. These were deduced from [3].

The analysis of the structure system (linear static) was performed. The FE model was analysed for an applied tensile load of 22 kN in direction Z. The stress and strain distributions of each material (core/cladding, resin-rich region, composite host) obtained from the analysis are shown in Figs. 3–5. Table 9 shows the comparison between experimental and finite element results using maximum displacement comparisons.

The difference shown in Table 9 seems significant, but the obvious non-linear and interfacial damage phenomena described in the next section, could account for at least, part of this disparity. The plotted strains in each of the plots in Fig. 5 are at the maximum load of 22 kN.

5. Analytical modelling

In this section, the exposition of an embedded fibre-optic-induced damage is provided using continuum mechanics and energy balance principles.

Assuming orthotropic material properties and plane stress conditions, the stiffness matrix generalised by Hooke's law relation is modified to allow for the fibre-optic inserts as follows:

$$\begin{bmatrix} Q_{11} & Q_{12} & 0 \\ Q_{11} & Q_{22} & 0 \\ 0 & 0 & Q_{66} \end{bmatrix}_{\text{Damaged}} = \begin{bmatrix} Q_{11} & Q_{12} & 0 \\ Q_{11} & Q_{22} & 0 \\ 0 & 0 & Q_{66} \end{bmatrix}_{\text{Without Fibre-Optic Inserts}} - \begin{bmatrix} \Theta_{11} & \Theta_{12} & 0 \\ \Theta_{11} & \Theta_{22} & 0 \\ 0 & 0 & \Theta_{66} \end{bmatrix}, \quad (1)$$

Table 8
Material properties used in the FEA analysis

Material	E_x (GPa)	E_y (GPa)	E_z (GPa)	v_{xy}	v_{xz}	v_{yz}
Carbon-epoxy	10.2	10.2	102	0.3	0.03	0.03
Fiber optic core	72.5	72.5	72.5	0.17	0.17	0.17
Fiber optic cladding	72.5	72	72.5	0.17	0.17	0.17
Resin-rich region	102	102	102	0.17	0.17	0.17

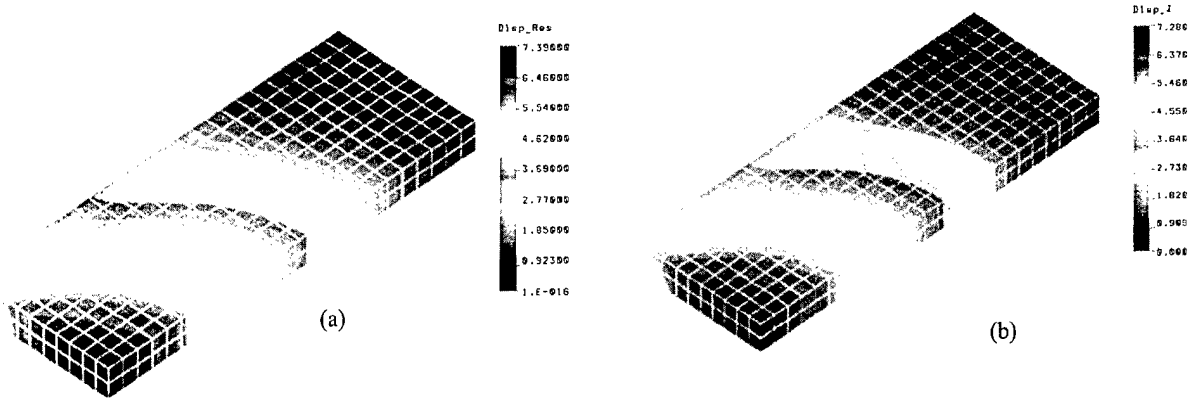

Fig. 5. (a) and (b) Resultant displacement and that in the Z-direction ($\Delta\ell_z$).

Table 9
Comparison of the experimental and FEA results

	Displacement $\Delta\ell_{z\max}$ (mm)
Experimental	0.64
FEA	0.283

where Θ is a stiffness loss parameter similar to that described by Zhang and Soutis [6] as an in situ damage effective function (IDEF).

If the tested samples in this study are schematically represented as shown in Fig. 6, then the following analytical considerations can be introduced.

The general stress–strain relationship is

$$\sigma_{ij} = 2\mu e_{ij} + \lambda\delta_{ij}e_{kk}, \tag{2}$$

where μ and λ are Lame's constants and are defined below. σ is the induced stress and e is the strain. δ_{ij} is the Kroneker delta as defined by Segal [4]

$$\mu = \frac{E}{2(1+v)} \quad \text{and} \quad \lambda = \frac{Ev}{(1+v)(1-2v)}, \tag{3}$$

where E and v are the Young's modulus and Poisson's ratio, respectively.

5.1. Strain energy decomposition

The total volume of the composite under consideration is V and that for an individual resin-rich eyelet plus an optical fibre is Γ. If the outstanding 'unaffected' composite volume is Ω, the general strain energy decomposition equation for the case shown in Fig. 6 is

$$\int_V \left(\int_0^{e_{ij}} \sigma de_{ij}\right) dV = \int_\Omega \left(\int_0^{e_{ij}} \sigma de_{ij}\right) d\Omega + \sum_1^n \int_\Gamma \left(\int_0^{e_{ij}} \sigma de_{ij}\right) d\Gamma, \tag{4}$$

where n is the number of resin-rich eyelets.

Eq. (4) assumes perfect bonding between the optical fibre and the polymer matrix composite. At this stage of the analysis, no disbonds or material imperfections are assumed to be present.

When Eq. (2) is substituted into the LHS of Eq. (4) and after integrating, the overall strain energy, U, is

$$U = \int_V \left(\mu e_{ij}e_{ij} + \frac{\lambda}{2}e_{kk}^2\right) dV. \tag{5}$$

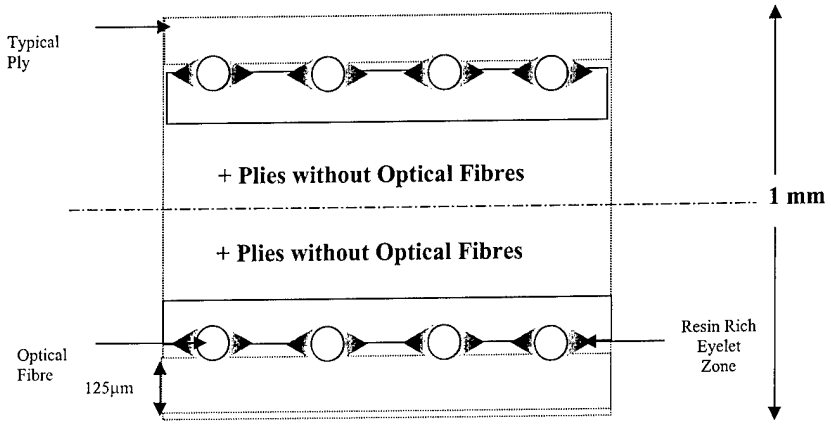

Fig. 6. A cross-sectional schematic of the composite panel tested in this study (not to scale).

Introducing the damage entity tensor, d_{ij}, described by Talreja [5],

$$d_{ij} = \int_s a_i n_i \, \mathrm{d}S, \tag{6}$$

where a and n are 'activity' and normal vectors acting on the surface S. The damage mode tensor is thus defined as

$$D_{ij} = \frac{1}{V} \sum_{k=1}^{m} \left[(d_{ij})_k \right], \tag{7}$$

where m is the number of identifiable damage zones.

From the markedly diminished failure load for the densely packed optical fibre placements shown in Table 6, it appears a transformation of entities takes place when deformation occurs as proposed in Eq. (8). Here, the strain energy component of the resin-rich eyelet as described in Eq. (4) gets transformed to either the stiffness reduction entity described in Eq. (1) and/or the damage mode entity tensor described in Eq. (7).

$$\sum_{1}^{n} \int_{\Gamma} \left(\int_{0}^{e_{ij}} \sigma_{ij} de_{ij} \right) \mathrm{d}\Gamma \Rightarrow \begin{cases} D_{ij} = \frac{1}{V} \sum_{k=1}^{m} \left[(d_{ij})_k \right] \\ \begin{bmatrix} \Theta_{11} & \Theta_{12} & 0 \\ \Theta_{11} & \Theta_{22} & 0 \\ 0 & 0 & \Theta_{66} \end{bmatrix}. \end{cases} \tag{8}$$

It is this transformation in Eq. (8) that is thought to be responsible for the degradation in mechanical properties as shown in Table 6. Here, the density is dramatically increased compared to the samples in Table 5 and the spatial location is moved from the centre to near the surface.

6. Conclusion

This study provides a unique look at the structural integrity analysis of composite structures with embedded OF. This analysis calls for caution in the use of OF in composite structures, where the accepted tenet is that 'embedding OF is perfectly safe in composite structures when deployed under general guidelines'.

A FE and analytical model was developed to study and predict the behaviour of the stress/strain fields of the material system under consideration here. The results of this analysis show that strain is successfully transferred from the carbon-epoxy host to the core/cladding of the optical fibre through the primary resin-rich region, which acts as interface. The results obtained from the FE analysis plotted in Figs. 3–5 are compared with those obtained from the experimental results. The comparison serves to verify the validity of the FE model and if the analytical parameters defined in Eqs. (1), (7) and (8) can be decomposed further to measurable entities, a truly circuitous validation exercise can be realised using analytical, experimental and computational tools.

References

[1] Culshaw B, Gardiner PT. Smart structures – the relevance of optical fibres. Fiber and Integrated Optics 1993;2:353–73.
[2] Hadzic R. Optical fibre embeddability in composite structures, Draft M.S. thesis, RMIT University, Melbourne, Australia, 1999.
[3] Matthews FL, Rawlings RD. Composite materials: engineering and science. London: Chapman & Hall; 1995.
[4] Segal LA. Mathematics applied to continuum mechanics. General Publishing Company, 1987.
[5] Talreja R. Damage mechanics of composite materials based on thermodynamics with internal variables. In: Cardon AH, Verchery G, editors. Durability of polymer-based composite systems for structural applications. London: Elsevier, 1991. p. 65–79.
[6] Zhang J, Fan J, Soutis C. Analysis of multiple matrix cracking in $[\pm\theta_m/90_n]_s$ composite laminates. Composites 1992;23(5):291–8.

ELSEVIER

Composite Structures 47 (1999) 767–779

COMPOSITE STRUCTURES

www.elsevier.com/locate/compstruct

The shear properties of woven carbon fabric

M. Nguyen [a,*], I. Herszberg [a], R. Paton [b]

[a] *The Sir Lawrence Wackett Centre for Aerospace Design and Technology, RMIT University, G.P.O. Box 2476V, Melbourne, Vic. 3001, Australia*
[b] *Cooperative Research Centre for Advance Composite Structures Ltd. (CRC-ACS), 506 Lorimer Street, Fishermens Bend, Vic. 3207, Australia*

Abstract

This paper presents experimental and theoretical studies of the shearing properties of carbon plain weave fabrics and prepregs. The shearing characteristics of these materials are determined by the use of a picture frame shear rig which is loaded by a mechanical test machine. The shear force/angle curves are presented for the experiments conducted with the various test materials. A proposed shear model based on previous research which idealizes the fabric yarns as beam elements is presented. Using fabric geometric and material parameters, the model predicts the initial slip region of the fabric, as well as the more dominant elastic deformation range. Comparisons of the experimental and theoretical results were conducted to validate the model. A discussion of the findings from the analysis is also given, with particular focus relating to the accuracy, limitations and advantages offered by such a model. Results indicated that the slip model gives modestly accurate predictions, whilst the elastic modulus model showed very good correlation with experimental data. © 2000 Published by Elsevier Science Ltd. All rights reserved.

Keywords: Shearing; Fabric model; Slip; Elastic modulus

Nomenclature

λ	eigen value solution
α, β, ϕ	eigen value fabric parameter functions
γ	shear angle
δ	maximum yarn deflection height
μ	coefficient of friction
A, B, C, D	model coefficients
a, b, c	positions along yarn deflection model
a_s	slip distance acting along contact length
d_c	effective yarn contact length
E	elastic tensile modulus
F	shear force along shear bar linkage
F_c	reaction force at position c
f	elemental shear force in an arbitrary direction
f_1, f_2	elemental shear force in 1, 2 direction
h	yarn crimp height
I	yarn cross-sectional area moment of inertia
k	spring constant
L	total specimen fabric length
M, N, O, P	coefficients of shear model solution
m	internal moments
P_1, P_2	pitch spacing in 1, 2 direction
R	resultant shear frame force
s_1, s_2	tow spacing in 1, 2 direction
t	tensile force
t_1, t_2	elemental tension force in 1, 2 direction
V	yarn normal force
v_{ab}	yarn deflection along length ab
v_{bc}	Yarn deflection along length bc
w_1, w_2	tow widths in 1, 2 direction
X, Y	coordinate axes
X_1, X_2	arbitrary lengths along the X-direction
$x_1, x_2, \ldots, x_8$	fabric architectural parameters

1. Introduction

The forming behaviour of fabric preforms is of important consideration for the manufacture of composite components. The ability of the fabric material to

* Corresponding author.
E-mail address: minh@boomerang.aero.rmit.edu.au (M. Nguyen).

0263-8223/99/$ - see front matter © 2000 Published by Elsevier Science Ltd. All rights reserved.
PII: S0263-8223(00)00051-9

conform to various shapes is highly dependent on the fabric architecture, which in turn will influence the resultant mechanical properties of the composite part. During preform forming, two major deformation mechanisms are considered to be important; these being simple shear and shear-slip (refer to Fig. 1). Of these mechanisms in relation to woven fabrics, simple shear has been indicated to be the more dominant behaviour [1].

In undergoing fabric shearing, it was initially suggested by Mack and Taylor [2] that the reinforcement behaves as a pin-jointed mesh, whereby the tows rotate or trellis about the fabric cross-overs. By further assuming that the yarns are inextensible and incompressible, Potter [3], Robertson [4], Van West [5] and Long [6], employed it to map the fabric draping behaviour over shapes of varying profiles. The outcome of these research efforts was to reinforce the concept that the ability of fabrics to shear is a particularly important forming characteristic. This characteristic enables the manufacture of 2-dimensional preforms into complex 3-dimensional shapes. Further work by McBride [7] showed that during fabric shearing, the spatial positioning of the fabric architecture will vary, such that local increases in the fibre volume fraction will occur.

Investigation conducted by Tam and Gutowski [8] with fibre-aligned materials identified in-plane and inter-ply shear as important parameters influencing the forming behaviour of aligned fibre-reinforced composites. Results showed that when the material experiences high angles of shearing, wrinkling of the fabric occurred. Woven fabrics differ from aligned fibre materials, as trellising or rotation of the yarn is the dominant deformation mechanism. Also the effect of inter-ply shear becomes an influential deformation mechanism, when stacks of fabric plies are required to undergo forming simultaneously [9]. However, when high angles of material shear are induced into woven fabrics, they too exhibit similar behaviour to aligned fibre materials; whereby wrinkling occurs due to a build-up of in-plane compressive forces.

The characterization of the fabric shear properties has predominantly consisted of testing the materials within a shear rig fixture which resembles a picture frame [10,11]. Results using a variety of glass and carbon fabrics have indicated that the shearing behaviour can be divided into two distinct regions. Before fabric lock-up, whereby low shearing loads are required; and after lock-up, which is characterized by a sudden increase in the load generally accompanied with material wrinkling. Fabric lock-up is described as when high angles of yarn rotation occur such that the fabric architecture becomes 'jammed', and this jamming effect results in a rapid increase in the shearing force. Further results from these tests have indicated that regardless of the weave type, the fabrics all exhibited similar trends in shear deformation.

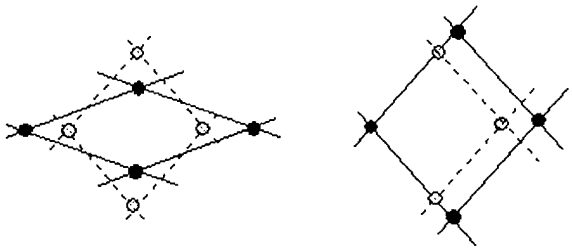

Fig. 1. Major mechanisms for fabric deformation.

By considering a plain woven unit cell and assuming that yarn rotation about the region of overlap behaves as a pin-jointed mesh. Prodromou and Chen [12] provided a geometric model to predict the occurrence of fabric lock-up. Recent work by Wang [13], highlighted that this fabric lock-up angle is highly dependent on the type of shear testing method employed. By characterizing the fabric shear behaviour of a material with the bias-extension and simple shear rail test, results showed that there were noticeable differences between the fabric locking angles obtained.

Early attempts to model the plain-weave fabric architecture typically assumed the yarn cross-section was circular and various inferences were made about the amount of yarn crimp [14,15]. Presently it is evident that the yarns can be more aptly described as elliptical, and that variations in the elliptical cross-sectional profile exist along the length of the yarn [16]. Though the understanding of the fabric architecture has progressed, there exists a critical need to provide models which accurately describe the shear properties of fabric preforms. Research into modelling the shear properties is scarce and there currently only exist a handful of methods. Initial attempts by Grosberg and Park [17] idealized the yarns as beam structural elements, allowing the ability to predict both the initial and elastic shear modulus of the fabric. Two disadvantages are considered to be associated with this model. Firstly the presentation of the theoretical solution is in a form not particularly suitable for practical use, and secondly, the model does not consider undulation of the yarns.

Modelling by Katabawa et al. [18–20] did incorporate yarn undulation, but assumed a linear function of the torsional moments required to induce fabric shearing. The various coefficients used to characterize this linear function, could not be defined theoretically and hence were experimentally solved. Elaboration of this model by Ye [21], enabled the contact force at the yarn cross-overs to be determined, though both the models by Grosberg and Park, and Katabawa et al. showed quite good correlation with experimental results. Validation consisted of comparisons with cloth, polyester and wool

fabrics, which are not suitable reinforcement materials for advanced composites.

More recent developments by Sinoimeri and Dréan [22] used energy methods to study the fabric shear properties. The introduction of a rheological model allowed tow slippage to be accounted. Unfortunately this model suffers from the use of arbitrarily coefficients to predict the fabric shearing behaviour, and that there is limited reference to the fabric architectural parameters within the model itself.

In this paper, a formulation for the shear properties of plain woven fabrics is presented. Theoretical solutions are generated from the model and are compared with experimental results obtained from a shear rig test fixture. A discussion on the findings is given, with particular focus on the accuracy, limitations and benefits offered by such a model.

2. Experimental

2.1. The picture frame experiment

Experimental investigation of the shearing behaviour of dry and prepreg fabrics was carried out using a picture-frame apparatus. The aim of this experiment is to determine the relationship between shearing angle and load for different weave architectures (i.e., variable pattern and fabric parameters). An illustration of the shear frame apparatus which is essentially a square four-bar linkage is shown in Fig. 2. A removable brace was designed to allow transport and loading of the apparatus so as to minimize fabric shearing prior to testing.

Experiments were carried out at ambient temperature, with force and displacement history recorded into a personal computer. This type of testing apparatus has been used successfully to characterize the shear properties of dry fabrics [10,12] and composite laminates [11].

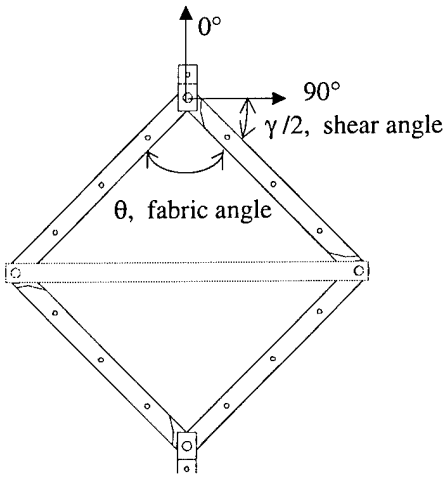

Fig. 2. Schematic of the picture frame, with removable brace attached.

A variety of carbon fabrics were tested, with their properties summarized in Table 1. For each material, a minimum of five tests were conducted. The test materials also consisted of two carbon plain weave prepregs. These prepregs were comprised from T300 and T650 yarns and impregnated with Hexcel F593 and Hexcel F584 modified epoxy resin, respectively.

An important characteristic of fabric deformation is when the material experiences high shearing angles (γ), resulting in the fabric architecture becoming 'jammed'. This jamming is also commonly referred to as fabric locking, the effect of which increases the forces required to deform the fabric and also leads to wrinkling. During this experimental investigation, locking of the fabric is defined when wrinkling of the material within the picture frame was observed to occur.

2.2. Procedure

The fabric test size is 240 mm × 240 mm, minus a 25 mm radius quadrant cut from each corner. This quadrant is required so that rotation of the hinges can occur freely. The test material is then placed into the fixture via a clamping arrangement located along each bar linkage. Care is taken to ensure that the weft and warp tows are positioned parallel to the frame. The shear frame is loaded into an INSTRON 45 kN screw driven testing machine and the brace then removed.

To minimize the viscosity behaviour of the prepregs, testing was carried out at a rate of 5 mm min^{-1}. Picture frame testing for a range of dry and impregnated fabrics has typically used shear rates of 10 mm min^{-1}. However, a reduced loading rate of one half this speed is not expected to significantly alter the material shearing characteristics. This speculation is supported with work from Wang [23], who showed that minimal variation of the shear modulus was observed for test speeds ranging from 1 to 10 mm min^{-1}.

2.3. Test results

Fig. 3 shows the shear frame picture rig deforming at 0°, 15°, 30° and 47° of shear, and the corresponding position of the rig deformation on the shear force/angle curve. White lines drawn 50 mm in from the edge of the bar linkages, show that there is a uniform state of shearing occurring within this highlighted region. The shear force/angle relationships for the fabrics listed in Table 1 are plotted in Fig. 4. A number of observations are obtained from these results.

- PW (1K) fabric exhibited a steeper shear curve compared to the PW (3K) material. This is thought to occur because of the PW (1K) having a combination of a small tow size and compact weave structure. The result is to increase the frictional resistance acting at the fabric cross-overs. Similar results have been noticed

Table 1
Specifications of fabrics used in experimentation

Fabric type (code)	Construction (tows cm^{-1})	Areal weight ($g\ m^2$)	Nominal thickness (mm)	Measured locking angle (γ, deg)	Calculated locking angle (γ, deg)
PW (1K)	6.4 × 6.5	90	0.20	46	40
PW (3K)	4.6 × 4.5	198	0.24	50	44
2/2 twill (3K)	5.2 × 5.3	220	0.32	72	–
2/2 twill (6K)	4.3 × 4.4	375	0.43	64	–
PW-prepreg (T300)	4.7 × 4.8	280	0.30	38	31
PW-prepreg (T650)	4.8 × 4.9	270	0.28	34	22

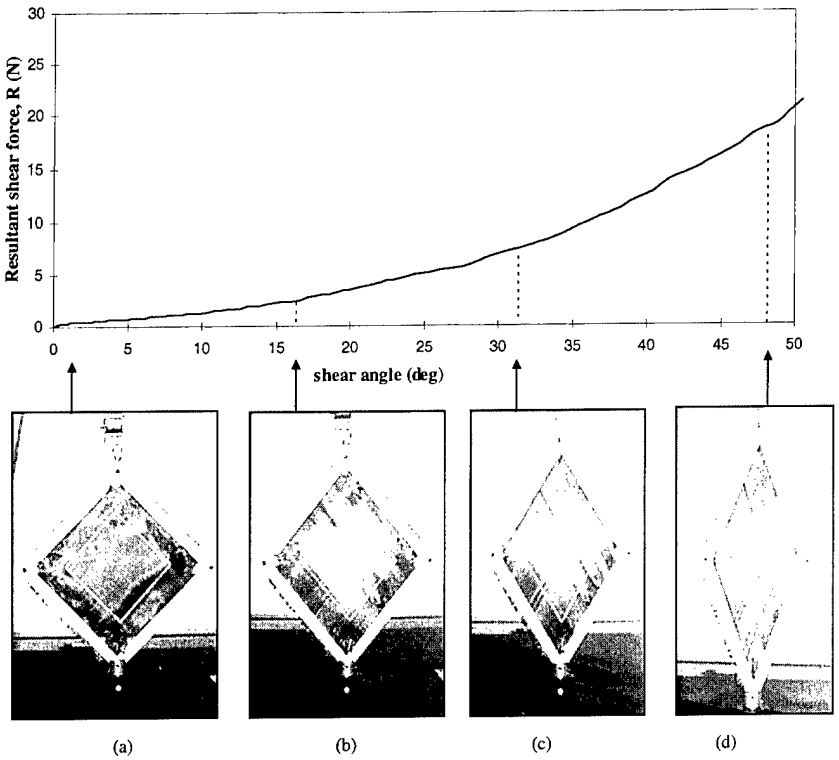

Fig. 3. Different stages of fabric shear deformation, tested at a nominal rate of 5 mm/min, corresponding to various positions of a PW (3K) shear deformation history at (a) 0°, (b) 15°, (c) 30°, (d) 47°.

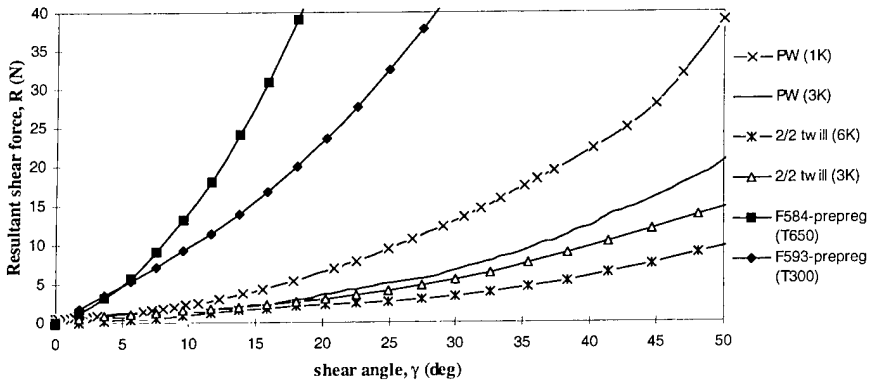

Fig. 4. Fabric and prepreg shear force/angle relationships for the material types listed in Table 1.

and various discussions relating to these observations have been given [12,24].

- Impregnation of fabric with resin as in the case of prepregs has the effect of increasing the material's shear modulus compared to dry fabrics. Results further indicate that the PW-prepreg (T650) has a much higher shear modulus compared to that of the PW-prepreg (T300). This variation between the shearing properties is considered to be due to the difference in the resin properties.
- Despite the weave type, both dry fabrics and the prepregs exhibit similar shear deformation behaviour, which can be described as parabolic in nature.
- As twill weave fabrics require low deformation loads, these materials experience fabric lock-up at much higher angles of shear. Consequently they are considered to be more 'conformable' than plain weaves, because of their ability to be contoured to complex shapes before the occurrence of wrinkling.

3. The shear models

Grosberg et al. [25] demonstrated that the trends for fabric shearing typically consist of three stages; the initial region, where shear is due to the flexural deformation of the tows; the mid-region, where shear resistance becomes dominated by a bearing load type contact; and the last region, where there is a rapid load increase due to 'jamming' of the fabric structure. As the fabric undergoes these deformation phases, the material architecture must change so that the different phases can be accommodated. Henceforth, it is necessary to both understand and describe the fabric architecture if a model is to be developed.

3.1. Definition of fabric architecture

To model the shearing property of the plain weave fabrics, an idealized repeating, geometrically symmetrical cell section is depicted in Fig. 5. Though there are different ways to how the cell can be represented [16], modelling of fabric shear properties has generally consisted of the following pattern.

In determining the fabric deformation characteristics using this unit cell structure, undulation of the yarns is not considered. The implications of this assumption on the accuracy of the theoretical results are discussed further in Section 5. By specifying a set of geometric parameters as shown in Fig. 5 with the material elastic properties, mathematical expressions for the initial slip and elastic modulus regions can be derived.

Fig. 6(a) shows a representation of the square shear rig deforming from a state of $\gamma = 0$, through to a shear angle of γ. As the fabric material is sheared, the forces acting on the bar linkages can be discretized into shear and tensile

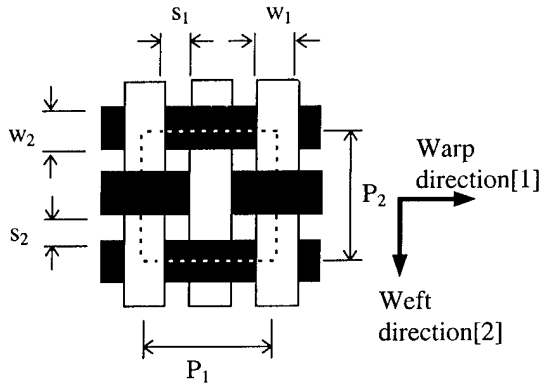

Fig. 5. Illustration showing the full repeating and geometrically symmetrical unit cell of the plain weave fabric structure.

force components acting perpendicular and parallel to the fabric tow. This is shown Fig. 6(b). At low angles of shearing ($0° \rightarrow 2°$), if the theory of small angle approximations is utilized [26], then the acting tensile force component will have negligible magnitude and hence can be ignored. Consequently for this deformation range, which is referred to as the initial slip region, the fabric material is considered to be in a state of pure shear (Fig. 6(c)).

3.2. The initial slip region

This region of deformation has been extensively dealt with by Grosberg and Park [17], and in obtaining the solution a number of key assumptions were presented, which are as follows:

1. As the initial region of slip exists for only small angles of shear, the model can be idealized to be in a state of pure shear, as shown in Fig. 6(c) where the elemental shear forces can be described as

$$f_1 = F\,P_1/L, \quad f_2 = F\,P_2/L.$$

2. The yarn contact lengths (d_c) acting at the cross-overs, are the same lengths in both directions.
3. Yarns are inextensible during the shearing process.
4. Deformation of the yarns is considered to be only due to bending.

It was necessary to understand the process of how this initial slip model was determined, as these principles provided the fundamentals in the development and improvement of the more important and dominant elastic modulus model. During reformulation of the solution presented by Grosberg and Park, two major modifications were incorporated, which were the re-definition of the normal force (V) and revision of the solution itself.

3.2.1. The normal force (V)

In woven fabrics, the undulation of the yarns will exert pressure at the cross-overs, which in turn induces frictional resistance to shearing. The definition of this normal force was initially provided by experimental and theoretical work by Pierce [14]. By considering the

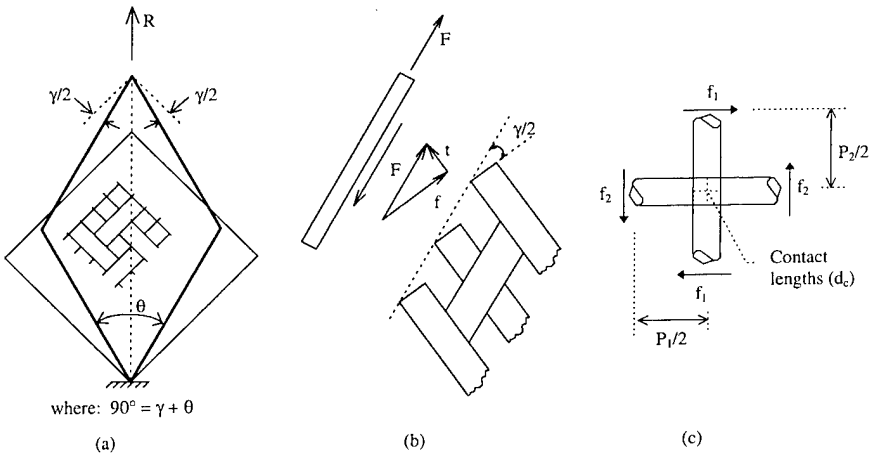

Fig. 6. (a) Fabric shearing under applied load (R). (b) As the applied load increases, the shearing forces acting along the bar linkages (F) can be resolved into components of tension (t) and shear (f) acting parallel and perpendicular to the tows. (c) For the unique case of the initial slip region as the shear angles are assumed to be small, the fabric can be idealised to be in a state of pure shear.

problem from a structural point of view, Katabawa et al. [20] idealized the yarns as beam elements. These beams whose ends are attached to fixed wall supports, enable the prediction of the normal contact force of the yarn using material and geometric parameters from the fabric architecture.

However, if the beams are rigidly attached to the wall and then deflection at the centre occurs by application of a normally applied load, this condition would invalidate a key assumption whereby the yarns are inextensible. To overcome this inconsistency, the yarn undulation behaviour is suggested to be more accurately modeled as a beam, having a pin and roller support, as shown in Fig. 7. Hence the normal force can be approximated as

$$V = \frac{48\,E\,I\,h}{P_{1,2}^3}, \tag{1}$$

where P_1 or P_2 refer to the pitch length in the warp or weft directions, respectively.

3.2.2. Revised solution

Using the problem statement, boundary conditions and theory as described by Grosberg and Park, a reformulation of the solution was performed. Comparisons of Grosberg and Park's and the revised solutions indicate that though both are dimensionally correct, there exists a small discrepancy which has a considerable influence on the overall results, this difference being the presence of cubic power terms present in the solution provided by Grosberg and Park, compared to square power terms in the revised equation. The extent and impact of these differences in describing the shearing properties of woven fabrics will be investigated and discussed in a future article.

The revised fabric shearing solution, incorporating the normal force function as described in Eq. (1) for the initial slippage region is as follows:

$$\gamma = \frac{F}{8\,E\,I\,L}\left[P_2\left[L - d_c\left(1 - \frac{a_s}{d_c}\right)\right]^2 + P_1\left[L - d_c\left(1 - \frac{a_s}{d_c}\right)\right]^2\right] \tag{2}$$

$$\gamma : 0 \rightarrow \frac{a_s}{d_c} = 1,$$

$$F = \frac{\mu\frac{V\,d_c}{24}\left(\frac{a_s}{d_c}\right)^2\left(3 - 2\frac{a_s}{d_c}\right)}{\frac{1}{4L}\left[P_2\left[L - d_c\left(1 - \frac{a_s}{d_c}\right)\right] + P_1\left[L - d_c\left(1 - \frac{a_s}{d_c}\right)\right]\right]} \tag{3}$$

$$\gamma : 0 \rightarrow \frac{a_s}{d_c} = 1.$$

d_c is determined from methods as described from Grosberg and Park [17].

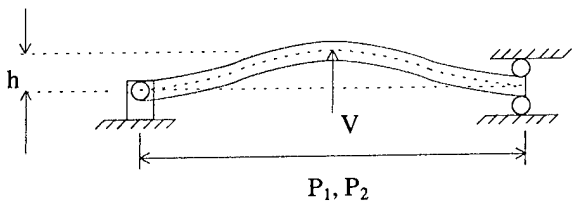

Fig. 7. Idealised bending of a fibre yarn.

3.3. The elastic modulus region

Grosberg et al. [25] elaborated on the shear modelling work by Grosberg and Park [17] by next considering the elastic shear modulus region. Unfortunately the solution provided is not presented in a manner which makes comprehension easy, particularly if it is desirable to understand how fabric parameters influence the material shear characteristics. The complexity of the equations is further exacerbated by the use of Fourier series to

express the deflected yarn modal shape. To overcome these drawbacks, a model is proposed which uses the same assumptions, boundary conditions and problem statement as initially set up by Grosberg et al., but varies by its approach in determining and defining the solution for the elastic shear modulus of plain woven fabrics.

3.3.1. Analysis

The analysis still maintains the geometrically symmetrical unit cell, however for this region, the mechanism in which fabric shearing occurs is different. As high angles of yarn rotation occur, the contact area between adjacent yarns near the fabric cross-overs will increase. This contact resistance to fabric shearing is now assumed to be more dominant than the frictional restraints acting about the yarn cross-overs. The idealization of this contact resistance to fabric shearing, takes the form of a spring bearing load mechanism. It is further assumed that this mechanism acts through a point located at the end of the cross-over contact length, d_c. This concept is illustrated in Fig. 8.

Tow rotation for this model deformation state is able to occur via a pin-joint acting about the tow cross-overs. Grosberg et al. argued that this is plausible as there is now constant frictional resistance about the tow overlap region after complete slippage has taken place. Furthermore, as the majority of the resistance to fabric shearing will be dominated by the spring contact force, the contribution of friction in resisting shear is expected to be small to minimal. As the fabric continues to be sheared, the shear forces acting on the bar linkages can be separated into tension and shear components acting parallel and perpendicular to the tows, respectively (Fig. 6(b)). By considering that these force components act on one-half of a yarn (as the unit cell is symmetrical), the problem can be described by a free body diaphragm as seen in Fig. 8(b) and Fig. 9.

3.3.2. Model expression

The amount of vertical yarn-deflection along the length X_1 and X_2 can be described as

$$v_{ab} = A\cos(\lambda X_1) + B\sin(\lambda X_1) - f_2/t_1\, X1 + \delta$$

$$X_1 : 0 \rightarrow (P_1 - d_c)/2, \tag{4}$$

$$v_{bc} = C\cos(\lambda X_2) + D\sin(\lambda X_2) + \left[\frac{f_2}{t_1}\left(\frac{P_1}{d_c} - 1\right) + \frac{2\delta}{d_c}\right]X_2$$

$$X_2 : 0 \rightarrow d_c/2, \tag{5}$$

where $\lambda = \sqrt{\frac{t_1}{E\,I}}$, and the elemental shear and tension forces acting on a single tow are described as

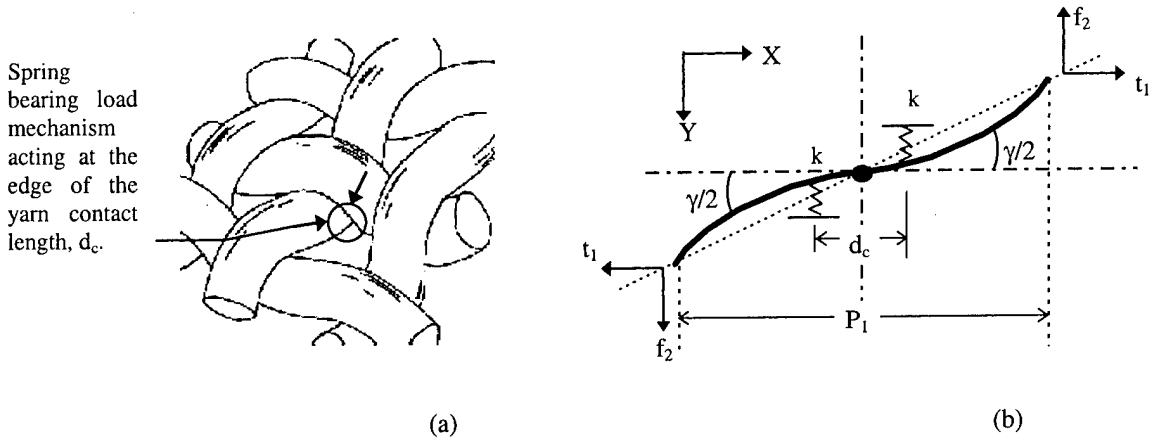

Fig. 8. (a) Point bearing loads acting at the edge of the cross-over contact length on a unit cell. (b) Representation in the form of a beam deflection diagram, showing a single yarn in a state of shear and tension with support springs.

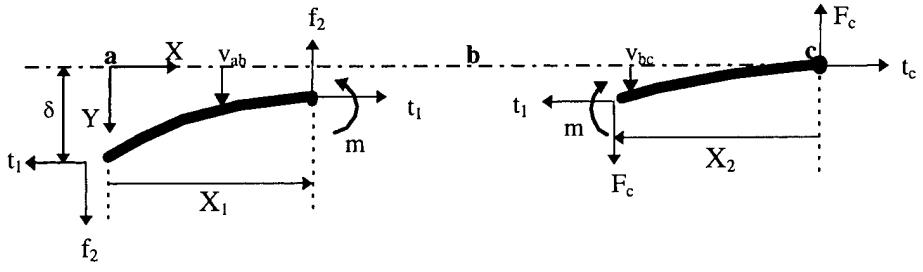

Fig. 9. Free body diagram of yarn deflection under tension and shear.

$$f_2 = \frac{F\ P_2}{L}\sin(\gamma/2), \qquad t_1 = \frac{F\ P_2}{L}\cos(\gamma/2). \tag{6}$$

3.3.3. Boundary conditions

A, B, C, D in Eqs. (4) and (5) are coefficients obtained from the boundary conditions. These boundary conditions are

1. at
$X_2 = 0, \quad v_{bc} = 0,$
2. at
$X_2 = d_c/2, \quad v_{bc} = \frac{2t_1\ \delta}{k\ d_c} - \frac{f_1\ P_1}{k\ d_c},$
3. at
$X_1 = (P_1 - d_c)/2, \quad v_{ab} = \frac{2t_1\ \delta}{k\ d_c} - \frac{f_1\ P_1}{k\ d_c},$
4.
$$\frac{-\partial\ v_{ab}}{\partial X_1}\left(\frac{1}{2}(P_1 - d_c)\right) = \frac{\partial\ v_{bc}}{\partial X_2}\left(\frac{d_c}{2}\right).$$

The maximum tow deflection (δ) will occur when $X_1 = 0$. This will result in Eq (4) being

$$\delta = A + \delta \quad \therefore A = 0. \tag{7}$$

If the boundary conditions are used to obtain the coefficient A, then results will show that the solution of A is non-zero. However the expression of A is also a function of δ and hence for Eq. (7) to be satisfied, δ must equal the expression given in Eq. (8).

$$\delta = \frac{\lambda\left[\frac{-f_2\ P_1}{k\ d_c} + \frac{f_2\ d_c}{2t_1}\left(\frac{P_1}{d_c} - 1\right)\right]\cot\frac{\lambda\ d_c}{2} + \lambda\left[\frac{-f_2\ P_1}{k\ d_c} + \frac{f_2}{2t}(P_1 - d_c)\right]\cot\frac{\lambda\ (P_1 - d_c)}{2} + \left[-\frac{f_2}{t_1}\left(\frac{P_1}{d_c} - 2\right)\right]}{\lambda\left(1 - \frac{2t_1}{k\ d_c}\right)\left(\cot\frac{\lambda\ d_c}{2} + \cot\frac{\lambda\ (P_1 - d_c)}{2}\right) - \frac{2}{d_c}}. \tag{8}$$

3.3.4. Solution

The maximum yarn shear angle as a result of shearing and tensile deformation along the warp direction can be approximated as

$$\frac{\gamma}{F} = \frac{2\ P_2}{L\ P_1}\sin\frac{\gamma}{2}\left\{\frac{\lambda\left[\frac{-P_1}{k\ d_c} + \frac{d_c}{2t_1}\left(\frac{P_1}{d_c} - 1\right)\right]\cot\frac{\lambda\ d_c}{2} + \lambda\left[\frac{-P_1}{k\ d_c} + \frac{1}{2t_1}(P_1 - d_c)\right]\cot\frac{\lambda\ (P_1 - d_c)}{2} + \left[-\frac{1}{t_1}\left(\frac{P_1}{d_c} - 2\right)\right]}{\lambda\left(1 - \frac{2t_1}{k\ dc}\right)\left(\cot\frac{\lambda\ d_c}{2} + \cot\frac{\lambda\ (P_1 - d_c)}{2}\right) - \frac{2}{dc}}\right\}$$
$$+ \frac{2\ P_1}{L\ P_2}\sin\frac{\gamma}{2}\left\{\frac{\lambda\left[\frac{-P_2}{k\ d_c} + \frac{dc}{2t_2}\left(\frac{P_2}{d_c} - 1\right)\right]\cot\frac{\lambda\ d_c}{2} + \lambda\left[\frac{-P_2}{k\ dc} + \frac{1}{2t_2}(P_2 - d_c)\right]\cot\frac{\lambda\ (P_2 - d_c)}{2} + \left[-\frac{1}{t_2}\left(\frac{P_2}{d_c} - 2\right)\right]}{\lambda\left(1 - \frac{2t}{k_1\ d_c}\right)\left(\cot\frac{\lambda\ d_c}{2} + \cot\frac{\lambda\ (P_2 - d_c)}{2}\right) - \frac{2}{d_c}}\right\}, \tag{9}$$

$$\gamma/2_{warp} = \frac{\delta}{P_1/2}. \tag{10}$$

As the unit cell is symmetrical, the tow shear angle in the weft direction can also be approximated as

$$\gamma/2_{weft} = \frac{\delta}{P_2/2}. \tag{11}$$

Hence the total shear angle of the warp and weft yarns is described as

$$\gamma = \gamma/2_{warp} + \gamma/2_{weft}. \tag{12}$$

Results for the expression of the total shear force (F) along a bar linkage as a function of the shear angle (γ) are given in Eq. (9). To simplify this solution, it is allowed that $P_1 = P_2$ due to yarn symmetry and that the co-tangent trigonomic function is re-expressed using polynomial approximation terms. The final solution for the shear force as a function of two unknown variables, shear angle (γ) and the spring constant (k) is given in the form of a cubic equation

$$M(k,\gamma)\ F^3 + N(k,\gamma)^2\ F + O(k,\gamma)\ F + P(k,\gamma) = 0, \qquad \gamma : 0 \to 90° - \arcsin(2\ W/P) \tag{13}$$

where the coefficients of the solution M, N, O, P are in terms of the fabric material and geometric parameters. Note that the solution is theoretically valid up to the state when fabric locking occurs.

$$M = \frac{15x_2}{2\alpha^5} + \frac{15x_2}{2\beta^5} - \frac{15x_5}{2\beta^5} - \frac{15x_7}{2\alpha^5},$$
$$N = -\frac{15x_1}{2\alpha^5} - \frac{15x_2}{2\beta^5} + \frac{3x_2}{\alpha^3} + \frac{3x_2}{\beta^3} + \frac{15x_4}{2\beta^5} - \frac{3x_5}{\beta^3} + \frac{15x_6}{2\alpha^5} - \frac{3x_7}{\alpha^3},$$
$$O = -\frac{3x_1}{\alpha^3} - \frac{3x_2}{\beta^3} + \frac{x_2}{\alpha} + \frac{x_2}{\beta} - x_3 + \frac{3x_4}{\beta^3} - \frac{x_5}{\beta} + \frac{3x_6}{\alpha^3} - \frac{x_7}{\alpha} + x_8,$$
$$P = -\frac{x_1}{\alpha} - \frac{x_1}{\beta} + \frac{x_4}{\beta} + \frac{x_6}{\alpha}$$

where

$$x_1 = -\gamma\ \tan(\gamma)\frac{P_2\ \phi}{L\ k\ d_c}, \quad x_5 = \frac{2(P_1 - d_c)\ \phi}{P_1\sin(\gamma)},$$
$$x_2 = \frac{\gamma\ \phi}{\cos(\gamma)}, \quad x_6 = -\frac{4P_2\ \phi}{L\ k\ d_c},$$

$$x_3 = \frac{2\gamma}{d_c \cos(\gamma)}, \quad x_7 = \frac{2d_c}{P_1 \sin(\gamma)}\left(\frac{P_1}{d_c} - 1\right)\phi,$$

$$x_4 = -\frac{4P_2.\phi}{L_2\ k\ d_c}, \quad x_8 = \frac{4}{P_1 \sin(\gamma)}\left(\frac{P_1}{d_c} - 2\right)$$

and finally where

$$\alpha = \sqrt{\frac{P_2 \sin(\gamma)}{L\ E\ I}}\left(\frac{d_c}{2}\right),$$

$$\beta = \sqrt{\frac{P_2 \sin(\gamma)}{L\ E\ I}}\left(\frac{P_1 - d_c}{2}\right),$$

$$\phi = \sqrt{\frac{P_2 \sin(\gamma)}{L\ E\ I}}.$$

By defining an appropriate spring constant (k) with the fabric material and geometric properties, the shear force (F) can be determined from Eq. (13) for a given value of the shearing angle (γ).

One drawback of the model from a theoretical aspect is that it is unable to accurately predict shear forces at regions of very low shear. This is because the model assumes that there are always components of shear and tension acting on the fabric tows for the solution to be valid. This does not reflect the physical condition in the unique case of when $\gamma = 0$, when the shear force on the frame will be zero. To cater to this discrepancy between experimental and theoretical solution when $\gamma = 0$, the theoretical solution is slightly modified by using a normalized factor of $F|_{\gamma=0}$. This factor is determined by assigning a spring constant, and evaluating the shear force from Eq. (13) for $\gamma = 0$. The modification of the solution in terms of this normalized factor is now expressed as

$$F_{\text{mod}} = F|_{\gamma:0\to\pi/2} - F|_{\gamma=0}. \tag{14}$$

Henceforth the resultant force required to deform the trellis frame (R) can be determined as

$$R = 2\ F_{\text{mod}} \cos(45 - \gamma/2). \tag{15}$$

4. Modelling results

To investigate the effectiveness of this model, the analysis as discussed in Section 3 was used to model the initial slip region and elastic modulus behaviour, of a range of plain weave dry fabrics and prepregs as detailed in Table 1.

4.1. Material property input

The four plain weave fabric configurations considered and their corresponding geometric and material properties required for the model validation are given in Table 2. Fabric geometric properties were obtained from observations using a stereo microscopic.

Although it is well known that the yarn cross-sectional area varies along the length of the yarn, for simplicity of the analysis, these cross-sectional profiles are generalized by having a constant elliptical shape. This allows the area moment of inertia (I) to be defined based on the yarn geometry. The empirical spring constant values were selected so that the theoretical solution would correlate closely with the experimental trends.

4.2. The initial slip model

Fig. 10(a) and (b) show the corresponding shear force and shear angle relationship for plain weave fabrics of 1K and 3K tow sizes, respectively, for the initial slip region. This region is typically characterized by the initially high rise in the shear modulus followed by levelling of the curve. Results indicate that the model provides modest correlation where initial slippage occurs and the magnitudes of the shear force within this range.

Using linear interpolation, Table 3 shows the average predicted shear modulus in comparison with the experimental values for this fabric deformation zone. These results indicate that there is a 44% and 35% difference between the average experimental and model shear moduli for PW (1K) and PW (3K), respectively. For prepreg fabrics, no calculations for the initial region of fabric slip were performed. It is evident from Fig. 10(c) that prepregs do not exhibit the same initial slip trends as compared to dry fabrics. This difference is attributed to prepregs having the introduction of resin into the fabric architecture. This resin influence on the material shear properties is discussed later in Section 5.

4.3. The elastic modulus model

Using the simplified solution as provided by Eq. (13) and the inputs as given by Table 2, the elastic model trends for the dry fabrics and prepregs are compared with experimental results. These comparisons are shown in Figs. 11 and 12. They show that there is generally good agreement with the experimental trends from zero shear, up to the angle of fabric locking.

For the shearing range of 0° to approximately 30°, the model underestimates the preform shear modulus, with variations from the experimental results ranging from 2% to 14%. The larger errors within the model generally arise in predicting regions of low shear and are considered to be due to the influence of the normalizing factor. As the shear angle increases, the influence of this normalizing factor decays and hence accuracy is improved.

Results also indicate there is a phase where the model goes from underestimating to overestimating the material shear properties. For prepregs, this transitional phase occurs after fabric locking, whereas for fabrics this happens before locking. Why the model behaves like

Table 2
Main parameters required for model validation

Parameter	Units	PW (1K)	PW (3K)	PW-prepreg (T300)	PW-prepreg (T650)
P_1	(mm)	3.15	4.26	4.22	4.20
P_2	(mm)	3.04	4.32	4.30	4.15
W_1	(mm)	1.20	1.51	1.80	1.95
W_1	(mm)	1.16	1.46	1.80	1.90
s_1	(mm)	0.41	0.61	0.41	0.25
s_2	(mm)	0.40	0.70	0.45	0.18
L	(mm)	240	240	240	240
Yarn thickness	(mm)	0.08	0.11	0.15	0.14
E	(GPa)	210	220	220	230
I	(m^4)	3.1×10^{-16}	1.17×10^{-16}	2.9×10^{-16}	2.61×10^{-16}
d_c	(mm)	0.48	0.52	0.47	0.51
k	(N/m)	13500	5000	35000	65000

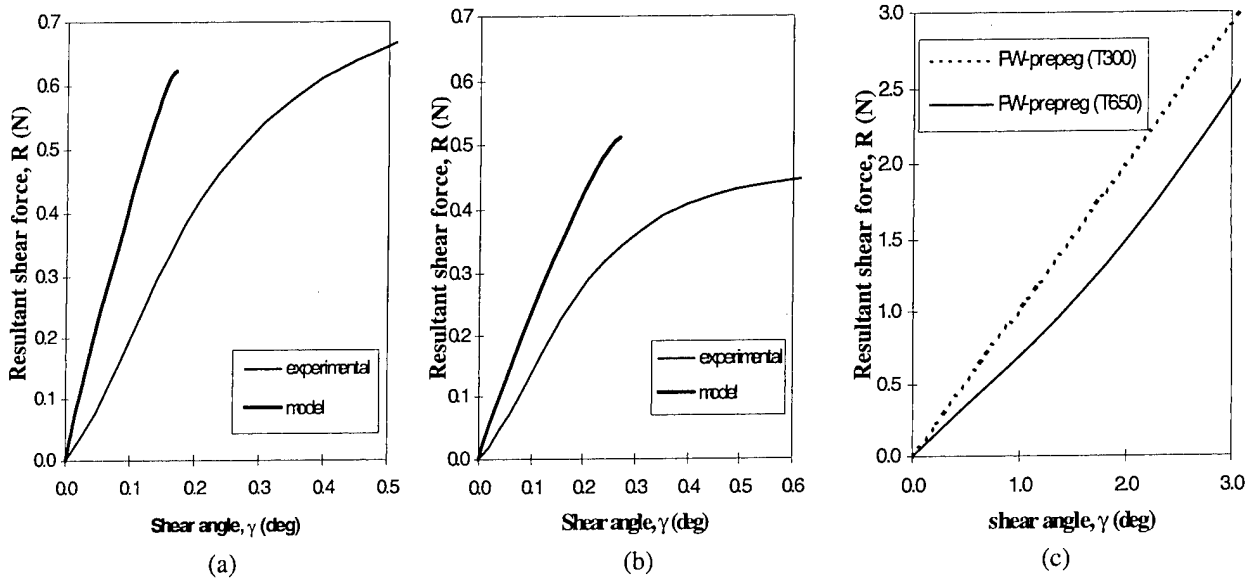

Fig. 10. Shear force/angle relationship at the initial slip region for (a) PW (1K) with experimental and model trends, (b) PW (3K) with experimental and model trends and (c) experimental trends for both prepregs.

Table 3
Predicted and experimental shear modulii and angles of shear for the initial fabric slip region

	Shear modulus (N/deg)		Slip region (deg)	
	Experiment	Model	Experiment	Model
PW (1K)	2.5	3.6	$0 \rightarrow 0.40$	$0 \rightarrow 0.18$
PW (3K)	1.4	1.9	$0 \rightarrow 0.35$	$0 \rightarrow 0.25$

this is not fully understood, however overall, the accuracy of the solution is still maintained regardless of where the model transitional phase is situated.

As stated in Section 3.3.3, the elastic modulus model is valid up to where fabric locking occurs. Analysis of the model's accuracy beyond the lock angle, shows that there is still reasonably good correlation with the experimental results. This is particularly evident for the prepreg materials and the PW (3K) fabric. These results highlight the possible application of the elastic modulus model to predict shear properties beyond fabric lock-up.

5. Discussion of results

The picture-frame experiment has been successfully used to examine the shearing behaviour of carbon plain weave dry fabrics and prepreg materials at ambient temperature. The findings are summarized in Fig. 4,

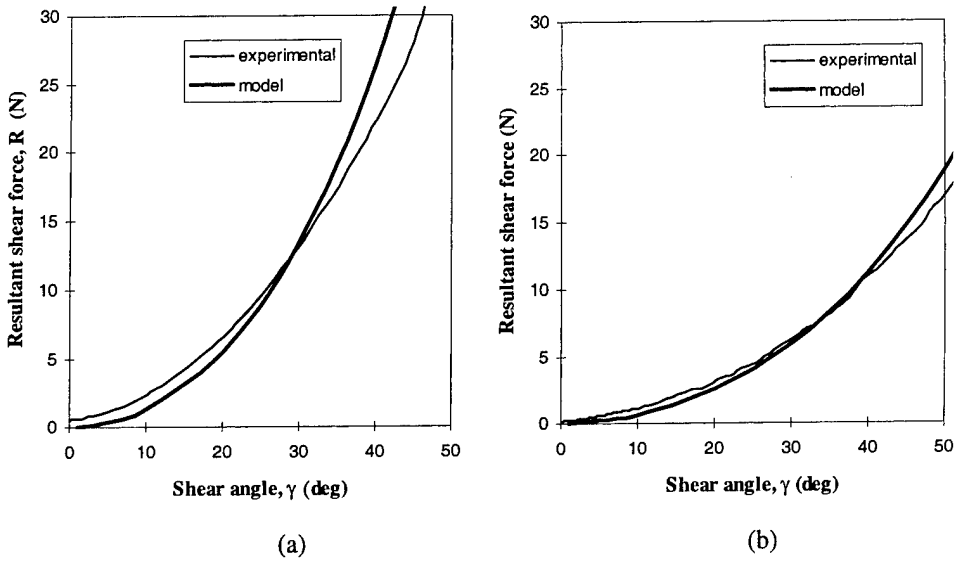

Fig. 11. Comparison of theoretical and experimental results for (a) PW (1K) with $k = 13500$ N/m and (b) PW (3K) with $k = 5000$ N/m.

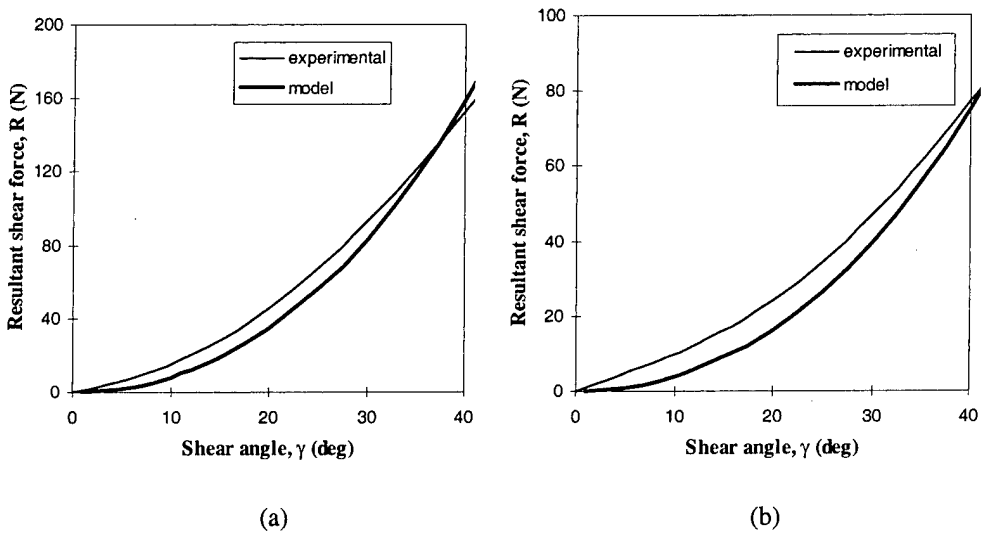

Fig. 12. Comparison of theoretical and experimental results for (a) PW-prepreg (T650) $k = 65000$ N/m and (b) PW-prepreg (T300) with $k = 35000$ N/m.

which shows that the shear modulus of the materials is lowest for twill weave fabrics and highest for prepregs. Because of the ability of twill weaves to undergo high angles of shear, they are better suited for forming applications, as wrinkles are induced at a later stage during the manufacturing process.

Previous works on the characterization of the shear properties for both dry and impregnated fabrics of varying architectures have exhibited similar results to that presented in this paper [10,12]. For instance, experimental values of the fabric locking angles, agreed well with work conducted by Breuer [10], who reported that the critical fabric shear angle ranged around 40° for carbon plain weaves and 60° for carbon twill weaves. Though Breuer does not describe how the lock angles were defined during testing, results from this experimental work bear similarities to results as presented by Breuer. It is hence assumed that a similar criterion, whereby locking is defined as when wrinkles occur during shear testing, was probably used.

In attempting to theoretically predict the locking angle, Prodromou and Chen [12] provided a geometric model based on the plain weave unit cell to define a point after which fabric lock-up occurs. This model is described as

$$\theta = \arcsin \frac{W}{P/2}, \tag{16}$$

where θ is the fabric lock angle, W the thickness of the yarn and P the pitch of the unit cell as described in Fig. 5. Estimations of the fabric locking angle using this formulation showed good correlation with experimental results (Table 1).

A limitation in the use of beam theory to predict the shear response of fabric preforms is the inability of the model to cater for yarn crimping. Katabawa et al. [20] showed that the influence of the yarn crimp angle (though generally small), when combined with shear will cause fabric deformation as a result of the bending and torsional moments created. The effect of not considering yarn torsion for the initial slip model, may be one plausible explanation as to why there exist large discrepancies between the theoretical and experimental results. However this does not exclude practical reasons for such differences, which could include incorrect material handling or slight misalignment of the fabric during loading within the picture-frame shear rig.

Having considered the influence of yarn crimping and reasons as to why the theoretical and experimental results differ for the initial slip region. It is worth noting that the angles and shear forces associated with this region, are of extremely small magnitudes when compared to the total range of the fabric deformation. Hence, it is expected that there may be practical limitations with the utilization of such a model. Nevertheless this initial slip model is of significant importance, as it provides important fundamentals on which the elastic modulus model is based.

Results from the elastic modulus model show that there is good correlation with experimental data with an acceptable level in the margin of error. The accuracy of the correlation within this fabric deformation range also validates the assumption that the effects of yarn crimping can be considered to be negligible. The significance of this deformation region compared to the initial slip region is apparent, as it represents a large proportion of the preform shear properties up till fabric lock-up. Generally, the shear properties of the preform after fabric lock-up has occurred are not required, as wrinkles within the material will already be present.

It was noticed that there were difficulties in determining the effective contact length (d_c) used in both the initial slip and elastic modulus models, when applying the methodology prescribed by Grosberg and Park [17]. During the evaluation of this length, it was realized that the models are highly sensitive to values of yarn thickness. Yarn thickness is an important parameter, because of its relationship to the yarn cross-sectional area moment of inertia via a cubic power term. Consequently small variations in the measured tow dimensions can be hugely exacerbated, which in turn will directly influence estimations of not only the contact length, but the solution itself.

The use of a dry fabric model to predict the shear behaviour of visco-elastic prepregs, suggests that the deformation mechanisms acting within prepregs are similar to that of dry fabrics. The introduction of resin into the fabric structure is considered to have two effects on the mechanisms of shear deformation. Firstly, it will introduce greater frictional constraints acting at the yarn cross-overs, and secondly, the elastic stiffness of the dry fabric yarns will be increased. The overall effect is to require higher shearing forces for the same degree of fabric shear. Consequently as shown in Fig. 10(c), prepregs do not exhibit the initial slip trends and so no slip predictions were performed. Rather the entire prepreg deformation region up to fabric locking is described by the elastic modulus model.

Currently the model relies on defining the spring constant (k), so that model generation is as accurate as possible. As this value is presently empirical, further modelling is required so that a theoretical description can be obtained. In comparing the current model with existing solutions, one common theme is that all have incorporated various forms of empirical and semi-empirical coefficients. The uniqueness of the solution presented is that it not only combines all the unknown variables into a single entity (k), but this factor also represents the physical mechanics required for fabric shear deformation. Furthermore, the breakdown of the solution into a cubic function, whose coefficients form parameters relating to the fabric geometric and material properties, enables the application of the solution to be relatively straightforward.

6. Conclusions and summary

From the current work the following conclusions were obtained:

- The picture frame test experiment is able to adequately characterize the shear deformation behaviour of both dry fabrics and prepregs.
- The region in which initial fabric slip occurs contains very low magnitudes of shear force and shear angle in comparison with the entire range of fabric deformation.
- Overestimation of the shear modulus within the initial slip region is thought to occur because the model ignores yarn undulation. This effect would need to be incorporated to improve the accuracy of the solution.
- Beam bending theory is a satisfactory analytical method which can be employed to predict the elastic modulus of prepregs and dry fabrics. Due to the accuracy of the solutions obtained, this validates the assumption that the influence of yarn crimping can be ignored during modelling of the elastic modulus.

- The definition of the spring constant (k) is an important factor in determining the accuracy of the solution. Currently this is an arbitrary value in which further research needs to be undertaken to characterize it from a theoretical aspect.

Finally, the present formulation easily models variation of the plain weave fabric architecture. This makes it a useful tool to understand and quantify how changes in the fibre architecture during manufacturing influence fabric shear properties.

References

[1] Long AC, Rudd CD, Blagdon M, Smith P. Characterizing the processing and performance of aligned reinforcements during preform manufacture. Composites: Part A 1996;27A:253–547.

[2] Mack C, Taylor HM. The fitting of woven cloth to surfaces. J Text Inst 1956;47:477–89.

[3] Potter KD. The influence of accurate stretch data for reinforcements on the production of complex structural mouldings. Composite 1979;11:161–7.

[4] Robertson RE, Hsiue ES, Yeh GSY. Continuous fiber rearrangements during the moulding of fiber composites. Polym Compos 1984;53:191–7.

[5] Van West BP, Pipes RB, Keefe M. A simulation of the draping of bidirectional fabrics over arbitrary surfaces. J Text Inst 1990;4:448–60.

[6] Long AC, Rudd CD, Blagdon M, Smith P. Characterising the processing and performance of aligned reinforcements during preform manufacturing. Composites: Part A 1996;27A:247–53.

[7] McBride TM, Chen J. Unit-cell geometry in plain-weave fabrics during shear deformations. Compos Sci Technol 1997;57:345–51.

[8] Tam AS, Gutowski TG. The kinematics for forming ideal aligned fibre composites into complex shapes. Compos Manuf 1990;1(4):219–28.

[9] Nguyen M. Investigations of the single diaphragm forming technique. Cooperative Research Centre for Advanced Composite Structures (CRC-ACS) Draft report, 1999.

[10] Breuer U, Neitzel M, Ketzer V. Reinicke. Deep drawing of fabric-reinforced thermoplastics: wrinkle formation and their reduction. Polym Compos 1996;17(4):643–7.

[11] McGuinness GB, Ó Brádaigh CM. Characterization of thermoplastics composite melts in rhombus-shear: the picture frame experiment. Composites: Part A 1998;19A:115–32.

[12] Prodromou AG, Chen J. On the relationship between shear angle and wrinkling of textile composite preforms. Composites: Part A 1997;28A:491–503.

[13] Wang J, Page JR, Paton R. Experimental investigation of the draping properties of reinforced fabrics. Compos Sci Technol 1998;58:269–80.

[14] Pierce FT. The geometry of cloth structure. J Text Inst 1937;45–95.

[15] Olofsson B. A general model of fabric as a geometric-mechanical structure. J Text Inst 1964:541–537.

[16] Kuhn JL, Charalambides PG. Modelling of plain weave fabric composite geometry. J Compos Mater 1999;33(3):188–220.

[17] Grosberg P, Park BJ. The mechanical properties of woven fabrics, Part V: The initial modulus and the frictional restraint in shearing of plain weave fabrics. Text Res J 1966:420–431.

[18] Kawabata S, Niwa M, Kawai H. The finite deformation theory of plain-weave fabrics Part I: the biaxial-deformation theory. J Text Inst 1973;64(2):21–46.

[19] Kawabata S, Niwa M, Kawai H. The finite deformation theory of plain-weave fabrics Part II: the uniaxial-deformation theory. J Text Inst 1973;64(2):47–61.

[20] Kawabata S, Niwa M, Kawai H. The finite deformation theory of plain-weave fabrics Part III: the shear-deformation theory. J Text Inst 1973;64(2):62–85.

[21] Ye L, Daghyani HR. Characteristics of woven fibre fabric reinforced composites in forming process. Composites: Part A 1997;28A:869–74.

[22] Sinoimeri A, Drean JY. A study of the mechanical behaviour of the plain-weave structure by using energy methods: fabric shear. J Text Inst 1996;87(1):120–9.

[23] Wang J, Paton R, Page JR. Forming properties of thermoset fabric prepregs at room temperature and elevated temperature. Cooperative Research Centre for Advanced Composites (CRC-ACS) technical memorandum, 1998.

[24] Golden K, Rogers TG, Spencer AJM. Forming kinematics of continuous fibre reinforced laminates. Compos Manuf 1991;2(3):167–278.

[25] Grosberg P, Leaf AV, Park BJ. The mechanical properties of woven fabrics, Part VI: the elastic shear modulus of plain-weave fabrics. Text Res J 1968:1085–1100.

[26] James Stewart. Calculus. 2nd ed. Brooks/Cole, 1991.

ELSEVIER

Composite Structures 47 (1999) 781–787

COMPOSITE STRUCTURES

www.elsevier.com/locate/compstruct

The bending properties of integrally woven and unidirectional prepreg T-sections

R.S. Thomson [a], P.J. Falzon [a], A. Nicolaidis [a], K.H. Leong [a,*], T. Ishikawa [b]

[a] *Cooperative Research Centre for Advanced Composite Structures Ltd. (CRC-ACS), 506 Lorimer Street, Fishermens Bend, VIC 3207, Australia*
[b] *National Aerospace Laboratory (NAL), Airframes Division, Composite Structures Section, 6-13-1 Ohsawa, Mitaka, Tokyo 181-0015, Japan*

Abstract

The relative bending properties of T-sections produced from three-dimensional (3D) integrally woven preforms and unidirectional prepreg have been investigated with respect to their stress–strain behaviour, skin-stiffener separation loads and fracture behaviour. These tests were carried out to simulate localised skin-stiffener separation that is normally responsible for the failure of postbuckling blade-stiffened composite structures. It has been found that the woven T-sections performed better than their prepreg counterpart in terms of initial and peak failure loads, while at the same time also sustaining less damage which is more contained. Finite element analysis has been carried out to ascertain the suitability of the modified three-point bend test, which also successfully modelled the deformed shape of the T-sections and their critical skin-stiffener separation forces. © 2000 Elsevier Science Ltd. All rights reserved.

Keywords: T-sections; Bending; Prepreg; 3D woven; Postbuckling

1. Introduction

Postbuckling composite structures typically comprise a thin skin that is reinforced with hat or blade stiffeners. Whilst these structures have the potential for reduced weight and improved structural performance, they suffer from one major weakness which is premature separation of the stiffeners from the skin due to the poor through-the-thickness properties of laminated composites [1]. Three-dimensional (3D) multilayer woven composites have been shown to be effective for improving the translaminar properties of laminated composite structures with the introduction of reinforcing fibres in the thickness direction of the laminate. Achievable on conventional industrial looms, 3D weaving also has an added advantage in that complex shaped preforms can be produced in one piece, thus potentially reducing overall manufacturing cost.

Researchers, such as Leong et al. [2], have shown that the choice of weave pattern and binder path can affect the amount of fibre crimping, and hence, in-plane properties of 3D woven composites. Soden et al. [3] further demonstrated that the level of through-the-thickness fibre interlinkage can significantly affect the failure behaviour of integrally woven T-sections. To assess the efficacy of using 3D weaving for producing cost-efficient postbuckling blade-stiffened panels with improved stiffener pull-out performance, T-sections which resemble a skin-to-stiffener junction in such panels were produced using integrally woven preforms and prepreg materials and tested in bending. The primary difference between the two test samples is in the manner by which the skin and stiffener are constructed. In the woven preforms, the stiffener and skins are integrally linked by fibres, whilst in the prepreg samples, such fibre interconnectivity is not present. The experimental studies were complemented with numerical analysis using the Finite Element (FE) method. Both the results of the bend tests and the FE analysis are reported in this paper. Postfailure examinations using ultrasonic C-scanning and optical microscopy were carried out to identify and understand the fracture mechanisms responsible for failure, and these findings are also presented in the paper.

It is noteworthy that this work forms the precursor to a larger collaborative programme between the Cooperative Research Centre for Advanced Composite Structures Ltd. (CRC-ACS) in Australia and the National

* Corresponding author. Tel.: +61-3-9646-6544; fax: +61-3-9646-8352.
E-mail address: khlcrcas@ozemail.com.au (K.H. Leong).

0263-8223/99/$ - see front matter © 2000 Elsevier Science Ltd. All rights reserved.
PII: S0263-8223(00)00054-4

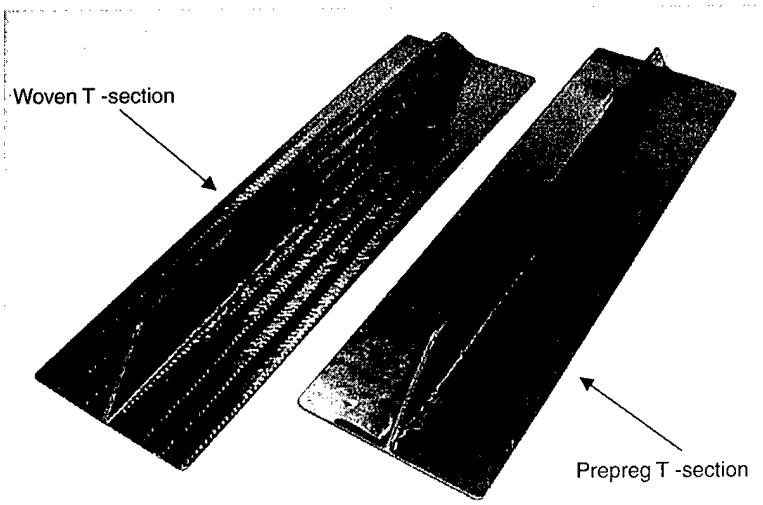

Fig. 1. Photograph of the T-section specimens.

Aerospace Laboratory (NAL) in Japan to investigate the potential of integrally woven blade-stiffened panels for postbuckling composite structures.

2. T-section design and manufacture

The T-sections used in this work measured nominally $200 \times 65 \times 25$ mm^3, and were manufactured from either integrally woven preforms (woven samples) or unidirectional prepreg materials (prepreg samples).

The multilayer woven preforms were produced on an automatic Jacquard loom from 3 k carbon tows. The preforms contained fibres in only the longitudinal and transverse orientations, and outer two-dimensional off-axis plies were added during the consolidation stage. The woven samples were manufactured with M18™ epoxy resin film using the Resin Film Infusion (RFI) technique. The prepreg samples were produced from Fibredux 914C™, which is an epoxy-based system. The conventional vacuum bag autoclave curing technique was used to consolidate the two sets of test samples. The woven and prepreg test samples, shown in Fig. 1, both had quasi-isotropic layups in the skin, and extra longitudinal reinforcement were used in the stiffeners. They were loaded to failure in three-point bending using the configuration shown in Fig. 2 to simulate the induced peeling at the T-joint normally encountered for post-buckling blade-stiffened panels.

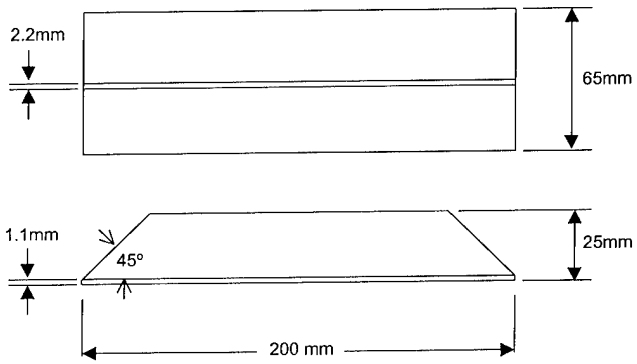

Fig. 2. Nominal dimensions of the T-section samples.

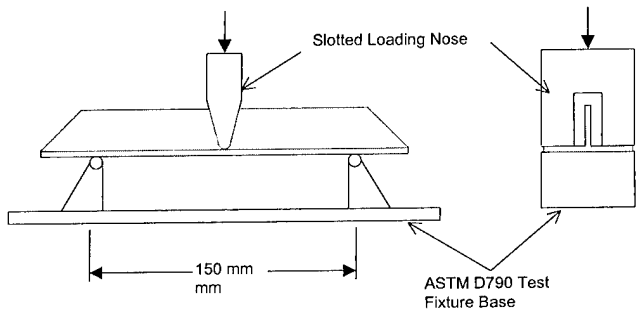

Fig. 3. Schematic diagram of test configuration.

3. Test methodology

The tests were conducted using the modified three-point bend procedure illustrated in Fig. 3. A slotted loading nose was used to apply the load directly to the skin, thus inducing bending in the skin and a normal force tending to cause skin-stiffener separation. The base of the test rig consisted of an ASTM D790 three-point bend fixture. Tests were conducted in a screw-driven,

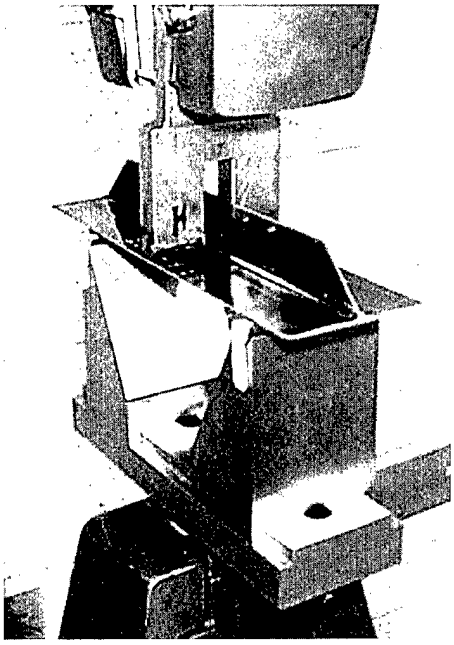

Fig. 4. Experimental test set-up.

universal testing machine under displacement control at a rate of 1.0 mm min^{-1}. The test set-up is more clearly shown in Fig. 4. A total of three and five specimens were tested for the woven and prepreg samples, respectively.

4. Analysis

An FE analysis of the T-sections was performed to determine the forces acting at the skin-stiffener interface under the proposed test conditions. The FE model, shown in Fig. 5, consisted of 1318 four-noded, quadrilateral plate elements. Spring elements were used to connect the stiffener to the skin so that the interface forces could be extracted. The mesh itself was refined towards the skin-stiffener interface region and the centre of the model to ensure accurate representation of the forces in this region. To simulate the loading used during testing, loads were applied at a point on the skin 7.5 mm from the stiffener centreline. The model was simply supported with a span of 150 mm, as shown in Fig. 5. MSC.NASTRAN was used to conduct the analysis and because relatively large deflections were expected to occur, the analysis included the effects of geometric nonlinearity.

The typical deformed shape is shown in Fig. 6 which demonstrates the localised effect of skin bending. This deformed shape is similar to that expected in a post-buckling structure where a buckle peak terminates at a stiffener. The normal forces acting along the skin-stiffener interface under 1.0 kN of applied load are plotted in Fig. 7. It will be noted that the peak force acts over a length of approximately 30 mm. The peak itself is rather sharp indicating that the peak stresses will be very localised. The shear flow along the stiffener interface under 1.0 kN of applied load is also plotted in Fig. 7 which demonstrates that shear is not present in the region of

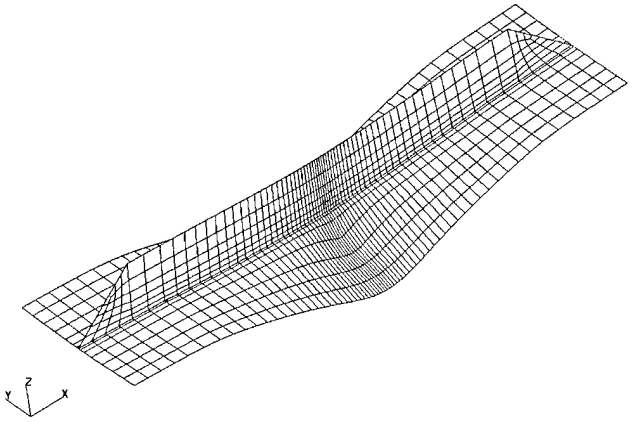

Fig. 6. Predicted deformed shape of the T-section.

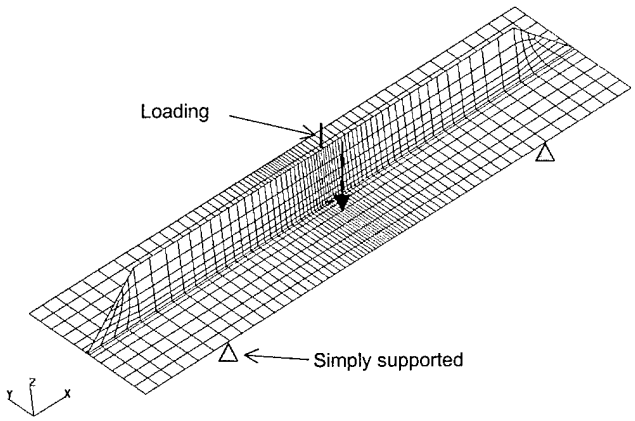

Fig. 5. Finite element model of the T-section.

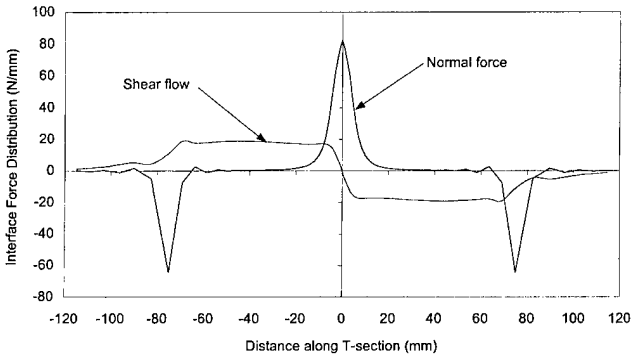

Fig. 7. Predicted normal and shear force distributions along the skin-stiffener interface under 1 kN of load.

the peak normal force. Therefore, interface failure of the specimens would be the result of the normal force only.

5. Test results

5.1. Stress–strain behaviour and damage accumulation

The results of the three-point-bending tests of the woven and prepreg T-sections are summarised in Tables 1 and 2, respectively, while their representative load-displacement curves are presented in Fig. 8. In both cases, the load–displacement behaviour was generally linear until initial failure occurred, which was associated with an audible acoustic emission and a small drop in load. The load picked up with continued loading and it increased with small failures, audibly noted, occurring at regular intervals until a peak load was achieved. A steady reduction in load was then experienced until catastrophic failure was observed.

Table 1
Summary of the woven T-section test results

Specimen ID	Initial failure load (kN)	Peak load (kN)
STWP-1	1.68	4.10
STWP-2	1.80	3.91
STWP-3	1.74	4.00
Average	1.74	4.00

Table 2
Summary of the prepreg T-section test results

Specimen ID	Initial failure load (kN)	Peak load (kN)
STPP-1	1.40	3.16
STPP-2	1.32	3.18
STPP-3	1.20	3.11
STPP-4	0.98	2.85
STPP-5	0.99	3.12
Average	1.18	3.08

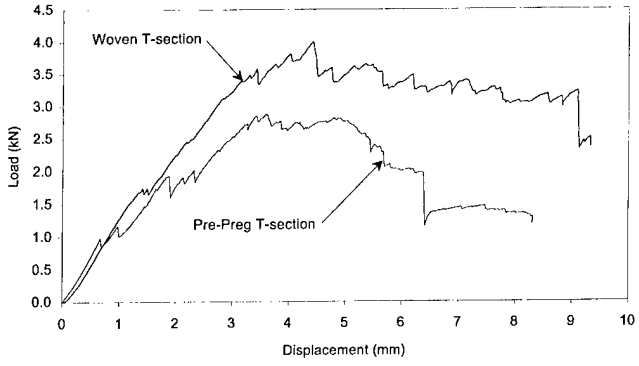

Fig. 8. Comparison of typical load–displacement curves for the woven and prepreg T-sections.

In the case of the woven samples, the ultimate load was typically associated with failure of the skin in bending. For the prepreg samples, on the other hand, initial failure appeared to be localised under the loading points in the form of fibre breakage and matrix cracking. Final failure modes included delaminations formed through separation of the stiffener from the skin, splitting and peeling of the outer plies, as well as localised fibre breakage. The stiffeners were either partially or completely (in one sample) split as a result of the local bending forces.

5.2. Failure loads

A comparison of the initial and ultimate failure loads on the woven and prepreg T-sections is presented in Fig. 9. The initial failure load and the peak load of T-sections manufactured from the woven preform (*viz.* 1.74 and 4.00 kN, respectively) were both significantly higher than those manufactured from prepreg tape (*viz.* 1.18 and 3.08 kN, respectively). In addition, the tests showed that the initial failures were less severe in the woven preform specimens and a higher load could be sustained following that preliminary load drop. The visible effects of failure were also significantly reduced in the woven preform specimens (compare Figs. 10 and 11).

5.3. Failure modes

5.3.1. Ultrasonic C-scan

The extent of damage sustained by the T-sections due to bending was assessed using the ultrasonic C-scanning technique. Fig. 12 shows representative C-scan images of both the woven and prepreg T-sections after ultimate failure. The scans clearly show that delamination has occurred in the skin of both samples, however, in the case of the prepreg T-sections, it appears that the delamination has also propagated into the stiffener.

The projected damage areas for each specimen were calculated from the C-scan images and summarised in

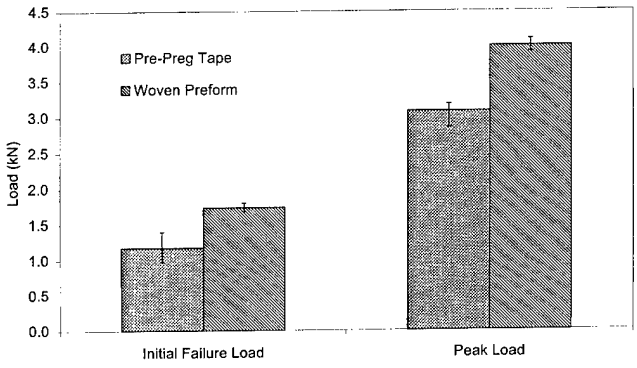

Fig. 9. Summary of failure loads of the T-section tests.

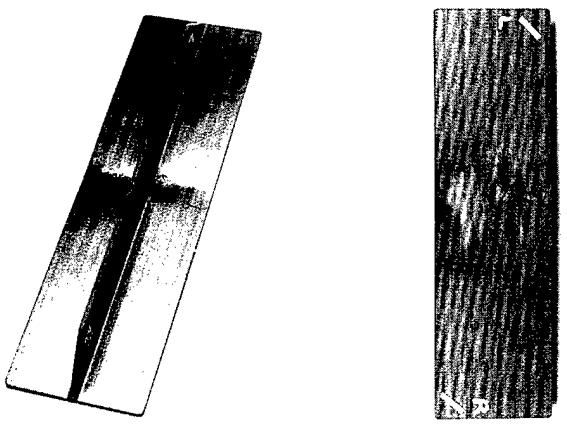

Fig. 10. Typical visible damage following testing of the woven T-section.

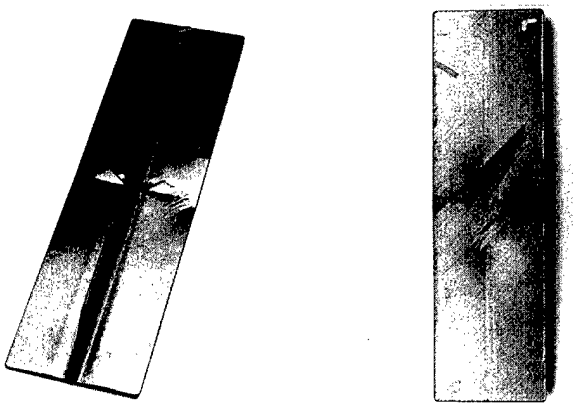

Fig. 11. Typical visible damage following testing of the prepreg T-section.

Fig. 13. Notwithstanding the observed scatter in the results, overall, the damage sustained in the skin was less severe in the woven than in the prepreg samples. This is also true when considering the total damage sustained by the T-sections since only the stiffener of the prepreg T-sections suffered any damage.

5.3.2. Microscopy

Selected specimens were sectioned, ground and polished, and then studied under the microscope to more accurately identify the locations and types of damage that were present in the T-section samples. It was observed that delamination in the woven T-sections occurred in the interfaces between the integrally woven preform and the off-axis plies. Note from Fig. 14(a) that the fibre crossover at the T-junction of the sample impeded the propagation of the delamination crack into the stiffener. On the other hand, delamination occurred in more than one set of interfaces in the prepreg T-section. As exemplified in Fig. 14(b), the delamination in the skin carried on into the stiffener unhindered resulting in partial, or in one specimen total, splitting. In addition, Fig. 14 also illustrates the difference in the severity of skin-stiffener separation in terms of delamination crack opening at the T-junction.

6. Discussion

Three-point bend tests were carried out on two different sets of carbon/epoxy composite T-sections – one manufactured from woven preforms and the other from prepreg tape – to simulate localised skin-stiffener separation that is normally responsible for the failure of postbuckling blade-stiffened composite panels.

The extent and spread of damage observed in the two sets of T-section samples were consistent with their respective microstructures and the recorded failure loads. By using an integrally woven design, the initial failure load of the T-sections was improved by 48% and the peak load by a further 30% compared with the prepreg design. These impressive improvements stemmed from the fact that, contrary to the prepreg microstructure, the

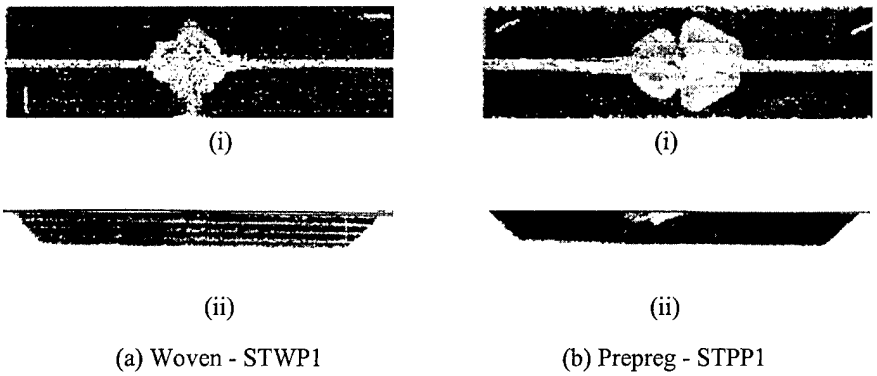

Fig. 12. Representative C-scan images of the failed T-sections.

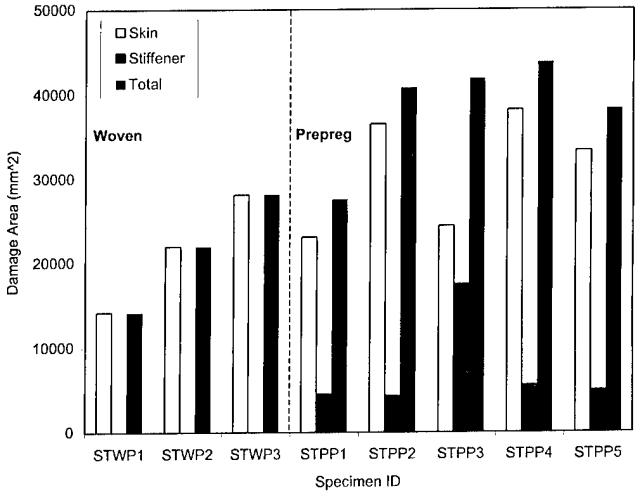

Fig. 13. Relative projected damage area of the woven and prepreg T-sections.

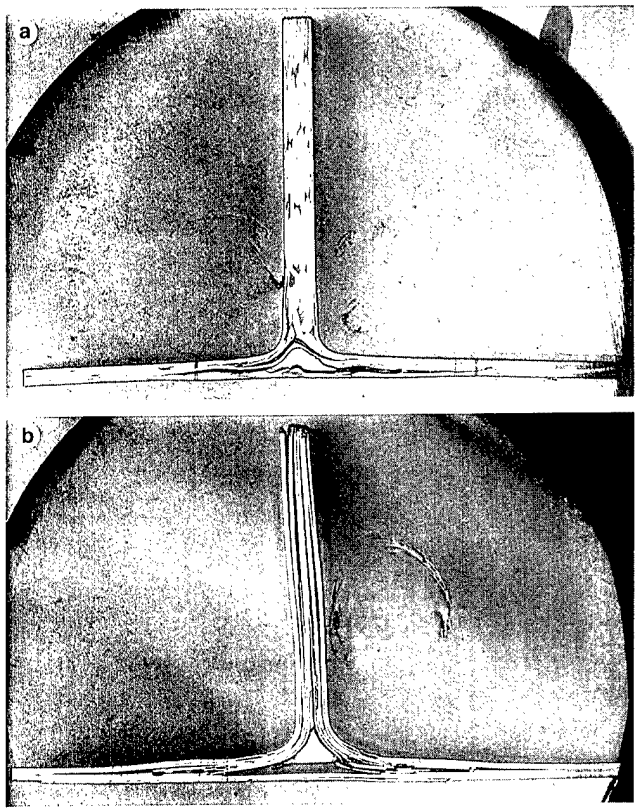

Fig. 14. Micrographs of cross-sections showing the extent of damage in the (a) woven, and (b) prepreg, T-sections.

woven microstructure possesses a relative more complex array of fibre paths which effectively act as crack inhibitors and stoppers. Therefore, larger amounts of fracture energy need to be expended for delamination cracks to propagate in the woven, than in the prepreg, T-sections. Consequently, although having sustained a greater load before failure, the degree of damage in the former was observed to be less severe. Further, the fibre crossover at the T-junction of the woven sample also meant that it would be more difficult for the delamination cracks to spread from the skin into the stiffener, which is believed to have contributed to the better failure loads exhibited by these T-sections. In terms of total damage area, the average delamination size in the woven sample was only approximately half that of the prepreg T-section.

It is important to note that despite not having through-the-thickness reinforcement over the whole cross-section, the 3D integrally woven design in the woven sample does carry some advantage nonetheless for enhancing the stiffener-skin separation loads. From the present work, it also appeared to suggest that failure would be less catastrophic than its prepreg counterpart. Furthermore, for structural designs which have a requirement for a thick cross-ply core layup, the use of this method could be particularly cost-effective.

It is noteworthy that finite element analysis was used initially to ascertain the suitability of the test which in turn successfully highlighted the necessary modifications to the standard three-point bend test that were needed in order to simulate skin-stiffener separation. The FE analysis was able to predict the typical deformed shape of the T-sections during bending which resembled that expected in a postbuckling panel where a buckle peak terminates at a stiffener, and this deformation was observed experimentally for the samples under study. The analysis also indicated that the peak normal force was very localised while the shear force flows along the stiffener interface away from the region of the peak normal force. This suggested that interface failure of the specimens was a result of only the normal force.

7. Conclusions

In conclusion, the three-point bend tests used in this investigation successfully duplicated failure via skin-stiffener separation, thus providing a relatively quicker and cheaper technique for assessing different skin-stiffener designs for improved postbuckling blade-stiffened structures. It was found that T-sections manufactured from 3D integrally woven preforms outperformed their prepreg counterpart in bending in terms of failure loads, both initial as well as ultimate, and the degree and spread of damage. By comparing with a prepreg design, the 3D woven concept studied here is being extended to actual blade-stiffened panels subjected to shear and compression loads to demonstrate its efficacy for enhancing skin-stiffener separation strength in large-scale postbuckling structures.

Acknowledgements

Thanks are due to M. Crossthwaite, M. McVilley (CRC-ACS) and M. Matsushima (NAL) for their assistance in specimen preparation, mechanical testing and ultrasonic C-scanning, respectively.

References

[1] Sheppard AT, Leong KH, Kelly DW, Raju J. Comp Struct 1998;41(3/4):341.
[2] Leong KH, Lee B, Herszberg I, Bannister MK. Comp Sci Tech 1999;60(1):149.
[3] Soden J, Weissenbach G, Hill BJ. Comp A 1999;30(3):213.

ELSEVIER

Composite Structures 47 (1999) 789–796

COMPOSITE STRUCTURES

www.elsevier.com/locate/compstruct

Computer modelling of impact on curved fibre composite panels

Zafer Leylek [a], Murray L. Scott [a,*], Steve Georgiadis [b], Rodney S. Thomson [c]

[a] *Sir Lawrence Wackett Centre for Aerospace Design Technology, Department of Aerospace Engineering, Royal Melbourne Institute of Technology, GPO Box 2476V, Melbourne, Vic. 3001, Australia*

[b] *Aerospace Technologies of Australia Limited, 226 Lorimer Street, Port Melbourne, Vic. 3207, Australia*

[c] *Cooperative Research Centre for Advanced Composite Structures Limited, 506 Lorimer Street, Fishermens Bend, Vic. 3207, Australia*

Abstract

This paper presents results of a finite element (FE) analysis study into low energy impact on curved composite panels. The aim of this study was to determine the accuracy and efficiency of a non-linear explicit FE code, MSC.Dytran, and compare results to published experimental data. The study also looked at impact response as a function of composite panel curvature, composite mesh density, impactor weight, velocity and size, and various suggestions are made for improving the accuracy and efficiency of FE analysis procedures in composite low energy impact studies. The paper presents 265 explicit computer simulation results, which show that non-linear FE analysis does provide accurate, efficient and conservative solutions provided various guidelines are followed. © 2000 Elsevier Science Ltd. All rights reserved.

Keywords: Impact; Explicit FE simulation; Impact damage

1. Introduction

Advanced fibre composite materials are widely used in aerospace structures due to their superior properties such as high strength to weight ratio. Structures manufactured from these materials are being used increasingly in both secondary and primary structures, however their susceptibility to impact is a significant constraint on further application. Impact of foreign objects, even at low velocity, can result in extensive internal damage of composite structures and significantly reduce their residual strength.

Low velocity impact is hazardous for laminated structures because it is often non-visible or barely visible and hence difficult to detect. Such damage can be caused by dropped tools during maintenance operations, or by hail and runway debris during take-off or landing. To design composite structures with impact resistance and damage tolerance, an understanding of impact behaviour and damage mechanisms is necessary. This paper presents modelling procedures to simulate impact events and predict associated structural responses, which will assist in the design of advanced composite structures.

The impact behaviour of composite panels can be described as a highly geometric non-linear and dynamic phenomenon. To precisely model impact scenarios and predict the impact response, the finite element (FE) analysis code MSC.Dytran, which utilises explicit methods to solve geometric non-linear dynamic contact problems, has been used. The effects of curvature on the impact characteristics of fibre composite panels are investigated and models with varying mesh size, impact energy levels and impactor geometry are studied. A number of studies have shown that low impact energy simulations can provide accurate and efficient results [1–6].

2. Test specimen

The composite model used in this investigation is outlined in [1], which was used as the basis for this composite impact simulation. The main objective of the current work was to verify the FE modelling with the experimental data published in this reference. The specimens were 16-ply flat or curved panels with $[45/0/-45/90]_{2s}$ lay-ups with ply thickness of 0.127 mm. Test specimen mechanical properties are presented in Table 1

* Corresponding author. Tel.: +61-3-9647-3090; fax: +61-3-9647-3050.

E-mail addresses: m.scott@rmit.edu.au (M.L. Scott), steve.georgiadis@australia.boeing.com (S. Georgiadis), rodney@duigen.dsto.defence.gov.au (R.S. Thomson).

0263-8223/99/$ - see front matter © 2000 Elsevier Science Ltd. All rights reserved.
PII: S0263-8223(00)00055-6

Table 1
Composite panel mechanical properties in [1]

Longitudinal modulus E_1 (GPa)	138.00
Transverse modulus E_2 (GPa)	8.96
In-plane shear modulus G_{12} (GPa)	6.00
Transverse shear modulus G_{23} (GPa)	3.52
Transverse shear modulus G_{13} (GPa)	6.00
Poisson's ratio v_{12}	0.30

and all simulated specimens were 127 mm wide and 228.6 mm long. The model specimens were fully clamped along all edges with no translation or rotation. Specimens were subjected to impact normal to the surface.

3. FE formulation

The FE code uses a Lagrangian explicit method to carry out the transient solution. The Newmark [7] method is used to carry out integration with respect to time where, all parameters for t_n are known, t_{n+1} can be calculated using the following equation of motion

$$Ma'_{n+1} + Cv'_{n+1} + Kd'_{n+1} = F^{\text{ext}}_{n+1}, \tag{1}$$

where M is the mass matrix, C the damping matrix, K the stiffness matrix, F^{ext} the external load vector, a'_{n+1} the acceleration at t_{n+1}, v'_{n+1} the velocity at t_{n+1}, d'_{n+1} is the displacement at t_{n+1}.

The estimates of d'_{n+1}, v'_{n+1} and a'_{n+1} are given by

$$d'_{n+1} = d_n + v_n\Delta t + \frac{(1-2\beta)a_n\Delta t^2}{2} + \beta a'_{n+1}\Delta t^2, \tag{2}$$

$$v'_{n+1} = v_n + (1-\gamma)a_n\Delta t + \gamma a'_{n+1}\Delta t, \tag{3}$$

$$a'_{n+1} = \frac{F^{\text{ext}}_{n+1} - Cv^*_n - Kd^*_n}{M + C\gamma\Delta t + K\beta\Delta t^2}, \tag{4}$$

where γ and β are constants and

$$d^*_n = d_n + v_n\Delta t + \frac{(1-2\beta)a_n\Delta t^2}{2}, \tag{5}$$

$$v^*_n = v_n + (1-\gamma)a_n\Delta t. \tag{6}$$

The composite panels are modelled using multi-layered orthotropic composite element. The elastic stress–strain relationship between the fibre and matrix stresses and strains can be written as

$$\begin{bmatrix}\sigma_{11}\\ \sigma_{22}\end{bmatrix} = \frac{1}{1-v_{12}v_{21}}\begin{bmatrix}E_{11} & v_{12}E_{22}\\ v_{21}E_{11} & E_{22}\end{bmatrix}\begin{bmatrix}\varepsilon_{11}\\ \varepsilon_{22}\end{bmatrix}. \tag{7}$$

The shear–strain relationship is given as

$$\gamma_{12} = \frac{1}{G_{12}}\sigma_{12}. \tag{8}$$

The stress and strains are evaluated at $t + \frac{1}{2}\Delta t$.

4. Impact parameters

Computational impact simulation of composite structures is a relatively new area of research. Debate continues in relation to the mechanisms and key parameters of impact damage. Furthermore, studying impact damage through FE simulation introduces variables such as mesh density and element type that need to be considered.

Since this research program aims to validate experimental results published in [1], the variables are selected so that an accurate comparison can be made. That is, the impactor mass, velocity and diameter for results in given in [1] are 12.7 mm, 1.134 kg and 1.89 m/s, respectively. Three parameters are defined for each variable. Hence, one lower and one higher parameter are used. The impact parameters under investigation are as follows:

- Panel radius of curvature: flat, 127 mm and 762 mm.
- Mesh density: 10×10, 25×25 and 50×50.
- Impactor size diameter: 6.35 mm, 12.7 mm and 25.4 mm.
- Impactor mass: 0.5 kg, 1.134 kg and 2.0 kg.
- Impactor velocity: 1.0 m/s, 1.89 m/s, 2.5 m/s.

The above combination of impactor mass and velocities yield 9 impact energy levels: 0.25, 0.567, 0.896. 1.00, 1.5625, 2.03, 3.54, 3.58 and 6.25 J.

It is assumed that impact is a function of the parameters listed above. Hence in order to obtain a clear understanding of composite impact behaviour and the variables described above, all possible parameter combination was investigated; a total of 265 simulations has been completed. Fig. 1 shows the scheme used to conduct this investigation where 243 simulations were undertaken. Another 22 simulations were completed where the only variable considered was composite curvature. This was done so that a clear comparison between nonlinear FE analysis and experimental data published in [1] could be made. The impact energy was 2.03 J, the impactor diameter was 12.7 mm and the composite panel radius of curvature ranged from 50.4 to 1625 mm.

The predominant parameter used in describing impact damage is taken as the contact force. Contact force represents the total force applied to the composite panel at every time increment. Internal energy also provides a valuable indicator of impact damage and is also used as a tool in determining impact effects on composite structures. Other parameters considered are impactor velocity and composite structure kinetic energy.

It should be noted here that internal stresses and strains were not considered in this study. Although these stresses and strains ultimately determine the structural impact response and residual strength after impact, analysing such a large amount of data and drawing reasonable conclusions is a formidable task. Also, in the absence of a reliable failure criterion, which can be used universally, the true effect of stress and strain analysis

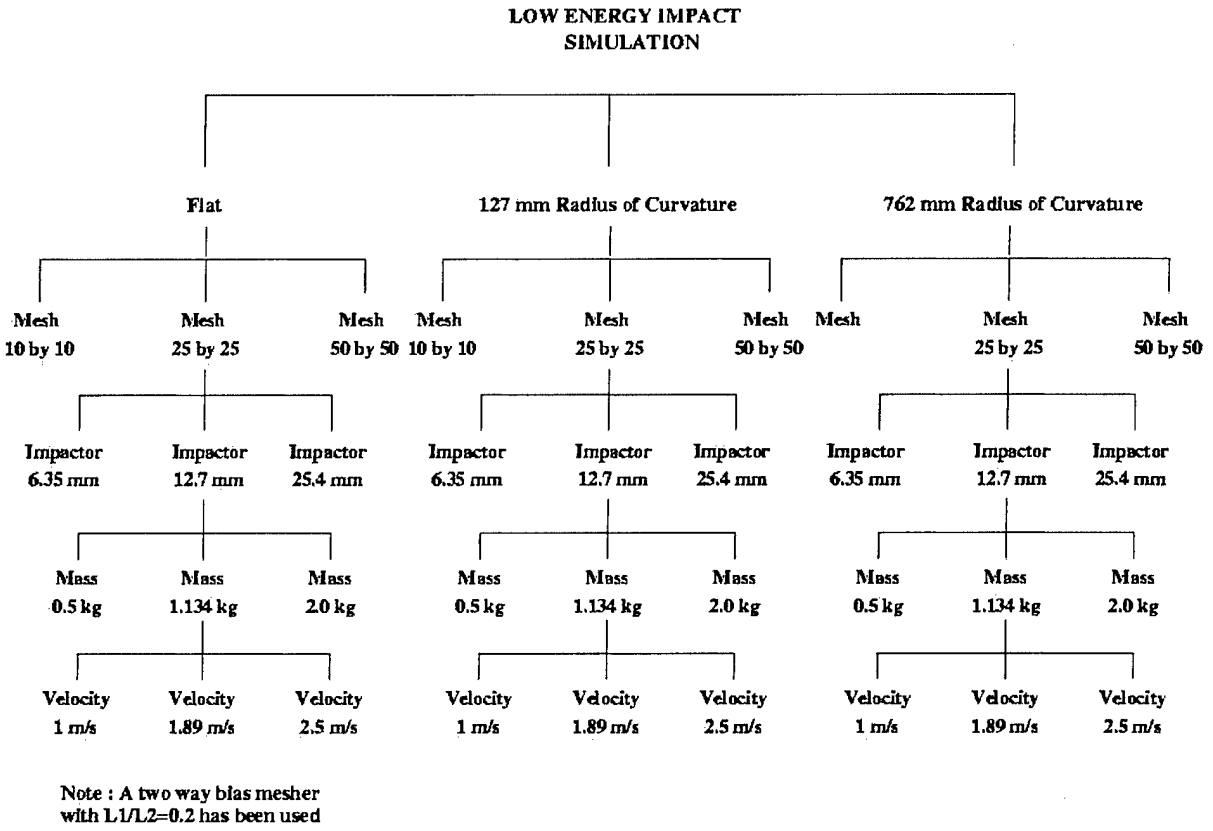

Fig. 1. Scheme used in the investigation of low energy impact as a function of composite panel curvature, mesh density, impactor size, mass and velocity.

cannot be efficiently employed at this stage. Although such analyses have drawbacks, detailed investigation of the internal stresses, strains and energy levels of the panels will be the subject of subsequent research by the authors.

5. Analysis technique

The simulation technique uses MSC.Patran (and XDEXTR) for pre- and post-processing, and MSC. Dytran to carry out the explicit Lagrangian non-linear simulation. The Lagrangian integration technique is suited to solid–solid interaction problems where the time-step is relatively large when compared to the Eulerian method. The Eulerian method is suited to solid–fluid interaction where smaller time-steps are required and computation efficiency is not a main issue. The composite panel is modelled using quadrilateral elements. A two-way bias mesh is employed with $L1/L2 = 0.2$. This means that the edge length ratio of the inner/middle element to the outer-most element is 1:5. This technique was used because the impact location was at the centre of the panel, and therefore a greater mesh density was required in this region. Fig. 2 shows a 25×25 mesh model with a 101.6 mm radius of curvature.

The impactor ball is modelled using three and four sided shell elements. The geometry of the impactor was generated using a rigid ellipse generator and then transformed into shell elements. The impactor is modelled as a rigid structure where the ball does not elastically deform and its mass, moment of inertia and velocity can be arbitrarily defined. Modelling the impactor this way vastly improves calculation time and efficiency, and does not consume valuable computer resources. Since impact energy levels are relatively low it is assumed that the errors involved are very low. Fig. 3 shows a 12.7 mm diameter ball used in impact simulation.

The simulations were conducted on an SGI Origin 200 with 2×180 MHz Processors (64 bit MIPS RISC R10000 CPU with R10010FPU) running IRIX 6.5.4 (UNIX) system. The time required to run a 10×10 mesh panel was approximately 5–6 min, 25–35 min for a 25×25 mesh panel, and 240–360 min for a 50×50 mesh panel.

6. Results and discussion

6.1. Comparison of FE results and experimental data

It was found that non-linear explicit simulation of composite impact yielded reasonably accurate results.

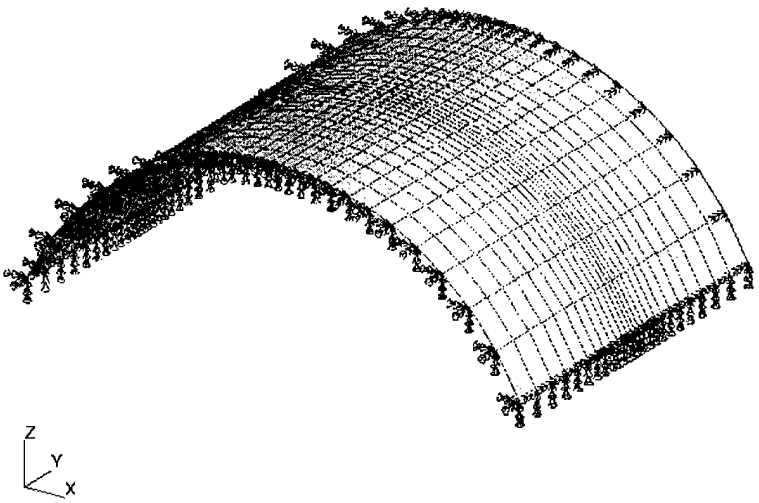

Fig. 2. A composite panel with 101.6 mm radius of curvature having a mesh density of 25×25.

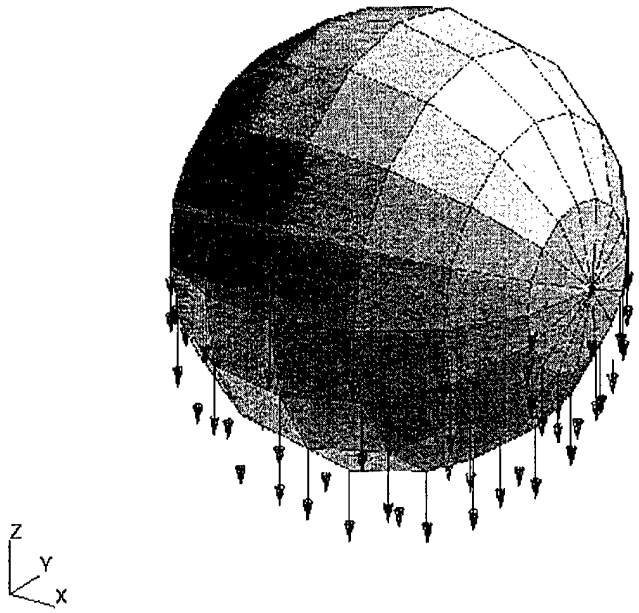

Fig. 3. Rigid 12.7 mm diameter impactor consisting of three and four sided elements.

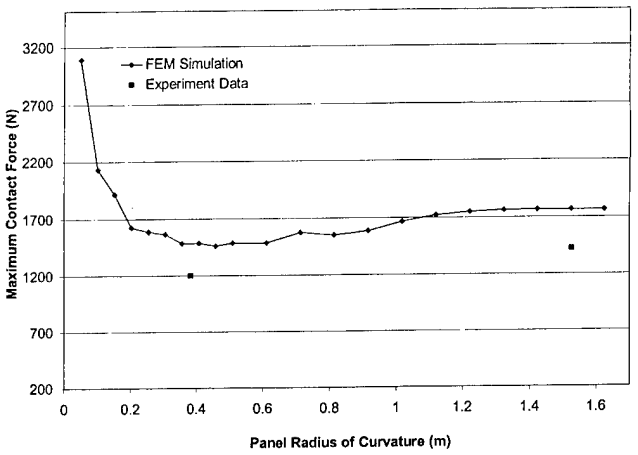

Fig. 4. Comparison of experimental data vs computer simulation results where impactor energy level is 2.03 J (impactor diameter is 12.7 mm and mesh density is 25×25).

Twenty composite impact simulations were conducted in order to compare explicit simulation results to experimental data published in [1]. The composite panel curvature ranged from 50.4 to 1625 mm. Fig. 4 shows a comparison of the experimental and simulation results. From this figure, it can be seen that the simulation provided quite accurate results. Note that the simulation results are for a 25×25 composite panel with an impactor energy of 2.03 J (mass is 1.134 kg and velocity is 1.89 m/s) and impactor diameter is 12.7 mm, hence the efficiency of computing resources and time is considered to be relatively high.

Simulation results exhibit the general trend expected in curved composite panel response, that is, for highly curved panels, the impact contact force is relatively high. As the radius of curvature increases, the impact contact force decreases then proceeds to take on a constant value. This is consistent with the experimental data published in [1]. It should also be noted that computer simulation results show a slightly conservative output, which further enhances its attractiveness in providing an efficient technique for modelling impact in practice.

6.2. Internal energy and composite curvature

Internal energy plots do not show the same trend that is seen in contact force diagrams. Fig. 5 is a typical internal energy vs time plot. The trend that is seen in this particular figure can be found in low impact simulations with varying panel curvature, mesh density and impactor size. Fig. 5 shows a "bell curve" response where the internal energy does not return to 0 J. This is due to the

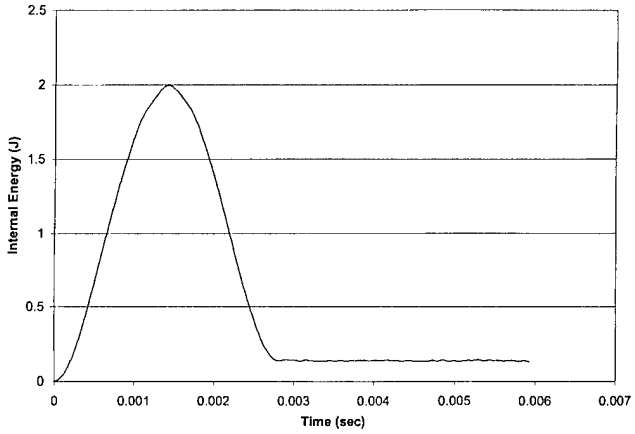

Fig. 5. Internal energy vs time for a composite panel with 101.6 mm radius of curvature (impactor diameter size is 12.7 mm and mesh density is 25×25).

fact that structural damping is assumed to be negligible when considering short period impact response and is not incorporated into the FE model.

As expected, the variation of maximum impact internal energy vs composite panel curvature is constant, as shown in Fig. 6. The maximum internal energy for a composite panel impacted with a 12.7 mm impactor at 2.03 J (mass = 1.134 kg, velocity = 1.89 m/s) having a 25×25 mesh density is approximately 2 J.

6.3. Impact time and composite panel radius of curvature

The impactor contact time response is inversely proportional to maximum contact force. Fig. 7 shows the variation of contact time as a function of composite panel radius of curvature. It shows that the contact time for small radii of curvature is very low. Contact times increase with panel radius of curvature, and reach a constant value at approximately 5 ms.

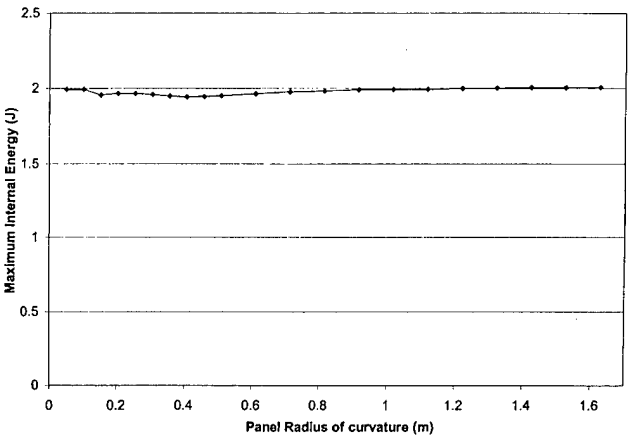

Fig. 6. Maximum internal energy vs composite panel curvature (impactor diameter is 12.7 mm and mesh density is 25×25).

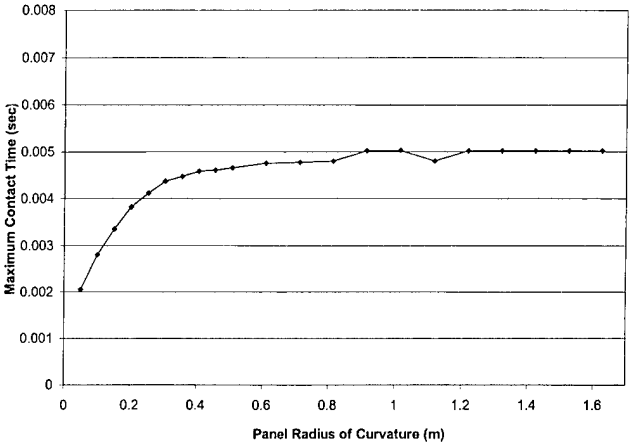

Fig. 7. Maximum contact time vs composite curvature (impactor diameter is 12.7 mm and mesh density is 25×25).

6.4. Mesh density effects on impact response

Impact energy and force response curves show composite panel modal fluctuations to occur at very high frequencies. Modal fluctuations are also observed in published experimental data [1–6]. The major differences between the computational solution and experimental data are the frequency and magnitude of the fluctuations. The FE solution shows smaller fluctuations with higher frequencies. This phenomenon may be associated with three factors: inaccuracies in the computational technique and the impact parameters employed; the composite model is not considered to have any structural damping; and impact response data are observed for a very short period of time and testing equipment may not be capable of observing such high frequency/low amplitude fluctuations. Also, results show that for higher impact energies and mesh densities, amplitude decreases and frequency increases. This trend also occurs in respect of composite panel curvature, that is, modal amplitude decreases and response frequency increases as composite panel radius of curvature decreases.

Another reason for observing such high frequency fluctuations may be related to the impactor modelling technique. Since the impactor was modelled as a rigid (no deformation) structure, the interaction between the composite panel and ball will not exactly represent the experimental case. The impactor does not deform hence the excitation load that the ball provides at each time-step will not exactly simulate experimental conditions. Since impact energy is relatively low and the study does not focus on accurately describing modal fluctuations, the impactor model was not altered. Such modifications would result in a very large trade-off against efficiency and computer resources.

Computer simulation shows that high mesh density does not improve the results dramatically. At low energy levels, the results are identical. However, instability is

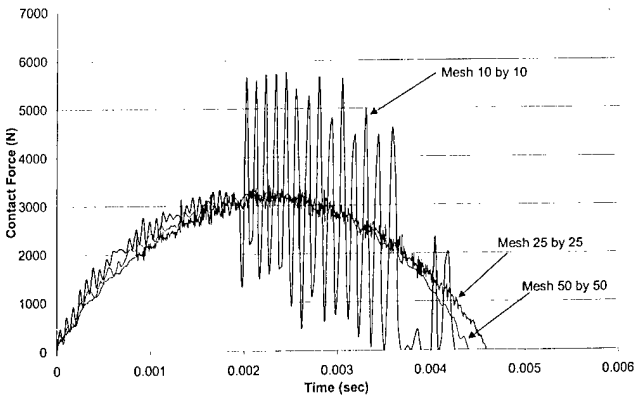

Fig. 8. Instability mode of a composite panel where impact energy is 6.25 J (impactor diameter is 6.35 mm and radius of curvature is 127 mm).

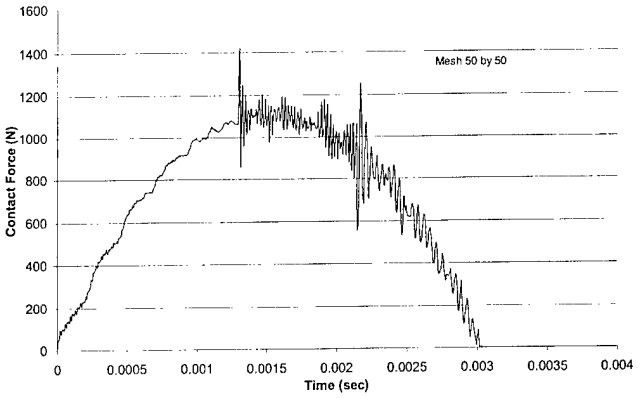

Fig. 9. Instability mode of a composite panel where impact energy is 0.5675 J (impactor diameter is 25.4 mm, 50×50 mesh density and radius of curvature is 127 mm).

observed with low mesh density at higher impact energy levels. This instability initiates at maximum contact force and propagates until there is no contact. Energy levels of 2.03 J and above were all unstable for composite structures having a 10×10 mesh density. This phenomenon can be seen in Fig. 8.

Another form of instability is also seen in composite panels having a 50×50 mesh structure which exhibit local/momentary instability that is not observed in panels with low mesh densities, as seen in Figs. 9 and 10. A local peak is observed around the maximum contact force region. This peak does not represent the general response of the structure. This trend is not seen in published experimental data [1–6]. The peaks seen in experimental data occur over a larger period of time. The response after a very large peak levels out into a stable solution. This phenomenon can be observed clearly in highly curved composite panels having large mesh densities. These localised peaks have been omitted from the investigation, as they do not represent true fibre composite panel behaviour. Plotting maximum contact force vs impact energy clearly shows this phenomenon.

Eliminating unstable solutions seen in panels having 10×10 mesh elements and localised peaks in 50×50 mesh panels yields a highly linear curve. Including these localised peaks shows the extent of instability and inaccuracy in the solution. It should be noted here that the unstable contact force solutions discussed above do not appear in the internal energy plot. The internal energy levels at contact force instability exhibit normal behaviour, that is, the random scatter observed in maximum contact force vs time is not seen in internal energy vs time. This holds true for flat, 127 and 762 mm radius composite panels.

6.5. Non-linear FE efficiency

The computing time associated with increasing the mesh density is observed to increase dramatically. The

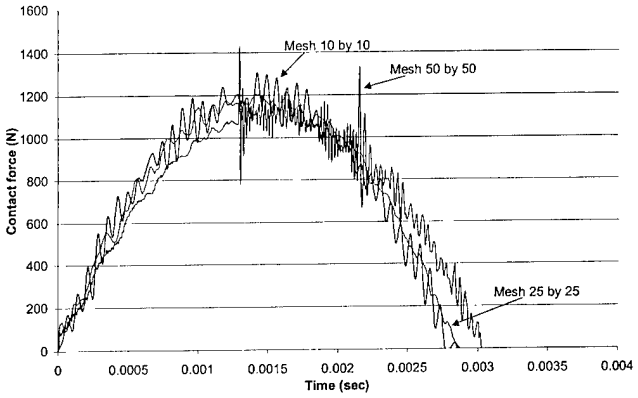

Fig. 10. Instability mode of a composite panel where impact energy is 0.5675 J (impactor diameter is 25.4 mm and radius of curvature is 127 mm).

use of finer meshed structures is therefore inefficient. It is found that a composite curved panel simulation takes 5 min for a 10×10 mesh, 25–35 min for a 25×25 mesh, and 240–360 min for a 50×50 mesh. Since there is almost no improvement in the simulation output, using a very fine mesh for contact energy and force calculations can not be justified. However, this may not be the case when internal stresses at given time intervals are required.

6.6. Critical parameters in impact damage

Impactor energy level and momentum are determined to be the critical parameters for maximum contact force and internal/distortional energy. As can be seen in Figs. 11 and 12, contact force varies approximately linearly with energy level and momentum (unstable points not included). The relationship between contact force and impact energy yields a response gradient of

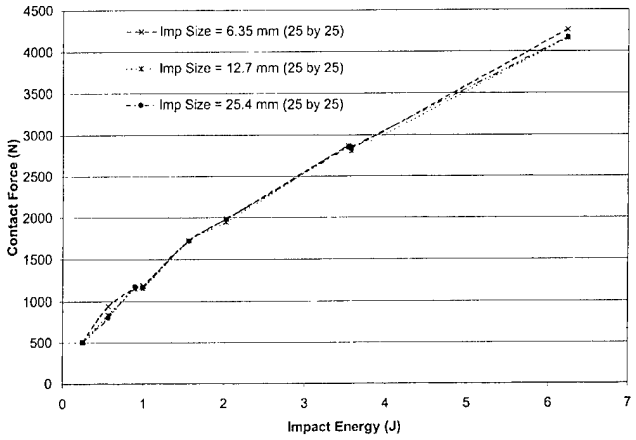

Fig. 11. Maximum contact force vs impact energy where mesh density is 25×25 and panel is flat.

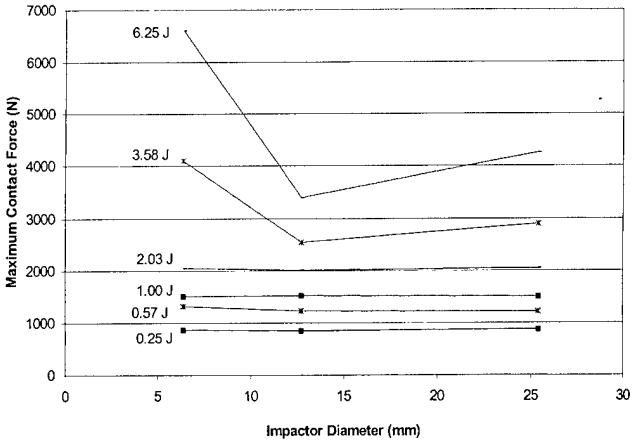

Fig. 13. Maximum impact force vs impact diameter where mesh density is 25×25 and composite panel is flat.

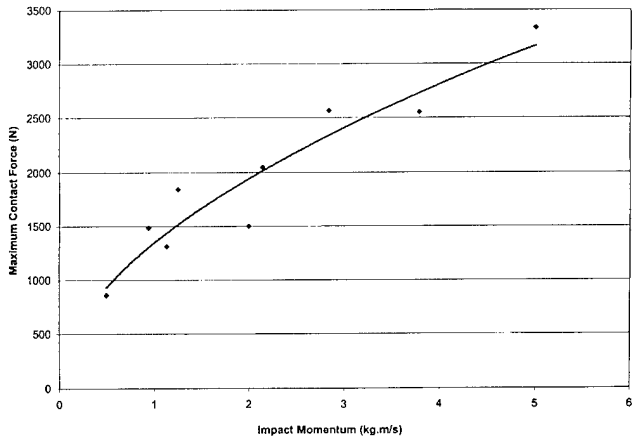

Fig. 12. Maximum contact force vs impact momentum (impactor diameter is 6.35 mm, mesh density is 25×25 and radius of curvature is 127 mm).

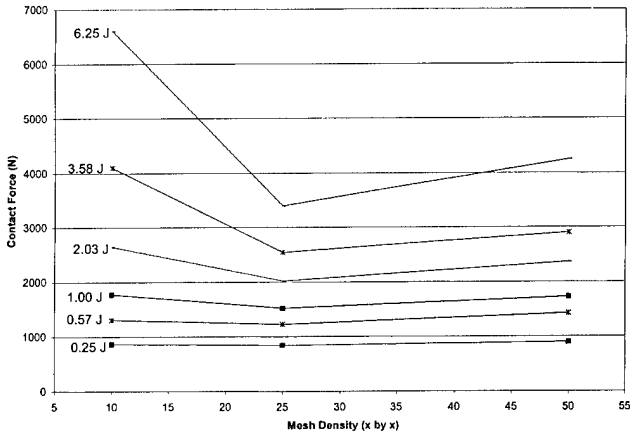

Fig. 14. Maximum contact force vs mesh density where impactor diameter is 12.7 mm and composite radius of curvature is 127 mm.

650–1100 N/J with scatter increasing with impact energy level. Various combinations of impactor mass and velocity have been used. Contact time between impactor and composite panel increases with mass. Impactor size does not alter contact time response.

6.7. *Effects of impactor size and mesh density on impact response*

The study looked at the effects of impactor geometry. The impactor is modelled as a rigid hollow sphere, which does not deform in any mode. The impactor mass is chosen without the need to alter material properties. Impactor diameters of 6.35, 12.7 and 25.4 mm were chosen. The impactor size did not alter maximum force, internal and kinetic energy. Fig. 13 shows a plot of maximum impact force vs impactor diameter for various curved composite panels and impact energy levels. A mesh density vs impact response curve shows that at low energy levels the impact response is constant; this trend can be seen up to approximately 2 J. Above this energy level, the impact response as a function of mesh density is more complex; Fig. 14 demonstrates this phenomenon.

A panel with a 10×10 mesh density produces larger maximum contact forces when compared to 25×25 and 50×50 mesh panels. This variation occurs at relatively high impact energy levels and is due to numerical instability; this can be seen in Fig. 8 for a 10×10 mesh instability. It is observed that the maximum contact forces for unstable solutions are relatively higher for 25×25 and 50×50 mesh panels. As the mesh density increases to 25×25, the maximum contact force reaches a minimum and then starts to increase again. Increasing mesh density refines the FE simulation process and the impact solution provides a stable and accurate values.

7. Conclusion

This study into non-linear FE analysis of low velocity impact on curved composite panels has shown that computer simulation can yield accurate and efficient results. This was shown to be true as results for FE analyses of curved panels closely matched data published in [1]. It was shown that for low radii of curvature, contact forces are relatively large. These impact forces reduce to a constant level as the panel radius of curvature increases. The relative element ratio of impactor and composite panel mesh plays an important role in obtaining sound impact response data, as various modes of instability were observed. Computational time and efficiency dropped significantly with large mesh structures. The investigation looked at a relatively small component of composite impact damage and the modelling technique that can be used to study such behaviour. However, this research has demonstrated that non-linear FE analysis can be used as an accurate and efficient tool in modelling low energy impact response of curved fibre composite structures.

References

[1] Ambur DR, Starnes JH. Effect of curvature on the impact damage characteristics and residual strength of composite plates, AIAA 98-1881, April 1998.
[2] Cantwell WJ, Morton J. The influence of varying projectile mass on the impact response of CFRP. Compos Struct 1989;13:101–14.
[3] Delfosse D, Poursartip A, Coxon BR, Dost EF. Non-penetrating impact behavior of CFRP at low and intermediate velocities. In: Martin RH, editor. Composite Materials: Fatigue and Fracture – Fifth Volume, ASTM STP 1230, American Society for Testing and Materials, Philadelphia, 1995, pp. 333–50.
[4] Jackson KE, Fasanella EL. Crashworthy Evaluation of a 1/5-Scale Model Composite Fuselage Concept, NASA/TM-1999-209132, April 1999.
[5] McGowan DM, Ambur DR. Compression Response of a Sandwich Fuselage Keel Panel With and Without Damage, NASA Technical Memorandum 110302, February 1997.
[6] Palazotto A, Perry R, Sandhu R. Impact response of graphite–epoxy cylindrical panels. AIAA J 1992;30(7):1827–32.
[7] Annon., MSC/DYTRAN User's Manual Version 4, The MacNeal–Schwendler Corporation, Los Angeles, CA, 1997.

ELSEVIER

Composite Structures 47 (1999) 797–804

COMPOSITE STRUCTURES

www.elsevier.com/locate/compstruct

Micromechanics models for the elastic constants and failure strengths of plain weave composites ☆

Ping Tan, Liyong Tong *, Grant P. Steven

Department of Aeronautical Engineering, University of Sydney, Bldg J07, Sydney, NSW 2006, Australia

Abstract

In this paper, two models are presented for plain weave composites. One is finite element analysis (FEA) model for elastic constants, namely, sinusoidal yarn model. Another is analytical model for failure strengths, namely, sinusoidal beam model. The FEA model is generated by interfacing an in-house computer code with FEA software strand6, and the analytical model is developed using the theory of elasticity. Numerical studies are carried out using the present models to investigate the effects of some major geometrical parameters on the properties of plain weave composites. It is concluded that the failure strengths are closely related to the fiber volume fraction of a yarn, and the mechanical properties are closely related to the overall fiber volume fraction of the composites. An experimental testing program is conducted for T300/934 plain weave composites to validate the developed models. A good agreement exists between the predicted and measured results. © 2000 Elsevier Science Ltd. All rights reserved.

Keywords: Sinusoidal yarn model; Sinusoidal beam model; Elastic constant; Failure strength; Plain weave composites; FEA model

1. Introduction

Composite materials have been increasingly used in modern structural designs that require the components and structures with special material properties. To tailor the composites to these specific requirements, it is necessary to evaluate their mechanical properties and failure strengths for a wide range of the architecture parameters. Analytical and finite element analysis (FEA) models provide a cost-effective tool to determine the mechanical properties and failure strengths, as well as to investigate the effects of some major geometrical parameters on the mechanical behavior for composites. The objective of the research work reported in this paper is the development of the FEA and analytical models for prediction of the elastic constants and failure strengths for plain weave composites.

Earlier researches on two-dimensional (2D) woven fabric-reinforced composites were carried out by Ishakawa and Chou [1–4]. These works were basically restricted to one-dimension. Later, various analytical methods and FEA models for predicting mechanical properties of 2D woven composites were developed, including one-dimensional (1D) model [5]; 2D models [6–8], and three-dimensional (3D) model [9,10]. In these 3D models, the crimps in plain weave composites were introduced through the angular yarn paths, whereas a smooth curve would be more realistic.

In this paper, a 3D FEA model, namely sinusoidal yarn model, is presented for prediction of elastic constants of plain weave composites. This 3D FEA model is capable of producing a 3D representation and visualization of any plain weave unit cell, and can be extended to establish the model for predicting failure strength for plain weave composites. Thus, an analytical model, namely, sinusoidal beam model, is also proposed in this paper. This analytical model is used in conjunction with the maximum stress criterion, and employed to investigate the effects of some major geometrical parameters on failure strengths for T300/934 plain weave composites. Both sinusoidal yarn and beam models are developed based on the plain weave unit cell and validated via the corresponding experimental results.

2. Sinusoidal yarn model for elastic constants of plain weave composites

In order to predict the elastic constants for plain weave composites more accurately, a flexible 3D FEA

☆ This work has been carried out as part of the CRC-ACS Ltd. research program

* Corresponding author. Tel.: +61-2-9351-6949; fax: +61-2-9351-4841.

E-mail address: ltong@aero.usyd.edu.au (L. Tong).

0263-8223/99/$ - see front matter © 2000 Elsevier Science Ltd. All rights reserved.
PII: S0263-8223(00)00056-8

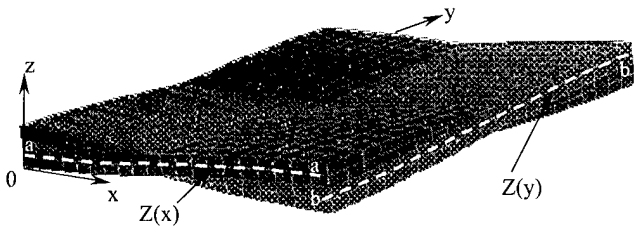

Fig. 1. 3D FEA mesh for a plain weave unit cell (removing the matrix from the model).

model, namely sinusoidal yarn model, is developed under the iso-strain assumption. This model is established at the yarn level. The yarn path is chosen to be sinusoidal, and a strictly lenticular cross-section formed by two sinusoidal curves is utilized in this model. The FEA mesh of the model is generated by interfacing an in-house computer code with the FEA software Strand6 [11] using eight-node brick and six-node wedge elements (see the FEA mesh in Fig. 1). The central line path for a warp yarn (e.g., white dashed curve a–a in Fig. 1) and that for a weft yarn (e.g., white dashed curve b–b in Fig. 1) can be expressed as

$$Z(i) = \frac{l_z}{4}\sin\left(\frac{\pi i}{l_i} - \frac{\pi}{2}\right) + \frac{l_z}{2} \tag{1}$$

($i = x$ for a warp yarn, $i = y$ for a weft yarn).

Some major parameters for plain weave composites, e.g., impregnated yarn orientation, fiber volume fraction, and mechanical properties of composite constituents are included in the model. The required geometrical parameters for a plain weave unit cell can be evaluated by averaging the data measured from the scans of the realistic cross-sections, which were obtained using the image analysis system and Iphoto Plus software.

The mechanical properties for the plain weave composite constituents are assumed to be homogeneous, and isotropic for matrix and orthotropic for impregnated fiber yarns with respect to their principal material axes. The elastic constants of an impregnated yarn can be obtained using the micromechanics equations proposed by Chamis [12], fiber volume fractions of yarns, and the mechanical properties of composite constituents. Hence, following the similar analysis procedure, boundary conditions, and strain vectors used for the undulated or angular yarn FEA models developed previously [10], the required elastic constants for plain weave composites can be evaluated using the present sinusoidal yarn model.

Except for the elastic constants, failure strength is another important parameter required in practical structure design. In the following section, an analytical model is proposed to predict the failure strengths of plain weave composites.

3. Sinusoidal beam model for failure strengths of plain weave composites

In this section, development of a sinusoidal beam model is briefly described, and the numerical study is conducted for investigating the effects of some major geometrical parameters on the failure strengths of plain weave composites.

3.1. Model development

Fig. 2 shows a schematic of the sinusoidal beam model, in which the warp yarn is considered to be a sinusoidal beam. This beam is subject to an external load P_x at each end of the warp yarn (i.e., sinusoidal beam) and supported by an elastic foundation, which is introduced to model the supporting effect of the matrix. As an approximation, both ends of the warp yarn are assumed to be simply supported, i.e., the deflection and bending moment at both ends are zero. Two continuity conditions (i.e., the same deflection and the same slope) must be satisfied at each end of the warp yarn. Based on the sinusoidal beam model shown in Fig. 2, we obtain

$$-E_w(x)I_w(x)\left[\frac{d^4W(x)}{dx^4} - \frac{d^4W_0(x)}{dx^4}\right] + P_x\frac{d^2W(x)}{dx^2} - K(x)[W(x) - W_0(x)] = 0, \tag{2}$$

where P_x is the external loading along the x direction, $W_0(x)$ and $W(x)$ are, respectively, the deflection of the warp yarn prior to loading and after loading, $E_w(x)$ is the longitudinal Young's modulus of a warp yarn, and $I_w(x)$ is the second moment of cross-sectional area of a warp yarn. $K(x)$ is the equivalent constant of the elastic foundation. All of these parameters are the functions of the coordinate (x).

The normal stress acting on the cross-section of the sinusoidal beam consists of two parts, i.e., uniform normal tensile stress across the beam cross-section $\sigma_{tw}(x)$, and the linearly distributed bending stress $\sigma_{bw}(x,y)$. The maximum bending stress in the sinusoidal beam is given by

$$\sigma_{bw}(x,y) = \frac{M(x)}{2I_w(x)}T_{max}(x,y), \tag{3}$$

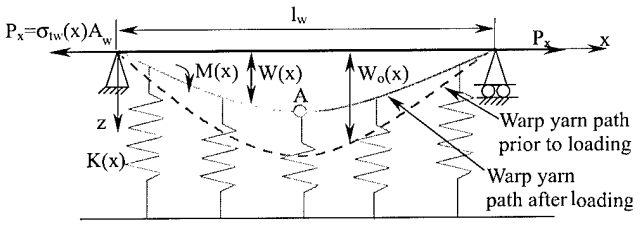

Fig. 2. A schematic of a sinusoidal beam model.

where $T_{\max}(x,y)$ is the maximum thickness of the sinusoidal beam at the coordinate (x, y).

The normal tensile stress $\sigma_{tw}(x)$ is obtained by

$$\sigma_{tw}(x) = \frac{P_x}{A_w(x)}, \tag{4}$$

where $A_w(x)$ is the sinusoidal beam cross-sectional area located at the coordinate (x).

Hence, the maximum normal stress acting on the cross-section of a sinusoidal beam at the coordinate (x, y) is

$$\sigma_{wmax}(x,y) = \sigma_{tw}(x) + \sigma_{bw}(x,y) = \frac{P_x}{A_w(x)} + \frac{M(x)}{2I_w(x)} T_{\max}(x,y). \tag{5}$$

When $\sigma_{wmax}(x,y)$ attains the ultimate longitudinal tensile strength for a warp yarn, σ_{lt}^{w}, the composite material is considered to fail at the coordinate (x, y). Therefore, for plain weave composites, the failure criterion under the tensile loading in the x direction is

$$\frac{P_x}{A_w(x)} + \frac{M(x)}{2I_w(x)} T_{\max}(x,y) = \sigma_{lt}^{w}. \tag{6}$$

3.2. Assumptions and geometrical parameters

As noticed from the formulas used in the sinusoidal beam model, a number of important parameters should be measured and evaluated before predicting the failure strength in the x or warp yarn direction. These parameters are the warp yarn paths, $W_0(x)$ and $W(x)$, longitudinal Young's modulus for a warp yarn, $E_w(x)$, cross-sectional parameters, $A_w(x)$, $I_w(x)$ and $T_{\max}(x,y)$, the equivalent constant of the elastic foundation, $K(x)$ and the ultimate longitudinal failure strength of a warp yarn under the tensile loading, σ_{lt}^{w}.

On the basis of the assumptions in the sinusoidal yarn model developed above, the warp yarn paths prior to and after loading can be obtained, respectively, by

$$W_0(x) = h_0 \sin\frac{\pi x}{l_w}, \tag{7}$$

$$W(x) = h \sin\frac{\pi x}{l_w}, \tag{8}$$

where h_0 and h are, respectively, the maximum amplitudes of the deformed warp yarn segment prior to and after loading, and l_w is the warp yarn span length.

The cross-sectional area for a warp yarn is assumed to be constant in the present investigation for simplifying the calculation and given by

$$A_w = A_w(x) = \int_{-l_f/2}^{l_f/2} [Z_1(y) - Z_2(y)]\,dy, \tag{9}$$

where $Z_1(y)$ and $Z_2(y)$ are the functions for two sinusoidal curves shown in Fig. 3, which are consistent with those used in the sinusoidal yarn model. The expressions for $Z_1(y)$ and $Z_2(y)$ are

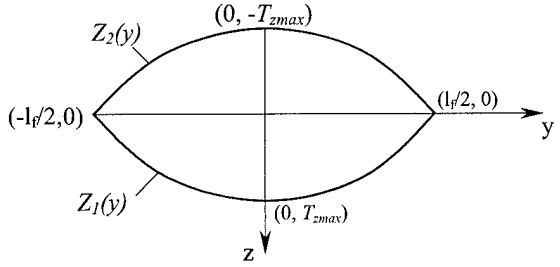

Fig. 3. A schematic of a warp yarn cross-sectional shape.

$$Z_1(y) = T_{z\max} \sin\left(\frac{\pi y}{l_f} + \frac{\pi}{2}\right), \tag{10}$$

$$Z_2(y) = -T_{z\max} \sin\left(\frac{\pi y}{l_f} + \frac{\pi}{2}\right), \tag{11}$$

Substituting Eqs. (10) and (11) into (9), we obtained

$$A_w = 2\int_{-l_f/2}^{l_f/2} T_{z\max} \sin\left(\frac{\pi y}{l_f} + \frac{\pi}{2}\right) dy = \frac{4T_{z\max} l_f}{\pi}, \tag{12}$$

where l_f is the width of the warp yarn.

Due to the assumption of constant yarn cross-section, $I_w(x)$ can also be considered to be an invariant, I_w, and $T_{\max}(x,y)$ is considered to be a function of coordinate (y). Hence, the second moment of cross-sectional area of a warp yarn is obtained by

$$I_w = \int_A z^2\,dA = \int_{-l_f/2}^{l_f/2} \int_{Z_2(y)}^{Z_1(y)} z^2\,dz\,dy = \frac{8 l_f T_{z\max}^3}{9\pi}. \tag{13}$$

The maximum thickness of the warp yarn located at the coordinate (y), $T_{\max}(y)$, is given by

$$T_{\max}(y) = 2Z_1(y). \tag{14}$$

For the sake of simplifying the calculation, the equivalent constant of the elastic foundation, $K(x)$, is considered to be invariable K and should be a function of the warp yarn width. It can be evaluated by

$$K = K(x) = E_m \times l_f. \tag{15}$$

Since the mechanical property of a warp yarn is assumed to be homogenous and orthotropic with respect to its principal axes, the longitudinal Young's modulus of a warp yarn $E_w(x)$ is considered to be a constant, E_w.

3.3. Longitudinal and transverse failure strengths

Based on the above assumptions and geometrical parameters, Eq. (2) can be represented as

$$-E_w I_w h\left(\frac{\pi}{l_w}\right)^4 + E_w I_w h_0\left(\frac{\pi}{l_w}\right)^4 - \sigma_{tw}(x)A_w h\left(\frac{\pi}{l_w}\right)^2 - E_m l_f h + E_m l_f h_0 = 0. \quad (16)$$

Rearranging the above equation gives

$$h = \frac{E_w I_w\left(\frac{\pi}{l_w}\right)^4 + E_m l_f}{E_w I_w\left(\frac{\pi}{l_w}\right)^4 + \sigma_{tw}(x)A_w\left(\frac{\pi}{l_w}\right)^2 + E_m l_f} h_0. \quad (17)$$

Since the bending moment in the warp yarn segment is obtained using

$$M(x) = -E_w I_w\left[\frac{d^2W(x)}{dx^2} - \frac{d^2W_0(x)}{dx^2}\right] = -E_w I_w\left[-\frac{h\pi^2}{l_w^2} + \frac{h_0\pi^2}{l_w^2}\right]\sin\frac{\pi x}{l_w}. \quad (18)$$

By substituting Eq. (17) into (18), we obtain

$$M(x) = -\frac{E_w I_w\left(\frac{\pi}{l_w}\right)^4 \sigma_{tw}(x)A_w h_0 \sin\frac{\pi x}{l_w}}{E_w I_w\left(\frac{\pi}{l_w}\right)^4 + \sigma_{tw}(x)A_w\left(\frac{\pi}{l_w}\right)^2 + E_m l_f}. \quad (19)$$

Hence, the maximum tensile stress caused by $M(x)$ is

$$\sigma_{bw}(x) = \frac{T_{z\,max}E_w\left(\frac{\pi}{l_w}\right)^4 \sigma_{tw}(x)A_w h_0}{E_w I_w\left(\frac{\pi}{l_w}\right)^4 + \sigma_{tw}(x)A_w\left(\frac{\pi}{l_w}\right)^2 + E_m l_f}\sin\frac{\pi x}{l_w}, \quad (20)$$

which is located at $z = -T_{z\,max}$ (see Fig. 3).

Assuming

$$\sigma_{tw}(x) = \frac{\sigma_x}{V_{A_w}}, \quad (21)$$

Where σ_x is the external stress applied to the specimen in the warp yarn or x direction, V_{A_w} is the overall cross-sectional area fraction of the warp yarn on the unit cell cross-section perpendicular to the x axis, and given by

$$V_{A_w} = \frac{A_w}{l_z l_y}, \quad (22)$$

where l_y and l_z are, respectively, the unit cell dimensions in the y and z directions.

Substituting the required parameters into the failure criterion (i.e., Eq. (6)), we obtain

$$\frac{\sigma_x}{V_{Aw}} + \frac{T_{z\,max}E_w\left(\frac{\pi}{l_w}\right)^4 \frac{\sigma_x}{V_{Aw}}A_w h_0}{E_w I_w\left(\frac{\pi}{l_w}\right)^4 + \frac{\sigma_x}{V_{Aw}}A_w\left(\frac{\pi}{l_w}\right)^2 + E_m l_f}\sin\frac{\pi x}{l_w} = \sigma_{1t}^w. \quad (23)$$

Therefore, for any given location x_0, the corresponding ultimate tensile stress can be obtained using Eq. (23). Along the whole length of a warp yarn segment, a minimum value of the applied stress $\sigma_{x\,min}$ can be identified together with the corresponding location. This minimum stress $\sigma_{x\,min}$ is chosen to be the longitudinal tensile failure strength in the x or warp yarn direction for plain weave composites, and the corresponding location is regarded as where the initial failure occurs when the specimen supports the axial loading in the x direction. It is noted that the initial failure occurs at point A in Fig. 2. This finding is consistent with that using 3D macro/micro FEA modeling approach developed previously [13]. The above analytical procedure can also be extended to predict the transverse failure strength in the weft yarn or y direction for plain weave composites.

3.4. Parametric study

In order to investigate the effects of some major geometric parameters on the failure strengths for plain weave composites, Eq. (23) is employed for the T300/934 plain weave composite under the tensile loading. The relevant mechanical properties and failure strengths of the composite constituents are, respectively, listed in Tables 1 and 2, and the required geometrical parameters are listed in Table 3. In Table 3, the unit cell length l_x and unit cell width l_y were obtained by averaging those measured from the realistic cross-sections of T300/934 plain weave composites. The unit cell thickness l_z was calculated by dividing the specimen thickness with the lamina layer number. The maximum amplitudes of the deformed yarn segment prior to loading h_0 was chosen to be a quarter of l_z (i.e., $l_z/4$). The values for $T_{z\,max}$, l_w and l_f are, respectively, chosen to be the same as h_0, l_x, l_y. Based on these data, the failure strengths for the T300/934 plain weave composites can be obtained using the sinusoidal beam model developed above.

Table 1
Elastic constants of constituents and impregnated yarn for T300/934 plain weave composites [14][a]

Composite constituents	Material	E_1 (GPa)	E_2 (= E_3) (GPa)	G_{12} (= G_{13}) (GPa)	G_{23} (GPa)	ν_{12} (= ν_{13})	ν_{23}
Fiber	(T300)	220	13.8	11.35	5.5	0.2	0.25
Matrix	Epoxy resin (934)	4.1	4.1	1.454	1.454	0.41	0.41
Impregnated yarn	(T300/934)	173.11	10.84	6.361	4.165	0.246	0.302

[a] Subscripts 1, 2 and 3 indicate the quantities in the longitudinal, transverse and through-the-thickness directions, respectively.

Table 2
Failure strengths for the plain weave composite constituents [13,15]

Composite constituents	Materials	Longitudinal tensile failure strength σ_{1t} (MPa)	Transverse tensile failure strength σ_{2t} (MPa)
Fiber	T300	3102.3	74.93
Matrix	Epoxy resin 934	27.6	27.6
Impregnated yarn	T300/934	2428.48	58.66

Table 3
Geometrical parameters for T300/934 plain weave composites [14]

l_x (mm)	l_y (mm)	l_z (mm)	h_0 (mm)	$T_{z\max}$ (mm)	l_w (mm)	l_f (mm)	V_f^o (%)
2.1 ± 0.13	2.1 ± 0.13	0.22	0.055	0.055	2.1	2.1	50.1

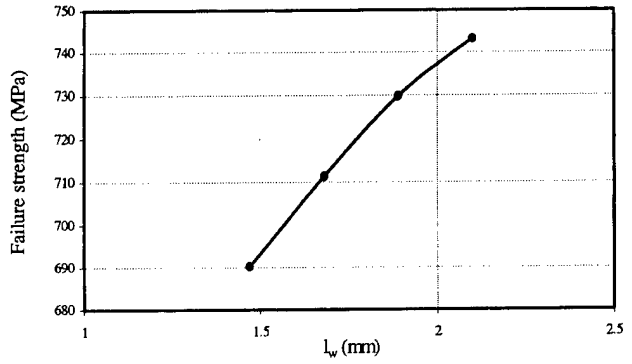

Fig. 4. The predicted tensile strength vs. the warp yarn span length l_w.

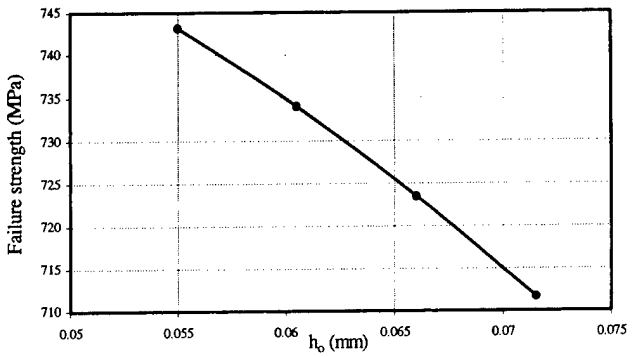

Fig. 5. The predicteds tensile strength vs. the maximum amplitude of the initial deflection h_0.

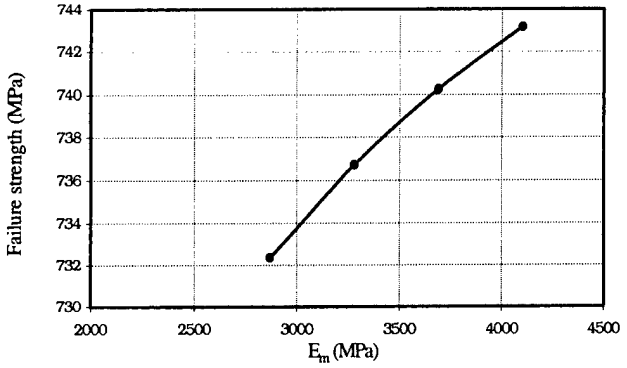

Fig. 6. The predicted tensile strength vs. the Young's modulus of matrix E_m.

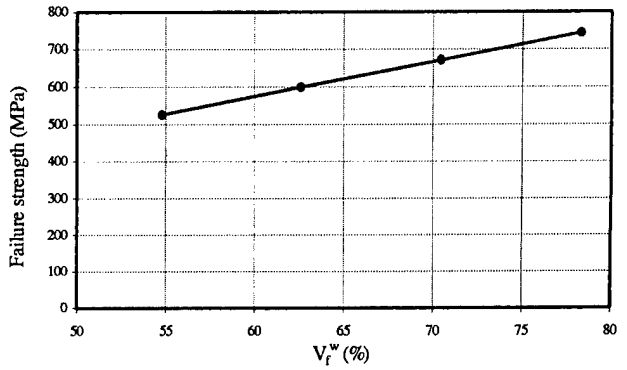

Fig. 7. The predicted tensile strength vs. the fiber volume fraction of warp yarn V_f^w.

Figs. 4–7 show, respectively, the variation trends of the failure strength in the x direction vs. l_w, h_0, E_m and V_f^w. From these figures, it is noted that 30% decrease in l_w results in a 7% decrease in the longitudinal failure strength for the sinusoidal beam along the x direction. A 30% increase in h_0 causes a 4.2% decrease in the failure strength. These findings are reasonable since the reduction of l_w and increase in h_0 lead to a further curved beam, in which the maximum bending stress becomes more important. The influence of E_m is slight. For example, the failure strength only increases 1.5% when E_m increases 42.86%. This is evident since when E_m or the elastic constant of the equivalent foundation increases, the foundation becomes stiffer and deflection produced by the external force is smaller than that on a soft foundation. This small deflection causes smaller bending stress, which further causes greater failure strength. However, the effect of the fiber volume fraction of warp yarn V_f^w is significant. A 42.86% increase in V_f^w results in 41.33% increase in the failure strength in the x direction,

Table 4
Lay-up sequence and thickness of laminate specimens

Specimen group	Stack sequence	Thickness of laminates (mm)	Purpose	Number of specimens
x-type	$[0°]_8$	1.75	Test for E_1, ν_{12}, σ_{1t}	6
y-type	$[90°]_8$	1.75	Test for E_2, σ_{2t}	6
xy-type	$[+45°/-45°]_{4s}$	1.75	Test for G_{12}	6

since it yields 42.86% increase in the ultimate longitudinal failure strength and 41.43% increase in the longitudinal Young's modulus for a warp yarn. This results in higher failure strength in the x direction for plain weave composites.

4. Experimental investigation

In order to validate the sinusoidal yarn model and sinusoidal beam model developed above, 18 tests were carried out for T300/934 plain weave composites. The specimen preparation, testing procedure, experimental results, and comparisons between the predicted and measured results are discussed in this section.

4.1. Specimen preparation and testing procedure

In this experimental investigation, two panels were made from T300/934 (3K-70-PW) graphic/epoxy prepreg woven fabrics. These panels were produced by laminating eight layers of the prepreg woven fabric sheets to produce the required specimen thickness about 1.75 mm. The stacking sequence of laminate specimens is balanced and symmetric. The panel laid up in 0° is used to investigate the in-plane Young's moduli, Poisson's ratio, as well as failure strengths in the x and y directions, and that in +45°/−45° is used to evaluate the in-plane shear modulus. The lay-up sequence and the thickness of the laminate specimens are listed in Table 4, where the *x-type* and *y-type* specimens were obtained by cutting the 0° panel along the warp and weft yarn directions, respectively. For the *xy-type* specimens, they were cut from the +45°/−45° Panel along the 45° with respect to the warp yarn direction. All specimens laminated from prepreg plain weave fabric sheets were cured in an autoclave following a curing cycle reported in Ref. [14].

The configuration of the specimens is in accordance with the ASTM D 3039-76 [16]. A strain gauge with $120 \pm 0.3\ \Omega$ gauge resistance and $2.13 \pm 1\%$ gauge factor was located at the middle length of a specimen. This strain gauge can be used for measuring the strains in both the longitudinal and transverse directions. Static tension tests were performed by Instron machine. The specimens were tested at a room temperature (26°C) and at a cross-head speed of 1 mm/min. Two computer data acquisition systems, driven by the software packages Instron Merlin and Labview were, respectively, used to record the cross-head movement, the applied axial load and the strain gauge readings. The Instron Merlin software package was used to collect the cross-head movement and applied load. The Labview software was used to measure the four channel strain gauges in addition to the cross-head movement and the applied load. The cross-head movement and the applied load were recorded by both systems for the purpose of cross checking.

4.2. Testing results and comparison

Table 5 tabulates the testing results for the in-plain Young's modulus E_1 and E_2, Poisson's ratio ν_{12}, shear modulus G_{12}, tensile failure strength σ_{1t} (i.e., σ_{xt}) and σ_{2t} (i.e., σ_{yt}) of T300/934 plain weave composites. The geometrical parameters for a T300/934 plain weave unit cell and the overall fiber volume fraction V_f^o are the same as those listed in Table 3, in which the overall fiber volume fraction V_f^o was evaluated using the following equation

$$V_f^o = \frac{N \times \rho_A}{T \times D}, \tag{24}$$

where N is the number of ply for the laminate specimen, ρ_A the fiber area weight (g/m^2), D the fiber density (g/cc) and T is the thickness of laminate specimen [17]. For T300/934 plain weave composites used in this testing investigation, N, T, ρ_A and D are, respectively, equal to 8, 1.75 mm, 194 g/m^2 and 1.77 g/cc [18].

Using the sinusoidal yarn model, the elastic constants for a T300/934 plain weave unit cell can be predicted based on the unit cell geometrical parameters in Table 3 and the mechanical properties of the composite constituents in Table 1, then they are tabulated in Table 6. These predicted values are compared favorably with those available in Ref. [19], and the present testing

Table 5
Measured elastic constants and failure strengths for T300/934 plain weave composites

	E_1, E_2 (GPa)	ν_{12}	G_{12} (GPa)	σ_{1t}, σ_{2t} (MPa)
Min.	58.19	0.042	4.04	477.37
Avg.	59.43	0.049	4.35	515.05
Max.	62.03	0.052	4.51	585.27
S.D.	1.37	0.003	0.17	45.80

Table 6
Comparisons of the elastic constants for T300/934 plain weave composites

Item	E_1 (GPa)	E_2 (GPa)	E_3 (GPa)	ν_{12}	ν_{13}	ν_{23}	G_{12} (GPa)	G_{13} (GPa)	G_{23} (GPa)
FEA model $V_f^v = 50.1\%$	56.5	56.5	10.18	0.043	0.45	0.45	4.28	2.86	2.86
Test	59.4	59.4	–	0.049	–	–	4.353	–	–
Ref. [19]	53.09–60.67	53.09–60.67	–	0.05	–	–	3.1–6.205	–	–

Table 7
Comparisons of the failure strength for T300/934 plain weave composites

Plain weave	Sinusoidal beam model	Test
Failure strength (MPa)	743.16	515.05 ± 45.80

results. The differences between the present predicted and experimental results are 4.9% for E_1 and E_2, 12.2% for ν_{12} and 1.7% for G_{12}. The differences between predicted results and the average values reported in Ref. [19] are 0.7% for E_1 and E_2, 14% for ν_{12} and 8% for G_{12}.

By employing the sinusoidal beam model (i.e., Eq. (23)), and the data listed in Tables 2 and 3, the tensile failure strength for plain weave composites are obtained. They are listed in Table 7 and compared with the present testing results. From Table 7, it is noted that the sinusoidal beam model overestimates the failure strength for T300/934 plain weave composites. One of the major reasons is that for a realistic yarn segment, its cross-sectional area may be quite different from the ideal yarn cross-sectional area used in the present models. For example, the average yarn cross-sectional area obtained by averaging the data measured from the realistic yarn cross-sections is generally greater than that used in the present models, i.e., sinusoidal yarn model and sinusoidal beam model. Thus, in these models, the fiber volume fraction in a sinusoidal yarn or beam should be selected to be larger than that in a realistic yarn in order to keep the overall fiber volume fraction in the present models to be the same as that for a realistic composite. This causes a larger longitudinal Young's modulus and ultimate tensile failure strength of a yarn to be employed in the present sinusoidal beam model, which may be the major reason that the sinusoidal beam model overestimates the failure strength for plain weave composites. In addition, the maximum amplitudes of the realistic deformed warp or weft yarn segment prior to loading h_0 are generally larger than that used in the present model, which was obtained by dividing the specimen thickness by four times of the layer number. Hence, in order to predict the failure strength of plain weave composite more correctly, a nominal yarn fiber volume fraction V_f^n, is introduced and obtained by

$$V_f^n = \frac{V_f' \times A_y}{A_y^n}, \tag{25}$$

where A_y^n is the nominal yarn cross-sectional area and equal to 0.166 mm^2 for the T300/934 plain weave composites used, which was obtained by averaging the cross-sectional areas measured from the realistic yarn cross-sections. V_f' is the yarn fiber volume fraction used in the sinusoidal yarn model and equal to 78.28%, which was evaluated based on the unit cell geometry and the total fiber volume fraction of plain weave composites. A_y is the yarn cross-sectional area used in the sinusoidal yarn model and equal to 0.147 mm^2. These data (i.e., V_f', and A_y) were also used in the sinusoidal beam model above. Based on these data, the nominal fiber volume fraction of a yarn for the T300/934 plain weave composites can be obtained and equal to 69.3%. Hence, using the relevant equations, the longitudinal Young's modulus and failure strength for a warp yarn are obtained, and equal to 153.7 GPa and 2150.33 MPa, respectively. By employing Eq. (12), the geometrical parameter $T_{z\max}$ can be evaluated based on the nominal warp yarn cross-sectional area A_y^n, and equal to 0.0621 mm. The nominal thickness of unit cell l_z is chosen to be four times of $T_{z\max}$, and the nominal maximum amplitudes of the deformed warp yarn segment prior to loading h_0 is assumed to be the same as $T_{z\max}$. Based on these nominal data, the corresponding failure strength for T300/934 plain weave composite is re-calculated using the present sinusoidal beam model, and equal to 651 Mpa. The difference between this predicted and testing results is 26%.

5. Conclusions

A sinusoidal yarn model and a sinusoidal beam model are developed to predict the elastic constants and failure strengths of plain weave composites, respectively. The numerical study using the sinusoidal beam model reveals that the failure strength in the warp yarn direction increases with the increase in the warp yarn span length and decrease in the maximum amplitude of initial warp yarn deflection prior to loading. The increases in Young's modulus of matrix, fiber volume fraction of a yarn, longitudinal Young's modulus and ultimate tensile

failure strength for a yarn yield the increase in the failure strength. In addition, it is noted from the numerical study that for the composite materials, the elastic constants are closely related to the overall fiber volume fraction of the composite, and the failure strength is closely related to the fiber volume fraction of a yarn.

For qualitatively verifying the presented models, eighteen T300/934 plain weave specimens are tested. It is noted that a reasonably good agreement existed between the predicted and measured results.

Acknowledgements

Ping Tan is supported by an Australian Postgraduate Award (APA), a Supplementary Scholarship in the Aeronautical Engineering Department of the University of Sydney and CRC-ACS Supplementary Scholarship. She would like to thank Mr Radu Turcanu for the assistance provided in the experimental test.

References

[1] Ishikawa T, Chou TW. Elastic behaviour of woven hybrid composites. Journal of Composite Material 1982;16(1):2–19.

[2] Ishikawa T, Chou TW. In-plane thermal expansion and thermal bending coefficients of fabric composites. Journal of Composite Material 1983;17(2):92–104.

[3] Ishikawa T, Chou TW. One-dimensional micromechanical analysis of woven fabric composites. AIAA Journal 1983;21(1):1714–21.

[4] Ishikawa T, Chou TW. Nonlinear behaviour of woven fabric composites. Journal of Composite Material 1983;17(5):399–413.

[5] Zhang YC, Harding J. A numerical micromechanics analysis of the mechanical properties of a plain weave composite. Computer and Structures 1990;36(5):839–44.

[6] Naik NK, Shembekar PS. Elastic behaviour of woven fabric composites: I – Lamina analysis. Journal of Composite Material 1992;26(15):2197–225.

[7] Shembekar PS, Naik NK. Elastic behaviour of woven fabric composites: II – Laminate analysis. Journal of Composite Material 1992;26(15):2226–46.

[8] Naik NK, Shembekar PS. Elastic behaviour of woven fabric composites: III – Laminate design. Journal of Composite Material 1992;26(17):2523–41.

[9] Hewitt JA, Brown D, Clarke RB. Computer modelling of woven composite materials. Composites 1995;26:134–40.

[10] Tan P, Tong L, Steven GP. A 3D modeling technique for predicting the linear elastic properties of opened-packing woven fabric unit cell. Composite Structures 1997;38(1-4):261–71.

[11] STRAND6 reference manual and user guide. Sydney, Australia: G + D Computing Pty Ltd, September 1993.

[12] Chamis CC. Simplified composite micromechanics equations for hygral, thermal, and mechanical properties. SAMPE Quarterly, April 1984:14–23.

[13] Tan P, Tong L. Steven GP. A 3D Macro/Micro FEA modeling approach for tensile failure behavior of woven composites. In: Proceedings of the Second Australian Congress on Applied Mechanics (ACAM-99), Canberra. 10–12th February 1999:189–194.

[14] Tan P, Tong L, Steven GP. A flexible 3D FEA modeling approach for predicting the mechanical properties of plain weave unit cell. In: Proceedings of the Eleventh International Conference on Composite Materials, vol. V, Gold Coast, Australia, 14–18th July 1997:67–76.

[15] Sih GC, Skudra AM. Failure mechanics of composites. Handbook of composites, vol. 3. Amsterdam: Elsevier, 1985.

[16] Carlsson LA, Gillespie JW. Dalaware composites design encyclopedia. Technomic Publishing Company, 1992.

[17] Composite manufacturing of tooling. CRC-AS Short course note, 1994.

[18] Anonymous, ICI fiberite material handbook. Arizona, USA: Tempe, 1989.

[19] BOEING, Advanced composites handbook, 1986.

ELSEVIER

Composite Structures 47 (1999) 805–812

COMPOSITE STRUCTURES

www.elsevier.com/locate/compstruct

Reinforcement of concrete beam–column connections with hybrid FRP sheet

Jianchun Li [a,*], Steve L Bakoss [a], Bijan Samali [a], Lin Ye [b]

[a] *Centre for Built Infrastructure Research, Faculty of Engineering, University of Technology, Sydney, NSW 2007, Australia*

[b] *Centre for Advanced Materials Technology, Department of Mechanical and Machatronic Engineering, University of Sydney, Sydney, NSW 2006, Australia*

Abstract

The paper describes the results of tests on prototype size reinforced concrete frame specimens which were designed to represent the column–beam connections in plane frames. The tests were devised to investigate the influence of fibre reinforced plastic (FRP) reinforcement applied to external surfaces adjacent to the beam–column connection on the behaviour of the test specimens under static loading. Of particular interest under static loading was the influence of FRP reinforcement on the strength and stiffness of beam–column connection. As a key to the study, the hybrid FRP composites of E-glass woven roving (WR) and plain carbon cloth, combined with chopped strand mat (CSM), glass fiber tape (GFT) with a vinyl-ester resin were designed to externally reinforce the joint of the concrete frame. The results show that retrofitting critical sections of concrete frames with FRP reinforcement can provide signification strengthening and stiffening to concrete frames and improve their behaviour under different types of loading. The selections of types of FRP and the architecture of composites in order to improve the bonding and strength of the retro-fitting were also discussed. © 2000 Elsevier Science Ltd. All rights reserved.

Keywords: Concrete structure; Strengthening; Rehabilitation; Hybrid FRP composite; Wrapping technique

1. Introduction

A widely adopted technique for retrofitting concrete structure is to use steel jackets placed around existing concrete columns [1,2]. The use of steel encasement to provide lateral confinement to the concrete in compression has been studied extensively [3,4], and has shown increase in the compression load carrying capacity and ductility of the concrete columns. However, the shortcomings of this technique are that it suffers from corrosions as well as inherent difficulties during practical applications.

Fibre reinforced plastic (FRP), on the other hand, is increasingly being used to reinforce concrete, masonry and timber structures. The load carrying capacity and serviceability of existing structures can be significantly augmented through externally retrofitting critical sections with FRP sheeting. In recent years FRP materials with wide range of fibre types of glass, aramid or carbon provide designers with an adaptable and cost-effective construction material with a large range of modulus and strength characteristics. Comparing with traditional rehabilitation techniques, the FRP composites have high specific strength/stiffness, flexibility in design and replacement as well as robustness in unfriendly environments. With FRP composites it is possible and also necessary to achieve the best strengthening results by optimising the constitute materials and architecture. Optimisation of the constitute materials and architecture becomes essential in order to utilise the superiority of FRP composites in application of rehabilitation [5–9]. It was found that winding of carbon fiber/epoxy composites around square concrete columns can increase the load carrying capacity by 8–22%, depending on the amount of fibres used and treatments of substrate surface [10]. The use of resin infusion technique was shown to contribute to substantial improvements in composite wrapping efficiency, and the use of woven glass roving, as the reinforcement in composites wrapping, was found to significantly increase both load carrying capacity and deformation resistance capacity of the concrete stubs [2]. Furthermore, through the use of glass/carbon hybrid reinforcements with an epoxy resin, replication of initial performance of concrete stubs subjected to deterioration

* Corresponding author. Tel.: +61-2-9514-2651; fax: +61-2-9514-2633.

E-mail address: l.jinchun@uts.edu.au (J. Li).

0263-8223/99/$ - see front matter © 2000 Elsevier Science Ltd. All rights reserved.
PII: S0263-8223(00)00057-X

was shown possible, with a simultaneous further improvement in load carrying capacity. In terms of the effects of orientation and thickness of the composites warps, it was found that the predominant use of reinforcements in the hoop direction would result in high efficiency [11]. Despite the large number of research carried out, one shortcoming of most studies has been that they were limited to simple small size components, such as concrete cylinders, rather than real structures. Furthermore, it is essential to study the optimisation of composites architectures in terms of cost effectiveness including materials and processing methods. This implies that the reinforcement of infrastructure with FRP composites should utilise the advantages of various materials, not only carbon fibers with epoxy resin, but also glass fiber or hybrid of carbon/glass fibres with other polymer resins. In this experimental investigation, a hybrid of carbon/*E*-glass with vinyl-ester resin composites jacket was designed to reinforce a typical building components, namely a column–beam connection. Static tests were then conducted on FRP reinforced and non-reinforced specimens with extensive instrumentation to study the influence of the designed composite reinforcement.

The investigation reported in the paper forms part of a collaborative research program between the University of Technology, Sydney and the Centre for Advanced Materials Technology, the University of Sydney in relation to application of advanced fibre composites to strengthen, stiffen and hence rehabilitate concrete structures.

2. Experimental procedures

Three prototype size reinforced concrete frame specimens, representing typical concrete column–beam connection, were designed for this study. Geometry of the specimens with location of FRP composite reinforcement is illustrated in Fig. 1. Among three specimens, two of them are as-is concrete beam–column connection type (none composites-reinforced (Non-CR) specimens) and one specimen was reinforced by the hybrid of carbon fiber and glass fibre composites around the column–beam joint (composites-reinforced (CR) specimen). All three specimens were pre-cast using standard commercial mix grade 40 concrete. The steel reinforcement of the concrete specimens are also shown in Fig. 1. Concrete compression tests based on the Australian Standard (AS 1012–1986) were conducted on the samples taken during the concrete pour in order to determine the modulus of elasticity and ultimate compression strength (UCS) of the concrete.

2.1. Composites architecture

One of the three concrete frame specimens was reinforced with hybrid composites. The hybrid composites consists of four basic architectures, namely E-glass woven roving (WR/600 g/m^2), chopped strand mat (CSM-300 g/m^2), carbon cloth (plain weave-200 g/m^2) and glass fibre tape (GFT-250 g/mm^2). The details of the composites architecture are shown in Table 1 and Fig. 2. Details of lay-up are illustrated in Fig. 3. WR and carbon cloth are a multi-directional reinforcement with biaxial plain weaving which provide equivalent strength in both axial and hoop directions. They play the basic reinforcement role in this composites architecture. GFT applying at hoop direction provides very good confinement and enhances structural integrity. The selection of resin curing systems is mainly concerned with the resin gel-time at ambient temperature, which is critical to wrapping process. In general, cold setting resin systems (ambient temperature curing) can be used when wet lay-up process is applied. Since no lay-up machine is available for the wrapping process described in this study, the hand lay-up method was used. The vinyl-ester

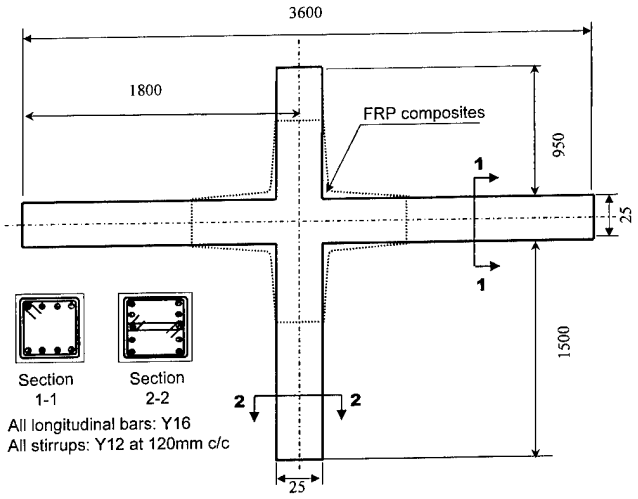

Fig. 1. Geometry details of test specimens (no to scale).

Table 1
Details of five composite systems with a composite architectures

Layers	Total fibre weight (g/m^2)	Description of wrap architectures	Thickness (mm)
Tap	250	Two layers glass tape wrap	0.95
CSM1	300	One layer of E-glass	0.45
WR	600	One layer of glass WR	1.00
Plain	200	Three layers of carbon cloth	1.00

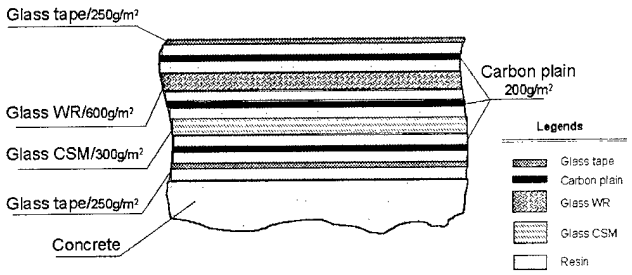

Fig. 2. Schematic illustration of FRP composites architecture used in this study.

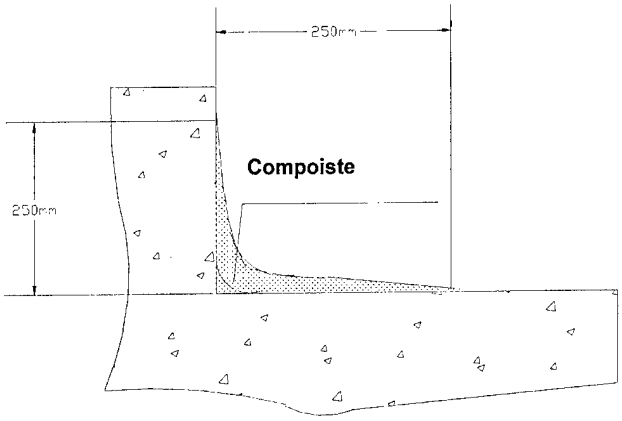

(a)

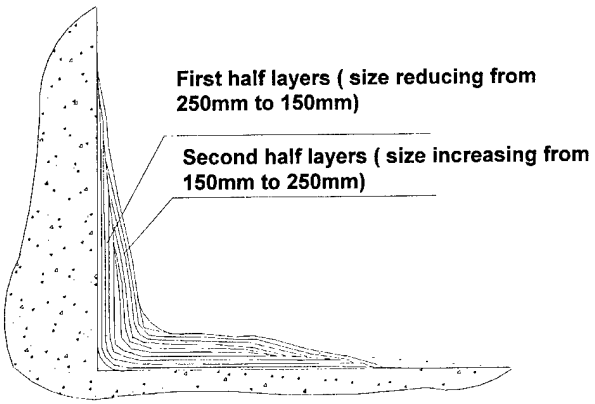

(b)

Fig. 3. Some details of FRP composites lay-up.

resin, Dastar-R/VERPVE/SW/TP, was mixed with 1.5% of MEKP (methyl-ethyl-ketone-peroxide), 0.4% of Co-Nap (Cobalt napthenate), and 0.5% of DMA (Dimethylaniline) at ambient temperature. The resin cures at ambient temperature. The weight ratio between resin and fibre layers was 1:1.5 for WR/CSM layers and 1:0.8 for carbon cloth, respectively. The concrete frame was wrapped by a lames-wool roller and a consolidating roller. Before laying the first fibre layer, the concrete surfaces were cleaned up using acetone, and a thin resin coat was applied to seal micro holes on the surface of concrete columns. However, further surface treatment such as sanding surface to expose the aggregates was intentionally avoided. Each composite layer was wetted with the resin and rolled onto the concrete frame to ensure full consolidation.

2.2. Design of static tests

The static tests of the concrete frame specimens were setup in a horizontal plane. The three supports of the concrete frame (no load applied) were roller type as shown in Fig. 4. The end at which load was applied was also a roller type support, however, horizontal movements were obviously not prevented. In order to provide the ideal roller type boundary conditions at each end as designed, a special setup was developed with combination of rollers and a swivel head at each supporting/loading point (Fig. 5). Four 1000-kN-hydraulic jacks were used in the tests. Among them, the only active jack was the jack that applied loads, while others were simply acting as adjustable packing to providing the reactions.

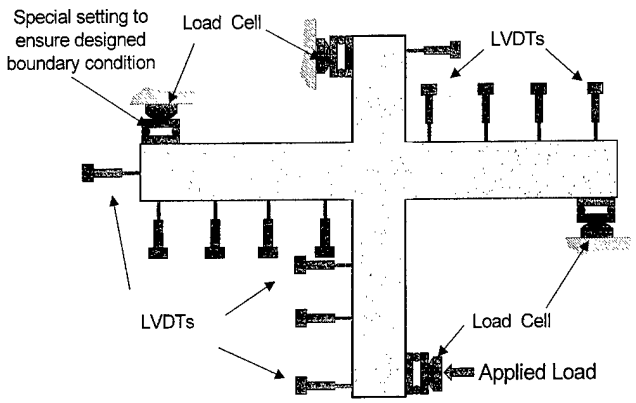

Fig. 4. Illustrative sketch of test set-up for static test.

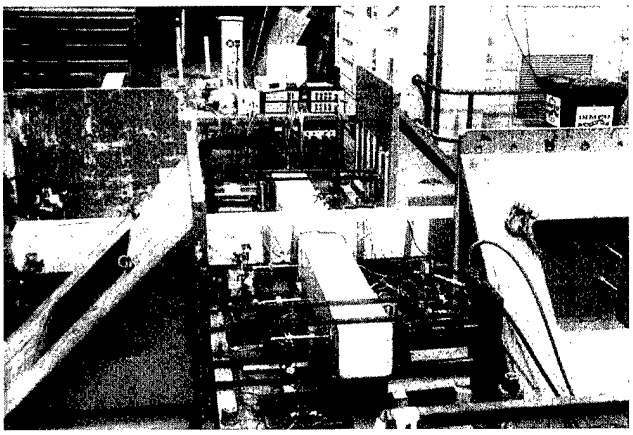

Fig. 5. Set-up for static test of concrete frame.

2.3. Instrumentation and data logging

Applied load as well as reaction forces were measured using four 998.8 kN load cells located in each of four supporting/loading positions. In order to obtain detailed flexural deflection curves for the concrete frame specimens, twelve linear variable displacement transducers (LVDTs) with a range from ±2.5 to ±50 mm were used at strategic locations to measure the flexural deflections. Extensive strain gauging was designed to capture the stress distribution of the testing specimens in order to validate tests and gain an insight into the behaviour of the concrete frame with or without FRP reinforcement. The total number of strain gauges was 56 for each specimen, in which 28 strain gauges (5 mm) were located on steel rebars and the rest (30 mm strain gauges) were located on the external surface of the concrete frame specimens. Locations of the strain gauges were arranged so that the strains on various points of the cross sections could be captured. A typical strain gauge arrangement for most measured cross sections is shown in Fig. 6. Locations of strain gauges inside the section are shown in Fig. 7.

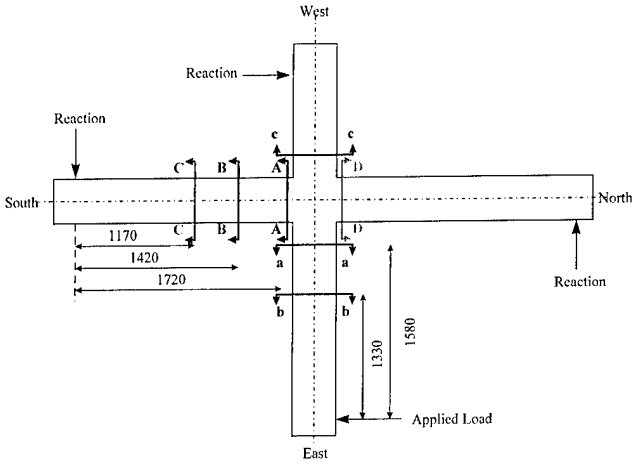

Fig. 6. Location of cross sections of the concrete frame for strain gauging.

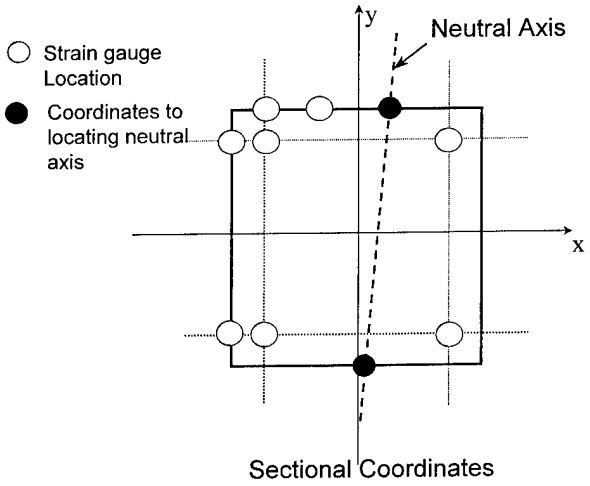

Fig. 7. Location of strain gauges in both beam and column sections.

2.4. Test procedure

Designations of test specimens and a brief description are given in Table 2. Prior to being formally tested at service load level, the first non-CR specimen was subjected to a series of investigative tests mostly loaded at the service load level of 40 kN with one single overload up to 50 kN. The second non-CR specimen and the CR specimens were not subjected to any loading until the initial service load level tests. All ultimate load tests were conducted after every specimen was exposed to about 100 cycles of cyclic loading at service load levels.

3. Results and analysis

In order to determine the influence of FRP composites, five sets of tests were conducted on the three specimens including three tests at service load levels and two at the ultimate load level. For every test, logged data consisted of four load records, twelve deflection records and 56 or 64 strain records.

3.1. Validation of the static tests

To validate the performed tests, the static equilibrium for each test was verified as follows:

Equilibrium of external loads: As redundancy was avoided in design of these tests and load cells were placed at each loading or reaction point, it was convenient to check equilibrium of the load/reaction forces through simple statics. Table 2 shows that the equilibrium of external loads was satisfied.

Table 2
Applied load and reactions for typical tests (unit: kN)

Specimen ID	Description	Applied load (East)	Reaction 1 (West)	Reaction 2 (North)	Reaction 3 (South)
C1-6-25b	First none-CR beam	25	23.3	18.3	19.7
C3-9-28	Second none-CR beam	25	24.5	16.6	16.5
C2-6-9a	CR beam	25	25.1	21 (16.4[a])	20.1

[a] Measurement was corrected by an additional load cell.

Equilibrium of forces and equilibrium of moment on cross sections: In order to calculate the internal forces and sectional moments, strains on the designated sections were required. To process the measured strains on a given cross section, the following assumption was made: the strains vary linearly through the cross sections. In other words the strains at a given cross section can be represented by a strain plane. Under this assumption, least square method with the two explanatory variables was adopted to obtain the strain plane for each given cross section using values of six measured strains. Fig. 8 shows comparison of the measured strain values and those calculated from the least square fitting. The strain values used in subsequence evaluations or calculations were obtained from calculated strain planes. For the validation of the equilibrium of internal forces in a given cross section, forces were calculated by integration of resulting stresses in tension and compression zones, respectively. The concrete was assumed to carry only compression loads and steel rebars (with FRP composites in some cases) were considered as the main load carriers in the tension zone. Equilibrium states that the resultant force in the compression zone should be equal to that in the tension zone. Moments at a given cross section were firstly calculated through integration of stresses in the section. They were compared to those calculated by using measured loads multiplied by the lever arms. Details of formulae pertained to these

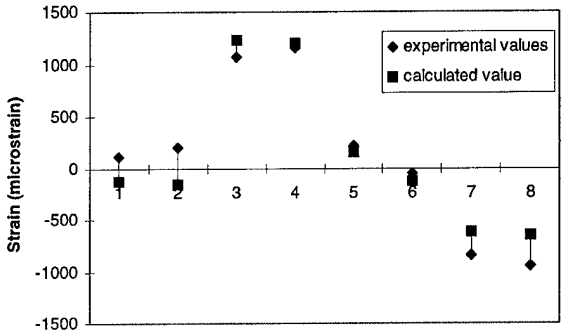

Fig. 8. Comparison of measured vs calculated strain values from least square fitting.

Table 3
List of calculated internal force and moments at section A-A of a non-CR specimen

Test no	C3-9-28	Section A-A		
Given data	Elastic modulus of concrete	28.4 GPa	Elastic modulus of steel	200 GPa
	Loads	16.6 kN	Distance from loading to section	1.720 m
Calculation of the force				
	Concrete (kN)	Steel (kN)		Total (kN)
Compression section	−109.9	−20.6		−130.6
Tensile section		127.5		127.5
Calculation of the moment				
	Concrete (kNm)	Steel (kNm)		Sub-total (kNm)
Compression section	1.1E + 04	4.3E + 02		1.2E + 04
Tensile section		1.6E + 04		1.6E + 04
Total moment by integration of stress			2.80E + 04 kNm	
Total moment by direct calculation			2.86E + 04 kNm	

Table 4
List of calculated internal force and moments at section A-A of a CR specimen

Test no	C2-6-9a	Section A-A		
Given data	Elastic modulus of concrete	28.4 GPa	Elastic modulus of FRP composite	14 GPa
	Loads	16.6 kN	Distance from loading to section	1.720 m
Calculation of the force				
	Concrete (kN)	Steel (kN)	Composite	Total (kN)
Compression section	−153.3	−27.0	−15.6	−195.9
Tensile section		198.7	41.8	240.5
Calculation of the moment				
	Concrete (kNm)	Steel (kNm)	Composite (kNm)	Sub-total (kNm)
Compression section	1.6E + 04	4.8E + 02	1.1E + 03	1.7E + 04
Tensile section		2.6E + 04	7.6E + 03	3.4E + 04
Total moment by integration of stress			5.10E + 04	
Total moment by direct calculation			5.31E + 04	

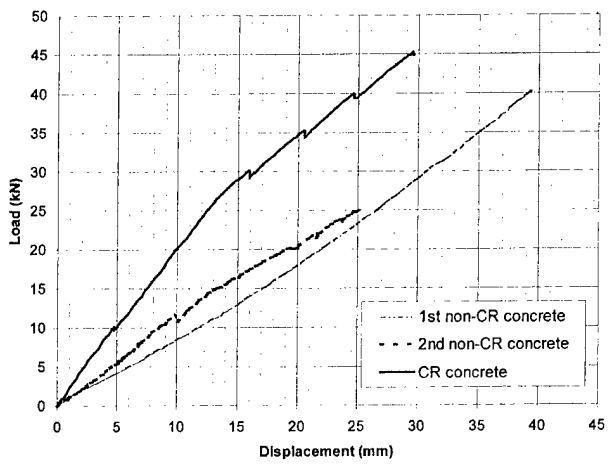

Fig. 9. Comparison of load vs deflection of CR and non-CR specimens (service level loading).

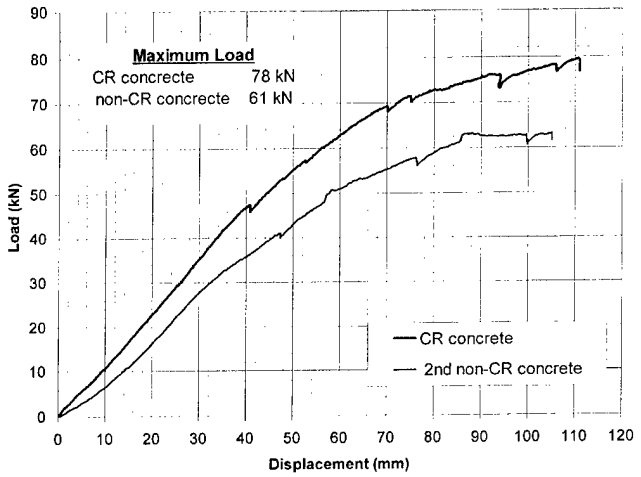

Fig. 10. Comparison of load vs deflection of CR and non-CR specimens in ultimate loading test.

calculations are presented in Appendix A. As shown in Tables 3 and 4, equilibrium is validated.

3.2. Load–deflection curves

Comparison of load–deflection curves for CR and non-CR specimens at both service load and ultimate load levels are shown in Figs. 9 and 10. About 45% increase in stiffness was observed due to the presence of FRP composites reinforcement (service load level). Results of the ultimate loading test indicated an increase in load carrying capacity of CR specimen of approximately 30% due to the presence of FRP composites.

3.3. Analysis of the strain results

To evaluate change of strain in steel rebars due to FRP reinforcement, a parameter was defined, namely "average strain reduction". It is defined as

$$\text{Average strain reduction } (\%) = \frac{P-R}{P} \times 100\%,$$

where P is the average of maximum section strains of the two none composites-reinforced (non-CR) specimens and R is the maximum section strain of composites-reinforced (CR) specimen at the same load level. Tables 5 and 6 summarise the typical comparison of maximum/minimum strains between non-CR and CR specimens and average strain reduction in various cross sections at same load level (see also Fig. 11). If one takes the mean of the average strain reductions for all beam-sections, it yields strain reduction factor of 51%. In same way, the mean of the average strain reductions for all column-sections is 55%. The average strain reduction can be used as an indication of external FPR reinforcement efficiency.

Table 5
Comparison of the maximum strains in the rebars for beam sections (unit: με)

Beam section		A-A section		B-B section		C-C section		D-D section	
Specimen ID	Description	Max	Min	Max	Min	Max	Min	Max	Min
C1-6-25b	First none-CR beam	998	−171	863	−289	617	−248	1259	−145
C3-9-28	Second none-CR beam	860	44	948	−243	1031	−214	953	−73
C2-6-9a	CR beam	488	−33	385	−146	531	−97	421	−78
Average strain reduction (%)		47	N/A	57	N/A	36	N/A	62	N/A

Table 6
Comparison of the maximum strains in the rebars for column sections (unit: με)

Beam section		a-a section		b-b section		c-c section	
Specimen ID	Description	Max	Min	Max	Min	Max	Min
C1-6-25b	First none-CR beam	879	34	857	−234	816	267
C3-9-28	Second none-CR beam	816	−321	612	−285	665	31
C2-6-9a	CR beam	528	−111	362	−165	170	71
Average strain reduction (%)		38	N/A	51	N/A	77	N/A

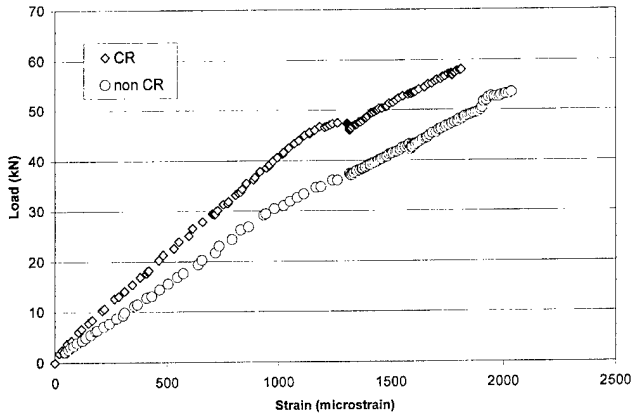

Fig. 11. Comparison of strains of CR and non-CR specimens in steel rebars at a given section.

3.4. Discussions on applied composites architecture

Results from both service load level tests and ultimate load test of the concrete frames show that the proposed composites architecture successfully enhanced the original structure in terms of stiffness and load carrying capacity. It is interesting to note that although the elastic modulus of FRP composites is only approximately half of that of concrete, the increase in stiffness and load carrying capacity of a reinforced concrete was significant. Despite of absence of special surface treatment of concrete before the application of FRP composite reinforcement, the bonding between the concrete and composites did not fail. This may be owing to the lower elastic modules of hybrid composites. There is an indication that low modulus FRP may provide better reinforcement/retrofitting for concrete structures because of low tensile strength in concrete. In the lay-up design, the gradual change of thickness is essential. It will reduce possible stress concentration in the FRP composites which could cause delamination or cracking. However, it is important to point out that because only a limited number of specimens were studied, some of these conclusions may be biased. It is suggested to conduct more tests to confirm these results.

4. Conclusions

As results of this study, the following conclusions can be drawn:

1. Tests on prototype size reinforced concrete frame specimens, designed to represent the column–beam connections in plane frame, have been successfully conducted. Test results were validated through equilibrium checks.
2. Designed hybrid composites consisting of roving cloth, carbon cloth, and chapped strand mat and glass fibre tape demonstrated effectiveness in reinforcing concrete structures. The results from the tests show significant increases in stiffness and load carrying capacity due to reinforcement provided by hybrid FRP composites. The results also show that optimisation is important in reinforcing concrete structures to achieve good results with low cost.
3. The results of static tests also suggest that hybrid carbon/E-glass fibre composites with low elastic modulus may contribute to good bonding and non-delamination. However, this needs to be confirmed by more tests.
4. It is also suggested that further investigation be carried out including reinforcing damaged concrete frame specimens, cyclic loading and using different composites architectures.

Appendix A

Assuming that at a given cross section of beam/column strain distribution is linear, for the given section, strain can then be expressed in form of

$$\varepsilon(x,y) = ax + by + c, \tag{A.1}$$

where a, b, c are constants.

Consider a two explanatory variables regression model

$$Y_i = \beta_0 + \beta_1 x_{i1} + \beta_2 x_{i2} + e_i, \tag{A.2}$$

where x_{i1} represents the ith observation on explanatory variable X_1 and x_{i2} denotes the ith observation on second explanatory variable X_2.

One can obtain a best fit strain plane from measured strain in a given section.

Under linear strain distribution assumption, a closed form solution for force and moment at the cross section using strain data can be obtained by double integration. In compression zone for the concrete (refer to Fig. 12), one obtains:

$$\begin{aligned} F_l &= \int_s \int E\epsilon \,\mathrm{d}S \\ &= E\int_{-125}^{125}\left[\int_{-125}^{-(by+c)/a} \varepsilon(x,y)\,\mathrm{d}x\right]\mathrm{d}y \\ &= -E\left\{125^3 a - 2\times 125^2 c + \frac{125}{3a}(125^2 b^2 + 3c^2)\right\}, \end{aligned} \tag{A.3}$$

where E is the modulus of the elasticity of concrete; a, b and c are constants in Eq. (A.1); F_l is the resultant force in the compression zone.

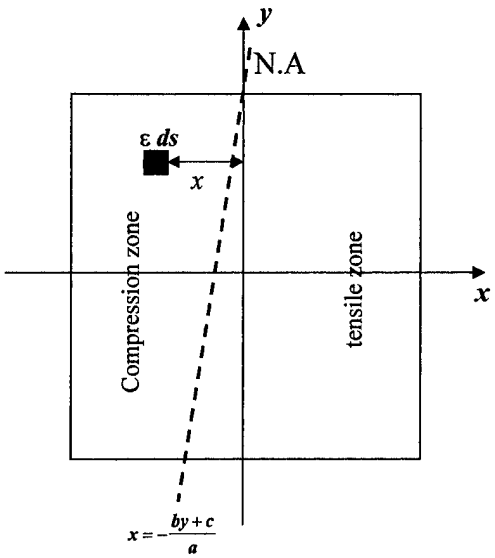

Fig. 12. Schematic drawing of a typical cross section of concrete frames.

$$M_I = E\int_s\int x\varepsilon(x,y)\,\mathrm{d}S = E\int_{-125}^{125}\left[\int_{-125}^{-(by+c)/a} x\varepsilon(x,y)\,\mathrm{d}x\right]\mathrm{d}y = E\left\{\frac{125c}{3a^2}(125^2b^2+c^2) - 125^3c + \frac{2}{3}\times 125^4 a\right\}, \tag{A.4}$$

where M_I is the moment at the compression zone.

For steel rebars and composites (if applied):

$$F_{IS} = \int_s\int E_s\varepsilon(x,y)\,\mathrm{d}s \quad \text{and} \qquad F_{IC} = \int_s\int E_c\varepsilon(x,y)\,\mathrm{d}s, \tag{A.5}$$

where F_{IS} and F_{IC} are forces in steel rebars and composite, respectively.

In tension zone, only steel rebars and composite count, formulae are similar to Eq. (A.5).

References

[1] Karbhari VM. Strengthening of concrete column stubs through resin infused composite wraps. J Thermoplastics Compos Mater 1993;6:93–107.

[2] Japan Concrete Institute. Handbook for retrofitting of existing reinforced concrete structures. Gihodo-shuppan [in Japanese].

[3] Fuelong RW. Strength of steel-encased concrete beam columns. ASCE J Struct Eng 1967;93:113–24.

[4] Knowles RB, Park R. Strength of concrete filled steel tubular columns. ASCE J Struct Eng 1969;95:2565–87.

[5] McKenna JK, Erki MA. Strengthening of reinforced concrete members using externally applied steel plates and fibre composite sheets – a survey. Can J Civ Eng 1994;21:16–24.

[6] Triantafillou TC, Deskovic N, Deuring M. Strengthening of concrete structures with pre-stressed fibre reinforced plastic sheets. ACI Struct J 1992;89:224–35.

[7] Priestley MJ, Fyfe E, Seible F. Column retrofitting using fibre glass/epoxy jackets. In: Proceedings of the First Annual Seismic Workshop. Cal. Treans, Sacramento, 1991. p. 217–24.

[8] Triantafillou TC, Plevris N. Post-strengthening of R/C beams with epoxy bonded fibre composite material. In: Advanced composite materials in civil engineering structures, Proc. Specialty Conference, Las Vegas, NV., ASCE, 1991. p. 245–56.

[9] Tanaka T, Yagi K. Retrofit method with carbon fibre for reinforced concrete structures. Adv Compos Mater 1994;4:183–95.

[10] Katsumata H, Kobatake Y, Takeda T. A study on strengthening with carbon fibre for earthquake-resistant capacity of existing reinforced columns. In: Proceeding of the Ninth World Conference on Earthquake Engineering, Tokyo, 1988. p. 517–22.

[11] Howie I, Karbhari VM. Effect of two sheet composite wrap architecture on strengthening of concrete due to confinement: I – Experimental studies. J Reinforced Plastics and Composites 1995;14:1008–30.

ELSEVIER

Composite Structures 47 (1999) 813–819

COMPOSITE STRUCTURES

www.elsevier.com/locate/compstruct

Development of a composite cargo door for an aircraft

H.G.S.J. Thuis *

National Aerospace laboratory NLR, Voorsterweg 31, 8316 PR Marknesse, Netherlands

Abstract

Nowadays, aircraft manufacturers are not only looking for ways to reduce the structural weight of their aircraft but they are also searching for structural concepts that will lead to a cost reduction. One way to realize a cost reduction is to design a component with a high level of part integration since this will lead to a reduction in labor intensive trimming and assembly costs. By using composites in combination with new fabrication concepts this part integration becomes feasible. One of these new fabrication concepts is resin transfer moulding (RTM) with pre-pregs. In traditional RTM processes, dry fiber pre-forms are positioned in a mould cavity. After the mould is closed, resin is injected into the mould and the fibers are impregnated. In the RTM process described in this paper, parts of the dry pre-form are replaced by pre-preg. After closure of the mould, the mould is heated and the resin in the pre-preg starts to melt. Then RTM resin is injected into the mould. The pressure of the RTM resin is used to pressurize the pre-preg. The main advantage of this fabrication concept is that sub-preforms can be made very easily in pre-preg that would be very difficult to make with dry fabric due to the lack of tack. Another advantage is that the RTM process time is reduced, because only a small quantity of resin has to be injected. In order to demonstrate the feasibility of this fabrication concept, a hat-stiffened cargo door concept was developed. Two doors were made. The doors were tested by applying a pressure difference to the door of 0.12 MPa. Both doors did not fail during the tests. © 2000 Elsevier Science Ltd. All rights reserved.

Keywords: Resin transfer moulding; Composite cargo door

1. Introduction

In the framework of the BRITE EURAM project, Advanced PRImary COmposite Structures (APRICOS), structural components for a composite fuselage of an aircraft were developed. The components ranged from discrete stiffened fuselage panels, beams, frames and a cargo door (see Fig. 1). The main goal of the program was to achieve a cost reduction of at least 20% by using composites instead of metals. The National Aerospace Laboratory NLR was responsible for developing a fabrication concept for a composite cargo door. The paper presents a description of the cargo door. The mould and fabrication concept developed for producing the door is presented in detail, followed by a brief description of the test program and a presentation of the test results.

2. Description of the door

The door represents an inwards-opening generic cargo door for an aircraft category like the Airbus A320. The purpose of the program was to develop a cost effective fabrication concept for this category of fuselage doors. Since only two doors had to be produced as deliverables of the program, it was decided not to develop a curved door but a non-curved door in order to limit tooling costs. However, the fabrication and tooling concept developed had to be valid also for producing curved doors.

During flight conditions the door will only be loaded by the pressure difference between the pressure in the fuselage and the atmospheric pressure. This means that design limit load for the door is 0.06 MPa. Design ultimate load is $2.0 \times 0.06 = 0.12$ MPa.

The cargo door concept is based on an outer skin that is stiffened by a lattice of hat-stiffeners, integrated pin-locks, door-stops and two hinge points (see Fig. 2). Fig. 3 shows a cross-section of a cargo door with a schematic presentation of the door-stops and the pin-locks (note that the cargo door in the figure has a curvature, whereas the door described in this paper is flat).

* Fax: +31 527 248604.
E-mail address: thuis@nlr.nl (H.G.S.J. Thuis).

0263-8223/99/$ - see front matter © 2000 Elsevier Science Ltd. All rights reserved.
PII: S0263-8223(00)00058-1

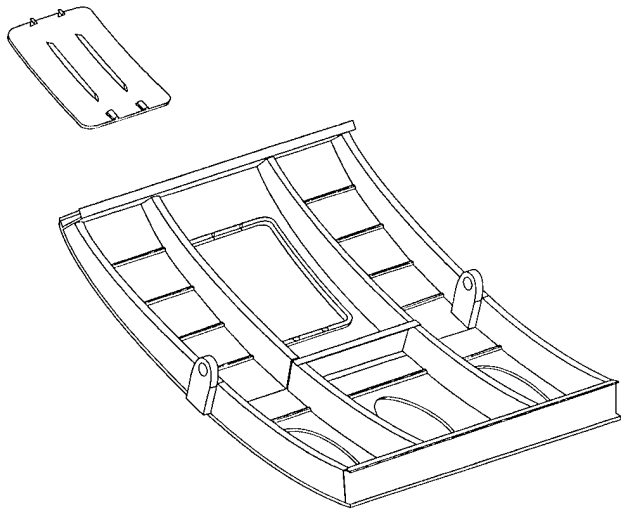

Fig. 1. Composite fuselage demonstrator.

Inside the lattice of hat-stiffeners a foam core is present. This foam core is only present for fabrication purposes and was not taken into account in the strength analyses. Each intersection of two hat-stiffeners is reinforced with four corner reinforcements (see Fig. 2). Ten aluminum inserts are incorporated in the door. After curing the door, these metal inserts will be machined to form respectively door-stops and pin-locks (see Fig. 2).

The finite element code B2000 [1] was used to design the door. B2000 is NLR's testbed for computational structural mechanics. The finite-element model comprised half a door and was composed of 753 nine-noded QUAD elements (see Fig. 4). The optimization module B2OPT [2] within B2000 was used to optimize the door for minimal weight with maximum values for the stresses as constraints. In order to facilitate the optimization, the following nine laminate design variables were defined (see Fig. 2):

1. the thickness of the 0° plies in the skin,
2. the thickness of the 90° ply in the skin,
3. the thickness of the ±45° plies in the skin,
4. the thickness of the 0° ply in the hat-stiffeners,
5. the thickness of the ±45° plies in the hat-stiffeners,
6. the thickness of the ±45° ply in the corner reinforcements.

Not only design variables but also the following side constraint was defined. The thickness of both the optimized skin and optimized hat-stiffeners had to be at least 1.4 mm each, in order to allow a repair with counter sunk fasteners in case the door will be damaged.

The Tsai–Hill criterion was used as a failure criterion. The optimum design was found after 13 optimization cycles.

In order to minimize milling, drilling and assembly costs it was decided to fabricate the door (including the metal inserts) in a single fabrication cycle. Due to the complexity of the door, the resin transfer moulding (RTM) fabrication concept was selected, since making the door with pre-preg in the autoclave would become very cumbersome. However, injection of a component of this size and this complexity would become very risky with the traditional RTM as fabrication process:

- the injection time would probably expand the pot life of the RTM resin at injection temperature;
- reproducibility in impregnating every spot of the preform during the RTM process would be difficult to guarantee.

Therefore it was decided to make the hat-stiffeners and corner reinforcements from pre-preg and use the pressure of the RTM resin during the RTM process to pressurize the pre-preg. In this way injection time is dramatically reduced because the hat-stiffeners and corner reinforcements are already impregnated and the risk of dry spots in the cured door is nearly eliminated.

The next paragraphs describe the different elements that compose the door: the foam core, the metal inserts, the skin, the lattice of hat-stiffeners, and the corner reinforcements.

3. The foam core

Fig. 5 presents an overview of the foam core for which Rohacell 71 WF was used. This foam was selected because it has a low density and is able to withstand a pressure of 0.4 MPa. This is very important since during the RTM process a resin injection pressure of 0.4 MPa was used. The total weight of the foam core was 1400 g.

4. The metal inserts

Fig. 5 presents the location of the aluminum inserts in the assembled foam core. After curing the door, these metal inserts were machined to form door-stops and pin-locks. In order to reduce the weight of the aluminum inserts, holes were drilled into these inserts. After drilling, these holes were filled with Rohacell 71 WF. The weight of the metal insets was 5750 g.

5. The skin

The skin was composed of dry carbon fabric Lyvertex G808 220 g/m^2. This fabric has 90% of its fibers in the warp direction and 10% of its fibers in the weft direction. The lay-up of the skin pre-form was [+45, −45, 0, 90, 0, −45, +45] with a total thickness of 1.4 mm. The size of the skin pre-form was 900 mm × 900 mm. A pre-form of dry fabric of this size is very difficult to handle due to the lack of tack of the single layers. Therefore the skin preform was stabilized by stitching the edges of the skin

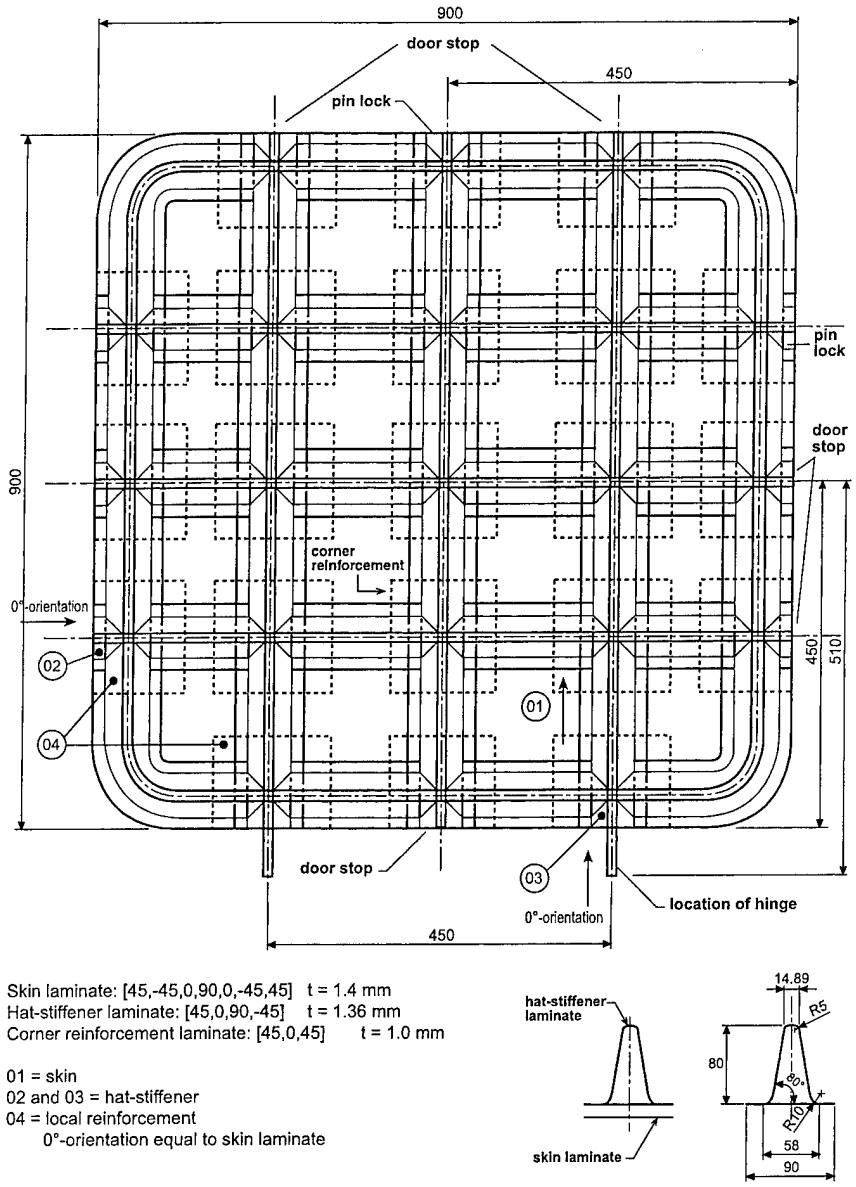

Fig. 2. Drawing of the door concept.

pre-form with a 2×40 tex Kevlar stitching fiber. The RTM-6 epoxy resin was used to impregnate the skin pre-form.

6. The hat-stiffeners

The hat-stiffeners were composed of Fiberite HMF carbon 977-2A-35-6KHTA-5H-370-T2 pre-preg fabric. This pre-preg was selected because tests on interlaminar shear specimens, made of RTM-6 resin and carbon fabric and the 977-2A-35-6KHTA-5H-370-T2 pre-preg, demonstrated compatibility between these two systems. The lay-up of the hat-stiffeners was [+45, 0, 90, −45]. The thickness of the hat-stiffeners was 1.4 mm.

7. The corner reinforcements

The corner reinforcements were composed of Fiberite HMF carbon 977-2A-35-6KHTA-5H-370-T2 pre-preg fabric. The lay-up of the corner reinforcements was [+45, 0, +45]. The thickness of the corner reinforcements was 1.0 mm.

8. The mould concept

As mentioned before the RTM fabrication concept was used to fabricate the door. The goal was to develop a stand alone tooling concept (with no need for an oven or an autoclave) in which the door could be produced

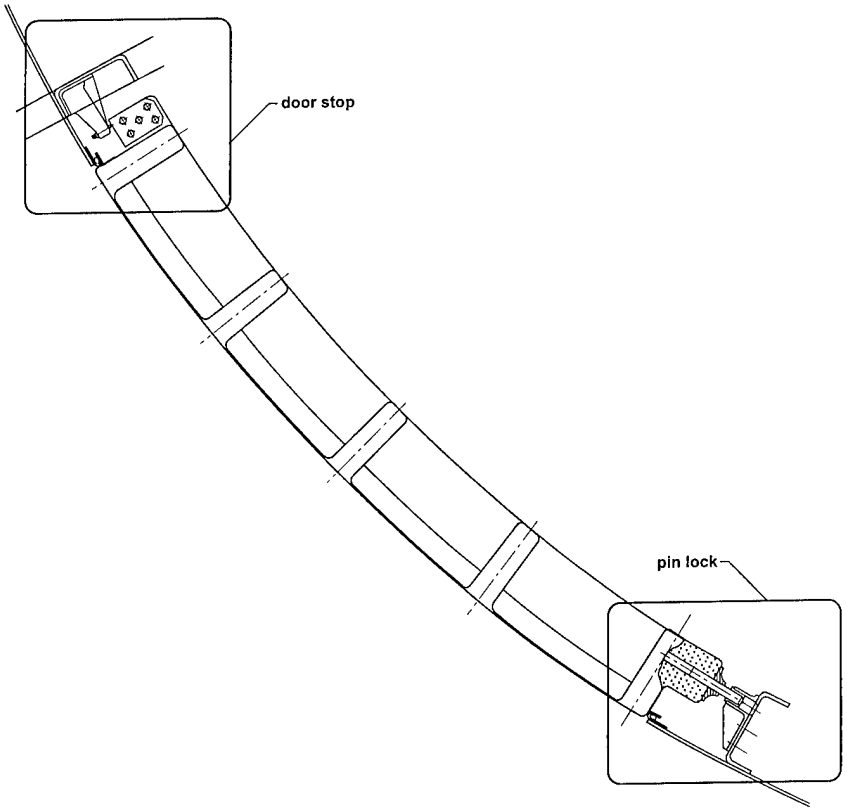

Fig. 3. Schematic cross-section of the hat-stiffened door with pin-locks and door-stops.

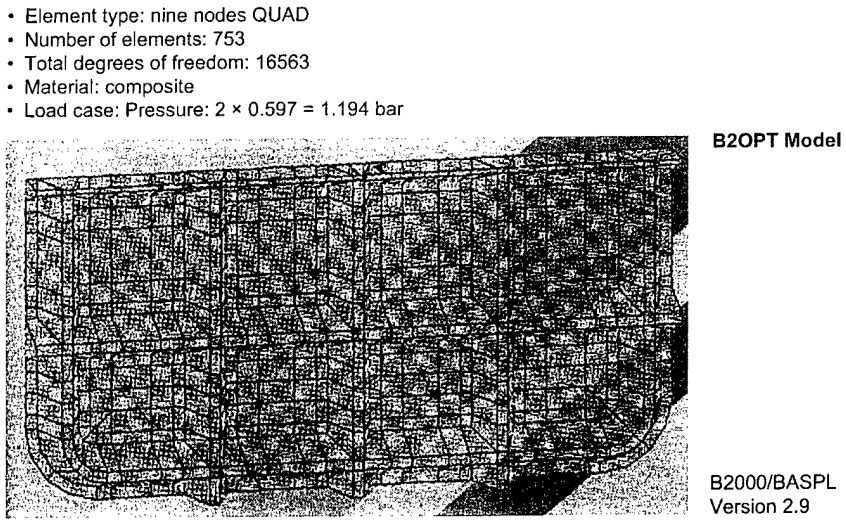

Fig. 4. Finite element model of the hat-stiffened door.

with tight (reproducible) outer dimensional tolerances. For example, the tolerance on the thickness of the different elements (skin, hat-stiffeners and corner reinforcements) was 0.1 mm. In order to make these tight tolerances feasible a stiff two-side mould had to be developed since the pressure used during the RTM process was 0.4 MPa. By incorporating electrical heating elements into the mould, no oven or autoclave was needed. This resulted in a mould concept with the following elements:

- A steel bottom frame.
- An aluminum bottom plate (see Fig. 6). The bottom plate had an injection circuit at the edges of the plate and one vent located at the center of the plate. This

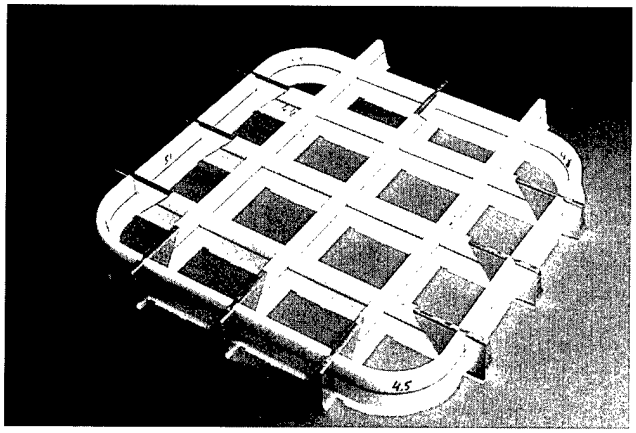

Fig. 5. Overview of Rohacell 71WF foam core and metal inserts.

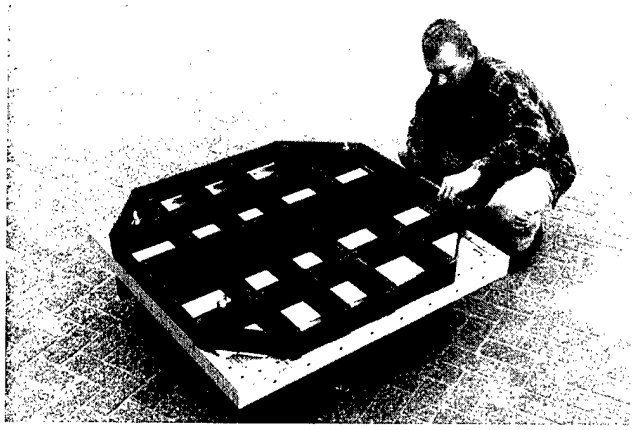

Fig. 6. Aluminium bottom plate and steel top frame.

radial injection strategy was selected to minimize injection time. Holes were drilled in the mould in which electrical heating elements were inserted before the RTM cycle.

- A composite top mould with integral electrical heating wires (see Fig. 7). It was technically not necessary to use a composite top mould since the top mould could also be made of metal. However, the composite top mould was developed in order to gain insight in the behavior of composite moulds for RTM with internal electrical heating wires. The experiences gained with this composite mould will not be presented in this paper.
- A steel top frame. Fig. 6 presents a picture of the metal top frame and the aluminum bottom plate. The picture provides a good insight in the size of the mould.

9. The fabrication concept

Two doors were made. Each door (including its metal inserts) was made during a single RTM fabrication cycle.

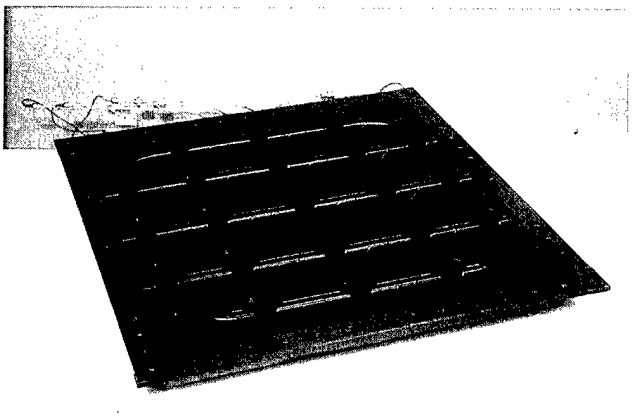

Fig. 7. Composite top mould with internal electrical heating wires.

During this fabrication cycle the following steps were distinguished:

- Laminating the hat-stiffeners with pre-preg on laminating blocks and pre-compacting the laminates under vacuum for at least 10 min.
- Laminating the corner reinforcements with pre-preg on laminating blocks and pre-compacting the laminates under vacuum for at least 10 min.
- Preparation of the dry fabric skin pre-form by stitching the edges with a Kevlar stitching wire.
- Positioning of the pre-preg corner reinforcements in the composite top mould.
- Positioning the pre-preg hat-stiffeners in the composite top mould.
- Positioning the dry fabric skin pre-form in the aluminum bottom mould.
- Assembly of the top and bottom mould.
- Assembly of the steel bottom and top frames.
- Applying vacuum to the mould for 3 h.
- Heating the assembled mould to 120°C by heating the electrical heating wire in the composite top mould and by heating electrical heating elements inside the aluminum bottom mould.
- Injection of RTM-6 resin into the bottom mould with a pressure of 0.4 MPa. The pressure of the RTM-6 resin will pressurize the pre-preg. The total injection time was approximately 25 min.
- Heating the mould to 160°C after the skin was impregnated with resin.
- Curing the pre-preg and the skin laminate at 160°C for 4 h.
- De-moulding the cured product.
- Machining the metal inserts and the corners of the door.

The weight of the machined door including the foam core and the metal inserts was 13.47 kg.

Fig. 8 presents one of the two doors after being machined. Fig. 9 presents a detail of a machined pinlock.

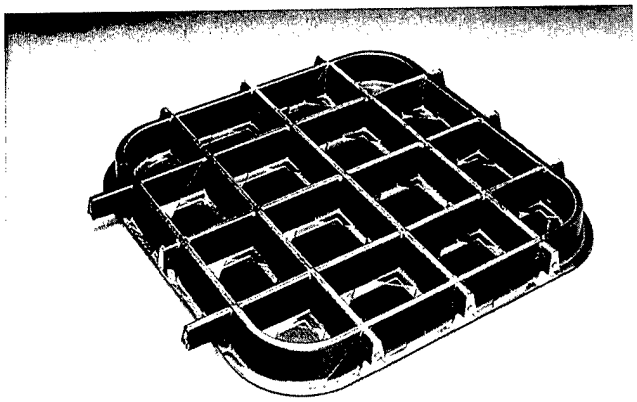

Fig. 8. Composite cargo door after machining.

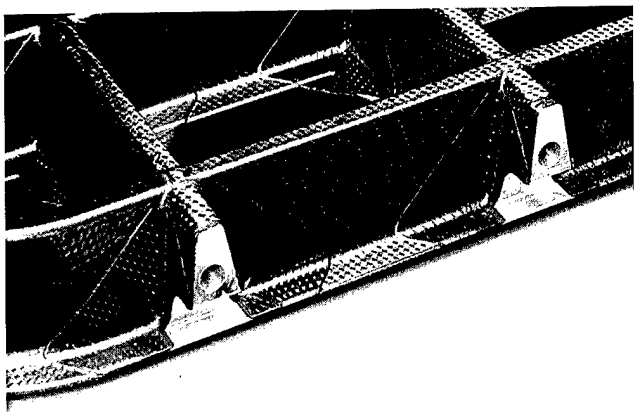

Fig. 9. Detail of a machined pinlock.

At this moment the cost comparison between a metal and the composite cargo door has not been made yet.

10. Testing the doors

The main goal of testing the doors was to demonstrate sufficient load carrying capability. In order to facilitate the tests on the doors a pressure box was designed and fabricated. Before being tested, the doors were mounted to the pressure box and all gaps between the door and the pressure box were sealed. Then the pressure inside the pressure box was gradually increased. The maximum pressure difference applied was 0.12 MPa. During the tests the displacement of the skin was

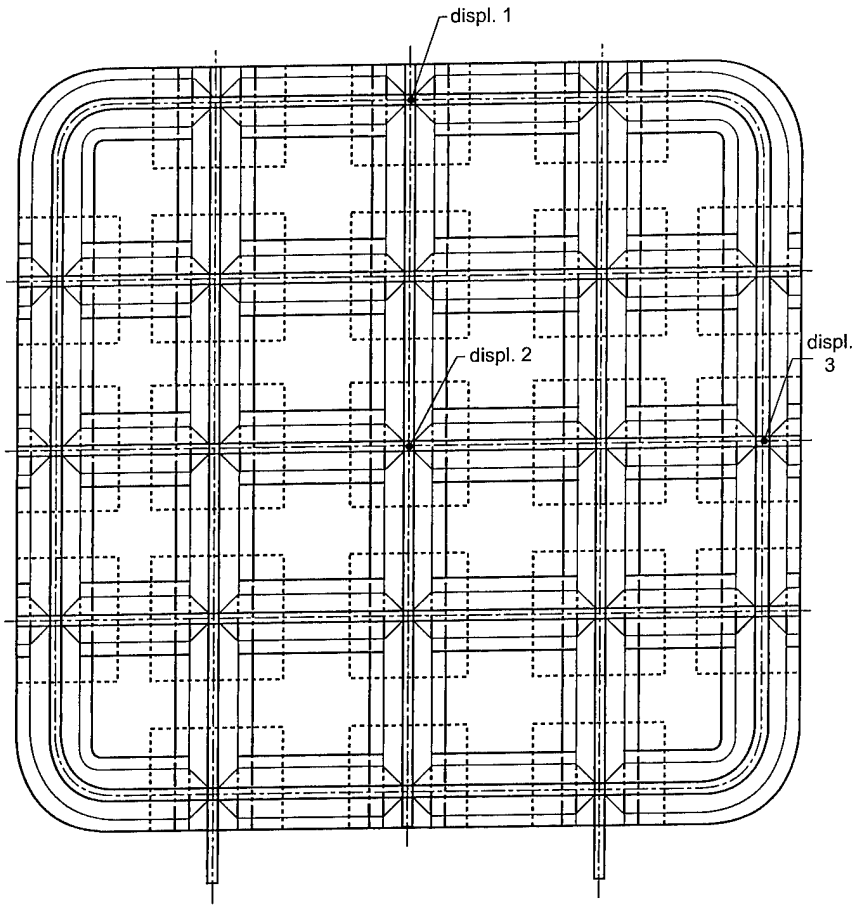

Fig. 10. Location of the displacement transducers.

Table 1

Test	Pressure difference (MPa)	Displ. 1 (mm)	Displ. 2 (mm)	Displ. 3 (mm)
1	0.119	3.4	7.2	2.3
2	0.118	3.5	7.4	2.4
3	0.118	3.4	9.7	2.7

measured at three locations (see Fig. 10) by linear displacement transducers.

Both doors were tested according to the following test program:

- *Test no.* 1
  - Test on door no. 1 to design ultimate load (0.12 MPa pressure difference). The door did not fail at this load level.
- *Test no.* 2
  - Test on door no. 2 to design ultimate load (0.12 MPa) pressure difference).
  - Applying two impact damages to door no. 2: a 30 Joule impact in the skin resulting in a barely visible impact damage (dent depth of 0.9 mm) and a 30 Joule impact in the skin under a hat-stiffener resulting in a puncture.
- *Test no.* 3
  - Test on door no. 2 to failure. Failure occurred at 1.2 bar pressure difference (design ultimate load), hence demonstrating the damage tolerance of the door.

Table 1 presents the measured displacements at maximum load of the doors during these tests.

11. Conclusions

A fabrication concept for producing a composite hat-stiffened door was developed successfully by combining dry fabrics with pre-preg during the RTM process.

Two doors were fabricated and tested. The tests not only demonstrated a sufficient load carrying capability of both doors but also damage tolerance of the doors. The cost evaluation will be carried out later.

References

[1] Merazzi S. B2000 – a modular finite element analysis system, Version 1.0, Memorandum SC-85-041 U. Amsterdam: National Aerospace Laboratory, 1985.

[2] Arendsen P. The B2000 optimization module: B2OPT, NLR-Report TP 94116 L. Amsterdam: National Aerospace laboratory, 1994.

ELSEVIER

Composite Structures 47 (1999) 821–825

COMPOSITE STRUCTURES

www.elsevier.com/locate/compstruct

An evaluation of higher-order effects on the eigenfrequencies of composite structures

Paolo Gaudenzi *, Rolando Carbonaro

Dipartimento Aerospaziale, Università di Roma "La Sapienza", Via Eudossiana 16, 00184 Rome, Italy

Abstract

The evaluation of the performances of higher-order models for the simulation of the response of laminated structures, namely in the prediction of global response characteristics such as the eigenfrequencies, is considered. An FEM analysis based on single-layer higher-order models has been carried out and the results for various cases of stacking sequences and aspect ratios have been compared. The same results have also been compared with the ones obtained with the classical laminate theory (CLT) in order to establish the predicting capability of the models and their utility in real practice. © 2000 Elsevier Science Ltd. All rights reserved.

Keywords: Eigen frequencies; Laminated plates; Higher-order effects

1. Introduction

It is widely recognised that the effect of the transverse shear deformation may be important in the evaluation of the global response of a composite plate, as the deflection, the eigenfrequencies, the buckling critical loads. As it is well known, the classical laminate theory (CLT), based on Kirchhoff hypothesis, is not adequate to represent this effect. The Mindlin–Reissner plate theory (a transverse shear deformable (SD) theory) takes into account the presence of out-of-the-plane shear deformation by assuming that every straight segment normal to the middle plane, in the undeformed configuration, remains straight but nor normal in the deformed configuration. On the other hand, a model of a composite plate based on SD theory requires the evaluation of the shear correction factor that depends on the type of stacking sequence.

For many years, many other theories, capable of capturing both local and global "higher-order" effects, not included in the CLT and SD theories, have been carried out. Noor [1] was among the first to illustrate their effect in dynamics by applying a difference method based on three-dimensional elasticity theory to analyse the free vibration behaviour of simply supported squared orthotropic laminated plates. Phan and Reddy [2] approached the problem of bending, vibration and stability of laminated plates by using a C^1 continuous model, developed by Reddy in previous studies [3], based on a higher-order shear deformation theory (HSDT). Barboni and Gaudenzi [4] developed a class C^0 of C° finite elements, based on a single-layer higher-order deformation theory, for evaluating local and global aspects of isotropic and laminated plates.

Also multi-layer higher-order theories have been proposed to analyse global aspects and in particular local aspect as the interlaminar stresses in composite plates. These theories are characterised by an assumed displacement field along the thickness z, which allows discontinuities in the derivative with respect to z, in order to impose the continuity of the displacements and the discontinuity of the strains at the interfaces of a laminated plate. Di Sciuva [5] proposed a zig–zag displacement model to approach global aspects for squared simply supported (0/90/0) laminated plates. This model allows the contact conditions for the displacements and the transverse shearing stresses at the interfaces to be satisfied simultaneously. The use of this approach seems to be more appropriate for the evaluation of local effects such as stress field concentrations, as in the paper by Gaudenzi et al. [6] who assumed a layerwise polynomial expansion along the thickness direction for displacements to represent the complicated pattern of stress distribution. More

* Corresponding author. Tel.: +39-06-4458-5304; fax: +39-06-4458-5670.

E-mail address: paolo@gaudenzi.ing.uniromal.it (P. Gaudenzi).

0263-8223/99/$ - see front matter © 2000 Elsevier Science Ltd. All rights reserved.
PII: S0263-8223(00)00059-3

recently other authors devoted their research efforts to the same problem such as in the case of Wu and Chen [7], Mota Soares et al. [8]. From the previously cited studies, some general conclusions can be drawn about the determination of free undamped vibration in laminated plates (see also [9]): the transverse shear deformation effect is more relevant as the thickness of the plate or the anisotropy degree of the composite material increase. Moreover, this effect increases with the mode order. As a consequence, if in the evaluation of dynamic response, the shear effects are neglected (as in the case of CLT theory), then the eigenvalues (vibration frequencies) are in general overestimated. Better agreement among the results of aforesaid models and the ones of SD theory can be reached. But, as already said, in this case the problem of choosing the appropriate shear correction factor, which is stacking sequence dependent, will occur.

Corresponding to this extended modelling effort no adequate assessment studies were conducted to establish the real cost/benefit trade-off in the choice of the adopted model in terms of computational effort and modelling capabilities. Sometimes the modelling effort is not correspondent to an effective improvement of predicting capability especially if global effects are considered. In the case of prediction of deflection and, even more, for the evaluation of buckling critical loads and eigenfrequencies, it is clear, from the cited literature, that there is no need for multi-layer higher-order approaches. The use of higher-order models can be restricted to simple single-layer higher-order models.

The aim of the present work is to evaluate the performances of simple higher-order models as compared to CLT (Kirchhoff) plate model for the prediction of eigenfrequencies of laminated plates. Moreover the evaluation of the global higher-order effect for different eigenmodes and the degree of refinement of the numerical prediction performed with a higher-order model are also studied. To reach this goal, an FEM analysis based on this type of modelling has been carried out. The results for various cases of stacking sequences, power series expansions and mesh refinements are also illustrated to determine first the convergence of the procedure and then to measure the predicting capabilities of the various higher-order models. In this way the use in practice of such models would be more appropriately assessed.

2. Finite element modelling

In the general formulation of a plate model based on a single-layer higher-order theory, the displacements can be represented in the following form:

$$\begin{aligned} U(x,y,z) &= \sum_{i=0}^{L} u_i(x,y) \times z^i, \\ V(x,y,z) &= \sum_{i=0}^{M} v_i(x,y) \times z^i, \\ W(x,y,z) &= \sum_{i=0}^{N} w_i(x,y) \times z^i. \end{aligned} \tag{1}$$

If the laminated plate is infinitely long in the y-direction (see Fig. 1) and the loading is uniform along the same direction (cylindrical bending), then we can rewrite Eq. (1) in the simplified form as shown in Eq. (2).

$$\begin{aligned} U(x,z) &= \sum_{i=0}^{L} u_i(x) \times z^i, \\ V(x,z) &= v_0(x), \\ W(x,z) &= \sum_{i=0}^{N} w_i(x) \times z^i. \end{aligned} \tag{2}$$

We now consider a generic strip of unitary width and develop for it a finite element approach.

The equilibrium for the generic finite element in dynamic condition will be represented by the virtual work Eq. (3), written in the absence of applied external forces for a single element

$$\int_{v_e} \left\{\tilde{\varepsilon}(x,z,t)\right\}_e \{\sigma(x,z,t)\}_e \, dv_e + \int_{v_e} \left\{\tilde{S}(x,z,t)\right\}_e^T \rho \frac{\partial^2 \{S(x,z,t)\}_e}{\partial t^2} \, dv_e = 0, \tag{3}$$

where the subscript "$\sim$" denotes a virtual quantity, $\{S(x,z,t)\}_e = \{U(x,z,t), V(x,z,t), W(x,z,t)\}_e^T$ is the displacement vector, $\{\varepsilon(x,z,t)\}_e$ the vector in which the strain components are collected, $\{\sigma(x,z,t)\}_e$ the vector of stress components, ρ is the density.

The displacement vector can be represented as follows:

$$\{S(x,z,t)\}_e = [Z(z)] \times \{s(x,t)\}_e, \tag{4}$$

where the matrix $[Z(z)]$ that express the displacement assumptions as far as the z-direction is concerned:

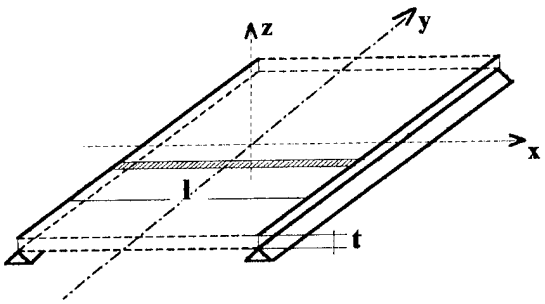

Fig. 1. Geometry of the examined structure.

$$[Z(z)] = \begin{bmatrix} 1 & z & z^2 & \dots & z^L & 0 & 0 & 0 & 0 & \dots & 0 \\ 0 & 0 & 0 & \dots & 0 & 1 & 0 & 0 & 0 & \dots & 0 \\ 0 & 0 & 0 & \dots & 0 & 0 & 1 & z & z^2 & \dots & z^N \end{bmatrix}$$

and $\{s(x,t)\}_e = \{u_0(x,t), u_1(x,t), \dots u_L(x,t), \ v_0(x,t), w_0(x,t), w_1(x,t), \dots w_N(x,t)\}_e^T$ is the vector of the generalised displacements.

On the basis of the usual finite element method procedure, the generalised displacement vector $\{s(x,t)\}$ can be represented in terms of nodal displacement $\{\delta(t)\}$ and shape functions $[N(x)]$.

$$\{s(x,t)\}_e = [N(x)]\{\delta(t)\}_e. \tag{5}$$

As a consequence the strain components will be written as

$$\{\varepsilon(x,z,t)\}_e = [D][Z][N]\{\delta(t)\}_e \tag{6}$$

being $[D]$ the matrix containing derivative operators which define the strain components in terms of the displacements.

By substituting the expressions (5) and (6) into the virtual work formulation for the generic element (3), after a variable separation and the usual assemblage of the contribution of the various elements, the global equation of the free vibrations of the present structure will be easily obtained.

$$[K]\{\delta\} - \omega^2[M]\{\delta\} = 0, \tag{7}$$

where ω represents the generic eigenvalue joined to the eigenequation (6) and $[K]$, $[M]$ are respectively the stiffness matrix and the mass matrix which have the following expressions:

$$[K] = \sum_e \int_{v_e} ([D][Z][N])^T [Q_k]([D][Z][N])\, dv_e,$$

$$[M] = \sum_e \int_{v_e} \rho[[Z][N]]^T [[Z][N]]\, dv_e,$$

where the summation operators are symbolically expressing the assemblage of the global stiffness and mass matrix by taking into account all the elements.

3. Numerical simulation

The main physical parameters of the material are summarised in Table 1. This material is characterised by ratios between the coefficients of the stiffness matrix C_{11}/C_{44} or C_{11}/C_{55} around 50, a value very far from the ratio $E/G \cong 3$ of an isotropic material. In this case the effects of transverse shear deformations cannot be considered negligible.

Table 1
Lamina characteristics

E_{11} (KN/mm^2)	172.369
$E_{22} = E_{33}$ (KN/mm^2)	$E_{11}/25$
$G_{12} = G_{13}$ (KN/mm^2)	$5 * E_{22}$
G_{23} (KN/mm^2)	$2 * E_{22}$
$\nu_{12} = \nu_{13} = \nu_{23}$	0.25
Density (kg/m^3)	1500

The numerical simulation has been developed for the following stacking sequences:

$$[0/90/0],\ [+45/-45]_s,\ [+30/-30]_s,\ [+45/-45/0/90]_s$$

and considering the simply-supported end constraints (see Fig. 1) for the examined structure.

Three single-layer higher-order models have been adopted for the present analysis respectively shown as models (1)–(3):

(1) $U(x,z) = u_0 + zu_1; \quad V(x,z) = v_0; \quad W(x,z) = w_0,$

(2) $U(x,z) = u_0 + zu_1 + z^2u_2 + z^3u_3; \quad V(x,z) = v_0;$
$W(x,z) = w_0,$

(3) $U(x,z) = u_0 + zu_1 + z^2u_2 + z^3u_3; \quad V(x,z) = v_0;$
$W(x,z) = w_0 + zw_1 + z^2w_2.$

The model (1) is like an SD (shear deformable) model of Reissner–Mindlin theory, with the principal difference, that here a corrective shear factor has not been included. The other two models allow a curved shape in the deformed configuration for every straight segment normal to the middle plane. The only difference between these last two models is that a transverse normal strain in the thickness direction has been allowed in the latter.

All the results of the numerical simulations have compared to those ones obtained with the CLT theory for which the exact solution is available in the hypothesis of simply supported boundary conditions:

$$\omega_n = \left(\frac{n\pi}{l}\right)^2 \sqrt{\frac{D_{11}}{\rho}}, \quad n = 1,2,\dots, \tag{8}$$

where D_{11} represents the coefficient of flexural stiffness that is defined as indicated in Eq. (9).

$$D_{11} = \frac{1}{3}\sum_{k=1}^{N} (Q_{11})_k (z_k^3 - z_{k-1}^3). \tag{9}$$

4. Convergence analysis

First, a convergence analysis has been developed. The diagrams of the eigenvalues as a function of the number of elements for the first four modes and for two different laminated plates with stacking sequences [0/90/0] and $[+45/-45/0/90]_s$ are respectively shown in Figs. 2 and 3. A higher-order model type (1) and a fixed ratio $l/t = 20$ (length/thickness) for the plate have been considered in both cases. All the values are normalised with respect to the corresponding CLT value set equal to 100.

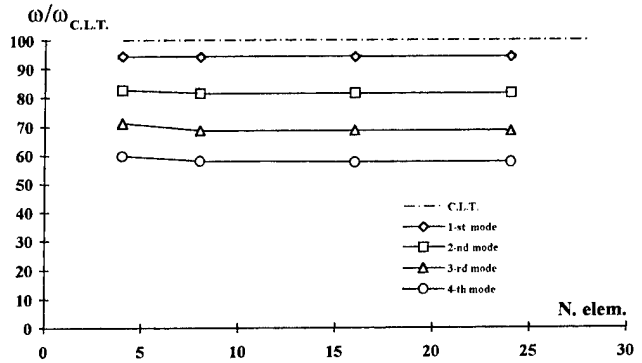

Fig. 2. Convergence analysis. Eigenvalues for the first four modes obtained with a ratio $l/t = 20$ and a [0/90/0] lay up, model type (1).

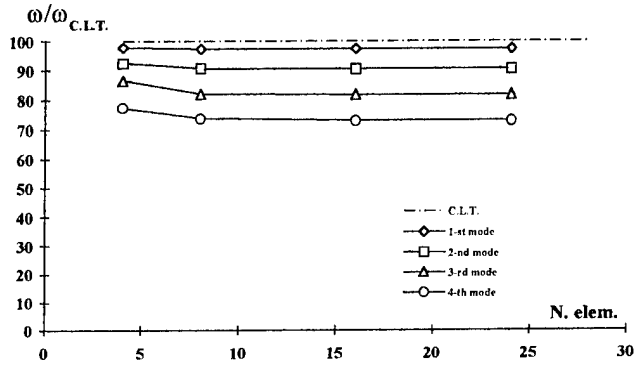

Fig. 3. Convergence analysis. Eigenvalues for the first four modes obtained with a ratio $l/t = 20$ and a $[+45/-45/0/90]_s$ lay up, model type (1).

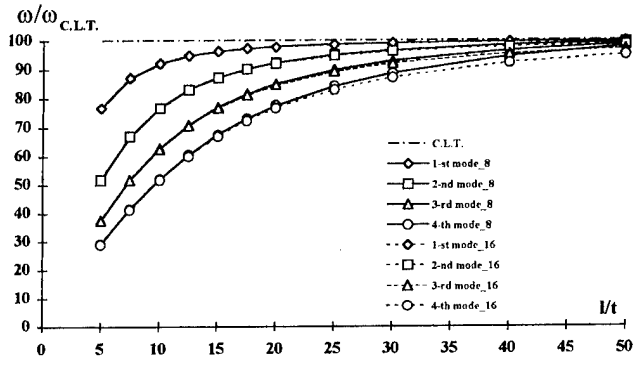

Fig. 4. Convergence analysis. Eigenvalues for the first four modes as a function of the ratio l/t and for different mesh refinement. $[+45/-45/0/90]_s$ lay up and higher order model type (1).

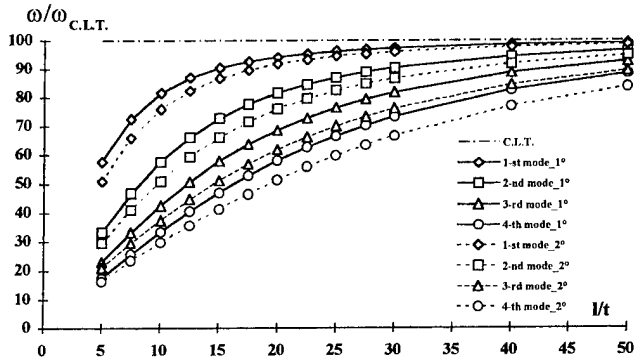

Fig. 5. Comparison between the results of models (1) and (2). Eigenvalues for first modes obtained varying the ratio l/t; [0/90/0] lay up.

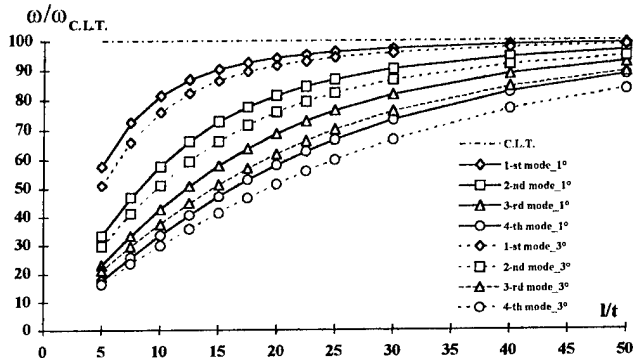

Fig. 6. Comparison between the results of models (1) and (3). Eigenvalues for first four modes obtained varying the ratio l/t; [0/90/0] lay up.

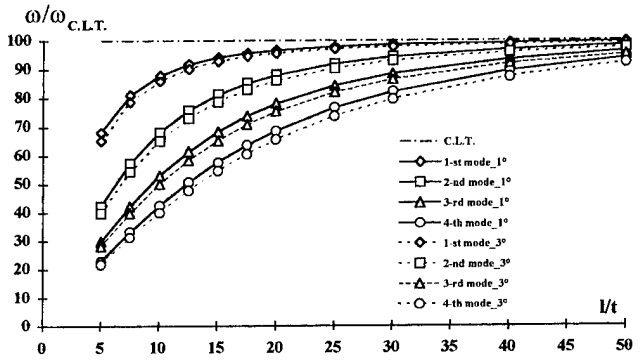

Fig. 7. Comparison between the results of models (1) and (3). Eigenvalues for first four modes obtained varying the ratio l/t; $[+30/-30]_s$ lay up.

As it is possible to note by examining these two diagrams, there is a rapid convergence in both cases; indeed, the eigenvalues are captured with only eight elements. As expected, the more the order of the mode increases the more the effect of the shear deformation is evident.

By comparing the two diagrams, it can be shown that the shear deformation effect depends not only upon the order of the mode but also the lay up: there is a approximate reduction equal to 45% for the [0/90/0] laminate in the 4th mode, while for the $[+45/-45/0/90]_s$ laminate this reduction is only equal to 25%.

The comparison between the results obtained for two meshes, respectively, 8 and 16 elements all of equal length, considering a $[+45/-45]_s$ stacking sequence and the model type (1) are shown in the diagram of

Fig. 4. Again, it is confirmed that an eight-element mesh is sufficient for evaluating the effect.

5. Comparison of the results

The eigenvalues for the first four modes, normalised with respect to the corresponding CLT value, as a function of the ratio l/t for models (1) and (2) are displayed and compared in Fig. 5. The considered stacking sequence is [0/90/0]. As it is possible to note in this diagram, the error between the models (1) and (2) cannot reach a value higher than 5%; while the error between model (1) and CLT is much higher.

The comparison between the results of model (1) and model (3) is shown in Fig. 6. From this figure and the previous one, it is evident there is no significant variation of results by using model (3) instead of model (2).

A similar comparison is shown in Fig. 7. Now the considered stacking sequence is $[+30/-30]_s$. Also this effect is dependent upon the stacking sequence. In this case the difference between the results of models (1) and (3) is not really significant from a practical viewpoint.

6. Conclusions

An evaluation of the global effects on the eigenfrequencies of a composite structure in cylindrical bending has been performed.

The study has highlighted the transverse shear deformation effect and higher-order effects as a function of the thickness of the plate evaluated in terms of the ratio l/t.

The reduction of the frequencies, especially for thick plates, with respect to CLT models is mostly captured by the first-order higher-order model and depends upon the stacking sequence.

Simple higher-order models (3rd degree of polynomial expansion in z) give corrections of the order of maximum few percents for the first modes. A further increase of the order of the model, if only low order modes are examined, seems not to be necessary.

References

[1] Noor AK. Free vibrations of multilayered composite plates. AIAA J 1972;11 (7):1038–39.
[2] Phan ND, Reddy JN. Analisys of laminated composite plates using a higher-order shear deformation theory. Internat J Numer Methods Engrg 1985;21:2201–19.
[3] Reddy JN. A simple higher-order theory for laminated composite plates. J Appl Mech 1984;51:745–52.
[4] Barboni R, Gaudenzi P. A class of C0 finite elements for the static and dynamic analysis of laminated plates. Comput & Structures 1992;44(6):1169–78.
[5] Sciuva MD. Bending, vibration and buckling of simply supported thick multilayered orthotropic plates: an evaluation of a new displacement model. J Sound Vibration 1986;105(3):425–42.
[6] Gaudenzi P, Barboni R, Mannini A. A finite element evaluation of single-layer and multi-layer theories for the analysis of laminated plates. Comp Struct 1995;30:427–40.
[7] Wu CP, Chen WY. Vibration and stability of laminated plates based on a local high order plate theory. J Sound Vibration 1994;177(4):503–20.
[8] Franco Correia VM, Mota Soares CM, Mota Soares CA. Higher-order models on the eigenfrequency analysis and optimal design of laminated composite structures. Comp Struct 1997;39:237–53.
[9] Gaudenzi P. Problemi di Analisi Strutturale di Piastre in Composito: Importanza del Comportamento 3D nei Problemi Statici, Dinamici e Termoelsatici. Tesi di Dottorato in Ingegneria Aerospaziale, Università di Roma "La sapienza" (in Italian), 1989.

ELSEVIER

Composite Structures 47 (1999) 827–833

COMPOSITE STRUCTURES

www.elsevier.com/locate/compstruct

A study on stress and vibration analysis of a steel and hybrid flexspline for harmonic drive

Han Su Jeon [a,*], Se Hoon Oh [b]

[a] *Technology Planning Team, Korea Institute of Industrial Technology Evaluation and Planning, Dongjak-gu 156-010, South Korea*
[b] *Department of Mechanical Design and Production Engineering, Chungang University, Dongjak-gu 156-756, South Korea*

Abstract

The conventional speed reducer uses the concept of rigid bodies, but the harmonic drive is operated by the elastic theory. As for this, harmonic drive shows different characteristics in operation principles and analysis compared to the conventional ones. Flexspline with components of harmonic drive can generate repeated vibration by the wave generator. Thus flexspline should have a good vibration characteristic. In this paper, a study on stress, deformation and related vibration characteristics using the finite element method tool has been carried out on the flexspline as a part of speed reducer. The damping ratio of composite flexspline is also five times as high as that of the steel flexspline. As a result of this study, composite flexspline has shown an improved quality compared to the conventional steel flexspline at the natural frequency, stiffness and damping capacity. © 2000 Published by Elsevier Science Ltd. All rights reserved.

Keywords: Harmonic drive; Robot speed reducer; Stress analysis; Vibration; Natural frequency

1. Introduction

Harmonic drive has several characteristics, for instance, a high precision, compactness, light-in-weight property and high reduction ratio characteristics compared with the conventional speed reducer. In modern industrial fields, a speed reducer requires a good driving torque, low backlashes and precise transmission characteristic of power. The harmonic drive has been applied as an actuator of robot, driving parts of measurement system, semiconductor manufacturing system, etc. The conventional speed reducer uses the concept of rigid bodies, but the harmonic drive is operated by the elastic theory. As for this, harmonic drive shows different characteristics in operation principles and analysis compared to the conventional ones. It is composed of flexspline, circular spline and wave generator. The wave generator has an oval cam type, which is operated by the input power and contacted with a flexspline. The circular spline has a rigid ring type with an internal gear. The flexspline has a thin circular cup type, it is the main component of a harmonic drive, which can generate a repeated vibration by the wave generator. With such a reason, the flexspline should have flexibility and good vibration characteristics.

In this paper, the application of steel and steel-composite hybrid materials as material of the flexspline in harmonic drive was analysed. It is important for the design of flexspline to consider a tooth and dimension in the harmonic drive was analysed. But circular spline has an internal gear type and good strength compared to flexspline. Many researchers have conducted studies to improve performance since Musser had invented a harmonic drive [1–3]. The purpose of the study is investigation of a stress and vibration characteristic to apply advanced materials such as carbon-fiber epoxy and glass-fiber epoxy composite materials from analysis of the dynamic characteristic of the harmonic drive. Analysis was performed on a three-dimensional model using an analytic output of the mathematical equation by the tooth elastic deformation.

In this paper, stress analysis and vibration characteristics were calculated using ANSYS [4], a commercial finite element analysis software for various types of conditions. Analysis has been performed on two kinds of models, one is a steel flexspline, the other is a steel-composite hybrid flexspline model, which is bonded to the interior part of the flexspline.

* Corresponding author.

0263-8223/99/$ - see front matter © 2000 Published by Elsevier Science Ltd. All rights reserved.
PII: S0263-8223(00)00060-X

2. Analysis of the steel flexspline

The flexspline has a thin cup type and an external gear profile in the open side. It is symmetric for the center line in static state, the wave generator to insert in flexspline and assemble with a circular spline, when harmonic drive was operating. A part of the flexspline's tooth is in contact with the circular spline's tooth near the major shaft when wave generator inserts in flexspline. In general, tooth contacts are about 10–30% of the total tooth number when harmonic drive was operating. Thus stress distribution cannot be symmetric for center line when the wave generator inserts in flexspline. When input power transfers from the wave generator to tooth of the flexspline, flexspline takes a strong twist deformation, which makes a stress concentration in some points. The flexspline was analyzed by the finite element method. It is useful to use a shell element without aspect ratio and geometric distortion, which can be generated in three-dimensional elements. Shell element cannot consider thickness direction in joint parts, and cannot make a modeling with external gear. Though flexspline is a thin shell type, three-dimensional elements have to be used [5]. Flexspline is loaded a bending stress by the structural condition. Model uses a three-dimensional hexagonal 8-node element with a 7840 element number. The contact part elements were further divided to improve results' accuracy. Model uses a cylindrical coordinate system to consider a symmetric structure for center line and a local coordinate system to draw a gear profile. Tooth profile was drawn with approximate data in modeling, because it was a very difficult and complex problem connected with shell of flexspline. It makes it possible to diminish modeling time and calculation time. Especially, it was calculated from a mathematical equation like the working point and gear profile to preserve accuracy of analysis of results using analytic output.

In this section, Table 1 shows the property of the steel. When flexspline and circular spline contact each other with parts of gear, for instance distributed loading of the input forces gear action. Distributed force is acted on the gear by the calculated data from theoretical equation.

Fig. 1 shows the analysis model of the steel flexspline. As a result of this analysis, the maximum tension stress has 152 MPa on the radial direction, which appears in contact parts with circular spline. Especially, that appears in dedendum of the tooth, which took the largest deformation placed by the major axis of the flexspline. And the maximum of the tension stress has 745 MPa in the circumferential direction, which appears in contact parts with circular spline.

Table 1
Properties of the steel

Tensile modulus (GPa)	210
Shear modulus (GPa)	80
Poisson's ratio	0.3
Tensile strength (MPa)	1000
Density (kg/m^3)	7850

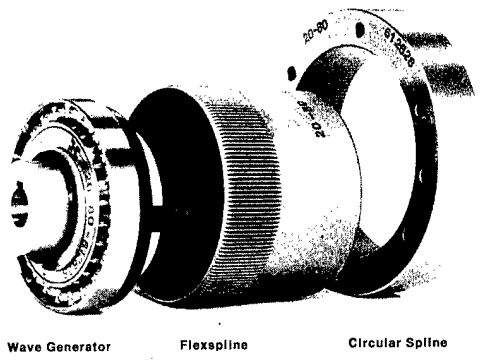

Fig. 1. Components of the harmonic drive.

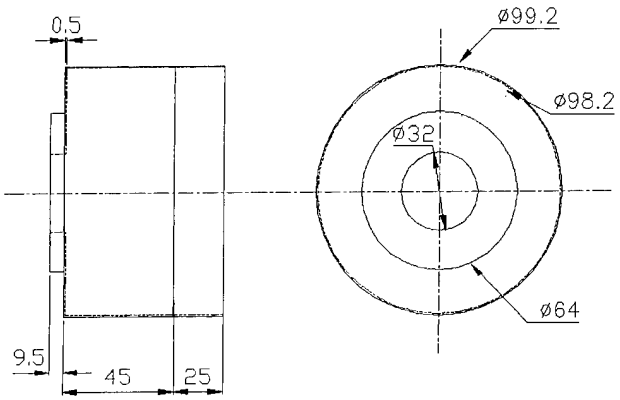

Fig. 2. Specification and dimension of the steel flexspline.

As a result of this analysis, the stress of circumferential direction is about five times larger than the radial stress. These results were very similar to the experimental test, conducted by Ishida using the strain gage for steel flexspline [6].

Stress distribution of the circumferential direction on gear section is shown in Fig. 2. Von Mises stress distributions for steel flexspline model are shown in Figs. 3 and 4. The maximum stress is shown in dedendum of gear, which position is the major axis. Stress distribution is shown symmetric on the major axis. The maximum stress is about 558 MPa. The maximum stress in the circumferential direction was 4.9 times larger than that in the radial direction.

3. Stress analysis of the steel-composite hybrid flexspline

The steel-composite hybrid flexspline was applied as composite material on some parts of flexspline. This was bonded to the interior part of flexspline.

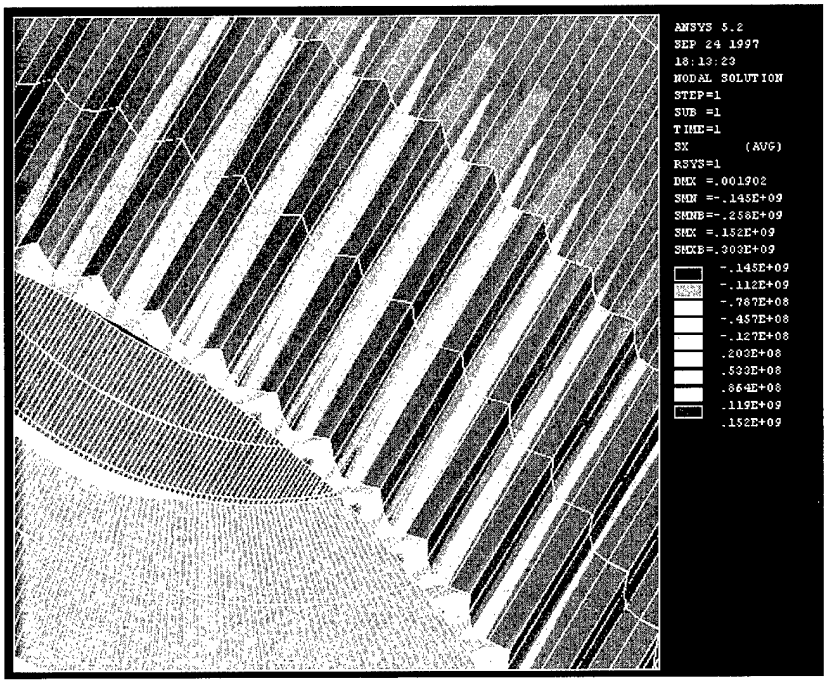

Fig. 3. Stress distribution of the circumferential direction on gear section.

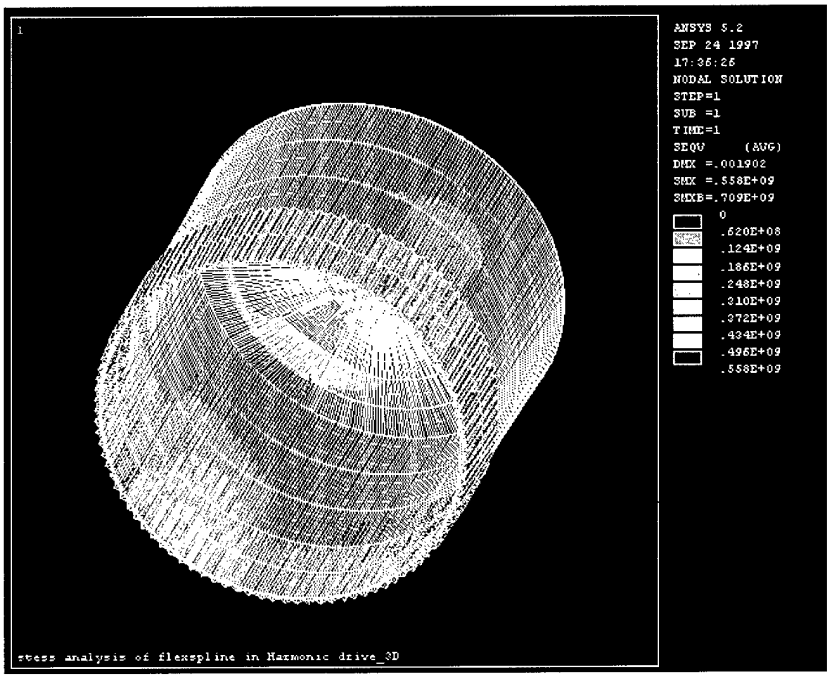

Fig. 4. Von Mises stress distributions.

In this study, two kinds of composite materials are considered like carbon-fiber and glass-fiber epoxy composite materials. These materials have a high specific stiffness (E/ρ) and specific strength (S/ρ) compared with conventional steel materials. The applied material on the interior part of flexspline is shown in Fig. 5.

There are two kinds of methods to use composite material in flexspline. One is as-occurred hybrid flexspline, the other is adhesively bonded hybrid flexspline. In this study, consider the first method. Bonded method on the flexspline is most popular using the bonded ring-shaped surface of conventional steel flexspline. And

there are several types of joint methods, namely single lap joint, double lap joint, scarf lap joint, stepped lap joint, etc. The single lap joint is most popularly used in this field. Due to the design and manufacturing method, it is simple and has low cost than other joint methods. Bonding thickness (BT) and stacking angle have variable values as main factors. BT 0.1, 0.5 and 1.0 mm and stacking angle ±30°, ±45° and ±60° make a diagonal loop and layer. Thickness of composite material is 0.6 mm, and width is 15 mm as shown in Fig. 5. Table 2 shows the mechanical properties of the composite materials. Steel parts of flexspline use the same element as steel model, and composite parts of flexspline use a layered structure element for bonded, that is simple bonded with steel parts. It has a merit of not needing to use two elements to make a bond with composite parts. Tables 2 and 3 show properties for composite materials and bonded materials. As a result of this, stress distribution pattern is a very similar phenomenon compared to steel model. Von Mises stress distribution of steel-composite hybrid flexspline is shown in Fig. 6. The maximum tension stress is 526 MPa on the gear section. Fig. 7 shows a stick graph for various types of conditions. Compared to composite materials, carbon-fiber epoxy hybrid model has a lower value than glass-fiber epoxy hybrid model for Von Mises stress. The glass-fiber epoxy composite hybrid model has a few different values with respect to BT and stacking angle. But car-

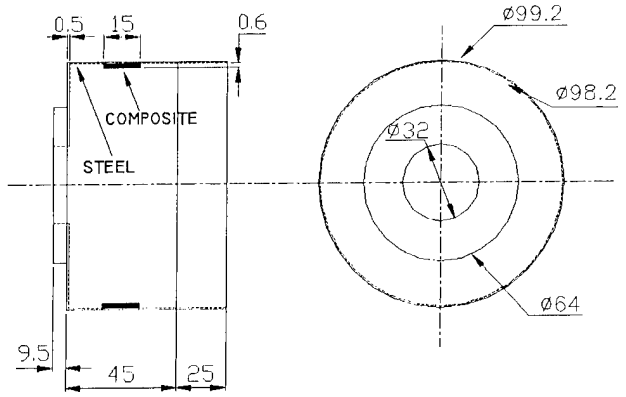

Fig. 5. Specification and dimension of the steel-composite hybrid flexspline.

Table 2
Properties of the composite materials

	Carbon-fiber epoxy	Glass-fiber epoxy
E_L (GPa)	130	43.5
E_T (GPa)	8.0	5.0
G_{LT} (GPa)	6.0	5.0
ν_{LT} (GPa)	0.28	0.25
ρ (kg/m^3)	1661	1997

Table 3
Properties of the epoxy resin (IPCO 9923)

Tensile modulus (GPa)	1.3
Shear modulus (GPa)	0.46
Poisson's ratio	0.41
Tensile strength (GPa)	45.0
Shear strength (GPa)	29.5
Lap shear strength (GPa)	13.7
Density (kg/m^3)	1200

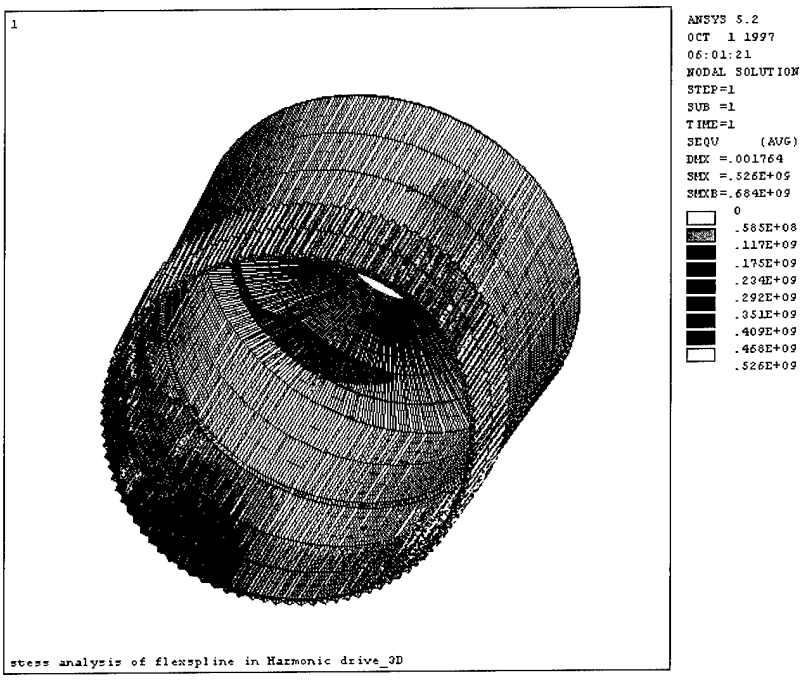

Fig. 6. Von Mises stresses of the carbon-fiber epoxy hybrid flexspline (BT: 1.0 mm, ±60°).

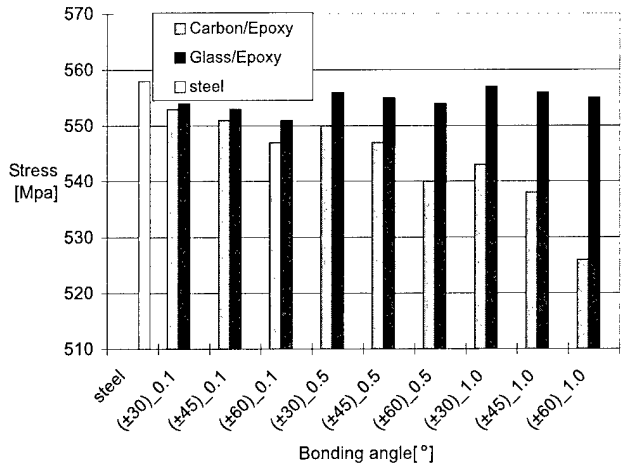

Fig. 7. Maximum Von Mises stresses with respect to materials.

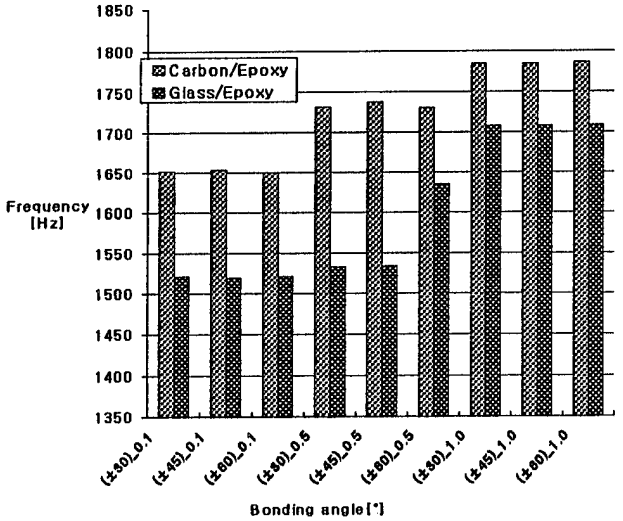

Fig. 8. The first natural frequency of the steel-composite hybrid flexspline.

bon-fiber epoxy hybrid model has a slight decline for Von Mises stress values. There is a 3.83% decline value for BT variance.

As a result of this, the Von Mises stress of carbon-fiber epoxy hybrid flexspline has a 5.73% lower value than that of the steel flexspline model. The displacement of the carbon-fiber epoxy composite hybrid flexspline has a 7.16% lower value than that of the steel flexspline model, but glass-fiber epoxy hybrid flexspline has a little difference than that of the steel model. The carbon-fiber epoxy hybrid model with a BT 1 mm and stacking angle ±60° has good characteristics for Von Mises and displacement.

4. Vibration characteristics of the steel-composite hybrid flexspline

Composite materials can be made to have high static stiffness and damping because composite materials can be composed of two materials, one has high Young's modulus and the other has high damping. The wave generator makes flexspline move repetitively. As the natural frequency of the flexspline is affected by driving frequency of wave generator, harmonic drive has a short life and bad transmission characteristics. Natural frequency of radial direction and damping capacity are the main factors in vibration characteristics, and the other factors are such as BT and joining technology in hybrid model.

In this study, BT and stacking angle were considered. The first natural frequency of carbon-fiber epoxy hybrid model was 7.7 times higher than that of the steel model and 4.5% higher than that of the glass-fiber epoxy hybrid model on the same condition. The first natural frequency of the carbon-fiber epoxy hybrid model was slightly higher with the increase of stacking angle and

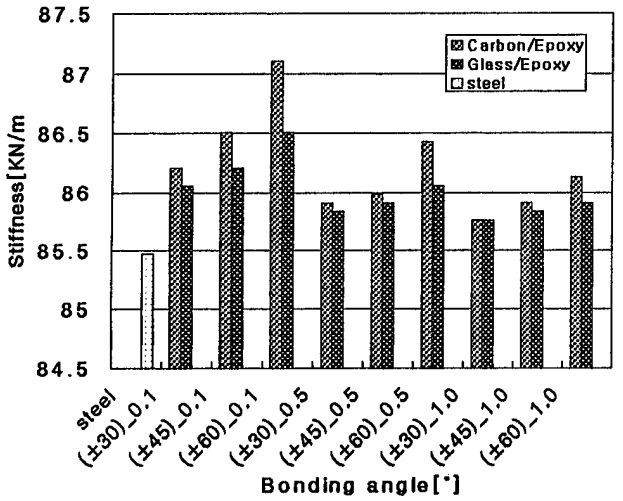

Fig. 9. Radial spring constant of the steel-composite hybrid flexspline.

BT. But that of the glass-fiber epoxy hybrid model had a little difference with the increase of stacking angle and BT. As a result of this, carbon-fiber epoxy hybrid model has a good vibration characteristic with respect to a stacking angle ±60°, BT 1 mm. Fig. 8 shows variation of the first natural frequency with respect to bonding angle and thickness.

A stiffness of flexspline at the maximum displacement was considered, when constant force of 100 N was acted on flexspline in the radial and circumferential directions. Flexspline must have the flexibility on the radial direction to improve a vibration characteristic, and the stiffness on the circumferential direction to preserve an accurate motion transmission. Figs. 9 and 10 show variations of stiffness about bonding angle for different materials and conditions.

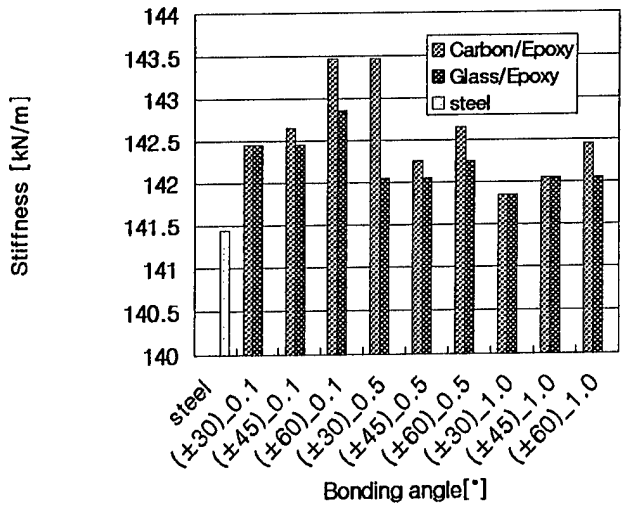

Fig. 10. Torsional spring constant of the steel-composite hybrid flexspline.

The ratio of radial and circumferential spring constants was 0.603 for steel, but for that of carbon-fiber epoxy and glass-fiber epoxy hybrid models were, respectively, 0.607, 0.605. As the ratio of radial and circumferential spring constants is similar to these materials, it is possible to use a flexspline for ratio of spring constant.

5. Damping capacity of the steel-composite hybrid flexspline

The damping capacity of flexspline was investigated for different materials, when a constant force of 100 N was acted on the flexspline during 0.6 s. To observe the damping effects during 9.4 s the constant force with respect to displacement and time was removed on the working points. For this purpose, transient analysis method was used such as ANSYS. Fig. 11 shows a transient graph with respect to displacement and time, when 100 N forces removed from the steel flexspline during 0.4 s.

Magnification graph of the displacement parts after constant force is removed is shown in Fig. 12. The transient graph of steel model shows a sine wave pattern with about 2 s frequency. The displacement of steel model is 23 times higher than that of steel-composite hybrid model on the same condition. The damping capacity of the steel-composite hybrid model was better with the increase of the BT and stacking angle. In general, the damping capacity of carbon-fiber epoxy hybrid model was 0.15% higher than that of glass-fiber epoxy hybrid model. To compare steel with steel-composite hybrid model about damping capacity, carbon-fiber epoxy hybrid model with BT 1.0 mm and stacking angle ±60° had 5.6 times more effect than the steel model.

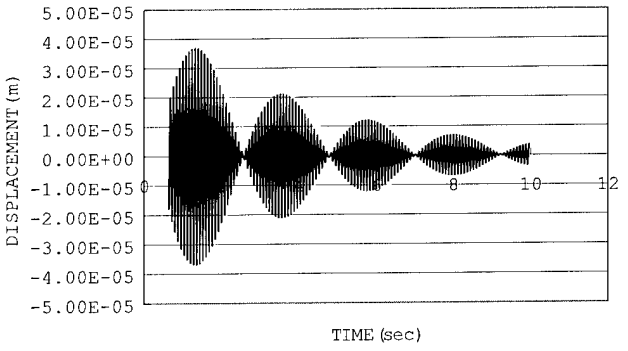

Fig. 11. Transient graph with respect to displacement and time when 100 N force is removed from the steel flexspline during 0.94 s.

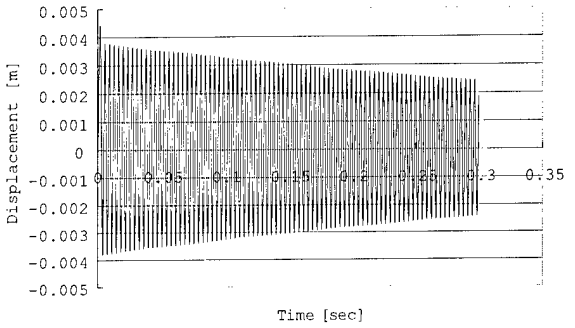

Fig. 12. Transient graph with respect to displacement and time when 100 N force is removed from the carbon-fiber epoxy hybrid flexspline during 0.94 s (BT: 1.0 mm, ±60° carbon/epoxy).

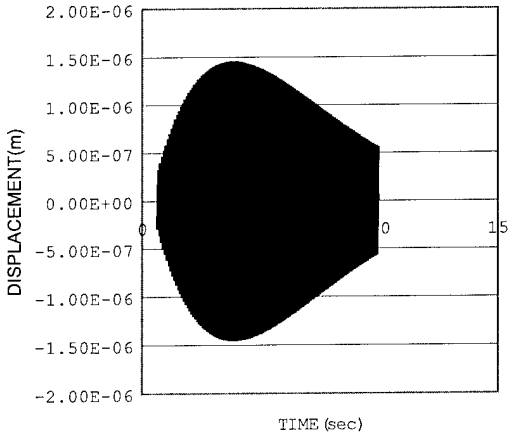

Fig. 13. Displacement of 1 p't in steel flexspline.

It was found that the damping effects of the steel-composite hybrid flexspline are better than that of the steel flexspline, when the actual force of 294 N was acted on. Figs. 13 and 14 show transient graphs with respect to materials. According to the graphs, transient phenomenon was approximately zero during 0.18 s on the carbon-fiber epoxy hybrid flexspline. But transient

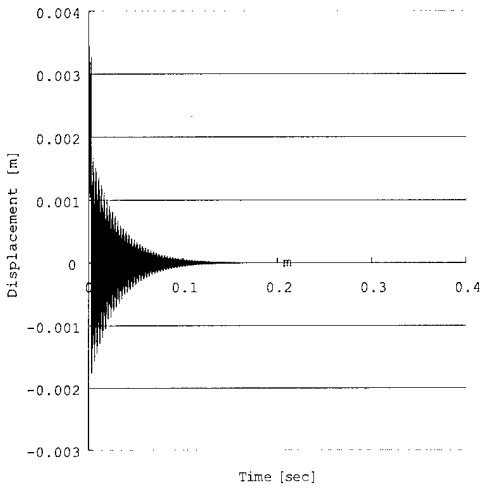

Fig. 14. Displacement of 1 p't in steel-composite hybrid flexspline.

phenomenon of the steel flexspline was approximately zero during 0.9 s.

6. Conclusions

In this paper, a study on stress and related vibration characteristics using the numerical analysis tool, has been carried out on the flexspline as part of speed reducer.

Analysis has been applied to two kinds of models, which are steel flexspline and steel-composite hybrid flexspline with carbon-fiber epoxy and glass-fiber epoxy composite materials. The stress, stiffness and damping capacity were investigated as a vibration characteristic.

According to results of this study, the stress ratios of radial and circumferential directions have similar values with respect to materials. Steel-composite hybrid model can be used as a component of the harmonic drive. The Von Mises stress of carbon-fiber epoxy hybrid model was 5.73% lower than that of the steel model and the first natural frequency was 7.7 times higher than that of steel model. Displacement of the steel-composite hybrid model is 23 times lower than that of the steel model.

The damping capacity, natural frequency and Von Mises stress of the steel-composite hybrid model are better with the increase of the BT and stacking angle. Especially, carbon-fiber epoxy hybrid model has a better characteristic than the glass-\ epoxy hybrid model.

Acknowledgements

This research was supported by Chungang University research grants in 1998.

References

[1] Muser CW. Strain Wave Gearing, United States Patent, No. 2,906,143.
[2] Kiyosawa Y, Takizawa N, Ohkura T, Yamamoto Y. A New Strain Wave Gearing, JSME, 23–26 November 1991, p. 1132–6.
[3] Tuttle TD. Understanding and modeling the behavior of a harmonic drive gear transsmision, MIT Technical Report 1365, MIT Artificial Intelligence Lab., 1992.
[4] Swanson Analysis System Inc., ANSYS Revision 5.0, Vol. III Element & Vol. XI, Dynamic.
[5] Se Hoon Oh, Seung Hwan Chang, Dai Gil Lee. Improvement of the dynamic properties of the steel-composite hybrid flexspline for a harmonic drive. Compos Struct 1997;38(1–4):251–60.
[6] Takeshi Ishida, Teruki Hidaka, et al. Bending stress on flexible spline of strain wave gearing. JSME 1993;59(567).

ELSEVIER

Composite Structures 47 (1999) 835–843

COMPOSITE STRUCTURES

www.elsevier.com/locate/compstruct

CONTENTS OF VOLUMES 44–47

Volume 44 Number 1

1 Studies in the matrix dominated failures of composite joints
R. JONES, J. P. G. SAWYER & W. K. CHIU (Australia)

17 Composite repairs to cracks in thick metallic components
R. JONES & W. K. CHIU (Australia)

31 Buckling and vibrations of unsymmetric laminates resting on elastic foundations under in-plane and shear forces
M. A. AIELLO & L. OMBRES (Italy)

43 A method for modeling the local and global buckling of delaminated composite plates
H. KIM & K. T. KEDWARD (USA)

55 Free vibration behaviour of helically wound cylindrical shells
C. B. SHARMA, M. DARVIZEH (UK) & A. DARVIZEH (Iran)

63 Performance of concrete beams prestressed with aramid fiber-reinforced polymer tendons
H. A. TOUTANJI & M. SAAFI (USA)

71 Modeling failure in notched plates with micropolar strain softening
T. C. KENNEDY (USA)

Volume 44 Numbers 2–3

81 Dynamic analysis for laminated composite beams
A. S. BASSIOUNI, R. M. GAD-ELRAB & T. H. ELMAHDY (Egypt)

89 Recent research on enhancement of damping in polymer composites
I. C. FINEGAN & R. F. GIBSON (USA)

99 Structural testing of DARPA/BIR composite army bridge treadway
J. B. KOSMATKA (USA)

117 Effect of thickness on the large elastic deformation behavior of laminated shells
R. A. CHAUDHURI & R. L. HSIA (USA)

129 Modeling of the torsional behavior of plasma sprayed copper
B. KAAYOU, K. E. ATCHOLI (France) & J. VANTOMME (Belgium)

137 Shear deformable user finite element for MARC to model composites with taper
B. B. HOFMAN & O. O. OCHOA (USA)

145 The free vibrations of rectangular composite plates with point-supports using static beam functions
Y. K. CHEUNG (Hong Kong) & D. ZHOU (China)

155 Durability characteristics of concrete columns confined with advanced composite materials
H. A. TOUTANJI (USA)

163 Fatigue life prediction of circular notched CFRP laminates
J. S. HUH & W. HWANG (South Korea)

169 An examination of a higher order theory for sandwich beams
S. R. SWANSON (USA)

179 Life extension of acoustically fatigued panels using add-on dampers
W. K. CHIU, U. SIOVITZ, S. C. GALEA & L. L. KOSS (Australia)

189 Composite beam analysis with arbitrary cross section
A. TAUFIK, J. J. BARRAU & F. LORIN (France)

195 Design, analysis, and optimization of composite leaf springs for light vehicle applications
E. SANCAKTAR & M. GRATTON (USA)

205 Response of composite beam under low-velocity impact of multiple masses
K. Y. LAM & T. S. SATHIYAMOORTHY (Singapore)

Volume 44 Number 4

221 Similitude study for a laminated cylindrical tube under tensile, torsion, bending, internal and external pressure. Part I: governing equations
C. S. CHOUCHAOUI & O. O. OCHOA (USA)

231 Similitude study for a laminated cylindrical tube under tension, torsion, bending, internal and external pressure. Part II: scale models
C. S. CHOUCHAOUI, P. PARKS & O. O. OCHOA (USA)

237 Failure mode maps for honeycomb sandwich panels
A. PETRAS & M. P. F. SUTCLIFFE (UK)

253 Graphite/epoxy honeycomb core sandwich permeability under mechanical loads
D. E. GLASS, V. V. RAMAN, V. S. VENKAT & S. N. SANKARAN (USA)

263 Compression, flexure and shear properties of a sandwich composite containing defects
A. P. MOURITZ & R. S. THOMSON (Australia)

279 Buckling and free vibration of non-homogeneous composite cross-ply laminated plates with various plate theories
M. E. FARES & A. M. ZENKOUR (Egypt)

289 On the computation of interface stresses by finite elements for sandwich materials
V. MANET (France)

297 Non-homogeneous response of cross-ply laminated elastic plates using a higher-order theory
A. M. ZENKOUR & M. E. FARES (Egypt)

Volume 45 Number 1

1 Fabrication and testing of composite isogrid stiffened cylinder
T. D. KIM (JAPAN)

7 Ovalization analysis of fiber-reinforced plastic poles
S. IBRAHIM & D. POLYZOIS (CANADA)

13 Buckling of woven GFRP cylinders under concentric and eccentric compression
A. Y. ELGHAZOULI, M. K. CHRYSSANTHOPOULOS & I. E. ESONG (UK)

29 Fracture mechanics using a 3D composite element
B. G. FALZON, D. HITCHINGS & T. BESANT (UK)

41 Mechanical property distribution of CFRP filament wound composites
T. P. PHILIPPIDIS, D. J. LEKOU & D. G. AGGELIS (GREECE)

51 Flexural analysis of laminated composite plates
P. SUBRAMANIAN (INDIA)

71 A failure mechanism-based approach for design of composite laminates
G. NARAYANA NAIK & A. V. KRISHNA MURTY (INDIA)

Volume 45 Number 2

81 Impact damage prediction and failure analysis of heavily loaded, blade-stiffened composite wing panels
J. F. M. WIGGENRAAD (The Netherlands), X. ZHANG & G. A. O. DAVIES (UK)

105 Laminated composite open profile sections: first order shear deformation theory
S. S. MADDUR & S. K. CHATURVEDI (USA)

115 Large deflection of composite laminated plates under transverse and in-plane loads and resting on elastic foundations
H.-S. SHEN (People's Republic of China)

125 Analytical simulation of stress wave propagation in composite materials
B. PARGA-LANDA, S. VLEGELS, F. HERNÁNDEZ-OLIVARES (Spain) & S. D. CLARK (UK)

131 Effective elastic properties of triangular grid structures
J. HOHE & W. BECKER (Germany)

147 Elastic response of a typical CFRP payload fairing due to separation impulse
V. RAMAMURTI, S. RAJARAJAN & G. V. RAO (India)

155 Interlaminar stresses at the free corners of a laminate
W. BECKER, P. P. JIN & P. NEUSER (Germany)

Volume 45 Number 3

163 3-D global/local analysis of composite hip prostheses – a model for multiscale structural analysis
S. SRINIVASAN, J. R. DE ANDRADE, S. B. BIGGERS JR. & R. A. LATOUR JR. (USA)

171 Stress distribution around triangular holes in anisotropic plates
V. G. UKADGAONKER & D. K. N. RAO (India)

185 Modeling of cracked thick metallic structure with bonded composite patch repair using three-layer technique
J. J. SCHUBBE & S. MALL (USA)

195 Stress distribution in sandwich beams under tension
C. GIN-BOAY, S. LEONG-KEEY & C. LEE-SOON (Singapore)

205 Symmetric deformation analysis of symmetric laminated plates including transverse shear and normal effects
J.-F. HE & S.-W. ZHANG (People's Republic of China)

227 A new theory for accurate thermal/mechanical flexural analysis of symmetric laminated plates
J. S. M. ALI, K. BHASKAR & T. K. VARADAN (India)

233 Validation of two-dimensional calculations of free edge delamination in laminated composites
J. H. A. SCHIPPEREN & F. J. LINGEN (The Netherlands)

Volume 45 Number 4

241 A study of fastener pull-through failure of composite laminates. Part 1: Experimental
A. BANBURY & D. W. KELLY (Australia)

255 A study of fastener pull-through failure of composite laminates. Part 2: Failure prediction
A. BANBURY, D. W. KELLY & L. K. JAIN (Australia)

271 A simplified beam analysis of the end notched flexure mode II delamination specimen
W. DING & M. T. KORTSCHOT (Canada)

279 Optimum design of cross-sectional profiles of pultruded box beams with high ultimate strength
L.-H. GAN, L. YE & Y.-W. MAI (Australia)

289 Compressive behaviour of CFRP laminates repaired with adhesively bonded external patches
C. SOUTIS, D-M. DUAN & P. GOUTAS (UK)

303 A theoretical study on shear strengthening of reinforced concrete beams using composite plates
G. GENDRON, A. PICARD & M.-C. GUÉRIN (Canada)

311 Internal pressure loading of segmented-stiffness composite cylinders
M. W. HYER & J. C. RIDDICK (USA)

321 Erratum

Volume 46 Number 1

1 Development of a specialised finite element for the analysis of composite structures with ply drop-off
A. MUKHERJEE & B. VARUGHESE (India)

17 Internally pressurized elliptical composite cylinders
M. W. HYER & J. M. MCMURRAY (USA)

33 Postbuckling analysis of delaminated composite beams by differential quadrature method
S. MORADI & F. TAHERI (Canada)

41 Damping studies in fiber-reinforced composites – a review
R. CHANDRA, S. P. SINGH & K. GUPTA (India)

53 Failure of orthotropic plates containing a circular opening
H. A. WHITWORTH & H. MAHASE (USA)

59 Dynamic instability analysis of circular conical shells
M. GANAPATHI, B. P. PATEL, C. T. SAMBANDAM (India) & M. TOURATIER (France)

65 Transient response of floating composite ship section subjected to underwater shock
S. W. GONG & K. Y. LAM (Singapore)

73 Effective elastic properties of hexagonal and quadrilateral grid structures
J. HOHE, C. BESCHORNER & W. BECKER (Germany)

Volume 46 Number 2

91 Layer-wise closed-form theory for geometrically nonlinear rectangular composite plates subjected to local loads
G.-Q. LI (Switzerland)

103 Partial-mixed formulation and refined models for the analysis of composite laminates within an FSDT
F. AURICCHIO & E. SACCO (Italy)

115 Two shear deformable finite element models for buckling analysis of skew fibre-reinforced composite and sandwich panels
C. SARATH BABU & T. KANT (India)

125 Exact solution for axisymmetric thick laminated shells
K. DING & L. TANG (People's Republic of China)

131 Delamination behavior of spliced Fiber Metal Laminates. Part 1. Experimental results
T. J. DE VRIES, A. VLOT & F. HASHAGEN (The Netherlands)

147 Delamination behavior of spliced Fiber Metal Laminates. Part 2. Numerical investigation
F. HASHAGEN, R. DE BORST & T. DE VRIES (The Netherlands)

163 Modeling of vibration damping in composite structures
A. MAHER, F. RAMADAN & M. FERRA (Egypt)

171 Optimum design of composite structures with ply drop using genetic algorithm and expert system shell
J.-S. KIM, C.-G. KIM & C.-S. HONG (South Korea)

189 Nonlinear free flexural vibrations/post-buckling analysis of laminated orthotropic beams/columns on a two parameter elastic foundation
B. P. PATEL (India), M. GANAPATHI (India) & M. TOURATIER (France)

Volume 46 Number 3

197 Non-linear vibration of composite laminated plates by the hierarchical finite element method
P. RIBEIRO (Portugal) & M. PETYT (UK)

209 Statistical aspects of strength size effect of laminated composite materials
A. TABIEI & J. SUN (USA)

217 On an orthotropic model for progressive degradation
V. B. HAMMER & P. PEDERSEN (Denmark)

229 Free vibration of composite beams featuring interlaminar bonding imperfections and exposed to thermomechanical loading
U. ICARDI (Italy)

245 Postbuckling analysis of tailored composite plates with progressive damage
A. T. BARANSKI & S. B. BIGGERS (USA)

257 Non-linear bending analysis of composite laminated plates using a refined first-order theory
M. E. FARES (Egypt)

267 Impact energy absorption characteristics of glass fiber hybrid composites
S. S. CHEON, T. S. LIM & D. G. LEE (South Korea)

279 The delamination buckling of single-fibre system and interply hybrid composites
S.-F. HWANG & C.-P. MAO (Republic of China)

289 Plate waves in multi-directional composite laminates
J. LEE (Korea)

299 Compressive strength of unidirectional composites: evaluation and comparison of prediction models
N. K. NAIK & R. S. KUMAR (India)

Volume 46 Number 4

309 Micro-mechanical approach and algorithm for the study of damage appearance in elastomer composites
M. BRIEU & F. DEVRIES (France)

321 A new finite element for buckling analysis of laminated stiffened plates
Y. V. SATISH KUMAR & M. MUKHOPADHYAY (India)

333 On the stress analysis of cross-ply laminated plates and shallow shell panels
K. P. SOLDATOS (UK) & X. SHU (China)

345 Optimisation of geometrically non-linear composite structures based on load–displacement control
C. A. CONCEIÇÃO ANTÓNIO (Portugal)

357 An analytical study of the effect of slamming pressures on the interlaminar behaviour of composite panels
B. PARGA-LANDA (Spain), S. VLEGELS (Spain), F. HERNÁNDEZ-OLIVARES (Spain) & S. D. CLARK (UK)

367 High performance 3D-analysis of thermo-mechanically loaded composite structures
R. ROLFES, J. NOACK & M. TAESCHNER (Germany)

381 Post-buckling behaviour of thermoplastic matrix composite laminates subjected to pure shear
P. GAUDENZI, R. BARBONI, G. MORMINO & P. DINARDO (Italy)

387 Architecture and composite structure of hornet cuticle (Insecta, Hymenoptera)
J. S. ISHAY, L. LITINETSKY & D. M. STEINBERG (Israel)

395 Nonlinear finite element analysis of stress and strain distributions across the adhesive thickness in composite single-lap joints
G. LI, P. LEE-SULLIVAN & R. W. THRING (Canada)

405 A damping analysis of composite laminates using the closed form expression for the basic damping of Poisson's ratio
J. H. YIM (South Korea)

413 Indentation resistance of sandwich beams
A. PETRAS & M. P. F. SUTCLIFFE (UK)

Volume 47 Numbers 1–4

425 Editorial
I. H. MARSHALL (UK)

427 Foreword

429 Australian Composite Structures Society Composite Structures Award

431 Bonded composite repair of fatigue-cracked primary aircraft structure
A. BAKER (Australia)

445 Matrix dominated time dependent failure predictions in polymer matrix composites
H. F. BRINSON (USA)

457 Analysis and development of the angular twist type torque-meter
Y. D. CHEONG, J. W. KIM, S. H. OH & C. W. LEE (South Korea)

463 A simulation study on the thermal buckling behavior of laminated composite shells with embedded shape memory alloy (SMA) wires
H. J. LEE, J. J. LEE & J. S. HUH (South Korea)

471 A resin film infusion process for manufacture of advanced composite structures
B. QI, J. RAJU, T. KRUCKENBERG & R. STANNING (Australia)

477 Evaluation of elastic properties of 3-D (4-step) regular braided composites by a homogenisation method
C. ZUORONG, Z. DECHAO (People's Republic of China), M. LU (People's Republic of China, Australia) & L. YE (Australia)

483 An engineering approach for predicting residual strength of carbon/epoxy laminates after impact and hygrothermal cycling
B. QI & I. HERSZBERG (Australia)

491 Numerical investigation on thermal response of oil-heated tool for manufacture of composite products
Y. DING, W. K. CHIU & X. L. LIU (Australia)

497 Composite robot end effector for manipulating large LCD glass panels
J. H. OH, D. G. LEE & H. S. KIM (South Korea)

507 Composite heddle frame for high-speed looms
D. G. LEE, C. S. LEE, J. H. OH & H. S. JEON (South Korea)

519 Crack path selection in piezoelectric bimaterials
Q.-H. QIN & Y.-W. MAI (Australia)

525 Damage detection of CFRP laminates using electrical resistance measurement and neural network
D.-C. SEO & J.-J. LEE (South Korea)

531 Development of semianalytical axisymmetric shell models with embedded sensors and actuators
I. F. PINTO CORREIA, C. M. MOTA SOARES, C. A. MOTA SOARES (Portugal) & J. HERSKOVITS (Brazil)

543 Evaluation of durability and strength of stitched foam-cored sandwich structures
J. H. KIM, Y. S. LEE, B. J. PARK & D. H. KIM (South Korea)

551 Experimental and numerical study of the impact behavior of SMC plates
S.-M. LEE, J.-S. CHEON & Y.-T. IM (South Korea)

563 External failure pressure of a frangible laminated composite canister cover
T. Y. KAM, J. H. WU & W. T. WANG (Taiwan)

571 Flexure of pultruded GRP beams with semi-rigid end connections
G. J. TURVEY (UK)

581 Heat transfer and cure analysis for the pultrusion of a fiberglass-vinyl ester I beam
X. L. LIU & W. HILLIER (Australia)

589 Synthesis of in situ Al–TiB_2 composites using stir cast route
K. L. TEE, L. LU & M. O. LAI (Singapore)

595 Influence of SiC particles on mechanical properties of Mg based composite
B. W. CHUA, L. LU & M. O. LAI (Singapore)

603 Mesh design in finite element analysis of post-buckled delamination in composite laminates
T. E. TAY, F. SHEN, K. H. LEE (Singapore), A. SCAGLIONE & M. DI SCIUVA (Italy)

613 In situ synthesis of TiC composite for structural application
L. LÜ, M. O. LAI & J. L. YEO (Singapore)

619 On the dynamic response of metal matrix composite panels to uniform temperature loading
E. FELDMAN & R. GILAT (Israel)

625 Optimal design of piezolaminated structures
C. M. MOTA SOARES, C. A. MOTA SOARES & V. M. FRANCO CORREIA (Portugal)

635 Optimum in situ strength design of laminates under combined mechanical and thermal loads
J. WANG (People's Republic of China) & B. L. KARIHALOO (UK)

643 Post-fire mechanical properties of marine polymer composites
A. P. MOURITZ & Z. MATHYS (Australia)

655 Prediction of shrinkage and warpage in consideration of residual stress in integrated simulation of injection molding
D.-S. CHOI & Y.-T. IM (South Korea)

667 Resistance welding of carbon fibre reinforced thermoplastic composite using alternative heating element
M. HOU, M. YANG, A. BEEHAG, Y.-W. MAI & L. YE (Australia)

673 Stress analysis of adhesively-bonded lap joints
S.-C. HER (ROC)

679 The active buckling control of laminated composite beams with embedded shape memory alloy wires
S. CHOI, J. J. LEE, D. C. SEO & S. W. CHOI (South Korea)

687 The mechanical performance of 3D woven sandwich composites
M. K. BANNISTER, R. BRAEMAR & P. J. CROTHERS (Australia)

691 Application of thermodynamic calculation in the in-situ process of Al/TiB_2
N. L. YUE, L. LU & M. O. LAI (Singapore)

695 Thermal buckling and postbuckling analysis of a laminated composite beam with embedded SMA actuators
J. J. LEE & S. CHOI (South Korea)

705 Thermo-mechanical behaviour of shape memory alloy reinforced composite laminate (Ni–Ti/glass-fibre/epoxy)
Z. SU, H. MAI (People's Republic of China), M. LU (People's Republic of China, Australia) & L. YE (Australia)

711 Residual compressive strength of laminated plates with delamination
H. CHEN & X. SUN (People's Republic of China)

719 Design and evaluation of various section profiles for pultruded deck panels
L. H. GAN, L. YE & Y.-W. MAI (Australia)

727 On the mechanical behaviour of aging and recycled paper structures under cyclic humidity
S. DILLON, R. JONES & V. BUZZI (Australia)

737 Composite repairs to rib stiffened panels
T. TING, R. JONES, W. K. CHIU, I. H. MARSHALL (Australia) & J. M. GREER (USA)

745 Smart structure for composite repair
Y. L. KOH, N. RAJIC, W. K. CHIU & S. GALEA (Australia)

753 Impact resistance and tolerance of interleaved tape laminates
A. DUARTE, I. HERSZBERG & R. PATON (Australia)

759 Structural integrity analysis of embedded optical fibres in composite structures
R. HADZIC, S. JOHN & I. HERSZBERG (Australia)

767 The shear properties of woven carbon fabric
M. NGUYEN, I. HERSZBERG & R. PATON (Australia)

781 The bending properties of integrally woven and unidirectional prepreg T-sections
R. S. THOMSON, P. J. FALZON, A. NICOLAIDIS, K. H. LEONG (Australia) & T. ISHIKAWA (Japan)

789 Computer modelling of impact on curved fibre composite panels
Z. LEYLEK, M. L. SCOTT, S. GEORGIADIS & R. S. THOMSON (Australia)

797 Micromechanics models for the elastic constants and failure strengths of plain weave composites
P. TAN, L. TONG & G. P. STEVEN (Australia)

805 Reinforcement of concrete beam–column connections with hybrid FRP sheet
J. LI, S. L. BAKOSS, B. SAMALI & L. YE (Australia)

813 Development of a composite cargo door for an aircraft
H. G. S. J. THUIS (Netherlands)

821 An evaluation of higher-order effects on the eigenfrequencies of composite structures
P. GAUDENZI & R. CARBONARO (Italy)

827 A study on stress and vibration analysis of a steel and hybrid flexspline for harmonic drive
H. S. JEON & S. H. OH (South Korea)

FROM ELSEVIER SCIENCE...
SCIENCE PUBLISHER TO THE WORLD

CONTENTS DIRECT

A FREE alerting service by E-mail for Elsevier Science journals

ContentsDirect allows you unrivalled access to the Tables of Contents pages of Elsevier Science journals in the following subject areas:

- Chemistry and Chemical Engineering
- Clinical Medicine
- Computer Science
- Earth and Planetary Sciences
- Economics, Business and Management Science
- Engineering, Energy and Technology
- Environmental Science and Technology
- Life Sciences
- Materials Science
- Mathematics
- Physics and Astronomy
- Social Sciences
- Multidiscipline

What does ContentsDirect provide?

- Journal title
- Volume and issue number
- Title of paper
- Names of authors
- Page details
- Anticipated publication date
- News and offers

Why register to ContentsDirect?

- Provides via E-mail advance notice of forthcoming papers, allowing you to reserve the issue at your library.
- Provides an invaluable information resource to scientists and researchers requiring the very latest information on soon-to-be published papers.
- Keeps you at the forefront of current research.
- Enables you to create a personal archive of key journal contents in your field of interest.

How to register for ContentsDirect:

- The quickest way to register for **ContentsDirect** is via Elsevier Science home page on the world wide web.
- Registration is simple and the selection of titles is provided by access to drop down menus of all subject classifications plus a complete listing of all titles available.
- If you wish to select new titles or amend your existing selection - simply re-visit the web site and personally make your changes.

ContentsDirect

Register now! **ContentsDirect**

www.elsevier.com/locate/ContentsDirect

www.elsevier.nl/locate/ContentsDirect

www.elsevier.co.jp/locate/ContentsDirect

NB If you can't access the web - please note that you can still register by sending an E-mail to **cdsubs@elsevier.co.uk**

8Z-MPD/2

AVAILABLE AT YOUR FINGERTIPS...

ELSEVIER SCIENCE CATALOGUE

Features include:

ELSEVIER SCIENCE

Catalogue on INTERNET

- ORDER YOUR **FREE** SAMPLE COPY OF *JOURNAL/ BOOK TITLE* TODAY BY CHECKING ITS CATALOGUE ENTRY

Other features include:-

- All the journals, with complete information about journal editors and editorial boards
- Listings of special issues and volumes
- Listings of recently published papers for many journals
- Complete descriptions and contents lists of book titles
- Clippings of independent reviews of published books
- Book series, dictionaries, reference works
- Electronic and CD-ROM products
- Full text search facilities
- Ordering facilities
- Print options
- Hypertext links
- Alerting facility for new & forthcoming publications
- Updated monthly

TRY IT TODAY!

http://www.elsevier.nl/

For further queries please contact:-

Customer Support Department
Tel: +1 (212) 633 3730
Fax: +1 (212) 633 3680
E-mail: usinfo-f@elsevier.com

Customer Support Department
Tel: +31 (20) 485 3757
Fax: +31 (20) 485 3432
E-mail: nlinfo-f@elsevier.nl

ELSEVIER SCIENCE

Catalogue on INTERNET

CO815/P6

ELSEVIER | PERGAMON | NORTH HOLLAND | EXCERPTA MEDICA

Receive Regular News of Elsevier's Publications

Elsevier Science mails information on new and existing publications regularly. If you would like to be added to the mailing list please send us your name and full mailing address, indicating your fields of interest:

a subject areas

- Chemistry and Chemical Engineering
- Clinical Medicine
- Computer Science
- Earth and Planetary Sciences
- Economics, Business and Management Science
- Engineering, Energy and Technology
- Environmental Science and Technology
- Life Sciences
- Materials Science
- Mathematics
- Physics and Astronomy
- Social Sciences

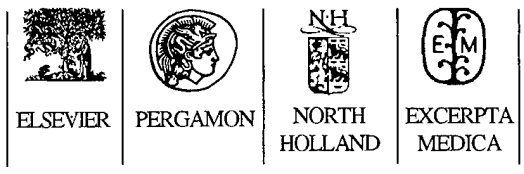

Regional Sales Offices

For customers in Europe, Middle East and Africa
Elsevier Science
Regional Sales Office
Customer Support Department
P.O. Box 211
1000 AE Amsterdam
The Netherlands
Tel: (+31) 20 485 3757
Fax: (+31) 20 485 3432
E-mail: nlinfo-f@elsevier.nl

For customers in the United States & Canada
Elsevier Science
Regional Sales Office
Customer Support Department
P.O. Box 945
New York, N.Y. 10159-0945
U.S.A.
Tel: (+1) 212 633 3730
Toll Free number for North-American customers: 1-888-4ES-INFO (437-4636)
Fax: (+1) 212 633 3680
E-mail: usinfo-f@elsevier.com

For customers in Japan
Elsevier Science
Regional Sales Office
Customer Support Department
9-15 Higashi-Azabu
1-chome
Minato-ku
Tokyo
106-0044 Japan
Tel: (+81) 3 5561 5033
Fax: (+81) 3 5561 5047
E-mail: info@elsevier.co.jp

For customers in Asia and Australasia
Elsevier Science
Regional Sales Office
Customer Support Department
No. 1 Temasek Avenue
#17-01 Millenia Tower
Singapore 039192
Tel: (+65) 434 3727
Fax: (+65) 337 2230
E-mail: asiainfo@elsevier.com.sg

For customers in Latin America
Elsevier Science
Regional Sales Office
Rua Sete de Setembro 111/16
Andar
20050-002 Centro
Rio de Janeiro - RJ
Brazil
Tel: (+55) 21 509 5340
Fax: (+55) 21 507 1991
E-mail: elsevier@campus.com.br

CO815/P5

BACK ISSUES OF THIS JOURNAL

SAVE UP TO 25% BY PURCHASING COMPLETE SETS

Customers wishing to purchase complete sets can do so at a saving of 25% off the individual volume price.

MICROFORM EDITIONS

Back issues in microform of Elsevier Science research journals are also available. For further information please apply to your nearest Elsevier Science office.

BACK ISSUES PRICE LIST

Full details of the rates of back issues of all Elsevier Science journals can be found in our Back Issues Price List. Please contact your nearest Elsevier Science office for a copy.

Back issues of this and all other Elsevier Science journals are available in hard copy. New subscribers to a journal may purchase back issues of that publication in hard copy edition at 25% discount off the standard price. Elsevier Science maintains stocks of back issues and orders may be placed with confidence at your nearest Elsevier Science office. Should any issue of a volume be temporarily out of stock at the time of ordering, a high quality photoduplicated copy will be supplied at no extra charge to complete your order.

Regional Sales Offices

For customers in Europe, Middle East and Africa
Elsevier Science, Regional Sales Office, Customer Support Department, P.O. Box 211, 1000 AE Amsterdam, The Netherlands
Tel: (+31) 20 485 3757, Fax: (+31) 20 485 3432, E-mail: nlinfo-f@elsevier.nl

For customers in the United States & Canada
Elsevier Science, Regional Sales Office, Customer Support Department, P.O. Box 945, New York, N.Y. 10159-0945, U.S.A.
Tel: (+1) 212 633 3730, Toll Free number for North-American customers: 1-888-4ES-INFO (437-4636), Fax: (+1) 212 633 3680
E-mail: usinfo-f@elsevier.com

For customers in Japan
Elsevier Science, Regional Sales Office, Customer Support Department, 9-15 Higashi-Azabu, 1-chome, Minato-ku, Tokyo, 106-0044 Japan
Tel: (+81) 3 5561 5033, Fax: (+81) 3 5561 5047, E-mail: info@elsevier.co.jp

For customers in Asia and Australasia
Elsevier Science, Regional Sales Office, Customer Support Department, No. 1 Temasek Avenue, #17-01 Millenia Tower, Singapore 039192
Tel: (+65) 434 3727, Fax: (+65) 337 2230, E-mail: asiainfo@elsevier.com.sg

For customers in Latin America
Elsevier Science, Regional Sales Office, Rua Sete de Setembro 111/16 Andar, 20050-002 Centro, Rio de Janeiro - RJ, Brazil
Tel: (+55) 21 509 5340, Fax: (+55) 21 507 1991, E-mail: elsevier@campus.com.br

ELSEVIER | PERGAMON | NORTH HOLLAND | EXCERPTA MEDICA

CO815/P4

JOURNAL PACKAGES

Money-saving ways
to buy journals such as...

Atmospheric Environment
Biochemical Pharmacology
Environmental Pollution
Life Sciences
Neuropharmacology
Neuroscience
Tetrahedron Letters
Trends in Pharmacological Sciences

Which libraries benefit?

Those libraries which take all the journals from a package will see an immediate benefit and saving. Libraries which take all but one of the journals may find that they can buy the missing title for a nominal amount.

Take advantage of these packages

Subscription Agents have been informed about these money-saving packages and are in a position to help librarians take advantage of the savings offered. Contact your nearest Regional Sales Office directly for more information and help.

ELSEVIER

PERGAMON

NORTH HOLLAND

EXCERPTA MEDICA

Regional Sales Offices

For customers in Europe, Middle East and Africa
Elsevier Science
Regional Sales Office
Customer Support Department
P.O. Box 211
1000 AE Amsterdam
The Netherlands
Tel: (+31) 20 485 3757
Fax: (+31) 20 485 3432
E-mail: nlinfo-f@elsevier.nl

For customers in the United States & Canada
Elsevier Science
Regional Sales Office
Customer Support Department
P.O. Box 945
New York, N.Y. 10159-0945
U.S.A.
Tel: (+1) 212 633 3730
Toll Free number for
North-American customers:
1-888-4ES-INFO (437-4636)
Fax: (+1) 212 633 3680
E-mail: usinfo-f@elsevier.com

For customers in Japan
Elsevier Science
Regional Sales Office
Customer Support Department
9-15 Higashi-Azabu
1-chome
Minato-ku
Tokyo
106-0044 Japan
Tel: (+81) 3 5561 5033
Fax: (+81) 3 5561 5047
E-mail: info@elsevier.co.jp

For customers in Asia and Australasia
Elsevier Science
Regional Sales Office
Customer Support Department
No. 1 Temasek Avenue
#17-01 Millenia Tower
Singapore 039192
Tel: (+65) 434 3727
Fax: (+65) 337 2230
E-mail: asiainfo@elsevier.com.sg

For customers in Latin America
Elsevier Science
Regional Sales Office
Rua Sete de Setembro 111/16
Andar
20050-002 Centro
Rio de Janeiro - RJ
Brazil
Tel: (+55) 21 509 5340
Fax: (+55) 21 507 1991
E-mail: elsevier@campus.com.br

CO815/P1

A Guide to Submitting Manuscripts on Disk

Elsevier Science is now publishing all manuscripts using electronic production methods, and therefore needs to receive the electronic files of your article with the hardcopy of the accepted version. Below are some general points to enable us to use your files.

Always supply good quality originals of your artwork with the hardcopy of the manuscript, as we cannot guarantee the usability of electronic graphic files. Electronic files of **accepted** manuscrpts can be submitted on floppy disk, CD or over the FTP (see http://ftp.elsevier.co.uk for further information).

To help us:
1. Name your files using the correct software extension, e.g. Fig1.cdr, tb1-6.xls, text.doc, fig1a.eps, fig1.tif, etc.
2. Save text on a separate disk from the graphics.
3. Please label all disks with your name, journal to be published in, software (e.g. Word 7, Adobe Illustrator 6.0), compression software if used, hardware used (e.g. Mac, PC) and file names.
4. It is essential that the electronic and hardcopy versions are **identical**. The hardcopy will be used as the definitive version of the article.

Text

We can accept most word-processing formats, (ideally Microsoft Word or WordPerfect). Please check the style of the individual journal to which the manuscript is to be submitted, particularly the reference style, so that fewer changes have to be made, thus reducing the possibility of errors being introduced. Most formatting codes will be removed or replaced on processing your article so there is no need for you to use excessive layout styling. In addition, do not use options such as automatic word breaking, justified layout, double columns or automatic paragraph numbering (especially for numbered references). However do use bold face, italic, subscripts, superscripts etc.

When preparing tables, if you are using a table grid, please use only one grid for each separate table and not a grid for each row. If no grid is being used, use tabs to align columns not spaces.

Please follow this order when you create your manuscript: Title, Authors, Affiliations, Abstract, Keywords, Main text, Acknowledgements, Appendix, References, Vitae, Figure legends and then Tables. **Do not import the Figures into the text file.**

Graphics

Computer-generated illustrations and halftones or line/tones (either colour or black and white) are acceptable. (Note: most journals charge for colour printing, so check if it is really necessary and refer to individual journal instructions.) Since we cannot guarantee the usability of graphic files, original hardcopies of all illustrations must accompany the accepted printout of the manuscript in all cases.

The following points should be taken into consideration when preparing electronic graphic files:
TIFF or EPS files are preferred. Suggested packages for line graphics are Adobe Illustrator (version 3.0 or above), Freehand and Corel Draw. Graphics made in WordPerfect or Word generally have too low a resolution. Files of scanned line graphics can be accepted preferably at a resolution of 1000 dpi, for scanned halftones (300 dpi) and scanned line/tones (500 dpi).

Colour should be scanned in at 300 dpi, (500 dpi for colour line/tones). With CMYK electronic files include a 4-colour machine or cromalin proof and check that all the separations (if provided) are colour coded.

Try to create your graphics near to the size they will be finally printed at by looking at previously published manuscripts. This will help with the lettering and resolution of your files, as the resolution will be lost if we have to enlarge a file and lettering may need re-keying if the file has to be reduced significantly. The final font size should be about 6-8 pt. Always use the standard Adobe set of fonts.

If you require any further information about electronic submission, please contact:
Author Services, Log-in Department
Elsevier Science
The Boulevard, Langford Lane
Kidlington, Oxford OX5 1GB, UK
E-mail: authors@elsevier.co.uk
Fax: +44 (0) 1865 843905
Tel: +44 (0) 1865 843900

Please note that if any file proves to be unusable we reserve the right to publish your article from the hardcopy supplied.

Composite Structures — Instructions to Authors

Submission of Papers

Authors are requested to submit their original manuscript and figures with three copies to the Editor: Prof. I. H. Marshall, 36 Gogoside Road, Largs, Ayrshire, Scotland KA30 9LX, UK or to any member of the Editorial Board.

All papers should be written in English and will be independently refereed.

Submission of a paper implies that it has not been published previously, that it is not under consideration for publication elsewhere, and that if accepted it will not be published elsewhere in the same form, in English or in any other language, without the written consent of the publisher. All papers should be written in English. All papers will be independently refereed.

Types of Contributions

Research papers; review articles; case studies; technical notes; book reviews; reports of conferences and meetings; letters to the Editor.

Manuscript Preparation

General: Manuscripts must be typewritten, double-spaced with wide margins on one side of white paper. Good quality printouts with a font size of 12 or 10 pt are required. The corresponding author should be identified (include a Fax number and E-mail address). Full postal addresses must be given for all co-authors. Authors should consult a recent issue of the journal for style if possible. An electronic copy of the paper should accompany the final version. The Editors reserve the right to adjust style to certain standards of uniformity. Authors should retain a copy of their manuscript since we cannot accept responsibility for damage or loss of papers. Original manuscripts are discarded one month after publication unless the Publisher is asked to return original material after use.

Paper Length: Generally, the size of the manuscript should not exceed 6000 words or about 12 printed pages.

Abstracts: The Abstract should be of about 100–150 words, reporting concisely on the purpose and results of the paper.

Text: Follow this order when typing manuscripts: Title, Authors, Affiliations, Abstract, Keywords, Main text, Acknowledgements, Appendix, References, Vitae, Figure Captions and then Tables. Do not import the Figures or Tables into your text. The corresponding author should be identified with an asterisk and footnote. All other footnotes (except for table footnotes) should be identified with superscript Arabic numbers.

Symbols: The SI system should be used for all scientific and laboratory data; if, in certain instances, it is necessary to quote other units, these should be added in parentheses. Temperatures should be given in degrees Celsius. The unit billion' (10^9 in America, 10^{12} in Europe) is ambiguous and should not be used.

References: All publications cited in the text should be presented in a list of references following the text of the manuscript. In the text refer to references by a number in square brackets on the line (e.g. Since Sonti[1]), and the full reference should be given in a numerical list at the end of the paper.
References should be given in the following form:
1. Sonti SS, Davalos JF, Zipfel MG, Gang Rao HVS. A review of wood cross tie performance. Forest Products Journal 1995;45(9):55–58.
2. Hetenyi M. Beams on elastic foundation. Ann Arbor, MI: University of Michigan Press, 1946.
3. Adali S. Lay-up optimization of laminated plates under buckling loads. In: Turvey GJ, Marshall IH, editors. Buckling and postbuckling of composite plates. London: Chapman and Hall, 1995. p. 329–365.
4. Adali S, Verijenko VE, Galileev SM, Matrosov AV. Method of initial function in three-dimensional analysis of laminated composite structures. In: Composites Modelling and Processing Science, Proceedings of the 9th International Conference on Composite Materials (ICCM/9), Madrid, 12–16 July 1993. p. 23–30.

Illustrations: All illustrations should be provided in camera-ready form, suitable for reproduction (which may include reduction) without retouching. Photographs, charts and diagrams are all to be referred to as 'Figure(s)' and should be numbered consecutively in the order to which they are referred. They should accompany the manuscript, but should not be included within the text. All illustrations should be clearly marked on the back with the figure number and the author's name. All figures are to have a caption. Captions should be supplied on a separate sheet.
Line drawings: Good quality printouts on white paper produced in black ink are required. All lettering, graph lines and points on graphs should be sufficiently large and bold to permit reproduction when the diagram has been reduced to a size suitable for inclusion in the journal. Dye-line prints or photocopies are not suitable for reproduction. Do not use any type of shading on computer-generated illustrations.
Photographs: Original photographs must be supplied as they are to be reproduced (e.g. black and white or colour). If necessary, a scale should be marked on the photograph. Please note that photocopies of photographs are not acceptable.
Colour: Where colour figures are required, the author will be charged accordingly. Further details of cost are available from Author Services, at Elsevier Science.

Tables: Tables should be numbered consecutively and given a suitable caption and each table typed on a separate sheet. Footnotes to tables should be typed below the table and should be referred to by superscript lowercase letters. No vertical rules should be used. Tables should not duplicate results presented elsewhere in the manuscript, (e.g. in graphs).

Electronic Submission

Authors should submit an electronic copy of their paper with the final version of the manuscript. The electronic copy should match the hardcopy exactly. Always keep a backup copy of the electronic file for reference and safety. Full details of electronic submission and formats can be obtained from Author Services at Elsevier Science.

Proofs

Proofs will be sent to the author (first named author if no corresponding author is identified of multi-authored papers) and should be returned within 48 hours of receipt. Corrections should be restricted to typesetting errors; any others may be charged to the author. Any queries should be answered in full. Please note that authors are urged to check their proofs carefully before return, since the inclusion of late corrections cannot be guaranteed. Proofs are to be returned to the Log-in Department, Elsevier Science, The Boulevard, Langford Lane, Kidlington, Oxford OX5 1GB, UK.

Offprints

Fifty offprints will be supplied free of charge. Additional offprints and copies of the issue can be ordered at a specially reduced rate using the order form sent to the corresponding author after the manuscript has been accepted. Orders for reprints will incur a 50% surcharge. Authors who pay for colour illustrations will receive an additional 100 offprints free of charge.

Copyright

All authors must sign the 'Transfer of Copyright' agreement before the article can be published. This transfer agreement enables Elsevier Science Ltd to protect the copyrighted material for the authors, but does not relinquish the author's proprietary rights. The copyright transfer covers the exclusive rights to reproduce and distribute the article, including reprints, photographic reproductions, microfilm or any other reproductions of similar nature and translations. Includes the right to adapt the article for use in conjunction with computer systems and programs, including reproduction or publication in machine-readable form and incorporation in retrieval systems. Authors are responsible for obtaining from the copyright holder permission to reproduce any figures for which copyright exists.

Author Services

For queries relating to the general submission of manuscripts (including electronic text and artwork) and the status of accepted manuscripts, please contact Author Services, Log-in Department, Elsevier Science, The Boulevard, Langford Lane, Kidlington, Oxford OX5 1GB, UK. E-mail: authors@elsevier.co.uk, Fax: +44 (0) 1865 843905, Tel: +44 (0) 1865 843900.

COMPOSITE STRUCTURES

0263-8223(199912)47:1-4;1-D

(Abstracted/indexed in: *Applied Mechanics Reviews; Current Contents/Engineering, Computing and Technology; Engineering Index; Materials Information; Materials Science Citation Index; Metals Abstracts; Polymer Contents; Science Citation Index*)

The Elsevier Science Catalogue can be accessed in *http://www.elsevier.nl* or *gopher.elsevier.nl*

CONTENTS

Volume 47 Numbers 1–4 1999

Special Issue: Tenth International Conference on Composite Structures

Guest Editors: I. H. Marshall & R. Jones

For contents see p. iii

CONTENTS direct

This journal is part of **ContentsDirect**, the ***free*** alerting service which sends tables of contents by e-mail for Elsevier Science books and journals. You can register for **ContentsDirect** online at: **www.elsevier.nl/locate/contentsdirect**

ELSEVIER

02017